NASA/CP—2002-211212/VOL1

Sixth Microgravity Fluid Physics and Transport Phenomena Conference

Plenary and Sessions 1–6

November 2002

The NASA STI Program Office . . . in Profile

Since its founding, NASA has been dedicated to the advancement of aeronautics and space science. The NASA Scientific and Technical Information (STI) Program Office plays a key part in helping NASA maintain this important role.

The NASA STI Program Office is operated by Langley Research Center, the Lead Center for NASA's scientific and technical information. The NASA STI Program Office provides access to the NASA STI Database, the largest collection of aeronautical and space science STI in the world. The Program Office is also NASA's institutional mechanism for disseminating the results of its research and development activities. These results are published by NASA in the NASA STI Report Series, which includes the following report types:

- TECHNICAL PUBLICATION. Reports of completed research or a major significant phase of research that present the results of NASA programs and include extensive data or theoretical analysis. Includes compilations of significant scientific and technical data and information deemed to be of continuing reference value. NASA's counterpart of peer-reviewed formal professional papers but has less stringent limitations on manuscript length and extent of graphic presentations.

- TECHNICAL MEMORANDUM. Scientific and technical findings that are preliminary or of specialized interest, e.g., quick release reports, working papers, and bibliographies that contain minimal annotation. Does not contain extensive analysis.

- CONTRACTOR REPORT. Scientific and technical findings by NASA-sponsored contractors and grantees.

- CONFERENCE PUBLICATION. Collected papers from scientific and technical conferences, symposia, seminars, or other meetings sponsored or cosponsored by NASA.

- SPECIAL PUBLICATION. Scientific, technical, or historical information from NASA programs, projects, and missions, often concerned with subjects having substantial public interest.

- TECHNICAL TRANSLATION. English-language translations of foreign scientific and technical material pertinent to NASA's mission.

Specialized services that complement the STI Program Office's diverse offerings include creating custom thesauri, building customized databases, organizing and publishing research results . . . even providing videos.

For more information about the NASA STI Program Office, see the following:

- Access the NASA STI Program Home Page at *http://www.sti.nasa.gov*

- E-mail your question via the Internet to help@sti.nasa.gov

- Fax your question to the NASA Access Help Desk at 301–621–0134

- Telephone the NASA Access Help Desk at 301–621–0390

- Write to:
  NASA Access Help Desk
  NASA Center for AeroSpace Information
  7121 Standard Drive
  Hanover, MD 21076

NASA/CP—2002-211212/VOL1

Sixth Microgravity Fluid Physics and Transport Phenomena Conference

Plenary and Sessions 1–6

Abstracts and presentations of a conference cosponsored by
the NASA Office of Life and Microgravity Sciences and Applications and
the Fluid Physics and Transport Phenomena Discipline Working Group
and hosted by NASA Glenn Research Center and
the National Center for Microgravity Research on Fluids and Combustion
Cleveland, Ohio, August 14–16, 2002

National Aeronautics and
Space Administration

Glenn Research Center

November 2002

Contents were reproduced from author-provided presentation materials.

Contents were reproduced from the best available copy as provided by the authors.

Trade names or manufacturers' names are used in this report for identification only. This usage does not constitute an official endorsement, either expressed or implied, by the National Aeronautics and Space Administration.

Available from

NASA Center for Aerospace Information
7121 Standard Drive
Hanover, MD 21076

Available electronically at http://gltrs.grc.nasa.gov

PREFACE

The Sixth Microgravity Fluid Physics and Transport Phenomena Conference provides us with the opportunity to view the current scope of the Microgravity Fluid Physics and Transport Phenomena Program and conjecture about its future. The Microgravity Program has become part of the newly established Office of Biological and Physical Research (OBPR), NASA's fifth Enterprise.

Meanwhile, we commenced the long-awaited and exciting era of conducting Microgravity Fluid Physics experiments on the International Space Station (ISS). We successfully completed the Physics of Colloids in Space (PCS) experiment on ISS and launched the Investigating Structure of Paramagnetic Aggregates of Colloidal Emulsions (InSPACE) experiment that will be conducted later this year.

The excitement of utilizing ISS was tempered, however, by its cost problems that negatively impacted the research budget available for developing flight experiment facilities and hardware. As a result, the Microgravity Fluid Physics discipline took a significant budget reduction that caused deferral/discontinuation of a number of flight investigations that had successfully completed their peer-reviews and received their endorsement. The budget supporting the principal investigators was also negatively impacted, though to a smaller extent. On the positive side, the Fluids Integrated Rack (FIR) that supports much of fluid physics experiments survived these budget reductions. Also the subsequent support of the research community through letters to Congress and to NASA clearly showed how the research community values the Microgravity Fluid Physics and Transport Phenomena Program.

In March, NASA Administrator Sean O'Keefe created the Research Maximization And Prioritization (REMAP) Task Force to perform an independent review and assessment of research priorities for the entire scientific, technological, and commercial portfolio of the Agency's Office of Biological and Physical Research (OBPR) and to provide recommendations on how the office can achieve its research goals. The panel report was released on July 10, 2002. The recommendations of this panel placed almost all of the research content of the Microgravity Fluid Physics Program in Priority 1 or 2 putting the program in an advantageous position as NASA begins to implement the recommendations of the panel.

The program currently has a total of 106 ground-based and 16 candidate flight principal investigators. A look at the collection of abstracts in this document clearly shows both the high quality and the breadth of the ongoing research program. One can easily notice many established world-class scientists as well as investigators who are early in their career poised to achieve that stature. We hope that many of the participants in this conference will perceive microgravity fluid physics as an exciting and rewarding area of research and choose to participate in the NASA Research Announcement released in December 2001. Proposals submitted to the fluid physics research area are due December 2, 2002. More information can be found at the following Web site:
http://research.hq.nasa.gov/code_u/nra/current/NRA-01-OBPR-08/index.html

The content of the Microgravity Fluid Physics and Transport Phenomena Program is well aligned with OBPR's mission of "conducting basic and applied research to support human exploration of space and to take advantage of the space environment as a laboratory for scientific, technological, and commercial research." The fluid physics discipline has a major role in the Physical Sciences Division's goal of developing a rigorous, cross-disciplinary scientific capability, bridging physical sciences and biology to address NASA's human and robotic space exploration goals.

We have implemented a number of changes in the format of this conference based on the inputs received from the participants. We have expanded plenary sessions to include all presentations, eliminated parallel sessions and expanded the exposition session with poster presentations. We hope that this will allow the participants to get a better picture of the overall program through the plenary presentations and promote focused discussion/dialogue through poster presentations. The Discipline Working Group has provided the much-needed guidance in planning the content and the format of this conference. As in the past, we elected to go with a virtual proceedings of the presentation charts that will be available on the World Wide Web at http://www.ncmr.org/events/fluids2002.html. In this regard we acknowledge the support of our principal investigators who have provided us timely inputs of their charts and abstracts and accommodated our format requirements. This cooperation was critical in implementing this and is very much appreciated.

This conference has been organized and hosted by the National Center for Microgravity Research on Fluids and Combustion under the leadership of its Director, Professor Simon Ostrach. I would like to acknowledge the extensive efforts of Ms. Christine Gorecki and other members of the Center in planning, organizing, and hosting the conference and in preparing the proceedings and conference materials. Sincere appreciation is offered to the authors for providing the abstracts and presentation charts in a timely manner and to the members of the Microgravity Fluids Physics Branch of the NASA Glenn Research Center for their many contributions.

Finally, I would like to express my gratitude to all of the conference participants for their contributions to the success of this conference.

Dr. Bhim S. Singh
Fluid Physics Discipline Lead Scientist
NASA Glenn Research Center
21000 Brookpark Road
Cleveland, Ohio 44135
Phone: 216–433–5396
Fax: 216–433–8660
E-mail: bhim.s.singh@grc.nasa.gov

ACKNOWLEDGMENTS

This conference was made possible by the efforts of many people. We acknowledge the contributions of the following individuals:

Fluid Physics and Transport Phenomena Discipline Working Group
- G. Paul Neitzel (chair), Georgia Institute of Technology
- Bhim Singh (vice-chair), NASA Glenn Research Center
- J. Iwan D. Alexander, Case Western Reserve University/National Center for Microgravity Research
- Bradley Carpenter, NASA Headquarters
- Francis Chiaramonte, NASA Headquarters
- Stephen Davis, Northwestern University
- Donald Gaver, Tulane University
- Joel Koplik, City College of the City University of New York
- G.P. Peterson, Rensselaer Polytechnic Institute
- Matthew Tirrell, University of California Santa Barbara
- David Weitz, Harvard University

Session Chairs
Plenary Sessions
- J. Iwan D. Alexander, NCMR/Case Western Reserve University
- Noel Clark, University of Colorado
- Amir Faghri, University of Connecticut
- Donald Gaver, Tulane University
- R. Glynn Holt, Boston University
- Gareth McKinley, Massachusetts Institute of Technology
- Simon Ostrach, NCMR/Case Western Reserve University
- Ramkumar Parthasarathy, The University of Oklahoma
- Jack Salzman, Chief, Microgravity Science Division, NASA Glenn Research Center
- Eric Shaqfeh, Stanford University
- Mary Silber, Northwestern University
- Paul Steen, Cornell University
- Theo Theofanous, University of California, Santa Barbara
- Eric Weeks, Emory University
- David Weitz, Harvard University

National Center for Microgravity Research on Fluids and Combustion
- Simon Ostrach, Director
- Thomas Labus, Deputy Director
- J. Iwan D. Alexander, Fluids Senior Scientist
- Christine Gorecki, Conference Coordinator

Conference Team
- J. Iwan D. Alexander
- Christine Gorecki
- Sandra Jones
- Beatrix Norton
- Cindy Rosenberger
- Norman Weinberg
- William Yanis

The Logistics and Technical Information Division and its support service contractors, particularly Kristen Easton, Caroline Rist, Lori Feher, Amy Fennell, Diane Furiga, Chris Sanyk, and Gayle DiBiasio.

TABLE OF CONTENTS

Opening Plenary

Microgravity Fluid Physics and Engineering: Fundamental and Applied Research
E. Trinh, NASA Headquarters 1

NASA Research Announcement
Francis Chiaramonte and Brad Carpenter, NASA Headquarters 12

Biofluids of Living in Space: Gas Mixing in the Periphery of the Lung
G. Kim Prisk, University of California, San Diego 24

Session 1: Colloids and Soft Condensed Matter 90

Recent Results From the Physics of Colloids in Space
David A. Weitz, A Bailey, R. Christianson, S. Manley, V. Prasad, P. Segre, U. Gasser, and L. Cipelletti, Harvard University; A. Schoefield and P. Pusey, University of Edinburgh; M. Doherty and A. Jankovsky, NASA Glenn Research Center; and T. Lorik, W. Shiley, J. Bowen, C. Kurta, and J. Eggers, ZIN Technologies, Inc 91

Physics of Hard Sphere Experiment: Scattering, Rheology and Microscopy Study of Colloidal Particles
Z-D. Cheng, J. Zhu, S-E. Phan, W.B. Russel, and P.M. Chaikin, Princeton University; and W.V. Meyer, National Center for Microgravity Research 133

Two-Dimensional Streptavidin Crystals on Giant Lipid Bilayer Vesicles
Pasut Ratanabanangkoon, Stanford University; Michael Gropper and Rudolf Merkel, Technical University of Munich; and Alice P. Gast, Massachusetts Institute of Technology 161

Optically-Excited Waves in 3D Dusty Plasmas
John Goree, University of Iowa 163

Electrically Guided Assembly of Colloidal Particles
W.D. Ristenpart, I.A. Aksay, and D.A. Saville, Princeton University 192

Self-Assembly of Colloidal Particles on Template Structures
Arjun G. Yodh, University of Pennsylvania 194

Molecular Dynamics Simulations of Crystallization of Hard Spheres
Igor Volkov, Pennsylvania State University; Marek Cieplak, Polish Academy of Sciences and Pennsylvania State University; Joel Koplik, City University of New York City College; and Jayanth R. Banavar, Pennsylvania State University 211

Session 2: Fluid Physics of Interfaces 222

Dynamics and Instability of Triple Junctions of Solidifying Eutectics: Flow-Modified Morphologies
S. Davis, Northwestern University 223

Electrohydrodynamically Driven Chaotic Advection in Drops
Thomas Ward and G.M. Homsy, University of California, Santa Barbara 240

The Effects of Ultrathin Films on Dynamic Wetting
Xia Chen and Stephen Garoff, Carnegie Mellon University; and Enrique Ramé, National Center for Microgravity Research 242

Passive and Active Stabilization of Liquid Bridges in Low Gravity
David B. Thiessen, Wei Wei, and Philip L. Marston, Washington State University 253

Molten-Metal Droplet Deposition on a Moving Substrate in Microgravity: Aiding the Development of Novel Technologies for Microelectronic Assembly
C.M. Megaridis and I.S. Bayer, University of Illinois at Chicago; D. Poulikakos, Swiss Federal Institute of Technology; and V. Nayagam, National Center for Microgravity Research 272

Non-Coalescence in Microgravity: Science and Technology
G. Paul Neitzel, Georgia Institute of Technology 293

Shadowgraph Study of Gradient Driven Fluctuations
Gennady Nikolaenko and David S. Cannell, University of California, Santa Barbara 325

Session 3: Complex Fluids 345

Particle Segregation in a Flowing Suspension Subject to High-Gradient Strong Electric Fields
Andreas Acrivos and Zhiyong Qiu, City University of New York City College; Boris Khusid and Nikolai Markarian, New Jersey Institute of Technology 346

Sheet Flows, Avalanches, and Dune Migration on Earth and Mars
James Jenkins, Cornell University 370

Gravitational Instability in Suspension Flows
Ileana C. Carpen and John F. Brady, California Institute of Technology 386

Dynamics of Charged Dust Near Surfaces in Space
Joshua E. Colwell, Mihály Horányi, Scott Robertson, and Amanda A. Sickafoose, University of Colorado, Boulder 395

Microgravity-Driven Instabilities in Gas-Fluidized Beds
Anthony J.C. Ladd, University of Florida; and David A. Weitz, Harvard University 417

Studies of Gas-Particle Interactions in a Microgravity Flow Cell
Michel Y. Louge, James T. Jenkins, Haitao Xu, and Anthony Reeves, Cornell University 435

Dynamics of Sheared Granular Materials
Lou Kondic, New Jersey Institute of Technology; and Brian Utter and Robert P. Behringer, Duke University 453

Session 4: Multiphase Flow and Phase Change 476

Fluid Dynamics of Bubbly Liquids
Y.H. Tsang and D.L. Koch, Cornell University; and A. Sangani, Syracuse University 477

Measurements of Turbulence Attenuation by a Dilute Dispersion of Solid Particles in Homogeneous Isotropic Turbulence
John K. Eaton and Wontae Hwang, Stanford University 515

A Mechanistic Study of Nucleate Boiling Under Microgravity Conditions
V.K. Dhir and G.R. Warrier, University of California, Los Angeles 529

Investigation of Body Force Effects on Flow Boiling Critical Heat Flux
Issam Mudawar and Hui Zhang, Purdue University; and Mohammad M. Hasan, NASA Glenn Research Center 553

Length Scale and Gravity Effects on Boiling Heat Transfer
Jungho Kim and Christopher Henry, University of Maryland.....579

Constrained Vapor Bubble Experiment
Peter C. Wayner, Jr., Joel L. Plawsky, Ling Zheng, and Ying-Xi Wang, Rensselaer Polytechnic Institute....606

Separation of Carbon Monoxide and Carbon Dioxide for Mars ISRU
M. Douglas LeVan and Krista S. Walton, Vanderbilt University; John E. Finn, NASA Ames Research Center; and K.R. Sridhar, University of Arizona.....620

Session 5: Biological Fluid Physics (Biological Fluid Mechanics and Biological Self Assembly).....636

Assembly of Colloidal Materials Using Bioadhesive Interactions
Daniel A. Hammer, Amy L. Hiddessen, Valeria Tohver, and John C. Crocker, University of Pennsylvania; and David A. Weitz, Harvard University.....637

Microgravity Effects on Transvascular Transport and Vascular Control
M. Kim, M. Civelek, K. Ainslie, J. Garanich, N.R. Harris, and J.M. Tarbell, Pennsylvania State University.....658

Capillary Instabilities in the Microgravity Environment
David Halpern, University of Alabama; and James B. Grotberg, University of Michigan.....680

The Importance of Interfacial Stresses During Pulmonary Airway Reopening in Microgravity
D.P. Gaver, A.M. Bilek, and K.C. Dee, Tulane University.....714

Protein Virial Coefficients From Size Exclusion Chromatography
Seth Fraden, Joshua Bloustine, and Viatcheslav Berejnov, Brandeis University.....745

Micro-Fluid Dynamics in an Evaporating Sessile Droplet: Application to DNA Optical Gene Mapping
Hua Hu, Lei Li, and Ronald Larson, University of Michigan.....769

Non-Invasive Health Diagnostics Using Eye as a "Window to the Body"
Rafat R. Ansari, NASA Glenn Research Center.....800

Session 6: Dynamics and Instabilities.....831

Containerless Ripple Turbulence
Seth Putterman and William Wright, University of California, Los Angeles; and Walter Duval and Charles Panzarella, NASA Glenn Research Center.....832

Phase Separation, Density Fluctuations, and Boiling Near the Liquid-Gas Critical Point
John Hegseth, Ana Oprisan, and Arun Roy, University of New Orleans; and Vadim S. Nikolayev, Carole Lecoutre, D. Beysens, and Y. Garrabos, Université de Bordeaux.....855

Stratified Taylor-Couette Flow With Radial Gravity
John Hart and Dan Ohlsen, University of Colorado, Boulder; Randall P. Tagg, University of Colorado, Denver; and Patrick D. Weidman, University of Colorado, Boulder.....896

An Experimental Investigation of Incompressible Richtmyer-Meshkov Instability
J.W. Jacobs, University of Arizona; and C.E. Niederhaus, NASA Glenn Research Center.....919

The Use of Pulsatile Flow to Separate Species
R. Narayanan, University of Florida; and Aaron M. Thomas, University of Idaho.....938

Particle Proximity Sensors: A Novel Technique for Visualizing Particle Deposition in Suspension Flows
M. Yoda, B.C. Bailey, and U.C. Andresen, Georgia Institute of Technology 964

Effects of Gravity Modulation on the Convective Instabilities of a Horizontal Double-Diffusive Layer
Wen-Yau Chen, Cho Lik Chan, and C.F. Chen, University of Arizona 982

Author Index 1005

August 14, 2000
Opening Plenary Speaker

Physical Sciences Research Priorities and Plans in OBPR

Dr. Eugene Trinh
NASA Headquarters
Director for Microgravity Research Division

Sixth Microgravity Fluid Physics and Transport Phenomena Conference

Microgravity Fluid Physics and Engineering: Fundamental and Applied Research

OBPR

Physical Sciences Research Division

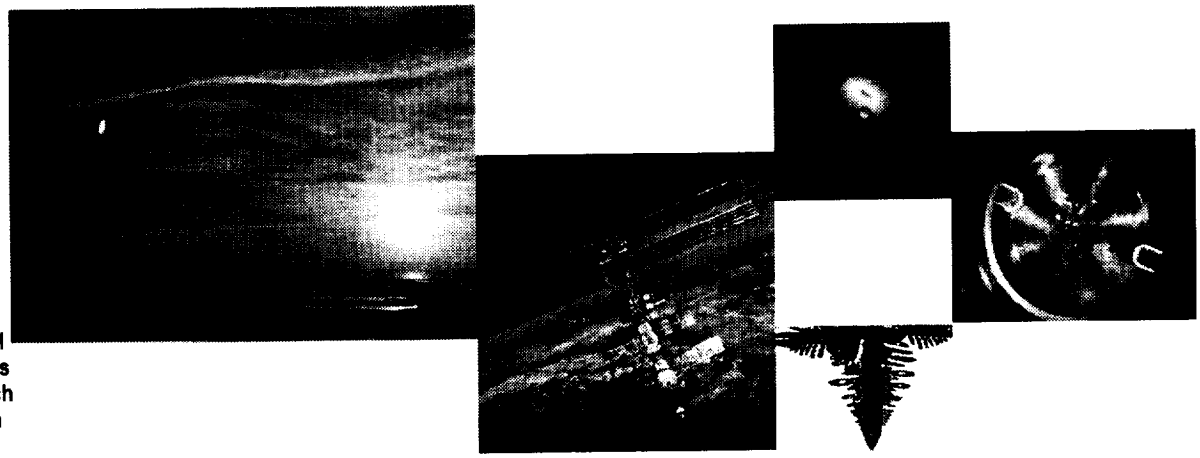

E. Trinh
Physical Sciences Research Division
OBPR / NASA

Beneficial Characteristics of the Space Environment

OBPR

Physical Sciences Research Division

- Long-term and significantly reduced gravitational acceleration (i.e. Extended Microgravity)
- Clear window to outer space
- Ultra-high vacuum
- Quiescent noise-free environment
- Human presence and creative interaction on some platforms
- Next frontier and NASA's domain to explore

Opportunity for unique and exciting research:

- *Directly participate in developing the enabling technologies for space exploration*
- *Exploit the unique experimental environment of space to unravel outstanding fundamental scientific mysteries*

Windows of Opportunity for Research Derived from Microgravity

10^{-2} to 10^{-6} g

OBPR

Physical Sciences Research Division

Convection-free Hydrostatic Pressure-free

- Quantum fluid properties
- ***Classical fluids & transport processes***
- ***Fluid-phase thermophysical properties***
- Diffusion-controlled processes
- ***Surface/Interfacial phenomena***
- Thermally-driven chemical reactions
- Materials synthesis & processing
- ***Morphological stability/pattern formation***
- ***Bio-fluids statics and dynamics***
- ***Multi-phase systems engineering***
- Physiological systems analysis
- Large scale systems modeling
- Gas-grain systems dynamics

Sedimentation-free

- Bose-Einstein condensates
- Critical phenomena/Phase transitions
- Supercritical fluids properties
- ***Multi-phase fluids physics***
- ***Colloid dynamics***
- ***Self-assembly/Meso-scale structures***
- Multi-component materials processing
- Cellular assembling mechanisms
- Bio-organisms interaction
- 3-D Tissue engineering
- ***Container-free experimentation***
- ***Spray and dust clouds dynamics***

NASA/CP—2002-211212/VOL1

Physical Sciences Research Program

Slide presented at the:
Fifth Microgravity Fluid Physics and Transport Phenomena Conference
Cleveland, Ohio, August 9-11, 2000

OBPR

Physical Sciences Research Division

Fluid Physics Program Dual Thrust:

- Peer-reviewed research based on scientific value and exploiting the advantages of the microgravity environment
- Peer-reviewed research based on engineering applications and relevant to human and robotic space exploration endeavor

The second component will be strengthened with a rigorous research program coordinated with other NASA enterprises

We really mean it now!

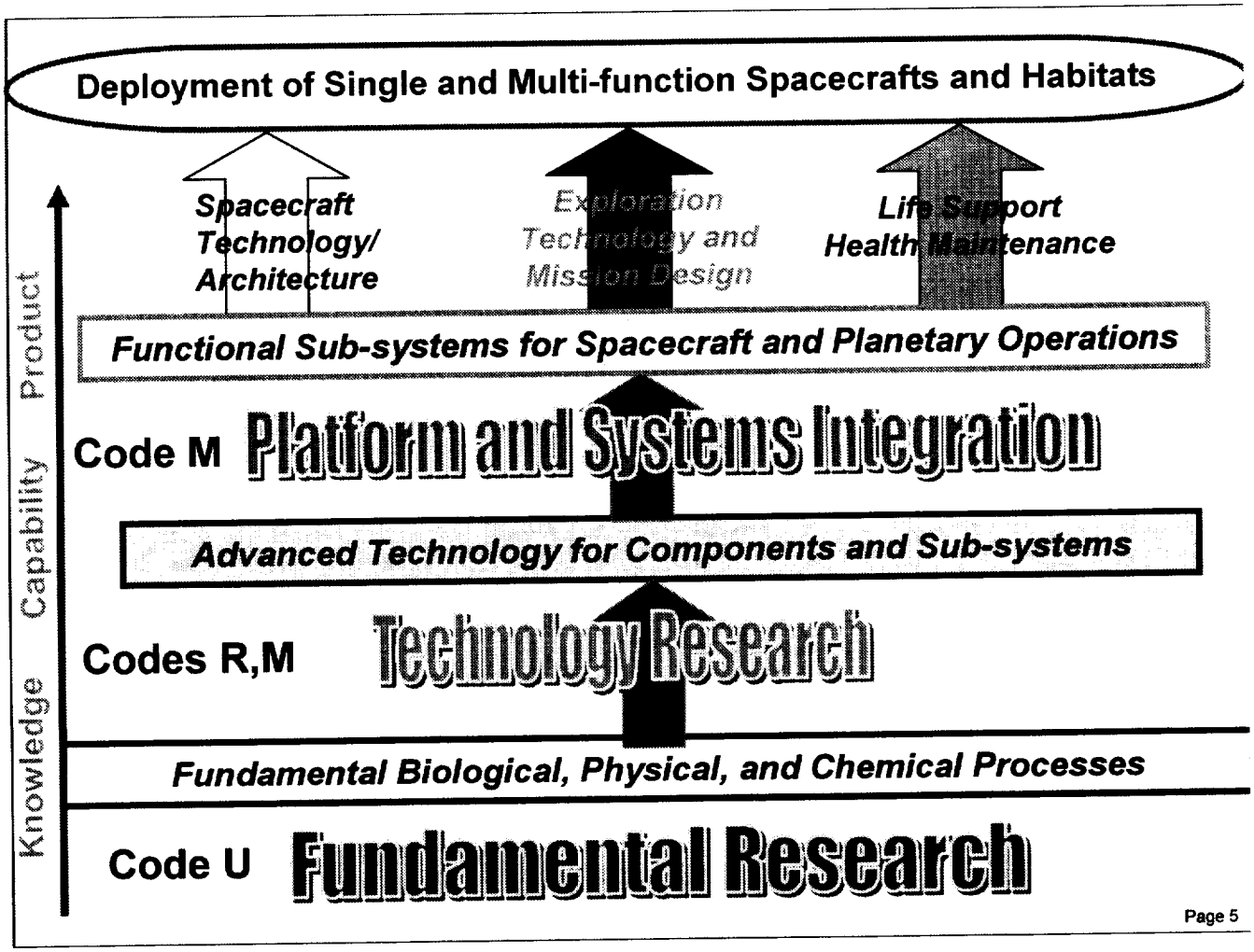
Deployment of Single and Multi-function Spacecrafts and Habitats
Spacecraft Technology/ Architecture
Exploration Technology and Mission Design
Life Support Health Maintenance
Functional Sub-systems for Spacecraft and Planetary Operations
Code M
Platform and Systems Integration
Advanced Technology for Components and Sub-systems
Codes R,M
Technology Research
Fundamental Biological, Physical, and Chemical Processes
Code U
Fundamental Research
Knowledge
Capability
Product
Page 5

Fundamental Research: Space-based Results and Ground-based Applications

- Surface-tension controlled drop equilibrium shapes and dynamics: Use of the unique microgravity environment to obtain benchmark data.
- The development and implementation of microgravity investigations has allowed ground-based applications to gather complementary information on the effects of external forces and initial shape deformation on gyrostatic equilibrium shape and nonlinear oscillation characteristics.

OBPR

Physical Sciences Research Division

- Theory validated for first stability limit
- No higher order bifurcation detected
- Effects of initial drop distortion measured
- Exact bifurcation velocity measured

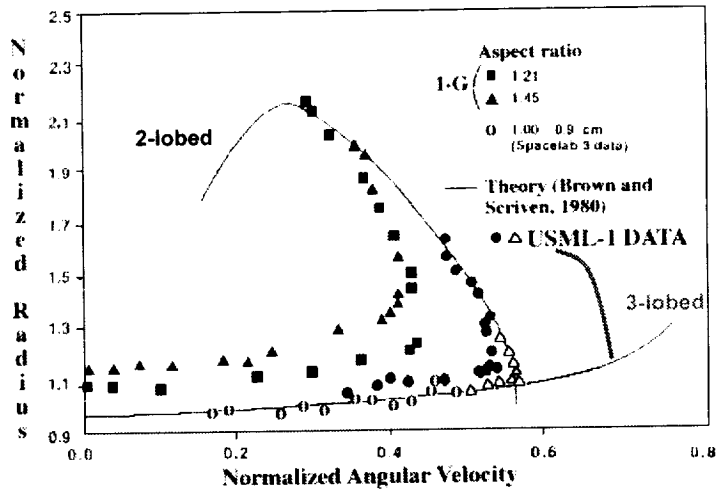

[Wang et al., J. Fluid Mech. 308,1 (1996)]

Fundamental Research: Space-based Results and Ground-based Applications

OBPR

Physical Sciences Research Division

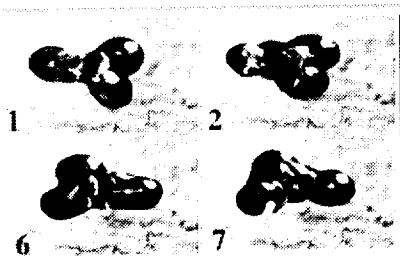

Ground-based 3-lobed Bifurcation

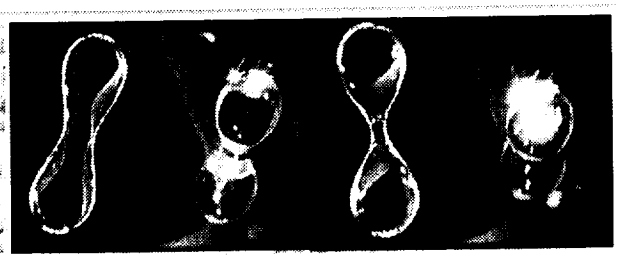

Space-based 2-lobed Bifurcation

"Three-lobed shape bifurcation of rotating liquid drops", K. Ohsaka and E.H. Trinh. Phys. Rev. Lett. 84, 1700 (2000)

Ground-based 2-lobed and toroidal shapes obtained with coated rolling drops

("Liquid Marbles", P. Aussillous and D. Quere, Nature 411,924 (2001))

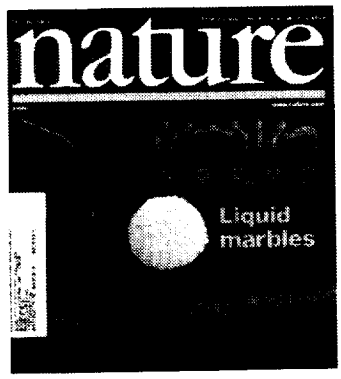

Nonlinear Oscillations

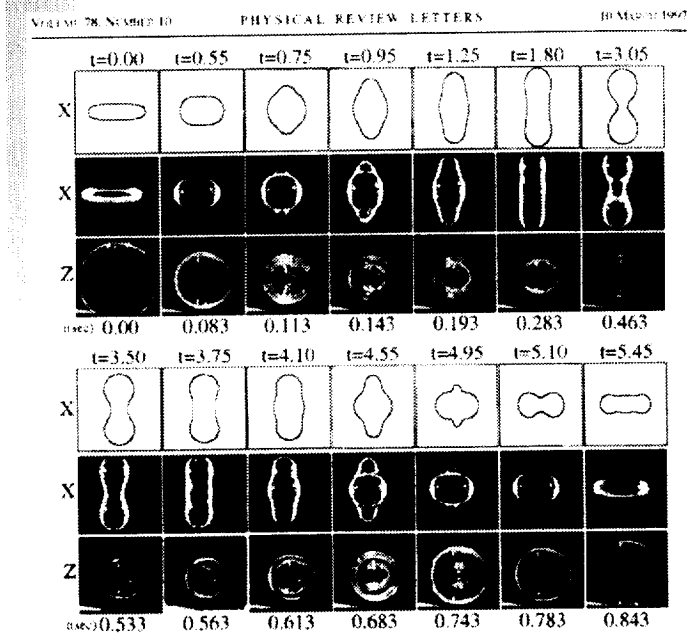

FIG. 1. Sequence of 14 frames showing single complete oscillation of a 6.6 cm³ drop that begins in a highly deformed oblate shape owing to a high intensity acoustic field, and which then oscillates after the acoustic field intensity is suddenly reduced. The top images in each row are the X (side) view, and the bottom images are the Z (top) view demonstrating the axisymmetric nature of the oscillation. The time of each frame is marked. Shown above the X view observations is a sequence of frames computed using the boundary integral method, assuming a Reynolds number of 660. The nondimensional time T shown with each frame is defined in the text. Note that the last two frames of the predictions differ from the observations, because the predictions are showing the center phase of the drop (which is dimpled in), whereas the observations are showing the front view image which cannot show the inward dimpling effect.

Microgravity Data

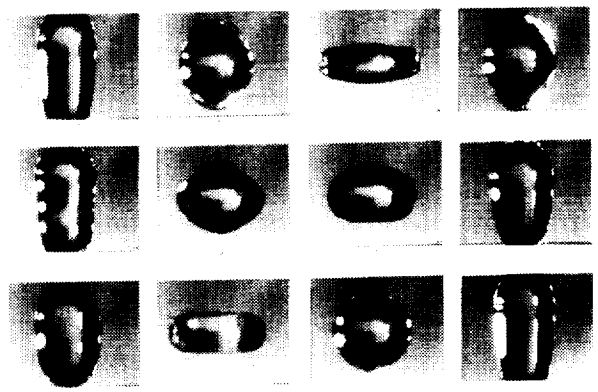

Ground-based Data.
Large amplitude oscillations obtained
By varying excitation mechanism

Fundamental Research: Space-based Results and Ground-based Applications

- Application to ground-based high-temperature thermophysical properties measurement by electrostatic levitation.

OBPR

Physical Sciences Research Division

- **An advanced sample levitation device developed by NASA**
- **Process refractory materials in high vacuum (metals, alloys and semiconductors)**
- **Studies of overheated as well as deeply undercooled liquids**
- **Non-contact diagnostic techniques for various thermo-physical properties**
- **Studies of phase transformation and development of new microstructures**

QuickTime™ and a Video decompressor are needed to see this picture

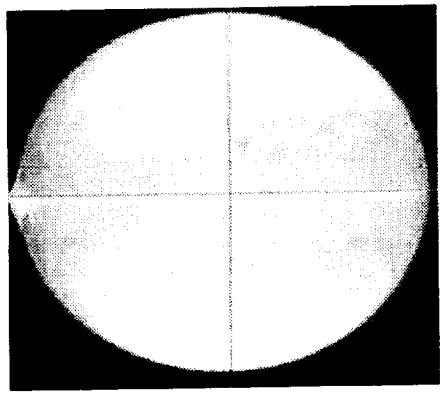

Figure: Molten Zirconium sphere at 2300 K

Fundamental Research: Applications to Mission-oriented Research

Vapor Bubble Removal from a Heated Surface

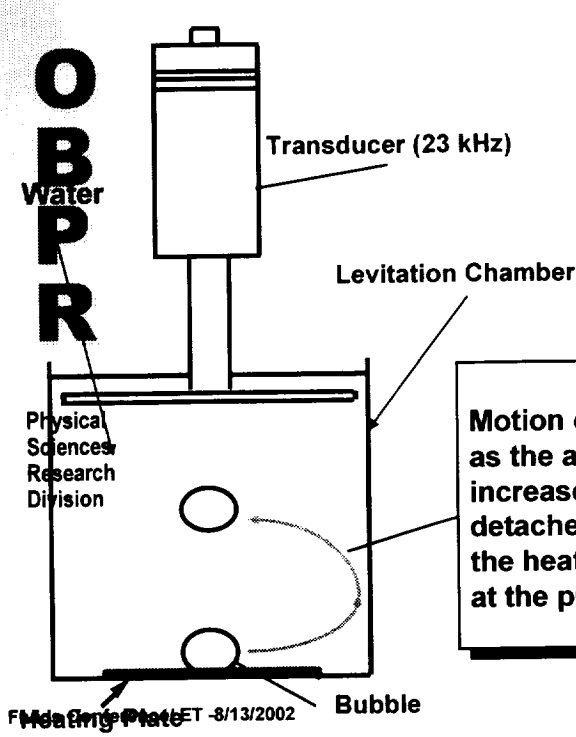

Motion of the vapor bubble as the acoustic pressure increases. The sound field detaches the bubble from the heated plate to trap it at the pressure node.

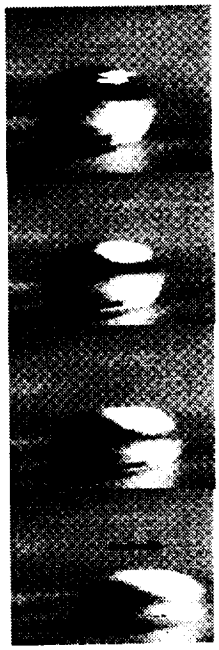

August 14, 2000
Opening Plenary Speaker

NASA Research Announcement

Fran Chiaramonte
NASA Headquarters
Office of Biological and Physical Research

Physical Science Research Division

Office of
Biological
& Physical
Research

Sixth Microgravity Fluid Physics and Transport Phenomena Conference

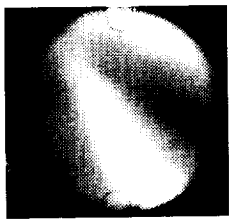

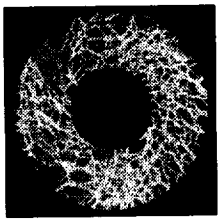

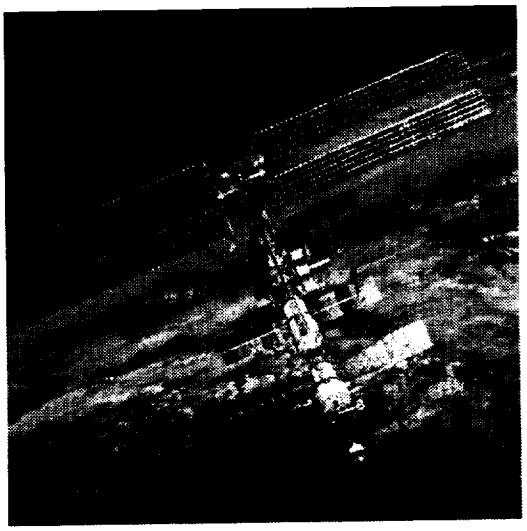

Francis Chiaramonte
Enterprise Scientist for Fluid Physics

Physical Science Research Division

Office of
Biological
& Physical
Research

2002 NRA for Fluid Physics

- NRA release changed from every 2 years to once a year
- Emphasis: Strategic and Fundamental Research
- 20 to 25 selections
- Mostly ground-based selections
- 1 or 2 flight selections possible if proposal is outstanding and compatible with existing hardware

Physical Science Research Division

Office of Biological & Physical Research

- Strategic Research (mission enabling)
  - Power generation and storage (radiators, boilers)
  - Space Propulsion (liquid management, propellant tank)
  - Life support (air revitalization, water recycling, waste processing, carbon dioxide collector)
  - Materials Handling and Transport (separation or filtration of solid particles (dust) from RF-processed gas streams)
  - Human health (respiration, bone loss, fluid shift, lung- reopening airways)

- Fundamental Research (Pursue major scientific issues or questions with potential technological impact, e.g. terrestrial applications.)
  - Colloid systems
  - Miscible interfaces
  - Granular flow
  - Multiphase flow
  - Etc.

Physical Science Research Division

Office of Biological & Physical Research

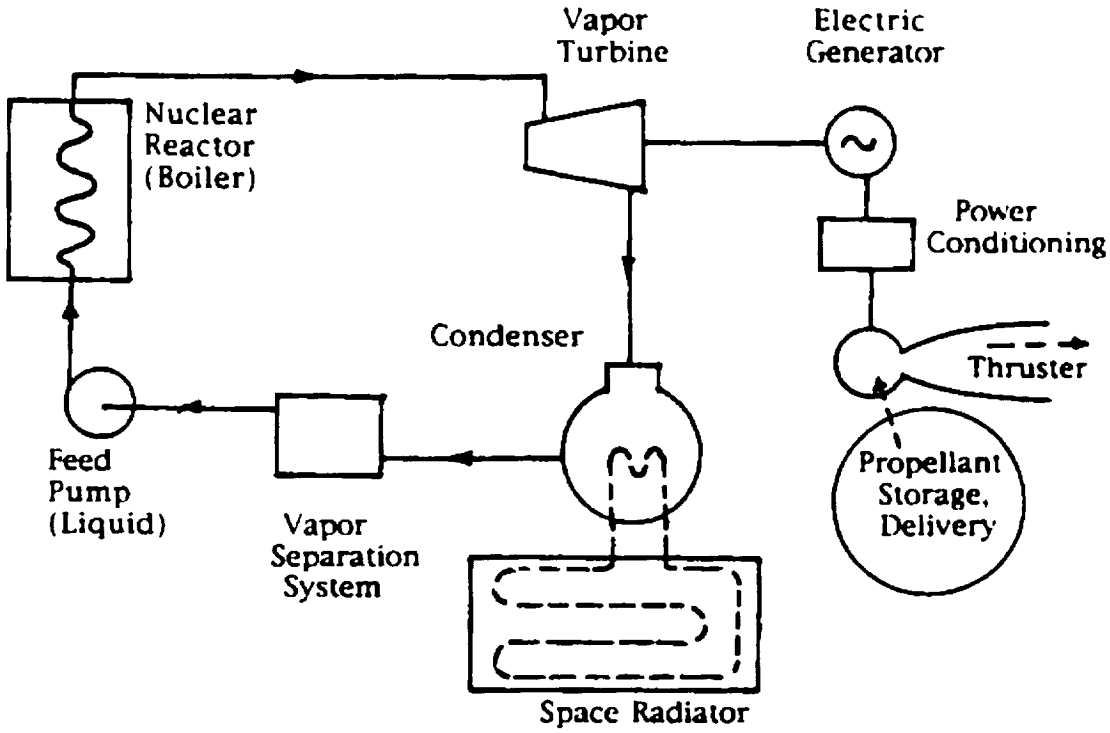

Schematic showing major elements of a nuclear electric propulsion system

Colloid-Polymer Samples

The PCS colloid-polymer samples are providing a much deeper study of the phase behavior of depletion-interactions that could lead to improved products such as paints, ceramics, and both food and drug delivery products.

Colloid-Polymer Critical Point Sample

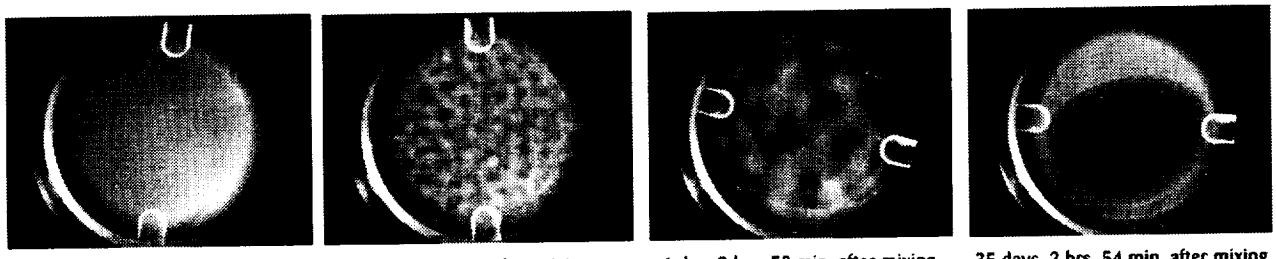

Immediately after mixing | 11 hrs, 45 min. after mixing | 1 day, 3 hrs, 50 min. after mixing | 35 days, 2 hrs, 54 min. after mixing

Results from Space

- Colloid-Polymer Critical Point Sample: Spontaneously demixes (phase separates) into colloid-rich and colloid-poor regions. In the absence of gravity, studied this process over four decades in length scale, from 1 micron to 1 centimeter. These results are the first to follow the process from its microscopic beginnings to the final, fully separated state.

Pool Boiling Experiment

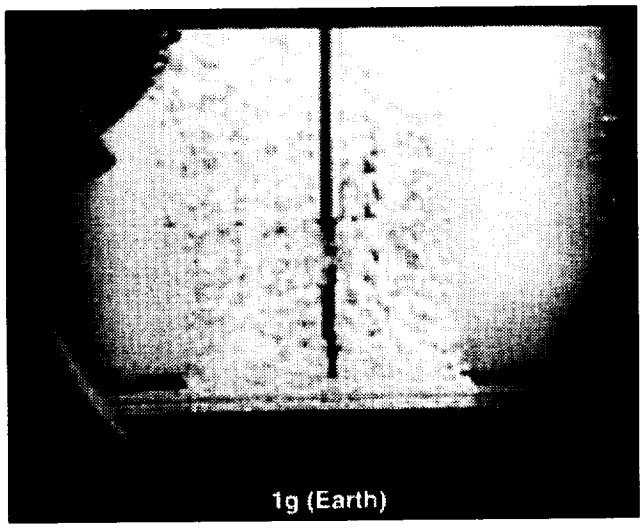

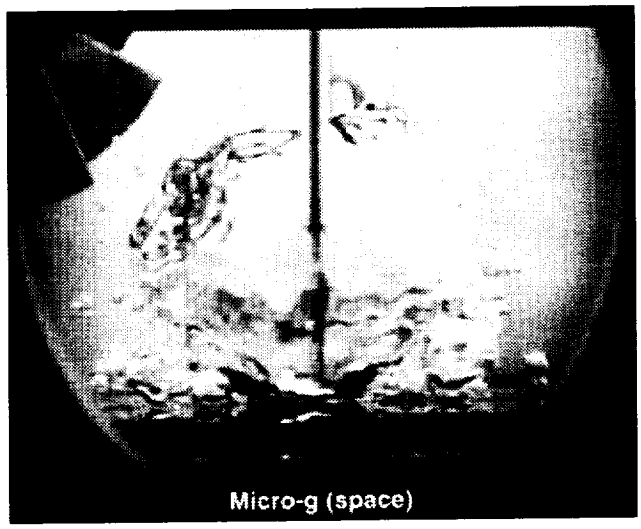

The Dynamics of Miscible Interfaces: A Space Flight Experiment (MIDAS)

Tony Maxworthy, University of Southern California
Eckart Meiburg, Univ. of CA - Santa Barbara

To better understand and develop predictive tools for flows such as in enhanced oil recovery, porous media etc.

Why:

Additional fluid stresses, caused by concentration gradients, is deemed important in the flow of miscible fluids. Such stresses are not represented by the commonly used Newtonian model.

"... Assessing the importance of the extra stresses represents a worthwhile fundamental scientific objective that will have important consequences in a variety of circumstances and applications...," SCR Panel, Sept. 2000.

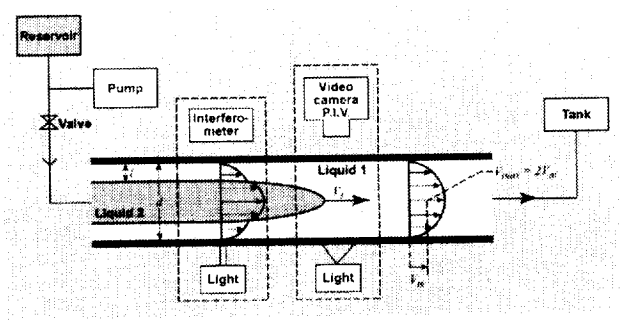

Schematic of proposed experiment.

FP-21	Final Peer Review Date: ~4/02	Flight Hardware Available: ~6/05

How:

- Study the process of displacement (fingering) of a viscous liquid by a miscible, less viscous liquid in a cylindrical tube in flow regimes inaccessible on Earth.
- Obtain the velocity field around the intruding finger by particle image velocimetry, and the concentration field by interferometry.
- Assess the importance of the additional fluid stresses by comparing experimental results with numerical predictions.

Impact:

- New predicitve tools can be developed and are important for progress in enhanced oil recovery, flows in porous media, fixed bed regeneration, and hydrology.

"... The foundation of the experiment is well established... Particular strengths of the experiment is its relative conceptual simplicity, the high qualifications of the Principal Investigators, and the compelling ground-based and computational work done ..." - SCR Panel, Sept. 2000.

Petitjeans, P. and Maxworthy, T., "Miscible Displacements in a Capillary Tube. Part 1 - Experiments", *J. Fluid Mech.* 326, 37 (1996).

Physical Science Research Division

- Where the FLUID PHYSICS Categories Fit: (one point of view)

- Strategic Research
  - Multiphase Flow and Heat Transfer
  - Biofluids
  - Interfacial Phenomena
  - Complex Fluids (Granular Flow)

- Fundamental Research
  - Complex Fluids (Colloids and Granular Flow)
  - Dynamics and Instabilities

Physical Science Research Division

Office of Biological & Physical Research

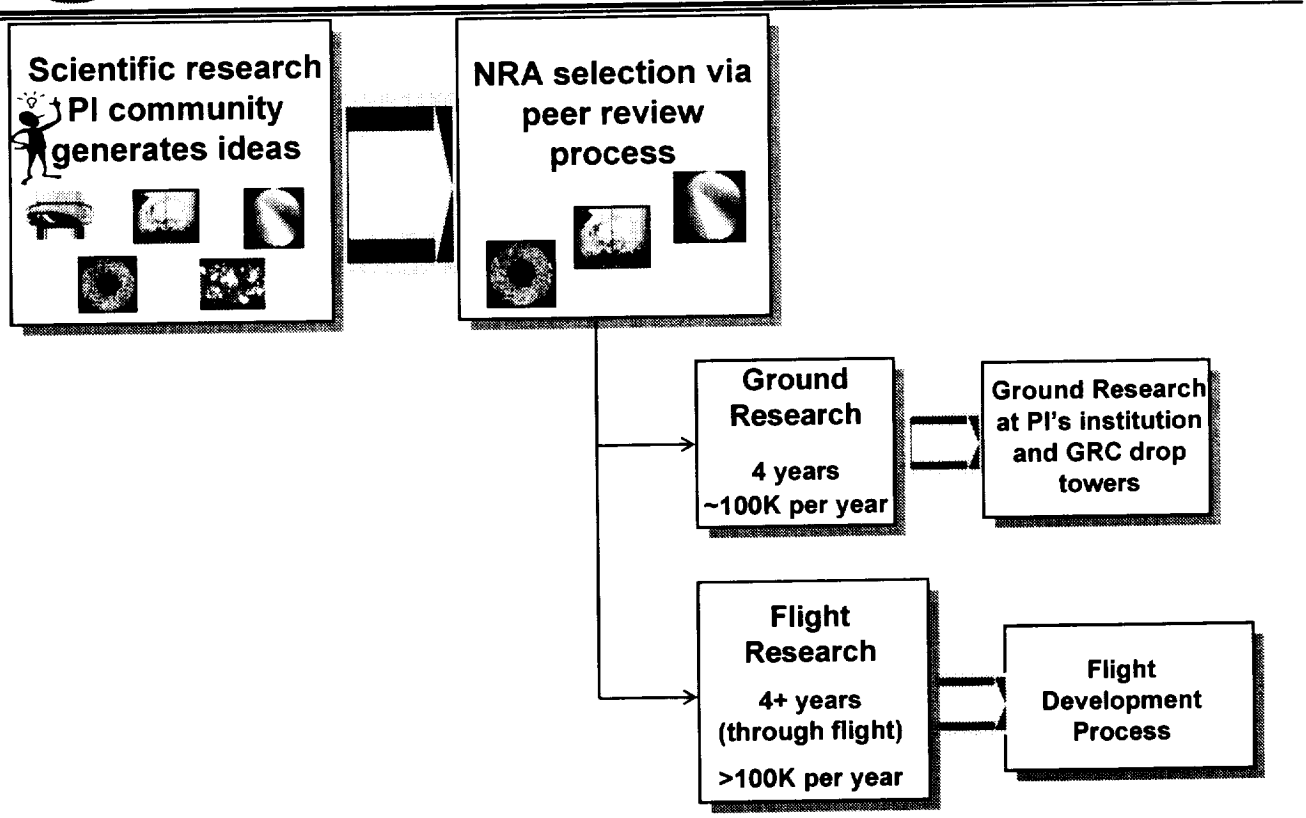

Physical Science Research Division

Office of Biological & Physical Research

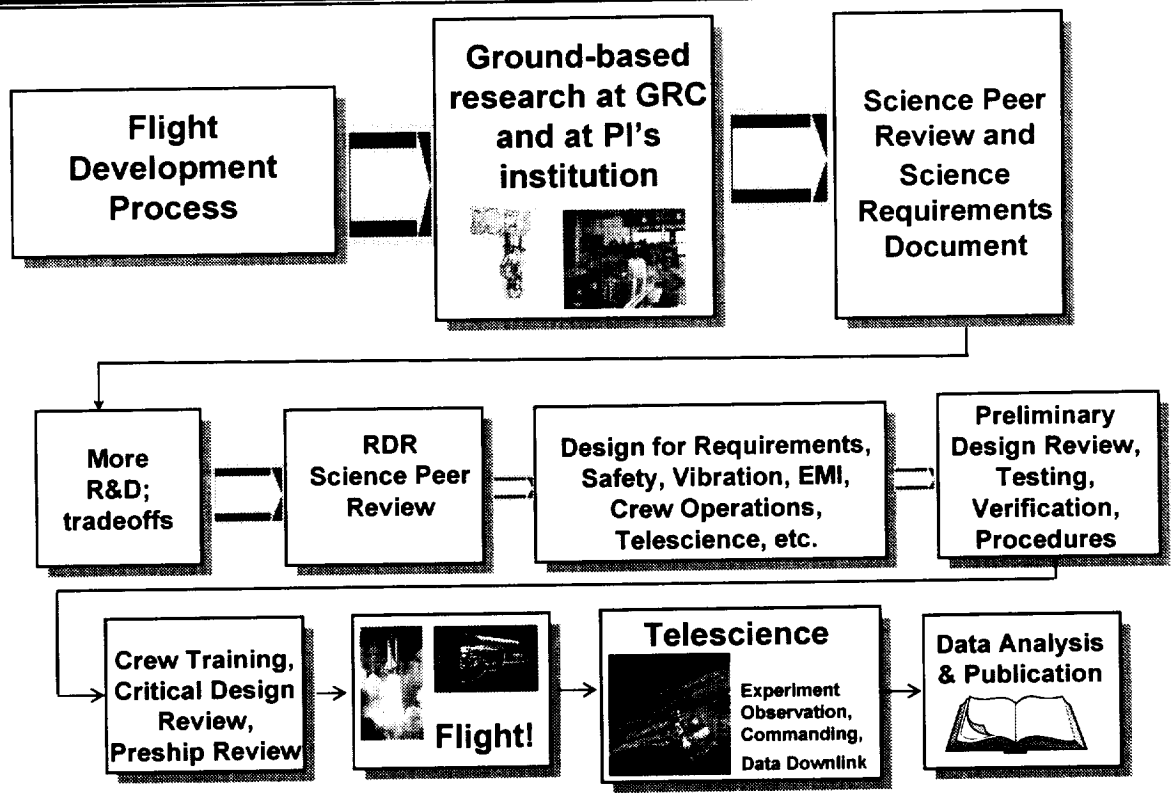

ISS and Ground-based Facilities

Fluids Rack

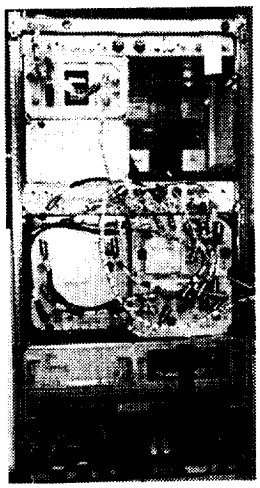

EXPRESS Rack

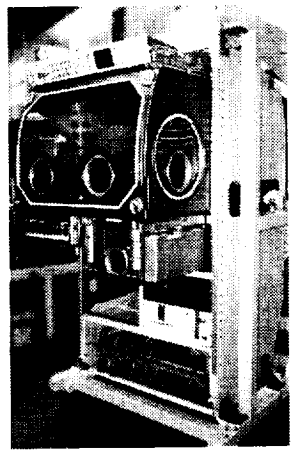

Glovebox

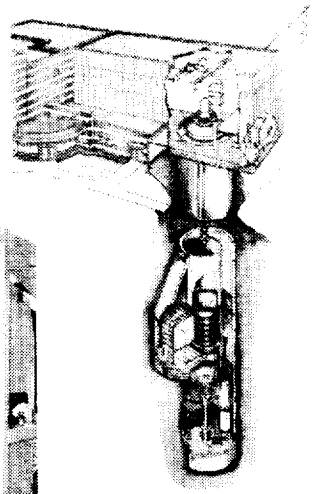

Drop tower

August 14, 2000
Opening Plenary Speaker

Biofluids of Living in Space

Kim Prisk
University of California, San Diego
Department of Medicine

Biofluids of living in space:

Gas mixing in the periphery of the lung

G. Kim Prisk, Ph.D.
Department of Medicine
University of California, San Diego

UCSD

Roadmap

- Lung overview
- Gravity and the lung

- Specific Examples
  - Diffusive-convective interactions in the periphery of the lung
  - Convective mixing in the periphery of the lung

- Other areas of interest

UCSD

Lung design

- Must meet the gas exchange needs of the body under maximum exercise
  - Oxygen consumption ~6 $l.min^{-1}$
  - Cardiac output of ~30 $l.min^{-1}$
- Passive diffusion only
  - Thin gas exchange barrier
  - Large gas exchange surface area

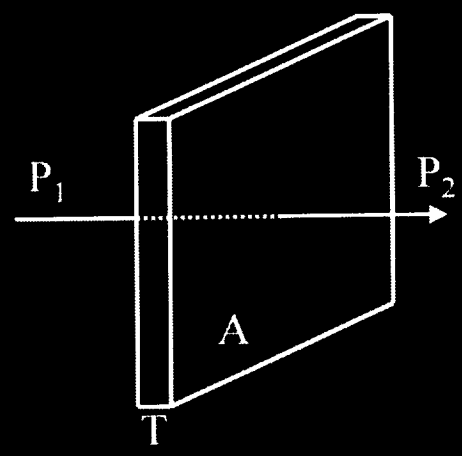

$$\dot{V}_{gas} = \frac{AD}{T}(P_1 - P_2)$$

Gas exchange membrane of

~50-100 m^2, ~0.7 μm thick

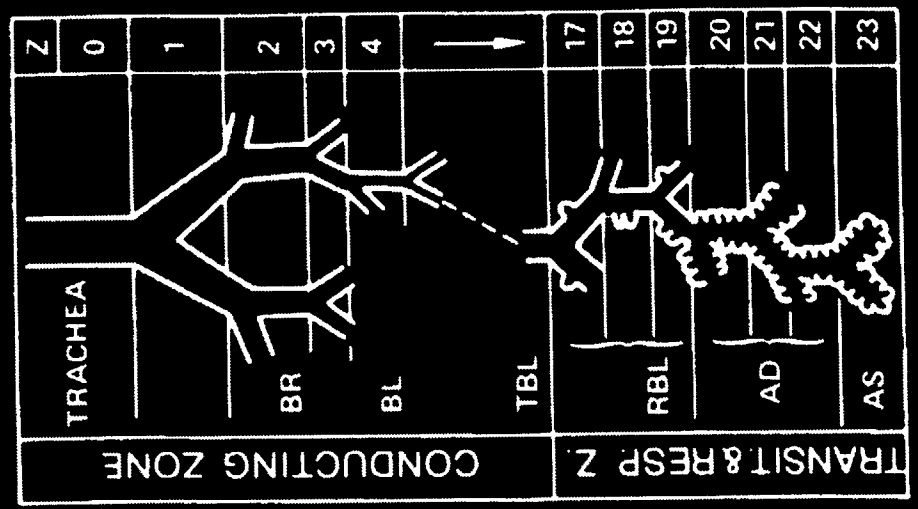
Z
0
1
2
3
4
17
18
19
20
21
22
23
TRACHEA
BR
BL
TBL
RBL
AD
AS
CONDUCTING ZONE
TRANSIT.&RESP. Z.

Lung Structure

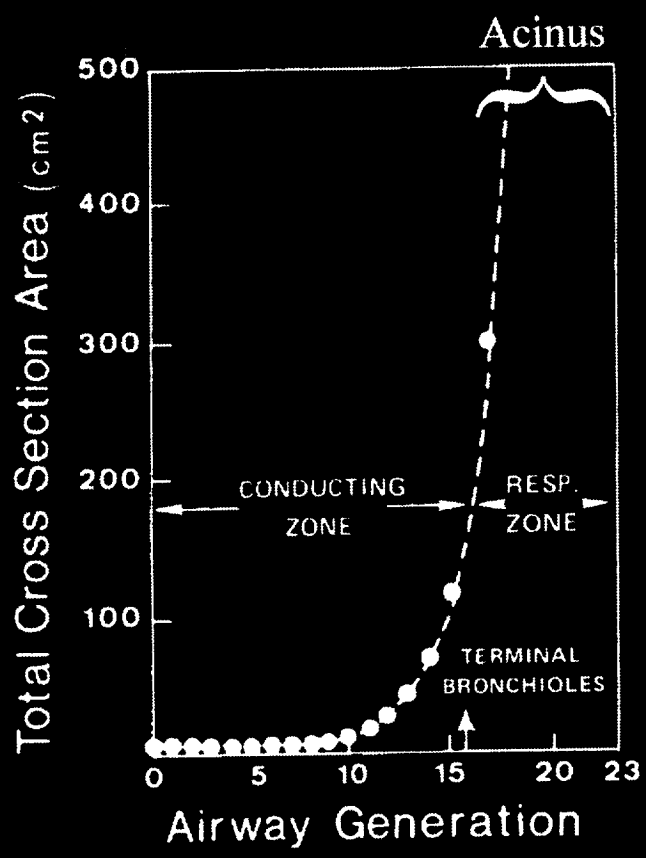

- Total airway cross-section increases rapidly towards the periphery of the lung
  - Trachea ~ 5 cm^2
  - Alveolar capillary membrane ~ 50-100 m^2
- Airflow velocity decreases rapidly towards the periphery of the lung

UCSD

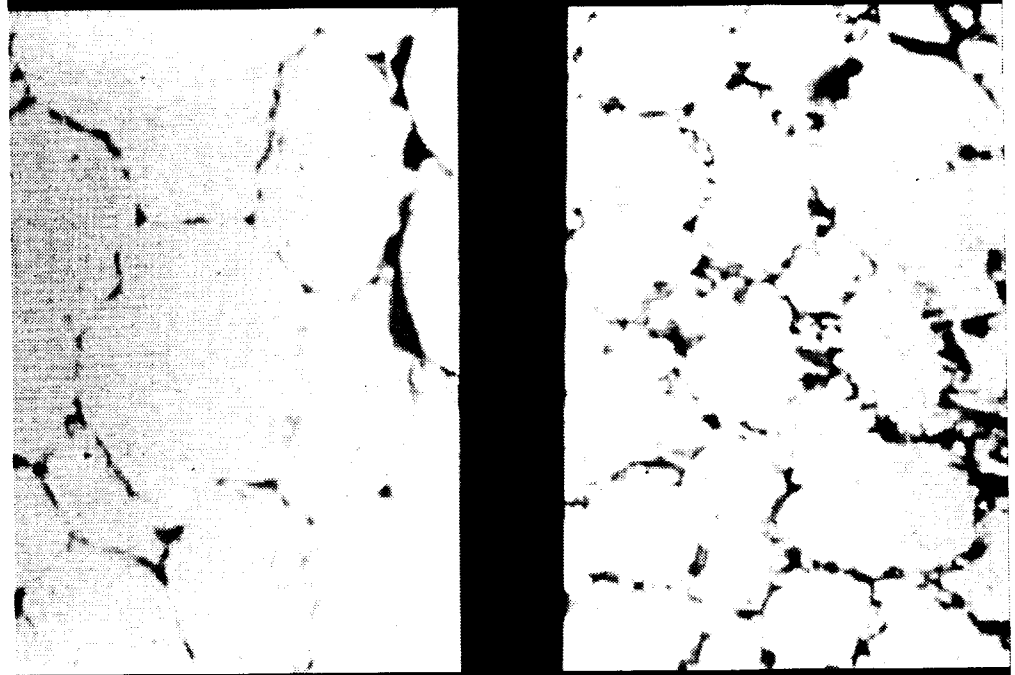

The lung in μG

Absence of Hydrostatic Forces

Increased thoracic blood volume

More even perfusion of lung

Absence of Mechanical Forces

Redistribution of pulmonary ventilation and volume

Changes in chest wall and abdominal mechanics

Unevenness of lung function is the hallmark of all pulmonary diseases

UCSD

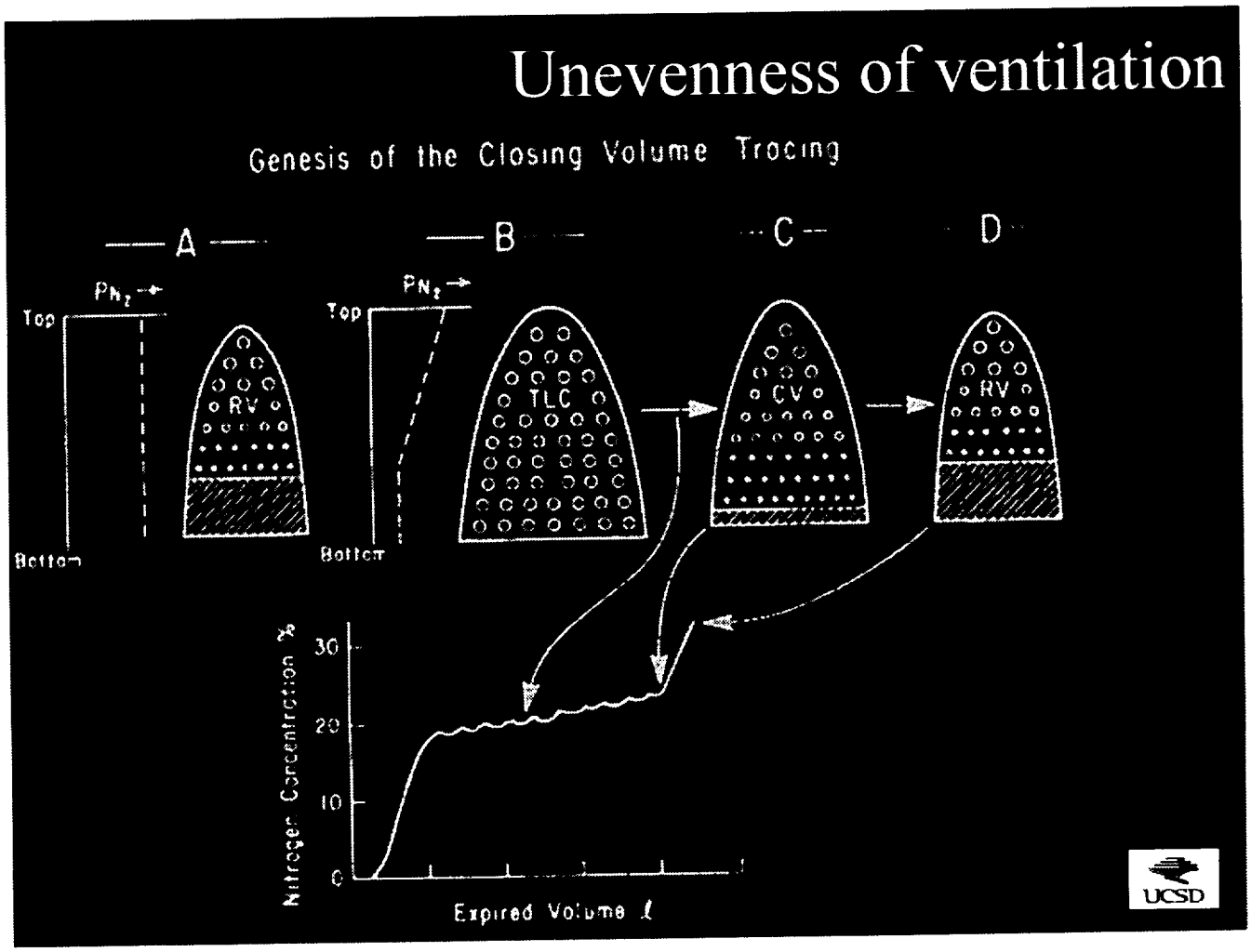
Unevenness of ventilation
Genesis of the Closing Volume Tracing
A
B
C
D
Top
Bottom
RV
TLC
CV
RV
Nitrogen Concentration %
30
20
10
0
Expired Volume l
UCSD

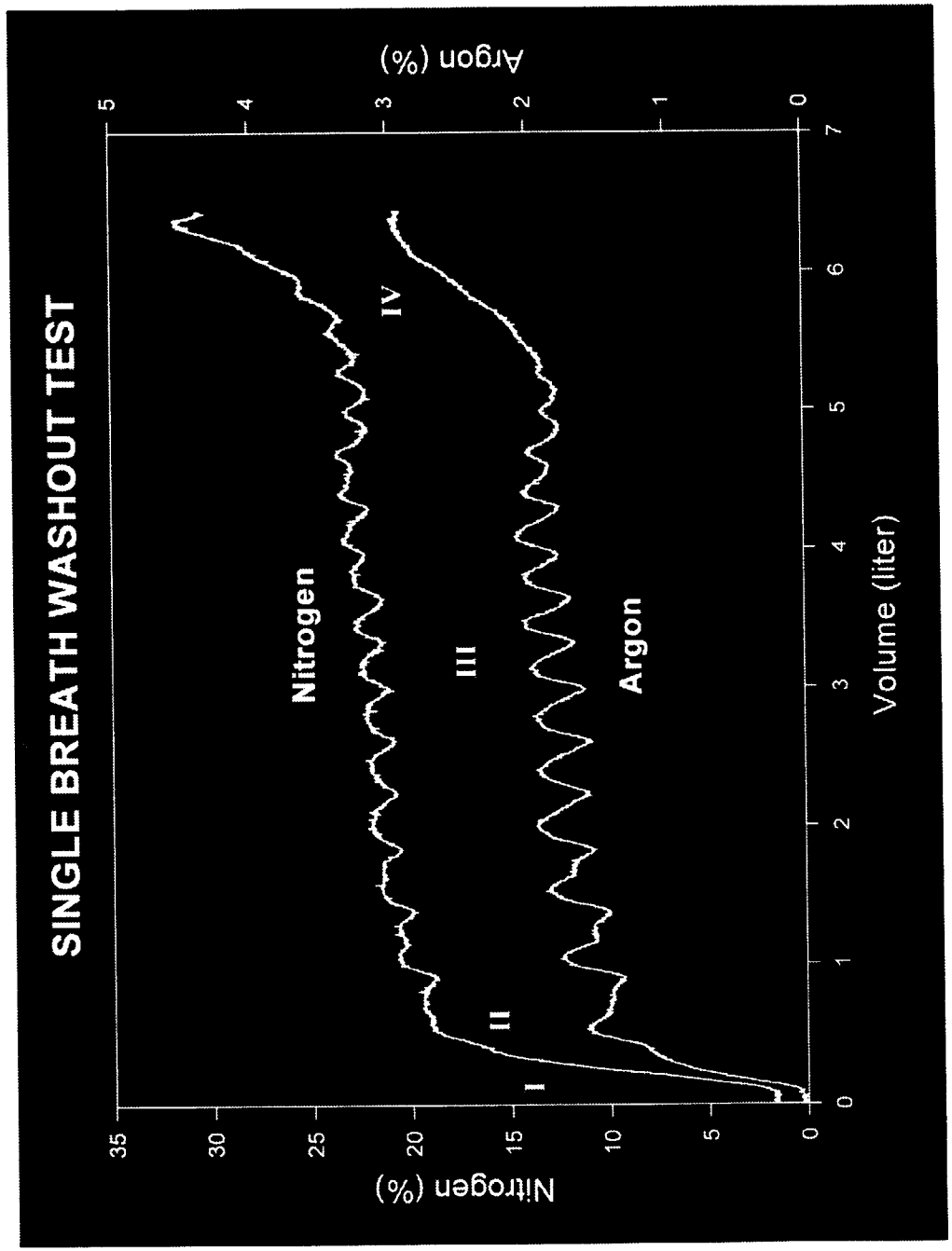
SINGLE BREATH WASHOUT TEST
Nitrogen
Argon
I
II
III
IV
Nitrogen (%)
Argon (%)
Volume (liter)
35
30
25
20
15
10
5
0
5
4
3
2
1
0
0
1
2
3
4
5
6
7

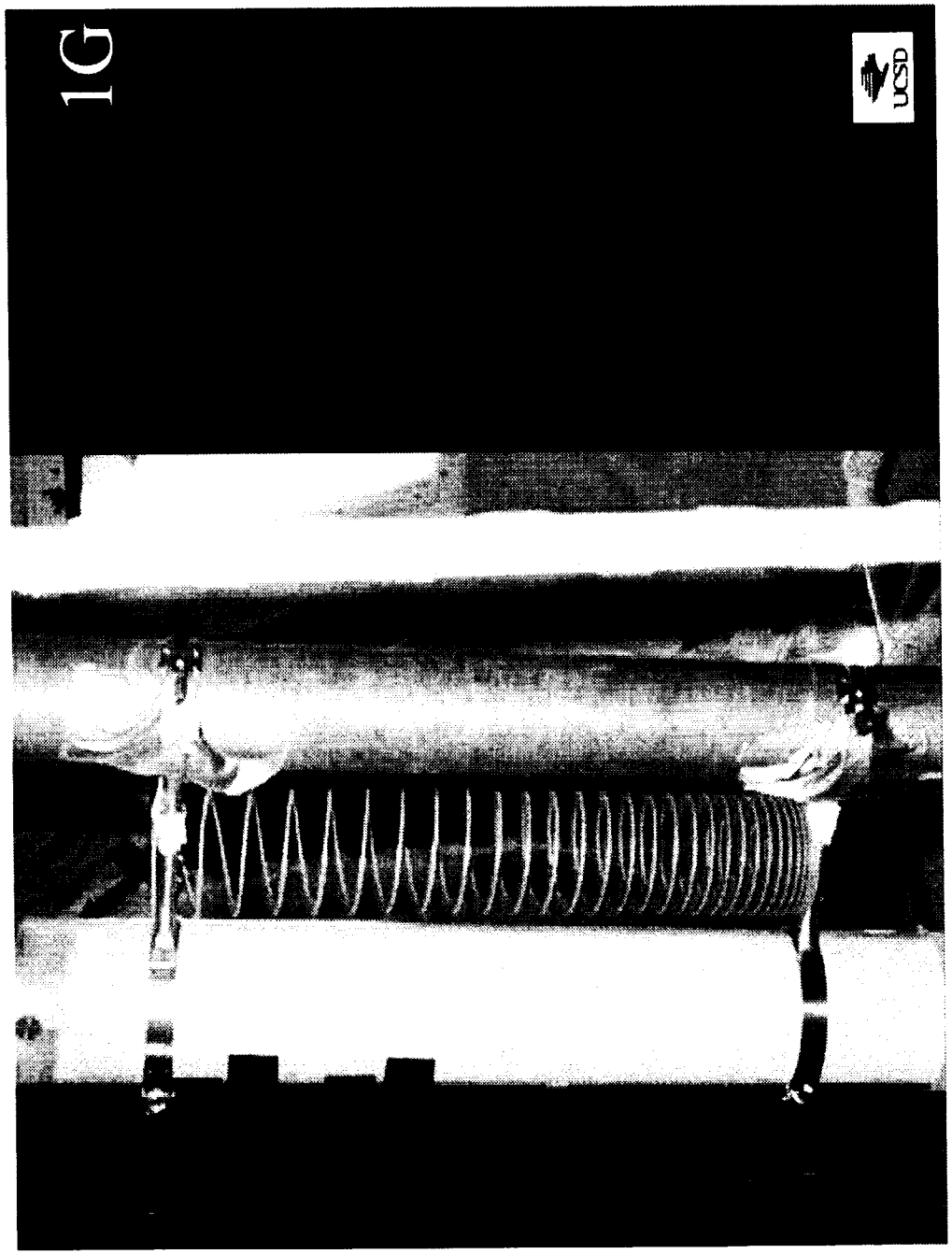
1G
UCSD

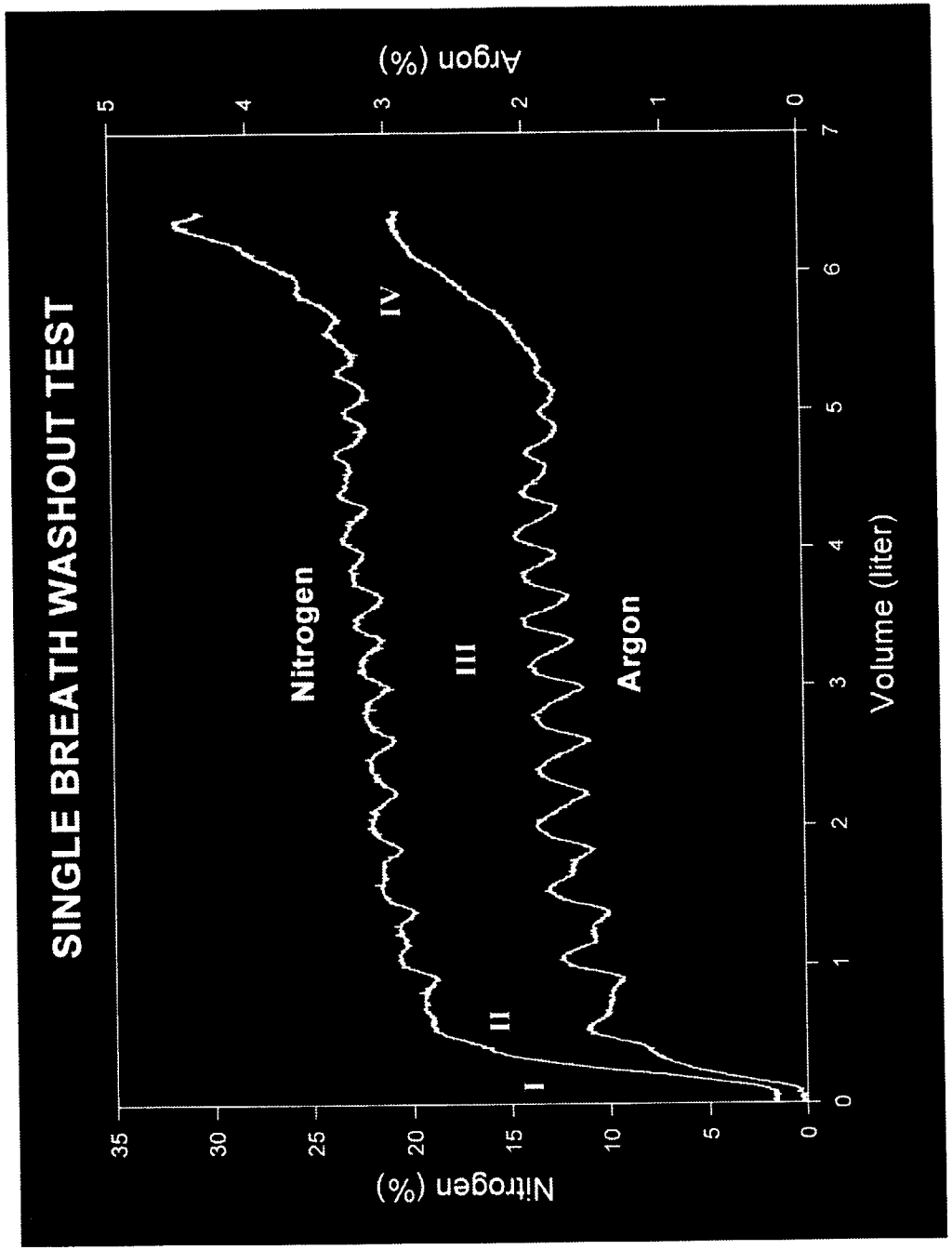
SINGLE BREATH WASHOUT TEST
Nitrogen (%)
Argon (%)
Volume (liter)
Nitrogen
Argon
I
II
III
IV
35
30
25
20
15
10
5
0
5
4
3
2
1
0
0
1
2
3
4
5
6
7

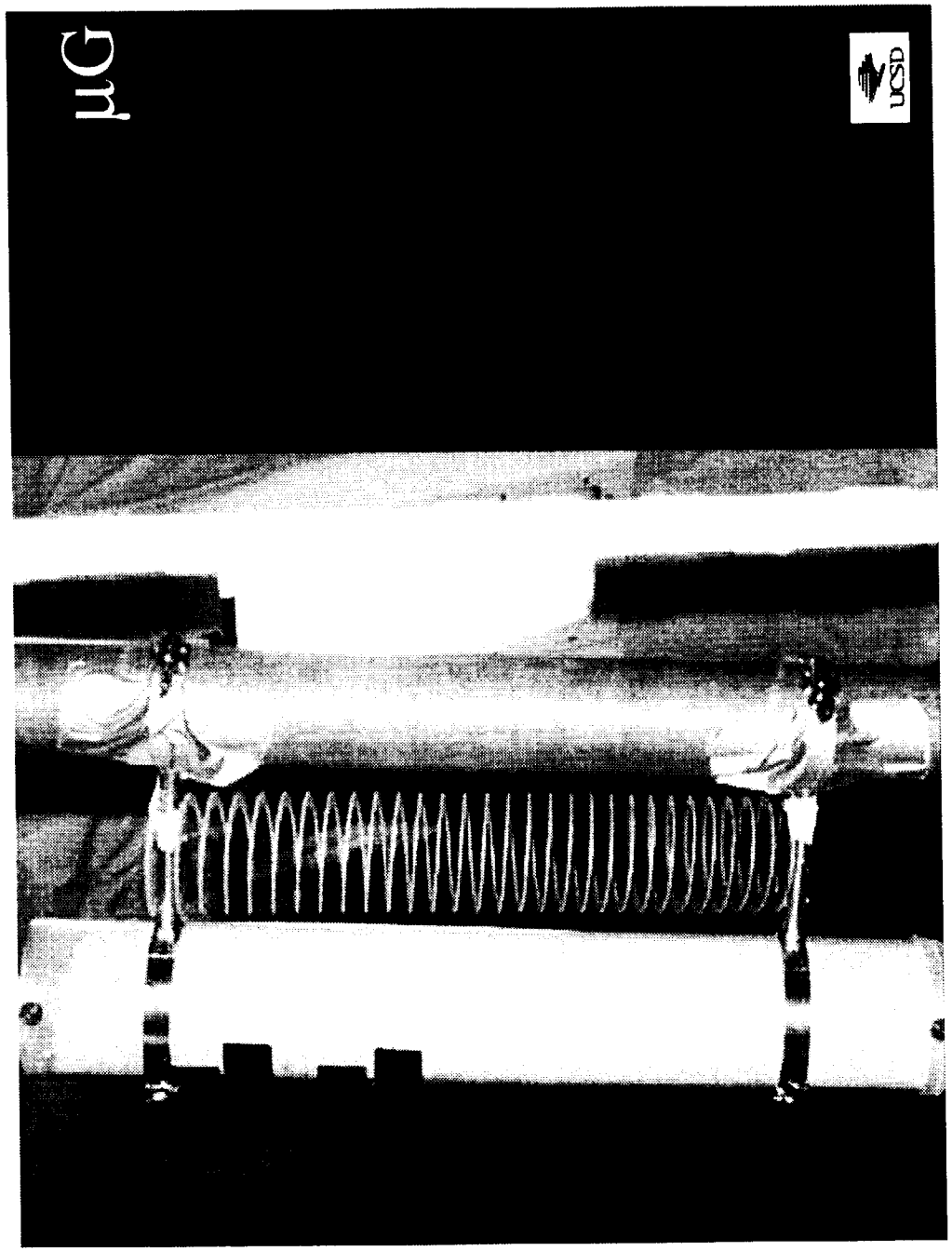
μG
UCSD

Sustained μG

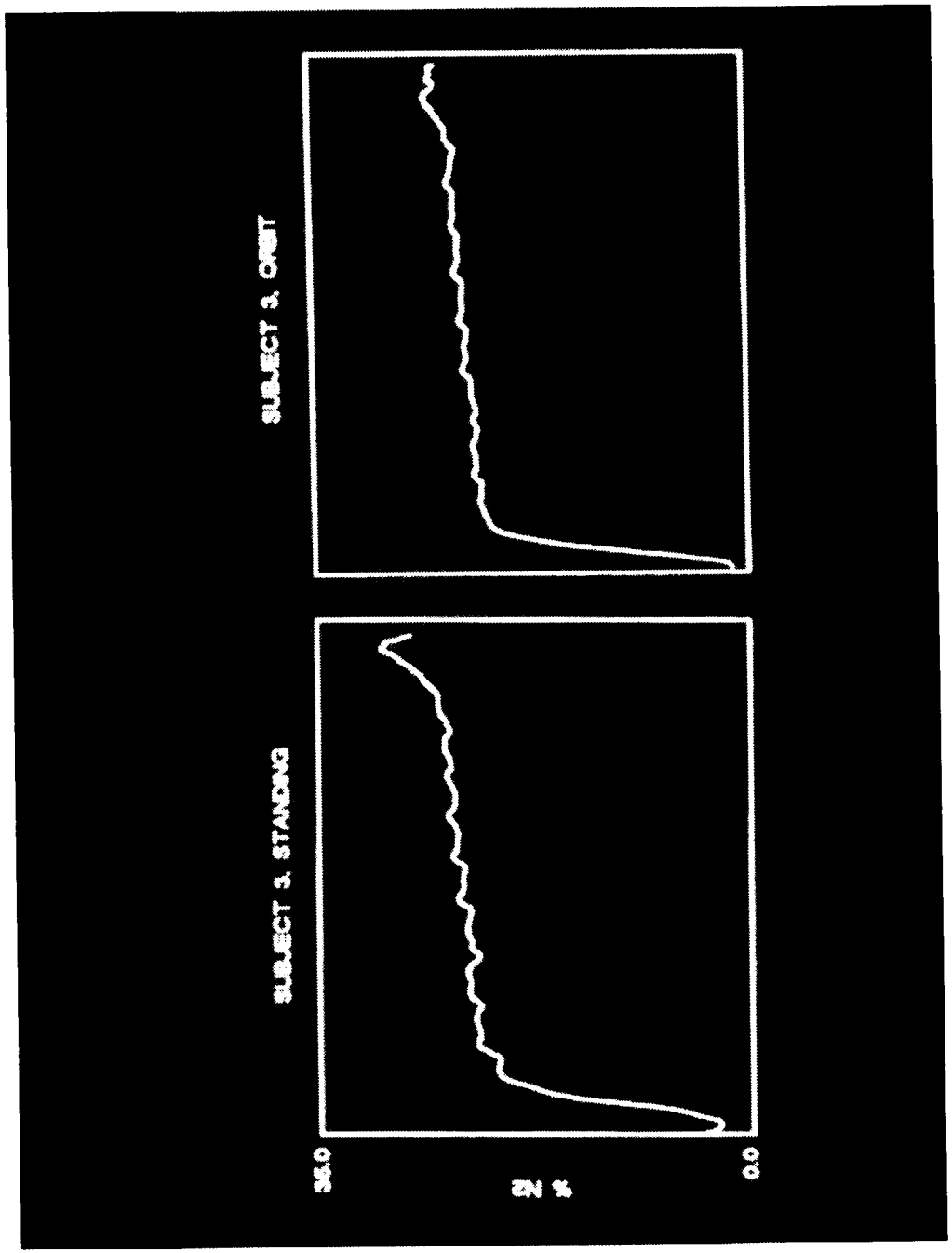
SUBJECT 3, STANDING
SUBJECT 3, ORBIT
56.0
0.0
% N2

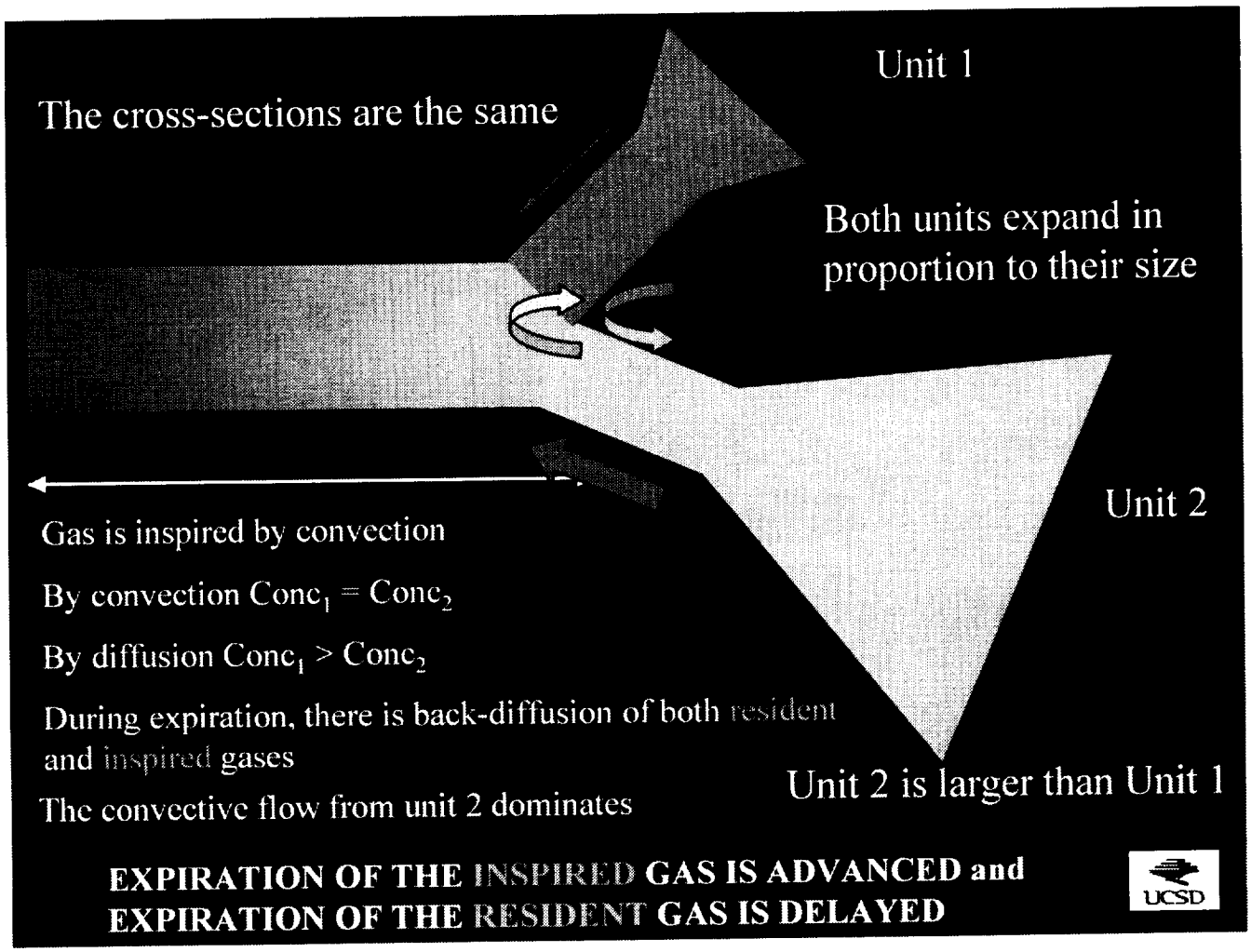
Unit 1
The cross-sections are the same
Both units expand in proportion to their size
Unit 2
Gas is inspired by convection
By convection $Conc_1 = Conc_2$
By diffusion $Conc_1 > Conc_2$
During expiration, there is back-diffusion of both resident and inspired gases
The convective flow from unit 2 dominates
Unit 2 is larger than Unit 1
EXPIRATION OF THE INSPIRED GAS IS ADVANCED and EXPIRATION OF THE RESIDENT GAS IS DELAYED
UCSD

Diffusive Pendeluft

- Only operative where transport due to diffusion and convection are comparable

  $P_e = ud/D \approx 1$
- Magnitude of the effect depends on the degree of asymmetry at the branch point
- For He this point is ~ the acinar entrance
- For SF_6 2-3 generations more peripheral

UCSD

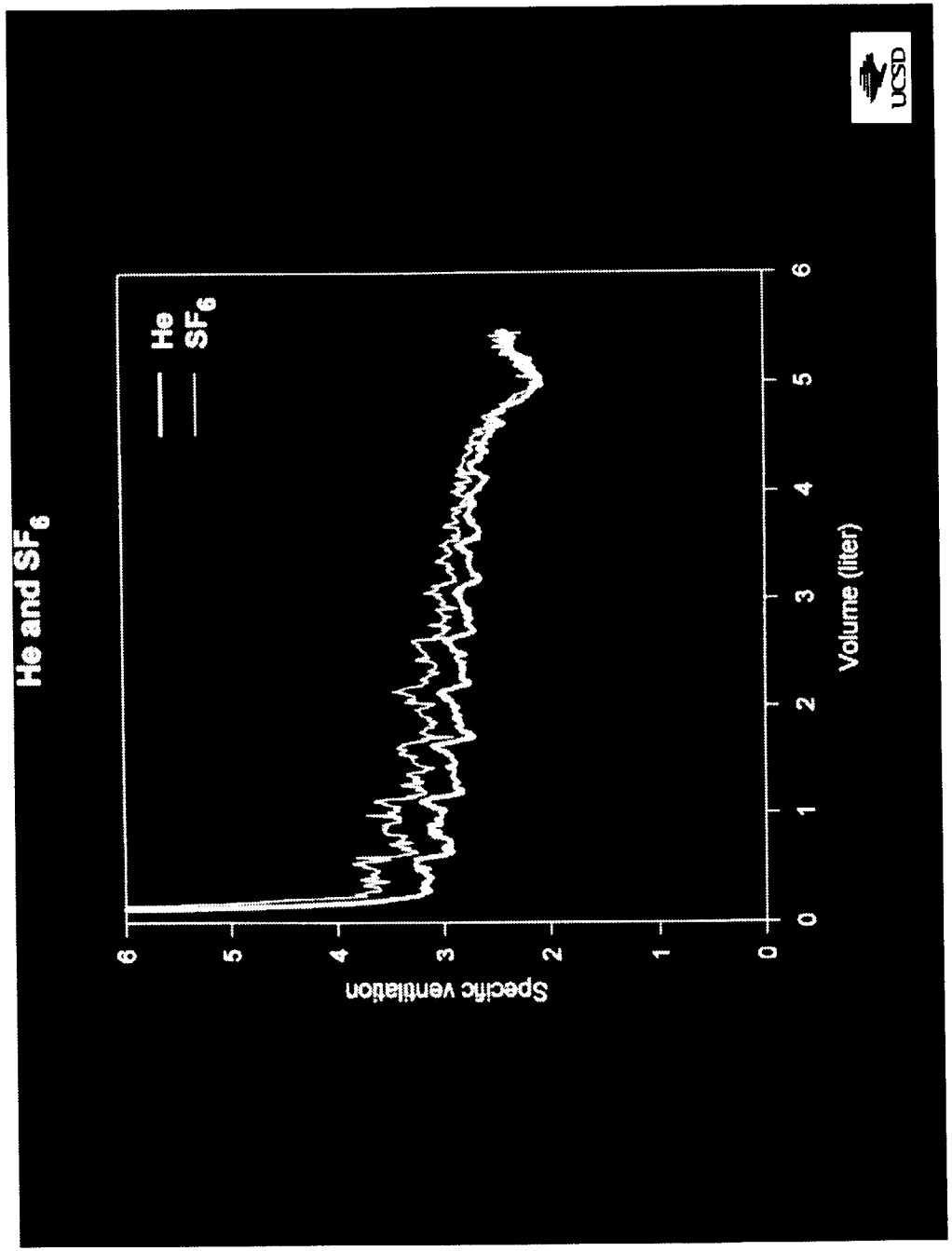
He and SF6
He
SF6
Specific ventilation
Volume (liter)
0
1
2
3
4
5
6
UCSD

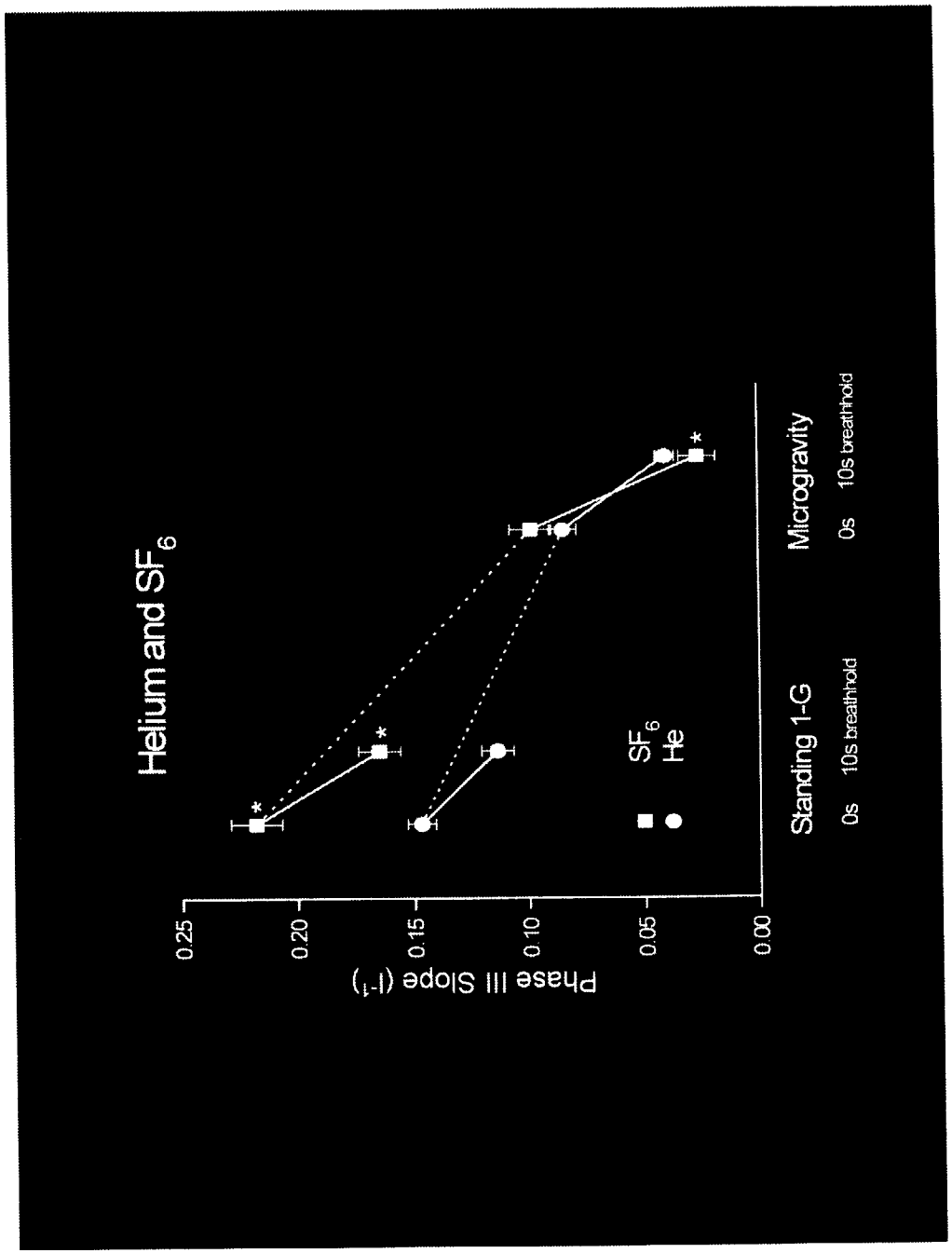
Helium and SF6
Phase III Slope (l-1)
0.25
0.20
0.15
0.10
0.05
0.00
SF6
He
Standing 1-G
Microgravity
0s
10s breathhold
0s
10s breathhold

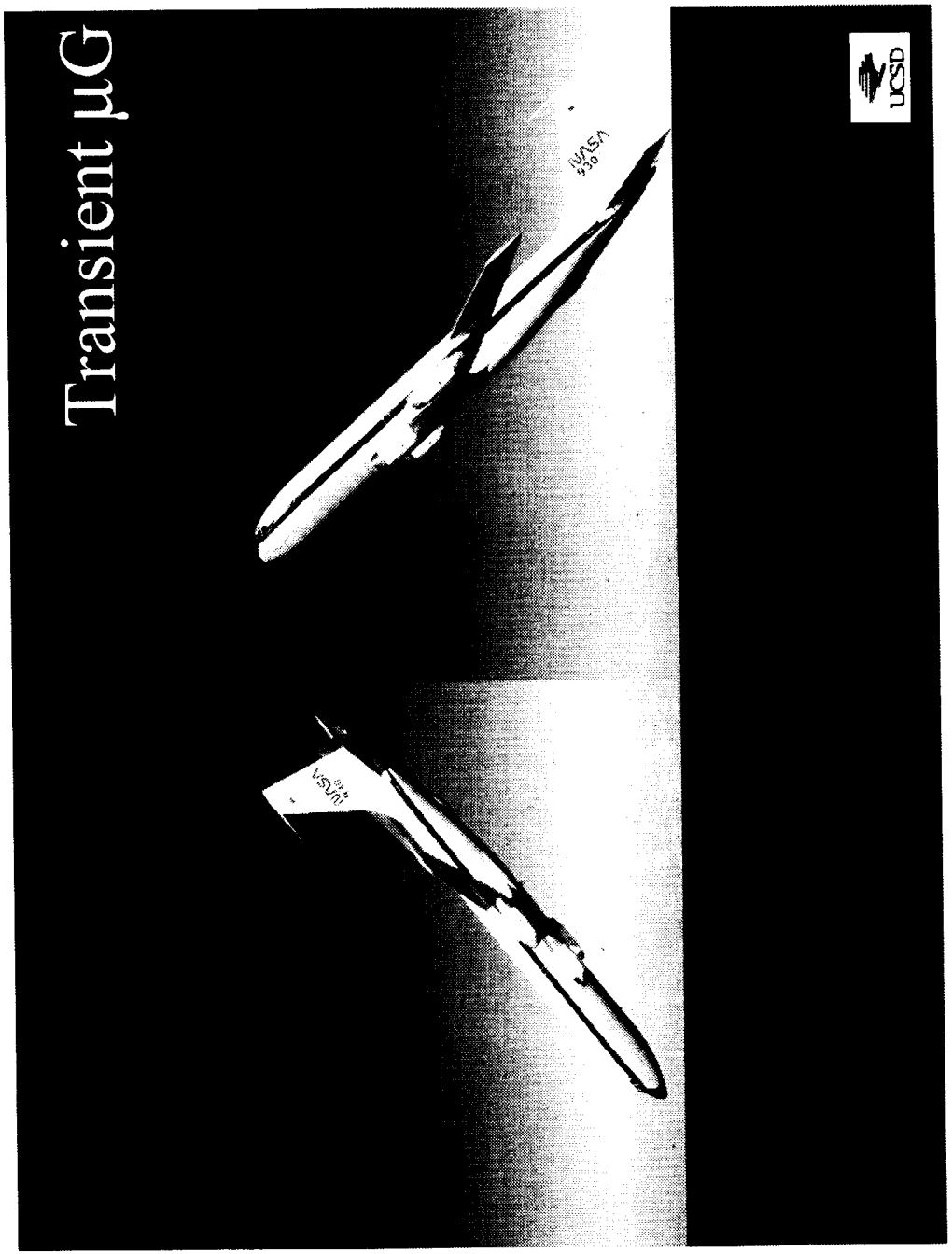
Transient μG
NASA
930
NASA
930
UCSD

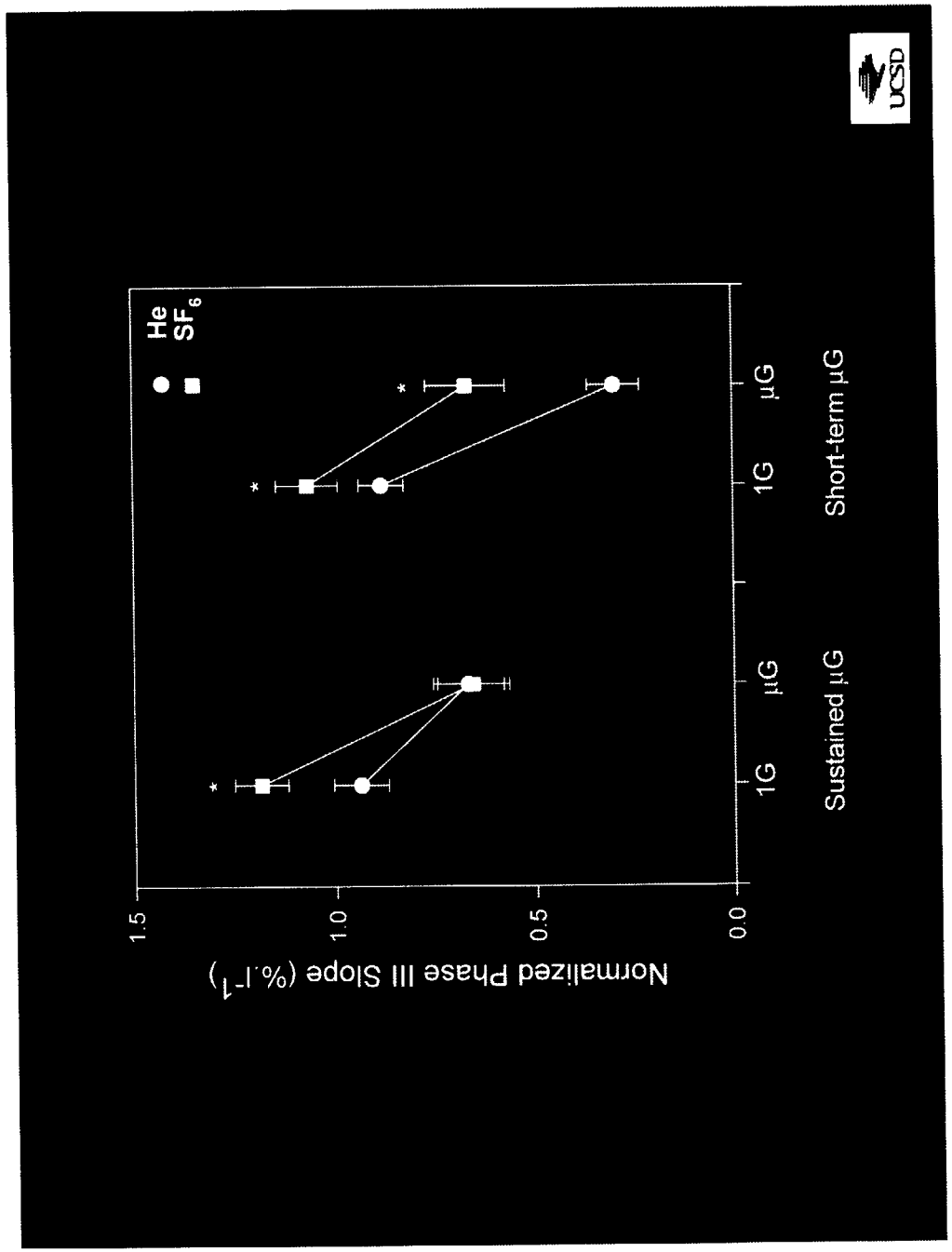
He
SF6
Normalized Phase III Slope (%.l-1)
1.5
1.0
0.5
0.0
1G
µG
1G
µG
Sustained µG
Short-term µG
UCSD

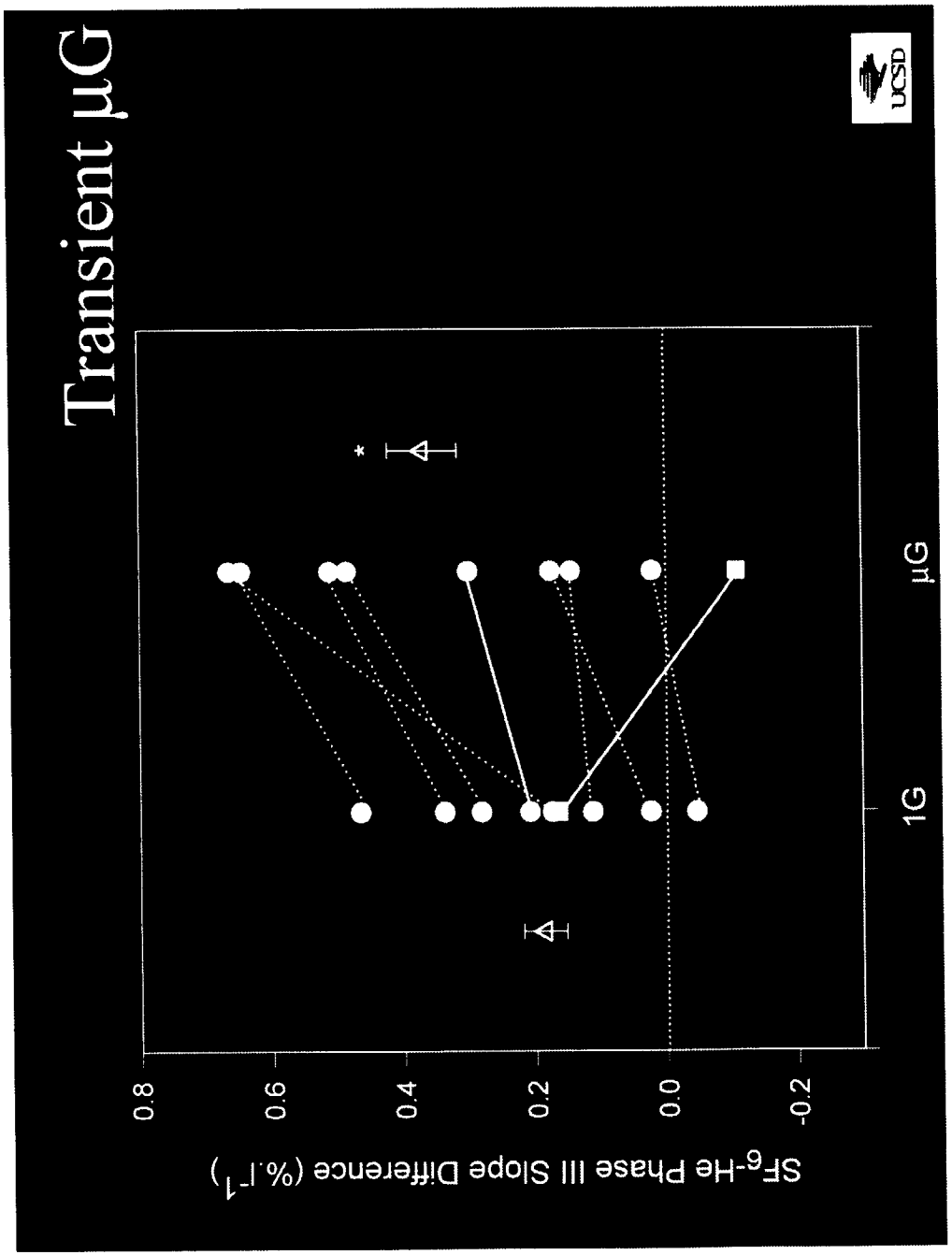
Transient µG
UCSD
SF6-He Phase III Slope Difference (%.l-1)
0.8
0.6
0.4
0.2
0.0
-0.2
1G
µG

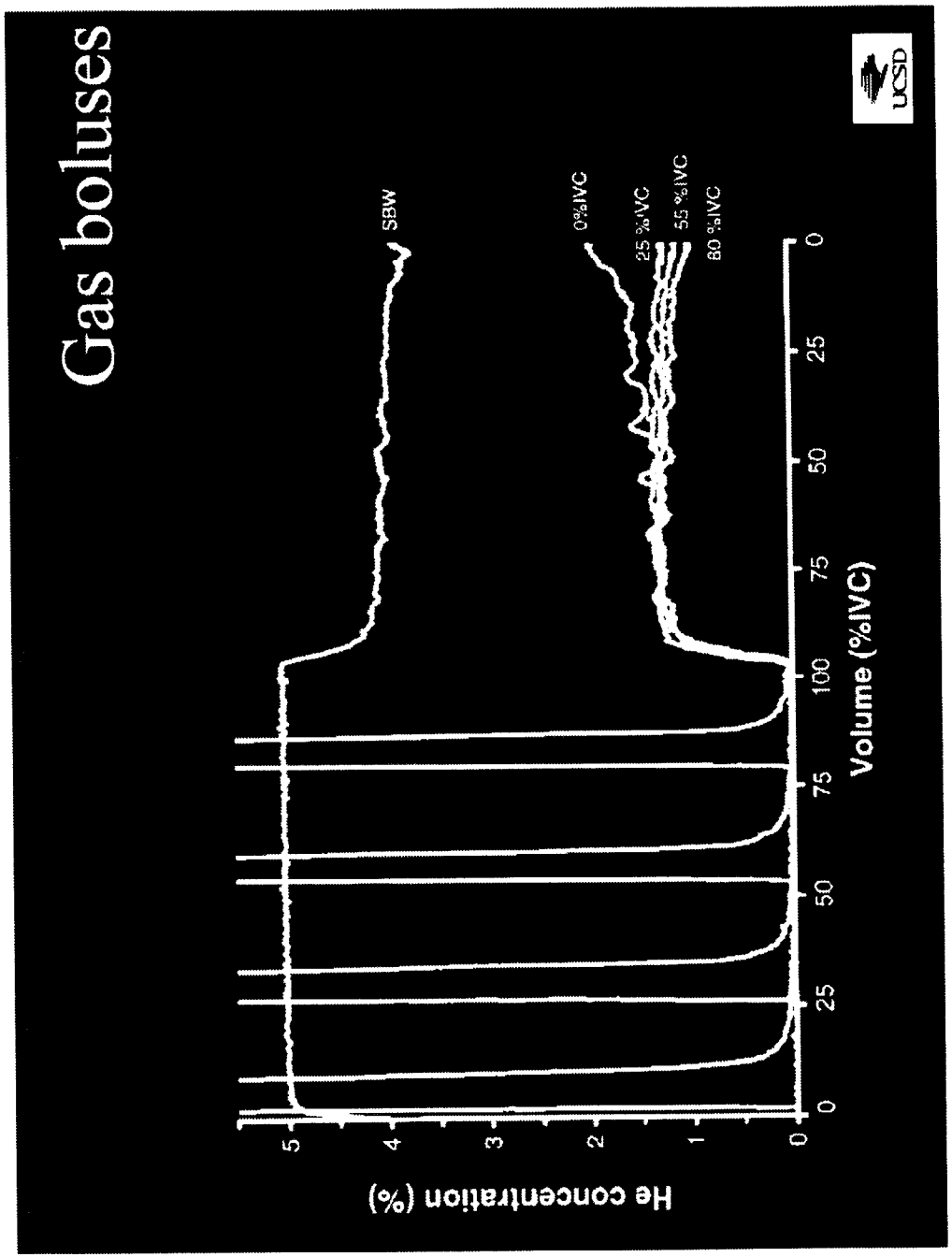
Gas boluses
He concentration (%)
5
4
3
2
1
0
0
25
50
75
100
75
50
25
0
Volume (%IVC)
SBW
0%IVC
25 %IVC
55 %IVC
80 %IVC
UCSD

Slope reconstruction

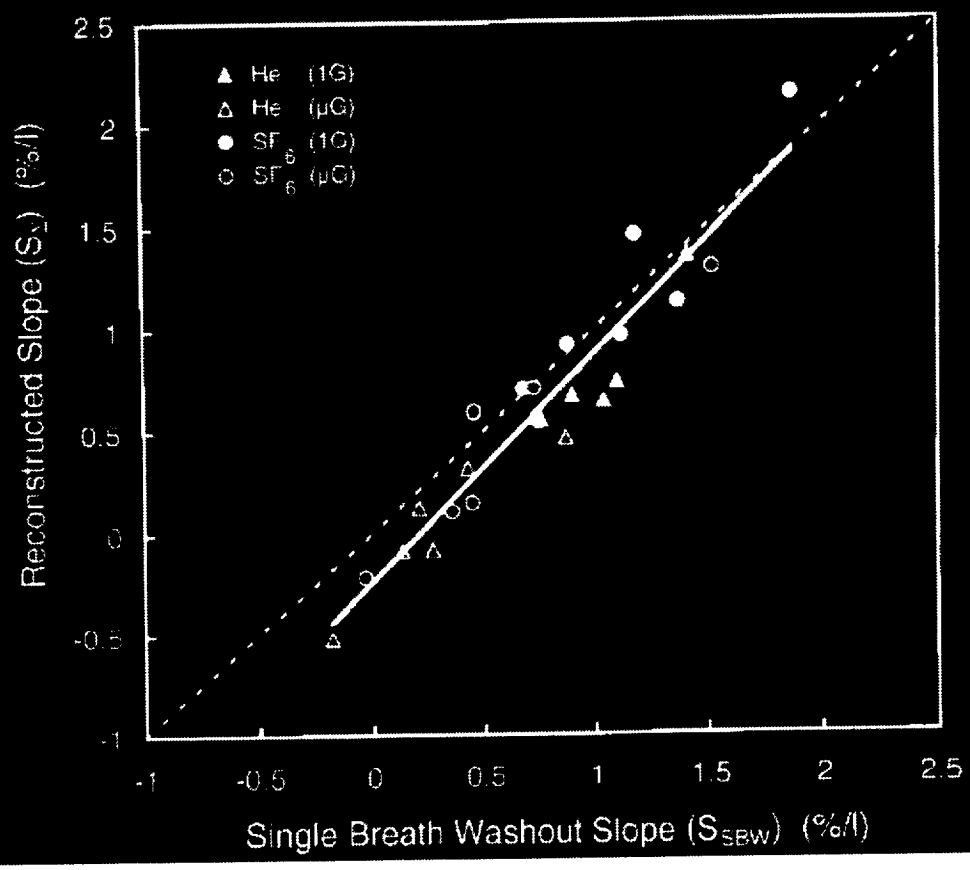

UCSD

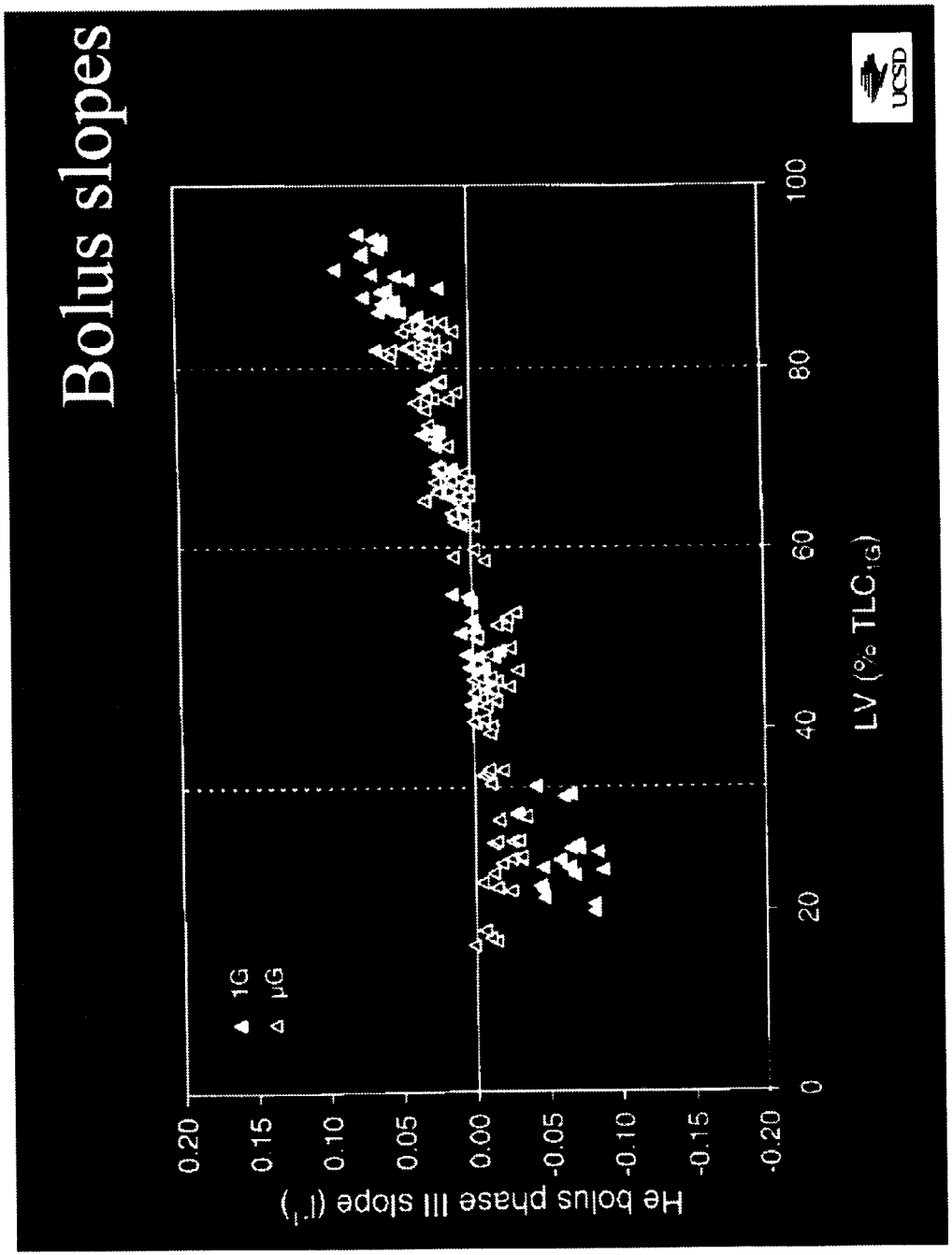
Bolus slopes
1G
μG
He bolus phase III slope (l⁻¹)
0.20
0.15
0.10
0.05
0.00
-0.05
-0.10
-0.15
-0.20
0
20
40
60
80
100
LV (% TLC1G)
UCSD

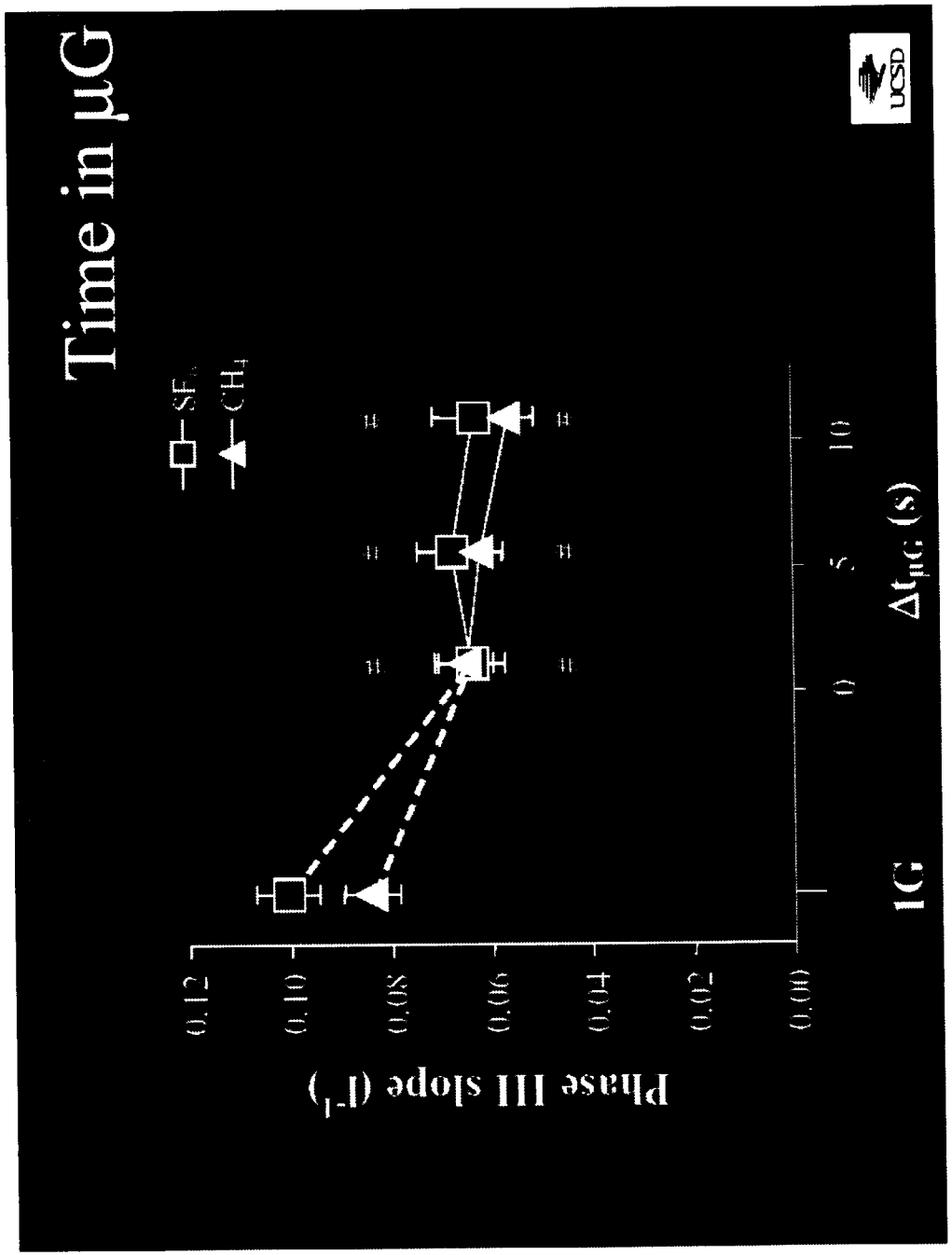
Time in μG
SF6
CH4
Phase III slope (T-1)
0.12
0.10
0.08
0.06
0.04
0.02
0.00
0
5
10
Δtμg (s)
1G
UCSD

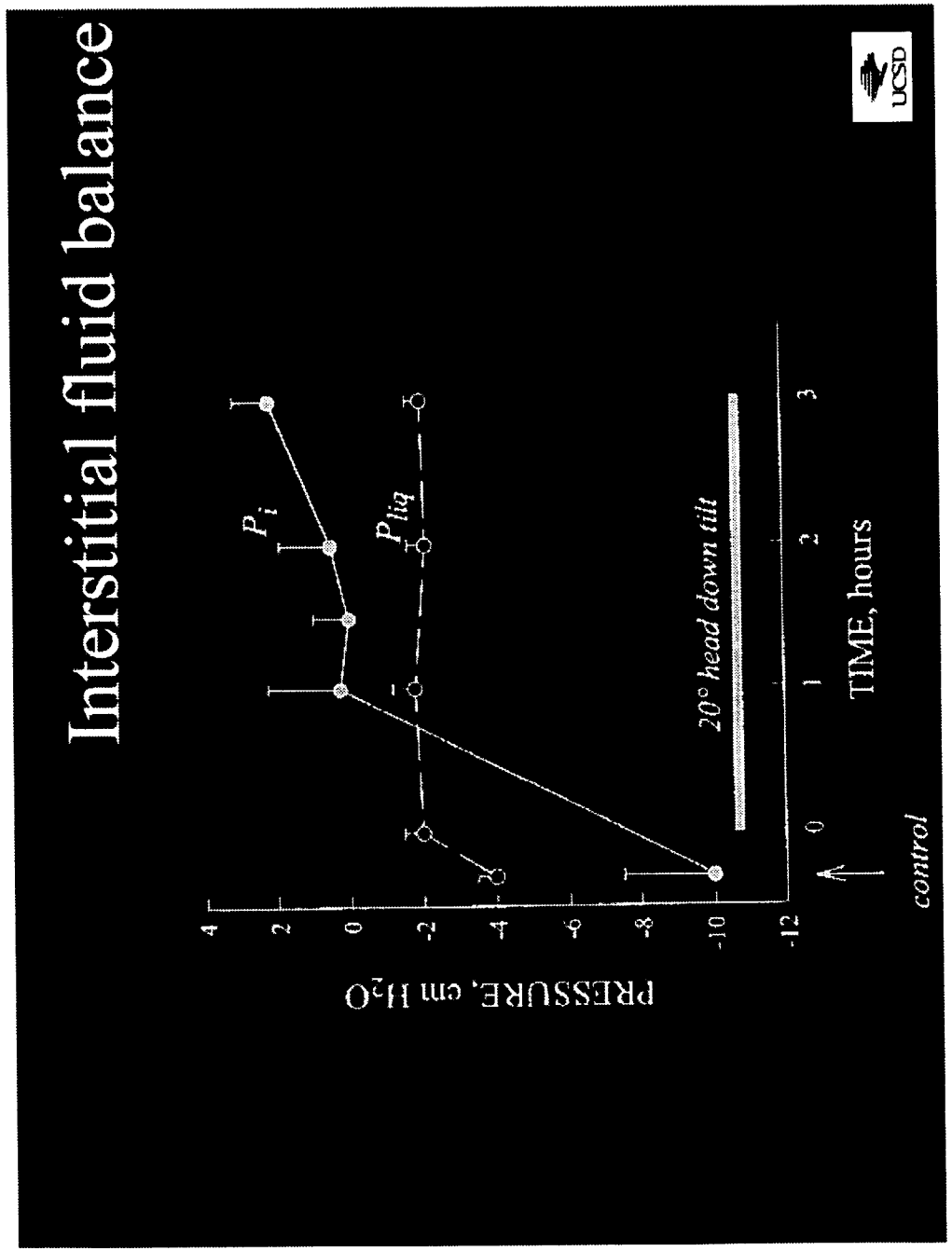
Interstitial fluid balance
PRESSURE, cm H2O
4
2
0
-2
-4
-6
-8
-10
-12
P_i
P_{liq}
20° head down tilt
0
1
2
3
TIME, hours
control
UCSD

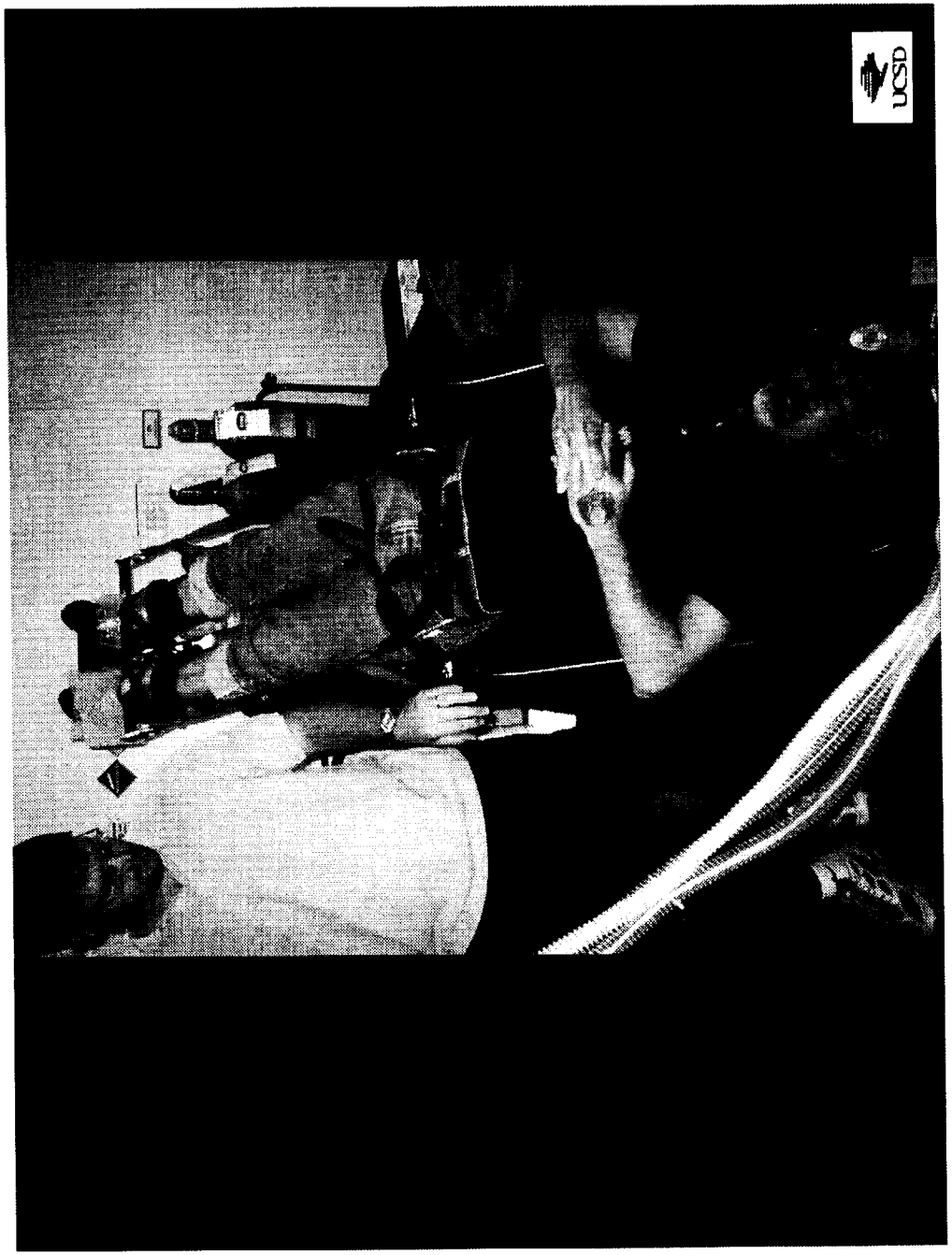
UCSD

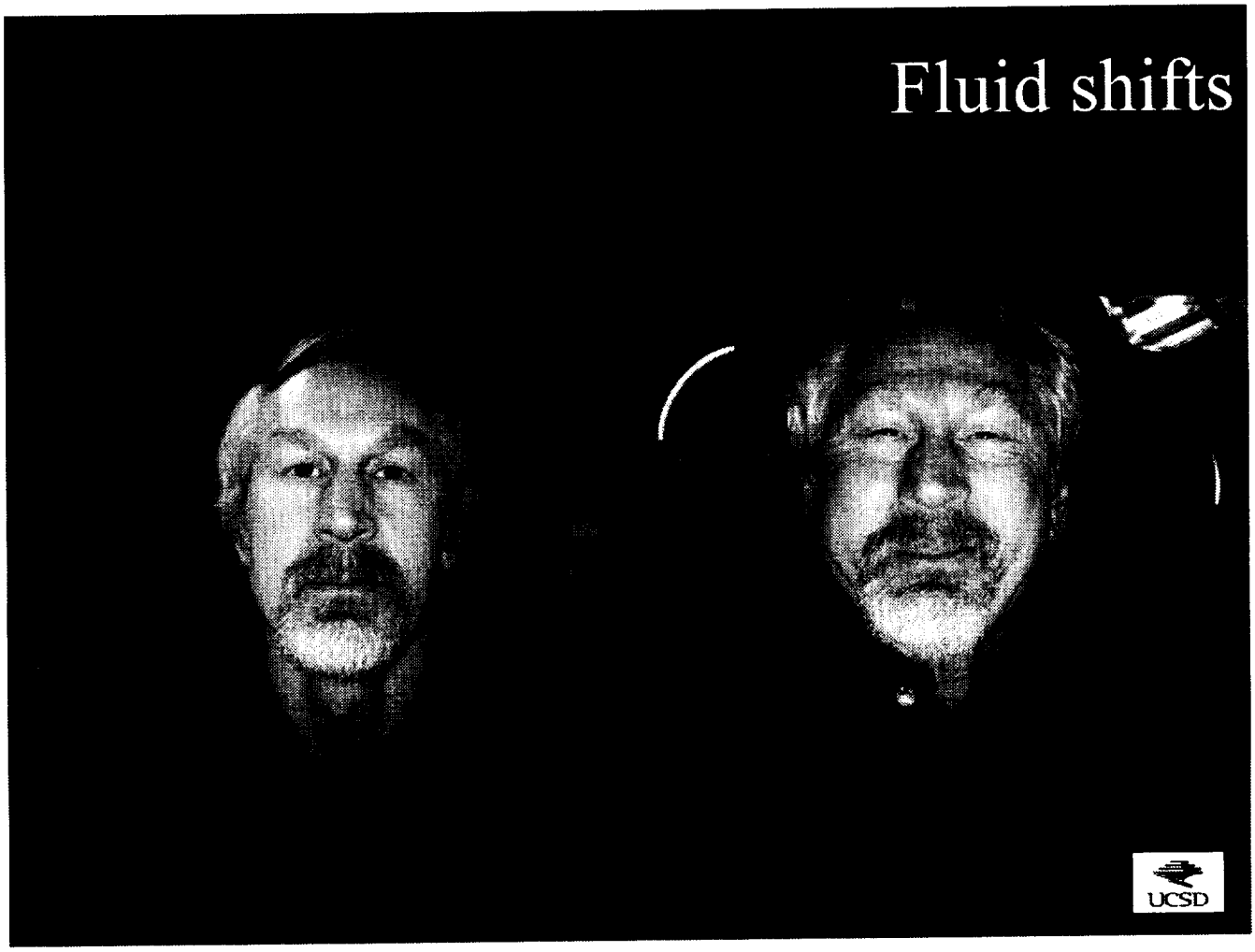
Fluid shifts
UCSD

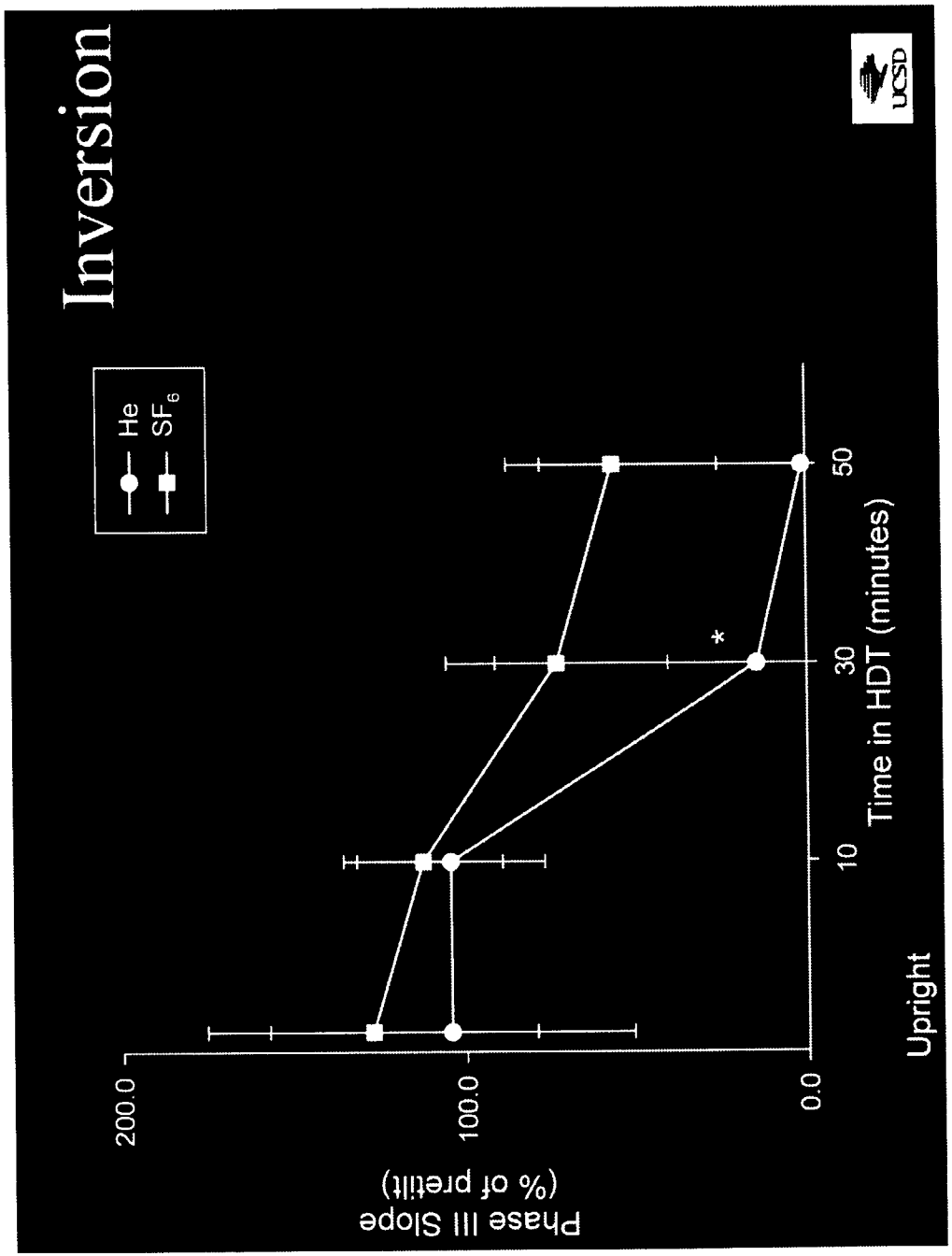
Inversion
He
SF6
200.0
100.0
0.0
Phase III Slope
(% of prefilt)
10
30
50
Time in HDT (minutes)
*
Upright
UCSD

Acinar gas mixing in μG

- In sustained μG, acinar gas mixing is substantially modified compared to 1G
  - Similar effects seen in HLT patients with rejection
  - Mechanism remains undetermined

  - Has a time constant sufficiently long that cannot be seen in transient microgravity

    and/or
  - Events below closing volume are important

  - Interstitial fluid balance may be important

UCSD

Aerosol deposition

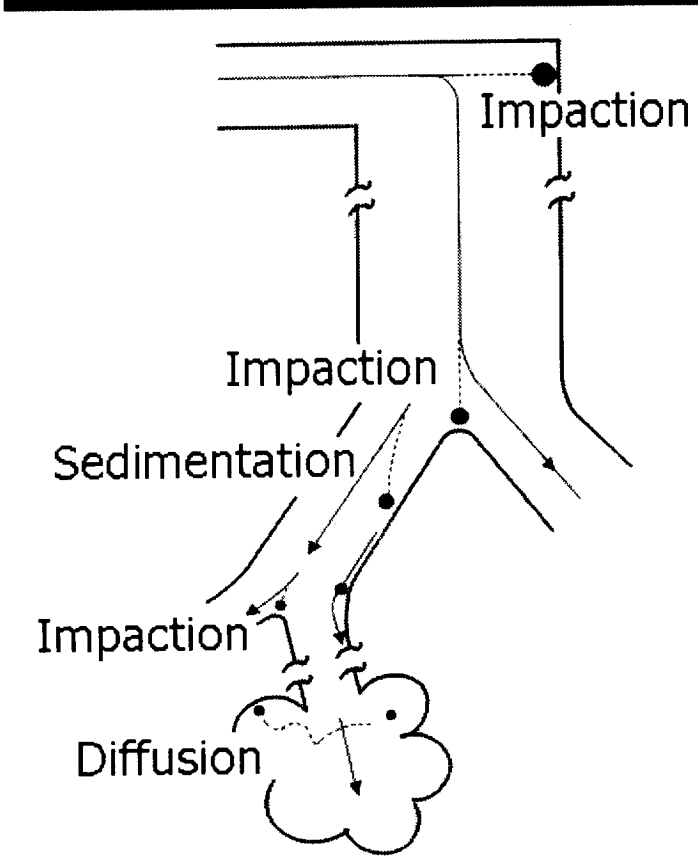

- Impaction: >5 μm
- Sedimentation: 0.5-8 μm
- Diffusion: <0.5 μm

UCSD

Health effects

- PM is a health risk
- Increase in risk of death from both long-term and short-term exposure
- Effects increase with decreasing particle size
  - $PM_{2.5} > PM_{10} > TSP$
- Uncertain mechanism linked to poor understanding of nature, site and magnitude of PM deposition

- Health effects include:
  - premature death
  - increased hospital admissions
  - increased emergency room visits
  - increased respiratory symptoms and disease
  - increased cardiovascular disease
  - decreased lung function
  - alterations of lung tissues and structure
- "At-risk" sub-populations:
  - elderly
  - asthmatics
  - children

UCSD

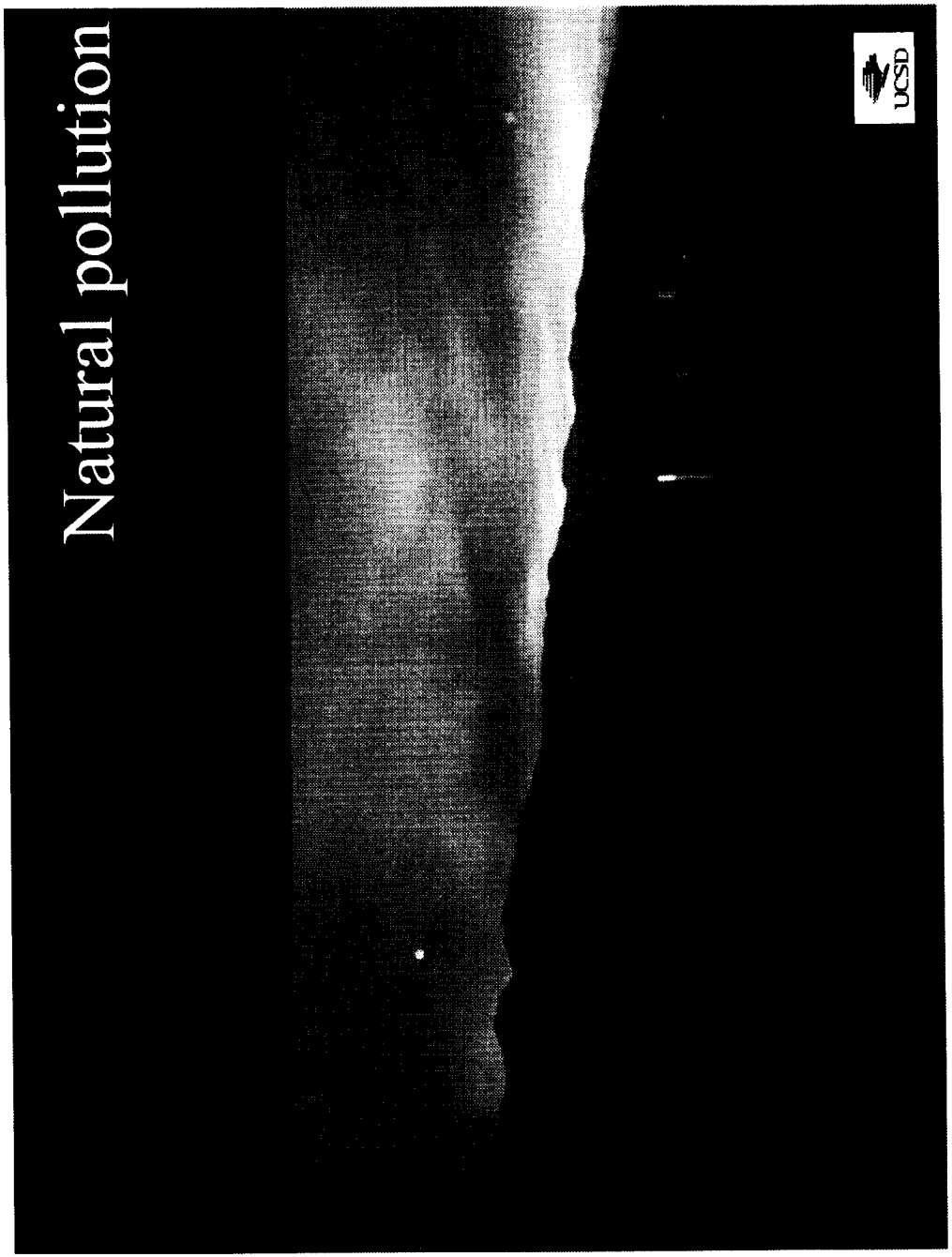
Natural pollution
UCSD

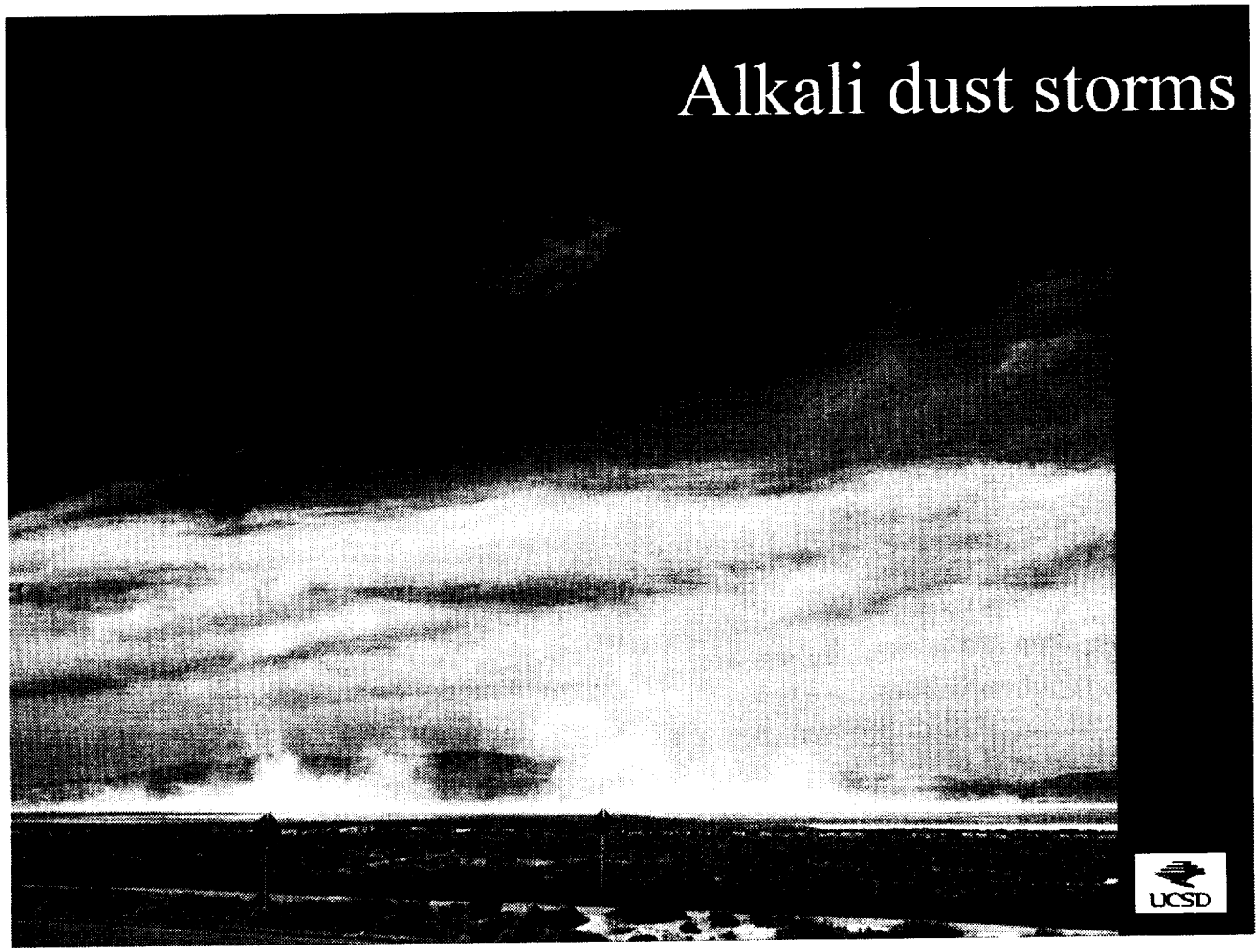
Alkali dust storms
UCSD

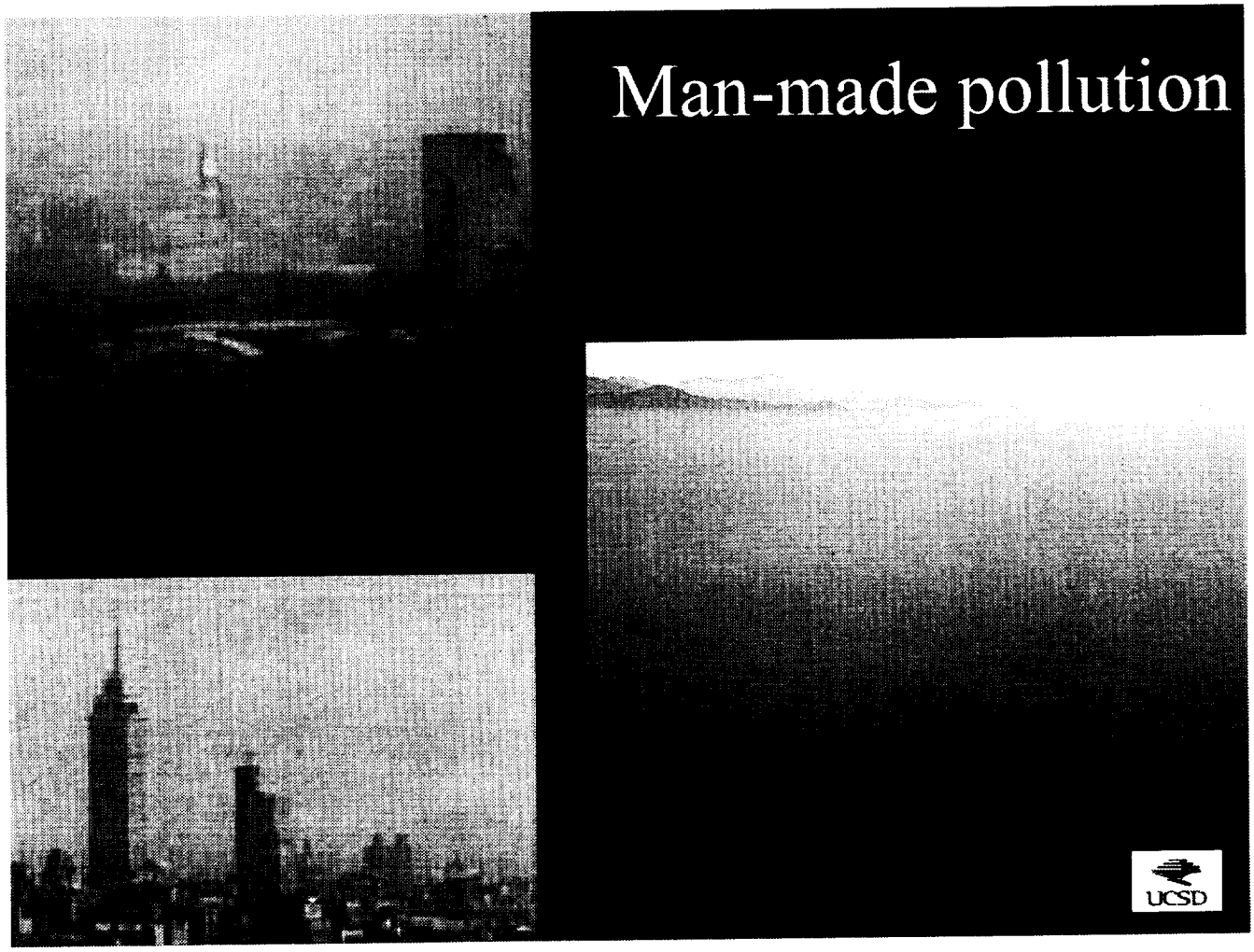
Man-made pollution
UCSD

Great fog of London

FIGURE 1.1

Daily Mean Pollution Concentrations and Daily Numbers of Deaths During the London Fog Episode of 1952

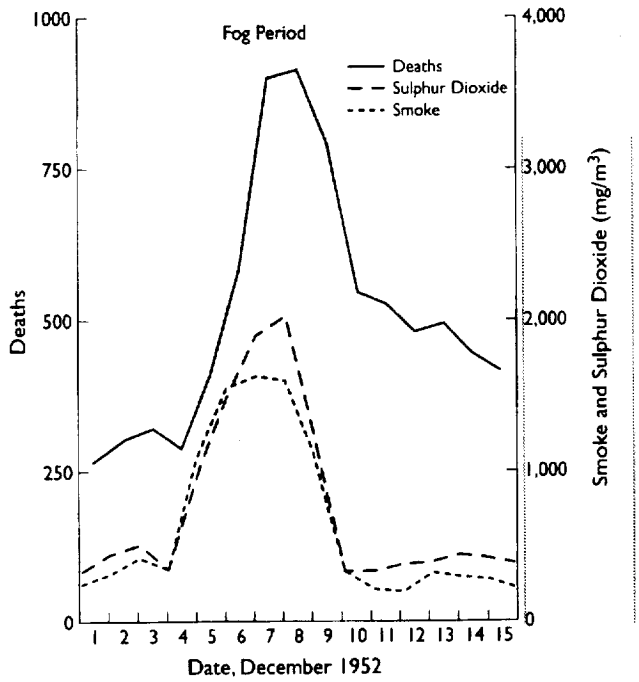

Source: Beaver, 1954

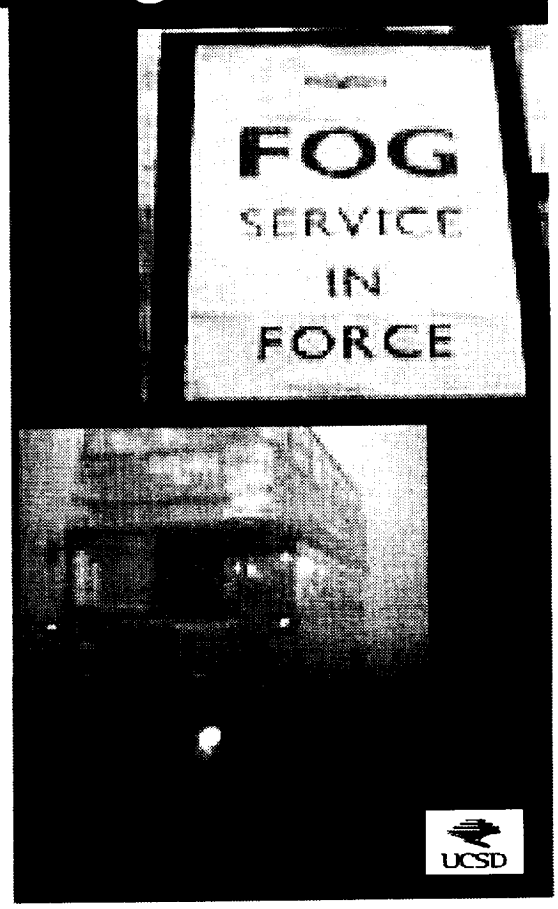

PM standards (EPA)

		Annual average ($\mu g/m^3$)	24h average ($\mu g/m^3$)
1971	TSP (<50 μm)	75	260
1987	PM_{10} (<10 μm)	50	150
1998	$PM_{2.5}$ (<2.5 μm)	15	65

UCSD

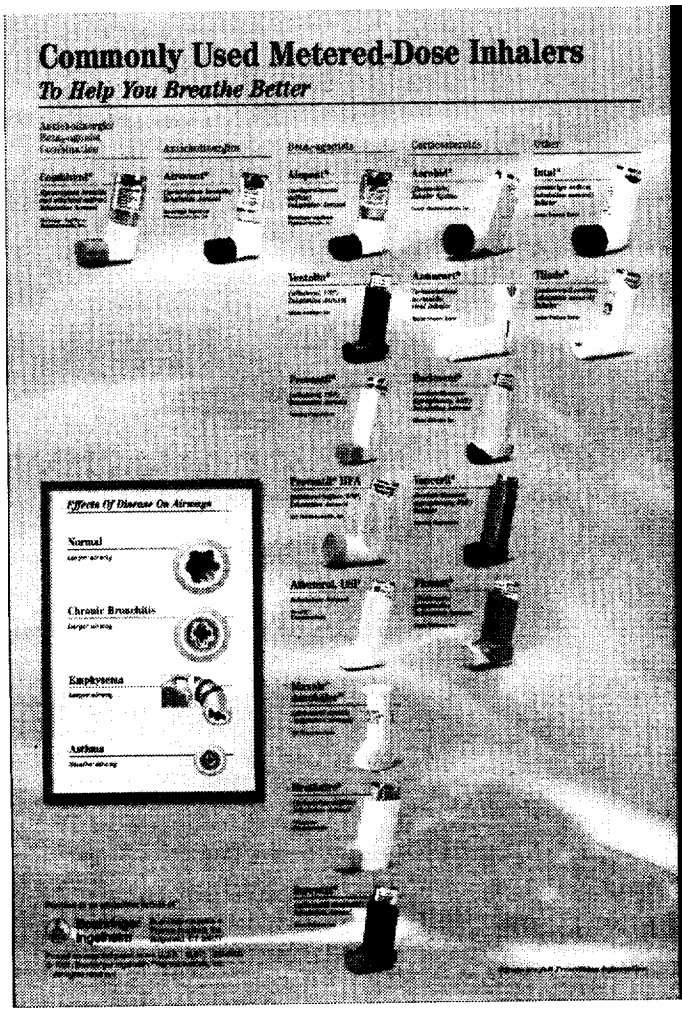

Drug delivery to the lungs

UCSD

Inhaled drugs

- β_2 agonist effect is enhanced if delivered to intended site of action (Lawrence and Patterson, *Adv. Intern. Med.* 1990).
- Inhaled corticosteroids in the upper airways are associated with fungal infections, hoarseness and cough (Konig, *J. Allergy Clin. Immunol.*, 1988).
- Drugs with systemic effects (e.g. pentamadine or ergotamine) should be delivered to the alveolar region of the lung, with minimum deposition in other regions (Hiller, In *Pharmaceutical inhalation aerosol technology*, 1992).

UCSD

Inhaled insulin

- Aerosolized insulin in testing (Cefalu. *Am. J. Respir. Crit. Care Med.* 2001.)
- Exubera (Pfizer)
  - dry powder formulation
  - effective blood sugar control
  - only 10-15% of delivered insulin is absorbed
- Could "spatial targeting" of delivery improve efficacy?

UCSD

Atmospheric contamination

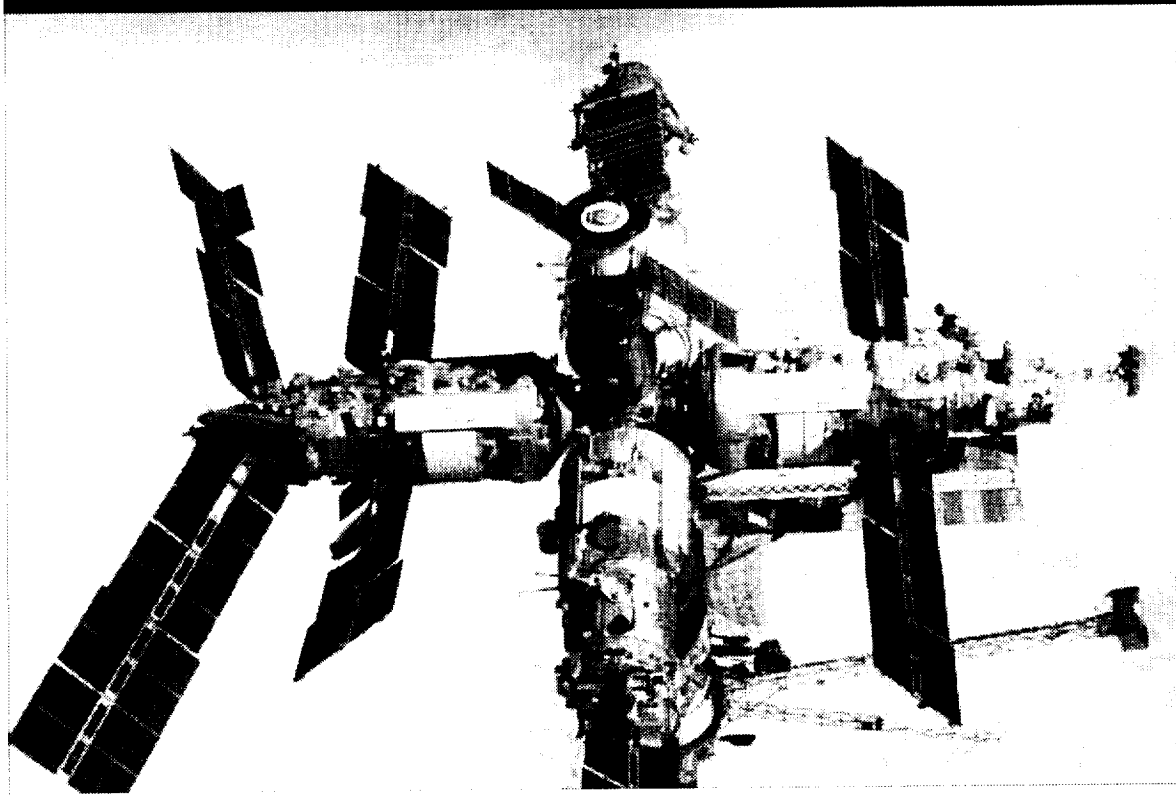

UCSD

Confined environments

UCSD

Mars dust

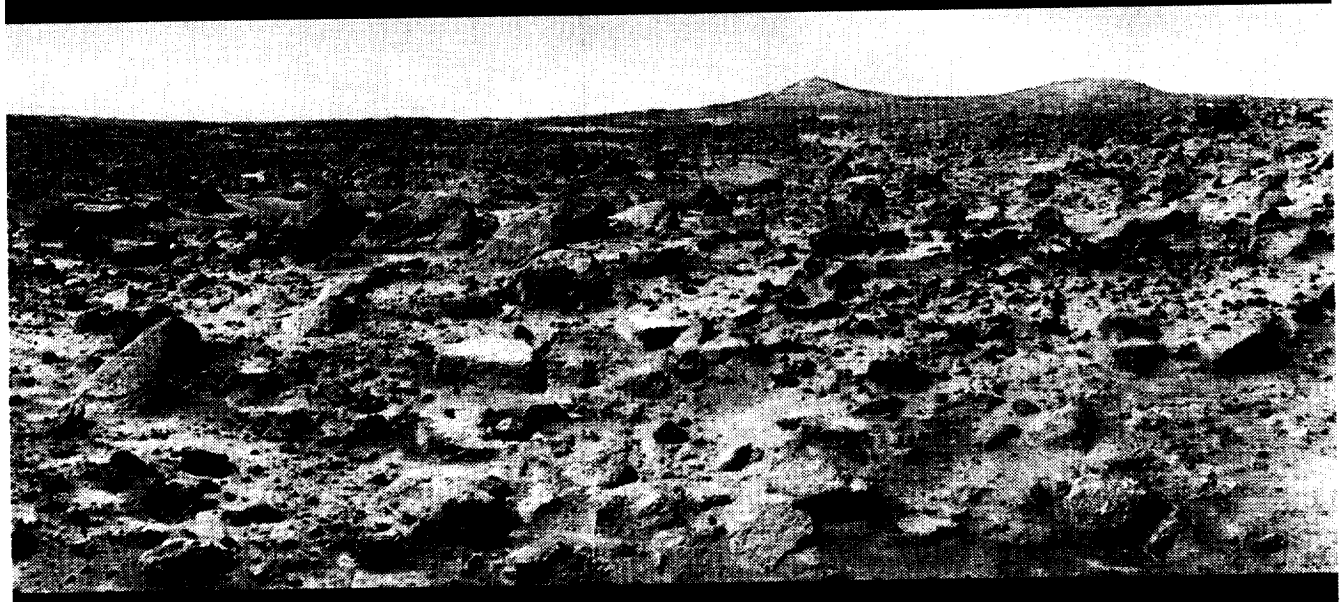

UCSD

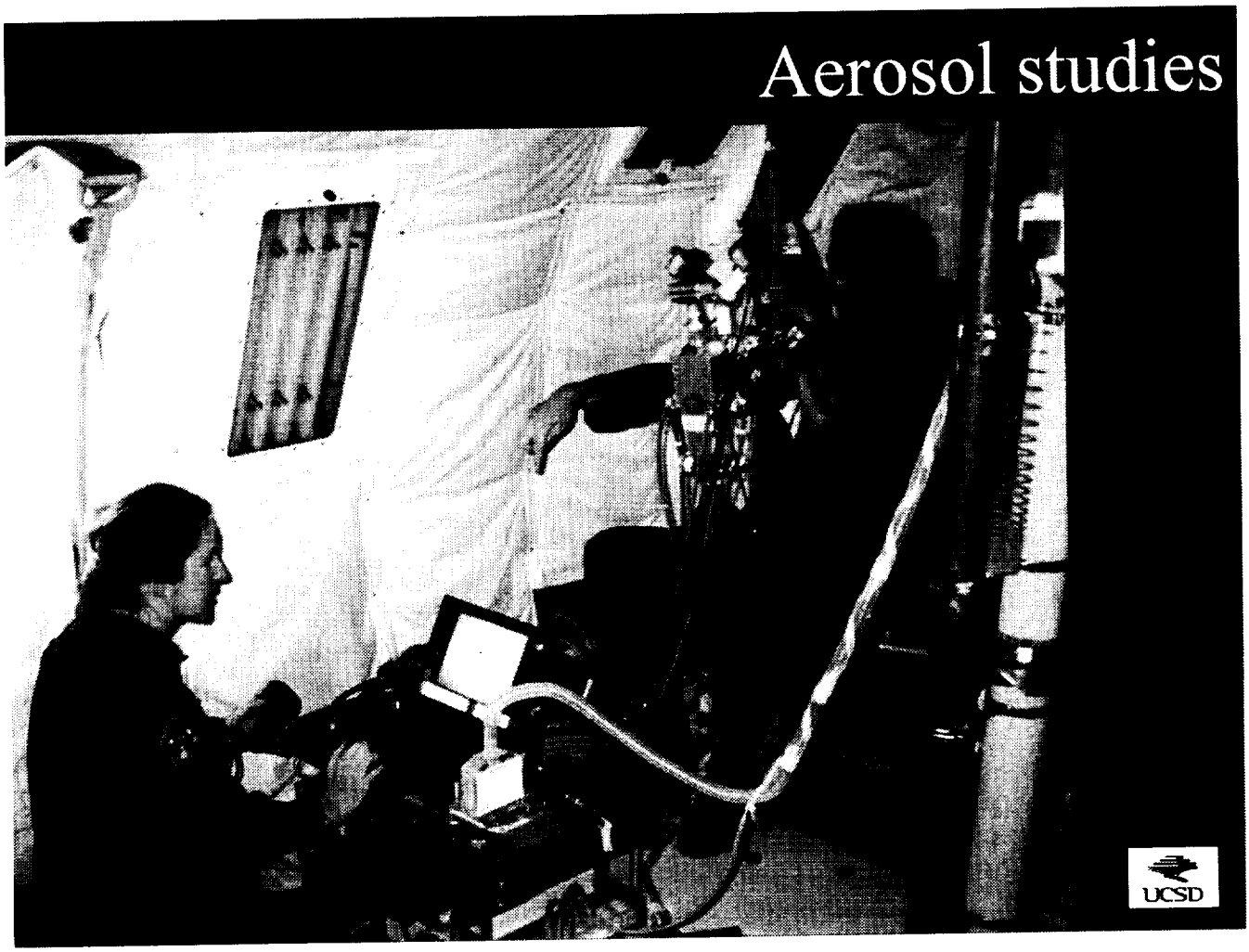
Aerosol studies
UCSD

Total deposition

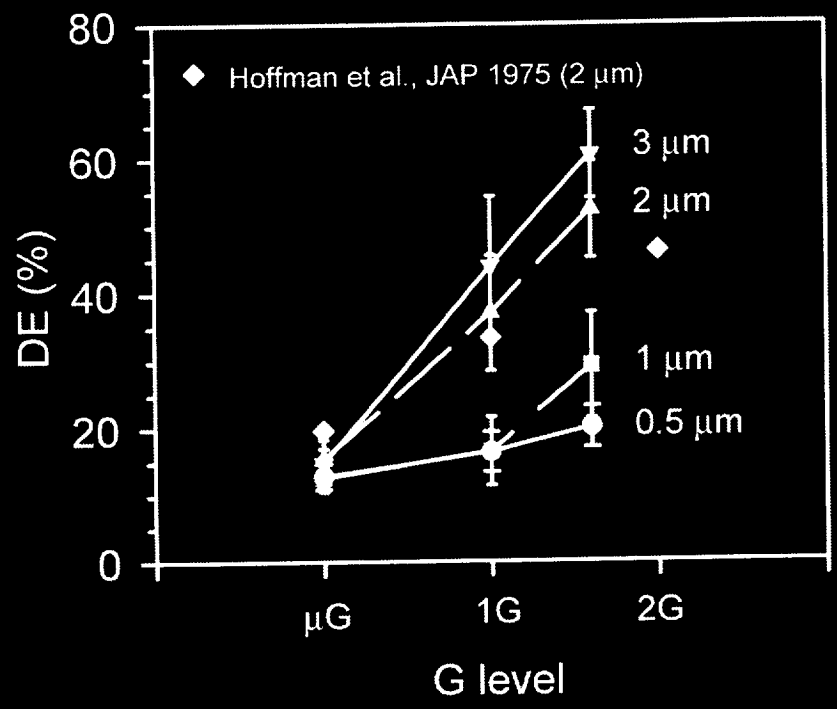

UCSD

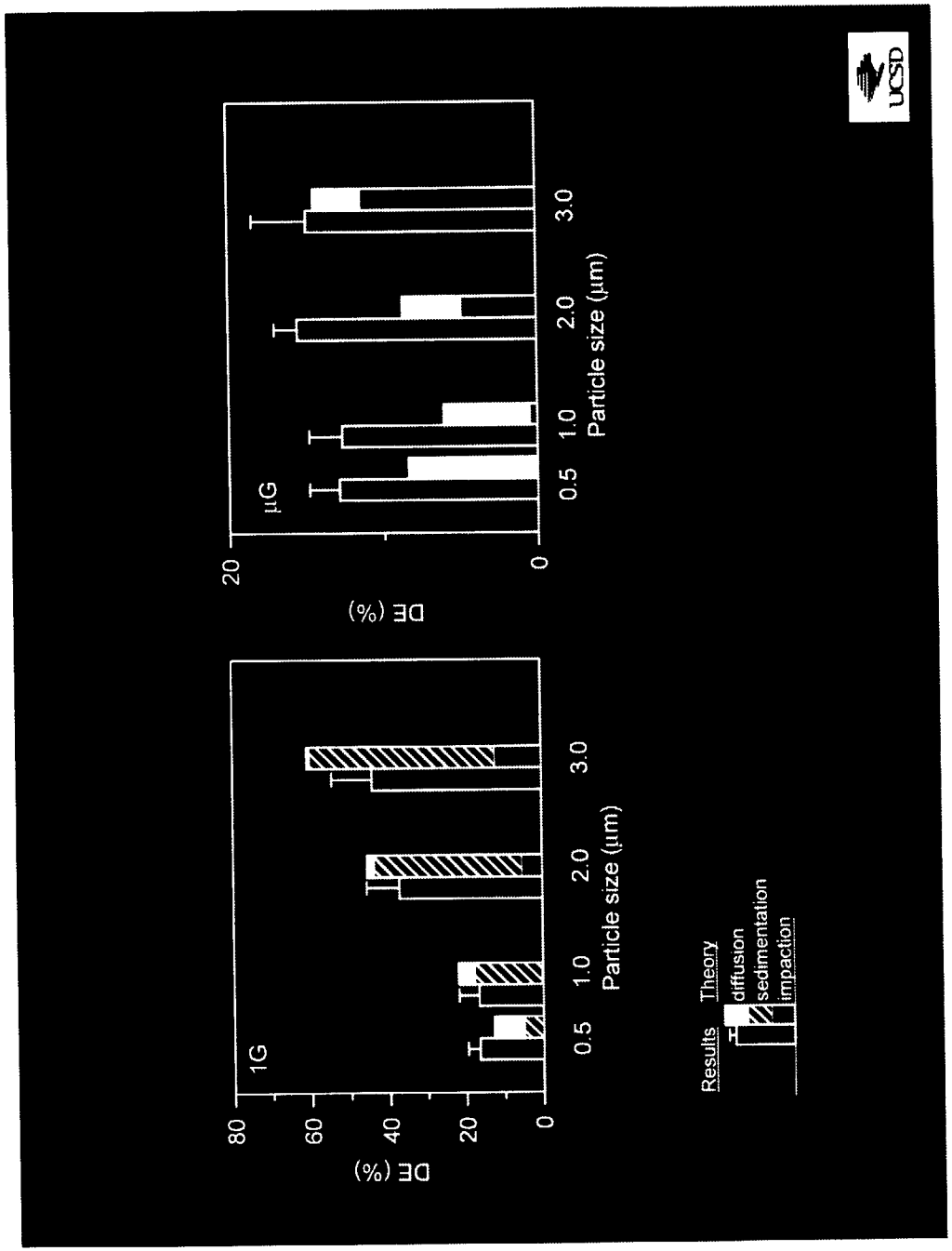
1G
DE (%)
80
60
40
20
0
0.5
1.0
2.0
3.0
Particle size (µm)
µG
DE (%)
20
0
0.5
1.0
2.0
3.0
Particle size (µm)
Results
Theory
diffusion
sedimentation
impaction
UCSD

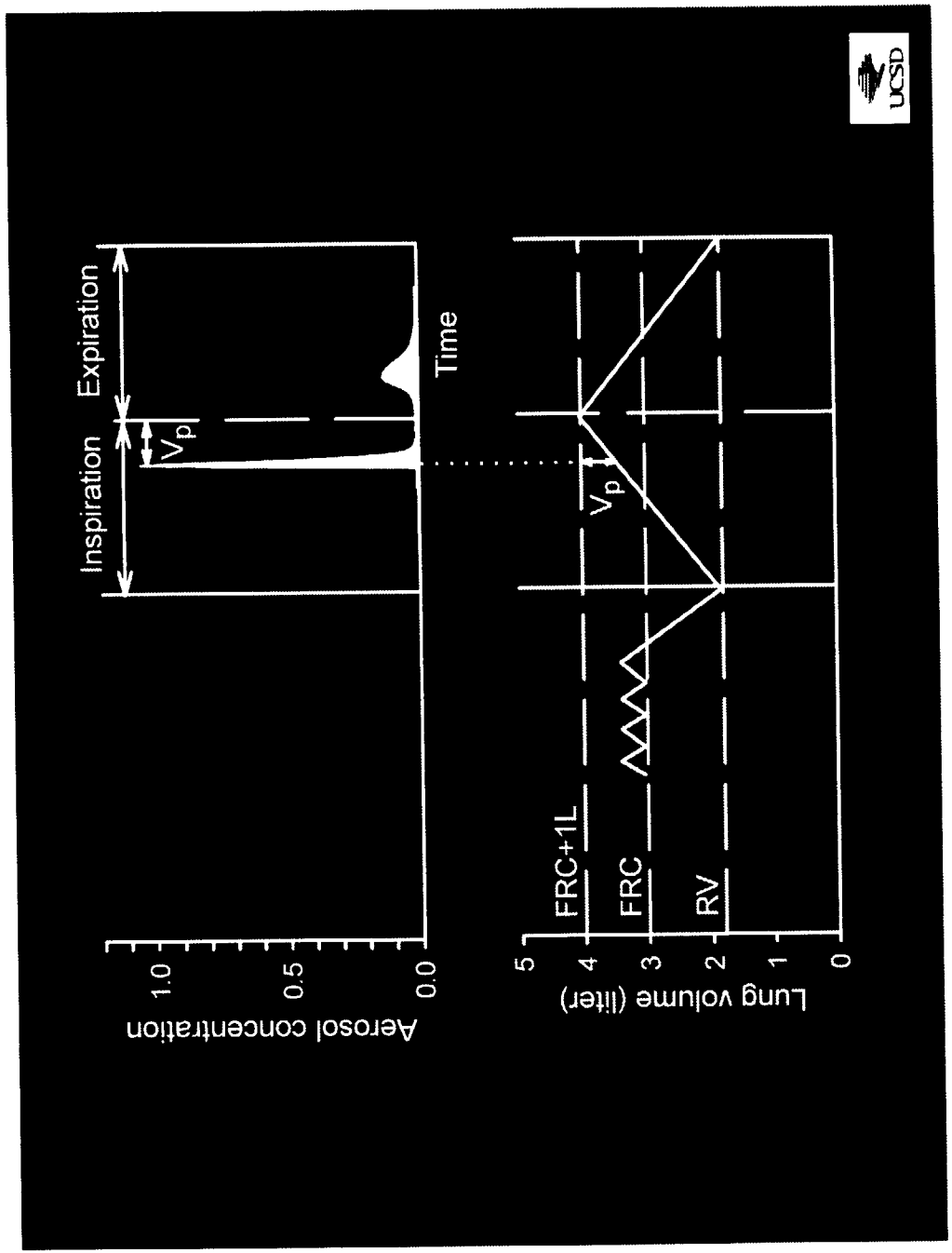
Inspiration
Expiration
V_p
Aerosol concentration
1.0
0.5
0.0
Time
Lung volume (liter)
5
4
3
2
1
0
FRC+1L
FRC
RV
V_p
UCSD

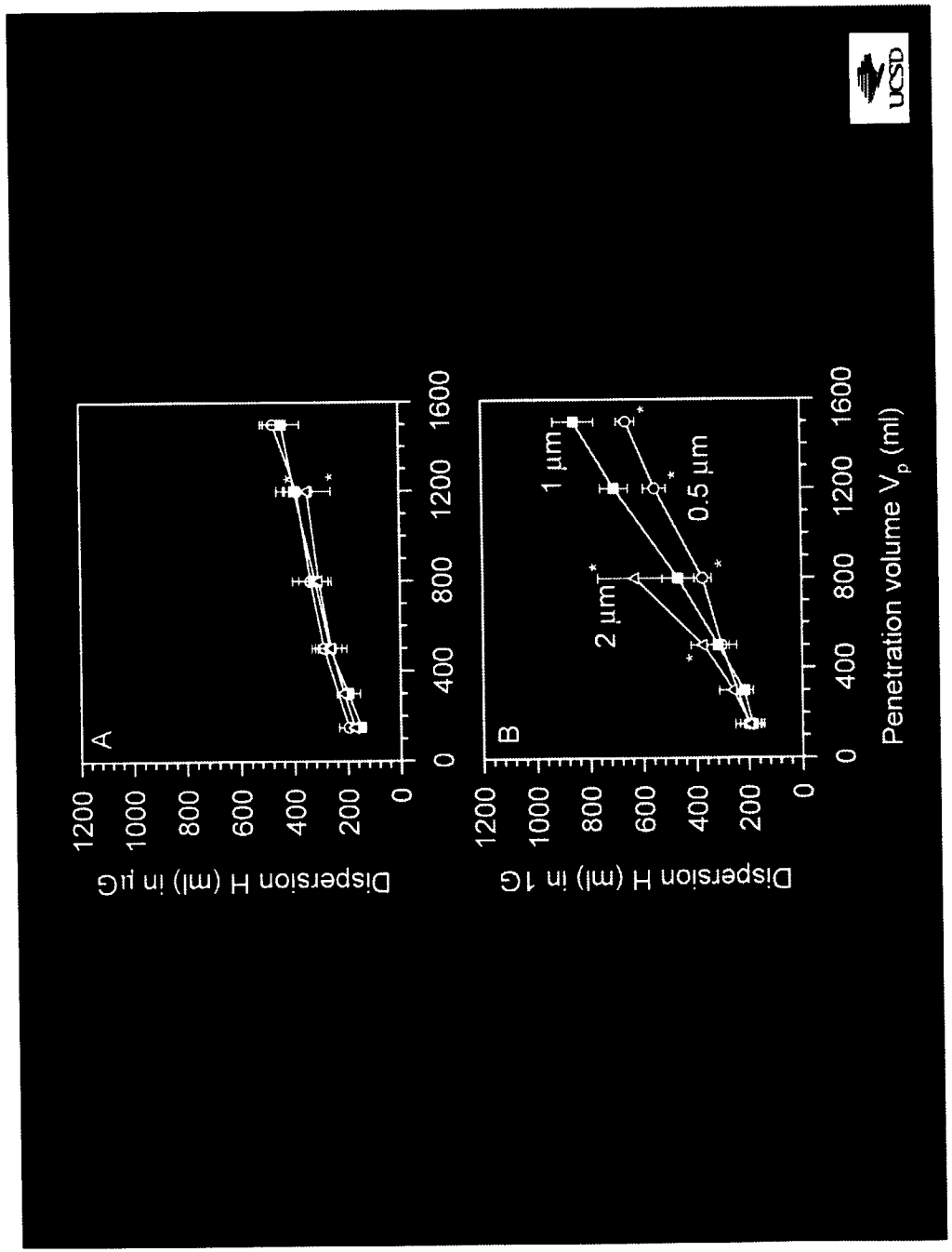
A
Dispersion H (ml) in μG
1200
1000
800
600
400
200
0
0
400
800
1200
1600
B
Dispersion H (ml) in 1G
1 μm
2 μm
0.5 μm
Penetration volume V_p (ml)
UCSD

Aerosols in μG

- Deposition unexpectedly high for small particles
  - Small aerosol particles are implicated in adverse health effects of pollutants
  - Suggests transport mechanism(s) that have been previously ignored
- Bolus dispersion shows persisting inhomogeneity in μG
  - Aerosol behaves as a non-diffusing gas
  - Consistent with gas mixing studies

UCSD

Mechanisms of enhanced deposition

- Diffusion
  - Characteristic diffusion distances only ~ 13μm for a 1μm sized particle, a small effect
  - Cardiogenic effects are small in the periphery
- Complex flow mixing
- Irreversible transport
  - Bifurcating geometry results in non-reversible flow with a net transport of particles towards the periphery

UCSD

Stretch & Fold – Theory

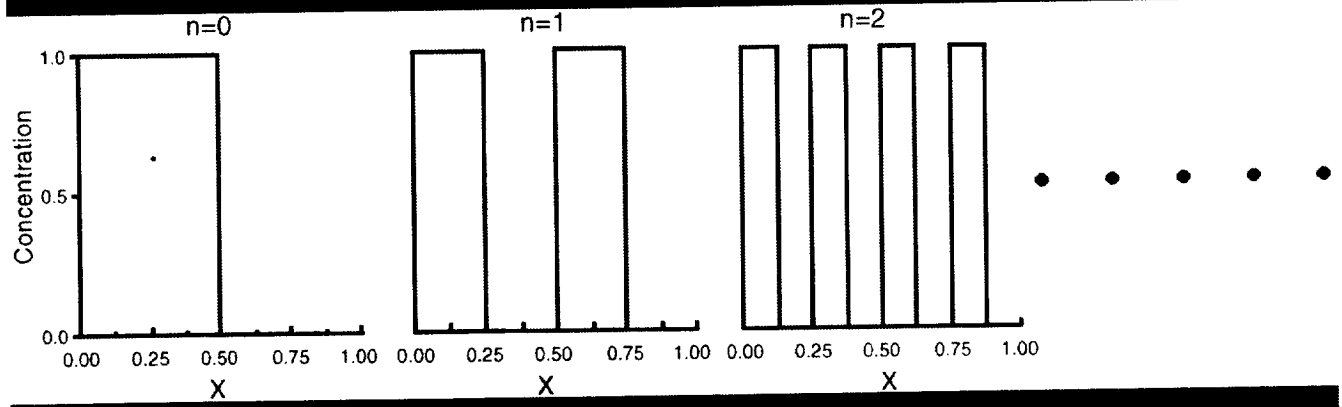

Butler and Tsuda

J. Appl. Physiol. 83: 800-809, 1997

UCSD

Stretch & Fold + Diffusion

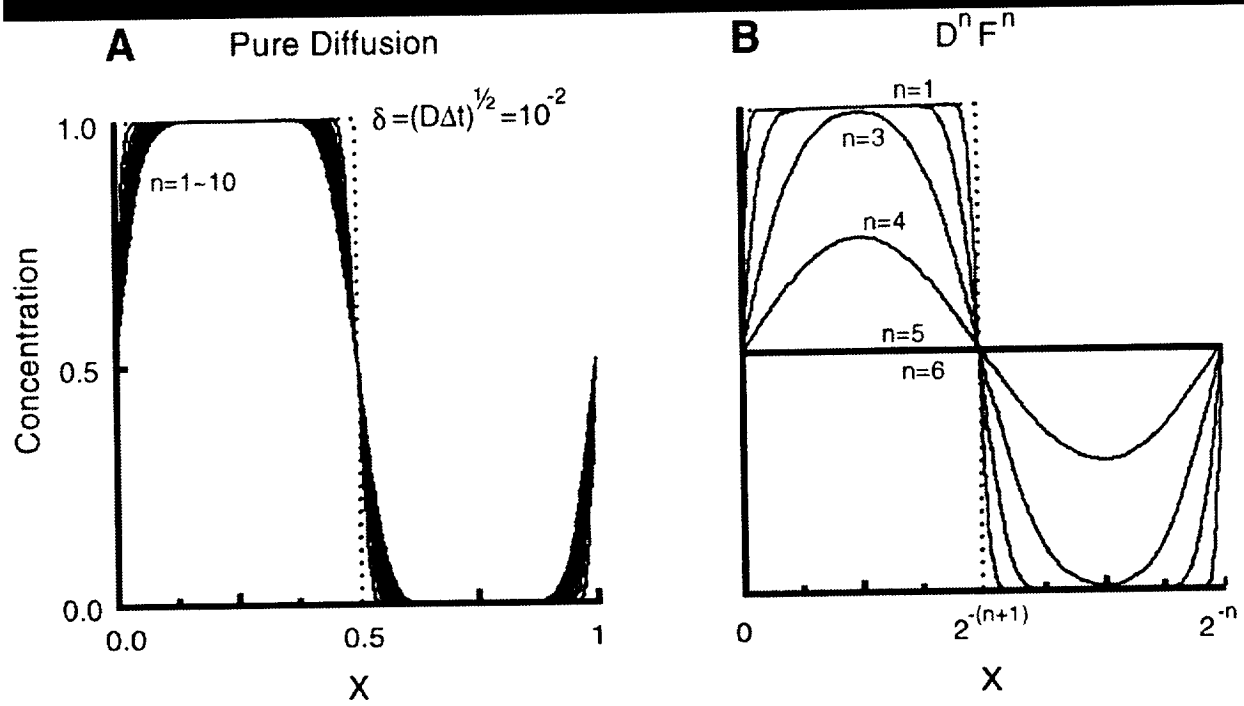

Butler and Tsuda
J. Appl. Physiol. 83: 800-809, 1997

Streamline mixing

$\phi = 5^{\circ}$

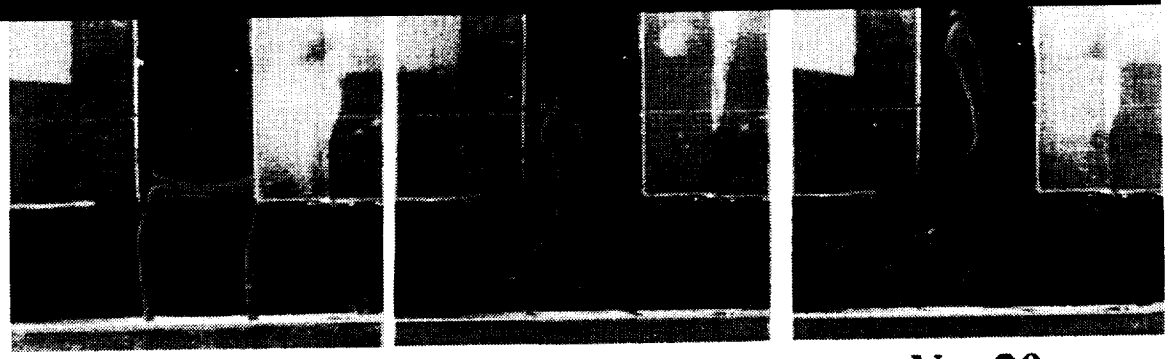

$N = 0$ $N = 8$ $N = 20$

Tsuda et al *J. Appl Physiol.* 86: 977-984, 1999

UCSD

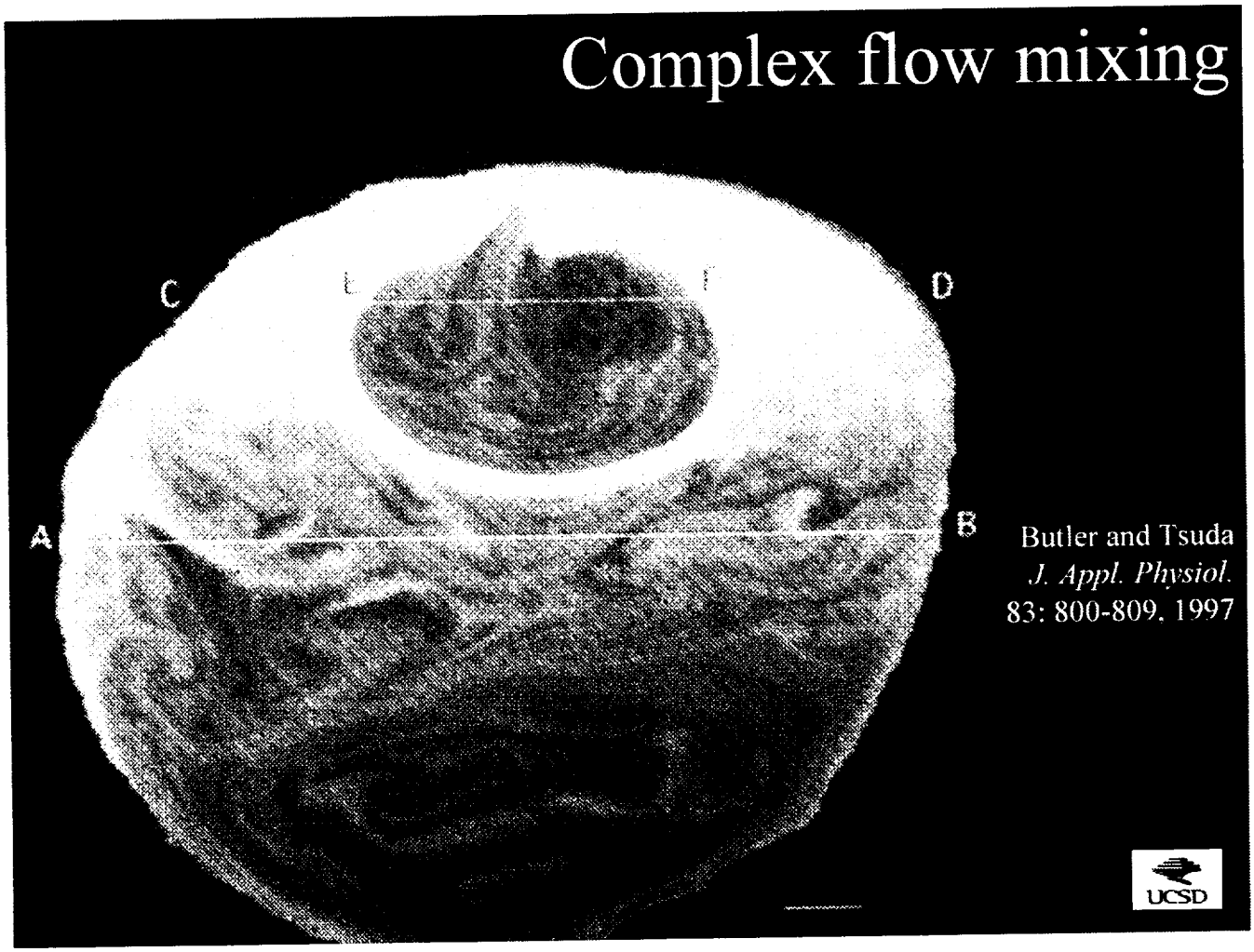
Complex flow mixing
C
D
A
B
Butler and Tsuda
J. Appl. Physiol.
83: 800-809, 1997
UCSD

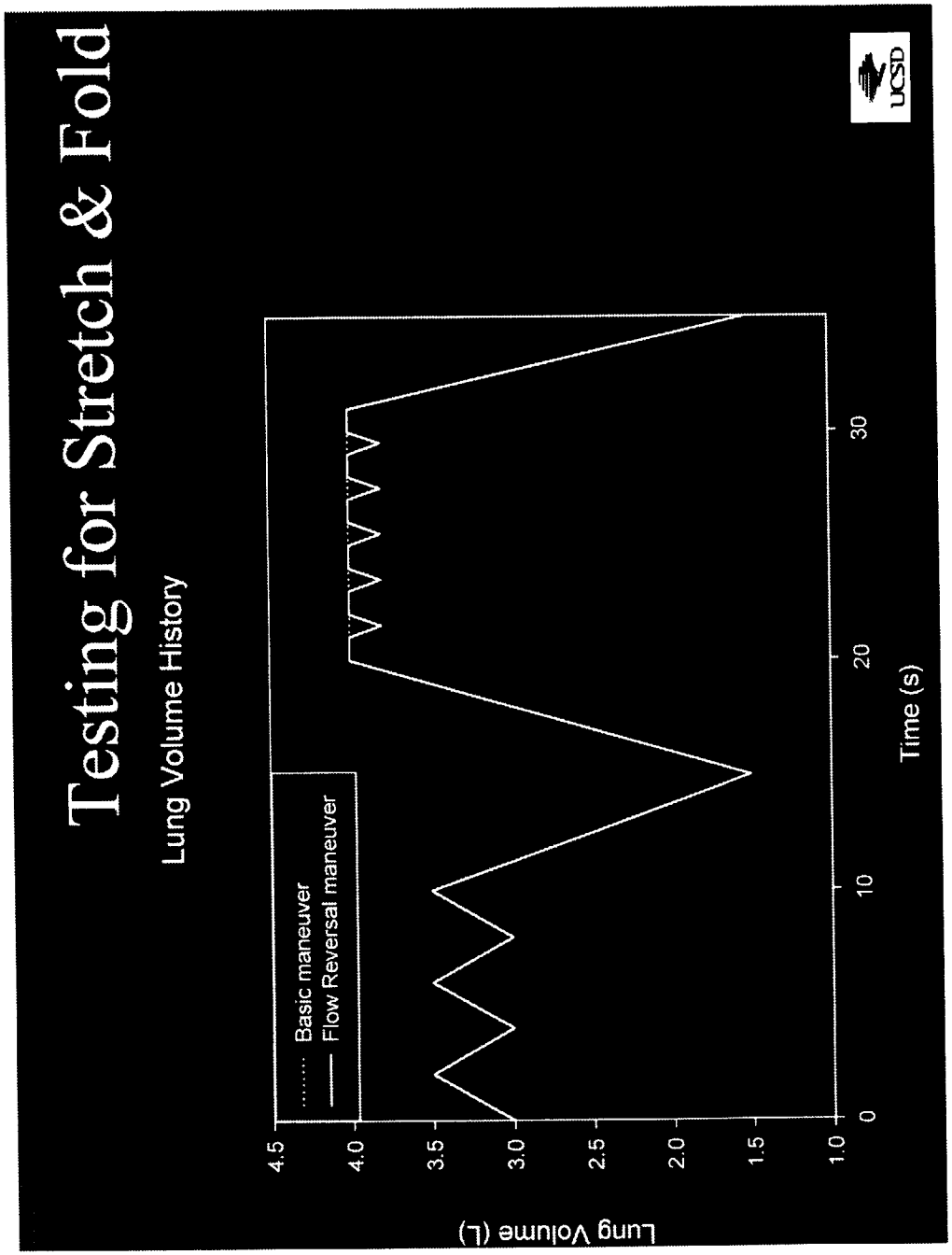
Testing for Stretch & Fold
Lung Volume History
Basic maneuver
Flow Reversal maneuver
Lung Volume (L)
4.5
4.0
3.5
3.0
2.5
2.0
1.5
1.0
0
10
20
30
Time (s)
UCSD

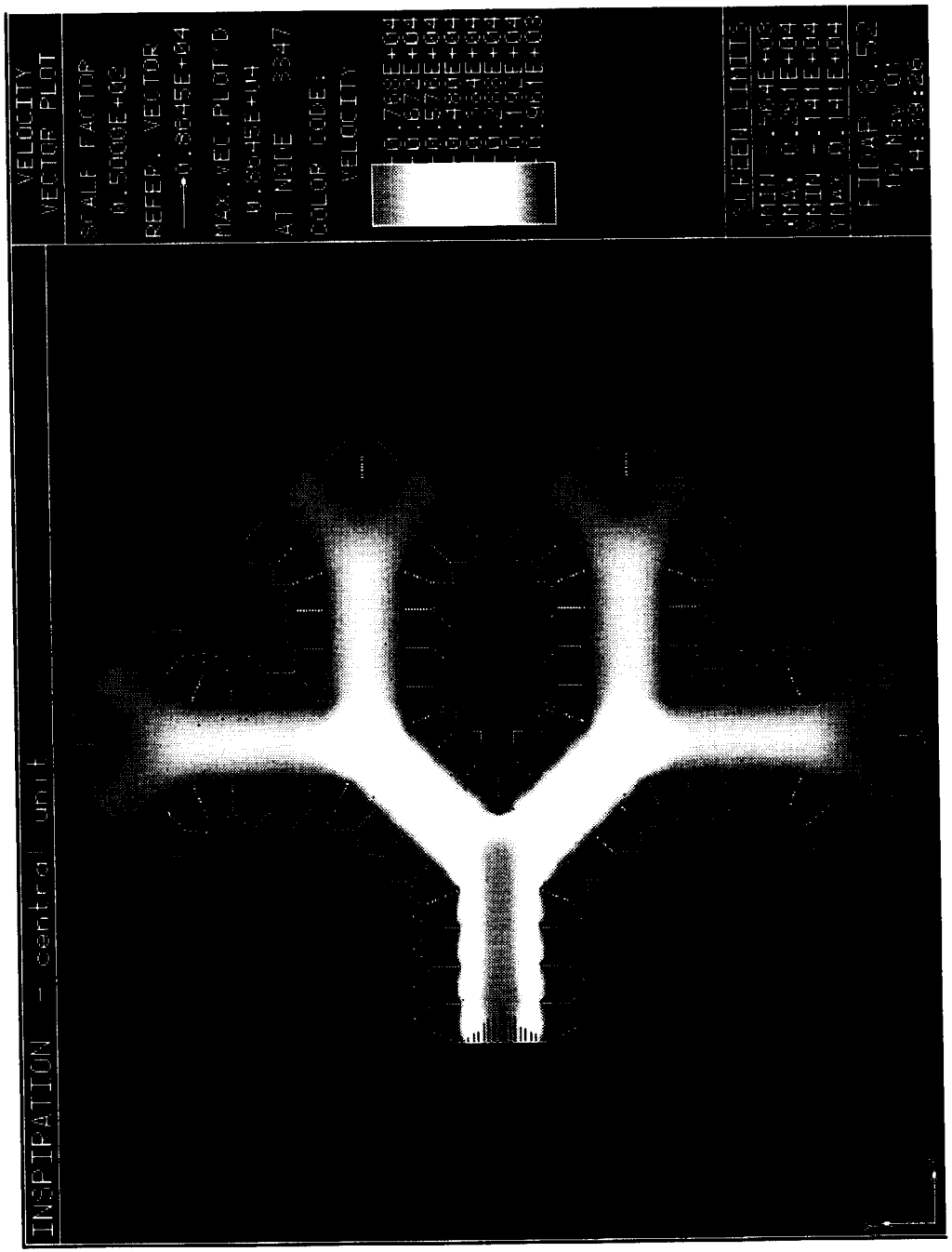
VELOCITY
VECTOR PLOT
SCALE FACTOR
0.5000E+02
REFER. VECTOR
0.8645E+04
MAX.VEC.PLOT'D
0.8645E+04
AT NODE 3347
COLOR CODE:
VELOCITY
0.768E+04
0.672E+04
0.576E+04
0.480E+04
0.384E+04
0.288E+04
0.192E+04
0.961E+03
SCREEN LIMITS
XMIN -.564E+03
XMAX 0.261E+04
YMIN -.141E+04
YMAX 0.141E+04
FIDAP 8.52
16 May 01
14:39:26
INSPIRATION - central unit

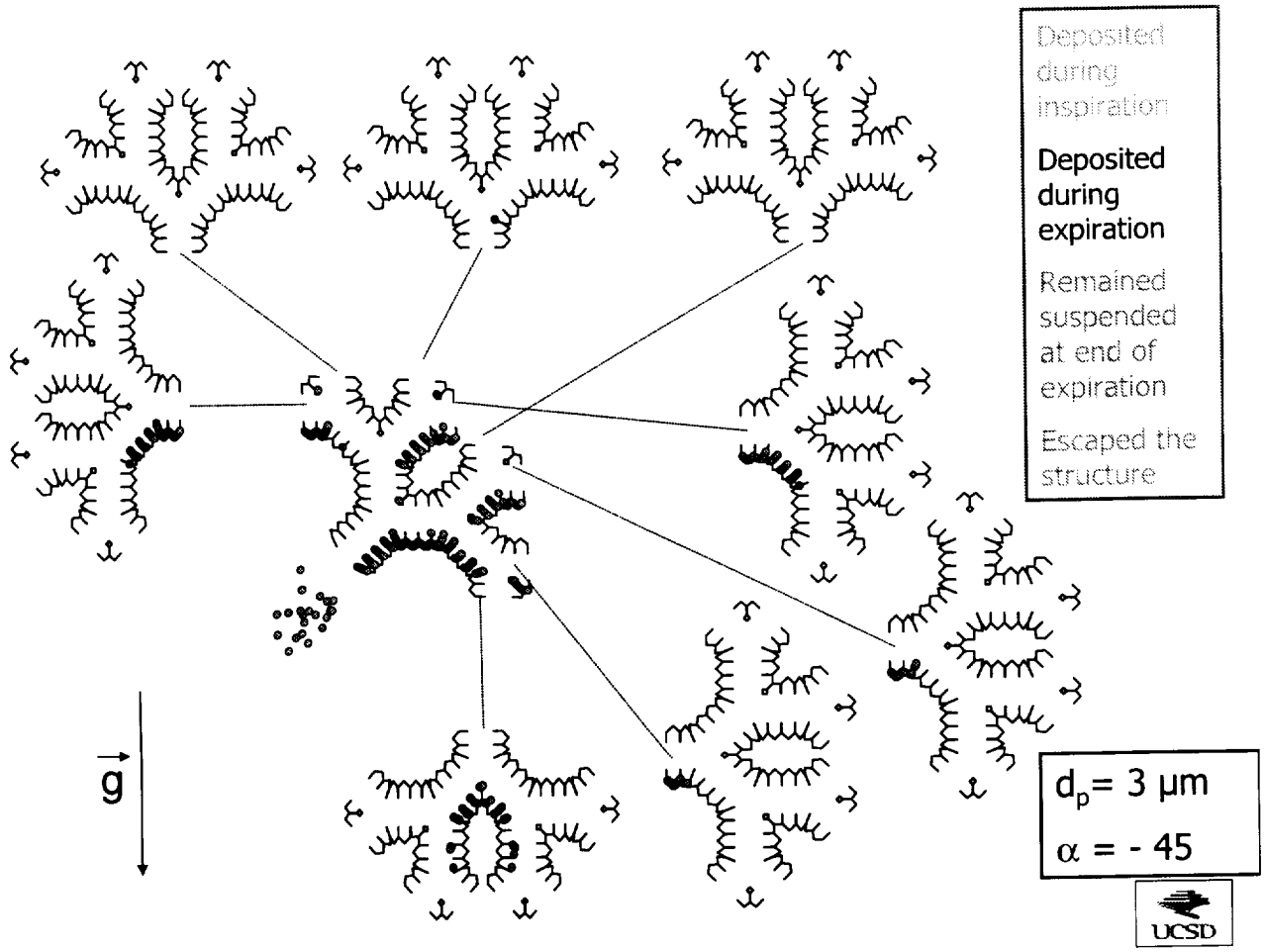
Deposited during inspiration
Deposited during expiration
Remained suspended at end of expiration
Escaped the structure
d_p= 3 μm
α = - 45
g
UCSD

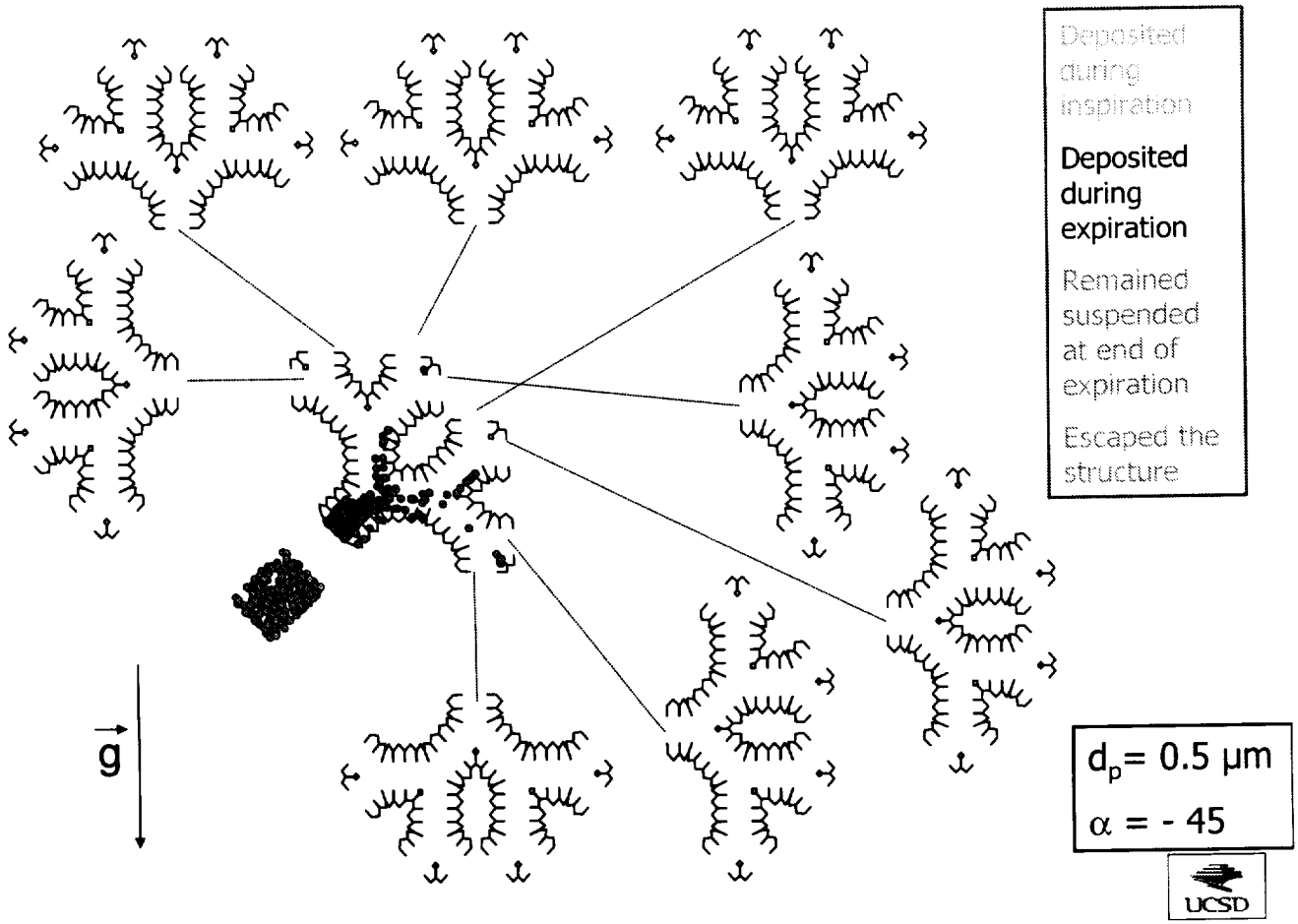
Deposited during inspiration
Deposited during expiration
Remained suspended at end of expiration
Escaped the structure
d_p= 0.5 μm
α = - 45
g
UCSD

Deposition in a 2-D structure

- For larger particles (3 and 5 μm) deposition is efficient and as expected
- For small particles (0.5 and 1 μm) many particles remain suspended within the structure after a complete breath cycle
  - These particles are transported peripherally during subsequent breaths where they <u>eventually deposit</u>

UCSD

Surface tension, viscosity and airway opening

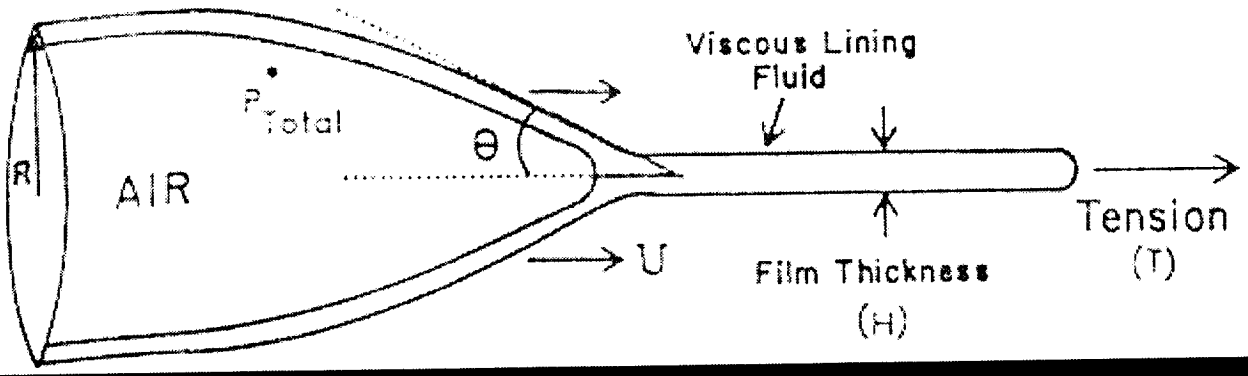

Gaver et al

J. Appl. Physiol.

69: 74 - 85, 1990

UCSD

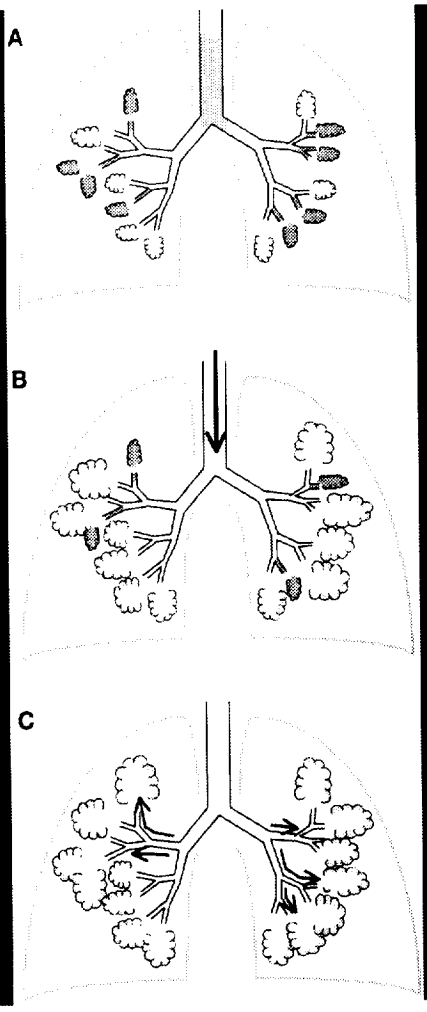

Sufactant dispersal in the lung

Espinosa & Kamm

J. Appl. Physiol.

86: 391-410, 1999

UCSD

Surfactant and airway reopening

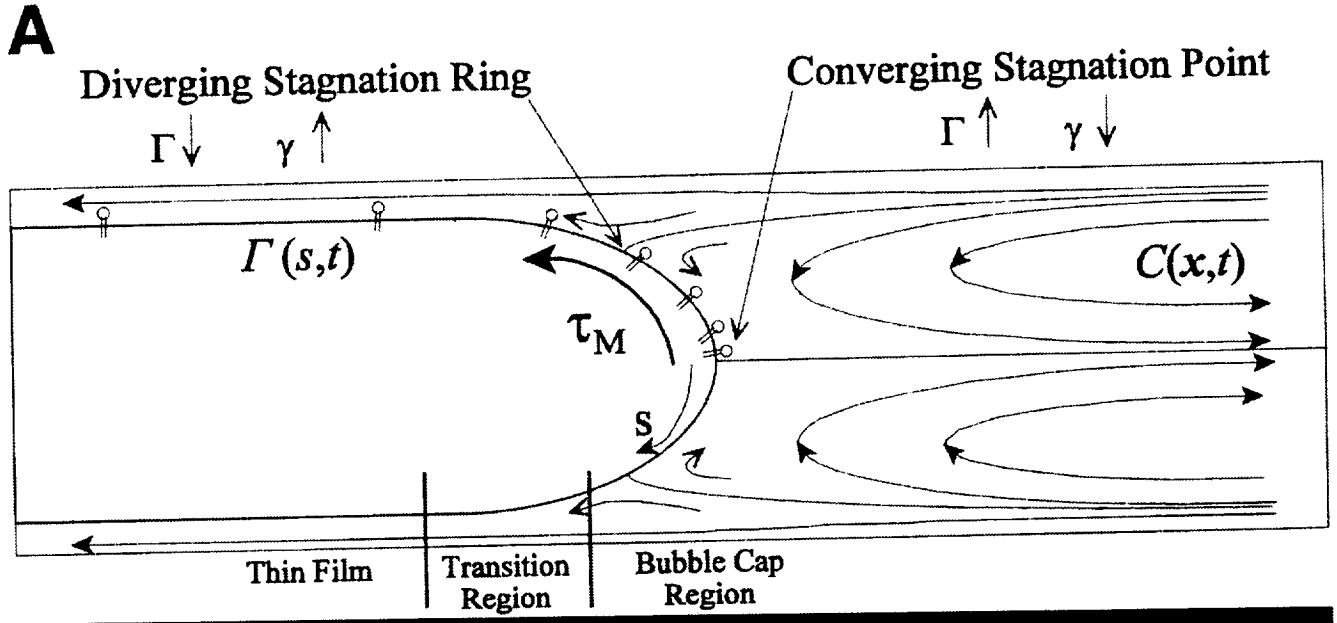

Ghadiale & Gaver

J. Appl. Physiol.

88: 493-506, 2000

UCSD

Capillary recruitment

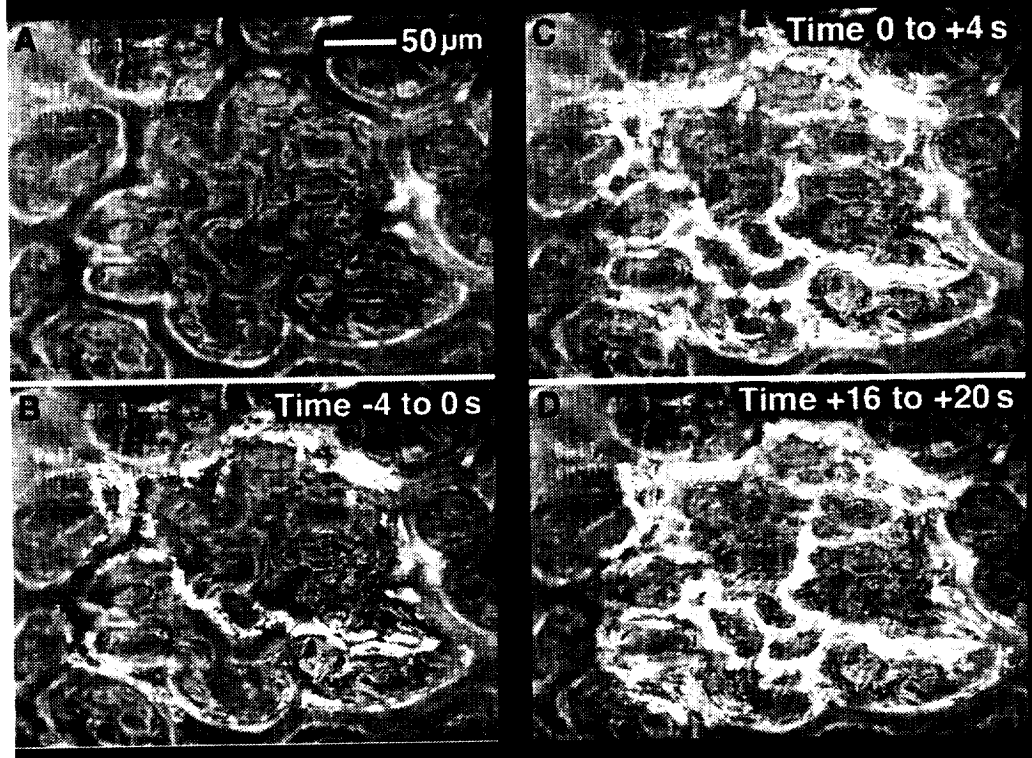

Jaryszak et al

J. Appl. Physiol.

89: 1233-1238, 2000

UCSD

RBC distribution and gas exchange

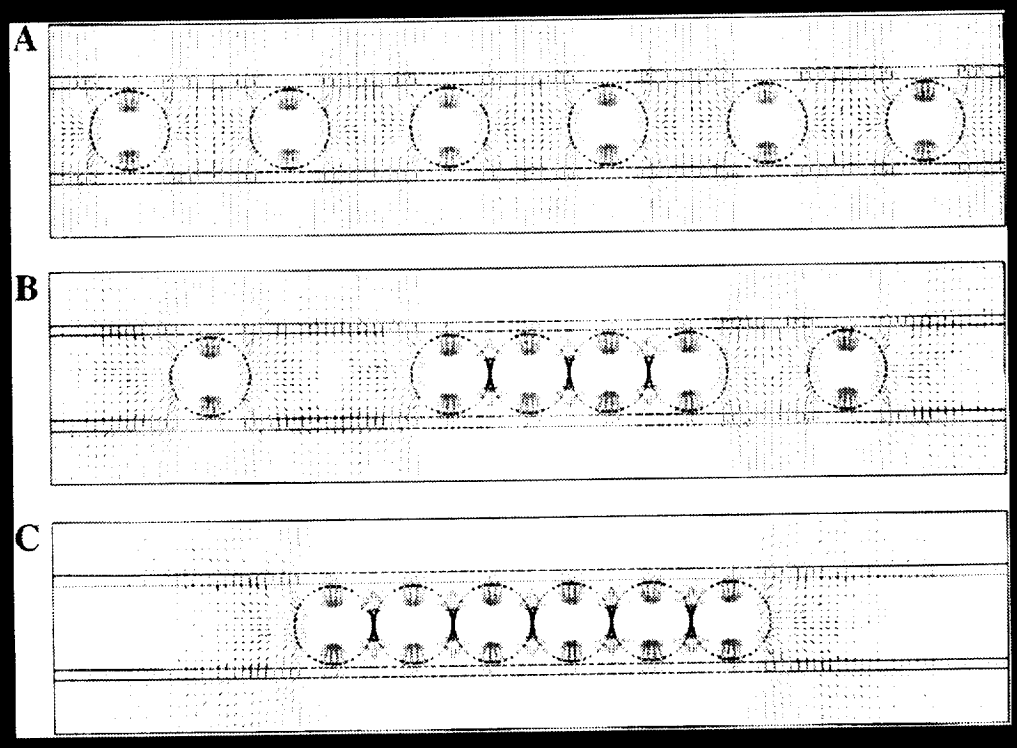

Hsia et al

J. Appl. Physiol.

86: 1460 - 1467, 1999

UCSD

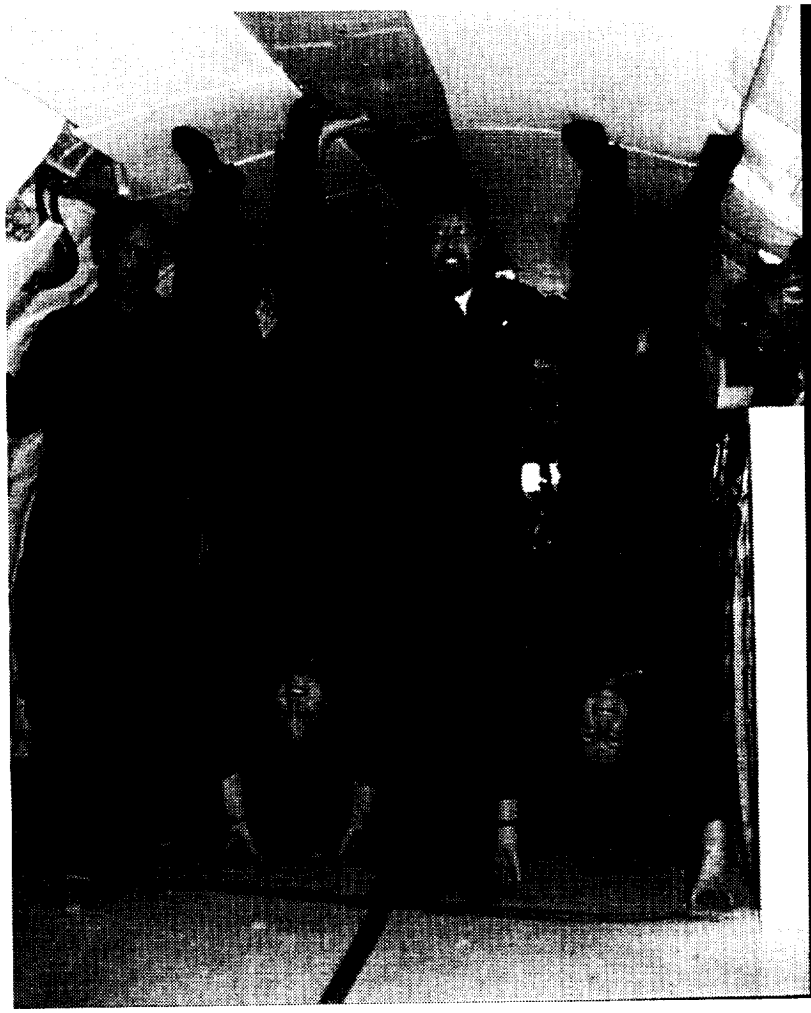

UCSD

- John West
- Kim Prisk
- Chantal Darquenne
- Harold Guy
- Ann Elliott
- Janelle Fine
- Trevor Cooper
- Jeff Struthers

Other Institutions

- Manuel Paiva
- Sylvia Verbanck
- Brigitte Dutrieue
- Dag Linnarsson

The crews

- and many more

UCSD

Session 1: Colloids and Soft Condensed Matter

RECENT RESULTS FROM THE PHYSICS OF COLLOIDS IN SPACE

David A. Weitz
Dept. of Physics and DEAS
Harvard University, Cambridge MA 02138

The PCS TEAM
A. Bailey,[1] R. Christianson, S. Manley, and V. Prasad, P. Segre,[2] U. Gasser,[3] L. Cipelletti[4]
Dept. of Physics and DEAS
Harvard University, Cambridge, MA,
1. Current address: Scitech Instruments, Vancouver, BC, Canada
2. Current address: NASA Marshall, Huntsville, AL
3. Current address: University of Konstanz, Germany
4. Current address: Universite' Montpellier II, 34095 Montpellier Cedex 05, FRANCE

A. Schoefield and P. Pusey,
University of Edinburgh, Edinburgh, UK

M. Doherty, and A. Jankovsky
NASA Glenn, Cleveland, OH

T. Lorik, W. Shiley, J. Bowen, C. Kurta, and J. Eggers
ZIN Technologies, Cleveland, OH

ABSTRACT

The Physics of Colloids in Space is an experiment which flew in the ISS. Data on several different samples of colloidal particles were obtained. They provided unexpected information about the behavior of the samples in microgravity. The data are currently being analyzed. The most recent findings will be discussed in this talk.

Physics of Colloids in Space

Dave Weitz Harvard

- ISS Experiment in Express Rack
- Flew April 2001 – June 2002
- Operated June 2001 – February 2002
- Preliminary Results
  - Binary Alloy Colloidal Crystals
    - AB_{13}; AB_6
  - Fractal Colloid Gels
  - Spinodal decomposition in colloid-polymer mixture

NASA/CP—2002-211212/VOL1

Physics of Colloids in Space

- SCIENCE TEAM
- **Harvard University**
  - Prof. David A. Weitz — Principle Investigator
  - Art Bailey (SciTek) — Science Lead
  - Rebecca Christianson — PDF
  - Suliana Manley, Vikram Prasad, Peter Lu — Graduate Students
  - Urs Gasser (Konstanz), Phil Segre (NASA), Luca Cipelletti (Montpellier) — Former PDF's
- **University of Edinburgh**
  - Prof. Peter N. Pusey — Co-Investigator
  - Andrew Schofield — PDF
- **GRC PROJECT MANAGEMENT**
  - Michael Doherty (GRC) — Project Manager
  - Amy Jankovsky (GRC) — Deputy Project Manager
- **HARDWARE AND OPERATIONS TEAM** (Zin Technologies)
  - Tibor Lorik, — Project Manager
  - Bill Shiley, John Bowen, Jeff Eggers — Software
  - Carol Kurta — Safety, Crew Training,
  - Kevin Dendorfer — Mechanical Tech.
  - Jim Greer — Designer

Harvard Science Team – Oct. 2001

Urs Gasser, Suliana Manley, Rebecca Christianson, Peter Lu, Vikram Prasad

NASA/CP—2002-211212/VOL1 94

Goals

- Study fundamental behavior of colloidal suspensions
- Develop new discipline of **"colloid engineering"**
- Fabricate new materials with colloidal precursors

- Integrated Light Scattering apparatus on ISS
- Eight Sample Cells
- Eight different experiments

- Microgravity essential
  - Eliminate sedimentation, convection
  - Eliminate differential sedimentation

NASA/CP—2002-211212/VOL1

PCS Test Section Internal Features

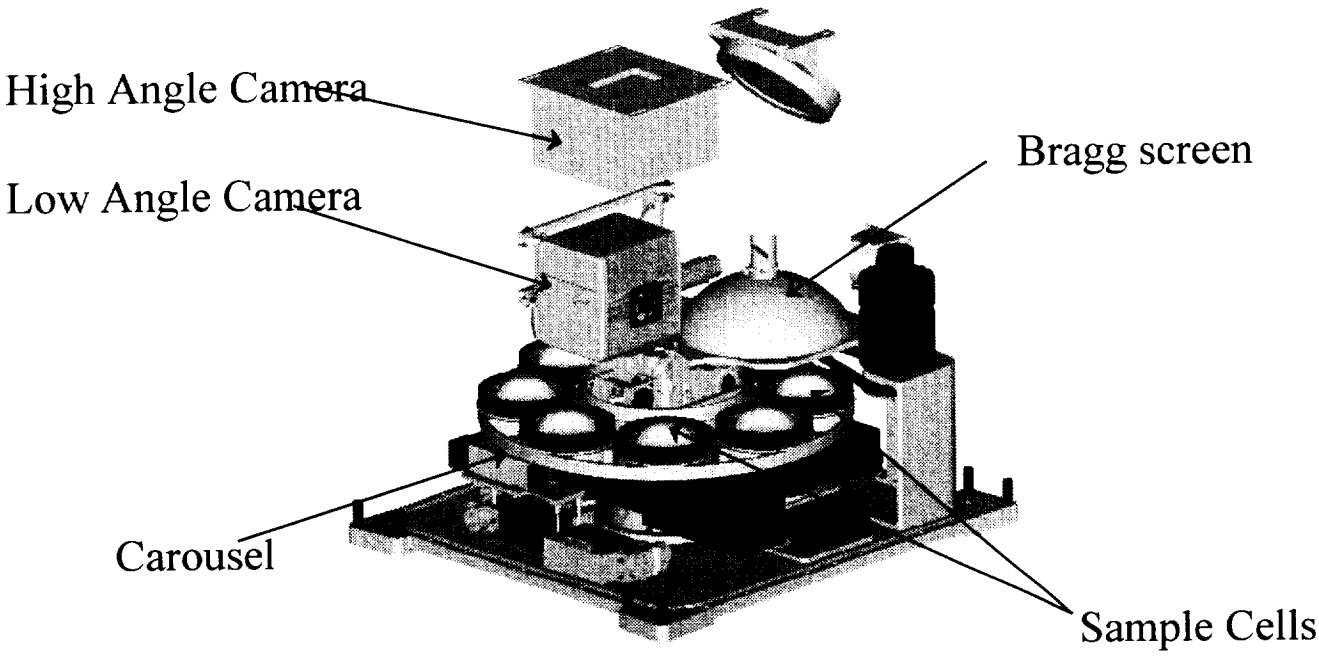

Note: For reference only, these components are not crew accessible
(Test Section side wall not shown)

NASA/CP—2002-211212/VOL1

PCS Science Diagnostics

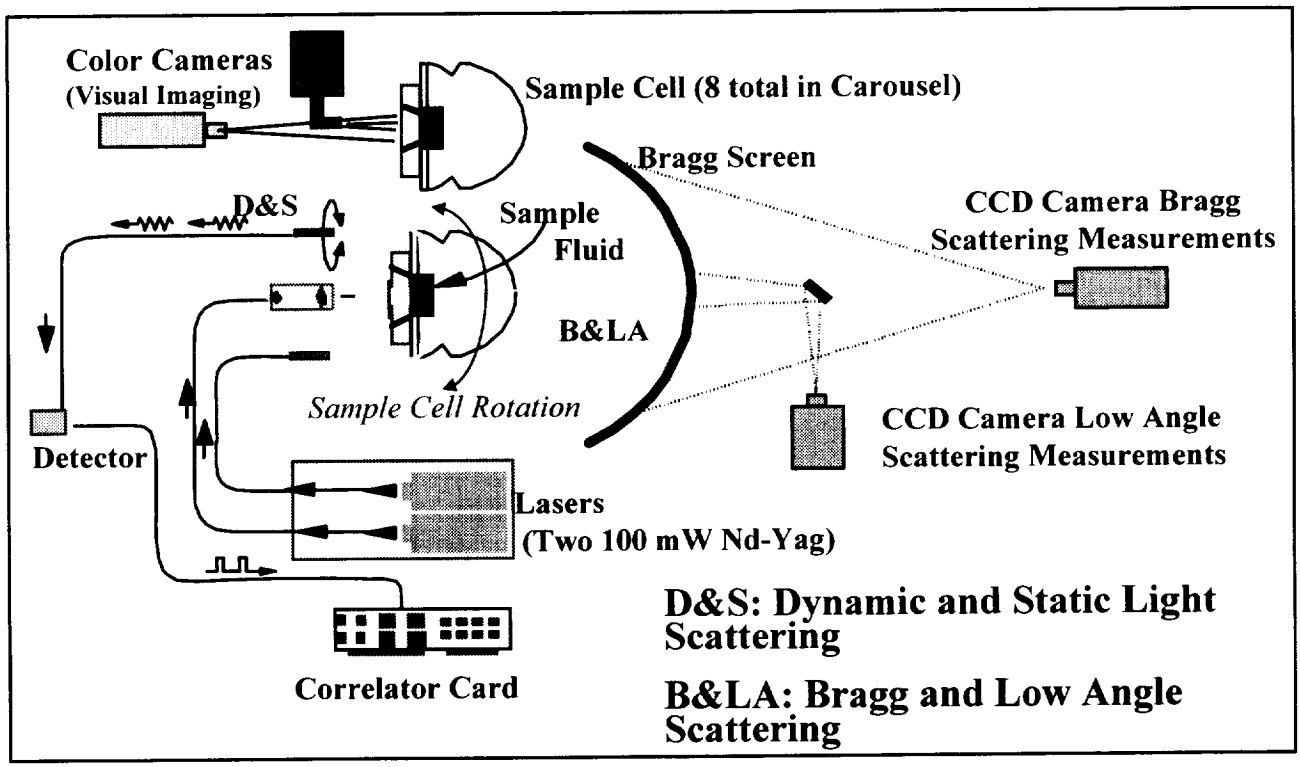

NASA/CP—2002-211212/VOL1 97

Sample Cell Carrousel

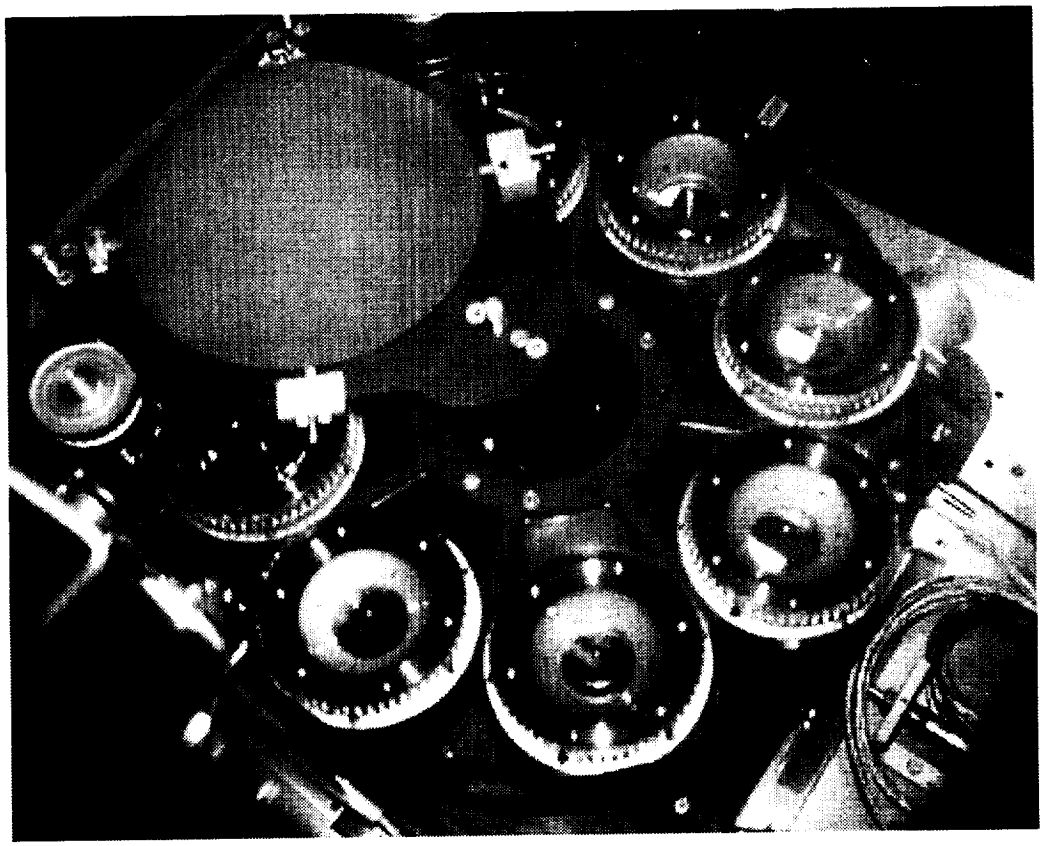

ISS Configuration

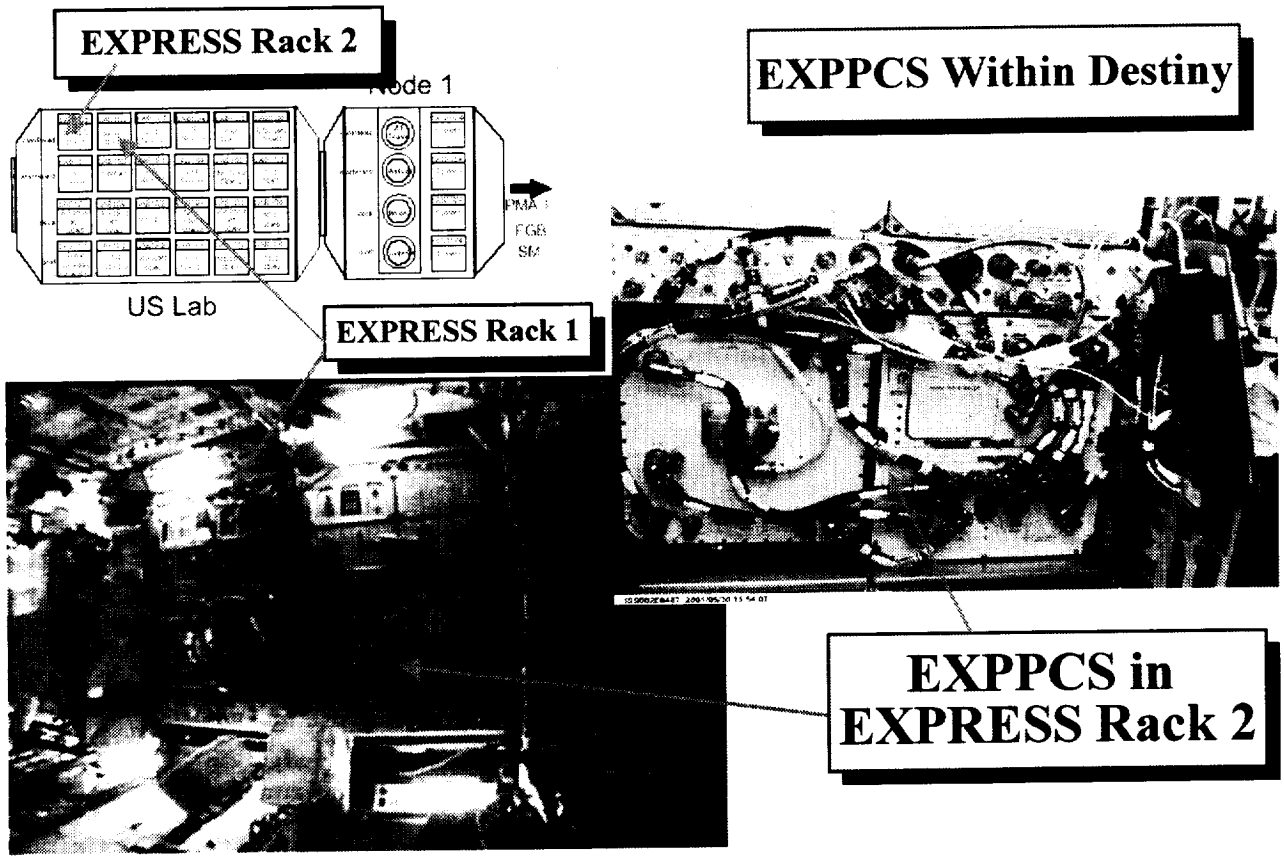

NASA/CP—2002-211212/VOL1 99

Colloid Samples

Binary Colloid Alloy Crystals
- 2 AB_6
- AB_{13}

Fractal Aggregates
- Colloid-polymer mixture
- 3 Polystyrene
- Silica

Colloid-polymer mixtures
- 2 Critical point
- Crystal

1 Colloidal Glass (Chaikin-Russel)

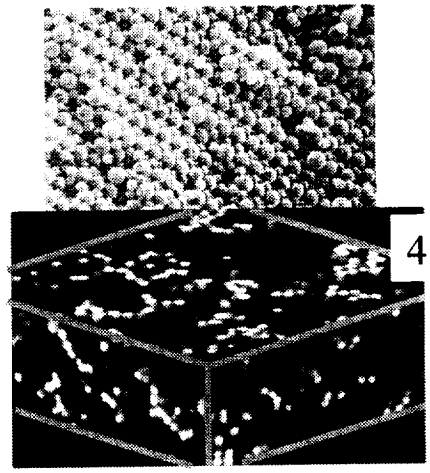

NASA/CP—2002-211212/VOL1

Binary Colloidal Crystals

- Mixtures of colloidal particles of different sizes
- First discovered in natural opal
- Model for crystallization in alloys and multi-component atomic systems
- Helps understand role of polydispersity

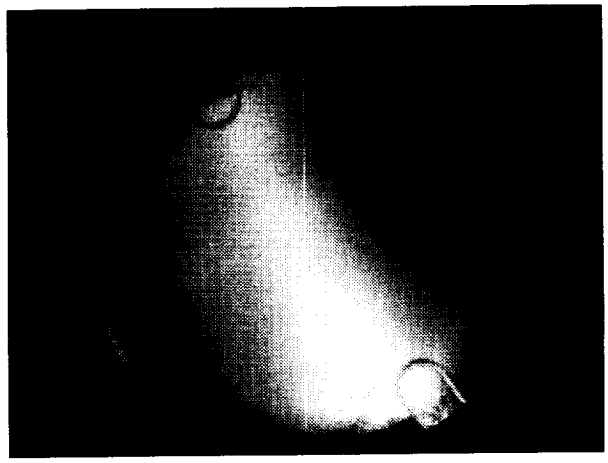

Driven by entropy

NASA/CP—2002-211212/VOL1

Binary Alloy Colloidal Crystals

Expected Structures based on packing

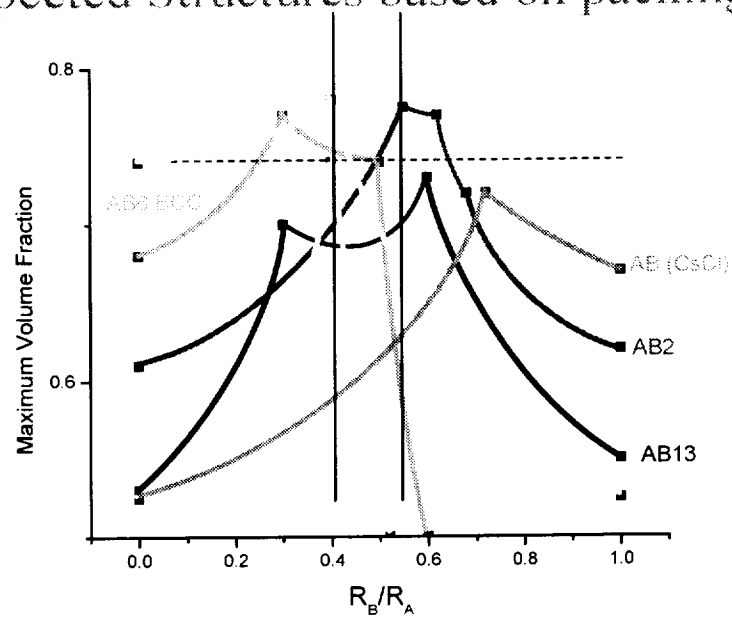

Doesn't work that well!!

- Hard sphere system → entropy determines free energy.
- Competition between configurational entropy and free volume per particle

AB_{13}

- Icosahedra of small particles, at center of simple cube of big particles
- Found in bimetallic alloys such as $NaZn_{13}$
- Stable at size ratios from 0.5-0.7

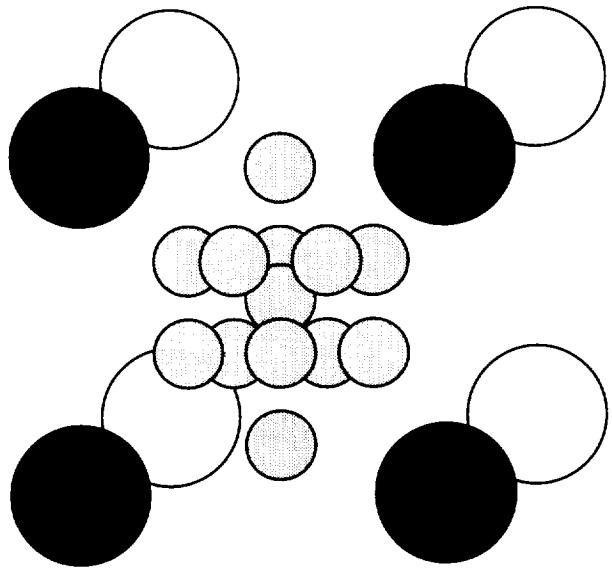

Driven by Entropy

NASA/CP—2002-211212/VOL1

AB_{13}

$R_B/R_A = 0.57$, $N_B/N_A = 19$

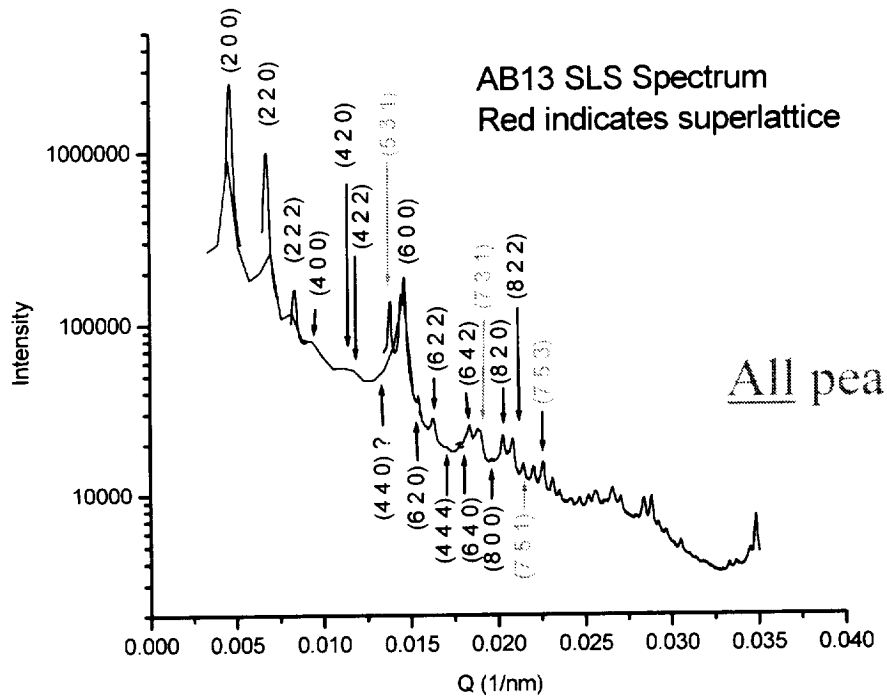

All peaks indexed!

NASA/CP—2002-211212/VOL1 104

Information from Scattering

- FWHM gives length scale of ordering
- Integrated area is proportional to the volume scattering.
- Position gives crystal lattice spacing and structure.

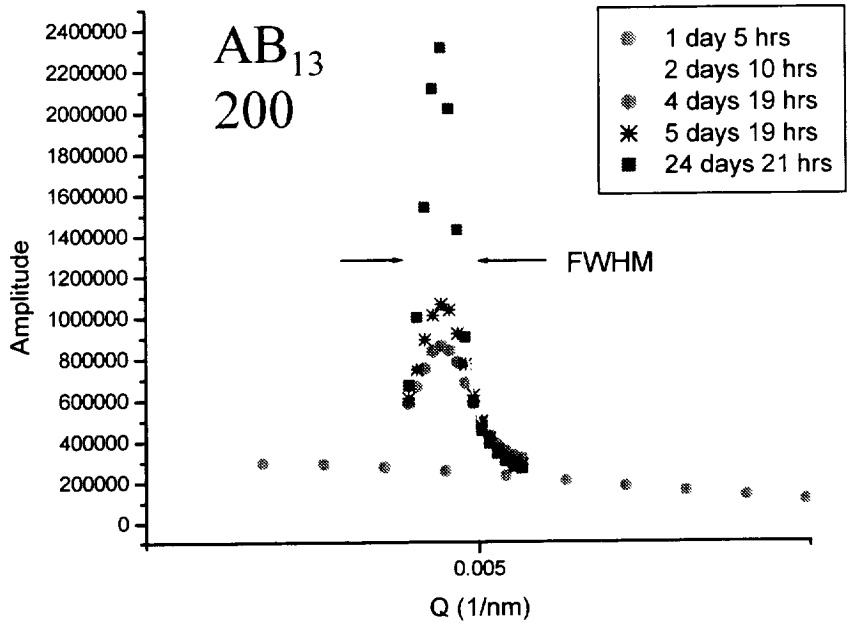

NASA/CP—2002-211212/VOL1 105

AB_{13}

FWHM

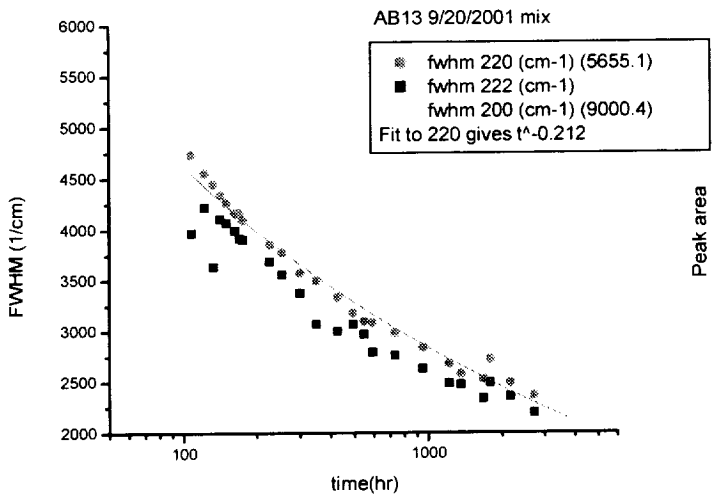

Area

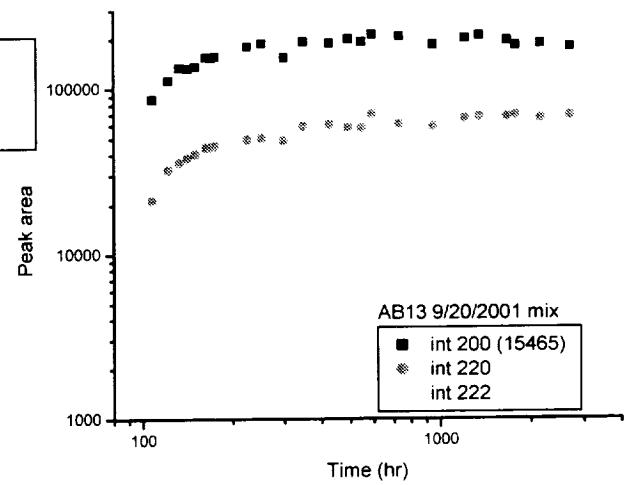

- Peak appears around 100 hrs after mix
- Long-time continued slow evolution
- First measure of growth dynamics

NASA/CP—2002-211212/VOL1 106

AB_6

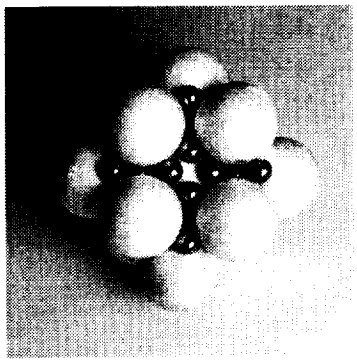

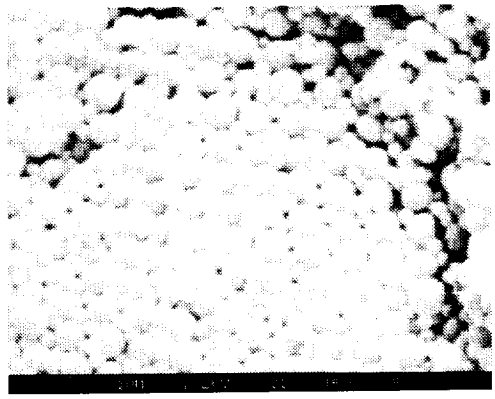

- AB6 occurs in three different structures: simple cubic, BCC and FCC, which occur at different size ratios from 0.3 to 0.4
- BCC is the fastest to crystallize, with crystals forming overnight at the optimal size ratio of 0.4

AB_6 Binary Alloy Crystal - BCC

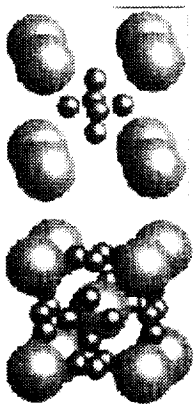

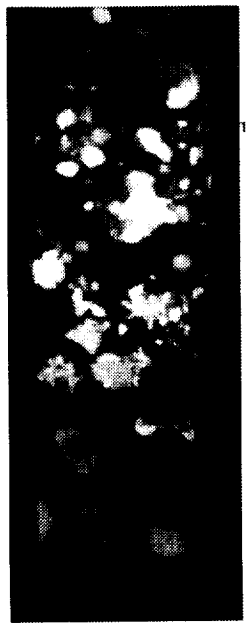

1 cm

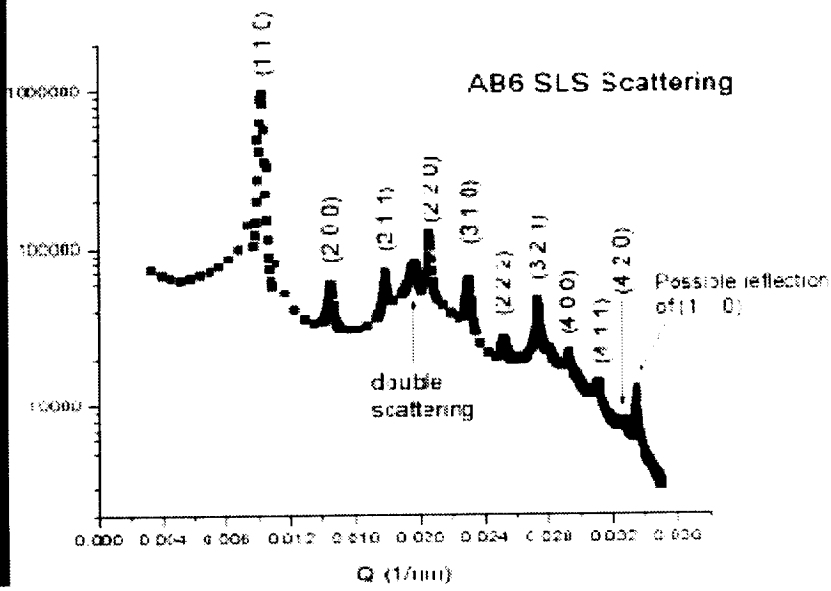

- Very intense Bragg scattering
- Very large crystals

NASA/CP—2002-211212/VOL1 108

AB_6 FWHM

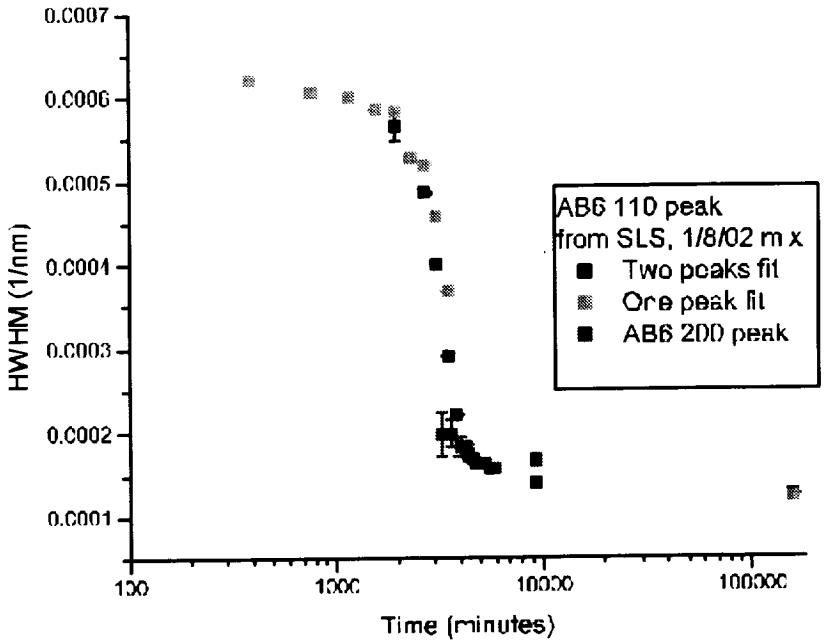

- Crystals form in ~40 hrs, half the time of AB_{13}
- Three distinct regions:
  - nucleation, crystallization, ripening?

NASA/CP—2002-211212/VOL1

AB_6 Binary Alloy Crystal

BCC 110 orientation

Confocal Microscope Images

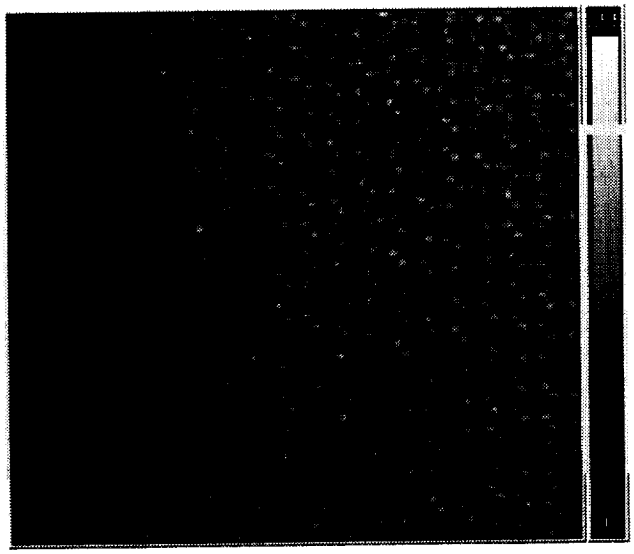

Small Particles

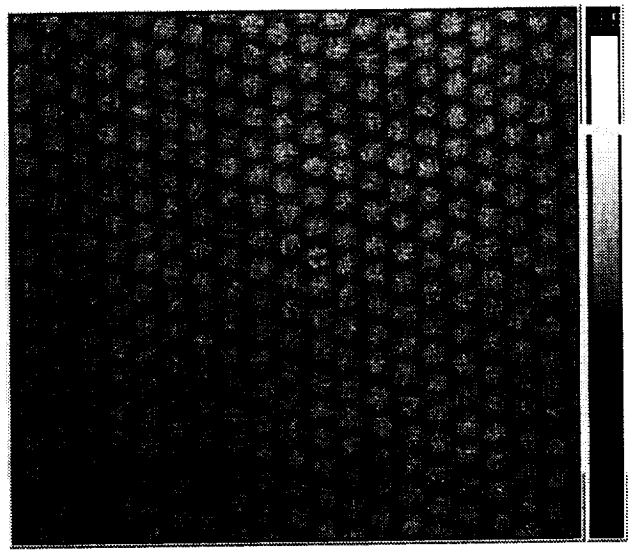

Large Particles

NASA/CP—2002-211212/VOL1

AB_6 Binary Alloy Crystal

BCC – 100 orientation

Confocal Microscope Images

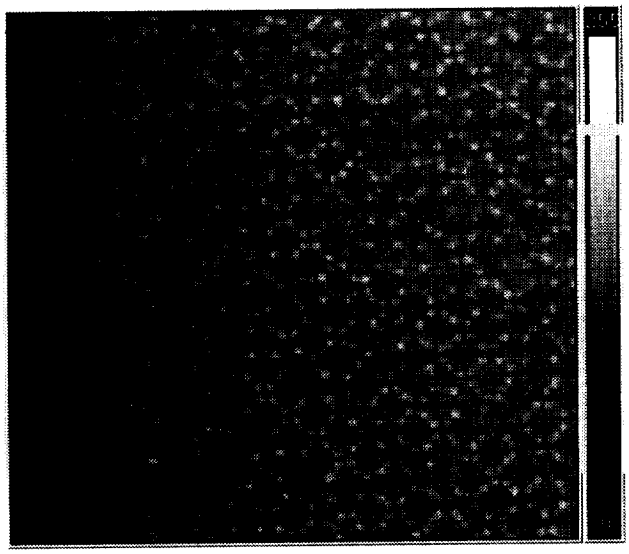

Small Particles

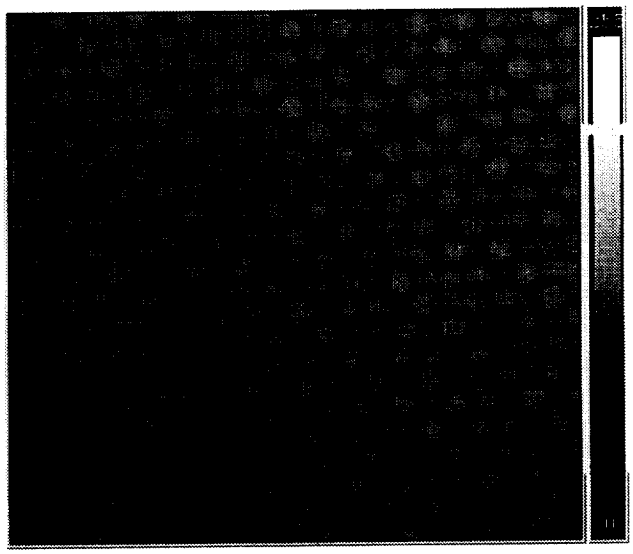

Large Particles

NASA/CP—2002-211212/VOL1 111

AB_6 Binary Alloy Crystal

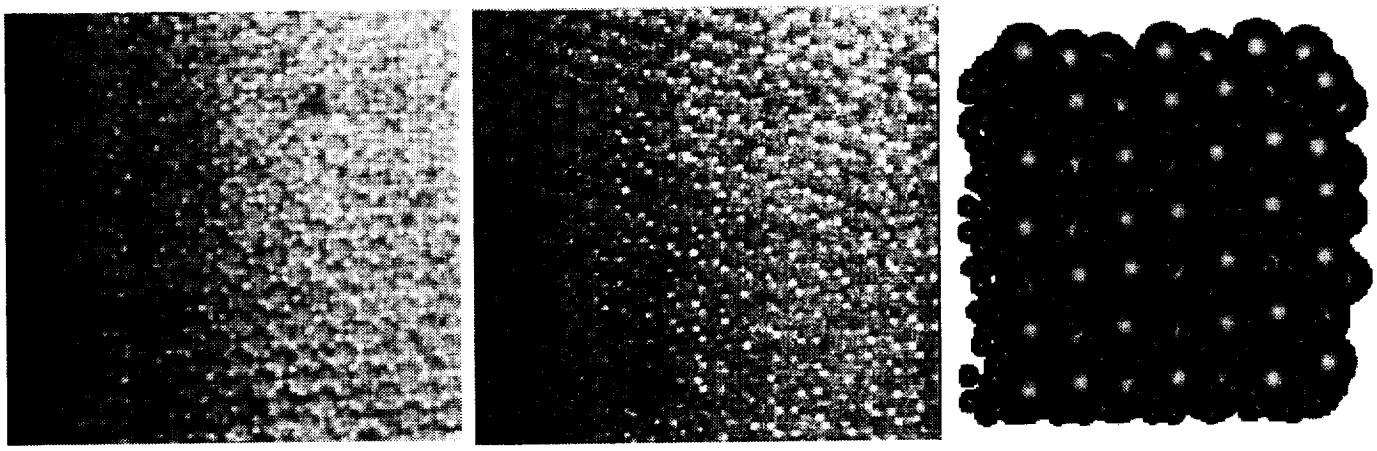

- Very well ordered FCC structure
- Small particles induce effective long-range intereaction
  - Creates highly ordered large particle lattice

NASA/CP—2002-211212/VOL1 112

Binary Alloy Colloidal Crystals

- Kinetics of growth of binary alloys
  - Crystals form, then anneal
- Very highly ordered colloidal crystals
  - Photonic uses – perfect crystals
    - Effective long-range interaction
  - Models for binary alloys
- LMM: Confocal microscopy in space

NASA/CP—2002-211212/VOL1 113

Colloidal Fractal Gels

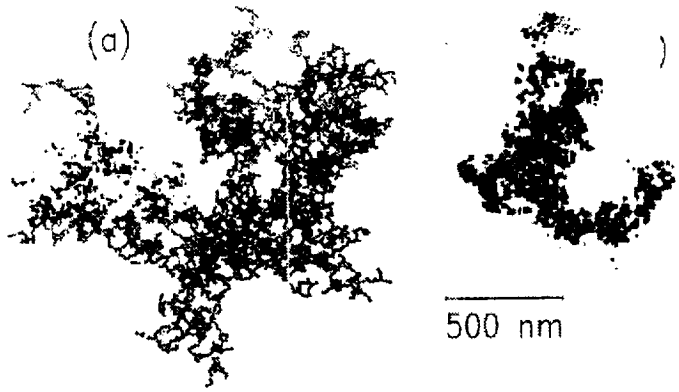

Network is fractal: $M \sim R^{df}$

Tenuous structures, must density match

- What are properties of very low ϕ gels?
- What is intrinsic limitation of gelation?
- How do gels age?

NASA/CP—2002-211212/VOL1 114

Sample Preparation

- 11 nm diameter colloidal spheres
- Screen charges with salt
  - van der Waals attraction

Polystyrene: $\phi = 8\text{x}10^{-6}$
Silica: $\phi = 2\text{x}10^{-4}$

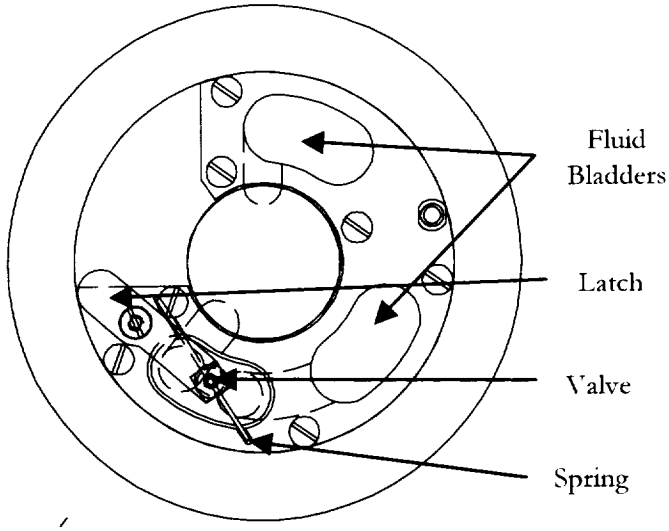

- On Board Mixer
- FCD cell

NASA/CP—2002-211212/VOL1 115

Polystyrene – Static Light Scattering

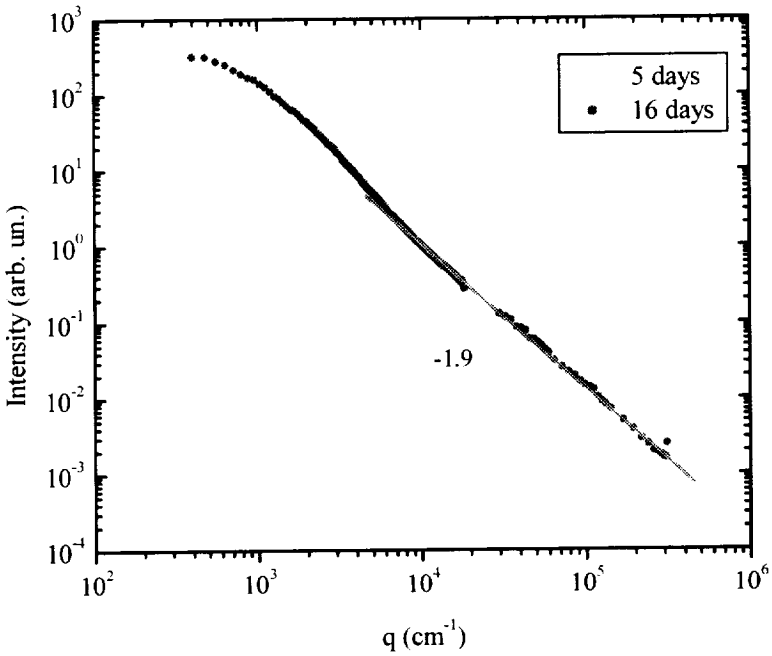

Fisher-Burford:
$I(\mathrm{I}) = \mathrm{I}(0)/[1+2/3(qR_c)^2]^{df/2}$
$d_f = 1.9$
$R_c = 2.5\ \mu\mathrm{m}$

Fractal Structure over very large range of length scales

NASA/CP—2002-211212/VOL1 116

Polystyrene – DLS and Low Angle DLS

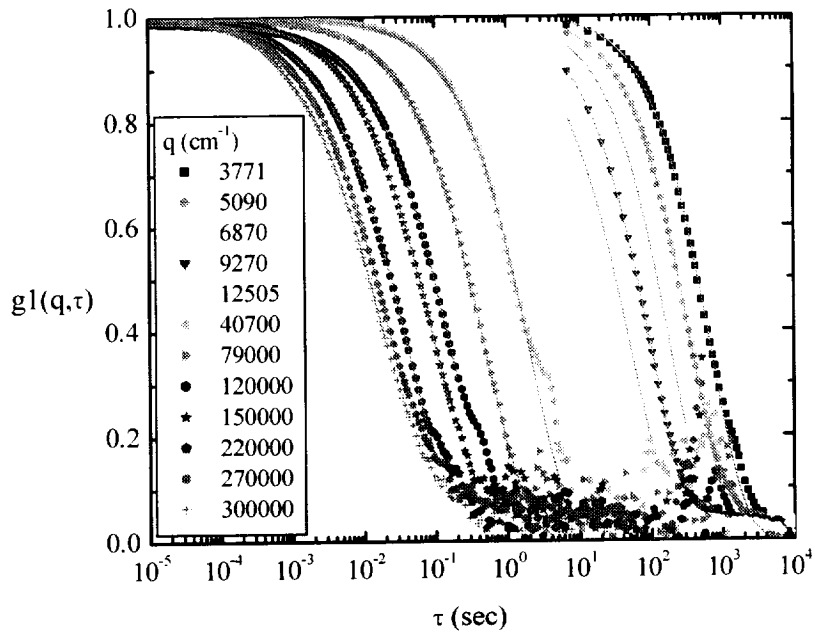

General fitting form: $g_1(q,\tau) \sim \exp(-(t/\tau)^p)$

Diffusion: $p = 1$

Internal modes: $p = 0.7$

NASA/CP—2002-211212/VOL1 117

Polystyrene – Early-time Low Angle DLS

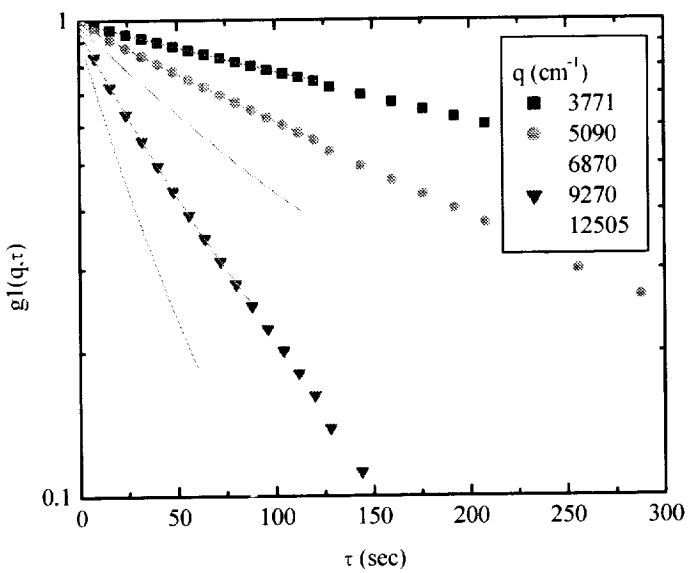

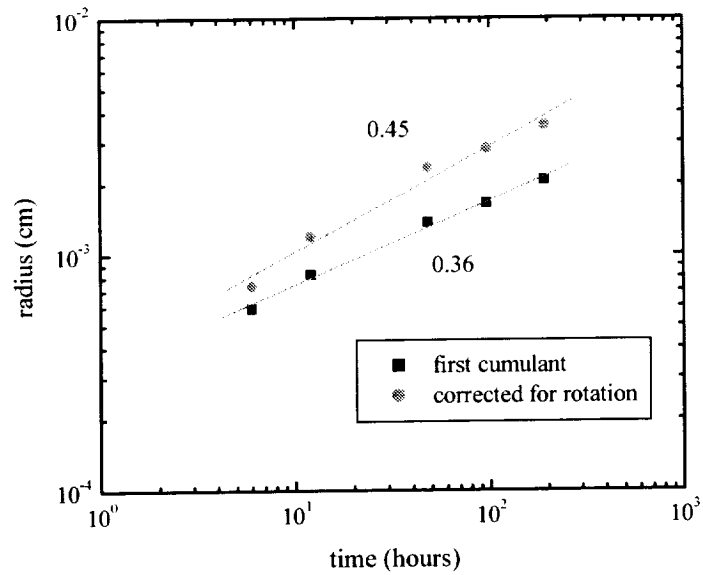

Diffusive: $g_1(q,\tau) \sim \exp(-q^2 D\ \tau)$
Stokes-Einstein relation: $a = kT/(6\pi\eta D)$
DLCA: $M \sim t$, $M \sim R^{df}$ so $R \sim t^{1/df}$

NASA/CP—2002-211212/VOL1 118

Scaling from fits - polystyrene

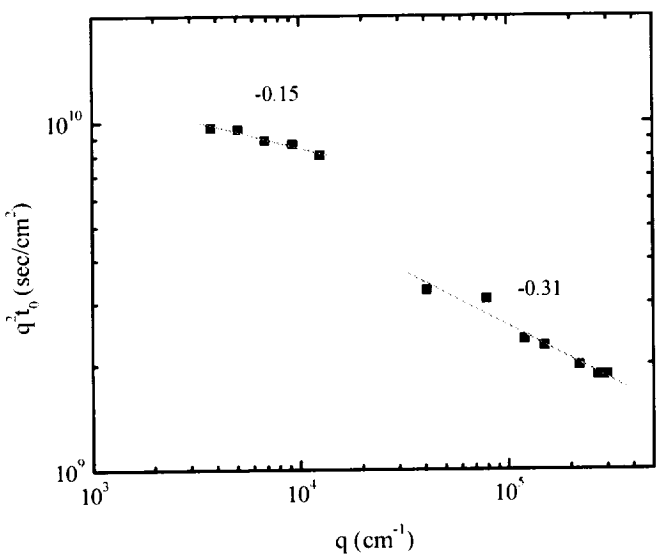

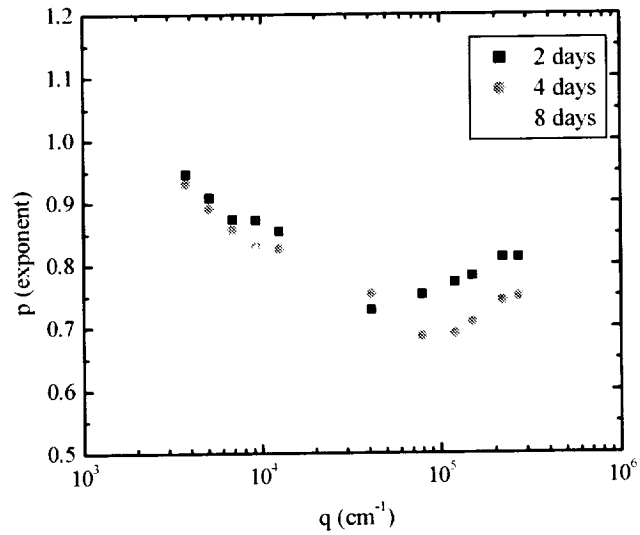

low q → $\tau \sim q^{-2}$ → diffusive
high q → $\tau \sim q^{(-2/p)}$, p=0.87, → internal modes

low q → $\tau \sim q^{-2}$ → diffusive
high q → $\tau \sim q^{(-2/p)}$, p = 0.65 – 0.8 → internal modes

Very large fractal clusters – not gelled yet

NASA/CP—2002-211212/VOL1 119

Thermal Limitation to gel formation?

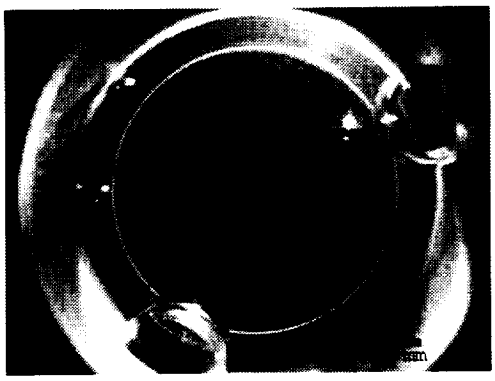

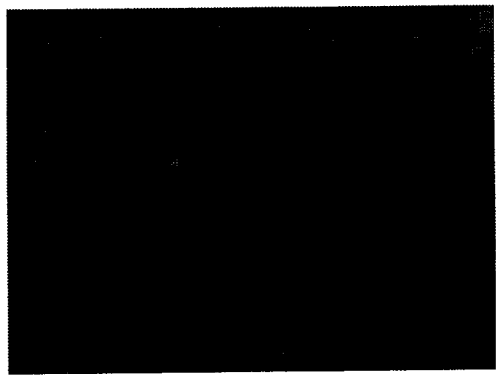

PCS photos
17 days

Buoyancy matched (6:4 D_2O:H_2O)

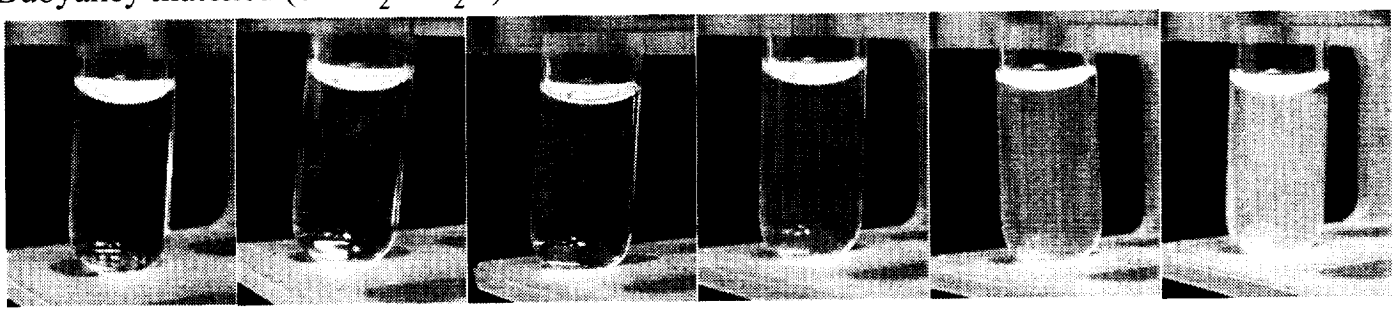

$\phi = 8x10^{-6}$ $\phi = 2x10^{-5}$ $\phi = 4x10^{-5}$ $\phi = 8x10^{-5}$ $\phi = 2x10^{-4}$ $\phi = 4x10^{-4}$

Ground photos courtesy of Darren Link

Silica – Static Light Scattering

- Can not buoyancy match
- Expect qualitatively different aging

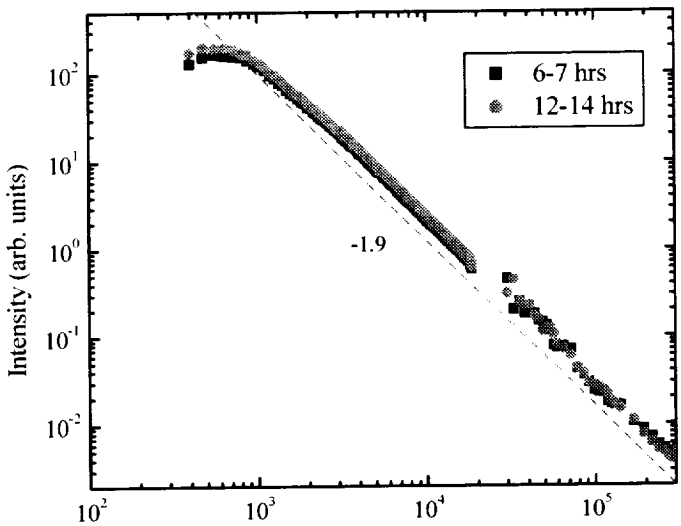

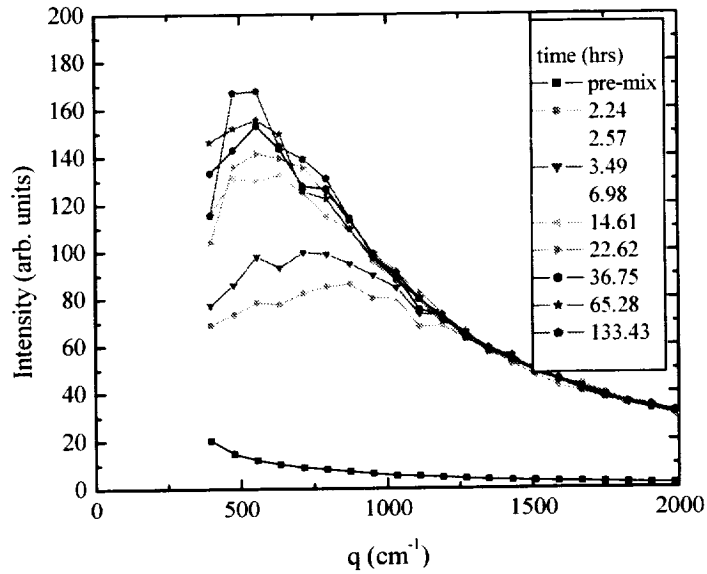

$d_f = 1.9$

$R_c \sim 2\pi/q_{max}$

NASA/CP—2002-211212/VOL1 121

Aging behavior: silica

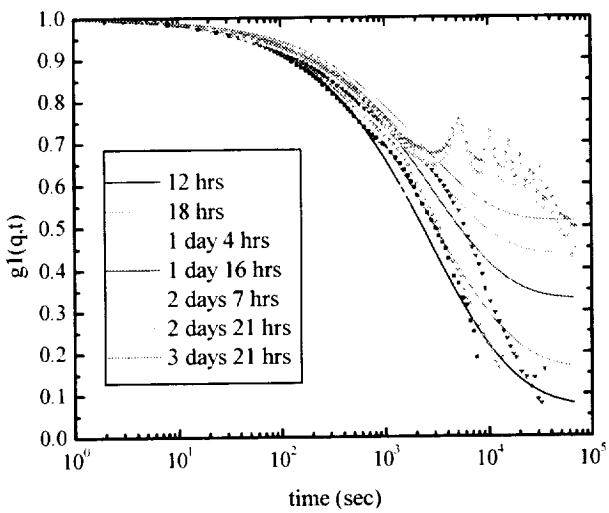

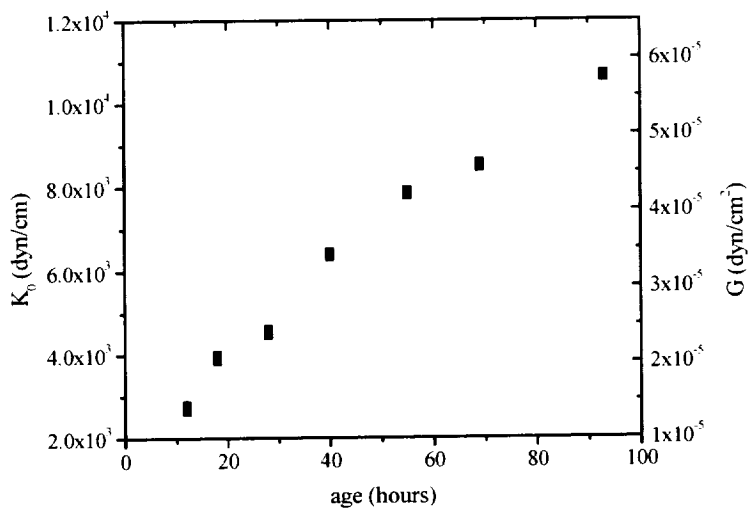

Aging results in stiffening – increase in κ_0.

NASA/CP—2002-211212/VOL1

NASA/CP—2002-211212/VOL1 123

Fractal Colloid Gels

- New understanding of structure and dynamics for large fractal structures
- Aging effects of colloidal gels
- Fundamental limitation of gelation

NASA/CP—2002-211212/VOL1

Colloid-Polymer Mixture Spinodal Decomposition

- Induce weak attraction between colloidal particle
  - Depletion attraction – add polymer
- Colloids model atoms
  - Directly visualize physics at "atomic" scale
- Phase separation
  - Fluid-rich and fluid-poor regions
- Driven by surface tension?

Spinodal Decomposition of Colloid Polymer

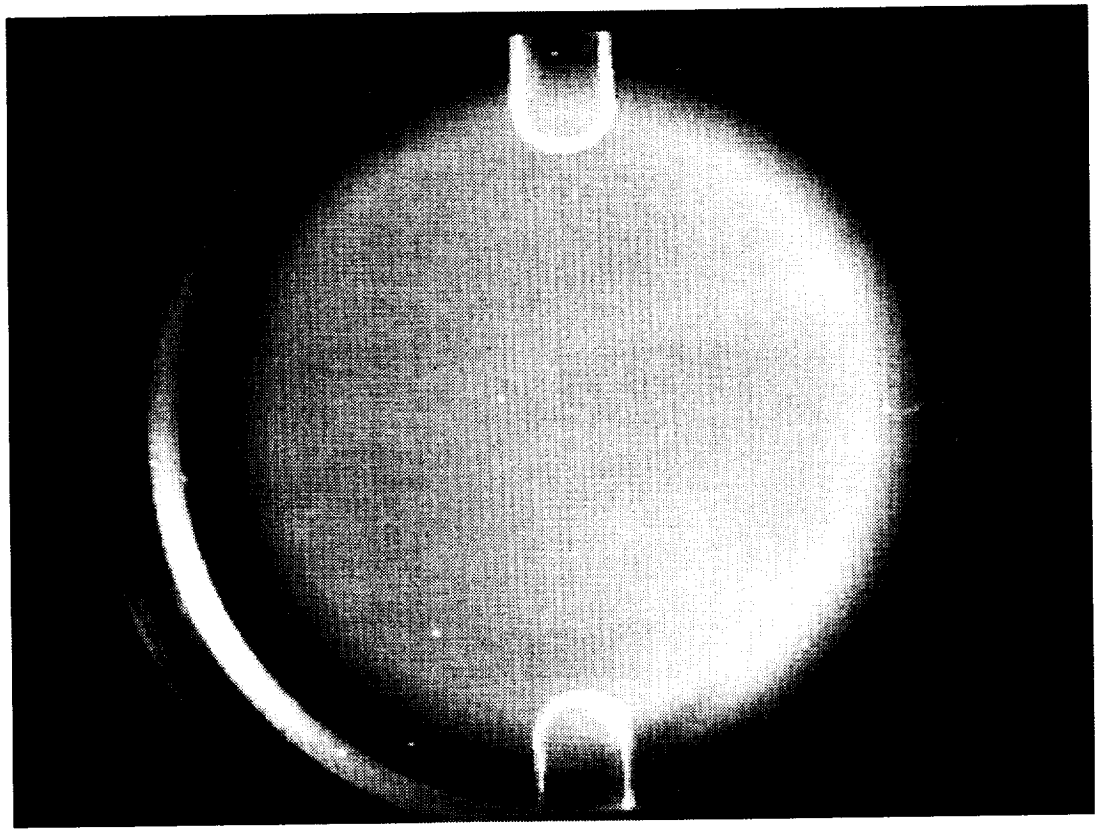

NASA/CP—2002-211212/VOL1 125

Col-Pol Critical Point: Sample Evolution

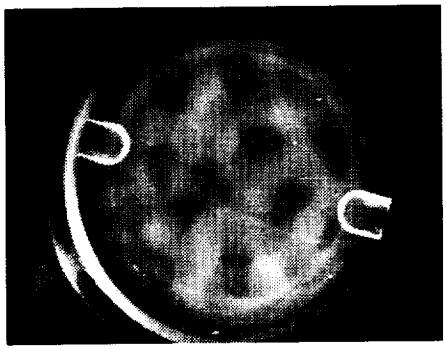

2. **3 hrs 50 min after mix**

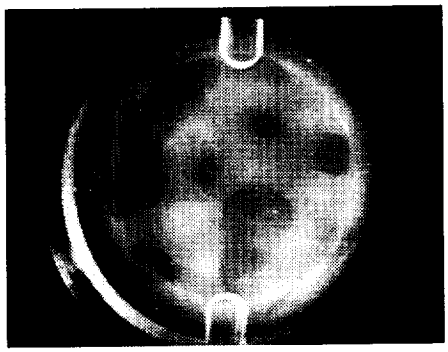

3. **13 hrs 24 min after mix**

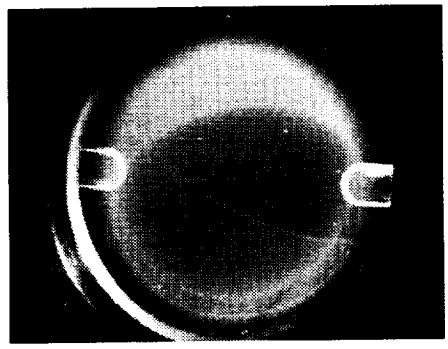

4. **35 Days, 2 hrs, 54 min after mix**

Large scale phase separation - Totally unprecedented

Structure is 10,000 times larger

Col-Pol Critical Point: Sample Evolution

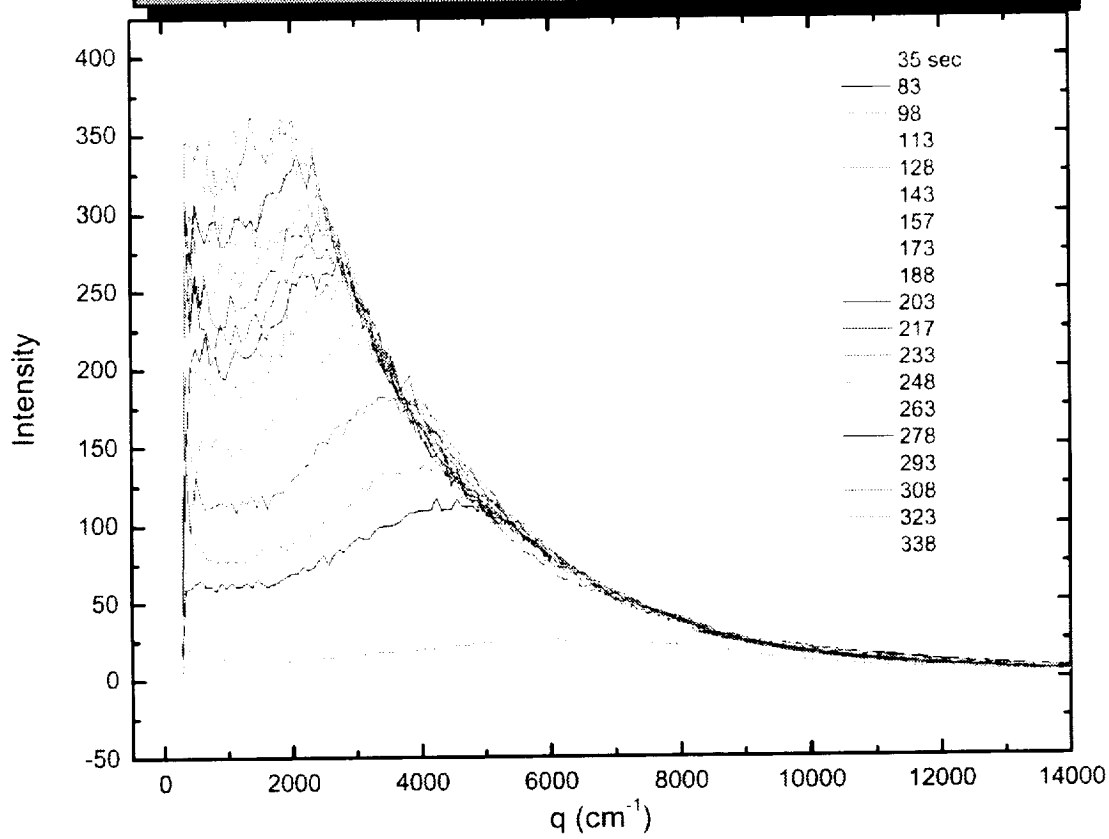

NASA/CP—2002-211212/VOL1 127

Motion of Interface between two drops

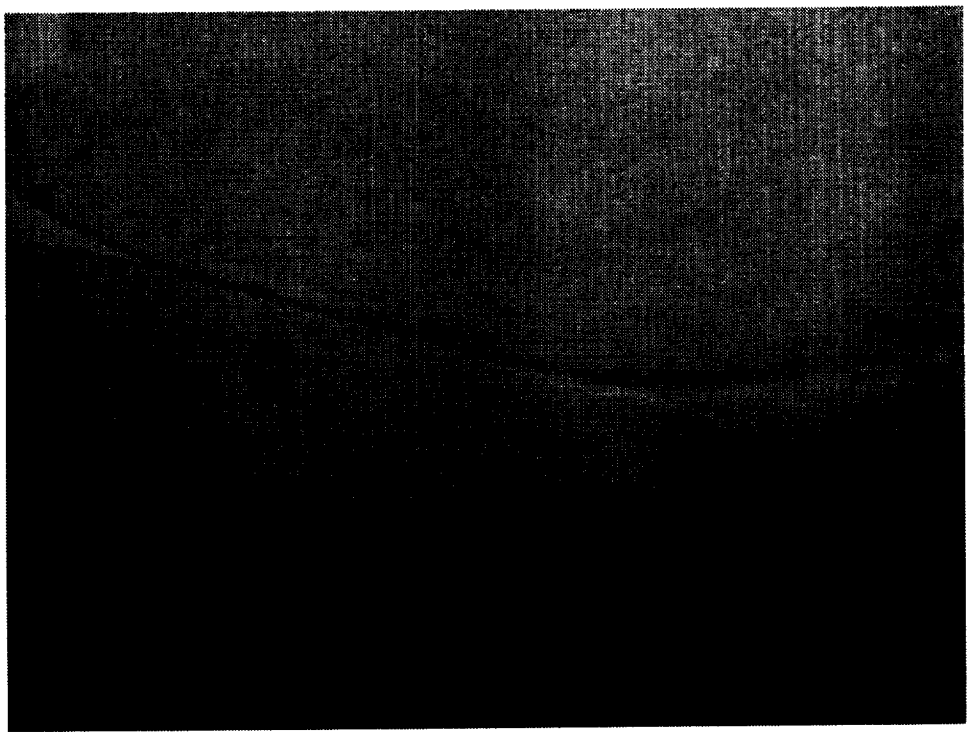

- Measure of surface tension?
- Measure of kinetics

NASA/CP—2002-211212/VOL1

Spinodal Decomposition of Attractive Colloids

- Large range of length scales
- 1 μm to 3 cm
- Hydrodynamics of late stages of spinodal decomposition
- Surface tension of colloidal particle mixtures
- Wide range of phase separation behavior possible

NASA/CP—2002-211212/VOL1

Important Criteria for Success

- Changeable sample cells
- Late delivery of samples to ensure up-to-date science
  - Planning to flight takes 5 – 7 years
- Flexible Apparatus
  - PCS-like apparatus first flow as PH^{A}SE (Chikin/Russel)
  - Unexpected results require creative solutions
- ISS resources highly constrained
  - Power
  - Crew time
  - Ground communication

NASA/CP—2002-211212/VOL1 130

Some Conclusions

- PCS quite successful
- Lead to new results for 5 different samples
  - New science
  - Importance for ground-based studied
- Raised even more new questions than answers
- GRC team facilitated research for science team
- Need better communication with astronauts
  - Commitment to research

NASA/CP—2002-211212/VOL1

For More Information...

See Rebecca at poster session: binaries, fractal gels

NASA GRC PCS Website:
http://microgravity.grc.nasa.gov/6712/PCS.htm
includes data on a sample by sample basis (constantly updated)

PI (group) at Harvard:
http://www.deas.harvard.edu/projects/weitzlab/
Dave's group and the scientific focus areas of interest

NASA GRC Microgravity:
http://microgravity.grc.nasa.gov/

NASA GRC Fluids Physics:
http://microgravity.grc.nasa.gov/MSD/MSD_htmls/fluids.html

Paul Chaikin at Princeton:
http://PUPGG.PRINCETON.EDU/www/jh/research/Chaikin_paul.htmlx

NASA/CP—2002-211212/VOL1

PHYSICS OF HARD SPHERE EXPERIMENT: SCATTERING, RHEOLOGY AND MICROSCOPY STUDY OF COLLOIDAL PARTICLES

Z-D Cheng, J. Zhu, S-E Phan, W. B. Russel, P. M. Chaikin*
Depts of Physics and Chem. Eng., and Princeton Materials Institute, Princeton University
Princeton, NJ 08544

W. V. Meyer
NCMR, NASA Glenn Research Center, Cleveland Ohio 44135

ABSTRACT

The Physics of Hard Sphere Experiment has two incarnations: the first as a scattering and rheology experiment on STS-83 and STS-94 and the second as a microscopy experiment to be performed in the future on LMM on the space station. Here we describe some of the quantitative and qualitative results from previous flights on the dynamics of crystallization in microgravity and especially the observed interaction of growing crystallites in the coexistance regime. To clarify rheological measurements we also present ground based experiments on the low shear rate viscosity and diffusion coefficient of several hard sphere experiments at high volume fraction. We also show how these experiments will be performed with confocal microscopy and laser tweezers in our lab and as preparation for the phAse II experiments on LMM. One of the main aims of the microscopy study will be the control of colloidal samples using an array of applied fields with an eye toward colloidal architectures. Temperature gradients, electric field gradients, laser tweezers and a variety of switchable imposed surface patterns are used toward this control.

Interaction between growing crystallites. One of the salient features, which has not been emphasized in previous experiments, is the existence of strong interactions between individual crystallites. In Fig1, from t=150s to about 800s, the size of the crystallites increases linearly $L=t^{\alpha}$, $\alpha \sim 1$, while the crystallinity X over this interval increases at a rate considerably less than L^3. Thus the number of crystallites decreases roughly as $N\_c=t^{-\gamma}$, $\gamma \sim 2.6$. This is unusual and contrasts with the classic theory that focuses on the nucleation and the growth in size of isolated crystallites. We identify this process as ``simultaneous coarsening and growth" in which small crystallites shrink and eventually disappear, causing the number of crystallites to decrease, while large crystallites keep growing, causing the measured average crystallites size to increase with time. The growth exponent for the size is about unity, resulting from the combination of normal diffusion limited growth and coarsening with the latter apparently due to direct transport from small to large

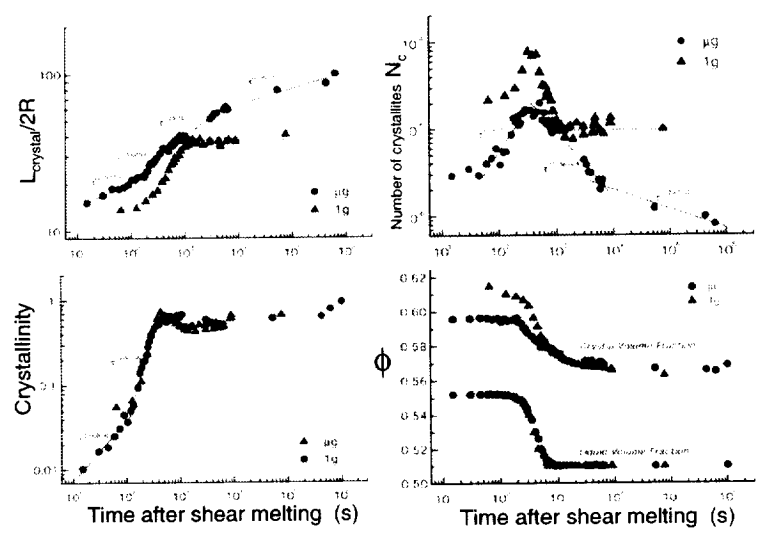

crystallites. Because of the different curvatures of these crystallites,\the smaller crystallites are under higher pressure from the Laplace or surface tension term and hence have a high internal volume fraction value. Therefore, the corresponding equilibrium liquid volume fraction surrounding a small crystallite is relatively higher than that surrounding a large crystallite. Mass transport, via these density gradients in the intervening fluid dispersion, moves particles from the small crystallites to the large ones.

Low Shear Rate Viscosity: For this study we used bare silica spheres with radius 244+/-10nm in index matching, high viscosity ethylene glycol and glycerol and a Zimm-Crother viscometer with shear stress as low as 10^{-5} Pa-S. Figure 2 shows the results plotted in a form consistent with the Doolittle equation: $\eta_0 / \mu = (\eta_\infty / \mu)(1 + A\exp[\gamma\phi/(\phi_{max} - \phi)])$ which provides a

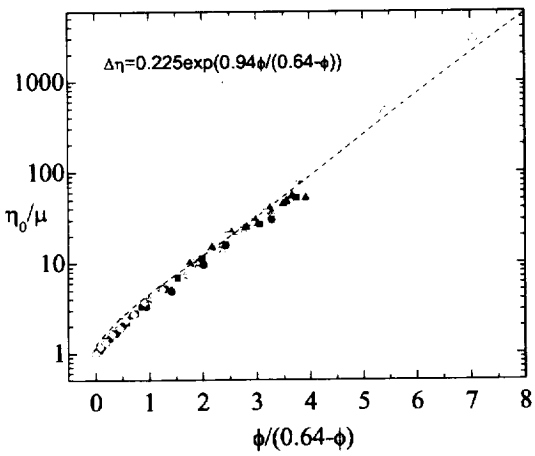

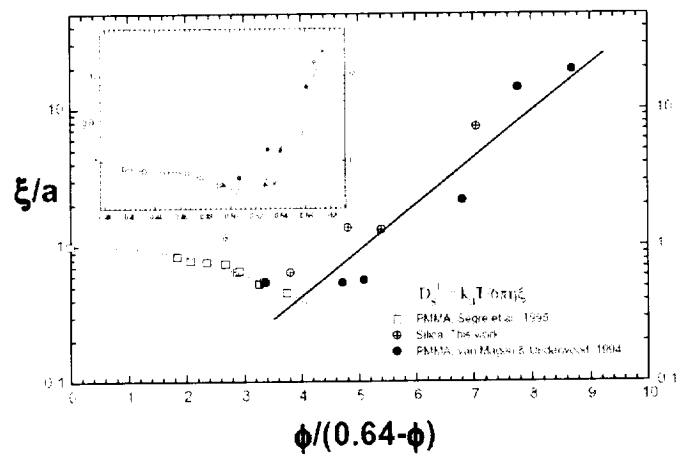

very good fit with γ=0.94, A=0.225 and ϕmax =0.64. For ϕ less than 0.50 there is excellent agreement with previous results on PMMA-PHSA suspensions. The literature suggests defining a dynamical correlation length by $\xi = kT/6\pi\eta(\varphi)D$, where η is the low shear viscosity and D is the long time self diffusion. Figure 3 shows a plot of this length vs ϕ. ξ changes behavior increasing rapidly just beyond the freezing ϕ ~0.5 and does not diverge at the glass transition ϕ=0.58, $\xi(\phi=0.58)$ =30a but rather appears to head for a divergence at ϕ=0.64 (random close packing). (At ϕ=0.58 ξ crosses the size of a critical nucleus.)

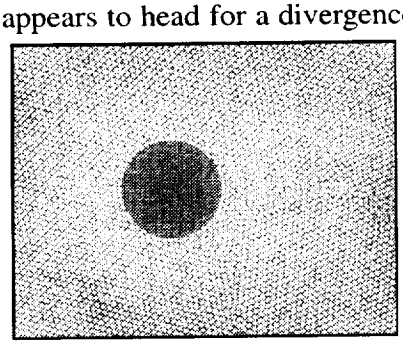

Rheology experiments on LMM will be performed using confocal microscopy and a probe particle whose motion is controlled by a laser tweezer. In Fig. 4 we show a 15μ particle suspended in a dense suspension of flourescently labeled PMMA hard spheres, so that the strain and strain rate can be monitored as the large particle is displaced. We will also discuss ground based experiments with lithographically patterned electric grids, and the effects of electric fields, Fig 5.

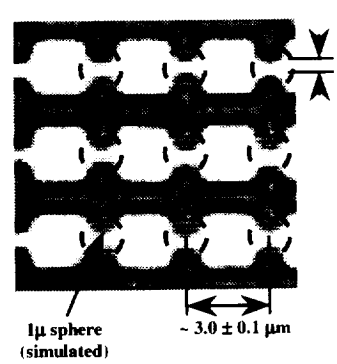

*P.I. chaikin@princeton.edu, 609 258-4338, FAX –6360

1)Z-D Cheng et al. Phys. Rev. Lett. **88**, 015501, (2002)
2) J. Stellbrink et al. Phys. Rev. E. **56**, R3772 (1997)

Physics of Hard Spheres Experiment: Microscopy of Colloidal Particles

Novel Control of Particle density and motion

Electric Field and Dielectrophoresis

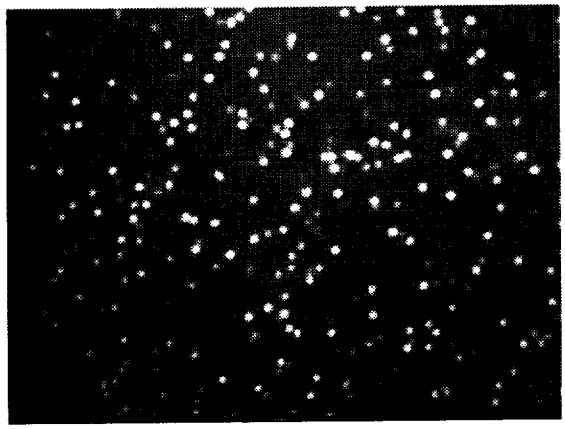

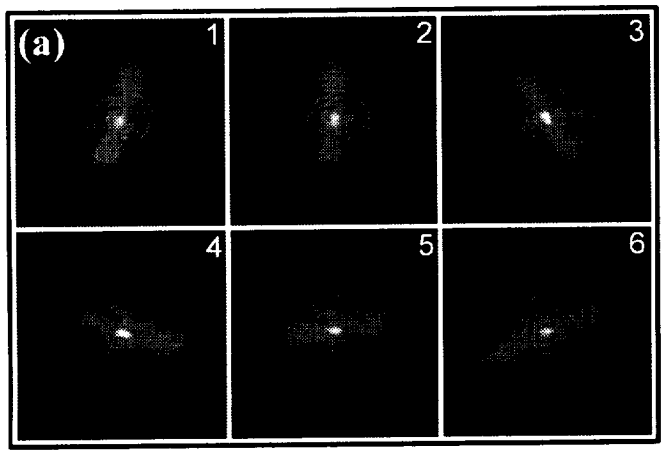

Colloidal Disks in Optical Tweezers
Colloidal Lighthouse
Switchback Oscillations

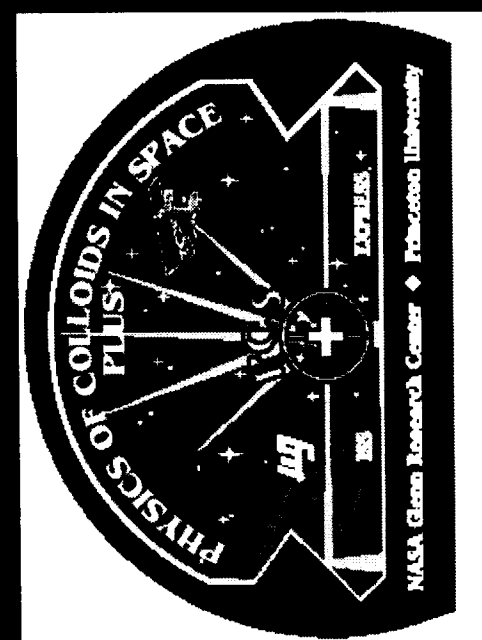
PHYSICS OF COLLOIDS IN SPACE
PLUS+
EXPRESS
NASA Glenn Research Center ◆ Princeton University

Dielectrophoresis

Particles drawn to high field

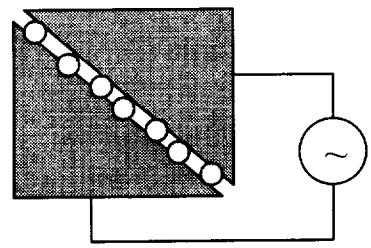

Force on particle depends on frequency and conductivity of solvent:

$$F(\omega) = 2\pi\varepsilon_m \operatorname{Re}\left(\frac{\varepsilon_p^* - \varepsilon_m^*}{\varepsilon_p^* + 2\varepsilon_m^*}\right)\left|\nabla E_0^2\right|$$

$$\operatorname{Re}\left(\frac{\varepsilon_p^* - \varepsilon_m^*}{\varepsilon_p^* + 2\varepsilon_m^*}\right) = \frac{(\sigma_p - \sigma_m)}{(1+\omega^2\tau^2)(\sigma_p + 2\sigma_m)} + \frac{\omega^2\tau^2(\varepsilon_p - \varepsilon_m)}{(1+\omega^2\tau^2)(\sigma_p + 2\sigma_m)}$$

AC off--AC on --- repeat six times
Change frequency to repulsion

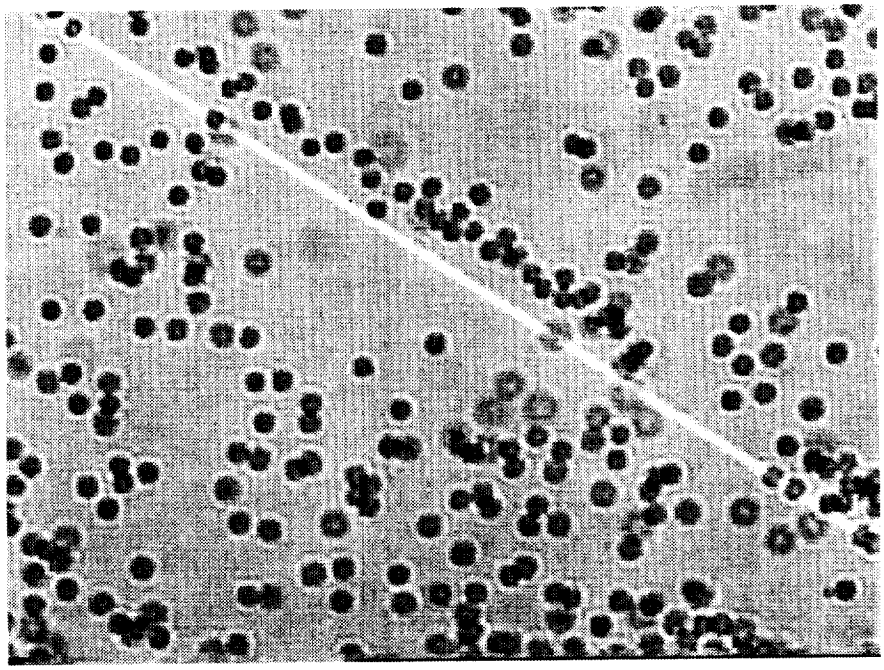

Attraction also works with PMMA in decalin-tetralin

Dielectrophoresis to control density

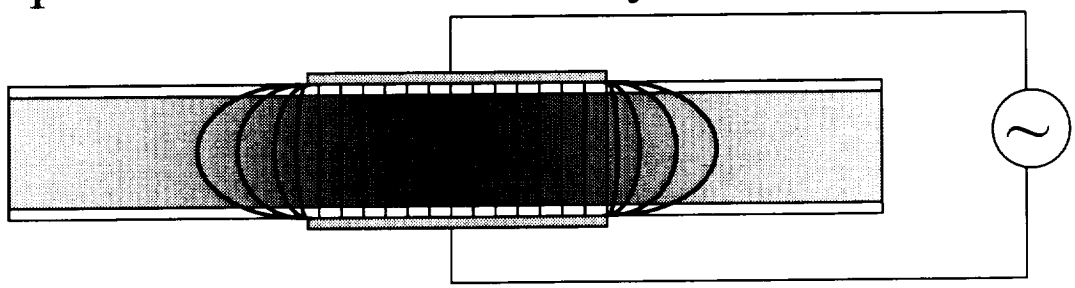

Particles with higher dielectric constant get sucked into region of high electric field

$$n \approx n_0 e^{\delta\varepsilon E^2 / 2k_B T}$$

For high density, interacting particles, field pressure balanced by osmotic pressure

$$\frac{\partial \Pi}{\partial x} = \frac{n}{2}\frac{\partial\left(\delta\varepsilon E^2\right)v_0}{\partial x} = \frac{\varphi}{2}\frac{\partial \delta\varepsilon E^2}{\partial x}$$

It works!

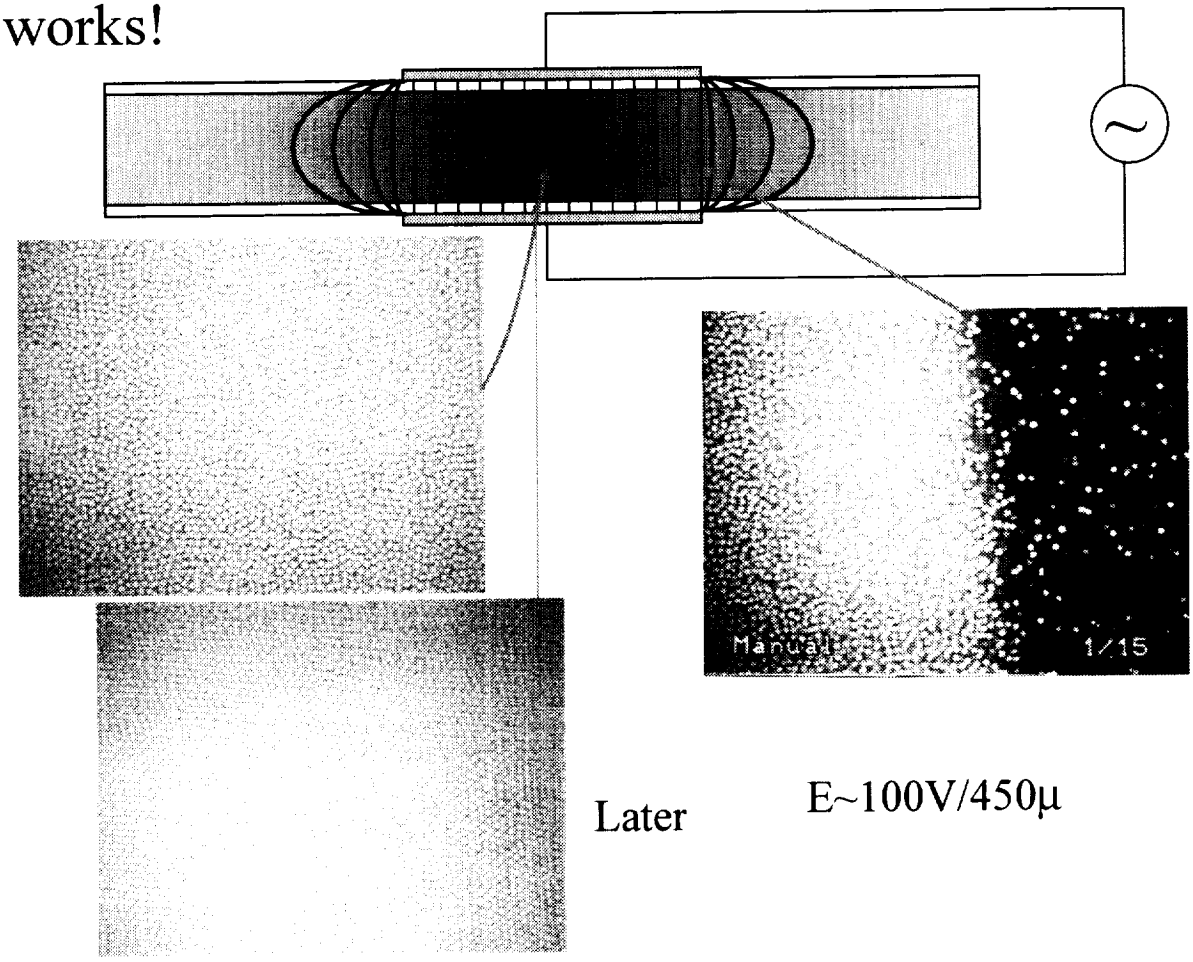

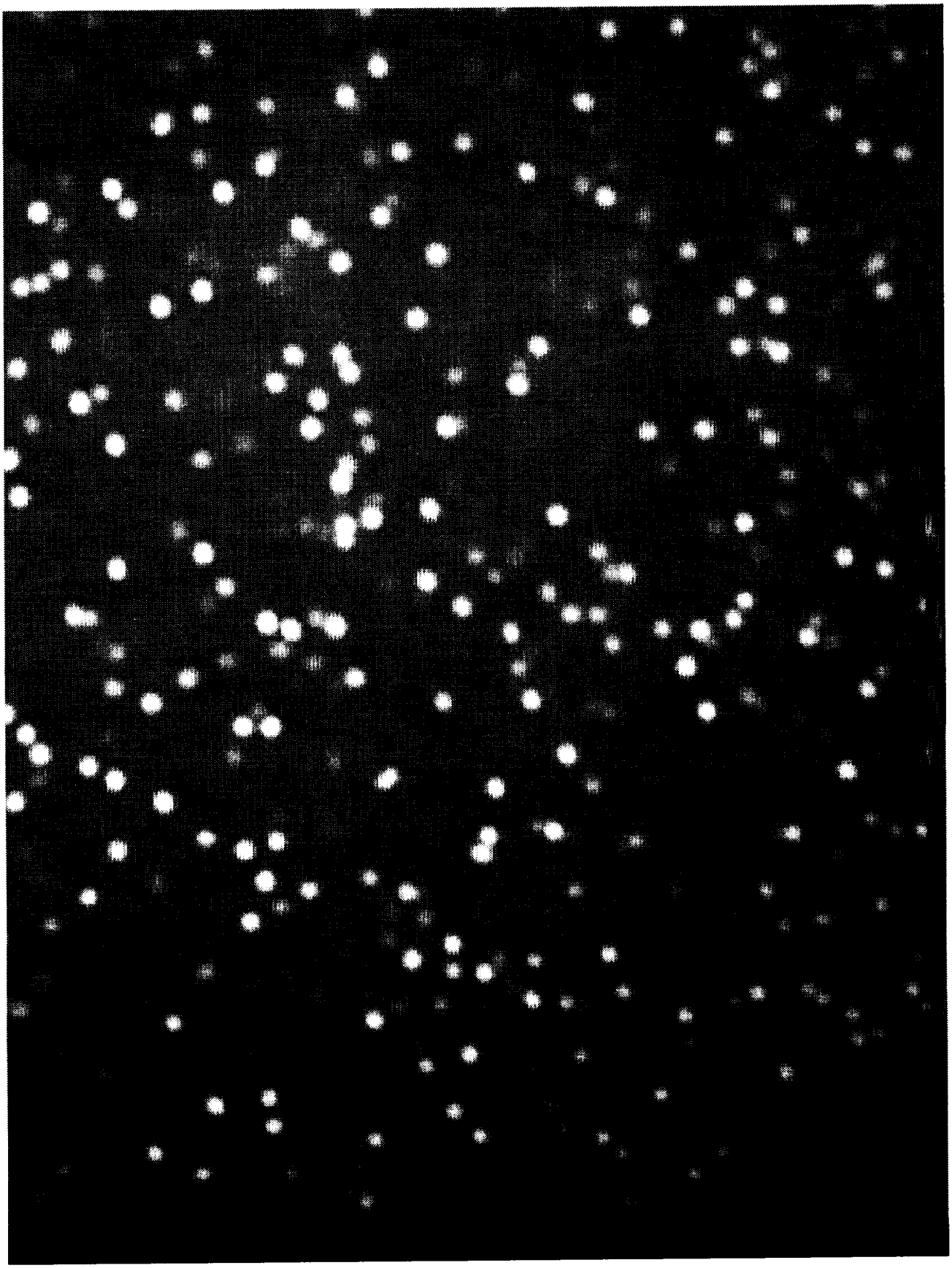

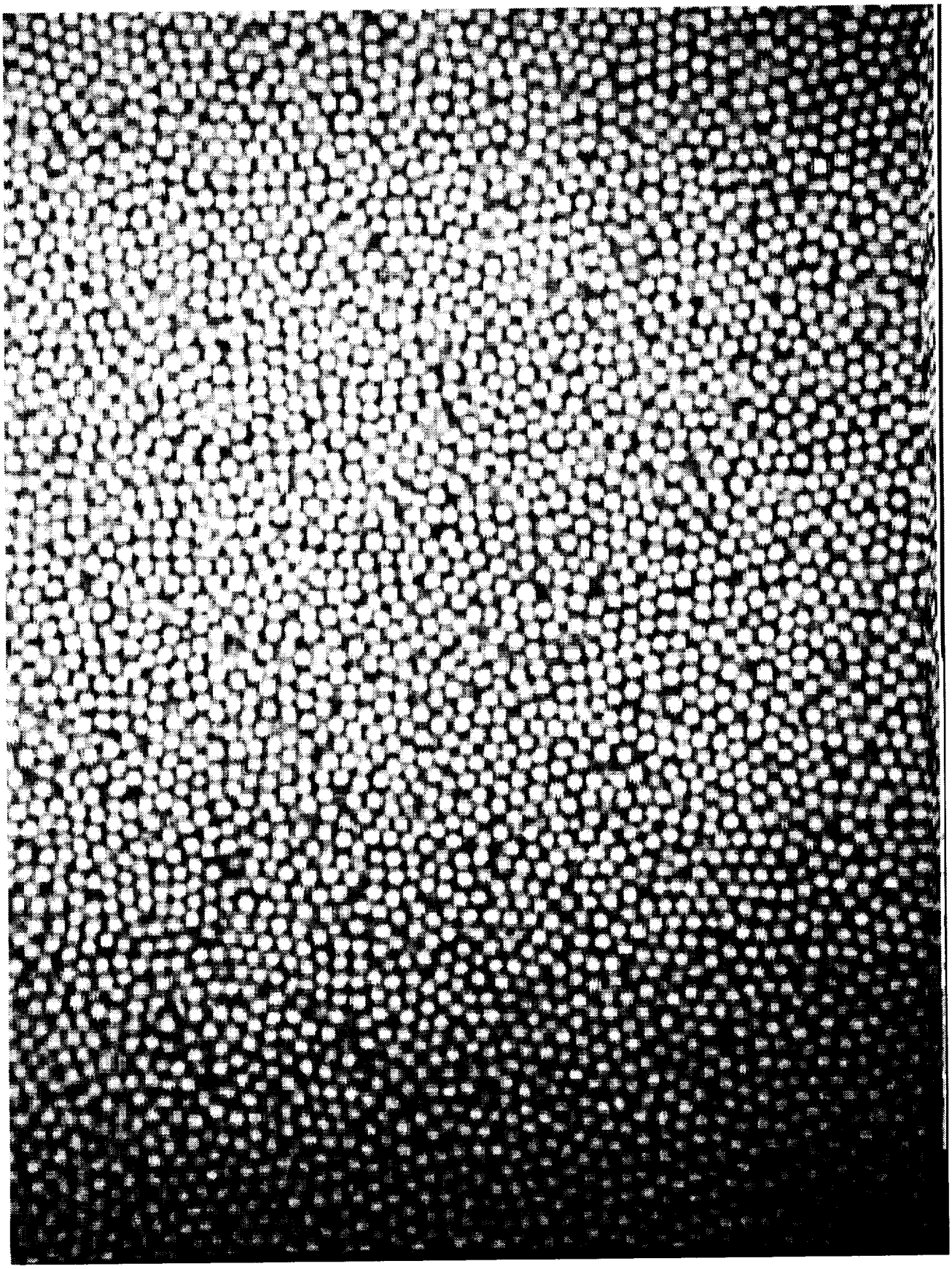

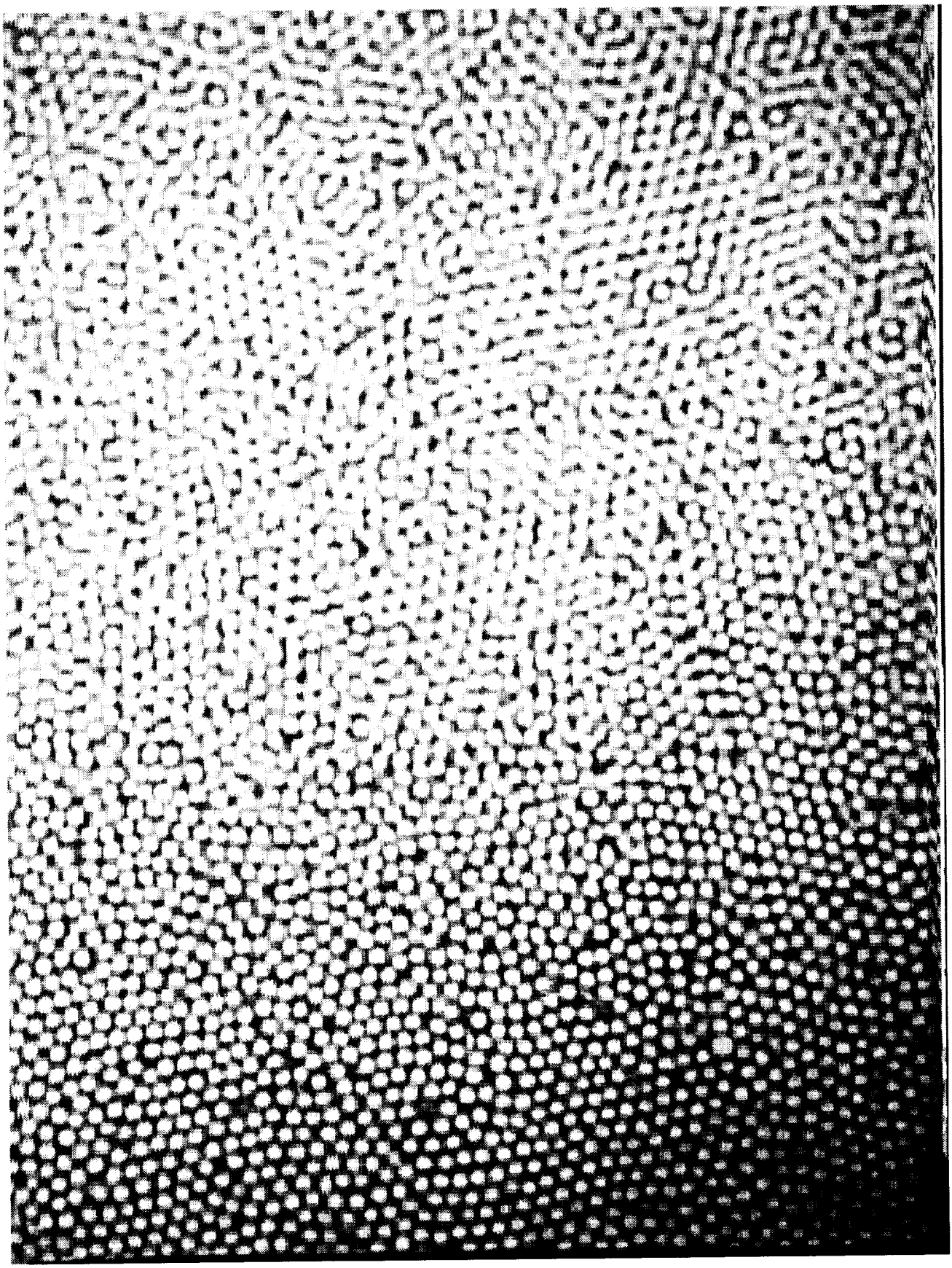

What About Electrorheological Fluid Chaining?

Dielectric sphere in field

$$P_{tot} = \frac{(\varepsilon - 1)}{(\varepsilon + 2)} E r^3$$

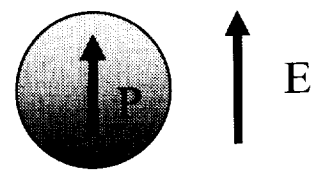

For density gradient want dipole in sphere $>k_BT$

$$P_{tot} \bullet E = \frac{(\varepsilon - 1)}{(\varepsilon + 2)} E^2 r^3 \sim \boxed{\frac{\delta\varepsilon}{3} E^2 r^3}$$

For no chains want dipole-dipole $<k_BT$

$$\frac{2P_{tot}^2}{(2r)^3} = \frac{\left(\frac{(\varepsilon - 1)}{(\varepsilon + 2)}\right)^2 E^2 r^6}{4r^3} \sim \boxed{\frac{(\delta\varepsilon)^2}{36} E^2 r^3}$$

Gradients and no chaining if: $\delta\varepsilon << 12$

Tailored Colloidal Particles
Ready to Lift-Off

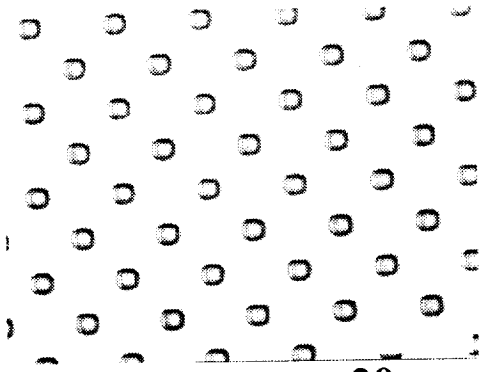

20 μm

disks!

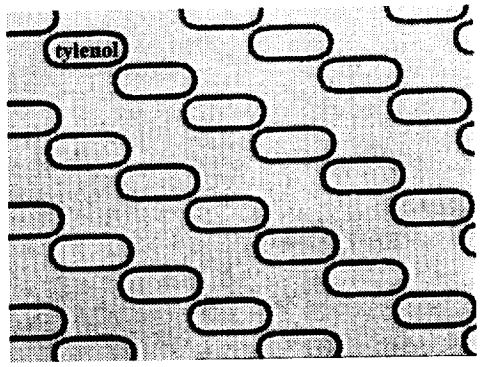

band-aids!

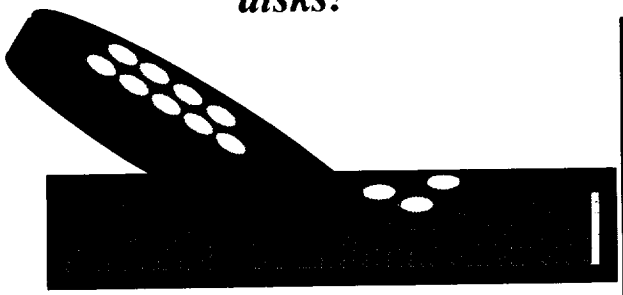

Sacrificial layer is dissolved upon immersion into solvent.

10^9 tailored colloids float off into solution

1 μl=(1 mm)^3 at closed packing.

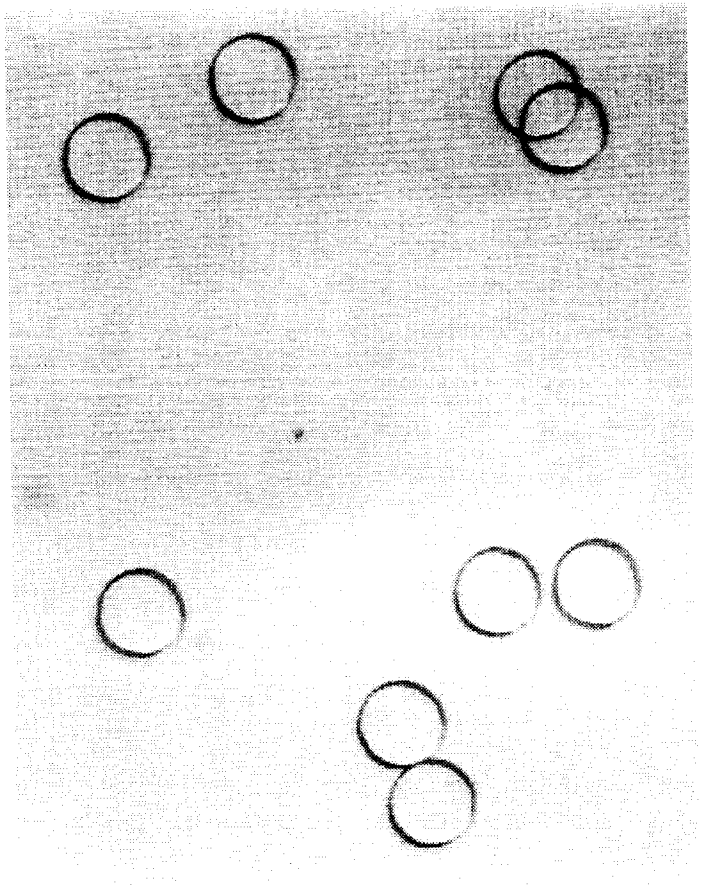

PMMA Donuts

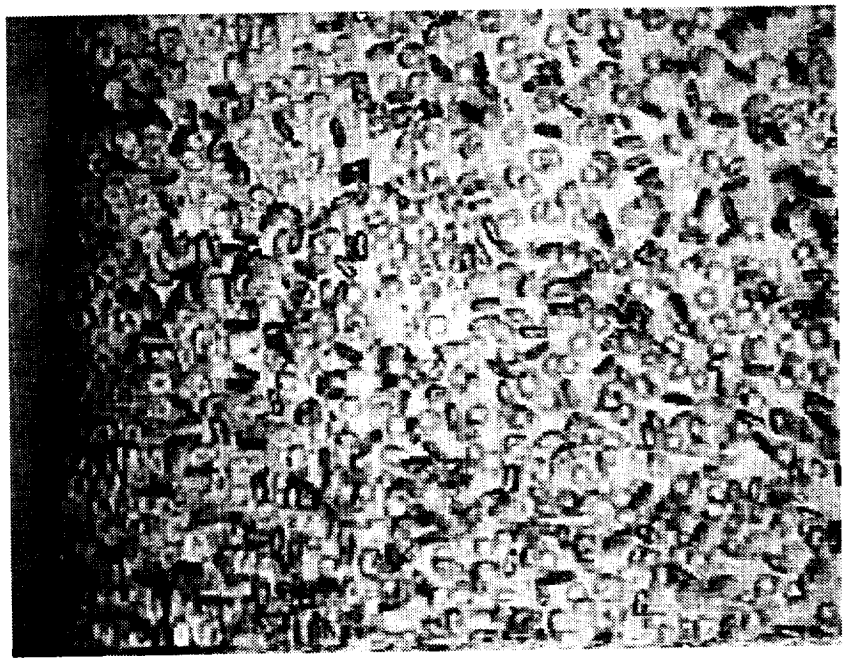

10 μm

Silicon Nitride Donuts

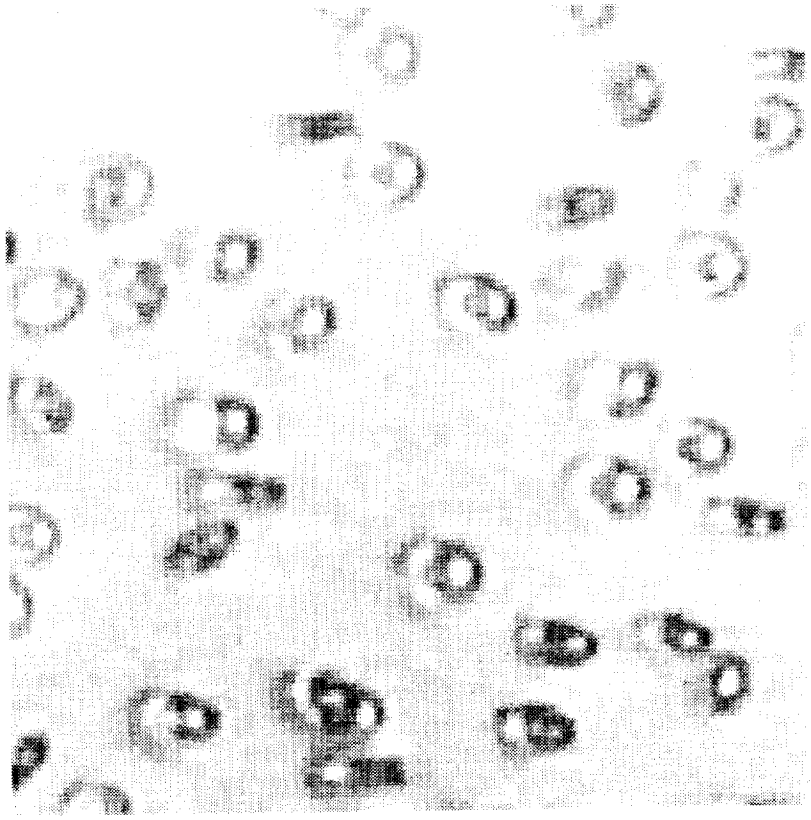

2 μm

Disks Align Edge-on and stably trap in tweezers

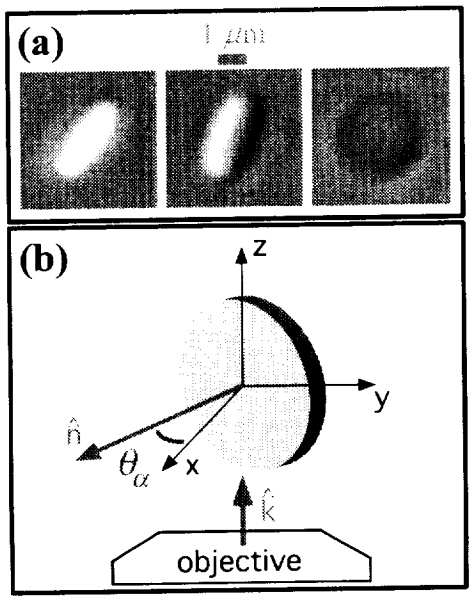

PRL next week

Works for both optically isotropic and birefringent disks
0.2-10μ, ~1:5 aspect ratio

With Birefringent Materials Get Torques

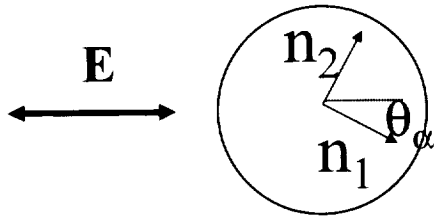

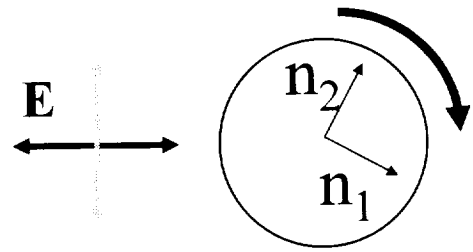

Linear Polarization

$$\tau = -\frac{2P_{eff}}{\omega_0}\sin(R)\sin(2\theta_\alpha)$$

Circular Polarization

$$\tau = \frac{2P_{eff}}{\omega_0}\sin^2(R/2)$$

$$R \approx 4\pi\Delta n a / \lambda$$

Rotates until n_1//E

Continuously Rotates

M. E. J. Friese et al. Nature 394, 348 (1998))
E. Higurashi et. Al. Phsy. Rev. E30, 2508 (1999)

α– eicosene Disks

Brownian Rotation

For PMMA disks get free Brownian rotation in Θ_R direction

For a-eicosene wax (CH_3-$(CH_2)_{17}$-$CH{=}CH_2$) disks get harmonically bound Brownian rotation:

$$\zeta\dot{\theta}_\alpha = \tau_R - \frac{2P_{eff}}{\omega_0}\sin(R)\sin(2\theta_\alpha)$$

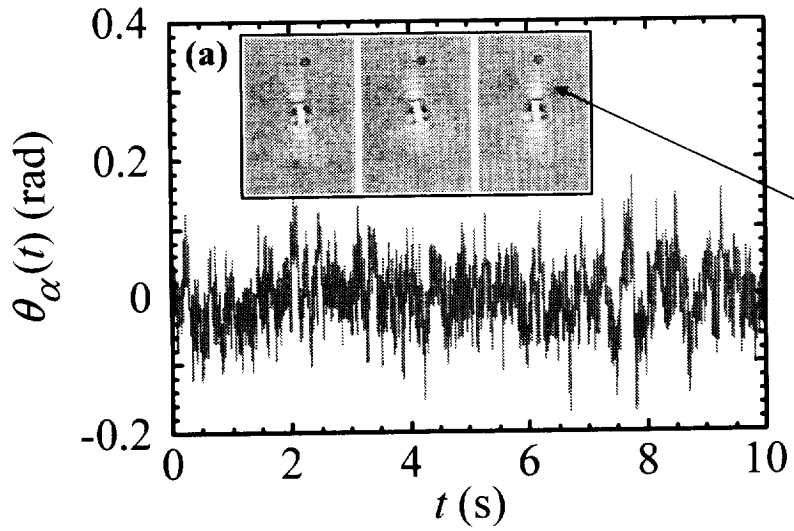

Note that reflection from disk faces gives a "Lighthouse Effect" in forward scattering. Allows accurate tracking of angular displacement

Fast video and/or photodiodes allow tracking over many orders in time

$$\left\langle \Delta\theta_\alpha^2(t) \right\rangle = \frac{2k_B T}{\kappa}\left[1-\exp(-\kappa t/\zeta)\right]$$

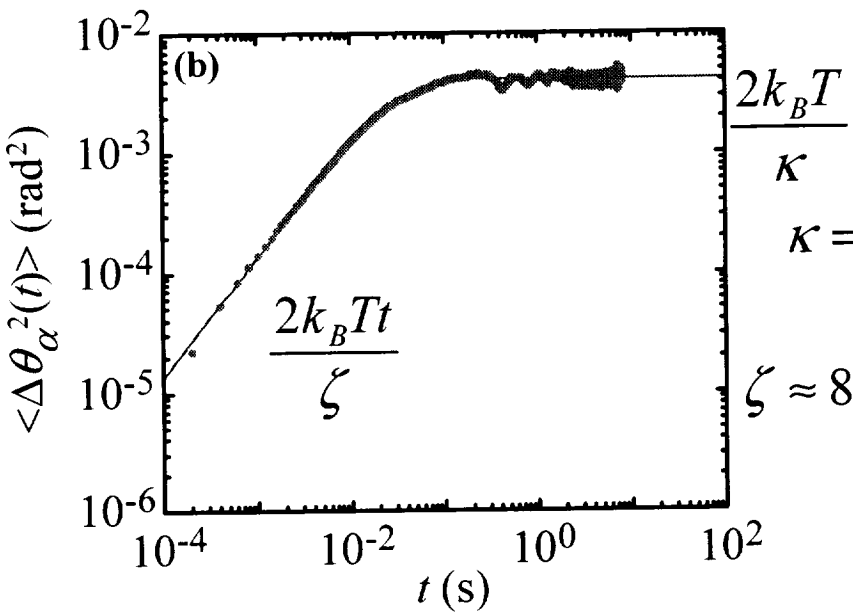

$$\kappa = \frac{4P_{eff}}{\omega_0}\sin(R)$$

$$\zeta \approx 8\pi\eta a^3 H(\rho)$$

Restoring force depends linearly on Power ~E_0^2

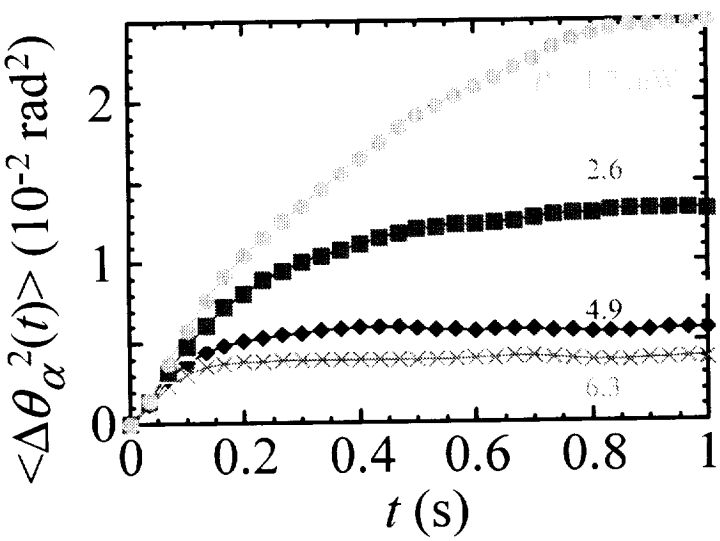

$$\frac{2k_BT}{\kappa}$$

$$\kappa = \frac{4P_{eff}}{\omega_0}\sin(R)$$

$$R \approx 4\pi\Delta na/\lambda$$

Can use rotational tracking for microrheology

In Circularly polarized light disks Rotate continuously

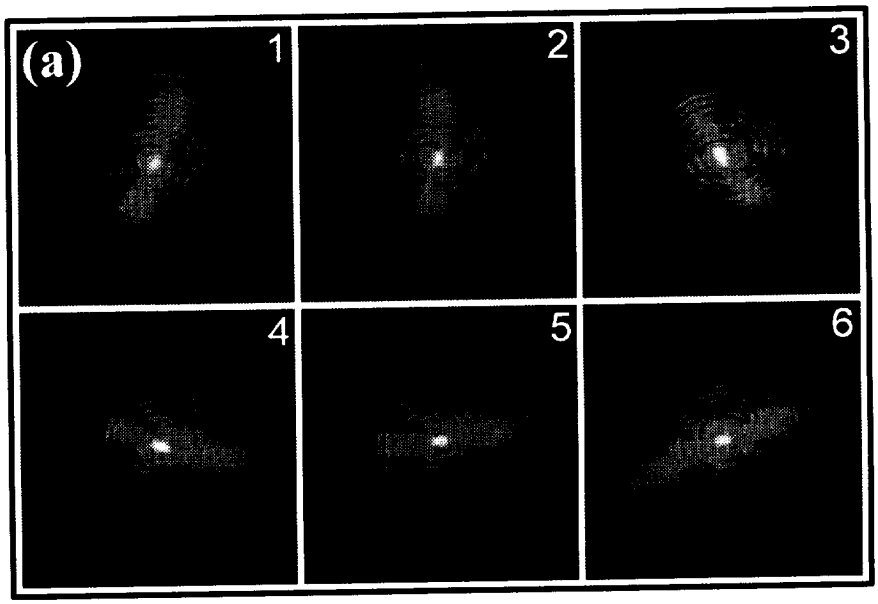

Rotation Rate proportional to power

$$\zeta\dot{\theta}_\alpha = \frac{2P_{eff}}{\omega_0}\sin(R/2)$$

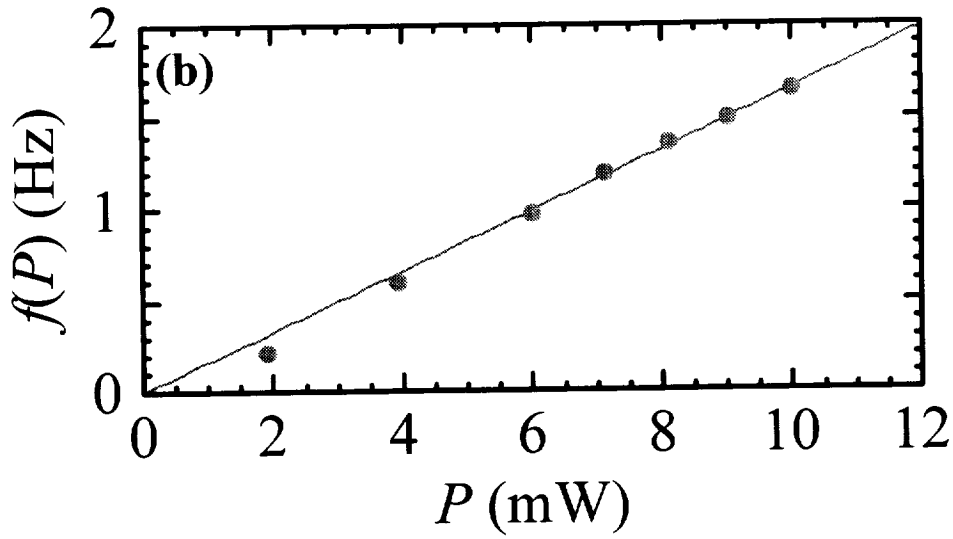

"Switchback Oscillations" result when disk is tweezed against back wall

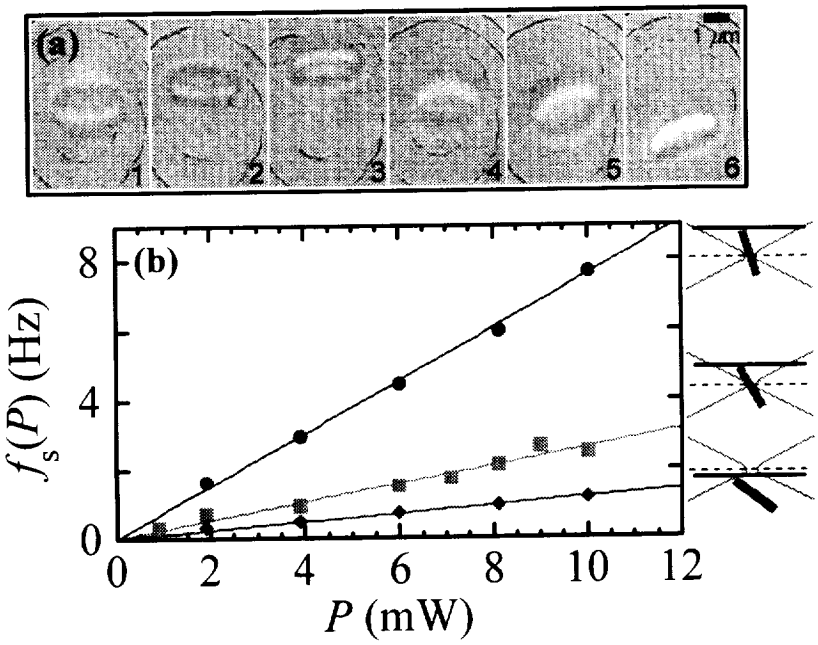

Forces and torques near wall

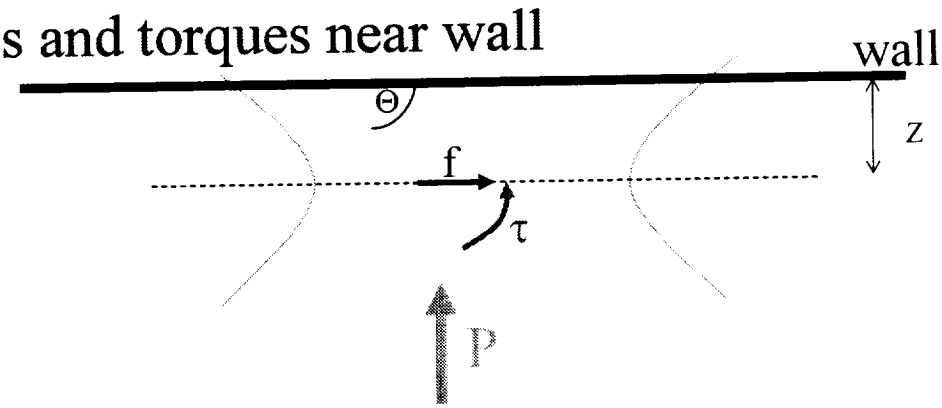

Forces f

- Restoring force of trap $-a_2 P x$
- Photon pressure on tilted disk $a_1 P \sin(\theta)\cos(\theta)$

Torques τ

- Restoring torque of trap $-a_5 P \sin(\theta)\cos(\theta)$
- Normal force wall - tilted disk $a_4 r P (r\cos(\theta) - z) r \sin(\theta)$
- Friction wall-tilted disk $a_6 (r\cos(\theta) - z) r \cos(\theta) \frac{dx}{dt}$

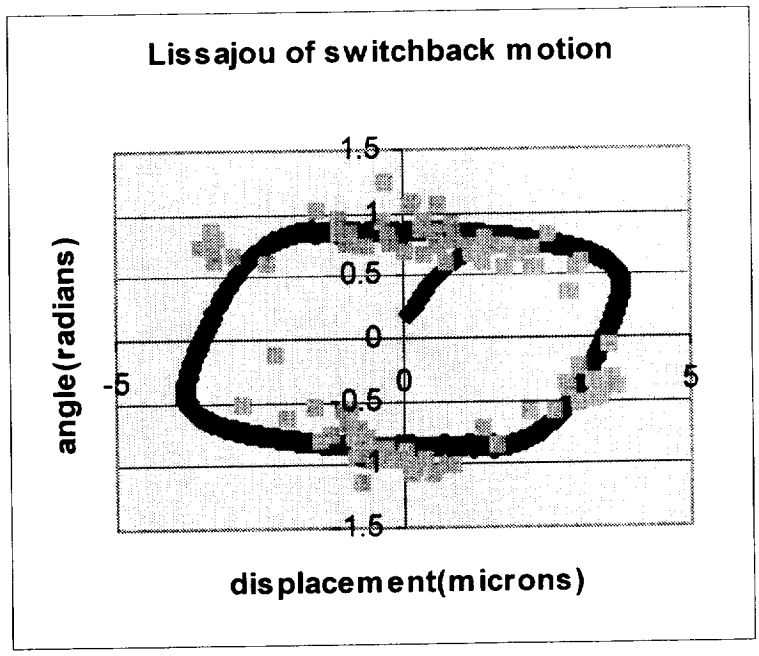

Data

Model

$$a_3 6\pi\eta r \frac{dx}{dt} = a_1 P \sin(\theta)\cos(\theta) - a_2 P x \qquad \text{force}$$

$$a_7 8\pi\eta r^3 \frac{d\theta}{dt} = \begin{bmatrix} a_4 r P(r\cos(\theta) - z) r \sin(\theta) - a_5 P \sin(\theta)\cos(\theta) \\ + a_6 (r\cos(\theta) - z) r \cos(\theta) \frac{dx}{dt} \end{bmatrix} \qquad \text{torque}$$

Conclusion

Microscopy allows:

- Control of density and growth through temperature Gradients and electric fields
- Studies and manipulation of mechanically and optically anisotropic particles
- New techniques for rheology and motility

TWO-DIMENSIONAL STREPTAVIDIN CRYSTALS ON GIANT LIPID BILAYER VESICLES

Pasut Ratanabanangkoon
Department of Chemical Engineering, Stanford University, Stanford, CA

Michael Gropper, Rudolf Merkel
Department of Biophysics, Technical University of Munich, Munich, Germany

Alice P. Gast
Department of Chemical Engineering, Massachusetts Institute of Technology, Cambridge, MA
Phone: (617) 253-1403; Fax: (617)-253-8388; e-mail: gast@mit.edu

ABSTRACT

Two-dimensional (2D) ordering of macromolecules is of particular interest due to their scientific importance as fundamental models for studying phase transitions and self-assembly. It is also a basis for the design and development of many biosensor and bioassay devices and engineered biomaterials. The ability to create and manipulate self-assembled structures of macromolecules requires a thorough understanding and control of the various intermolecular forces involved. In this study, we used 2D streptavidin crystallization as a model system to study 2D protein organization on lipid bilayers and their effect on bilayer properties.

We studied the crystallization of streptavidin on giant lipid bilayer vesicles. Giant Unilamellar Vesicles (GUVs) are composed of a single lipid bilayer membrane with sizes of approximately 10-100 microns in diameter. Due to the sensitivity to ionic species, they remain stable in only extremely low ionic strength solutions. Once bound to the vesicle surface, streptavidin crystallized to form a rigid polycrystalline shell surrounding the vesicle. The ability to create crystals on GUVs provides a means to study many crystals in a single experiment and in a microgravity environment. Transmission Electron Microscopy (TEM) images of negatively-stained vesicles revealed that the crystals are of the lowest-density C222 symmetry, and does not change with solution pH unlike those grown in high ionic strength conditions. The lack of higher density 2D crystal forms is due to the strong electrostatic repulsion. Despite the presence of only one crystal structure, the change in solution pH changed the macroscopic crystal morphology and crystal growth pattern, and the vesicles were distorted into either roughened spheres or football-shaped ellipsoids.

Micropipette aspiration of avidin-coated and streptavidin-coated vesicles revealed the unique mechanical properties of the protein-lipid membrane. Vesicles coated with the noncrystallizable avidin shows relatively similar elastic area expansion modulus to that of uncoated vesicles. The existence of crystalline domains on streptavidin-coated vesicles resulted in various unique mechanical properties. Rapid permanent deformation was observed at low strain, while a slower viscoelastic behavior was observed at higher deformation. Despite their extremely rigid appearance, the presence of an external polycrystalline shell does not increase the toughness of the vesicles beyond that of bare vesicles. The distinctive properties of the protein-lipid

composite membrane can be traced to the unique combination of streptavidin-streptavidin, streptavidin-phospholipid, and phospholipid-phospholipid interactions.

Three-dimensional reconstructed confocal microscopy images of two-dimensional streptavidin crystals (shown in black) on giant lipid bilayer vesicles. Scale bar represents 10 μm.

OPTICALLY-EXCITED WAVES IN 3D DUSTY PLASMAS

John Goree
Dept. of Physics and Astronomy, The University of Iowa, Iowa City, IA 52242

ABSTRACT

Flight experiments are planned for an interdisciplinary study of waves (i.e., phonons) in 3D Coulomb lattices. The experimental system will be a suspension of charged polymer microspheres in a gas-discharge plasma. This so-called "dusty plasma" is a macroscopic system where the microspheres arrange themselves, due to their mutual repulsion, in a lattice. Like a colloidal suspension, this lattice can be in a crystalline or liquid state. The particles are imaged directly using video microscopy.

These experiments are an extension of 2D experiments performed in the laboratory, under gravity conditions. Sedimentation due to gravity causes the microspheres to settle rapidly into a 2D layer that is levitated by the strong electric field near an electrode in a plasma. By eliminating gravity, it is possible to fill a 3D volume with the suspension.

Experiments will focus on the shear acoustic wave in the lattice. This kind of wave has particle motion that is transverse to the direction of wave propagation. Our experiments will exploit the low damping of a dusty plasma as compared to colloidal suspensions. We will excite the waves using a manipulation laser, which applies a radiation pressure on the particles. Particle motion will be measured *in-situ* using direct imaging with video microscopy. After the experiment, we will analyze the video data by computing the particle velocities and then analyzing the wave motion of the particles.

The experiment is to be performed on-orbit in ISS, with accommodation probably in the FIR. Preliminary tests of the experimental procedures will be done in parabolic aircraft flights.

The two experimental tasks for the flight experiments will be:

1. Study the dispersion relation (i.e., phonon spectrum) of sinusoidal waves and the propagation of pulsed waves. These experiments will be performed with plane waves.
2. Study the formation of Mach cones, which are the V-shaped wakes or shocks created by a supersonic disturbance. In this experiment, a moving laser spot is the supersonic disturbance.

These experiments build on our laboratory experience with these waves and Mach cones in a 2D lattice. This earlier work has been carried out as a ground-based project funded by the Fluid Physics discipline of NASA's microgravity program. Some of the results of these ground-based experiments are described below.

A 2D hexagonal lattice sustains two wave modes, for particle motion in the plane of the lattice. These modes are the longitudinal and transverse sound waves. We report experimental results, supported by theory and simulations, demonstrating the properties of these two waves.

The waves, which are observed by measuring the particle velocities, can be excited by two mechanisms in the lab: laser manipulation and thermal particle motion.

Using laser manipulation, we excited both modes. An argon laser beam was directed toward the lattice, where it pushed the particles about with a spatial and temporal variation that we controlled, using scanning mirrors. For low laser power, we verified that both waves obey their linear dispersion relations [1] for a Yukawa inter-particle repulsion. We found that this provides a method of measuring charge and screening length with considerable precision. In contrast to the longitudinal wave, the transverse mode has a dispersion relation with a more linear relationship of f vs. k, i.e., a more dispersionless characteristic over a wide range of k [2]. We found that Mach cones can be excited which consist not only of the longitudinal wave, as reported earlier [3], but also the transverse wave. A Mach cone is excited by a moving laser spot, as shown in the figure. The other waves are excited by a stationary sheet of light that is modulated temporally. By using a higher power for the laser sheet, we excited weakly nonlinear longitudinal waves, which propagated faster than the sound speed for small amplitude waves.

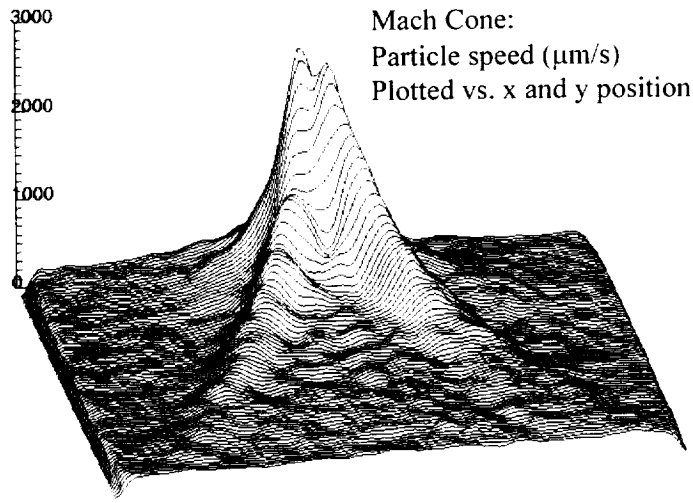

In the absence of external particle manipulation, we found that natural thermal particle motion consists of a spectrum of both kinds of waves, where the wave energy is distributed over values of f and k that satisfy the linear dispersion relation, as shown in the first figure [4].

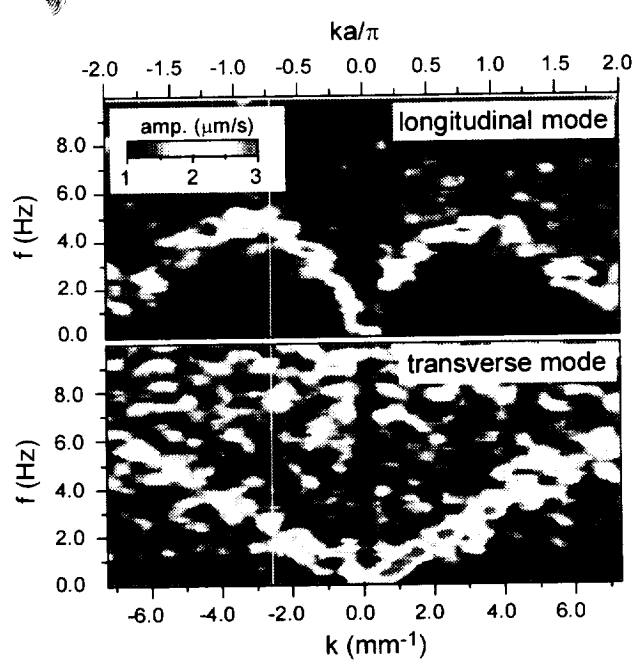

Phonon spectrum in the absence of laser manipulation. The wave amplitude is plotted vs. wavenumber over the first Brillouin zone, for propagation parallel to a primitive lattice vector.

[1] X. Wang, A. Bhattacharjee, and S. Hu, Phys. Rev. Lett. 86, 2569 (2001).

[2] S. Nunomura, D. Samsonov, and J. Goree, Phys. Rev. Lett. 84, 5141 (2000).

[3] V. Nosenko, J. Goree, Z.W. Ma and A. Piel, Phys. Rev. Lett. 88, 135001-1 (2002).

[4] S. Nunomura, J. Goree, S. Hu, X. Wang, A. Bhattacharjee and K. Avinash, Phys. Rev. Lett. (2002).

Optically-Excited Waves in 3D Dusty Plasmas

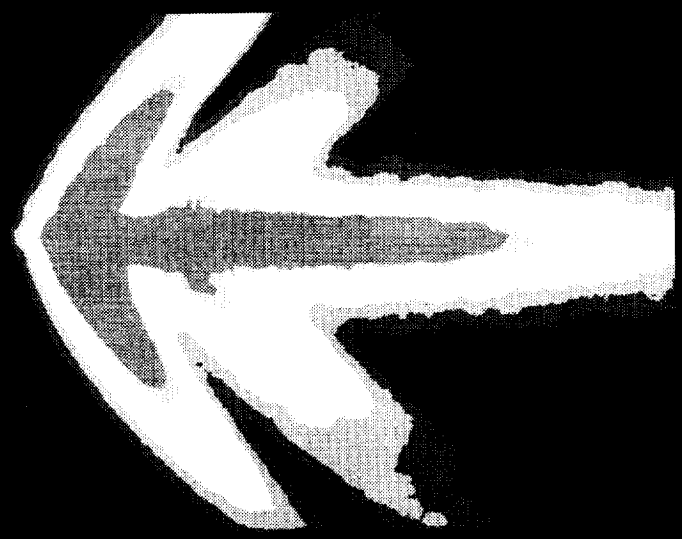

John Goree *The University of Iowa*

What is a dusty plasma?

plasma = electrons + ions

small particle of solid matter

- absorbs electrons and ions
- becomes negatively charged
- Debye shielding

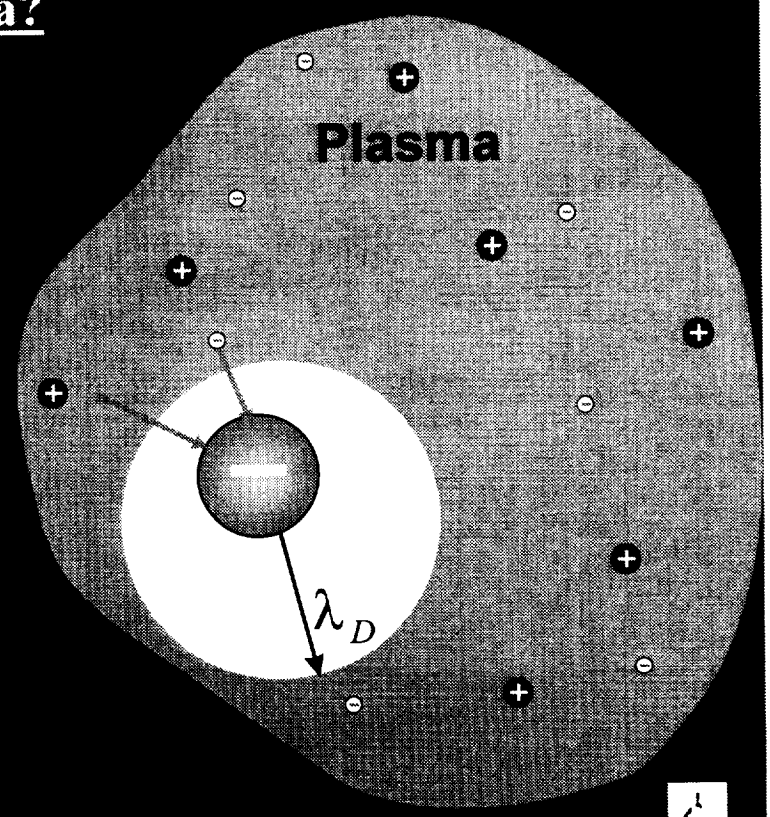

Who cares about dusty plasmas?

Solar system

- Rings of Saturn
- Comet tails

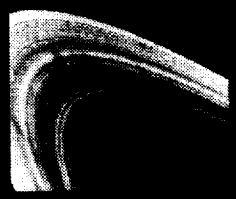

Manufacturing

- Particle contamination
  (Si wafer processing)
- Nanomaterial synthesis

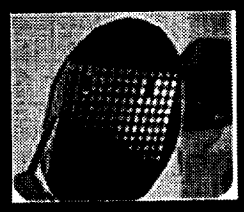

Basic physics

- Coulomb crystals
- Waves

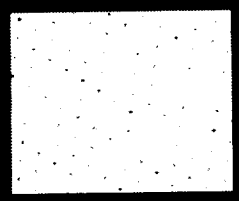

Forces Acting on a Particle

Coulomb

QE

Gravity

mg

Other forces:

- Gas drag
- Ion drag
- Thermophoresis
- Radiation Pressure

Electrostatic trapping of particles

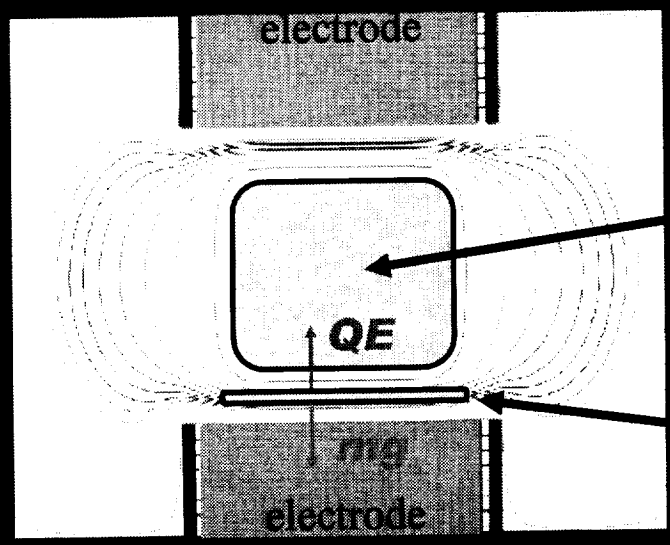

Equipotential contours

Without gravity, particles fill 3-D volume

With gravity, particles sediment to high-field region
⇒ 2-D layer

Particles

polymer microspheres

8 μm diameter

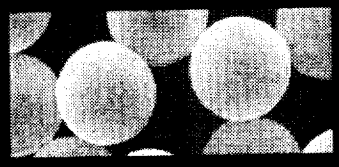

separation $a \approx 0.5$ mm

charge $Q \approx -10^4\, e$

Comparison to Colloidal Suspensions

Same:

- Coulomb repulsion
- Crystals

Different:

- Dusty plasma has much lower damping rate $\Longrightarrow$ wave propagation is easier

Experiments described in this talk

- 2D physics: *Ground-based*
- 3D physics: *Flight*

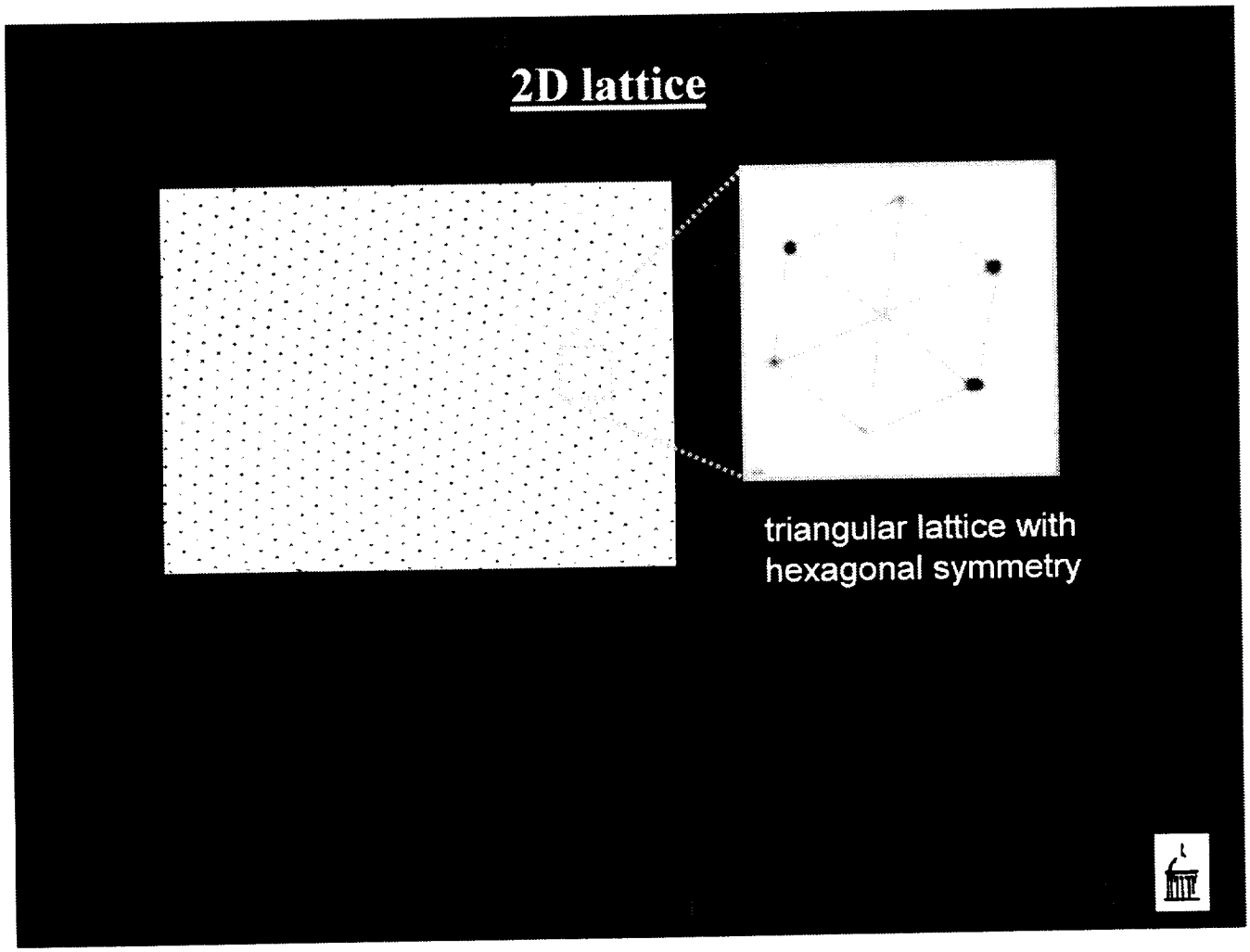
2D lattice
triangular lattice with
hexagonal symmetry

Two modes in a lattice

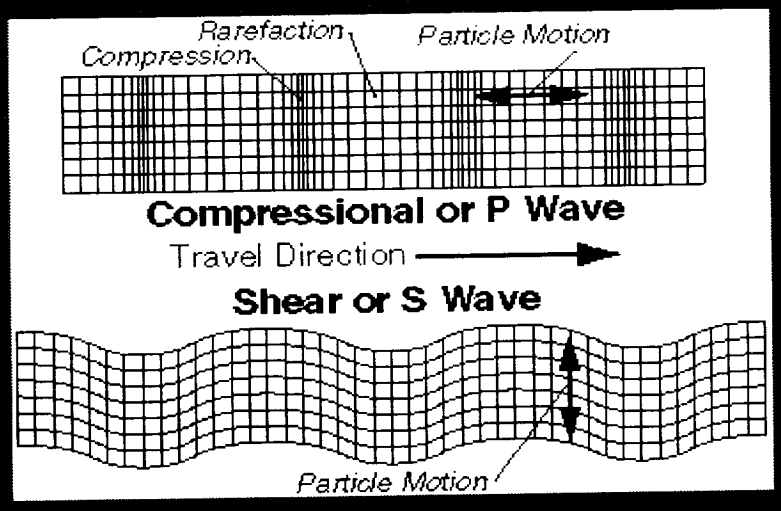

Dispersion relations in 2D triangular lattice

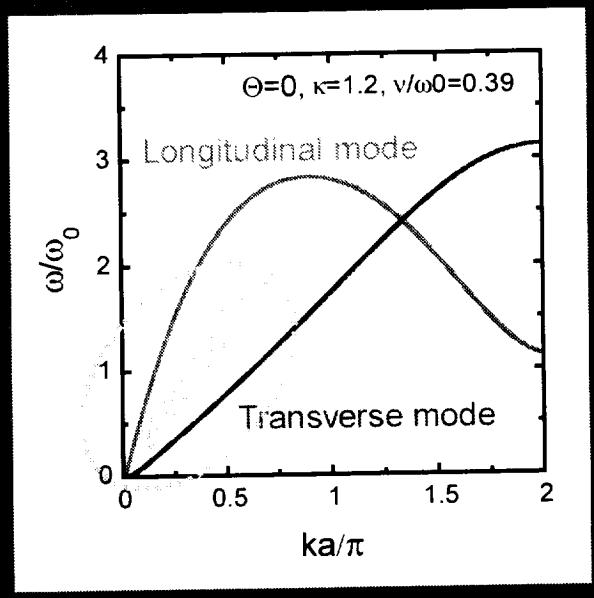

Wang *et al.* PRL 2001

Setup

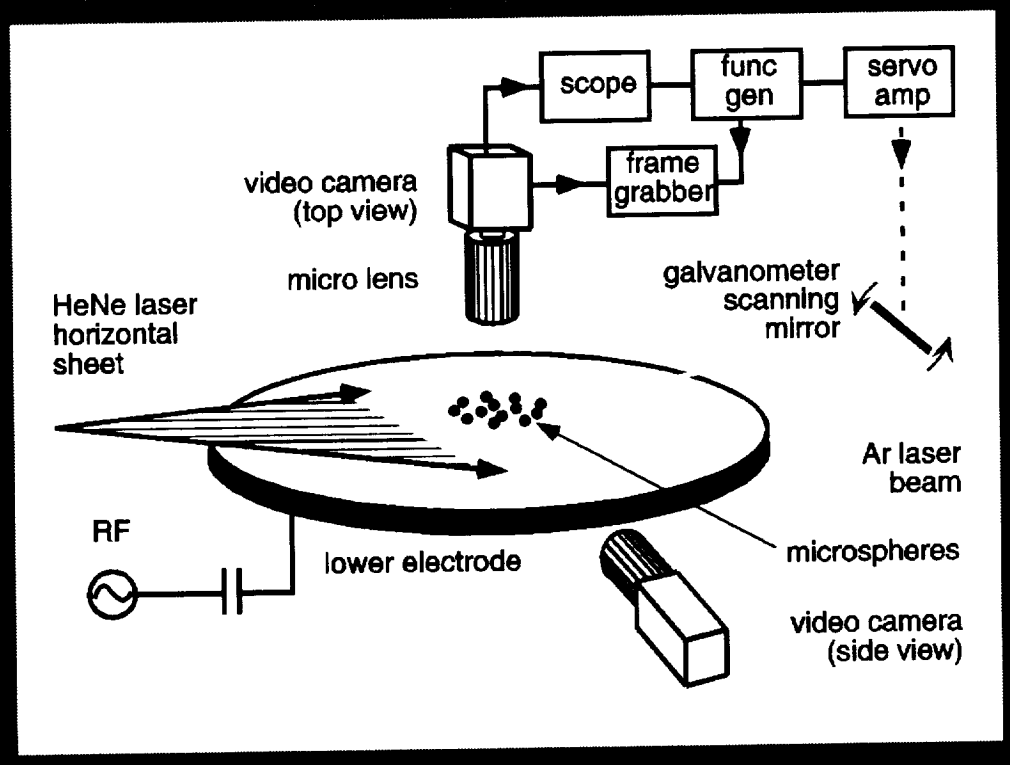
scope
func gen
servo amp
frame grabber
video camera (top view)
micro lens
galvanometer scanning mirror
HeNe laser horizontal sheet
Ar laser beam
RF
lower electrode
microspheres
video camera (side view)

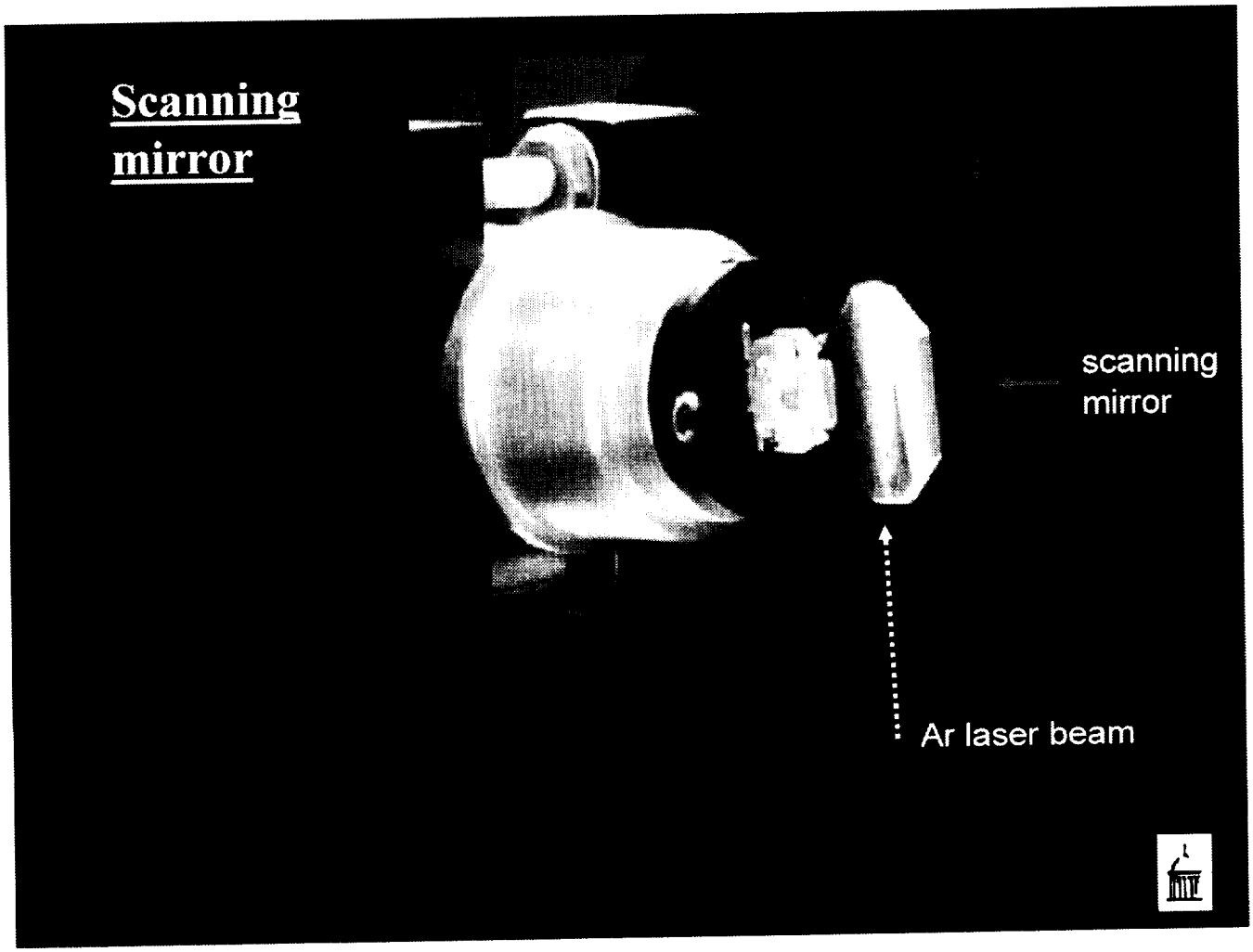
Scanning mirror
scanning mirror
Ar laser beam

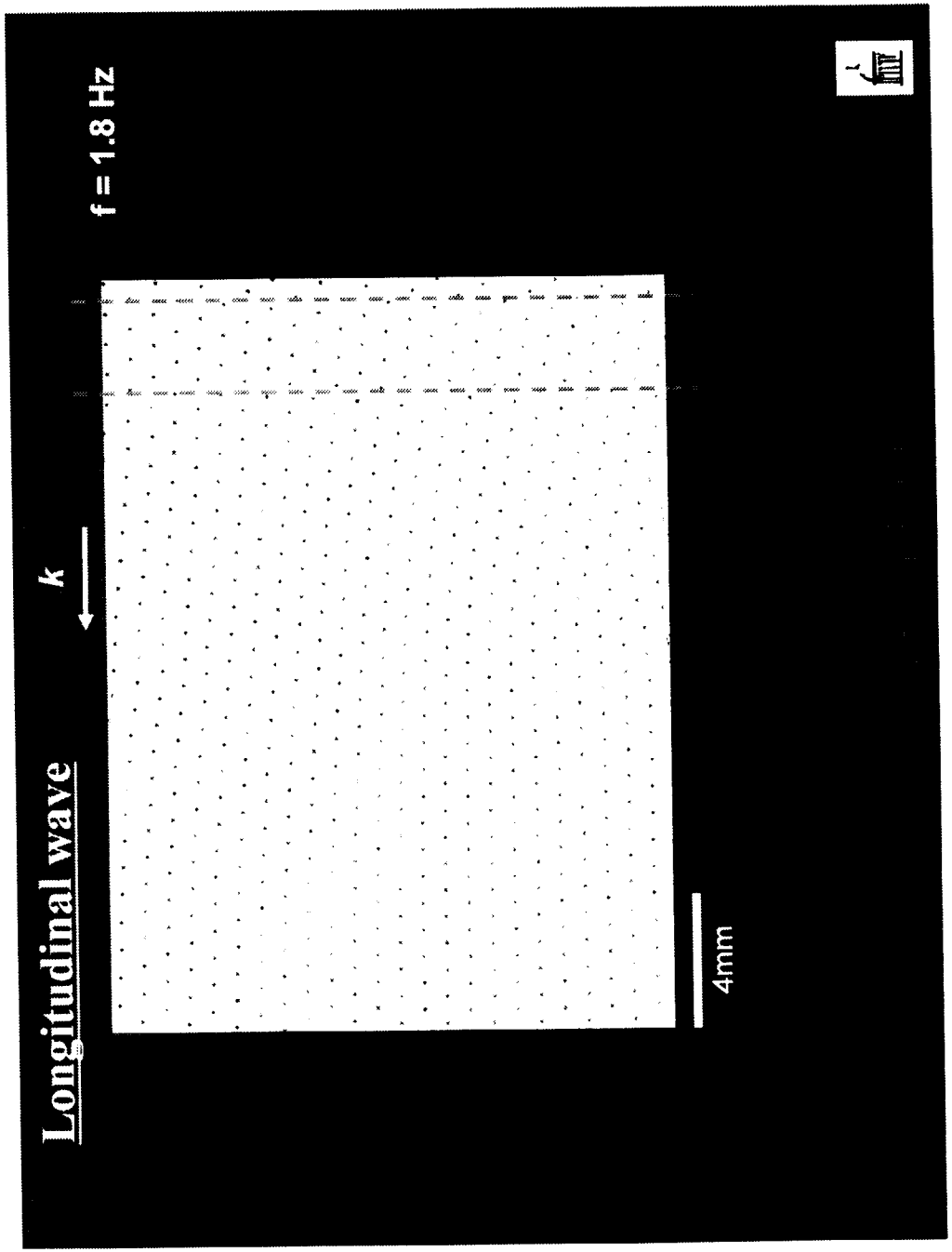
Longitudinal wave
k
f = 1.8 Hz
4mm

Random particle motion

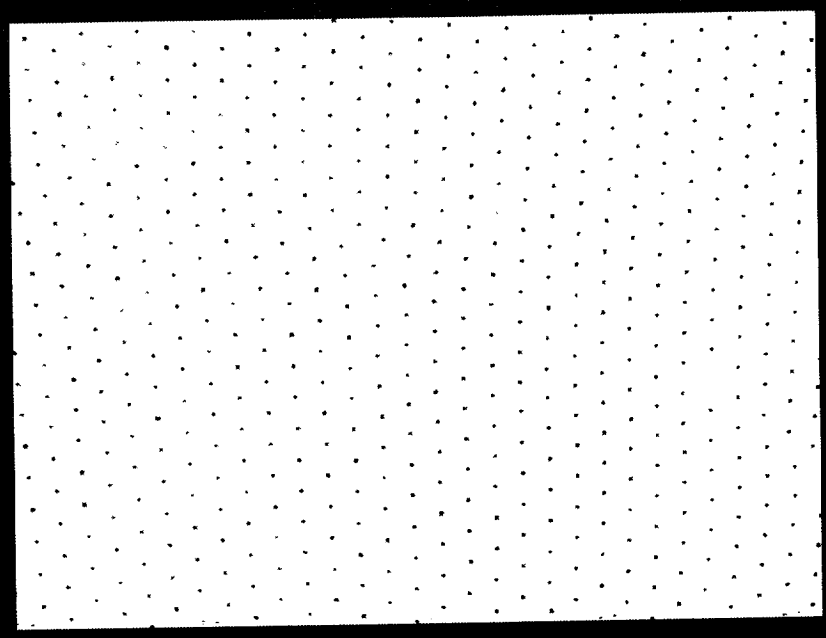

Phonon spectrum& sinusoidally-excited waves

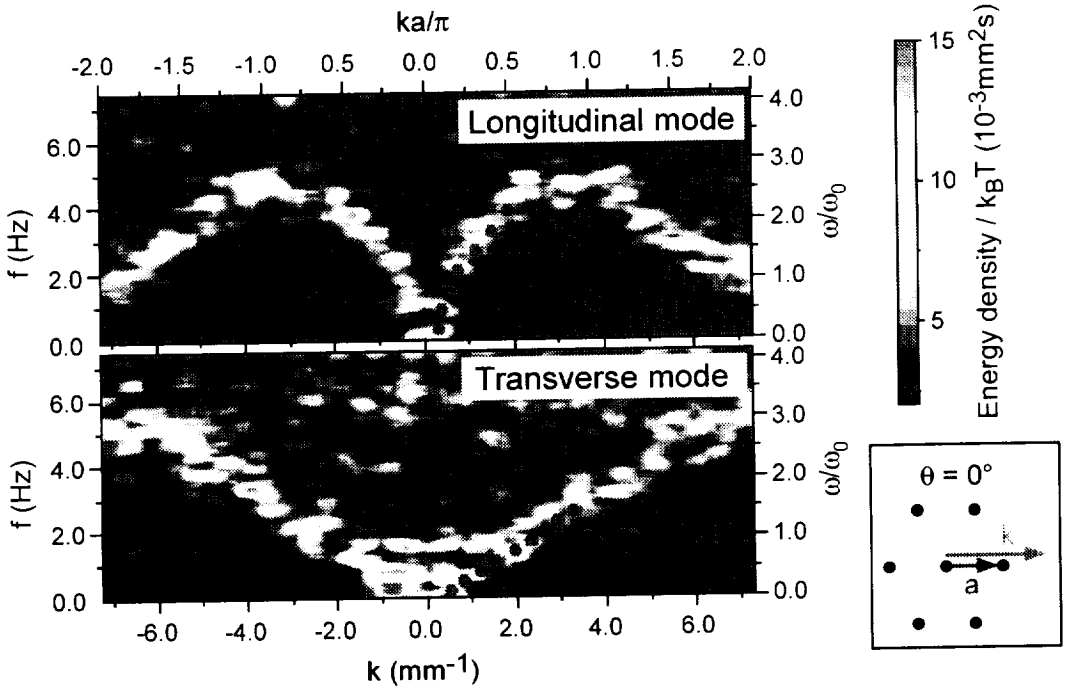

Nunomura *et al.* PRL 2002

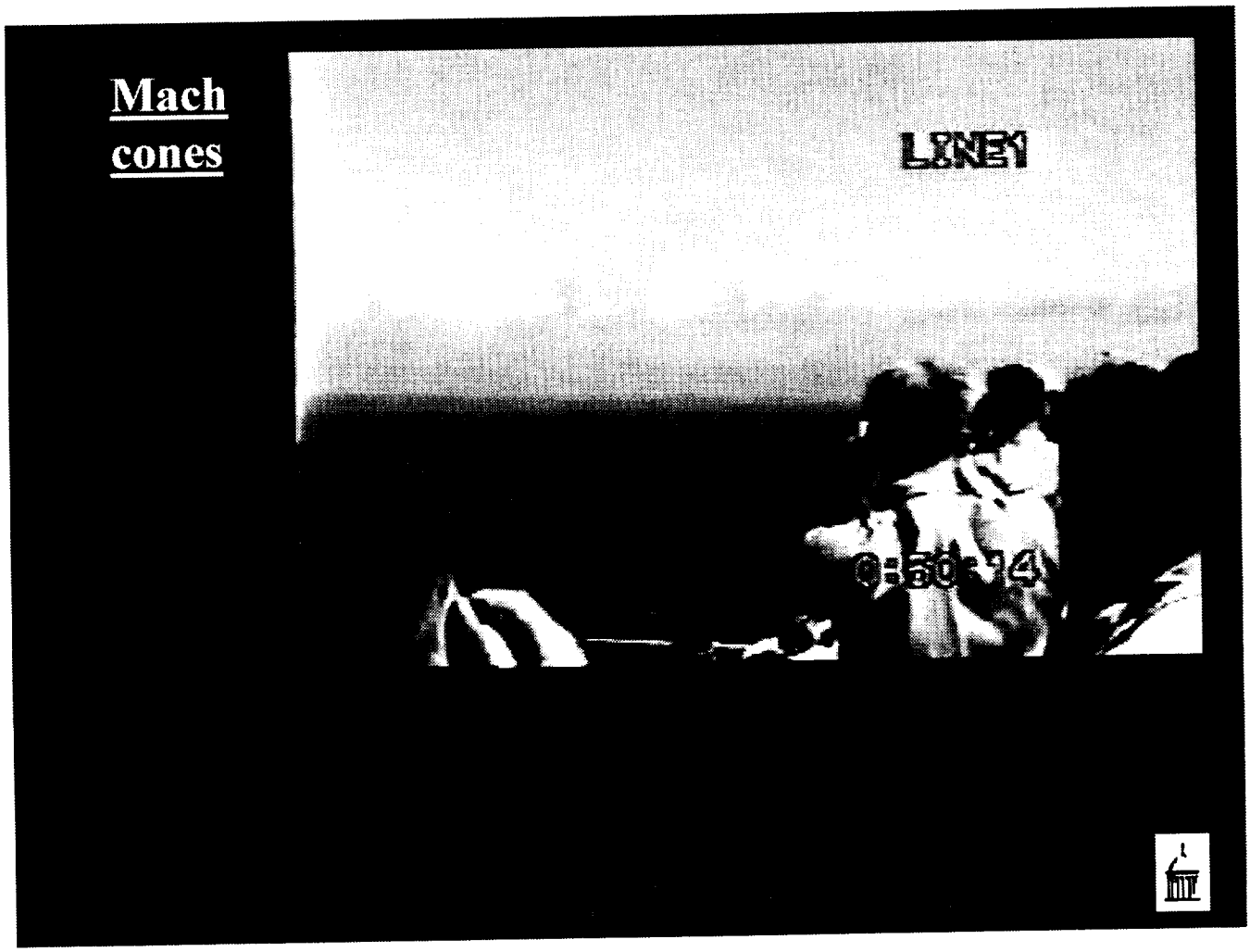
Mach
cones
LINE1
0:50:74

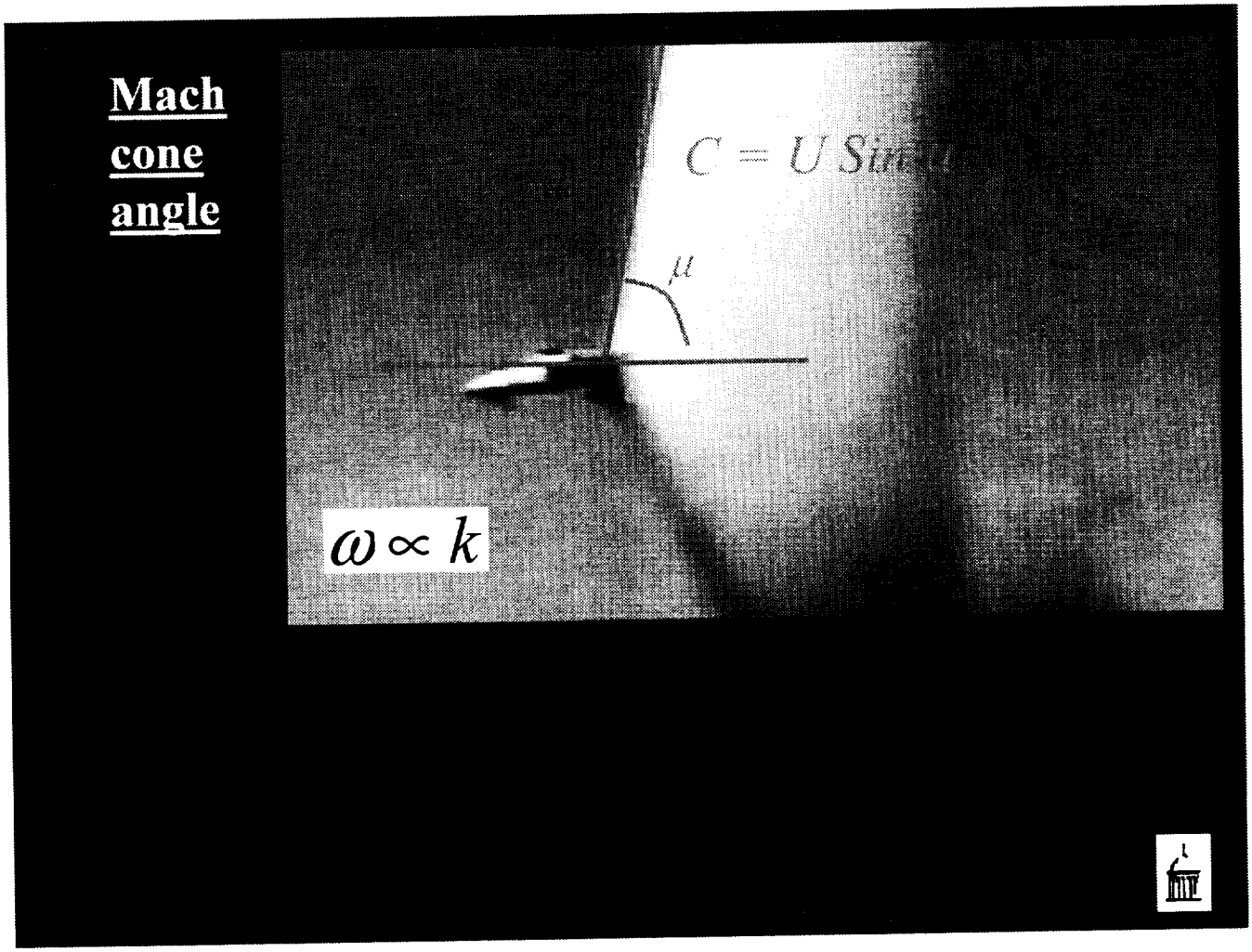
Mach
cone
angle
$C = U\,Sin$
μ
$\omega \propto k$

Ship's wake

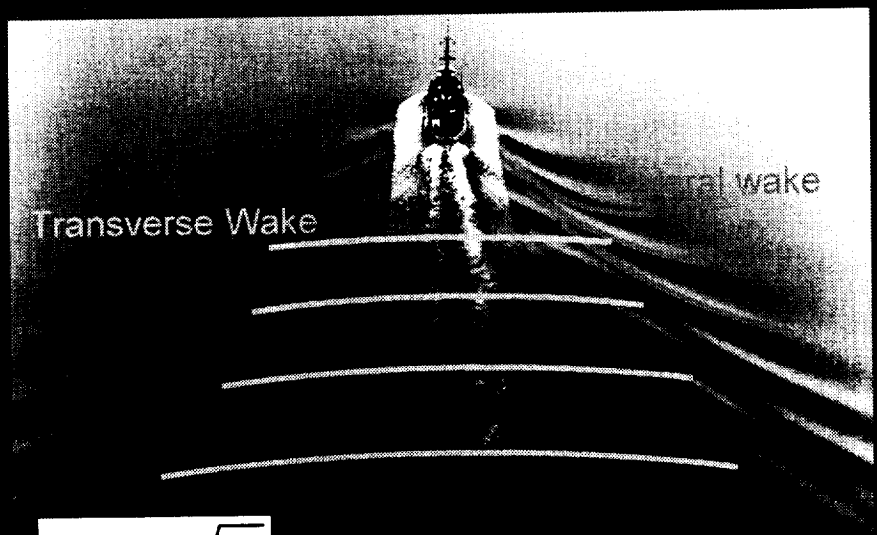

$$\omega \propto \sqrt{k}$$

Wake pattern is determined by dispersion relation

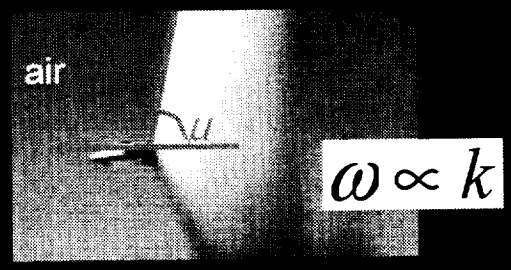

Mach cone

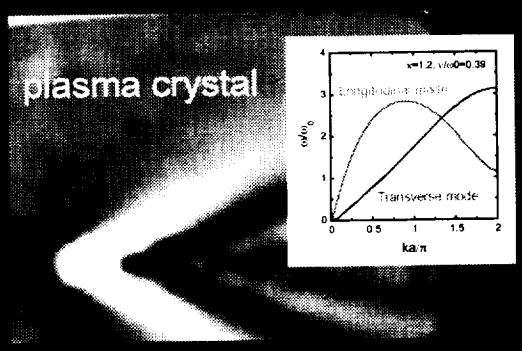

Has both features

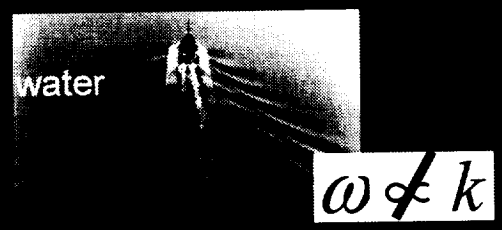

Lateral & transverse wakes

Mach cone excitation

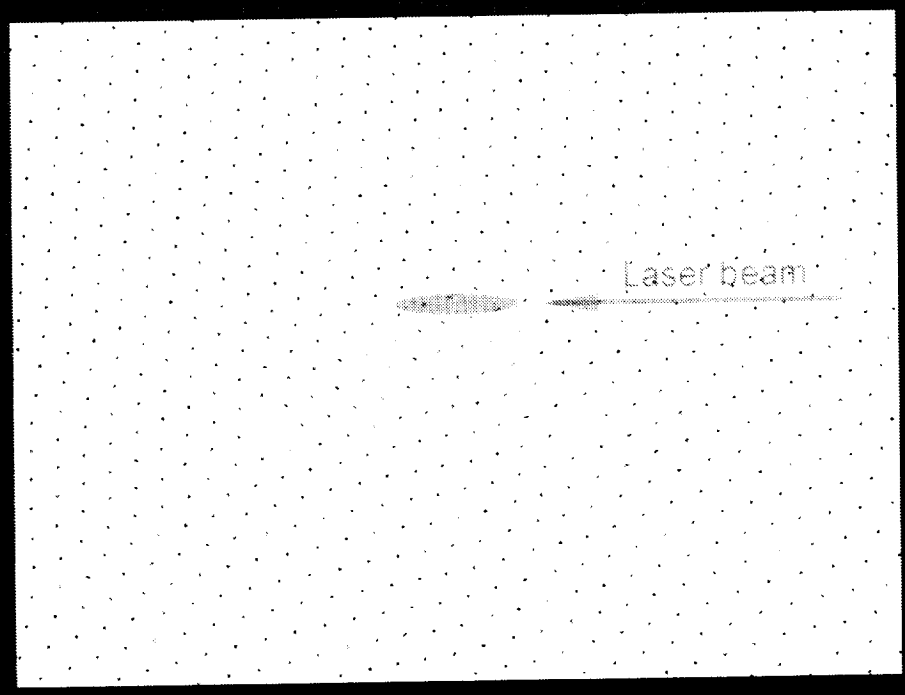

$V/C_L = 1.17$

Mach cone

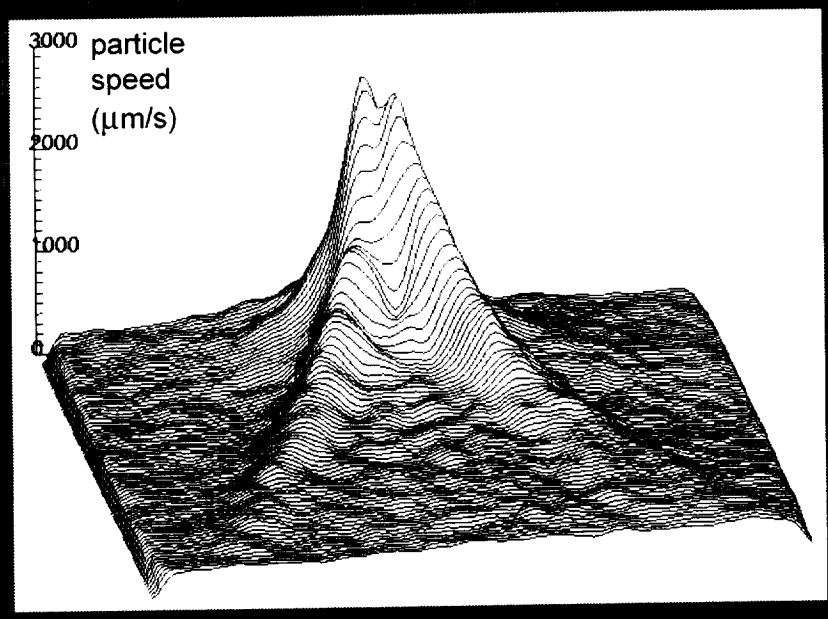

Nosenko *et al.* PRL 2002

Microgravity

3D physics

Predecessor microgravity experiments

1996-1998
Sounding
rockets
Morfill et al.,
PRL 1999

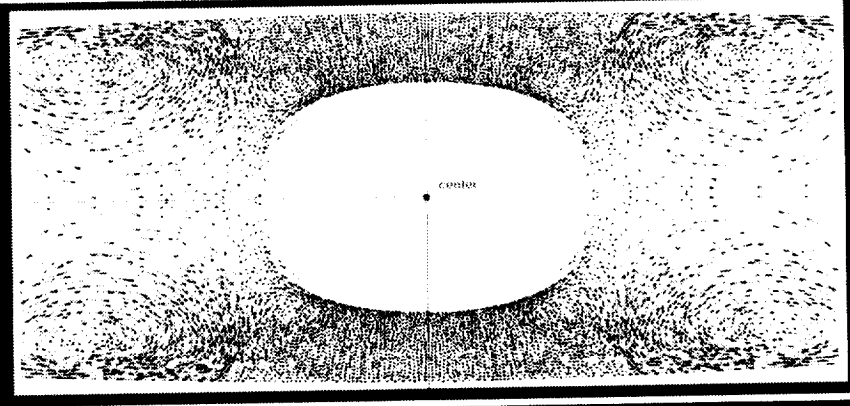

2001 – 2002
ISS - PKE
submitted to
Nature 2002

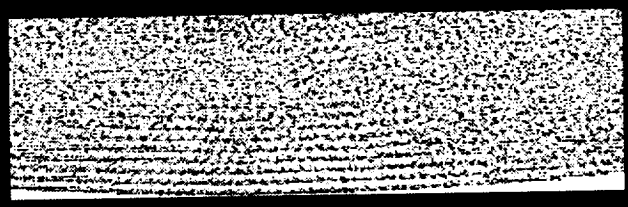

PKE vacuum chamber

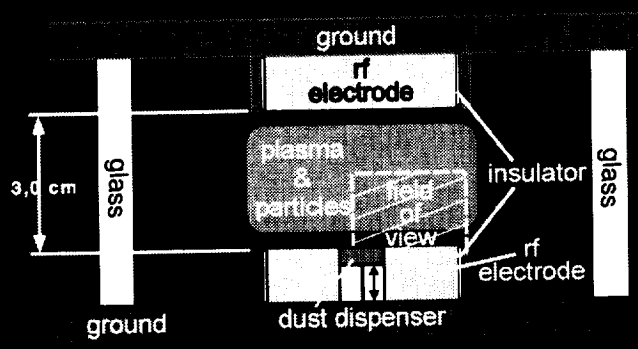

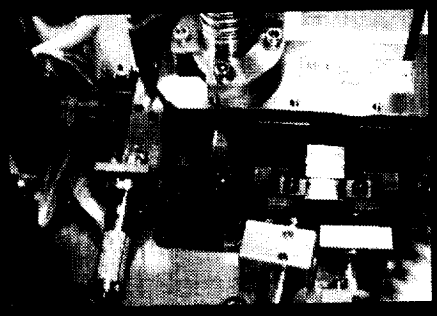

Laser sheets for illuminating particles

Cameras for imaging particles

Flight hardware concept for *optically-excited waves in 3D dusty plasmas*

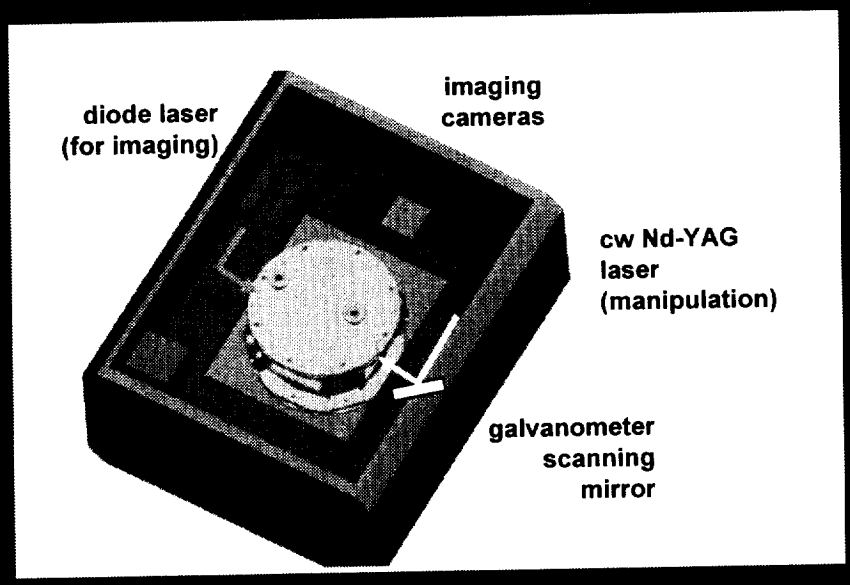

shown in a mid-deck locker: plasma chamber & optics

not shown: gas/vacuum, power, data

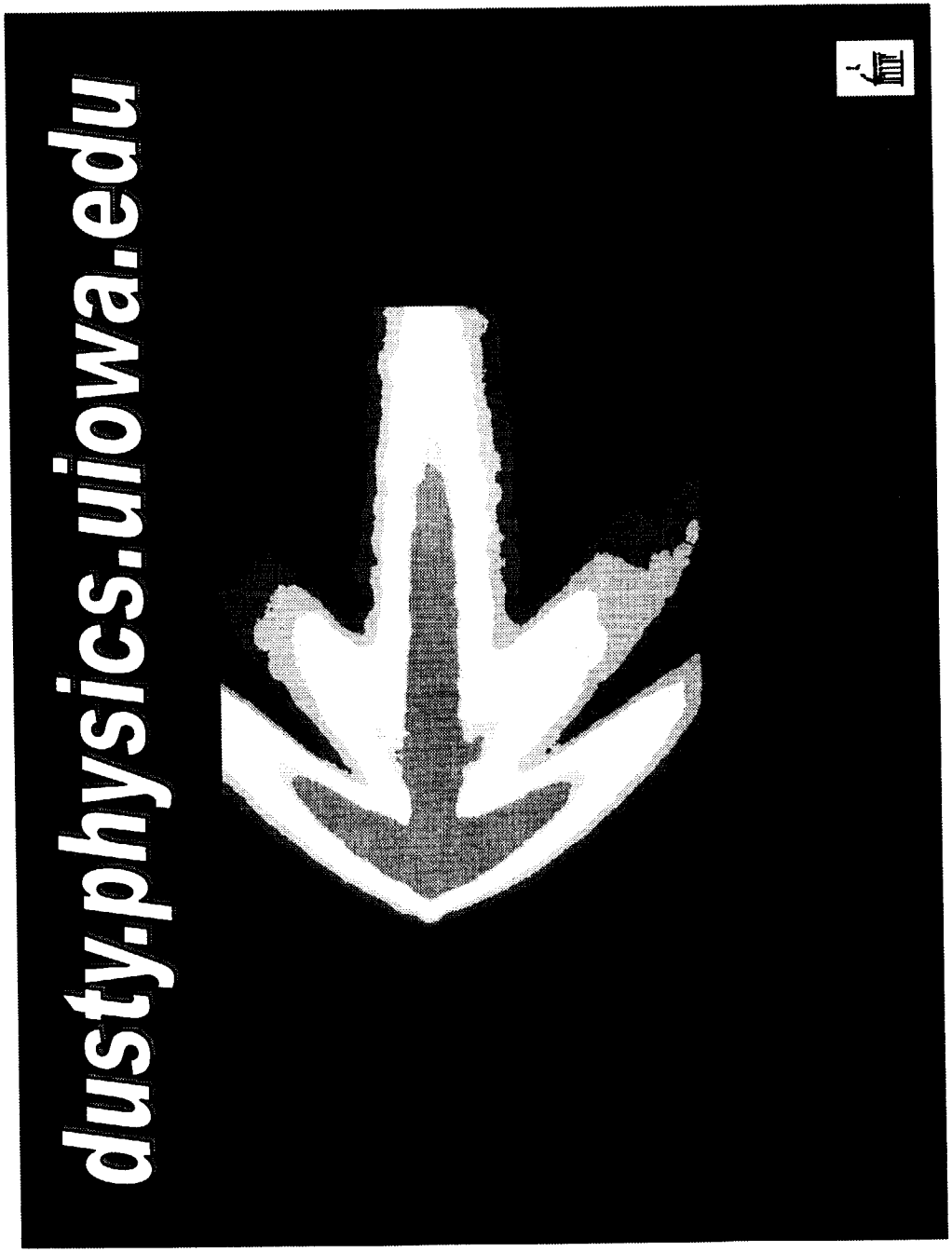
dusty.physics.uiowa.edu

ELECTRICALLY GUIDED ASSEMBLY OF COLLOIDAL PARTICLES

W. D. Ristenpart, I. A. Aksay, and D. A. Saville
Dept. of Chemical Engineering, Princeton University, Princeton, NJ 08544

In earlier work[1] it was shown that the strength and frequency of an applied electric field alters the dynamic arrangement of particles on an electrode. Two-dimensional 'gas,' 'liquid' and 'solid' arrangements were formed, depending on the field strength and frequency. Since the particles are similarly charged, yet migrate over large distances under the influence of steady or oscillatory fields, it is clear that both hydrodynamic and electrical processes are involved. Here we report on an extensive study of electrically induced ordering in a parallel electrode cell.

First, we discuss the kinetics of aggregation in a DC field as measured using video microscopy and digital image analysis. Rate constants were determined as a function of applied electric field strength and particle zeta potential (Fig.1). The kinetic parameters are compared to models based on electrohydrodynamic and electroosmotic fluid flow mechanisms

Second, using monodisperse micron-sized particles, we examined the average interparticle spacing over a wide range of applied frequencies and field strengths. Variation of these parameters allows formation of closely-spaced arrangements and ordered arrays of widely separated particles (Fig. 2). We find that there is a strong dependence on frequency, but there is surprisingly little influence of the electric field strength past a small threshold.

Last, we present experiments with binary suspensions of similarly sized particles with negative but unequal surface potentials. A a long-range lateral attraction is observed in an AC field. Depending on the frequency, this attractive interaction results in a diverse set of aggregate morphologies, including superstructured hexagonal lattices (Fig. 3). These results are discussed in terms of induced dipole-dipole interactions and electrohydrodynamic flow. Finally, we explore the implications for practical applications.

---

[1] M. Trau, D.A. Saville, I.A. Aksay, *Science* **1996**, 272, 706.

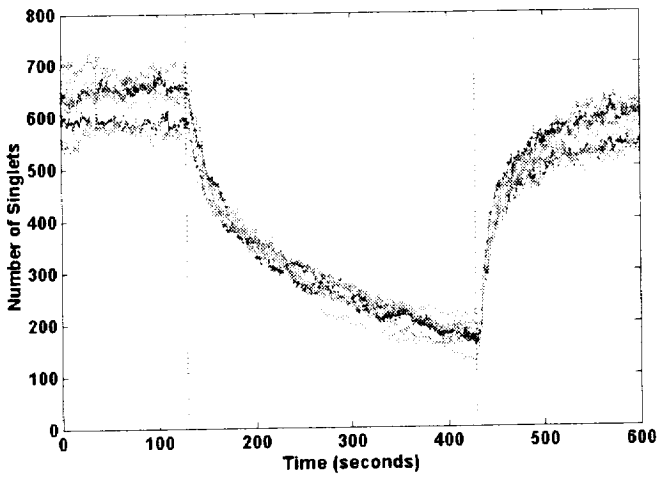

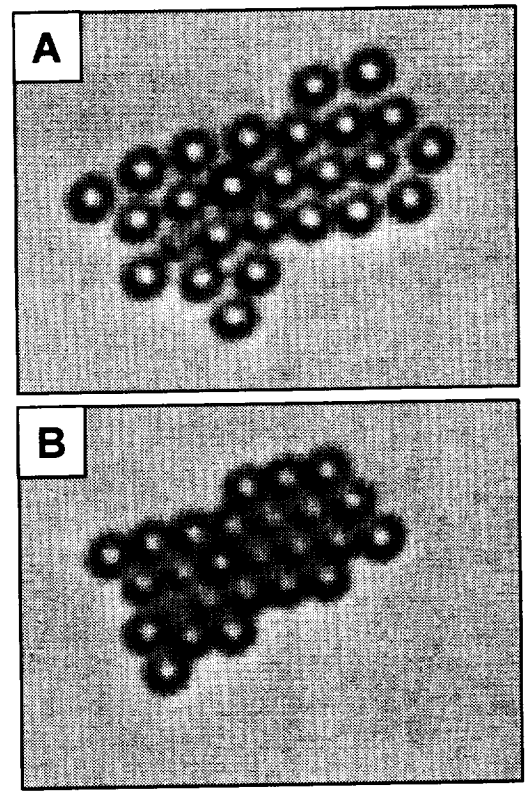

Fig.1 (Above). The concentration of singlets (individual particles) as a function of time for a 10 μA/cm2 applied field. The dashed vertical lines indicate the times at which the field was applied and removed, respectively. Upon application of the field, the concentration of singlets decreases as they join larger aggregates; the concentration increases once the field is removed and the aggregates disperse.

Fig. 2 (Top right). Optical micrographs of 2-μm silica particles on an electrode surface in a 40 V/mm AC field, oriented out of the page. **(A)** At 5 KHz, the particles exhibit simultaneous long-range lateral repulsion and attraction. **(B)** At 2 KHz, the particles come into close contact.

Fig. 3. (Below). Optical micrographs of binary suspensions (light particles are silica, dark particles are polystyrene, both 2-μm diameter) in a 40 V/mm, 2 KHz field. **(A)** Low magnification image of a region with low particle concentration; the particles form clusters typically composed of a silica particle surrounded by six polystyrene particles. **(B)** A higher magnification image of a binary superlattice.

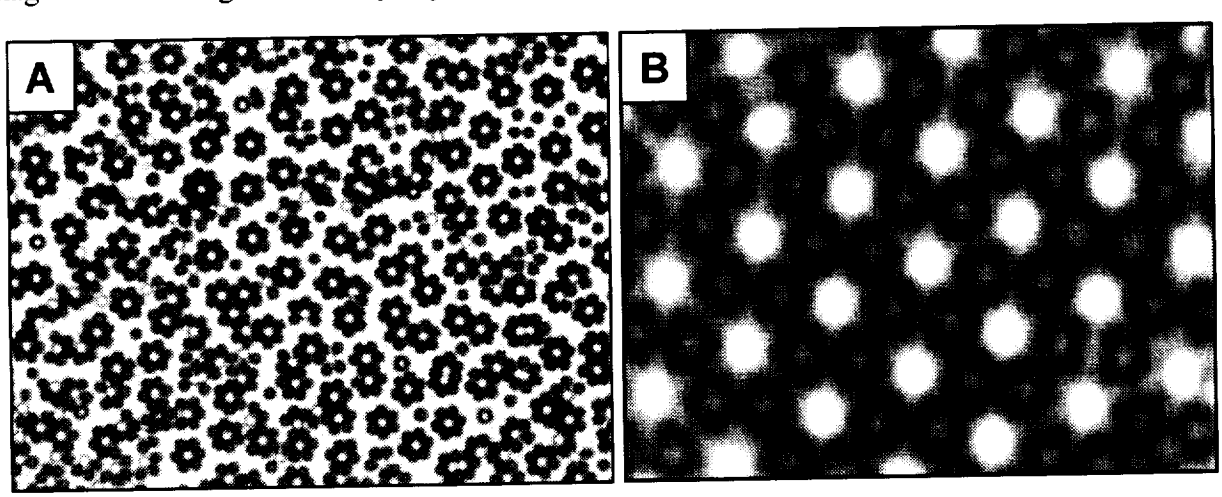

Self-assembly of Colloidal Particles on Template Structures

Arjun G. Yodh
Department of Physics & Astronomy
University of Pennsylvania
Philadelphia, PA 19104-6396
(215)898-6354 (O); x8-2010 (FAX) yodh@dept.physics.upenn.edu

Abstract

I will discuss recent experiments from my lab, which use surface templates to induce ordered colloidal structures. Particle assembly driven by entropic depletion, fluid convection, and sedimentation will be described. Confocal microscopy was used to visualize most of these samples.

SOFT MATTERS at PENN

1. Local and Bulk Rheological Properties from One- and Two-Point Microrheology**

2. Templates for Self-Assembly in Depletion-driven, Convective, and Sedimenting Colloids

Daniel Chen
Eric Weeks (Currently at Emory University)
John Crocker (Currently in Chem. Eng., PENN)
Ritu Verma (Currently Unilever)
Mohammad Islam
Josh Gruber
Alex Levine (Currently Univ. Mass., Amherst)
Tom Lubensky
Arjun G. Yodh Dept. of Physics & Astronomy, University of Pennsylvania

Acknowledgements: NASA, NSF

PLAN

1. Reminder about one- and two-point microrheology

2. Model System: Colloidal Particles in Semi-dilute DNA Solutions

3. Results

Goal of Microrheology

Track motions of tracer particles embedded in a complex fluid. Analysis yields viscoelastic properties of the medium.

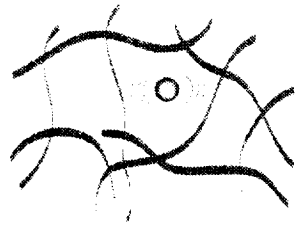

$G(\omega)$, η

Advantages over Conventional Rheology:

$$F = A\cos(\omega t)$$

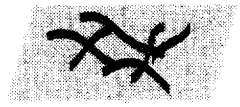

- Smaller Volumes (μl vs ml)
- Local properties
- higher frequencies.

Issues with microrheology:

- Local vs. Bulk Responses (Inhomogeneous media)

One-point Microrheology

*Mason & Weitz, PRL **74** (1995).*
*Gittes, Schnurrr, Olmsted, MacKintosh, Schmidt, PRL **79** (1997).*
*Mason, Ganesan, van Zanten, Wirtz, Kuo, PRL **79** (1997).*

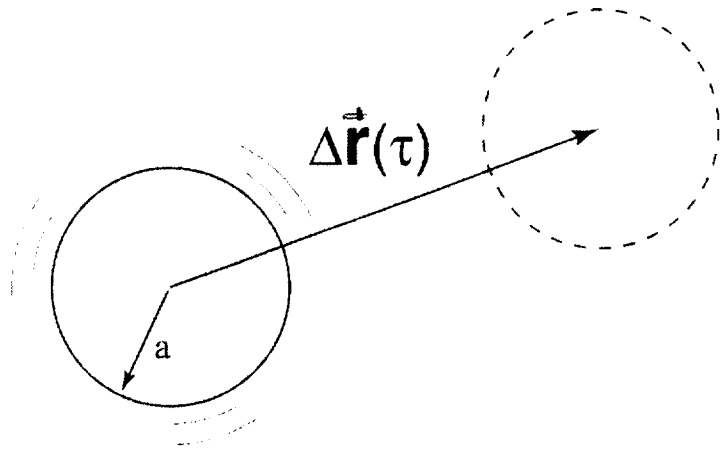

$$\langle \Delta\vec{\mathbf{r}}^2(\tau) \rangle = \langle \vec{\mathbf{r}}(t)\, \vec{\mathbf{r}}(t+\tau) \rangle = \text{MSD1}$$

$$\langle \Delta\mathbf{r}^2(\omega) \rangle = \text{Fourier Transform } \{ \langle \Delta\mathbf{r}^2(\tau) \rangle \}$$

$$\langle \Delta\mathbf{r}^2(\omega) \rangle = \frac{k_B T}{\pi a (i\omega G(\omega))}$$

Simple incompressible viscous media: $G(\omega) = -i\omega\eta$

$$\langle \Delta\mathbf{r}^2(\tau) \rangle = [\, k_B T / 6\pi a \eta \,]\, \tau$$

Conceptual Advance:

Deviations from $\langle \Delta\mathbf{r}^2(\tau) \rangle \propto \tau$ reveal viscoelasticity of surrounding media.

Inhomogeneous Materials

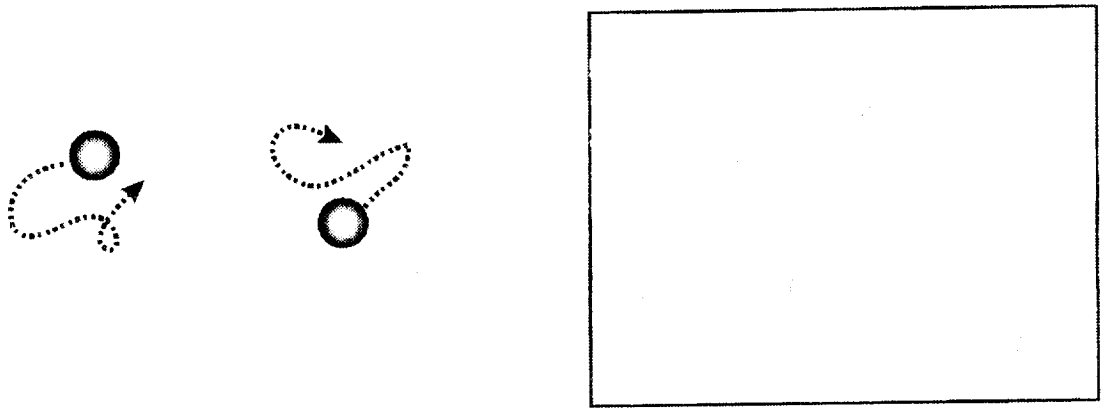

- Local pockets around embedded particles oversampled
- Ambiguity: local or bulk viscoelasticity, what is measured?

Examples: crosslinked gel, nonadsorbing polymer

Two-Point Microrheology

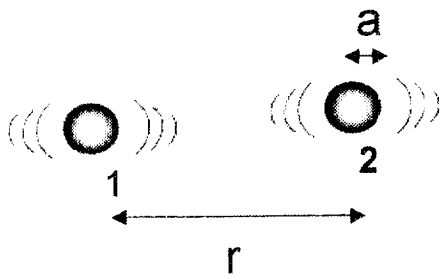

Cross Correlation

$D_{rr}(r,\tau) = \langle \Delta \vec{r}_1(r,\tau) \Delta \vec{r}_2(r,\tau) \rangle_{\text{distinct}} \sim 1/r$

Strain field ~ 1/r

$$D_{rr}(r,\omega) = \frac{k_B T}{2\pi r (i\omega G(\omega))} \quad , r >> a$$

Independent of a

MSD2 = $(2r/a)^* D_{rr}$

MSD2 = MSD1 for homogeneous fluids

Crocker, Valentine, Weeks, Gisler, Kaplan, Yodh, & Weitz [redacted] PRL, **85** (2000)

THEORETICAL JUSTIFICATION

Levine & Lubensky Phys. Rev. E ***65*** *(2002).*

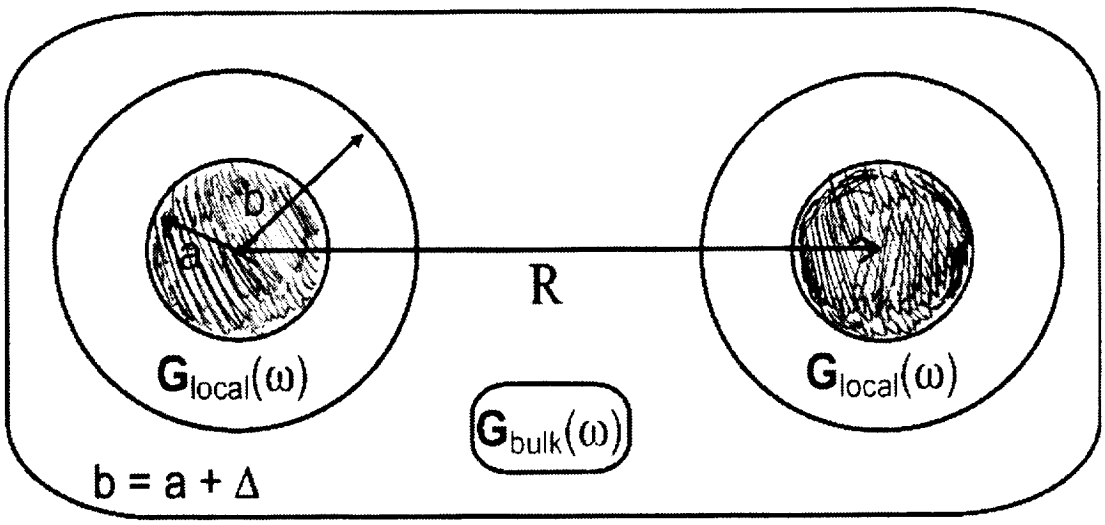

$$G_{1\text{-point}} = F(b/a,\ G_{local},\ G_{bulk})$$

$$G_{2\text{-point}} = F(b/a,\ \underset{\uparrow R}{}\ G_{local},\ G_{bulk}) \quad \underset{R \gg a,\, b}{\rightarrow} \quad G_{2\text{-point}} = G_{bulk}$$

$$G_{1\text{-point}} + G_{2\text{-point}} \quad \underset{\text{Theory}}{\rightarrow} \quad G_{local} \quad (b/a)$$

Test theory in a Model Semidilute Polymer: λ-DNA

Monodisperse, linear, semiflexible polymer

- N = 48,502 base pairs
- Contour length L = 16.5 μm
- Persistence Length L_p = 50 nm

Regime of behavior probed:

Semidilute (C>C*): Entanglements on length scale ξ

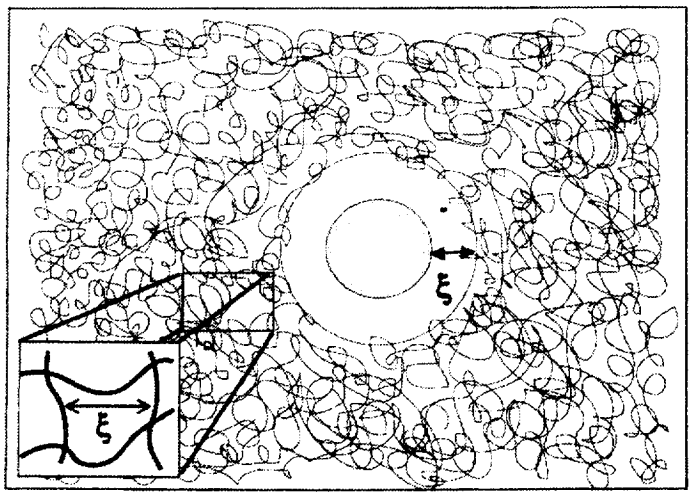

C* ~ 60 μg/ml for λ-DNA

Verma, Crocker, Lubensky, Yodh PRL 81 (1998)
" " " , Macromolecules 33 (2000)

INTERACTION POTENTIAL
for varying DNA Concentrations

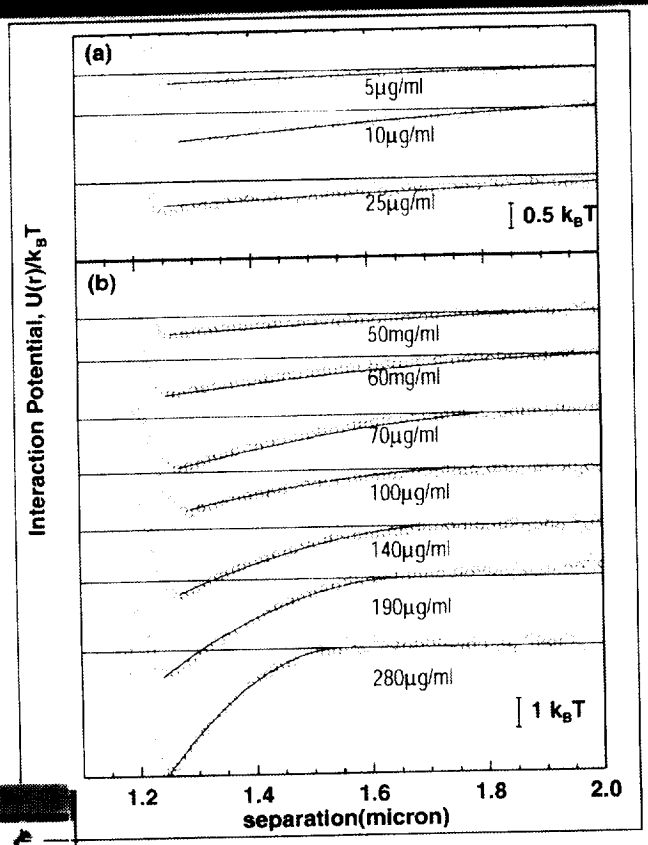

Dilute

1.2 μm Silica

λ-DNA

monodisperse, non-adsorbing

Semi-Dilute

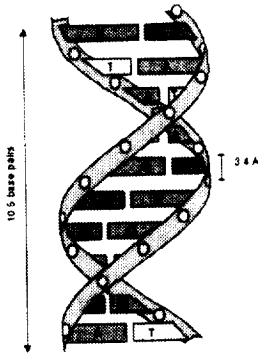

- 48,502 base pairs
- Radius of Gyration ~ 500nm
- Contour Length ~ 16 μm
- Persistence Length ~ 50nm
- Solvent: 10mM Tris-HCl, pH 8.0, 0.1mM EDTA

Depth ↑ ↓ Range

Experimental Parameters

Track spheres of 3 sizes at 4 different concentrations:
Essentially Semidilute

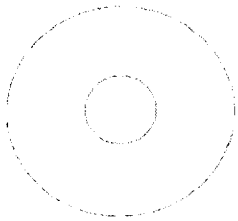

Small Particle
Low Conc.
($\sim c^*$)

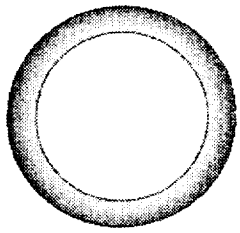

Large Particle,
High Conc.
($\sim 10c^*$)

- $2a = .46\,\mu m, .97\,\mu m, 2.0\,\mu m$
- Video tracking 60 Hz and 20 nm spatial resolution
- ~ 100 particles / frame
- 1 hour video yields ~ 10^8 positions

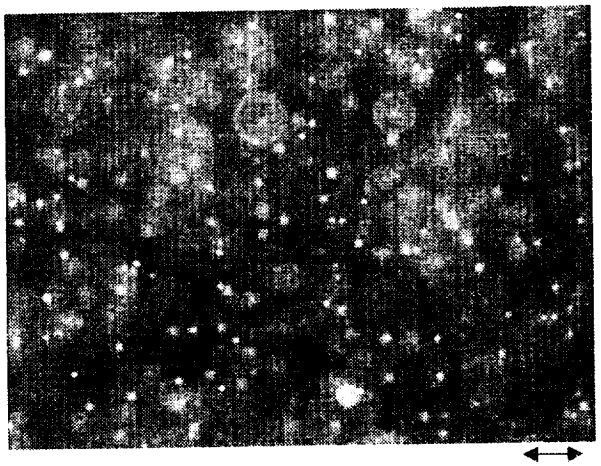

10 μm

Fixed particle size, increasing concentration

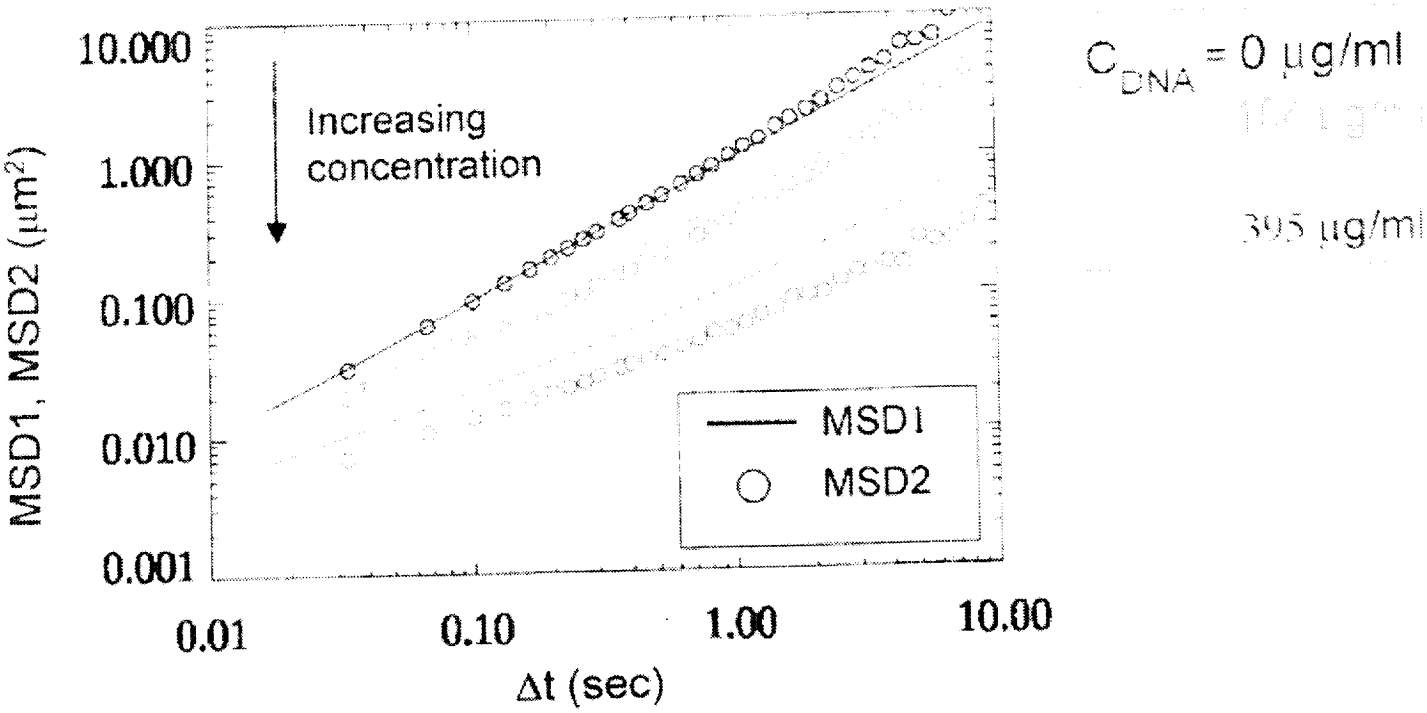

- Discrepancy between MSD1, MSD2 with increasing DNA concentration
- Evidence of local cavities forming around particles

G′ and G″ as a Function of Particle Diameter at Fixed Concentration

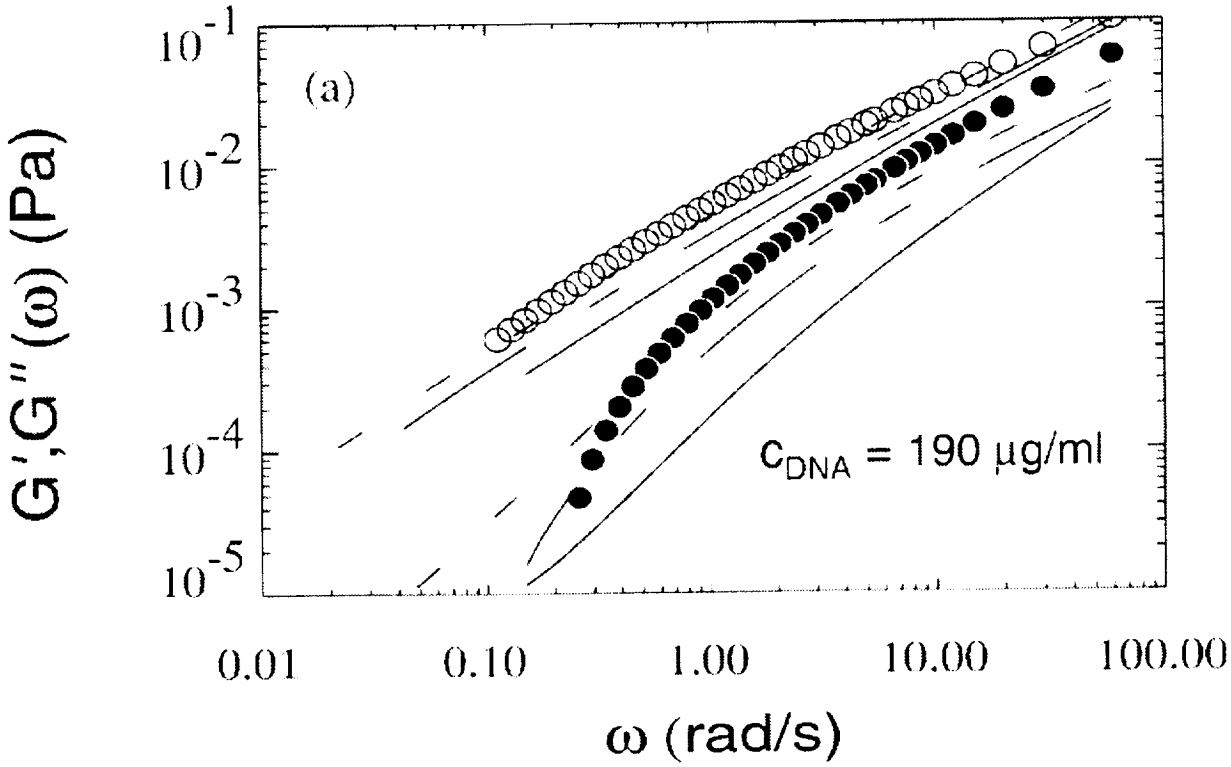

Filled and Open Circles: From MSD2
Lines: From MSD1 (2a = 2.0, 0.97, 0.46 microns)

SHELL THICKNESS

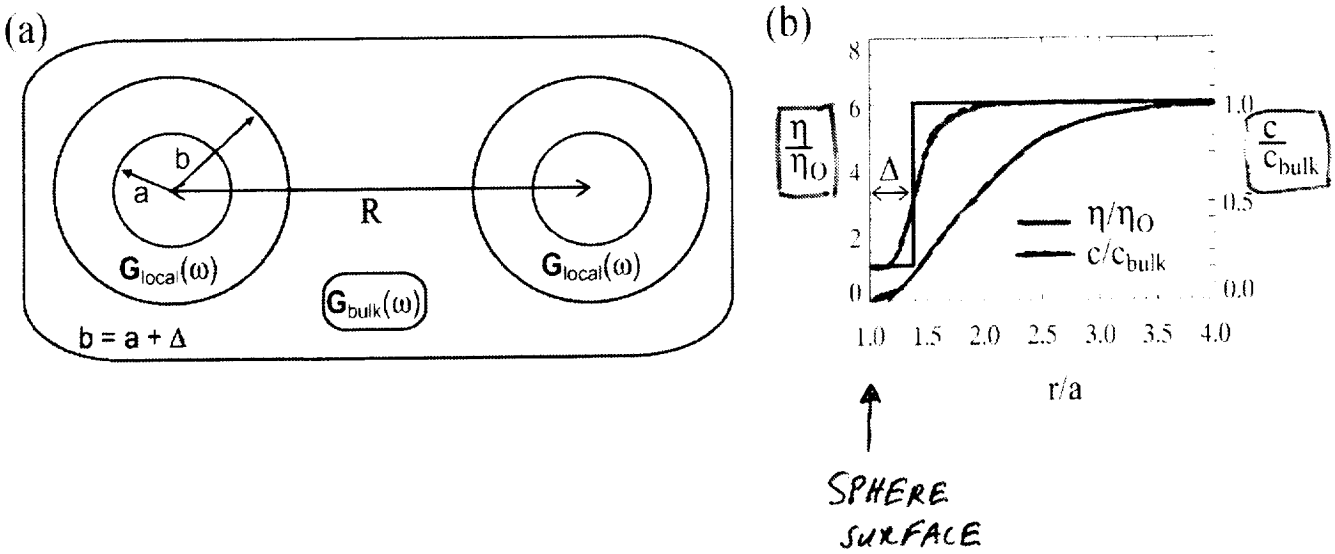

SPHERE SURFACE

Global Fit to all Concentrations and Particle Diameters and All ω to Extract Local Viscosity

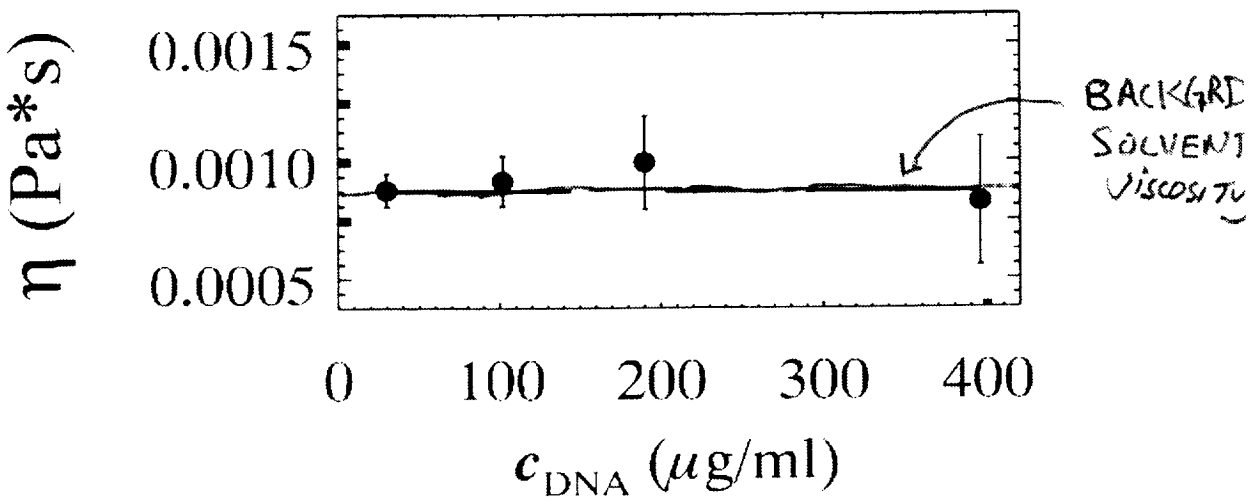

INPUT TO FITS

1. b/a from interaction measurements
2. G_{bulk} from $G_{2\text{-point}}$ measurements

$\Downarrow$ $G_{1\text{-point}}$ + THEORY

G_{local}, η_{local}

Derive $G_{2\text{-point}}$ (i.e. G_{bulk}) from estimated b/a, η_{local}, and measured $G_{1\text{-point}}$

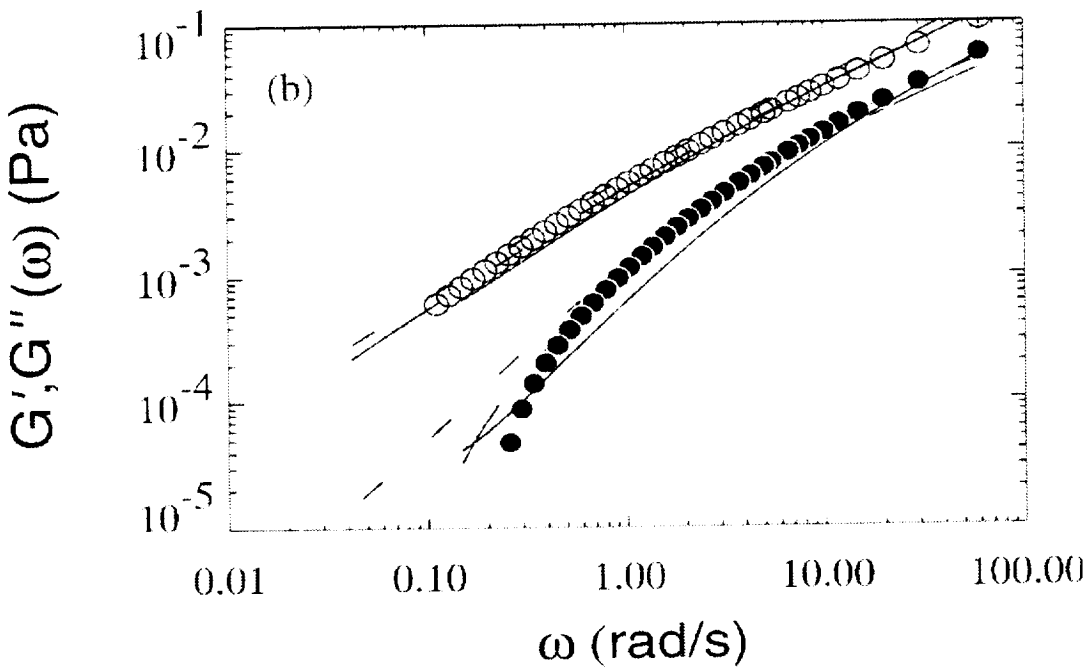

Summary

1. Local and bulk information from one- and two-point measurements.

2. Experiment and Theory hang together in model system.

3. Means to correct one-point to get G_{bulk}.

4. More work – continuum models, new systems....

Molecular dynamics simulations of crystallization of hard spheres

IGOR VOLKOV[†], MAREK CIEPLAK[§,†], JOEL KOPLIK[‡] & JAYANTH R. BANAVAR[†]

[†] Department of Physics, 104 Davey Laboratory, The Pennsylvania State University, University Park, Pennsylvania 16802

[§] Institue of Physics, Polish Academy of Sciences, 02-668 Warsaw, Poland

[‡] Benjamin Levich Institute and Department of Physics, City College of the City University of New York, New York, NY 10031

Colloidal suspensions exhibit a rich variety of behaviors and are interesting not only from a fundamental scientific viewpoint but also have significant technological applications. It is well-known that such systems self-assemble into a wide range of structures. Thus, they may be thought of as models of atomistic condensed matter systems with the distinct advantage of relevant length and time scales that are more readily accessible to experiments. The use of colloidal particles for engineering new materials is a relatively unexplored field which promises to revolutionize materials synthesis.

On earth, the effects of sedimentation and gravity-induced convection cloud, and sometimes can even radically alter, the intrinsic behavior of certain classes of colloidal systems. Because the binding energies of the crystalline phases are low and comparable to each other, gravity

can greatly influence the kinetics of formation and, indeed, the nature of the observed crystal structure.

Colloidal suspensions of hard spheres are model systems for studying the statistical mechanics of structural phase transitions. Such suspensions undergo an entropy-driven phase transition from fluid to crystal as a function of increasing volume fraction. Unlike comparable phase transitions in conventional sytems of condensed matter, the dynamics of such structural phase transitions can be monitored with 'atomic' resolution using conventional light microscopy. In hard sphere systems, at high volume fractions, glass formation competes with the nucleation and growth of the crystalline phase. The Chaikin-Russel experiments on the Space Shuttle have led to the striking result that samples of hard sphere colloids that remain glassy for more than a year on earth crystallize within a few weeks in a microgravity environment.

We have carried out molecular dynamics simulations of the crystallization of hard spheres. Our aim is to study the dynamics of colloidal systems, using microscopic probes which complement conventional earth and space-based measurements and probe the effects of weak gravitational forces, polydispersity and the effect of bounding walls on phase structure. The simulations employed an extensive exclusive particle grid method discussed by Isobe and the type and degree of crystalline order was studied in two independent ways. As in experiments, the structure factor was measured during crystallization and, in addition, the local order was monitored by means of rotational invariants.

We will present quantitative comparisons of the nucleation rates of monodisperse and polydisperse hard sphere systems and benchmark them against experimental results, we will show how the presence of bounding walls leads to wall-induced nucleation and rapid crystallization and we will discuss the role played by gravity in nucleation and crystal growth.

Molecular dynamics simulations of crystallization of hard spheres

Igor Volkov
The Pennsylvania State University

Marek Cieplak
The Pennsylvania State University
Institute of Physics, Polish Academy of Sciences

Joel Koplik
City College of the City University of New York

PENNSTATE

Hard spheres – simplest model of condensed matter

Colloidal suspensions – engineering new materials;
photonic crystals;
self assembly into wide range of structures

Earth – sedimentation and gravity-induced convection

Chaikin-Russel ; Weitz; Yodh

PENNSTATE

Extended exclusive particle grid method

*M. Isobe, Int. J. Mod. Phys. C **10**, 1281 (1999)*

Next collision event determined using binary tree

*M. Marin, D. Risso and P. Cordero, J. Comp. Phys. **109**, 306 (1993)*

Initial random configuration of hard spheres

*R. Jullien, P. Jund and D. Caprion, Phys. Rev. E **54**, 6035 (1996)*

Local structure

a) Identification of crystal like particles

b) Nature of local crystalline order

*P. J. Steinhardt, D. R. Nelson, M. Ronchetti, Phys. Rev. B. **28**, 784 (1983)*

*P. R. ten Wolde, M. J. Ruiz-Montero and D. Frenkel, J. Chem. Phys. **104**, 9932 (1996)*

Structure factor

*J. L. Harland and W. van Megen, Phys. Rev. E **55**, 3054 (1997)*

PENNSTATE

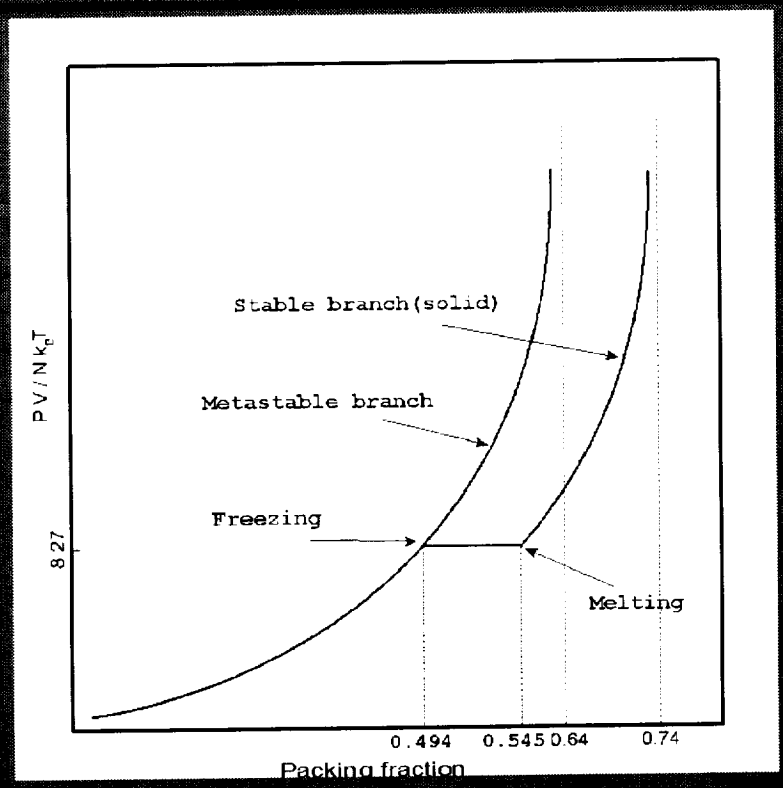

Schematic representation of the phase diagram of a system of hard spheres.

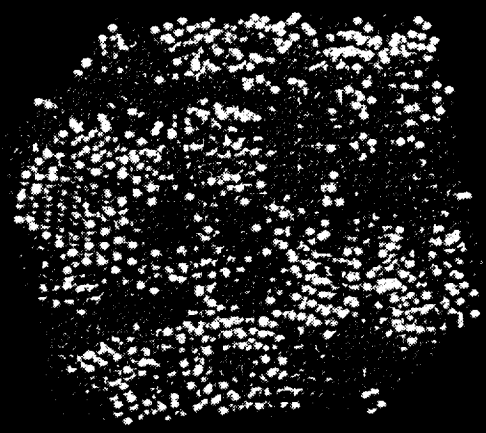

The snapshot of a system with volume fraction of 56% and periodic boundary conditions in the middle of the crystallization process. Here, red, yellow, green and blue particles correspond to liquid, hcp, fcc and bcc structures respectively. The particle sizes have been reduced to half their value for easier visualization.

PENNSTATE

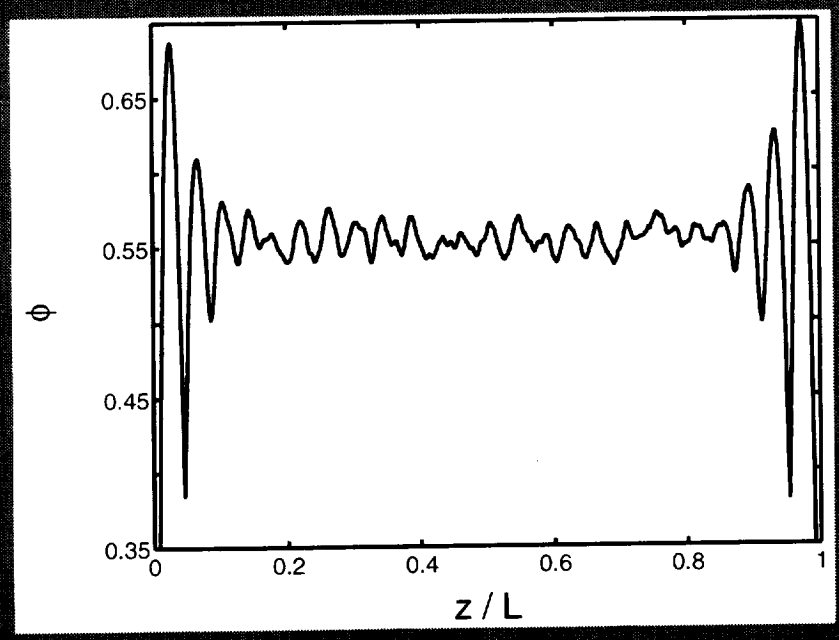

The density profile of a typical initial configuration of the system bounded by two walls with $\varphi = 55\%$. L is the distance between the two walls and is equal to 21.86 hard sphere diameters.

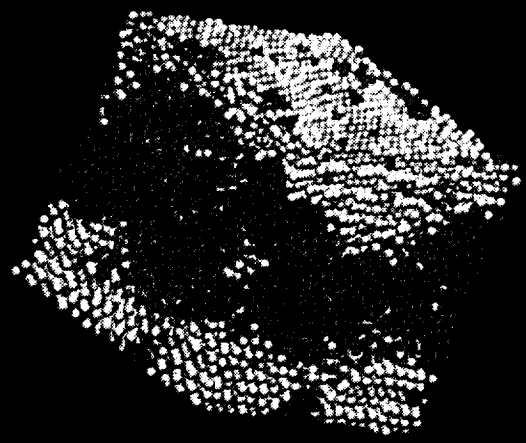

The snapshot of a system (φ = 56%) bounded by two walls in the middle of the crystallization process.

PENNSTATE

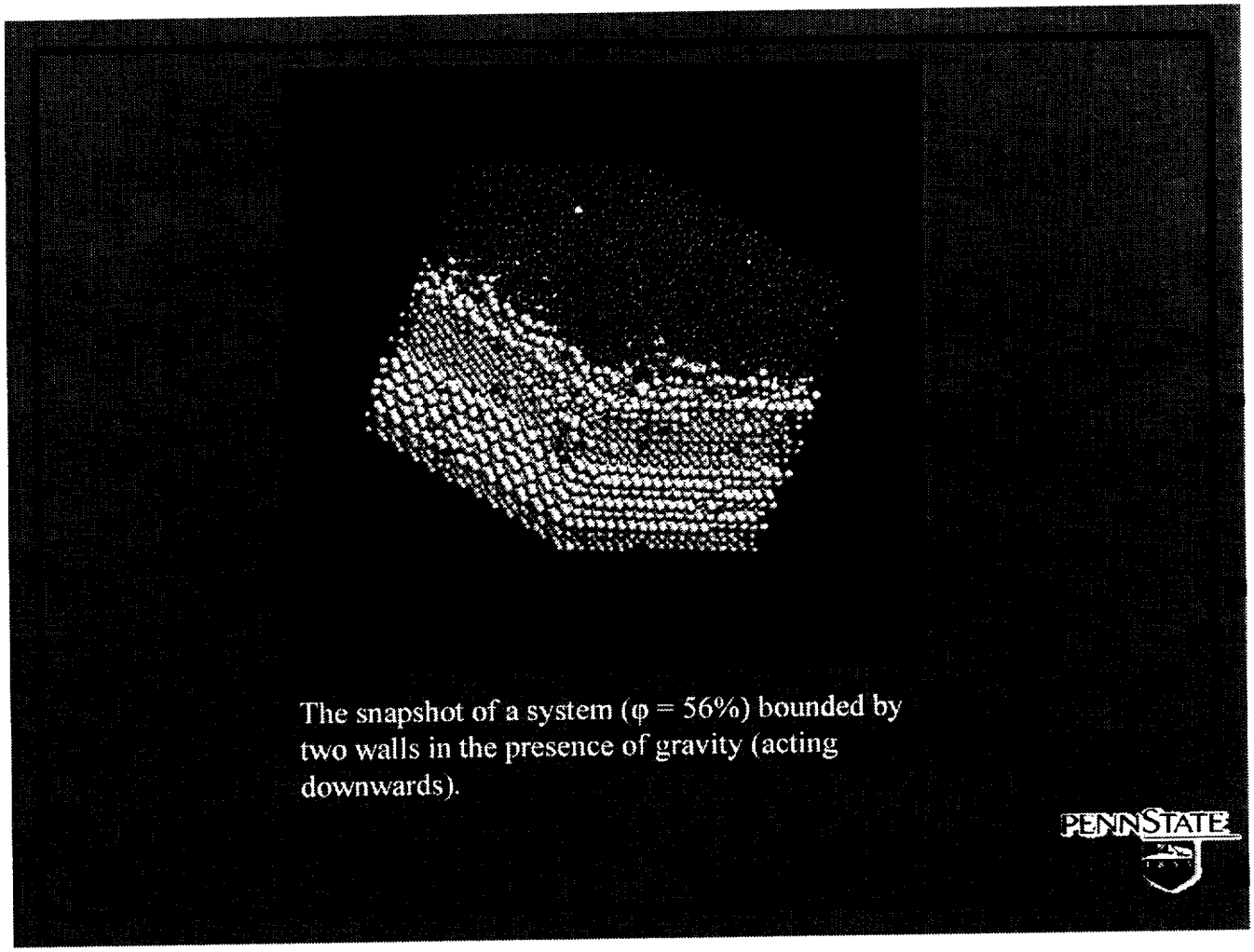
The snapshot of a system (φ = 56%) bounded by two walls in the presence of gravity (acting downwards).
PENNSTATE

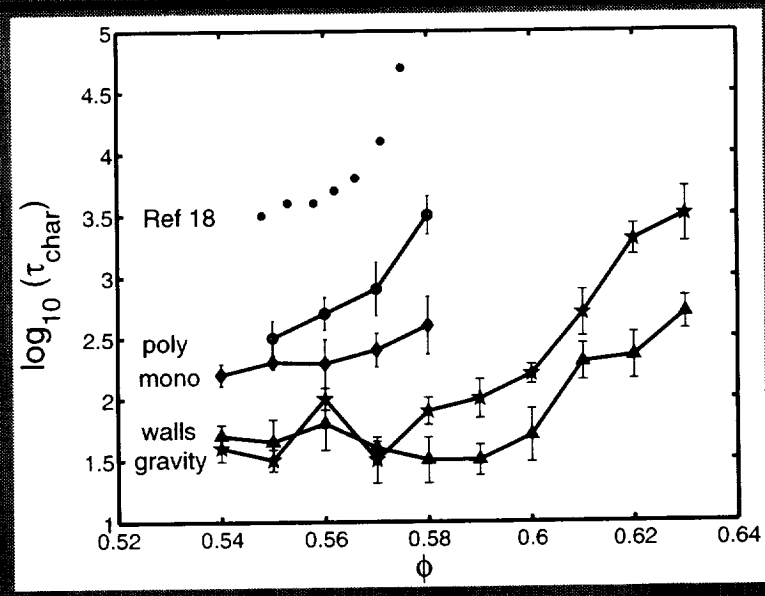

The logarithm of the characteristic crystallization times in units of the diffusional characteristic times.

Ref.18 *J. L. Harland and W. van Megen, Phys. Rev. E* **55**, *3054 (1997)*

PENNSTATE

Session 2: Fluid Physics of Interfaces

Dynamics and Instability of Triple Junctions of Solidifying Eutectics: Flow-Modified Morphologies

S. Davis
Northwestern University

Fluid motions impressed upon a eutectic crystal front during directional solidification result in an increase of the lamellar spacing. This flow-induced change of microstructures is analyzed analytically to show the relationship between spacing and the operating conditions. The resulting system is a set of ordinary differential equations which describe the evolution of triple junctions. In a weak-flow regime lamellar widths at the minimum undercooling have a scaling similar to that of Jackson and Hunt, modified by the flows. When the flows are strong, a new scaling law shows that the width is proportional to one-fourth power of the imposed shear rate. Lamellar phases then tilt into the flow. Only at large morphological numbers does the minimum undercooling point corresponds to the marginal stability limit. Simulations show that the flows promote pinching of unstable lamellae.

EUTECTICS: STEADY GROWTH, INSTABILITY, AND FLOW

STEPHEN H. DAVIS
NORTHWESTERN UNIVERSITY

CHEN, Y.-J AND DAVIS, S. H. (2001,2002)
ACTA MATERIALIA

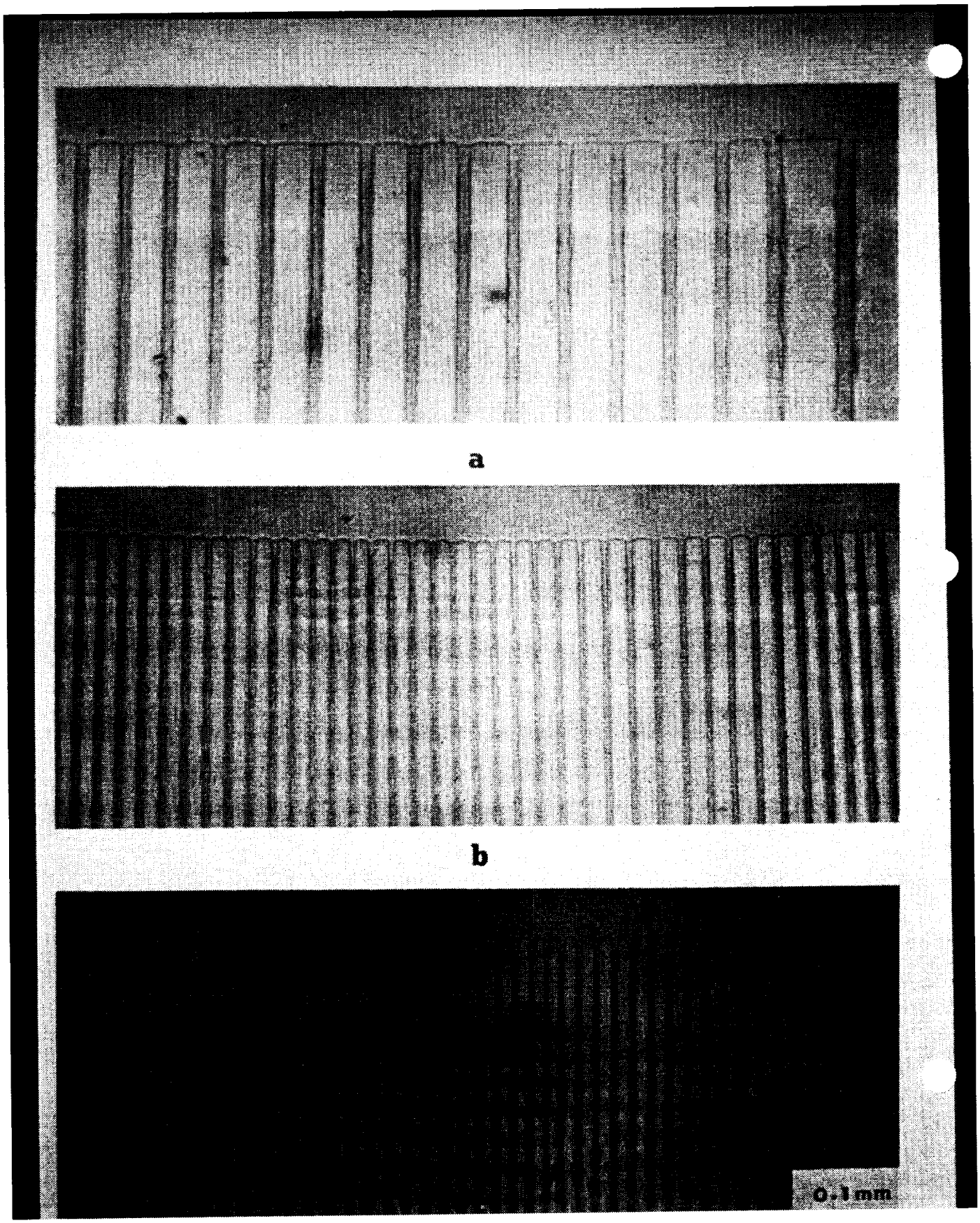
a
b
0.1mm

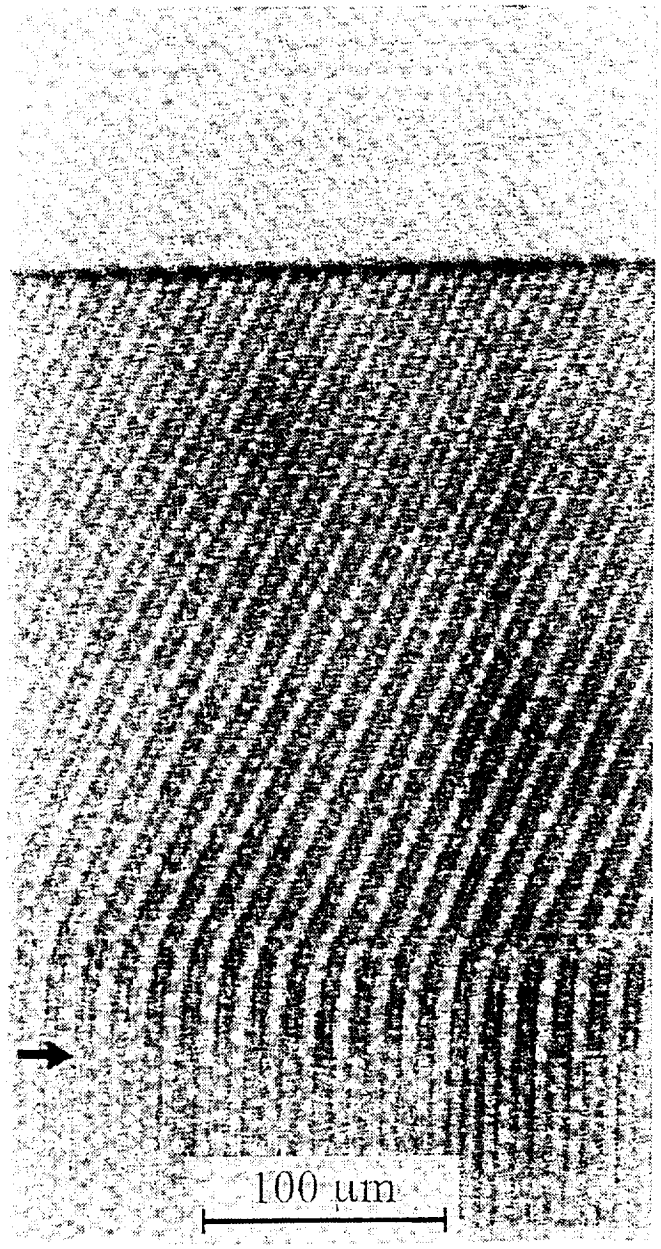

Figure 8.12. Observed transition to a stable, tilted steady-state morphology in thin-sample directional solidification of CBr_4–$C_2C\ell_6$ for $C^{\infty} \approx 0.21 \pm 0.02$ and $G_T \approx$ 80 K/cm. It results from a velocity jump from 0.85 to 3.3 μm/s applied at the time indicated by the arrow, which corresponds to a jump in λ/λ_m from approximately unity to 1.9 ± 0.1 (courtesy of G. Faivre and M. Ginigre). From to Karma and Sarkissian (1996). (Reprinted with permission of Metall. mater. Trans.)

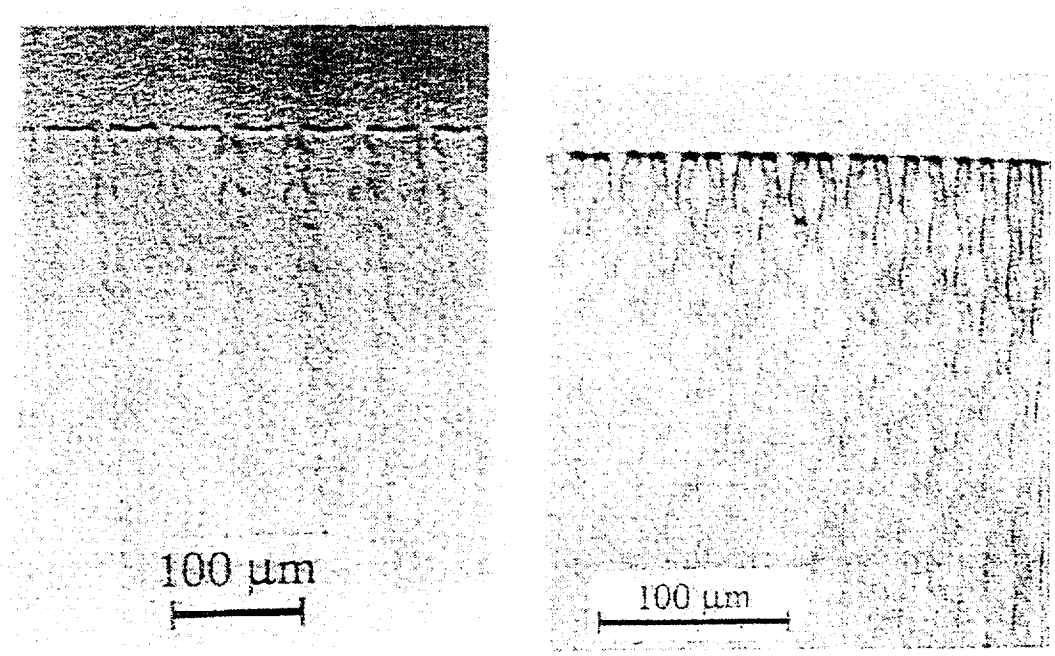

(a) (b)

Figure 8.15. Observed symmetric oscillatory morphologies in CBr_4–C_4Cl_6 observed by G. Faivre and M. Ginibre for $G_T \approx 80$ K/cm: (a) 1λ oscillations for $V = 0.51$ μm/s, $\Delta \approx 0 \pm 0.02$, and $\lambda/\lambda_m \approx 2.3 \pm 0.2$; and (b) 2λ oscillations for $V = 2$ μm/s, $\Delta \approx 0.21 \pm 0.02$, and $\lambda/\lambda_m \approx 1.2 \pm 0.1$. From Karma and Sarkissian (1996). (Reprinted with permission of Metall. mater. Trans.)

CONFIGURATION

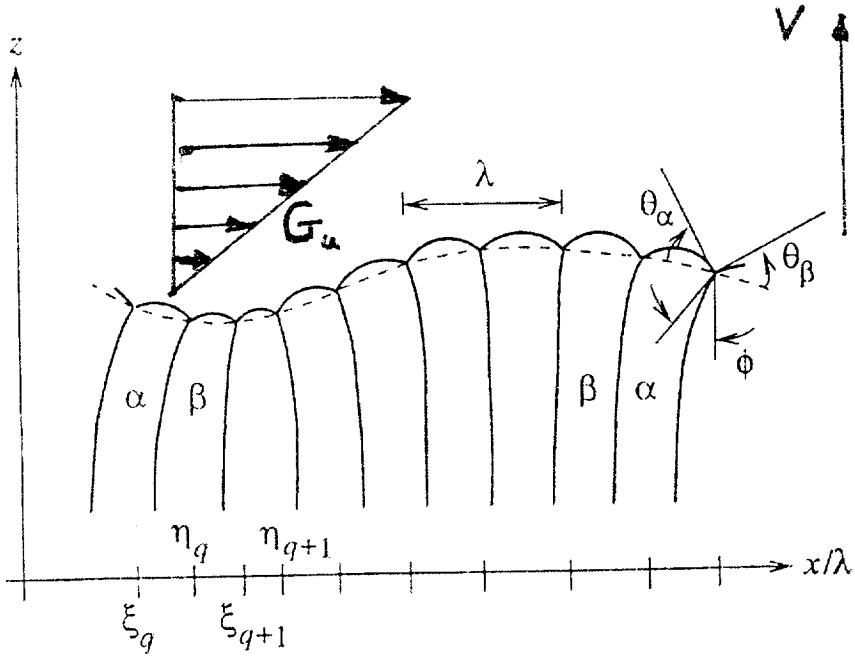

MODEL

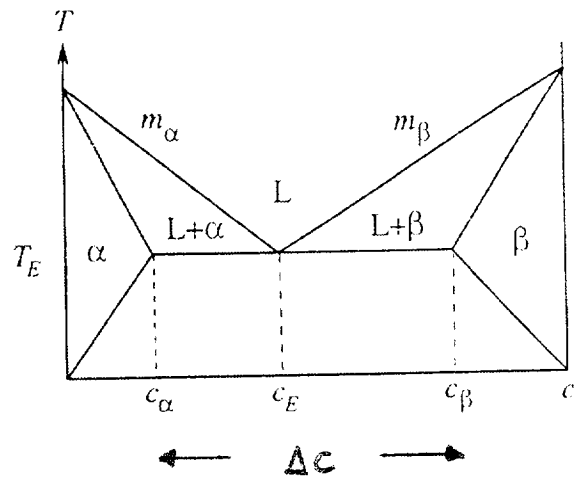

1. ONE-SIDED, FROZEN-TEMPERATURE DS
2. $p = \lambda V/D$
3. $S = G_u D/V^2$
4. STOKES FLOW
5. CONTACT LINES: $\gamma_\alpha + \gamma_\beta + \gamma_{\alpha\beta} = 0$
6. MAIN PARAMETERS: $s = \alpha, \beta$

$$M_s = -\frac{v_s m_s \Delta C}{G_T}\frac{V}{D}, \quad \Gamma_s = \frac{\gamma_s T_E}{-v_s m_s \Delta C L_v^s}\frac{V}{D}$$

$$\Omega_s = \frac{C_E - C_s}{\Delta C}$$

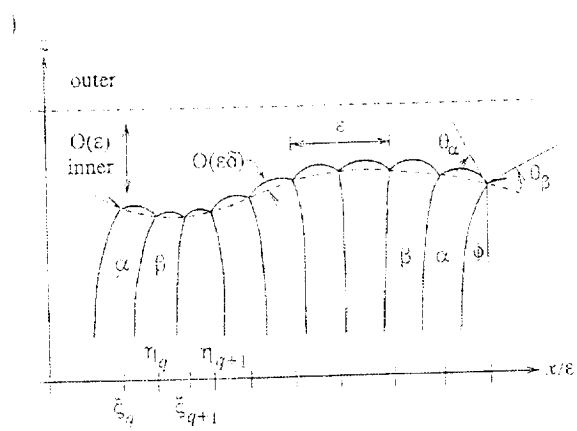

RESULTS: NO FLOW

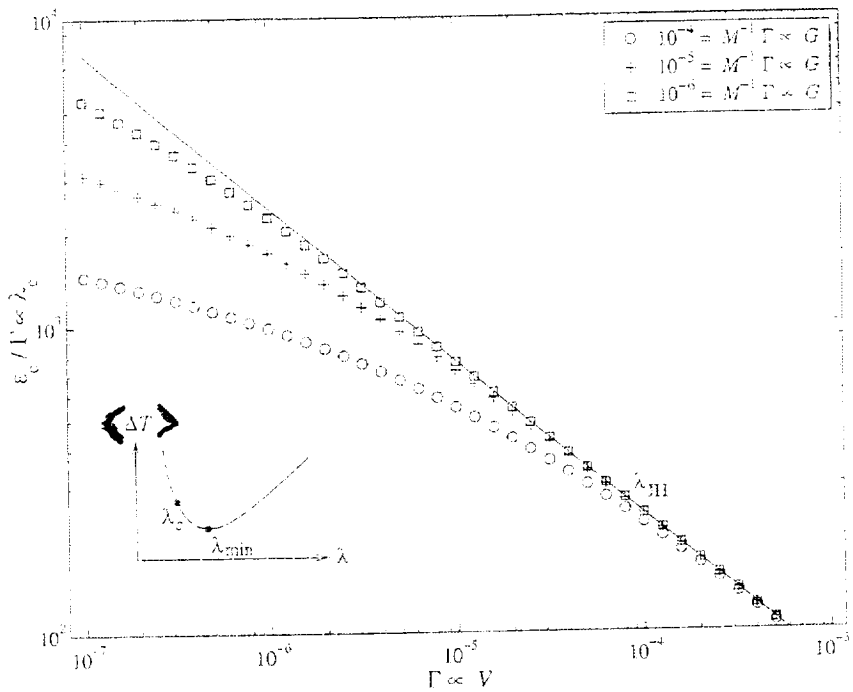

JACKSON AND HUNT (1966)

UNIFORM TEMPERATURE ON PLANAR INTERFACE

PLANAR INTERFACE

$$\Rightarrow \lambda_c = \lambda_m$$

CHEN AND DAVIS (2001)

GENERAL INTERFACIAL TEMPERATURE AND INTERFACE,

MATCHED ASYMPTOTICS

$$\Rightarrow \quad M_s \text{ LARGE}, \quad \lambda_c = \lambda_m, \quad V\lambda_c^2 = K_1$$

$$M_s \text{ SMALL}, \quad \lambda_c < \lambda_m, \quad V\exp\left[K_2\lambda_c\sqrt{G_T}\right] = K_3 G_T$$

RESULTS: FLOW

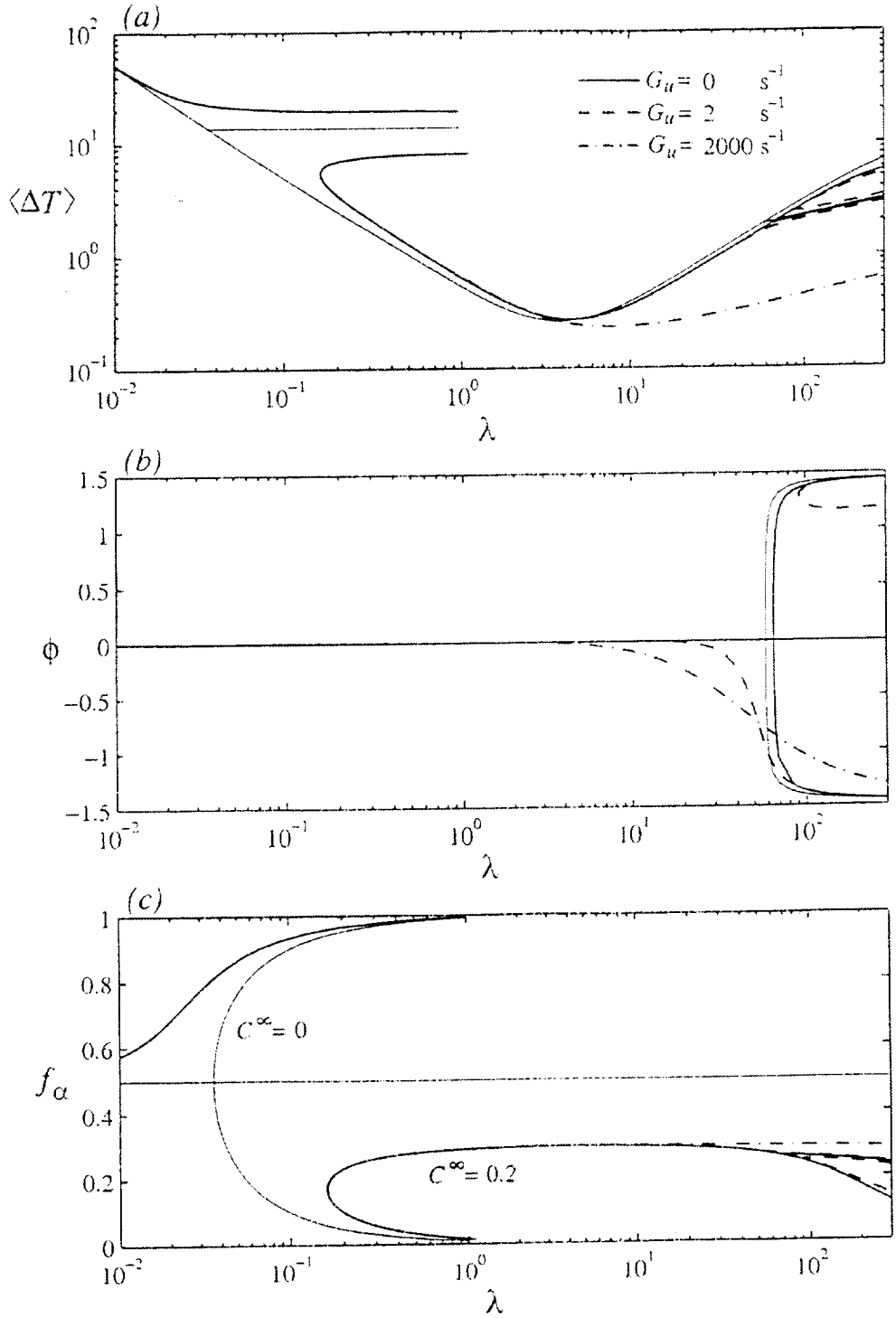

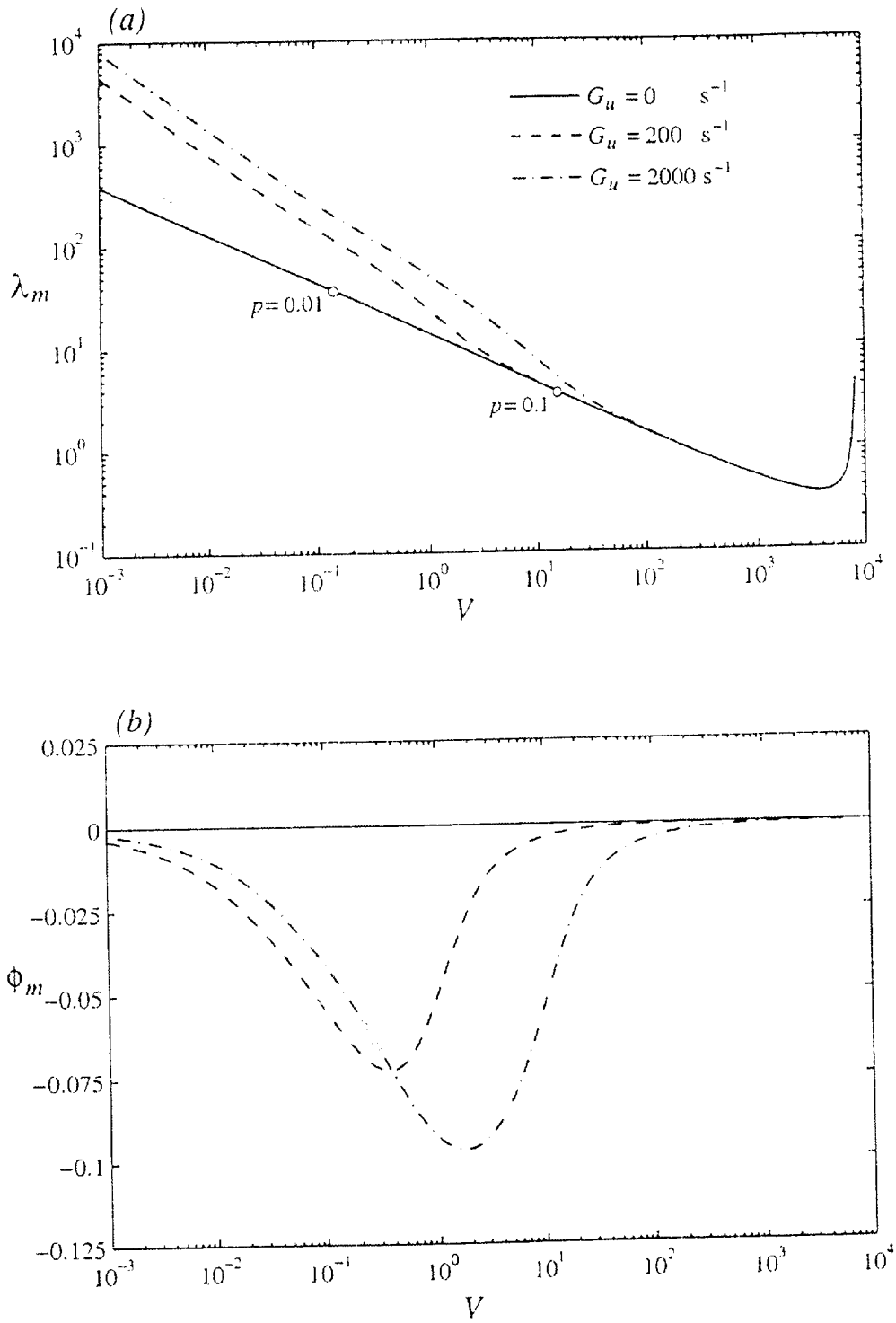

Fig 3

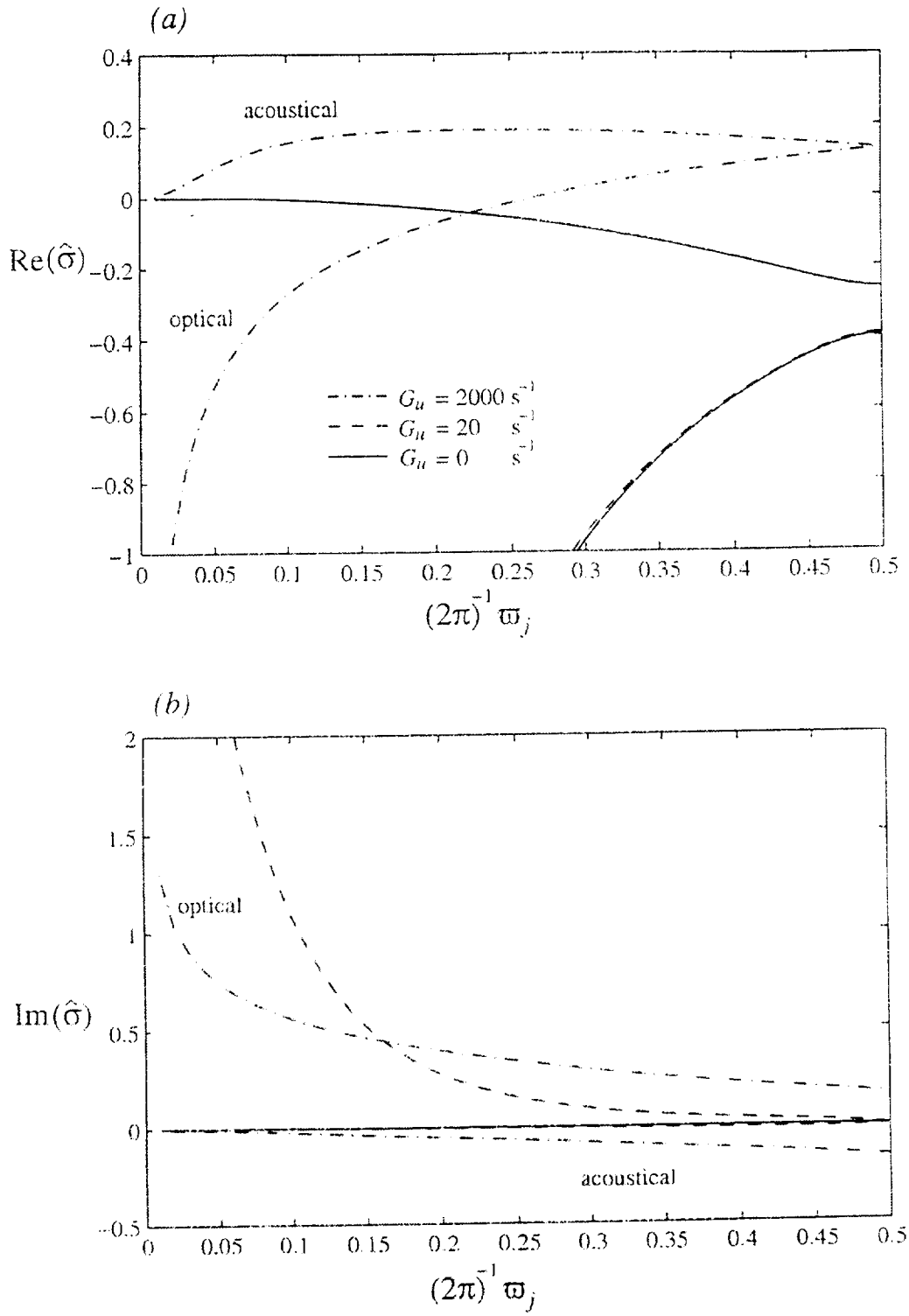
(a)
acoustical
optical
$G_u = 2000\ s^{-1}$
$G_u = 20\ s^{-1}$
$G_u = 0\ s^{-1}$
$\mathrm{Re}(\hat{\sigma})$
$(2\pi)^{-1}\varpi_j$
(b)
optical
acoustical
$\mathrm{Im}(\hat{\sigma})$
$(2\pi)^{-1}\varpi_j$

Fig 5

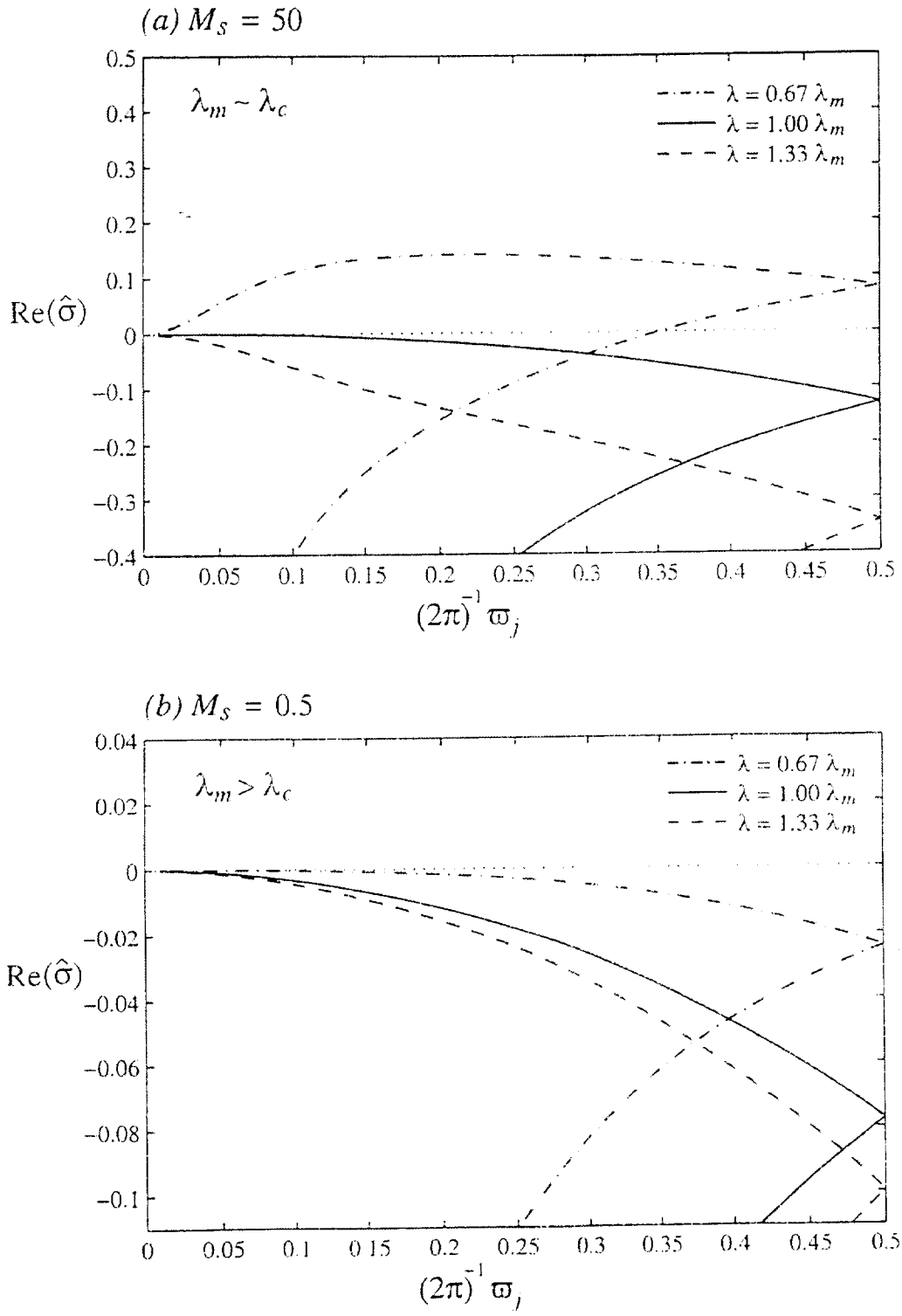
(a) M_s = 50
$\lambda_m \sim \lambda_c$
$\lambda = 0.67\,\lambda_m$
$\lambda = 1.00\,\lambda_m$
$\lambda = 1.33\,\lambda_m$
Re($\hat{\sigma}$)
$(2\pi)^{-1}\varpi_j$
(b) M_s = 0.5
$\lambda_m > \lambda_c$
$\lambda = 0.67\,\lambda_m$
$\lambda = 1.00\,\lambda_m$
$\lambda = 1.33\,\lambda_m$
Re($\hat{\sigma}$)
$(2\pi)^{-1}\varpi_j$

Fig 6

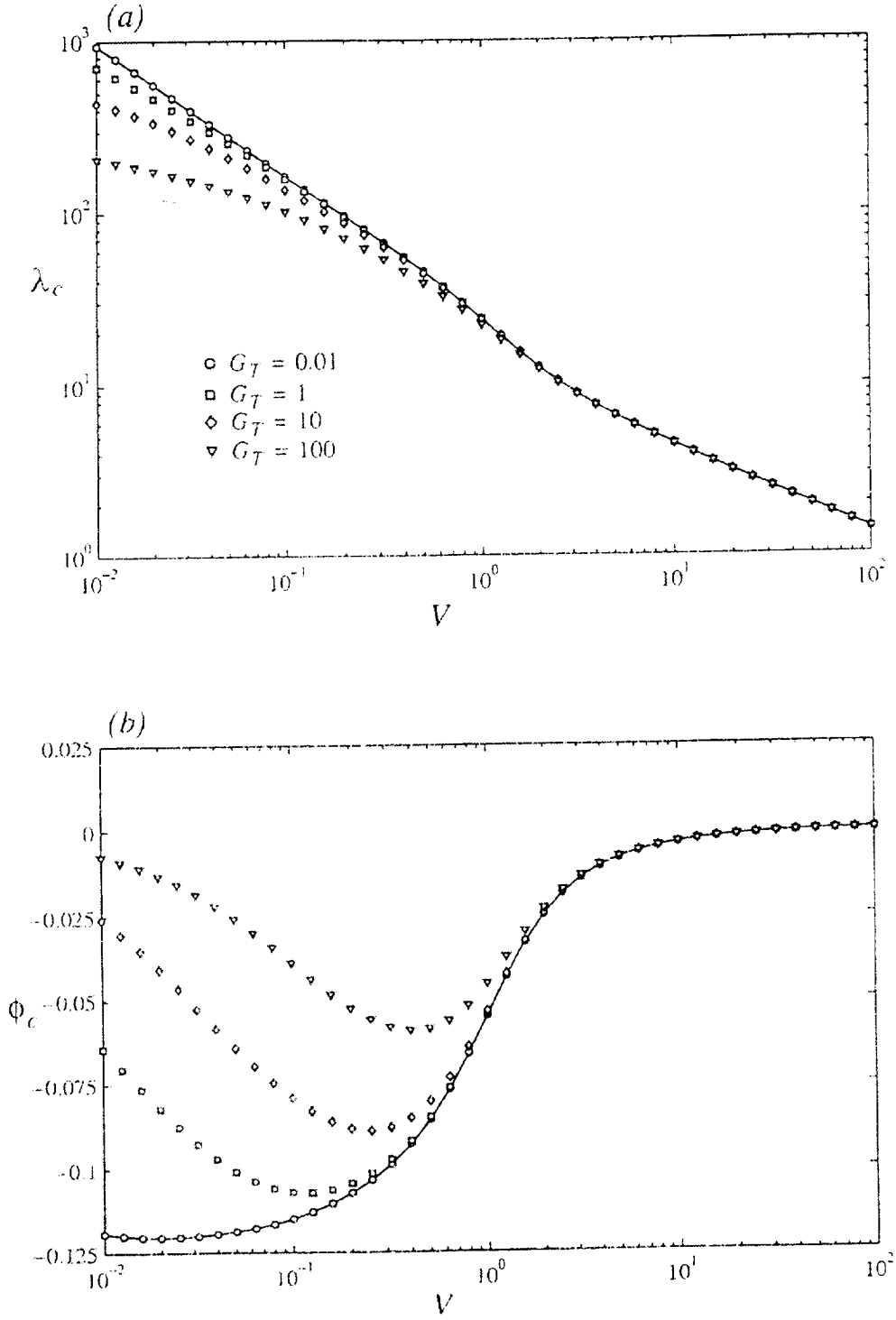
(a)
10^3
10^2
10^1
10^0
λ_c
G_T = 0.01
G_T = 1
G_T = 10
G_T = 100
10^{-2}
10^{-1}
10^0
10^1
10^2
V
(b)
0.025
0
-0.025
-0.05
-0.075
-0.1
-0.125
ϕ_c
10^{-2}
10^{-1}
10^0
10^1
10^2
V

Fig 7

SUMMARY OF RESULTS

	$M << 1$	$M >> 1$
$p^2 S << 1$	$p_m \sim p_{sm}\ [1 - p_{sm}^4 S^2]^{-1/2}$	$p_m \sim p_{JH}[1 - p_{JH}^4 S^2]^{-1/2}$
	$\phi_m \sim \frac{M_\alpha + M_\beta}{(M_\alpha \Gamma_\alpha)^{1/2} + (M_\beta \Gamma_\beta)^{1/2}} \phi_{sm}^3\ S$	$\phi_m \sim \left(\frac{1}{\Gamma_\alpha} + \frac{1}{\Gamma_\beta}\right) p_m^4 S^2$
$p^2 S >> 1$	$p_m \sim p_{sm}^{3/2} S^{1/4}$	$p_m \sim p_{JH}^{3/2} S^{1/4}$
	$\phi_m \sim -\frac{(M_\alpha + M\beta)}{(M_\alpha \Gamma_\alpha)^{1/2} + (M_\beta \Gamma_\beta)^{1/2}} p_{sm}^{1/3} S^{-1/4}$	$\phi_m \sim -\left(\frac{1}{\Gamma_\alpha} + \frac{1}{\Gamma_\beta}\right) P_{JH}^2$

WHERE

$p_{sm} = p_m$ at $S = 0$.

DYNAMICAL SYSTEMS

INSTABILITY FOR THE CASE $p << 1$

$\xi_q(t), \ \eta_q(t)$

DYNAMICAL SYSTEM

$$g_1\left(\dot{\eta}_q, \dot{\xi}_q \ , \eta_q, \xi_q, \ldots\right) = 0$$

$$g_2\left(\qquad\qquad\qquad \right) = 0$$

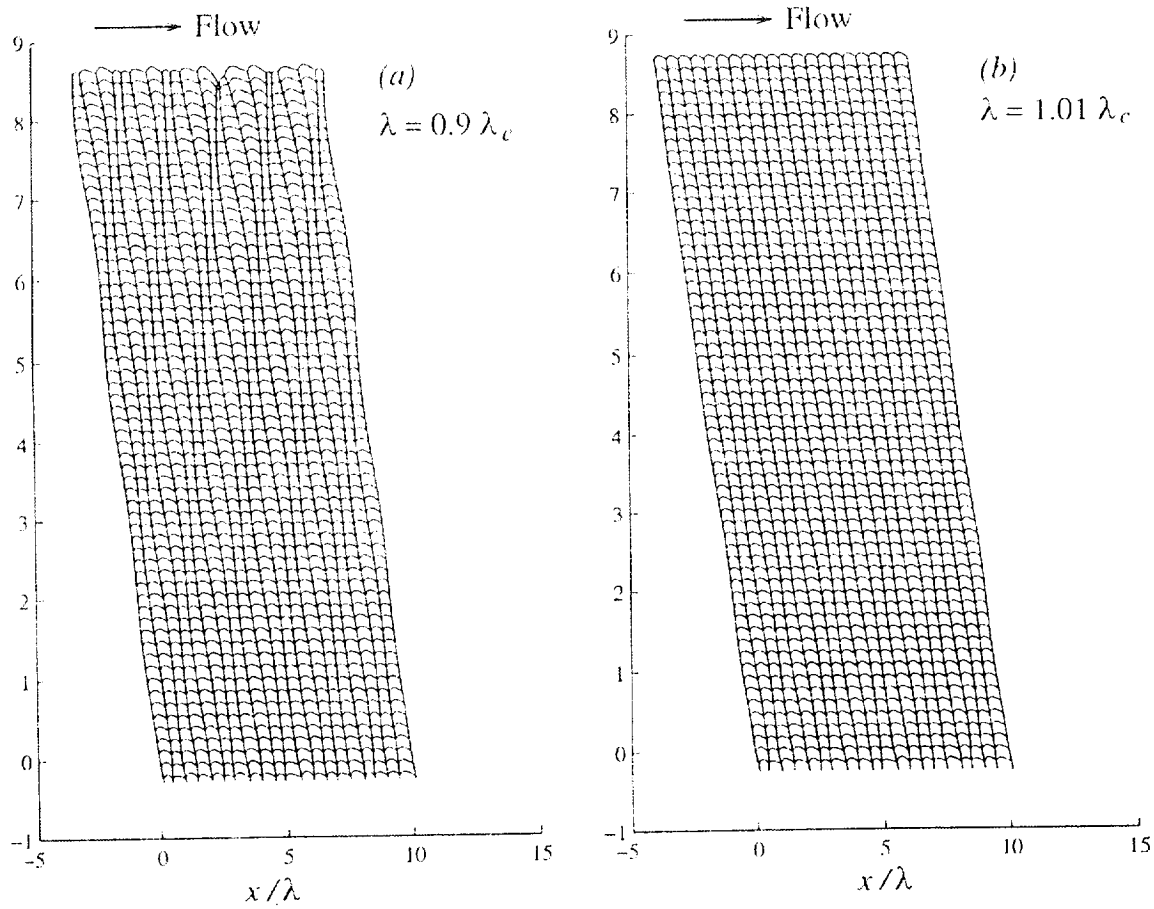

Fig 8

CONCLUSIONS

1. LONG-WAVE INSTABILITY

2. FLOW-INDUCED EFFECTS ON SPACING AND TILTING

3. NONLINEAR PINCHING

STEADY GROWTH:

p ARBITRARY - SYMMETRY-BREAKING BIFURCATIONS FOR $\lambda << 1$ AND $\lambda >> 1$

NO LEVER RULE WAVES

INSTABILITY: $p << 1$

$M >> 1 \qquad \lambda_c = \lambda_m$

$M << 1 \qquad \lambda_c < \lambda_m$

WHERE

$\lambda_c < \lambda_c \Rightarrow$ PINCHING IN FINITE TIME

FLOW PROMOTES PINCHING

ELECTROHYDRODYNAMICALLY DRIVEN CHAOTIC ADVECTION IN DROPS

Thomas Ward & G. M. Homsy*

Department of Mechanical Engineering
Engineering II Building, UCSB
Santa Barbara, CA 93106-5070

ABSTRACT

When a liquid drop of given dielectric constant, resistivity and viscosity is translating in a liquid of different dielectric constant, resistivity and viscosity under Stokes flow conditions in the presence of an electric field, the resulting internal circulation is a superposition of the Hadamard-Rybcynski circulation and the circulation first described theoretically by G. I. Taylor [1]. For sufficiently strong electric field strengths, the quadrapole structure of the Taylor circulation can cause an internal stagnation disk to occur [2]. Our interest is in the situation where a modulation of the electric field causes the stagnation disk to modulate its position, potentially leading to chaotic flows within the drop. The dimensionless electric field strength is characterized by $W = 4V(1+\lambda)/U$, where V is the maximum interfacial velocity of the Taylor circulation, U the translational velocity, and λ the viscosity ratio. The streamfunction for the flow is:

$$\psi = (r^4 - r^2)\sin^2(\theta) + W(t)\,(r^3 - r^5)\sin^2(\theta)\cos(\theta) \qquad (1)$$

$$W(t) = W_1 + W_2\cos(\varepsilon t), \qquad (2)$$

where ε is the dimensionless frequency, and W_1, W_2 are the amplitudes of the DC and AC components, respectively. We have found it useful to replace these parameters by a secondary set, ε, W_{max}, and $\delta = (1/W_1 - 1/W_2) - (1/W_1 + 1/W_2)$. As shown in Figure 1a, δ is the dimensionless distance the stagnation disk moves over one period of modulation. The advection equations corresponding to the flow in (1) were integrated by standard techniques, and it was found that the trajectories were chaotic over a wide range of parameters [3]. Figure 1b shows a typical Poincaré section, indicating that a large percentage of the drop may become well-mixed asymptotically over a large number of periods.

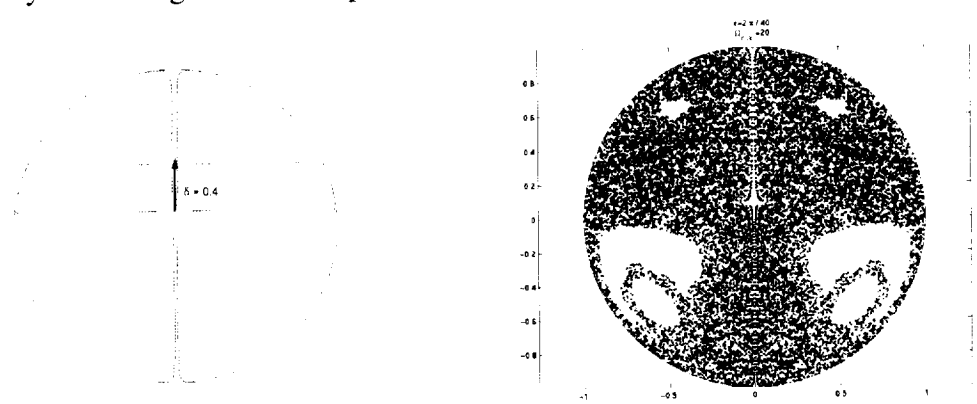

(a) (b)

Figure 1. (a) Schematic of circulation with modulated electric field.
(b) Poincaré section for the parameters: $W_{max} = 20$, $\varepsilon = 10$, $\delta = 0.4$

Experiments were conducted to test the predictions of rapid mixing on convective time scales. Drops of silicon oil were suspended in a small 60 mm x 120 mm x 120 mm test cell filled with castor oil, and subject to time-modulated axial electric fields with a wave form corresponding to eq(2). The drops were typically 5 mm in diameter and settled with typical speeds of $O(10^{-1}$ mm/s). Once formed, the drops were inoculated with small scattering particles and illuminated in an equatorial plane by an Argon-ion laser. Fields of $O(10^{-1}$ kV/mm) and frequencies of $O(10^{-2}$ Hz) resulted in typical values of $W_{max} = 20$, $\varepsilon = 8$, $\delta = 0.4$. The resulting advection of the particles was imaged by a CCD camera, which collected images over a number of modulation periods. In order to make comparisons between these images and the corresponding theory, the trajectories of a large number of particles (typically $O(10^4)$) were simulated, with initial positions approximately the same as in the experiments.

Figure 2a shows a typical image, recorded after 6 periods of modulation. As can be seen, the particles are not confined to the spherical section in which they began, and the mixing pattern has particular geometric features. The corresponding simulation for the same set of parameters is shown in Figure 2b. As can be seen, there is good qualitative agreement between the two.

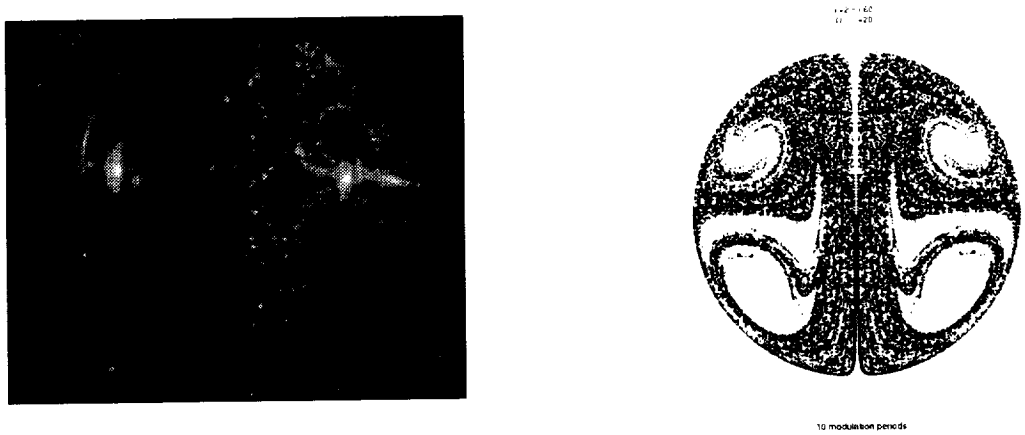

(a) (b)

Figure 2. Results for particle positions after 6 periods for the same conditions as in Figure 2. (a) experimental image. (b) simulation.

In summary, our work has shown that it is possible to drive chaotic advection within drops using time-modulated electrical stresses, and that the resulting mixing is rapid, being achieved over a few modulation periods, and is in good agreement between theory and experiment.

References
1. G. I. Taylor, *Proc. Roy. Soc.* **291A**, 159-166, 1966
2. L. S. Chang, T. E. Carlson, & J. C. Berg, *Int. J. Heat Mass Transfer,* **25**, 1023-1030, 1981.
3. T. Ward & G. M. Homsy, *Phys. Fluids*, **13**, 3521-3525, 2001.

* bud@engineering.ucsb.edu: (805) 893-2704(V) (805)-893-8651(F)

THE EFFECTS OF ULTRATHIN FILMS ON DYNAMIC WETTING

Xia Chen, Stephen Garoff
Dept. of Physics and Center for Complex Fluids Engineering
Carnegie Mellon University, Pittsburgh, PA 15213
Email: sg2e@andrew.cmu.edu
412-268-6877
412-681-0648 (fax)

Enrique Ramé
National Center for Microgravity Research on Fluids and Combustion
NASA Glenn Research Center, MS 110-3, Cleveland, OH 44135

ABSTRACT:

Dynamic wetting, the displacement of one fluid by another immiscible fluid on a surface, controls many natural and technological phenomena, such as coating, printing, spray painting and lubricating. Particularly in coating and spraying applications, contact lines advance across pre-existing fluid films. Most previous work has focused on contact lines advancing across films sufficiently thick that they behave as simple Newtonian fluids. Ultrathin films, where the film thickness may impinge on fundamental length scales in the fluid, have received less attention.

In this talk, we will discuss the effects of ultrathin polymer films on dynamic wetting. We measure the interface shape within microns of moving contact lines advancing across pre-existing films and compare the measurements to existing models of viscous bending for interfaces advancing across dry surfaces and "thick" (in the sense that they behave as liquids) films. In the experiments, we advance a contact line of 10-poise and 1-poise polydimethylsiloxane (silicone oil) across pre-coated films of the same fluid with thickness from a single chain thickness (~10 Å) through a couple of radii of gyration (100-200 Å) to films so thick they are likely bulk in behavior (10^3 Å). All films are physisorbed, i.e. they readily rinse from the surface. Thus, molecules in the film are not anchored to the surface and can move within the film if the hydrodynamics dictate such motion.

For films of the thickness of a single chain (~10 Å), our experiments indicate that the advancing fluid behaves just as it would if it advanced over a dry surface. For the thicker films (10^3 Å), we find behavior indicating that the molecules in the film are acting as a fluid with the bulk properties. In this regime, results for the two different fluids are identical when the experiments are performed at the same pre-existing film thickness and advancing capillary number, Ca. For film of thickness of a few radii of gyration (~100- 200 Å), the behavior depends on Ca of the advancing meniscus. At low Ca, the viscous bending of the interface near the contact line does not behave as it would on a dry surface. It has a lower curvature than expected. However, at higher Ca, the viscous bending is described by the model for spreading over a dry surface. These results show that the fluid flow in the film does behave differently than bulk as the film thickness becomes comparable to molecular length scale. But even more intriguing is the unusual velocity dependence of that behavior where the film behaves more solid-like at higher contact line speeds. We will discuss these results in terms of the properties of confined polymer melts.

NASA/CP—2002-211212/VOL1

The Effects of Thin and Ultrathin Films on Dynamic Wetting

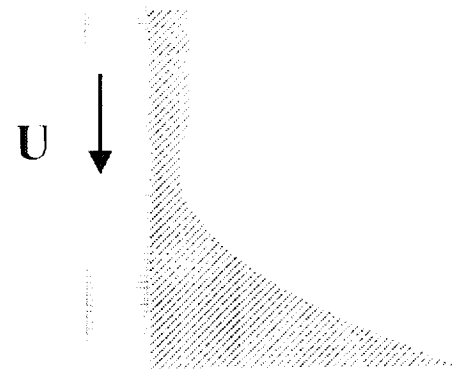

X. Chen, S. Garoff

Dept. of Physics,

Center for Complex Fluids Engineering

Carnegie Mellon University, Pittsburgh, PA 15213

E. Ramé

National Center for Microgravity Research,

NASA, Cleveland, OH 44135

Support: NASA

Wetting: Inherently a Mesoscale Phenomenon

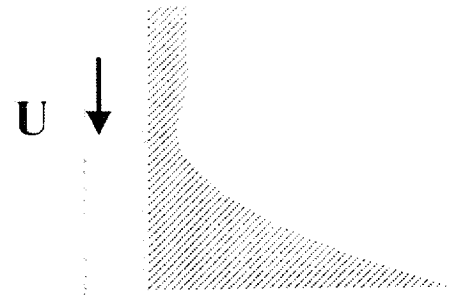

- Wetting controlled by the physics in region near contact line
  - Region decreases in size as contact line approached
  - Must cross to "nano-" or mesoscale
  - Many wetting regimes: mesoscale physics controls macro behavior
- Thus dynamic wetting
  - Provides a place to probe new mesoscale fluid physics
  - This mesoscale physics controls macro behavior
- How can we see this mesoscale physics?
  - Deformation of liquid/vapor interface sensitive to fluid motion on mesoscale
  - Fluid behavior on mesoscale not directly measurable
  - Measure wetting on micro and macro scales and infer mesoscale physics
- Today: use method to probe mesoscale physics of fluids confined in thin films

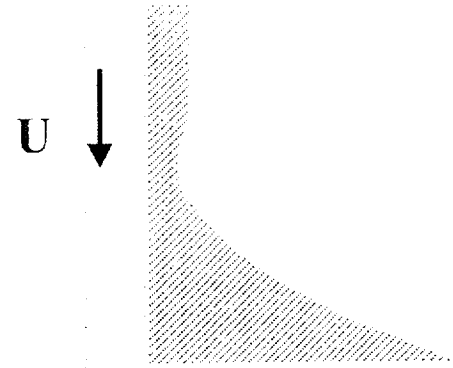

Main Points of Talk

- Advancing meniscus across a pre-existing film
  - Correct fluid mechanics near the contact line?
  - Properties of the material in the film?
- For thin (~ microns) films
  - Present models work within predicted limits
  - Test new models and computation beyond those limits
- For ultrathin (~ radius of gyration, 10 – 100Å) films
  - Viscous bending like that found on dry surfaces
  - Material in film: still a fluid?
- Microgravity: a critical tool to probe these questions

Two Analytic Models Which Might Describe Wetting

Bretherton-like

(Landau-Levich, Park & Homsy,…)

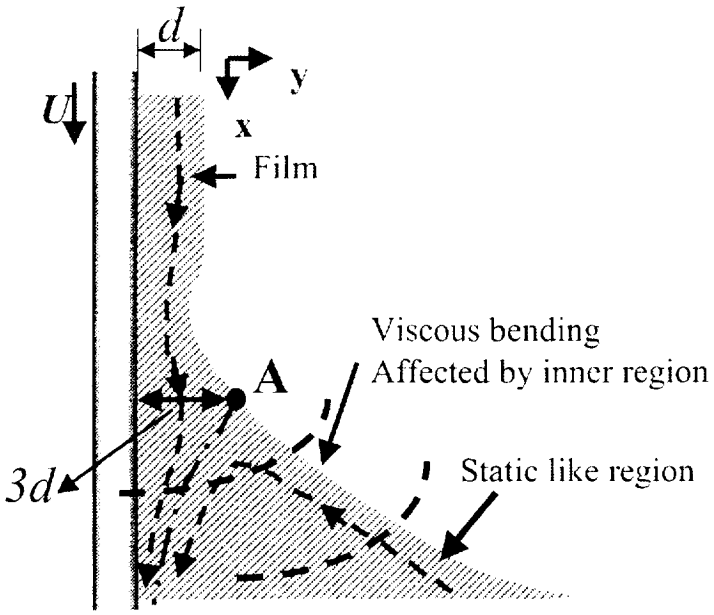

Cox

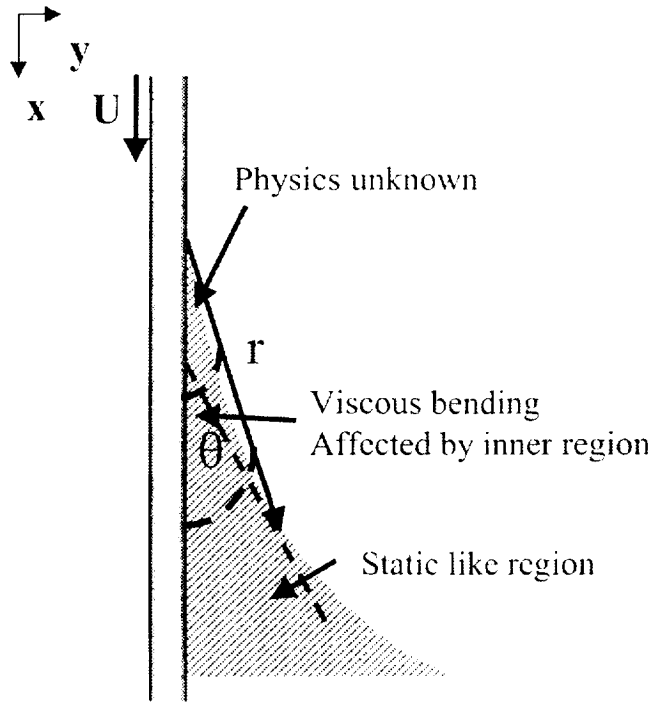

Experiments

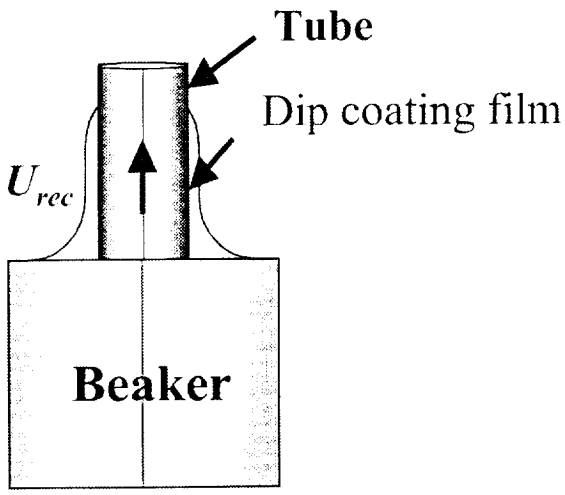

Recede to pre-coat films

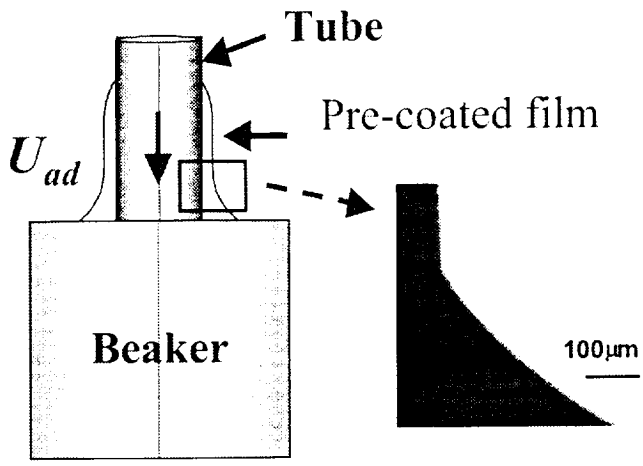

Advance at different speeds

- Digitize liquid-vapor interface shape
- Fit data to two models
- Explore viscous bending

Material System And Film Preparation

- Material used
  - PDMS (Polydimethylsiloxane) in bulk and films
  - Viscosity and radius of gyration
    - 1000 cP ($R_g \approx 100$ Å) and 100 cP ($R_g \approx 50$ Å)
  - Surface — Pyrex
- Films preparation
  - Dip coating (pure or from solvent)
  - Film thickness from 20 $\AA$ to 10 μm

For Micron Scale Films
Ready to Compare to New Computation

- $F = Ca^{2/3}_{adv}/Ca^{2/3}_{rec}$

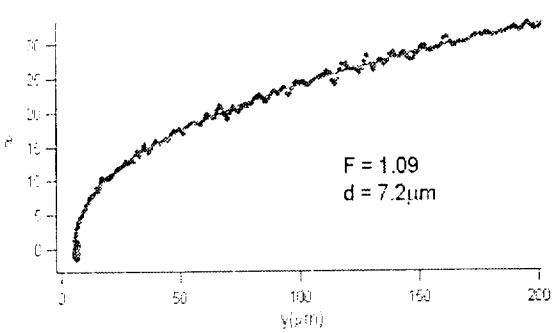

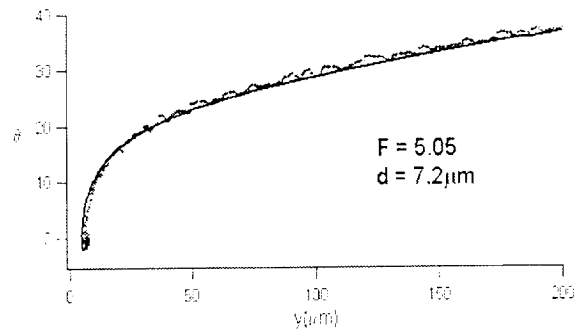

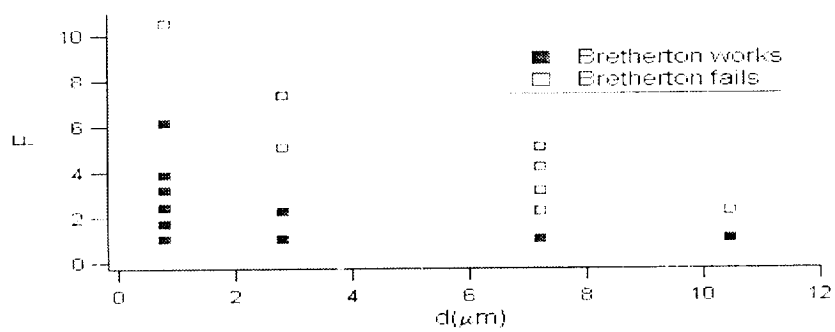

- Results as expected
  - Bretherton-like solution works for $F \leq 1$
  - Shapes independent of length scales of fluids
- New computation (Bose, Gaver, Homsy, …) and models (Hirasaki, Jensen)

Can Use Microscopic Scale Flow Visualization to Examine Position of Stagnation Point and Dividing Streamline

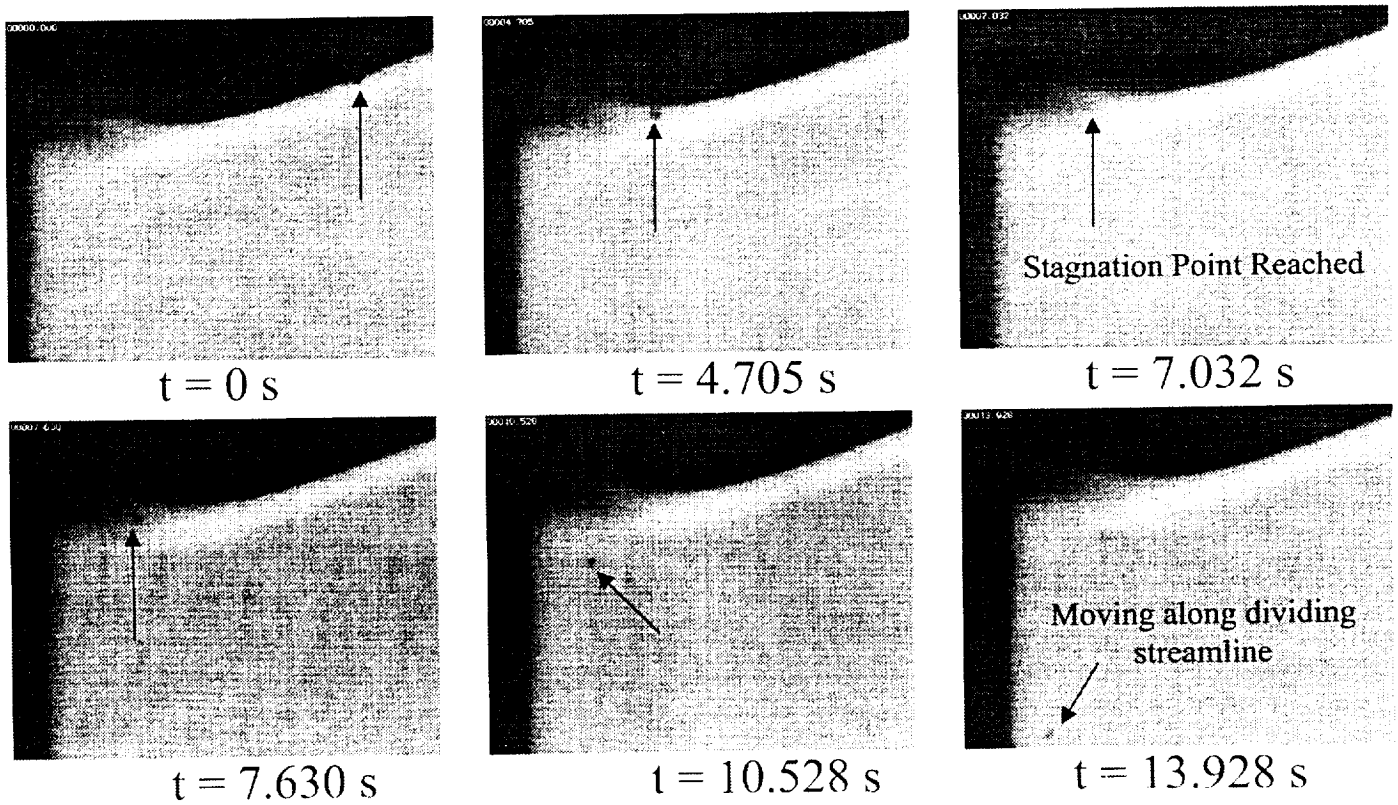

For Ultrathin Films, Viscous Bending More Closely Described by Cox Model

•Bretherton fails to describe viscous bending, not surprising, $F \geq 10^2$

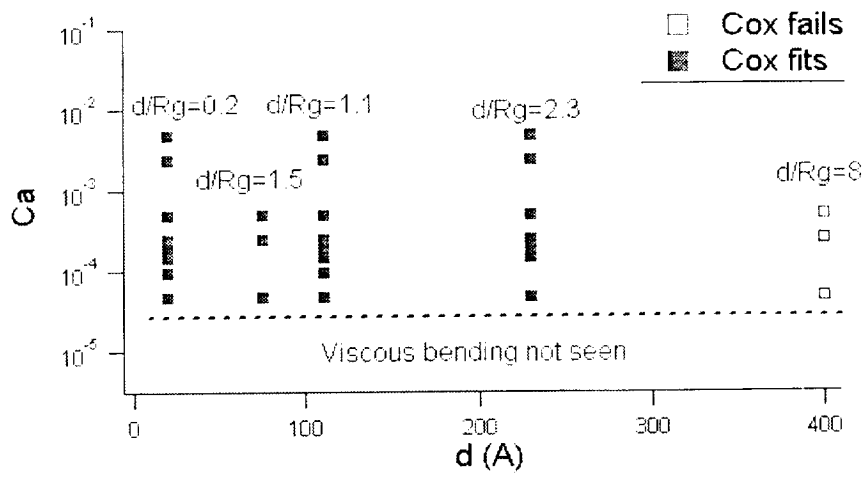

•Cox begins to describe viscous bending for ultrathin films

– Viscous bending characteristic of modulated wedge region for $d/R_g < 8$

– Is material in film beginning to behave as a viscoelastic fluid?

•More detailed hydrodynamic descriptions needed to determine if fluids in films becoming non-Newtonian

Contact Lines Advancing Over Pre-existing Thin Films

- Dynamic wetting – a probe of mesoscale physics in thin films
- Films much thicker than material length scales
  - Previous models adequate in limited Ca range
  - Stage set for testing new computations and models
- Films which approach material length scales
  - Fitting surprising
  - May be indicating material in film no longer simple fluid
  - Further development of fluid mechanics needed to clarify

PASSIVE AND ACTIVE STABILIZATION OF LIQUID BRIDGES IN LOW GRAVITY

David B. Thiessen, Wei Wei and Philip L. Marston*
Physics Department, Washington State University, Pullman, WA 99164-2814

ABSTRACT

The cylindrical liquid bridge of arbitrary size surrounded by air or vacuum is a fluid configuration that is essentially unique to the zero-gravity environment. An associated technology, which is enhanced in zero gravity, is the float-zone process of crystal growth, which involves a molten liquid bridge between a feed rod and the growing cylindrical crystal. There are several advantages to the crystal growth process in using long molten zones. Unfortunately, long liquid bridges are more susceptible to g-jitter [1]. Also, a cylindrical liquid bridge in zero gravity is unstable if its length exceeds its circumference, or stated in another way, when the slenderness, defined as the length to diameter ratio, exceeds π. This is the well-known Rayleigh-Plateau (RP) instability involving the growth of a varicose mode leading to breaking of the bridge. Stabilization of liquid bridges in air in the low-gravity environment of NASA's KC-135 aircraft has been demonstrated for slenderness values in excess of 4.0 using two techniques, passive acoustic stabilization (PAS) [2] and active electrostatic stabilization (AES) [3]. The PAS method is theoretically capable of stabilizing a bridge of any length, provided a sound field of appropriate dimension is available. The AES method in its current form controls only the (2,0) mode of the bridge, which is the varicose mode that becomes unstable when the slenderness (S) exceeds π. By controlling only the (2,0) mode, the current form of the AES method cannot stabilize cylindrical bridges beyond S=4.493 at which point the (3,0) mode becomes unstable. At present, the longest bridge stabilized on the KC-135 by the AES method had a slenderness of 4.4 [3]. The AES method has the advantage that it can be used to control both the frequency and damping of the (2,0) mode of the bridge. This would be useful in reducing the susceptibility of a long molten zone to g-jitter in that the (2,0) mode frequency could be shifted away from a particularly noisy vibration frequency band of the spacecraft and the response further reduced by control of the damping of the mode.

The principle behind the AES method is to sense the (2,0)-mode amplitude and then apply a mode-coupled feedback stress to control the mode dynamics. Two concentric ring electrodes are used to produce a Maxwell-stress distribution that couples into the (2,0) mode of the bridge. By applying a feedback stress in proportion to the (2,0)-mode amplitude with appropriate gain, the mode frequency can be raised and bridges can be stabilized beyond $S=\pi$. Models show that the stability is affected by the bandwidth of the controller and the (2,0)-mode damping. If the feedback stress is applied in proportion to the velocity of the mode amplitude with appropriate sign, the damping of the mode can be increased. Active control of damping has recently been demonstrated in Plateau-tank experiments. The dynamic response of a bridge to feedback control is predicted to be significantly different for bridges in air compared to those in a Plateau tank

because of the different nature of the viscous damping for the two cases. Boundary-layer damping at the free interface is much more important for the case of a Plateau-tank bridge.

Laboratory experiments: A new fluid system is being used in the Plateau-tank facility to allow for studies of bridge dynamics and active control of damping with the AES system. The bath fluid is a high-density (1.61 g/cc), low viscosity (0.77 cS), low dielectric constant, fluorinated liquid with low water solubility. The bridge liquid is an aqueous solution of CsCl, density matched to the bath (~52.3 wt% CsCl). The Ohnesorge number (ratio of viscous to inertial effects) for bridges with the new fluid system is around 0.003 which is close to that of a pure water bridge in air of the same diameter. The new system is still not dynamically similar to a bridge in air because the dynamics also depend on the density and viscosity ratios between the inner and outer fluids. Dynamics studies involve driving the (2,0) mode by modulating the electrode potentials and then cutting off modulation to allow for a free decay of the mode. Feedback can be active during the entire modulation and free-decay sequence. Results obtained with the new system show that mode damping increases in proportion to the velocity gain as expected. Also, by using negative velocity feedback, damping can be reduced to the point that the bridge spontaneously begins oscillating at the natural (2,0)-mode frequency leading to breakup of the bridge. By using both amplitude and velocity feedback, the mode frequency can be shifted upward and the damping increased.

KC-135 based experiments: KC-135 experiments performed in 2001 concentrated on passive acoustic stabilization. Real-time measurements of transducer power consumption and acoustic pressure were made while stabilizing a bridge. Also, progress was made on confirming the theoretical understanding of PAS by performing experiments with different bridge radii but the same acoustic wavenumber. The theory predicts optimum stabilization for a particular value of the wavenumber-radius product (kR~0.86) [2]. As expected, a bridge with a kR value significantly larger than the predicted optimum could not be stabilized. Because of the limited duration and quality of low gravity, studies of bridge dynamics on the KC-135 using the AES system in the manner described above for the Plateau-tank are very difficult. Some oscillation and free-decay measurements for a bridge in air without feedback were made on the KC-135 in 2000 [3]. The measured frequency and damping of the mode agreed reasonably well with theory [3]. Active damping of bridges in air would be investigated best on the ISS, although a demonstration on the KC-135 may be possible.

REFERENCES

[1] D. Langbein, "Crystal Growth from Liquid Columns," J. Crystal Growth **104**, 47-59 (1990).

[2] M. J. Marr-Lyon, D. B. Thiessen, and P. L. Marston, "Passive stabilization of capillary bridges in air with acoustic radiation pressure," Phys. Rev. Lett. **86**, 2293-2296 (2001); erratum **87** (20), 9001.

[3] D. B. Thiessen, M. J. Marr-Lyon, and P. L. Marston, "Active electrostatic stabilization of liquid bridges in low gravity," J. Fluid Mech. **457**, 285-294 (2002).

* marston@wsu.edu, phone: (509) 335-5343, FAX: (509) 335-7816

Passive and Active Stabilization of Liquid Bridges in Low Gravity

David B. Thiessen, Wei Wei and Philip L. Marston
Physics Department, Washington State University

RECENT PUBLICATIONS

M. J. Marr-Lyon, D. B. Thiessen, F. J. Blonigen, and P. L. Marston, "Stabilization of electrically conducting capillary bridges using feedback control of radial electrostatic stresses and the shapes of extended bridges," *Phys. Fluids* **12**, 986-995 (2000).

M. J. Marr-Lyon, D. B. Thiessen, and P. L. Marston, "Passive stabilization of capillary bridges in air with acoustic radiation pressure," *Phys. Rev. Lett.* **86**, 2293-2296 (2001).

D. B. Thiessen, M. J. Marr-Lyon, and P. L. Marston, "Active electrostatic stabilization of liquid bridges in low gravity," *J. Fluid Mech.* **457**, 285-294 (2002).

Sixth Microgravity Fluid Physics and Transport Phenomena Conference
August 14-16, 2002
Cleveland, OH

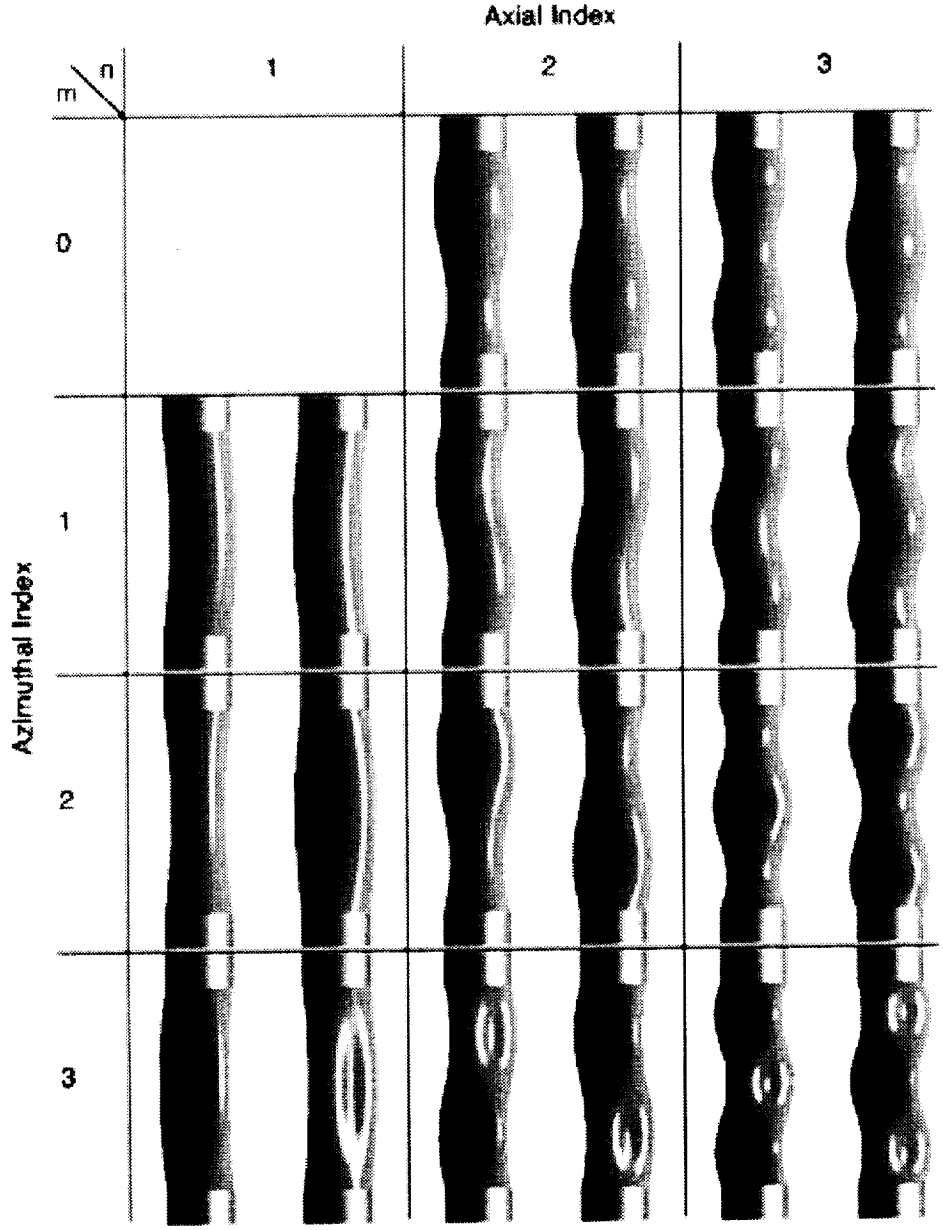

Capillary modes on a cylindrical bridge (mode shapes shown 180 degrees out of phase).

slenderness $S = L/2R$

(2,0) mode

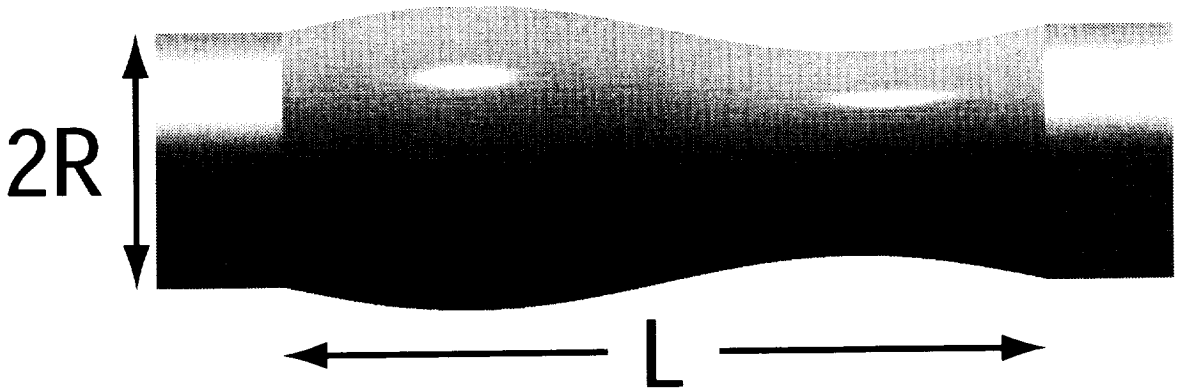

Rayleigh-Plateau limit, $S_2 = \pi$

(3,0) mode

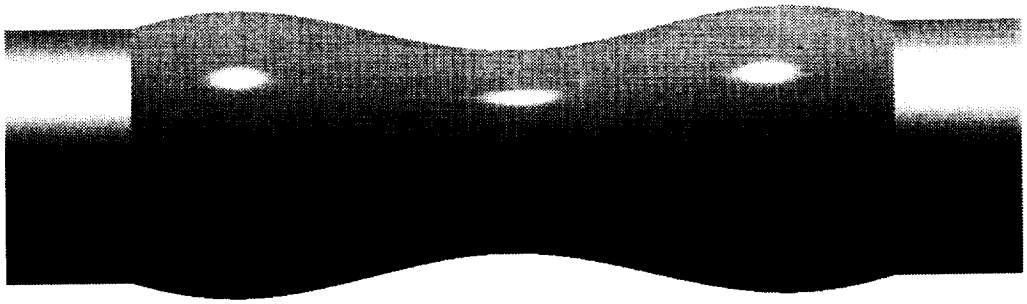

Stability limit, $S_3 = 4.4934...$

Passive Acoustic Stabilization Method (PAS)

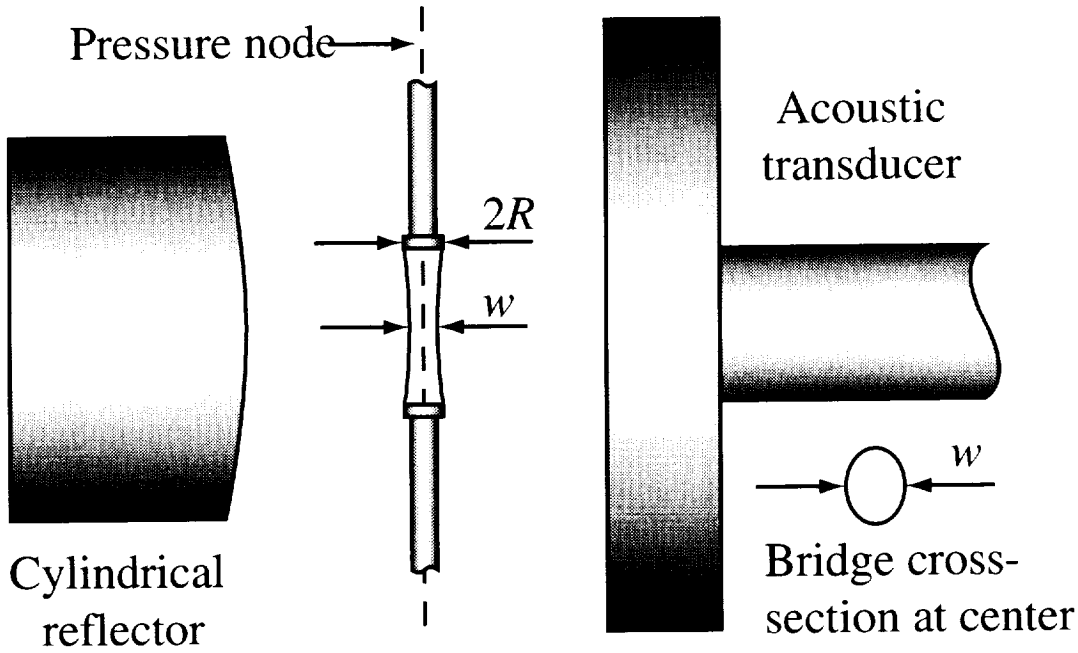

Active Electrostatic Stabilization (AES)

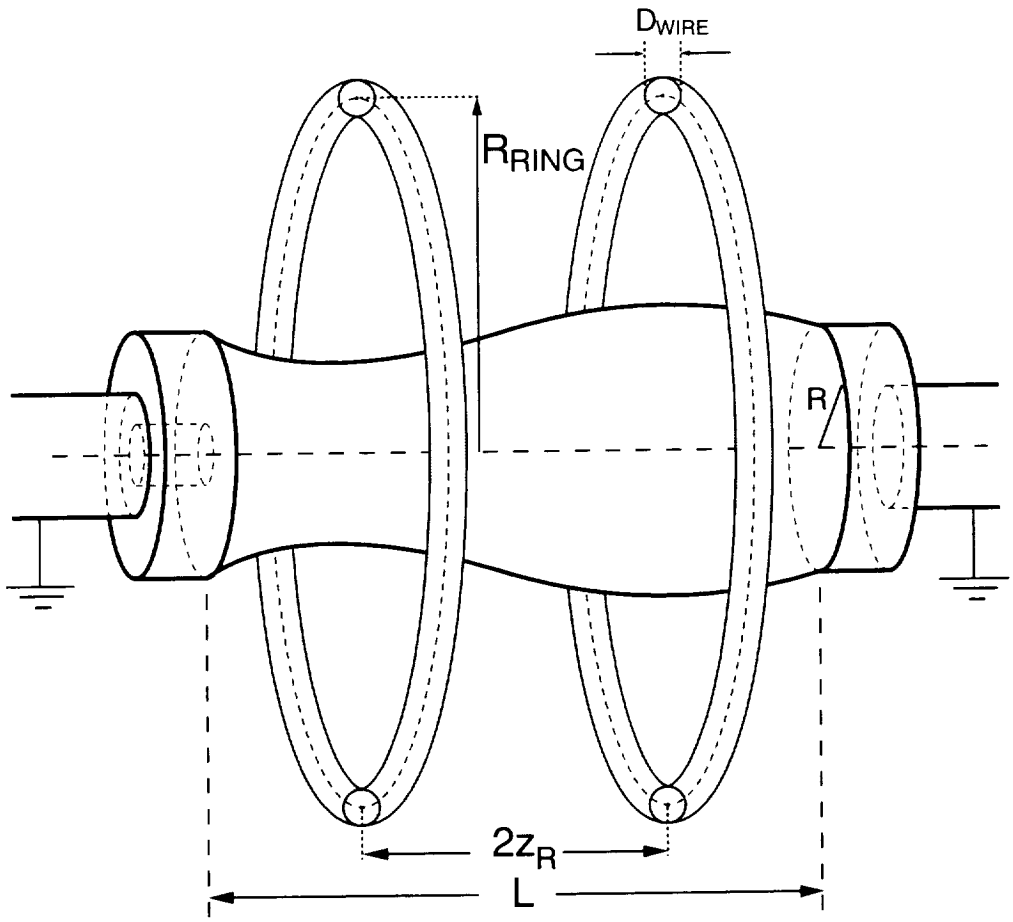

Schematic of a liquid bridge suspended between circular supports. Concentric ring electrodes are also shown. Circular supports are grounded. Shifting the potential of the left electrode away from ground potential produces an outward Maxwell stress on the necked portion of the bridge.

Potential Applications

Float Zone (FZ) Crystal Growth

- long molten zone has advantages for control of temperature gradient in crystal and for producing planar solid/melt interface
- active damping of g-jitter induced oscillations using AES method
- mode frequency shifting (PAS or AES)
- control of grown-crystal diameter by control of meniscus angle using AES

Other Possible Applications

- control breakup of liquid jet (AES or PAS)
- general control of free liquid surface dynamics through mode-coupled feedback stress (AES)

Status of AES Experiments

Plateau Tank:

- stabilization beyond Rayleigh-Plateau limit confirmed (up to (3,0)-mode stability limit)
- active damping confirmed

*KC-135 (bridge in air):

- stabilization of (2,0) mode confirmed, stability envelope pushed over many flights (rarely reaching (3,0)-mode limit)
- demonstrated free-decay measurements

Accessible Ohnesorge numbers larger than for practical FZ systems.

* over 1200 parabolas were flown on the KC-135 for the combined PAS & AES development

Need for Long-Duration Low Gravity

- Plateau-tank system cannot be made dynamically similar to a bridge in air as a consequence of enhanced boundary-layer damping
- low-g duration on KC-135 too short to make dynamical measurements of low-Ohnesorge-number systems of interest for practical applications

Characteristic Dimensions

length scale	R	(tip radius)
time scale	$\left(\rho_i R^3/\sigma\right)^{1/2}$	
pressure scale	σ/R	(Laplace pressure)

Nondimensional Parameters

$S = L/2R$	slenderness
$\mu = \mu_o/\mu_i$	viscosity ratio
$\rho = \rho_o/\rho_i$	density ratio
$C = \mu_i/\left(\rho_i \sigma R\right)^{1/2}$	Ohnesorge number

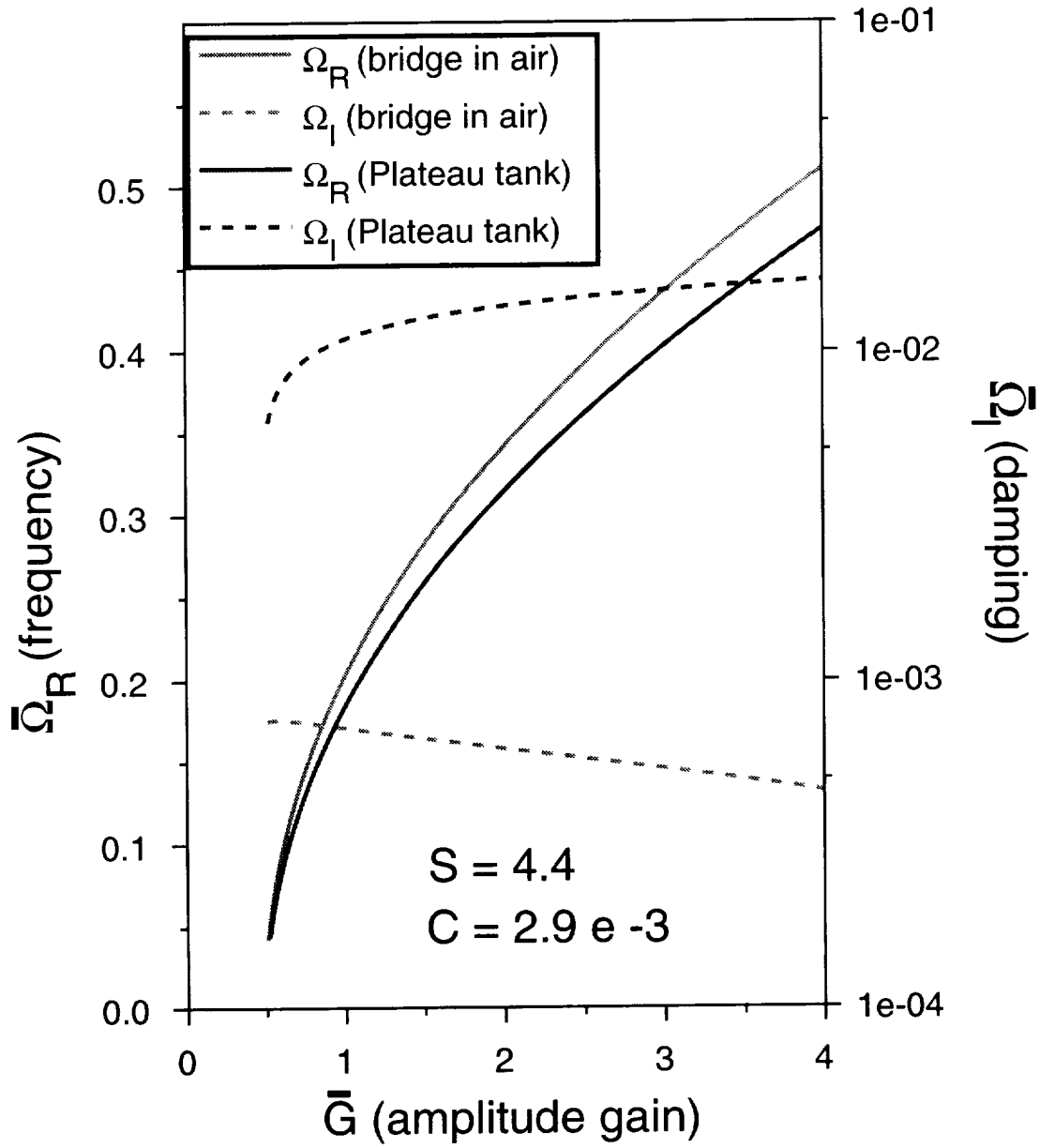

Comparison of model predictions of frequency and damping versus feedback gain for two identical bridges except that one is surrounded by air and the other by a density-matched fluid (Plateau tank). The damping behavior is dramatically different.

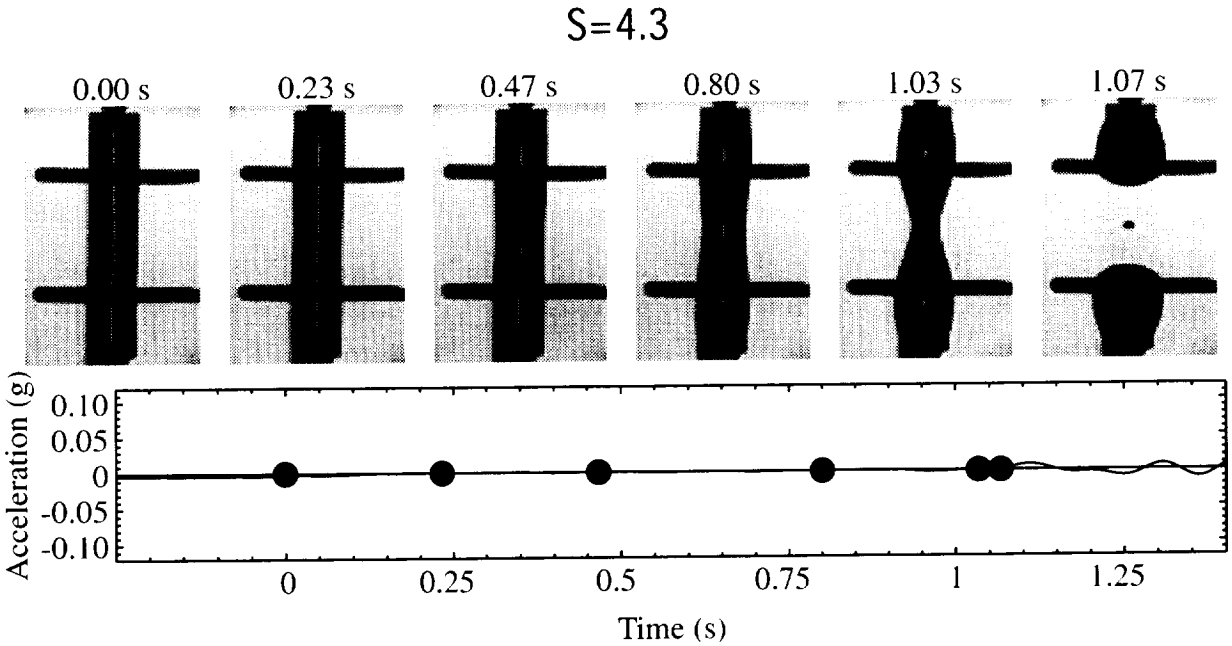

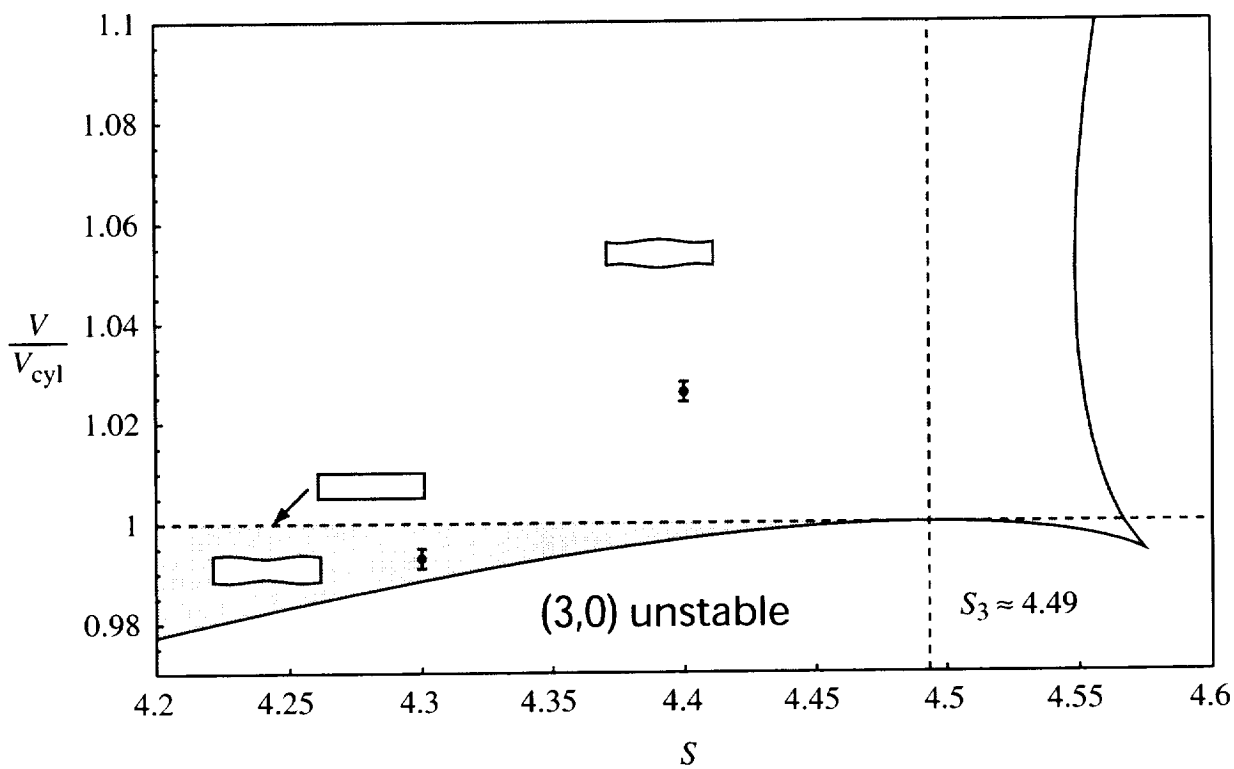

(3,0)-mode stability boundaries in volume-slenderness space showing two of the best results obtained on the KC-135. Images of the slenderness 4.3 result are shown above along with the corresponding accelerometer trace.

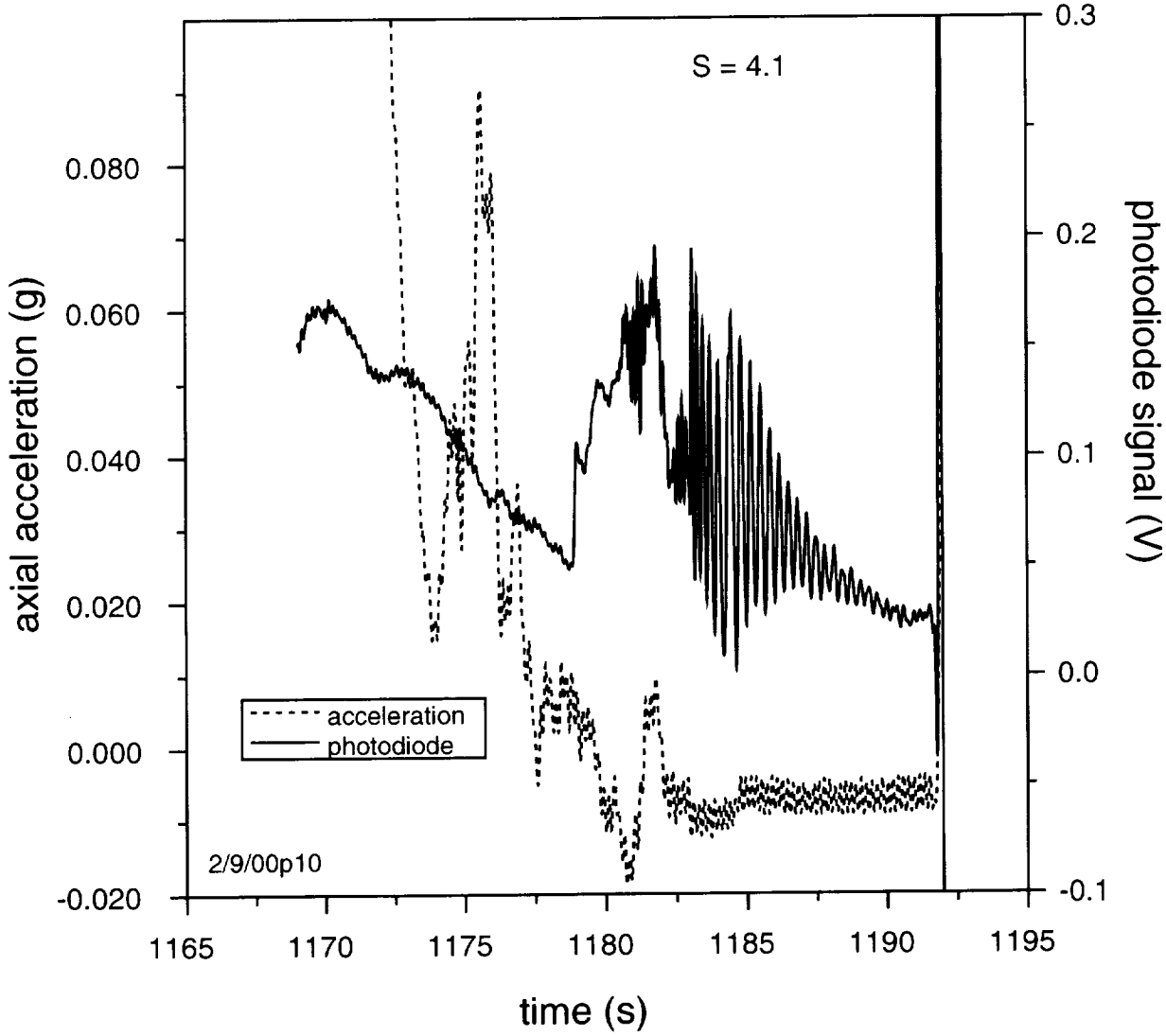

Stabilization results from KC-135 flight. The (2,0) mode of a bridge stabilized to slenderness 4.1 is accidentally excited by g-jitter and decays slowly.

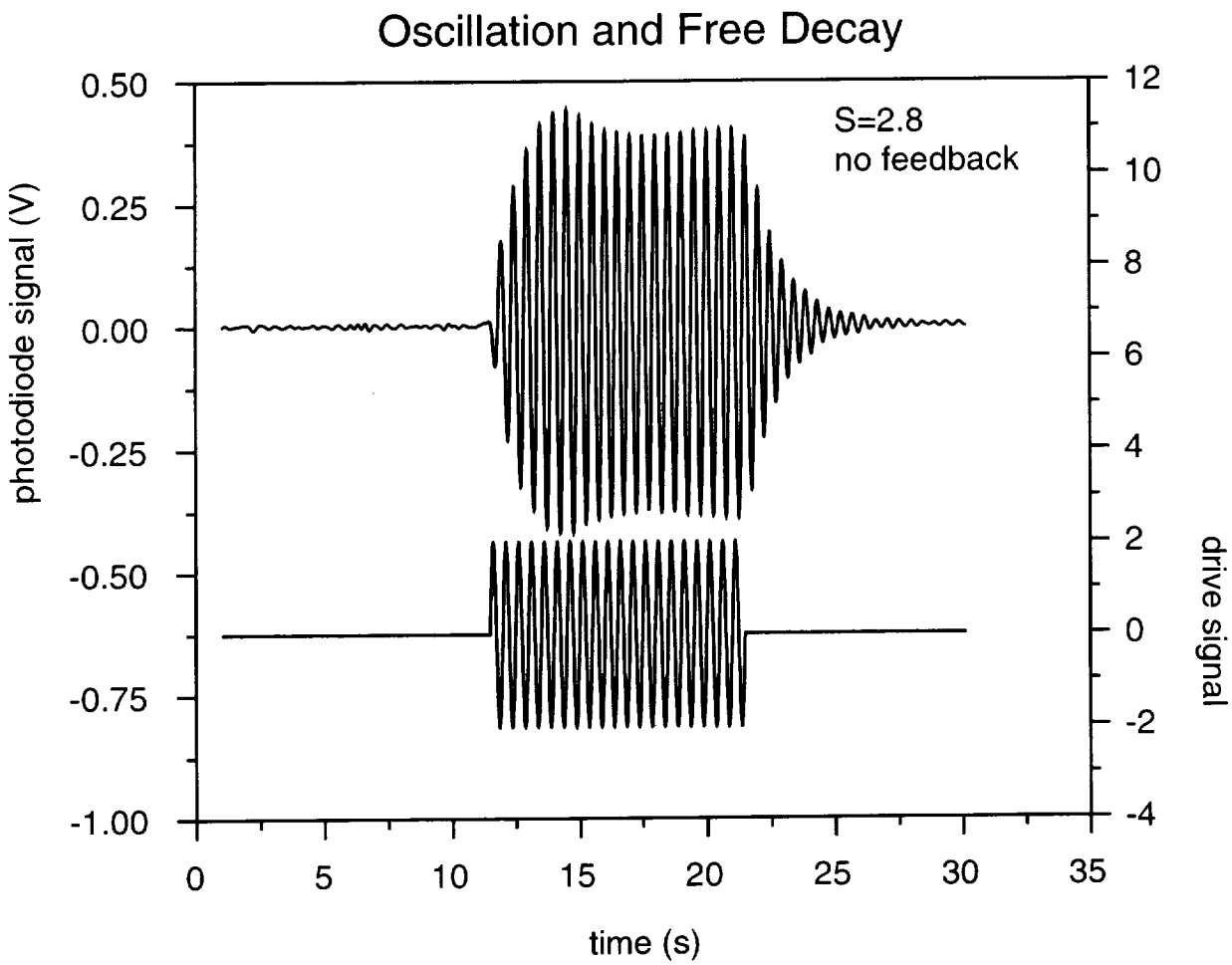

Plateau tank

bridge liquid: H_2O + CsCl (52 wt% CsCl)

bath: HFE-7500 (3M product)

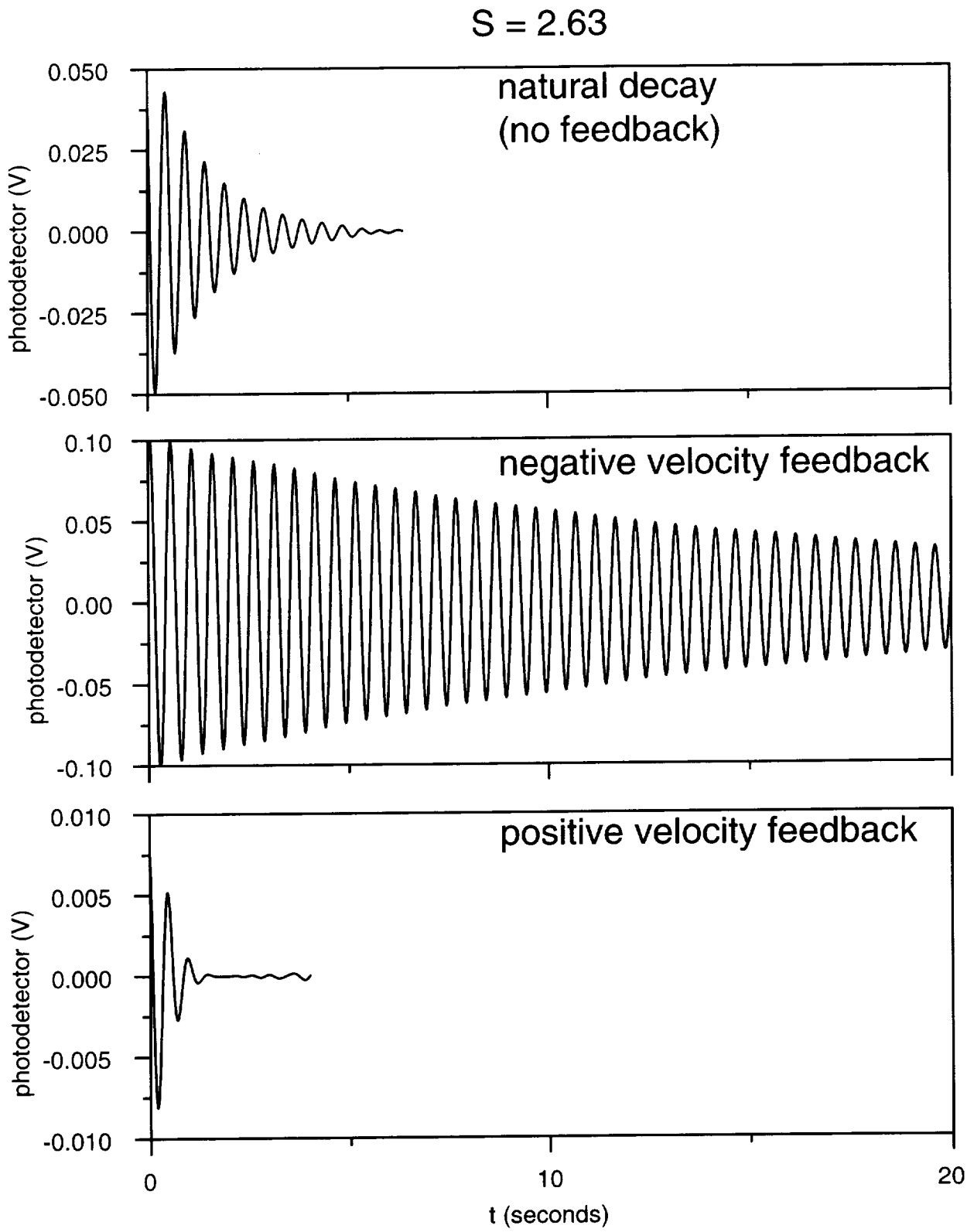
S = 2.63
natural decay
(no feedback)
negative velocity feedback
positive velocity feedback
photodetector (V)
0.050
0.025
0.000
-0.025
-0.050
0.10
0.05
0.00
-0.05
-0.10
0.010
0.005
0.000
-0.005
-0.010
0
10
20
t (seconds)

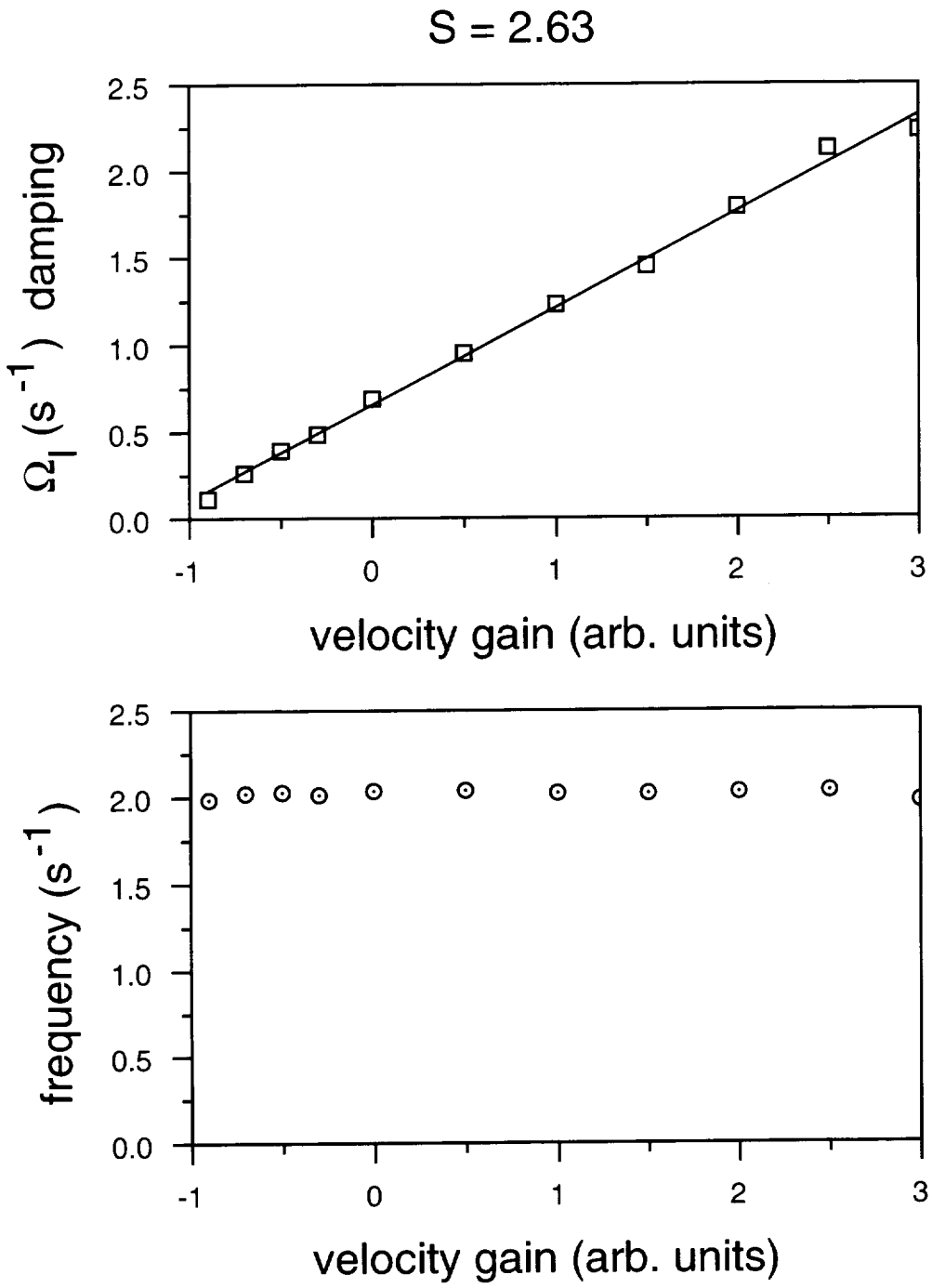
S = 2.63
Ω_I (s^{-1}) damping
2.5
2.0
1.5
1.0
0.5
0.0
-1
0
1
2
3
velocity gain (arb. units)
frequency (s^{-1})
2.5
2.0
1.5
1.0
0.5
0.0
-1
0
1
2
3
velocity gain (arb. units)

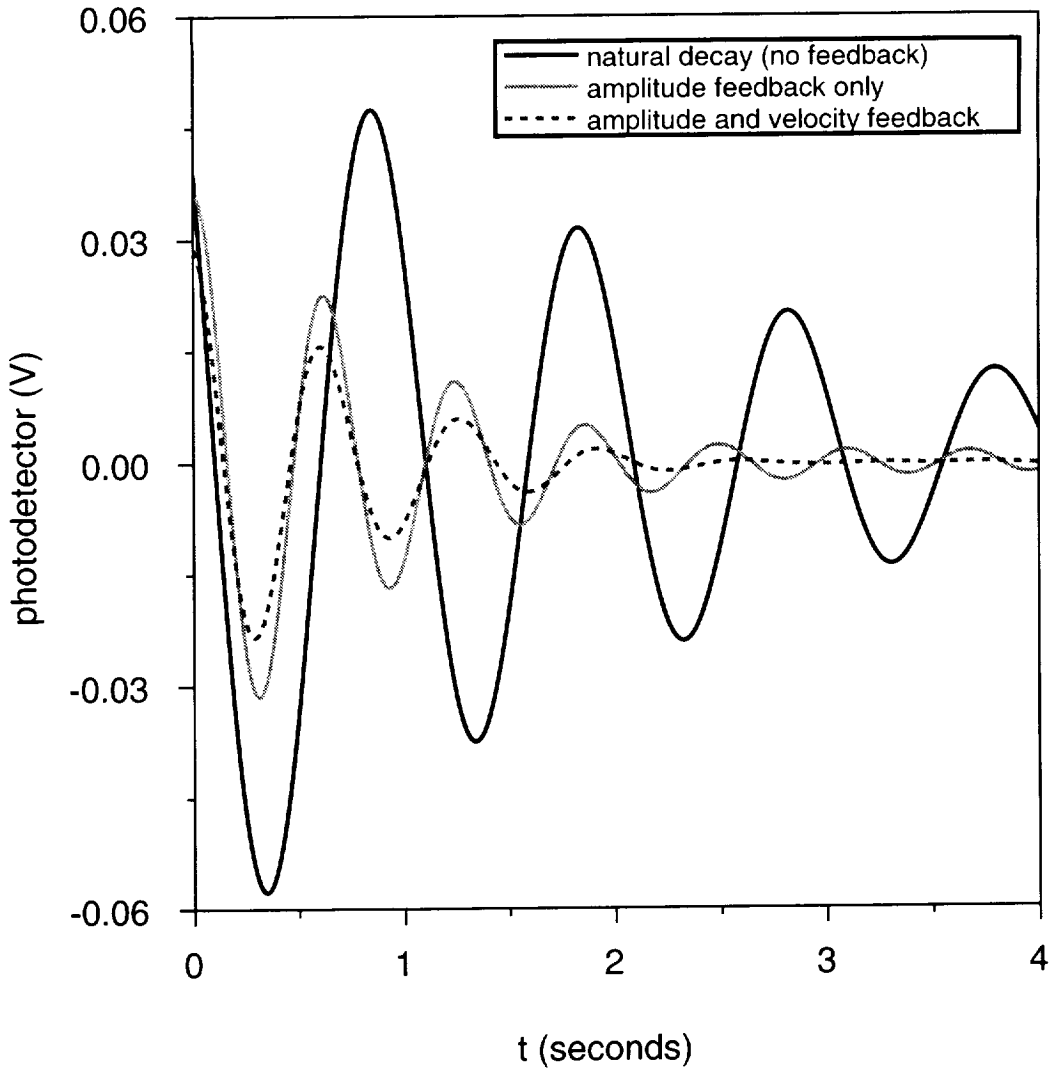

Plateau-tank results for S = 2.97.

Future Directions

Plateau Tank:

- continue quantitative tests of bridge model with feedback stresses (AES)
- explore limits of active damping (AES)
- test novel stabilization methods

KC-135 (ISS would be preferred platform):

- AES: demonstrate active damping for bridge in air (may be difficult on KC-135)
- PAS: measure bridge-mode oscillations in sound field (may be difficult on KC-135)

Theory:

- incorporate improved bridge dynamics model (Nicolas and Vega (2000)) in order to make predictions at low Ohnesorge number

MOLTEN-METAL DROPLET DEPOSITION ON A MOVING SUBSTRATE IN MICROGRAVITY: AIDING THE DEVELOPMENT OF NOVEL TECHNOLOGIES FOR MICROELECTRONIC ASSEMBLY

C. M. Megaridis,* I. S. Bayer
Department of Mechanical and Industrial Engineering, University of Illinois at Chicago

D. Poulikakos
Institute of Energy Technology, Swiss Federal Institute of Technology, Zurich, Switzerland

V. Nayagam
National Center for Microgravity Research, Cleveland, Ohio

ABSTRACT

Driven by advancements in microelectronics manufacturing, this research investigates the oblique (non-axisymmetric) impact of liquid-metal droplets on flat substrates. The problem of interest is relevant to the development of the novel technology of on-demand dispension (printing) of microscopic solder deposits for the surface mounting of microelectronic devices. The technology, known as solder jetting, features on-demand deposition of miniature solder droplets (30 to 120μm in diameter) in very fine, very accurate patterns using techniques analogous to those developed for the ink-jet printing industry. Despite its promise, severe limitations exist currently with regards to the throughput rates of the technology; some of these limitations are largely due to the lack of the capability for reliable prediction of solder bump positioning and shapes, especially under ballistic deposition conditions where the droplet impact phenomena are inherently three-dimensional.

The study consists of a theoretical and an experimental component. The theoretical work uses a finite element formulation to simulate numerically the non-axisymmetric (3-D) fluid mechanics and heat transfer phenomena of a liquid solder droplet impacting at an angle α on a flat substrate (Fig. 1). The work focuses on the pre-solidification regime. The modeling of the most challenging fluid mechanics part of the process has been completed successfully. It is based upon the full laminar Navier-Stokes equations employing a Lagrangian frame of reference. Due to the large droplet deformation, the surface (skin) as well as the volumetric mesh have to be regenerated during the calculations in order to maintain the high accuracy of the numerical scheme. The pressure and velocity fields are then interpolated on the newly created mesh. The numerical predictions are being tested against experiments, for cases where wetting phenomena are not important. For the impact parameters used in the example shown in Figs 2, 3 (We = 2.38, Fr = 16300, Re = 157), the droplet rolls along the substrate, but its shape remains practically axisymmetric for all impact angles within the range from 0 to 60 deg. Figure 2 exemplifies the results, showing this rolling motion at an impact angle α=45 deg. Interestingly, the substrate/droplet contact area during the recoiling phase of the impact is not a monotonically decreasing function of time (Fig. 3).

* M/C 251, 842 W. Taylor St., Chicago IL 60607-7022; cmm@uic.edu; fax: (312) 413 0447; tel: (312) 996 3436

The experimental component of the research tests the numerical predictions and provides necessary input data (contact angles) for the theoretical model. The experiments are performed in microgravity (2.2s drop tower of the NASA GRC) in order to allow for the use of mm-size solder droplets, which make feasible the performance of accurate measurements, while maintaining similitude of the relevant fluid dynamic groups (*Re, Fr, We, Ste*). Preliminary oblique impact experiments have been performed using water droplets in normal gravity. Figure 4 shows the definition of the two extreme values of contact angle (front θ_F, rear θ_R), as viewed from a direction normal to the plane of impact. Figure 5 compares the measured temporal variations of these two angles for an impact case where α=27deg, We = 11.7, Fr = 20.5 and Re = 1530. It is seen that the oscillatory behavior of the two angles is not in phase, indicating the complex interaction between the bulk fluid motion and the motion of the free surface.

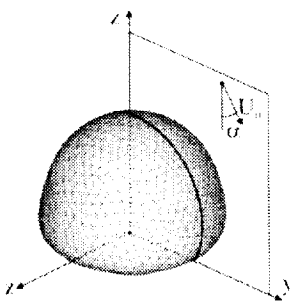

Fig. 1: Problem configuration.

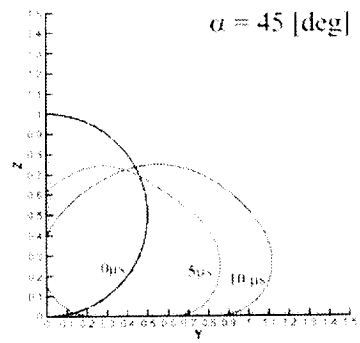

Fig. 2: Time sequence of droplet profiles as predicted by the model.

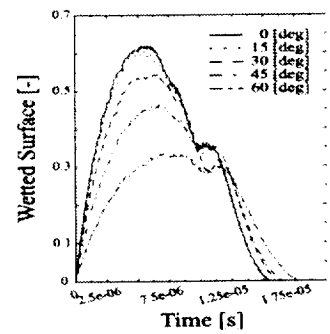

Fig. 3: Evolution of the contact area for various impact angles.

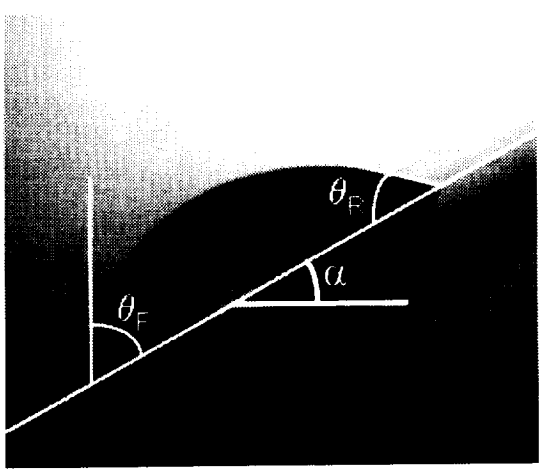

Fig. 4: Definition of front (θ_F) and rear (θ_R) contact angle in the impact of a droplet on an inclined plate.

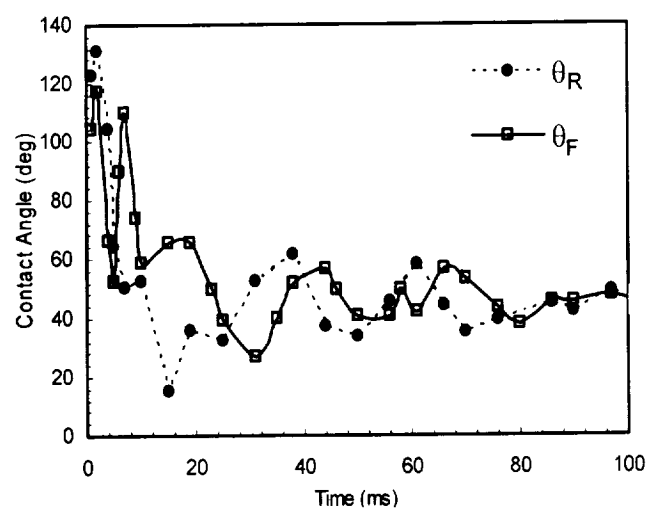

Fig. 5: Temporal variation of front and rear contact angles (Fig. 4) for an experiment with α= 27deg, We = 11.7, Fr = 20.5 and Re = 1530.

Molten-Metal Droplet Deposition on a Moving Substrate in Microgravity: Aiding the Development of Novel Technologies for Microelectronic Assembly

C. M. Megaridis, I. S. Bayer

Department of Mechanical and Industrial Engineering
University of Illinois at Chicago, Chicago, Illinois

D. Poulikakos, V. D. Butty

Institute of Energy Technology, Swiss Federal Institute of Technology
Zurich, Switzerland

V. Nayagam

National Center for Microgravity Research, Cleveland, Ohio

Sixth Microgravity Fluid Physics and Transport Phenomena Conference
August 14-16, 2002, Cleveland OH

Grant NAG3-2456

Outline

- Problem Description and Industrial Relevance
- Objectives
- Why Microgravity?
- Methodology
  - Theoretical
  - Experimental
- Results
  - Theoretical
  - Experimental
- Conclusions
- Future Plan

Droplet and Particle Technology Lab, UIC

Problem Description

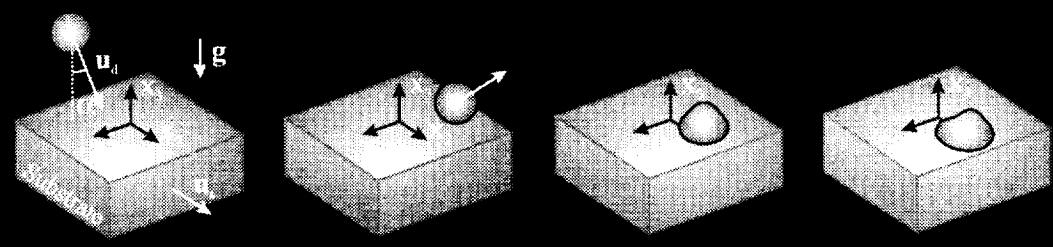

- **Fluid dynamics with simultaneous heat transfer and solidification of molten metal droplets impacting onto flat smooth substrates**
- **Non-axisymmetric geometry (impact angle α, moving substrate). Special cases:**
  - **offset (oblique) impact on stationary substrate**
  - **orthogonal impact on moving substrate**

Droplet and Particle Technology Lab, UIC

Technology Relevance

Printing of microscopic (30-120μm diameter) solder droplets in surface mounting of microelectronic devices.

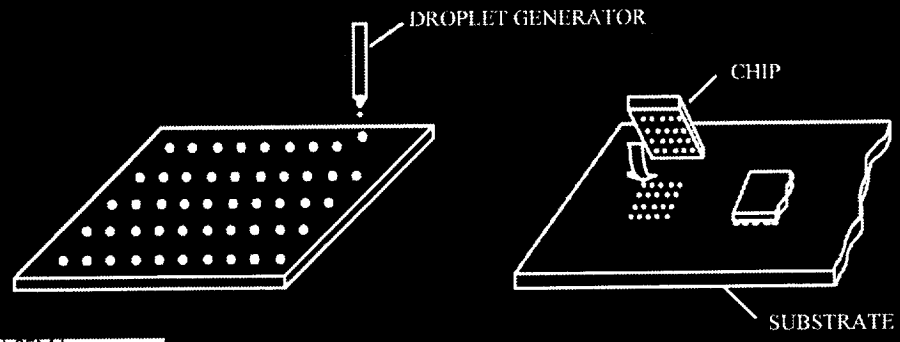

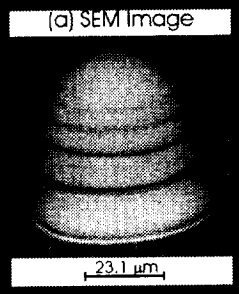

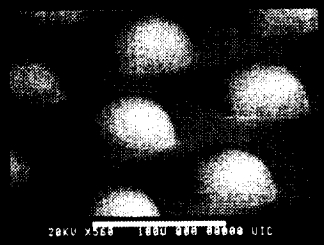

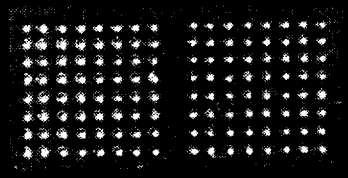

Droplet and Particle Technology Lab, UIC

Objectives

- Investigate fluid dynamics, heat transfer and simultaneous solidification of molten solder droplets during 3-D impact on flat smooth substrates.
- Create science base and identify influence of dominant process parameters in solder microdroplet dispensing. These are: droplet size and velocity; droplet impact orientation; droplet, substrate and ambient gas temperatures; contact angle between solder/substrate before and after solidification.
- Through a combination of experiments and numerical modeling, document systematically the effect of the relevant dimensionless groups (*Re, We, Fr, Ste, Pr, Ca,* etc.) and the physics they represent.

Droplet and Particle Technology Lab, UIC

Conditions of Practical Interest

63%Sn – 37%Pb eutectic solder (melting point 183°C)

Solder injection temperature 200 – 230°C

Droplet diameter 30 –120μm

Droplet injection velocity 1 – 3m/s

Ambient (N_2) temperature 20 – 150°C

Flight distance 1 – 5mm

Multi-layered smooth substrate

Substrate temperature 20 – 150°C

Droplet and Particle Technology Lab, UIC

Dimensionless Parameters

$$Re = \frac{V_0 d_0}{\nu}, \quad We = \frac{\rho V_0^{\,2} d_0}{\gamma}, \quad Fr = \frac{V_0^{\,2}}{d_0 g}$$

$$Oh = \frac{\mu}{(\rho \gamma d_0)^{1/2}} = \frac{(We)^{1/2}}{Re}, \quad Ca = \frac{\mu V_0}{\gamma}$$

$$Bo = \frac{\rho g d_0^{\,2}}{\gamma} = \frac{We}{Fr}, \quad Ste = \frac{c(T_m - T_{substrate})}{L}$$

Re **= O(100),** ***We*** **= O(1),** ***Fr*** **= O(1000)**

Oh **= O(10^{-2}),** ***Ca*** **= O(10^{-3}),** ***Bo*** **= O(10^{-3})**

Ste **= O(1)**

Droplet and Particle Technology Lab. UIC

Why Reduced Gravity?

Typical operating conditions in solder microdroplet dispensing correspond to:

$Re = O(100)$, $We = O(1)$ and $Fr = O(1000)$

To achieve similitude (based on *Re*, *We* and *Fr*) with mm-diameter droplet experiments, one should:

- reduce impact velocity by O(10)
- reduce surface tension coefficient of solder by O(10)
- reduce gravitational level by O(1000)

Reduced gravity is necessary to maintain relevance when performing large solder-droplet impact experiments. 2.2s drop tower is proper facility.

Droplet and Particle Technology Lab, UIC

Methodology

Experimental:

Performed at 2.2s drop tower to allow for the use of large (mm-diameter) solder droplets in the *Re, We, Fr* range of technological interest.

Theoretical:

Navier-Stokes models based on finite element techniques and detailed free-surface tracking. Necessary to provide in-depth understanding of fundamental transport phenomena in 3–D deposition process.

Experiments test the numerical predictions and provide necessary input data (contact angles) for the numerical model.

Droplet and Particle Technology Lab, UIC

Modeling Formulation and Results

- Physical Domain Equations

$$\partial_t \rho = -\rho \nabla \cdot \vec{u}$$

$$\rho \partial_t \vec{u} = \nabla \cdot \sigma + \rho \vec{g}$$

$$\partial_t \rho = \frac{1}{c^2} \partial_t p$$

$$\sigma_{i,k} = \mu\left(\partial_{x_i} u_k + \partial_{x_k} u_i\right) + \xi \delta_{i,k} \partial_{x_l} u_l - p \delta_{i,k} \qquad \xi = -\frac{2}{3}\mu$$

- Free Surface

$$\left(\sigma^{(2)} - \sigma^{(1)}\right)\vec{n} - \nabla^s \gamma = -\gamma\left(\nabla^s \cdot \vec{n}\right)\vec{n}$$

- Wall

$$\vec{u} = \vec{u}_w$$

Droplet and Particle Technology Lab, UIC

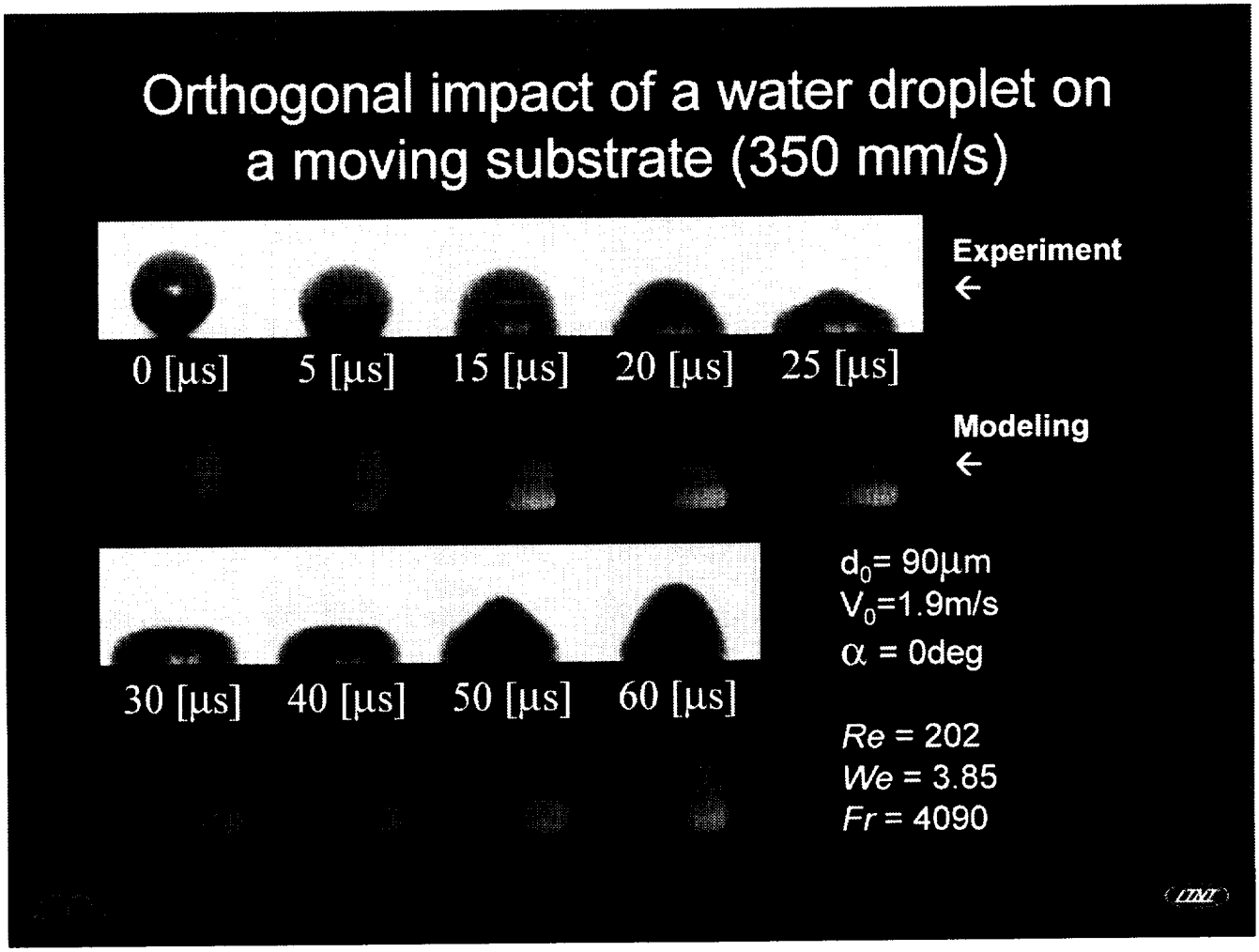
Orthogonal impact of a water droplet on a moving substrate (350 mm/s)
Experiment
0 [μs]
5 [μs]
15 [μs]
20 [μs]
25 [μs]
Modeling
30 [μs]
40 [μs]
50 [μs]
60 [μs]
d_0= 90μm
V_0=1.9m/s
α = 0deg
Re = 202
We = 3.85
Fr = 4090

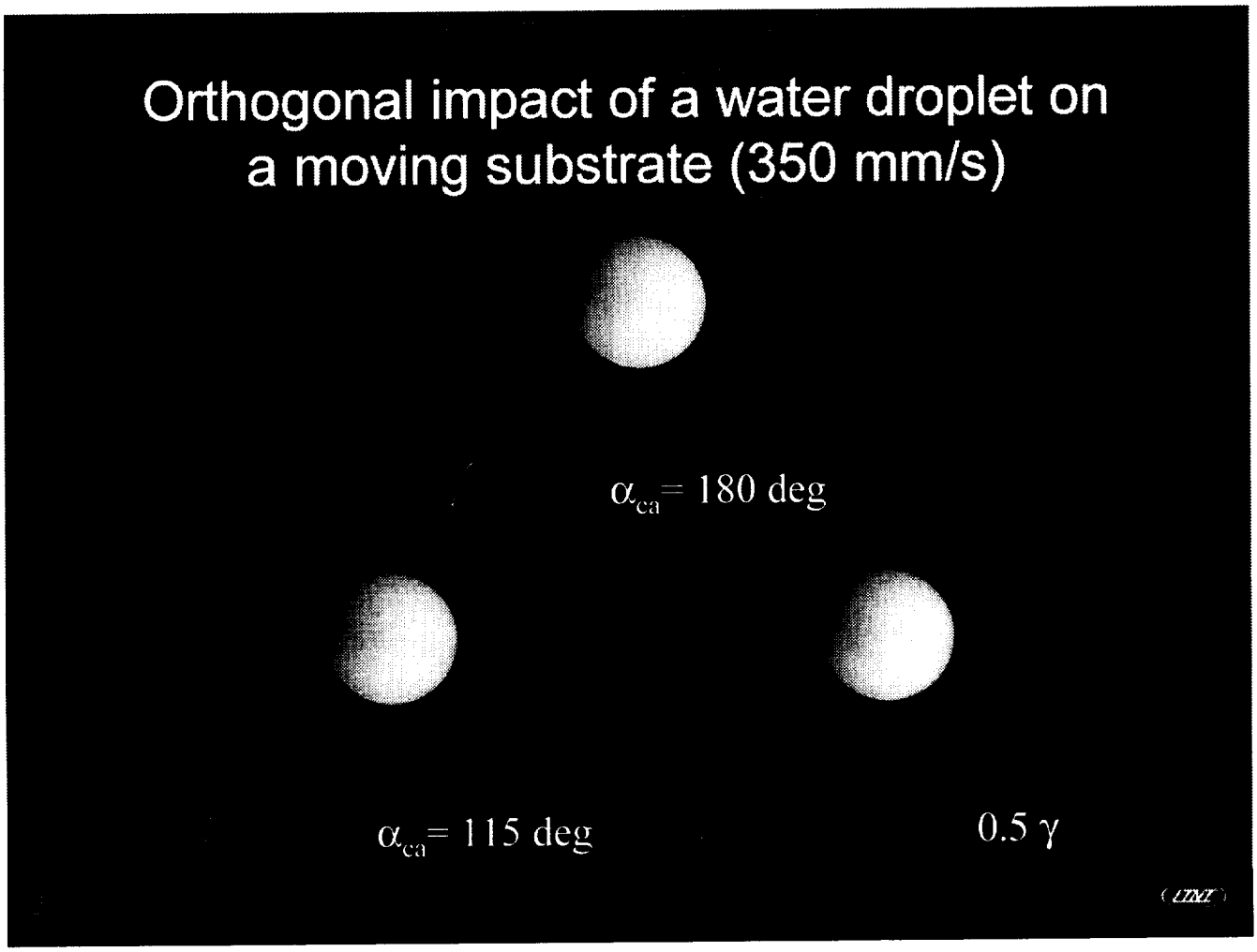
Orthogonal impact of a water droplet on a moving substrate (350 mm/s)
α_{ca}= 180 deg
α_{ca}= 115 deg
0.5 γ

Orthogonal impact of a water droplet on a moving substrate

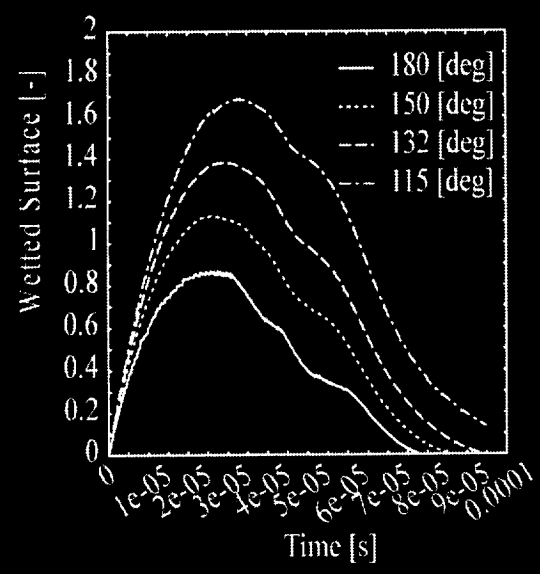

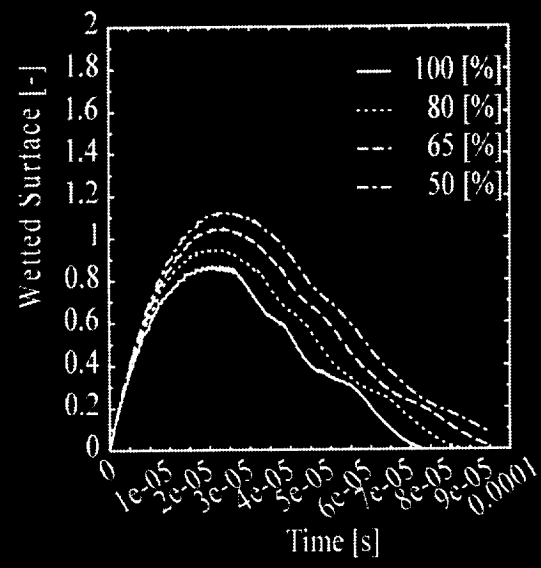

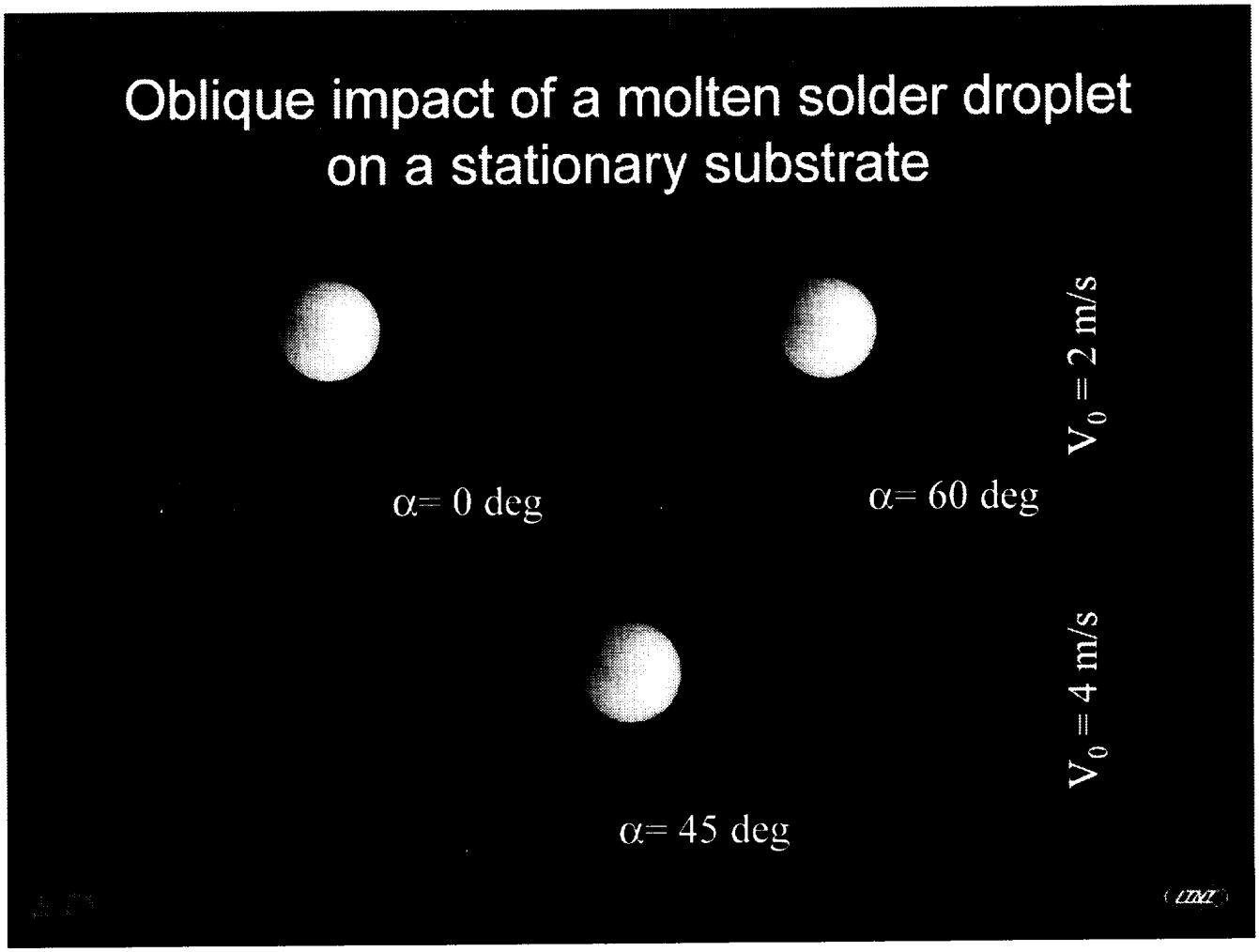
Oblique impact of a molten solder droplet
on a stationary substrate
α= 0 deg
α= 60 deg
α= 45 deg
$V_0 = 2$ m/s
$V_0 = 4$ m/s

Oblique impact of a molten solder droplet on a stationary substrate

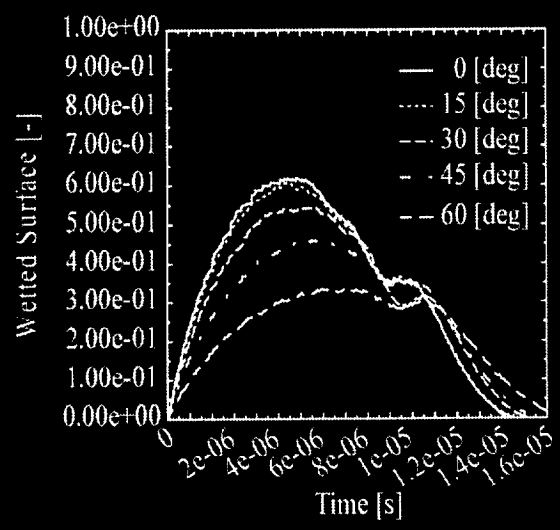

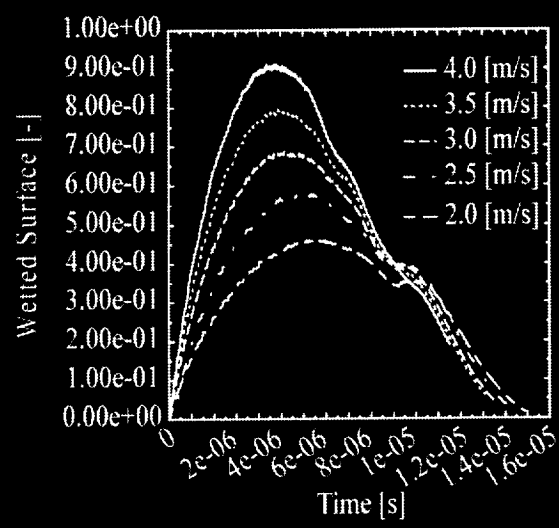

Experimental

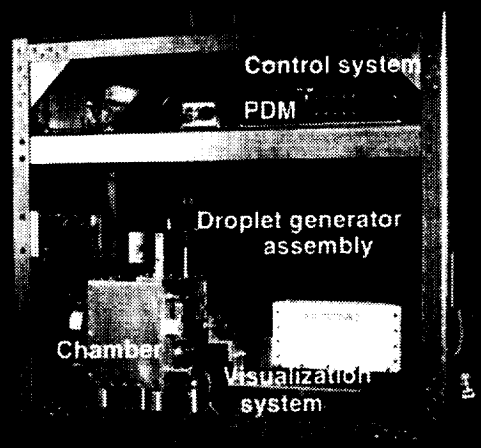

2.2s drop tower rig

Droplet and Particle Technology Lab, UIC

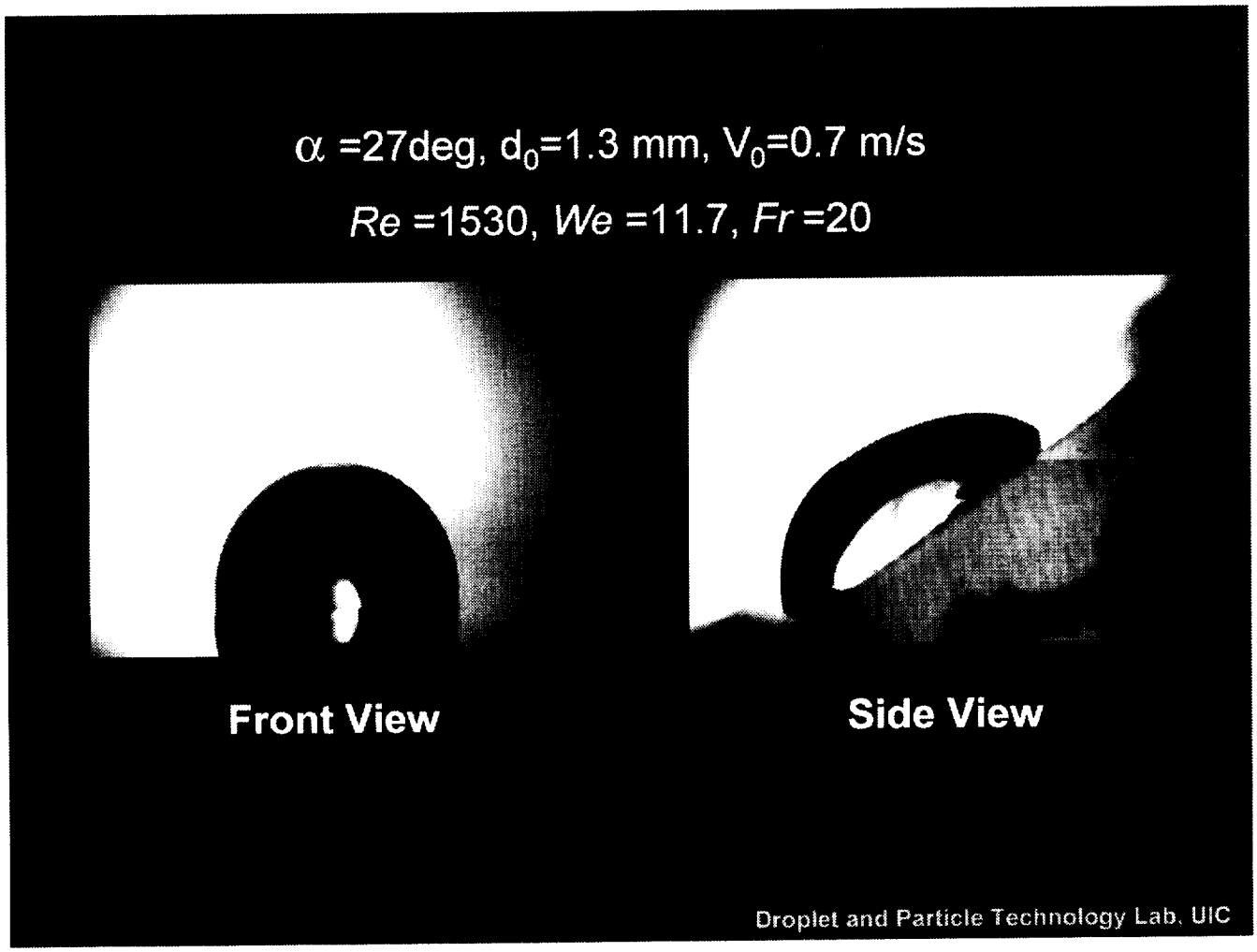
α =27deg, d0=1.3 mm, V0=0.7 m/s
Re =1530, We =11.7, Fr =20
Front View
Side View
Droplet and Particle Technology Lab, UIC

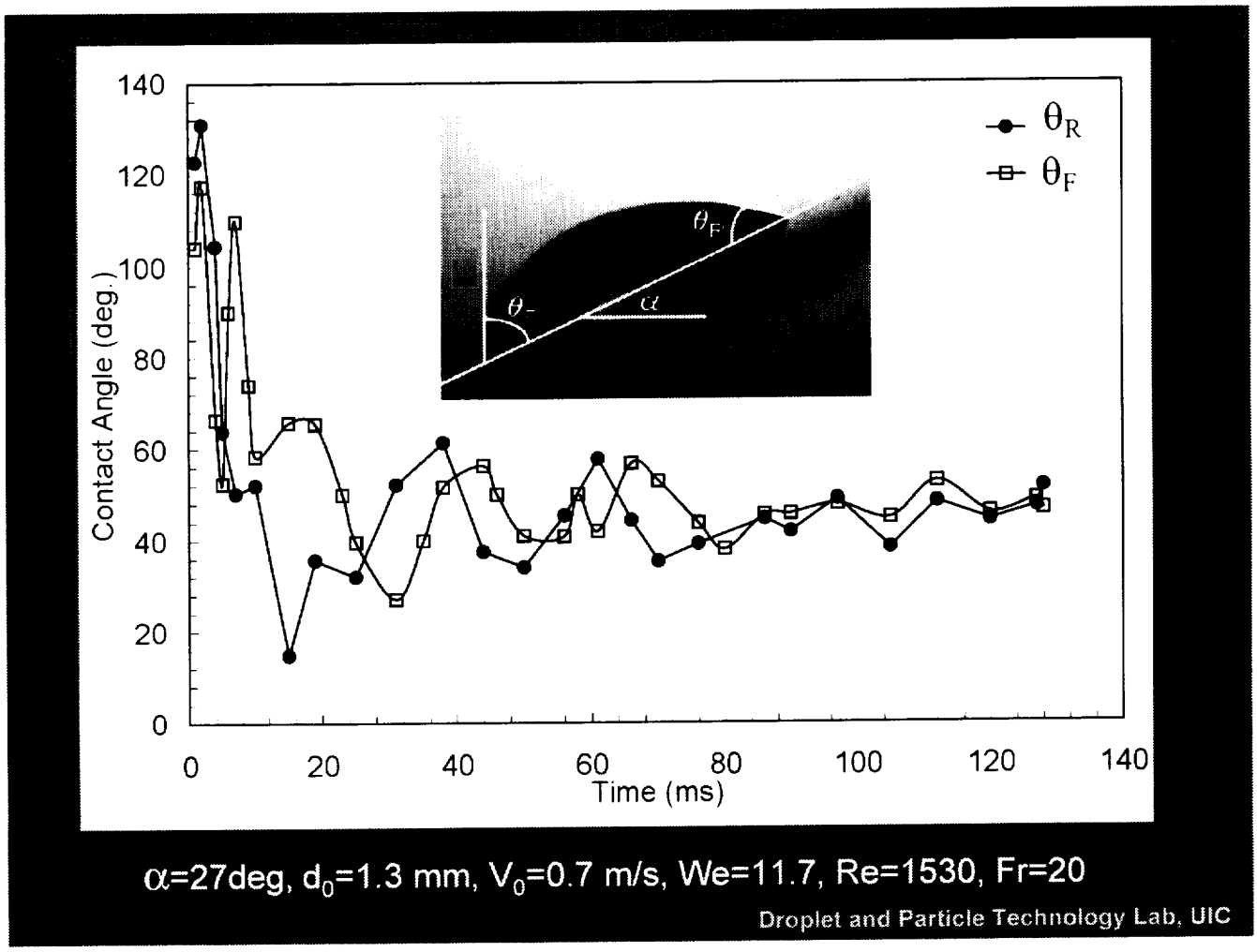
Contact Angle (deg.)
Time (ms)
0
20
40
60
80
100
120
140
θR
θF
θF
θ-
α
α=27deg, d0=1.3 mm, V0=0.7 m/s, We=11.7, Re=1530, Fr=20
Droplet and Particle Technology Lab, UIC

Conclusions

- A finite-element model implementing a stable surface fitting algorithm has been developed to simulate droplet 3-D impact dynamics. Rolling/translation has been demonstrated.
- Experimental instrumentation has been validated in 1-g. Preliminary reduced-gravity experiments being performed at the 2.2s drop tower.
- Good preliminary agreement between numerical and experimental results has been demonstrated for non-wetting cases.

NON-COALESCENCE IN MICROGRAVITY: SCIENCE AND TECHNOLOGY

G. Paul Neitzel
The George W. Woodruff School of Mechanical Engineering
Georgia Institute of Technology
Atlanta, GA 30332-0405
paul.neitzel@me.gatech.edu
404-894-3242 (Voice)
404-894-8496 (Fax)

ABSTRACT

In this project we examine non-coalescence and non-wetting phenomena driven by either thermocapillary convection or forced motion of one surface relative to the other. In both cases, the non-coalescence or non-wetting is enabled by the existence of a lubricating layer of gas that exists to keep the two surfaces in question from coming into contact with one another.

Recent progress has been made on several fronts: 1) measurement of the vibrational modes of pinned droplets; 2) development of an apparatus for the measurement of the frictional forces associated with a non-wetting droplet sliding over a solid surface; 3) measurements of the failure modes for non-wetting droplets and the influence of static electric charge on failure; and 4) numerical simulation of a two-dimensional non-wetting droplet revealing a possible explanation for why the phenomenon has not been able to be observed using water as the droplet liquid.

Issue 1) above is of relevance to the use of non-wetting droplets as positioning mechanisms and vibration dampers in a microgravity environment; issue 2) relates to the use of non-wetting droplets as nearly "frictionless" bearings in low-load applications. Understanding of the failure modes identified in 3) is of importance to any potential application and the numerical simulations conducted under 4) allow us to obtain information about these systems that is currently not available through experimentation Each of these topics will be discussed briefly during the presentation.

Recent Results on Permanent Non-Coalescence and Non-Wetting*

G. P. Neitzel[1], P. Nagy[1], M. I. Carnasciali[1],
P. Dell'Aversana[2], M. R. Vetrano[2],
J.-C. Chen[3] and C. W. Kuo[3]

[1]Georgia Institute of Technology, Atlanta, USA
[2]MARS Center, Naples, Italy
[3]National Central University, Chung-Li, Taiwan

*Supported by NASA, the Italian Ministry of Research and ASI

Georgia Tech

Thermocapillary Conditions

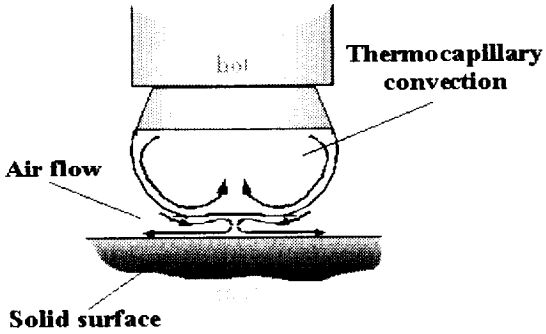

Isothermal Conditions

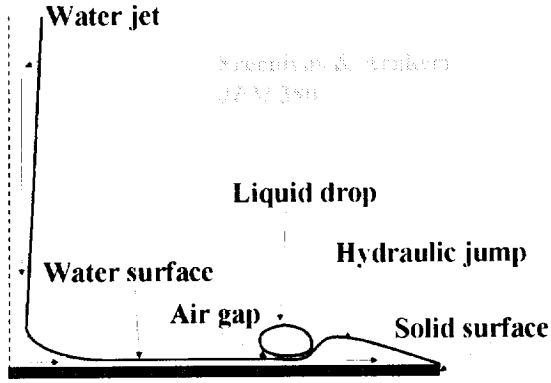

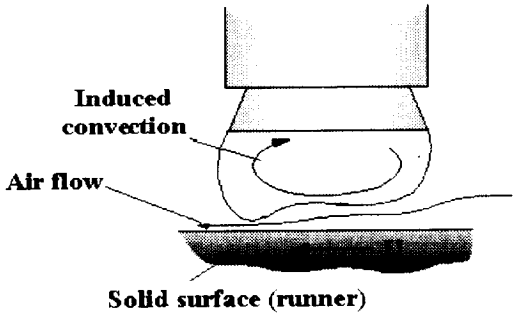

Overview

- Experimental and numerical studies are underway to investigate some properties of interest for non-coalescing and non-wetting systems.

- These properties are relevant to envisioned applications of such systems and include vibration response, failure mechanisms and frictional forces.

Vibration & Damping Characteristics

- If non-coalescing or non-wetting droplets are to be used in vibration-isolation applications, their own vibration characteristics are of interest.

- Experiments have been performed to determine the natural frequencies and damping rates for pinned, silicone-oil droplets.

Experimental Set-Up

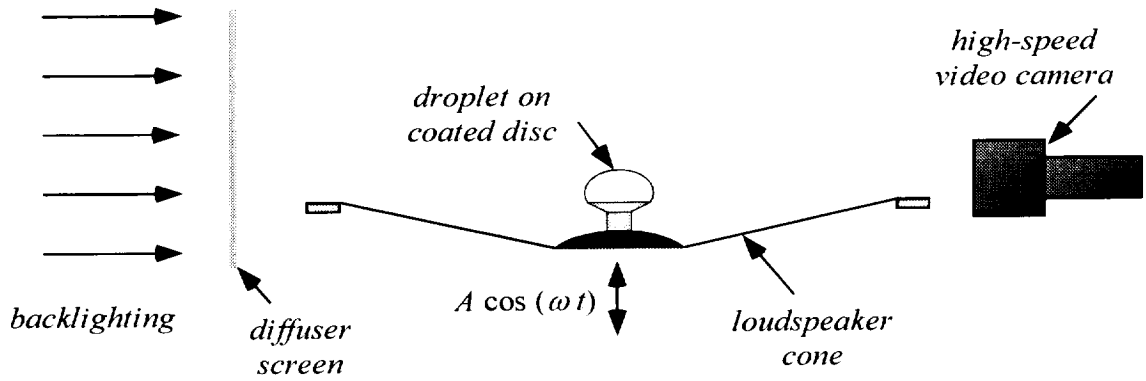

- Silicone-oil (1, 5, & 10 cS) droplets of various volumes are deposited onto sharp-edged 3, 5&7 mm Cu discs coated with Scotchguard.
- Loudspeaker-driven forcing is provided at various A and ω.
- Droplet shape changes following cessation of forcing are captured with high-speed (1000 ~3000 frames/s) video.

Mode Shapes

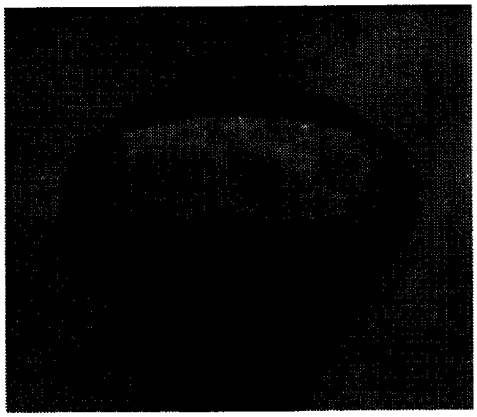

First Mode

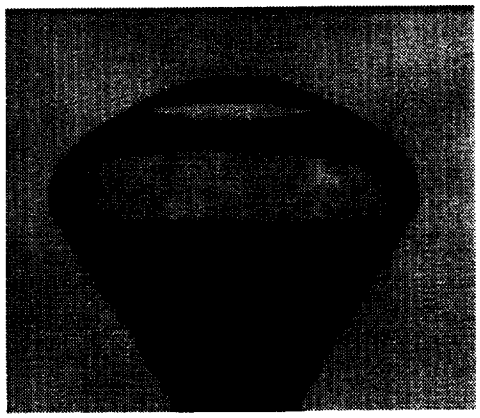

Second Mode

Damping Data

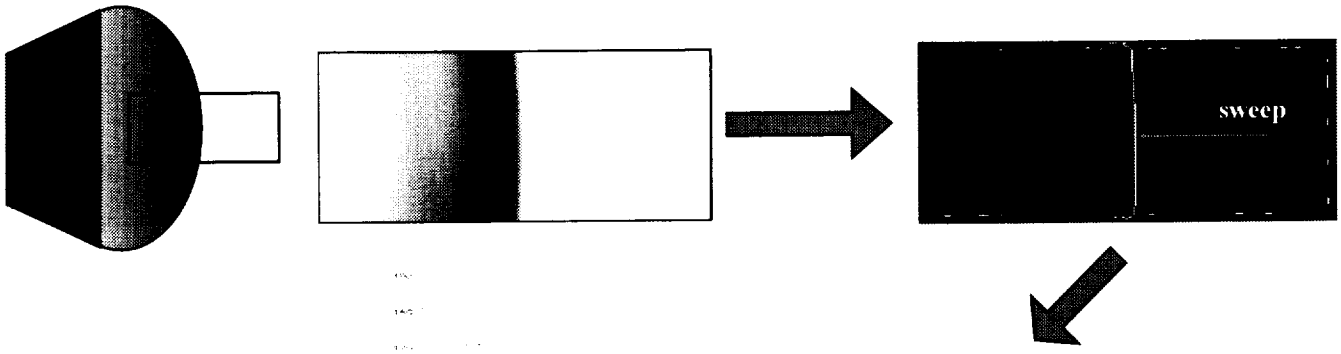

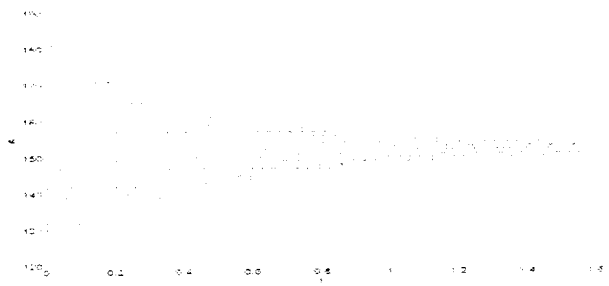

Pixel coordinate plotted against time

- Zoom to the region of interest
- Fit data to determine frequency ω and damping rate b

Dimensionless Parameters

- *Ohnesorge number* $Oh = \mu / \sqrt{\rho \sigma R}$

- *Strouhal number* $St = \omega R / U$

In the low-*Oh* limit, $U \sim \sqrt{\sigma / \rho R}$ (Taylor 1959) making the Strouhal number

$$St = \omega \sqrt{\frac{\rho R^3}{\sigma}}$$

Dimensionless Parameters (cont'd)

- *Volume parameter* V / R^3
- *Bond number* $Bo = \dfrac{\rho g R^2}{\sigma}$
- *Damping rate parameter* $\dfrac{bR^2}{\nu}$

Results - Frequency

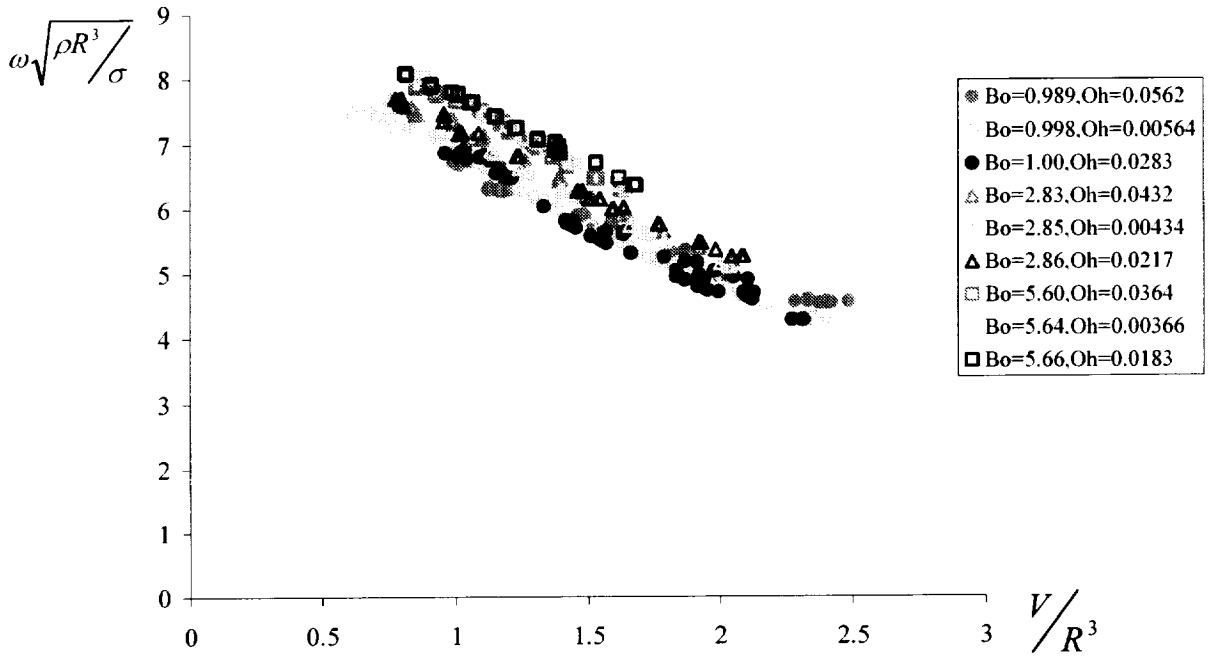

Results - Damping Rate

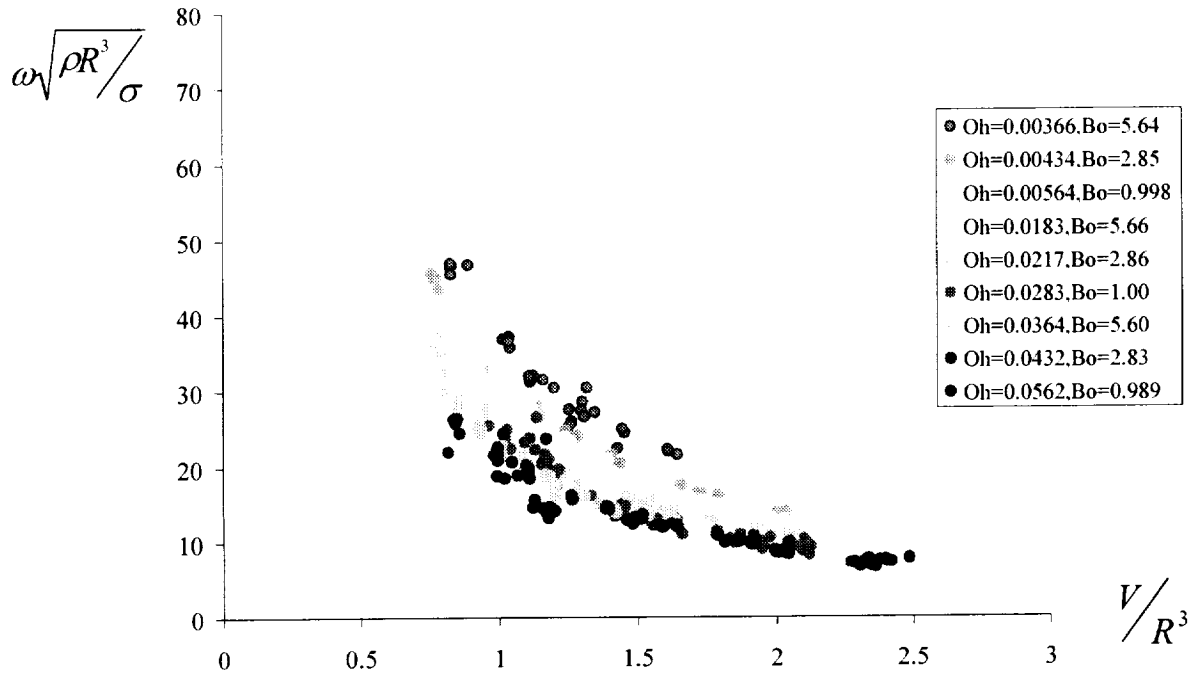

Georgia Tech

Failure Mechanisms in Non-Coalescing and Non-Wetting Systems

- We have demonstrated previously the load-carrying capacity of non-coalescing and non-wetting systems and have proposed their use as "frictionless" bearings.

- What are the failure mechanisms associated with these systems, non-wetting ones in particular?

Charles & Mason Results

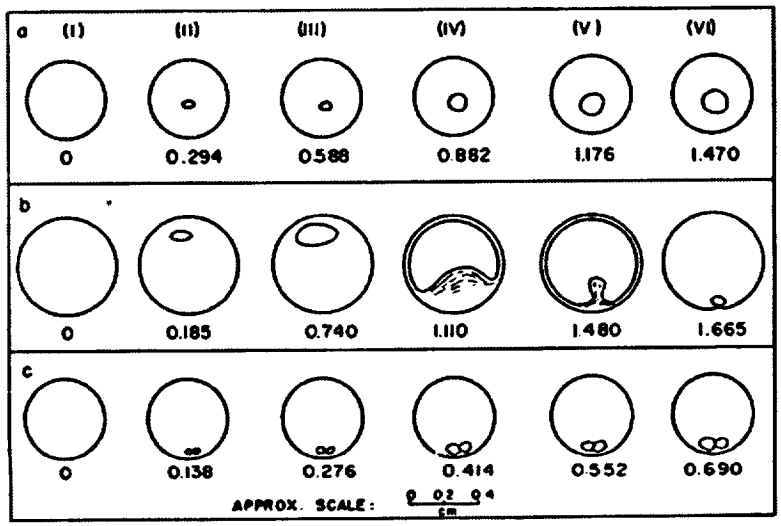

Relevant Quantities

- *Stabilizing*

  Lubrication pressure

  Vapor pressure

- *Destabilizing*

  Capillary forces

  van der Waals forces

  Applied (squeezing) forces

  Electrostatic forces

Thermocapillary Film Rupture Experiments

- Employed high-speed (5000 frames/s) digital photography.
- Rupture accomplished by increasing squeezing against non-wetted plate.
- In all cases, rupture occurred at the ridge (thinnest portion) of the lubricating film.

Mechanical Film Rupture of a Thermocapillary Non-Wetting Droplet

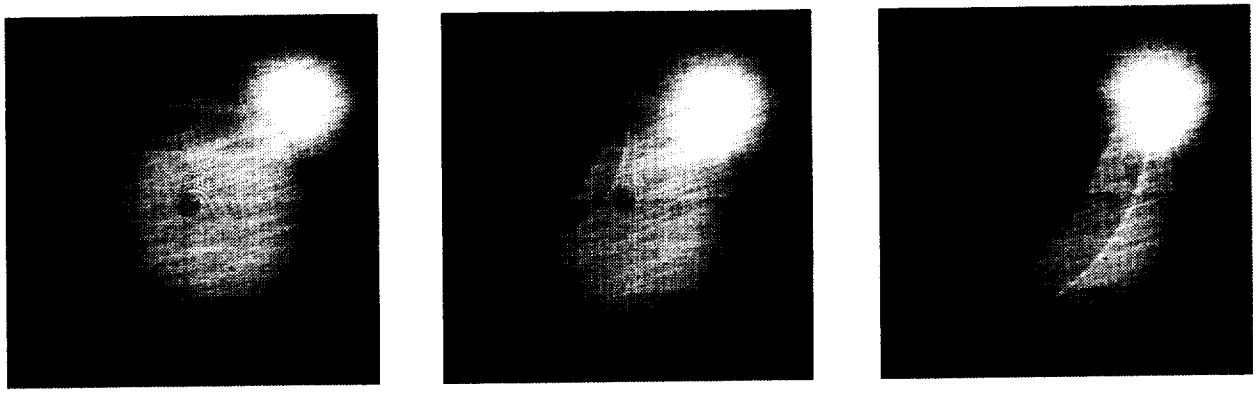

$t = t_0 + 1/3000$ s $\quad$ $t = t_0 + 3/3000$ s $\quad$ $t = t_0 + 7/3000$ s

Electrostatic Film Deformation
Non-Conductive Surface

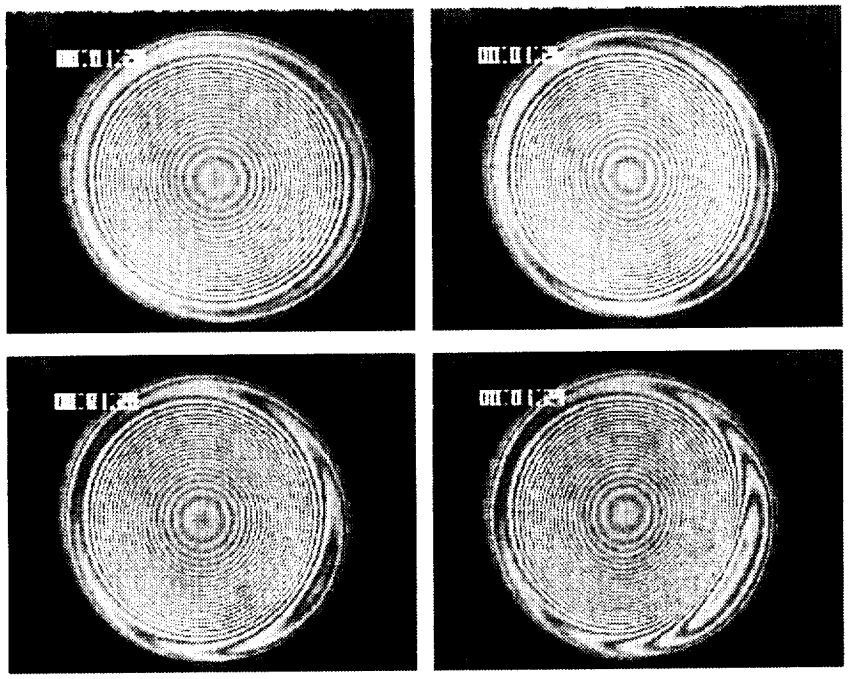

Controlled Electrostatic Rupture

- A controlled charge is applied to the upper surface of a coated glass plate using an electrostatic generator and high-voltage power supply.

- Potential measured with a field meter positioned 2.5 mm from upper glass surface.

- Critical voltages (fixed squeezing) are $O(100\text{V})$.

Electrostatic Film Rupture of a Thermocapillary Non-Wetting Droplet

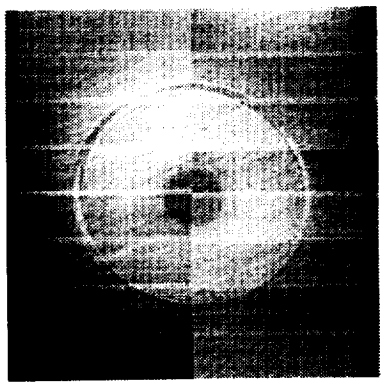

$t = t_0 + 1/3000$ s

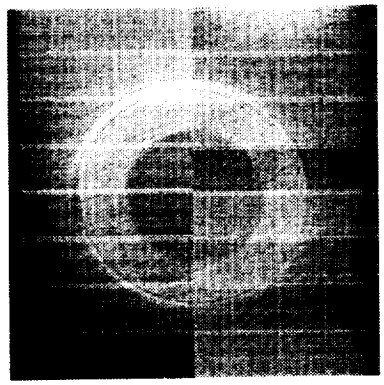

$t = t_0 + 2/3000$ s

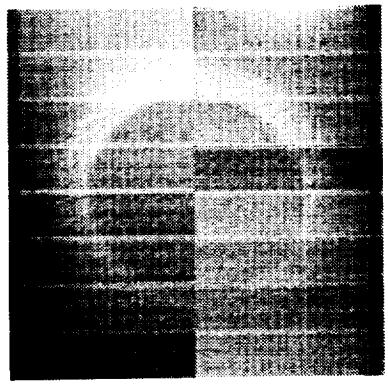

$t = t_0 + 3/3000$ s

Observation

- Rupture initiated at the center of the droplet was unanticipated.
- *Hypothesis*: Advection and accumulation of surface charge due to thermocapillary convection is responsible for observed results.
- *Test of hypothesis*: isothermal non-wetting experiments with electrostatic effect present demonstrated in next section.

Isothermal Non-Wetting

- Relative motion of the non-coalescing or non-wetting surfaces need not arise only due to thermocapillarity.

- Non-wetting of a silicone-oil drop against a glass disk has been demonstrated.

Isothermal Non-Wetting Apparatus

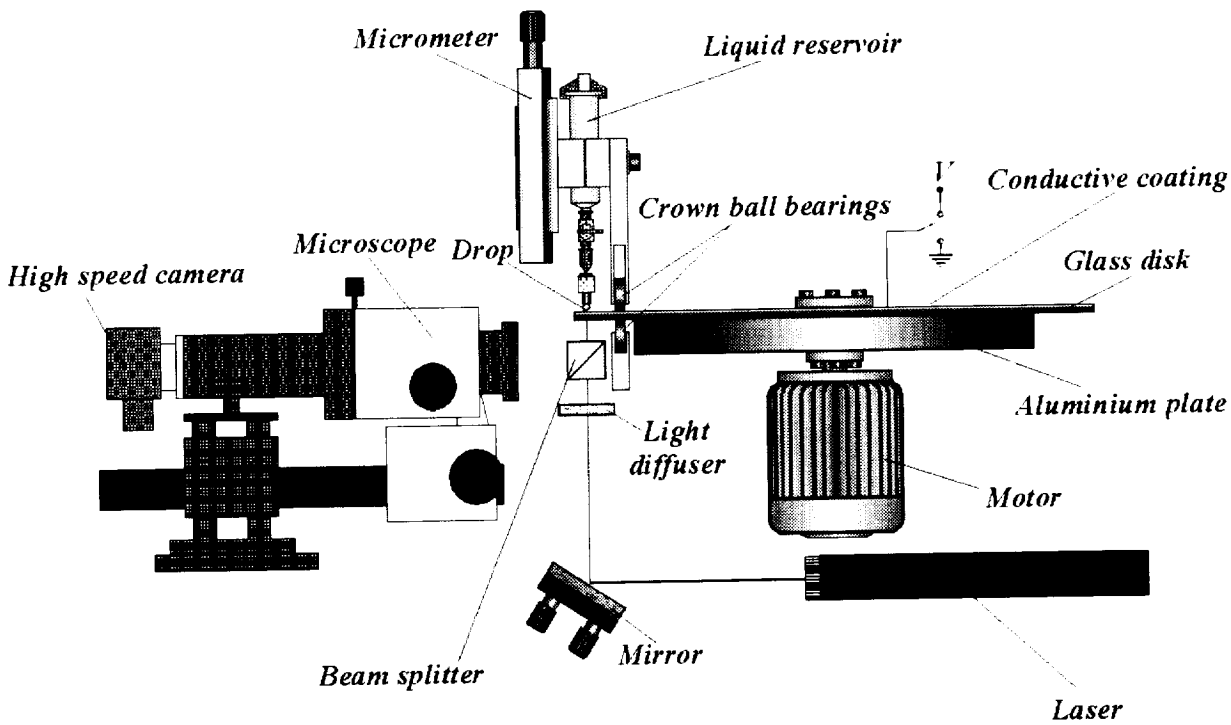

Lubricating Film Shapes

Thermocapillary
Non-wetting

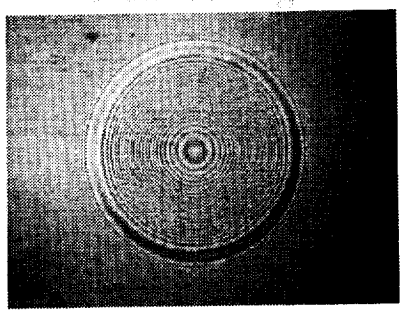

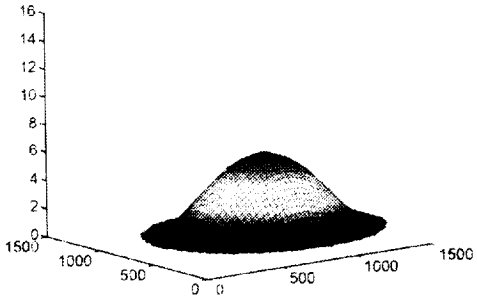

Sliding
Droplet

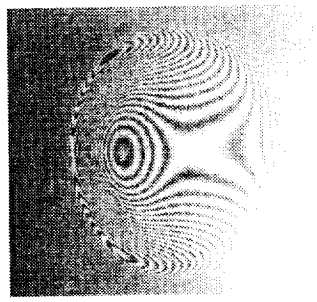

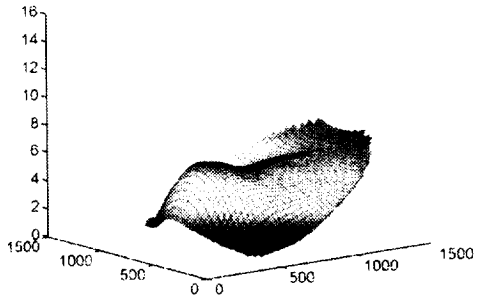

Transient Wetting - Spitting Instability

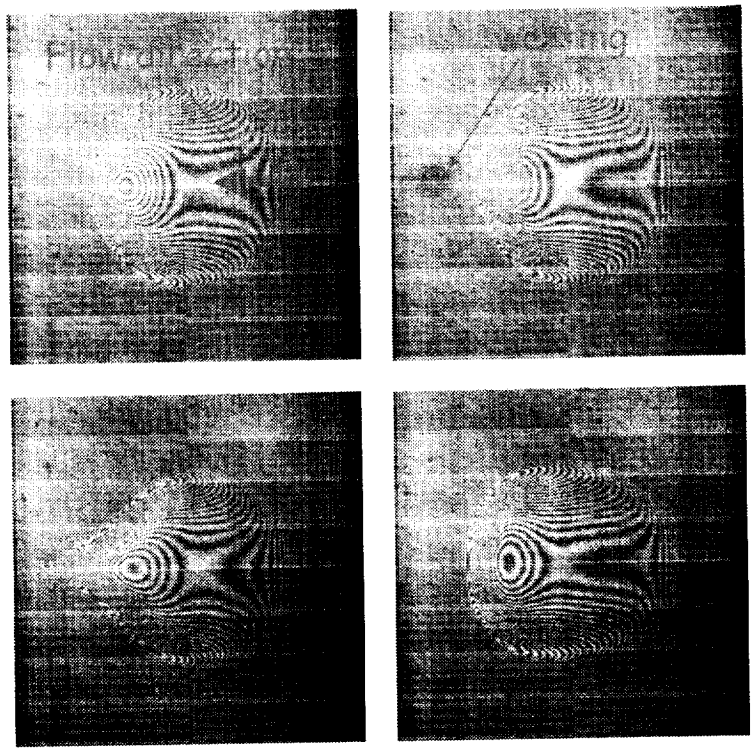

$t = t_0$

$t = t_0 + 1/3000$ s

$t = t_0 + 2/3000$ s

$t = t_0 + 5/3000$ s

Electrostatic Film Deformation of a Sliding Drop

5 cS silicone oil drop

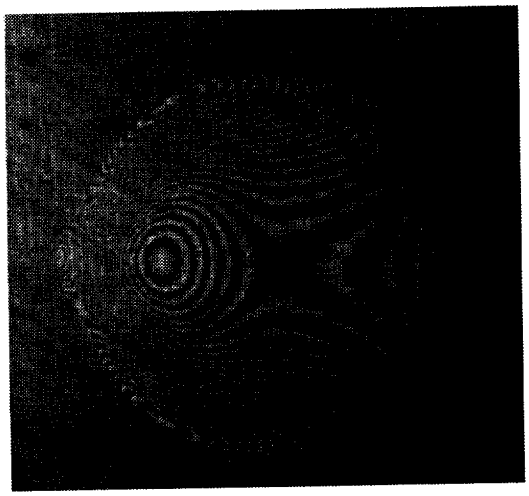

10,000 cS silicone oil drop

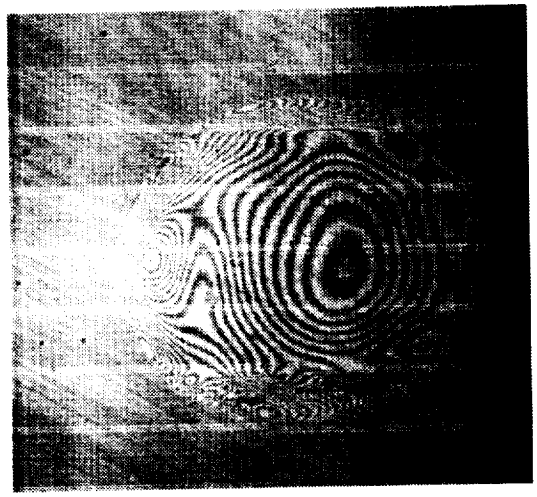

Same disk speed and applied voltages in both cases

Frictional Force Measurement

- Experiments are being developed to measure the frictional forces associated with an isothermal sliding, non-wetting droplet.
- Companion numerical simulations will also be performed.

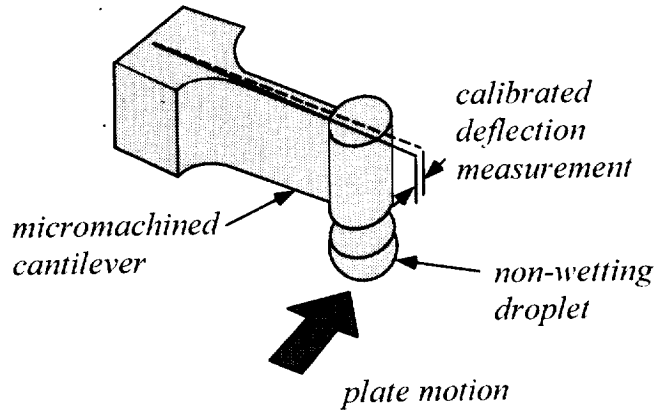

Non-Wetting Numerical Solutions

- Numerical solutions of the Navier-Stokes equations have been performed using FIDAP for a hot drop pressed against a cold plate.

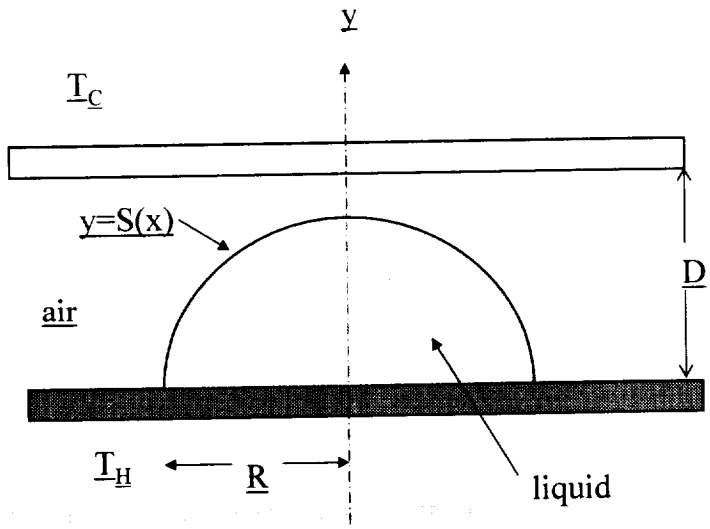

Finite-Element Mesh

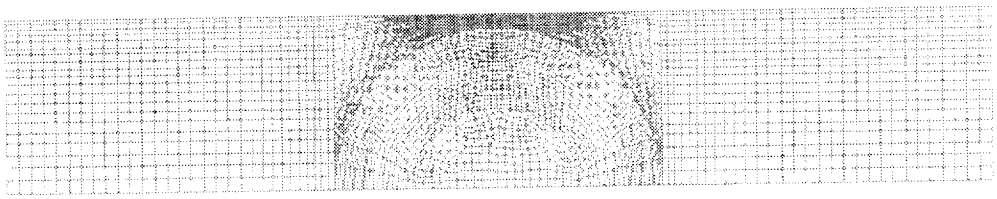

Streamlines and Isotherms
5cS Silicone Oil Drop

Streamlines

Isotherms

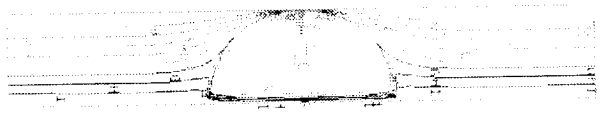

Pr = 74, Re = 136, Ca = 0.1076, D/R = 1.005

Silicone Oil vs Water

- An interesting result has been obtained relating to the behavior differences between 5 cS silicone oil and water.

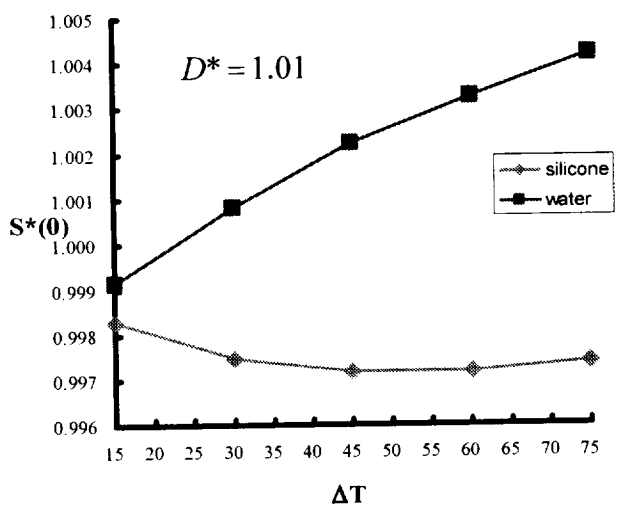

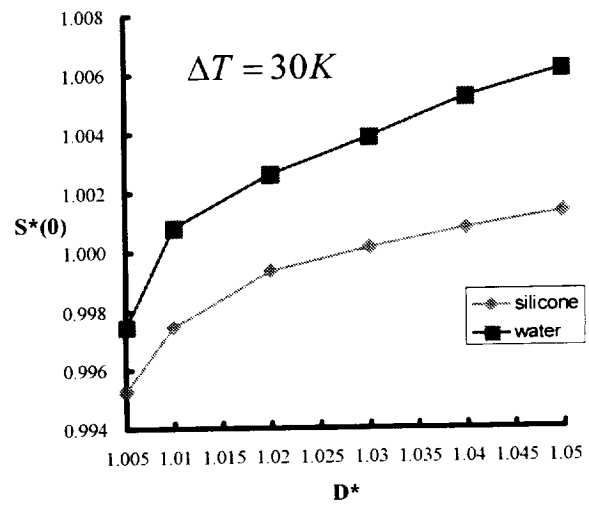

Georgia Tech

Summary

- Experiments have been performed to investigate the failure of lubricating films in non-wetting situations.
- Ridge rupture appears in situations not involving electrostatic-charge effects.
- Axisymmetric rupture appears to be provoked by the convection and accumulation of electrostatic surface charge.
- One can exploit electric charge to either break the lubrication film at a given time/place or to give it a particular shape.

SHADOWGRAPH STUDY OF GRADIENT DRIVEN FLUCTUATIONS

Gennady Nikolaenko and David S. Cannell
Department of Physics
UC Santa Barbara
Santa Barbara, CA 93106

ABSTRACT

A fluid or fluid mixture, subjected to a vertical temperature and/or concentration gradient in a gravitational field, exhibits greatly enhanced light scattering at small angles [1-3]. This effect is caused by coupling between the vertical velocity fluctuations due to thermal energy and the vertically varying refractive index. Physically, small upward or downward moving regions will be displaced into fluid having a refractive index different from that of the moving region, thus giving rise to the enhanced scattering [4]. The scattered intensity is predicted [5-7] to vary with scattering wave vector $\mathbf{q}$, as q^{-4}, for sufficiently large $\mathbf{q}$, but the divergence is quenched by gravity [8] at small $\mathbf{q}$. In the absence of gravity, the long wavelength fluctuations responsible for the enhanced scattering are predicted to grow until limited by the sample dimensions [9, 10]. It is thus of interest to measure the mean-squared amplitude of such fluctuations in the microgravity environment for comparison with existing theory and ground based measurements.

The relevant wave vectors are extremely small, making traditional low-angle light scattering difficult or impossible because of stray elastically scattered light generated by optical surfaces. An alternative technique is offered by the shadowgraph method, which is normally used to visualize fluid flows, but which can also serve as a quantitative tool to measure fluctuations [11, 12]. A somewhat novel shadowgraph apparatus and the necessary data analysis methods will be described. The apparatus uses a spatially coherent, but temporally incoherent, light source consisting of a super-luminescent diode coupled to a single-mode optical fiber in order to achieve extremely high spatial resolution, while avoiding effects caused by interference of light reflected from the various optical surfaces that are present when using laser sources.

Results obtained for a critical mixture of aniline and cyclohexane subjected to a vertical temperature gradient will be presented. The sample was confined between two horizontal parallel sapphire plates with a vertical spacing of 1 mm. The temperatures of the sapphire plates were controlled by independent circulating water loops that used Peltier devices to add or remove heat from the room air as required.

For a mixture with a temperature gradient, two effects are involved in generating the vertical refractive index gradient, namely thermal expansion and the Soret effect, which generates a concentration gradient in response to the applied temperature gradient. For the aniline/cyclohexane system, the denser component (aniline) migrates toward the colder surface. Consequently, when heating from above, both effects result in the sample density decreasing with altitude and are stabilizing in the sense that no convective motion occurs regardless of the magnitude of the applied temperature gradient. The Soret effect is strong near a binary liquid critical point, and thus the dominant effect is due to the induced concentration gradient. The results clearly show the divergence at low $\mathbf{q}$ and the predicted gravitational quenching. Results obtained for different applied temperature gradients at varying temperature differences from the critical temperature, clearly demonstrate the predicted divergence of the thermal diffusion ratio.

Thus, the more closely the critical point is approached, the smaller becomes the temperature gradient required to generate the same signal.

Two different methods have been used to generate pure concentration gradients. In the first, a sample cell was filled with a single fluid, ethylene glycol, and a denser miscible fluid, water, was added from below thus establishing a sharp interface to begin the experiment. As time went on the two fluids diffused into each other, and large amplitude fluctuations were clearly observed at low $\mathbf{q}$. The effects of gravitational quenching were also evident. In the second method, the aniline/cyclohexane sample was used, and after applying a vertical temperature gradient for several hours, the top and bottom temperatures were set equal and the thermal gradient died on a time scale of seconds, leaving the Soret induced concentration gradient in place. Again, large-scale fluctuations were observed and died away slowly in amplitude as diffusion destroyed the initial concentration gradient.

1. B. M. Law, R. W. Gammon, and J. V. Sengers, Light-scattering observations of long-range correlations in a nonequilibrium liquid, Phys. Rev. Lett. 60, 1554 (1988).
2. P. N. Segrè, R. W. Gammon, J. V. Sengers, and B. M. Law, Rayleigh scattering in a liquid far from thermal equilibrium, Phys. Rev. A 45, 714 (1992).
3. A. Vailati and M. Giglio, Giant fluctuations in a free diffusion process, Nature (London) 390, 262 (1997).
4. D. A. Weitz, Diffusion in a Different Direction, Nature, 390, 233 (1997).
5. T. R. Kirkpatrick, E. G. D. Cohen, and J. R. Dorfman, Light scattering by a fluid in a nonequilibrium steady state. II. Large gradients, Phys. Rev. A 26, 995 (1982).
6. R. Schmitz and E. G. D. Cohen, Fluctuations in a fluid under a stationary heat flux. II Slow part of the correlation matrix, J. Stat. Phys. 40, 431 (1985).
7. P. N. Segrè and J. V. Sengers, Nonequilibrium fluctuations in liquid mixtures under the influence of gravity, Physica A 198, 46 (1993).
8. A. Vailati and M. Giglio, q divergence of nonequilibrium fluctuations and its gravity-induced frustration in a temperature stressed liquid mixture, Phys. Rev. Lett. 77, 1484 (1996).
9. J. M. Ortiz de Zarate, R. Perez Cordon, and J. V. Sengers, Finite-size effects on fluctuations in a fluid out of thermal equilibrium, Physica A 291, 113 (2001).
10. J. M. Ortiz de Zárate and J. V. Sengers, Boundary effects on the nonequilibrium structure factor of fluids below the Rayleigh-Bénard instability, Preprint November, 2001.
11. M. Wu, G. Ahlers, and D. S. Cannell, Thermally induced fluctuations below the onset of Rayleigh-Bénard convection, Phys. Rev. Lett. 75, 1743 (1995).
12. S. P. Trainoff and D. S. Cannell, Physical Optics Treatment of the Shadowgraph, Physics of Fluids, 14, 1340 (2002).

Gradient Density Fluctuation

David Cannell and Gennady Nikolaenko

UC Santa Barbara

Marzio Giglio, Alberto Vailati and Fabrizio Croccolo

University of Milan

William Meyer

NASA Glenn Research Center

Supported by NAG3-2439 and the Italian Space Agency

Motivation

Basic Physics:

$$G(\mathbf{R},\tau) = < \delta\rho(\mathbf{R},\tau)\delta\rho(0,0) >$$

$$S(\mathbf{q},\omega) = FT[G(\mathbf{R},\tau)]$$

Normally short ranged and decays quickly, except near Critical Points

Becomes very long ranged when a fluid is subjected to a temperature gradient.

This effect is suppressed by gravity.

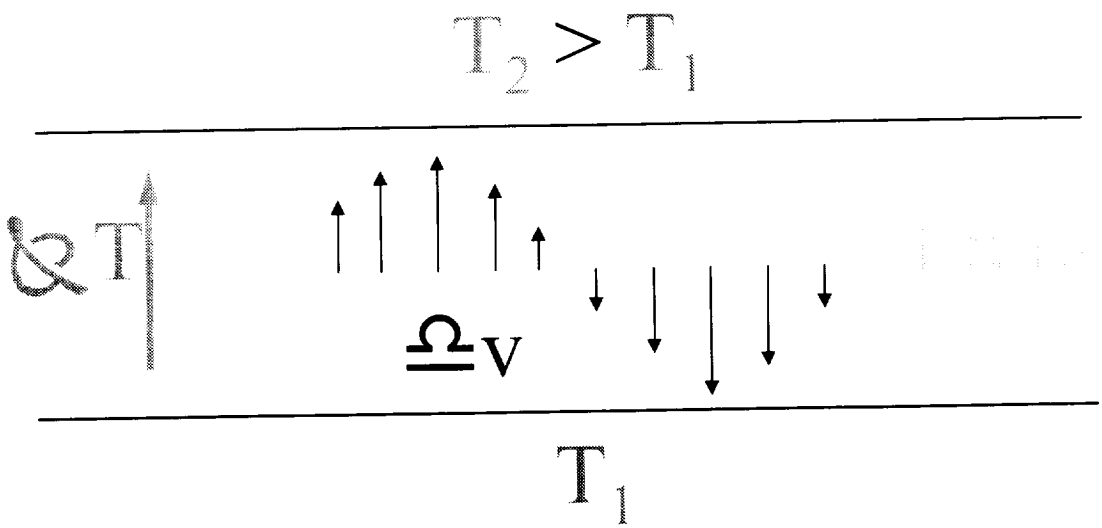

Thermally driven velocity fluctuations force colder more dense fluid into warmer less dense regions, and vice versa.

Result: Mode-mode coupling greatly enhances long-range density fluctuations.

Conceptual Physical Picture

Short wavelength fluctuations are suppressed by viscosity and thermal diffusion.

$$\tau = 1/(D_T q^2),\ 1/(\nu q^2)$$

$$q = 2\pi / \Lambda$$

Long wavelength fluctuations last long enough for buoyancy to be important.

Quenched by gravity.

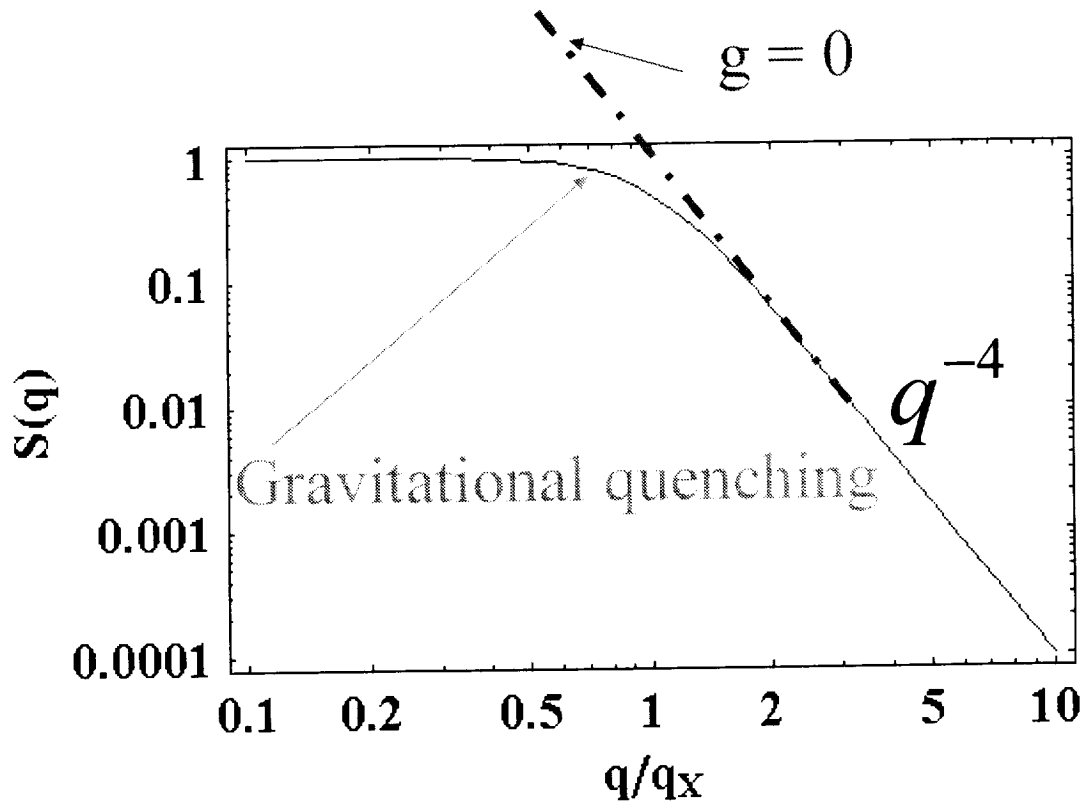

The structure factor S(q), predicted for a bulk fluid subjected to a thermal gradient.

Similar results hold for mixtures with a temperature and/or a concentration gradient.

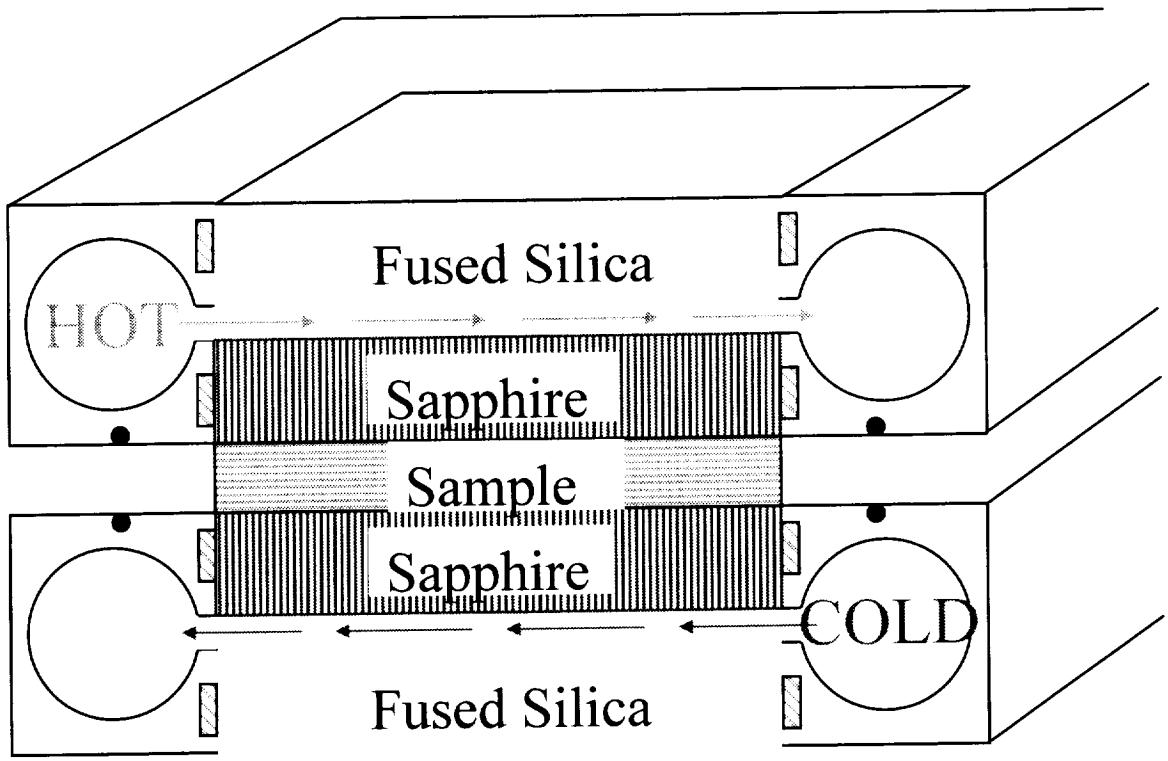

Cross section of the sample cell used to impose controlled thermal gradients on fluids.

Small angle scattering?
Interferometry?
Quantitative Shadowgraphy?

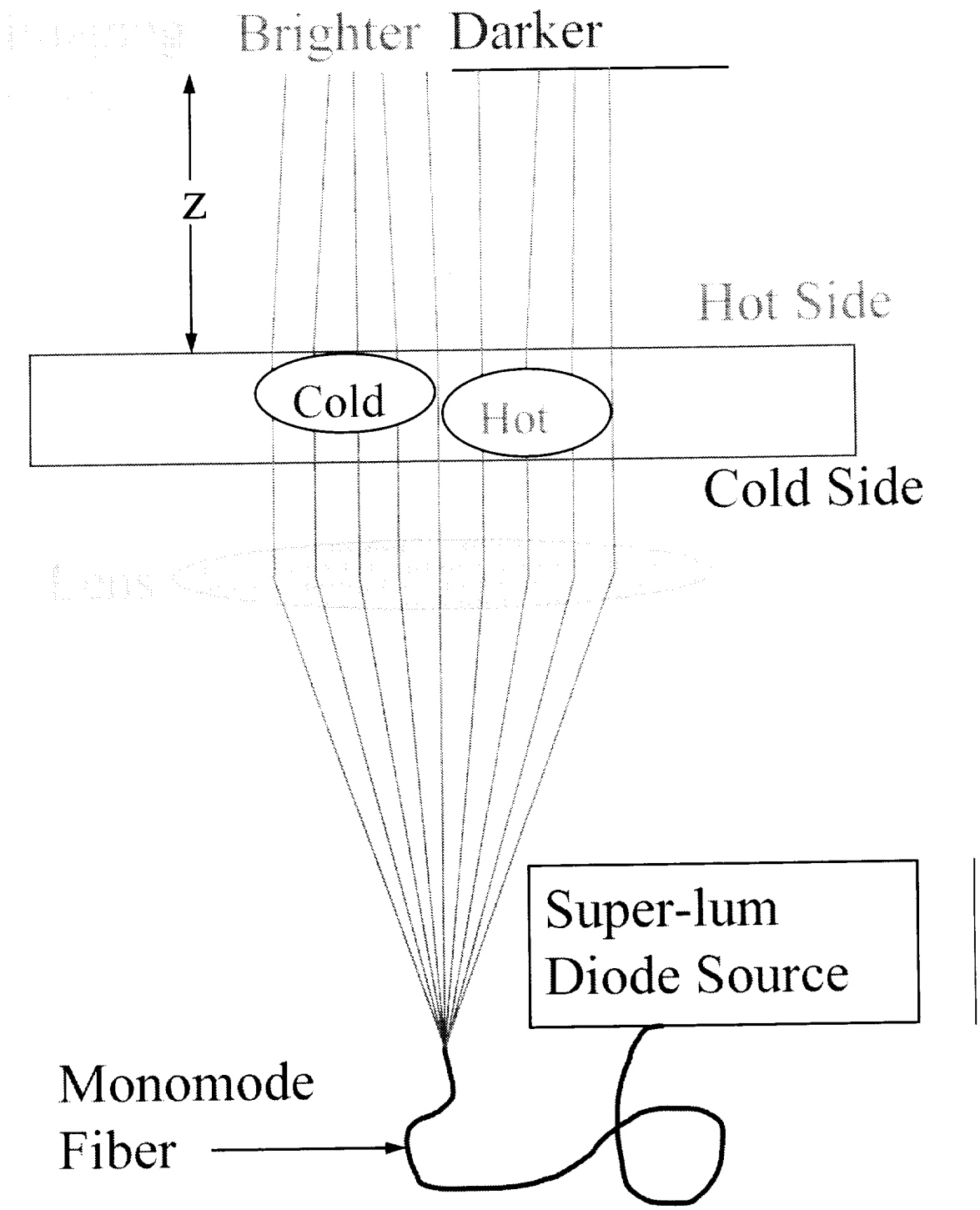
Brighter
Darker
z
Hot Side
Cold
Hot
Cold Side
Super-lum
Diode Source
Monomode
Fiber

Physical Optics Treatment

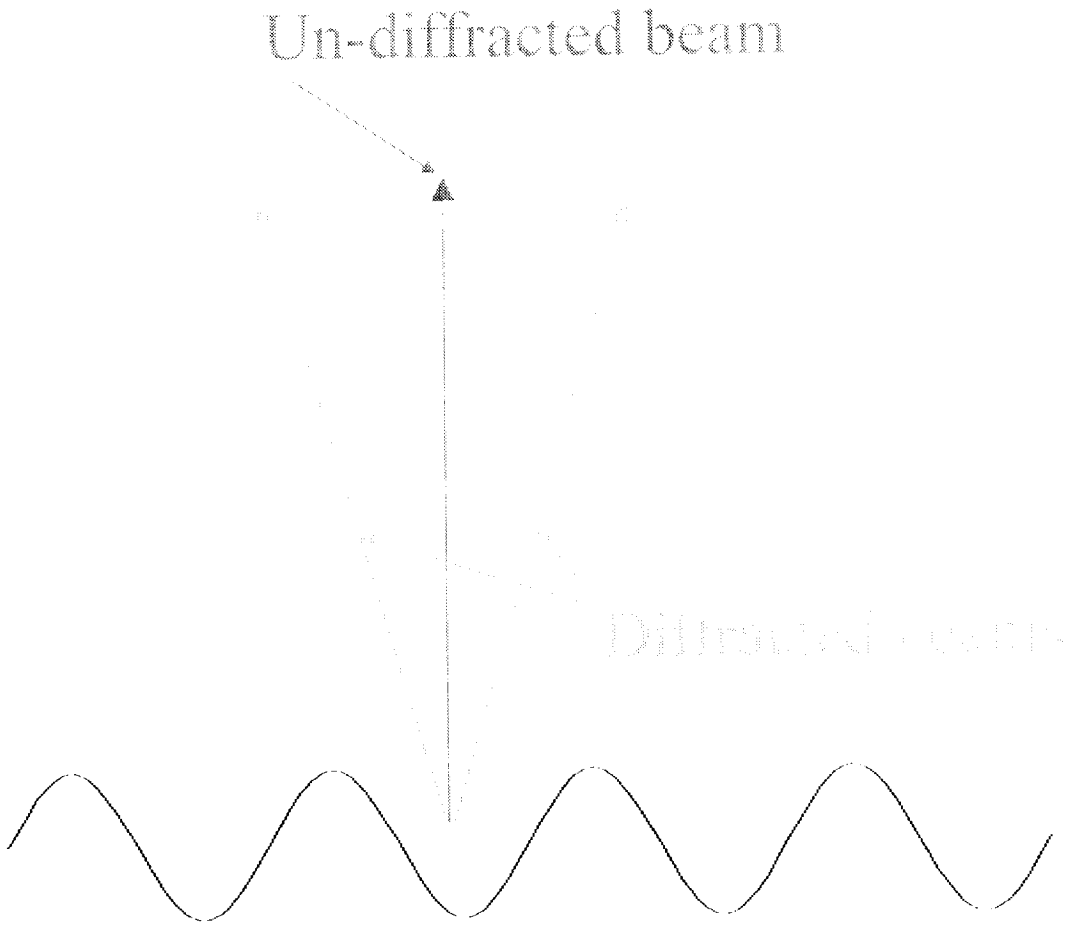

Wave fronts emerging from the sample are phase modulated.

2. Ratios of images quantify the fluctuations, $\delta I(x, y)$.

3. Fourier analysis of the ratio images reveals the spatial power spectrum of the fluctuations, $\delta I^2(\mathbf{q})$.

$$\delta I^2(\mathbf{q}) = A\ Sin^2(\mathbf{q}^2 z/(2k_o))\ S(\mathbf{q})$$

$$S(\mathbf{q}) = FT[G(\mathbf{R})]$$

Physics of Fluids, **14**, 1340 (2002).

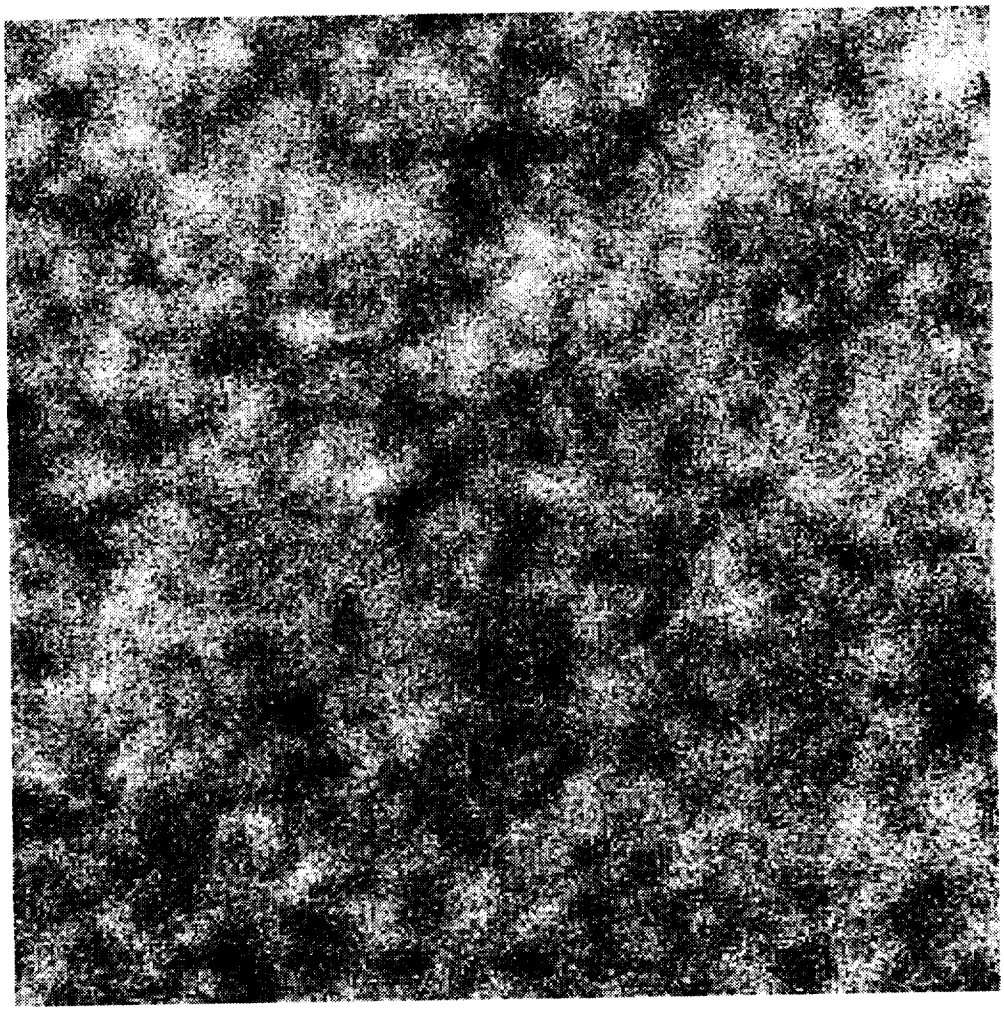

Ratio of two images taken 1 second Apart for aniline/cyclohexane at 40° C with a gradient of 160 K/cm.

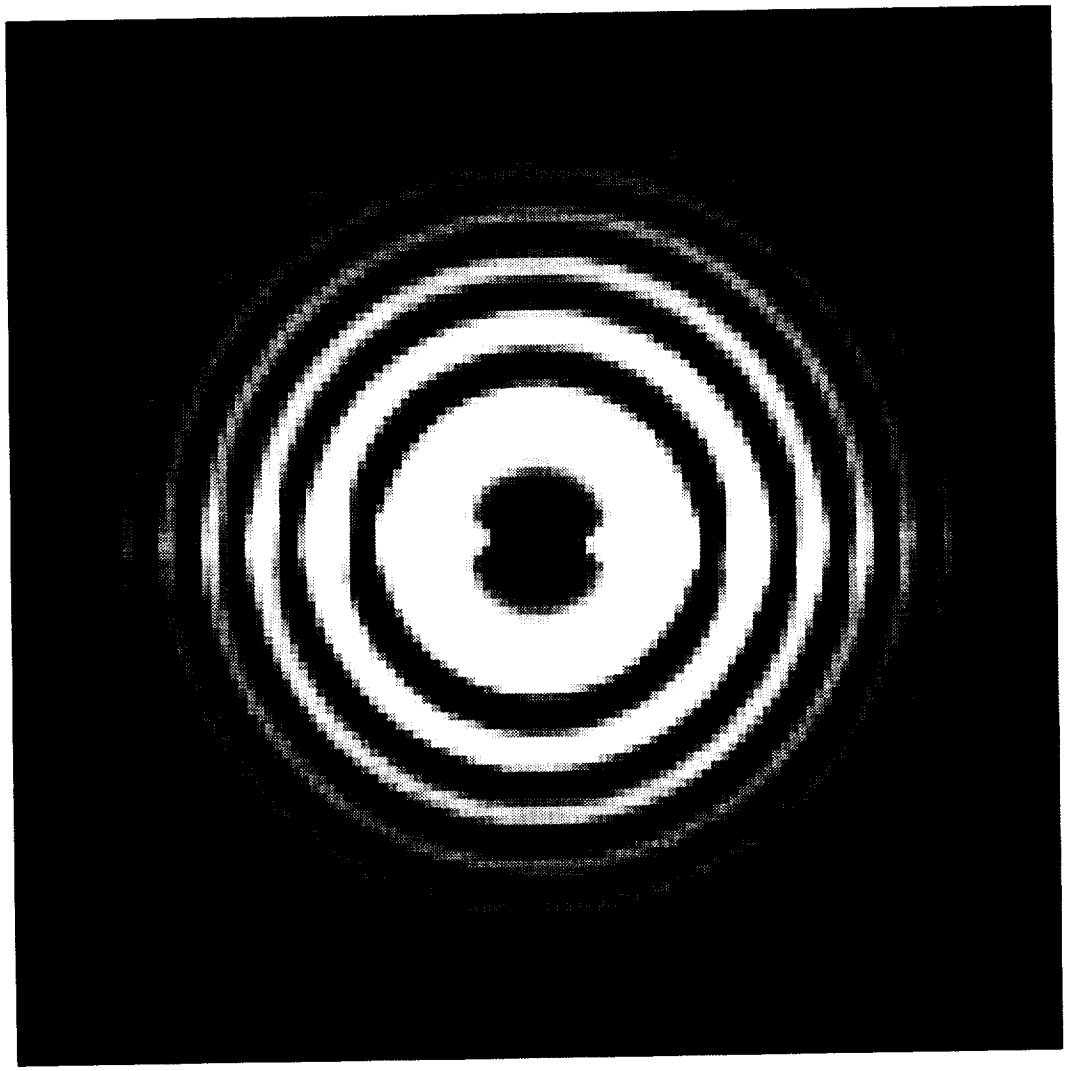

$I^2(\mathbf{q})$ for a 1 mm thick sample of 47 Wt.% aniline in cyclohexane at 40° C with a gradient of 160 K/cm. Measured at z = 18 cm.

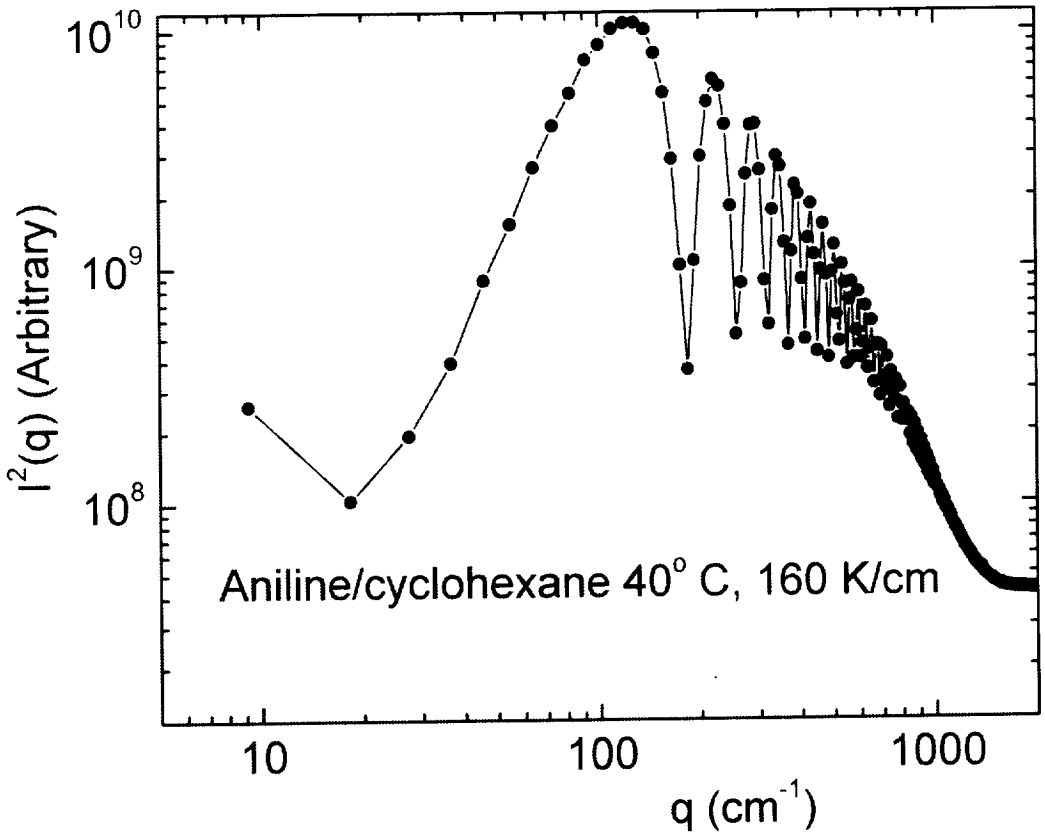

Log-Log plot of the spatial power spectrum of the fluctuations for the aniline/cyclohexane sample.

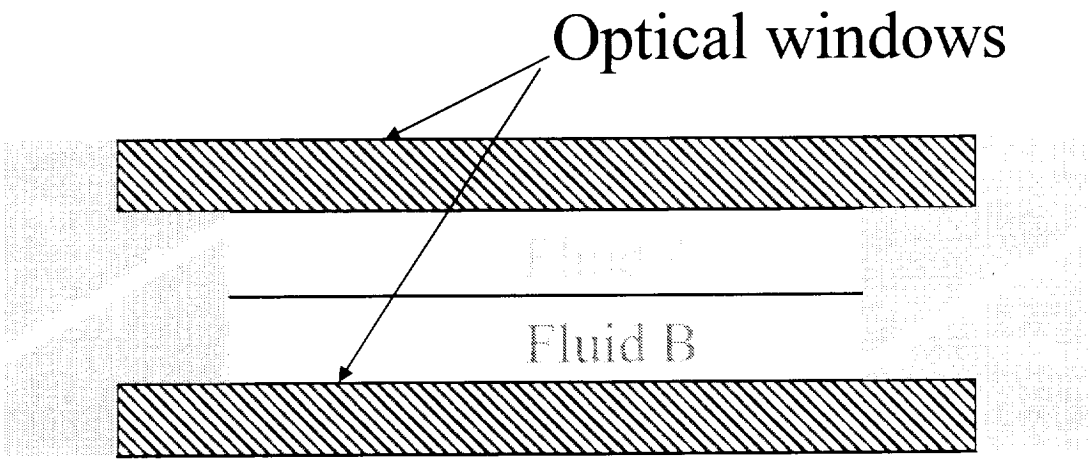

Cross section of the sample cell used to layer one fluid upon another, creating a flat interface.

A large concentration gradient is present for many hours, during the process of free diffusion.

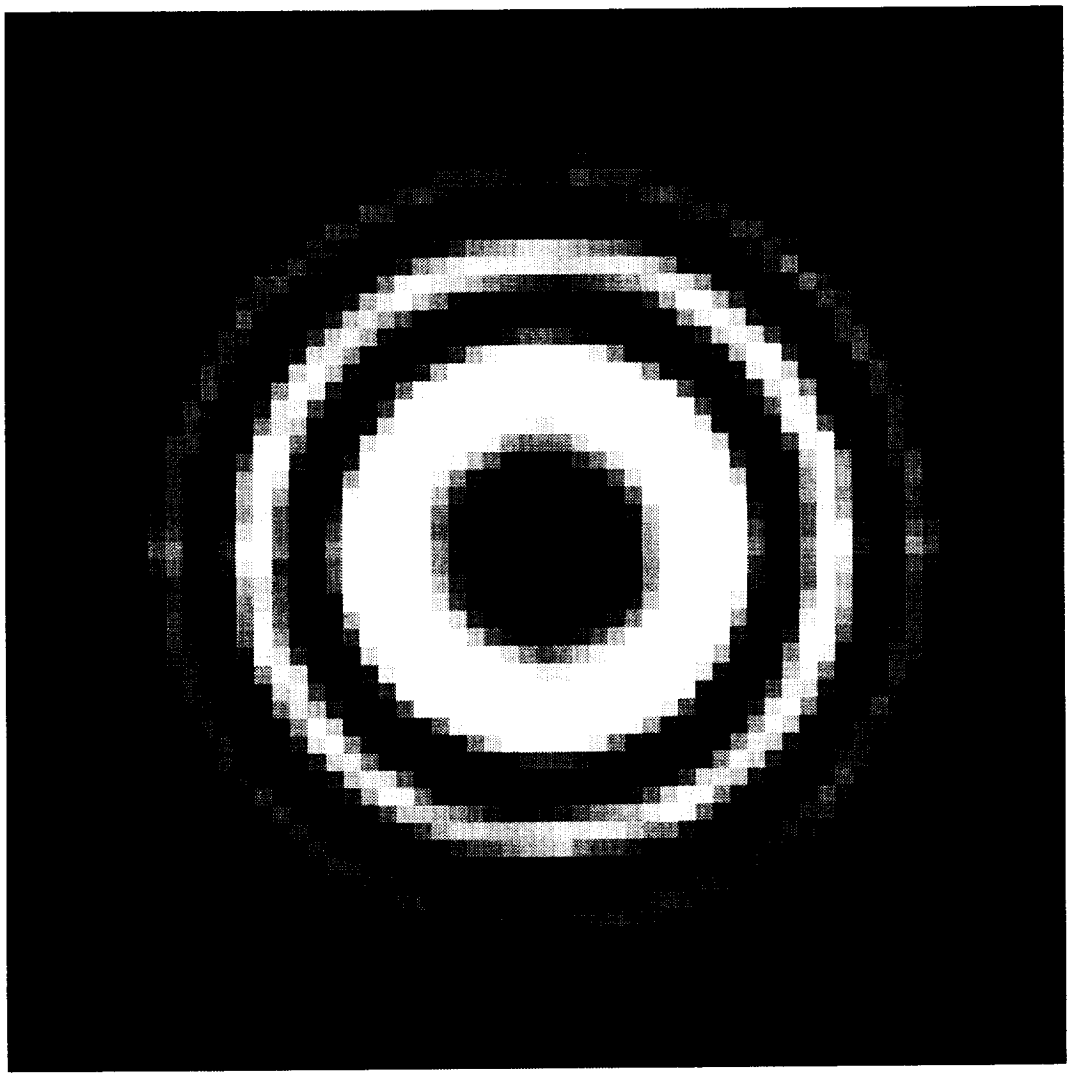

$I^2(\mathbf{q})$ for water diffusing into ethylene glycol.

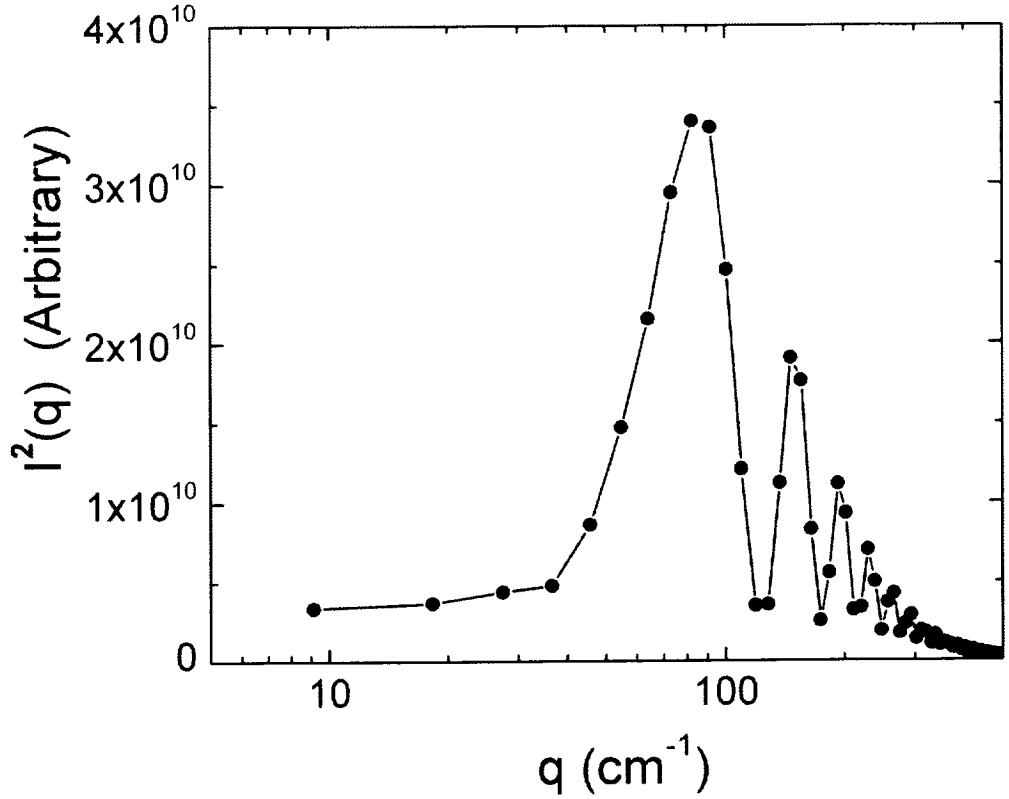

Log-Linear plot of the spatial power spectrum of the fluctuations for water diffusing into ethylene glycol.

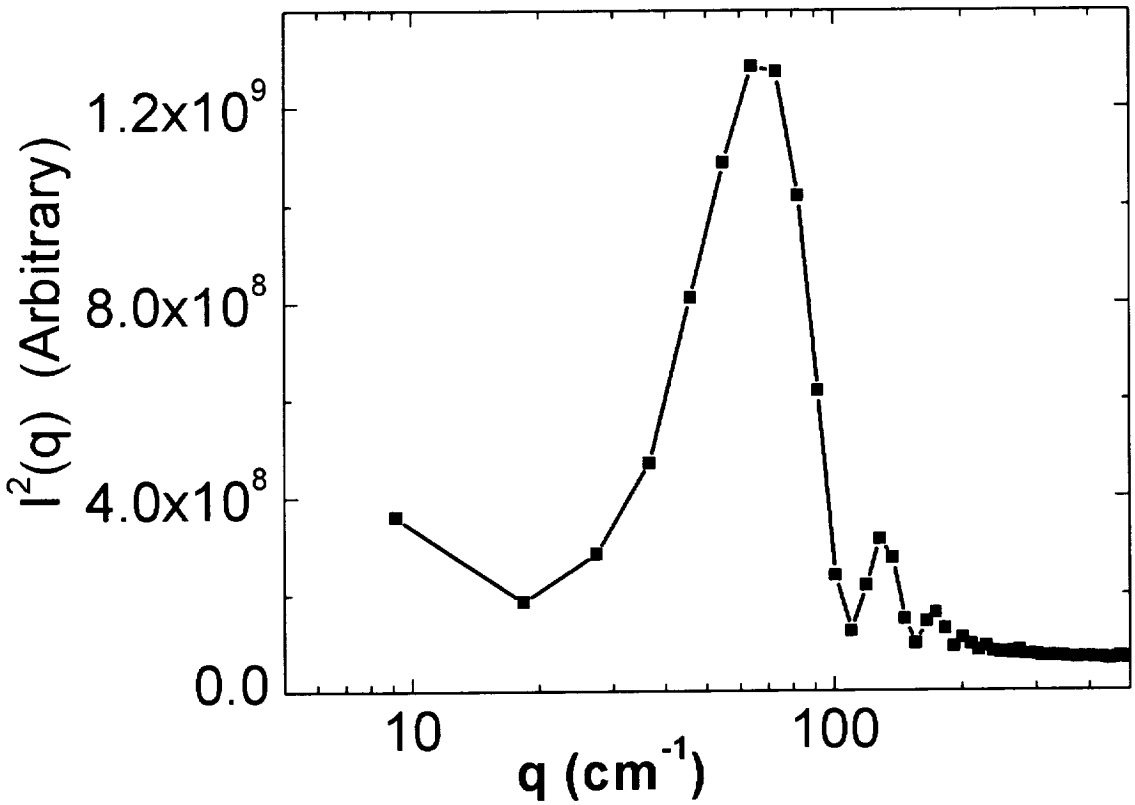

Log-Linear plot of the spatial power spectrum of the fluctuations for a 1 mm thick toluene sample with a gradient of 200 K/cm.

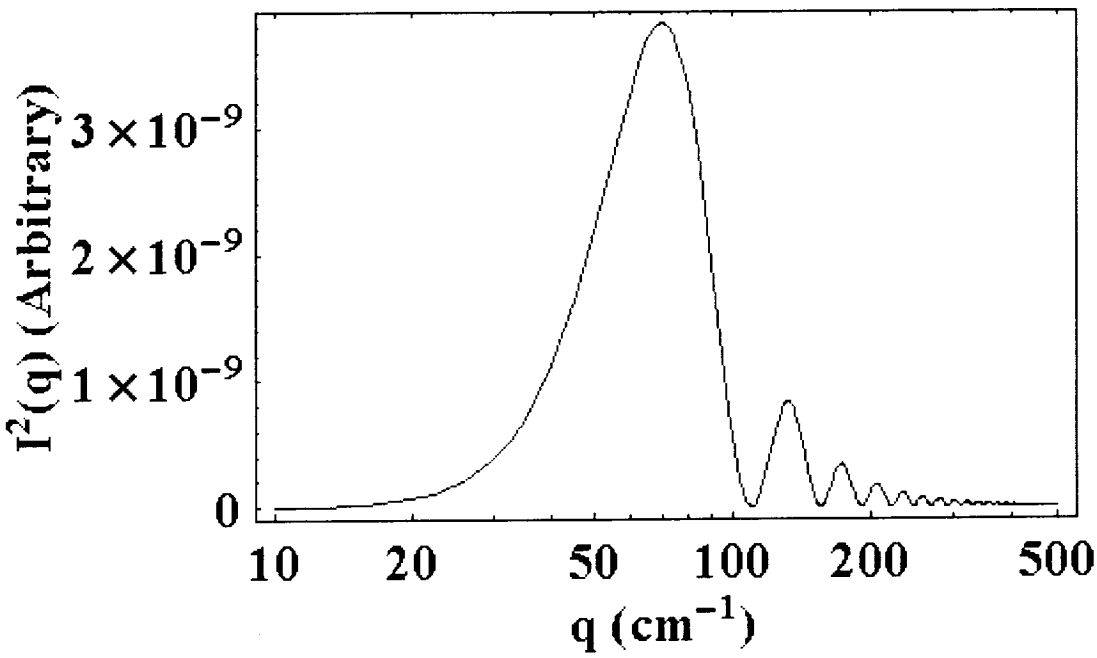

Log-Linear plot of the shadowgraph signal expected for a 1mm thick toluene sample subjected to a gradient of 200 K/cm, and with an imaging distance of 50 cm.

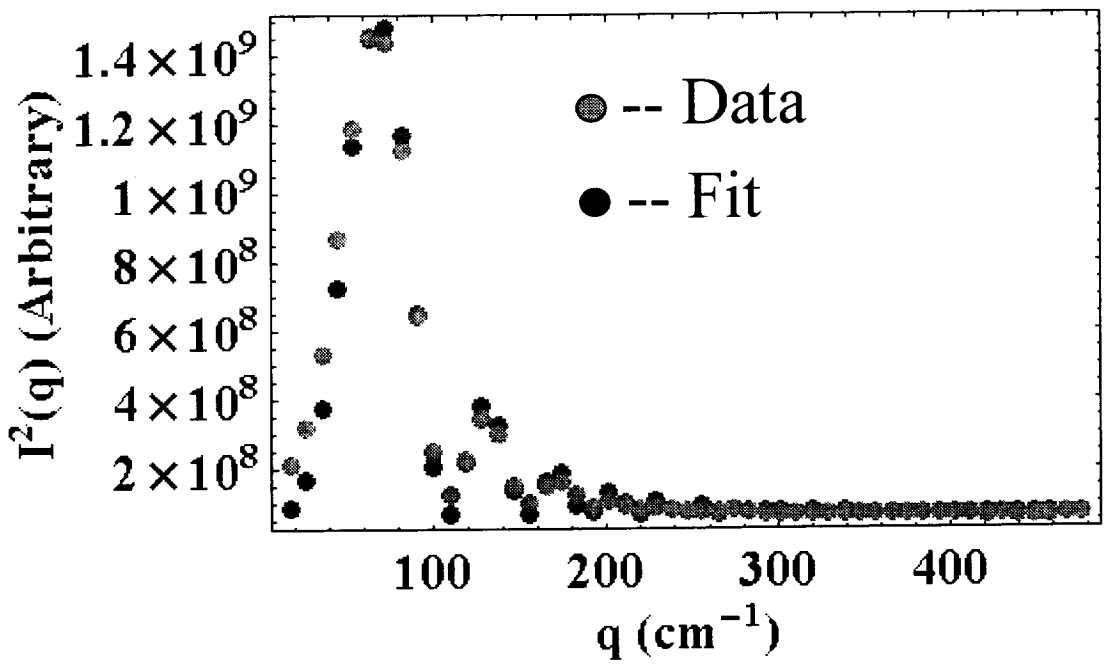

Results of fitting existing theory to the data for toluene. The theory* includes both gravity and finite-size effects.

* José Ortiz de Zárate and Jan. V. Sengers, Preprint (2002).

Session 3: Complex Fluids

PARTICLE SEGREGATION IN A FLOWING SUSPENSION SUBJECT TO HIGH-GRADIENT STRONG ELECTRIC FIELDS

Andreas Acrivos, Zhiyong Qiu
The City College of New York

Boris Khusid, Nikolai Markarian
New Jersey Institute of Technology

PI: Andreas Acrivos, The Levich Institute, The City College of New York, 140th Street & Convent Avenue, New York, NY 10031, Tel: 212-650-8159, Fax: (212) 650-6835; E-mail: acrivos@scisun.sci.ccny.cuny.edu

INTRODUCTION

The widespread use of electro-hydrodynamic devices and processes emphasizes a critical need for developing a comprehensive predictive theory capable of improving our fundamental understanding of the behavior of a suspension subject to an AC electric field and shear, and of facilitating the design and optimization of such devices. The currently favored approach to the qualitative interpretation of the AC-field driven manipulation of suspensions is based on a model which considers only the force exerted on a single particle by an external field and neglects the field-induced and hydrodynamic interparticle interactions both being inversely proportional to the interparticle distance raised to the power three. On the other hand, the purpose of the field-induced separation is to concentrate particles in certain regions of a device. This clearly raises the fundamental question regarding the extent to which we can neglect these slow decaying electrical and hydrodynamic collective interactions and rely on the predictions of a single-particle model. Another important issue that still remains open is how to characterize the polarization of a particle exposed to a strong electric field. The presentation will address both these questions.

EXPERIMENTAL DATA AND COMPARISON WITH SIMULATIONS

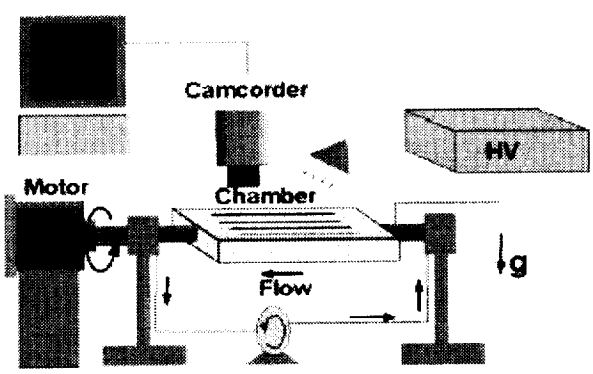

Figure 1. Setup

Experiments were conducted in a parallel-plate channel in which a 10^{-3} (v/v) suspension of heavy, positively polarized Al_2O_3 spheres was exposed to an AC field under conditions such that the field lines were arranged in the channel cross-section perpendicular to the streamlines of the main flow [1, 2]. To reduce the effects of the gravitational settling of the particles, the channel was slowly rotated (4 rpm) around a horizontal axis (Fig.1). Following the application of a high-gradient strong

AC field (~kV/mm), the particles were found to move towards both the high-voltage (HV) and grounded (GR) electrodes and to form "bristles" along their edges (Fig. 2).

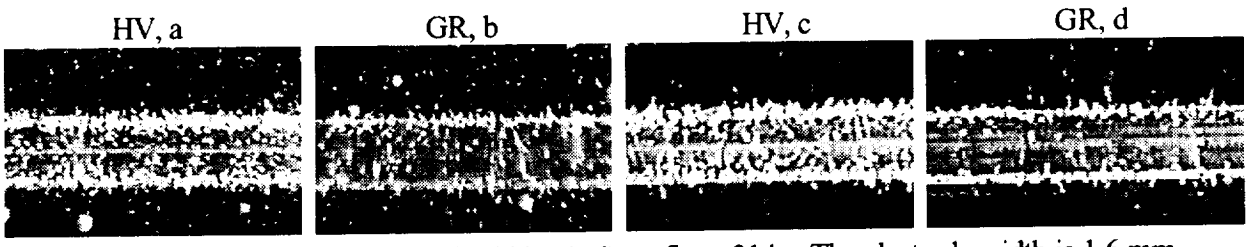

Figure 2. 1kV, 100Hz; (a,b) 20 ml/min, 383s; (c,d) no flow, 314 s. The electrode width is 1.6 mm

The process was modeled by computing the particle motions under the combined action of dielectrophoretic, viscous, and gravitational forces under conditions of negligibly small particle Reynolds numbers and neglecting the interparticle electric and hydrodynamic interactions. The model calculations required no fitting parameters because the particle polarizability was determined independently by measuring the frequency and concentration dependence of the complex dielectric permittivity of a suspension in a low-strength field (~ V/mm).

The predictions of this single-particle model were found to be consistent with the experimental data for the rate of particle accumulation on the electrodes. In particular, Fig. 3 shows the experimental and theoretical data on the kinetics of the particle aggregation on a high-voltage electrode in the middle of the channel for a 10^{-3} (v/v)-suspension following the application of an electric field. The data are plotted against the non-dimensional time, t/τ_d, with τ_d being the characteristic dielectrophoretic time [1, 2]. However, the interparticle interactions, even for initially very dilute suspensions, appear to govern the formation of the. aggregation pattern on the electrodes. The experiments suggested a two-step mechanism for the formation of the arrays of bristles (Fig.2) along the electrode edges, which arose from the interplay of the dielectrophoretic force that confined the particles near the electrode edge and the dipolar interactions of nearby particles.

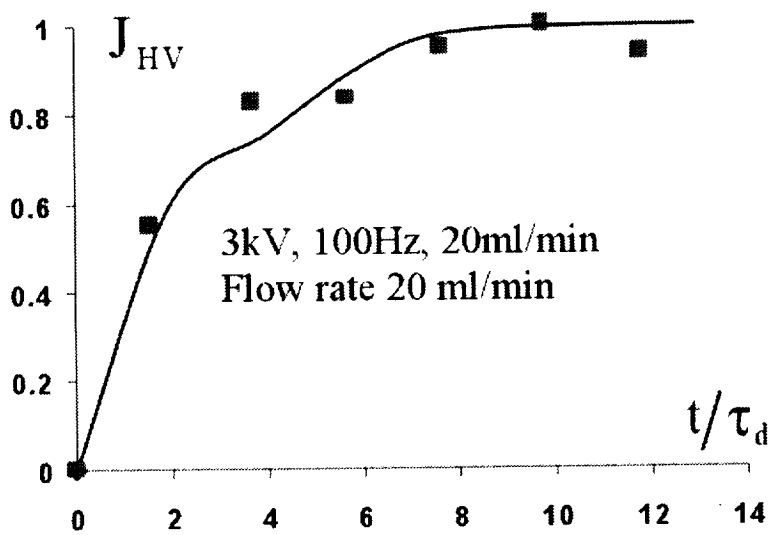

Figure 3. Amount of accumulated particles

REFERENCES

1. A. Dussaud, B. Khusid and A. Acrivos, J. Appl. Phys., 88, 5463 (2000).
2. Z. Qiu, N. Markarian, B. Khusid and A. Acrivos, J. Appl. Phys. (to appear, 2002)

PARTICLE SEGREGATION IN A FLOWING SUSPENSION SUBJECT TO HIGH-GRADIENT STRONG ELECTRIC FIELDS

Andreas Acrivos and **Zhiyong Qiu**
The Levich Institute at CCNY

Boris Khusid and **Nikolai Markarian**
New Jersey Institute of Technology

Sixth Microgravity Fluid Physics and Transport Phenomena Conference

August 14-16, 2002
Cleveland, OH

Support:
NASA Office of Biological and Physical Research

ELECTRO-HYDRODYNAMICS OF SUSPENSIONS

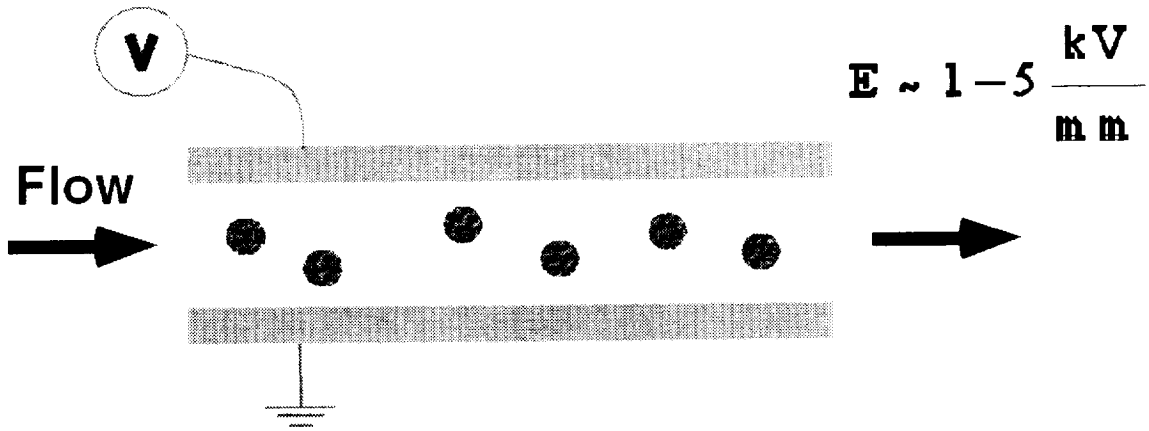

APPLICATIONS

Interactive control & manipulation of the particle motions and segregation

FIELD-INDUCED PHENOMENA

- **Particle interaction with a field**
- **Interparticle interactions**

PONDEROMOTIVE FORCE

The force acting on a particle subject to a gradient electric field is

$$\mathbf{F}_e = Q\mathbf{E} + (\mathbf{P}\cdot\nabla)\mathbf{E}$$

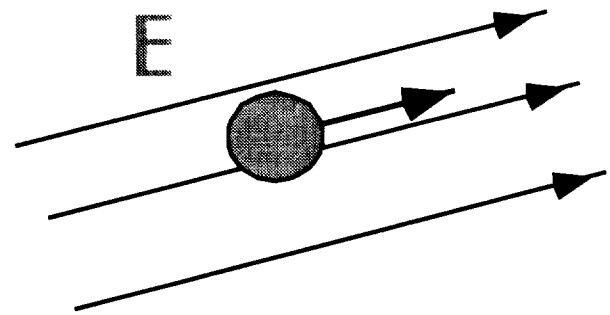

Electrophoresis is the motion of a charged particle in a DC field

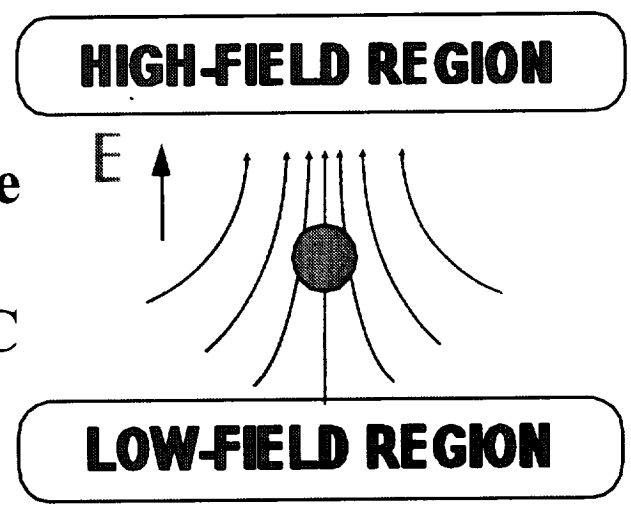

Dielectrophoresis is the motion of a neutral particle in gradient DC and AC fields

The time average dielectrophoretic force in an AC field

$$\langle \mathbf{F} \rangle = 2\pi\varepsilon_0\varepsilon_f a^3 \mathrm{Re}(\beta(\omega))\nabla E_{rms}^2$$

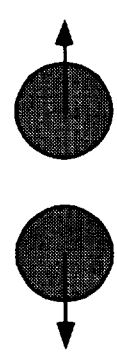

Positive $\mathrm{Re}(\beta)>0$ **dielectrophoresis**

Negative $\mathrm{Re}(\beta)<0$ **dielectrophoresis**

FIELD-INDUCED AGGREGATION

A homogeneous random arrangement of particles

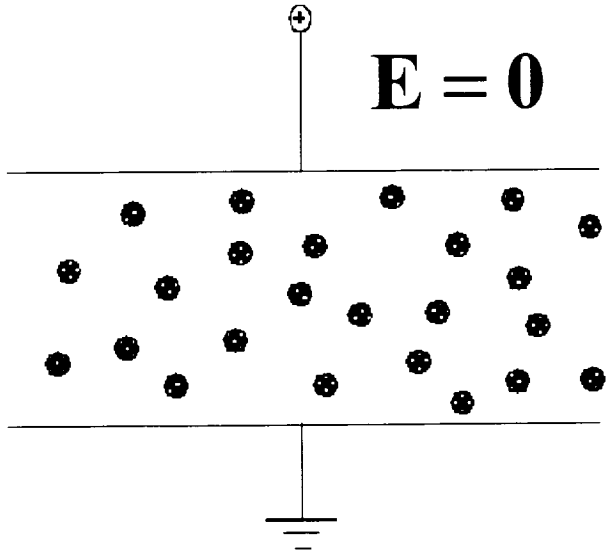

A variety of ordered aggregation patterns

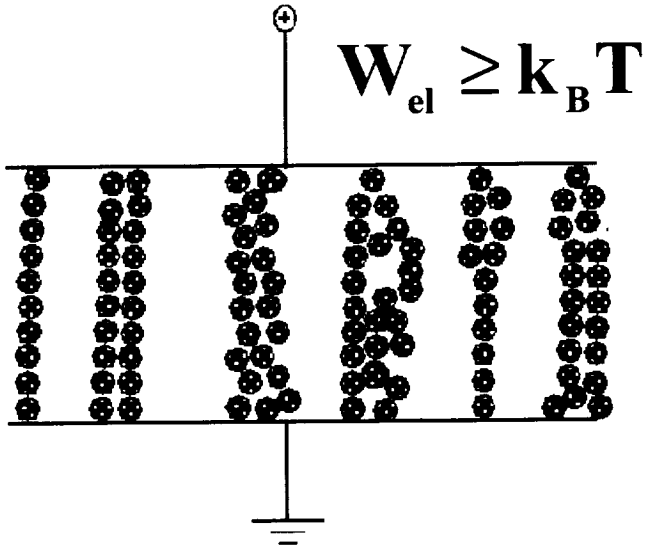

UNRESOLVED PROBLEMS

When the particles and the liquid are not perfectly insulating or perfectly conducting:

No quantitative verification of the expression for the electric force acting on a particle

No constitutive relations for electric energy and stress in non-dilute suspensions.

DIELECTRIC RESPONSE

The microscopic theory yields

$$\mathbf{D} = \varepsilon_0 \mathbf{E} + \mathbf{P}$$

Perfect dielectric responds instantaneously

$$\mathbf{D}(t) = \varepsilon_0 \varepsilon \mathbf{E}(t)$$

Not-perfect dielectric has a finite response time

$$\mathbf{D}(t) = \varepsilon_0 \int_0^\infty \varepsilon(t - t')\mathbf{E}(t')dt'$$

$$\mathbf{D}_\omega = \varepsilon_0 \varepsilon^*(\omega)\mathbf{E}_\omega$$

The complex dielectric permittivity

$$\varepsilon^* = \varepsilon' - i\varepsilon''$$

Energy dissipation

$$\langle Q_{el} \rangle = \omega \varepsilon_0 \varepsilon'' \langle \mathbf{E}^2 \rangle$$

FIELD-INDUCED PHASE SEPARATION

Microscopic theory for the field-induced phase transitions and dielectrophoresis in suspensions

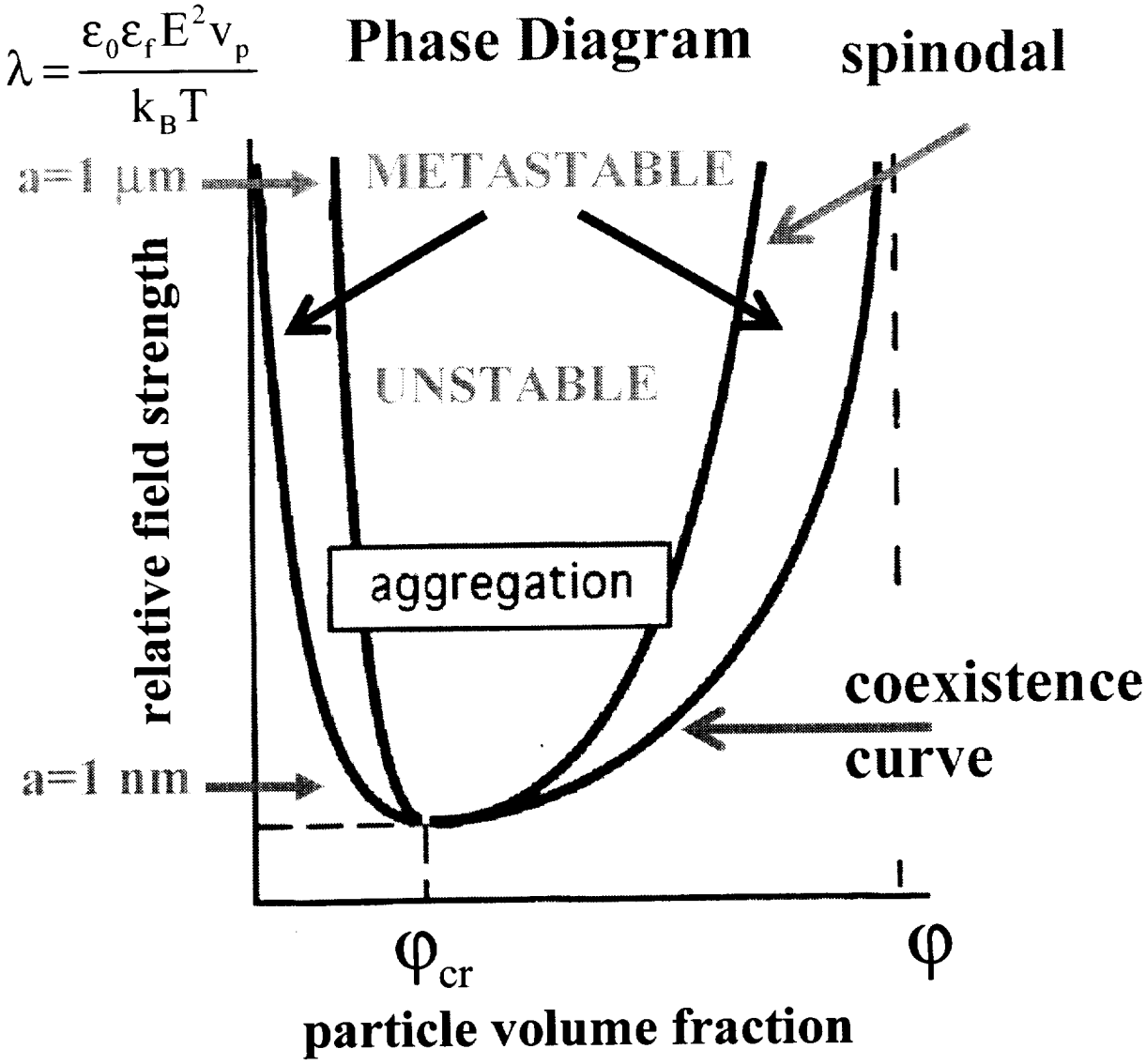

Khusid & Acrivos, *Phys Rev E*, 1995, 1996, 1999

DIELECTROPHORESIS IN NON-DILUTE SUSPENSIONS

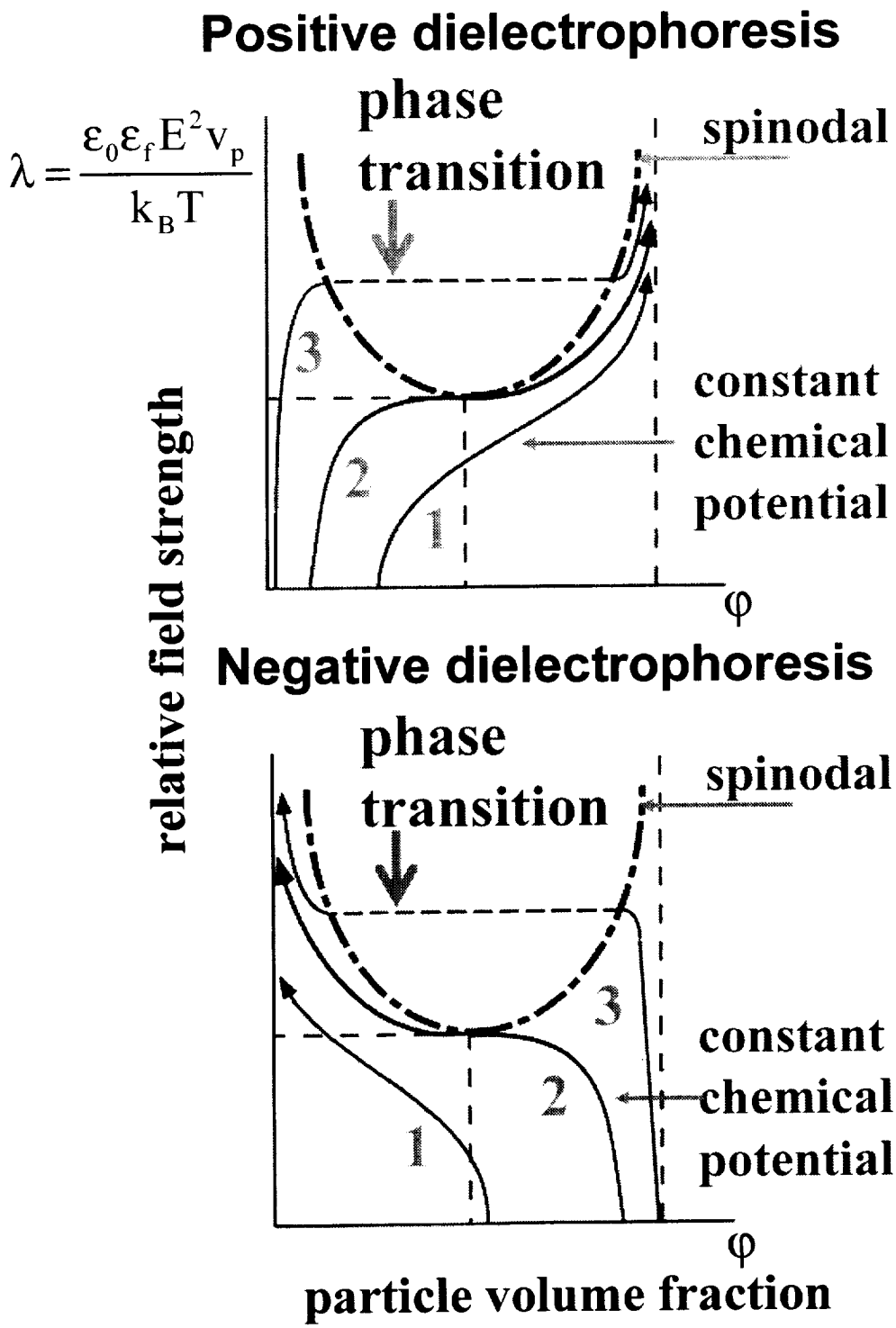

AGGREGATION IN GRADIENT FIELDS

Aggregation time

$$\tau_a \approx \frac{\eta_f}{\varepsilon_0 \varepsilon_f \left(\mathrm{Re}(\beta) E\right)^2} \xi(\varphi)$$

$$\xi \approx 0.4\left[(\pi/6\varphi)^{5/3} - 1\right] \qquad E \sim V_{rms}/d$$

Dielectrophoretic time

$$\tau_d = \frac{3 d^4 \eta_f}{a^2 \varepsilon_0 \varepsilon_f \left|\mathrm{Re}(\beta)\right| V_{rms}^2}$$

Aggregation-to-dielectrophoretic times ratio

$$\frac{\tau_d}{\tau_a} \approx \frac{3 d^2 \left|\mathrm{Re}(\beta)\right|}{a^2 \xi(\varphi)}$$

Homogeneous aggregation $\tau_d >> \tau_a$

Heterogeneous aggregation $\tau_d << \tau_a$

THE FOCUS OF OUR STUDIES

The synergism of electric and shear driven phenomena in a flowing suspension subjected to a high-gradient field

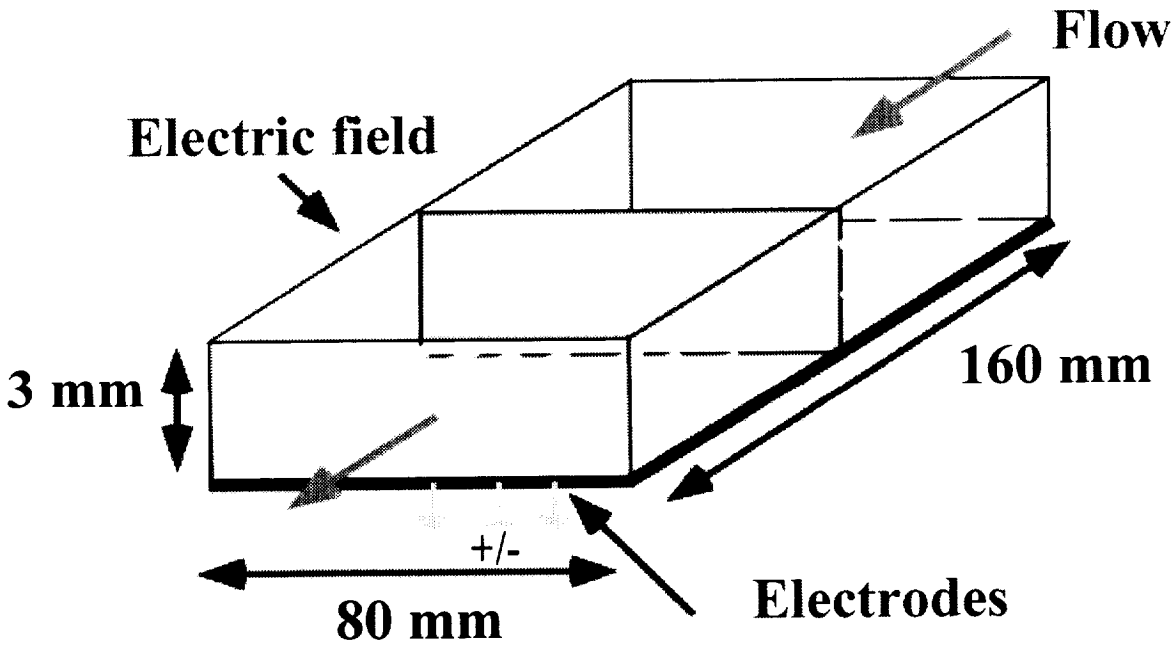

Dussaud, Khusid & Acrivos, *J Appl Phys*, 2000

NEGATIVE DIELECTROPHORESIS OF NEUTRALLY BUOYANT SPHERES

Dussaud, Khusid & Acrivos, *J Appl Phys*, 2000

- **Dielectric spectroscopy for measuring particle polarizability, E~ V/mm**

The Maxwell-Wagner model

$$\frac{\varepsilon_s^*(\omega,\varphi)-\varepsilon_f^*}{\varepsilon_s^*(\omega,\varphi)+2\varepsilon_f^*}=\varphi\beta(\omega)$$

- **Validation of equation for dielectrophoretic force, E~ kV/mm**

DIELECTRIC SPECTROSCOPY

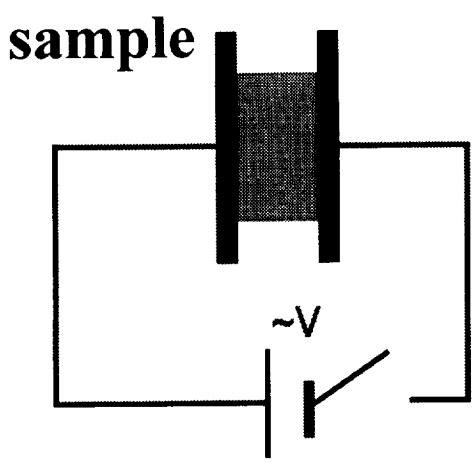

E~1 V/mm

DS measures the relation between time-varying voltage and current through a sample

NJIT W.M. Keck Laboratory

ROTATING ELECTRIC CHAMBER

Zero buoyancy limits the variation of the polarization mismatch between particles and fluid.

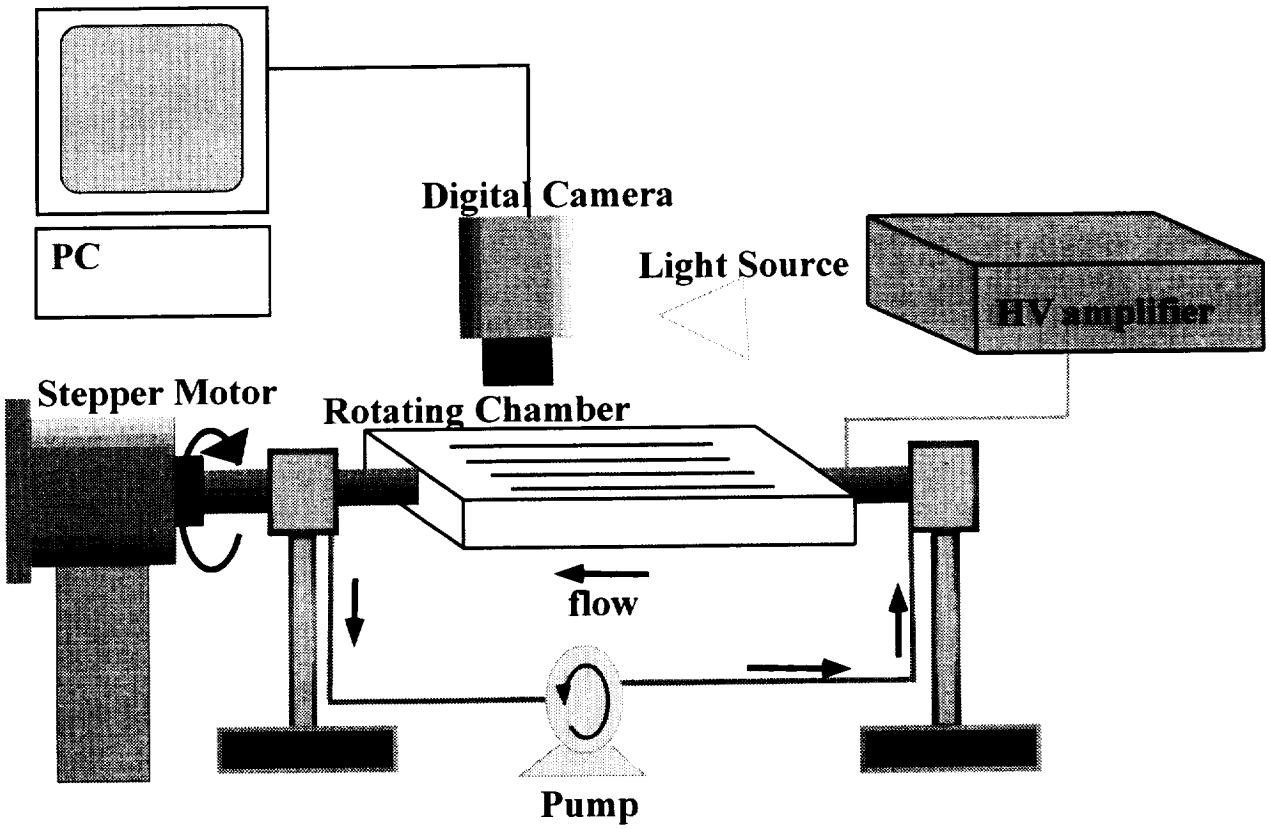

4 - 8 rpm

$$\langle g \rangle_{aver} = 0$$

centrifugal acceleration ~mg

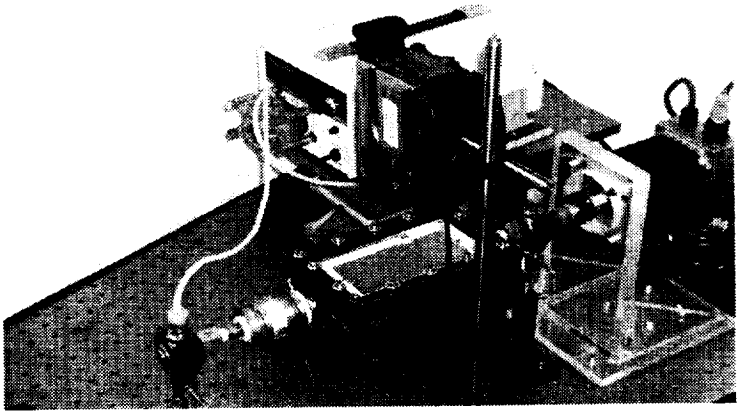

Qiu, Markarian, Khusid & Acrivos, *J Appl Phys*,2002

SUSPENSION OF HIGHLY POLARIZABLE PARTICLES

Al_2O_3 spheres (3.75 g/cm^3, D= 89.6 μm) in corn oil (0.92 g/cm^3, η_f=0.06 Pa·s)

The Maxwell-Wagner model

$$\mathrm{Re}\left(\frac{\varepsilon_s^* - \varepsilon_f^*}{\varepsilon_s^* + 2\varepsilon_f^*}\right)$$

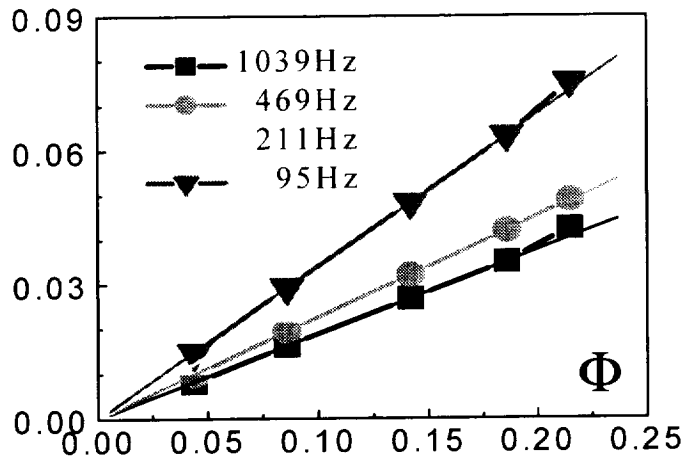

particle volume fraction

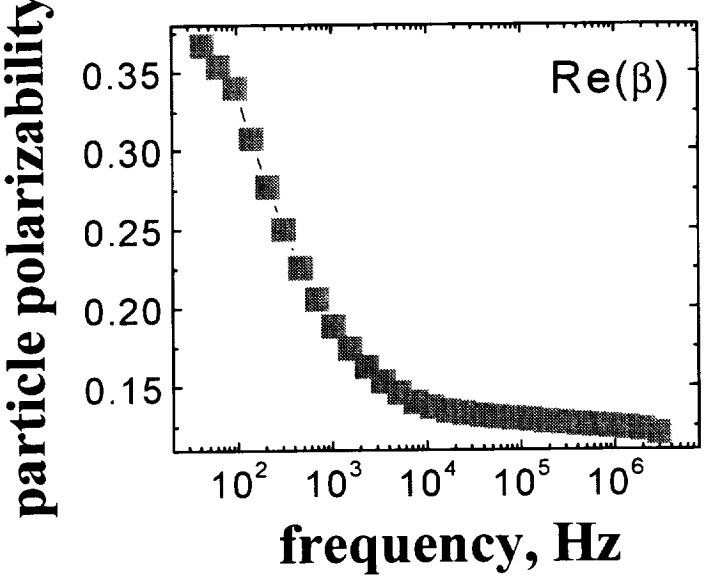

Broadband Dielectric Spectrometer, BDS-80, Novocontrol

FIELD-INDUCED SEPARATION

3 kV_{rms}, 100 Hz, 4 rpm

HETEROGENEOUS AGGREGATION

G

HV

G

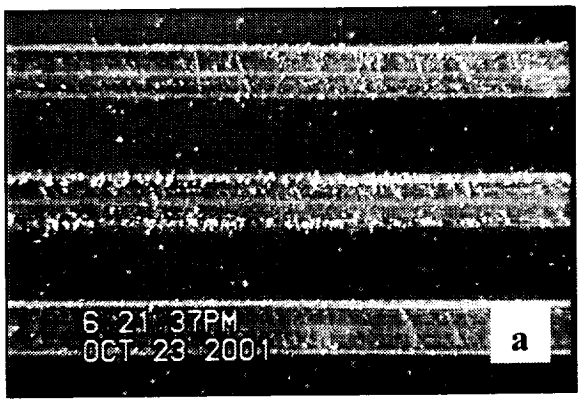

$$\varphi = 0.0001, \quad t = 637 \text{ s}$$

$$\frac{\tau_d}{\tau_a} \approx \frac{3d^2|\mathrm{Re}(\beta)|}{a^2\xi(\varphi)} \sim 4\cdot 10^{-3}$$

G

HV

G

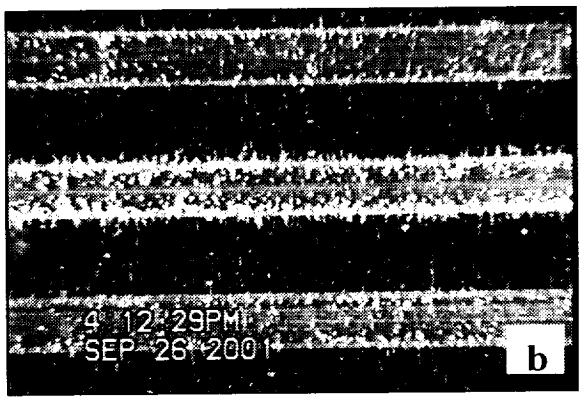

$$\varphi = 0.001, \quad t = 273 \text{ s}$$

$$\frac{\tau_d}{\tau_a} \approx \frac{3d^2|\mathrm{Re}(\beta)|}{a^2\xi(\varphi)} \sim 0.1$$

HOMOGENEOUS AGGREGATION

HV

G

HV

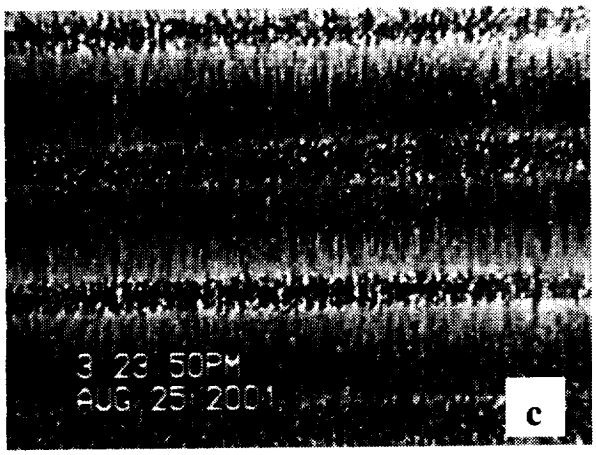

$$\varphi = 0.01, \quad t = 83 \text{ s}$$

$$\frac{\tau_d}{\tau_a} \approx \frac{3d^2|\mathrm{Re}(\beta)|}{a^2\xi(\varphi)} \sim 7$$

A SINGLE-PARTICLE MODEL

The balance of drag, dielectrophoretic, and gravitational forces

$$6\pi\eta a(\mathbf{u}-\mathbf{v}_f) = 2\pi\varepsilon_0\varepsilon_f a^3\,\mathrm{Re}(\beta)\nabla E_{rms}^2 + \frac{4}{3}\pi(\rho_p-\rho_f)a^3 g\mathbf{e}$$

The field-induced particle displacement

$$\frac{d\mathbf{r}}{dt}=\mathbf{u} \qquad \mathbf{r}|_{t=0}=\mathbf{r}_0$$

The characteristic time of dielectrophoresis

$$\tau_d = \frac{3d^4\eta_f}{a^2\varepsilon_0\varepsilon_f|\mathrm{Re}(\beta)|V_{rms}^2}$$

COMPUTATIONAL CELL

Laplace's equation & boundary conditions

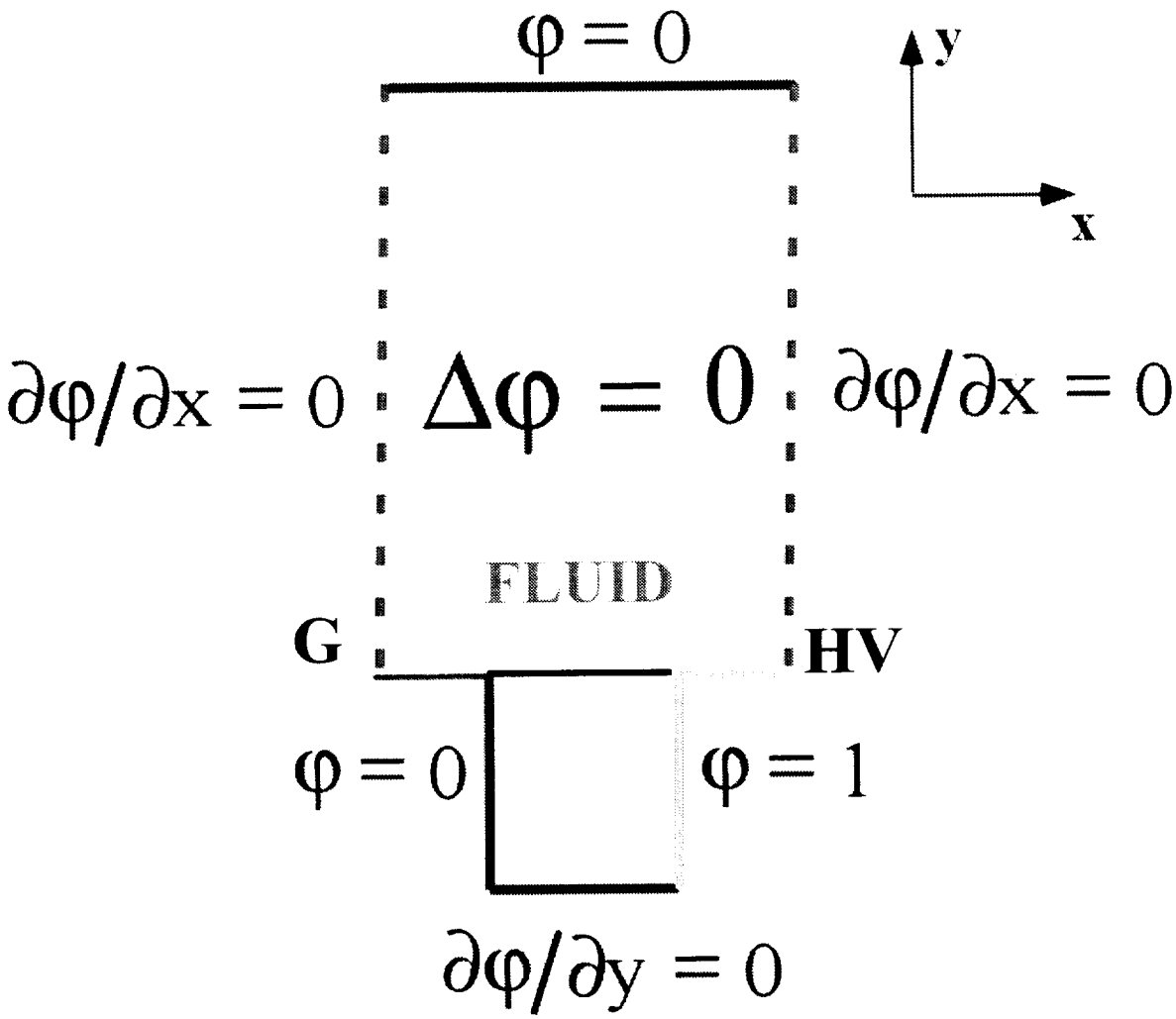

COMPUTED SQUARE OF THE FIELD STRENGTH

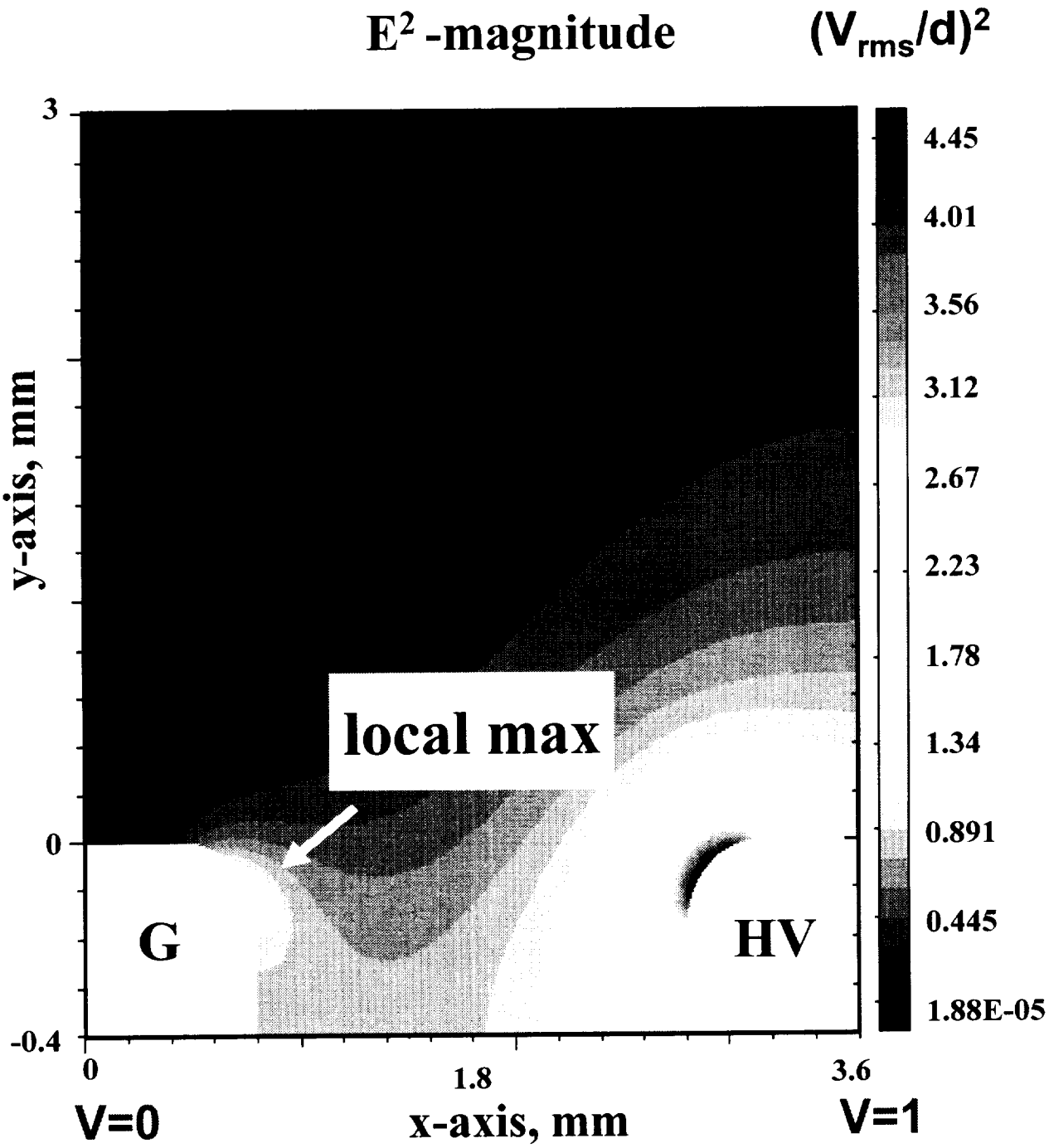

HETEROGENEOUS AGGREGATION

$V = 3\ kV_{rms}$, 100 Hz, 4 rpm, $\varphi = 0.001$

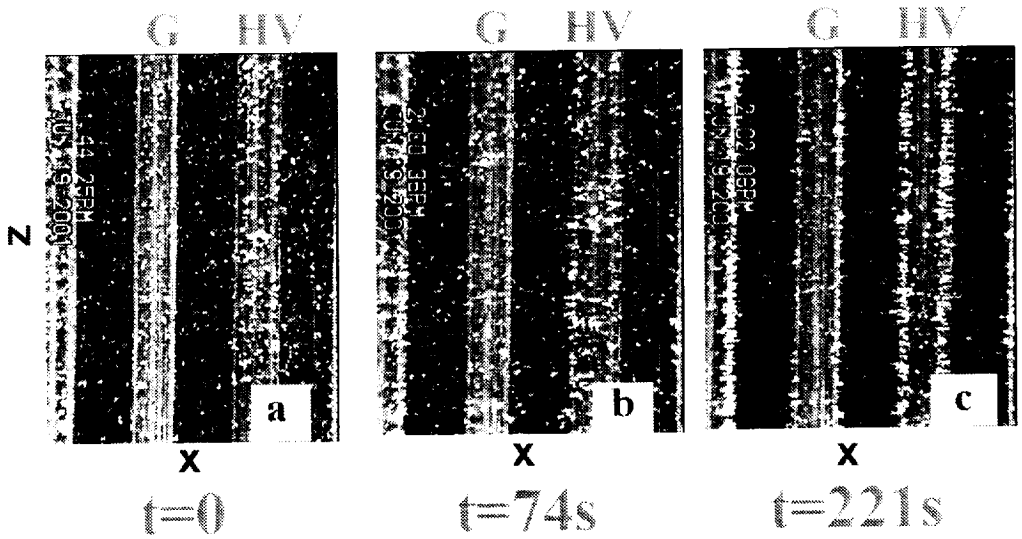

Simulations with 2400 particles

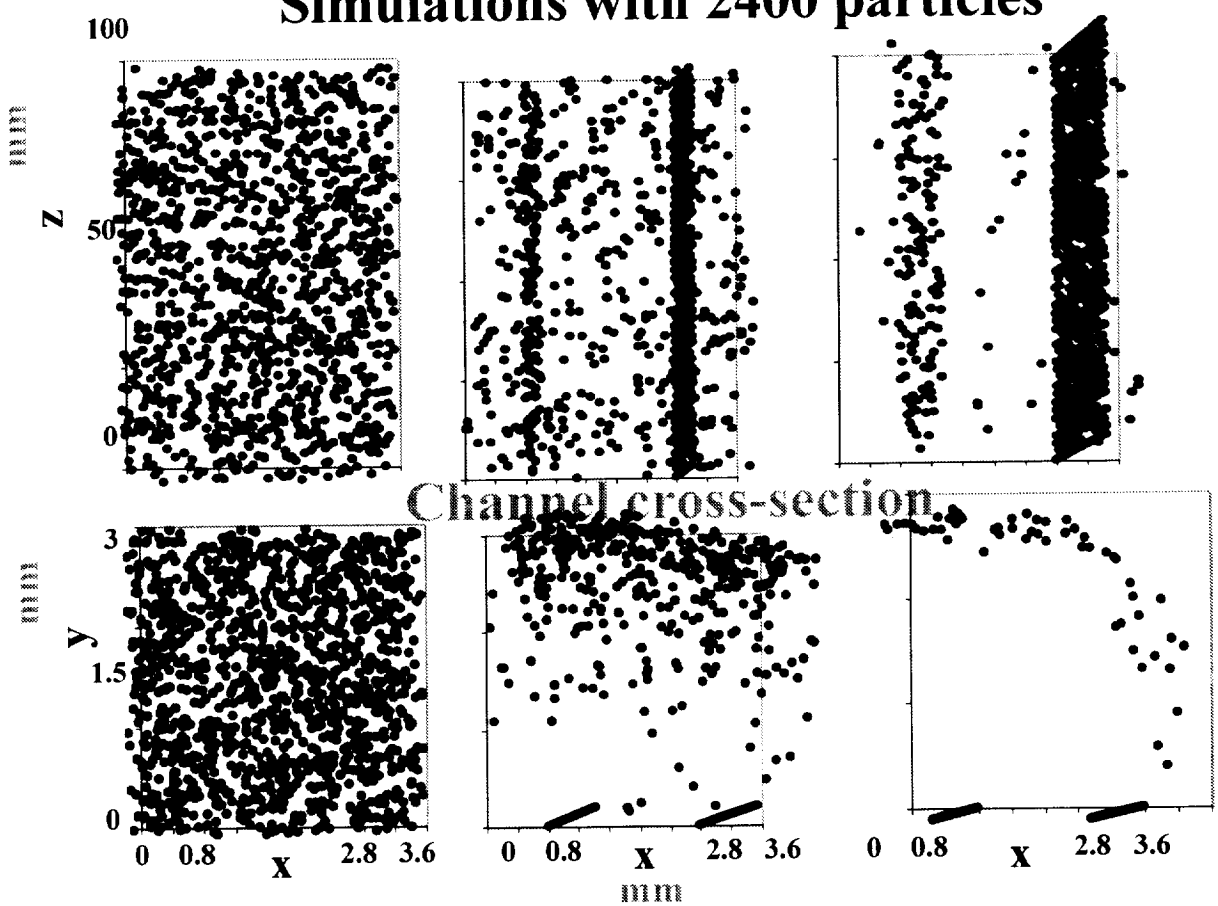

SIMULATIONS

Particle trajectories, $V = 3\ kV_{rms}$, 100 Hz, 4 rpm

Channel cross-section

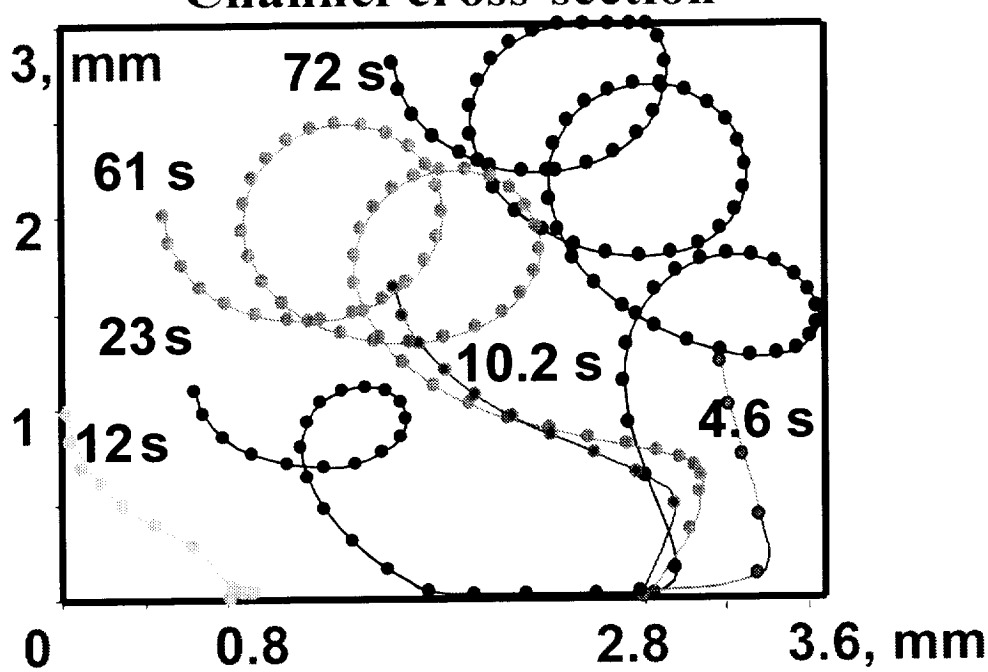

Effects of gravity, 3 kV_{rms}, 1 kHz, 4 rpm

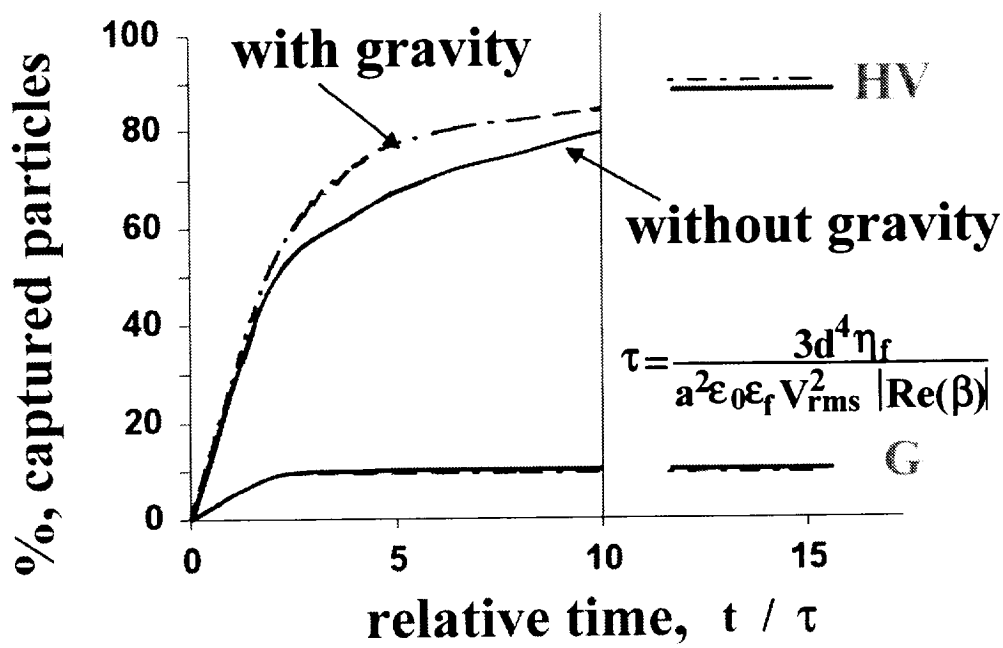

COMPARISON WITH EXPERIMENT

Measuring of gray level

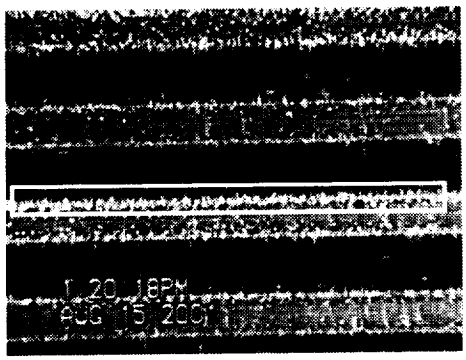

3 kV_{rms}, 100 Hz
t= 630 s

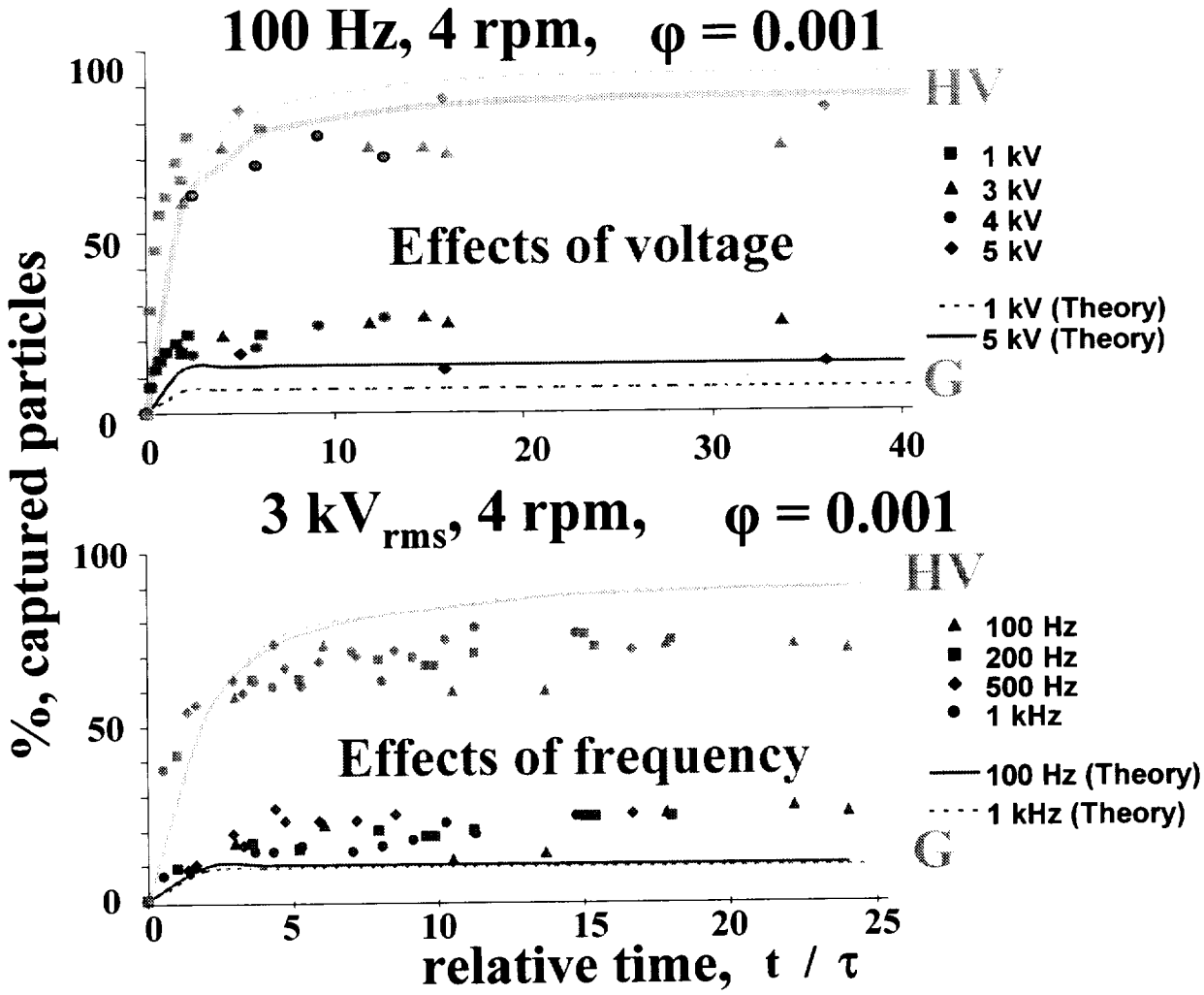

AGGREGATION PATTERN

1 kV_{rms}, 100 Hz, 4 rpm, $\varphi = 0.001$

Flow 20 ml/min | **Without Flow**

73 s | **69 s**

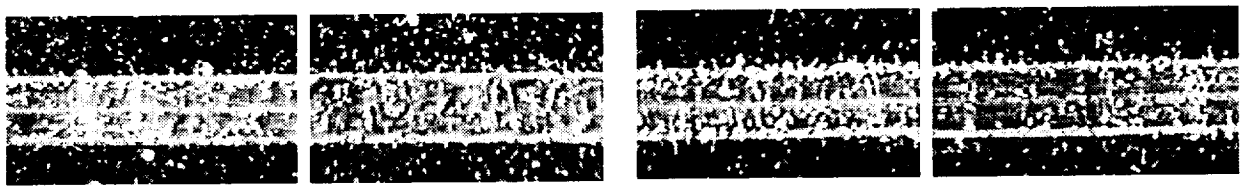

156 s | **149 s**

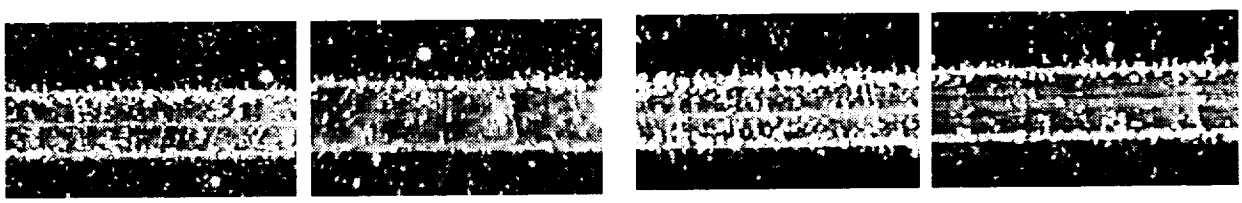

594 s | **617 s**

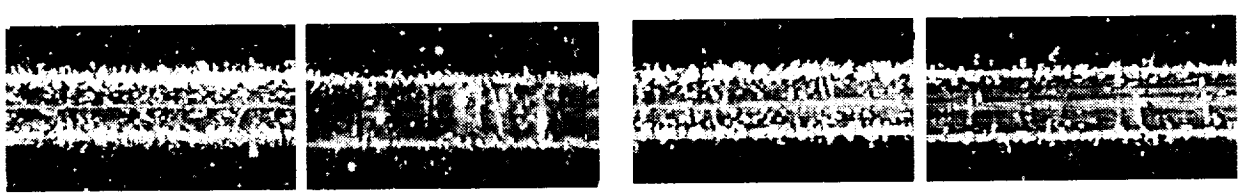

HV GR HV GR

Qiu, Markarian, Khusid & Acrivos, *J Appl Phys*,2002

MOTIVATION

$$\mathbf{E} = \mathbf{A}(\mathbf{r}, t)\cos\omega t$$

non-perfect dielectric fluid

other microscopic parameters

complex dielectric permittivity

Electric energy and stress

Can we express the electric energy and electric stress for a non-perfect dielectric fluid in terms of its complex dielectric permittivity or other microscopic parameters are required?

SHEET FLOWS, AVALANCHES, AND DUNE MIGRATION ON EARTH AND MARS

James Jenkins
Department of Theoretical and Applied Mechanics
Cornell University, Ithaca, NY 14853
jtj2@cornell.edu Tel: 606-255-7185, Fax: 607-255-2011

ABSTRACT

We provide an overview of our research on sheet flows and avalanches of granular materials, primarily in terrestrial conditions. Sheet flows are relatively thin, highly concentrated regions of grains that flow near the ground under the influence of a strong turbulent wind. In them grains are suspended by interparticle collisions and the velocity fluctuations of the turbulent gas. Avalanches are flows of dry, cohesionless granular materials that are driven by gravity down inclines against the frictional and collisional resistance of the grains of the bed.

In our study of sheet flows, we have extended existing theories that involve particle-particle and gas-particle interactions to apply to the conditions of a typical terrestrial sand dune during a sandstorm. This has involved the incorporation of both the viscous dissipation of the particle fluctuation energy due to the gas and the turbulent suspension of the grains due to velocity fluctuations of the gas. It has also involved an examination of several different boundary conditions at the bed and a more precise characterization of the conditions that apply at the top of a sheet flow, where the mean-free-path between collisions becomes comparable to the length of a ballistic trajectory. Solutions to the resulting differential equations have been obtained for both steady and unsteady fully-developed flow. The latter solutions provide information on the characteristic time to achieve a steady flow that plays a key role in dune formation.

In support of this modeling effort, experiments have been undertaken to provide a better understanding of the interaction of particles colliding with the bed, and the energy of the rebounding particle and additional ejected particles has been measured in two-dimensional situations.

The research on avalanches has focused on dense, frictional flows. Experiment and numerical simulations indicate that relatively thin dense flows, on the order of ten particle diameters, occur in layers. In these, momentum transfer occurs by rubbing between contacting particles and bumping between particles falling under gravity, rather than in collisions between freely flying particles. Thicker dense flows, on the other hand, do seem to involve collisional transfer of momentum. Theories based on the appropriated mechanisms of momentum transfer predict velocity profiles that are in agreement with those measured in experiment and numerical simulations, some of which have been carried out in the course of the research.

Dune Formation and Migration

J. Jenkins (Cornell), D. Hanes (Florida)

D. Bideau, G. Berton, F. Rioual, A. Valance
(Rennes)

Minimal Model for Formation and Migration
Sauermann & Herrmann

Dune:

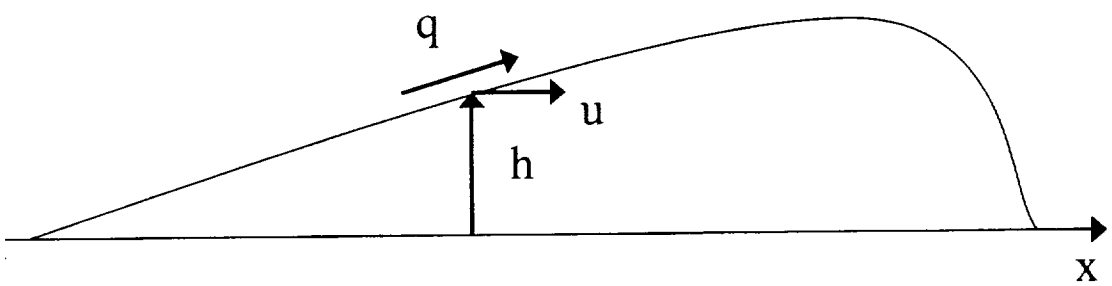

Mass balance:

$$\rho_s \frac{\partial h}{\partial t} + \frac{\partial q}{\partial x} = 0$$

$q(x)$ flux/depth

Kinematic boundary condition:

$$\frac{\partial h}{\partial t} + u\frac{\partial h}{\partial x} + v\frac{\partial h}{\partial y} = 0$$

$$-\frac{1}{\rho_s}\frac{\partial q}{\partial x} + u\frac{\partial h}{\partial x} \doteq 0$$

$u(x,t)$ bed velocity

Wind:

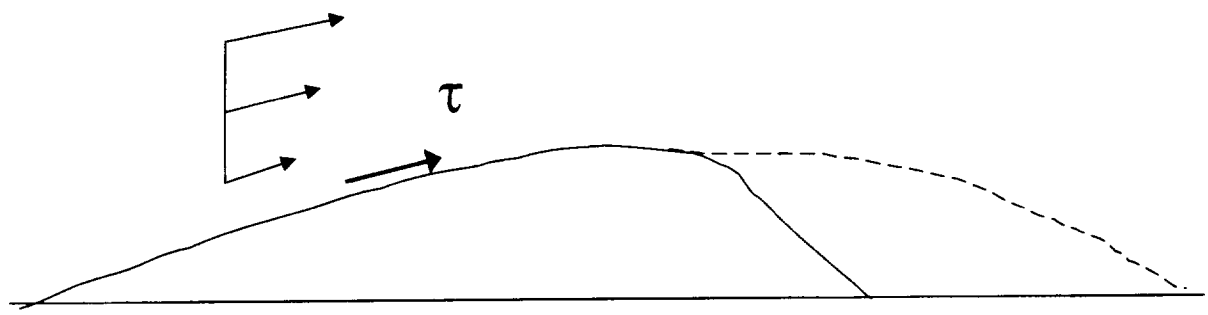

Wind shear stress $\tau(x) = \tau_0[1 + \hat{\tau}(x)]$

$$\hat{\tau}(x) = 4\left(\frac{1}{\pi}\int_{-\infty}^{\infty}\frac{h'}{x-\xi}d\xi + 0.3h'\right)$$

Sand:

Saturated flux $q_s = q_s(\tau)$

Saturation length $\ell_s = \ell_s(\tau)$

$$\frac{\partial q}{\partial x} = \frac{q}{\ell_s}\left(1 - \frac{q}{q_s}\right)$$

Goals: To determine $q_s(\tau)$ and $\ell_s(\tau)$.

Laboratory experiments on saltation in 2D and 3D for the splash function.

Field experiments to determine dune shape and to study heap-to-dune evolution.

Numerical simulations of saltation.

Solution of model equations for steady sheet flow.

Formulation of model equations for unsteady sheet flow.

*

Physical experiments, numerical simulations, and analytical studies of dense inclined flow.

Saltation

Individual grains, lifted from the bed by strong turbulent eddies, are accelerated by the drag of the mean turbulent shear flow, and, upon colliding with the bed, rebound and eject other particles.

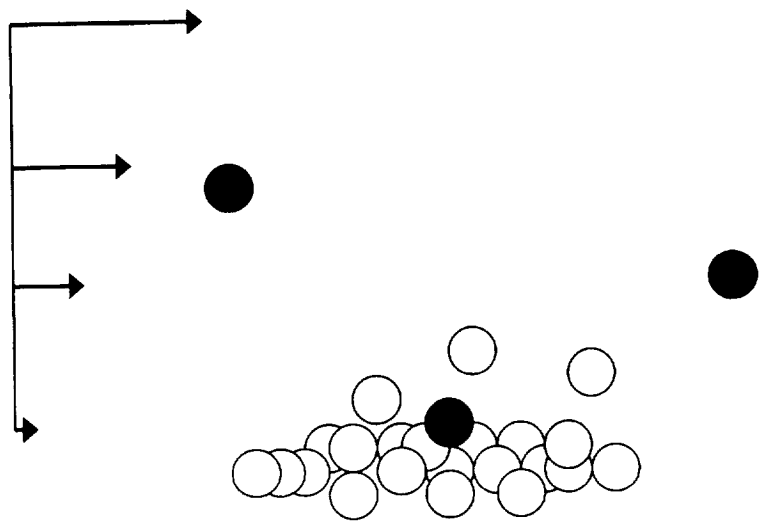

Sheet Flow

As the strength of the turbulent shear flow increases, saltating particles become more numerous and collisions between saltating particles become common. A concentrated region of particles is maintained above the bed by a gradient in the particle pressure.

Experimental setup

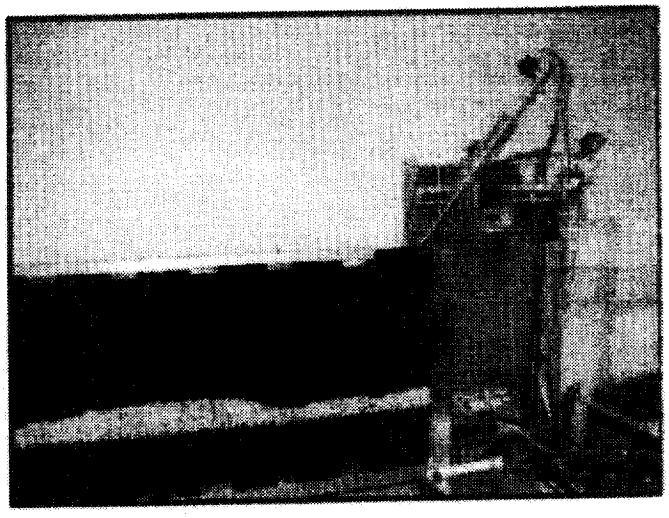

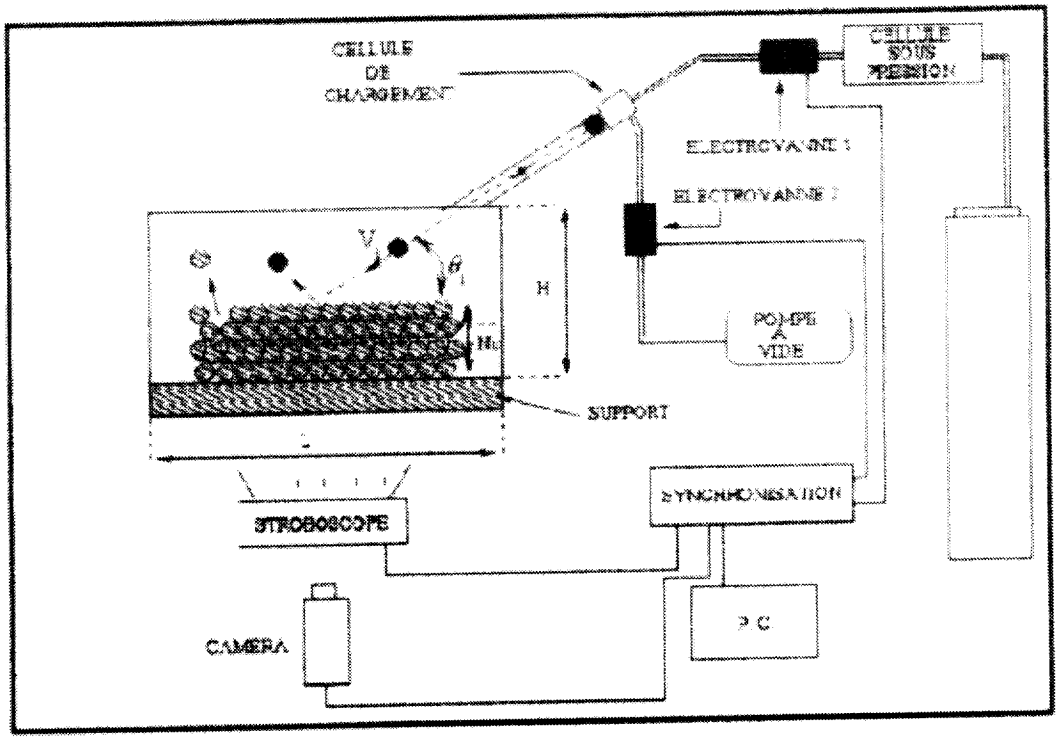

A typical collision:

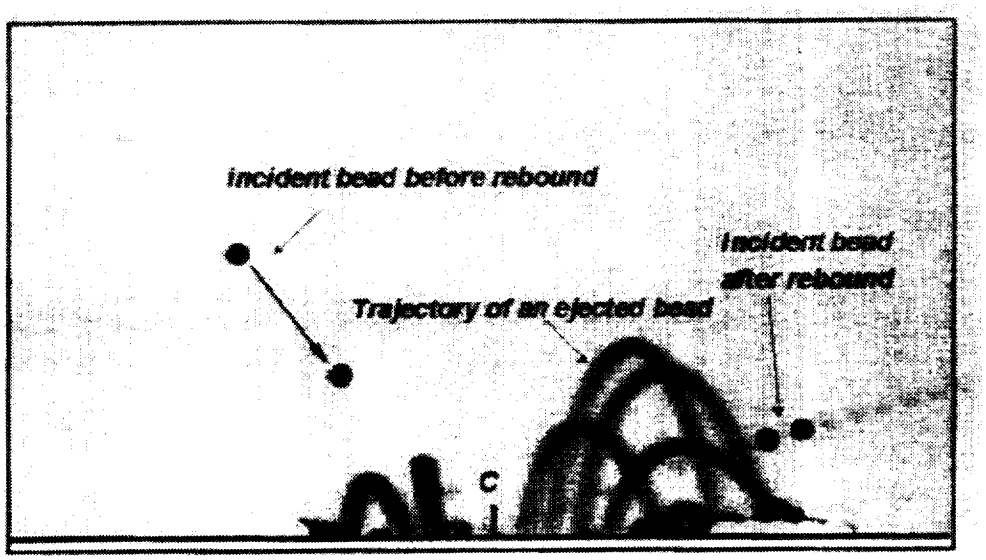

Statistics on the properties of the ejected beads

14

•Etude du Splash à 3 dimensions

Field experiments in Mauritania

- Barchan dunes

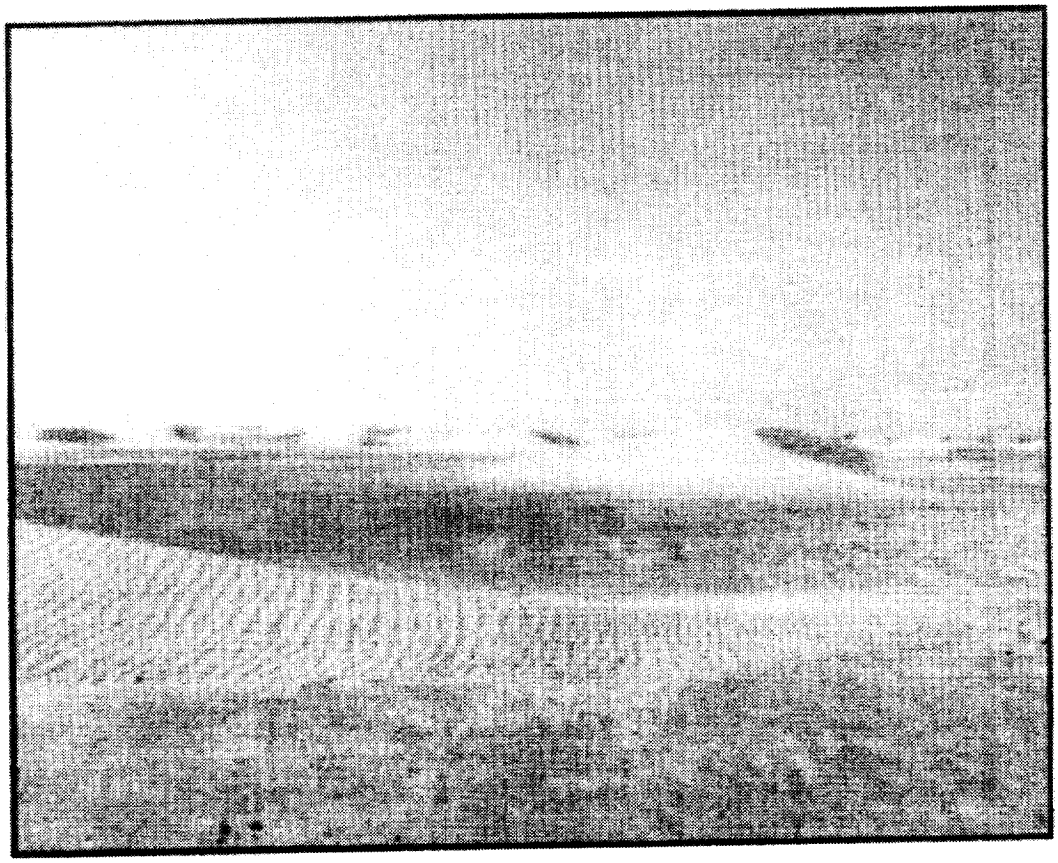

40

Heap-to-Dune Transition

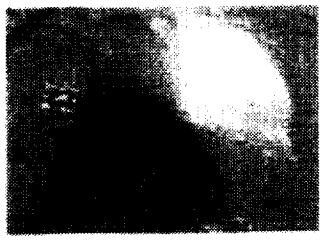

T= 0ms

T= 20 ms

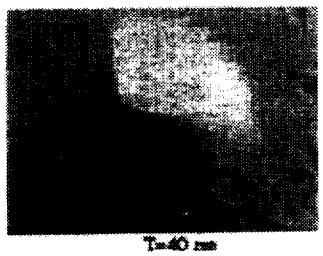

T=40 ms

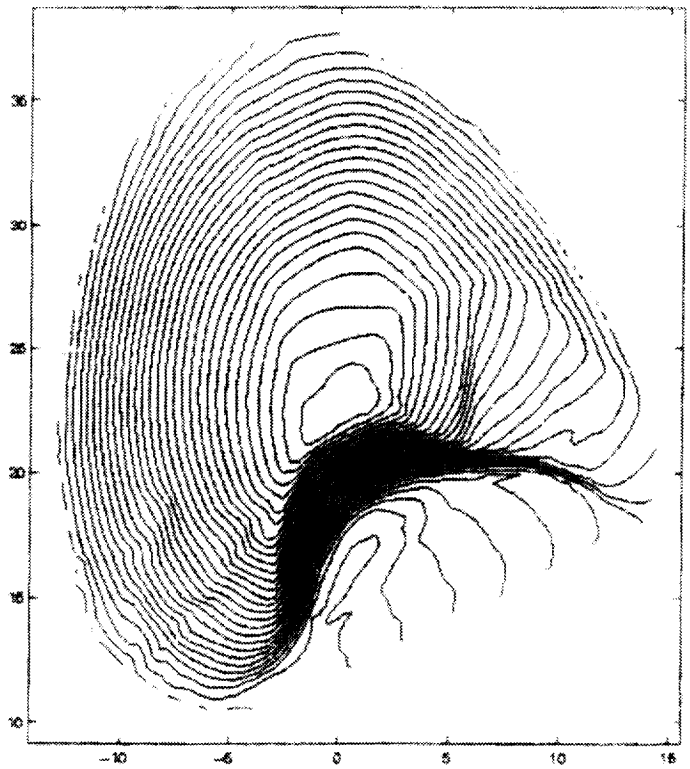

Sheet Flow of Sand in Air

$$D = 0.02 \text{ cm}, \ \rho_s / \rho_f = 2,200$$

$$\mu_f / \rho_f = 0.15 \text{ cm}^2 / \text{sec}, \ e = 0.85$$

Collisional pressure and turbulent suspension

Viscous dissipation of particle fluctuation energy and turbulent fluid energy

Erodible bed: $\nu = 0.55, \ Q \leq 0, \ u = U = 0$

Ballistic top: $p = 0.03; \ S \doteq 0, \ Q \doteq 0$

Sheet Flow

Sand:

$$\frac{d\nu}{dz} = L\frac{\left(\nu - \sqrt{\pi}\frac{F}{M}\frac{Q}{w}\right)}{\left[4Hw^2 + L(1-\nu)\frac{0.09}{0.165}\frac{C_D k^{1/2}\kappa(1-z)}{s_G}\right]}$$

$$\frac{dw}{dz} = L\frac{\sqrt{\pi}}{2}\frac{F}{M}\frac{Q}{p}$$

$$\frac{dQ}{dz} = L\left[6(1-e) - \frac{5\sqrt{\pi}}{12}\frac{1}{E}\left(\frac{FS}{p}\right)^2\right]\frac{pw}{\sqrt{\pi}F} + 3L\frac{\nu C_D}{s_G}w^2$$

$$\frac{du}{dz} = -L\frac{5\sqrt{\pi}}{2}\frac{Fw}{E}\frac{S}{p}$$

Wind:

$$\frac{dS}{dz} = L\frac{\nu C_D}{s_G}(U-u)$$

$$k^{1/2} = \frac{(0.09)^{1/2}}{0.165}\kappa(1-z)\left|U'\right|\left[\left(1+\Delta^2\right)^{1/2} - \Delta\right]$$

$$\Delta \equiv \frac{1}{(0.09)^{1/2}}\frac{C_D}{\left|U'\right|}\frac{\nu}{1-\nu}$$

$$\left|U'\right| \doteq \frac{1}{\kappa(1-z)}\left[\frac{(\tau-S)s_G}{(1-\nu)}\right]^{1/2}$$

$$\frac{dU}{dz} = -\frac{1}{2RL\hat{\kappa}^2(1-z)^2}$$

$$\times\left[\left\{1+\frac{4s_G(\tau-S)}{(1-\nu)}\left[RL\hat{\kappa}(1-z)\right]^2\right\}^{1/2} - 1\right]$$

$$\hat{\kappa} \equiv \kappa\left[\left(1+\Delta^2\right)^{1/2} - \Delta\right]$$

Velocities and Local Sand Flux

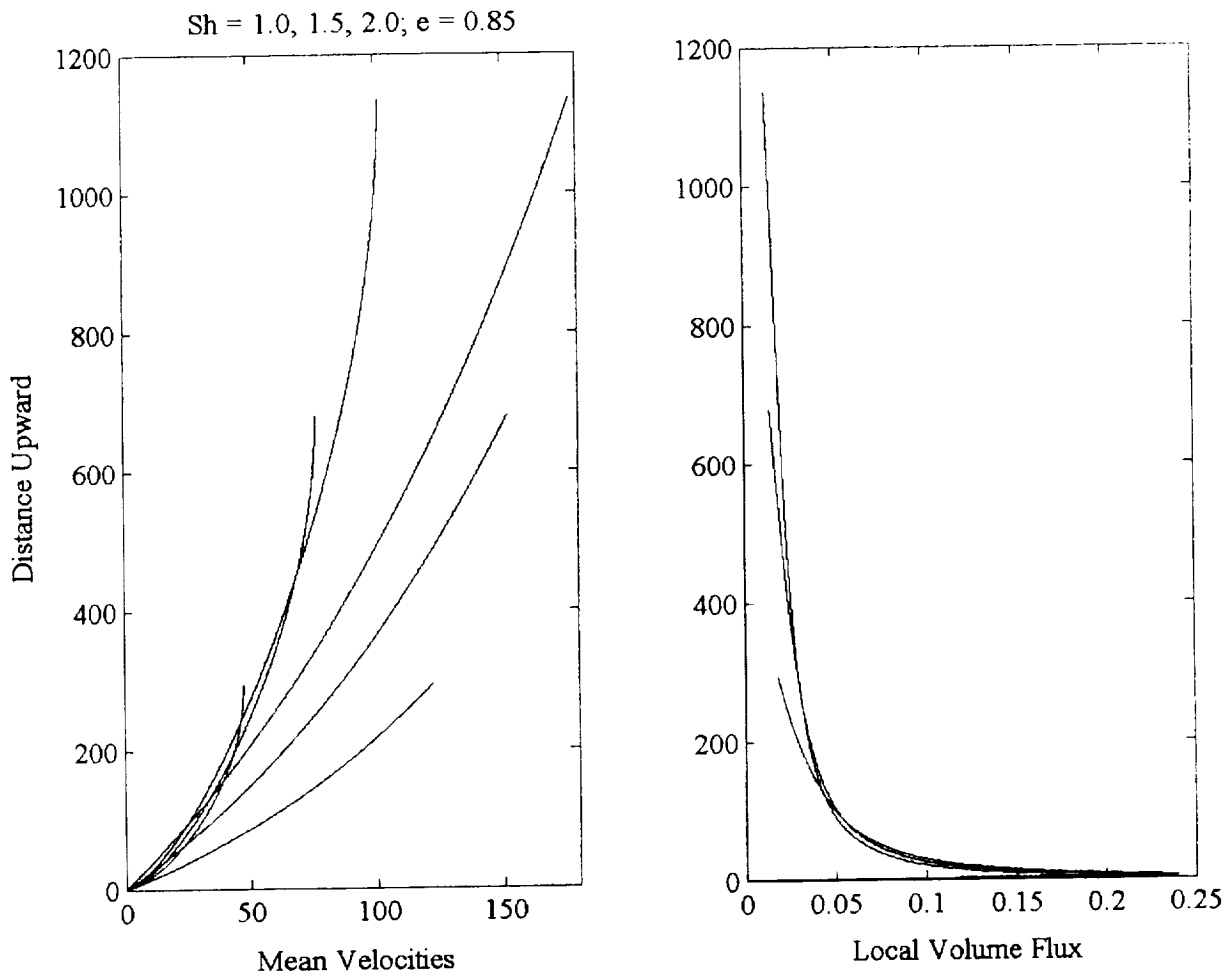

Sand flux/depth: $q = C\tau^{3/2}$

Conclusions

In a near-bed boundary layer of sand in air,

for wind speeds between 30 and 50 km/hr at the top of the layer, turbulent suspension is dominated by inter-particle collisions;

for increasing wind speeds above 50 km/hr, turbulent suspension becomes increasingly important;

for wind speeds decreasing below 30 km/hr, inter-particle collisions become less frequent than collisions with the bed and saltation plays the dominant role.

GRAVATIONAL INSTABILITY IN SUSPENSION FLOWS

Ileana C. Carpen and John F. Brady

Division of Chemistry and Chemical Engineering
California Institute of Technology
Pasadena, CA 91125
626-395-4183, 626-586-8743(Fax), jfbrady@caltech.edu

The gravity-driven flow of non-neutrally buoyant suspensions is shown to be unstable to spanwise perturbations when the shearing motion generates a density profile that increases with height. The instability is simply due to having heavier material over light. The wavelength of the perturbation is found to be on the order of the thickness of the suspension layer. The parameters important to the problem are the angle of inclination of the layer relative to gravity, the relative density difference between the particles and fluid, the ratio of the particle size to the suspension layer, and the bulk volume fraction of particles. An example showing the growth rate as a function of wave number is shown below.

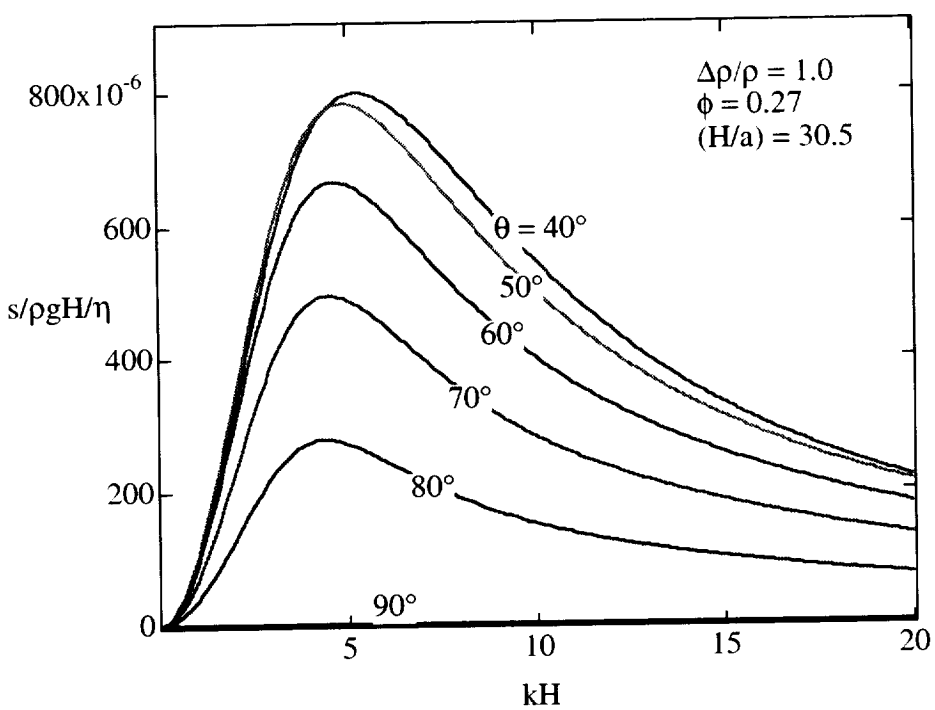

Gravitational Instability in Suspension Flows

Ileana C. Carpen & John F. Brady

Division of Chemistry & Chemical Engineering
California Institute of Technology
Pasadena, CA 91125

With help from: Z. Fang
And backed by: NASA

Particle Migration (e.g. channel flow)

- Neutrally buoyant, nonBrownian particles: $Re = 0, Pe = \infty$
- Shear-induced migration (Leighton & Acrivos 1987)

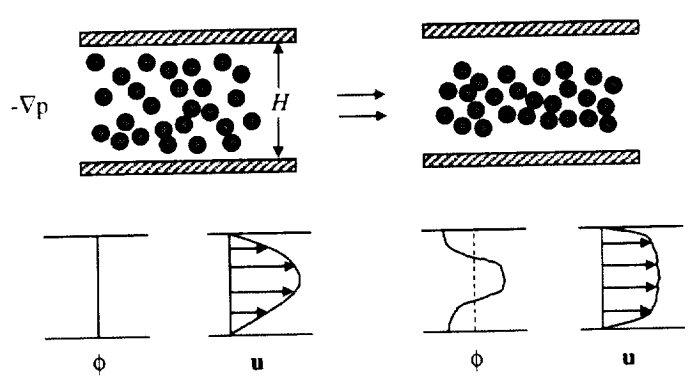

Pressure-driven flow of suspensions ($H/a = 30, \phi_A = 0.4$)

STOKESIAN DYNAMICS
PRESSURE-DRIVEN FLOW OF SUSPENSIONS

Jeffrey F. Morris, Prabhu R. Nott and John F. Brady

Department of Chemical Engineering
California Institute of Technology

Supported by the Office of Naval Research

Particle Migration

- When the shear rate varies as in pressure-driven flow, particles migrate from regions of high shear rate to low, accumulating at the channel center.
- This behavior can be modeled by writing mass and momentum balances for the particles and fluid -- two-phase flow equations.

Lyon & Leal (1998)

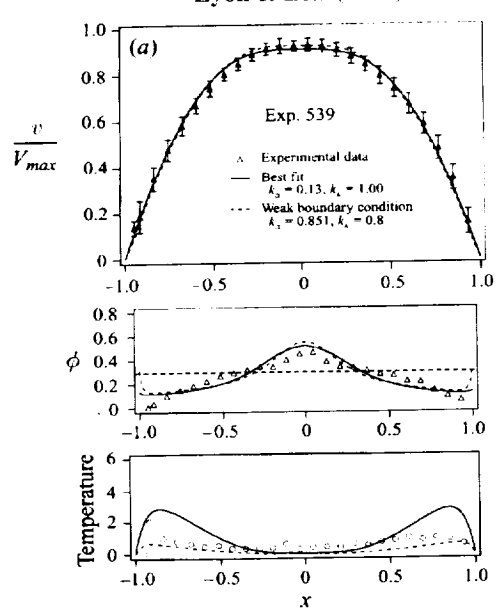

Page 2

Pressure-driven flow plus gravity (heavy particles)

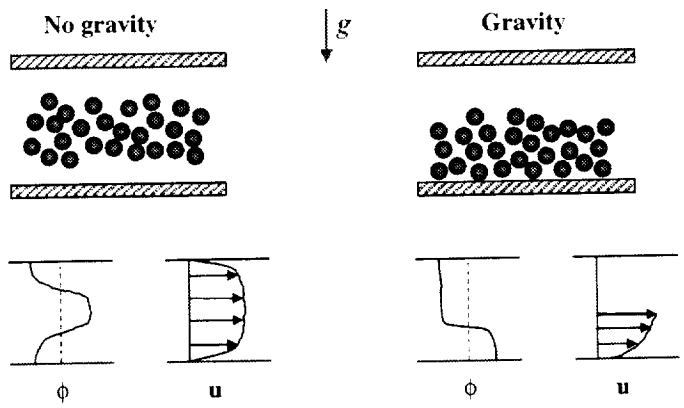

Pressure-driven flow plus gravity

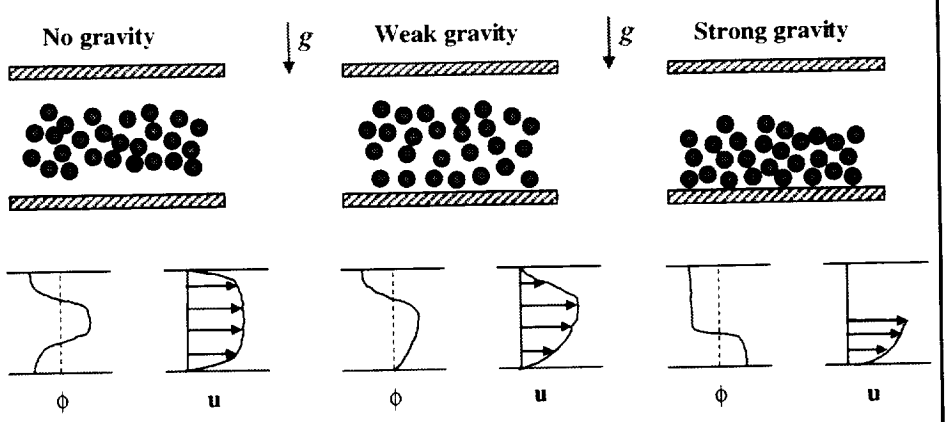

Page 3

Pressure-driven flow of dense suspensions (B = 0.01)

Negatively Buoyant Suspension

Particle Fraction:
$\phi^{A} = 0.40$

Channel Width:
$H / a = 30.54$

Modeling (gravity-driven flow)

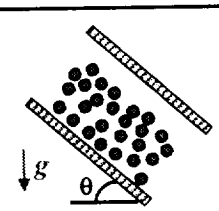

Suspension:

$$\nabla \cdot \langle \boldsymbol{u} \rangle = 0$$

$$\nabla \cdot \langle \sigma \rangle + \rho \boldsymbol{g} = 0$$

Particles:

$$\frac{\partial \phi}{\partial t} + \nabla \cdot \langle \boldsymbol{u} \rangle_p \phi = 0$$

$$\nabla \cdot \langle \sigma \rangle_p + \Delta\rho\phi\boldsymbol{g} - \frac{9}{2}\frac{\eta}{a^2}\frac{\phi}{f(\phi)}\left(\langle \boldsymbol{u} \rangle_p - \langle \boldsymbol{u} \rangle\right) = 0$$

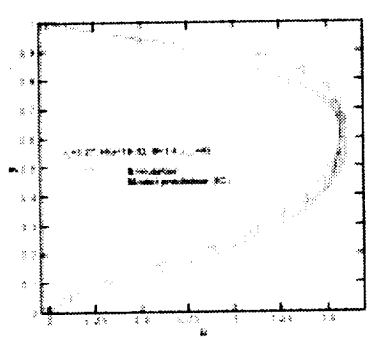

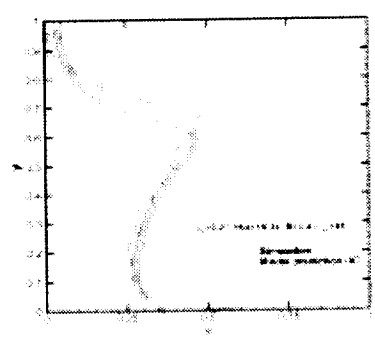

Page 4

Gravitational or Rayleigh-Taylor instability

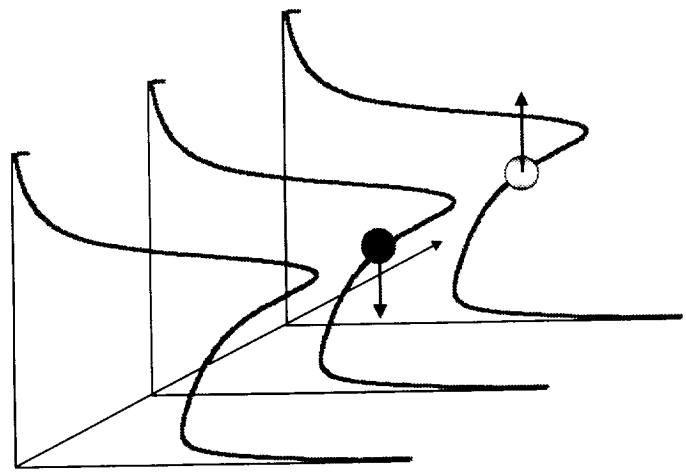

Gravity-driven flow in a channel

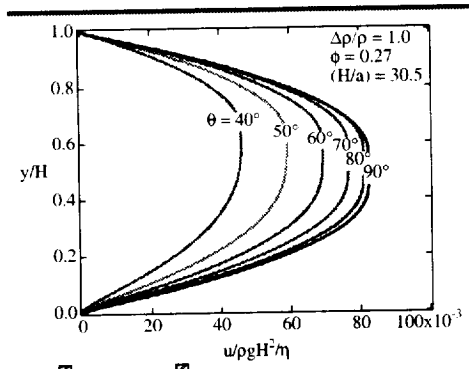

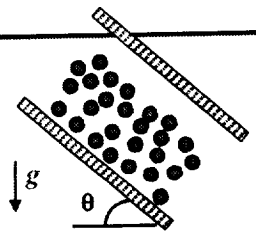

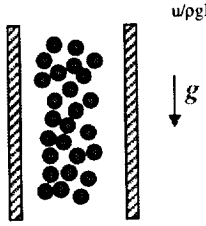

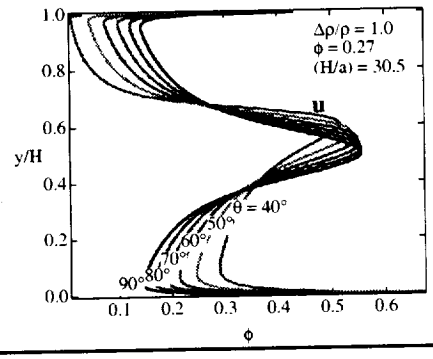

Spanwise Rayleigh-Taylor Instability

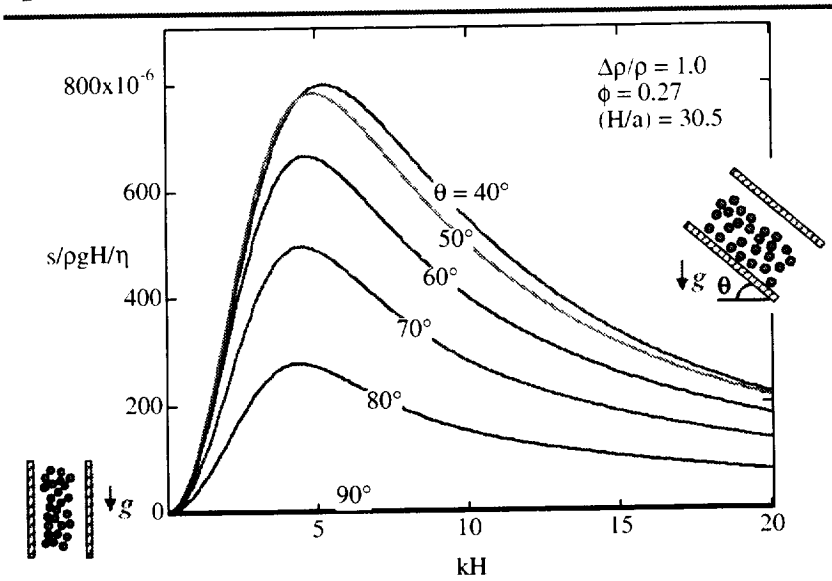

Rotating Drum Experiments (Granular Flow)

Fried *et al*, (*Phys. Fluids* 1998)

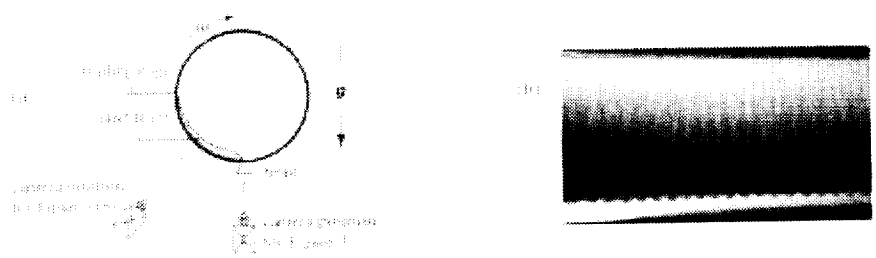

Filling fraction = 1.5%, rotation rate 13.8 rad/s, sand diameter = 0.182mm

Page 6

Pattern Formation in Granular Flows

Rapid granular flow down an inclined plane (Forterre and Pouliquen, *Phys. Rev. Letters* 2001).

sand diameter = 0.25mm

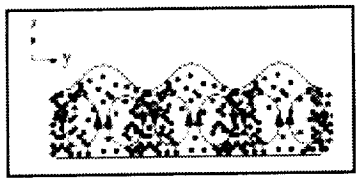

$\lambda \sim 3H$

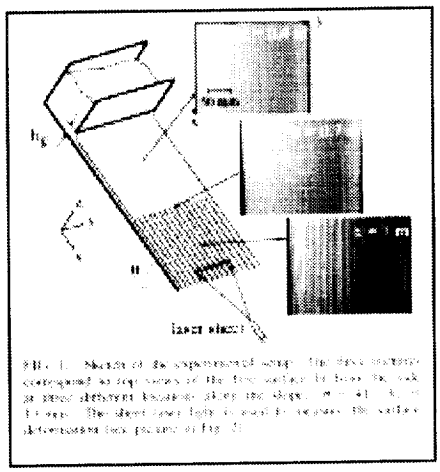

Conclusions

- **A gravitational instability may be present whenever the shearing motion generates an adverse (relative to gravity) particle concentration gradient. This applies to viscous suspensions as well as granular flows.**
- **The wavelength of the instability is set by the shear-induced concentration gradient ($\nabla\phi \sim 1/H$).**
- **The growth rate is determined by the characteristic time scale for the base flow (e.g. $\rho gH/\eta$) and the magnitude of the concentration gradient.**
- **The flow may be unstable in both the transverse (or spanwise) direction and in the longitudinal (or flow) direction. The latter case has a traveling wave component. Their combination can give rise to a chevron pattern.**
- **This mechanism may be important for pattern formation in a variety of multiphase flows.**

Pattern Formation in Suspensions

Thomas, *JFM* 1994; Zoueshtiagh & Thomas, *Phys. Rev. E* 2000

Spiral patterns formed by a dense suspension.

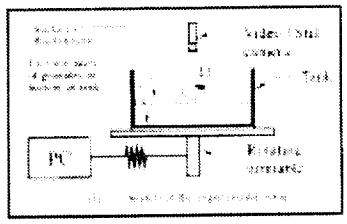

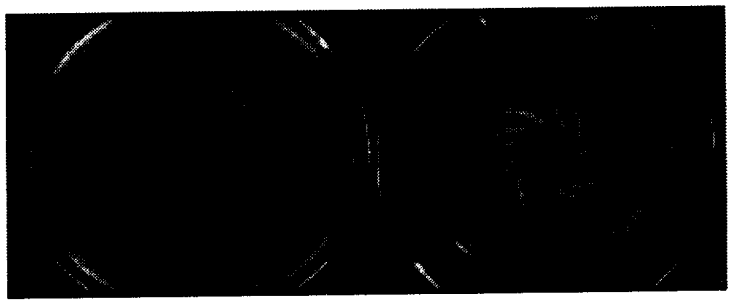

Gravitational instability: effects of parameters

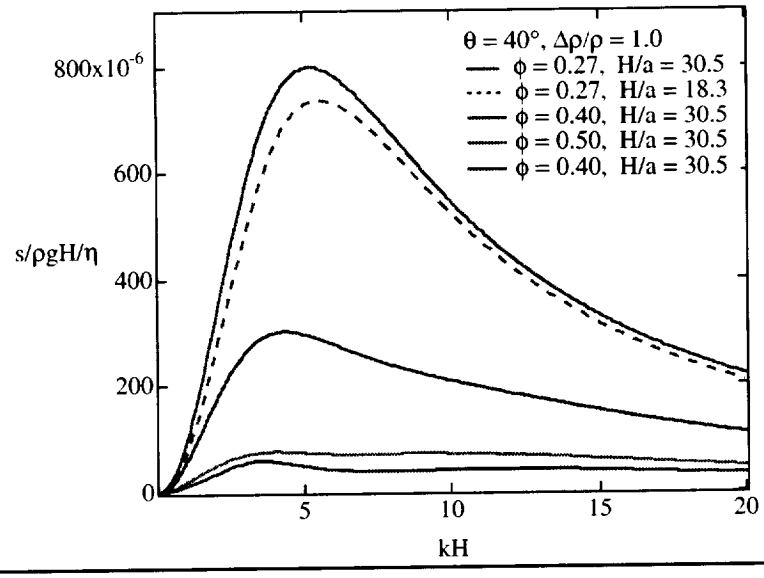

Page 8

DYNAMICS OF CHARGED DUST NEAR SURFACES IN SPACE

Joshua E. Colwell, Mihály Horányi, Scott Robertson, and Amanda A. Sickafoose
LASP, University of Colorado, Boulder CO 80309-0392, josh.colwell@lasp.colorado.edu,
303-492-6805, Fax: 303-492-6946

ABSTRACT

Objects in plasma, such as planetary bodies in the solar wind, charge to a floating potential determined by the balance between charging currents in the local plasma environment. In cases where secondary electron emission and photoemission are weak, objects will become negatively charged due to electron collection and will be surrounded by a plasma sheath. Solar ultraviolet radiation can produce a photoelectron sheath above the sunlit surface of airless planetary bodies. In both cases an electric field is present near the surface that can accelerate charged dust particles near the surface. Dust may be stably levitated if the electric force balances the gravitational force.

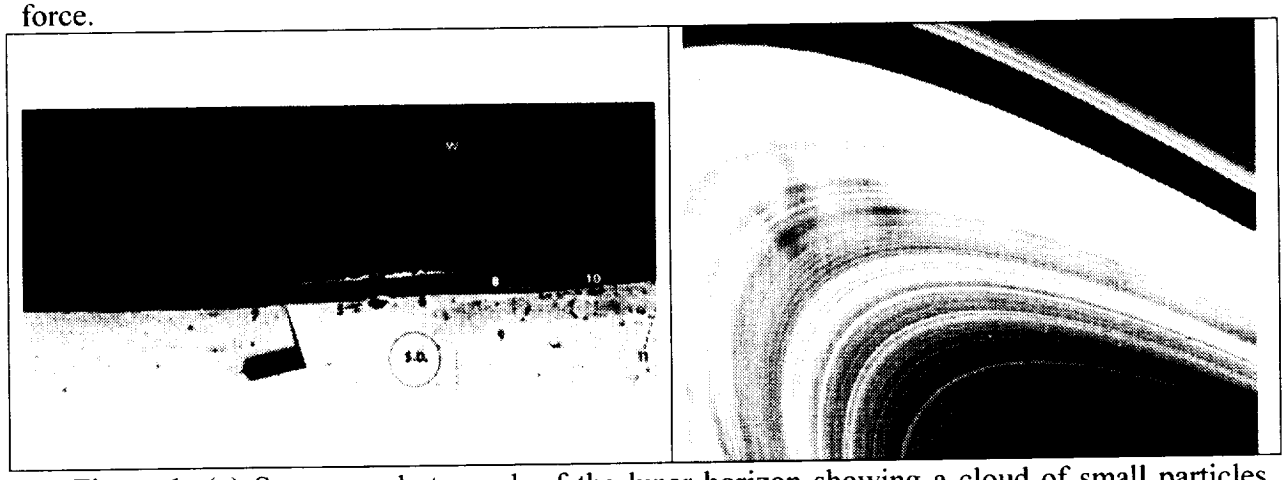

Figure 1: (a) Surveyor photograph of the lunar horizon showing a cloud of small particles suspended 1 m above the surface. The circle labeled "S.D." indicates the apparent size and direction to the Sun [1]. (b) Voyager 2 image of Saturn's rings. The dark smudges are "spokes" of dust particles lifted off the surface of the larger ring particles by electrostatic forces [2].

Experiments in a plasma sheath have shown that particles can be stably levitated with surface potentials consistent with those expected on planetary surfaces [3]. Our experiments have also shown that particles can be lifted off the surface by the electric field without any additional disturbance. This may explain the separation of dust from the surfaces of larger particles in Saturn's rings observed as "spokes" by local plasma presumably generated by an impact (Figure 1). Observations of smooth deposits of regolith in crater bottoms on the asteroid 433 Eros by the NEAR spacecraft suggest a transport mechanism for regolith [4]. Levitation of charged dust and transport in an inhomogeneous electric field is a possible explanation for the distribution of regolith on Eros and other asteroids. More generally, acceleration of charged dust in the near-surface sheath can lead to loss of fine-grained particles from objects with weak gravitational accelerations.

We have carried out experiments on charging, levitation, and transport of dust in plasma and photoelectron sheaths. A tungsten filament beneath the surface plate creates the primary electrons that ionize gas in the chamber. When the surface is biased to a sufficiently high voltage

(-40V to -80V), dust particles are lifted off the surface. Some of these particles, depending on size and mass, become stably levitated a few cm above the surface [3]. On objects with weaker surface gravity the particle size-dependent levitation height is higher.

In addition to levitation our experimental studies show that dust can be transported horizontally over a uniform surface in a uniform plasma sheath. We conducted experiments where a surface is partially covered by dust grains and partially clean. After cycling the plasma on and off, net transport of dust to the initially dust-free portions of the surface is observed. Further experiments will include topographical features on the surface simulating craters and rocks, and we will quantify the horizontal transport of dust in the sheath as a function of grain properties and plasma properties.

Simple numerical simulations also show a net transport of dust when inhomogeneities in the sheath are introduced. We calculate the trajectories of individual dust grains using a numerical integrator that simultaneously solves for the charge on the particle. The forces on the particle are gravity downward and the electric force resulting from the grain charge and the electric field normal to the model surface that is produced by the sheath. Although there are no horizontal forces in our initial simulations, horizontal transport occurs as a result of a combination of initial horizontal velocity components for dust lifted off the surface, the effects of topography, and discontinuities in the photoelectron sheath at the terminator. When dust particles enter shadow the sheath vanishes in this model, and the particle falls to the surface under the effects of gravity. In our simulations this leads to an accumulation of dust at the terminator. Dust also accumulates at the borders of topographical features such as blocks and craters (Figure 3).

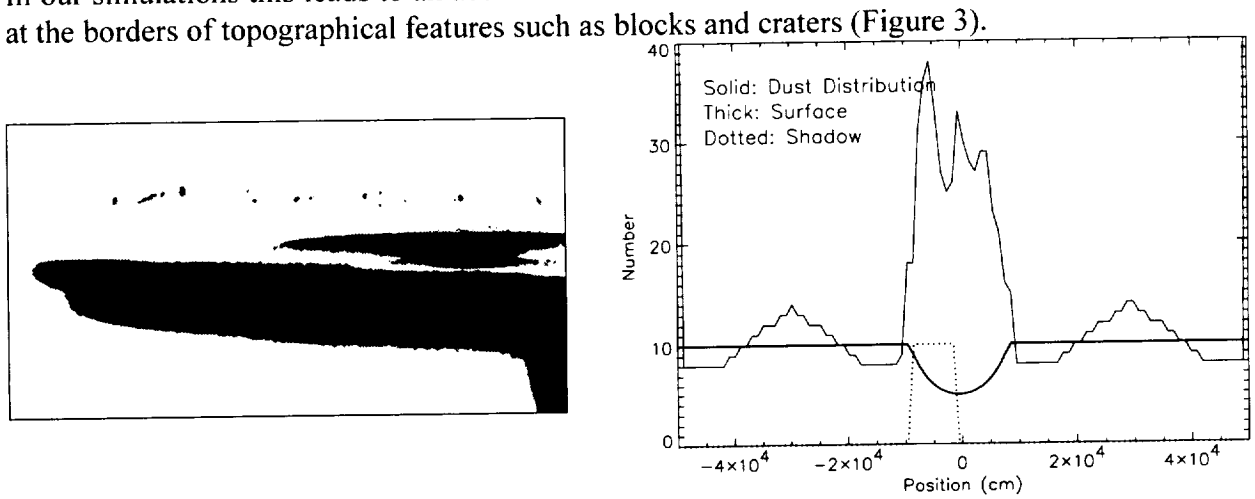

Figure 3: (a) Negative image of levitated dust in our laboratory experiment [3]. (b) Numerical simulation of dust accumulation in a crater on a low-surface-gravity object. Particles accumulate in the shadow where no electric force counteracts gravity. The piles on either side of the crater are edge effects of the simulation.

More realistic modeling of the sheath and the surface at these boundaries are planned, but the basic phenomenon of dust accumulation at shadow and topographical boundaries should persist.

REFERENCES

[1] Rennilson, J. J., and D. R. Criswell, *The Moon*, **10**, 121-142 (1974).

[2] Goertz, C. K., *Reviews of Geophysics*, *27*(2), 271-292 (1989).

[3] Sickafoose, A.A., J.E. Colwell, M. Horányi, and S. Robertson, *J. Geophys. Res.* (sub. 2002).

[4] Robinson, M. S., P. C. Thomas, J. Veverka, S. Murchi, B. Carcich, *Nature*, **413**, 396 (2001).

Dynamics of Charged Dust Near Surfaces in Space

Joshua Colwell, Mihály Horányi, Amanda Sickafoose
Laboratory for Atmospheric and Space Physics
Scott Robertson
Dept. of Physics
University of Colorado, Boulder

Mobile Dust in the Solar System

Dark radial streaks or "spokes" in Saturn's rings are believed to be dust particles lifted off the surface of larger ring particles by electrostatic forces. In this Voyager image, the spokes cast a shadow on the bright B ring whose particles are predominantly cm-sized and larger.

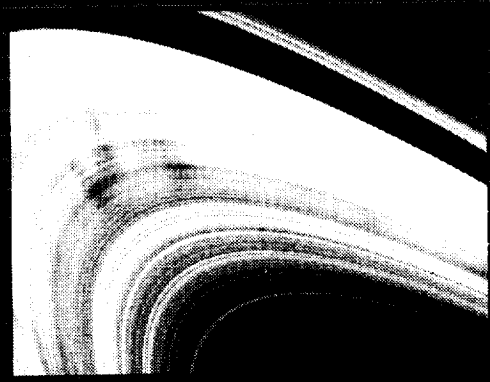

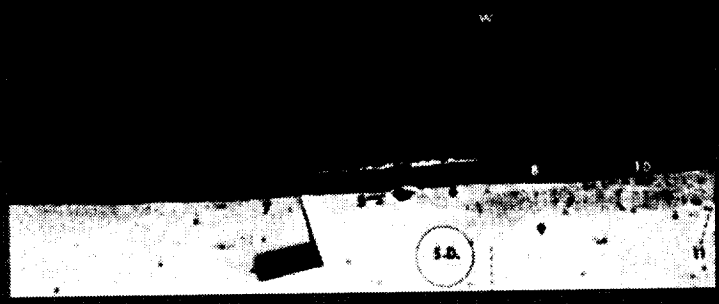

This Surveyor image of the lunar horizon shows a cloud of dust roughly one meter above the surface near lunar sunset. "S.D." indicates the size and direction of the solar disk (Rennilson and Criswell, 1974).

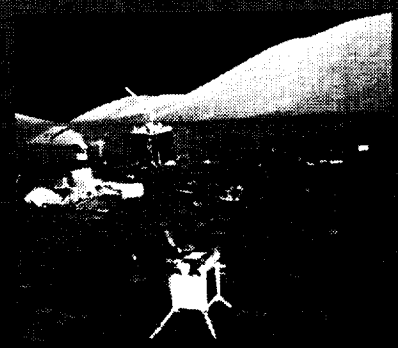

Evidence of dust transport across the lunar surface:LEAM data show degradation of dust sensors facing east, suggesting transport of dust from east to west across the terminator.

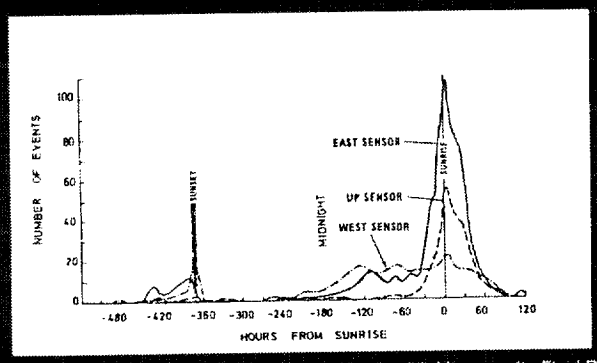

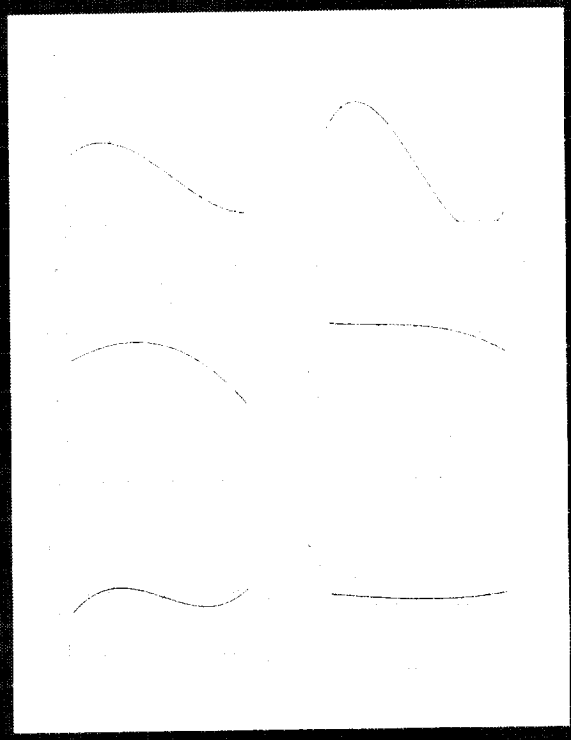

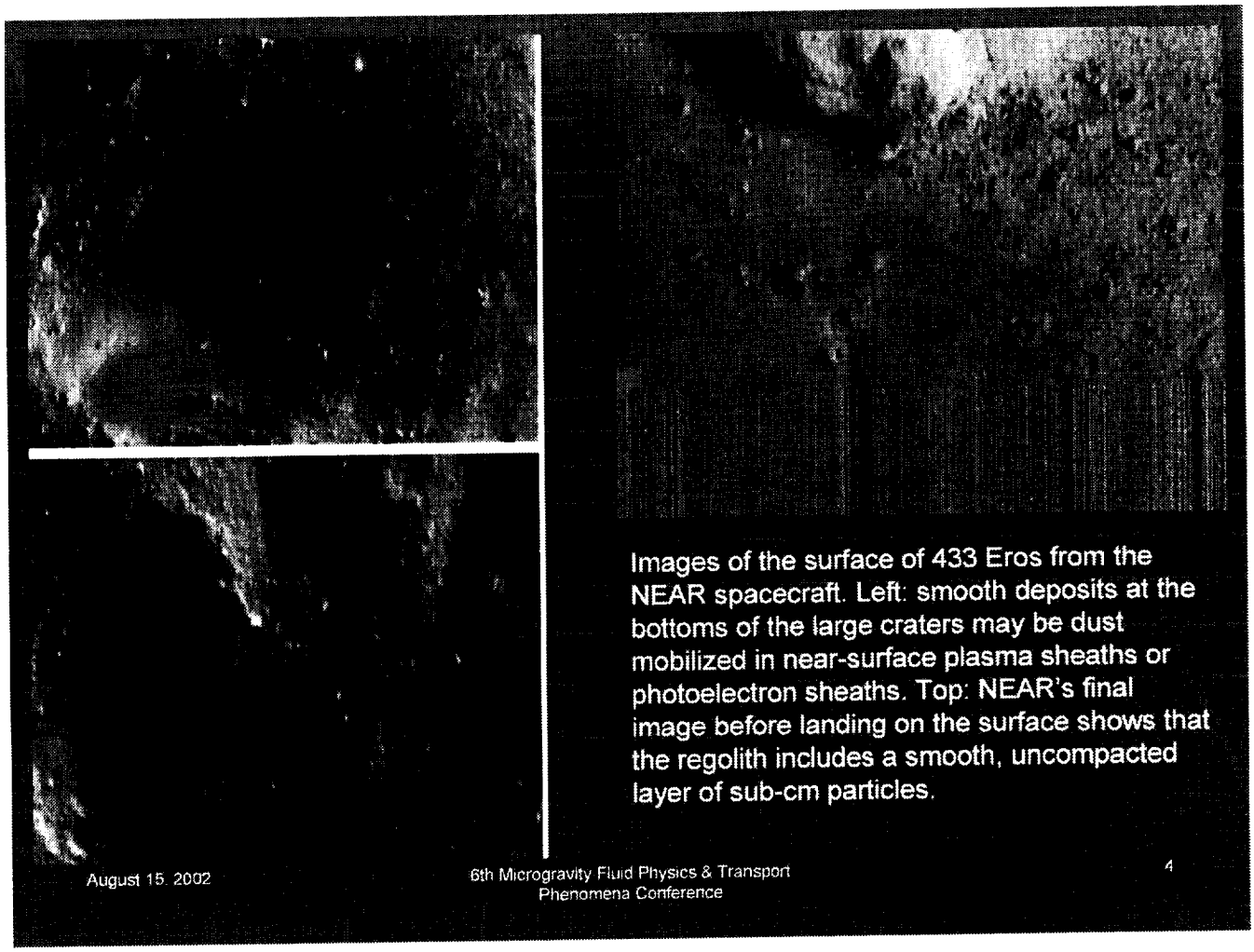
Images of the surface of 433 Eros from the NEAR spacecraft. Left: smooth deposits at the bottoms of the large craters may be dust mobilized in near-surface plasma sheaths or photoelectron sheaths. Top: NEAR's final image before landing on the surface shows that the regolith includes a smooth, uncompacted layer of sub-cm particles.
August 15, 2002
6th Microgravity Fluid Physics & Transport Phenomena Conference
4

Physics of Levitated Dust

- Photoemission of electrons from a surface creates a photoelectron sheath or a kind of electron exosphere above the surface.
- A surface in a plasma, such as the solar wind, will develop a plasma sheath if photoemission is weak or absent. The plasma sheath generates an electric field, E.
- The surface and dust grains beneath a plasma sheath have a negative charge due to collection of the faster electrons in the plasma.
- The surface bias allows particles to lift off the surface (electrostatic repulsion overcomes adhesion).
- Once in the sheath dust can achieve stable levitation due to the balance of the electric and gravitational force.

Sheath and Grain Potential

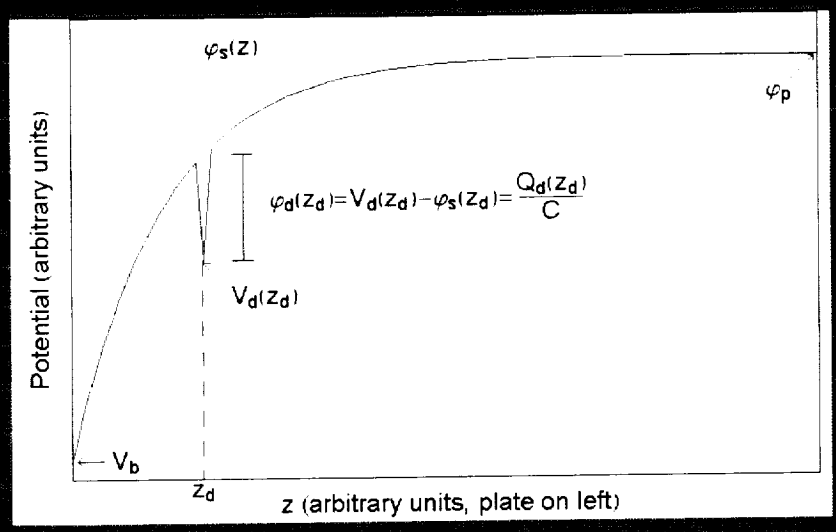

Schematic of the potential in a plasma sheath with a single dust particle. The dust particle potential with respect to the plasma sheath potential is φ_d, and the charge on the grain is Q_d. The electric field is given by the gradient in the sheath potential, $\varphi_s(z)$.

Role of Gravity

- Relevant forces: gravity (mg), electric (qE), adhesion and cohesion.
- $m \sim r^3$ and $q \sim r$, so for $mg \approx qE$ need particular particle size.
- Moon: $mg \approx -qE$ for: r=10μm at the surface
  r=0.1 μm at 100 km (smaller E)
- Asteroids, small moons, planetary rings:
  - Mg << qE for small particles (r~ 10 μm)
  - qE ~ adhesion, cohesion? Large E or mechanical disturbance required to break interparticle bonds.
- Earth: mg>qE unless E large.

Laboratory Experiments

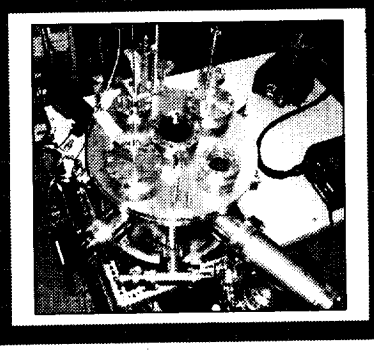

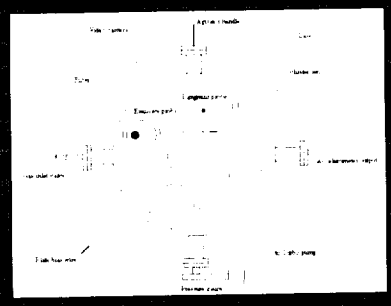

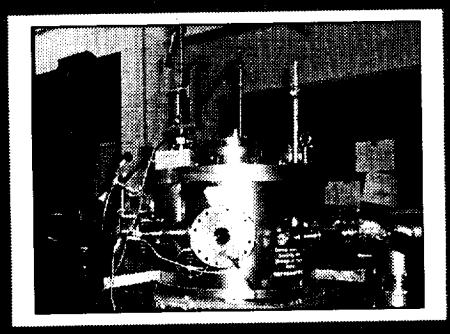

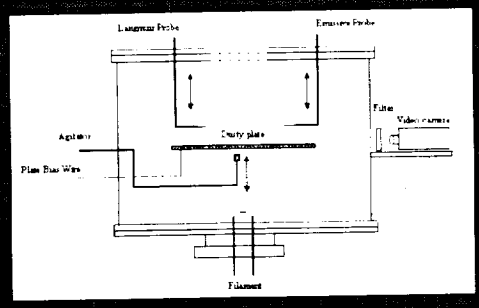

Dust Levitation

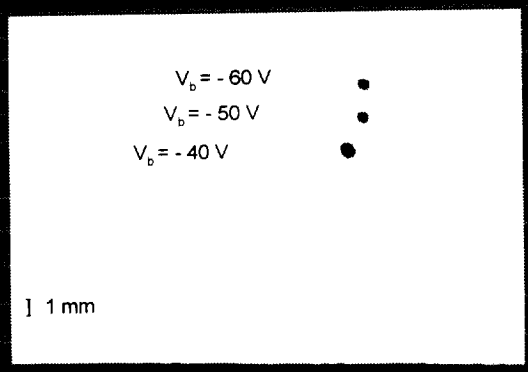

Negative of three superimposed digital photographs showing a stable, levitated polystyrene grain (10.0 μm in diameter) for the surface at three different biases : 40 V, 50 V, and 60 V. As expected, the grain is at the highest position away from the surface when the surface bias is most negative.

Dust Levitation

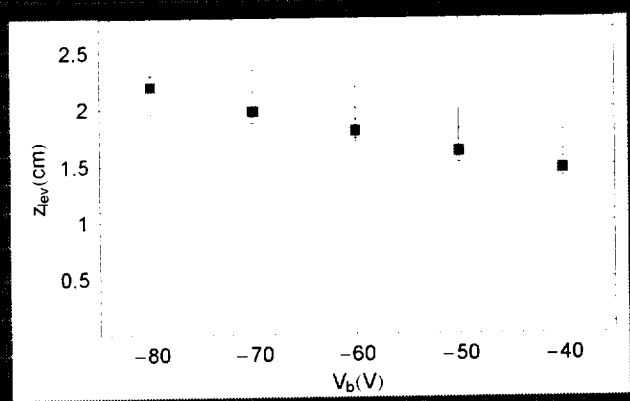

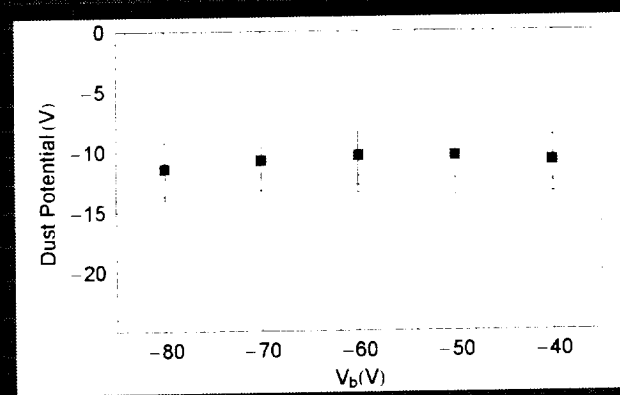

Levitation heights and grain potential as a function of the voltage bias on the surface in our experiment (squares) and predicted values from orbit motion limited (OML) theory (crosses) for 10 μm polystyrene spheres. As the surface is biased to larger negative voltages, the plasma sheath expands and the electric field is stronger leading to a higher levitation height even though the particle potential is roughly constant.

Dust Levitation

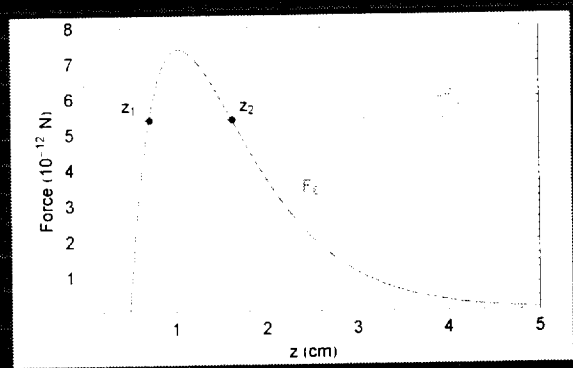

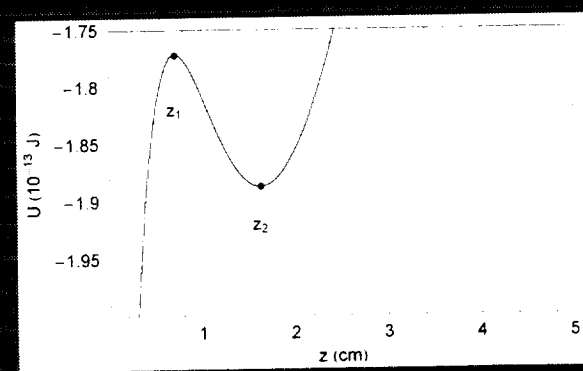

Left: electric and gravitational forces on a 10 μm polystyrene grain as a function of distance above the surface indicating two locations where the forces balance. The surface is biased to -40V.

Right: potential energy of the grain showing that the upper force-balance point is stable.

Grains can escape the surface if they are accelerated to escape velocity by F_E in the sheath.

Dust Levitation

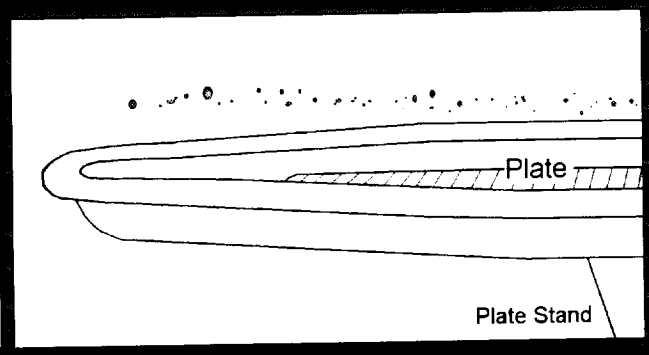

Image (left) and schematic of the experiment including the surface and a cloud of levitated JSC-1 dust grains 1.2 cm above the surface. The laser imaging system only shows those grains at a particular height above the surface. Additional grains are levitated above and below those shown here. Interparticle forces in this levitated cloud can lead to horizontal transport of dust in the sheath.

Dust Transport

- We have performed experiments to look for horizontal transport of dust in a plasma sheath.
- Spots of dust were placed on the surface and the plasma sheath was generated for varying periods of time.
- This is the first step in studying the formation of deposits in craters on asteroids and small satellites and possible migration of regolith.

Dust Transport

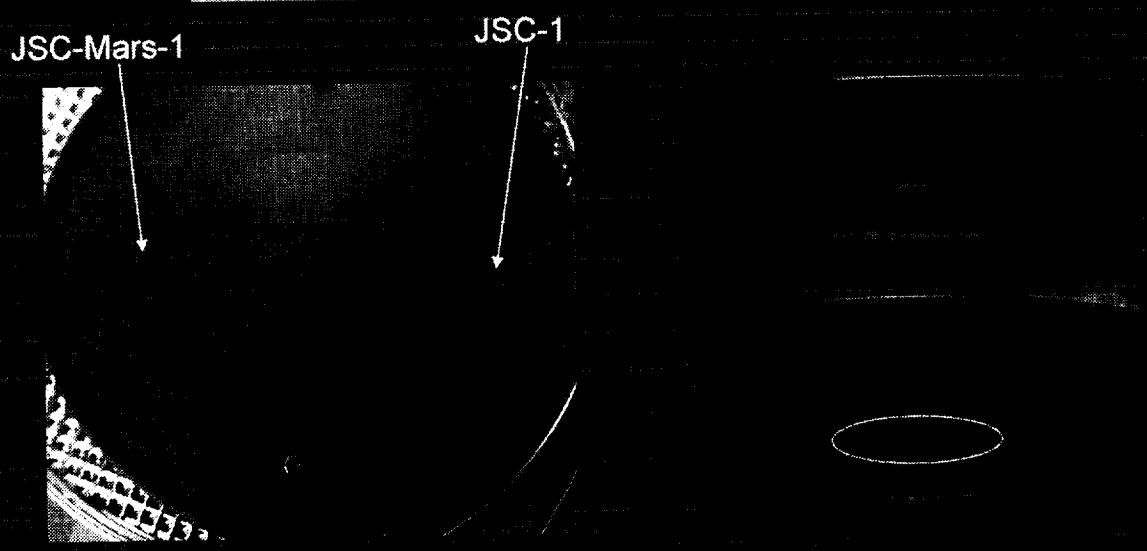

Left: normal view of the graphite surface with spots of JSC-Mars-1 and JSC-1 prior to turning on the plasma sheath. Right: Edge on view of the plate before (top) and after (bottom) running the plasma shows that the dust has spread to a larger area after being levitated in the sheath.

Dust Transport

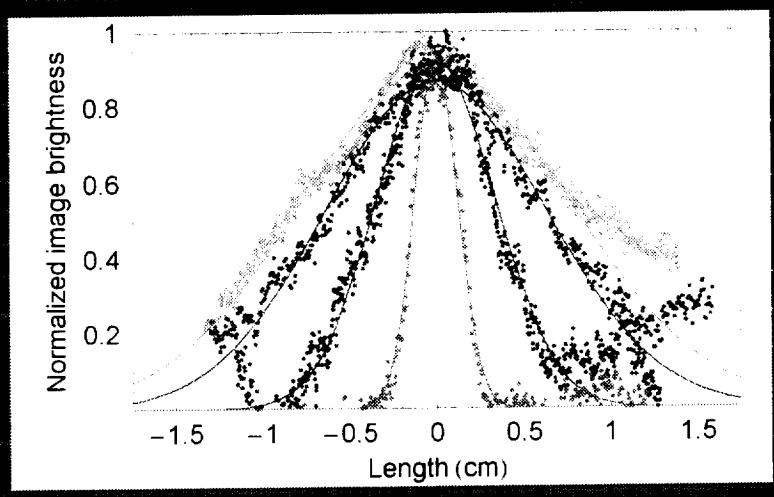

Spreading of JSC-Mars-1 in a plasma sheath as a function of time in the sheath. Red indicates the initial distribution of dust. Purple: after 15 minutes in the sheath; Blue: after 60 minutes; Green: after 120 minutes. Points are for an average of three runs at each duration, and solid lines are best-fit Gaussians.

Numerical Simulations

- 2D model of charged dust motion.
- Grains are launched one at a time from the surface with a range of velocities in two directions above a one-dimensional simulated "surface."
- Grain charge is calculated by current balance within the sheath and the trajectory is simultaneously integrated until the grain comes in contact with the surface.
- Particles with any horizontal component to their velocities fall to the surface as soon as they leave the photoelectron sheath and the upward electric force vanishes. This tends to make particles accumulate in shadowed areas where the surface potential is less and the electric field weaker. In our simulations this appears as an accumulation of dust at the sheath boundary, whether imposed arbitrarily, or as a result of shadowing.
- Topography impedes the horizontal motion of dust lifted off the surface. Particles tend to accumulate in depressions and next to elevated obstacles (blocks or boulders).

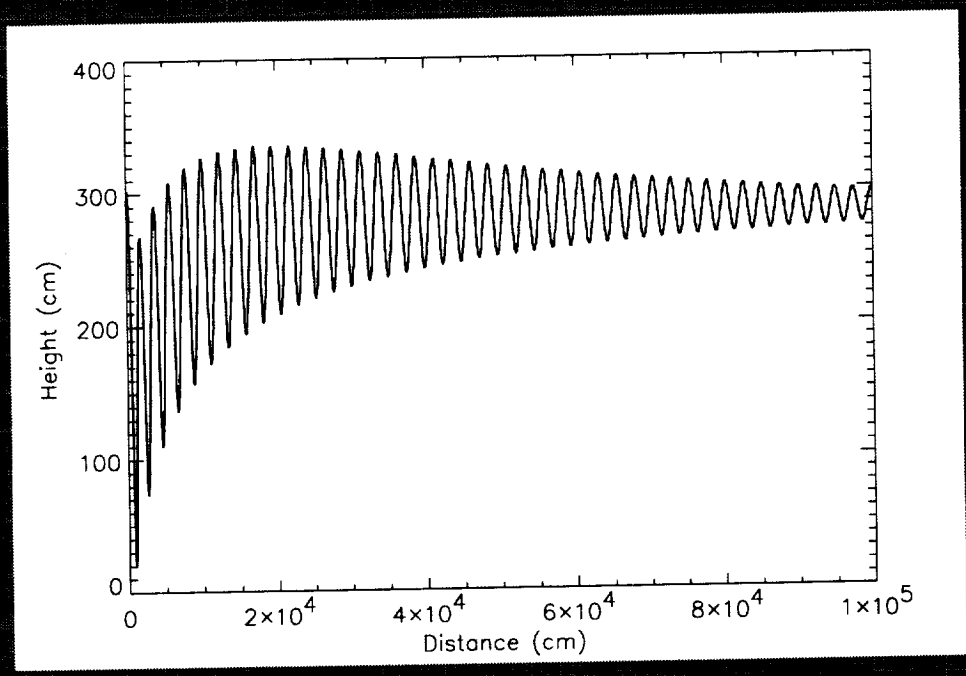

Example trajectory of dust particle levitated in photoelectron sheath. Particle is 0.1 micron radius launched from surface at ~5 m/s. Surface gravity matches that of Mercury.

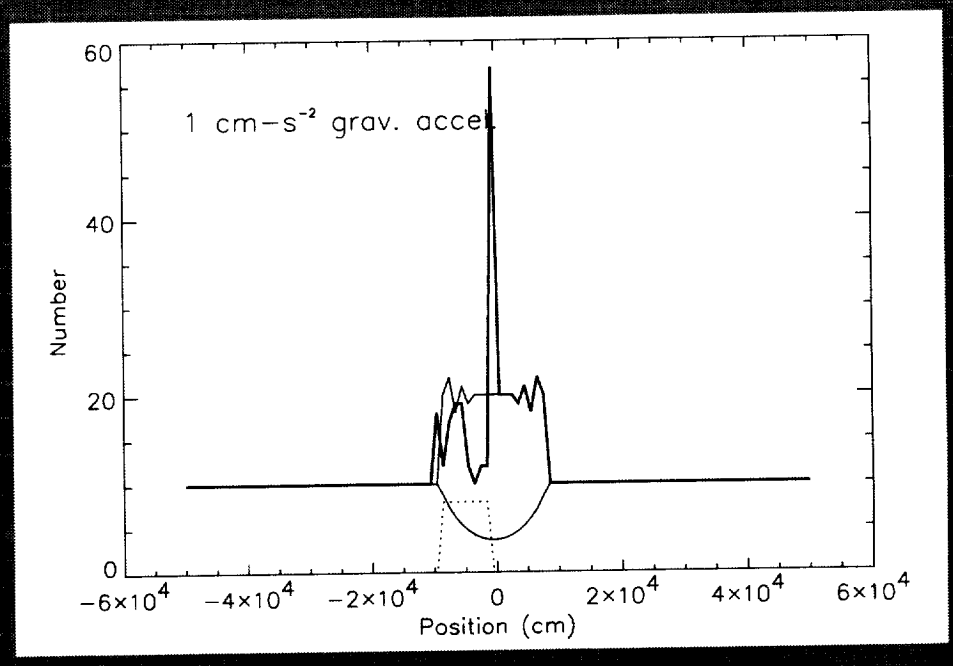

Distribution of final positions of dust particles for a surface with a simulated crater (thick line) and no sheath in the shadowed area (dotted line). Thin line shows final dust positions with a uniform sheath. Dust accumulates at the sheath boundary (where there is no upward electric force) and at the crater rim. Surface gravity is 1 cm-s^{-2}. Initial velocities are 1-100 cm/s.

Planned Work

- Experimental simulations of planetary surfaces including topography: craters and boulders. Look for *net* transport of dust.
- 3-D time-dependent numerical simulations including sheath profiles from experiments to extend results to parameters that cannot be simulated in the lab.
- Similar experiments with photoelectron sheath.
- Simulate diurnal cycle by cycling sheath off and on.

Summary

- Dust particles have been experimentally levitated in a plasma sheath.
  - Dust potential and levitation height match theory.
  - Levitated particles exposed to UV light levitated at a lower height due to decreased charge.
  - No external disturbance required to break cohesion at surface if voltage is high enough.
- Dust in a sheath undergoes horizontal transport.
- Changes in UV illumination and topography can lead to net transport of dust over a surface, providing an explanation for "ponds" of dust in crater bottoms on Eros.
- Net transport of dust over surfaces has broad-ranging implications for planetary science and spacecraft on surfaces.

MICROGRAVITY-DRIVEN INSTABILITIES IN GAS-FLUIDIZED BEDS

Anthony J.C. Ladd
University of Florida

David A. Weitz
Harvard University

A dense pack of solid particles can be fluidized by an upward flow of liquid, which counterbalances the gravitational force on the particles. The resulting suspension is stable for sufficiently small fluid velocities, although the particle dynamics are complex and still not fully understood. A packed particle bed can also be fluidized by a gas flow, but in this case a stable suspension of moving particles cannot be produced in earth's gravitational field. Kinetic theory of gas-fluidized beds predicts that the bed is always unstable to particle inertia, whichis several orders of magnitude larger than fluid inertia in this case. In order to study the onset of this particle-induced instability, the minimum fluidization velocity must be reduced by several orders of magnitude; we believe that this can be most successfully accomplished in a reduced gravity environment. We expect that in a microgravity environment it would be possible to explore the transition between stable and unstable flow regimes in gas-fluidized beds, and contrast the behavior of particle inertia (gas-fluidized) and fluid inertia (liquid fluidized) driven instabilities. However in this preliminary study the investigations of gas-fluidized systems will be done numerically. We will compare and contrast the stability conditions and flow patterns arising from increasing fluid inertia ($Re > 1$, $St \sim Re$) and increasing particle-inertia ($Re < 1$, $St > 1$). Laboratory experiments on liquid-fluidized beds are being used to validate the predictions of the numerical simulations.

In this talk I will summarize results from computer simulations of particles settling in a low-Reynolds number regime. Experimental measurements of the velocity fluctuations in a sedimenting suspension [1, 2] are independent of system size for sufficiently large containers. However, this observation is at odds with theoretical [3] and numerical [4, 5] predictions for a random distribution of particles. I will present new data for suspensions bounded by a rigid container, and compare them with results for homogeneous suspensions with periodic boundary conditions. Velocity fluctuations in vertically*inhomogeneous* suspensions are found to saturate under conditions similar to those found in laboratory experiments, while in vertically *homogeneous* suspensions the velocity fluctuations diverge with increasing container dimension (Fig. 1) [6].

The strikingly different behavior in the velocity fluctuations for the different boundary conditions is caused by the interfaces between the dense pack, the homogenous suspension, and the supernatent fluid. These interfaces are a sink for the fluctuation energy, which drains out of the system at a rate that is roughly proportional to the inverse of the cell height. Random density fluctuations convect to one of these two interfaces and are absorbed by the density gradient at the interface. A scaling argument suggests that convection of density fluctuations to the boundaries at

the top and bottom of the suspension leads to a correlation length proportional to the mean interparticle spacing $\alpha^{1/3}$.

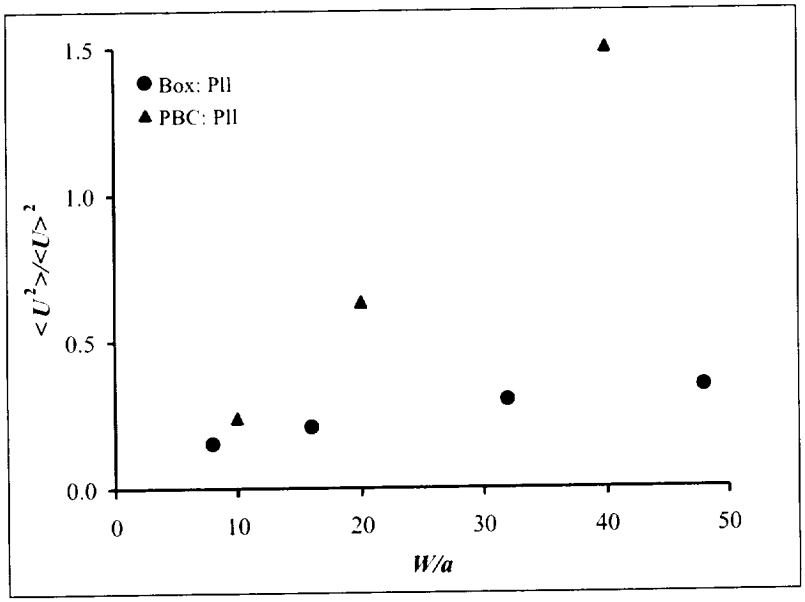

Figure 1. Fluctuations in the settling velocity as a function of container width a cell bounded in all three directions by no-slip walls (Box) and a cell that is periodic in all three directions (PBC). The statistical errors are comparable to the size of the symbols.

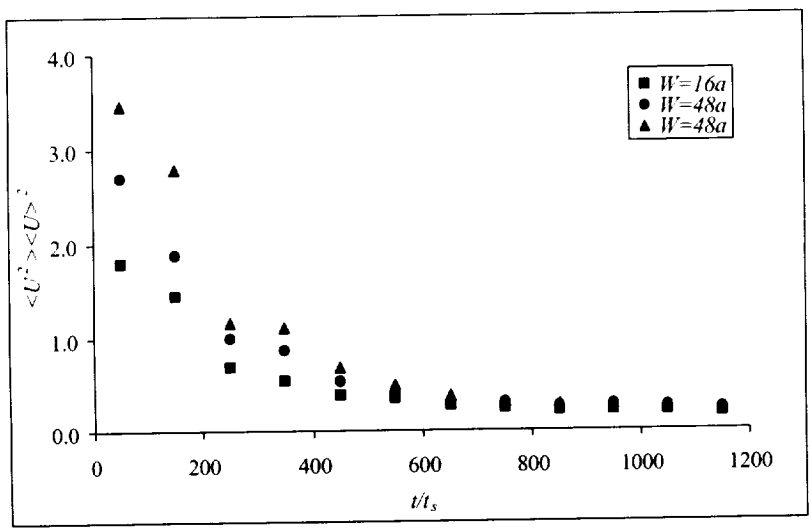

Figure 2. Time dependence of relative velocity fluctuations for different container widths.

1. Segrè, P.N., E. Herbolzheimer, and P.M. Chaikin, *Long-Range Correlations in Sedimentation.* Physical Review Letters, 1997. **79**(13): p. 2574-2577.
2. Nicolai, H. and E. Guazzelli, *Effect of the vessel size on the hydrodynamic diffusion of sedimenting spheres.* Physics of Fluids, 1995. **7**(1): p. 3-5.
3. Caflisch, R.E. and J.H.C. Luke, *Variance in the sedimentation speed of a suspension.* Phys. Fluids, 1985. **28**: p. 759.
4. Ladd, A.J.C., *Hydrodynamic Screening in Sedimenting Suspensions of non-Brownian Spheres.* Physical Review Letters, 1996. **76**(8): p. 1392-1395.
5. Ladd, A.J.C., *Sedimentation of homogeneous suspensions of non-Brownian spheres.* Physics of Fluids, 1997. **9**(3): p. 491-499.
6. Ladd, A.J.C., *Effects of container walls on the velocity fluctuations in sedimenting suspensions.* Phys. Rev. Lett., 2002. **88**: p. 048301.

NASA/CP—2002-211212/VOL1

Microgravity-driven instabilities in gas-fluidized beds

Tony Ladd
University of Florida
Dave Weitz
Harvard University

NASA Fluid Physics Meeting 2002

Sedimentation of monodisperse spheres

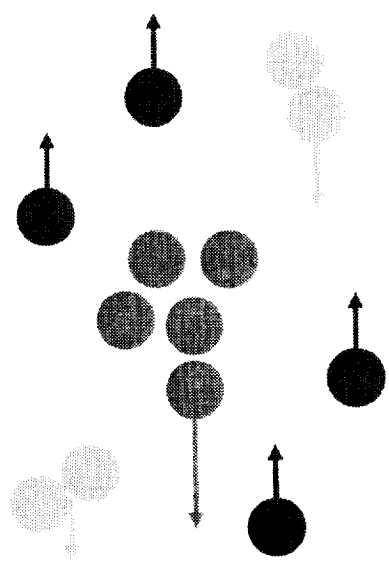

Clusters fall faster than isolated spheres:

$$U \propto \frac{M_C g}{R_C} \propto R_C^2$$

Displaced fluid sweeps isolated spheres upwards

Large fluctuations in particle velocity,

$$\sqrt{\langle U^2 \rangle} \approx \langle U \rangle$$

leads to hydrodynamic dispersion (diffusion)

Experimental and numerical investigation of fluidization/settling of suspended particles

- Macroscopic dynamics of a fluidized bed characterized by
  - (i) Reynolds number (fluid inertia) $Re = \rho_f UL / \mu$
  - (ii) Stokes number (particle inertia) $St = \rho_p UL / \mu$
- Focused on limiting case $Re \to 0,\ St \to 0$
  - Reynolds stress and particle stress << viscous stress
  - Stable bed (no macroscopic density fluctuations)
- Explored connections between fluctuations in particle velocity, microstructure, and boundary conditions
- Experiment data from PIV and DLS measurements
- Numerical simulations of particle dynamics in viscous fluid

Velocity-fluctuations controlled by long-range hydrodynamic interactions

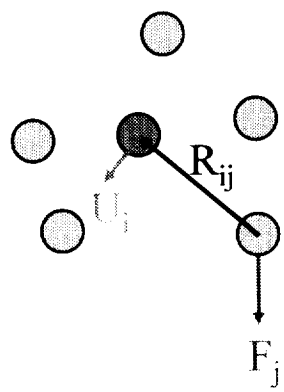

Velocity of a test-particle is affected by distant neighbors

$$U_i \sim \sum_{j \neq i} R_{ij}^{-1} F_j$$

Diverging particle velocity, $\propto L^2$ suppressed by backflow (Batchelor)

Also explains why $\langle U \rangle < U_0$

But fluctuations are unaffected by backflow

$$\langle U^2 \rangle \sim \int R^{-2} d^3R \sim L$$

Caflisch-Luke 1988

Experiments have shown that $\langle U^2 \rangle$ is independent of L

Do boundary conditions affect $<U^2>$? Bulk screening or surface effects?

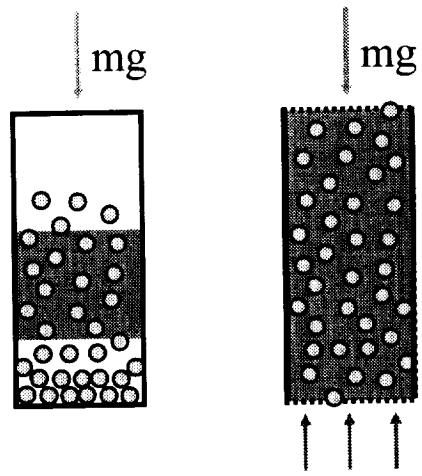

Sedimentation

Fluidization with PBC

Is there a "bulk" region in a sedimenting suspension?

Is there a steady state in a sedimenting suspension?

Computational details

- Cells 960*a*-1920*a* high; square X-section, width 8*a* - 60*a*
  - With and without walls at the top and bottom
- From 1000 to 70,000 solid particles
  - Volume fraction 2% &13%
- Up to 4×10^6 fluid grid points- particles are 3-5 grid points in diameter. Lattice-Boltzmann fluid solver.
- Largest simulations run for ~ 300 hours on 4X600 MHz P3
  - 150,000 time steps- Re ~ 0.2

Boundary conditions at the top and bottom make a qualitative difference to $<\Delta U^2>$

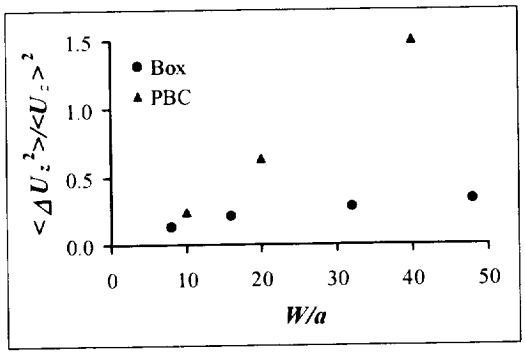

Fluctuations saturate in systems with container bottom (Box)
But fluctuations in homogenous suspensions diverge with W (PBC)

Sedimentation is not homogeneous

Effects of boundaries always present

No bulk screening

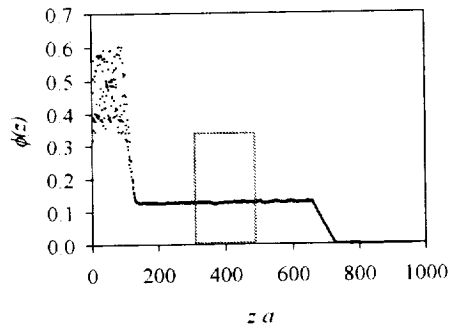

Time dependent fluctuations in vertically inhomogenous suspensions

- Fluctuations in homogeneous suspensions are size dependent and constant in time (indicated schematically by arrows)

•Initially amplitudes similar to homogeneous suspensions, but decay in time to quasi steady state
•Size-independent fluctuations for $W > 30a$
•Consistent with experiments of Segre et al. / Nicolai & Guazzelli

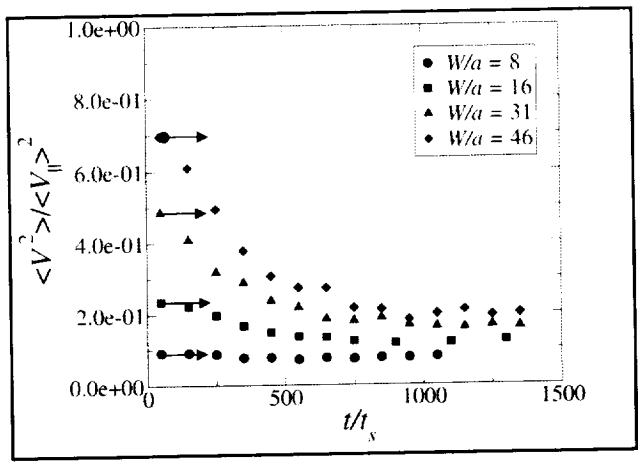

Scaling model for the correlation length

- Fluctuations drain to upper and lower interfaces (Hinch)
  - Convective velocity from balance of mass fluctuations $\delta N \propto N^{1/2} \propto \sqrt{\phi l^3}$ and drag force $\eta v_l l$:

$$v_l \sim U_0 \sqrt{\phi l / a}$$

  - Time to reach steady state ~ H/v_l
- Assuming steady state
  - Random source + diffusive decay leads to $<\delta U^2> \propto L$

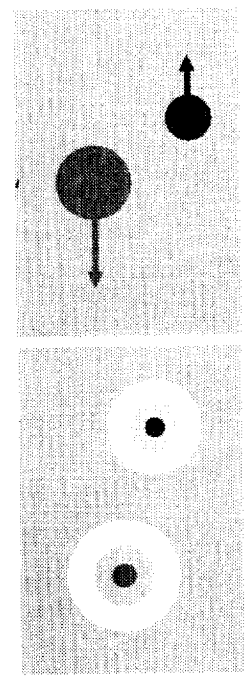

Diffusive growth + convection leads to a correlation length

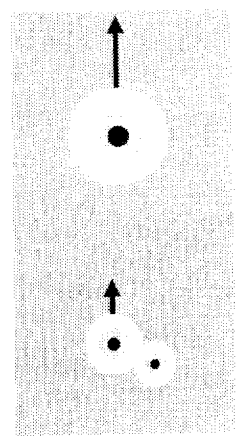

- Include convective decay

$$t_l \sim l/v_l \sim (\phi a / l)^{1/2} t_S$$

- Diffusion is source of large-scale fluctuations

$$t_D \sim l^2/D_H \sim (l/a)^2 t_S$$

- Critical length scale l_c where $t_D \sim t_l$
  - maximum size for a self-sustaining fluctuation $l_c \sim a\phi^{-1/3}$
- Consistent with experiment (Segre)

Velocity fluctuations are controlled by the suspension microstructure (no inertia)

Fluctuations in particle number density: $S(\mathbf{k}) = \langle n(\mathbf{k}) n(-\mathbf{k}) \rangle$

Drives fluctuations in particle velocity $\langle U^2 \rangle \sim \int S(\mathbf{k}) k^{-4} d\mathbf{k}$

HI

Equilibrium:
Homogenous (PBC): $S(\mathbf{k} \to 0) = C; \quad \langle U^2 \rangle \sim \frac{1}{k_{\min}} \sim L$

Ladd (1996)

For bounded $\langle U^2 \rangle$; $S(\mathbf{k} \to 0) \sim k_\perp^2;$ Levine et al. (1998)

Simulation data agrees with predictions of convection-diffusion model

$S(\mathbf{k})$ vanishes as $k_\perp \to 0$

Finite velocity variance

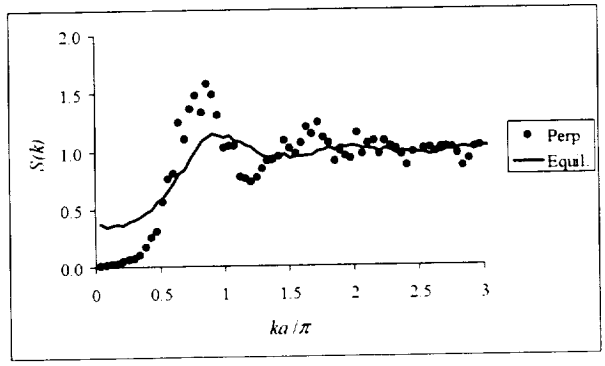

$$S(\mathbf{k}) \sim \frac{q^2}{q^2 + \Gamma q_\perp^2}$$

Renormalized convection-diffusion model:
Levine et al.

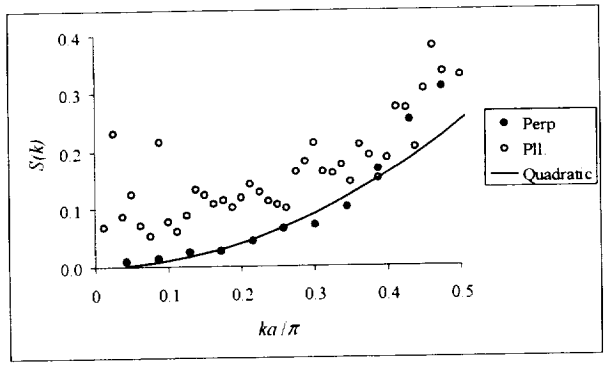

Dilute suspensions in large cells do not come to steady state

Velocity fluctuations in dilute suspensions (1% by volume) measured by PIV and DLS

a) in smaller cells (up to 150*a*) fluctuations decay to steady state

b) in larger cells fluctuations decay continuously, without ever reaching steady state

c) exponential decay with time constant proportional to container height

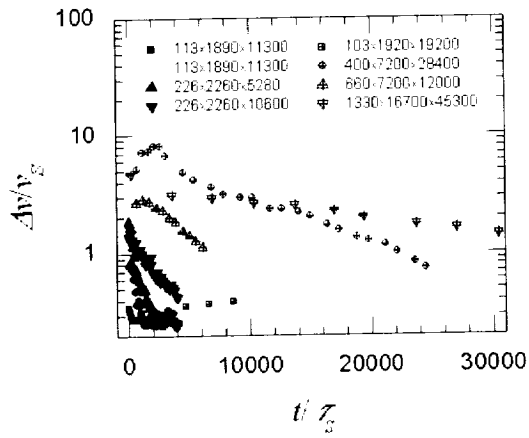

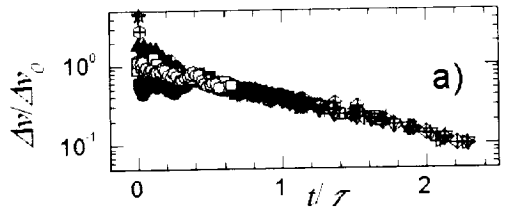

Dilute suspensions develop a broad interface between suspension and supernatent

- Driven by hydrodynamic dispersion
- No "self-sharpening":

$$U_{ss} = -\varphi\, dU/d\varphi << D/a$$

- Interface broadens approximately linearly with time
- Width of interface is of the order of the container height (> 10,000a)
- Stratification is another mechanism for damping velocity fluctuations (Luke 2000)
- Absence of steady state can be explained by the spreading front (Tee et al 2002)

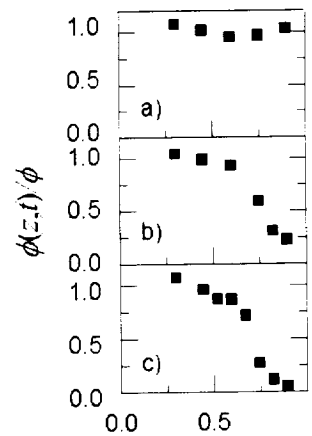

NASA/CP—2002-211212/VOL1

Summary

- Simulations have led to greatly increased understanding of fluctuations in a sedimenting suspension.
  - Macroscopic boundaries have qualitatively important effect on velocity fluctuations
  - Long-wavelength density fluctuations are damped during settling
  - $S(\mathbf{k} \to 0) \sim k_{\perp}^{2}$, in agreement with convection-diffusion model
- Experiments indicate additional phenomena in large cells at low solids concentrations
  - Results have been explained in terms of a stratification in the density profile

Future work

- Resolution of different mechanisms for damping velocity fluctuations. Identify boundaries in concentration and system size for the different mechanisms

- Systematic investigation of first effects of fluid and solid inertia
  - Theoretical prediction (Koch): $\langle U^2 \rangle \sim \sqrt{L}$
  - Gas-solid suspensions at low *Re*, but finite *St*
    - (reduced gravity environment)

- Simulations (experiments) of fluidized beds (steady state)

STUDIES OF GAS-PARTICLE INTERACTIONS IN A MICROGRAVITY FLOW CELL

Michel Y. Louge†, James T. Jenkins, Haitao Xu and Anthony Reeves
Cornell University, Ithaca, NY 14853

ABSTRACT

The NASA-Glenn Research Center is designing a microgravity flow cell in which to study the interaction of a flowing gas with relatively massive particles that collide with each other and with the moving boundaries of the cell. This cell will permit us to study suspensions over a range of laminar, steady, fully developed conditions where viscous forces dominate the gas flow and inertial forces proportional to the gas density are nearly eliminated. Unlike terrestrial flows, where the gas velocity must be set to a value large enough to support the weight of particles, the duration and quality of microgravity on the International Space Station will permit us to achieve suspensions in which the agitation of the particles and the gas flow can be controlled independently by adjusting the pressure gradient along the flow and the relative motion of the boundaries. To do this, we will use an axisymmetric Couette shearing cell permitting the independent control of the speeds of the moving inner and outer boundaries. This apparatus will be configured for two experiments on gas-solid interactions.

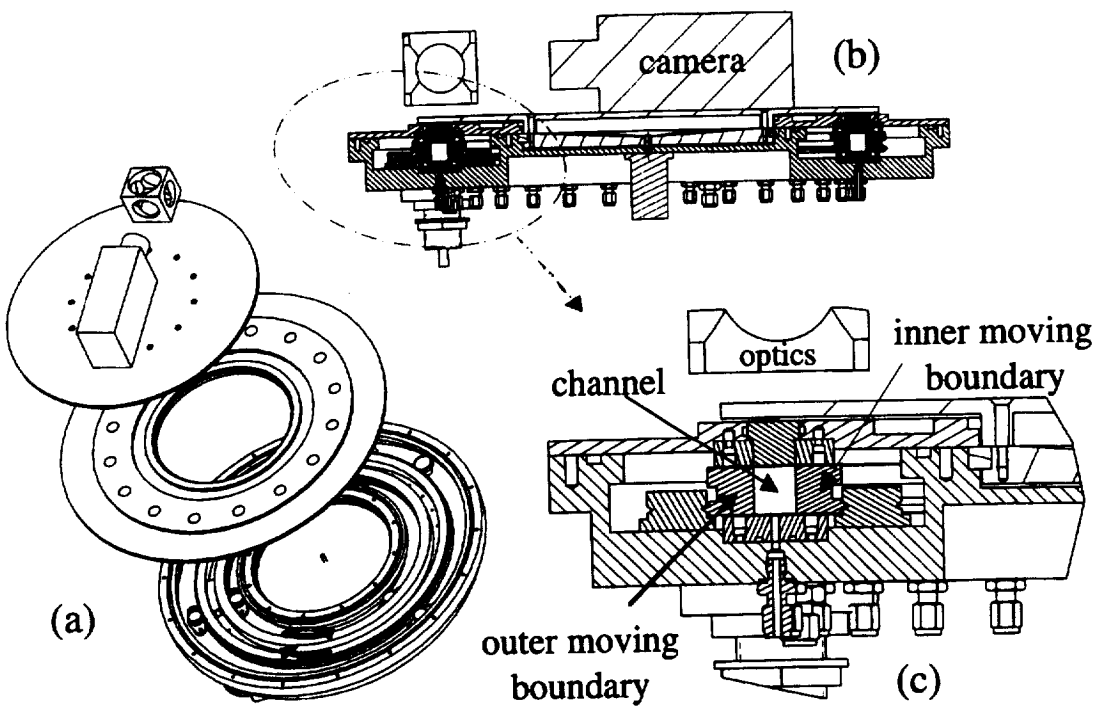

In the first series of experiments, we will characterize the viscous dissipation of the energy of the particle fluctuations when there is no relative mean velocity between gas and solids. We

† Sibley School of Mechanical and Aerospace Engineering, Cornell University, 192 Rhodes Hall, Ithaca, NY 14853, MYL3@cornell.edu, voice: (607) 255 4193, fax: (607) 255 1222.

recall that in the absence of a gas, individual impacts are so fast that the only time scale governing the granular phase is the inverse of γ, the shear rate imposed by the moving boundaries. At small particle Reynolds numbers, the gas introduces an additional viscous relaxation time $\theta_s = \rho_s d^2/18\mu_g$, where ρ_s, d and μ_g are, respectively, the density of the spheres, their diameter and the gas viscosity. In simple shear flows, Sangani et al. (1996) calculated values of the limiting Stokes number $St = \gamma \theta_s$ at which the particle fluctuation energy is equally dissipated by viscous and collisional interactions. Far above this limit, the shear rate is sufficient to ignore the viscous drag on the spheres.

In contrast, for these Viscous Dissipation Experiments, our intention is to reduce the boundary speed in successive tests until the Stokes number becomes small enough for the gas to affect the balance of fluctuation energy of the spheres. We will control the magnitude of the particle Reynolds number by adjusting the absolute pressure in the cell. At sufficiently low Stokes number, Sangani et al. (1996) showed that the granular fluctuation velocity scales as $\sqrt{T}/\gamma d \propto St/R_{diss}$, where $R_{diss}(\nu)$ is a coefficient characterizing viscous dissipation. In our experiments, we will infer R_{diss} by recording transverse profiles of granular temperature and comparing these with theoretical predictions.

The measurements will be accomplished by observing the flow through side walls and by using computer vision techniques to record transverse profiles of the mean and fluctuation velocities of the solids. In order to evaluate the role of non-continuum lubrication, we will also reduce the pressure of the apparatus and measure R_{diss} at increasing values of the molecular mean free path. Finally, we will perform experiments at Stokes and Reynolds numbers where the present theory is valid and also, in an effort to inform future theoretical work, at values when it is not.

In the second series of experiments, we will impose a gas pressure gradient on the shearing cell. The gradient will induce a relative velocity between the two phases, while the shearing will set independently the agitation of the solids. These Viscous Drag Experiments will be unique in exploring a regime where particle velocity fluctuations are determined by a mechanism other than interactions with the gas. In this regime, we will measure the dependence of R_{diss} and the drag coefficient R_{drag} on the solid volume fraction.

We will do so by recording the following variables and comparing these with theoretical predictions: mean gas volume flow rate through the flow channel, pressure gradient in the gas and transverse profiles of mean granular velocity, granular temperature and volume fraction. By reducing the pressure of the cell, we will also record the effects of particle Reynolds number on R_{drag}. Finally, we will record the cross-sectional mean solid volume fraction at several positions along the channel. This will permit us to monitor the flow development and the approach to steady-state, and it will contribute to measuring the required volume flow rate of gas through all branches of the flow channel.

REFERENCE

Sangani A.S., Mo G., Tsao H.-K., and Koch D.L., "Simple shear flows of dense gas-solid suspensions at finite Stokes number," *J. Fluid Mech.* **313**, 309-341 (1996).

NASA/CP—2002-211212/VOL1

Gas-particle interactions in a microgravity flow cell

Michel Louge
Cornell University

with James Jenkins, Haitao Xu,
Stephen Keast and Anthony Reeves

Sixth Microgravity Fluid Physics Conference
August 15, 2002
Cleveland, OH

CORNELL UNIVERSITY

IFPRI
International Fine Particle Research Institute

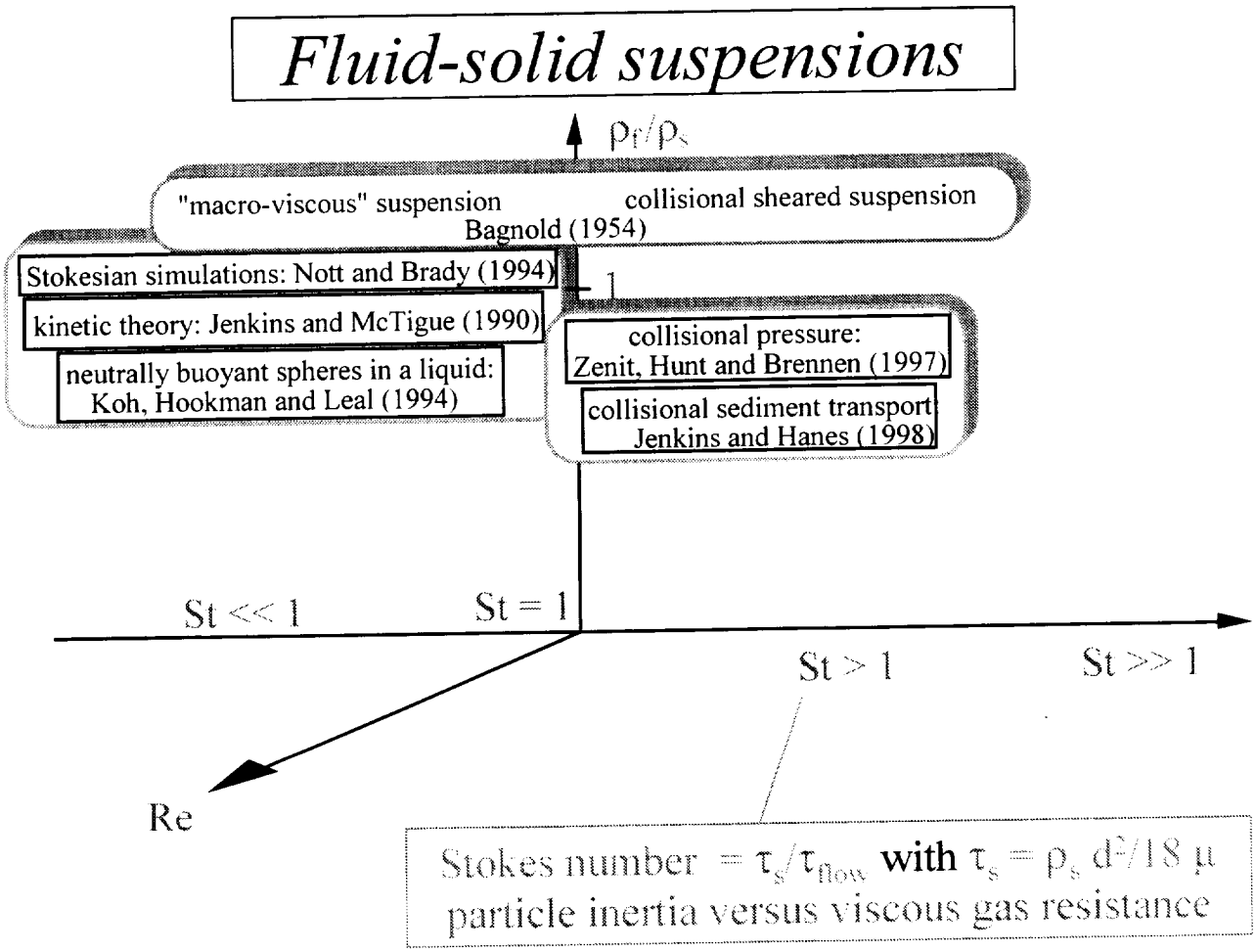
Fluid-solid suspensions
ρ_f/ρ_s
"macro-viscous" suspension
collisional sheared suspension
Bagnold (1954)
Stokesian simulations: Nott and Brady (1994)
1
kinetic theory: Jenkins and McTigue (1990)
neutrally buoyant spheres in a liquid: Koh, Hookman and Leal (1994)
collisional pressure: Zenit, Hunt and Brennen (1997)
collisional sediment transport: Jenkins and Hanes (1998)
St << 1
St = 1
St > 1
St >> 1
Re
Stokes number = τ_s/τ_{flow} with $\tau_s = \rho_s d^2/18\mu$
particle inertia versus viscous gas resistance

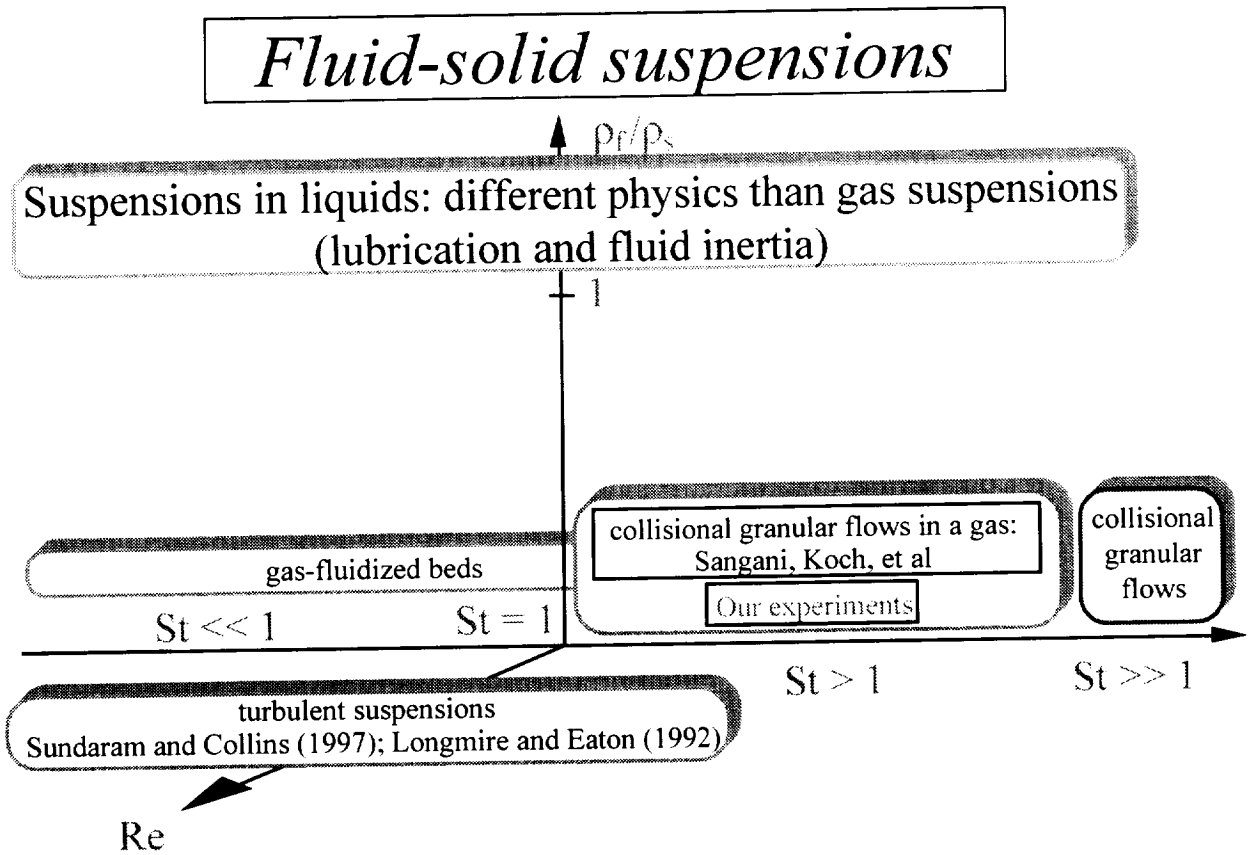
Fluid-solid suspensions
ρf/ρs
Suspensions in liquids: different physics than gas suspensions
(lubrication and fluid inertia)
1
collisional granular flows in a gas:
Sangani, Koch, et al
Our experiments
collisional
granular
flows
gas-fluidized beds
St << 1
St = 1
St > 1
St >> 1
turbulent suspensions
Sundaram and Collins (1997); Longmire and Eaton (1992)
Re

"Temperature" of a colliding granular material

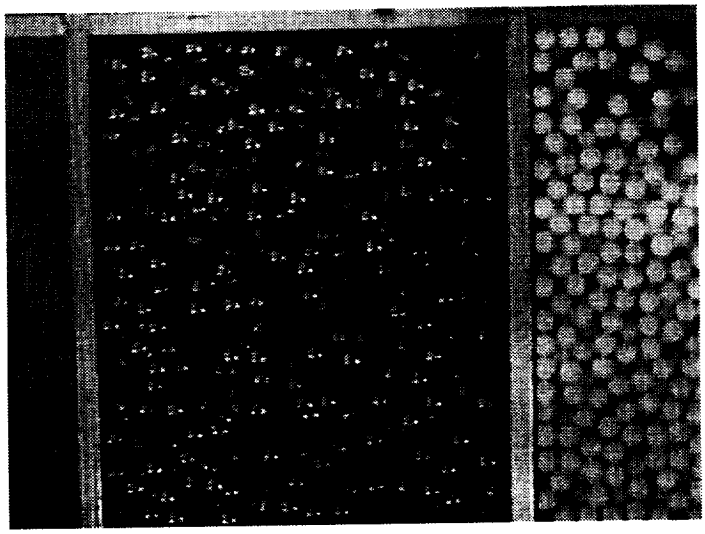

It measures the particle agitation.

"Temperature" of a colliding granular material

fluctuation velocity u_i

$$T = \frac{1}{3} m \overline{u_i u_i}$$

fluctuation kinetic energy of the grains

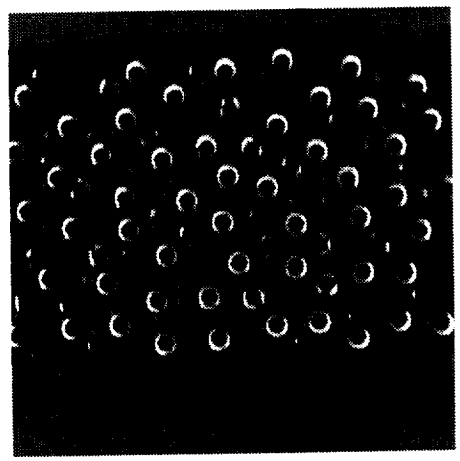

"granular temperature" ⇨ granular viscosity $\mu_s \propto \rho_s d \sqrt{T/m} f_\mu(\nu)$

⇨ granular conductivity $k_s \propto \rho_s d \sqrt{T/m} f_k(\nu)$

Objective

Characterize
the dissipation of granular temperature by the gas
and the effects of granular agitation on drag.

Benefits

Chemical engineering,
oil and energy industries.

Food, pharmaceutical,
mining industries,
planetary missions.

Solid transport.

Viscous dissipation of granular temperature

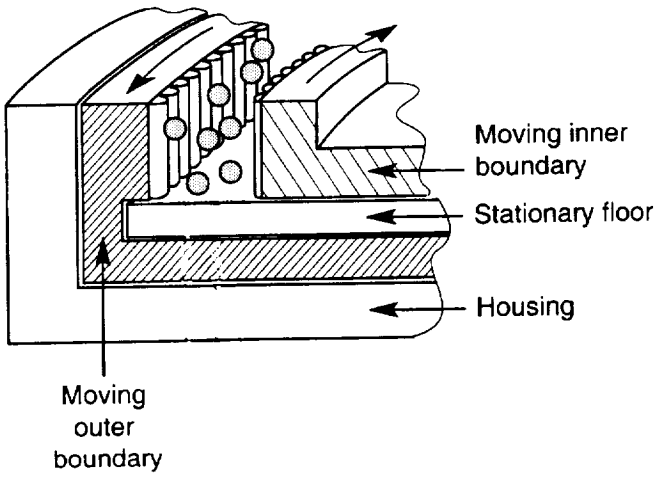

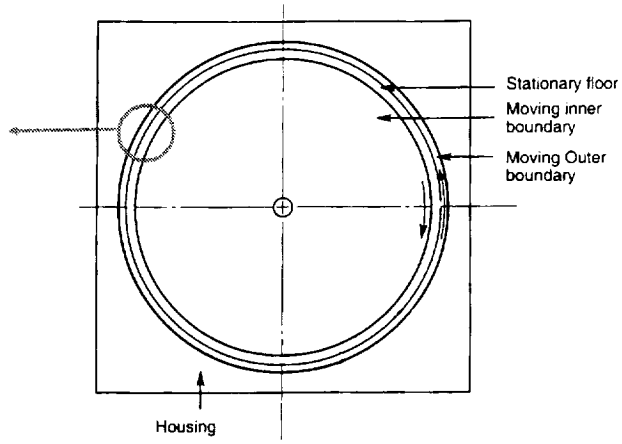

Reduce boundary speed until collisional and viscous dissipation of fluctuation energy are comparable.

Effects of gas viscosity on granular temperature

Solid density ρ_s, diameter d, granular temperature T,
normal restitution e, gas viscosity μ.

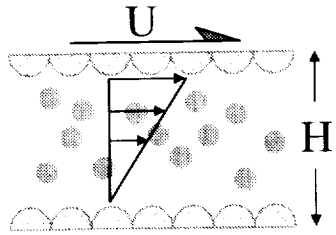

Collisional production ~ $\rho_s\, d\, \sqrt{T}\, (U/H)^2$

Fluctuation energy balance sets the granular temperature

Collisional dissipation ~ $(1-e)\, \rho_s\, T^{3/2}/d$

Viscous dissipation ~ $\mu\, R_{diss}\, T/d^2$

Low U: $(\sqrt{T}/U) \sim (\rho_s\, d^2/\mu)\, (U/H)\, (d/H)\, /R_{diss} \sim [St\, /R_{diss}]\, (d/H)$

Gas drag on agitated solids

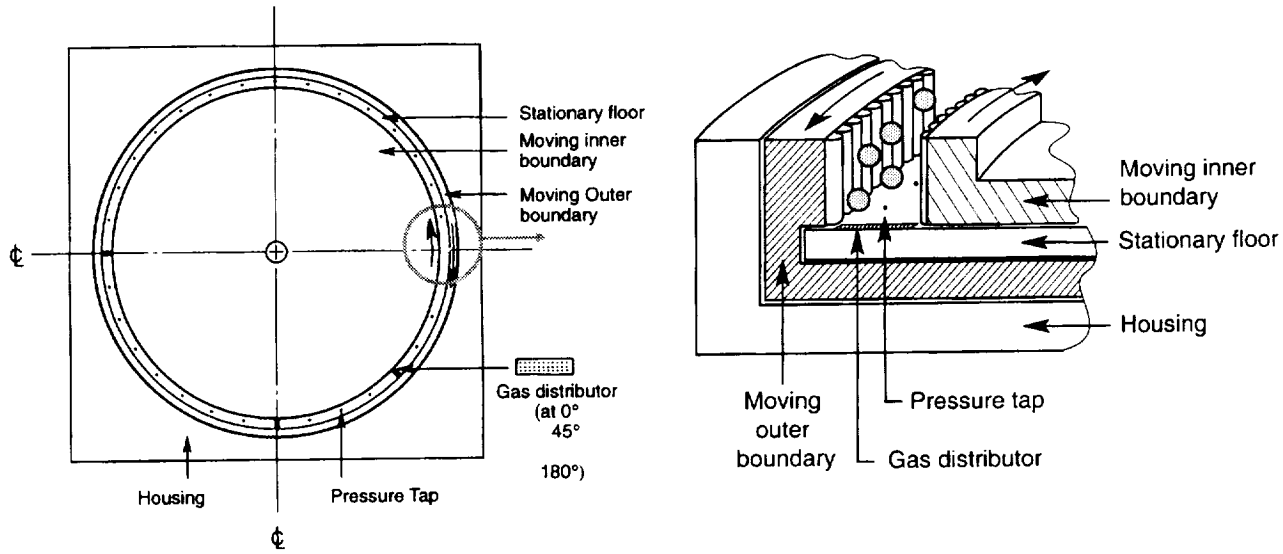

Impose a gas pressure gradient on the agitated, sheared granular material.

Flow development

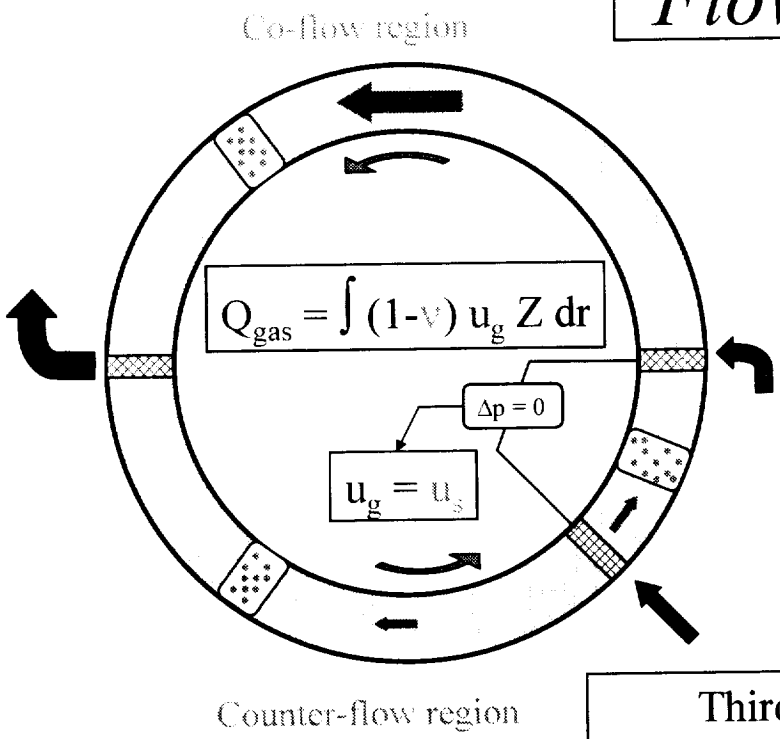

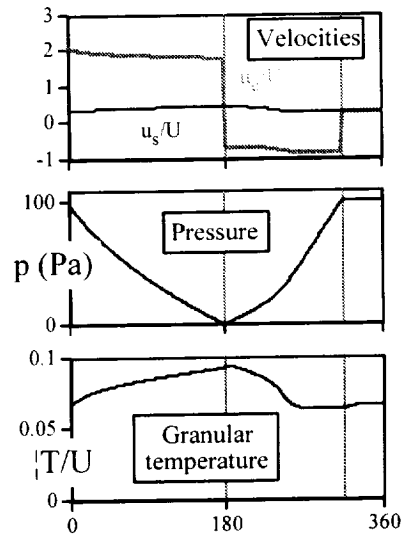

Third distributor to infer the gas volume flow rate in the fully-developed regions

Prototype cell

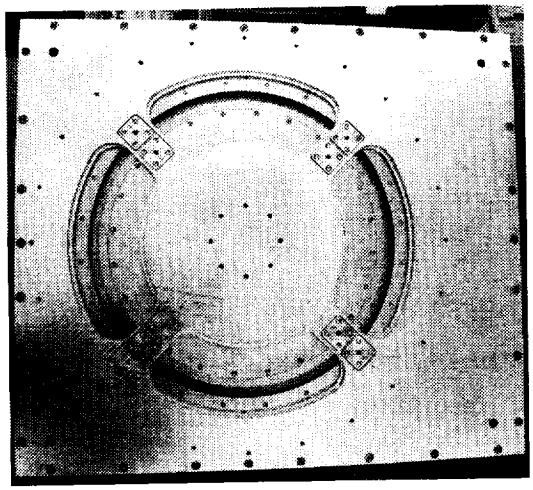

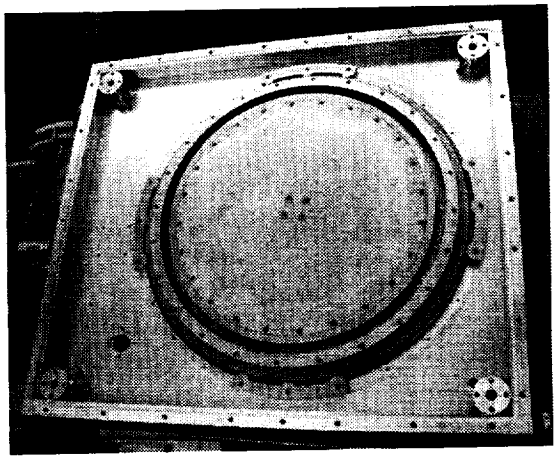

Tests of the isokinetic concept

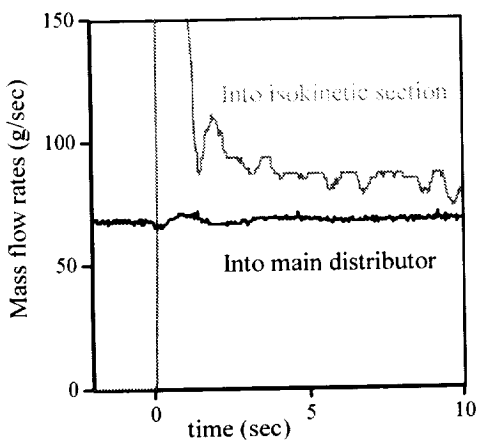

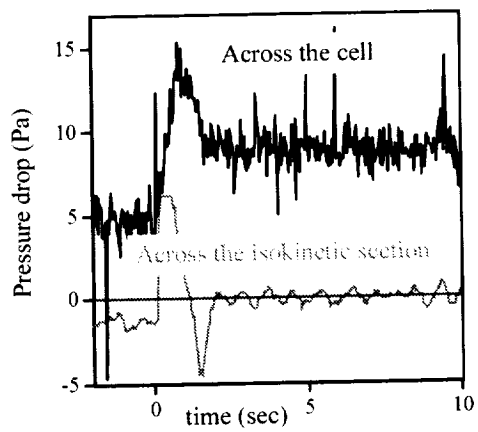

Add gas into the isokinetic section

Flight Tests

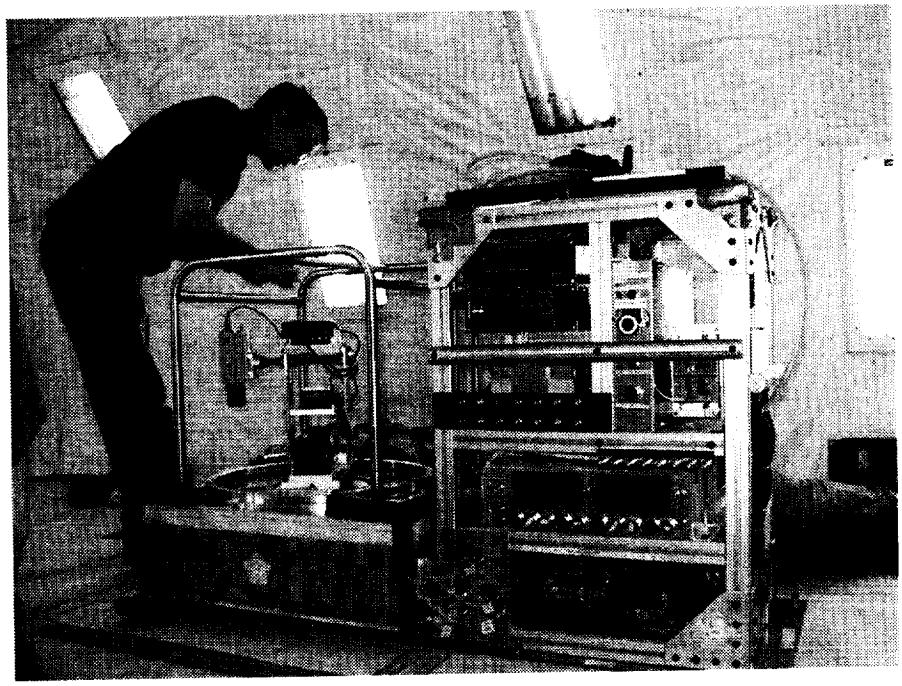

High-speed images

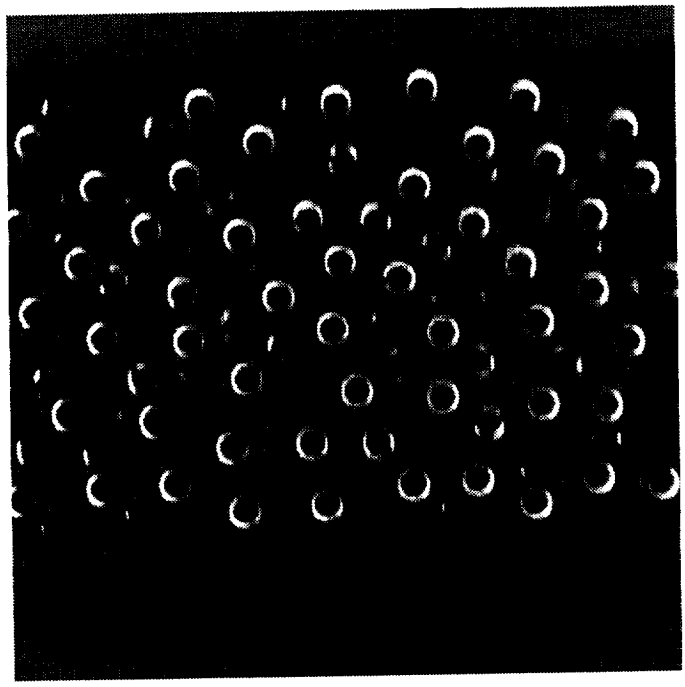

Accomplishments

- We manufactured a prototype of the apparatus.
- We gained experience with it on the KC-135 aircraft.
- We developed a theory for the flow.
- We prescribed scientific requirements for flight.

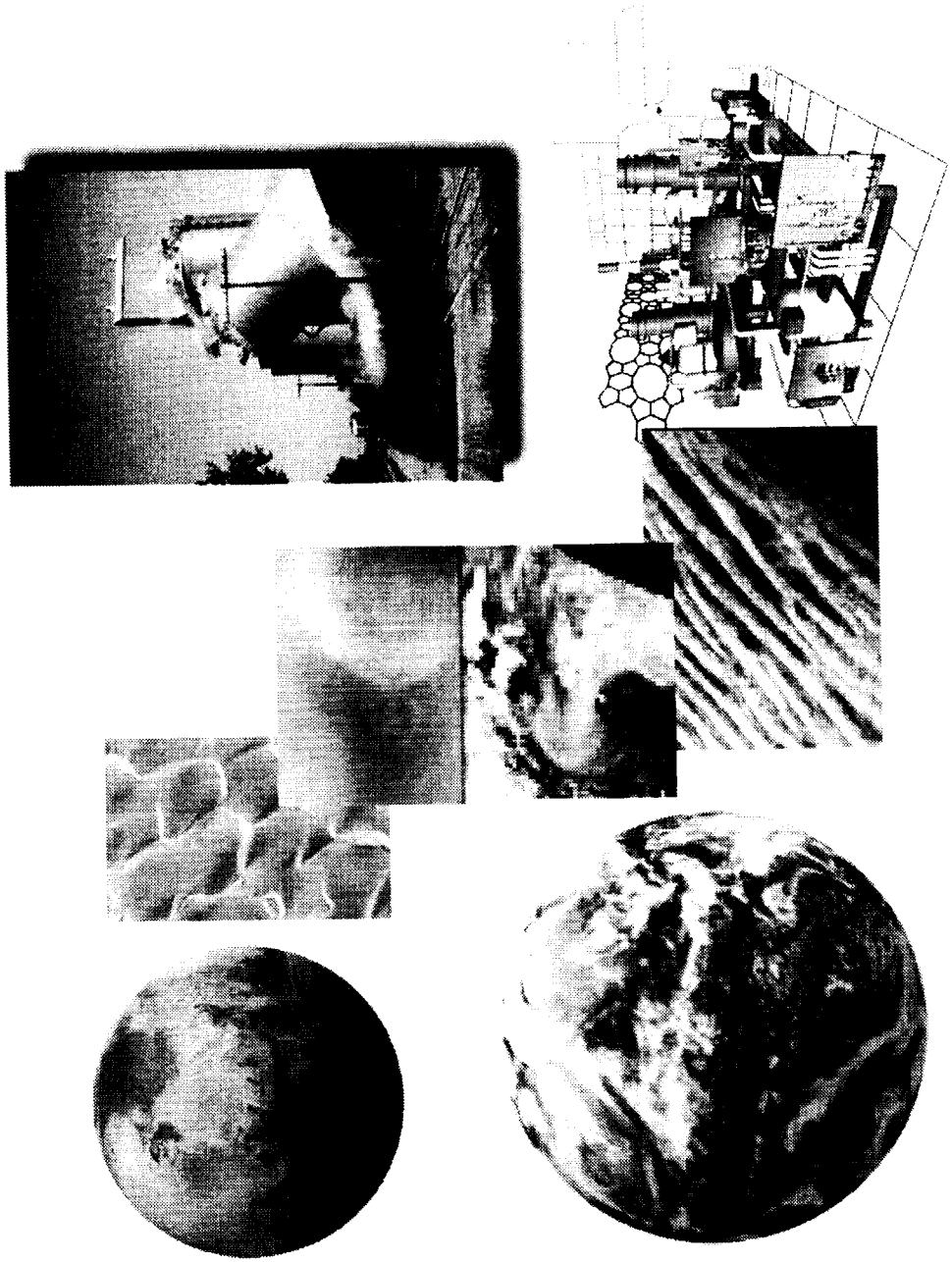

Dynamics of Sheared Granular Materials

Lou Kondic
Department of Mathematical Sciences and Center for Applied Mathematics & Statistics,
New Jersey Institute of Technology, Newark, NJ 07102

Brian Utter and Robert P. Behringer
Department of Physics and Center for Nonlinear and Complex Systems
Duke University, Durham, NC 27708

ABSTRACT

This work focuses on the properties of sheared granular materials near the jamming transition. The project currently involves two aspects. The first of these is an experiment that is a prototype for a planned ISS flight. The second is discrete element simulations (DES) that can give insight into the behavior one might expect in a reduced-g environment.

The experimental arrangement consists of an annular channel that contains the granular material. One surface, say the upper surface, rotates so as to shear the material contained in the annulus. The lower surface controls the mean density/mean stress on the sample through an actuator or other control system. A novel feature under development is the ability to 'thermalize' the layer–i.e. create a larger amount of random motion in the material, by using the actuating system to provide vibrations as well control the mean volume of the annulus. The stress states of the system are determined by transducers on the non-rotating wall. These measure both shear and normal components of the stress on different size scales. Here, the idea is to characterize the system as the density varies through values spanning dense almost solid to relatively mobile granular states. This transition regime encompasses the regime usually thought of as the glass transition, and/or the jamming transition.

Motivation for this experiment springs from ideas of a granular glass transition, a related jamming transition, and from recent experiments. In particular, we note recent experiments carried out by our group to characterize this type of transition (Howell et al. Phys. Rev. Lett. **82**, 5241 (1999)) and also to demonstrate/characterize fluctuations in slowly sheared systems (Miller et al. Phys. Rev. Lett. **77**, 3110 (1996)). These experiments give key insights into what one might expect in near-zero g. In particular, they show that the compressibility of granular systems diverges at a transition or critical point. It is this divergence, coupled to gravity, that makes it extremely difficult if not impossible to characterize the transition region in an earth-bound experiment.

In the DE modeling, we analyze dynamics of a sheared granular system in Couette geometry in two (2D) and three (3D) space dimensions. Here, the idea is to both better understand what we might encounter in a reduced-g environment, and at a deeper level to deduce the physics of sheared systems in a density regime that has not been addressed by past experiments or simulations.

One aspect of the simulations addresses sheared 2D system in zero-g environment. For low volume fractions, the expected dynamics of this type of system is relatively well understood. However, as the volume fraction is increased, the system undergoes a phase transition, as explained above. The DES concentrate on the evolution of the system as the solid volume fraction is slowly increased, and in particular on the behavior of very dense systems. For these configurations, the simulations show that polydispersity of the sheared particles is a crucial factor that determines the system response. Figures 1 and 2 below, that present the total force on each grain, show that even relatively small (10 %) nonuniformity of the size

of the grains (expected in typical experiments) may lead to significant modifications of the system properties, such as velocity profiles, temperature, force propagation, and formation of shear bands.

The simulations are extended in a few other directions, in order to provide additional insight to the experimental system analyzed above. In one direction, both gravity, and driving due to vibrations are included. These simulations allow for predictions on the driving regime that is required in the experiments in order to analyze the jamming transition. Furthermore, direct comparison of experiments and DES will allow for verification of the modeling assumptions. We have also extended our modeling efforts to 3D. The (preliminary) results of these simulations of an annular system in zero-g environment will conclude the presentation.

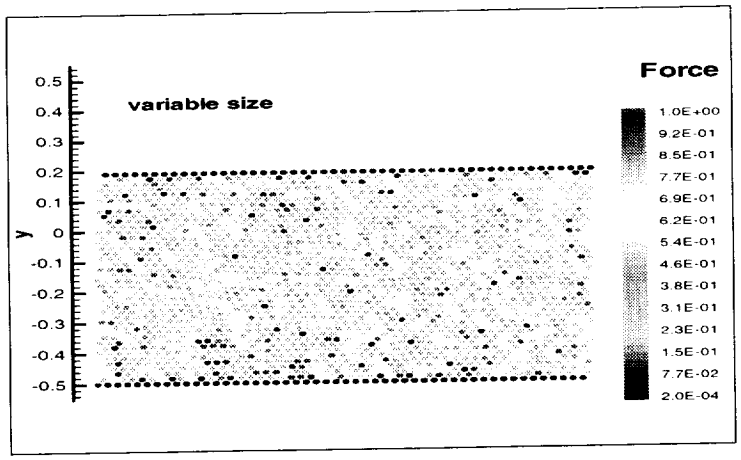

Figure 1: The (instantaneous) force experienced by the variable size particles; the volume fraction at the instant shown is approximately 0.9. The flow is driven by constant velocity motion of the upper wall in the $+x$ direction (left to right).

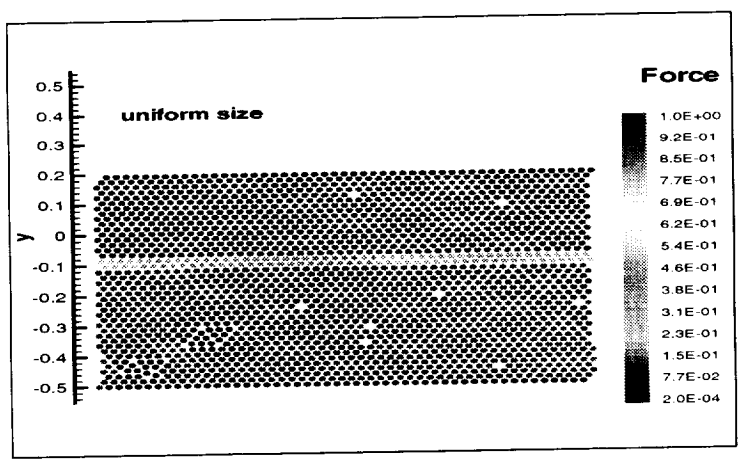

Figure 2: The force in the case of uniform size particles; all the other quantities are the same as in Fig. 1. Note formation of a shear band at $y \approx -0.1$; it should be mentioned that this particular shear band is just one of possible configurations characterizing the flow, and the manner in which the force propagates.

Dynamics of Sheared Granular Materials

By:

Lou Kondic, NJIT
Brian Utter, Duke
Robert P. Behringer, Duke

Presented at:

Sixth Microgravity Fluid Physics
and Transport Phenomena Conference
August '02

supported by NASA

Main goal

Understand the dynamics of a granular system as the volume fraction γ is modified between gas-like and solid-like
Analyze the phase transition which may occur in 3D zero-g experiment
Analogy to 2D? - see Howell et al. PRL (1999)
Discuss the parameters defining the system, in particular distribution of particle sizes

Techniques

Experimental
Computational (discrete element simulations)

This talk: Simulations

Discuss expected behavior in zero g
Analyze force propagation
Also: can we thermalize the system in non-zero g and expect to reach uniform states?

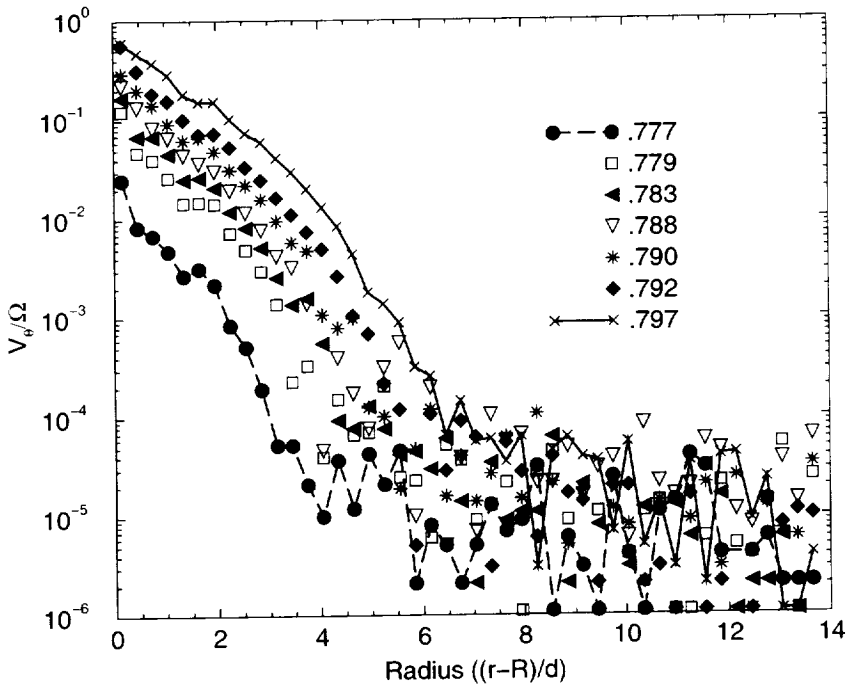

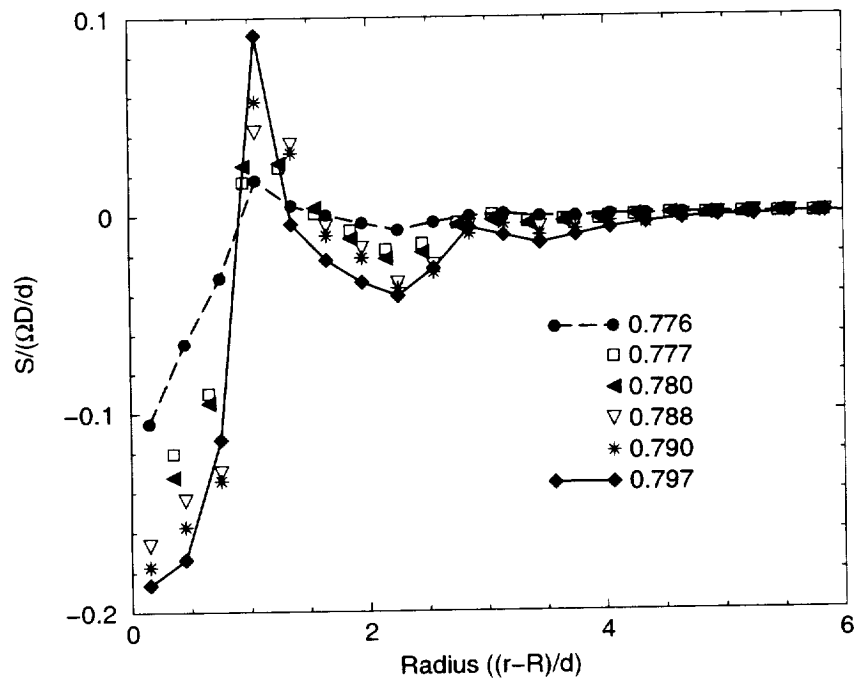

(from Howell et al, PRL (1999))

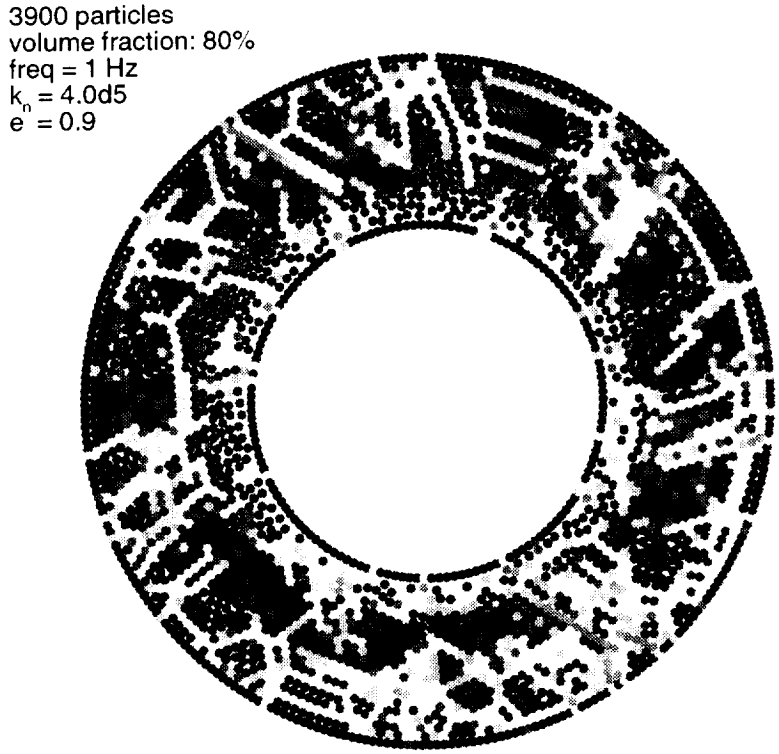

Experiment:

2D: Second-order phase transition as the volume fraction is decreased

2D: gravitational effects are reduced by using a horizontal system

3D (annular geometry): gravitational compaction does not allow to analyze dynamics close to γ_c

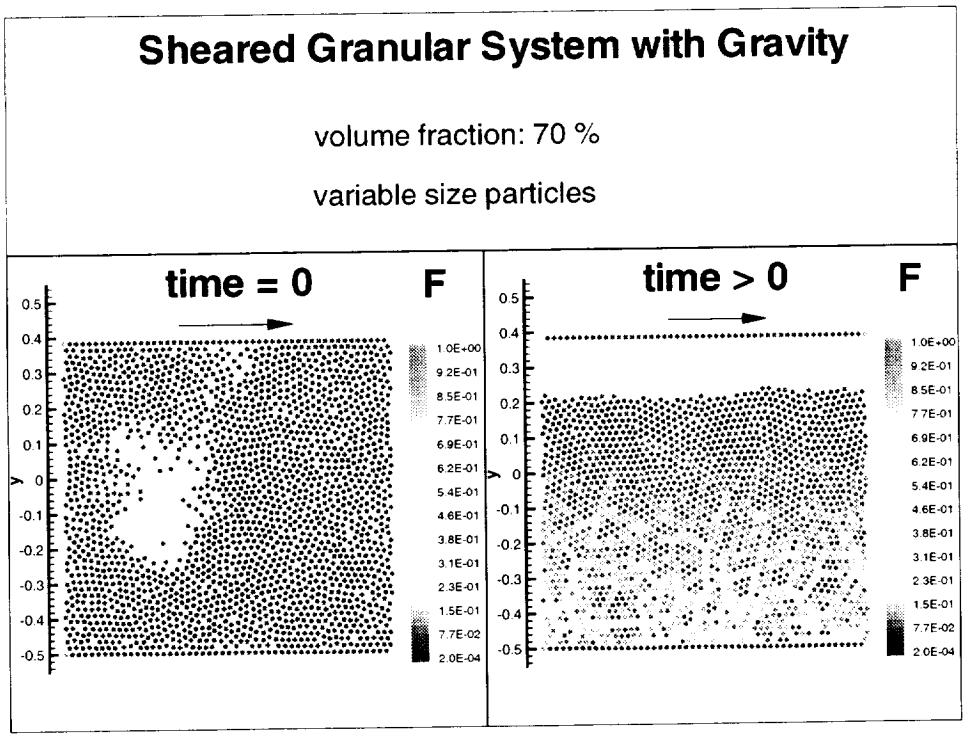

(an example of gravitational compaction)

Goal of Simulations

Analyze open (channel) (2D) Couette geometry to understand the basics of dynamics in 3D experiment in annular geometry and zero-g environment

Discrete element techniques

Linear force model with damping in normal and tangential directions

$$\mathbf{F}^n_{i,j} = \left[k(d - r_{i,j}) - \gamma_n \bar{m}(\mathbf{v}_{i,j} \cdot \mathbf{n})\right] \mathbf{n}$$

Tangential force

$$\mathbf{F}^t_{i,j} = min\left(-\gamma_s \bar{m} v_{rel}, \mu|\mathbf{F}_{i,j} \cdot \mathbf{n}|\right) \mathbf{s}$$
$$v_{rel} = \mathbf{v}_{i,j} \cdot \mathbf{s} + (r_i \Omega_i + r_j \Omega_j)$$
$$\mathbf{s} : \mathbf{s} \perp \mathbf{n}$$

γ_s tangentional damping
μ: Coulomb coefficient

Parameters chosen appropriately for (soft) photoelastic disks, (e.g. Howell and Behringer, PRL (1999))

This talk: periodic boundaries, rough walls

- Sheared system with slowly varying γ
- Switch on gravity as well as excitation

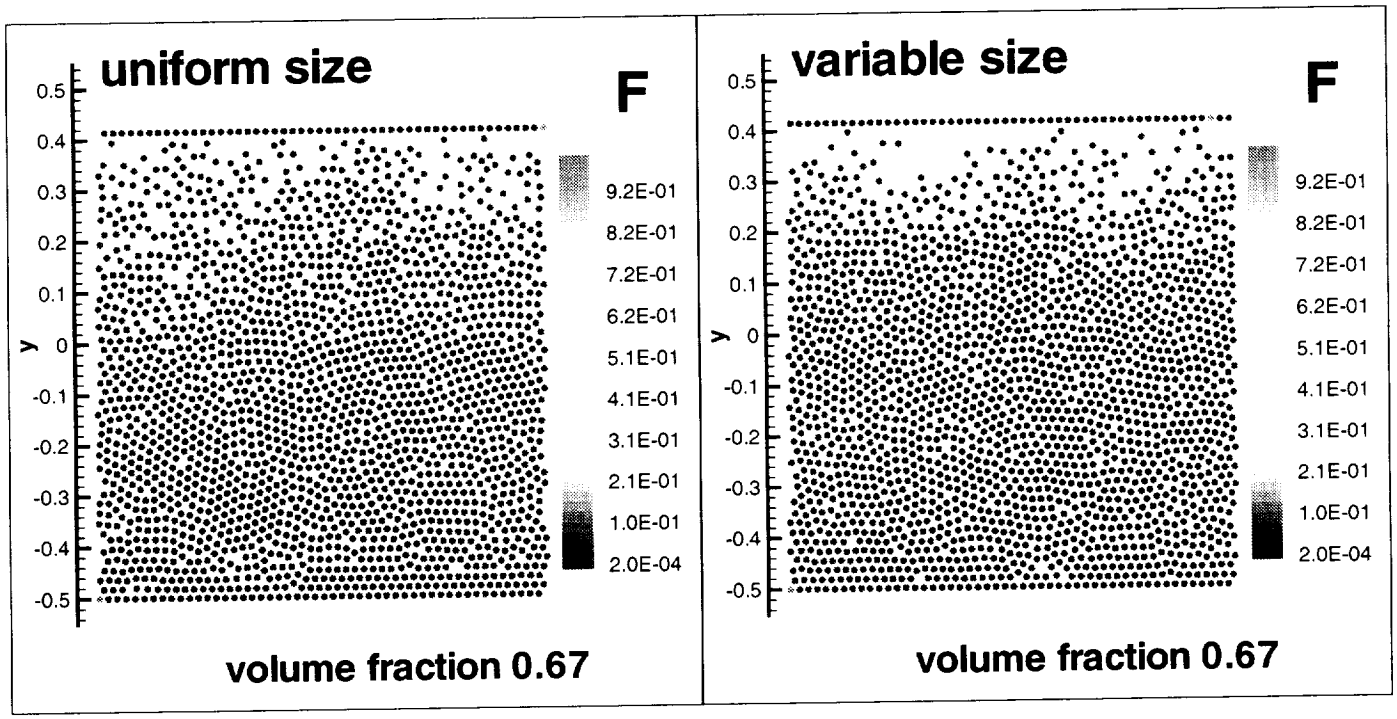
uniform size
F
y
0.5
0.4
0.3
0.2
0.1
0
-0.1
-0.2
-0.3
-0.4
-0.5
9.2E-01
8.2E-01
7.2E-01
6.2E-01
5.1E-01
4.1E-01
3.1E-01
2.1E-01
1.0E-01
2.0E-04
volume fraction 0.67
variable size
F
y
0.5
0.4
0.3
0.2
0.1
0
-0.1
-0.2
-0.3
-0.4
-0.5
9.2E-01
8.2E-01
7.2E-01
6.2E-01
5.1E-01
4.1E-01
3.1E-01
2.1E-01
1.0E-01
2.0E-04
volume fraction 0.67

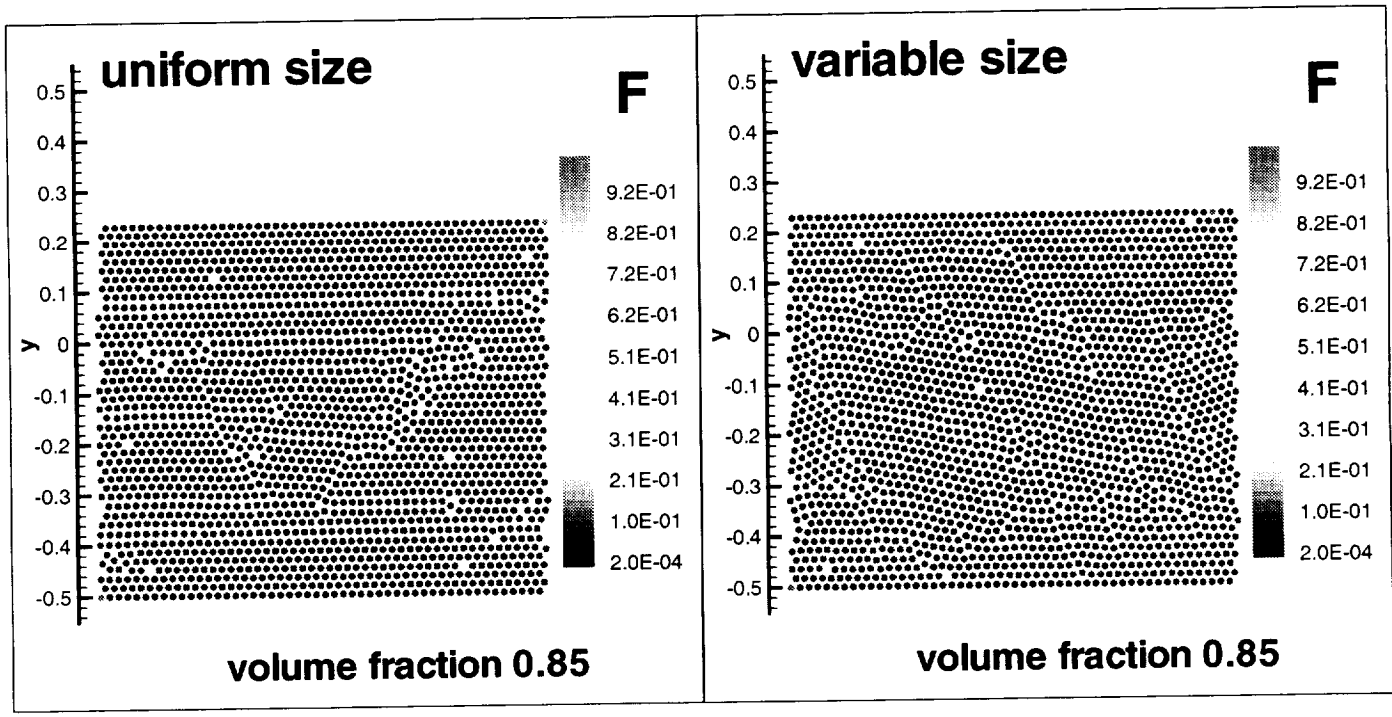
uniform size
F
y
0.5
0.4
0.3
0.2
0.1
0
-0.1
-0.2
-0.3
-0.4
-0.5
9.2E-01
8.2E-01
7.2E-01
6.2E-01
5.1E-01
4.1E-01
3.1E-01
2.1E-01
1.0E-01
2.0E-04
volume fraction 0.85
variable size
F
y
0.5
0.4
0.3
0.2
0.1
0
-0.1
-0.2
-0.3
-0.4
-0.5
9.2E-01
8.2E-01
7.2E-01
6.2E-01
5.1E-01
4.1E-01
3.1E-01
2.1E-01
1.0E-01
2.0E-04
volume fraction 0.85

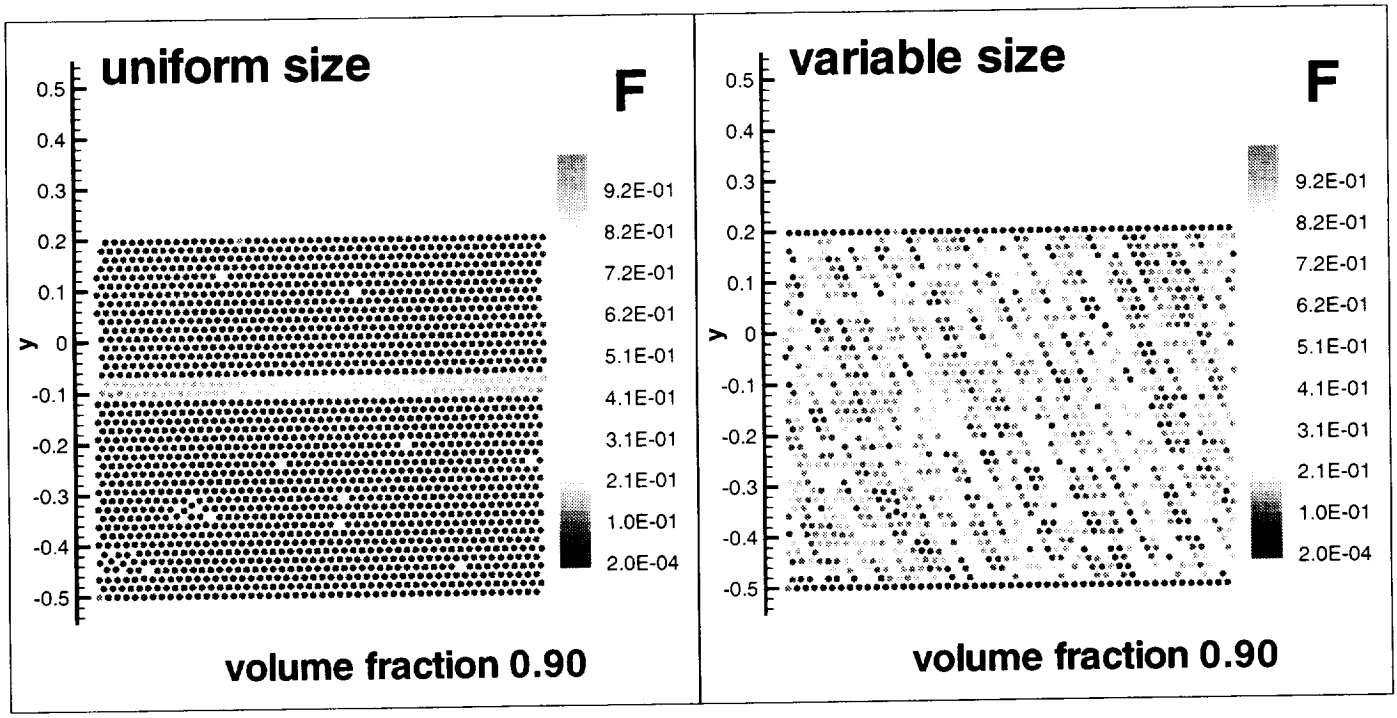
uniform size
F
y
0.5
0.4
0.3
0.2
0.1
0
-0.1
-0.2
-0.3
-0.4
-0.5
9.2E-01
8.2E-01
7.2E-01
6.2E-01
5.1E-01
4.1E-01
3.1E-01
2.1E-01
1.0E-01
2.0E-04
volume fraction 0.90
variable size
F
y
0.5
0.4
0.3
0.2
0.1
0
-0.1
-0.2
-0.3
-0.4
-0.5
9.2E-01
8.2E-01
7.2E-01
6.2E-01
5.1E-01
4.1E-01
3.1E-01
2.1E-01
1.0E-01
2.0E-04
volume fraction 0.90

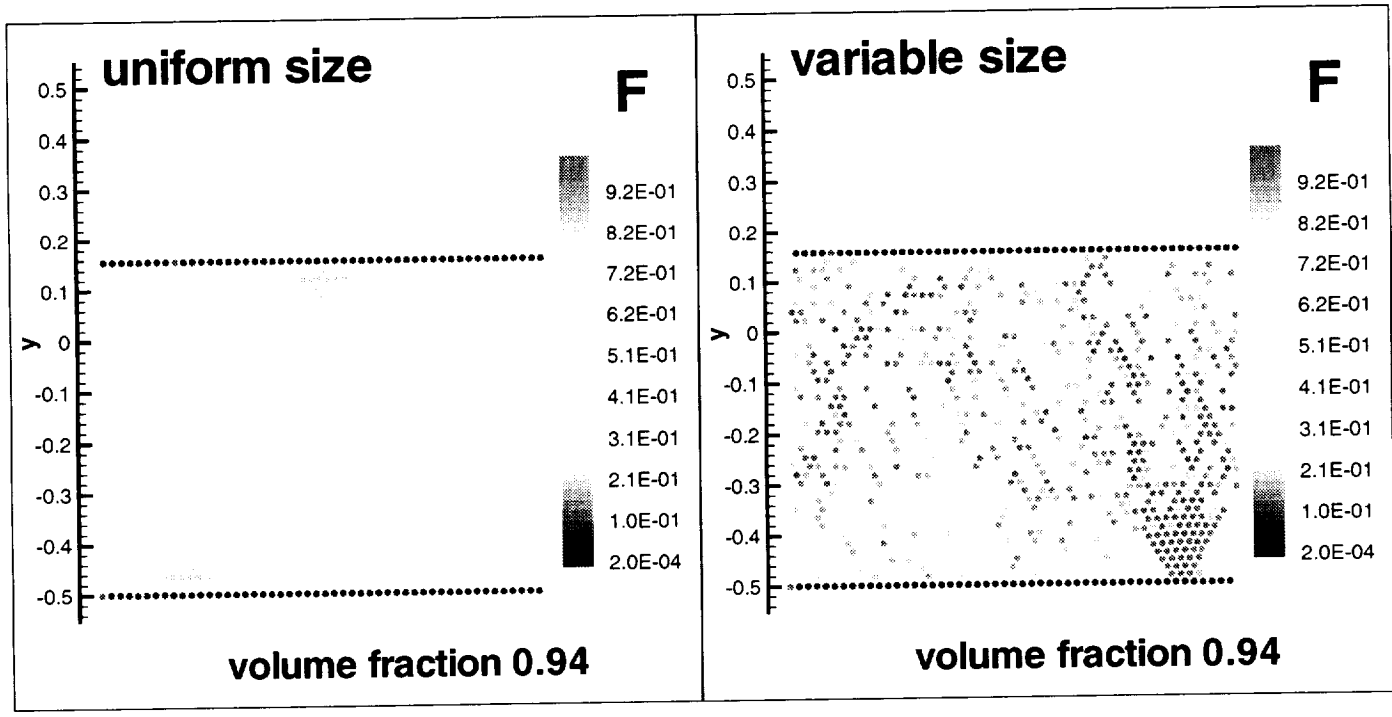
uniform size
F
y
0.5
0.4
0.3
0.2
0.1
0
-0.1
-0.2
-0.3
-0.4
-0.5
9.2E-01
8.2E-01
7.2E-01
6.2E-01
5.1E-01
4.1E-01
3.1E-01
2.1E-01
1.0E-01
2.0E-04
volume fraction 0.94
variable size
F
y
0.5
0.4
0.3
0.2
0.1
0
-0.1
-0.2
-0.3
-0.4
-0.5
9.2E-01
8.2E-01
7.2E-01
6.2E-01
5.1E-01
4.1E-01
3.1E-01
2.1E-01
1.0E-01
2.0E-04
volume fraction 0.94

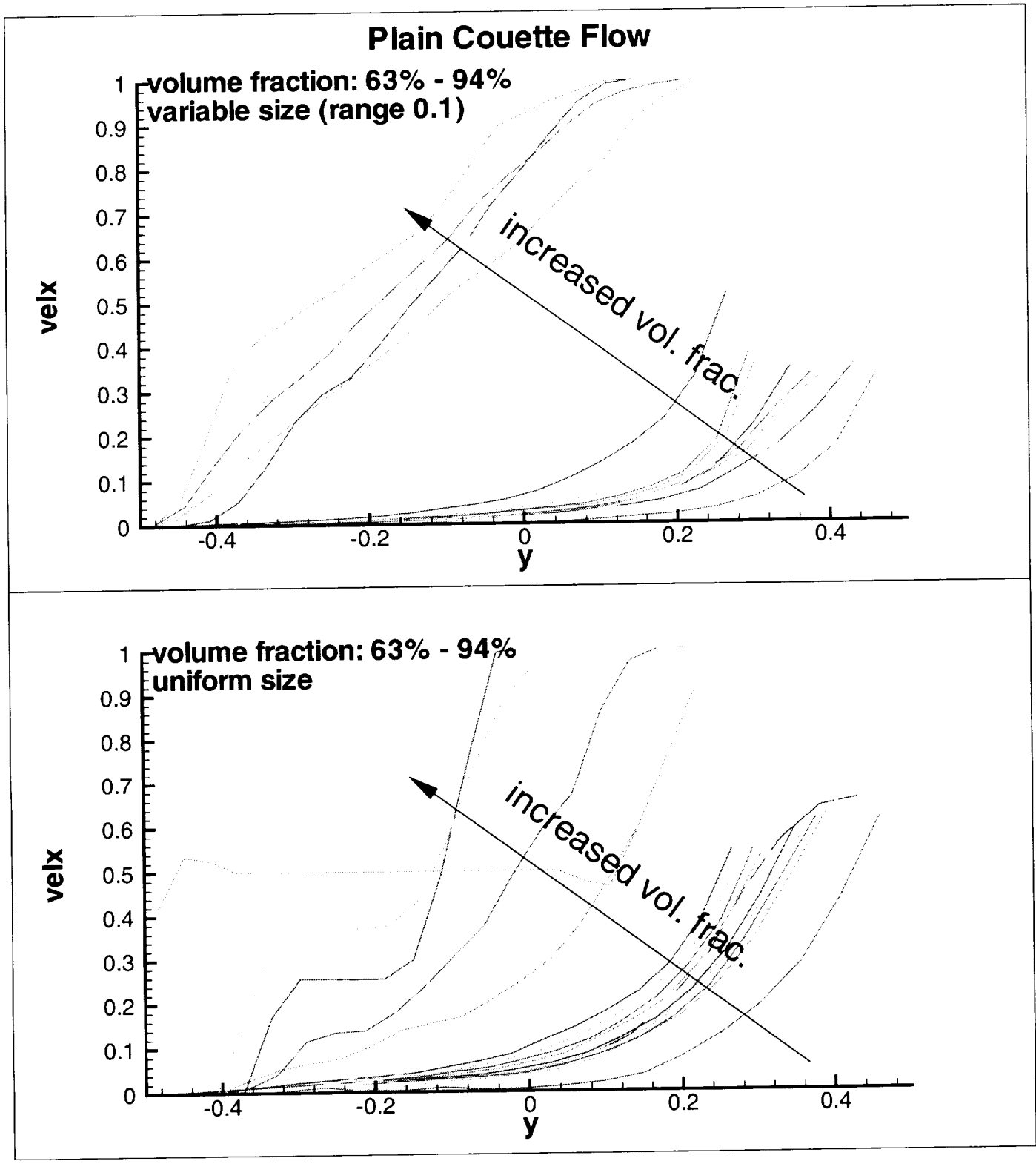
Plain Couette Flow
volume fraction: 63% - 94%
variable size (range 0.1)
increased vol. frac.
velx
y
volume fraction: 63% - 94%
uniform size
increased vol. frac.
velx
y

Low volume fractions: Gas-like regime

No significant difference between monodisperse and polydisperse materials

System dilated next to the shearing wall

Energy shared between kinetic and elastic

Higher temperature and elastic energy close to the shearing wall

Rate-independent system behavior

Shearing band formation for lower γ's similarly as in radial Couette geometry

(can this shearing band be *removed* by externally imposed excitations?)

Related works

Jenkins, Richman, Phys. Fluids '85

Walton, Braun, J. Rheol., '86

Campbell, Annu. Rev. Fluid Mech. '90

Hopkins, Louge, Phys. Fluids '91

Savage, JFM '98

...

High volume fractions

From exponential to linear velocity profiles (note: linear profiles are not observed in annular geometry!)

From gas-like to solid-like behavior: jamming

Significant differences between monodisperse and polydisperse systems:

Fracture occurs for monodisperse systems

Monodisperse systems are compressed easier (crystallization) $\rightarrow$ large difference in the stored elastic energy

Rate-dependent behavior for large volume fractions

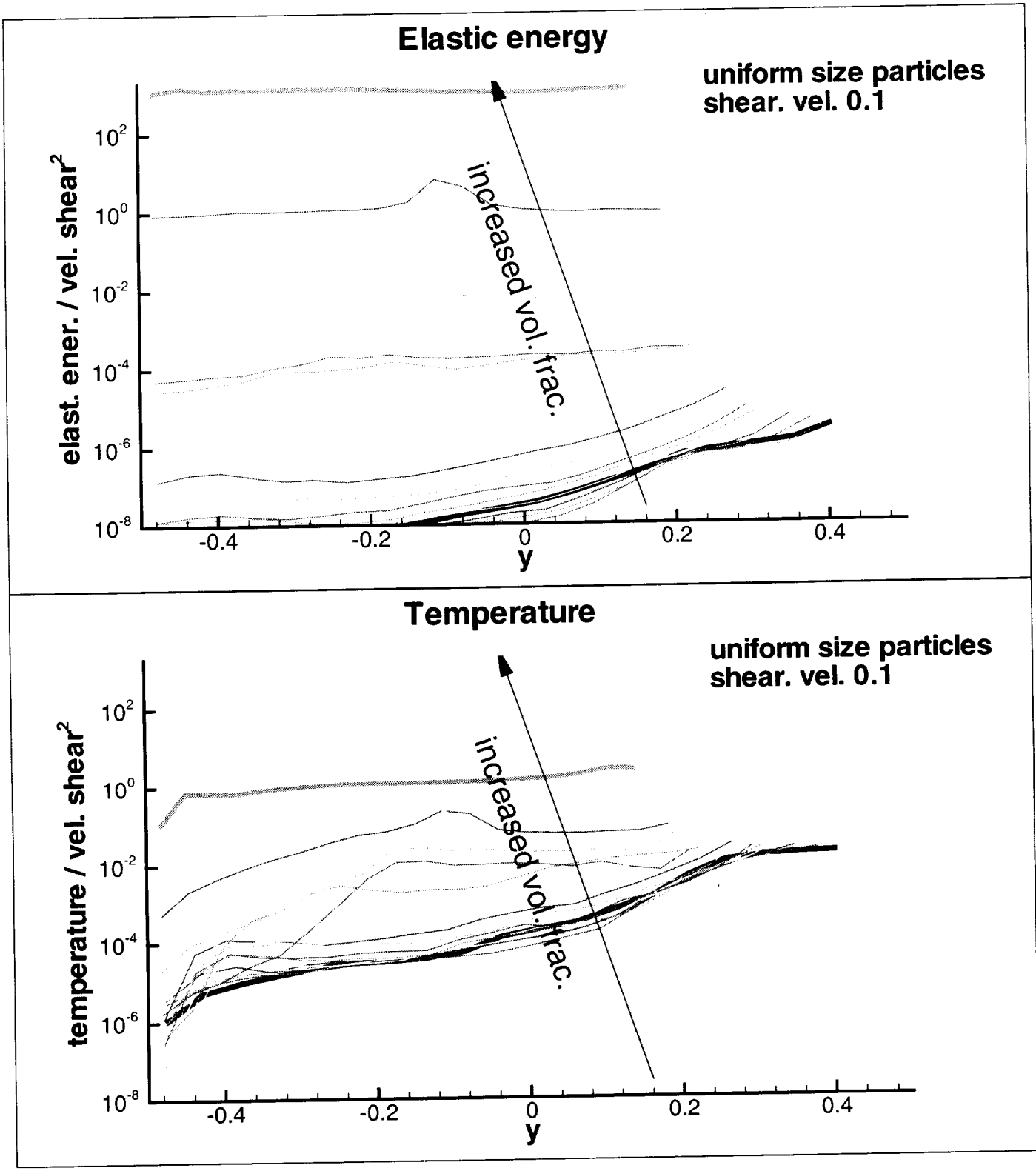
Elastic energy
uniform size particles
shear. vel. 0.1
elast. ener. / vel. shear^2
10^2
10^0
10^{-2}
10^{-4}
10^{-6}
10^{-8}
increased vol. frac.
-0.4
-0.2
0
0.2
0.4
y
Temperature
uniform size particles
shear. vel. 0.1
temperature / vel. shear^2
10^2
10^0
10^{-2}
10^{-4}
10^{-6}
10^{-8}
increased vol. frac.
-0.4
-0.2
0
0.2
0.4
y

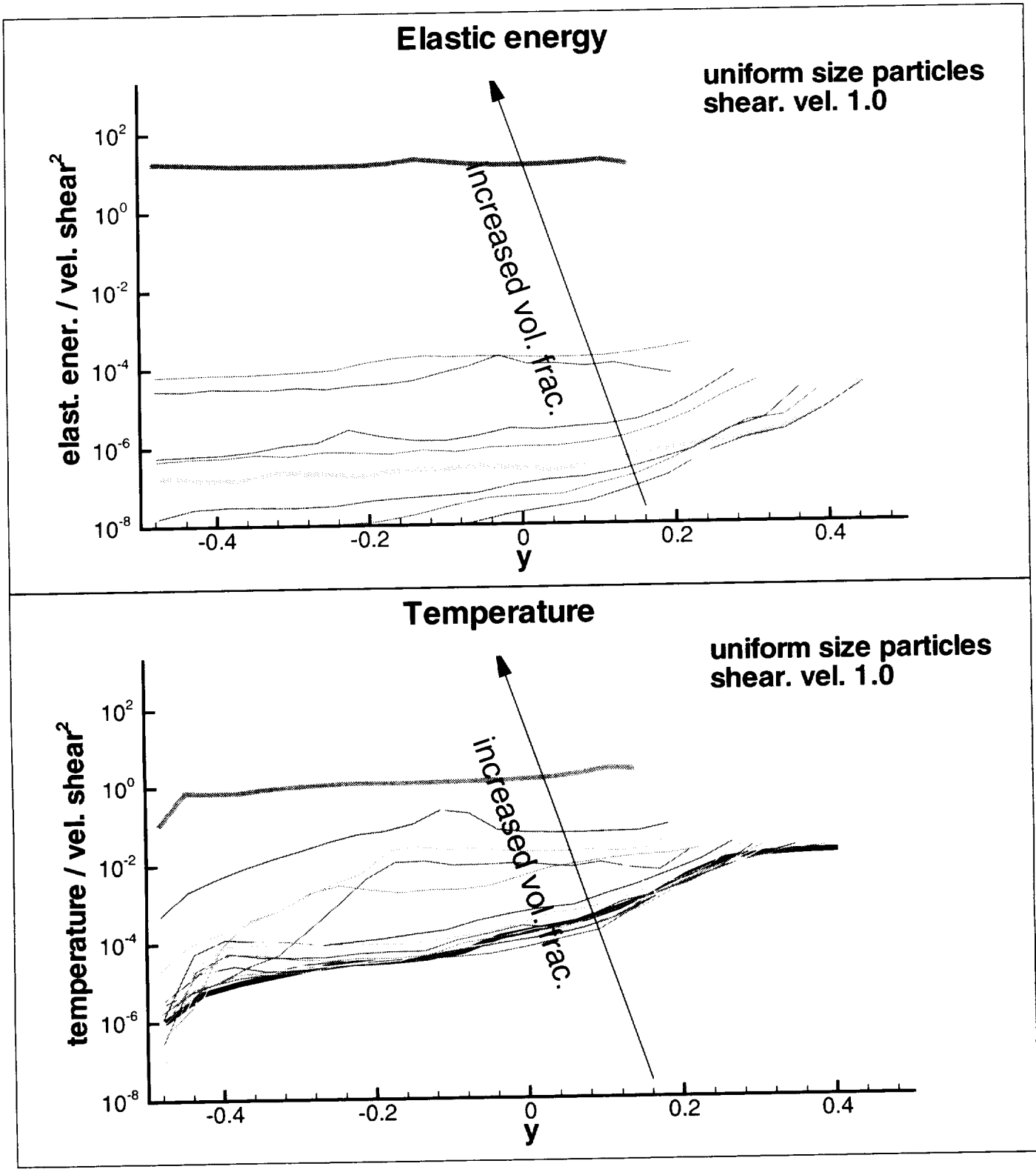
Elastic energy
uniform size particles
shear. vel. 1.0
elast. ener. / vel. shear^2
10^2
10^0
10^{-2}
10^{-4}
10^{-6}
10^{-8}
increased vol. frac.
-0.4
-0.2
0
0.2
0.4
y
Temperature
uniform size particles
shear. vel. 1.0
temperature / vel. shear^2
10^2
10^0
10^{-2}
10^{-4}
10^{-6}
10^{-8}
increased vol. frac.
-0.4
-0.2
0
0.2
0.4
y

Gravity plus excitations

If gravity is included, compaction results $\longrightarrow$ possible phase transition cannot be observed

Question: Can we excite (thermalize) the system so to reach uniformly sheared states? (Analogy: glasses, colloids, ...)

Consider:

Sheared system + gravity
Excitations through vibrated lower boundary

Analyze:

different modes of excitations
different Γ's
different ratios of shearing and thermalizing energy input
different volume ratios

Plain Couette Flow

volume fraction: 80%
variable size particles

(last 5 averages shown)

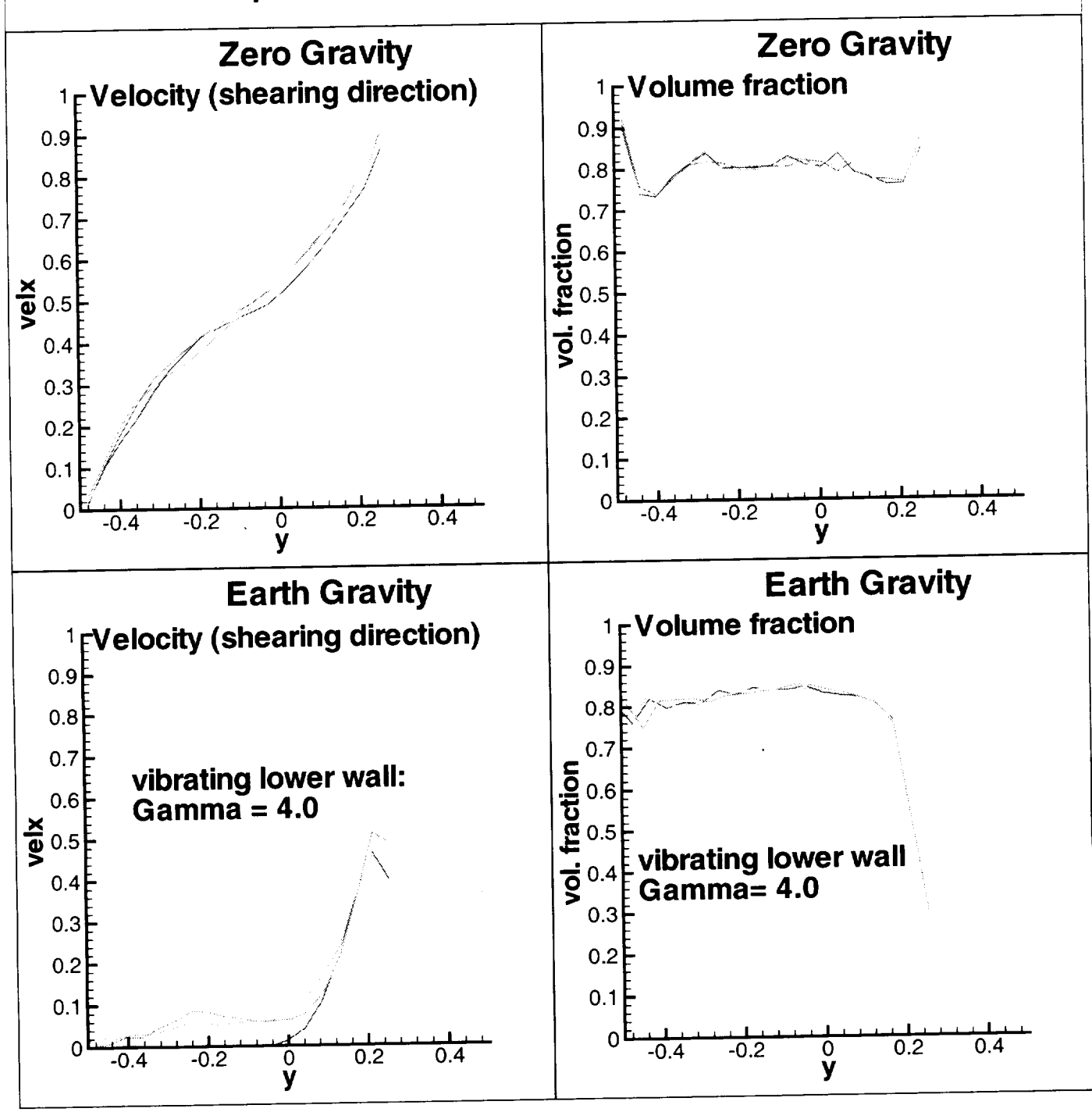

Answer: It is not easy to fight Gravity!

Difficult to produce uniform and dense granular system which responds to shearing
(there are also large forces resulting from excitations)

Suggestion of this study: will need to perform experiments (and simulations) in zero g to fully understand the problem

Current and Future Work

How relevant is the granular temperature? Do we need to consider a quantity that would also include elastic energy?

Understand better the influence of initial conditions (multiple solutions?)

Extend to 3D and analyze the influence of material parameters

Analyze the stress distribution in space and time

Understand the effect of geometry on the nature of the flow

Analyze in more detail the role of external excitations in both zero and nonzero g environment

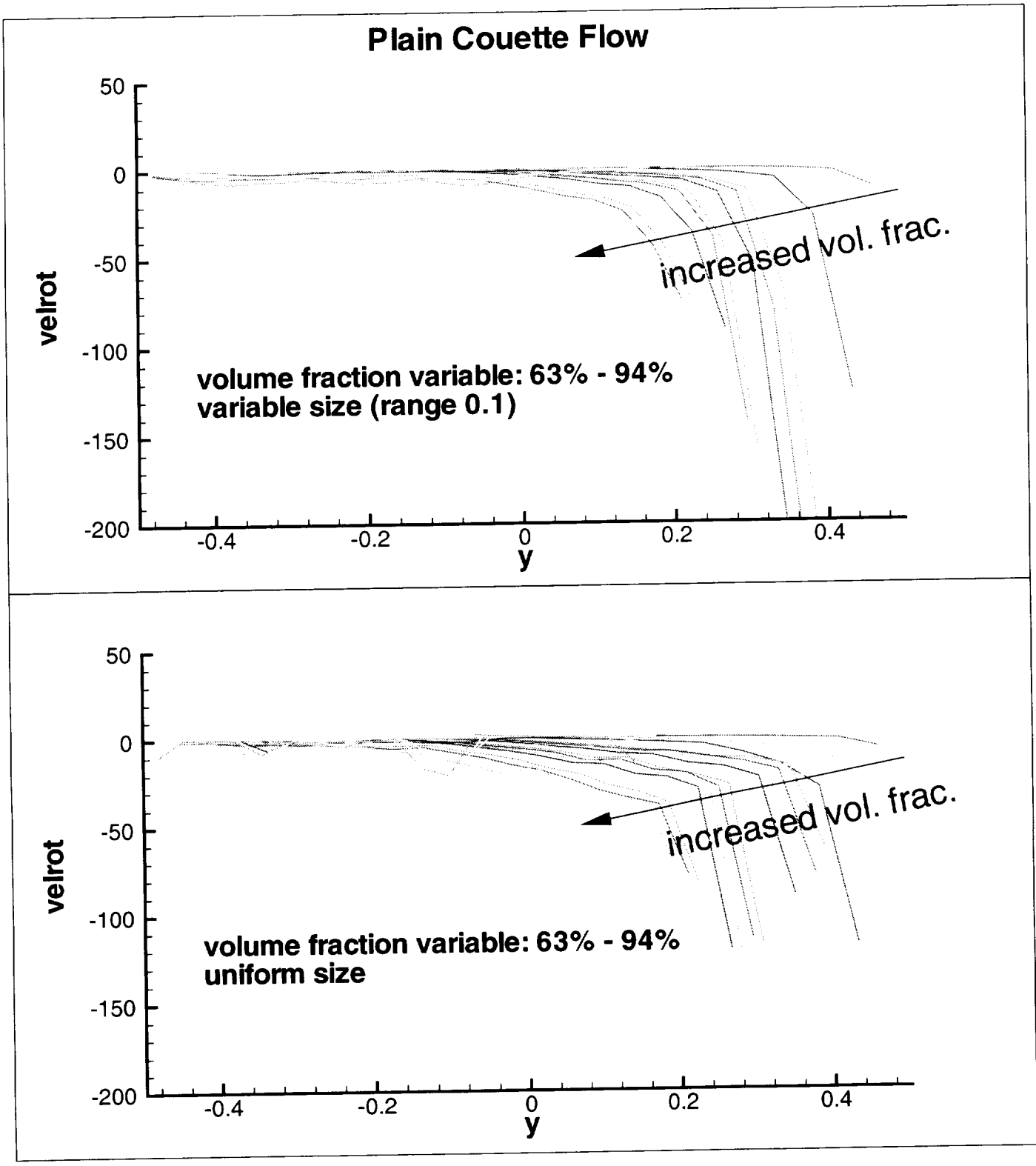
Plain Couette Flow
50
0
-50
-100
-150
-200
velrot
-0.4
-0.2
0
0.2
0.4
y
increased vol. frac.
volume fraction variable: 63% - 94%
variable size (range 0.1)
50
0
-50
-100
-150
-200
velrot
-0.4
-0.2
0
0.2
0.4
y
increased vol. frac.
volume fraction variable: 63% - 94%
uniform size

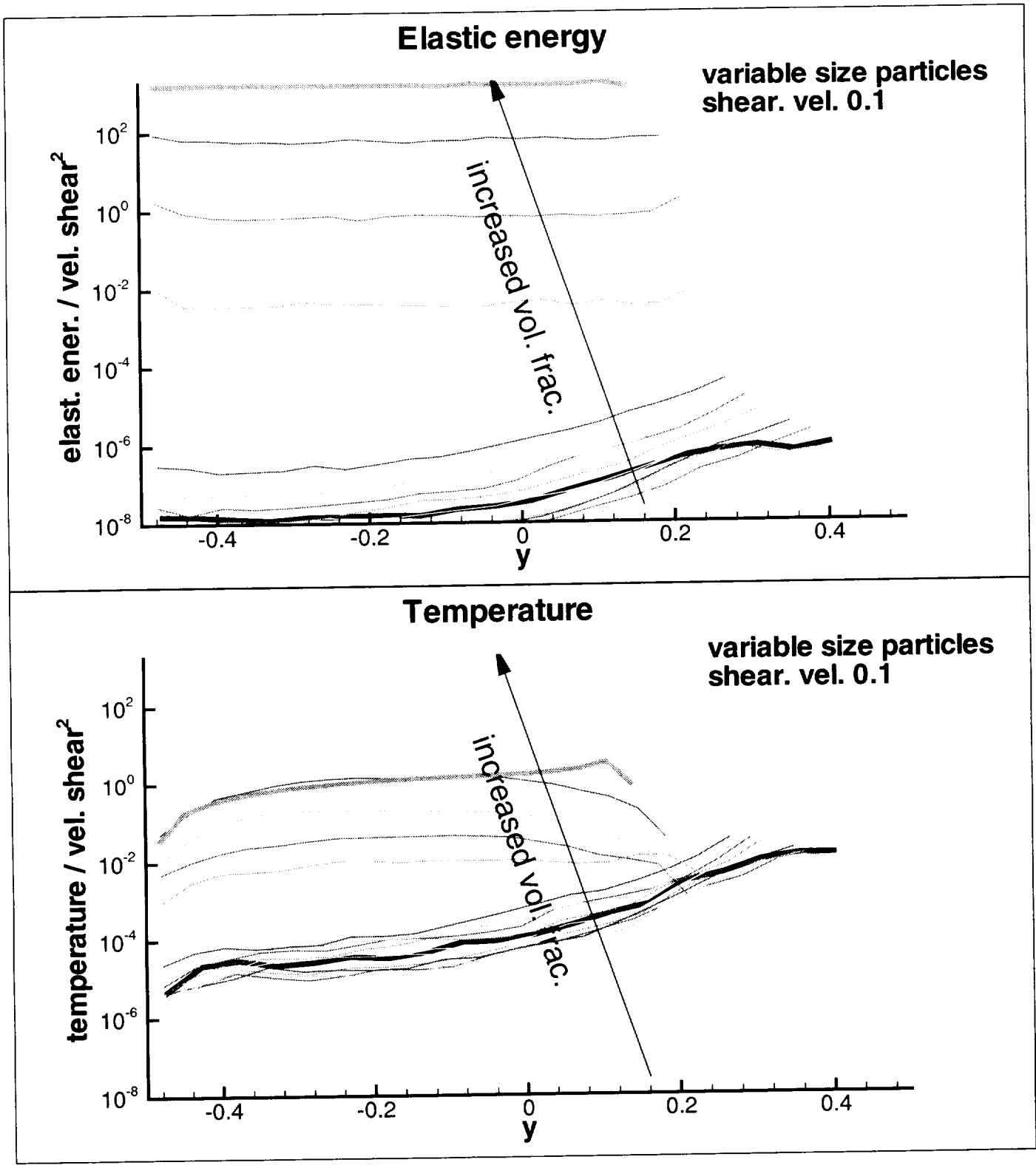
Elastic energy
variable size particles
shear. vel. 0.1
elast. ener. / vel. shear^2
10^2
10^0
10^{-2}
10^{-4}
10^{-6}
10^{-8}
increased vol. frac.
-0.4
-0.2
0
0.2
0.4
y
Temperature
variable size particles
shear. vel. 0.1
temperature / vel. shear^2
10^2
10^0
10^{-2}
10^{-4}
10^{-6}
10^{-8}
increased vol. frac.
-0.4
-0.2
0
0.2
0.4
y

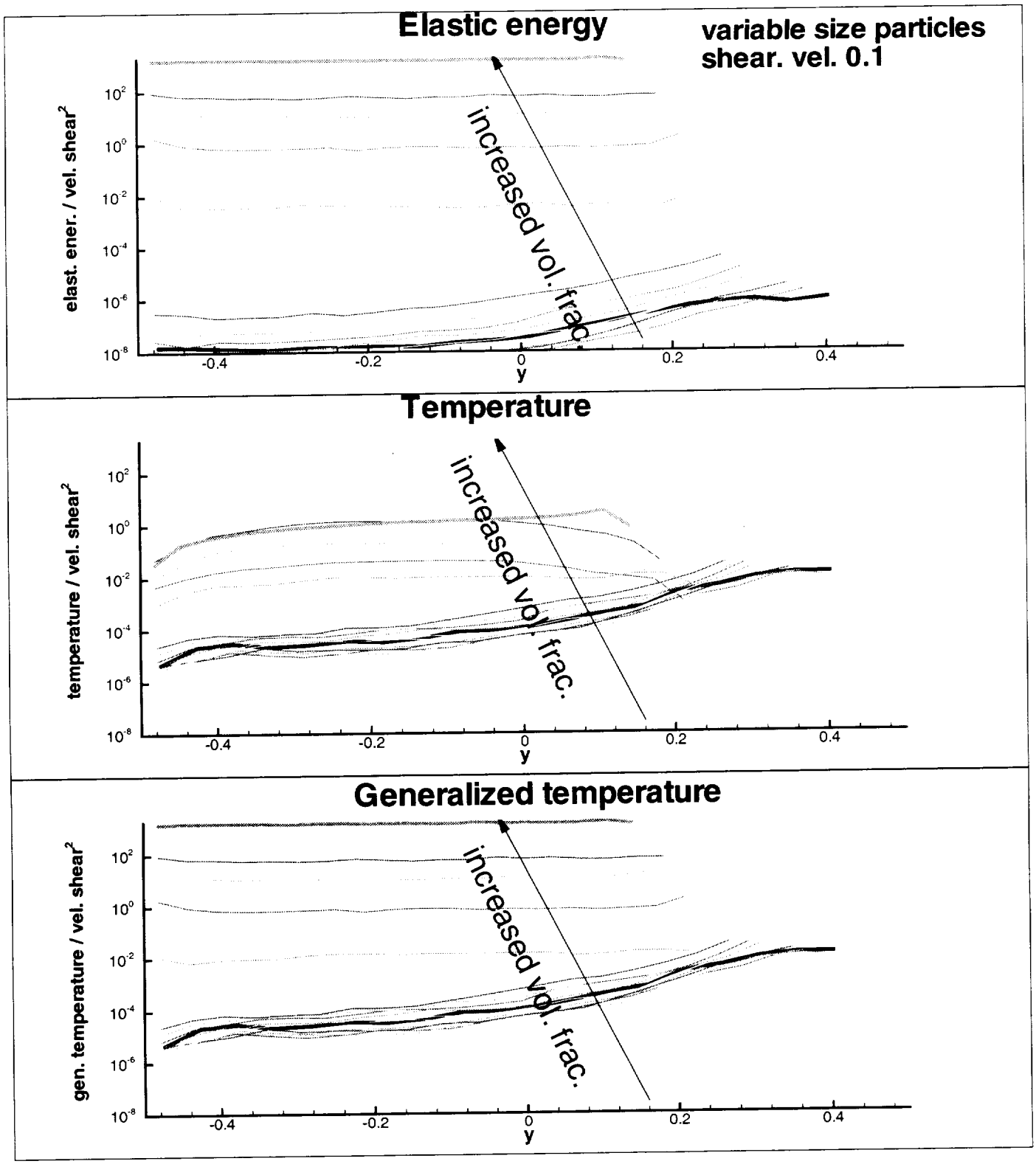
Elastic energy
variable size particles
shear. vel. 0.1
elast. ener. / vel. shear^2
increased vol. frac.
y
Temperature
temperature / vel. shear^2
increased vol. frac.
y
Generalized temperature
gen. temperature / vel. shear^2
increased vol. frac.
y

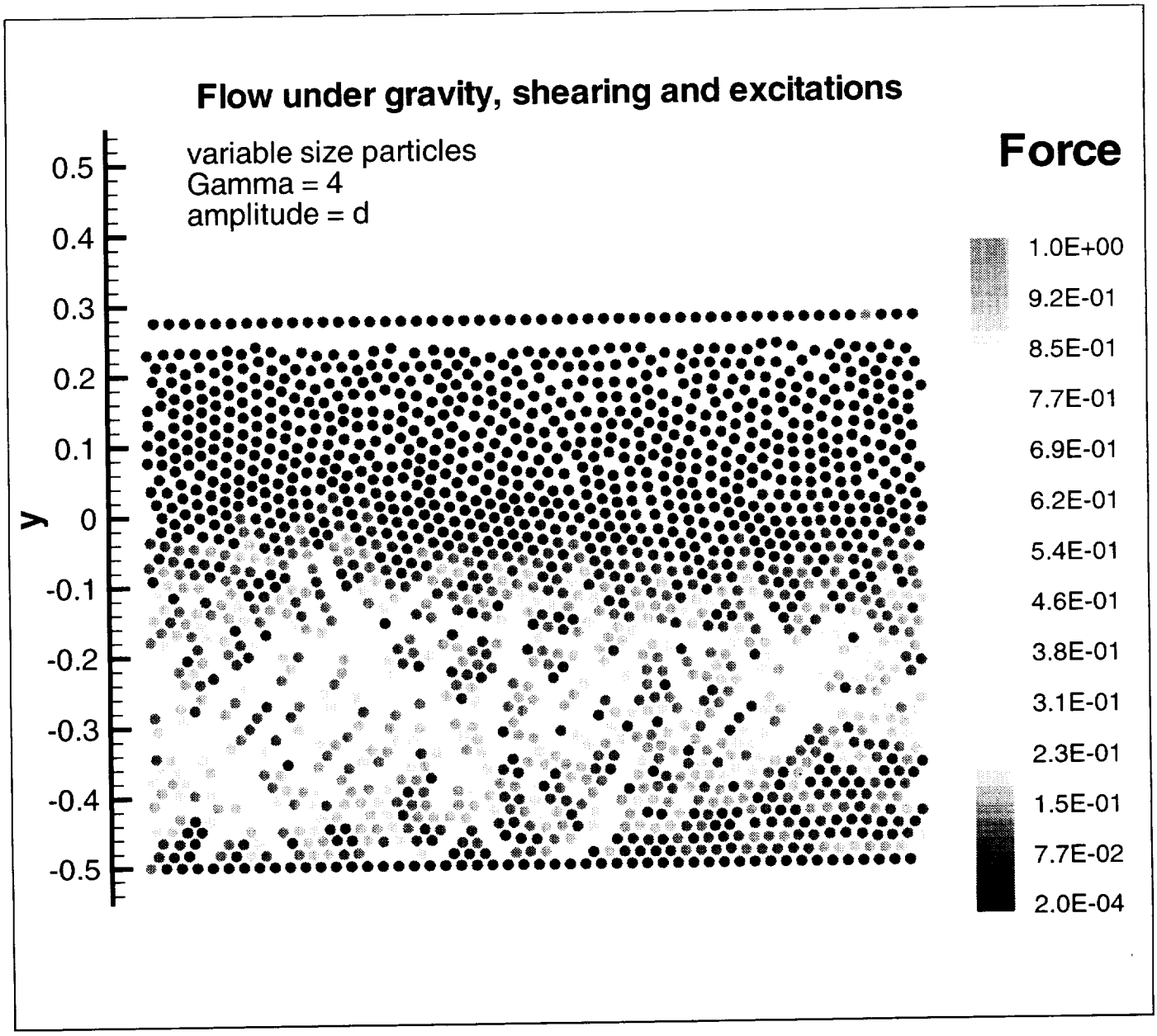
Flow under gravity, shearing and excitations
variable size particles
Gamma = 4
amplitude = d
Force
1.0E+00
9.2E-01
8.5E-01
7.7E-01
6.9E-01
6.2E-01
5.4E-01
4.6E-01
3.8E-01
3.1E-01
2.3E-01
1.5E-01
7.7E-02
2.0E-04
y
0.5
0.4
0.3
0.2
0.1
0
-0.1
-0.2
-0.3
-0.4
-0.5

Session 4: Multiphase Flow and Phase Change

FLUID DYNAMICS OF BUBBLY LIQUIDS

Y. H. Tsang, D. L. Koch
School of Chemical Engineering, Cornell University
Ithaca, NY 14853

A. Sangani
Department of Chemical Engineering, Syracuse University
Syracuse, NY 13244

ABSTRACT

Experiments have been performed to study the average flow properties of inertially dominated bubbly liquids which may be described by a novel analysis. Bubbles with high Reynolds number and low Weber number may produce a fluid velocity disturbance that can be approximated by a potential flow. We studied the behavior of suspensions of bubbles of about 1.5 mm diameter in vertical and inclined channels. The suspension was produced using a bank of 900 glass capillaries with inner diameter of about 100 μm in a quasi-steady fashion. In addition, salt was added to the suspension to prevent bubble-bubble coalescence. As a result, a nearly monodisperse suspension of bubble was produced. By increasing the inclination angle, we were able to explore an increasing amount of shear to buoyancy motion. A pipe flow experiment with the liquid beingrecirculated is under construction. This will provide an even larger range of shear to buoyancy motion. We are planning a microgravity experiment in which a bubble suspension is subjected to shearing in acouette cell in the absence of a buoyancy-driven relative motion of the two phases.

By employing a single-wire, hot film anemometer, we were able to obtain the liquid velocity fluctuations. The shear stress at the wall was measured using a hot film probe flush mounted on the wall. The gas volume fraction, bubble velocity, and bubble velocity fluctuations were measured using a homemade, dual impedance probe. In addition, we also employed a high-speed camera to obtain the bubble size distribution and bubble shape in a dilute suspension.

A rapid decrease in bubble velocity for a dilute bubble suspension is attributed to the effects of bubble-wall collisions. The more gradual decrease of bubble velocity as gas volume fraction increases, due to subsequent hindering of bubble motion, is in qualitative agreement with the predictions of Spelt and Sangani (1998) for the effects of potential-flow bubble-bubble interactions on the mean velocity. The ratio of the bubble velocity variance to the square of the mean is $O(0.1)$. For these conditions Spelt and Sangani predicted that the homogeneous suspension would be unstable and clustering into horizontal rafts will take place. Evidence for bubble clustering is obtained by analysis of video images. The liquid velocity variance is larger than would be expected for a homogeneous suspension and the liquid velocity frequency spectrum indicates the presence of velocity fluctuations that are slow compared with the time for the passage of an individual bubble. These observations provide further evidence for bubble clustering.

Inclination of the channel at angles between 2 to 10 degrees relative to gravity produces a variation in bubble volume fraction across the channel. The resulting buoyancy variation drives a shear flow in the channel and provides a means of observing the effects of weak shear on a bubbly liquid. The bubble velocity and volume fraction gradients increase with channel inclination and exhibit little or no dependence on the mean gas volume fraction. The tendency of buoyancy driven motion to cause the bubbles to accumulate on the upper wall is balanced by lift forces and by an effective bubble-phase diffusivity in the cross-channel direction. The bubble velocity gradient can be understood in terms of a balance of the component of the buoyancy force parallel to the channel walls and an effective viscosity associated with the Reynolds stresses produced by bubble-induced liquid velocity fluctuations. The effective viscosity required to explain the measured bubble velocity gradient is about 1000 times the viscosity of the suspending water. This magnitude is consistent with the liquid velocity fluctuations measured with the hot film anemometer.

In addition, we are studying the Reynolds number dependence of the average properties of the suspension by using a glycerin-water mixture. In a more viscous solution, the boundary layer may become thicker and the wake behind the bubble may become larger. As a result, vorticity may be created. A glycerin solution with a viscosity two times that of water will reduce the Reynolds number based on the bubble radius and the bubble terminal velocity by a factor of four to a value between 40 and 60 which is at the margin of the region for which the potential flow approximation is accurate.

A pipe flow apparatus with recirculation of the liquid has been designed and is under construction. This will provide a larger range of superficial liquid velocities (0.05 to 1 m/s) and liquid velocity gradients than can be achieved in the inclined channel. As a result, a stronger shear can be produced. This apparatus will allow us to study the bubble suspension where the liquid velocities will be of the same order of magnitude as the bubble rise velocity and the shear rates, γ, may approach U_t / a where U_t is the terminal bubble velocity and a the bubble radius. The ratio of the Reynolds number based on the pipe radius, R, to that based on a and γ scales like $(R / a)^2$. In order to study the suspension in the laminar regime and the bubbles being in the ignited state ($Re_a > 30$), and also to ensure a continuum suspension flow, a pipe ID of about 10 bubble diameters will be used. The pipe must have a large height (2.5 m) to ensure fully developed flow. A gas / water separator and a vent will be installed at the end of the test section where the gas will be vented to the atmosphere and the water will be recycled to the pipe entrance. A by-pass section with a pair of quick-closing and opening valves will be inserted between the test section and the separator in order to collect samples of suspension for measurement of the gas hold up. This will be used to calibrate the measurement of the gas volume fraction using the impedance probes. This new experimental setup will allow us to examine how the probes will respond when there is a significant mean liquid velocity.

The ground-based experiments will demonstrate the qualitative phenomenon of shear-induced, bubble-phase pressure that will be measured more quantitatively and in a more ideal setting in the microgravity experiment in which the effects of gravity and lift force will be eliminated.

Flows of bubbly liquids

Cornell team: D. L. Koch, Y. H. Tsang, R. Zenit

Syracuse team: A. S. Sangani, V. I. Kushch, P.D.M. Spelt

NASA GRC team: M. Hoffman, H. Nahra, C. Fritz, R. Dolesh, L. Dozier, …

Regimes of Suspension Behavior

(γ=10s^{-1} , water)

Brownian Colloidal	Viscous non-Brownian	Inertial
$Pe=\gamma a^2/D=1$ a=0.3 μm		$Re=\rho_f \gamma a^2/\mu_f=1$ $St=\rho_p \gamma a^2/\mu_f=1$ a=0.3 mm

Three tractable cases of inertial suspensions

Gas-solid suspensions with a = 5-50 microns

- Neglect gas inertia / retain particle inertia
- Stokes equations of motion for the gas phase

Bubbles in water with a = 0.5 mm

- Potential flow approximation
- Viscous effects confined (no boundary layer separation)

Granular materials (inelastic collisions; a=1 mm)

Kinetic theory and numerical simulations possible

Averaged equations for bubble suspensions

- Bubble phase:

$$\frac{\partial \phi}{\partial t} + \frac{\partial}{\partial x_j}(\phi w_j) = 0$$

$$n\frac{dI_i}{dt} = -\frac{\partial P_{ij}}{\partial x_j} + nF_i^b$$

$$n\frac{dT}{dt} = -\frac{\partial Q_j}{\partial x_j} + S$$

- Entire mixture:

$$\frac{\partial u_j}{\partial x_j} = 0$$

$$\frac{\partial}{\partial t}(1-\phi)u_i^L + \frac{\partial}{\partial x_j}(1-\phi)u_i^L u_j^l = -\frac{1}{\rho}\frac{\partial \Sigma_{ij}}{\partial x_j} + (1-\phi)g_i$$

Disperse-phase pressure

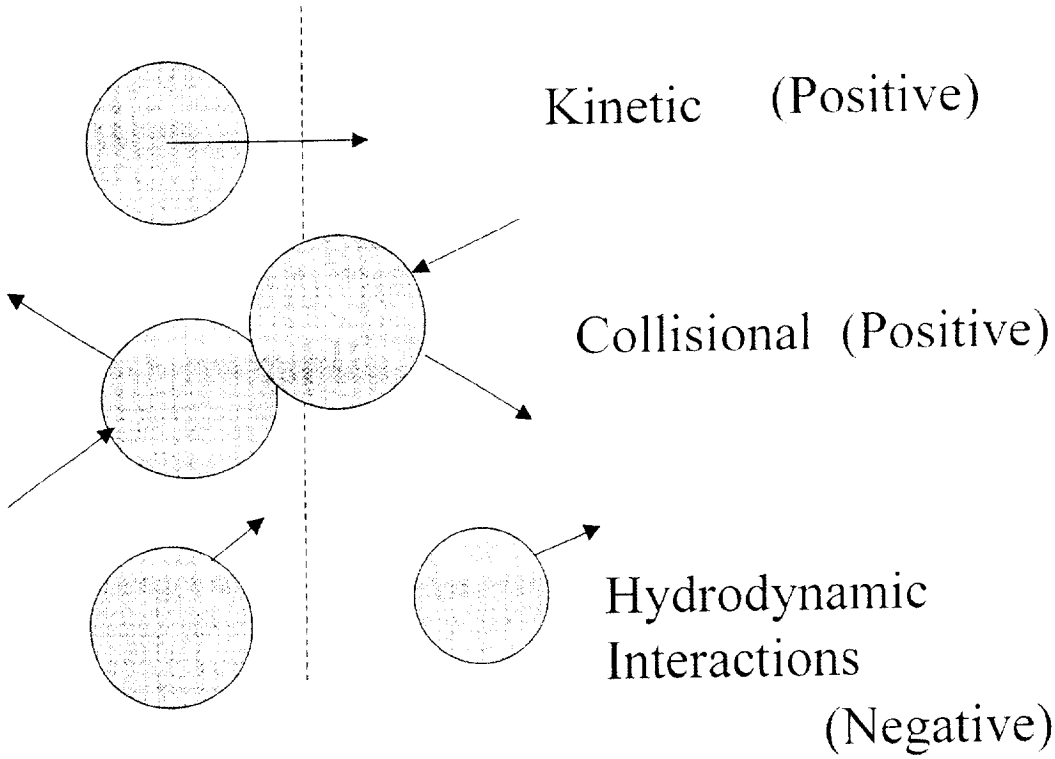

Stress depends on velocity variance and mean velocity

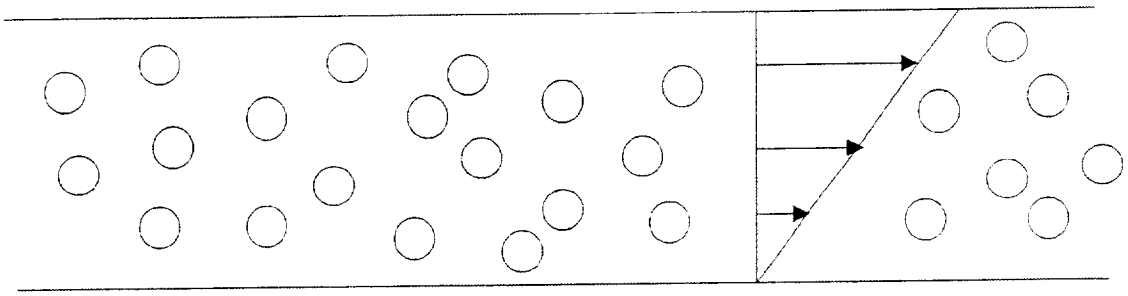

Kinetic theory relates disperse-phase pressure and viscosity to velocity variance or bubble-phase ``temperature''

Energy balance: Shear work =Viscous dissipation

SIMULATIONS OF SHEARED BUBBLE SUSPENISIONS (Kang et al 1997)

Solid line: kinetic theory; Diamonds: Simulations with hydrodynamic interactions; Pluses: Simplified simulations with bubbles replaced by particles of mass $(m/2)C_k(\phi)$ and drag coefficient $R_{\text{diss}}(\phi)$

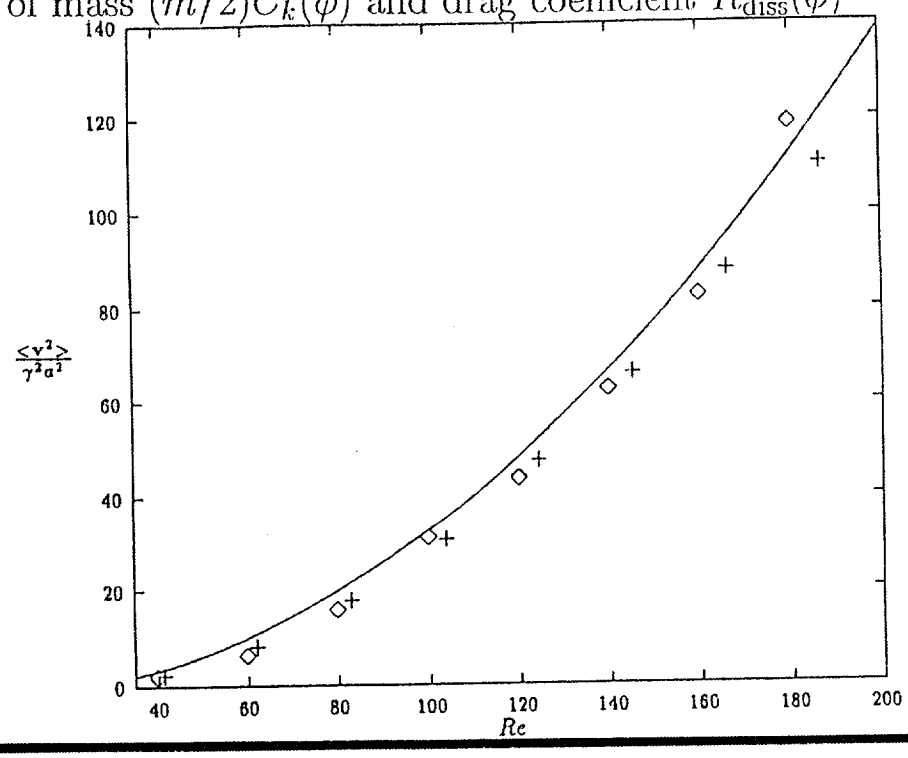

Proposed Experiment on ISS

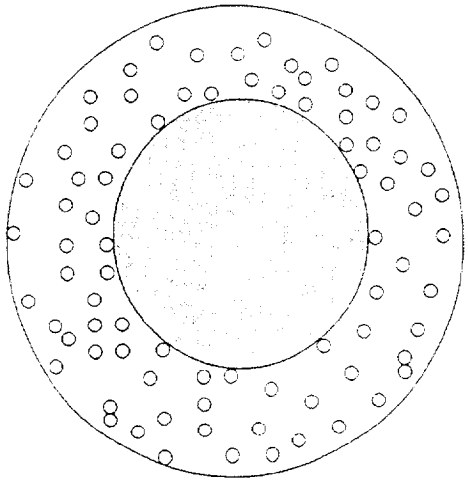

Centrifugal force = dispersed phase pressure gradient

Need for microgravity

- Density matching not possible
- Complications due to buoyancy (lift force, wake interactions, instability, etc.)
- Better control of Reynolds and Weber numbers
- One of the simplest flows
- Larger dispersed-phase pressure

Requirements

- Nearly monodisperse bubble suspension (Earth based / microgravity)
- Minimal coalescence
- Measurement of volume fraction and velocity distribution profiles

Coalescence Inhibition

- Surface-active impurities
- Electrolytes (Magnesium Sulfate, Salt)
  - -- No Marangoni effects
  - -- Short-range repulsive forces (hydration)

Inertial Multiphase Flows: Instrumentation

- High-speed video -- non-invasive, but limited to dilute suspensions.
- Dual-impedance probe for gas volume fraction, bubble velocity (mean and fluctuations), and bubble collision rates.
- Hot-film probe for liquid velocity.
- Flush-mounted hot-film probe for wall shear stress (Zenit *et al.*, 2001).

Experimental Study of Sheared Bubbly Liquids

- vertical channel inclined channel vertical pipe flow Couette in μg

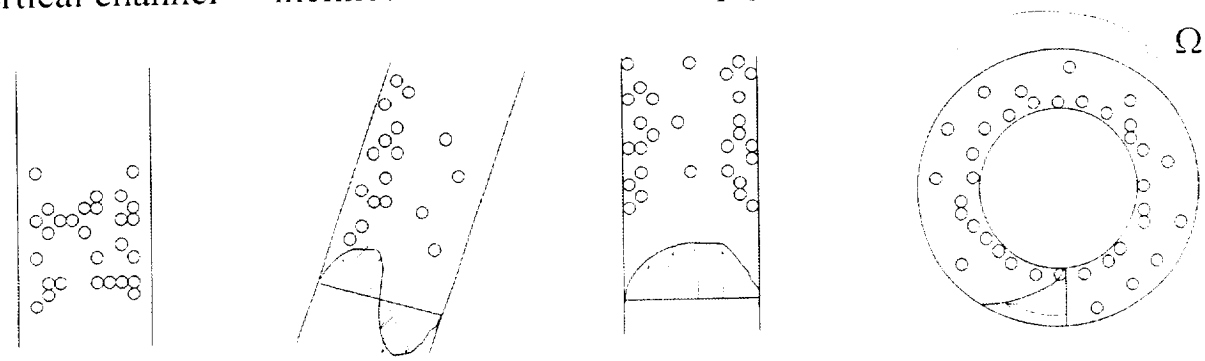

- The ratio of shear to buoyancy increases from left to right.
- Gravity-driven shear flow in an inclined channel.
- Pure shear flow in a Couette experiment in μg.

Experimental setup

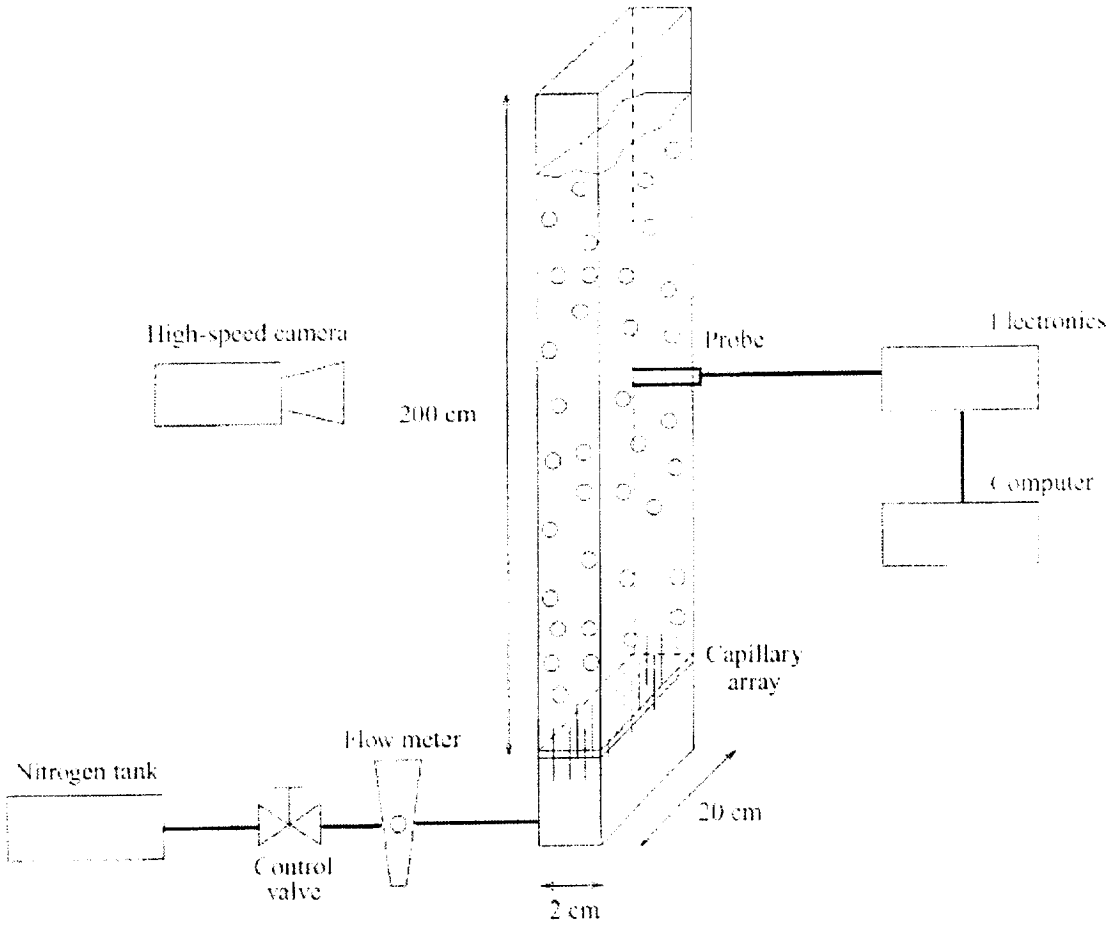

Bubble size and distribution

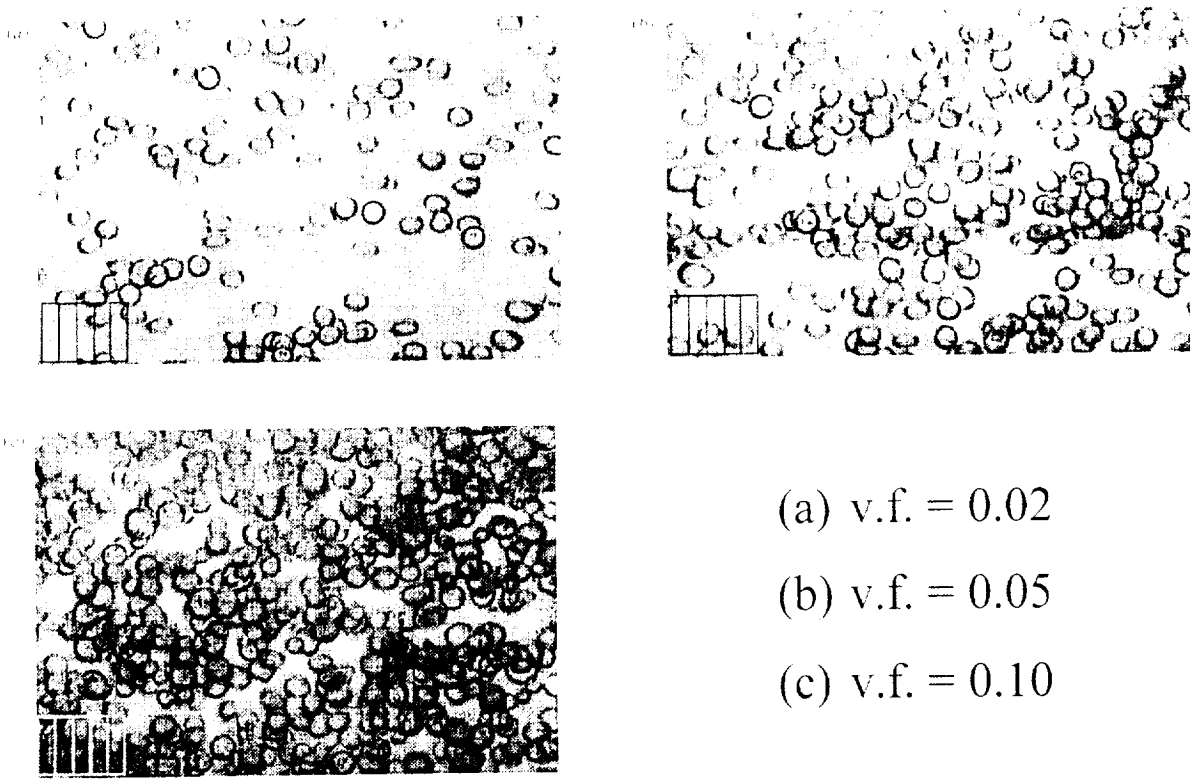

(a) v.f. = 0.02

(b) v.f. = 0.05

(c) v.f. = 0.10

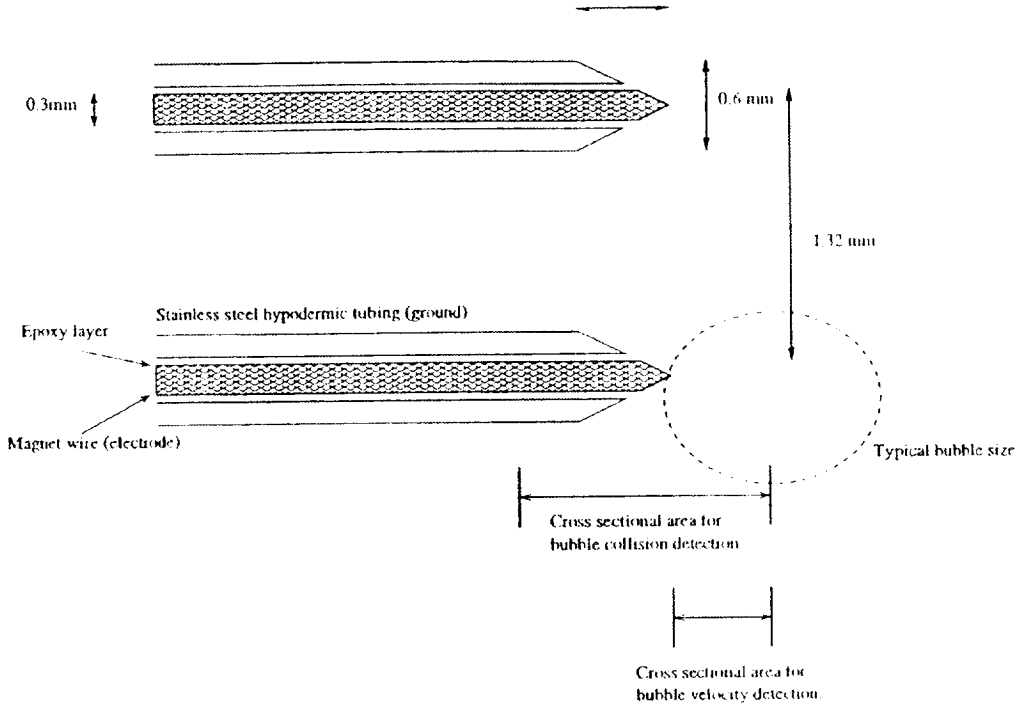
0.3mm
0.6 mm
1.32 mm
Stainless steel hypodermic tubing (ground)
Epoxy layer
Magnet wire (electrode)
Typical bubble size
Cross sectional area for bubble collision detection
Cross sectional area for bubble velocity detection

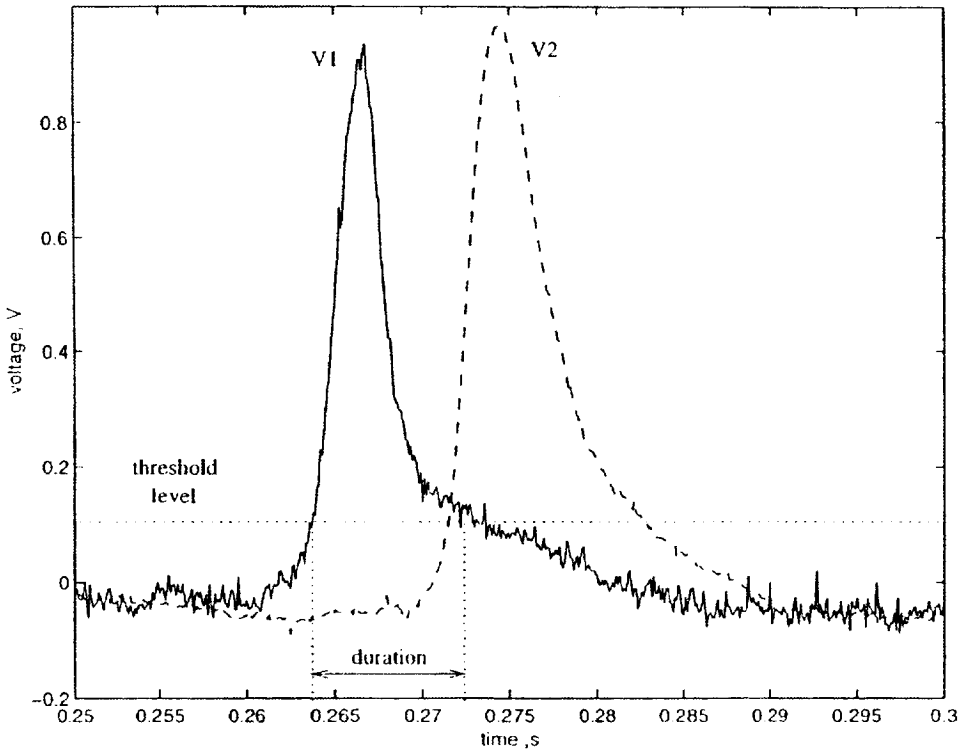
V1
V2
threshold level
duration
voltage, V
time ,s
0.8
0.6
0.4
0.2
0
-0.2
0.25
0.255
0.26
0.265
0.27
0.275
0.28
0.285
0.29
0.295
0.3

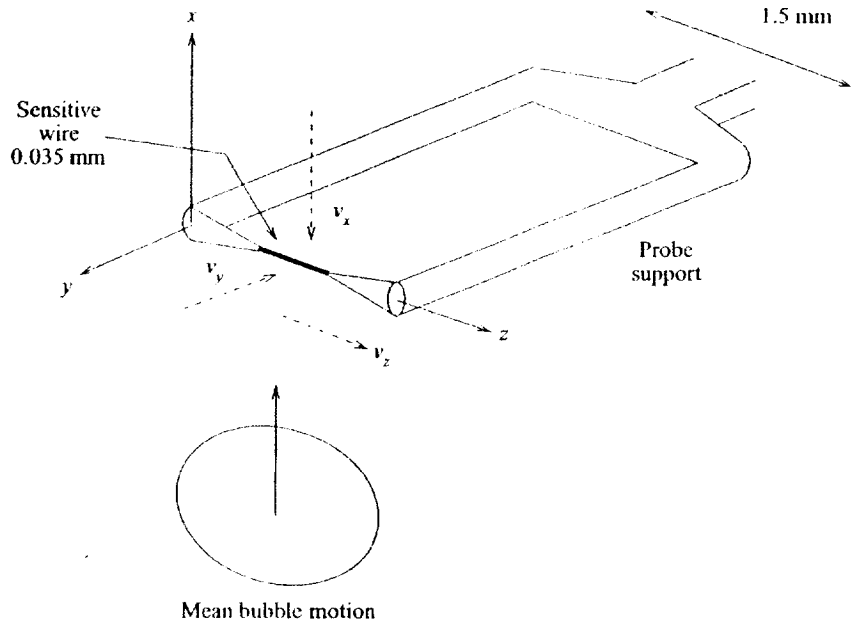

FIGURE 3. Sketch of the hot-wire probe and its orientation with respect to the mean bubble motion.

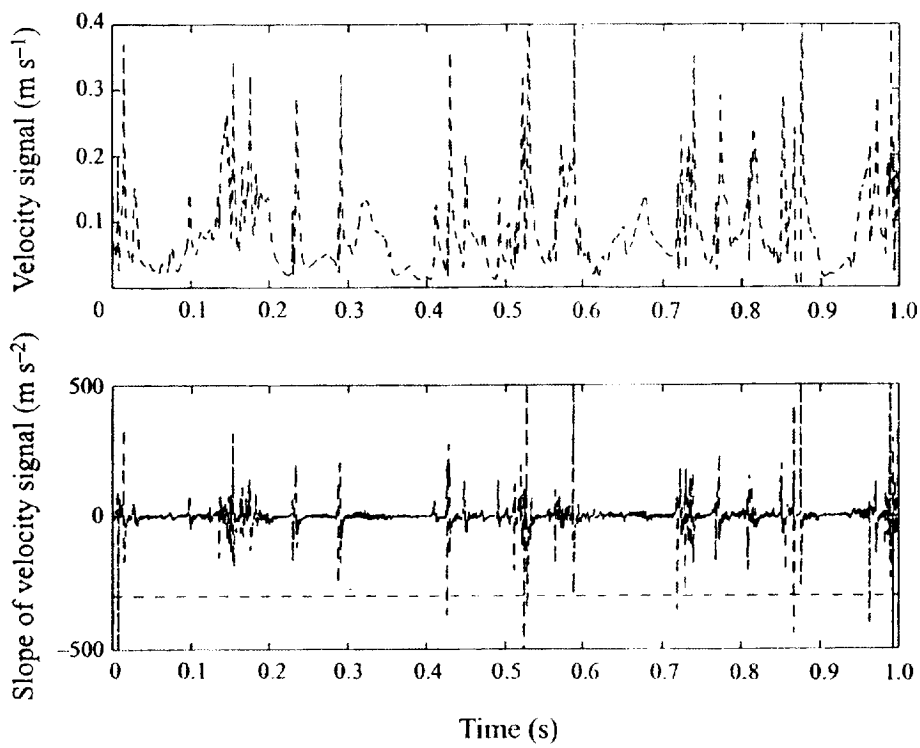

FIGURE 4. Typical fluid velocity signal and fluid velocity signal slope for a mean gas volume fraction of 0.05. The dashed line denotes the collision detection threshold level.

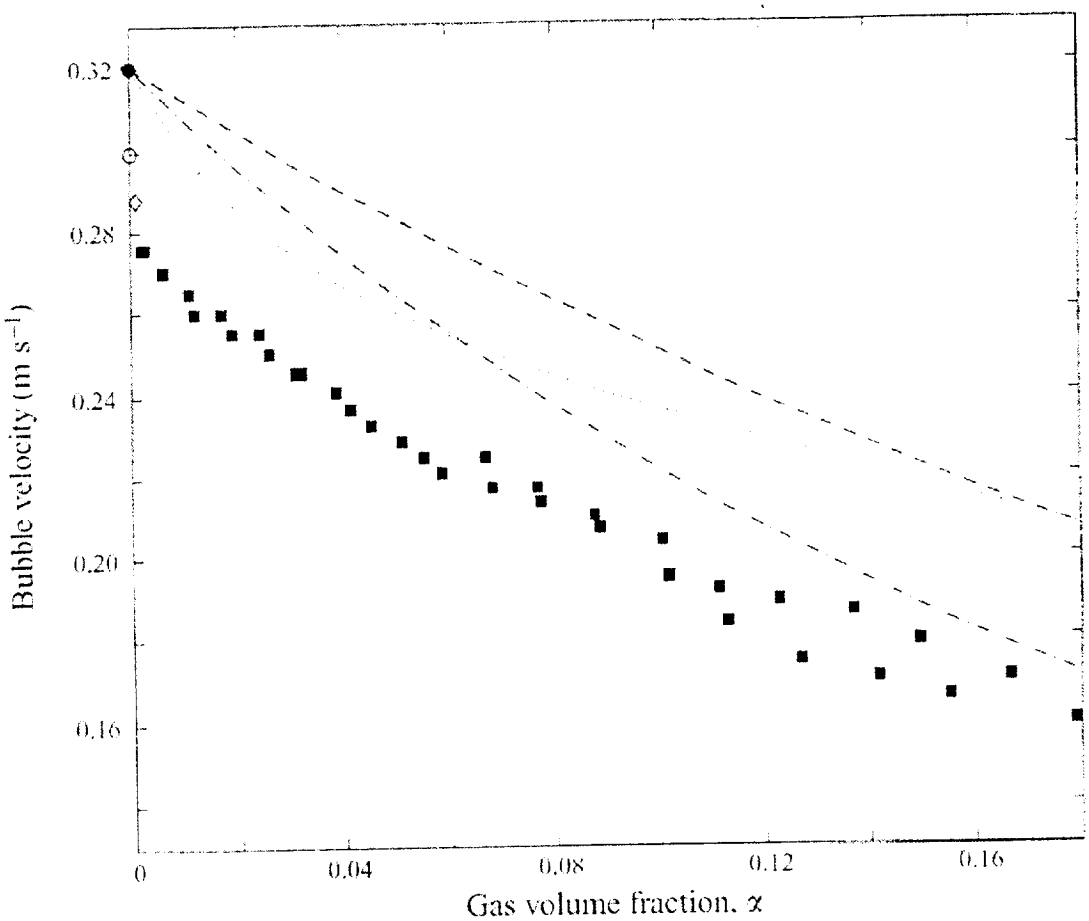
0.32
0.28
0.24
0.20
0.16
Bubble velocity (m s^{-1})
0
0.04
0.08
0.12
0.16
Gas volume fraction, α

Normalized bubble velocity variance, T_b/u_b^2
0.10
0.08
0.06
0.04
0.02
0
0.04
0.08
0.12
0.16
Gas volume fraction, χ

Bubble-wall collision

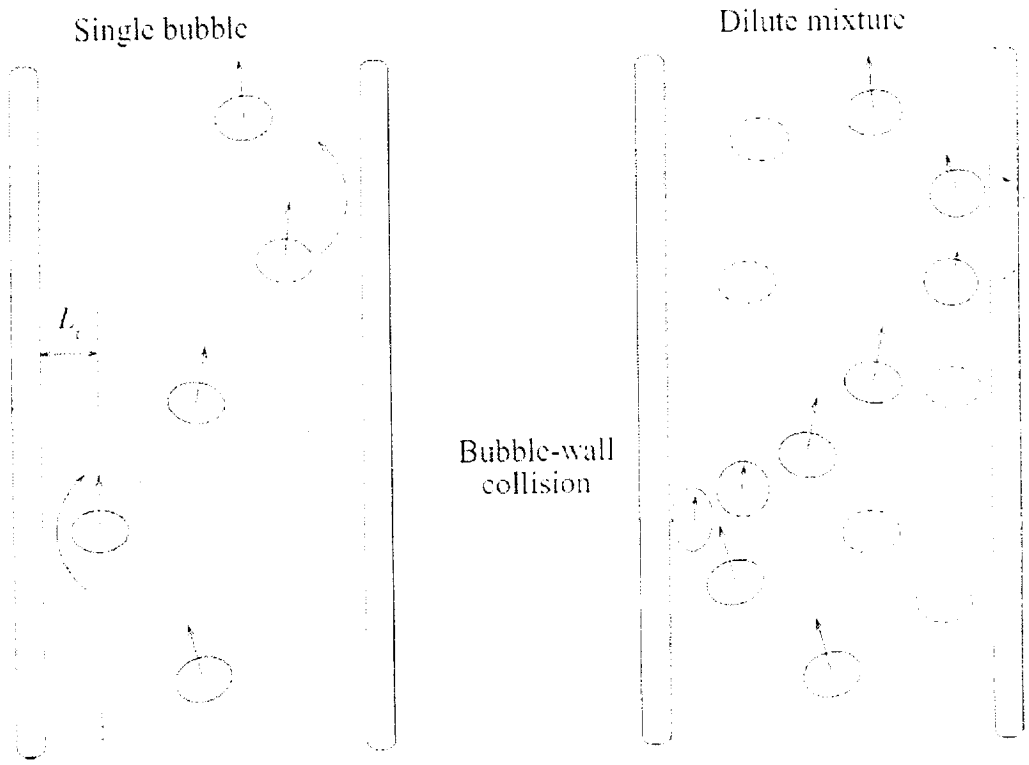

Vertical Channel: Fluid Velocity Variance

- The vertical velocity variance is larger than the horizontal variance at all gas volume fractions.

- The experimental values are much larger than theoretical prediction for a homogeneous suspension.

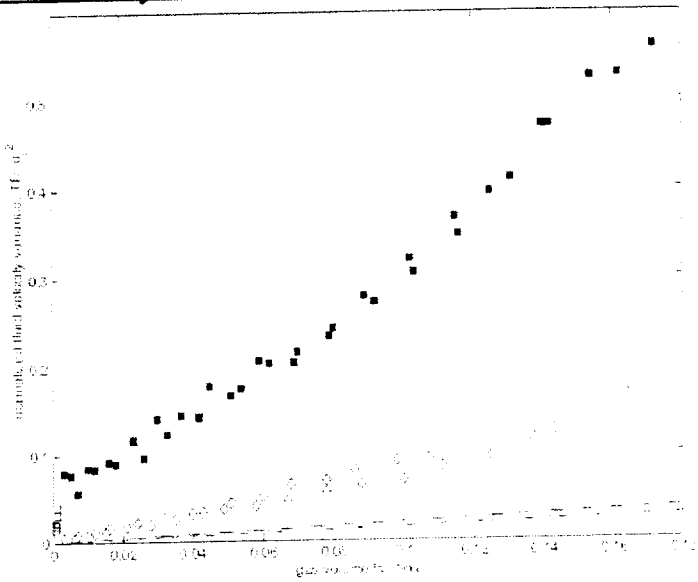

Vertical Channel: Power Spectrum

- Dashed line represents characteristic frequency of single bubble passing near the probe: $\omega_b = u_b / a = O(100) Hz$.

- Dashed-dotted line represents characteristic frequency of structures having the size of the channel width ($H = 2\ cm$):

  $\omega_H = u_b / H = O(10) Hz$.

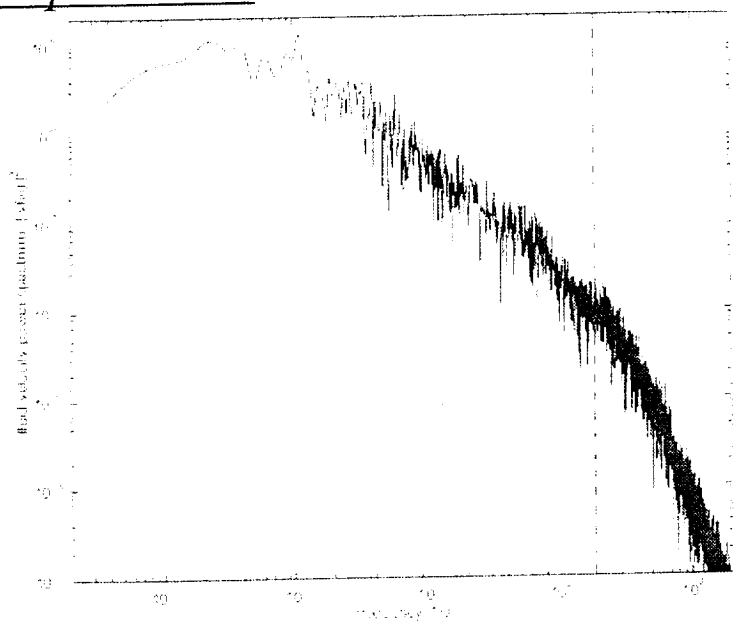

- Most energy confined in frequency less than ω_H; structures with size larger than bubble diameter.

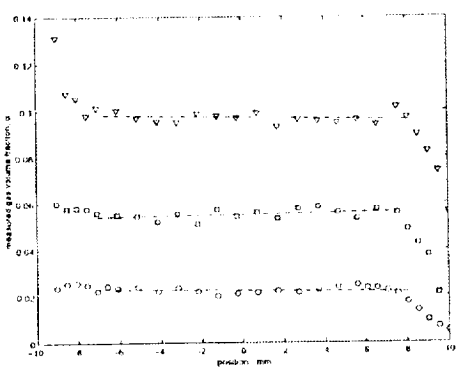

(a) $\theta = 0^o$

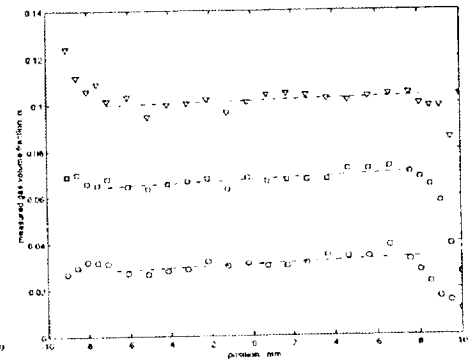

(b) $\theta = 2.5^o$

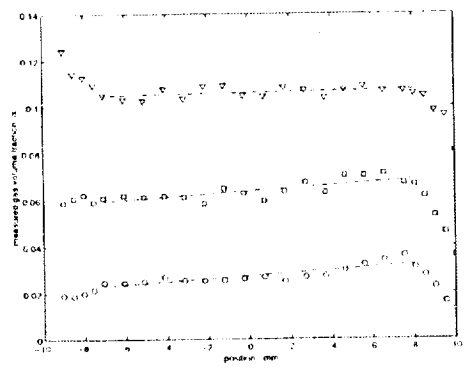

(c) $\theta = 5^o$

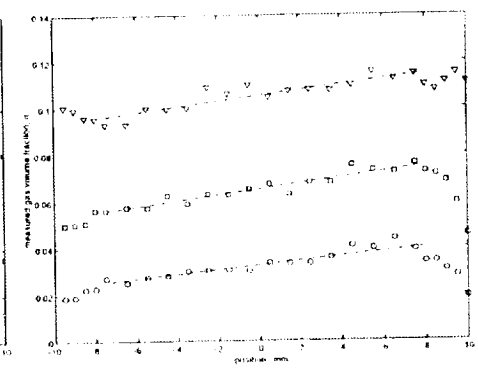

(d) $\theta = 7.5^o$

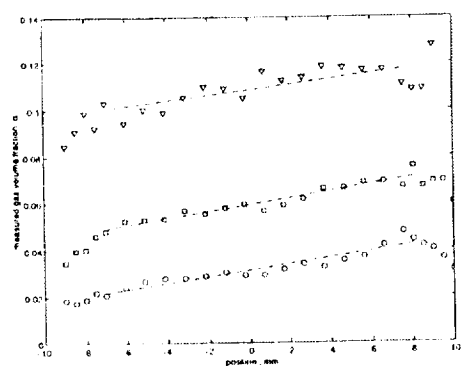

(e) $\theta = 10^o$

FIGURE 10. Gas volume fraction profiles for three typical hold ups. (o), α=0.02; (□), α=0.05; (∇), α=0.10, for four channel inclinations. The lines show best linear fits of the data excluding the near-wall regions.

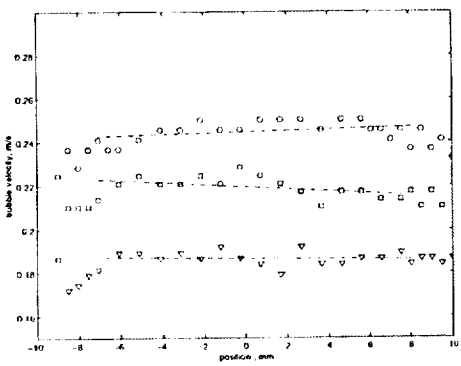

(a) $\theta = 0^o$

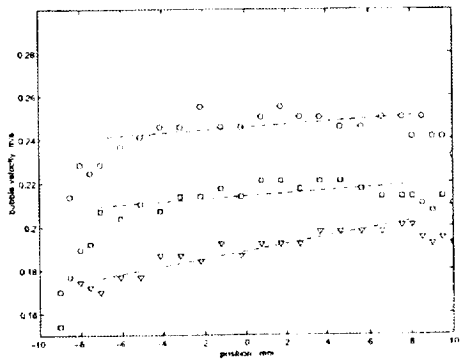

(b) $\theta = 2.5^o$

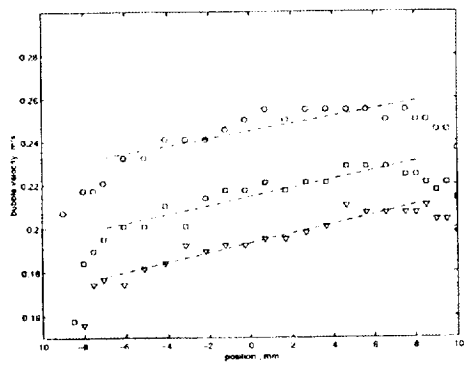

(c) $\theta = 5^o$

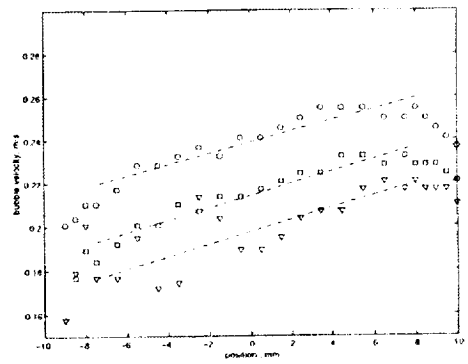

(d) $\theta = 7.5^o$

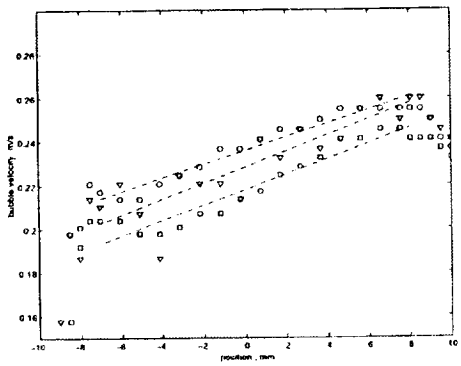

(e) $\theta = 10^o$

FIGURE 12. Bubble velocity profiles for three typical hold ups. (○), α=0.02; (□), α=0.05; (▽), α=0.10, for four channel inclinations. The lines show the linear best fits.

Inclined Channel: Bubble Velocity Gradient

- Non-dimensionalized by bubble diameter and velocity.
- Increases with inclination angle.
- Small dependence on volume fraction.

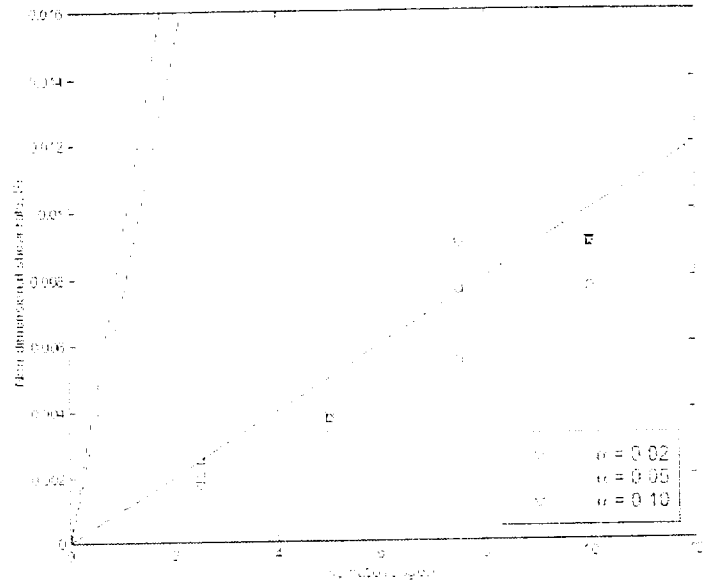

- Balancing the lift force exerted on bubbles by the component of gravity in the cross-channel direction, $\frac{\partial u_b}{\partial y} = \frac{2g\sin\theta}{v_b}$
- Simplified model overestimates bubble velocity gradient. Another effect may balance the gravity force in addition to life force.

Bubble Velocity Fluctuations: Hydrodynamic Diffusion or Bubble Phase Pressure?

- If $\tau_{diff} > \tau_{visc}$, bubbles in suspension relax to the local fluid velocity rapidly. Fluctuations in bubble velocity are strongly correlated with fluid velocity fluctuations. The bubbles are transported across the channel by hydrodynamic diffusion.

- If $\tau_{visc} > \tau_{diff}$, there is insufficient time for bubble velocities to relax to the local fluid velocity before they are transported into a region with a different fluctuating liquid velocity. It would be appropriate to use a kinetic theory. The bubble velocity distribution is assumed to be uncorrelated with the local fluid velocity.

Inclined Channel: Hydrodynamic Diffusion

- $\tau_{visc} = m / 12\pi\mu a \approx 0.05$ sec.
- $\tau_{diff} = H^2 / D = H / \sqrt{\langle u_b'^2 \rangle}$
- $\tau_{diff} > \tau_{visc}$,

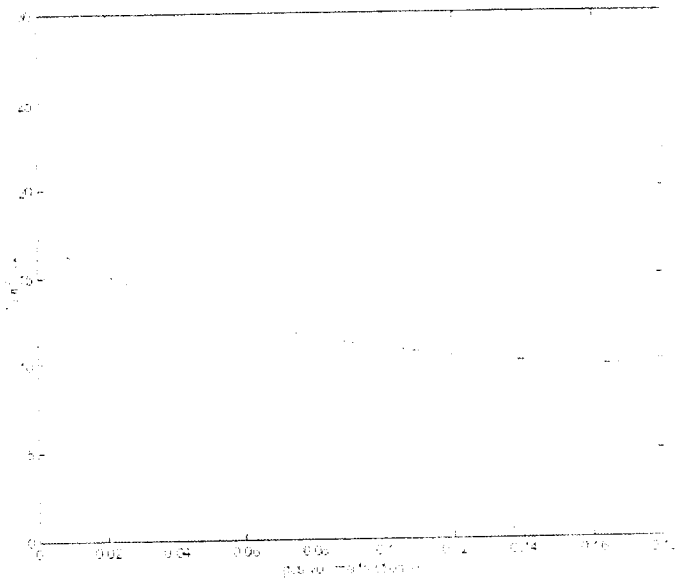

- Hydrodynamic diffusion is more appropriate to describe bubbles' fluctuating motion and their transport across the channel.

Inclined Channel: Diffusivity

- Diffusivity estimated on the basis of the measured bubble velocity variance (solid line) is comparable to the diffusivity that would be required to balance the buoyancy driven velocity (dashed line)

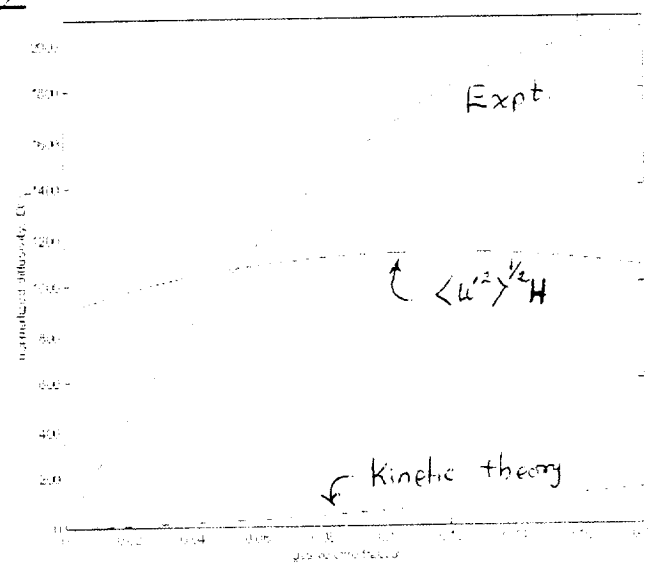

- Diffusivity estimated by the bubble phase pressure gradient from kinetic theory (dashed-dotted line) is much smaller than the other two.

- Inappropriate to use kinetic theory to describe the bubble phase pressure.

$$D_{expt} = \frac{(U_{buoy} - U_{Lift})\alpha}{\partial\alpha/\partial y}, \qquad D_{kin} = \frac{d^2}{36\mu}\left(\frac{\partial P}{\partial \alpha}\right)$$

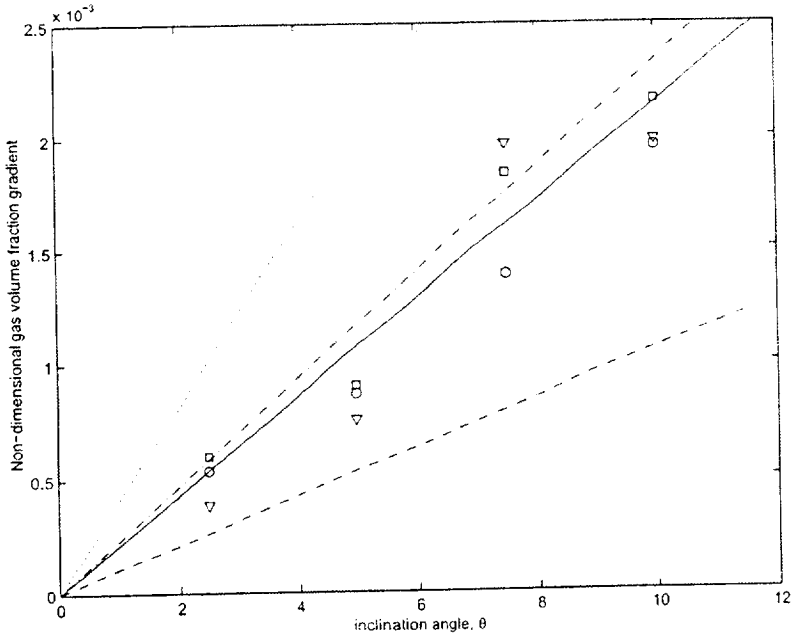

FIGURE 17. Comparison of the measured non-dimensional gas volume fraction gradient with predictions from equation 4.11. The predictions are for three mean gas volume fractions: (– – –), $\alpha = 0.02$; (– · –), $\alpha = 0.05$; (· · ·), $\alpha = 0.10$. The circles, squares and triangles refer to experiments with $\alpha = 0.02$, 0.05, and 0.10, respectively. The solid line shows a best fit to all of the experimental results, which exhibit little dependence on volume fraction.

Bubble phase pressure

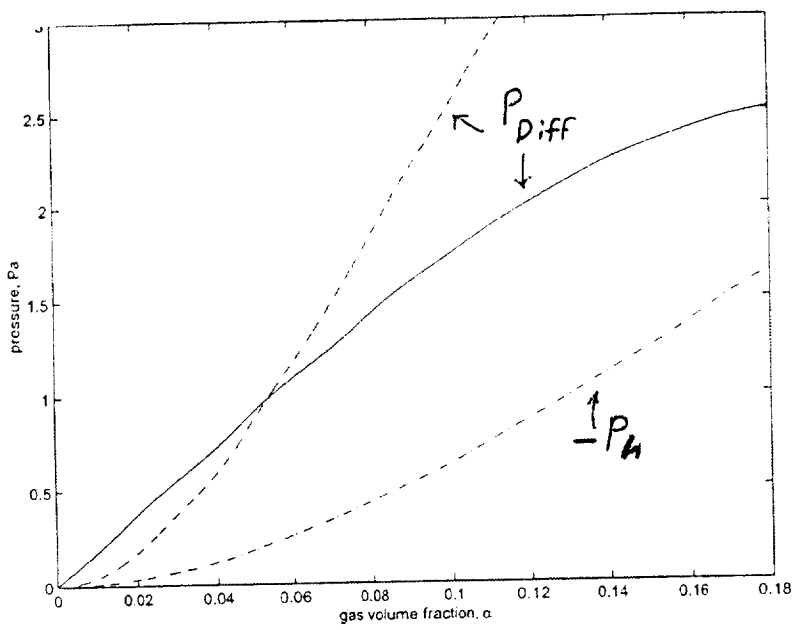

FIGURE 19. Bubble phase pressure obtained using equation 4.3 (solid line) and equation 4.10 (dashed line) for the diffusivity, and the negative of the Maxwell pressure (dashed dotted line) as functions of gas volume fraction.

Map of stability conditions

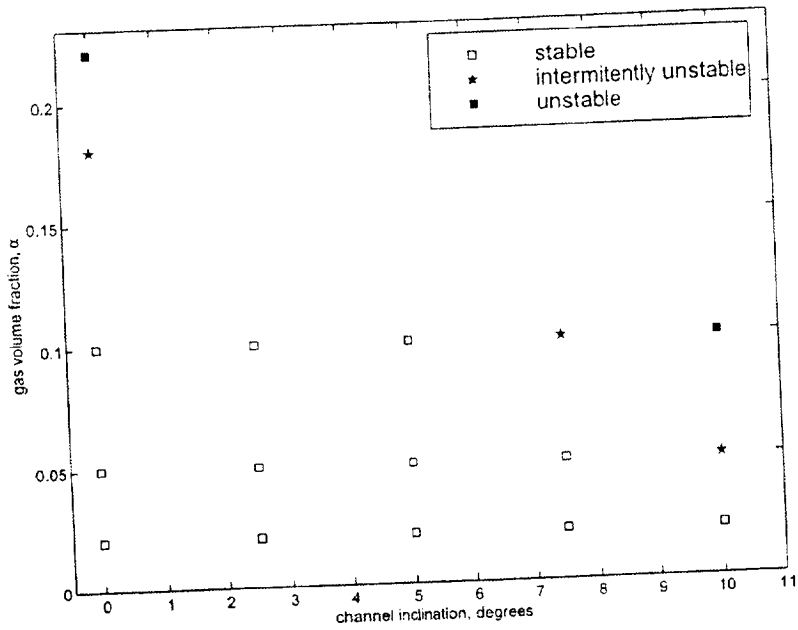

Bubble phase pressure gradient

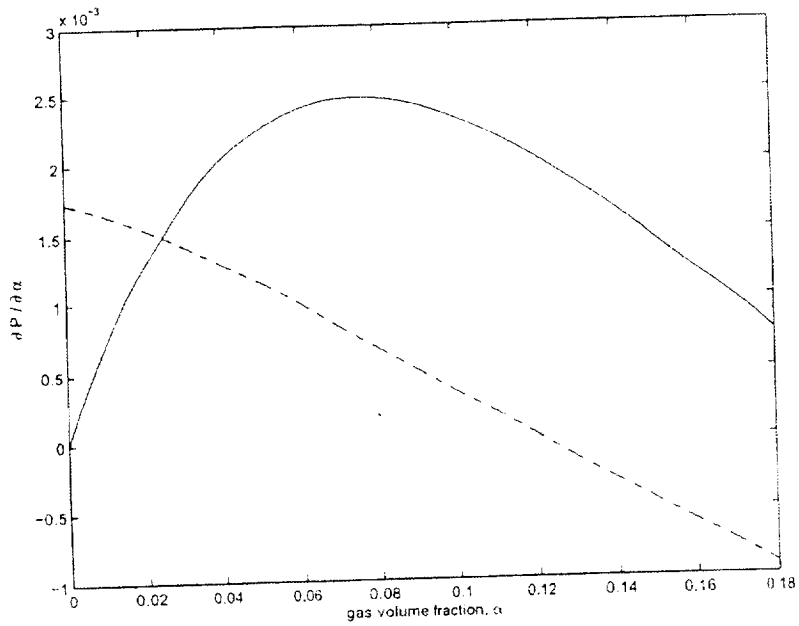

FIGURE 21. Gradient of the total bubble phase pressure with respect of the bubble concentration as a function of the gas volume fraction. The dashed and solid lines show the prediction of the pressure gradient based on equations 4.3 and 4.10 respectively.

Inclined Channel: Suspension Effective Viscosity

- Open symbols: effective viscosity calculated from bubble velocity and volume fraction gradients.

- Solid symbols: effective viscosity calculated from shear stress measurement and bubble velocity gradient.

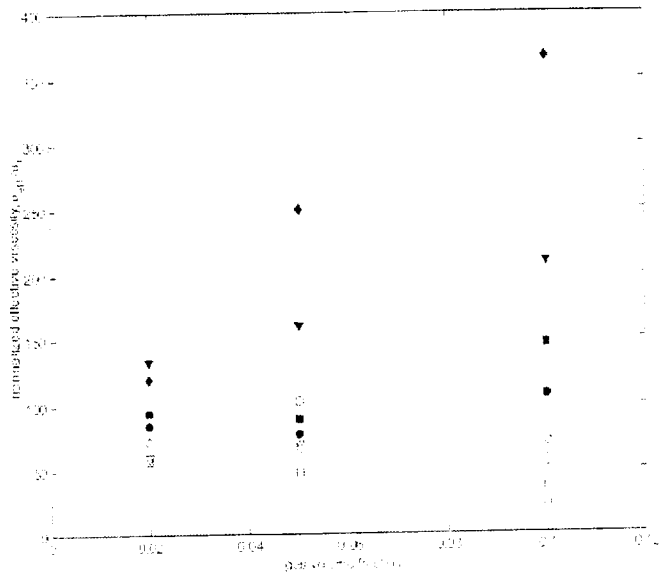

- The dispersed phase enhances the effective viscosity by 25 to 375 times that of the suspending water.

$$\mu_{eff}^{kinetic} < \mu_{eff} < \rho D$$

Bubbly liquids

- Millimeter-sized bubbles
- Large Reynolds number, small to moderate Weber number flows
- Wake effects minimal
- Potential flow approximation
- Small amounts of salt (inhibit coalescence)

Summary

- Generated nearly monodisperse bubble suspensions
- Developed probes for measuring volume fraction and velocity distribution of bubbles
- Flows in vertical and inclined channels influenced siginificantly by wall effects and flow instabilities

Summary (continued)

- Transport by liquid velocity fluctuations across the channel width
- Magnitude of fluctuations adequate to prevent cluster formations

MEASUREMENTS OF TURBULENCE ATTENUATION BY A DILUTE DISPERSION OF SOLID PARTICLES IN HOMOGENEOUS ISOTROPIC TURBULENCE

John K. Eaton and Wontae Hwang

Department of Mechanical Engineering
Stanford University
Stanford, California 94305
eaton@vk.stanford.edu, (v) 650-723-1971 (f) 650-723-4548

ABSTRACT

This research addresses turbulent gas flows laden with fine solid particles at sufficiently large mass loading that strong two-way coupling occurs. By two-way coupling we mean that the particle motion is governed largely by the flow, while the particles affect the gas-phase mean flow and the turbulence properties. Our main interest is in understanding how the particles affect the turbulence. Computational techniques have been developed which can accurately predict flows carrying particles that are much smaller than the smallest scales of turbulence. Also, advanced computational techniques and burgeoning computer resources make it feasible to fully resolve very large particles moving through turbulent flows. However, flows with particle diameters of the same order as the Kolmogorov scale of the turbulence are notoriously difficult to predict. Some simple flows show strong turbulence attenuation with reductions in the turbulent kinetic energy by up to a factor of five. On the other hand, some seemingly similar flows show almost no modification. No model has been proposed that allows prediction of when the strong attenuation will occur. Unfortunately, many technological and natural two-phase flows fall into this regime, so there is a strong need for new physical understanding and modeling capability.

Our objective is to study the simplest possible turbulent particle-laden flow, namely homogeneous, isotropic turbulence with a uniform dispersion of monodisperse particles. We chose such a simple flow for two reasons. First, the simplicity allows us to probe the interaction in more detail and offers analytical simplicity in interpreting the results. Secondly, this flow can be addressed by numerical simulation, and many research groups are already working on calculating the flow. Our detailed data can help guide some of these efforts. By using microgravity, we can further simplify the flow to the case of no mean velocity for either the turbulence or the particles. In fact the addition of gravity as a variable parameter may help us to better understand the physics of turbulence attenuation.

The experiments are conducted in a turbulence chamber capable of producing stationary or decaying isotropic turbulence with nearly zero mean flow and Taylor microscale Reynolds numbers up to nearly 500. The chamber is a 410 mm cubic box with the corners cut off to make it approximately spherical. Synthetic jet turbulence generators are mounted in each of the eight corners or the box. Each generator consists of a loudspeaker forcing a plenum and producing a pulsed jet through a 20 mm diameter orifice. These synthetic jets are directed into ejector tubes pointing towards the chamber center. The ejector tubes increase the jet mass flow and decrease the velocity. The jets then pass through a turbulence grid. Each of the eight loudspeakers is

forced with a random phase and frequency. The resulting turbulence is highly isotropic and matches typical behavior of grid turbulence.

Measurements of both phases are acquired using particle image velocimetry (PIV). The gas is seeded with approximately 1 micron diameter seeding particles while the solid phase is typically 150 micron diameter spherical glass particles. A double-pulsed YAG laser and a Kodak ES-1.0 10-bit PIV camera provide the PIV images. Custom software is used to separate the images into individual images containing either gas-phase tracers or large particles. Modern high-resolution PIV algorithms are then used to calculate the velocity field. A large set of image pairs are acquired for each case, then the results are averaged both spatially and over the ensemble of acquired images.

The entire apparatus is mounted in two racks which are carried aboard NASA's KC-135 Flying Microgravity Laboratory. The rack containing the turbulence chamber, the laser head, and the camera floats freely in the airplane cabin (constrained by competent NASA personnel) to minimize g-jitter. The floating rack with safety covers removed is shown in Figure 1. In a typical day of flying, we obtain quality data during about 20 of the 40 parabolas flown. Prior to taking off, a measured quantity of solid particles are loaded into the turbulence chamber. During the course of the experiments, there is attrition as particles become stuck in the corners of the box and in the synthetic jet actuators. For this reason, the particle mass loading for each image pair is calculated by the number of particles captured in the images. This increases the uncertainty in the particle loading. We are presently doing calibrations to reduce this uncertainty.

Results for 150 micron diameter particles are shown in Figure 2. The turbulent kinetic energy is reduced by approximately a factor of four for a mass-loading ratio of 0.3. It is interesting to note that the attenuation agrees closely with results from a parallel experiment on the centerplane of fully developed channel flow.

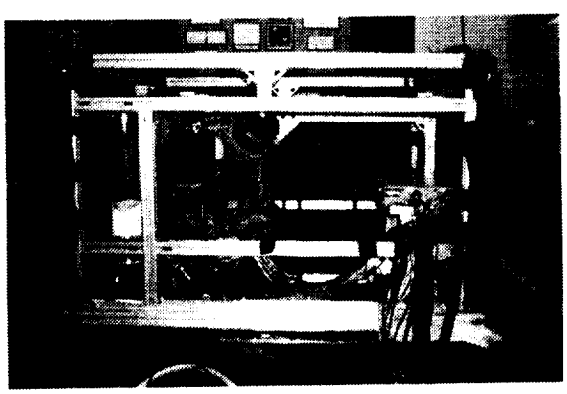

Figure 1. Free-floating rack

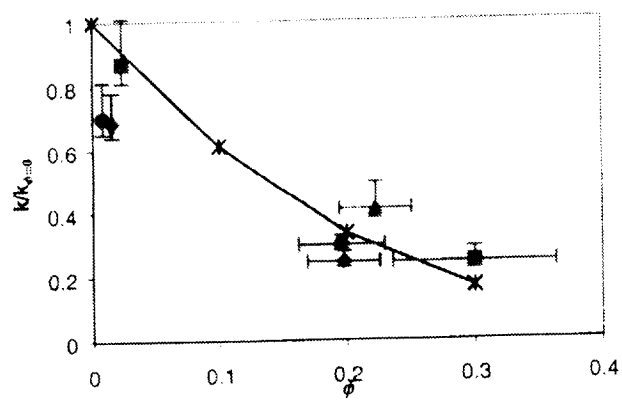

Figure 2. Attenuation of turbulent kinetic energy with 150 micron glass beads

NASA/CP—2002-211212/VOL1

Attenuation of Gas Turbulence by a Nearly Stationary Dispersion of Solid Particles

Principal Investigator: John Eaton
Research Assistants: Wontae Hwang, Patrick Cabral
Sponsor: NASA

Motivation

- Examples of particle-laden flow
  - pollution control, combustion of pulverized coal, pneumatic transport of powder, dust storms, …

- Carrier phase turbulence can be attenuated

$$\rho_p / \rho_f = O(1000)$$

$$d_p / d_f = O(1)$$

$$\dot{m}_p / \dot{m}_f = O(0.1 \sim 1)$$

Turbulence Attenuation

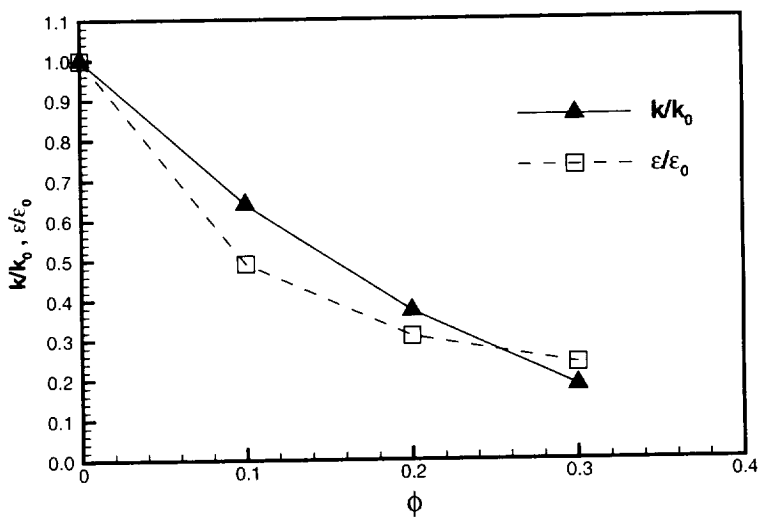

Turbulent kinetic energy and dissipation rate at the center plane of a turbulent channel flow laden with 150 μm glass beads (from Paris & Eaton, 2001)

Experimental Facility

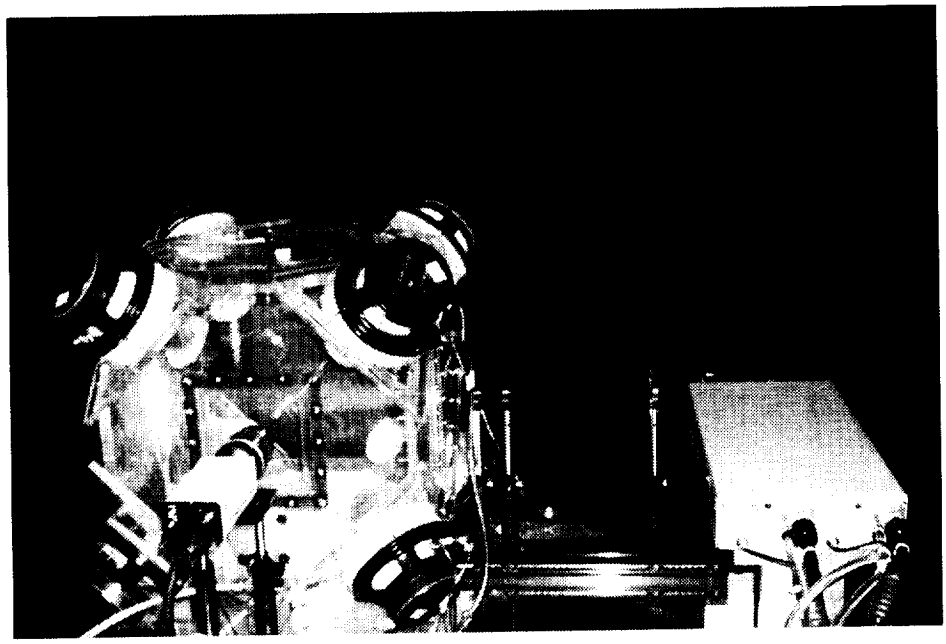

Forced Turbulence

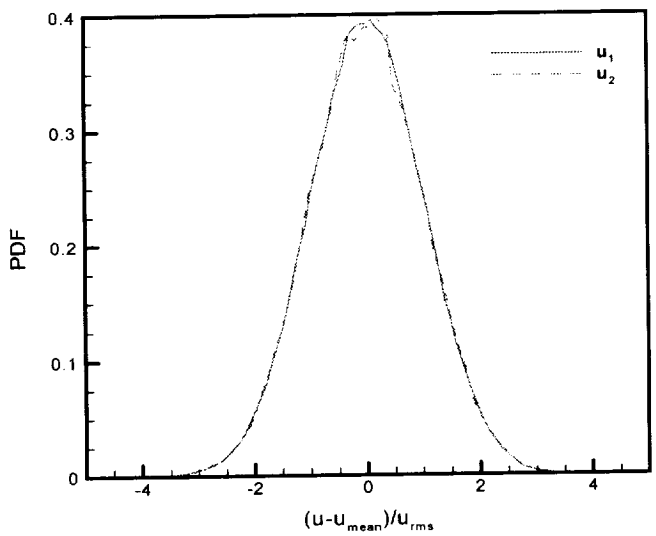

	x_1-dir.	x_2-dir.
U (m/s)	0.018	-0.083
u_{rms} (m/s)	0.85	0.83
Skewness	-0.045	-0.032
Kurtosis	2.98	2.93

q^2	ε	λ	Re_λ
2.1 m^2/s^2	12 m^2/s^3	3.6 mm	200

Two-point Velocity Correlations

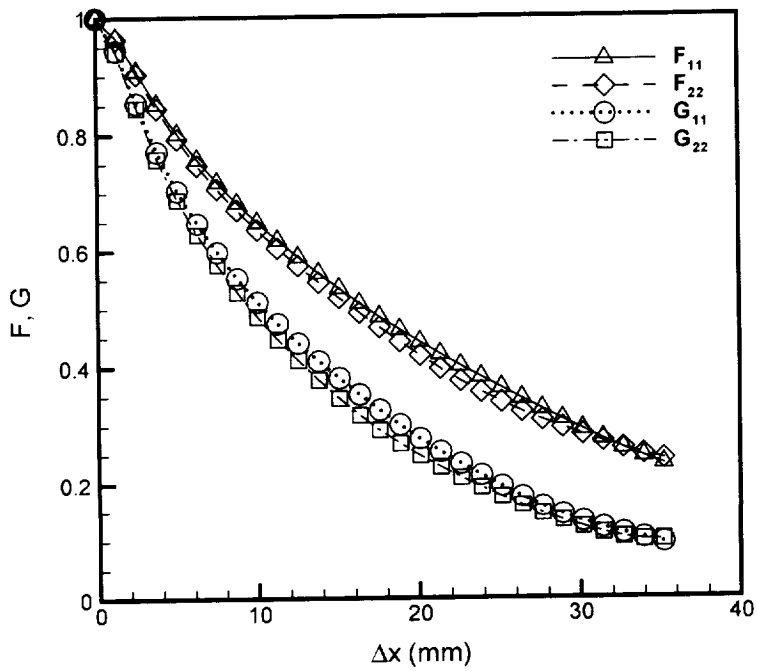

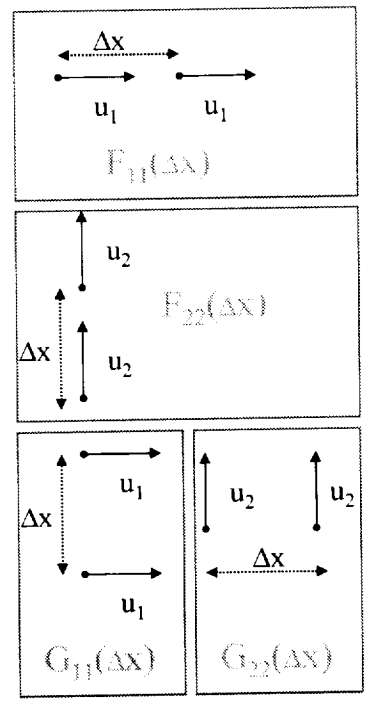

Eliminating Mean Particle Wakes

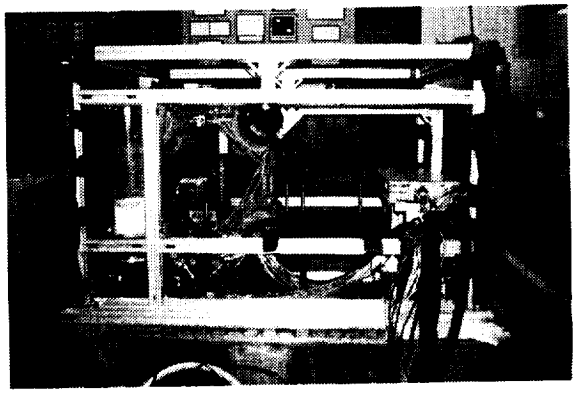

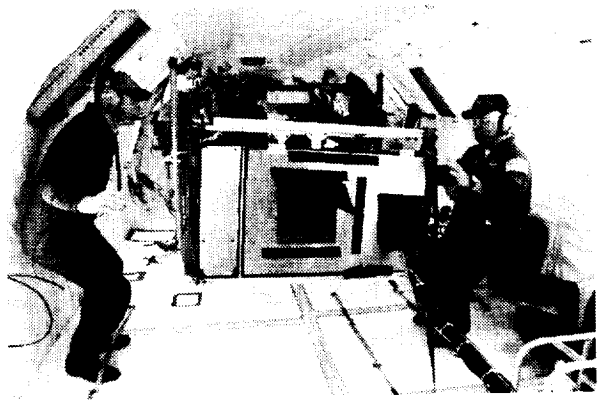

Image of Tracers and Particles

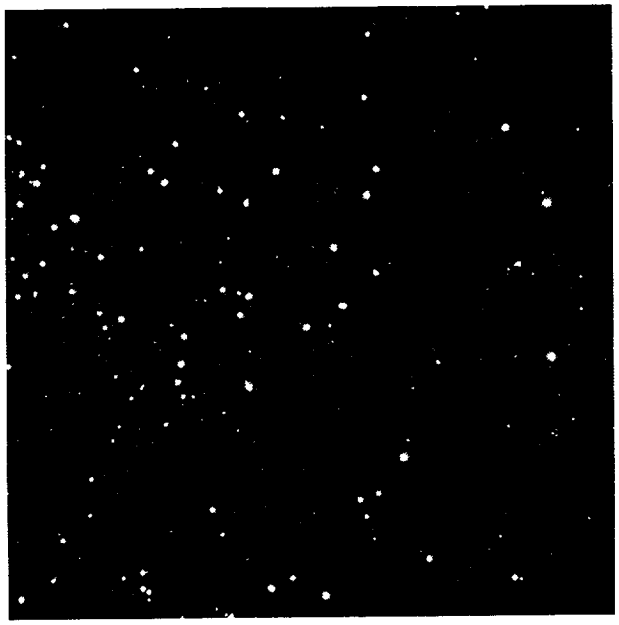

Particles: 150 μm glass
Tracers: 0.3 μm alumina

Separated Images

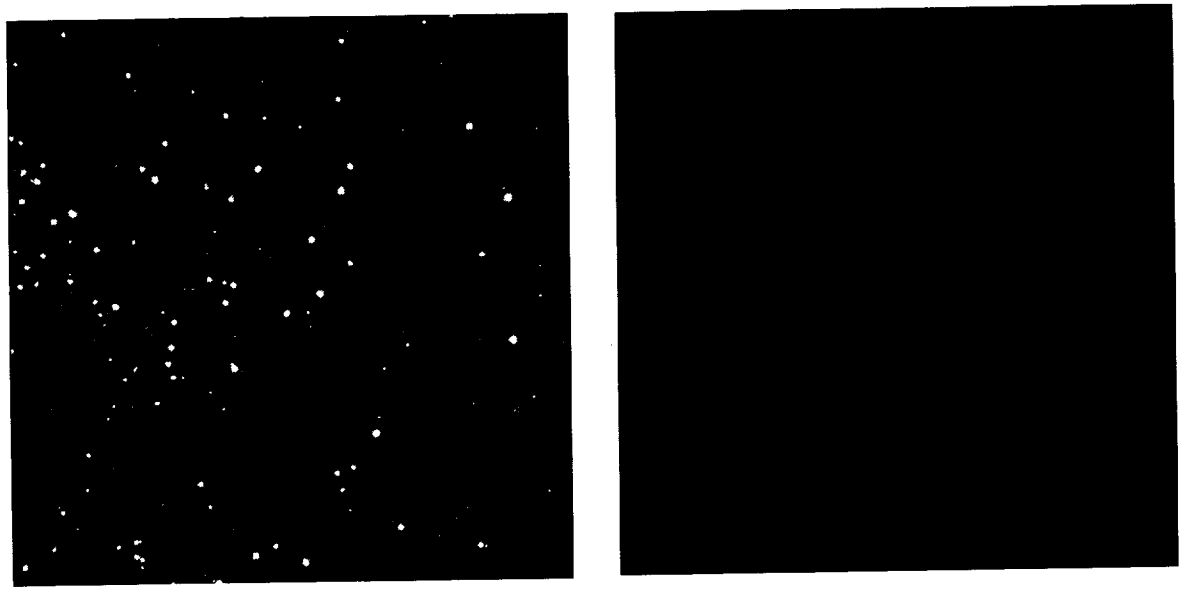

(a) 150 μm glass only (b) 0.3 μm alumina only

Instantaneous Velocity Fields

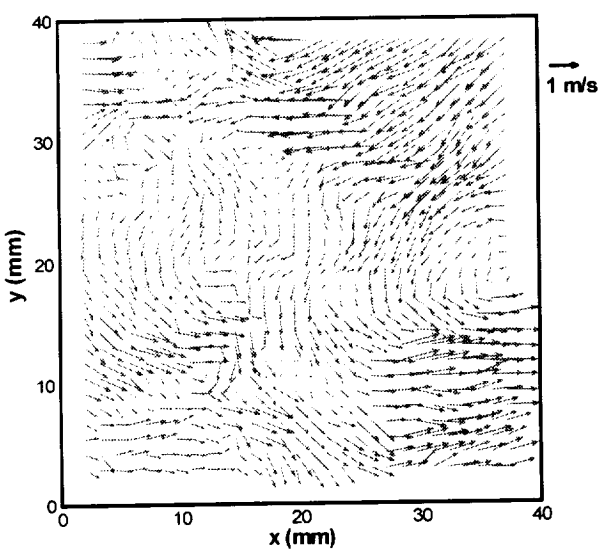

Unladen

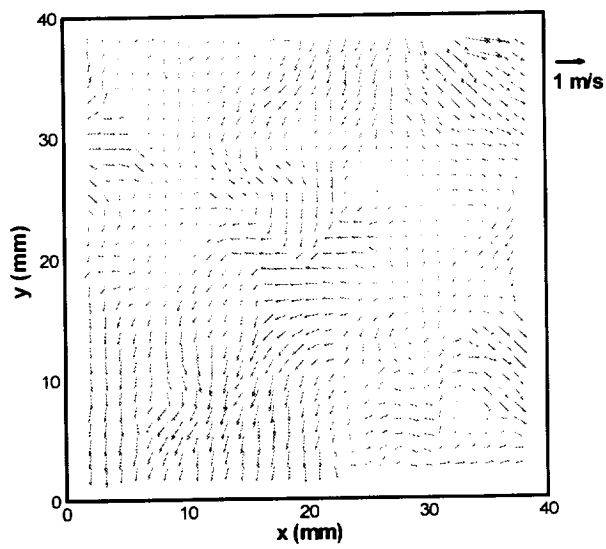

Laden with 150 μm glass

Attenuation of TKE

(with 150 μm glass beads)

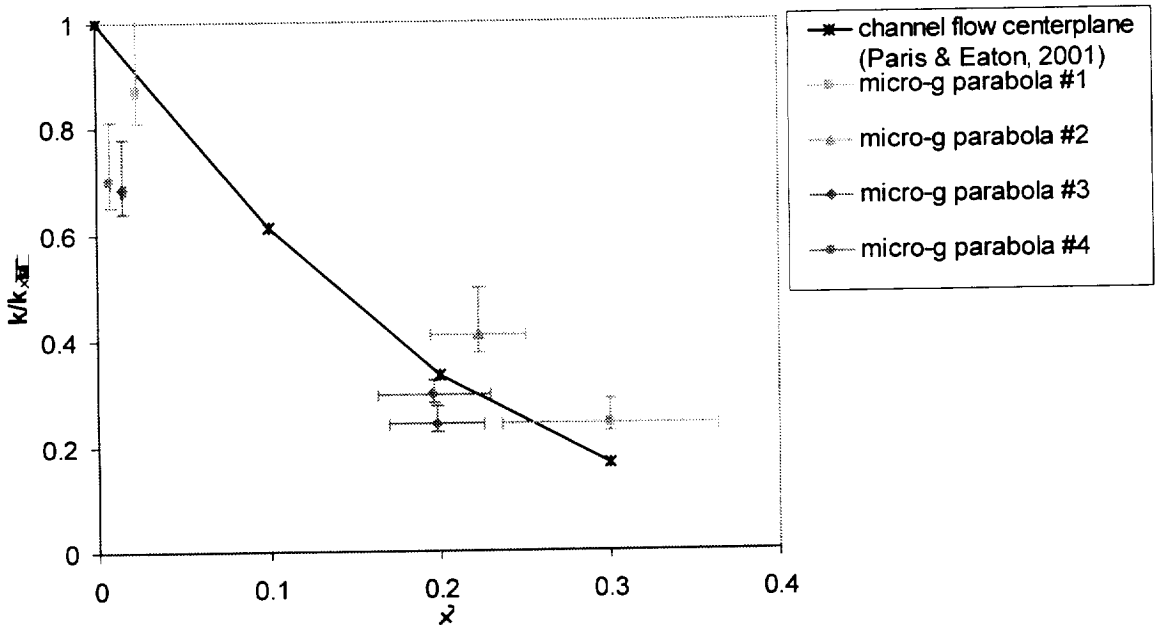

Summary & Future Work

- The turbulence chamber is capable of creating isotropic turbulence with small mean flow
- TKE is attenuated by suspended particles in microgravity
- Attenuation similar to channel centerplane

- Complete measurements with settling particles
- Highly resolved measurements for particle equation of motion

A Mechanistic Study of Nucleate Boiling Under Microgravity Conditions

V. K. Dhir and G. R. Warrier
Mechancial and Aerospace Engineering Department
School of Engineering and Applied Science
University of California, Los Angeles
Los Angeles, CA 90095-1597
Ph: (310) 825-8507, Fax: (310) 206-4830
Email: vdhir@seas.ucla.edu

ABSTRACT

The overall objective of this work is to study nucleate boiling heat transfer under microgravity conditions in such a way that while providing basic knowledge of the phenomena, it also leads to development of simulation models ad correlations that can be used as design tools for a wide range of gravity levels. In the study a building block type of approach is used and both pool and low velocity flow boiling are investigated. Starting with experiments using a single bubble, the complexity of the experiments is increased to two or three inline bubbles, to five bubbles placed on a two-dimensional grid. Finally, experiments are conducted where a large number of prescribed cavities nucleate on the heater and when a commercial surface is used. So far experiments have been conducted at earth normal gravity and in the reduced gravity environment of the KC-135 aircraft whereas experiments on the space station are planned. Modeling/complete numerical simulation of the boiling process is an integral part of the total effort.

Experiments conducted with single bubbles formed on a nucleation site microfabricated on a polished silicon wafer show that for gravity levels (g) varying from $1.5g_e$ to $0.01g_e$, the bubble diameter at departure varies approximately as $(g_e/g)^{1/2}$ and the growth period as (g_e/g). When bubbles merge either inline or in a plane, the bubble diameter at departure is found to be smaller than that obtained for a single bubble and shows a weaker dependence on the level of gravity. The possible reason is that as the bubbles merge they create fluid circulation around the bubbles, which in turn induces a lift force that is responsible for the earlier departure of the bubbles. The verification of this proposition is being sought through numerical simulations. Figures 1a, 1b, and 1c, respectively show the merger of two inline, three inline, and several bubbles in a plane in the low gravity environment of the KC-135 aircraft. After merger and before departure, a mushroom type of bubble with several stems attached to the heater surface is clearly evident. Local heat fluxes during growth and departure of a single bubble were also measured. It was found that during most of the growth period of the bubble, generally the wall heat flux decreased with time because of the increased dry area under the bubble. However, the heat flux increased rapidly just prior to departure of the bubble because of the transient conduction into the cold liquid rushing to fill the space vacated by the

bubble as the bubble base shrinks. The measured heat fluxes at various radial locations are found to be in qualitative agreement with the numerical predictions.

Single bubble studies at earth normal gravity have also been performed on surfaces oriented at different angles to the gravitational acceleration with flow parallel to the surface. It is found that in all cases the bubbles slide along the surface before lift-off from the surface. The lift force generated as a result of the relative motion between the sliding bubbles and the imposed flow is found to play an important role when the normal force due to buoyancy is reduced. An experimental apparatus for the study of the bubble behavior with imposed flow under reduced gravity conditions has been developed and will soon be employed for experiments in the KC-135 aircraft.

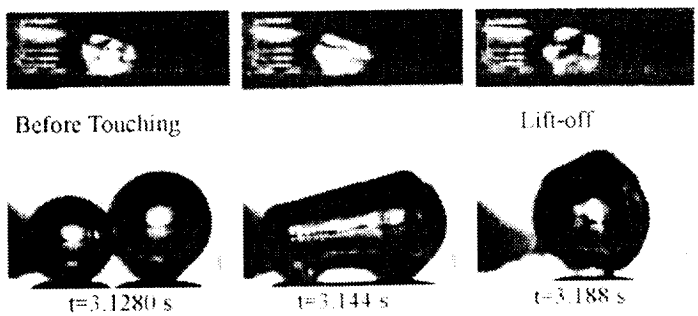

a. Two bubble merger.

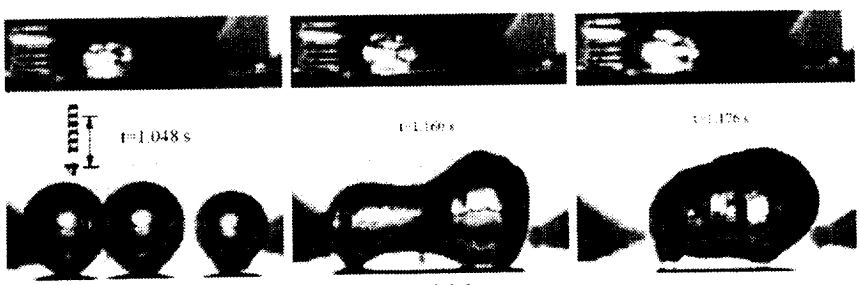

b. Three bubble merger.

c. Multiple bubble merger.

Figure 1. Photographs of bubble merger in the reduced gravity environment of the KC-135 aircraft with saturated water at one atmosphere pressure as the test liquid.

A MECHANISTIC STUDY OF NUCLEATE BOILING HEAT TRANSFER UNDER MICROGRAVITY CONDITIONS

P. I.

V. K. Dhir

School of Engineering and Applied Science, UCLA

Co P. I.

M. M. Hasan

NASA Glenn Research Center

Presented at

Microgravity Fluid Physics Conference, Cleveland, Ohio

August 15, 2002

PREDICTION OF NUCLEATE BOILING HEAT TRANSFER IN MICROGRAVITY

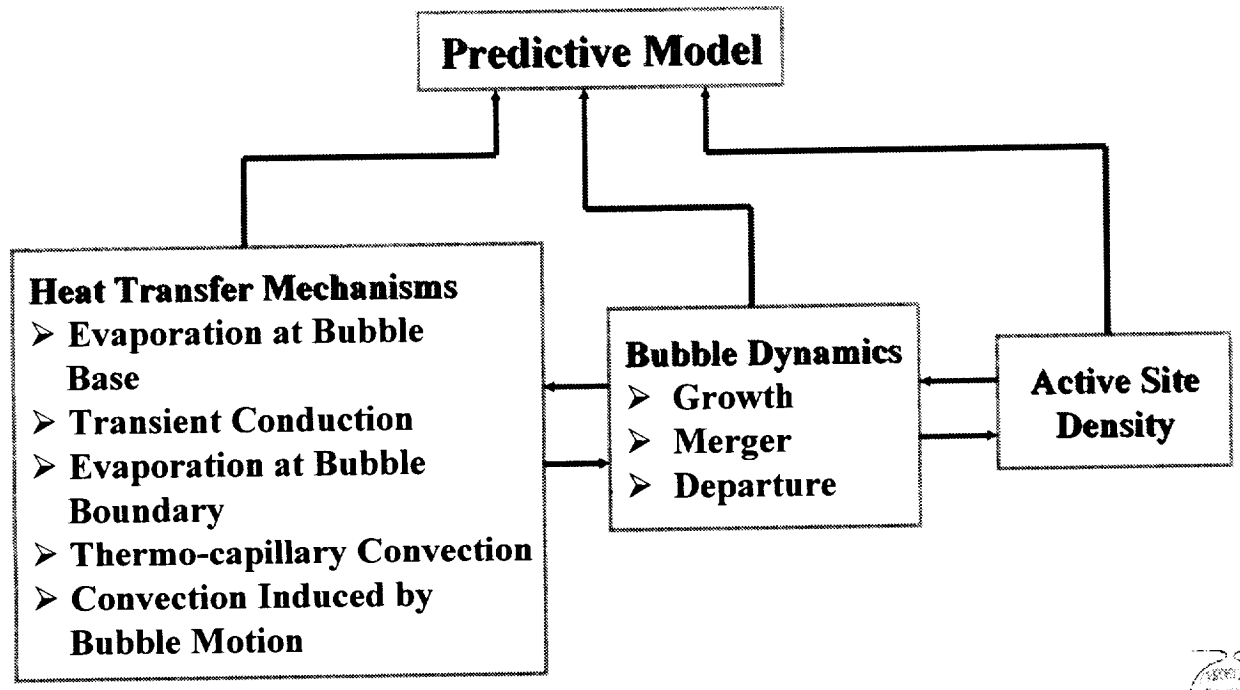

UCLA

APPROACH

- Building block type approach
  - Single bubble
  - Two – Three bubbles
  - Five bubbles on a two-dimensional grid
  - Multiple cavities on a heater surface
- Experiments at Earth normal gravity
- Experiments in the low gravity environment of the KC-135 aircraft
- Numerical simulations
- Experiments in the microgravity environment of the space station

APPROACH (contd.)

- Polished silicon wafers to be used as test surface
- Two liquids to be used so that the effect of surface tension and wettability can be investigated
- System pressure will be close to one atmosphere but the ratio of the liquid to vapor density for the two liquids will differ by atleast an order of magnitude
- Liquid subcooling is to be varied parametrically

EXPERIMENTS IN THE LOW GRAVITY ENVIRONMENT OF THE KC-135 AIRCRAFT

POOL NUCLEATE BOILING

Bubble Growth – Lift off Cycle

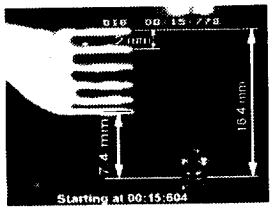

t = 0.17 s

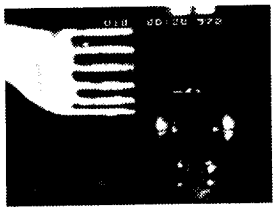

t = 4.97 s

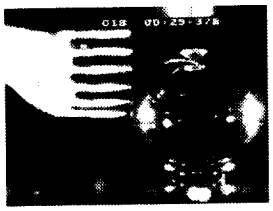

t = 9.77 s (Max. base)

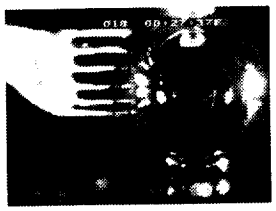

t = 11.77 s

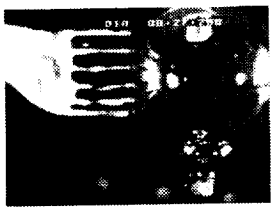

t = 12.15 s (Departure)

$\Delta T_{sub} = 0.3\ ^{o}C$, $\Delta T_w = 4.2\ ^{o}C$, $g_z = 0.02\ g/g_e$

POOL NUCLEATE BOILING (contd.)

Scaling of the Effect of Gravity on Bubble Lift-off Diameter and Growth Period

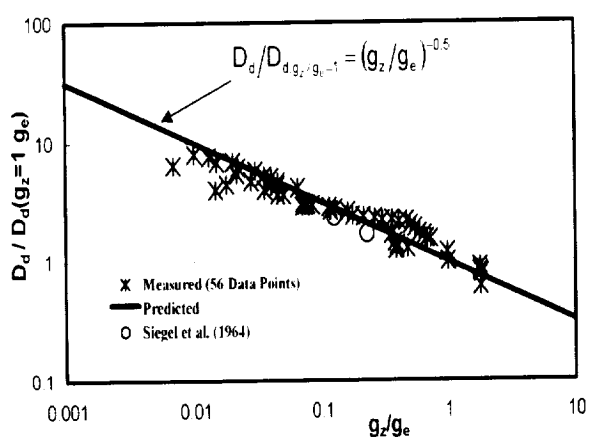

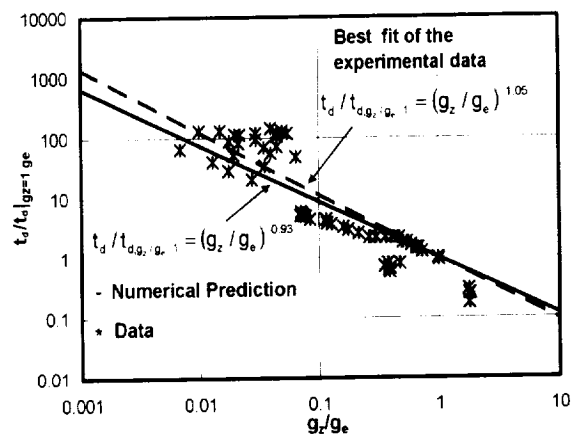

POOL NUCLEATE BOILING (contd.)

Single Bubble – Numerical Simulations

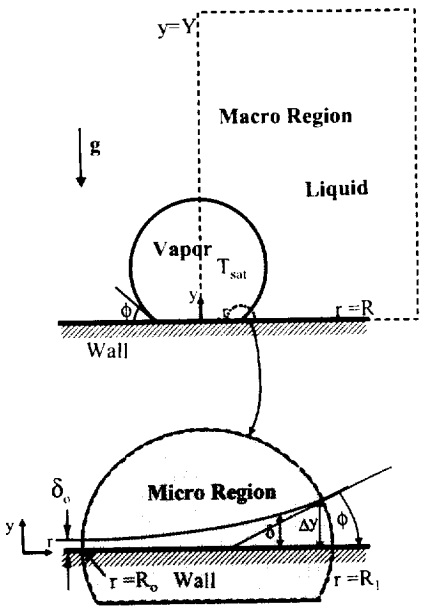

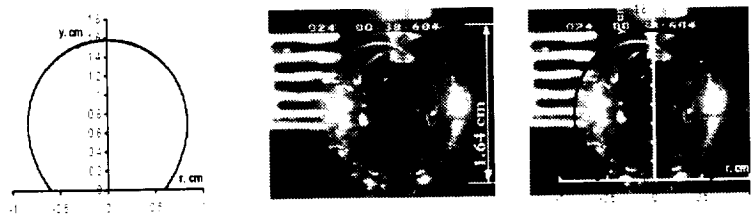

Comparison between measured and predicted bubble shapes for ΔT_w= 3.8°C, ΔT_{sub}= 0.4°C and g_z = 0.02 g_e

POOL NUCLEATE BOILING (contd.)

Single Bubble – Numerical Simulations

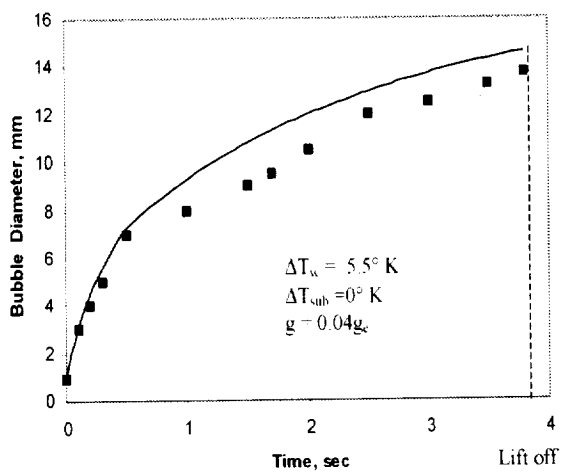

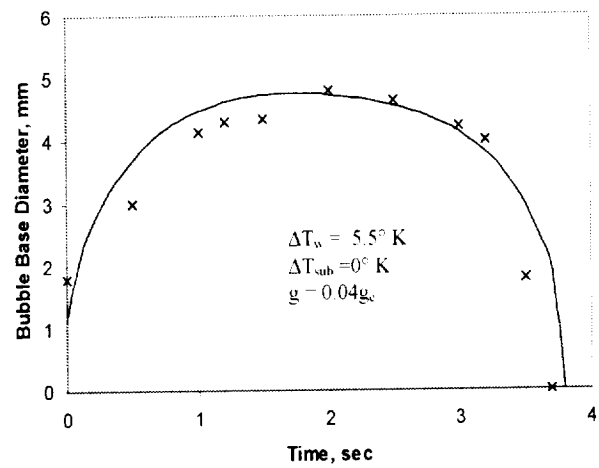

The variation of equivalent bubble diameter and bubble base diameter with time for $\Delta T_w = 5.5°C$, $\Delta T_{sub} = 0°C$, $g = 0.04g_e$

UCLA

POOL NUCLEATE BOILING (contd.)

Single Bubble Dynamics and Associated Heat Transfer

– Numerical Simulations

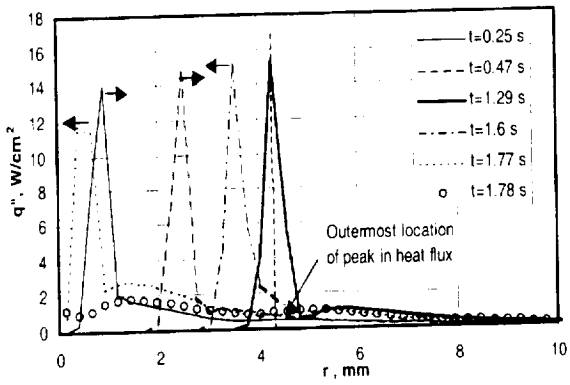

Local heat flux
$\Delta T_w = 8.5\ ^oC$, $g_z = 0.01 g_e$

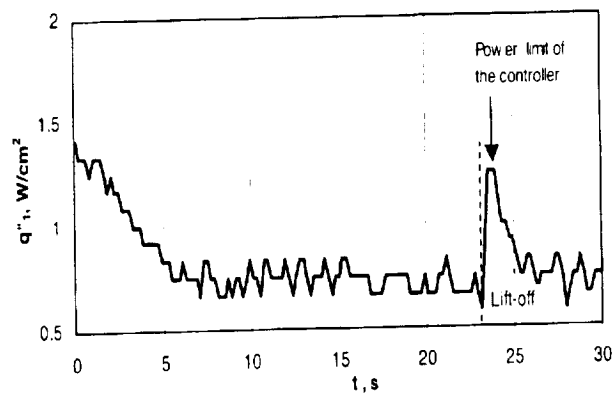

Heat flux from the elements underneath the cavity

UCLA

POOL NUCLEATE BOILING (contd.)

Single Bubble Dynamics

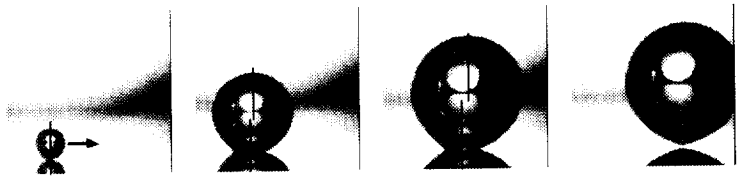

$\Delta T_{sub} = 0.6°C$, $\Delta T_w = 5.0°C$, $g_z = 0.021\ g_e$, $g_x = -0.009\ g_e$ and $g_y = -0.005\ g_e$

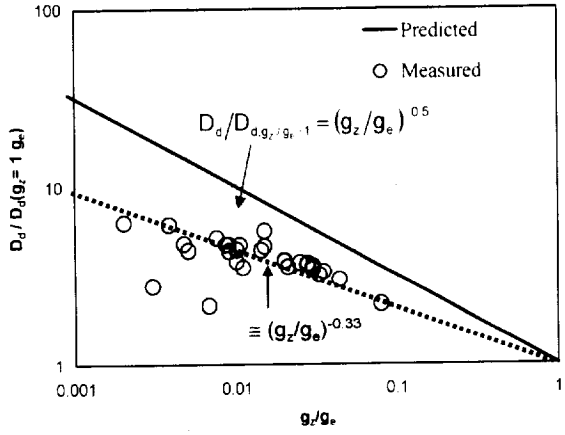

POOL NUCLEATE BOILING (contd.)

Bubble Merger

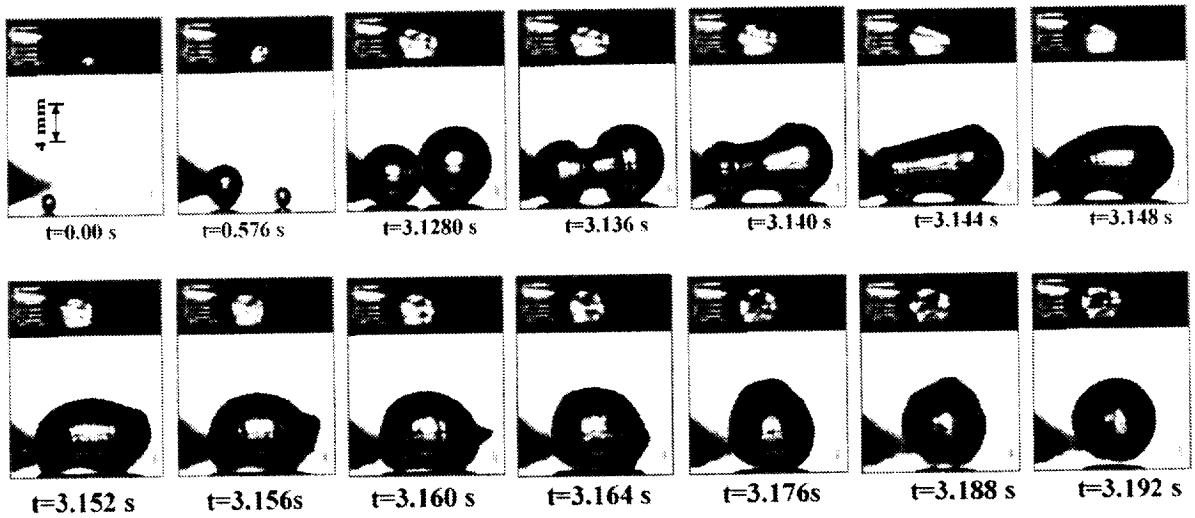

Two bubble merger at ΔT_{sub}=3.0 °C, T_w-T_{sat}=5.0°C, g_z=0.0033 g_e

POOL NUCLEATE BOILING (contd.)

Bubble Merger

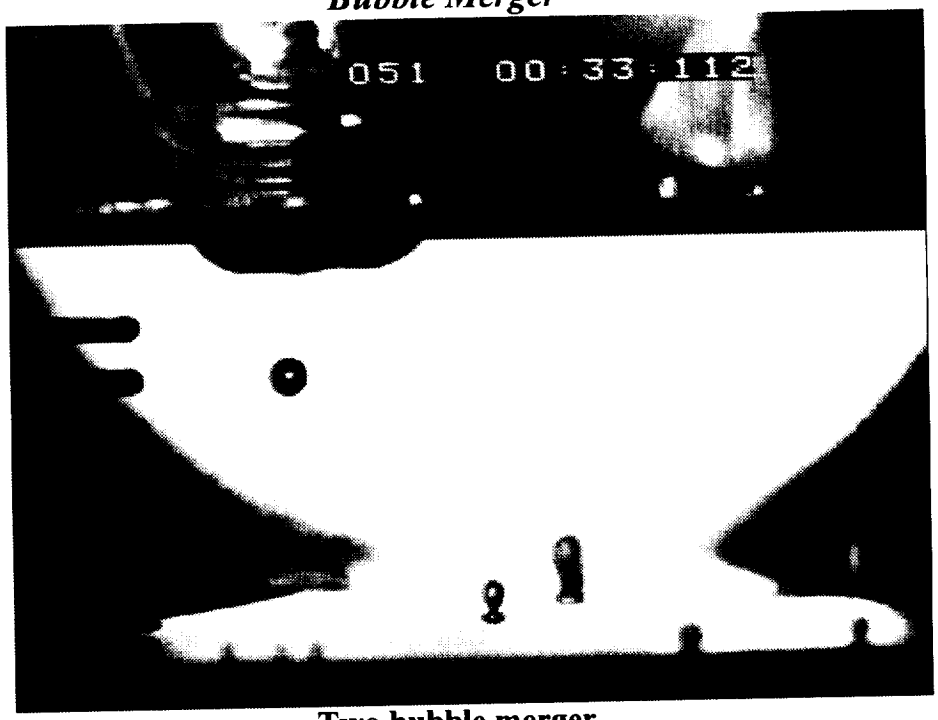

Two bubble merger

UCLA

POOL NUCLEATE BOILING (contd.)

Bubble Merger

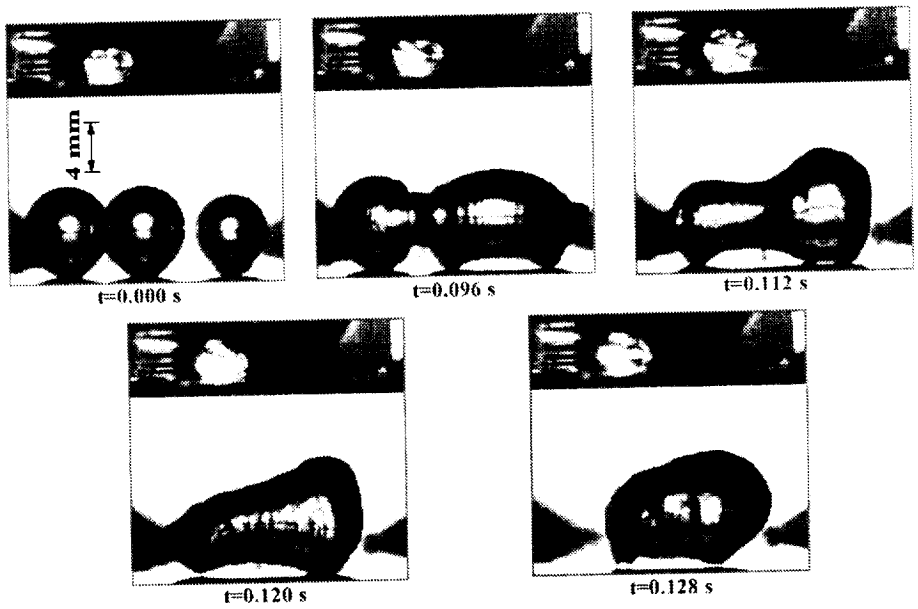

Three bubble merger at ΔT_{sub}=2.0 °C, T_w-T_{sat}=5.5°C, g_z=0.008 g_e

UCLA

POOL NUCLEATE BOILING (contd.)

Bubble Merger

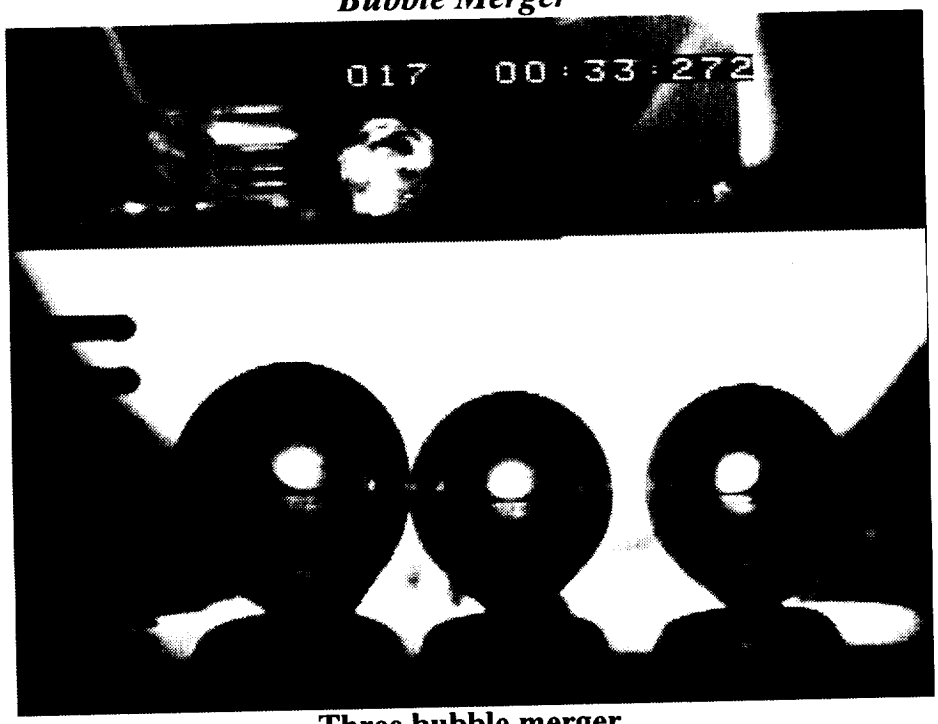

Three bubble merger

POOL NUCLEATE BOILING (contd.)

Bubble Merger

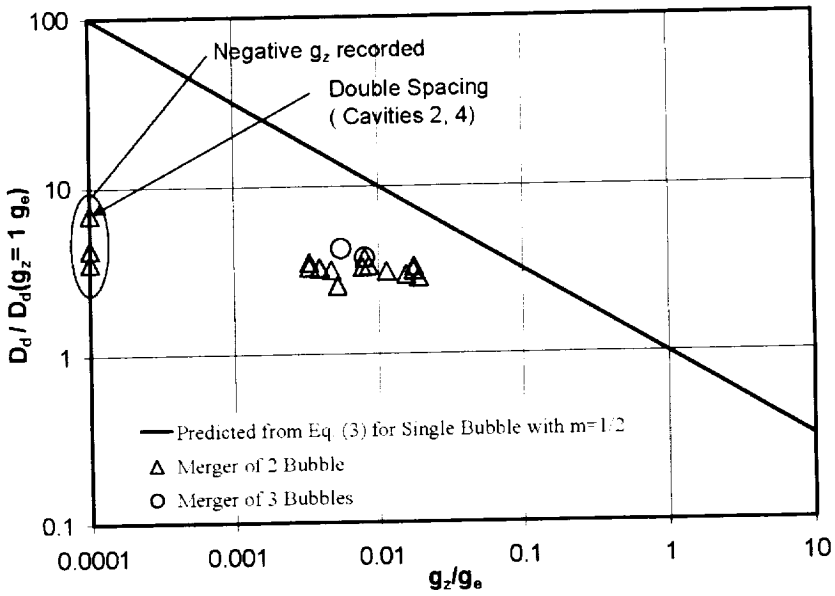

Bubble departure diameter with merger of two or three bubbles

POOL NUCLEATE BOILING (contd.)

Two Bubble Merger and Associated Heat Transfer – Numerical Results

$g_z = 0.04\ g_e$

Top view

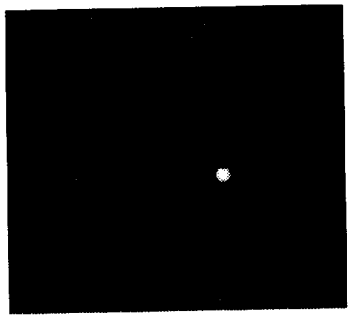

Front view

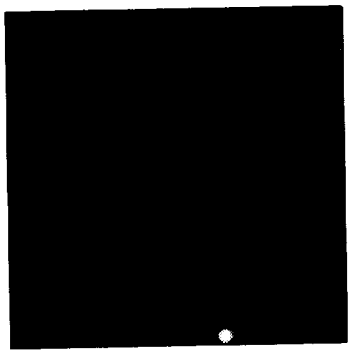

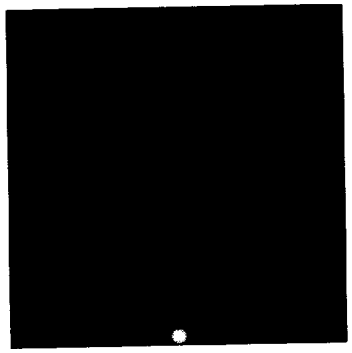

Side view

POOL NUCLEATE BOILING (contd.)

Two Bubble Merger and Associated Heat Transfer – Numerical Results

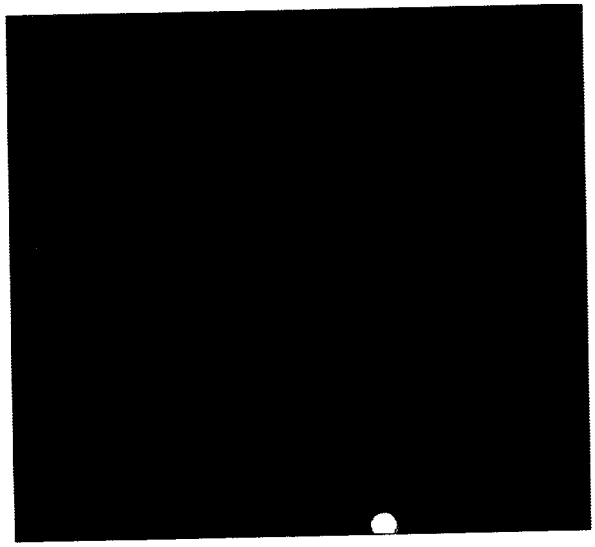

Velocity Field

17

UCLA

POOL NUCLEATE BOILING (contd.)

Two Bubble Merger and Associated Heat Transfer – Numerical Results

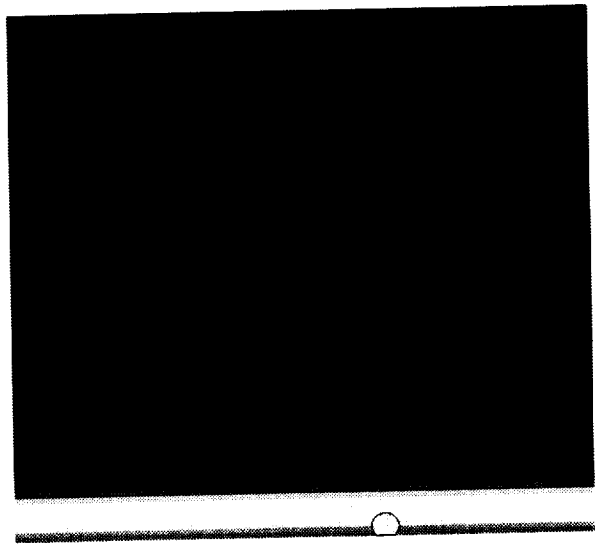

Temperature Field

18

UCLA

POOL NUCLEATE BOILING (contd.)

Three Bubble Merger – Numerical Results

$g_z = 0.01\ g_e$

Top view

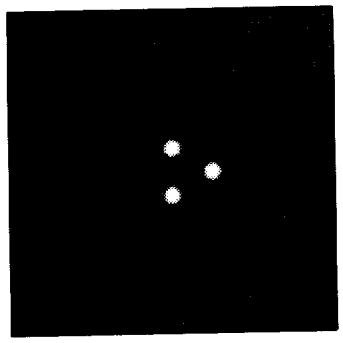

Front view

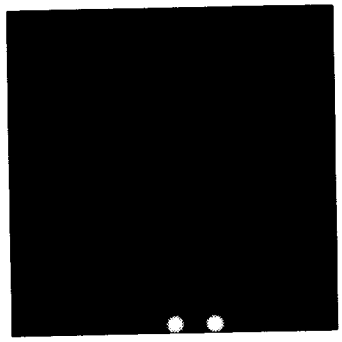

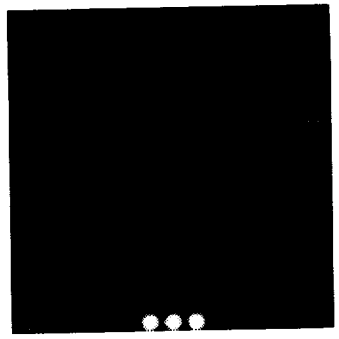

Side view

UCLA

POOL NUCLEATE BOILING (contd.)

Five Bubble Merger – Numerical Results

Top view

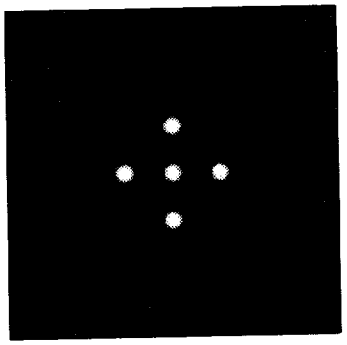

$g_z = 0.01\ g_e$

Front view

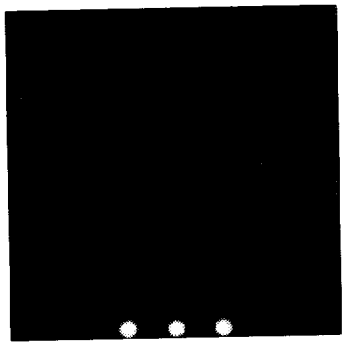

UCLA

POOL NUCLEATE BOILING (contd.)

Comparison of predicted and experimentally observed heat transfer with multiple nucleation sites active in $1g_e$ and $0.01g_e$

No of Cavities	1 g					0.01 g				
	Numerical				Exp.	Numerical				Exp.
	Q nc (W)	Q ev (W)	Q Total (W)	q_w (W/cm²)		Q nc (W)	Q ev (W)	Q total (W)	q_w (W/cm²)	
3	9.84	0.76	10.14	[illegible]		2.13	4.14	5.88	[illegible]	
5	9.84	1.26	10.34	[illegible]		2.13	6.37	8.01	[illegible]	

Domain Size = 40 mm x 40 mm, Wall superheat = 6.6 K

UCLA

CONCLUSIONS

- For single bubbles, the departure diameter scales as $g_z^{-1/2}$, whereas the growth period scales as g_z^{-1}
- Bubble merger and sliding motion of bubbles leads to a lift off force normal to the surface. As a result of this force, the bubble departure diameter is smaller than that for a stationary single bubble. The lift force weakens the dependence of bubble departure diameter on gravity
- Observed heat fluxes for up to 5 active cavities is generally higher than those predicted from numerical simulations
- The magnitude of gravity normal and along the surface are found to affect the dynamics of bubble departure

INVESTIGATION OF BODY FORCE EFFECTS ON FLOW BOILING CRITICAL HEAT FLUX

Issam Mudawar and Hui Zhang

Boiling and Two-phase Flow Laboratory
School of Mechanical Engineering, Purdue University
West Lafayette, IN 47907, USA
mudawar@ecn.purdue.edu
Fax: 765-494-0539
Tel: 765-494-5705

and

Mohammad M. Hasan

NASA Glenn Research Center
21000 Brookpark Road
Cleveland, OH 44135, USA

The bubble coalescence and interfacial instabilities that are important to modeling critical heat flux (CHF) in reduced-gravity systems can be sensitive to even minute body forces. Understanding these complex phenomena is vital to the design and safe implementation of two-phase thermal management loops proposed for space and planetary-based thermal systems. While reduced gravity conditions cannot be accurately simulated in 1*g* ground-based experiments, such experiments can help isolate the effects of the various forces (body force, surface tension force and inertia) which influence flow boiling CHF. In this project, the effects of the component of body force perpendicular to a heated wall were examined by conducting 1*g* flow boiling experiments at different orientations. FC-72 liquid was boiled along one wall of a transparent rectangular flow channel that permitted photographic study of the vapor-liquid interface at conditions approaching CHF. High-speed video imaging was employed to capture dominant CHF mechanisms. Six different CHF regimes were identified: Wavy Vapor Layer, Pool Boiling, Stratification, Vapor Counterflow, Vapor Stagnation, and Separated Concurrent Vapor Flow. CHF showed great sensitivity to orientation for flow velocities below 0.2 m/s, where very small CHF values where measured, especially with downflow and downward-facing heated wall orientations. High flow velocities dampened the effects of orientation considerably. Figure 1 shows representative images for the different CHF regimes.

The Wavy Vapor Layer regime was dominant for all high velocities and most orientations, while all other regimes were encountered at low velocities, in the downflow and/or downward-facing heated wall orientations. The Interfacial Lift-off model was modified to predict the effects of orientation on CHF for the dominant Wavy Vapor Layer regime. The photographic study captured a fairly continuous wavy vapor layer travelling along the heated wall while permitting liquid contact only in wetting fronts, located in the troughs of the interfacial waves. CHF commenced when wetting fronts near the outlet were lifted off the wall. The Interfacial Lift-off model is shown to an effective tool for predicting the effects of body force on CHF at high velocities.

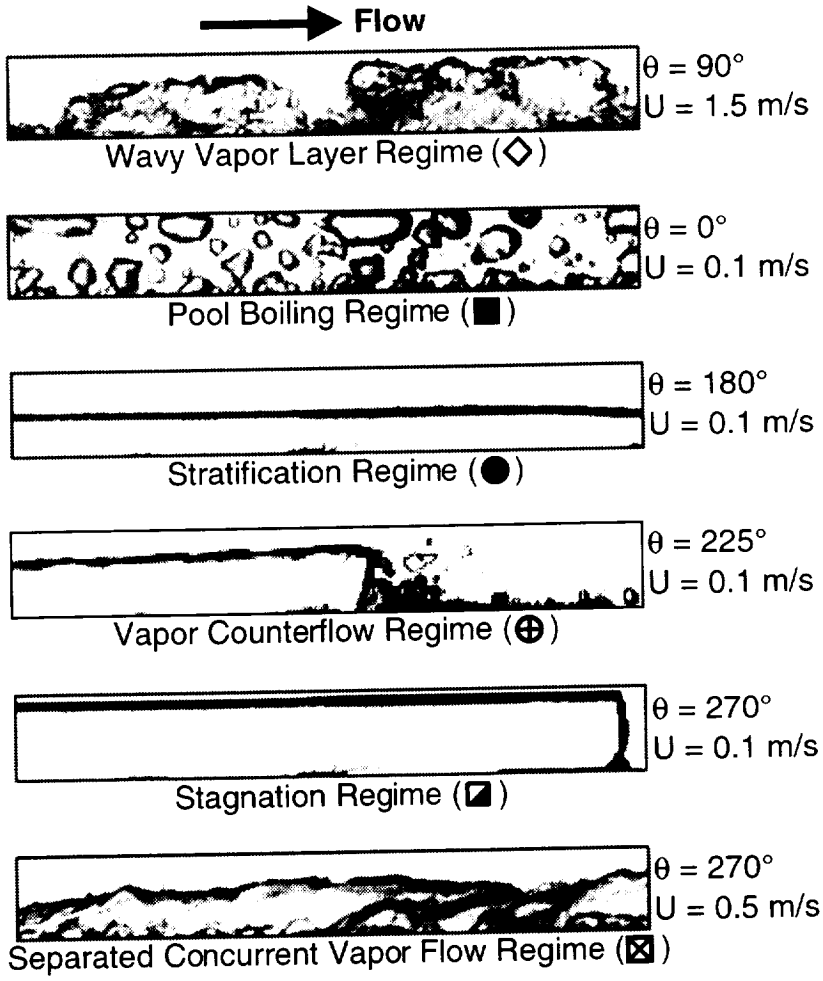

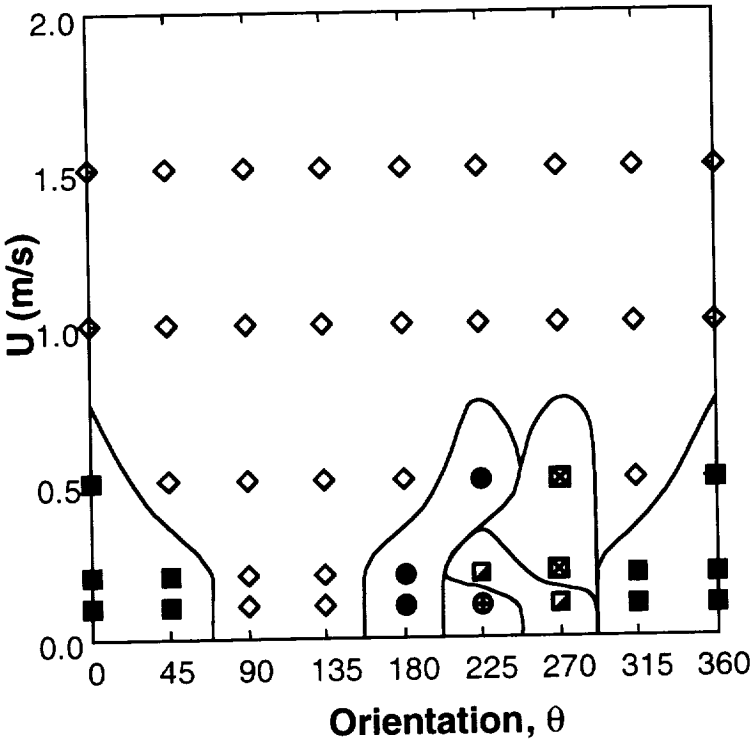

Figure 1 CHF regime map and representative flow characteristics for each regime.

NASA/CP—2002-211212/VOL1

Investigation of Body Force Effects on Flow Boiling Critical Heat Flux

Hui Zhang and Issam Mudawar
Boiling and Two-Phase Flow Laboratory
Purdue University

and

Mohammad M. Hasan
NASA Glenn Research Center

Background

- New thermal management schemes are needed for space systems to dissipate and transport heat from power, electronic and environmental sources of various sizes and power densities
- Two-phase loops greatly increase heat-load-to-weight ratio and ensure nearly isothermal heat transport over long piping distances
- Capillary forces in passive two-phase thermal management systems (heat pipes, loop heat pipes, capillary-pumped loops) can sustain only small pressure drops and coolant flow rates, limiting both heat flux and total heat load removal capabilities
- Mechanically-pumped two-phase loops may therefore become necessary for intense heat removal in future space systems

Flow Boiling CHF

- Critical heat flux (CHF) is a key design parameter for heat-flux-controlled devices
- Ability to predict CHF is of paramount importance to both the safety and reliability of a two-phase thermal management system
- Most previous reduced-gravity boiling studies have been focused on pool rather than flow boiling
- There are conflicting recommendations concerning the viability of pool boiling in microgravity
- Flow boiling is a proven method for enhancing CHF relative to pool boiling
- Bulk motion increases CHF by flushing bubbles away from the heated wall before they coalesce into an insulating vapor blanket, and by constantly replenishing the wall with bulk liquid

Flow Boiling CHF Models

- Previous CHF models were developed mainly for nuclear reactors, steam boilers, and vertical upflow
- Previously proposed CHF mechanisms:
  - Boundary Layer Separation
  - Bubble Crowding
  - Sublayer Dryout
  - Interfacial Lift-off
- Interfacial instabilities are very important to CHF modeling
- New applications are emerging which demand intense heat removal from relatively small surface areas; new CHF predictive tools are needed for those applications

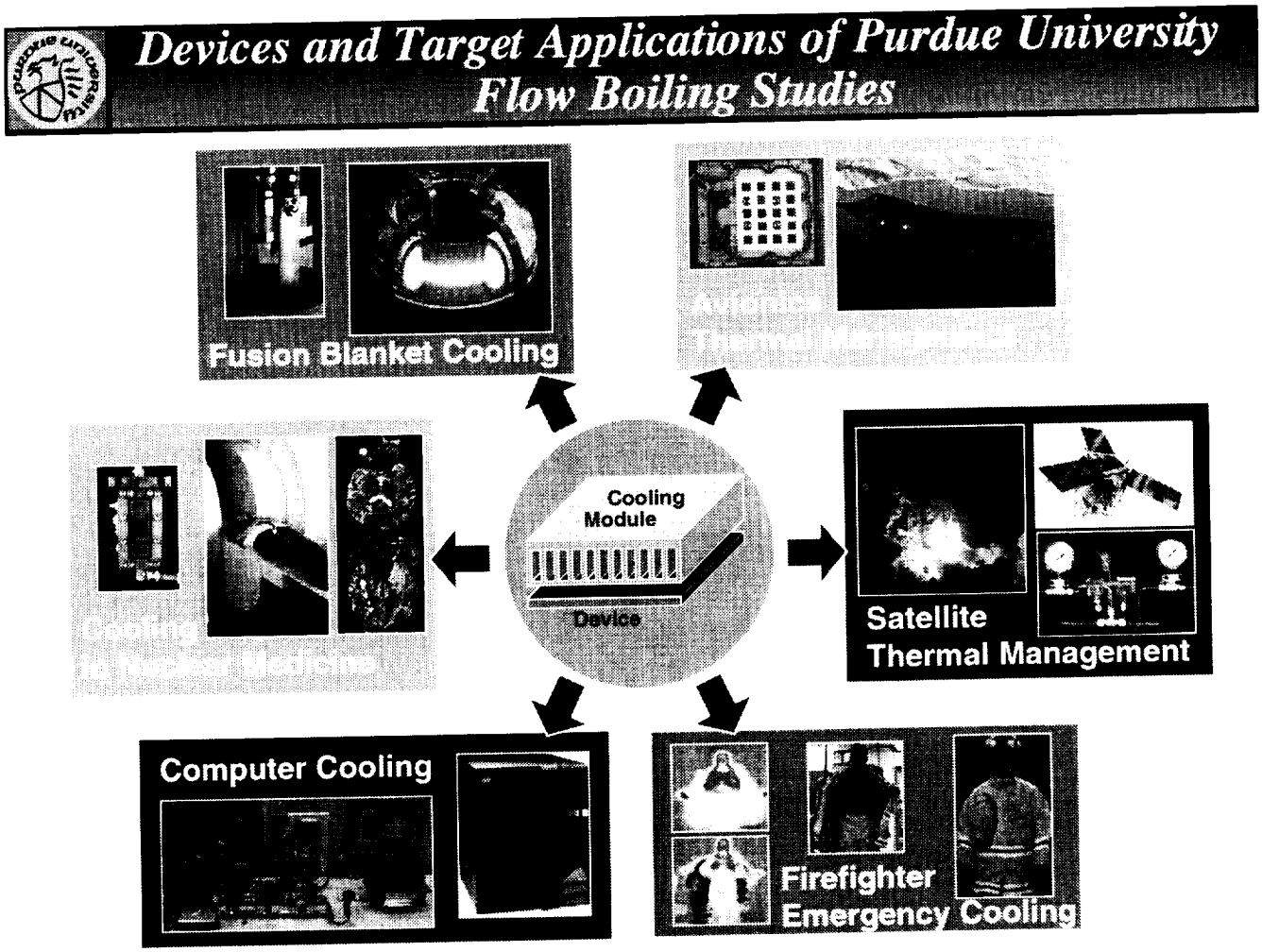
Devices and Target Applications of Purdue University Flow Boiling Studies
Fusion Blanket Cooling
Cooling Module
Device
Satellite Thermal Management
Computer Cooling
Firefighter Emergency Cooling

Pool Boiling CHF from a Horizontal Surface

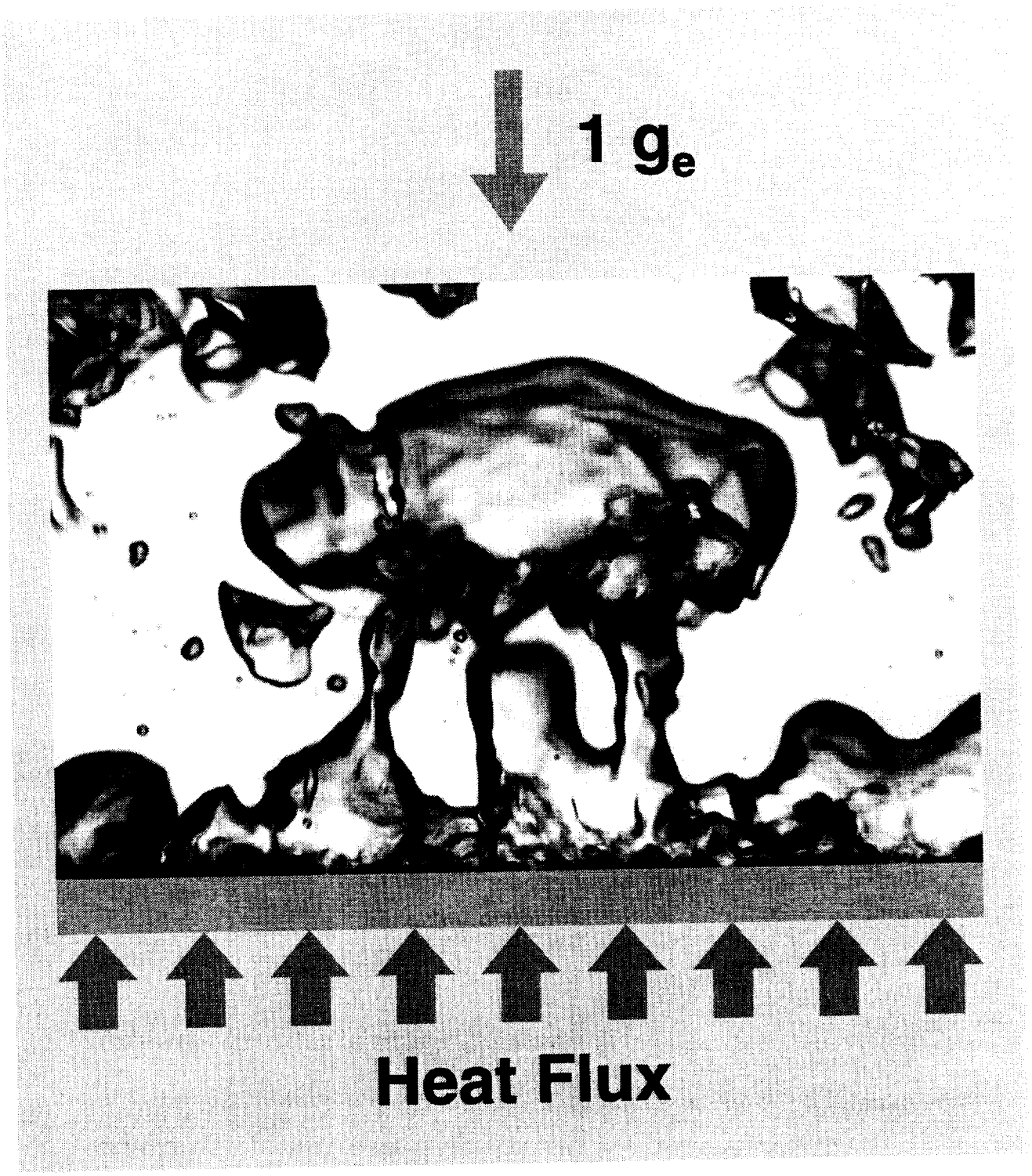

Pool Boiling CHF at Different Surface Orientations

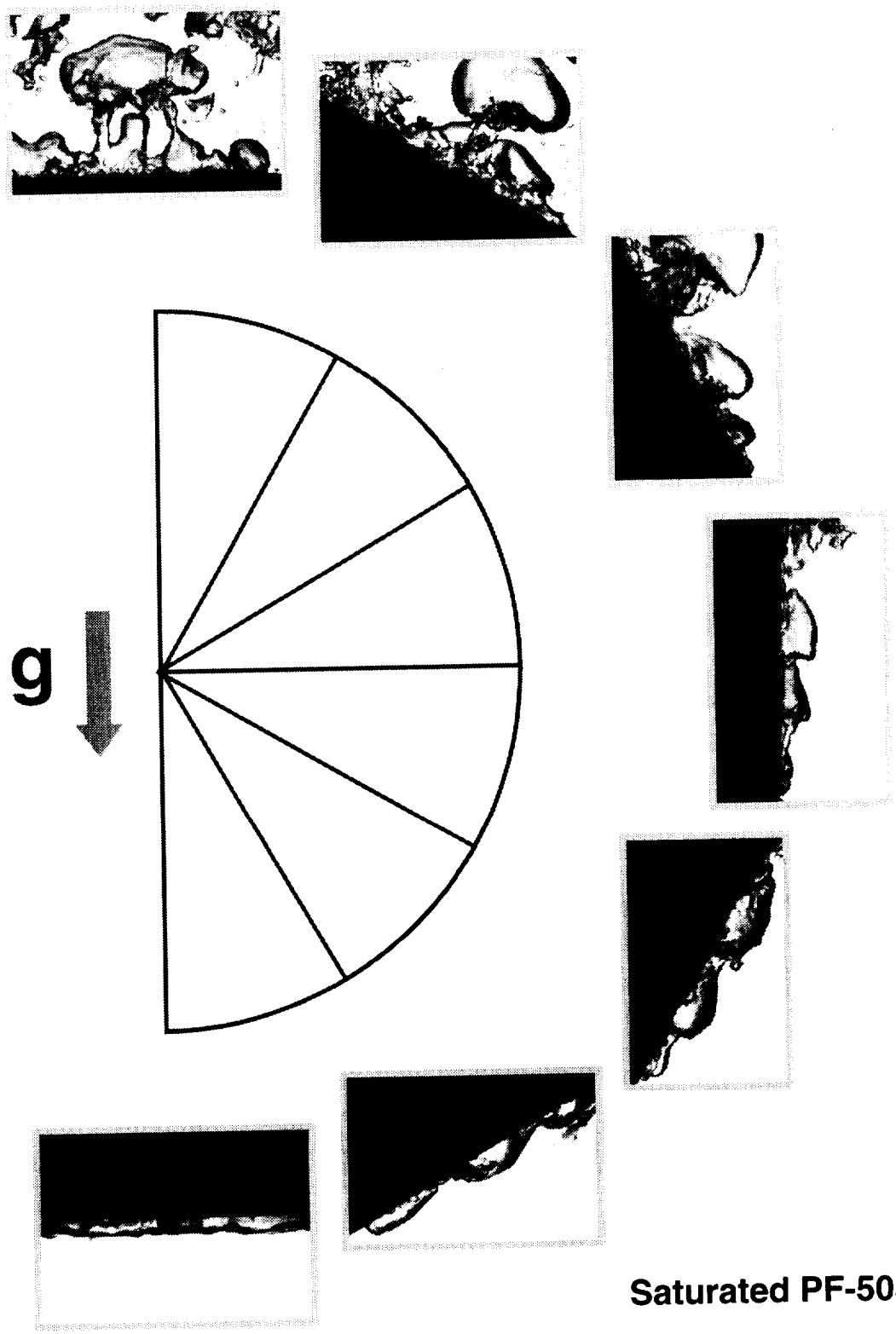

Saturated PF-5052

Wavy Vapor Layer

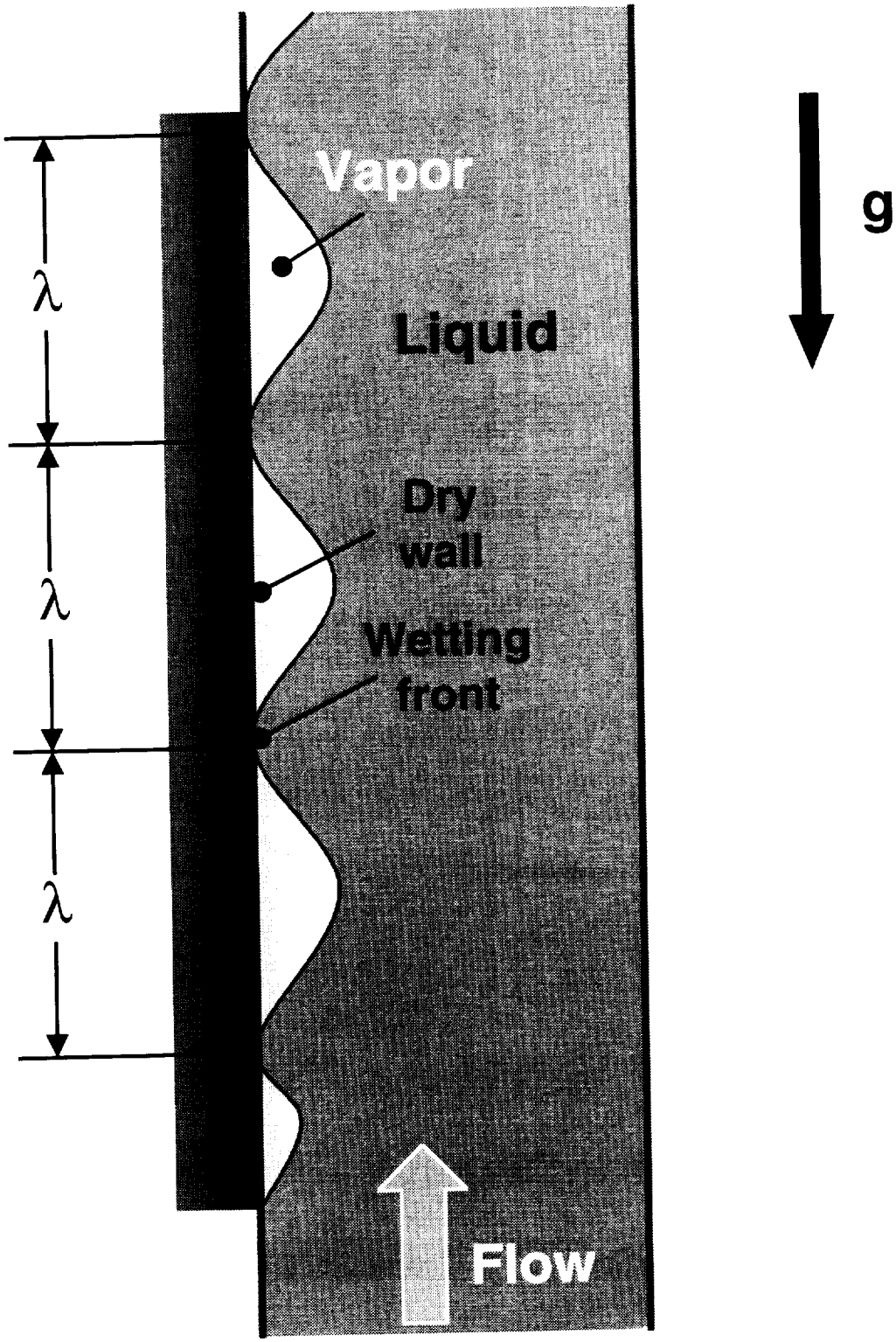

Long-Term Objective

Develop a comprehensive approach to predicting flow boiling CHF in reduced gravity, which can be used to guard against burnout of electronic and power devices in space thermal management systems

Approach

(1) Develop compact experimental apparatus to explore flow boiling CHF at different orientations in 1 g_e

(2) Develop photographic methods to investigate interfacial instabilities just prior to CHF

(3) Assess effects of body force, surface tension, and inertia on flow boiling CHF in 1 g_e by conducting experiments at different flow orientations over a broad range of flow velocities

(4) Identify CHF regimes corresponding to different orientations and different flow conditions

(5) Assess effectiveness of CHF models and correlations at predicting experimental data for different CHF regimes

Future:
Use same approach to explore flow boiling CHF in microgravity

Flow Boiling Module

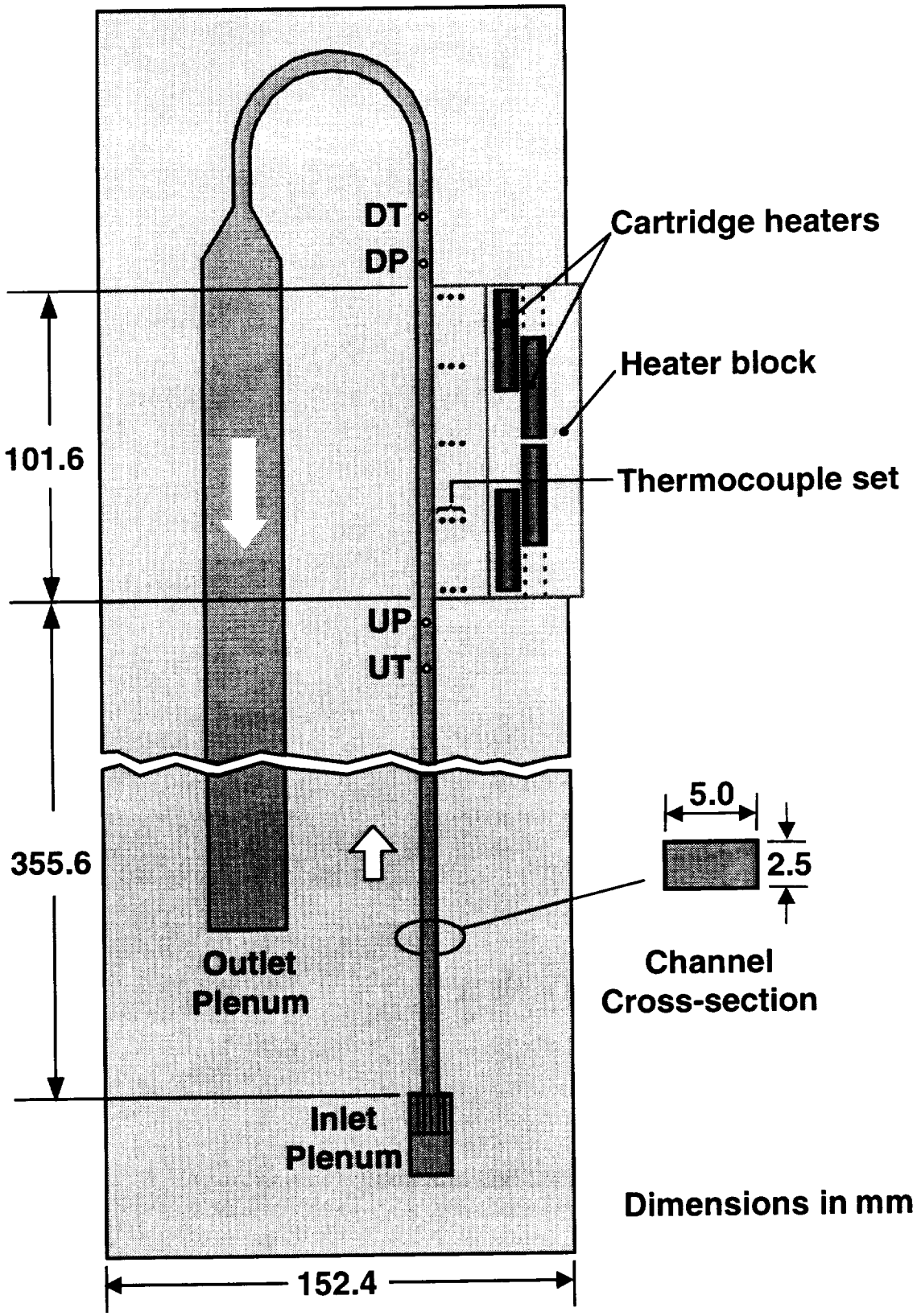

Test Module

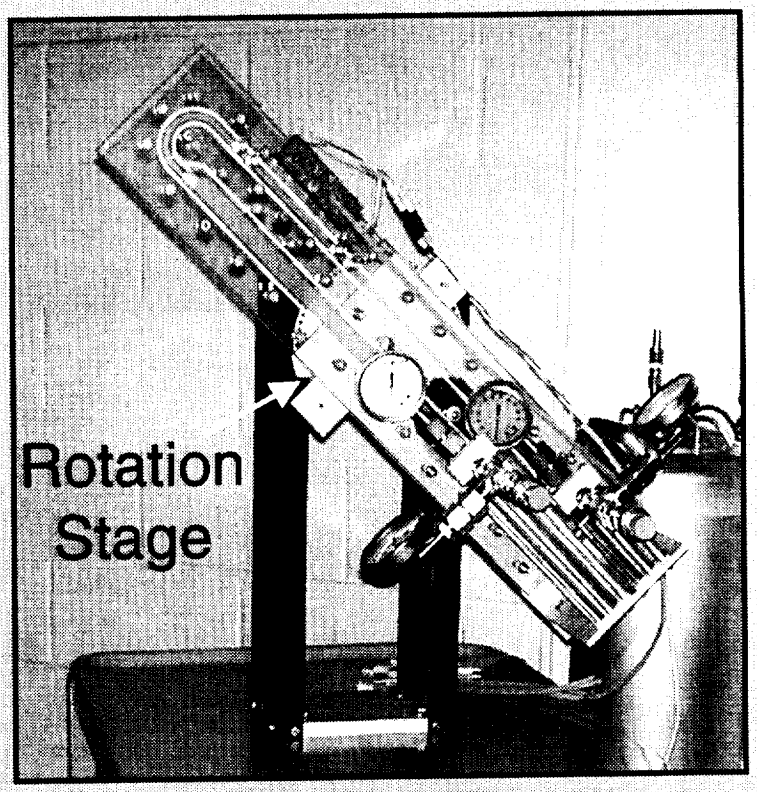

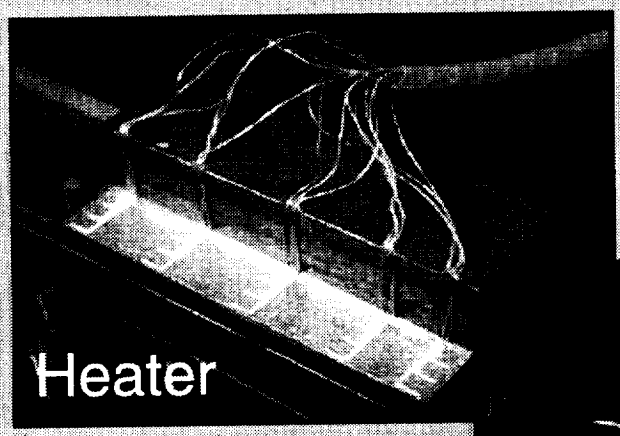

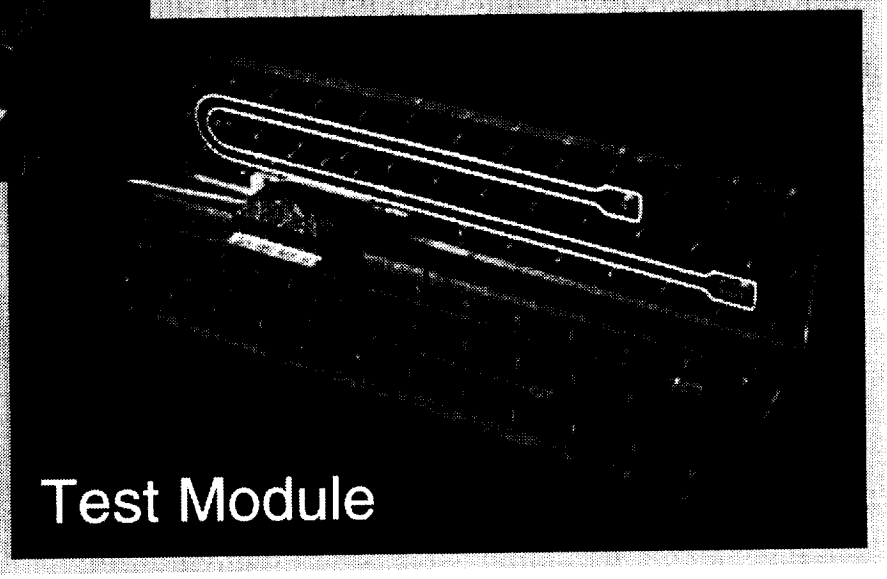

Test Apparatus

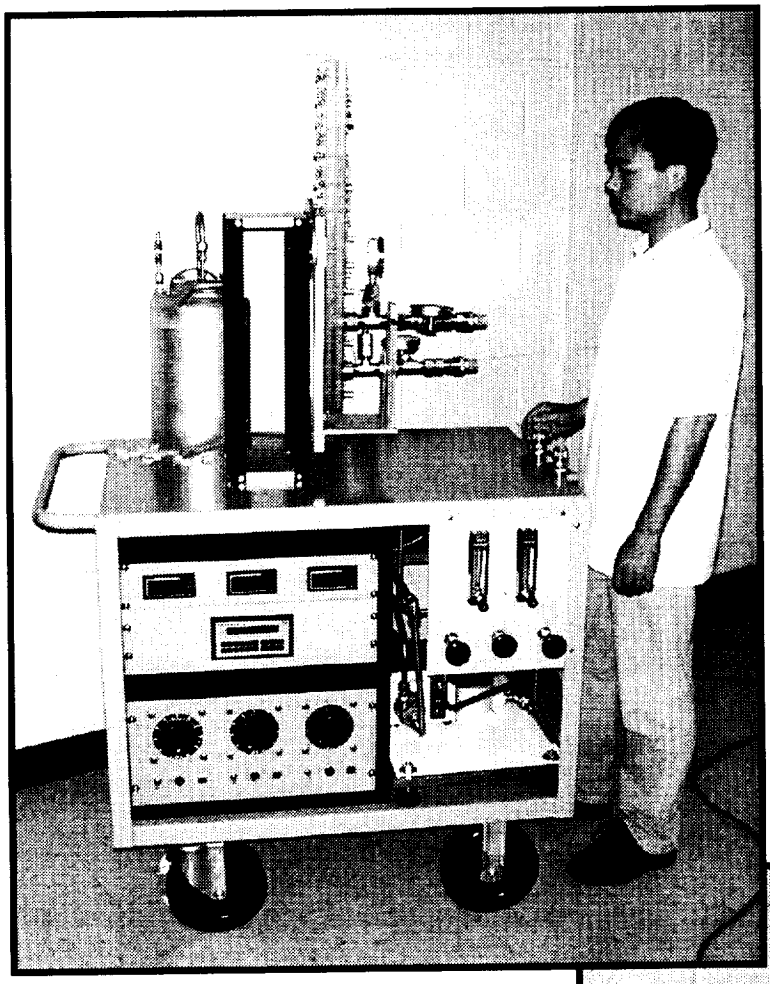

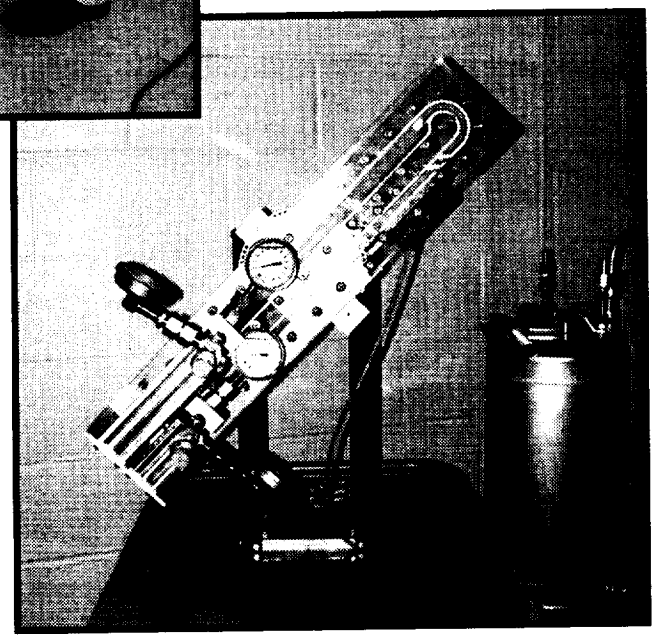

Orientation Nomenclature

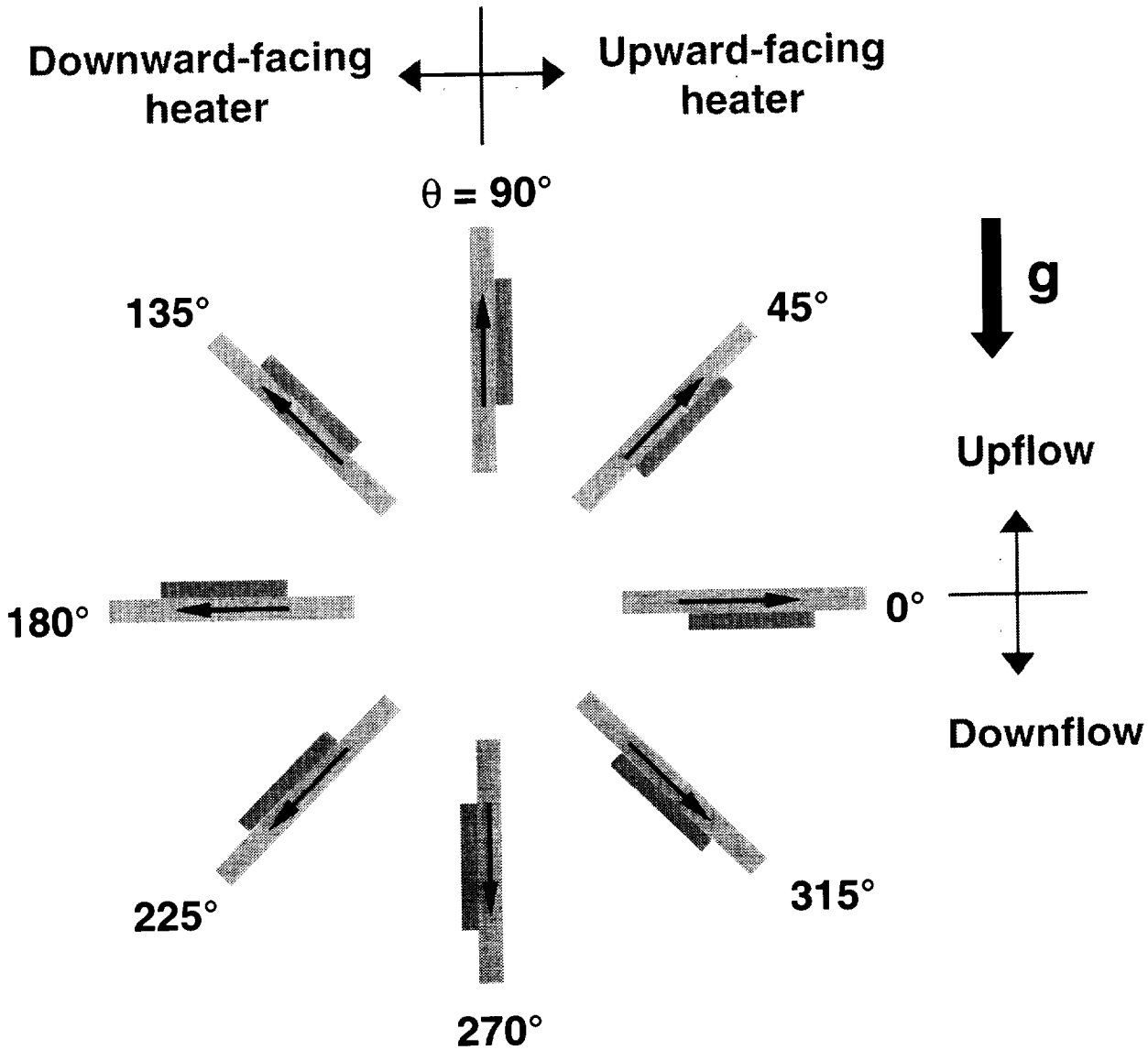

Vapor Behavior for Saturated Flow

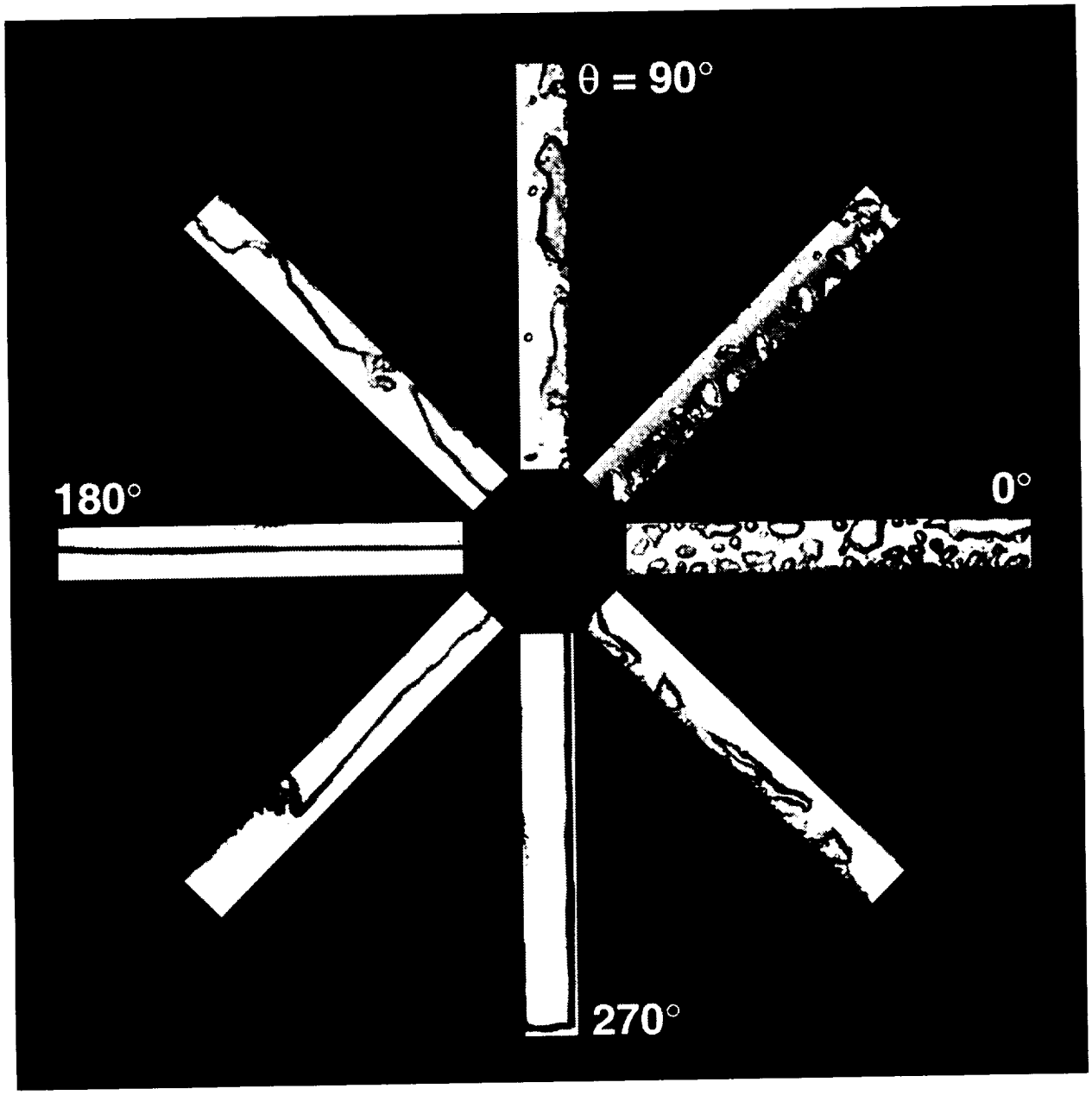

$\Delta T_{sub,o}$ = 3 °C, U = 0.1 m/s

Vapor Behavior for Saturated Flow

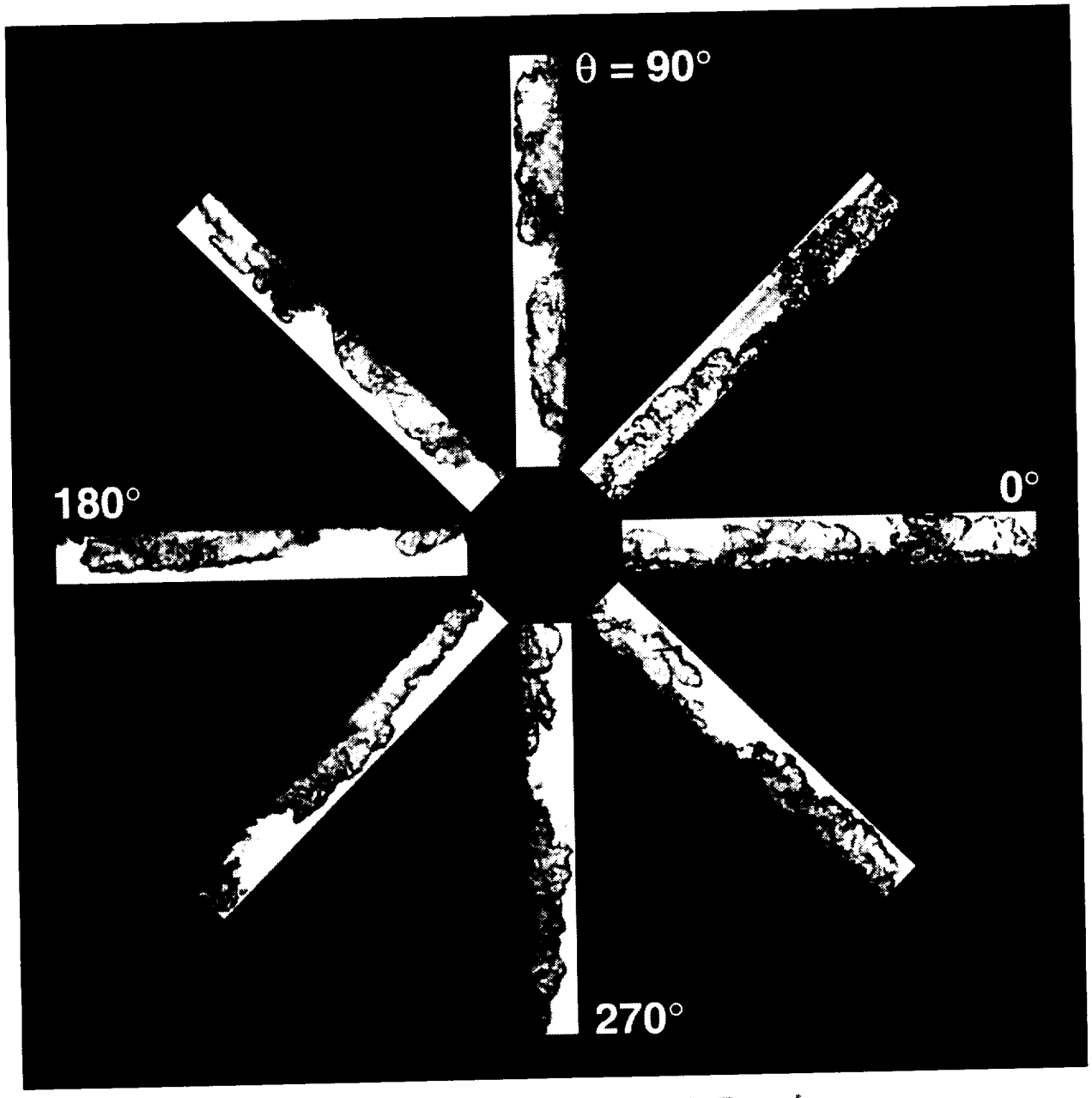

$\Delta T_{sub,o}$ = 3 °C, U = 1.5 m/s

CHF Variation with Orientation and Flow Velocity

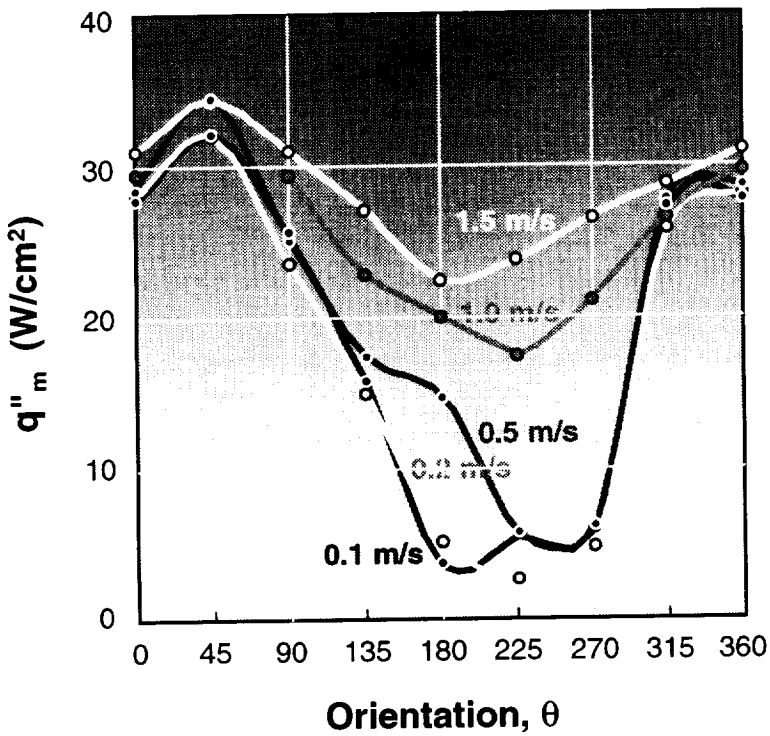

CHF Regime Map

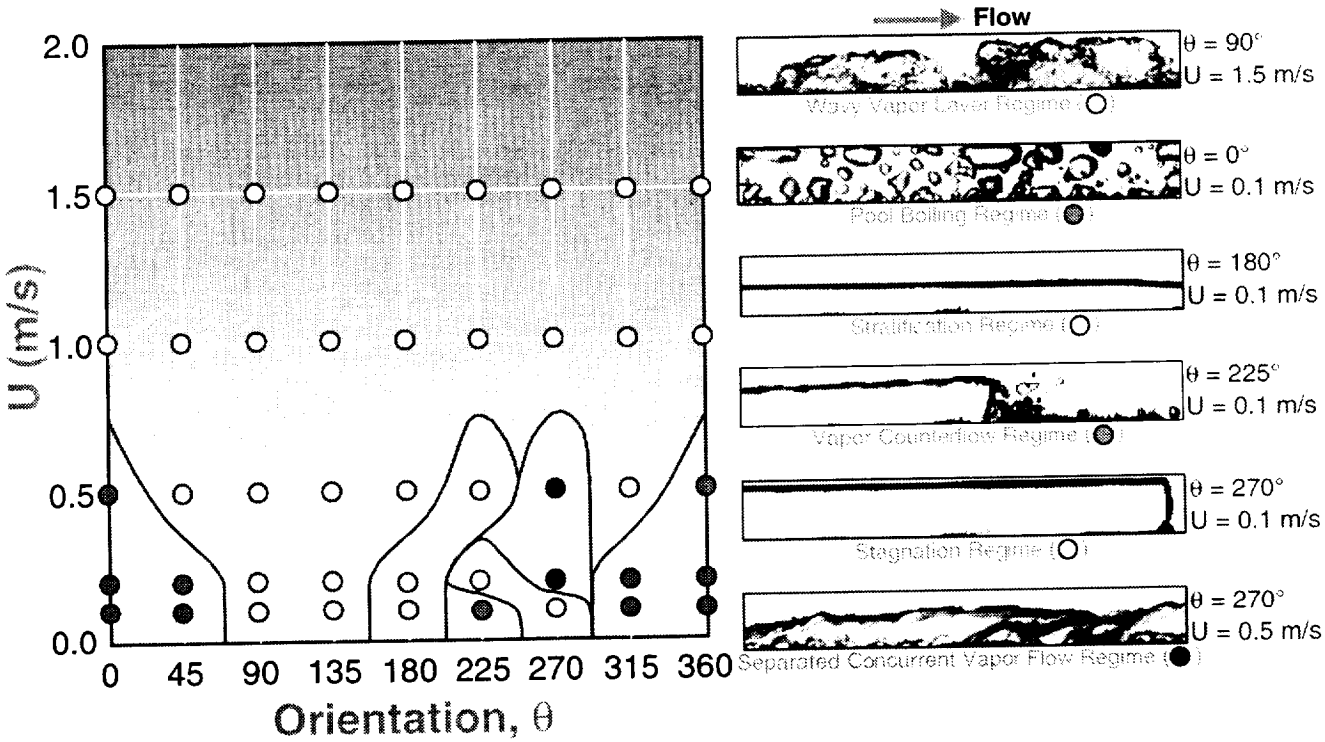

Comparison of Measured and Predicted CHF

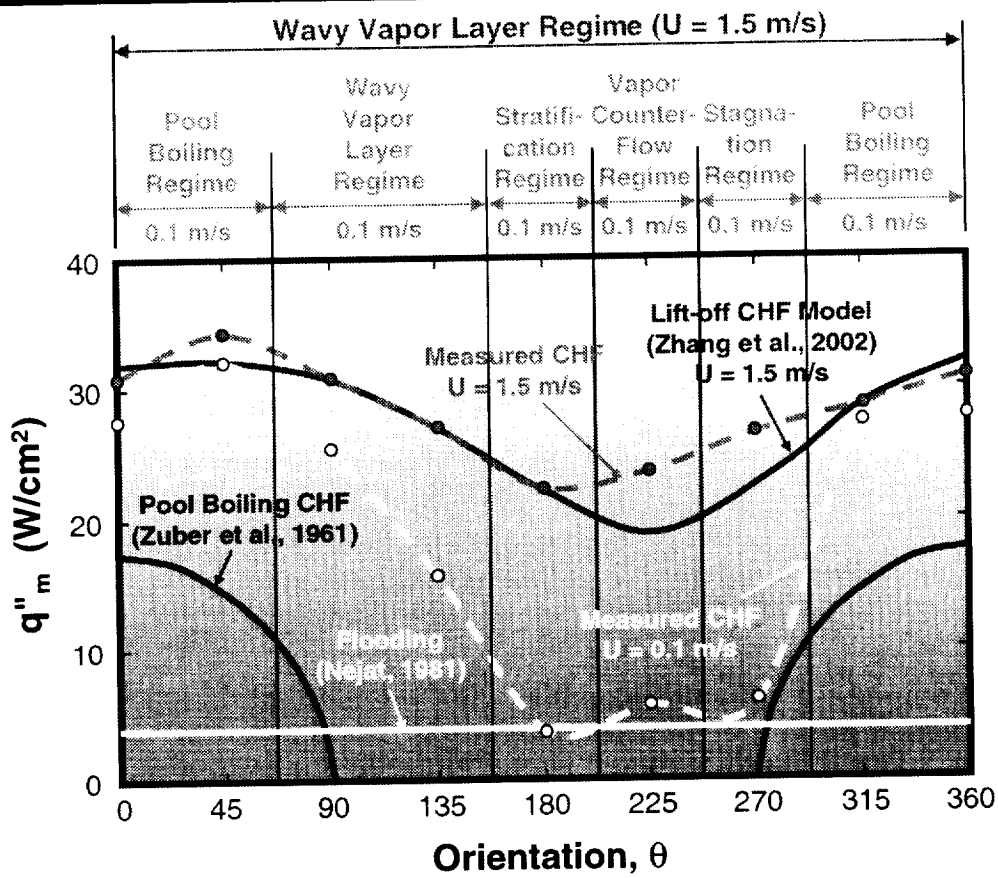

Conclusions

- CHF is very sensitive to orientation for flow velocities below 0.2 m/s
- At high velocities, CHF is less sensitive to orientation and increases with increasing velocity
- At low velocities, CHF for downflow and downward-facing heated wall orientations is much smaller than for upflow and upward-facing orientations
- The vapor layer characteristics fall into six different regimes

Conclusions

- At high velocities, CHF at all orientations is dominated by a Wavy Vapor Layer Regime. The vapor layer layer propagates along heated wall permitting liquid contact only in the troughs of interfacial waves. CHF occurs when the liquid contact regions are lifted from the wall due to intense vapor effusion

- At low velocities, CHF mechanism is dependant on flow/wall orientation:
  - Horizontal upward-facing:
    - Pool Boiling Regime
  - Upflow:
    - Wavy Vapor Layer Regime
  - Horizontal downward-facing:
    - Stratification Regime
  - Downflow:
    - Vapor Counterflow Regime
    - Stagnation Regime
    - Separated Countercurrent Vapor Flow Regime

Conclusions

- For Wavy Vapor Layer Regime,
  - Wavelength and wetting front length both increase in flow direction but their ratio remains constant
  - Lift-off of wetting fronts is closely related to wave curvature
- Interfacial Lift-off Model is very effective at capturing overall dependence of CHF on orientation in the Wavy Vapor Layer Regime
- Flooding limit is better suited to CHF prediction in low velocity downflow orientations

Effect of Body Force on Critical Wavelength

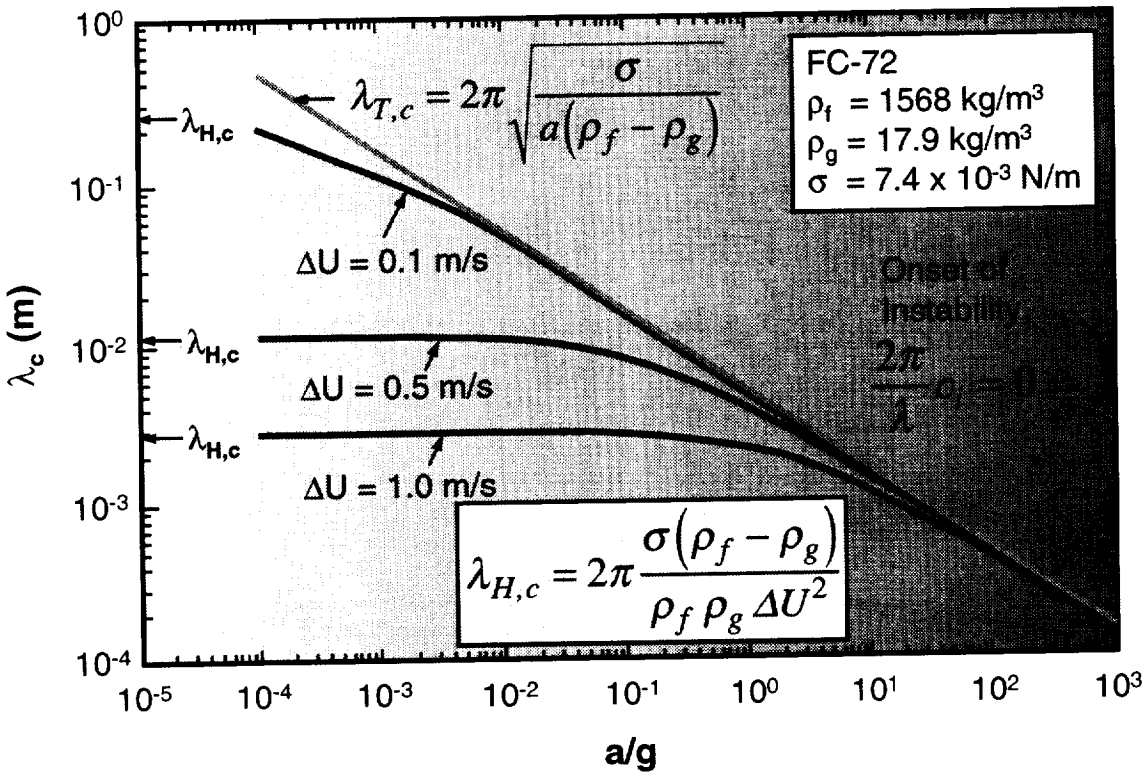

Conclusions

- This study points to minimum coolant velocities that can suppress body force effects
- These findings should be carefully confirmed in reduced gravity experiments
- Investigation of flow boiling CHF in reduced gravity is crucial to the safety and reliability of future space thermal management systems

LENGTH SCALE AND GRAVITY EFFECTS ON MICROGRAVITY BOILING HEAT TRANSFER

Jungho Kim and Christopher Henry
University of Maryland
Dept. of Mechanical Engineering
College Park, MD 20742

ABSTRACT

Boiling is a complex phenomenon where hydrodynamics, heat transfer, mass transfer, and interfacial phenomena are tightly interwoven. An understanding of boiling and critical heat flux in microgravity environments is of importance to space based hardware and processes such as heat exchange, cryogenic fuel storage and transportation, electronic cooling, and material processing due to the large amounts of heat that can be removed with relatively little increase in temperature. Although research in this area has been performed in the past four decades, the mechanisms by which heat is removed from surfaces in microgravity are still unclear. In earth gravity, buoyancy is an important parameter that affects boiling heat transfer through the rate at which bubbles are removed from the surface. A simple model describing the bubble departure size based on a quasi-static force balance between buoyancy and surface tension is given by the Fritz [1] relation:

$$Bo^{1/2} = 0.0208\,\theta$$

where Bo is the ratio between buoyancy and surface tension forces. For small, rapidly growing bubbles, inertia associated with the induced liquid motion can also cause bubble departure. In microgravity, the magnitude of effects related to natural convection and buoyancy are small and physical mechanisms normally masked by natural convection in earth gravity such as Marangoni convection can substantially influence the boiling and vapor bubble dynamics.

CHF is also substantially affected by microgravity. In 1-g environments, Bo has been used as a correlating parameter for CHF. Zuber's [2] CHF model for an infinite horizontal surface assumes that vapor columns formed by the merger of bubbles become unstable due to a Helmholtz instability blocking the supply of liquid to the surface. The jets are spaced λ_D apart, where

$$\lambda_D = 2\pi\sqrt{3}\left[\frac{\sigma}{g(\rho_l - \rho_v)}\right]^{1/2} = 2\pi\sqrt{3}L\,Bo^{-1/2} = \sqrt{3}\lambda_c$$

and is the wavelength that amplifies most rapidly. The critical wavelength, λ_c, is the wavelength below which a vapor layer underneath a liquid layer is stable. For heaters with Bo smaller than about 3 (heaters smaller than λ_D), the above model is not applicable, and surface tension effects dominate. Bubble coalescence is thought to be the mechanism for CHF under these conditions. Small Bo can result by decreasing the size of a heater in earth gravity, or by operating a large heater in a lower gravity environment. In the microgravity of space, even large heaters can have

low Bo, and models based on Helmholtz instability should not be applicable. The macrolayer model of Haramura and Katto [3] is dimensionally equivalent to Zuber's model and has the same dependence on gravity, so it should not be applicable as well. The goal of this work is to determine how boiling heat transfer mechanisms in a low-g environment are altered from those at higher gravity levels.

Boiling data using a microheater array was obtained under gravity environments ranging from 1.8 g to 0.02 g with heater sizes ranging from 2.7 mm to 1 mm. The boiling behavior for 2.7 mm at 0.02 g looked quite similar to boiling on the 1 mm heater at 1 g–the formation of a large primary bubble surrounded by smaller satellite bubbles was observed under both conditions. The similarity suggests that for heaters smaller than some fraction of l_c, coalescence and surface tension dominate boiling heat transfer. It also suggests that microgravity boiling can be studied by studying boiling on very small heaters.

[1] Fritz, W. (1935) "Berechnungen des Maximalvolumens von Dampfblasen", Phys. Z., Vol. 36, pp. 379-384.

[2] Zuber, N., (1959) "Hydrodynamics of Boiling Heat Transfer", AEC Report AECU-4439.

[3] Haramura, Y, and Katto, Y. (1983) "A New Hydrodynamic Model of the Ciritical Heat Flux, Applicable Widely to Both Pool and Forced Convective Boiling on Submerged Bodies in Saturated Liquids", Int. J. of Heat and Mass Transfer, Vol. 26, pp. 389-399.

Boiling Heat Transfer Mechanisms at Various Gravity and Length Scales

15 August, 2002

Jungho Kim

University of Maryland

John McQuillen and Joe Balombin

NASA Glenn Research Center

This work was sponsored by NASA HQ
Office of Biological and Physical Sciences

Outline

- Experimental Technique
- Some Earth Gravity Results
- Some Low Gravity Results
- Scaling Across Gravity and Length scales

Experimental Technique

Heater Array

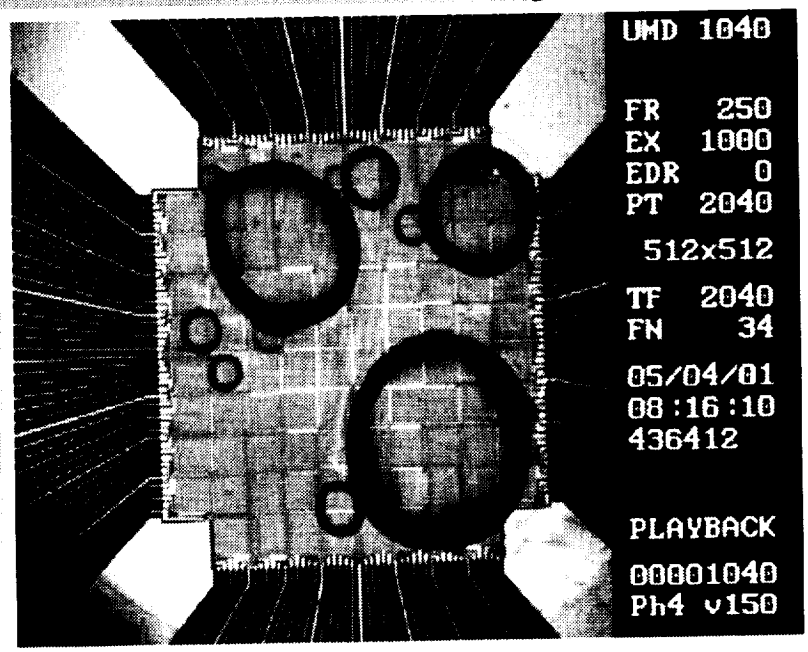

- Pt heaters on quartz substrate
- Heater resistance 200-1000 Ω
- 96 heaters in array

Heater Sizes

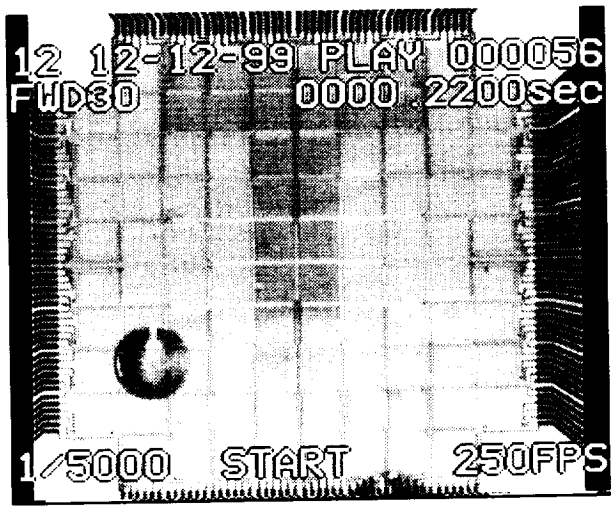

2.7 mm heater array

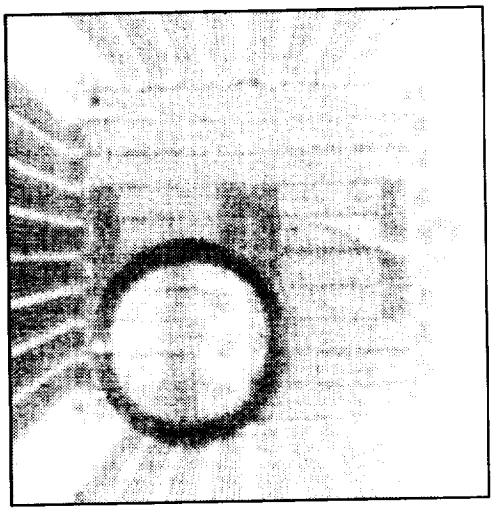

1.0 mm heater array

- Also have a 7 mm heater array

Feedback Circuits

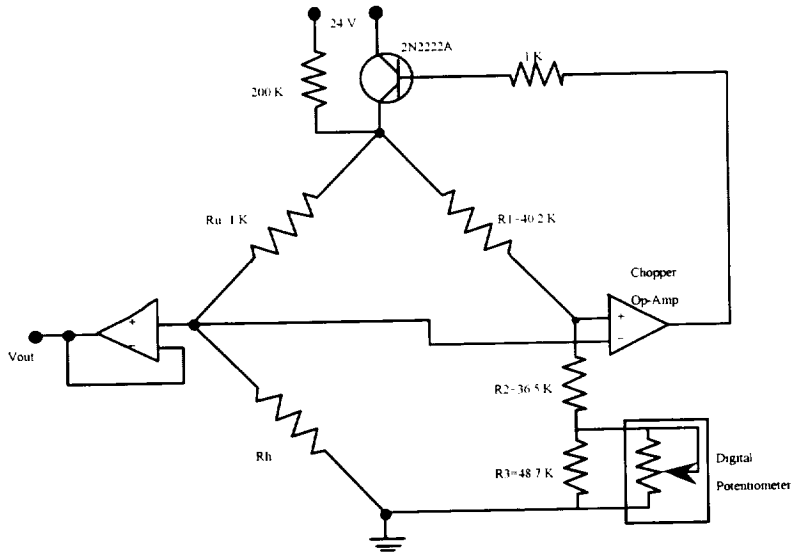

- 96 feedback circuits (one per heater)
- Constant temperature operation
- 15 kHz frequency response

Test Apparatus

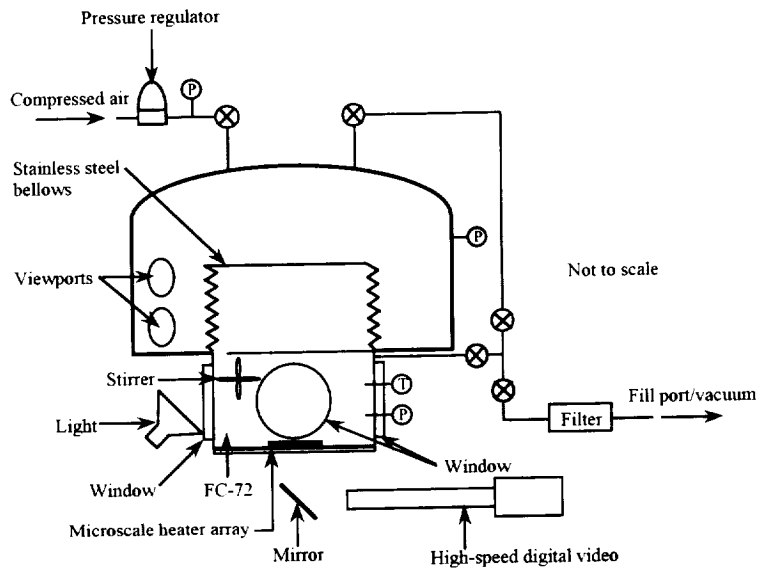

- **Prototype for Dr. H. Merte's shuttle payload**

Photograph of Test Rig

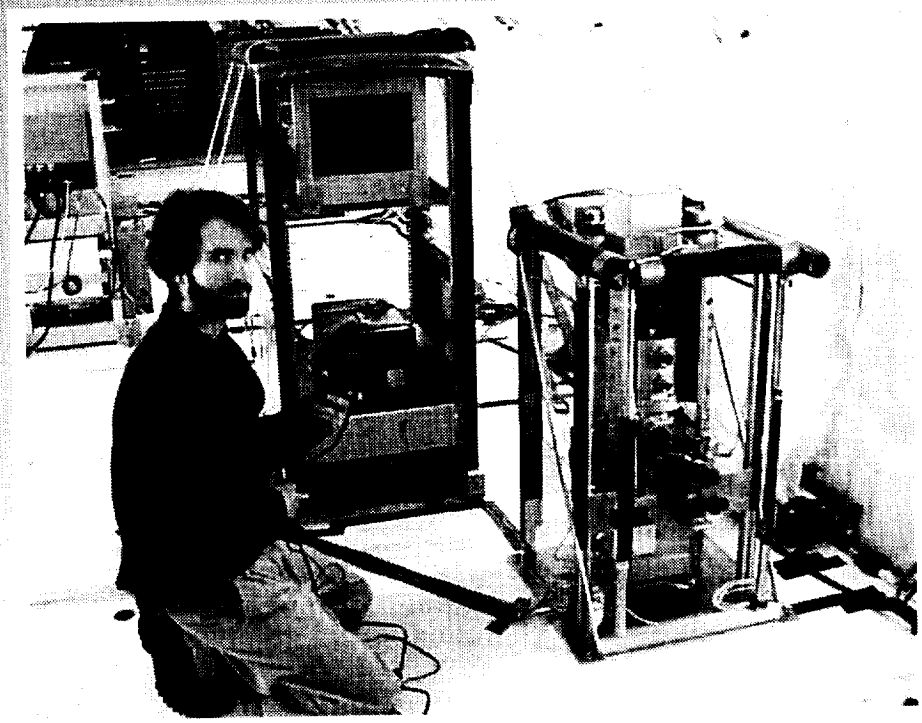

Earth Gravity Boiling Heat Transfer

Experiment Conditions

- Fluid is FC-72 (C_6F_{14})
- Pressure=1 atm (Tsat=57 °C)
- Heater temperature=76 °C
- Bulk liquid temperature= 52 °C

Side View Images of Triple Bubble Event

Nucleation

Departure

[ms]

Colorized Images

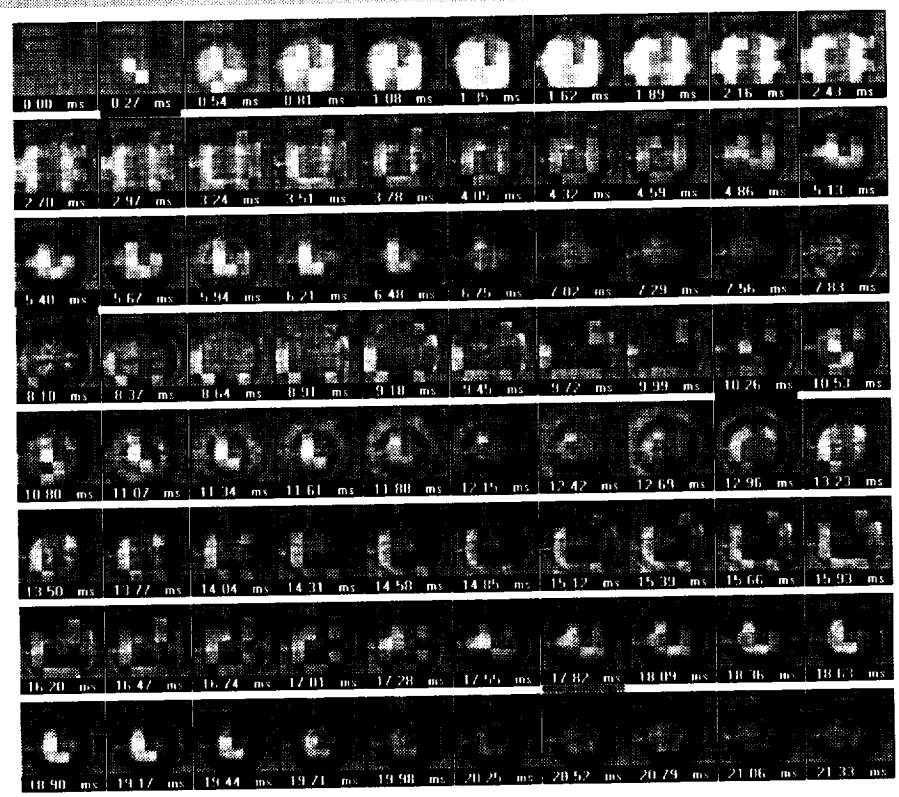

Nucleation

Departure

0

0.02 W

Triple Bubble Event Analysis

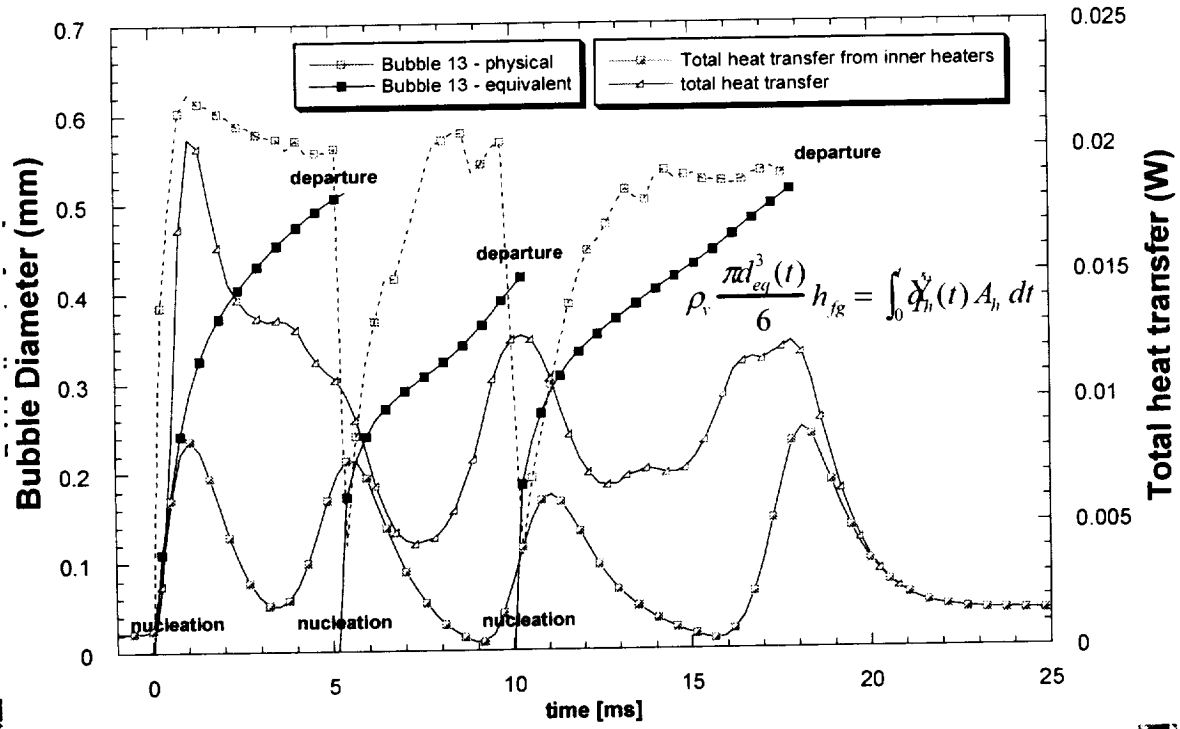

Low Gravity Boiling Heat Transfer

Low Gravity Environment

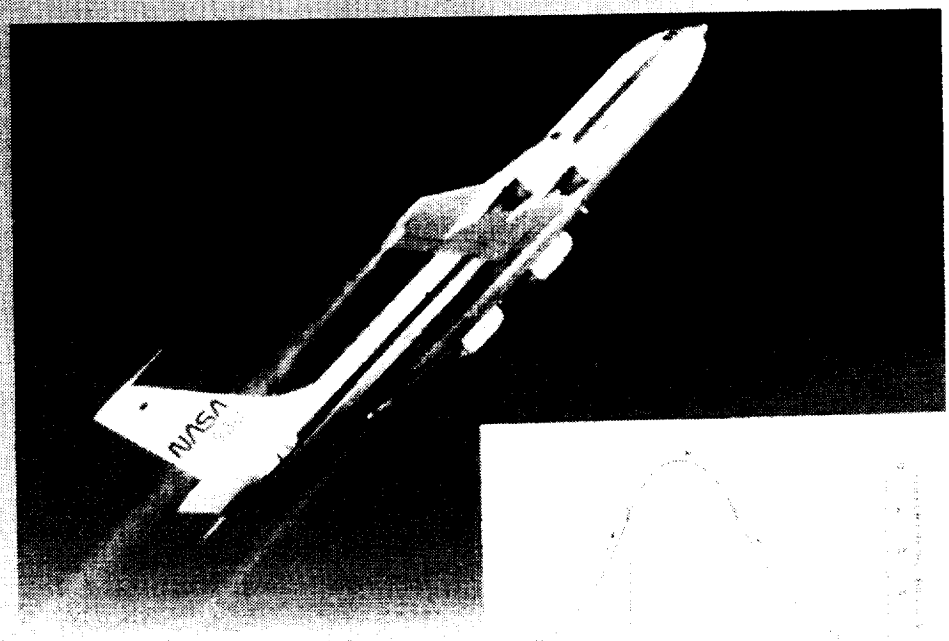

Space and Time Resolved Heat Flux Distribution

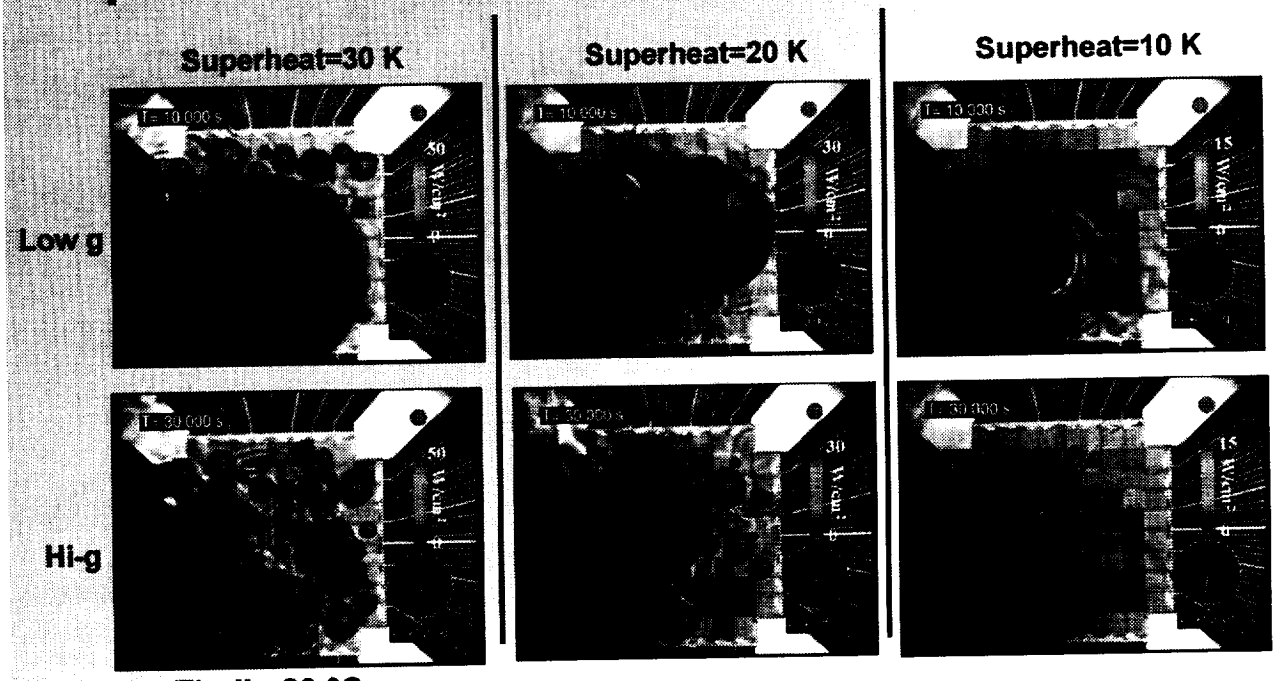

Tbulk=20 °C

(Colorization of images performed by the NASA GVIS Lab)

Low Gravity Boiling at Various Subcooling

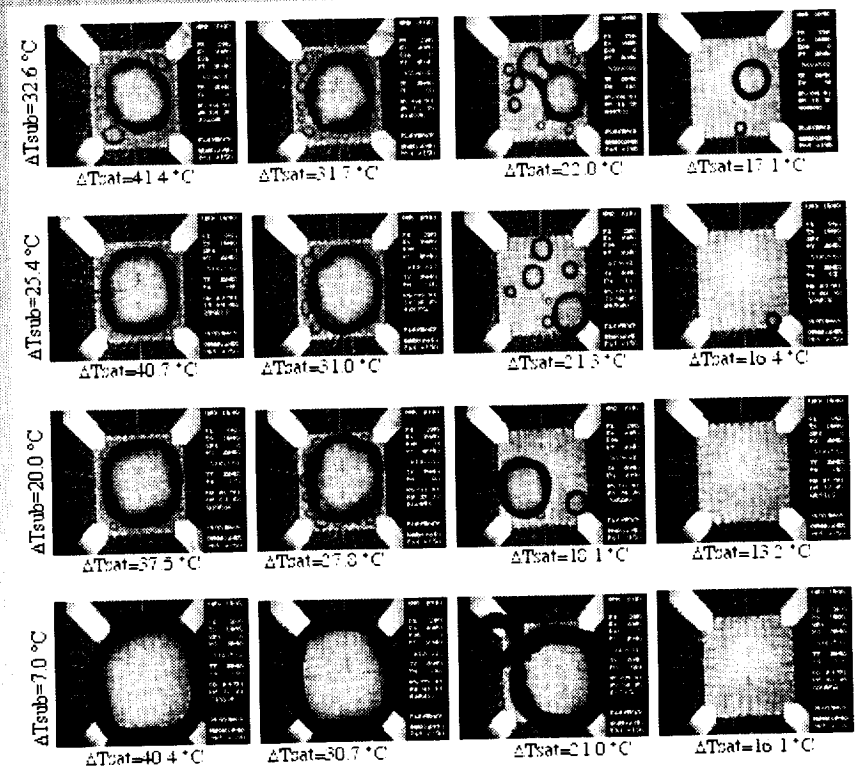

Time Averaged Heat Flux Distribution

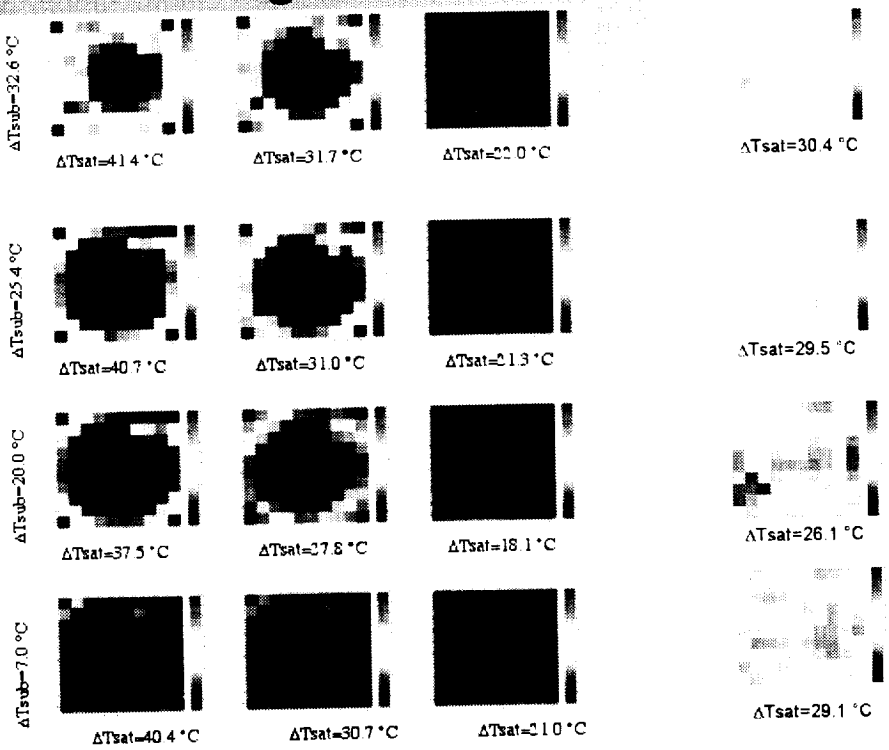

Low Gravity (0-55 W/cm²) **1 g (0-45 W/cm²)**

Boiling Curve in Low Gravity, 1 g, and Hi-g

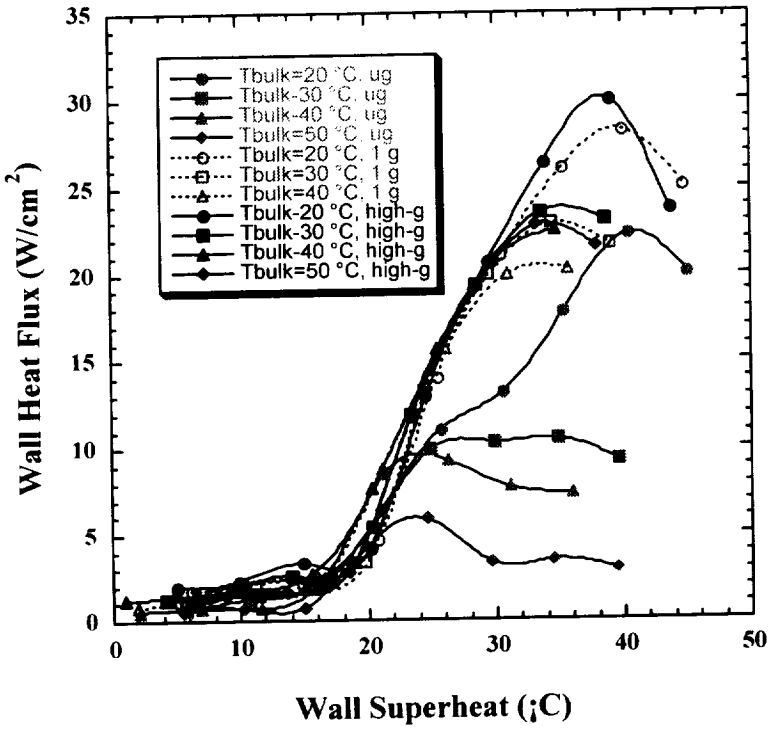

Scaling Boiling Heat Transfer Across Gravity Levels and Heater Sizes

Length and Gravity Effects: (Tbulk=28 C, Twall=90 C)

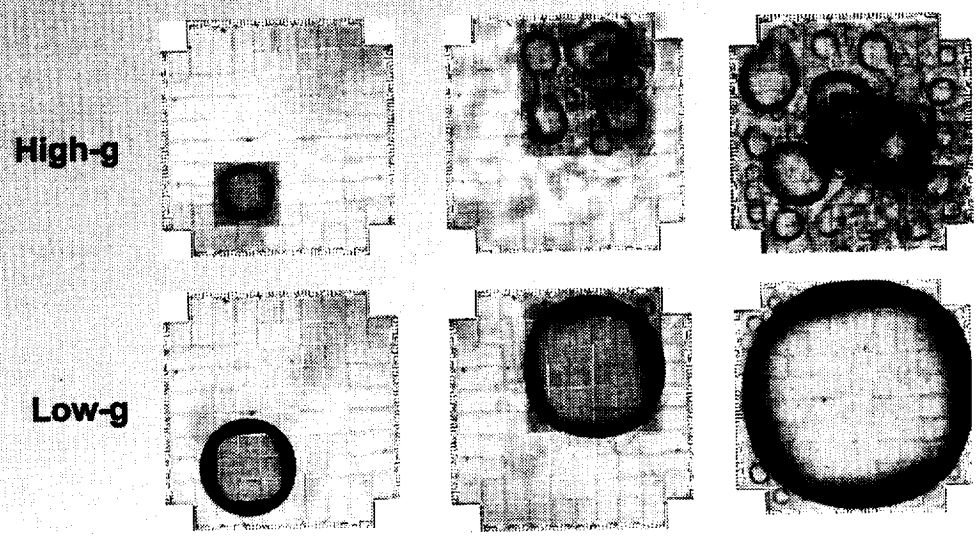

Length and Gravity Effects: (Tbulk=55 C, Twall=90 C)

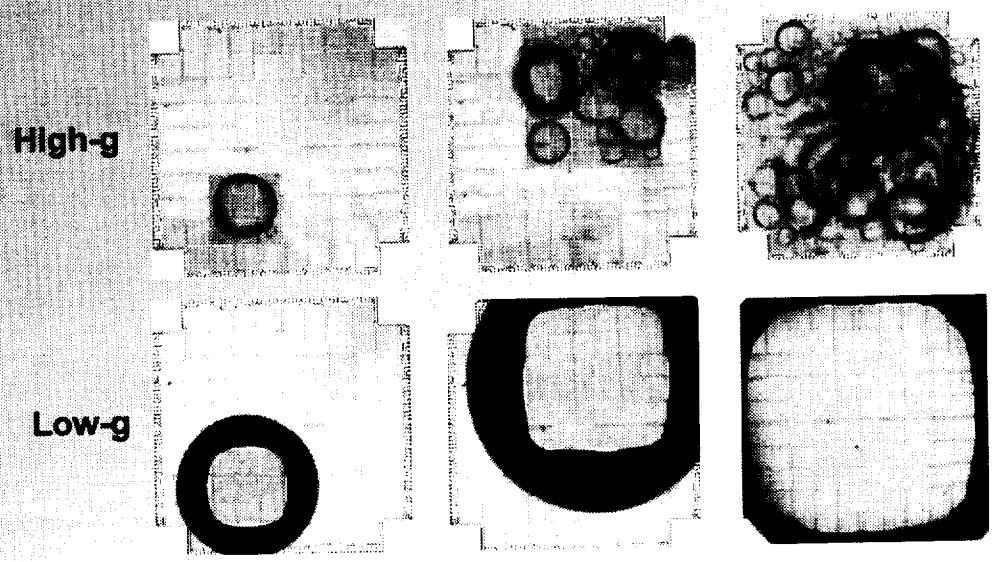

9 heaters 36 heaters 96 heaters

Dimensional Analysis

- $D_b = f\left[g, L_H, (T_{sat} - T_{bulk}), (T_{wall} - T_{sat}), (\rho_l - \rho_v), \sigma, c_p, h_{fg}, k, P, \mu\right]$
- 12 variables – 4 dimensions (M, L, θ, T) = 8 groups
- $\frac{D_b}{L_H} = [Bo][Ja_{sub}][Ja_{\sup}][L'][\Pr]\left[\frac{h_{fg}(\rho_l - \rho_v)}{P}\right]\left[\frac{h_{fg}^{1/2}\mu}{\sigma}\right]$

$$Bo = \frac{g(\rho_l - \rho_v)L_H^2}{\sigma} \qquad Ja_{sub} = \frac{c_p(T_{sat} - T_{bulk})}{h_{fg}} \qquad Ja_{\sup} = \frac{c_p(T_{wall} - T_{sat})}{h_{fg}}$$

$$L' = \frac{L_H P}{\sigma}$$

- If D_b/L_h is near unity for surface tension dominated flow, and we assume constant properties and pressure, then

$$[Bo] = [Ja_{sub}][Ja_{\sup}][L']$$

- Determine the g-level at which the primary bubble departs, and compute $Bo = f(Ja_{sub}, Ja_{sat}, L')$

Preliminary Boundary Between Gravity and Surface Tension Dominated Behavior

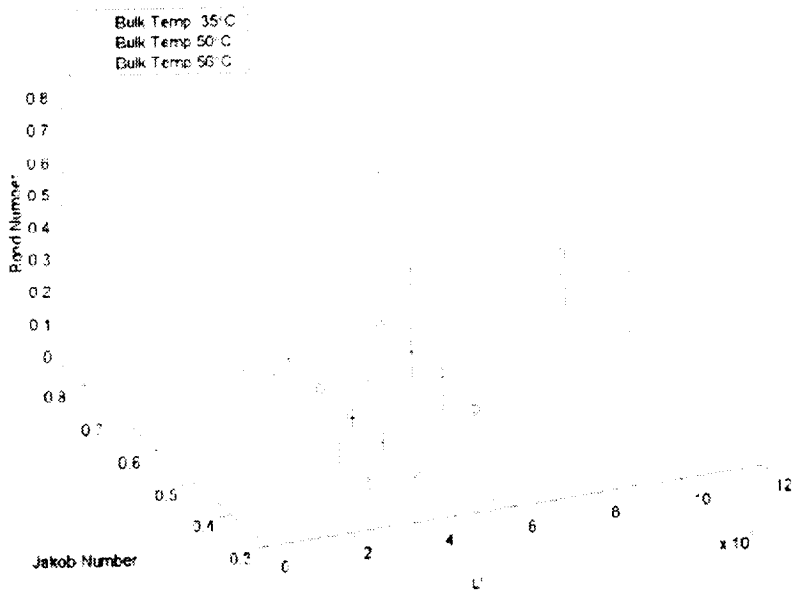

Acknowledgements

Graduate students: Fatih Demiray, Chris Henry, Jonathan Coursey

Undergraduate students: John Benton, Bob Kucner, Aaron Bird

NASA: John Yaniec, Jim Withrow, Mary Vickerman

Constrained Vapor Bubble Experiment

Peter C. Wayner, Jr., Joel L. Plawsky, Ling Zheng, and Ying-Xi Wang
Isermann Department of Chemcial Engineering
Rensselaer Polytechnic Institute
Troy, NY 12180

Microgravity experiments on the Constrained Vapor Bubble Heat Exchanger, CVB, are being developed for the International Space Station. In particular, we present results of a precursory experimental and theoretical study of the vertical Constrained Vapor Bubble in the Earth's environment. A novel non-isothermal experimental setup was designed and built to study the transport processes in an ethanol/quartz vertical CVB system.

Temperature profiles were measured using an in situ PC-based LabView data acquisition system via thermocouples. Film thickness profiles were measured using interferometry. A theoretical model was developed to predict the curvature profile of the stable film in the evaporator. The concept of the total amount of evaporation, which can be obtained directly by integrating the experimental temperature profile, was introduced. Experimentally measured curvature profiles are in good agreement with modeling results. For microgravity conditions, an analytical expression, which reveals an inherent relation between temperature and curvature profiles, was derived.

CONSTRAINED VAPOR BUBBLE:

EXPERIMENTAL STUDY OF CONTACT LINE DYNAMICS IN DROPLET EVAPORATION / CONDENSATION

Shripad Gokhale, Joel Plawsky and Peter C. Wayner, Jr.
Department of Chemical Engineering
Rensselaer Polytechnic Institute
Troy, New York, USA

SIXTH MICROGRAVITY FLUID PHYSICS AND TRANSPORT PHENOMENA CONFERENCE
AUGUST 14 - 16, 2002
CLEVELAND, OHIO

CONSTRAINED VAPOR BUBBLE

VERTICAL EXPERIMENTAL CELL

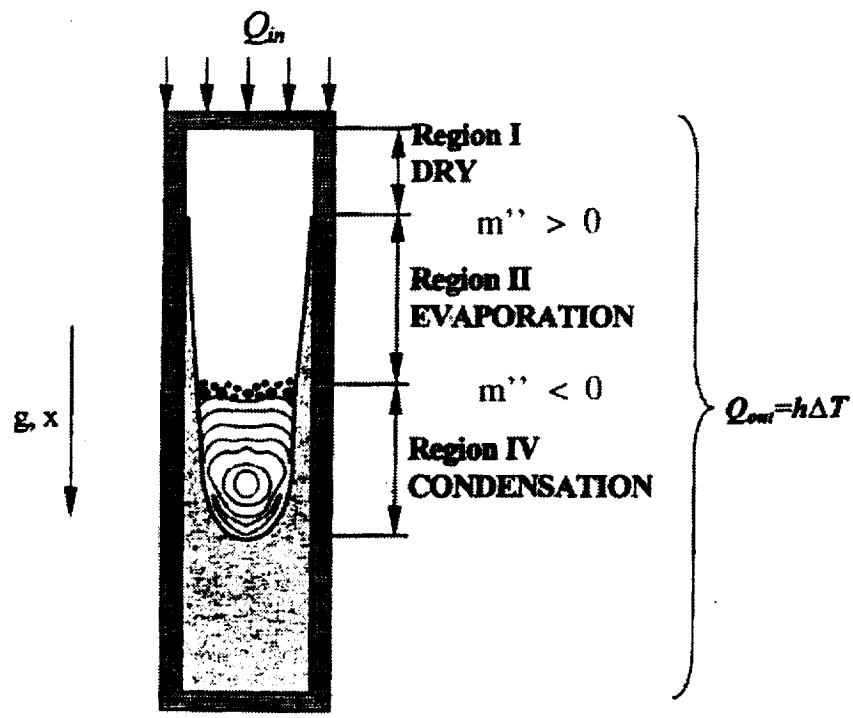

SQUARE QUARTZ CELL WITH SHARP CORNERS

INSIDE DIMENSIONS: 3 x 3 x 40 mm^3

SMALL REGIONS CAN BE EXPERIMENTALLY STUDIED USING A MICROSCOPE (e.g., DROPWISE CONDENSATION AT THE JUNCTION OF REGIONS II & IV)

VERTICAL GENERIC EXTENDED MENISCUS

SHAPE GIVES PRESSURE : $P_l = P_v - \sigma K - \Pi$

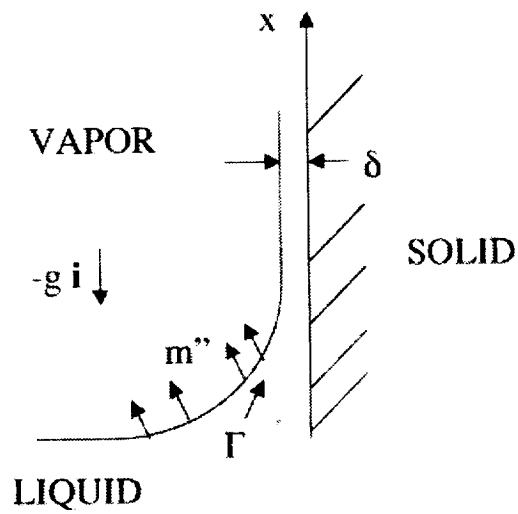

CHEMICAL POTENTIAL , μ

$$\mu_{ig} = \mu_i (T_l , P_l) + \rho_{lm} \, g \, x$$

KELVIN (ΔP) – CLAPEYRON (ΔT) EFFECTS ON μ

$$\Delta\mu_g = -[\sigma K + \Pi - \rho_{lm} \, g \, x] + \frac{\rho_{lm} \Delta h_m}{\bar{T}} [T_{lvx} - T_{vx}]$$

$$\Delta\mu_g = \rho_{lM} \, R T_{lv} \ln \frac{P_{vlvx}}{P_{vx}} \qquad at \quad x$$

$$IF \quad P_{vlvx} \neq P_{vx} \quad , \quad m'' \neq 0$$

3

CONDENSATION : n-BUTANOL ON QUARTZ

SESSILE DROP WITH LOW INTERFACIAL FLUX → 0

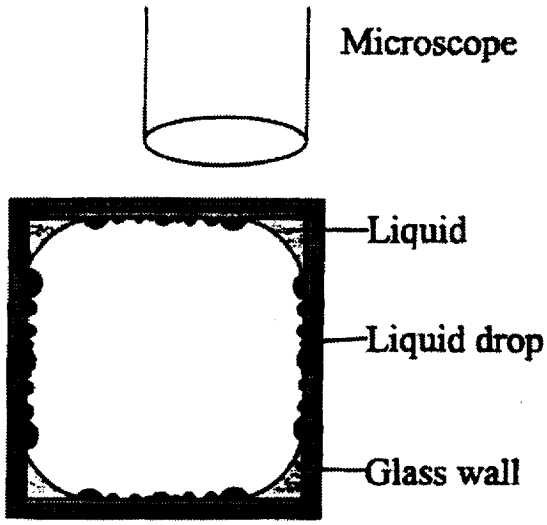

CVB CELL

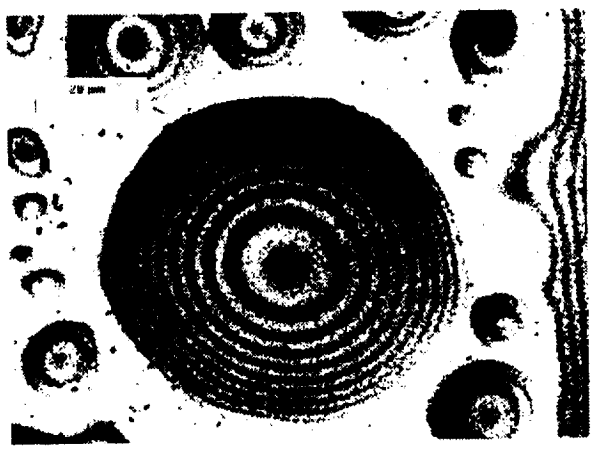

- NATURALLY OCCURRING INTERFERENCE FRINGES GIVE THE CONTACT ANGLE (SURFACE EXCESS FREE ENERGY), CURVATURE, VOLUME AND INTERFACIAL HEAT FLUX AS A FUNCTION OF TIME

- OBTAIN ENHANCED UNDERSTANDING OF THE CONTACT LINE REGION

HORIZONTAL EXPERIMENTAL SYSTEM

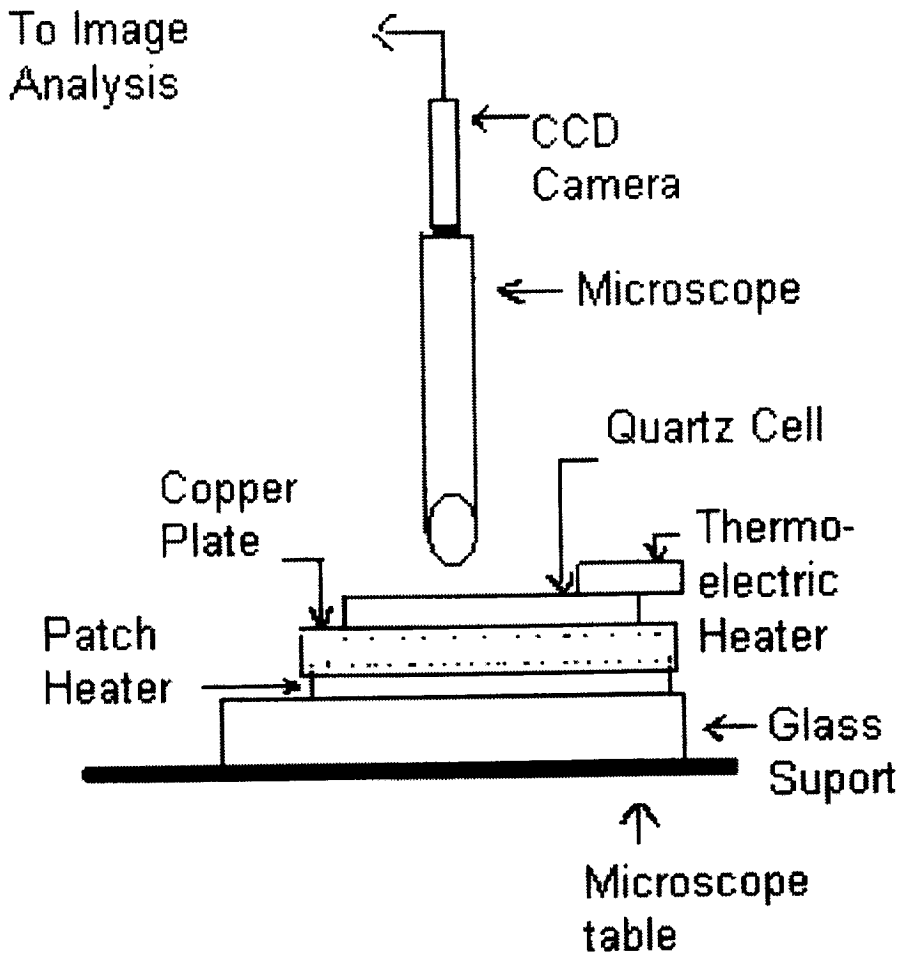

INSIDE DIMENSIONS OF CONSTRAINED VAPOR BUBBLE
QUARTZ CELL, CVB : 3 mm X 3 mm X 40 mm

PARTIALLY WETTING SYSTEM, $\theta > 0$

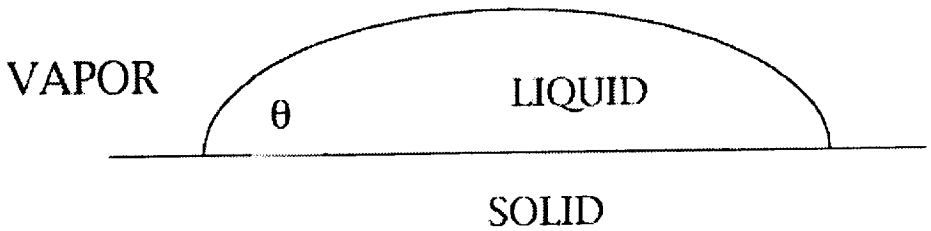

$$\sigma_l(\cos\theta - 1) = \Delta G(\delta_e)$$

$$\Delta G(\delta_e) = S^{LW}\left[\frac{d_o^2}{\delta_e^{\,2}}\right] + S^P \exp\left[\frac{d_o - \delta_e}{l}\right]$$

θ	[MEASURE] APPARENT CONTACT ANGLE AND CURVATURE
ΔG	EXCESS FREE ENERGY OF ADJACENT FILM
S	APOLAR AND POLAR COMPONENTS OF THE SPREADING COEFFICENT : $S^P = 0$ FOR N-BUTANOL / QUARTZ
l	CORRELATION LENGTH
d_o	EQUILIBRIUM CUT-OFF DISTANCE
δ_e	THICKNESS OF ADJACENT THIN FILM

RADIUS OF CURVATURE VERSUS TIME

CONDENSATION

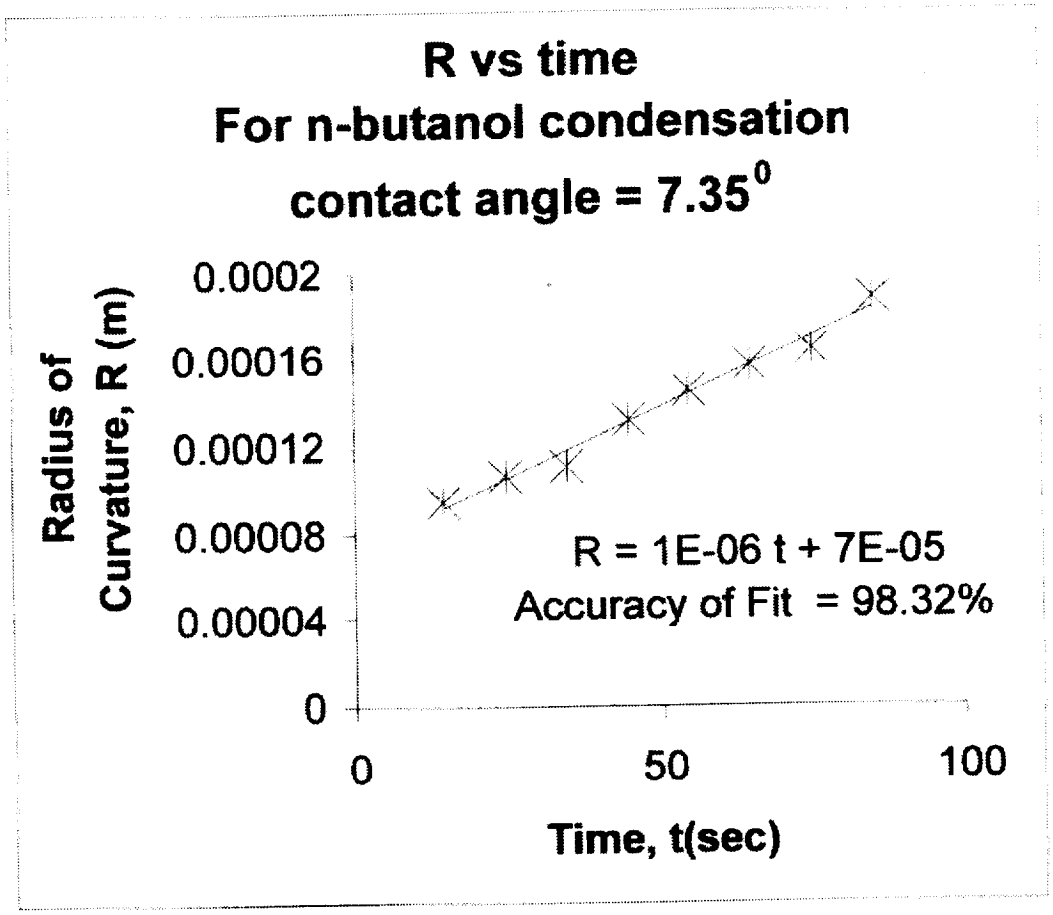

- RADIUS IS A LINEAR FUNCTION OF TIME
- ADDITIONAL DATA SHOWS THAT THE (ADVANCING) CONTACT ANGLE INCREASES WITH AN INCREASE IN THE CONDENSATION RATE

RADIUS OF CURVATURE VERSUS TIME

EVAPORATION

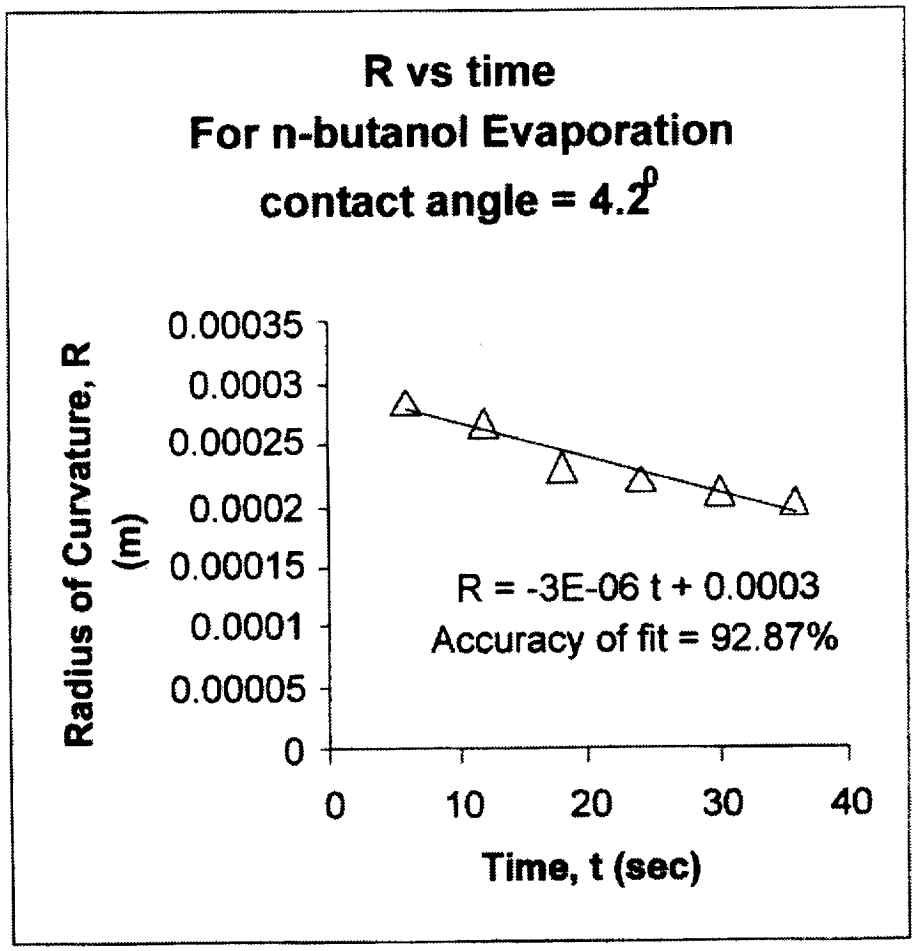

- RADIUS IS A LINEAR FUNCTION OF TIME

- ADDITIONAL DATA SHOWS THAT THE (RECEDING) CONTACT ANGLE DECREASES AS THE EVAPORATION RATE INCREASES.

CHARACTERISTIC INTERFACIAL VELOCITY VERSUS CONTACT ANGLE

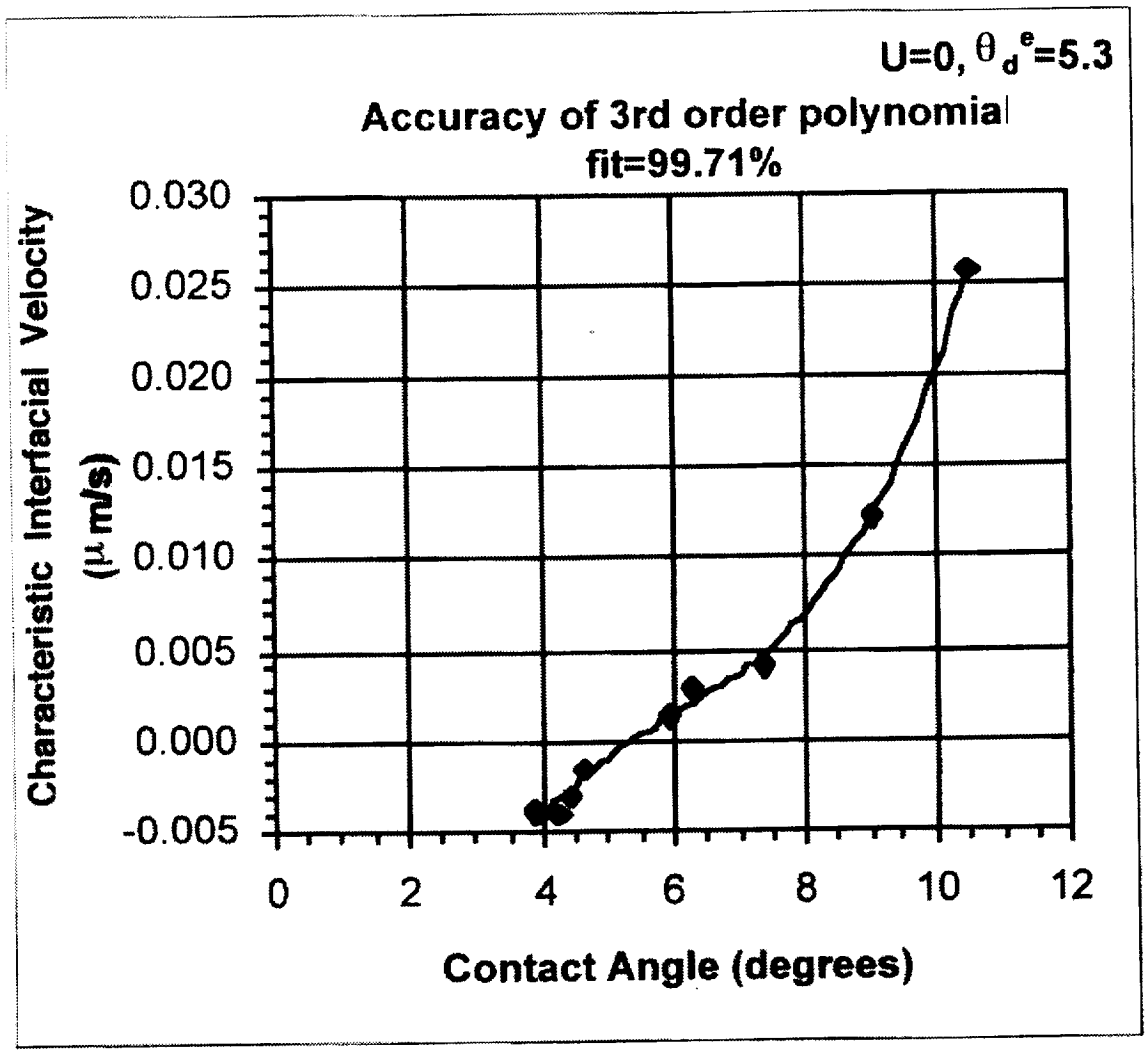

CONSISTENT WITH TANNER'S EQUATION : $U_d \propto \theta_d^3$

THE INTERFACE IS DYNAMIC

KELVIN – CLAPEYRON INTERFACIAL KINETICS

$$q''_{lv} = h_{lv}\,[T_{lvx} - T_{vx}] \qquad \textit{HEAT FLUX}$$

$$= h_{lv}^{cl}\,[T_{lvx} - T_{vx}] - h_{lv}^{kl}\,[\Pi + \sigma_{lv} K - \rho_l g x]$$

$$h_{lv}^{cl} = \left(\frac{C^2 M}{2\pi R T_{lv}}\right)^{0.5} \frac{M P_v \Delta h_m^2}{R T_v T_{lv}} \quad ; \quad h_{lv}^{kl} = \left(\frac{C^2 M}{2\pi R T_{lv}}\right)^{0.5} \frac{V_{lM} P_v \Delta h_m}{R T_{lv}}$$

---

for n-butanol at T = 45° C , P_v = 3.42 x 10^3 Pa.

$$q_{lv}'' = 5.02\,x10^5 \bullet (T_{lv} - T_v) + 0.320 \bullet (P_l - P_v)$$

e.g., radius of curvature of R_1 = 140 μm, ΔP_1 = 363 N/m^2

R_2 = 60 nm, ΔP = 680,000 N/m^2

with low flux, ΔT_1 = 2.3 x 10^{-4} is not measurable , ΔP_1 is

INTERFACIAL TEMPERATURE DIFFERENCE FROM DATA AND THE KELVIN – CLAPEYRON MODEL VERSUS TME

FOR CONDENSATION

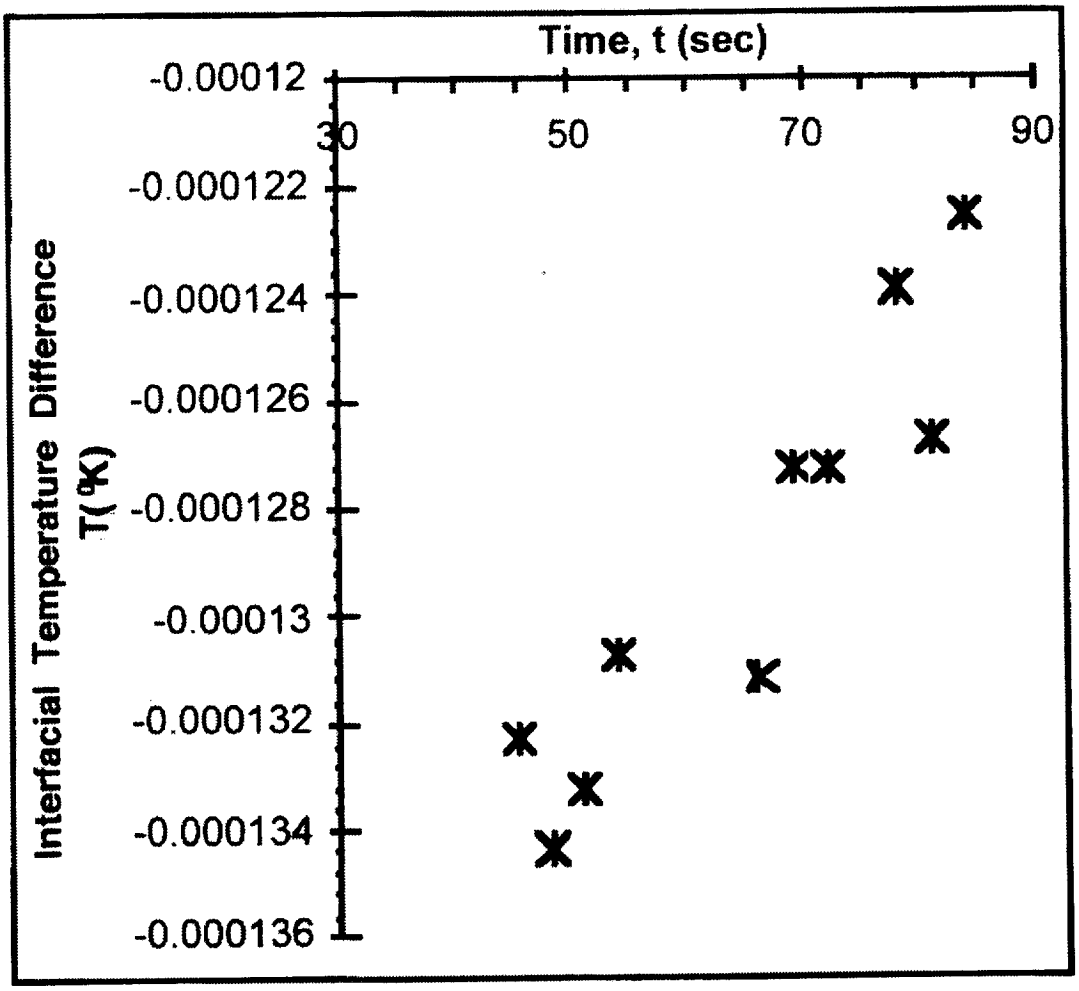

THE INTERFACIAL TEMPERATURE DIFFERENCE IS EXTREMELY SMALL AND CANNOT BE MEASURED ALTHOUGH THE PRESSURE JUMP CAN BE MEASURED

DROP MERGING INTO CORNER MENISCUS

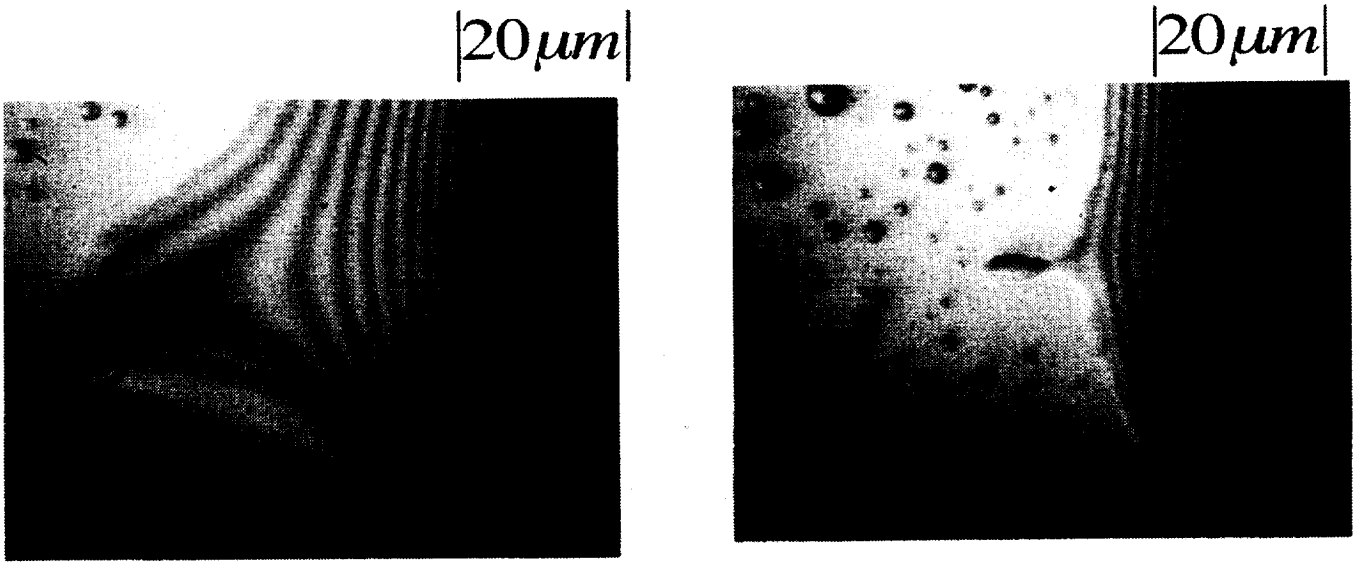

t = 0.66 sec. t = 2.64 sec.

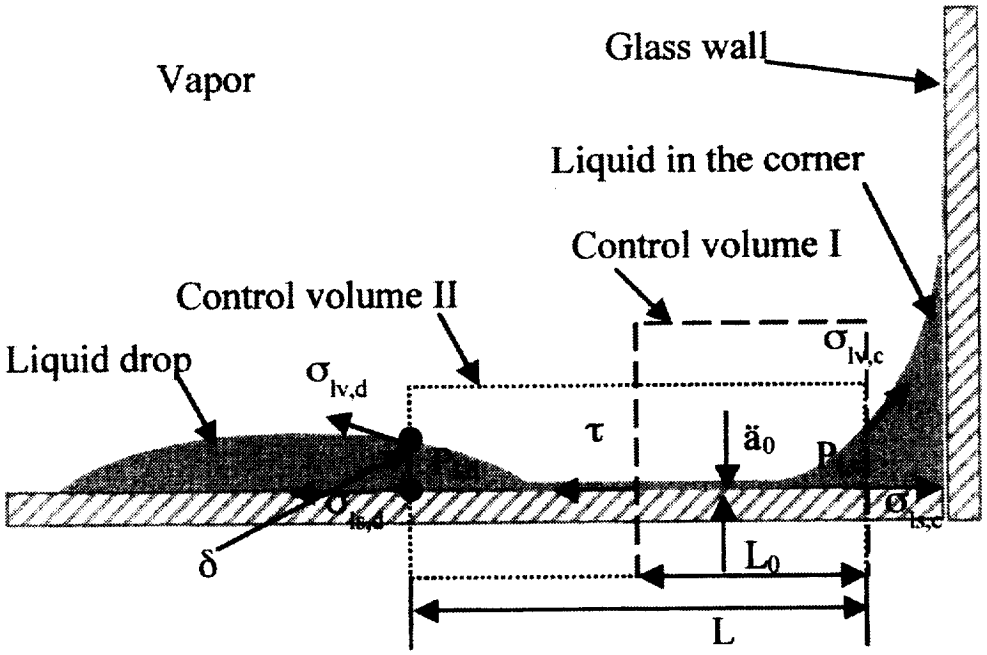

CONCLUSIONS

- EXPERIMENTAL AND THEORETICAL TECHNIQUES TO STUDY CONTACT LINE MOTION WITH PHASE CHANGE WERE DEVELOPED.

- AS THE RATE OF CONDENSATION INCREASES, THE CONTACT ANGLE OF THE (ADVANCING) CONTACT LINE INCREASES.

- AS THE RATE OF EVAPORATION INCREASES, THE CONTACT ANGLE OF THE (RECEDING) CONTACT LINE DECREASES.

- THE RESULTS ARE CONSISTENT WITH TANNER'S SCALING EQUATION : $U \propto (\Theta^3 - \Theta_O^3)$.

- THE EXCESS INTERFACIAL TEMPERATURE IS TOO SMALL TO MEASURE EXPERIMENTALLY WHEREAS THE INTERFACIAL PRESSURE JUMP CAN BE MEASURED EXPERIMENTALLY.

- THE RESULTS SUPPORT THE HYPOTHESIS THAT EVAPORATION/CONDENSATION IS AN IMPORTANT FACTOR IN CONTACT LINE MOTION.

SEPARATION OF CARBON MONOXIDE AND CARBON DIOXIDE FOR MARS ISRU

M. Douglas LeVan and Krista S. Walton
Department of Chemical Engineering, Vanderbilt University
VU Station B 351604, Nashville, TN 37235
m.douglas.levan@vanderbilt.edu
Ph: (615) 322-2441 Fax: (615) 343-7951

John E. Finn
Astrobiology Technology Branch, M/S 239-15
NASA Ames Research Center, Moffett Field, CA 94035-1000

K. R. Sridhar
Department of Aerospace and Mechanical Engineering
The University of Arizona, P.O. Box 210016, Tucson, AZ 85721

ABSTRACT

Human Exploration and Development of Space will require the use of fundamental process technologies for gas storage and separation. These are enabling technologies. In our research, we are designing, constructing, and testing an innovative, robust, low mass, low power separation device that can recover carbon dioxide and carbon monoxide for Mars ISRU (in-situ resource utilization). The work has broad implications for gas storage and separations for gas-solid systems; these are ideally suited for reduced gravitational environments. The work is also important for robotic sample return missions using ISRU and in lunar oxygen production from regolith using carbothermal reduction. This paper describes our overall effort and highlights our results on adsorption equilibrium determination and process design. A second paper will provide details on adsorption equilibrium measurement and adsorbent selection.

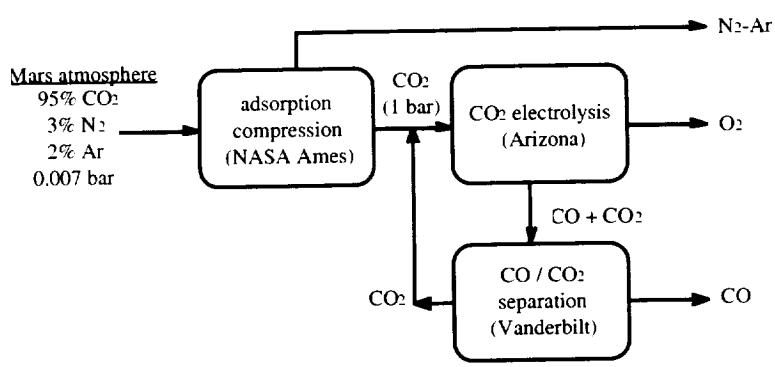

Figure 1: Flow diagram of a chemical system for conversion of Mars atmosphere to a N_2-Ar mixture and high-pressure CO_2, O_2, and CO.

As shown in Figure 1, this work is a collaborative effort involving the integration of an adsorption compressor developed at NASA Ames Research Center, a solid oxide electrolysis cell developed at the University of Arizona, and our separator. Solid oxide electrolyzers, such as electrolysis cells utilizing yttria-stabilized zirconia, can produce oxygen from planetary atmospheric carbon dioxide and reject carbon monoxide and unreacted carbon dioxide in a separate stream. The oxygen-production process is far more efficient if the high-pressure, unreacted carbon dioxide can be separated and recycled back into the feed stream. Additionally, the mass of the adsorption compressor can be reduced. Also, the carbon monoxide by-product is a valuable fuel for space exploration and habitation, with applications from fuel cells to production of hydrocarbons and plastics.

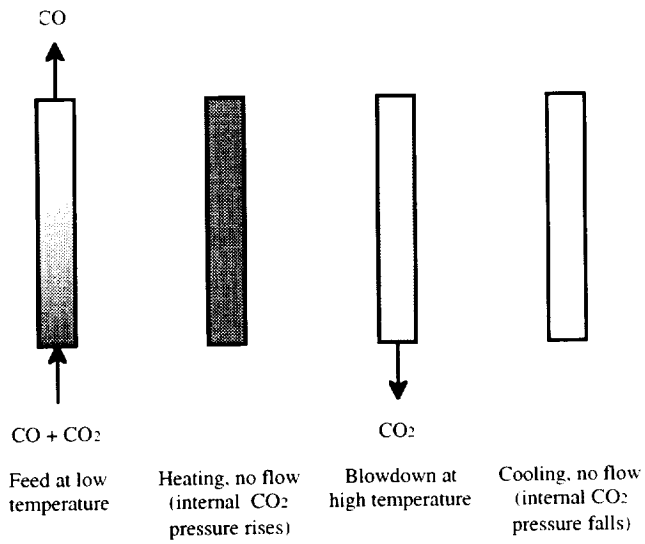

Figure 2: Four-step adsorption cycle for separation of CO and CO_2. CO is produced at the feed pressure (e.g., 1 bar); CO_2 product is expanded to a pressure determined by the zirconia cell's requirements.

Our separations cycle is shown in Figure 2. It combines concepts of temperature swing adsorption, pressure swing adsorption, and adsorption compression. The cycle will separate unreacted CO_2 such that it can be recycled back to re-feed the zirconia cell, permit essentially complete conversion of CO_2 to O_2 and CO in the integrated system, permit essentially complete recovery of CO, and be able to generate CO product at various purities.

With reference to the process steps shown in Figure 2, we seek an adsorbent high in CO_2 capacity and low in CO capacity, but which will release the CO_2 at elevated temperatures as pressure is reduced. We have measured pure component adsorption equilibrium for CO_2 and CO on many adsorbents using a gravimetric system. We have measured binary adsorption equilibrium for CO/CO_2 on the most promising adsorbents over wide temperature ranges using a volumetric system. We have developed process models for the cycle and are constructing the proof-of-concept CO/CO_2 separator. These will all be discussed.

NASA/CP—2002-211212/VOL1

Separation of Carbon Monoxide and Carbon Dioxide for Mars ISRU

M. Douglas LeVan and Krista S. Walton
Vanderbilt University, Nashville, Tennessee

John E. Finn
NASA Ames Research Center, Moffett Field, California

K. R. Sridhar
The University of Arizona, Tucson, Arizona

Relevance of ISRU to HEDS Missions

The NASA Strategic Plan:

- *Prepare to conduct human missions of exploration to planetary and other bodies in the solar system. The Enterprise relies on the robotic missions of the Space Science Enterprise to ...**demonstrate the feasibility of utilizing local resources to "live off the land."** Imagine commerce flourishing in space, with solar power satellites, or a Martian power plant to permit a permanent colony. These images are part of the Human Exploration and Development of Space (HEDS) Enterprise.*

- Chemical Processes are crucial for In-Situ Resource Utilization. They are ***enabling technologies***.

Goals

- Oxygen production from Martian atmosphere for propulsion
- Oxygen production from CO_2 for other applications
- CO as chemical reactant / fuel / propellant

- Development of low energy separation methods
- Contribute to gas storage methods

Water on Mars

NASA's Mars Odyssey - Gamma Ray Spectrometer

- South pole region - water ice in top meter of soil
- Low/mid latitudes - hydrogen bound to minerals

Conversion of Mars Atmosphere to N_2-Ar Mixture and High-Pressure CO_2, O_2, and CO

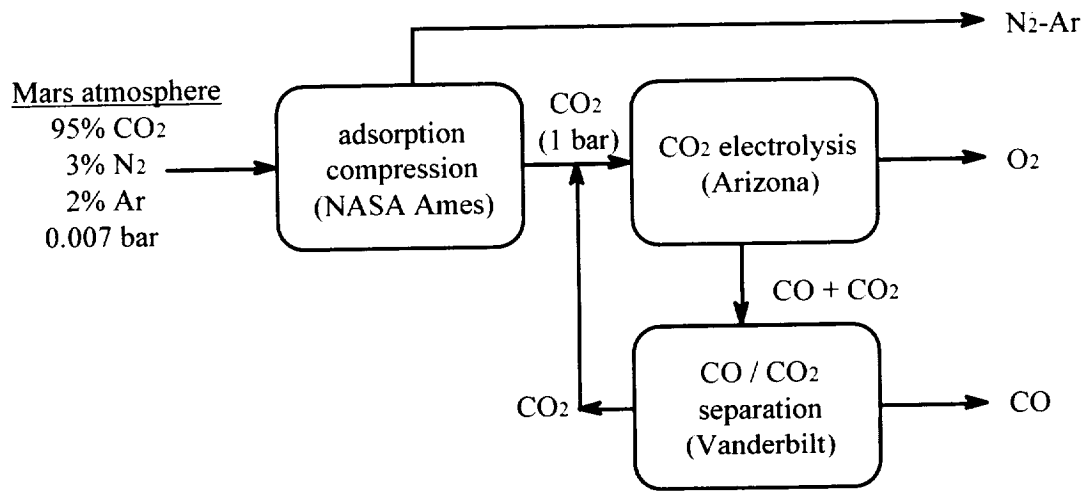

Adsorption Compressors

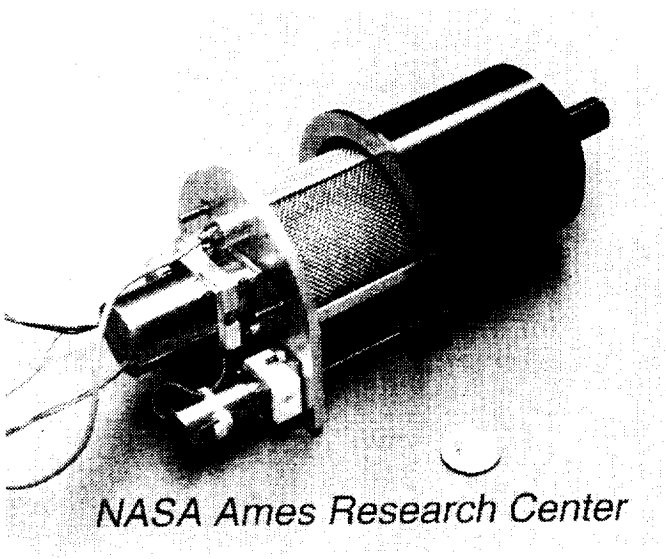

Solid Oxide Electrolysis Cell: Yttria-Stabilized Zirconia (YSZ)

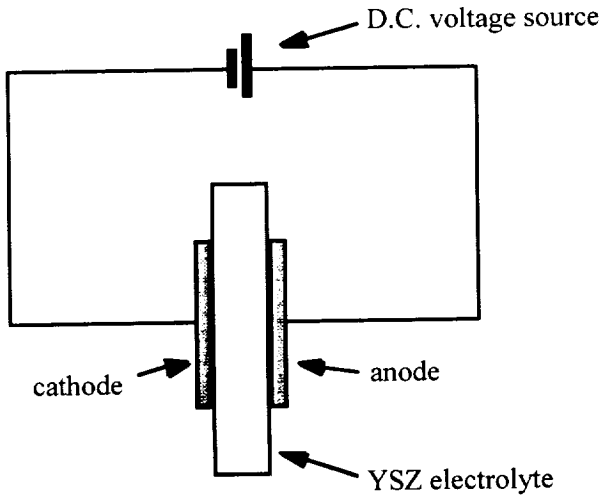

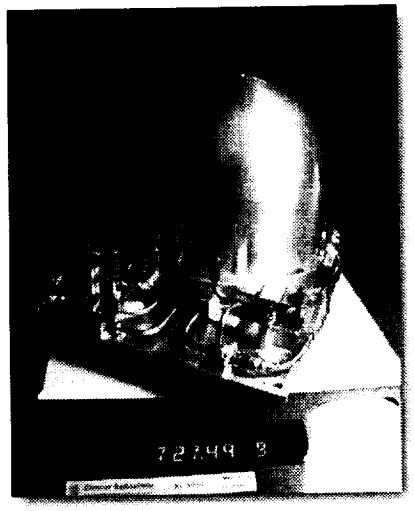

Four-Step Adsorption Cycle for CO/CO_2 Separation

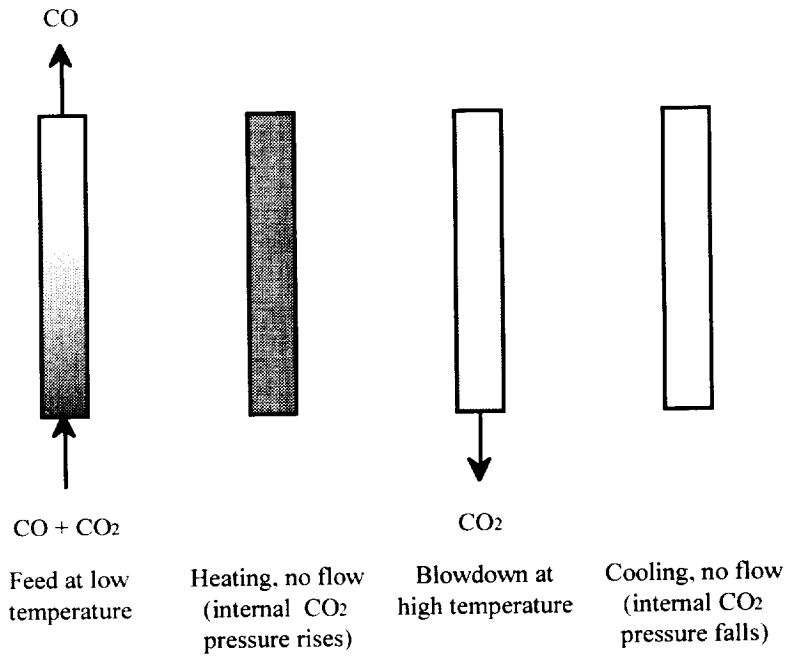

Adsorption Equilibria

- Gravimetric apparatus
  - CO_2 at 25 C
    - Seven adsorbents: NaY, 13X (NaX), 5A, 4A (NaA), 3A, Silicalite, BPL Carbon
  - CO at 25 C
    - Three Adsorbents: NaY, 13X (NaX), 5A
- Volumetric apparatus
  - CO_2 and CO at 25, 75, and 125 C
  - CO/CO_2 at 25 C
- Descriptions using Toth equation and Ideal Adsorbed Solution Theory

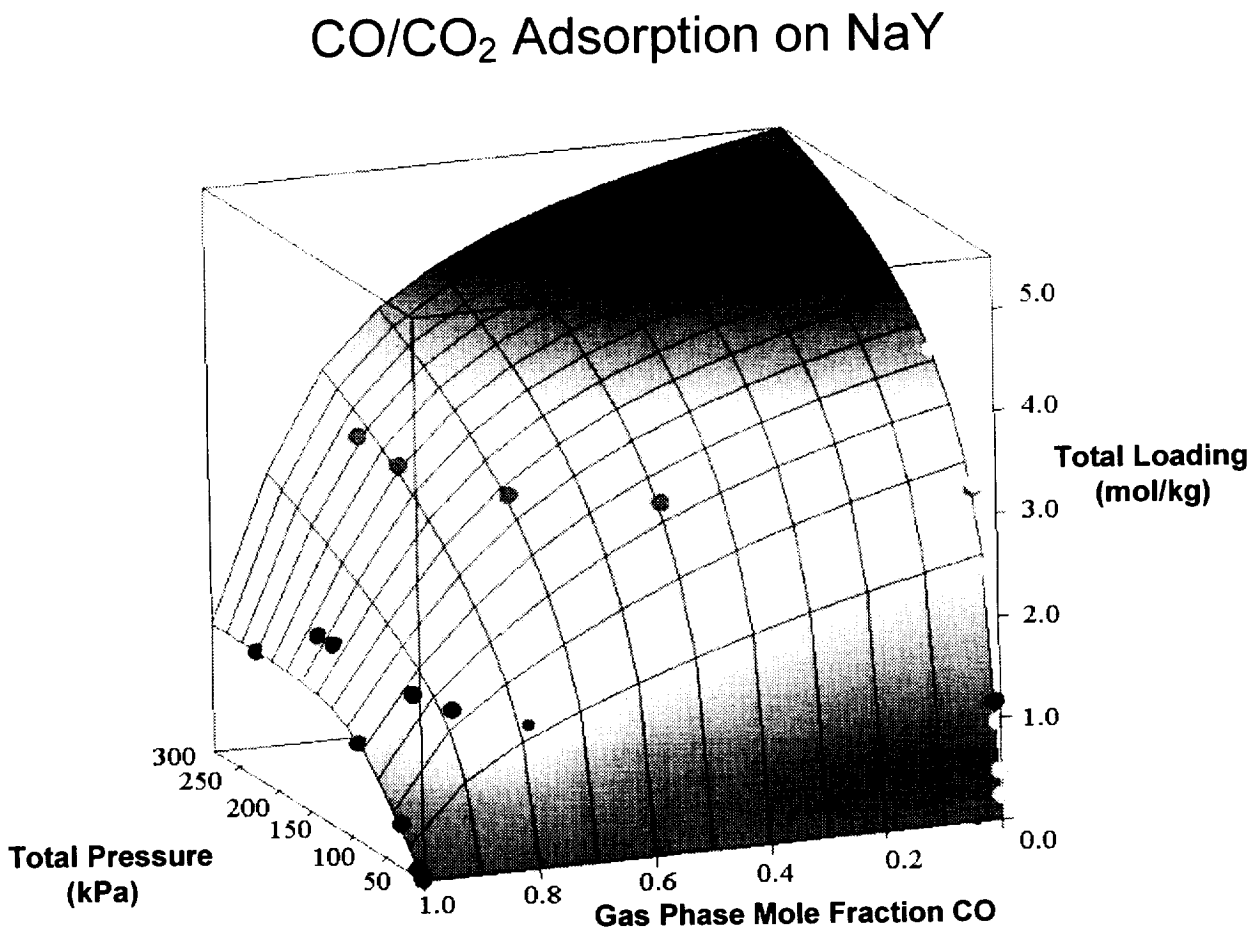
CO/CO2 Adsorption on NaY
Total Loading (mol/kg)
5.0
4.0
3.0
2.0
1.0
0.0
Total Pressure (kPa)
300
250
200
150
100
50
Gas Phase Mole Fraction CO
1.0
0.8
0.6
0.4
0.2

Cycle Steps and Path: CO_2 on NaY

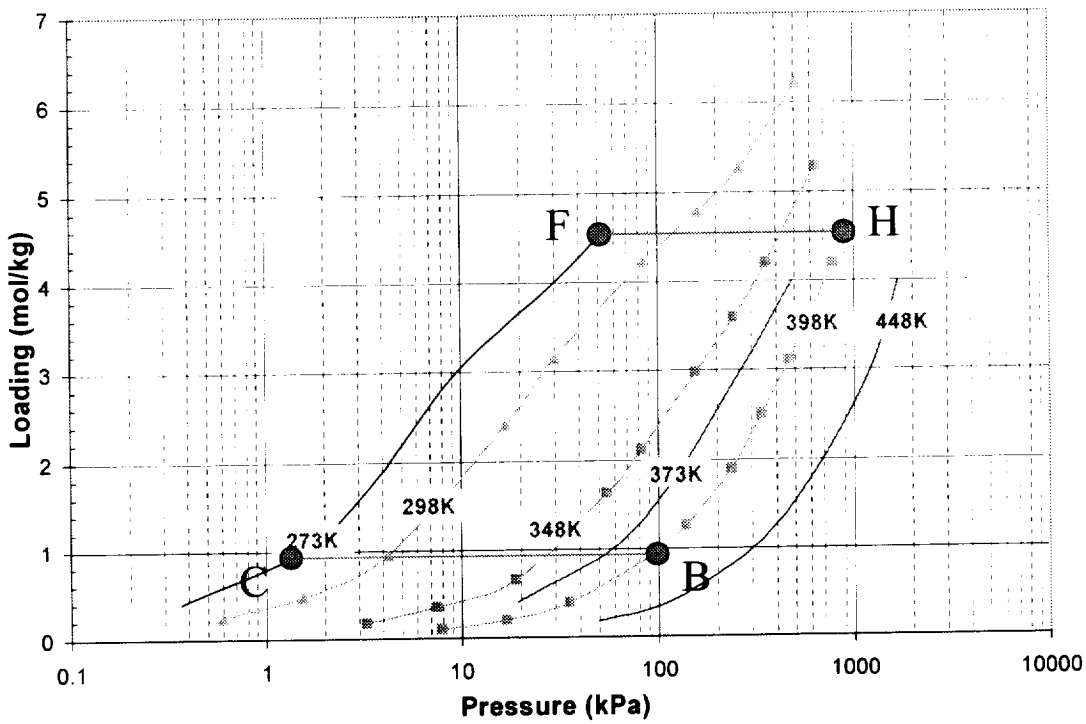

Calculations

- Cycle between 273 K and 398 K, 50% conversion per pass
- Equilibrium Loadings and Pressures for NaY:
  - End of Feed (273 K, 0.5 bar): 19.8 wt % CO_2
  - End of Blowdown (398 K, 1 bar): 4.3 wt % CO_2
  - End of Cooling (273 K, 4.3 wt % CO_2): 1.4 kPa
  - Feed Step Product: 98.6 mol % CO
- Similar end points for NaX (13X) are 18 wt % and 9 wt %
- "Practical Swing" between 6 and 18 wt % (i.e., 12 wt %) would be twice as efficient as swing of 6 wt % for NaX

Separator for CO/CO_2 Studies

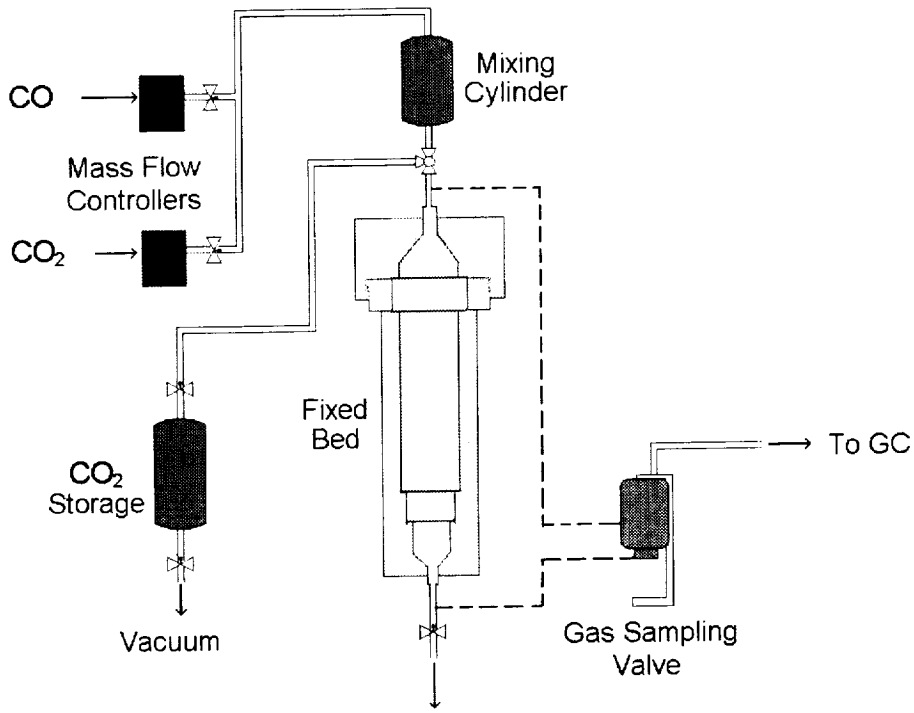

Conclusions

Two apparatuses have been constructed for adsorption equilibrium measurements. A third is under construction for studying the PSA/TSA separation cycle.

NaY zeolite is the best adsorbent for use for the CO/CO_2 separation. NaY has a high capacity for CO_2 at high partial pressures and low capacity at low partial pressures with very little adsorption of CO.

The Toth equation describes pure-component adsorption equilibrium well for both pure components.

The Ideal Adsorbed Solution Theory describes mixed gas adsorption equilibrium well for the CO/CO_2/NaY system.

NaY cuts adsorbent weight in half, compared to NaX (13X).

Our mathematical model has been developed. With a predictive model for binary adsorption equilibrium, computer simulations are now being performed to model the proposed PSA/TSA cycle.

Session 5:
Biological Fluid Physics
(Biological Fluid Mechanics and Biological Self Assembly)

ASSEMBLY OF COLLOIDAL MATERIALS USING BIOADHESIVE INTERACTIONS

Daniel A. Hammer, Amy L. Hiddessen, Valeria Tohver, and John C. Crocker
Departments of Bioengineering and Chemical Engineering, University of Pennsylvania, Philadelphia, PA 19104

David A. Weitz
Department of Physics and DEAS, Harvard University, Cambridge, MA 02139

ABSTRACT

We have pursued the use of biological crosslinking molecules of several types to make colloidal materials at relatively low volume fraction of colloidal particles. The objective is to make binary alloys of colloidal particles, made of two different colloidal particles coated with complementary biological lock-and-key binding molecules, which assemble due to the biological specificity. The long-term goal is to use low affinity lock-and-key biological interactions, so that the colloidal systems can anneal to form crystalline states.

We have used a variety of different surface chemistries in order to make colloidal materials. Our first system involved using selectin-carbohydrate (sialyl-Lewis^x) interactions; this chemistry is derived from immune system. This chemical interaction is of relatively low affinity, with time-scales for dissociation of several seconds. Furthermore, the adhesion mediated by these molecules can be reversed by the chelation of calcium atoms; thus assembled structures can be disassembled reversibly. Our second system employed avidin-biotin chemistry. This well-studied system is of high affinity, and is generally irreversible on a laboratory time-scale. Thus, we would expect selectin-carbohydrate interactions at high molecular density and avidin-biotin interactions to give kinetically-trapped structures; however, at low densities, we would expect significant differences in the structure and dynamics of the two materials, owing to their very different release rates.

We have also begun to use a third chemistry – DNA hybridization. By attaching single stranded DNA oligonucleotide chains to beads, we can drive the assembly of colloidal materials by hybridization of complementary DNA chains. It is well known that DNA adenosine-thymine (A-T) and guanine-cytosine (G-C) bases hybridize pairwise with a Gibbs free energy change of –1.7 kcal/mol per base; thus, the energy of the assembly can be modulated by altering the number of complementary bases in the DNA chains.

Using these different crosslinking molecules, we have assembled colloidal materials from different-sized colloidal particles, A and B. In the first sets of experiment, we used high densities of adhesion molecules, and 0.96 micron (A) and 5.5 micron (B) diameter particles. The high density of adhesion molecules means that the structures are kinetically trapped in non-equilibrium configurations. The structure of the suspension can be varied by changing the number ratio of the two types of colloidal particles, N_A and N_B, where A is the smaller particle. With carbohydrate-selectin or avidin-biotin interactions, large N_A/N_B leads to the formation of colloidal micelles, with the large center B particle surrounded by many smaller A particles (see Figure 1). As the ratio N_A/N_B decreases, the structures become more extended, approaching the formation of macro-Rouse polymers – extended linear chains where A beads are connected with intervening small B linkers.

When the structures are made with selectin-carbohydrate interactions, the chelation of calcium using EDTA can cause the structures to disassemble entirely. Also, the addition of EDTA prior to the mixing of the suspension can prevent the structures from forming.

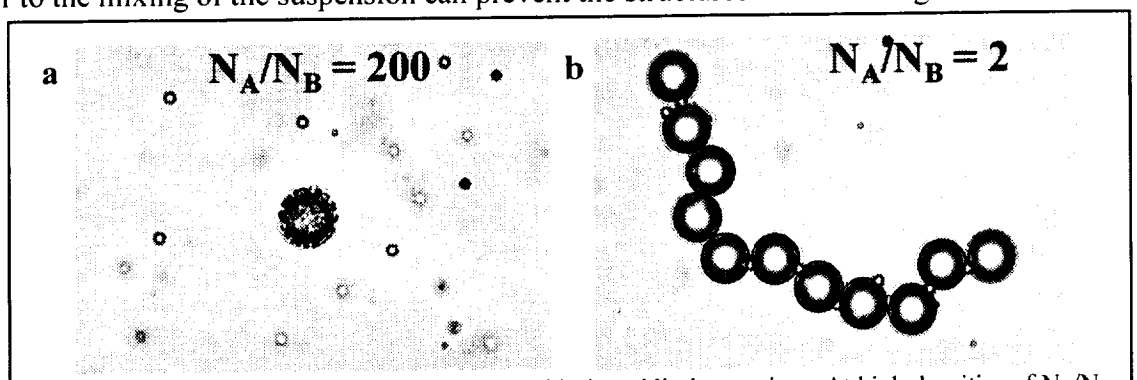

Figure 1. Assembly of colloidal structures using biotin-avidin interactions. At high densities of N_A/N_B (A), a large B particle is surrounded by many A particles. At low densities of N_A/N_B (B), extended chains are formed.

When the density of selectin-carbohydrate molecules is decreased, the binding of small A beads to the central B particle becomes transient. The time-scale for release of A particles from the surface of the central B particle is an increasing function of the molecular density. The density of molecules on the A particles can be changed by the concentration of molecular incubation, and verified with flow cytometry. The time scale of release of many particles can be tracked, and compared to a simple probabilistic binding model for molecular dissociation. The decay of bound (docked) particles can be fit to determine the intrinsic binding dissociation constants. The uni-molecular dissociation constant for sialyl-Lewis^x/E-selectin interactions determined this way is approximately 1 sec^{-1}, which corresponds to the off rate measured separately for this interaction by other laboratories.

We have also been measuring the rheology and assembly of resultant colloidal suspension using micro-rheometry. This has involved bulk rheological measurements, as well as the dynamics of colloidal assembly using confocal microscopy (where the smaller bead species, A, is fluorescent, and its position is tracked with time). At 10 % total volume fraction, and a bead ratio $N_A/N_B = 10$, colloidal materials assembled using avidin-biotin interactions exhibit a characteristic shear thinning behavior over a wide range of shear stresses. A long-term goal is to compare the time-constants for shear thinning behavior as a function of the density and strength of the biological molecules.

Finally, we have made significant progress in assembling small aggregates of colloidal particles that are crosslinked by DNA hybridization. Avidin-coated particles were coated with 30 base pair DNA sequences (a and b) that had 20 bp overlapping sequences. The sequences were made with biotin at the 5' end and the fluorescent dye Cy5 at the 3' end. The presence of the oligonucleotide strands on the beads was verified by fluorescence flow cytometry. Since the hydbridization of DNA depends on temperature and the length of overlap of the DNA bases, we will explore the effect of temperature and chain length on the ability for assemble stable colloidal structures using DNA hybridization with different lengths of chain overlap.

Acknowledgement: Authors wish to acknowledge support from the NASA Fluid Physics program. Requests for information and reprints should be addressed to Daniel A. Hammer, Department of Bioengineering, University of Pennsylvania, Philadelphia, PA 19104, hammer@seas.upenn.edu.

Assembly of Colloidal Materials Using Bioadhesive Interaction

Daniel A. Hammer
Departments of Bioengineering, Chemical Engineering,
and Institute of Medicine and Engineering
University of Pennsylvania

NASA Fluid Physics Meeting
August 16, 2002

Colloidal Assemblies → Colloidal Crystals

(a) Nonspecific Forces

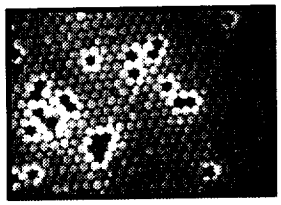

Guo, J. Ph.D. thesis, University of Illinois. **1997**

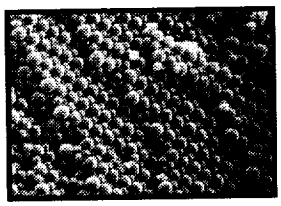

Barlett PRL **1992** *68* 25 3801

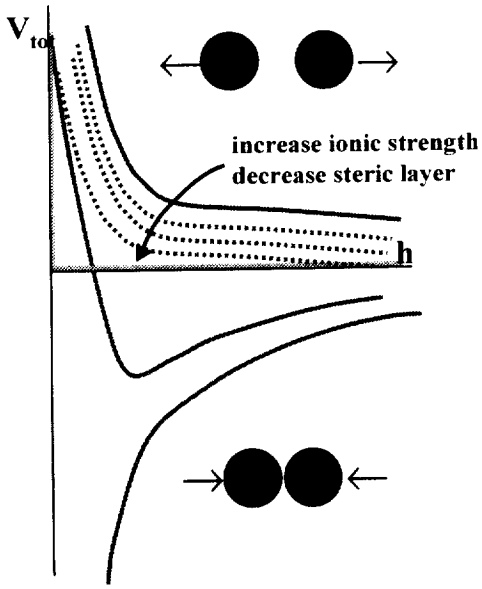

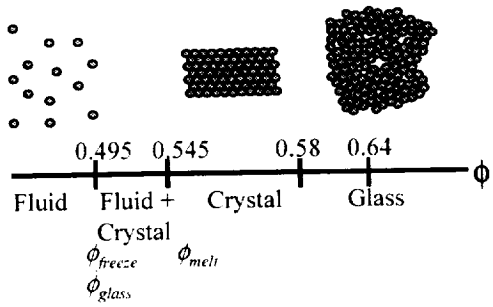

Narrow size distribution **Net repulsive interaction** **Entropically driven process**

(b) Specific Forces

Biotin-Avidin

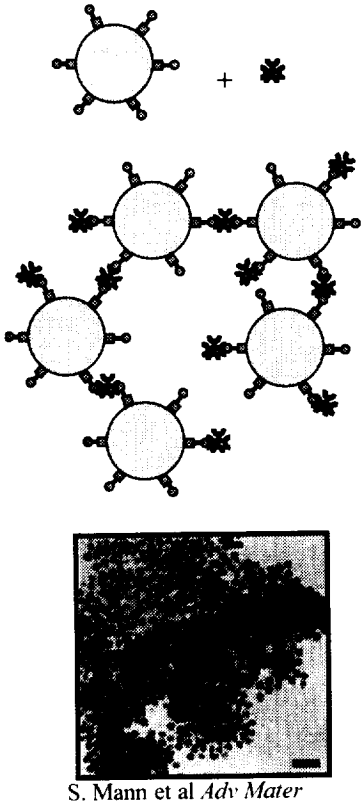

S. Mann et al *Adv Mater*
2000 *12* 2 147-150

Protein - carbohydrate

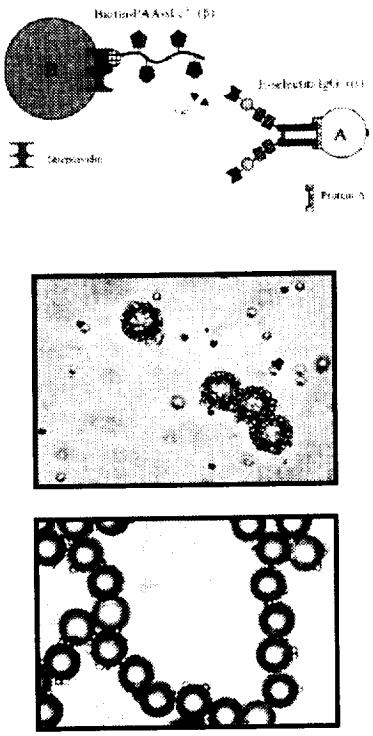

A. Hiddessen et al Langmuir
2000 *16* 25 9744-9753

DNA

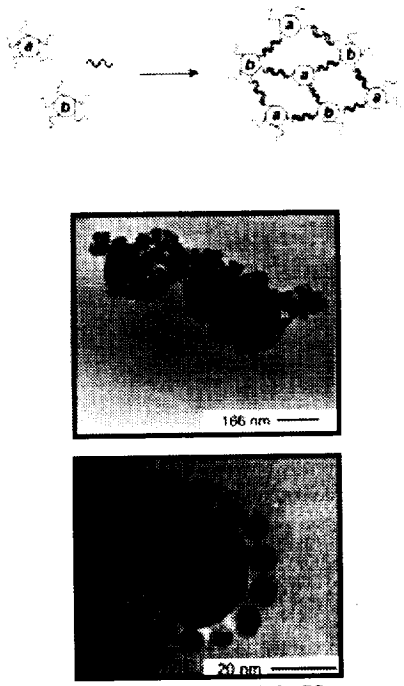

C. Mirkin et al *JACS*
1998 *120* 48 12574-12675

Objective

- To make colloidal crystals using weak biological self-assembly

E. Winfree

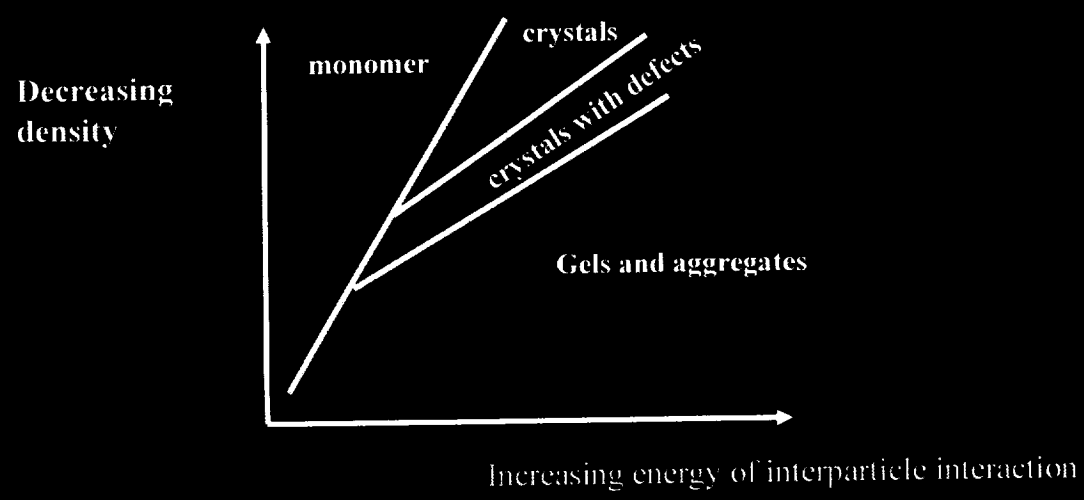

- Kinetic (self) annealing or temperature-driven annealing

Binary Alloys

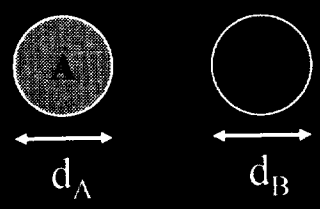

- Materials and may be varied (*organic/inorganic, magnetic, etc.*)

Parameters: Volume Fraction ϕ_A + = ϕ_T

Composition (or Number Ratio) $f = N_A/$

Diameter Ratio $\alpha = d_A/$

Energies , ε_A

$\varepsilon_{AA} = 0, \varepsilon_{BB} = 0, \varepsilon_{AB} < 0$

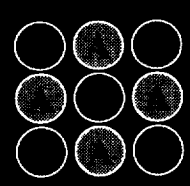

$f = 1, \alpha = 1$

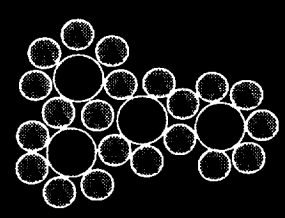

$f > 1, \alpha < 1$

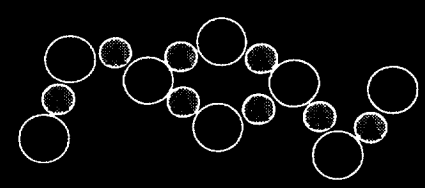

$f = 1, \alpha < 1$

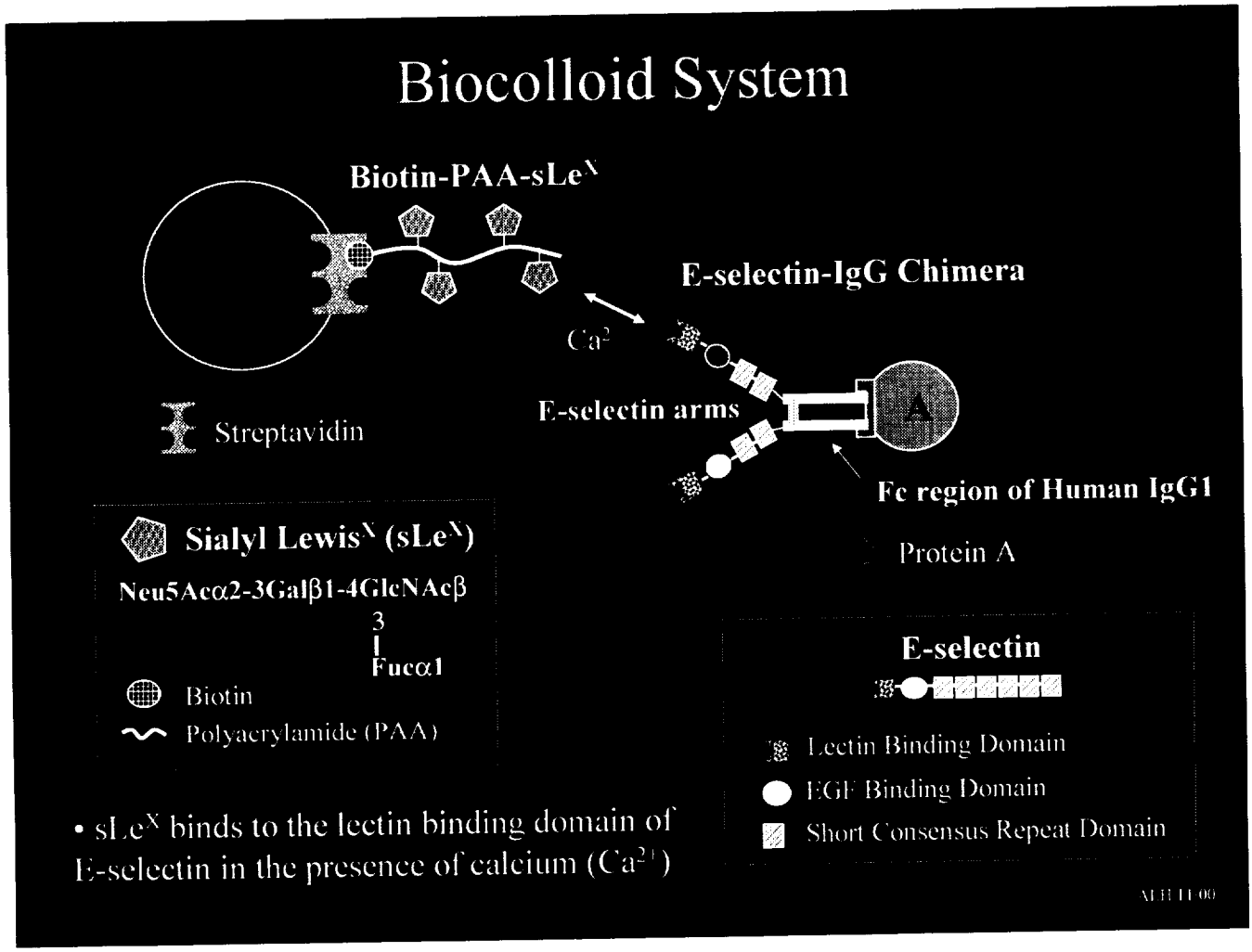
Biocolloid System
Biotin-PAA-sLe^X
E-selectin-IgG Chimera
Ca^{2}
E-selectin arms
Streptavidin
A
Fc region of Human IgG1
Protein A
Sialyl Lewis^X (sLe^X)
Neu5Acα2-3Galβ1-4GlcNAcβ
3
Fucα1
Biotin
Polyacrylamide (PAA)
E-selectin
Lectin Binding Domain
EGF Binding Domain
Short Consensus Repeat Domain
• sLe^X binds to the lectin binding domain of E-selectin in the presence of calcium (Ca^{2+})

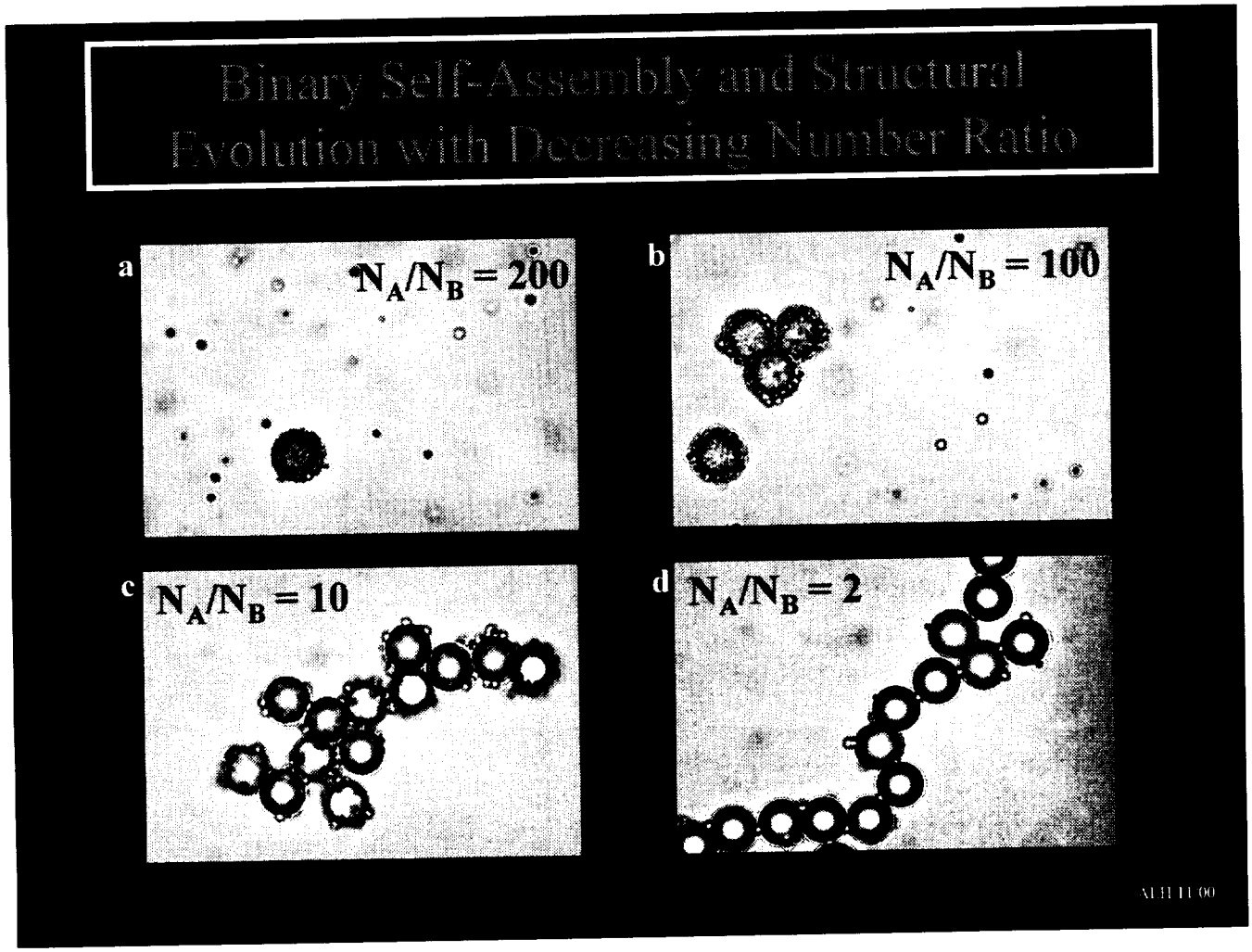
Binary Self-Assembly and Structural Evolution with Decreasing Number Ratio
a
$N_A/N_B = 200$
b
$N_A/N_B = 100$
c
$N_A/N_B = 10$
d
$N_A/N_B = 2$
AEH 11 00

Exploiting Calcium-dependent E-selectin/sLe^X Interactions to Manipulate Colloidal Assembly

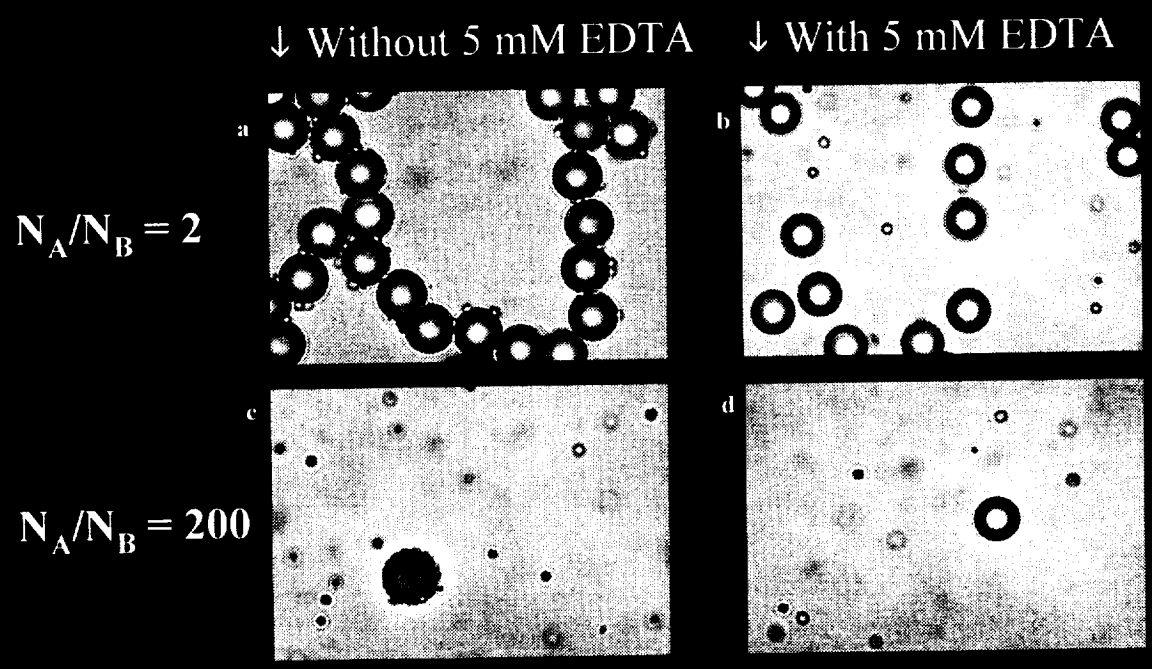

Self-assembly can be prevented by addition of EDTA (calcium chelator)

EDTA abolishes the interaction between E-selectin and sLe^X

Exploiting Calcium-dependent E-selectin/sLe^X Interactions to Manipulate Colloidal Assembly

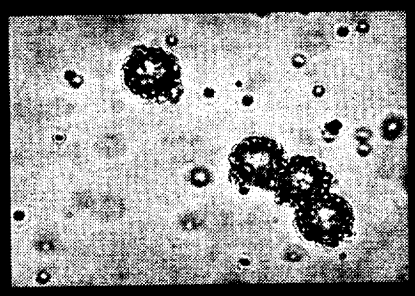

Self-assembly

E-selectin/sLe^X crosslinking

Addition of 5 mM EDTA

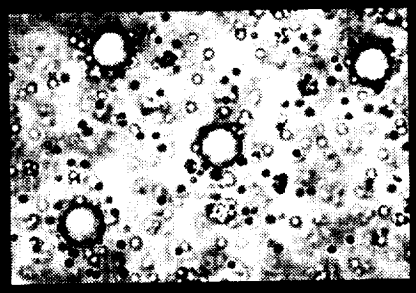

Disassembly

E-selectin/sLe^X crosslinking disrupted by chelation of calcium ions

Adding EDTA to aggregated suspensions can induce disassembly of binary colloidal structures crosslinked by E-selectin/sLe^X

ALH 11/00

Reversible Colloidal Interaction Using E-selectin/sLe^X

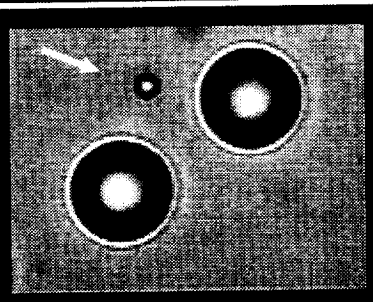

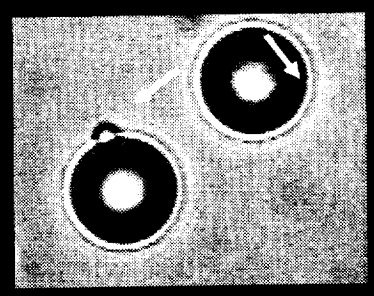

E-selectin/sLe^X bond(s) form

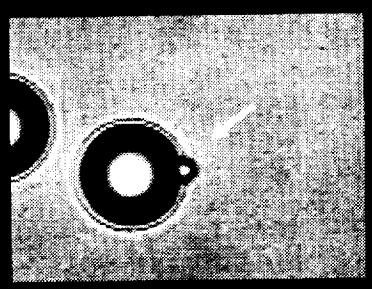

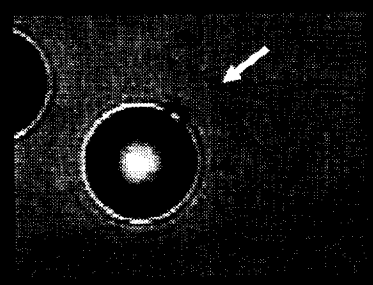

E-selectin/sLe^X bond(s) break

E-selectin/sLe^X crosslinking is reversible at lower molecular surface densities

ALH 11/00

Fraction of Particle Pairs Adherent vs. Time

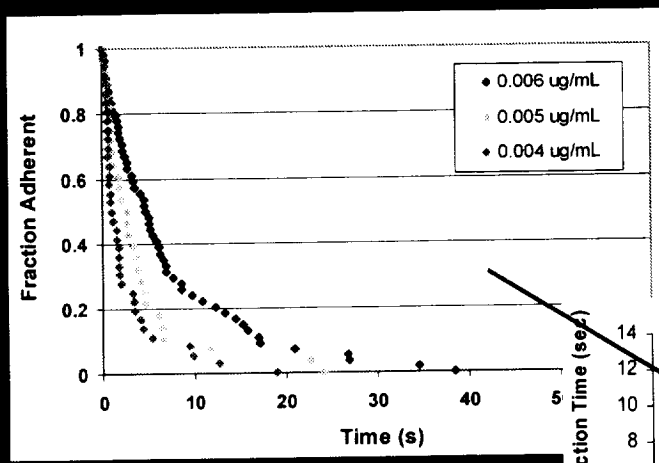

Tunable release times

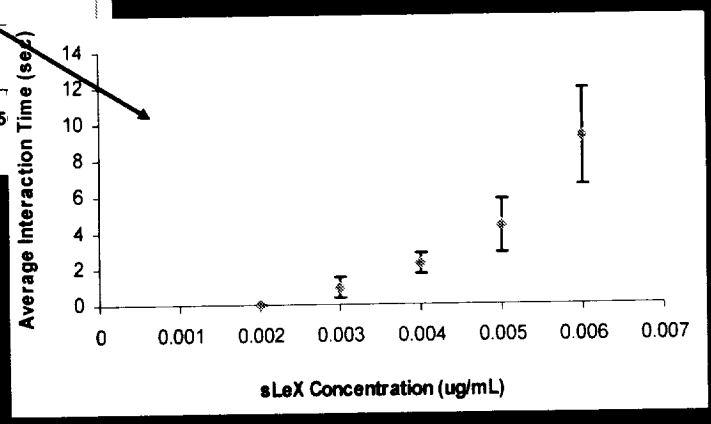

Suspect we need "Goldilocks" molecules for crystallization

DNA-mediated assembly

- Variable attraction (length, sequence choice, solution conditions)
- Helical formation reversible (temperature anneal, ionic strength)

DNA attached to beads via biotin-avidin chemistry

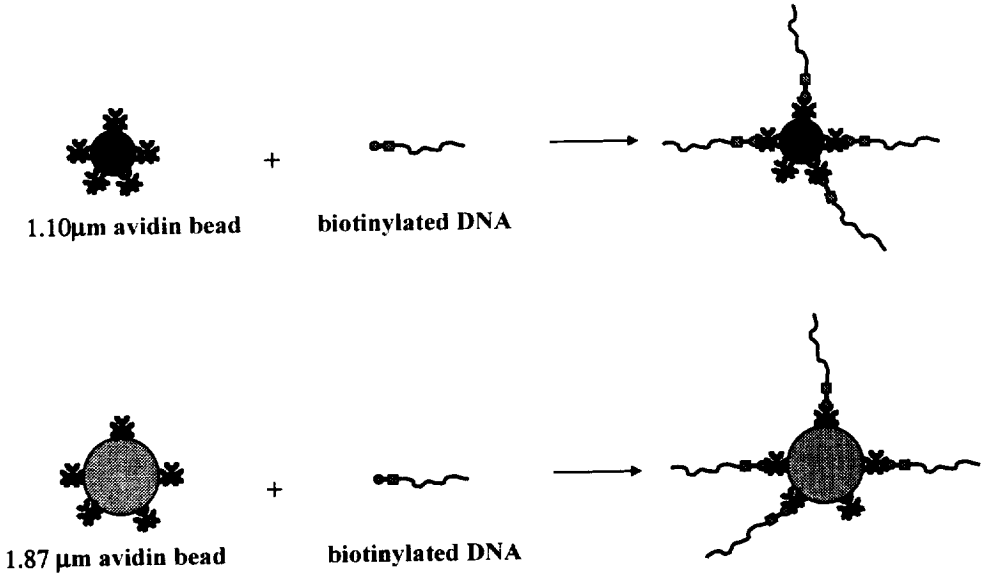

Schematics of DNA designs to link particles

(a)

Overlapping strands

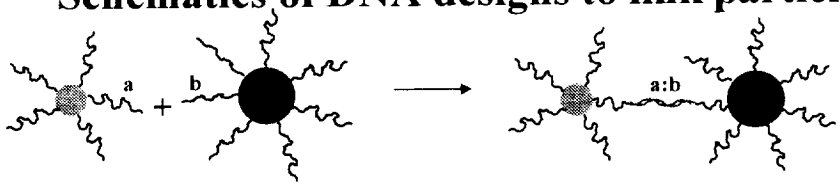

TTTCATTCAGTCCAGTCAGTTCATTTCCATCATATCA -biotin = b

a = biotin--AGTAAAGTTCAGGTATCAAGGTCAAAGTAAGTCAGGT

T_m =41°C

(b)

Third bridging strand

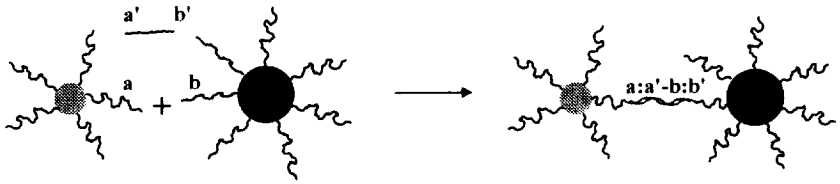

a'b' = TTTCATT—CAGTCCA

a = biotin-AGTAAAGTTCAGGTATCAAGGTCAAAGTAA GTCAGGTCAGTCAAGTAAAGGTAGTATAGT-biotin = b

T_m = 41°C

(c)

Bridging plus stabilizing strand

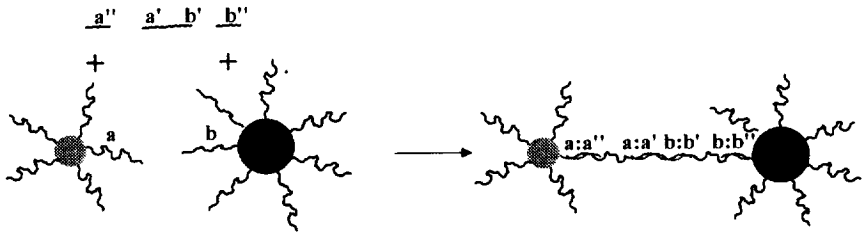

a'' = TCATTTCAAGTCCATAGTT a'b' =TTTCATT—CAGTCCA GTTCATTTCCATCATATCA = b''

a = biotin-AGTAAAGTTCAGGTATCAAGGTCAAAGTAA GTCAGGTCAGTCAAGTAAAGGTAGTATAGT-biotin = b

T_m = 49°C T_m = 41°C T_m = 51°C

Cytometry indicates successful conjugation and hybridization

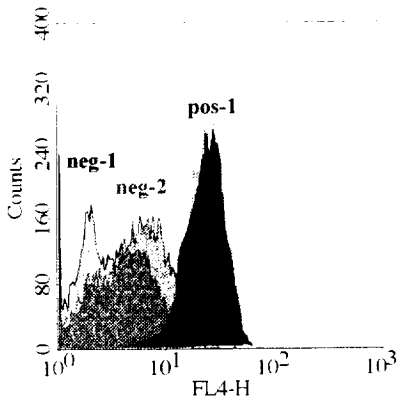

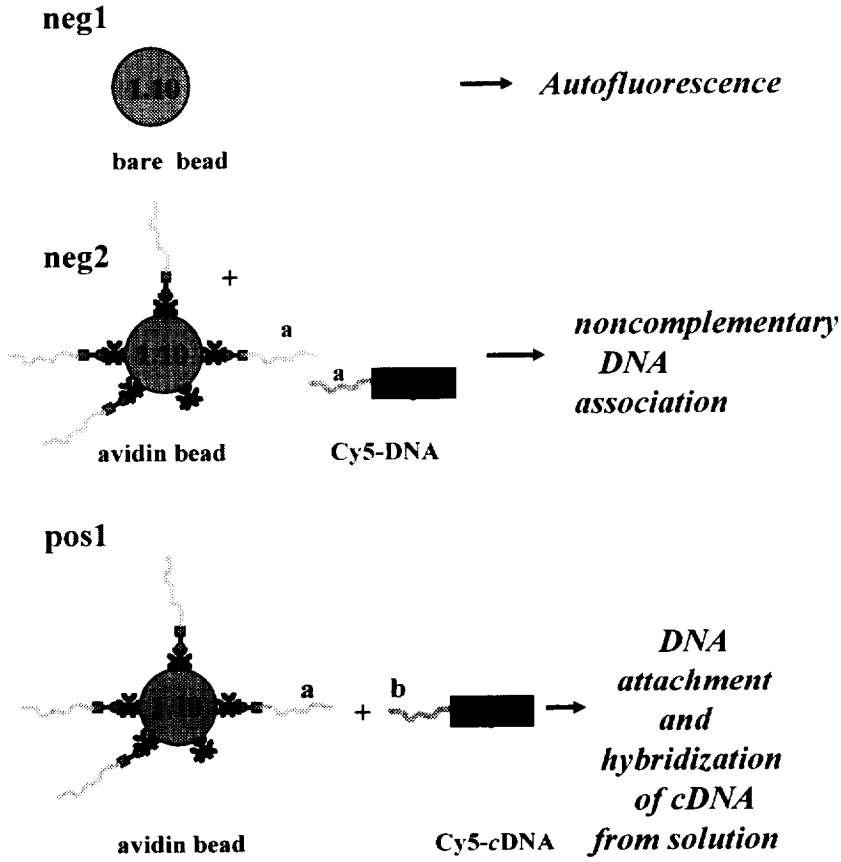

Optical Microscopy of Binary Mixtures

$N_A/N_B = 440$

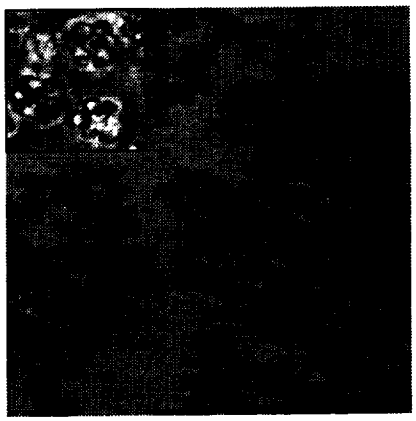

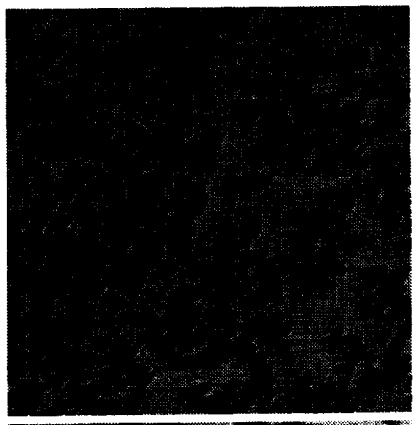

$N_A/N_B = 150$

$N_A/N_B = 50$

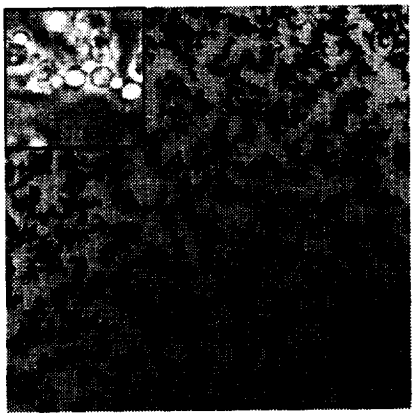

$N_A/N_B = 20$

Confocal Microscopy of Binary Mixtures

Smaller bead is fluorescent

$N_A/N_B = 440$

Colloidal micelles

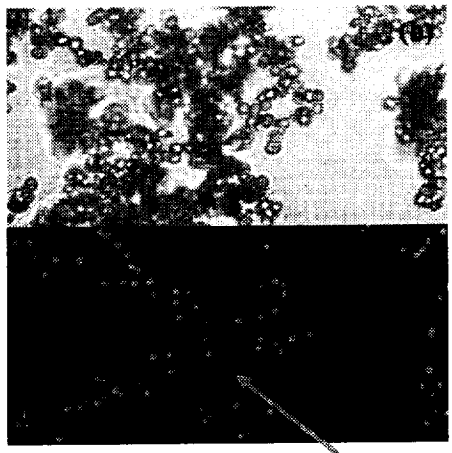

$N_A/N_B = 50$

Extended chains

Multiple chain binding – melting at temperatures ~ 40 C higher than the single chain melting T

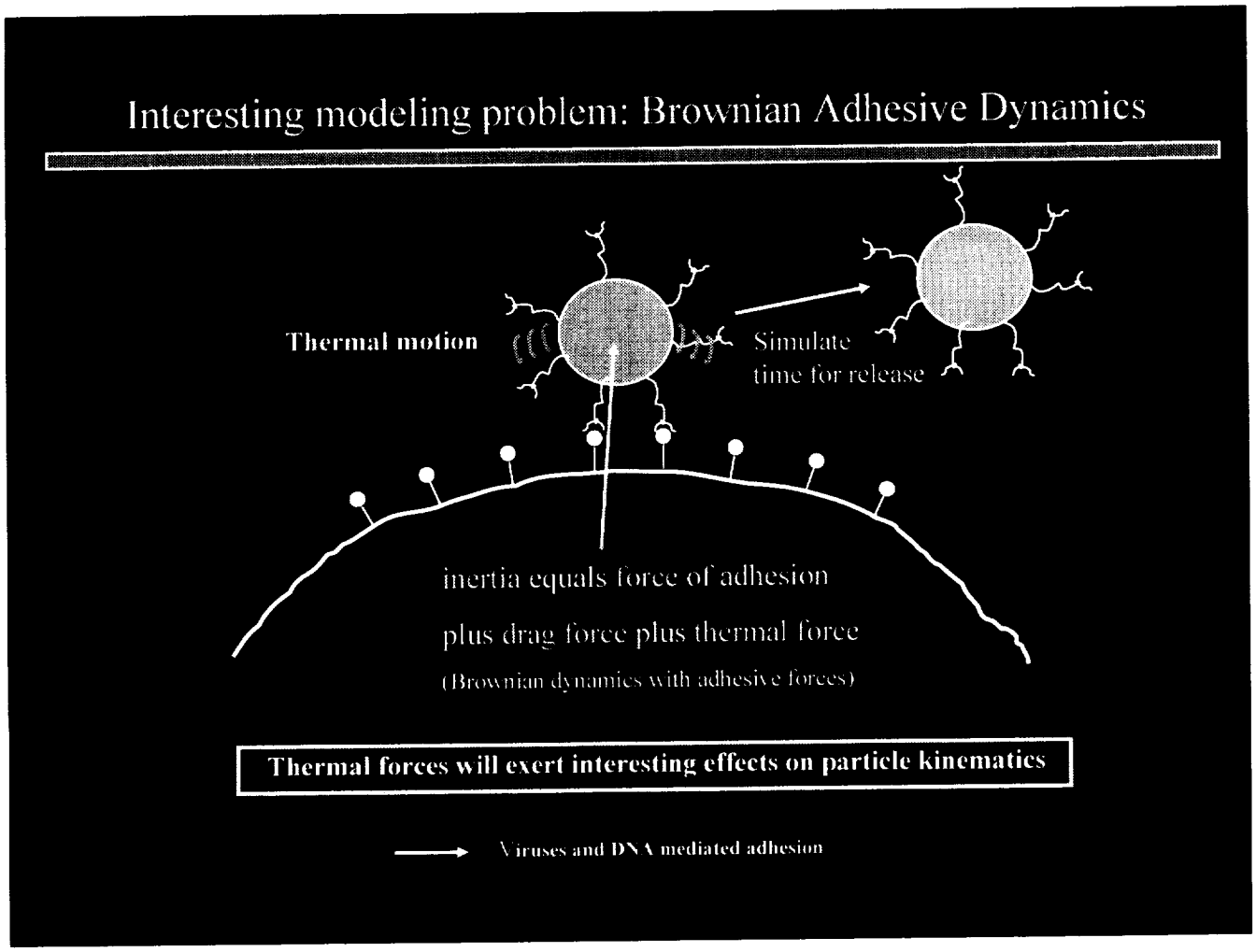
Interesting modeling problem: Brownian Adhesive Dynamics
Thermal motion
Simulate
time for release
inertia equals force of adhesion
plus drag force plus thermal force
(Brownian dynamics with adhesive forces)
Thermal forces will exert interesting effects on particle kinematics
Viruses and DNA mediated adhesion

Position (implicit with time)

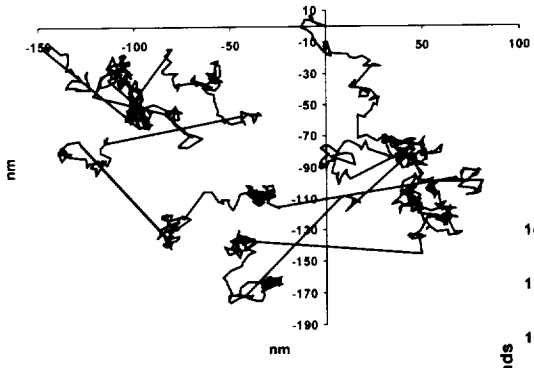

Bonding vs. time

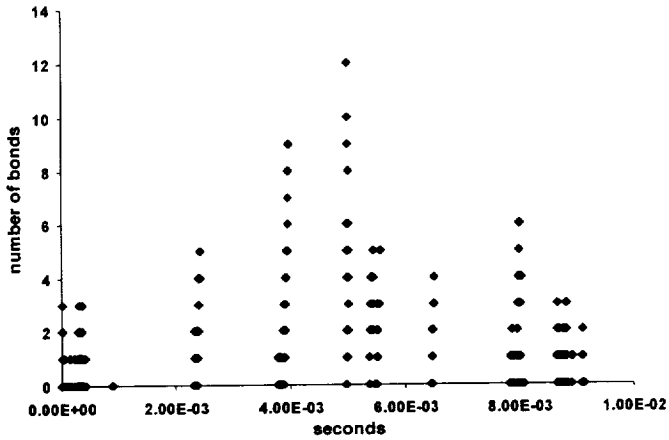

Summary & Acknowledgements

- **Novel colloidal materials made by biological crosslinking**
  - Wide range of kinetically trapped structures (different densities)
  - DNA shows great promise for tunable adhesion strength and annealing
- **Adhesive dynamics for simulation of docking of Brownian particles**
- **Attempt to make crystals**
  - Shorter strands, temperature annealing

Thanks to: *Amy Hiddessen*, *Valeria Tohver*, *Dave Weitz (Harvard)*, *John Crocker (Penn)*

Funding: *NASA Fluid Physics*, *Penn MRSEC*

MICROGRAVITY EFFECTS ON TRANSVASCULAR TRANSPORT AND VASCULAR CONTROL

M. Kim, M. Civelek, K. Ainslie, J. Garanich, N.R. Harris, J.M. Tarbell
Departments of Bioengineering and Chemical Engineering, The Pennsylvania State Univerity, University Park, PA, USA

ABSTRACT

Introduction: Microgravity alters transvascular pressure differential and transmural flow across blood vessel walls. We have hypothesized that changes in transmural flow alter fluid shear stress on vascular smooth muscle cells (SMC) and this in turn affects the state of contraction or "tone" of SMC. Since the cardiovascular system relies on SMC contraction in arterioles in response to changes in pressure ("myogenic response") to regulate blood flow to tissue beds which in turn affects transvascular exchange, we have investigated the effects of fluid flow shear stress on SMC contraction using both in vitro and in vivo models.

In Vitro Studies: Primary rat aortic SMC were expanded in cell culture flasks containing DMEM + 10% FBS. Then the cells were "starved" (maintained in DMEM, no FBS) in culture flasks for two to three days and then on quartz slides at sub-confluent density for two more days prior to experiments that were also run serum-free. SMC starving was necessary to induce the contractile phenotype. To study cell contraction in response to shear stress, sub-confluent cells on quartz slides were exposed to defined levels of steady shear stress in a parallel plate flow chamber for 30 minutes while being photographed under a microscope with a video camera. Reduction in cell area was interpreted as cell contraction and quantified in terms of percent area reduction. Intra-cellular calcium (Ca^{2+}) was imaged under flow in the parallel plate chamber using the calcium sensitive dye fura-2.

Cells in the contractile phenotype that were exposed to 25 dyne/cm^2 shear stress decreased their area significantly within 3 minutes and by more than 30% after 30 minutes. The threshold for contraction was about 7 dyne/cm^2. To our surprise, this contraction response was not accompanied by a response of intracellular Ca^{2+}. Additional experiments in calcium free media and with an intracellular calcium chelator also displayed a significant contraction response to shear stress confirming that shear-induced contraction is not mediated by intracellular Ca^{2+}. Additional pharmacological experiments suggested that the shear-induced contraction is mediated primarily through a Rho-kinase intracellular signaling pathway. In contrast, cells in the proliferative phenotype (maintained in serum) did not contract in response to shear stress but did display a marked intracellular Ca^{2+} response to shear.

In Vivo Studies: Fourteen male Wistar rats were anesthetized and the right carotid artery was cannulated to monitor systemic blood pressure, and for systemic injection of a mixture of bovine serum albumin (BSA) and 70 kD Ficoll in nine of the experiments. The BSA-Ficoll mixture was

used to increase plasma osmotic pressure which reduces transmural flow (J_v) and shear stress on SMC. The small intestine was exteriorized surgically and the mesentery was draped over a glass coverslip which was mounted on the stage of an inverted microscope. The mesentery was observed through a x40 objective (Nikon Plan Apo, 0.95 N.A.) using a 100-W halogen light source, and brightfield images were captured with a color camera and recorded for image analysis of vessel diameter. Arterioles having a baseline diameter of 20-30 microns were occluded with a glass micropipette to initiate a myogenic response. This technique has been performed previously for the hamster cheek pouch [1], where arteriolar pressure upstream of the occluder increased by 22.5%. Following the baseline occlusion, a mixture of dialyzed BSA and Ficoll was injected to increase the osmotic pressure, then a second occlusion was performed. After release of the second occlusion, maximal dilation of the arteriole (D_{max}) was obtained by exposure to papaverine to estimate % tone of the baseline diameter. The value of J_v normalized to the surface area S (J_v/S) was monitored during each occlusion by measuring the decreasing distance between the micropipette and the upstream red blood cells as described previously [2].

Baseline arteriolar tone ($1-D/D_{max}$) and J_v/S were well correlated, with tone increasing from 2% at $J_v/S = 0.002$ micron/sec up to 8% at $J_v/S = 0.013$ micron/sec. Although this is consistent with our hypothesis that J_v may control myogenic tone, it is also possible that both factors are related by hydrostatic pressure, an increase of which would be expected to increase both myogenic tone and transmural flow. To further investigate our hypothesis, we compared the myogenic response prior to and following infusion of the BSA-Ficoll osmotic solution. The osmotic solution attenuated J_v by ~50% relative to autologous plasma and reduced the myogenic constriction of arteriolar diameter by ~60%. The occlusion-induced increase in hydrostatic pressure was likely similar for the two data sets (osmotic solution and autologous plasma solution), based on the observation that the arteriole diameter was stretched initially by the same amount for both data sets.

Discussion: The in vitro results show that an increase in fluid shear stress causes SMC to contract in a calcium-independent manner suggesting that increased fluid shear stress on SMC associated with increased transmural flow may drive the myogenic response in arterioles. The in vivo results, which show that a reduction in transmural flow induced by an osmotic solution reduces the myogenic response, are consistent with the in vitro results. These experiments support a new hypothesis for the mechanical basis of the myogenic response that invokes fluid shear stress. The new hypothesis has important implications for vascular control and fluid shift in microgravity since transmural flow is altered by microgravity.

References

1. Lombard, J.H., Duling, B.R. (1977). *Circ. Res.*, vol. 41(3), pp. 365-373.
2. Harris, N.R., Benoit, J.N., Granger, D.N. (1993). *Am. J. Physiol.*, vol. 265, pp. H1623-H1628.

Principal Investigator: John M. Tarbell, Bioengineering Department, The Pennsylvania State University, University Park, PA 16802. email: jmt@psu.edu; tel. 814-863-4801; fax 814-865-7846.

Microgravity Effects on Transvascular Transport and Vascular Control

M. Kim, M. Civelek, K. Ainslie, J. Garanich, N.R. Harris and J.M. Tarbell

Departments of Bioengineering and Chemical Engineering, The Pennsylvania State University

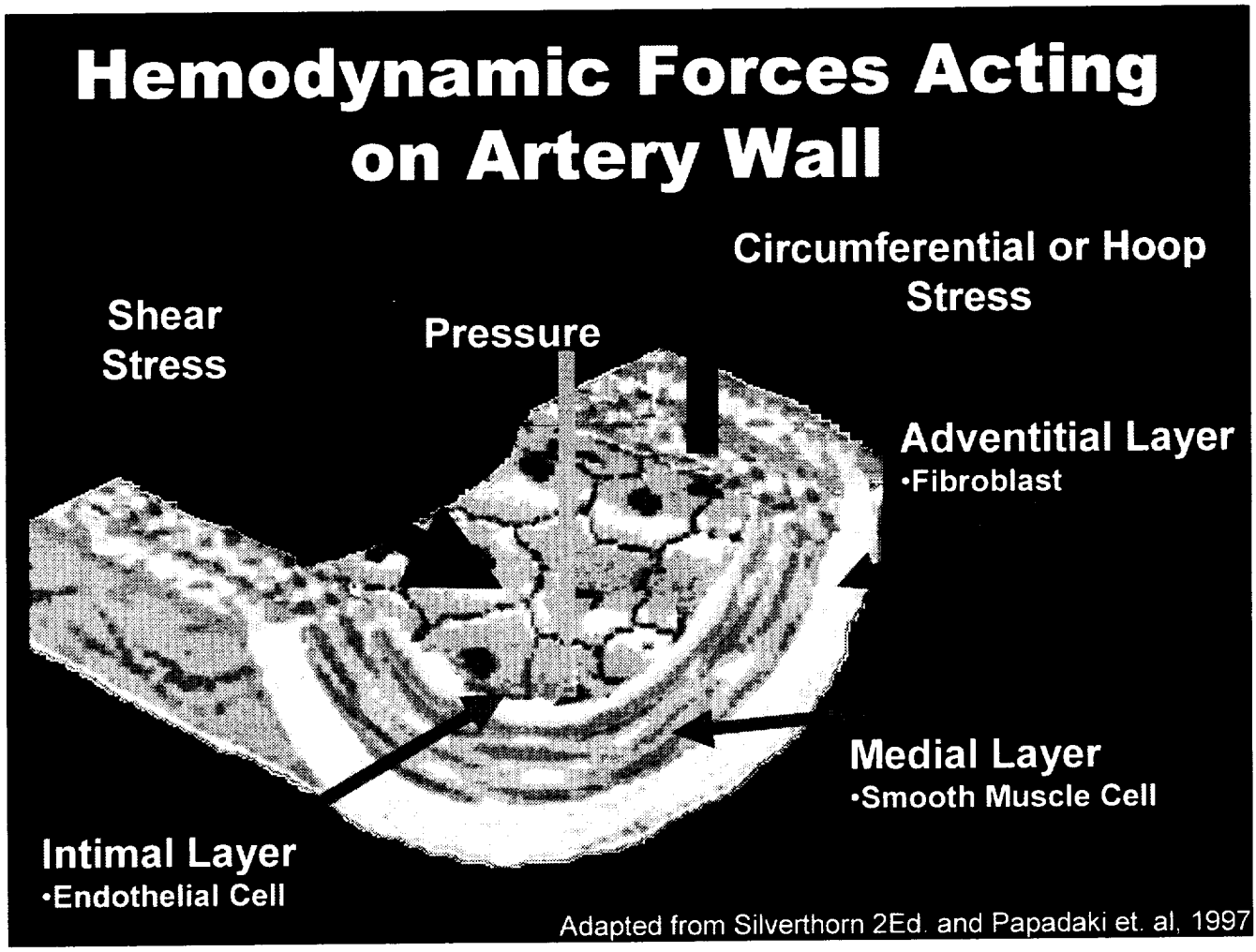
Hemodynamic Forces Acting on Artery Wall
Circumferential or Hoop Stress
Shear Stress
Pressure
Adventitial Layer
•Fibroblast
Medial Layer
•Smooth Muscle Cell
Intimal Layer
•Endothelial Cell
Adapted from Silverthorn 2Ed. and Papadaki et. al, 1997

SMC Exposure to Flow: Intact Vessel

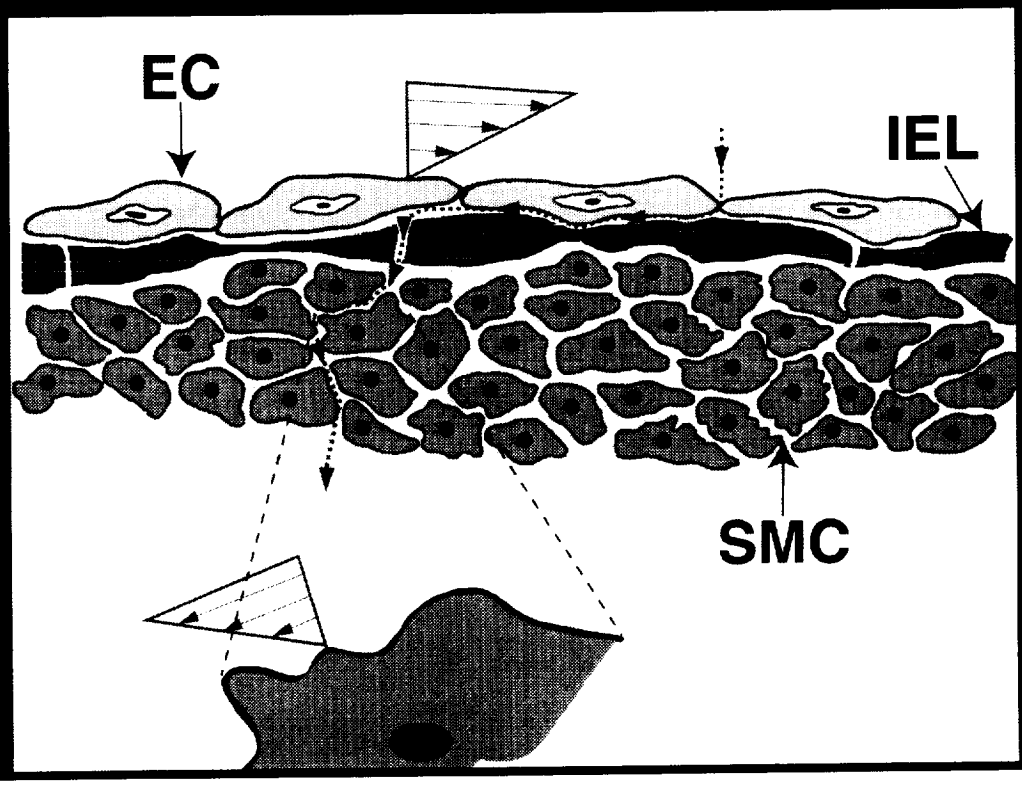

SMC Shear Stress Distribution

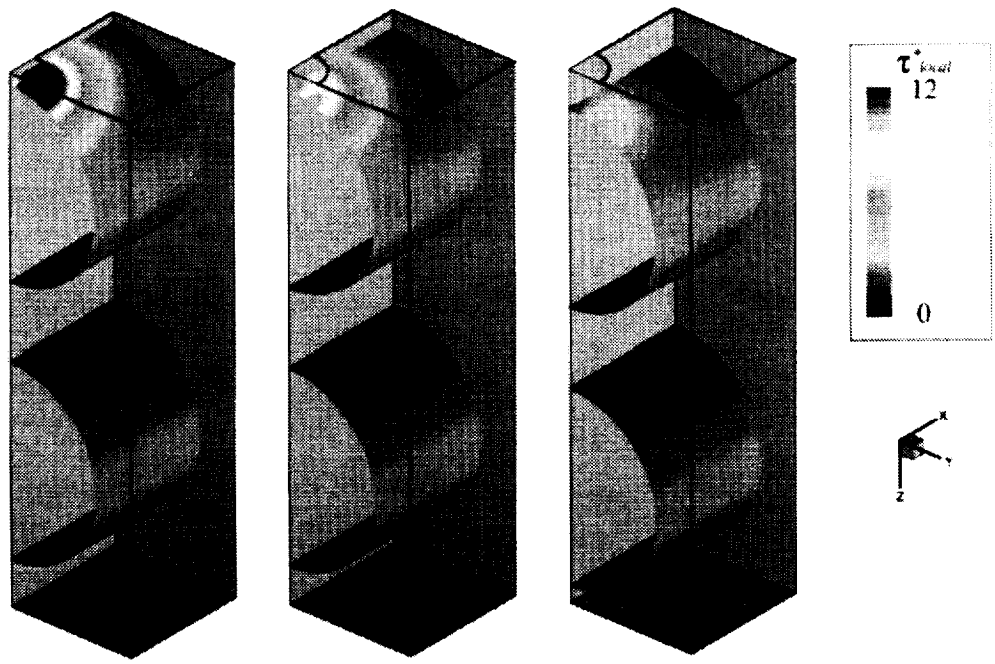

(1) $a = 0.20\,\mu m$ (2) $a = 0.36\,\mu m$ (3) $a = 0.80\,\mu m$

Myogenic Response

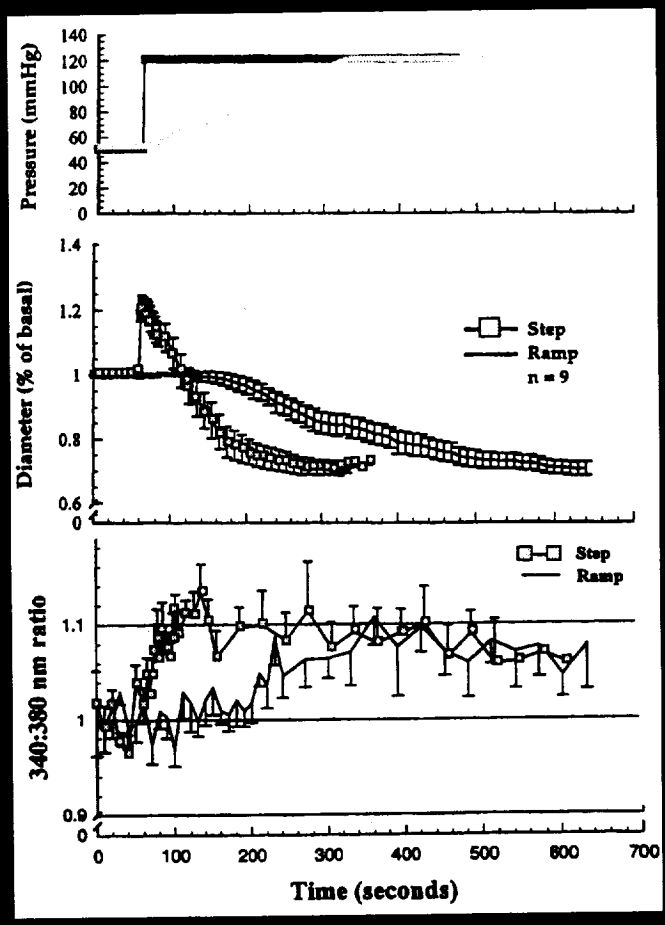

Hill et. al, 2000

SMC Phenotypes

Primary rat aortic SMC were expanded in cell culture flasks containing DMEM + 10% FBS. Then, depending on the experiment, SMC were treated in one of two ways in order to maintain them in a specific cell phenotype.

Proliferative Phenotype

SMC were maintained in DMEM + 10% FBS throughout the completion of experimentation.

Contractile Phenotype

SMC were "starved" (maintained in DMEM, no FBS) in culture flasks for two days and then on quartz slides for two more days prior to experiments, which were also run serum-free.

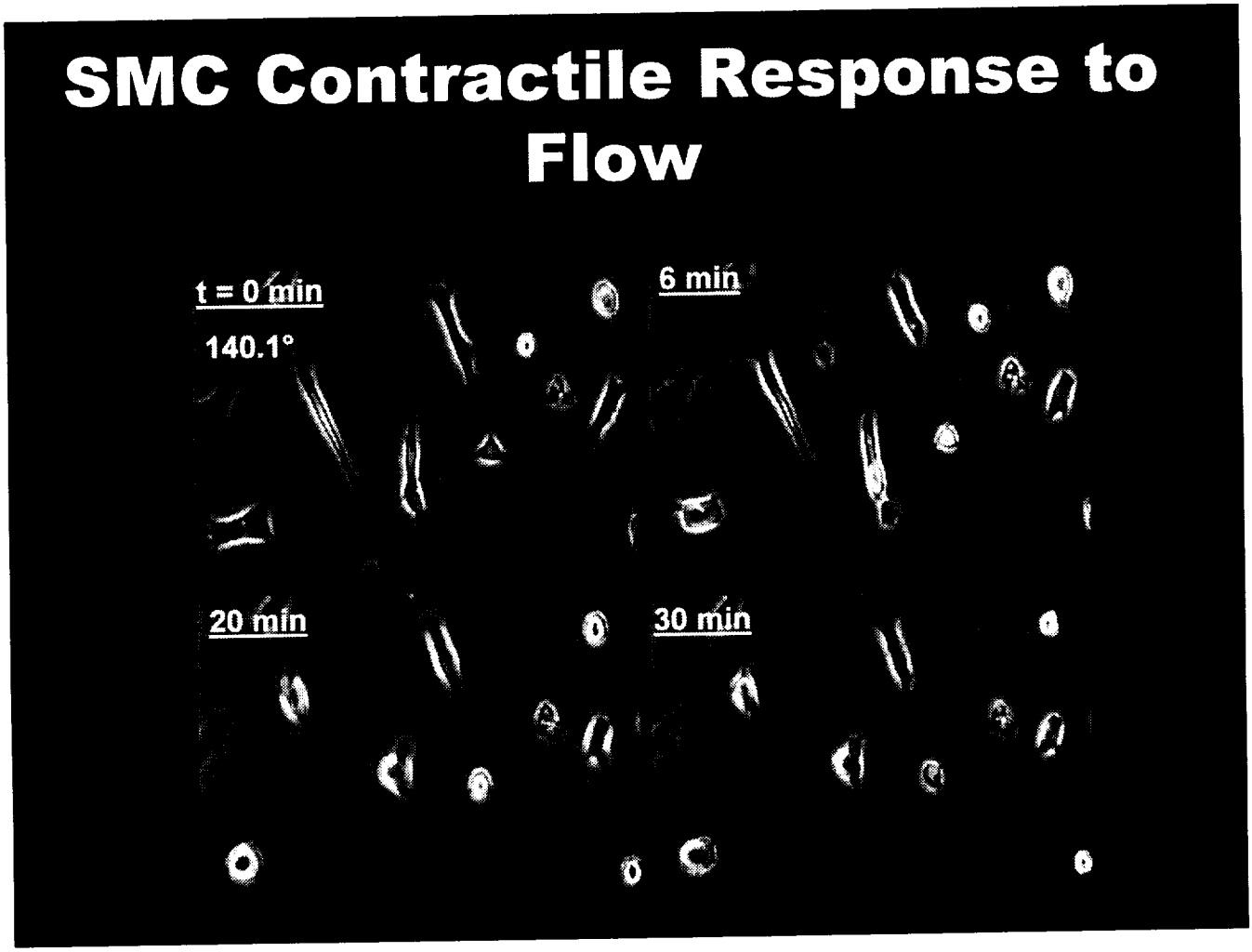
SMC Contractile Response to Flow
t = 0 min
140.1°
6 min
20 min
30 min

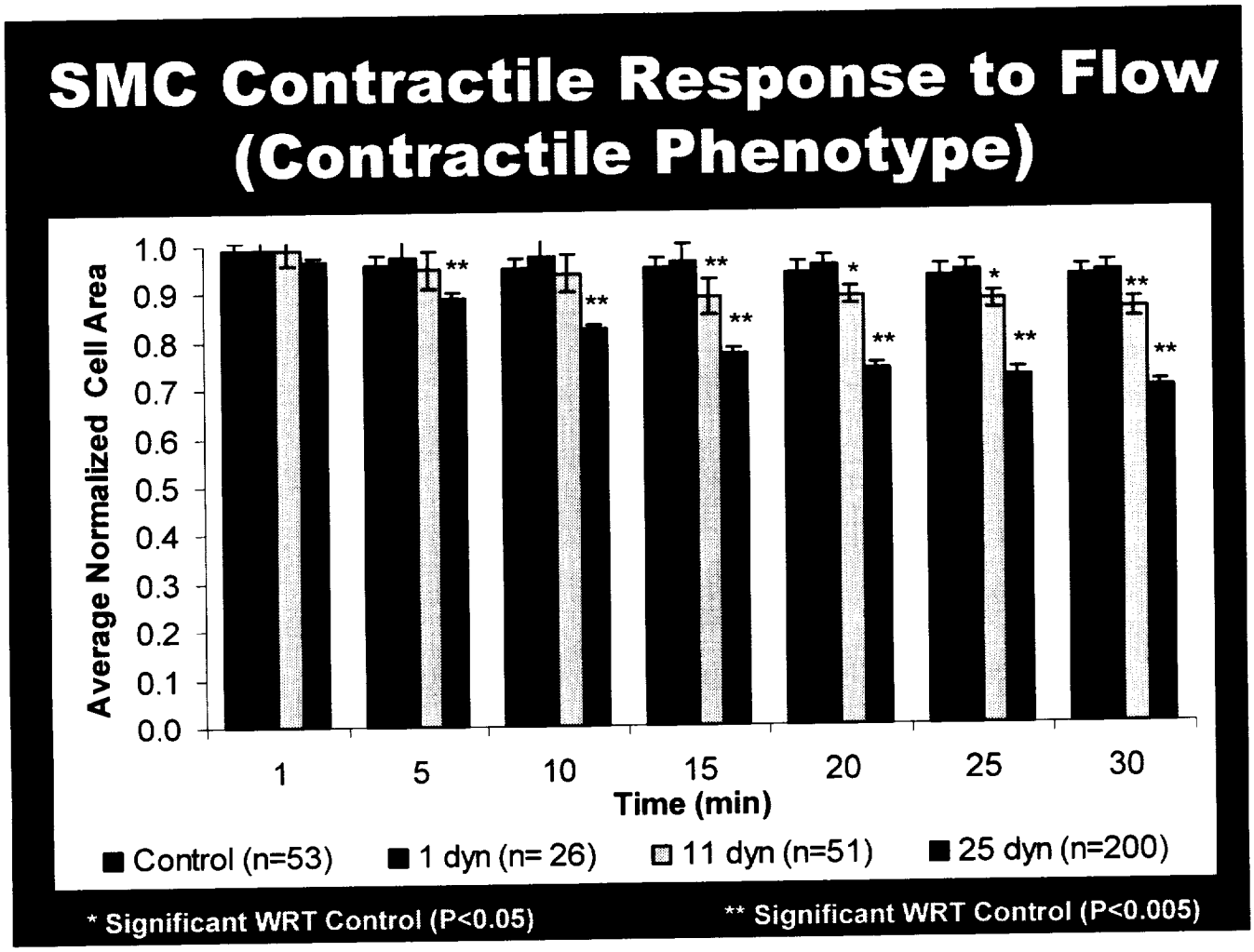
SMC Contractile Response to Flow
(Contractile Phenotype)
Average Normalized Cell Area
1.0
0.9
0.8
0.7
0.6
0.5
0.4
0.3
0.2
0.1
0.0
1
5
10
15
20
25
30
Time (min)
Control (n=53)
1 dyn (n= 26)
11 dyn (n=51)
25 dyn (n=200)
* Significant WRT Control (P<0.05)
** Significant WRT Control (P<0.005)

SMC Calcium Response to Flow (Contractile Phenotype)

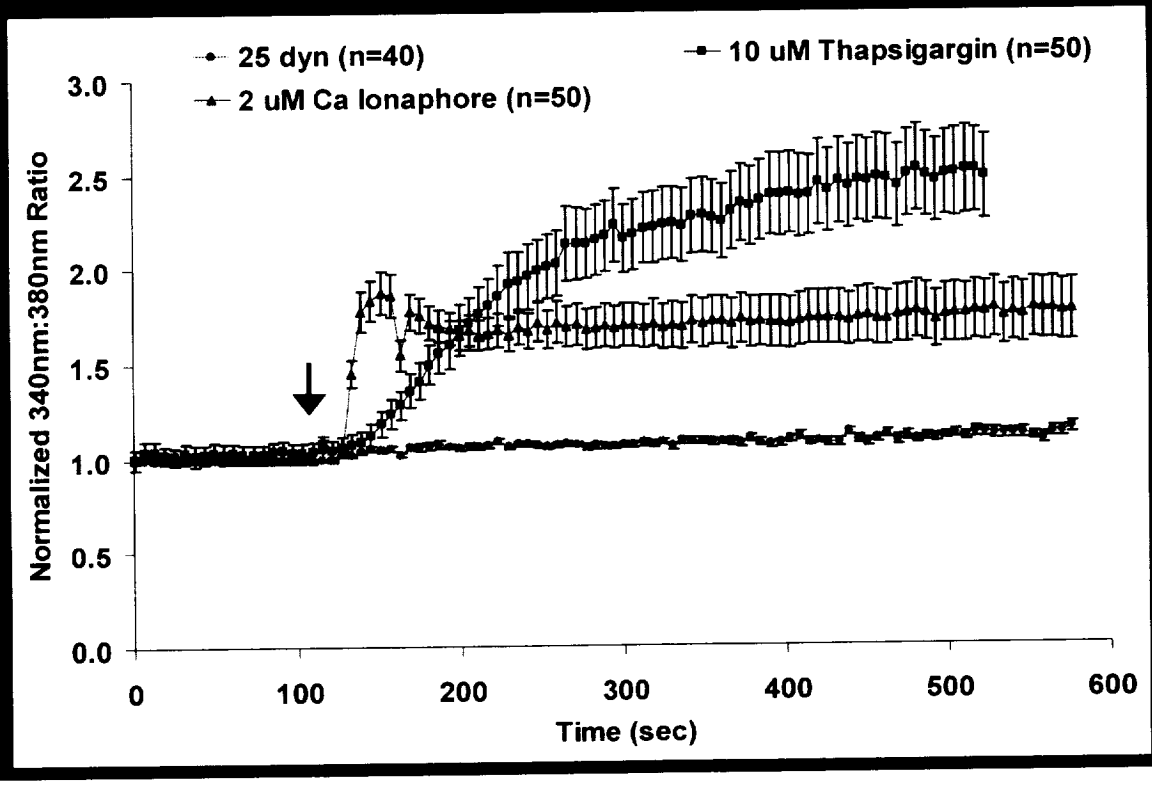

SMC Contractile Response to Flow (Proliferative Phenotype)

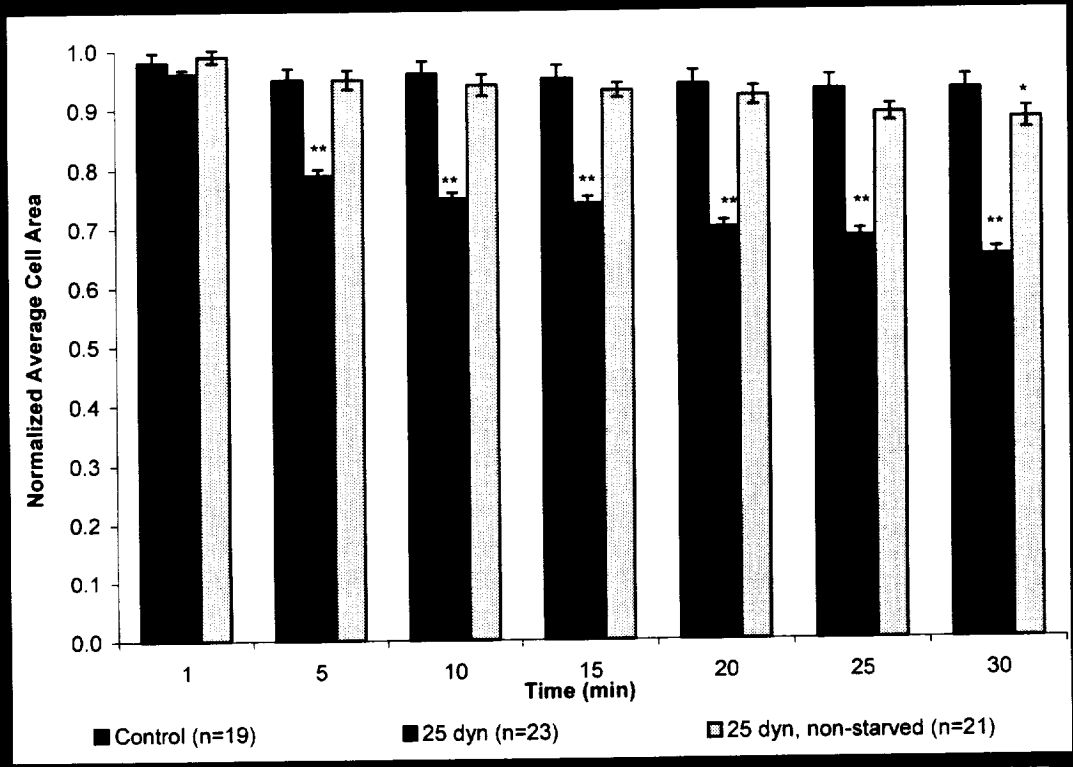

* Significant WRT Control (P<0.05)

** Significant WRT Control (P<0.005)

SMC Calcium Response to Flow (Proliferative Phenotype)

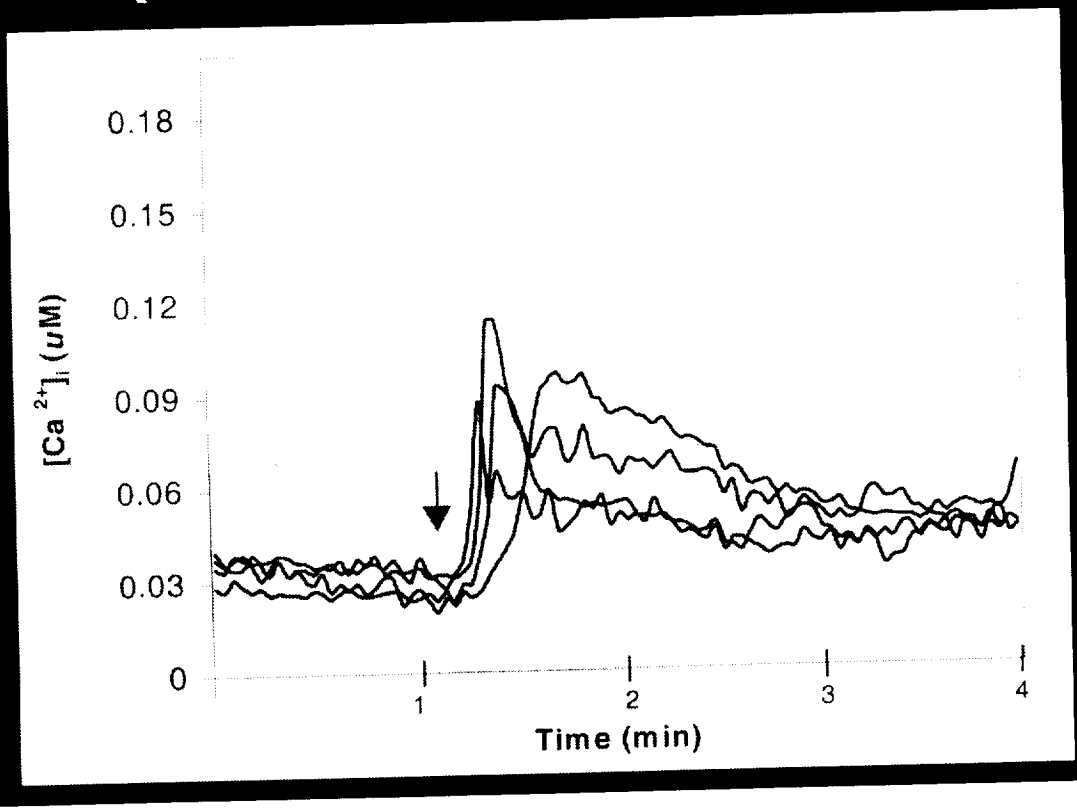

Rho-kinase pathway

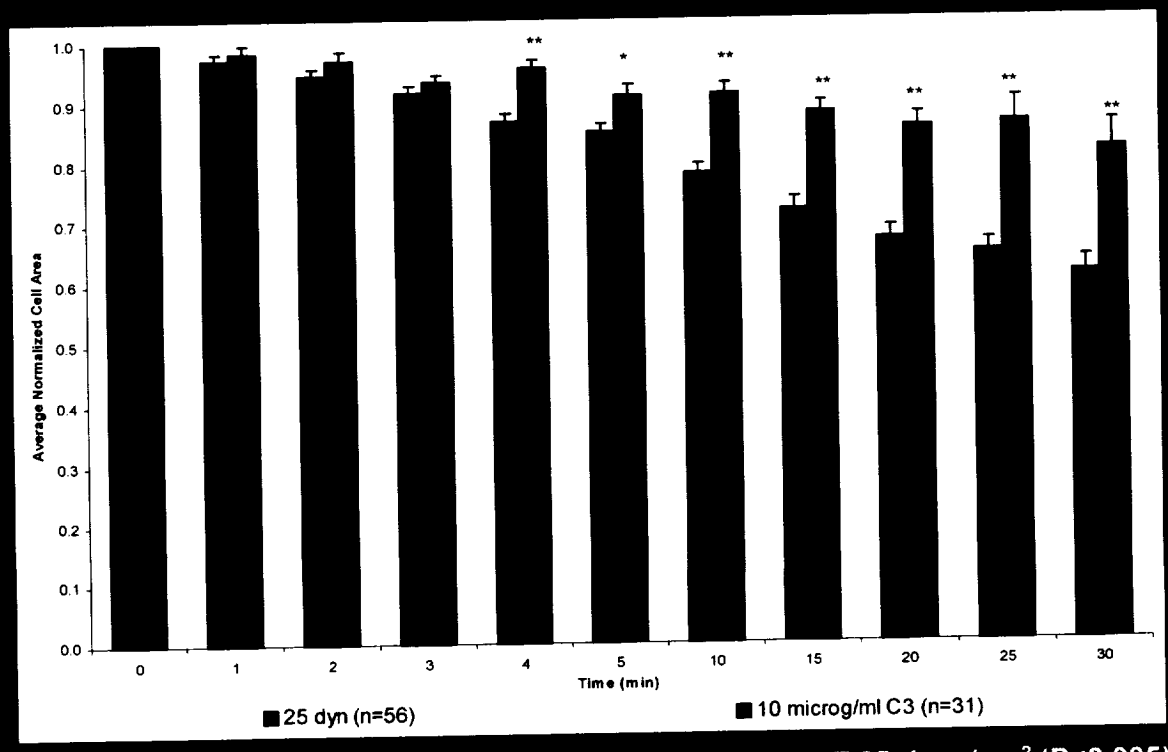

* Significant WRT 25 dyne/cm^2 ($P<0.05$) ** Significant WRT 25 dyne/cm^2 ($P<0.005$)

Conclusions

- SMC Experience Shear Stress Levels Comparable to EC
- SMC In Vitro Contract Significantly in Response to Shear Stress in a Calcium-Independent Manner

Method

1. Video microscopy of rat mesentry
   (normal wistar rats, 200~250 g)

2. Step change in pressure
   -> Measurement of arteriolar fluid filtration and myogenic constriction

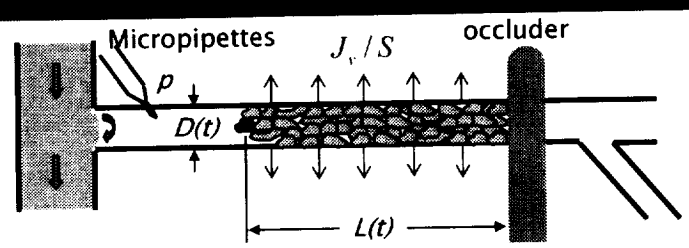

$$\frac{dVol}{dt} = J_v \Rightarrow J_v / S = \frac{dVol}{dt}\left(\frac{1}{S}\right) \quad where \quad S = \pi D(t) L(t)$$

3. Infusion of osmotic agents (BSA/Ficoll, 0.25 g)
   Superfusion of Adenosine (10^{-4} M)

Infusion of osmotic agents (BSA/Ficoll)

Filtration rate (N=11)

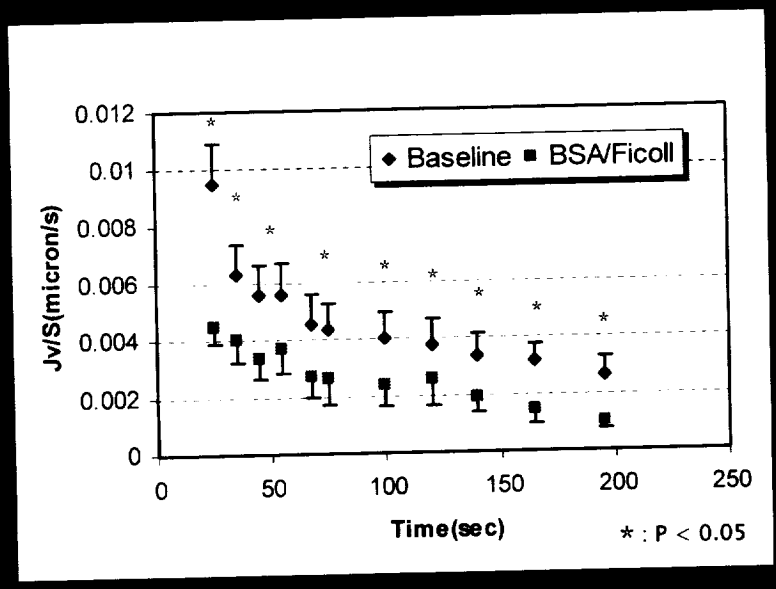

Infusion of osmotic agents (BSA/Ficoll)

Normalized diameter (N=11)

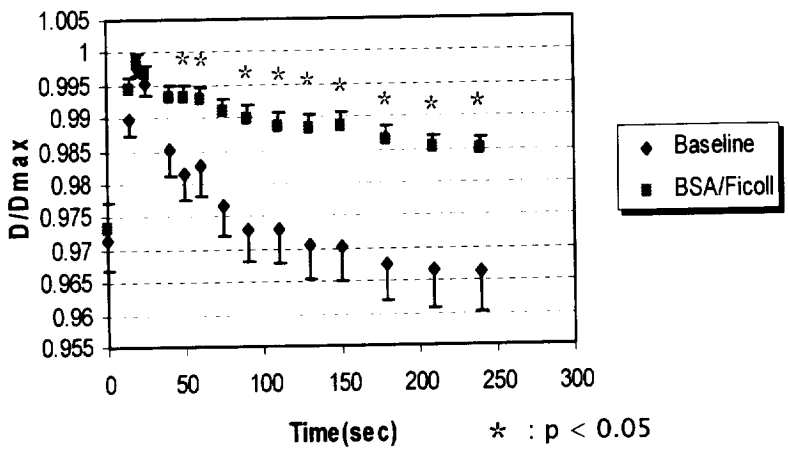

* : $p < 0.05$

Infusion of osmotic agents (BSA/Ficoll)

No change in flow condition between baseline and BSA/Ficoll experiments

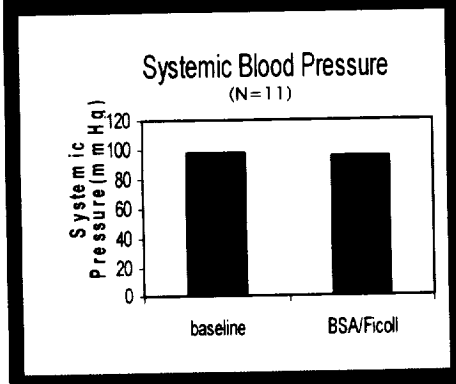

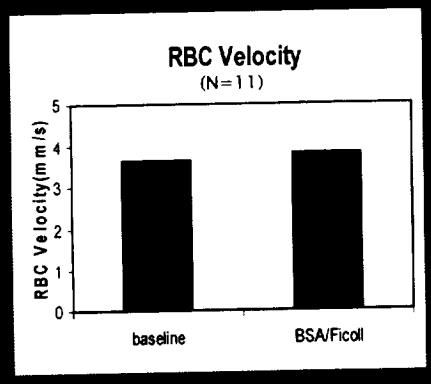

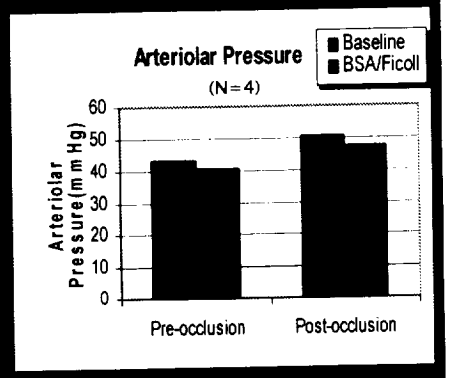

Infusion of osmotic agents (BSA/Ficoll)

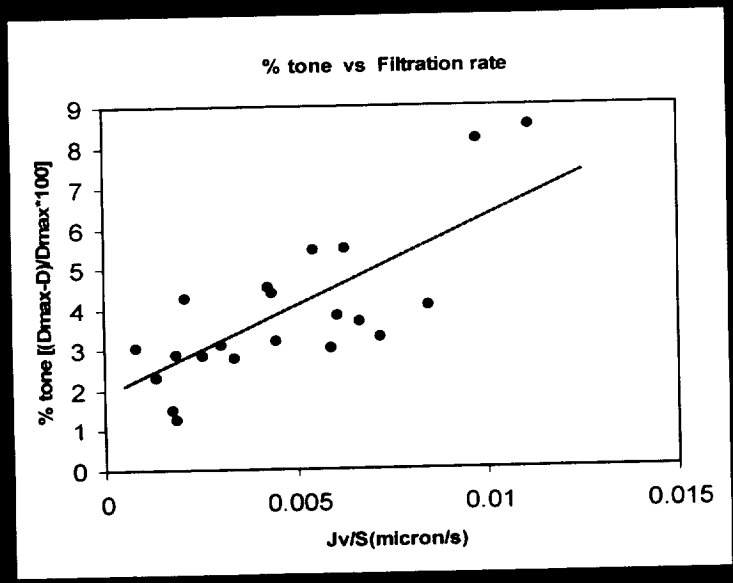

Superfusion of adenosine

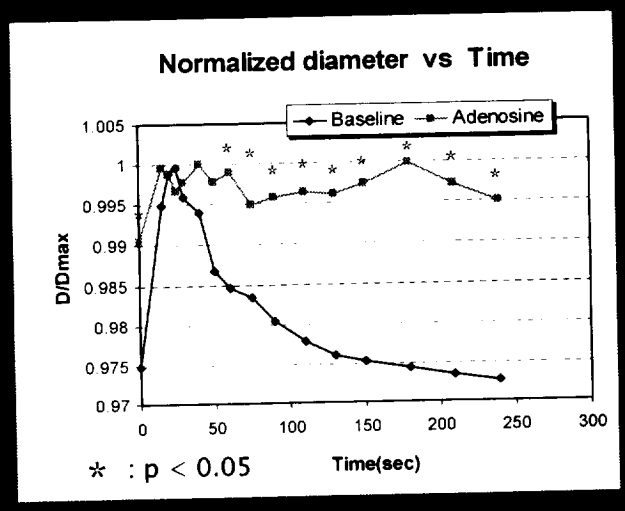

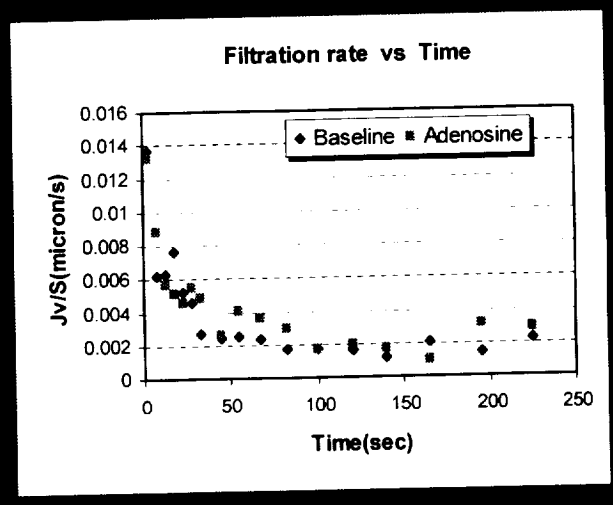

Conclusions

- The infusion of BSA/Ficoll attenuated Jv/S
- During the BSA/Ficoll occlusion, arteriolar diameter constricted much less compared to baseline occlusion
- Arteriolar constriction appears to be controlled by transmular fluid filtration

Capillary instabilities in the microgravity environment

David Halpern
Department of Mathematics
University of Alabama
Tuscaloosa AL 35487,

James B. Grotberg
Biomedical Engineering Department
University of Michigan
Ann Arbor, MI 48109

ABSTRACT

The lung consists of a network of bifurcating tubes that are coated with a thin viscous film. In the case of disease, the liquid film can form a meniscus which plugs the tube, thus obstructing gas exchange. The formation of the liquid meniscus is due to capillary driven instabilities which arise in the lining causing it to close up. Airflow can also be obstructed if the airway tube collapses in on itself. This occurs when the elastic forces of the tube are not large enough to sustain the negative fluid pressures inside the tube caused by surface-tension, and the tube collapses. Closure of the airway can be due to either, or a combination of, these mechanisms. In any case the instability is dependent on the surface tension of the liquid lining and the presence, or lack of, surfactants.

Premature babies, whose lungs have not developed sufficient surfactant to maintain the surface tension of the lung at a sufficiently low level for healthy functioning, are especially predisposed to problems caused by airway closure. In such cases, the patients can be treated with high frequency ventilation machines or surfactant replacement therapy or both Adults also are treated with ventilators for a variety of pulmonary conditions which can involve airway closure. For mechanical ventilation, the frequency of the breathing cycle, as well as the tidal volume, are two control parameters at the disposal of the clinician. Little is known, however, of the effect that these two parameters can have on the occurrence of airway closure. Indeed, if airways can be kept open by using some given machine frequency or amplitude, thus causing mechanical perturbations to the unstable interface, then this would important in the treatment of such patients.

In normal gravity, airway closure tends to occur in the lower regions of the lung, due to the weight of the lung above, and at the end of expiration when the lung volume, and hence airway radii, are smallest. The transient blockage of gas exchange in the affected tubes occurs in only part of the lung, the other portions remaining open. In the microgravity environment, airway closure is a potentially significant issue since ventilation and airway closure are more homogeneous, leaving less of the lung to be open during end expiration. Prevention of airway closure in this setting may be useful.

We model the phenomenon of airway closure by considering the stability of a thin film coating the inner surface of a rigid cylindrical tube. An oscillatory air (core) flow exerts

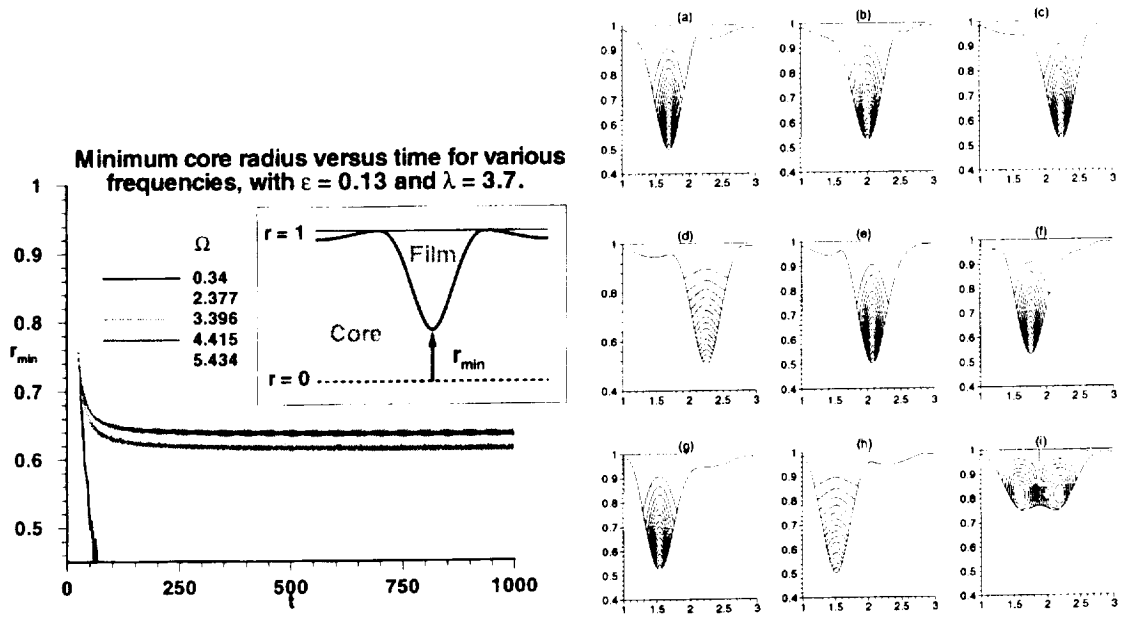

Figure 1: Left panel:Minimum core radius versus time for different values of the frequency parameter Ω for fixed amplitude λ and unperturbed film thickness ϵ. For sufficiently large frequency, closure is prevented since $r_{\min}$ does not approach zero. Right panel: Profiles of air-liquid interface and streamlines at different times during a cycle once an asymptotic state has been reached. The bulge deposits fluid to the film behind it as it moves from one side of the domain to the other, and picks up fluid from the film during the parts of the cycle when it reverses direction.

tangential and normal stresses on the air-liquid interface. The core flow is determined independently of the film flow by assuming that the core perceives the highly viscous film as a rigid boundary. We also consider the effects of a surfactant monolayer present at the air-liquid interface. Lubrication theory is used to derive an evolution equation for the position of the air-liquid interface which includes the effects of the core flow. This equation is coupled to a surfactant transport equation. Scaling analysis reveals several dimensionless parameters involving the frequency and amplitude of the periodic core pressure gradient, the thickness of the film, the tube radius, the viscosities of the fluids, the surface tension and surface-tension gradients due to the presence of the surfactant. When the core is passive, closure is possible provided the ratio of the unperturbed film thickness to tube radius exceeds a certain critical value. For the non-zero frequency case, it is shown that the core flow can stabilize the capillary instability and prevent closure. We find that there is a critical frequency above which closure does not occur, and that this critical frequency increases as the amplitude of the core flow decreases. An example of our computations is shown in figure 1.

Stabilization of thin liquid films by oscillatory shear stress: preventing airway closure

James B. Grotberg[1] & Peter Halpern[2]

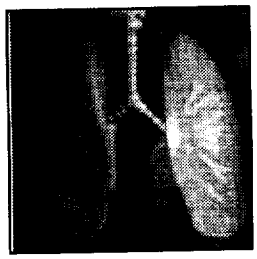

Airway Network of the Lung

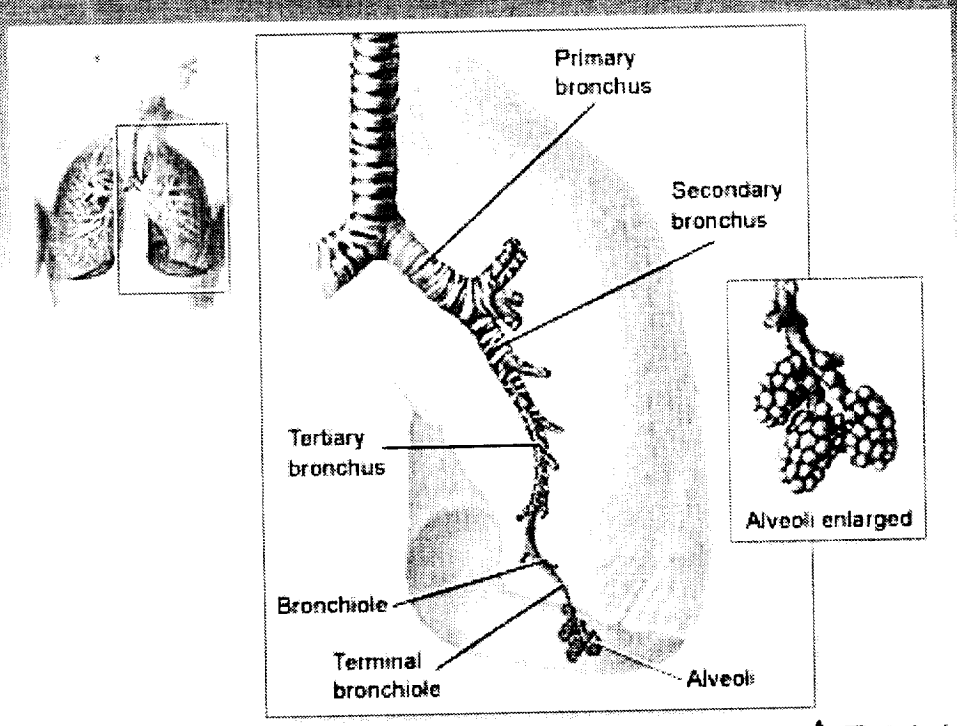

ADAM.

Gravity Effects on Ventilation Distribution

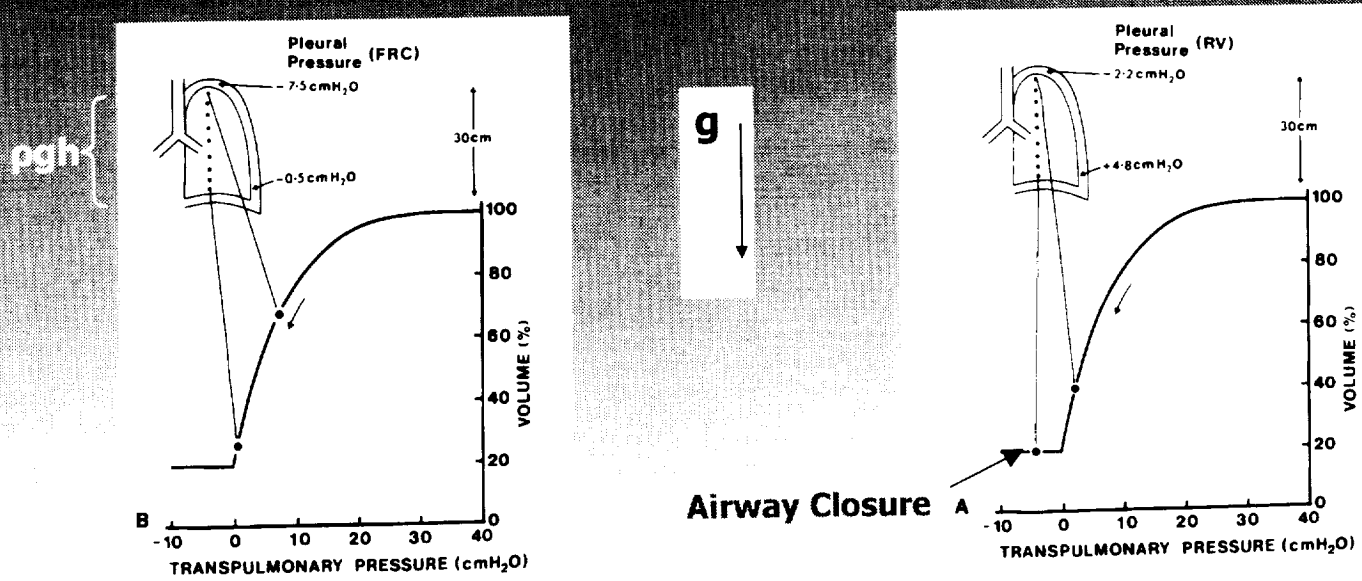

Mechanisms of Airway Closure
liquid
gas
Open Airway

Airway Closure in Normal Gravity

- Occurs in lower lung only
- Local atelectesis
- Regional ventilation inhomogeneity

Related Diseases

Small airways are highly compliant, liquid-lined tubes that can close under disease states such as

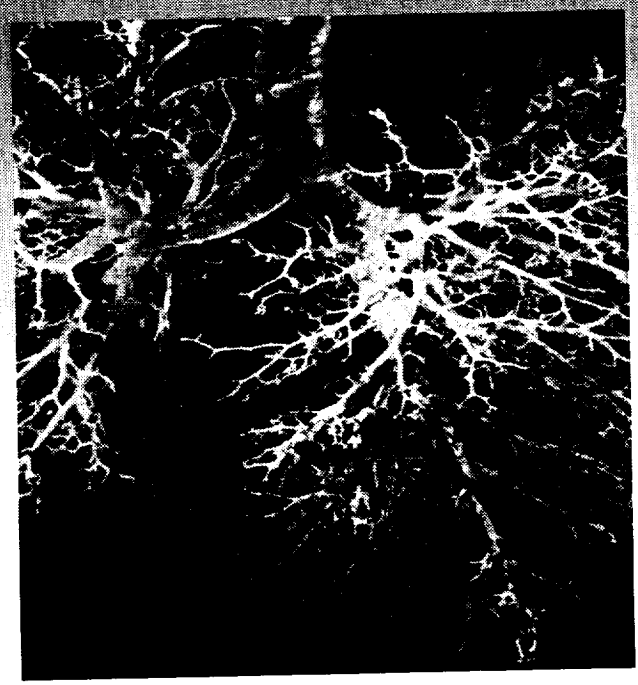

Other Core-annular Flows

- Unlubricated pipelining of crude-viscous oils

Capillary Instability

- Young-Laplace Equation

(surface-tension) X
Curvature of interface

Base State

a = Tube Radius
b = Uniform film radius
(a-b) = Film Thickness

ϵ = (a-b)/a

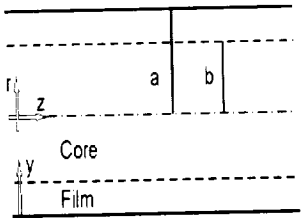

Perturbed State

Interface at $r^* = b + h^*(z,t)$
Disturbance wavelength λ^*

When h is small, $h \sim h_0 e^{qt + ikz}$
Where k = Wavenumber
q = Initial growth rate

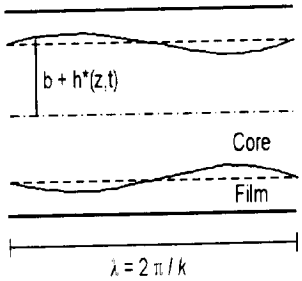

Rayleigh Instability:

$8 = 2\ B\ /k >$ Core Circumference $= 2\ B\ h$

Objectives

1. Derivation of evolution equation for deflection of air-liquid interface $h(z', t)$ using lubrication theory

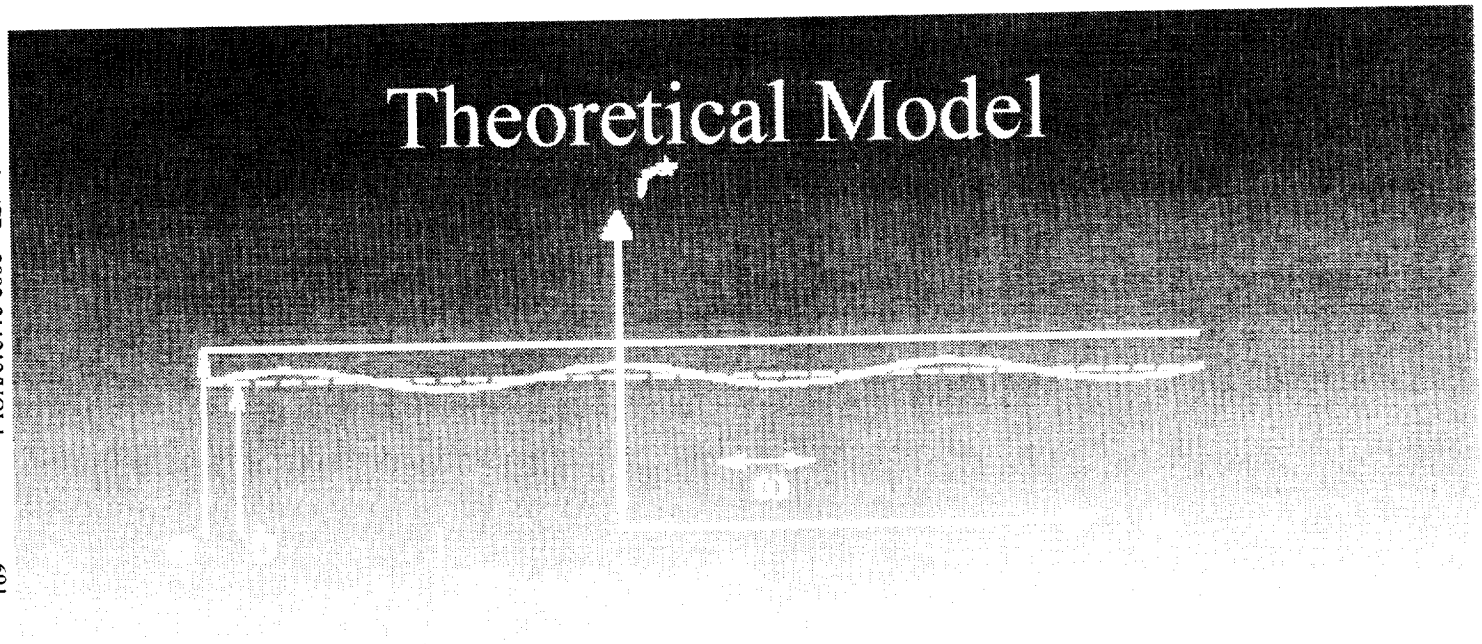

$$\lambda = V_T / \pi b^3 \qquad \Omega = \omega a / (\varepsilon^3 \sigma / \mu_f)$$

$$\varepsilon = \frac{a-b}{a}, \ \alpha^2 = \omega b^2 / \upsilon_c, \ Ca = \mu_c \omega L_T / \varepsilon^2 \sigma$$

Model Assumptions

1. Film consists of incompressible Newtonian fluid
2. Oscillatory core flow provides shear-stress at interface
3. Flow in thin film governed by lubrication theory

Lubrication Theory

Scale lengths on a, velocities on $U_{cap} = \varepsilon^3 \sigma/\mu$, time on a/U_{cap}, pressure on $\varepsilon\sigma/a$, $\varepsilon = 1 - b/a << 1$. Let $y = (1 - r)/\varepsilon$.

Axial Momentum : $\dfrac{\partial^2 w}{\partial y^2} = \dfrac{\partial p}{\partial z}$

Continuity : $\dfrac{\partial u}{\partial y} = \dfrac{\partial w}{\partial z}$

$\tau(z, t)$

$p_0(z, t)$

τ p_0

Lubrication Theory

Scale lengths on a, velocities on $U_{cap} = \varepsilon^3 \sigma/\mu$, time on a/U_{cap}, pressure on $\varepsilon\sigma/a$, $\varepsilon = 1 - b/a << 1$. Let $y = (1 - r)/\varepsilon$.

Axial Momentum : $\dfrac{\partial^2 w}{\partial y^2} = \dfrac{\partial p}{\partial z}$

Continuity : $\dfrac{\partial u}{\partial y} = \dfrac{\partial w}{\partial z}$

$\tau(z, t)$

$p_0(z, t)$

τ p_0

Core Flow

<u>Scales</u>: $t_c = \omega t_c^*$; $r_c = r_c^*/b$; $z_c = \delta z_c^*/b$
where $\delta = 2\pi b/\ell$; $p_c = \delta b p_c^*/\mu_a U_a$;
and $(u_c, w_c) = (u_c^*/(\delta U_a), w_c^*/U_a)$ where
$U_a = \omega L_T$ and $L_T = V_T/(\pi b^2)$ is the stroke length.

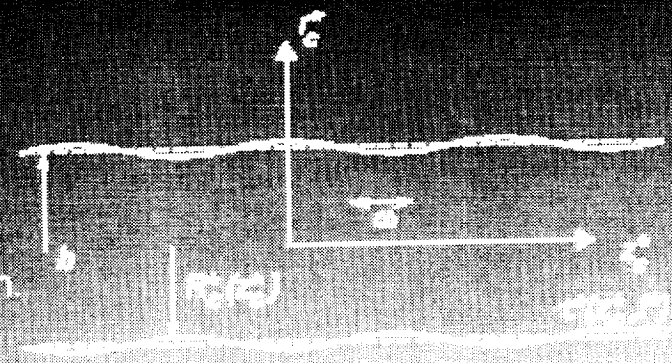

Airway Closure Experiment: Liquid Plug Formation

Goal: [redacted] that an oscillatory [redacted]ent closure.

Equations in Film Region $\varepsilon << 1$

Scales: $z = z^*/a$, $y = 1 - \varepsilon\, r^*/a$, $(u_f, w_f) = (u^*/(\varepsilon\, U_{cap}), w^*/U_{cap})$, $t = t^*/(a/U_{cap})$,
$p_f = p^*/(\varepsilon\sigma/a)$ where $U_{cap} = \varepsilon^2 \sigma/\mu$, $r = (a - h)/\varepsilon$.

Axial momentum:

$$\varepsilon^2 \left[w_{f_t} - \frac{u_f}{(1-\varepsilon y)} (r w_f)_y + w_{f_z} \right] = -p_{f_z} + \frac{1}{(1-\varepsilon y)} ((1-\varepsilon y) w_{f_y})_y + \varepsilon^2 \cdot \varepsilon$$

Radial momentum:

$$Re_f = \rho_f\, U_{cap}\, a / \mu_f$$

Core Flow $\delta << 1, \alpha = O(1), \alpha^2 \delta \lambda << 1$

Scales: $t_c = \omega t_c^*$; $r_c = r_c^*/b$; $z_c = \delta z_c^*/b$ where $\delta = \varepsilon b/\ell$; $p_c = \delta b p_c^* / \mu_e U_c$;
and $(u_c, w_c) = \left(u_c^*/(\delta U_c), w_c^*/U_c\right)$ where $U_c = \omega L_T$ and $L_T = V_T/(\pi b^2)$ is the stroke length.

Axial flow rate: $Q_c = \frac{1}{2}\sin(t_c + \varphi) \Rightarrow$ Pressure gradient: $\frac{\partial p_c}{\partial z_c} = B(z_c)\sin t_c$

Continuity equation: $\frac{1}{r_c}(r_c u_c)_{r_c} + w_{c_{z_c}} = 0$

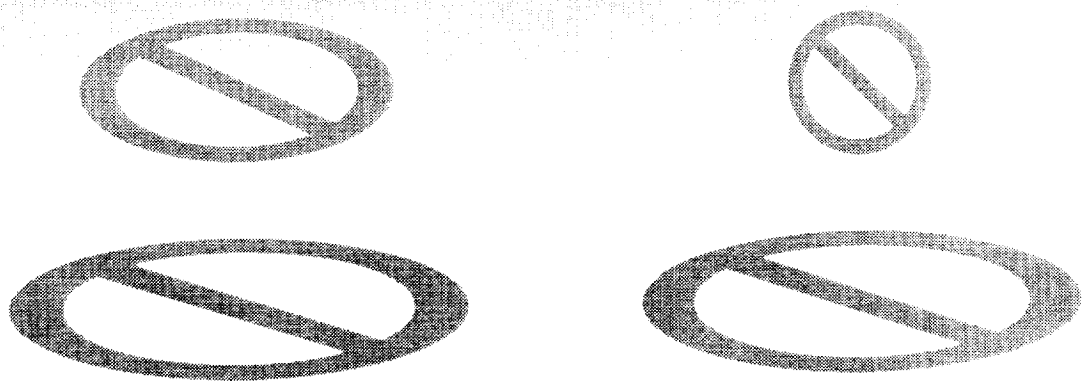

$\alpha = (\rho_c \omega/\mu_c)^{1/2} b$
$\lambda = L_T/b$

Boundary conditions

Film and core become uncoupled if $\Omega >> 1$ and $\Omega\lambda >> 1$

<u>No slip and no penetration at tube wall:</u> $w_f = u_f = 0$ Film bc

Interfacial boundary conditions (at $r = R(z, t) = 1 - \epsilon + \epsilon\, h(z, t)$, or $r_c = R_c(z_c, t_c)$):

Tangential stress: $w_{f_\theta} = -\frac{Ca}{1-\epsilon} w_{c_\theta} + O(\epsilon^2, \delta^2)$

Film bc

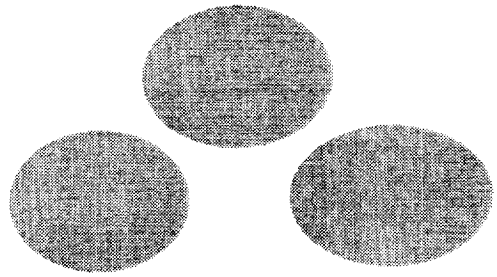

Core bc

$\Omega = \omega\, a / U_{cap}$ $Ca = \mu_T\, \omega\, L_T / (\epsilon^2 \sigma)$

Core Flow

The **axial velocity** is given by a longwave Womersley flow:

$$w_c(r_c, z_c, t_c) = \Re\left(\frac{iB(z_c)}{\alpha^2} \left(1 - \frac{J_0(\kappa_c r_c)}{J_0(\kappa_c R_c(z_c))} \right) e^{i(t_c - \pi/2)} \right)$$

The **core pressure gradient** is:

$$\frac{\partial p_c}{\partial y} = \alpha^2 \frac{\varepsilon}{(1-\varepsilon)^2} Ca\hat{B}(z) \sin \Omega t$$

$$\tau = -\frac{\partial w}{\partial y} = \alpha \frac{Ca}{(1-\varepsilon)^2} \Re\left(\hat{B}(z) \frac{J_1(\kappa R_w)}{J_0(\kappa R_w)} e^{i(\Omega t - \pi/4)} \right).$$

Evolution Equation for $h(z,t)$

Kinematic boundary condition

Computational Method

Initial Condition:

$$h(z,t) = A \cos(2\pi z/L)$$

Boundary Conditions: Spatially Periodic

Parameter estimates

- High frequency ventilation: 5-30 Hz
- Small tidal volumes: 10-100 ml
- Film viscosity: $\mu_L = 0.1$ Poise (10x water)
- Core viscosity: $\mu_c = 0.0002$ Poise (2x

Dimensionless parameter values

- Stroke length: $3.7 < \lambda < 37$
- Film time scale/core time scale: $1.7 < \Omega < 11$
- Womersley parameter : $0.4 < \alpha < 1$
- Core capillary number: $0.002 < Ca < 0.1$

Frequency

Animation Showing Closure

- $\varepsilon = 0.13, \Omega = 0.$
- Initial condition: amplitude is 1% of initial film thickness and wavelength gives fastest growth according to linear stability.

Film

Core

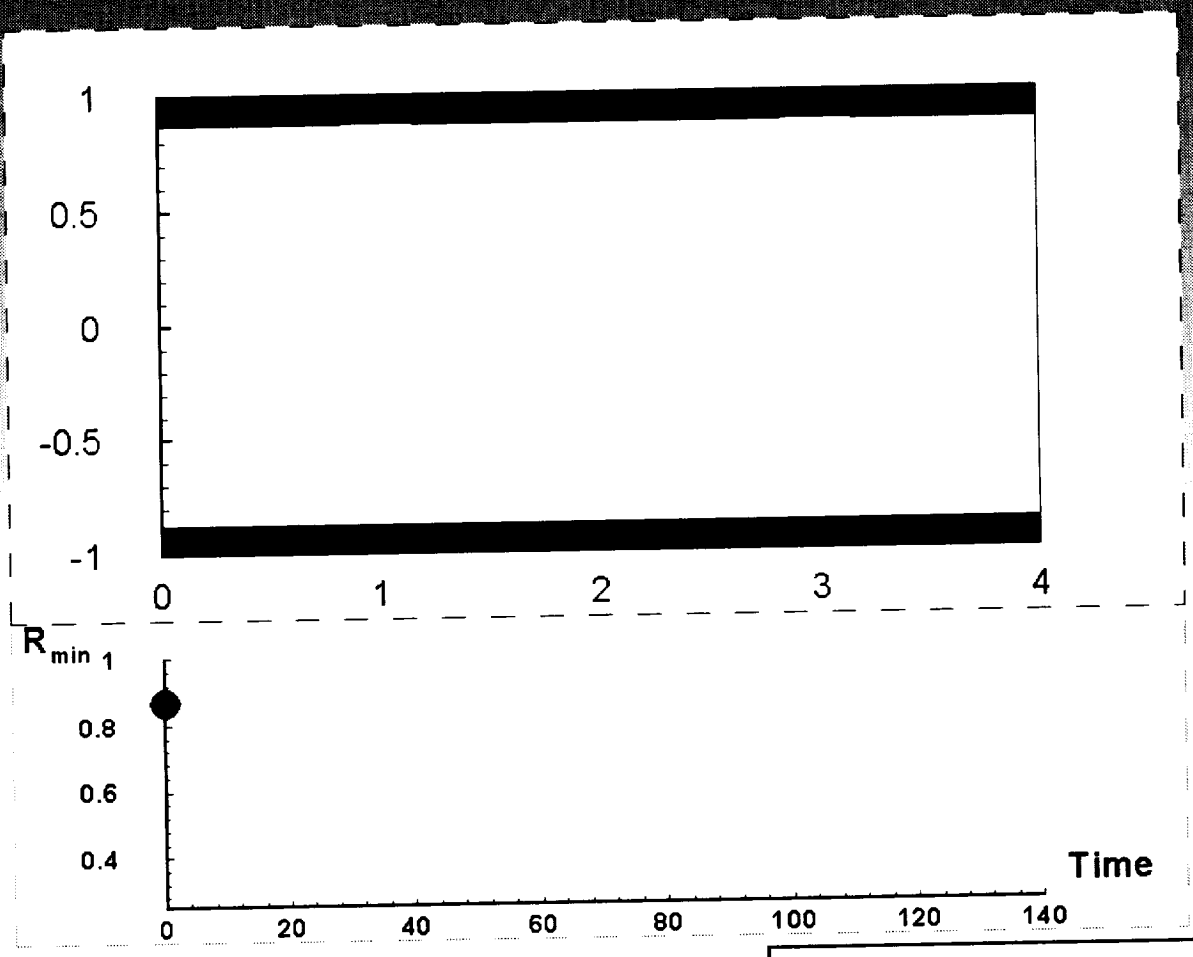

Click here to play movie

Animation Showing Saturation of Instability

- $\varepsilon = 0.13$, $\Omega = 3.40$, $\alpha = 0.61$, $\lambda = 14.86$.
- Initial condition: amplitude is 1% of initial

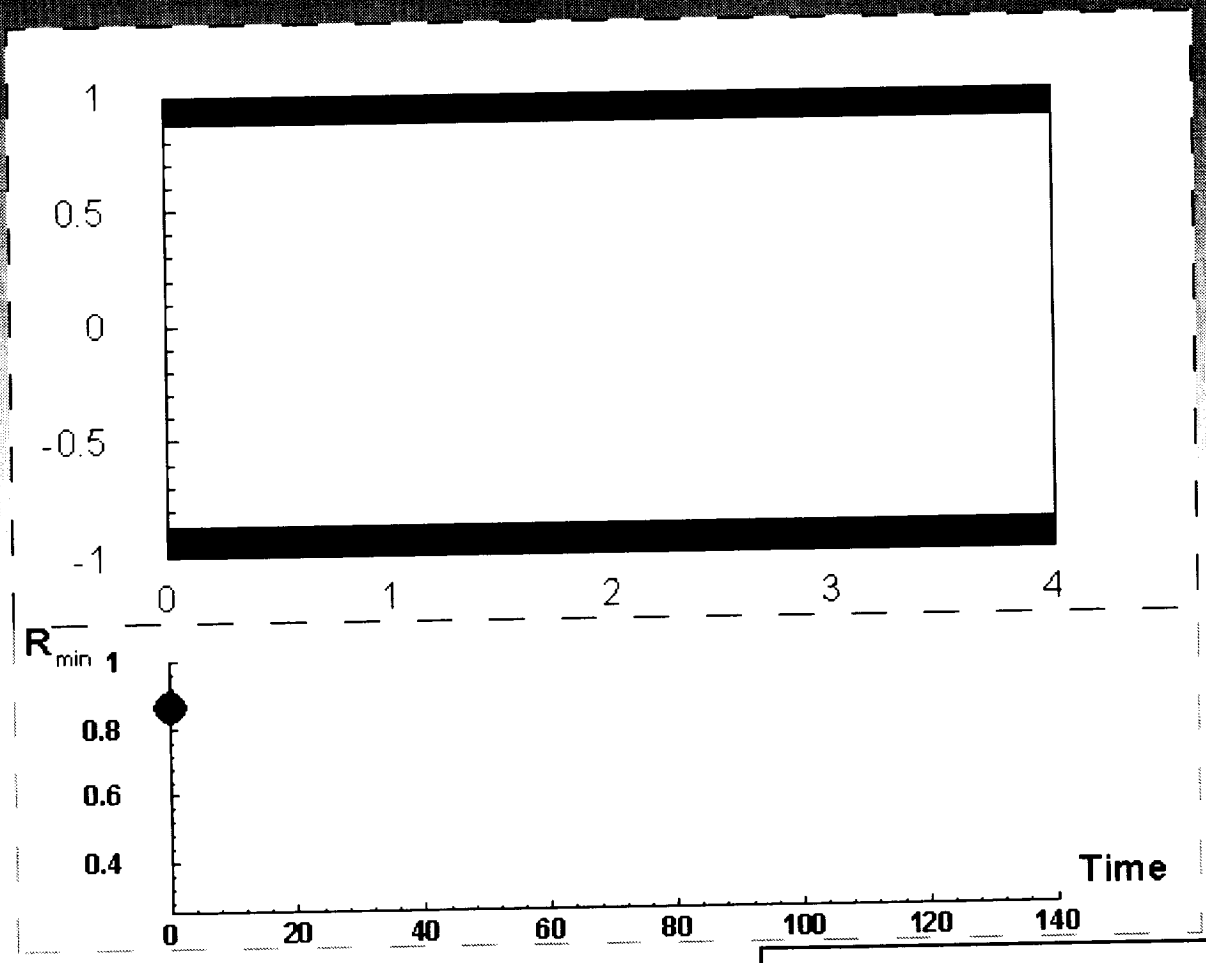

Click here to play movie

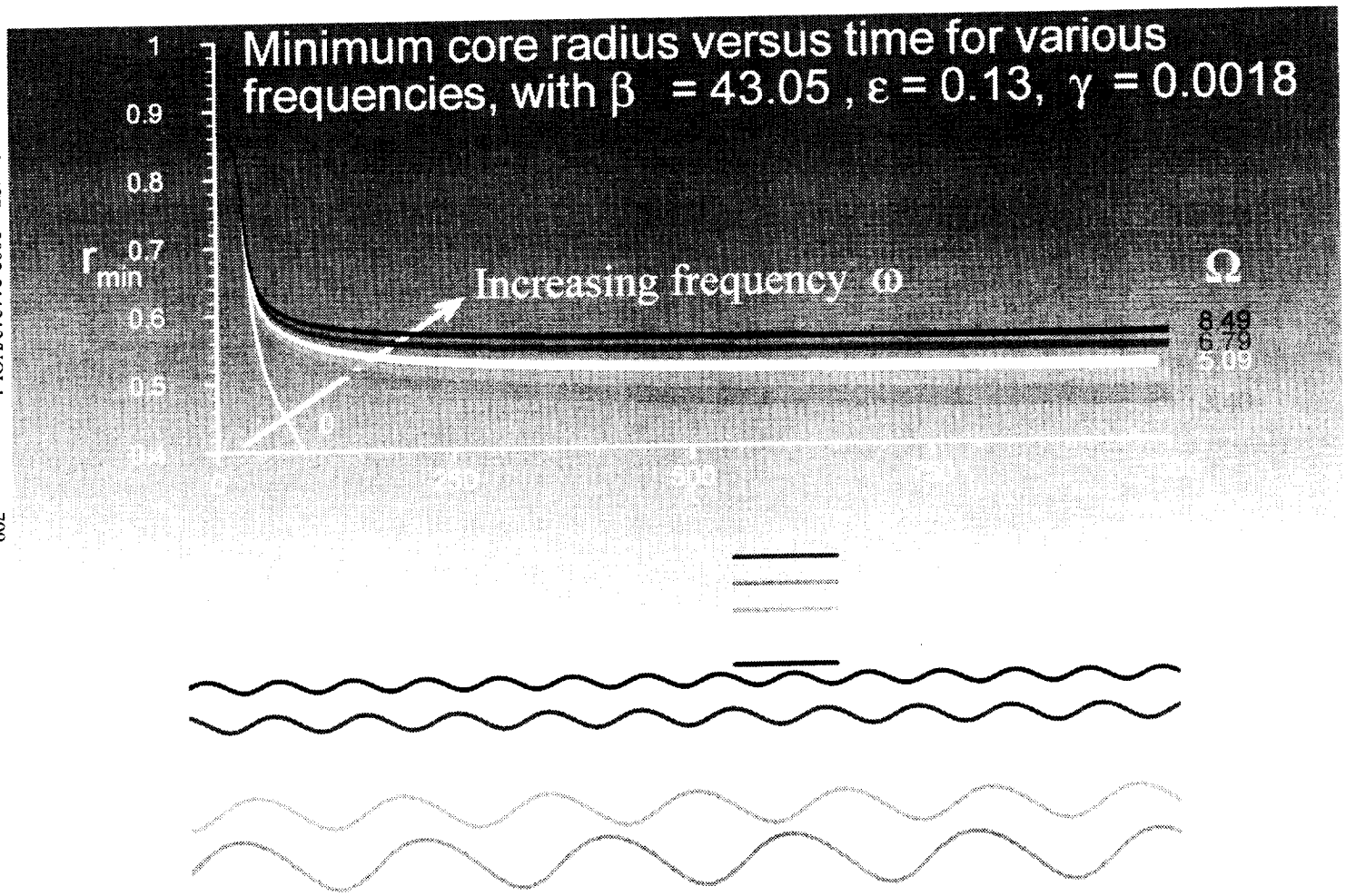
Minimum core radius versus time for various frequencies, with β = 43.05 , ε = 0.13, γ = 0.0018
r_{min}
1
0.9
0.8
0.7
0.6
0.5
0.4
0
250
500
750
1000
Increasing frequency ω
Ω
8.49
6.79
5.09

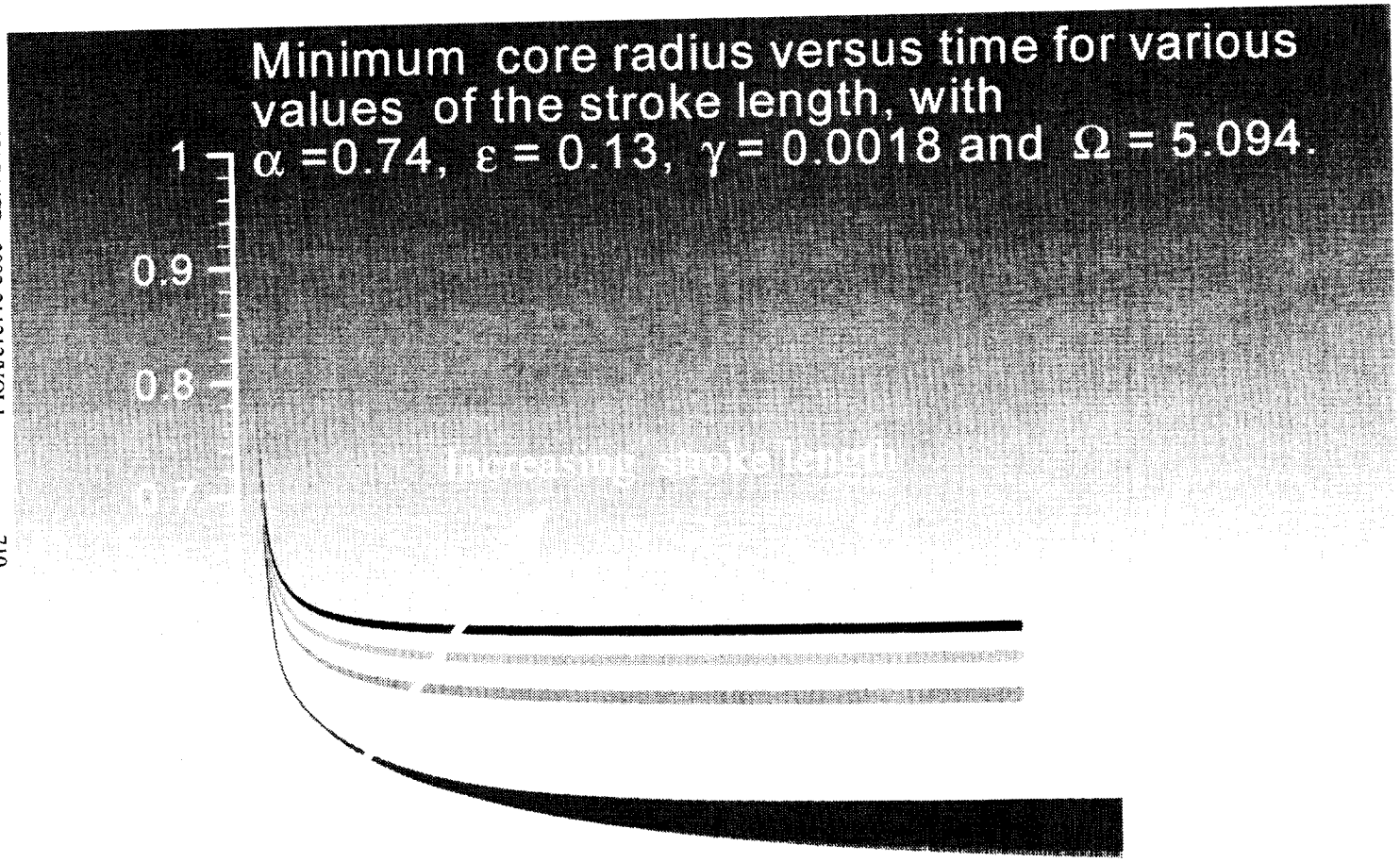
Minimum core radius versus time for various values of the stroke length, with
α =0.74, ε = 0.13, γ = 0.0018 and Ω = 5.094.
1
0.9
0.8
0.7
Increasing stroke length

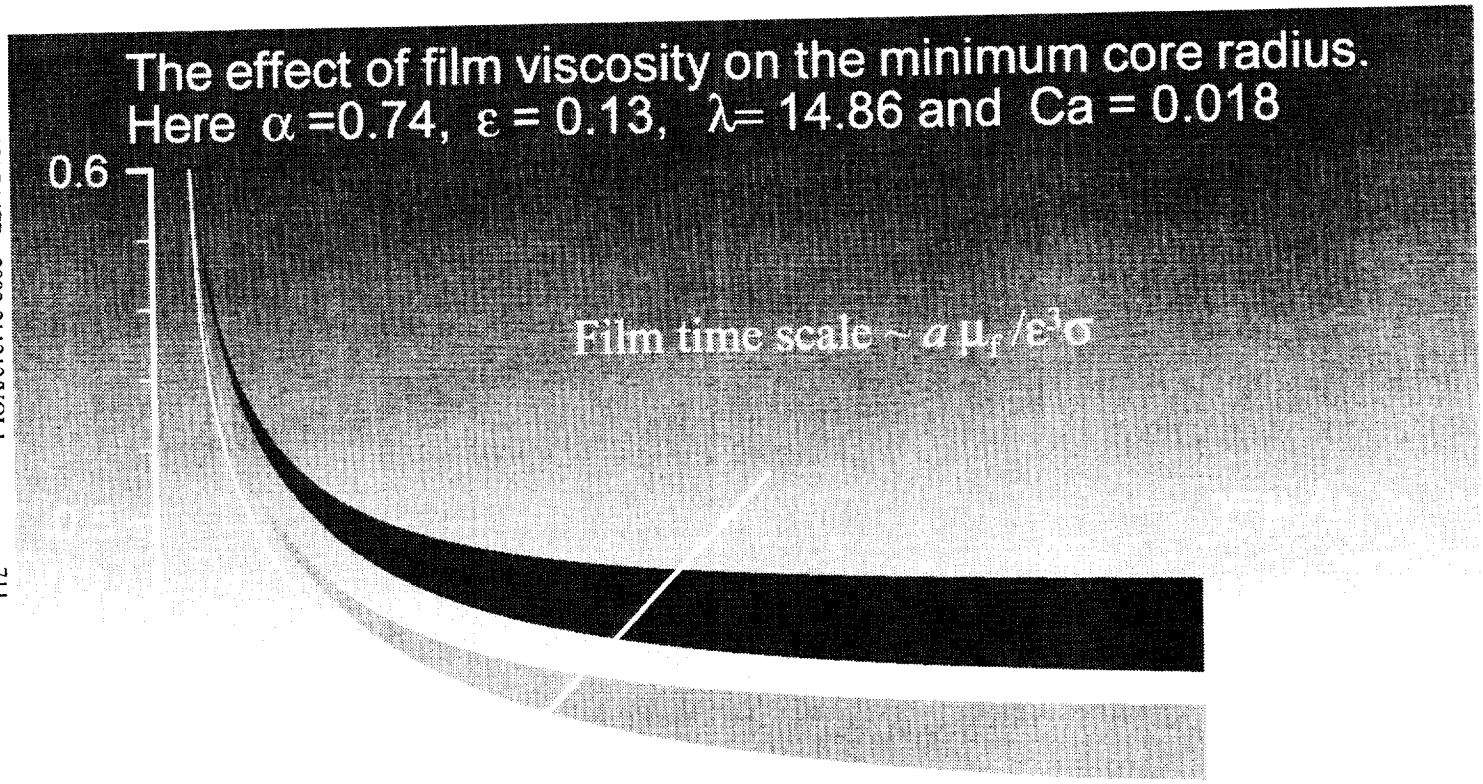
The effect of film viscosity on the minimum core radius.
Here α =0.74, ε = 0.13, λ= 14.86 and Ca = 0.018
0.6
Film time scale ~ α μf /ε³σ

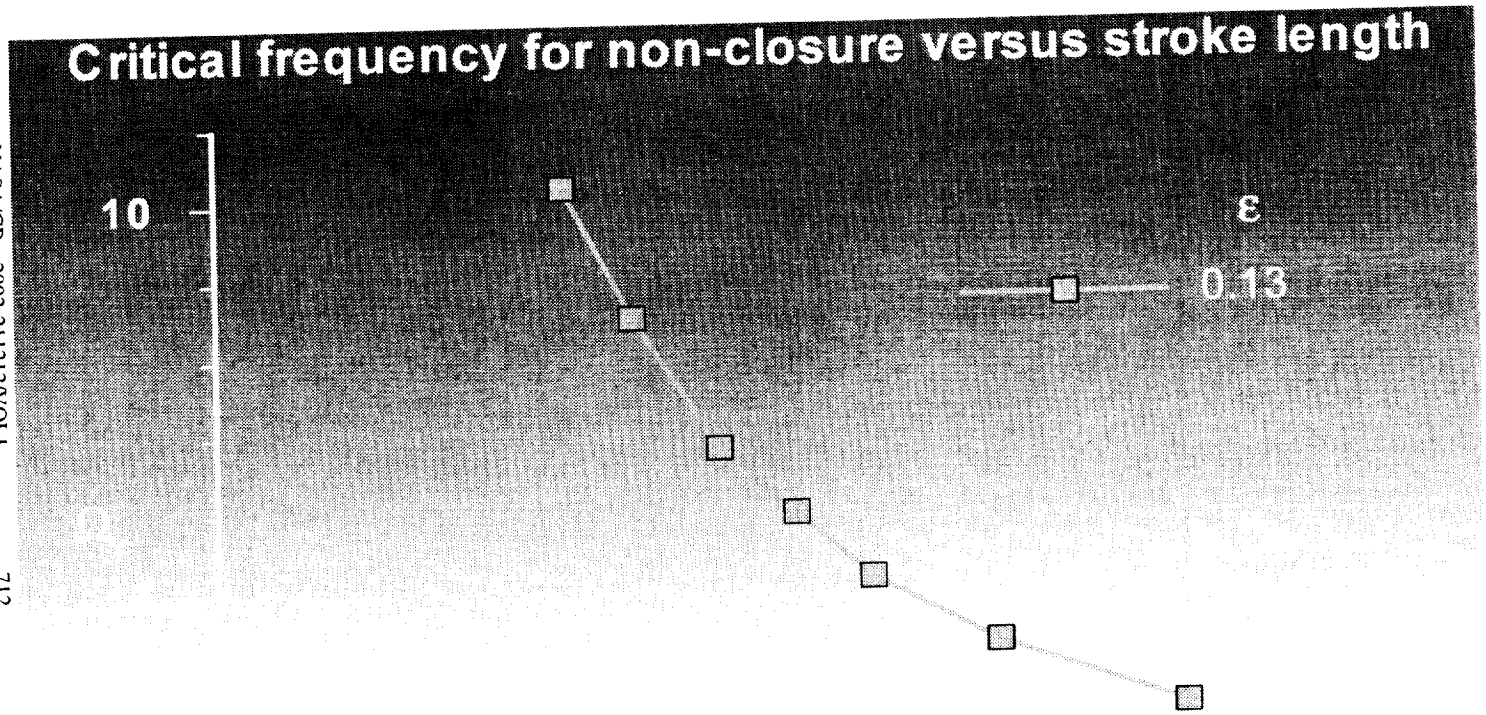
Critical frequency for non-closure versus stroke length
10
ε
0.13

Conclusions

- An oscillatory core flow can prevent liquid plug formation by saturating the capillary instability.
- Mechanism is a cyclic re-application of the growing liquid bulge to the cylinder wall.

THE IMPORTANCE OF INTERFACIAL STRESSES DURING PULMONARY AIRWAY REOPENING IN MICROGRAVITY

D.P. Gaver, A.M. Bilek, K.C Dee
Department of Biomedical Engineering, Tulane University, New Orleans, LA, USA

ABSTRACT

Pulmonary airway closure is a potentially dangerous event that can occur in microgravity environments and may result in limited gas exchange for flight crew during long-term space flight. Repetitive airway collapse and reopening subjects the pulmonary epithelium to large, dynamic, and potentially injurious mechanical stresses. During ventilation at low lung volumes and pressures, airway instability leads to repetitive collapse and reopening. During reopening, air must progress through a collapsed airway, generating stresses on the airway walls, potentially damaging airway tissues. The normal lung can tolerate repetitive collapse and reopening. However, combined with insufficient or dysfunctional pulmonary surfactant repetitive airway collapse and reopening produces severe lung injury. Particularly at risk is the pulmonary epithelium. As an important regulator of lung function and physiology, the degree of pulmonary epithelial damage influences the course and outcome of lung injury. Two companion studies, an experimental investigation and computational fluid dynamic simulation, are presented that address the hypothesis that the mechanical stresses associated with airway reopening inflict injury to the pulmonary epithelium.

Experimental Investigation

A parallel plate chamber lined with pulmonary epithelial cells was constructed as an idealized model of a collapsed segment of an airway where the walls are held in opposition by a viscous fluid. A fetal rat pulmonary epithelial cell line (CCL-149, ATCC) was cultured to confluence on a small (1 cm^2), square region of the upper plate. The narrow channel was filled a model airway lining fluid. Phosphate buffered saline including 0.1 mg/mL $CaCl_2$ and $MgSO_4$ (PBS) was used to model a surfactant-deficient airway lining fluid. A surfactant-containing airway lining fluid was approximated using Infasurf (ONY, Inc.) diluted to 1 mg/mL phospholipid concentration in PBS. Airway "reopening" was generated by the steady progression of a semi-infinite bubble of air down the length of the channel using a constant rate infusion pump (7 or 70 mL/min). For the control, slides were soaked in PBS for 5 minutes. A digital camera mounted above the channel collected sequential overhead images of the progressing bubble, which were used to calculate bubble velocity. Once removed from the apparatus, the slide was incubated with 1.2 μM Ethidium homodimer-1 (Eth-1) and 1.2 μM calcein AM (Molecular Probes). For each slide, the number of injured cells was recorded as the average number of Eth-1 stained nuclei counted in fluorescence microscopic images.

Fluid Dynamic Simulations

The bubble and parallel-plate flow chamber was modeled as a semi-infinite bubble progressing within a Hele-Shaw cell. In this model the walls were separated by a distance $2H$, with the semi-infinite bubble progressing in the x-direction with tip velocity U. The surface

tension, γ, was constant. The capillary number, $Ca = \mu U/\gamma$, representing the relative importance of viscous to surface tension effects on the bubble determines the dynamic response of the system. Stokes equations, $\nabla \mathbf{P} = \mu \nabla^2 u$ and $\nabla \bullet u = 0$, were solved using the boundary element method. The interfacial stress condition applied at the air-liquid interface was $|\sigma \bullet \hat{n}| = \gamma \kappa \hat{n}$, where $\sigma = -\mathbf{PI} + \mu(\nabla u + \nabla u^T)$ was the stress tensor, $\hat{n}$ was the unit normal, and κ was the interfacial curvature. For a given Ca, the system was simulated until a steady-state meniscus had developed and the stress-field and bubble geometry were determined.

Three potentially injurious components of the stress cycle associated with bubble progression – the shear stress, the shear stress gradient, and the pressure gradient – were analyzed. Regression relationships describing the behavior of these components as a function of Ca were determined for very small Ca ($5 \times 10^{-4} \leq Ca \leq 2 \times 10^{-3}$). Additionally, the thickness of the thin film deposited by bubble progression was estimated. Dimensionless values for the experimental flow conditions were extrapolated from the regression equations and redimensionalized.

Results and Discussion

For each condition the average number of injured cells per square centimeter was measured (Table 1). The control showed few injured cells. For the saline-occluded channels, bubble progression at both velocities produced significantly increased numbers of injured cells when compared to the control. The slow velocity resulted in a 66-fold increase in the number of injured cells and the fast velocity produced a 20-fold increase. The addition of Infasurf to the occlusion fluid reduced the number of injured cells to a level similar to the control. These results support the hypotheses that mechanical stresses associated with airway reopening injure pulmonary epithelial cells and that pulmonary surfactant in the normal lung protects the epithelium from injury due to airway reopening.

The stress component that best agrees with the experimentally observed trauma is the maximal pressure gradient (Table 1). Pressure gradients create a force imbalance on the cell membrane over the length of the cell. For a low profile, predominately flat cell or region of a cell, the non-uniformly distributed load can depress region of the cell stretching the membrane. For high profile cells or regions of a cell, such as the protrusion cause by the nucleus, where the normal forces of the cell surface are nearly opposite, a pressure gradient will pinch that region. The pinching can tear the membrane at the base of the protrusion or force fluid upward rupturing the top surface of the cell.

Table 1: Measured and calculated parameter values for the experimental conditions

Fluid	Q (mL/min)	Trauma (10^3 injured cells/cm^2)	γ (dyn/cm)	U (cm/s)	Ca $\times 10^{-3}$	$(\tau_s)_{max}$ (dyn/cm^2)	$(d\tau_s/dx)_{max}$ (dyn/cm^2/μm)	$(dP/dx)_{max}$ (dyn/cm^2/μm)	f (μm)
Control		0.60 ± 0.22							
PBS	7	39.80 ± 8.76 *†	70	0.27 ± 0.01	0.0386	15.5	0.209	6.65	1.3
PBS	70	12.04 ± 5.91 *†	70	2.70 ± 0.33	0.3857	34.3	0.211	3.36	6.0
Infasurf	7	0.80 ± 0.17	25	0.27 ± 0.02	0.1080	7.9	0.075	1.75	2.6
Infasurf	70	1.03 ± 0.74	25	2.42 ± 0.26	1.0800	17.5	0.077	0.88	11.9

PBS = Phosphate Buffered Saline (with Ca^{++} and Mg^{++}), Infasurf = 1mg/mL in PBS, Q = infusion rate, γ = surface tension, U = velocity, Ca = capillary number, $(\tau_s)_{max}$ = maximum shear stress, $(d\tau_s/dx)_{max}$ = maximum shear stress gradient, $(dP/dx)_{max}$ = maximum pressure gradient, f = film thickness, Note: H = 0.085 cm, * Significantly greater than control ($p < 0.01$), † Significantly greater than Infasurf for the same velocity ($p < 0.01$)

The Importance Of Interfacial Stresses During Pulmonary Airway Reopening In Microgravity

Donald P. Gaver
Anastacia M. Bilek
Anne-Marie Jacob
Kay C Dee

Department of Biomedical Engineering
Tulane University
New Orleans, LA

Airway Closure in Microgravity

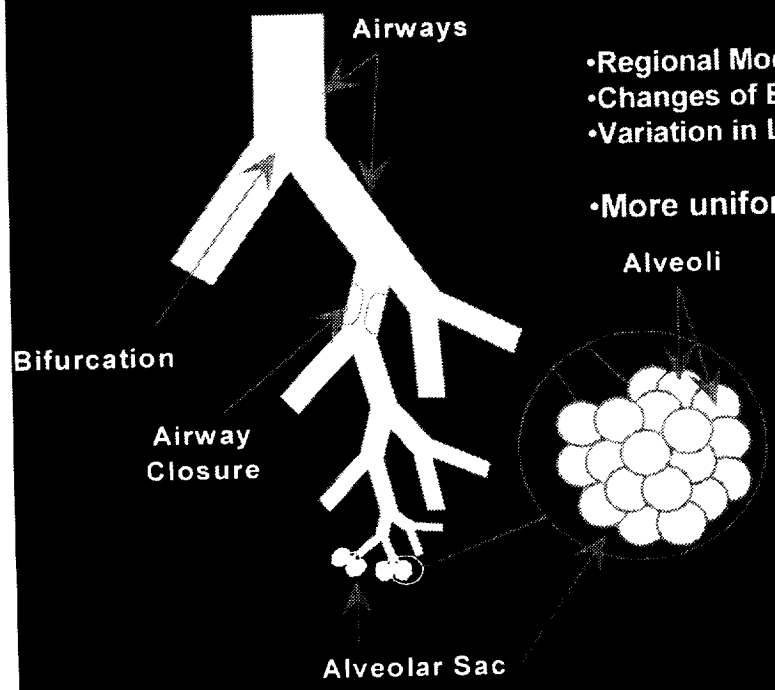

MICROGRAVITY CAUSES:

- Regional Modification of Ventilation
- Changes of Blood Perfusion
- Variation in Lung Capacity

- More uniform distribution of airway collapse

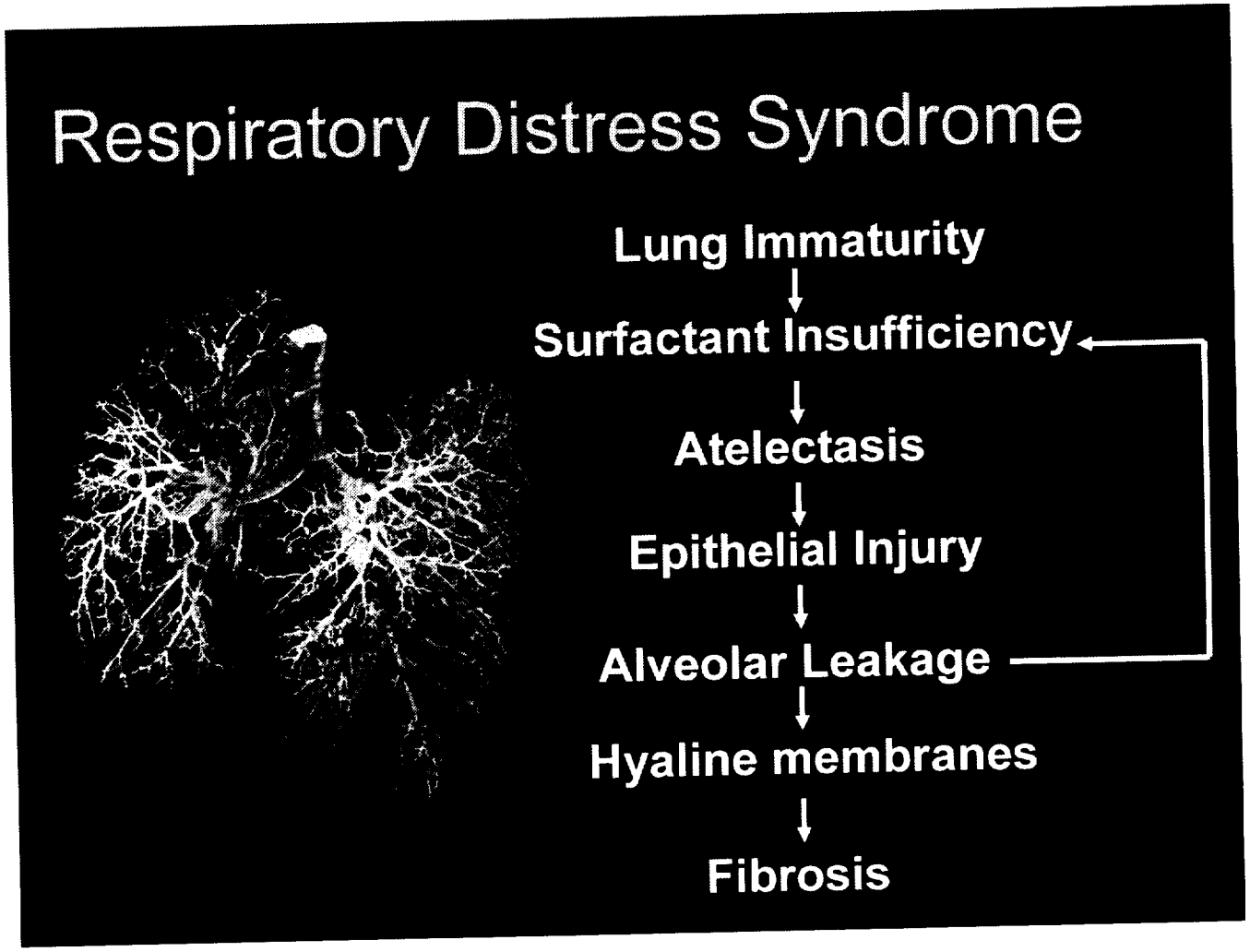
Respiratory Distress Syndrome
Lung Immaturity
Surfactant Insufficiency
Atelectasis
Epithelial Injury
Alveolar Leakage
Hyaline membranes
Fibrosis

Lung Pressure-Volume Zones of Injury

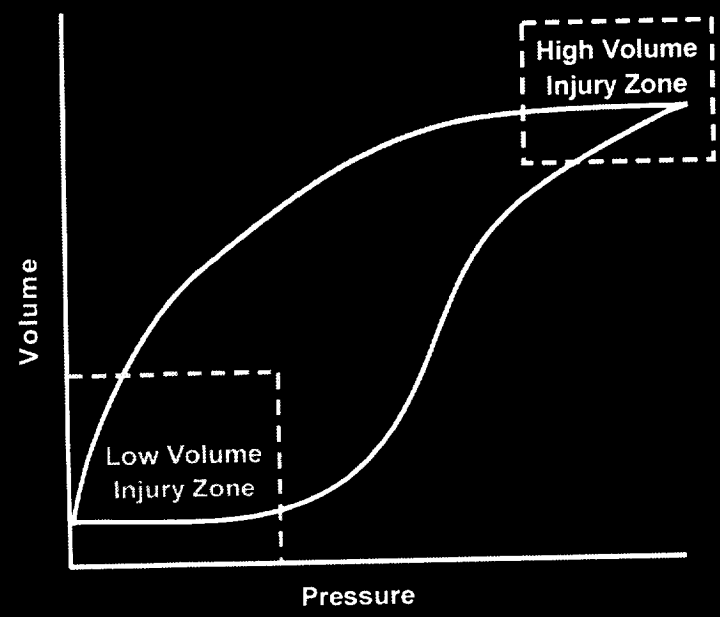

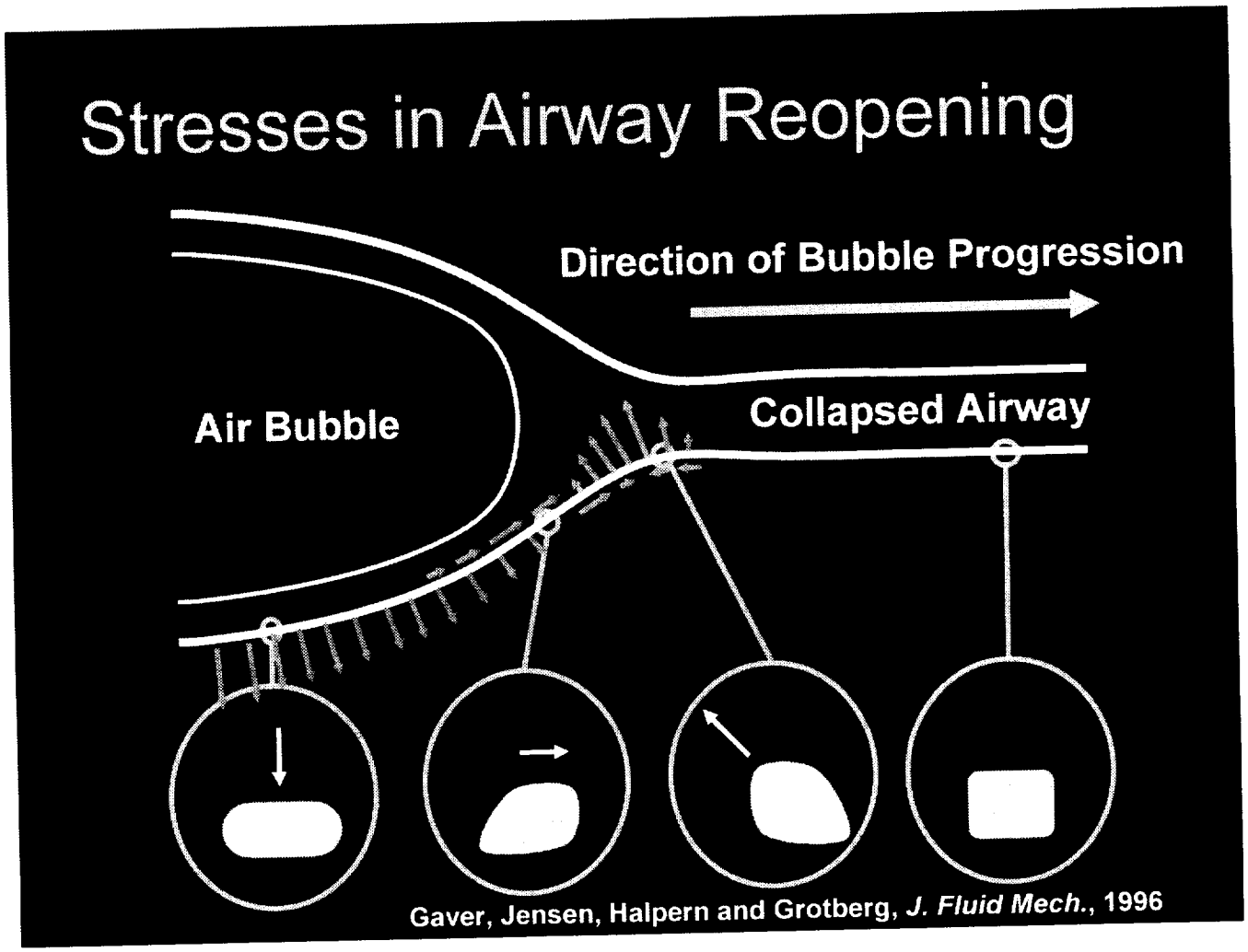
Stresses in Airway Reopening
Direction of Bubble Progression
Air Bubble
Collapsed Airway
Gaver, Jensen, Halpern and Grotberg, J. Fluid Mech., 1996

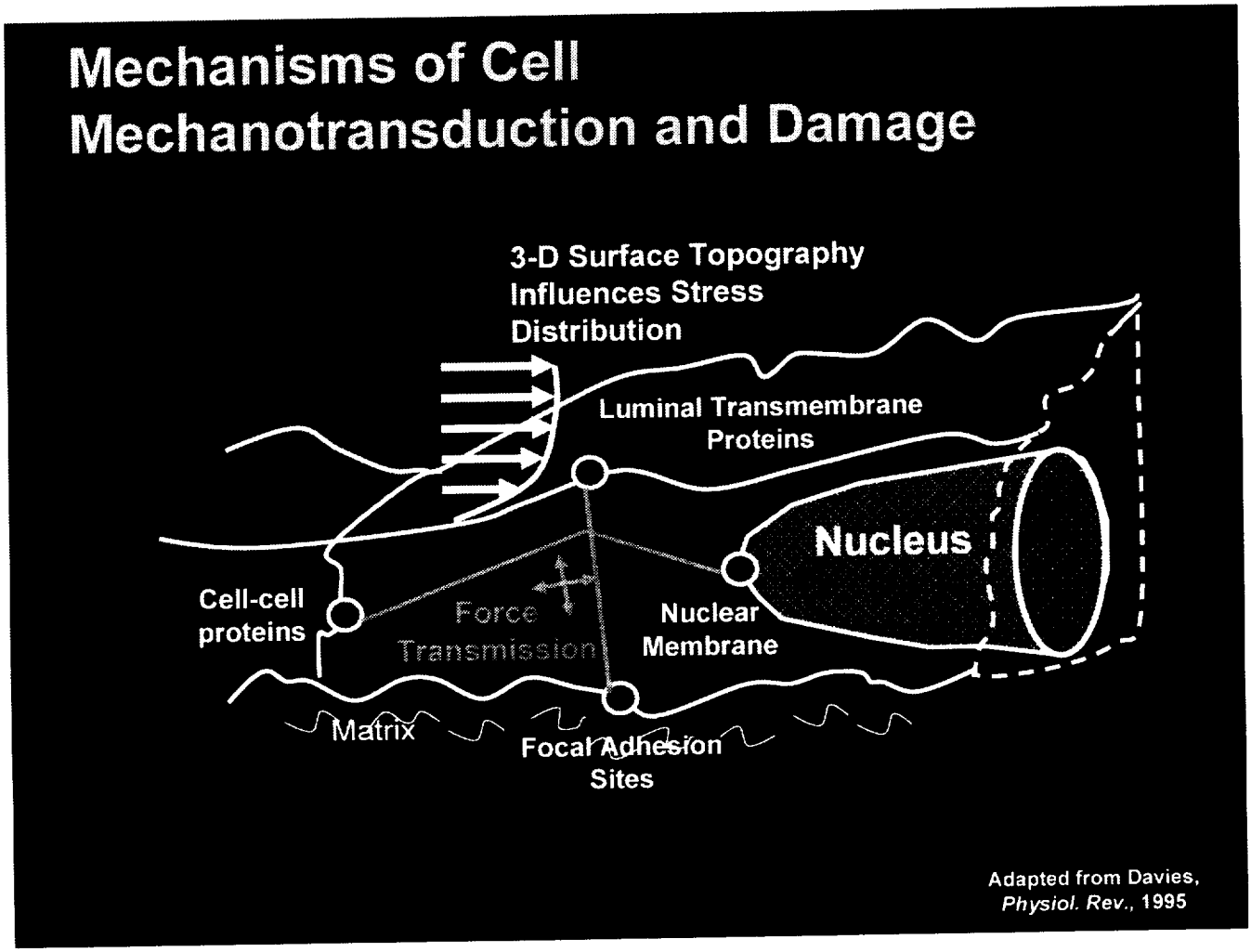
Mechanisms of Cell
Mechanotransduction and Damage
3-D Surface Topography
Influences Stress
Distribution
Luminal Transmembrane
Proteins
Nucleus
Cell-cell
proteins
Force
Transmission
Nuclear
Membrane
Matrix
Focal Adhesion
Sites
Adapted from Davies,
Physiol. Rev., 1995

Investigations of Cellular Trauma During Airway Reopening

Collaborators: K. C Dee and A. Bilek

Hypothesis:

Mechanical stresses during airway reopening cause cellular trauma contributing to focal epithelial cell death and basement membrane denudation seen in ALI.

Cell Culture Experiments

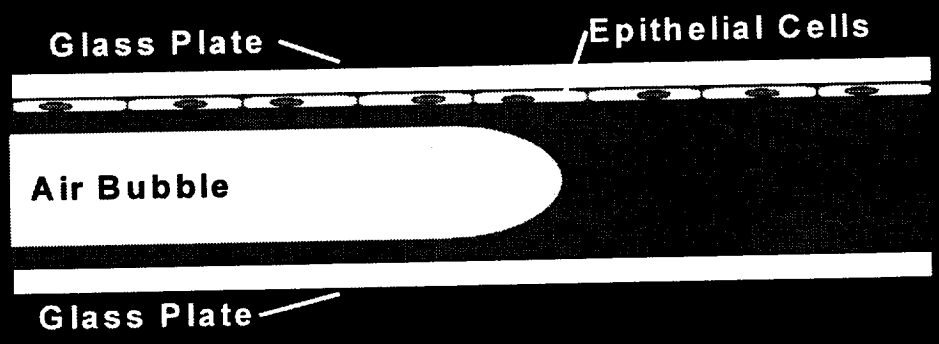

Lung epithelial cells were:

- **cultured in an idealized model of small airways,**
- **exposed to a moving finger of air under reopening conditions,**
- **examined for cellular trauma.**

Methods

- Lung epithelial cells (CRL-149, ATCC) cultured to confluence on glass microscope slides.
- The channel dimensions were 2.5 x 7.0 x 0.17 cm.
- Two velocities (0.27 and 2.7 cm/s) were assessed.
- Two occlusion fluids were assessed:
  - phosphate buffered saline (PBS) and
  - 1 mg/mL Infasurf (ONY, Inc., Buffalo, NY) in PBS.
- Cellular trauma was quantified using fluorescent staining (Live/Dead Kit, Molecular Probes).

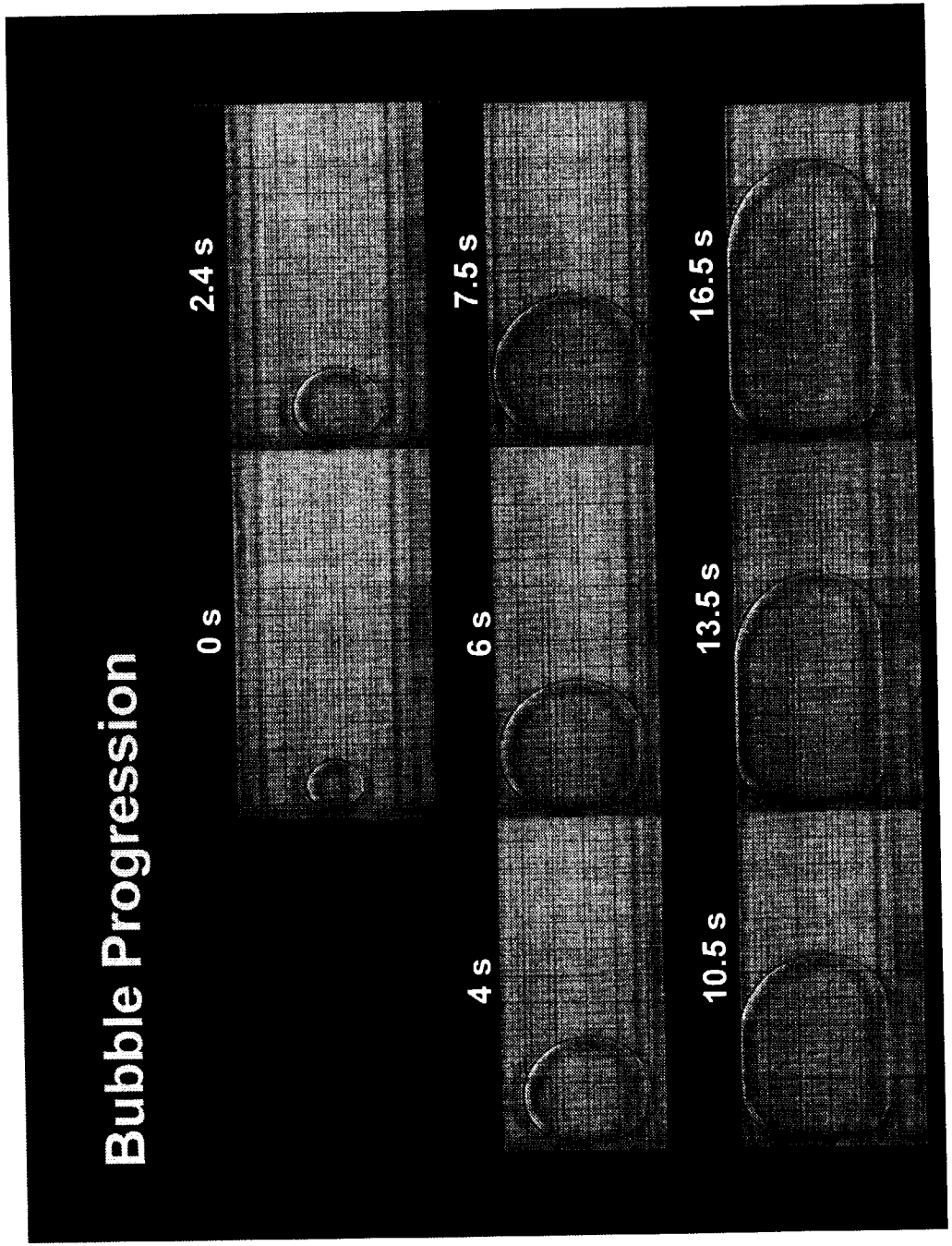
Bubble Progression
0 s
2.4 s
4 s
6 s
7.5 s
10.5 s
13.5 s
16.5 s

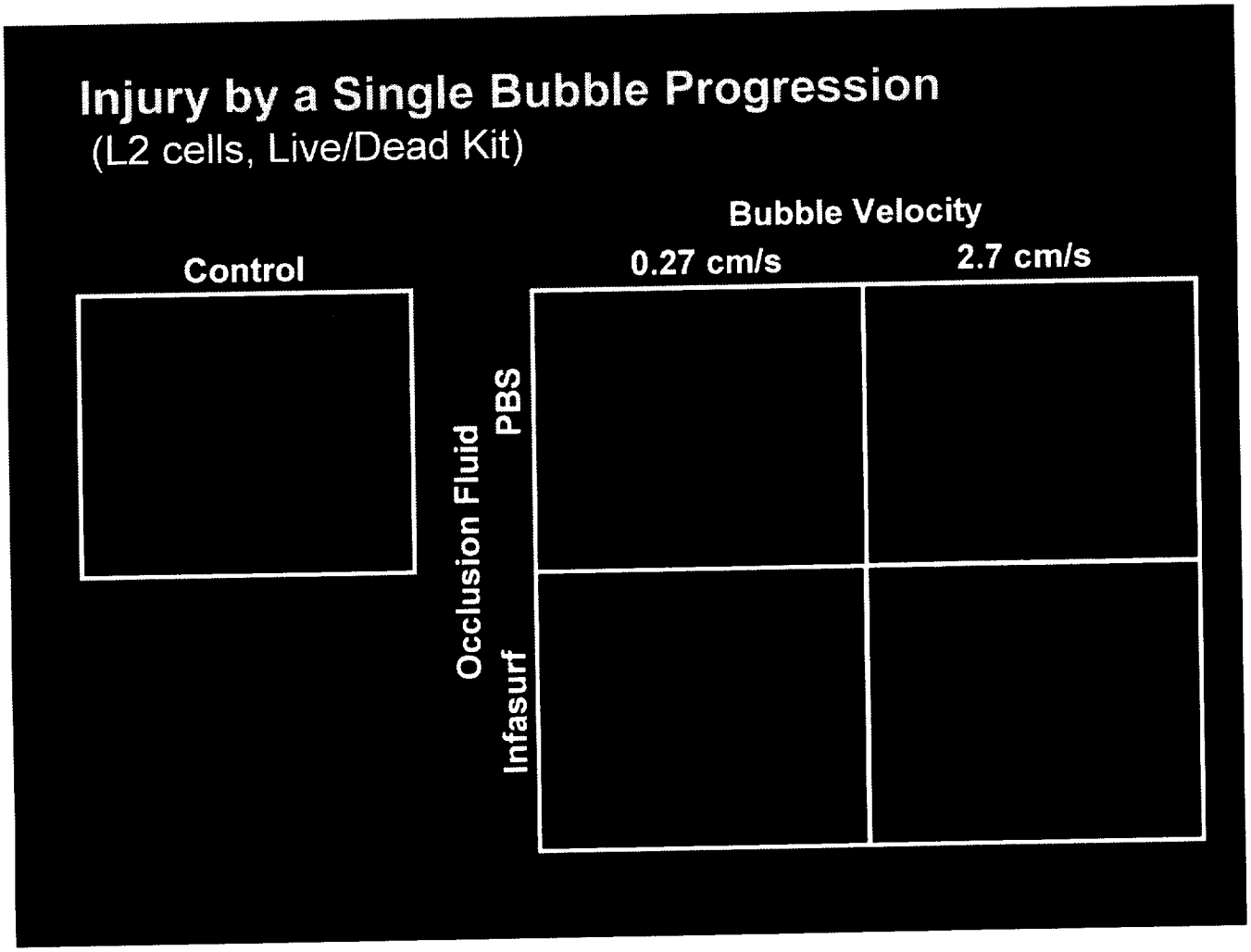
Injury by a Single Bubble Progression
(L2 cells, Live/Dead Kit)
Bubble Velocity
0.27 cm/s
2.7 cm/s
Control
Occlusion Fluid
PBS
Infasurf

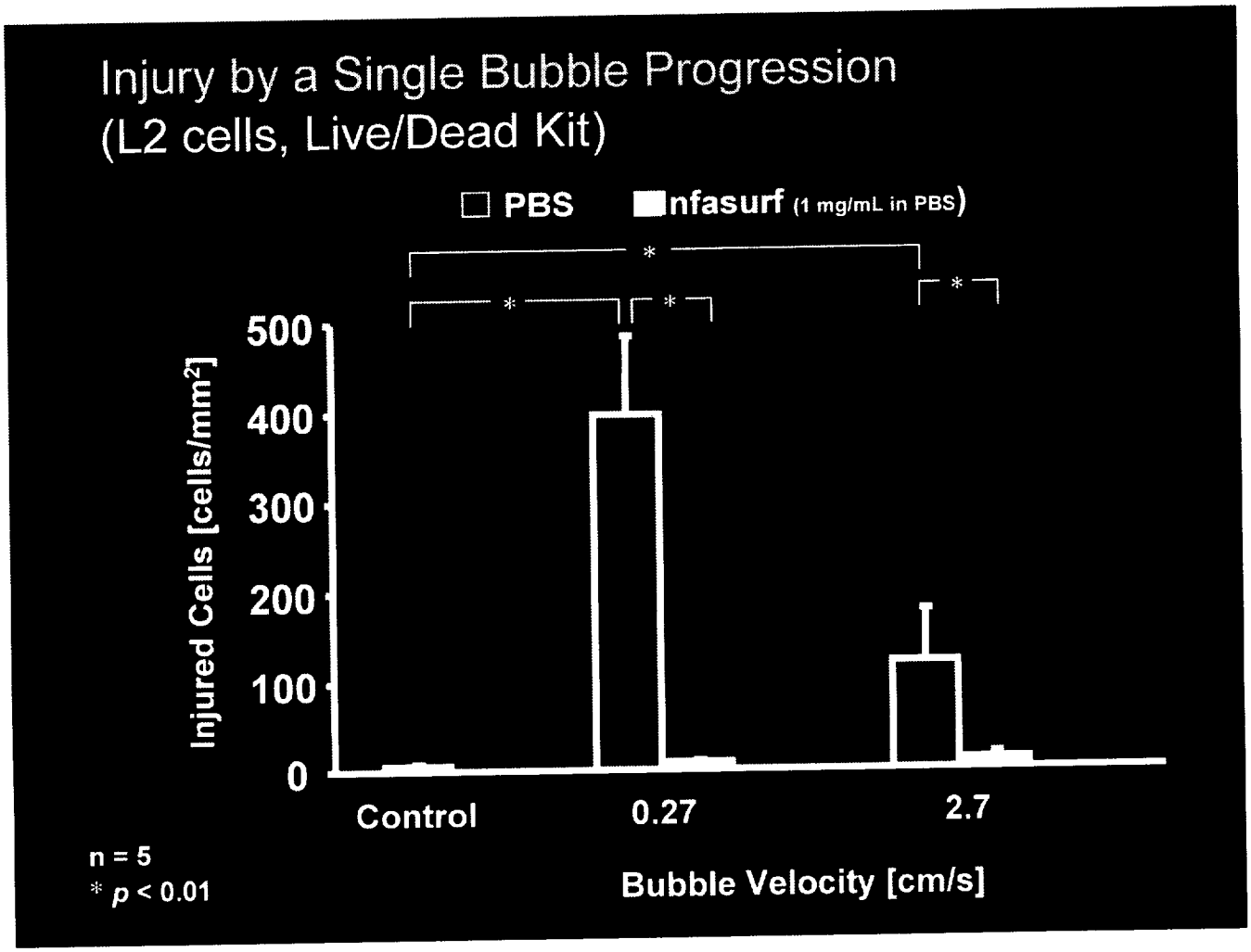
Injury by a Single Bubble Progression
(L2 cells, Live/Dead Kit)
PBS
nfasurf (1 mg/mL in PBS)
*
*
*
*
500
400
300
200
100
0
Injured Cells [cells/mm²]
Control
0.27
2.7
Bubble Velocity [cm/s]
n = 5
* p < 0.01

Experimental Conclusion

- Progression of an air-bubble across cells causes short-term disruption of the cell membrane
- The response is modulated by lowering the surface tension with surfactant
- The cell damage is likely to be due to mechanical stress.

Computational Investigation

- We model this system to identify the mechanical effects due to fluid-structure interaction.

Hypotheses of mechanisms:

- Shear stress
- Shear stress gradient
- Pressure gradient
- Topography

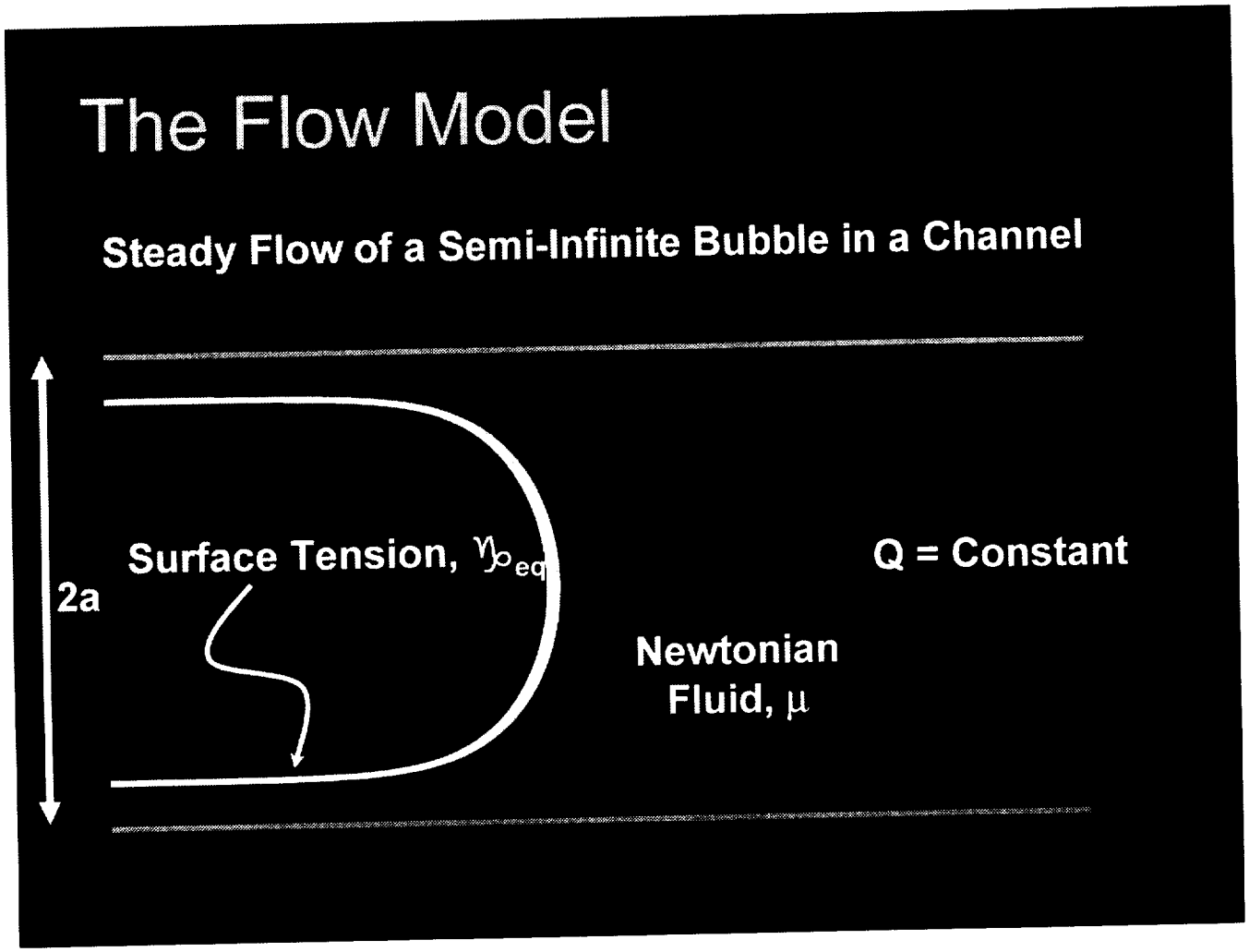
The Flow Model
Steady Flow of a Semi-Infinite Bubble in a Channel
2a
Surface Tension, γ_{eq}
Q = Constant
Newtonian
Fluid, μ

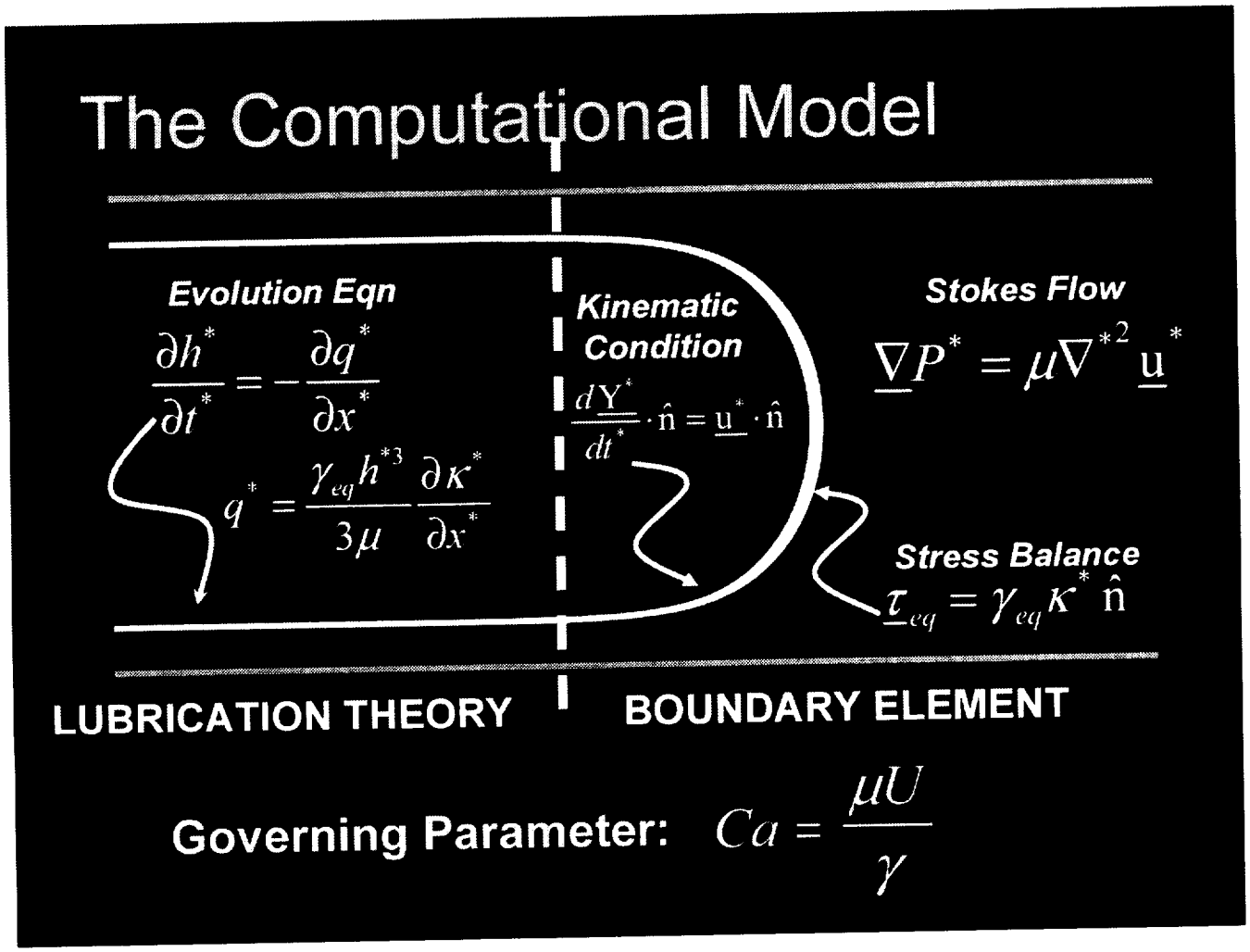
The Computational Model
Evolution Eqn
$\frac{\partial h^*}{\partial t^*} = -\frac{\partial q^*}{\partial x^*}$
$q^* = \frac{\gamma_{eq} h^{*3}}{3\mu} \frac{\partial \kappa^*}{\partial x^*}$
Kinematic Condition
$\frac{d\underline{Y}^*}{dt^*} \cdot \hat{n} = \underline{u}^* \cdot \hat{n}$
Stokes Flow
$\underline{\nabla} P^* = \mu \nabla^{*2} \underline{u}^*$
Stress Balance
$\underline{\tau}_{eq} = \gamma_{eq} \kappa^* \hat{n}$
LUBRICATION THEORY
BOUNDARY ELEMENT
Governing Parameter: $Ca = \frac{\mu U}{\gamma}$

Predictions of Cell Shear Stress

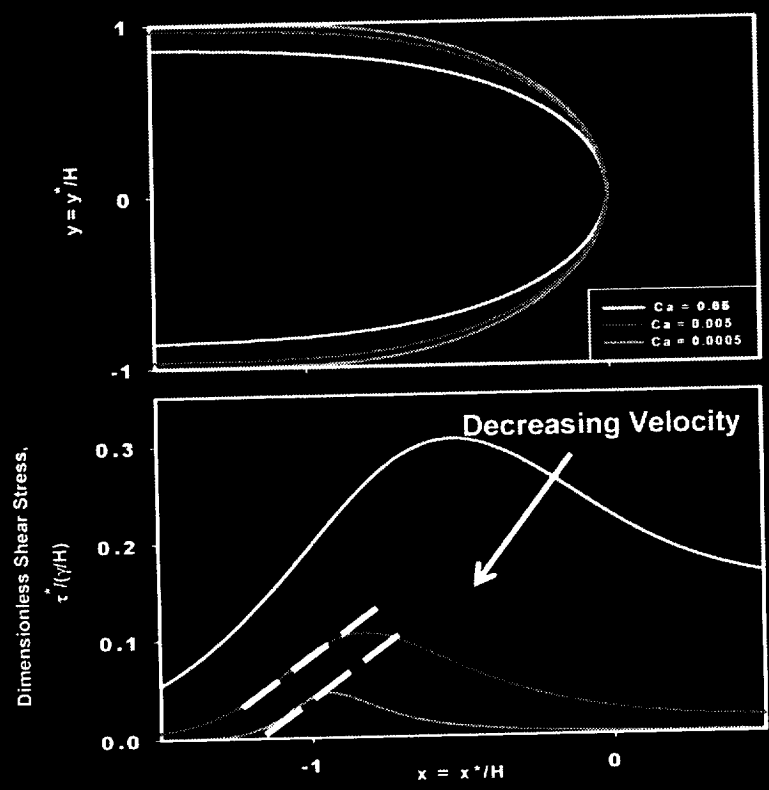

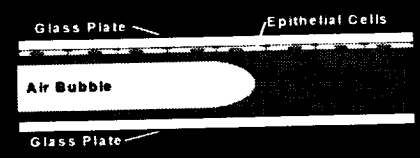

1. Shear Stress decreases with decreasing velocity

2. Shear Stress Gradient becomes nearly constant with decreasing velocity

Predictions of Cell Normal Stresses

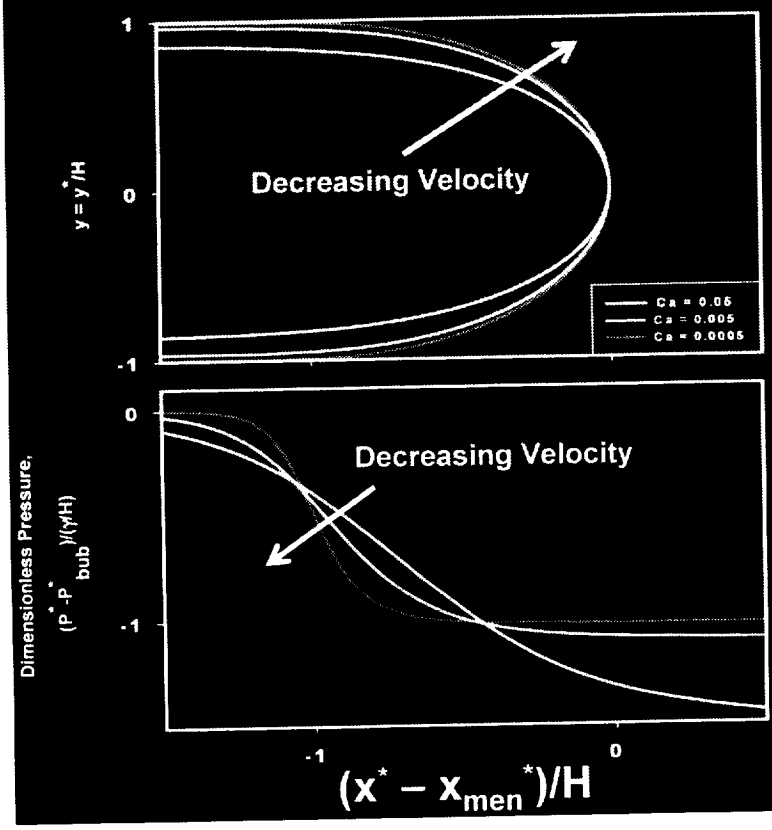

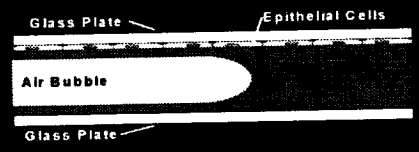

1. Film Thickness decreases with decreasing velocity
2. The pressure gradient on the cell surface increases with decreasing velocity

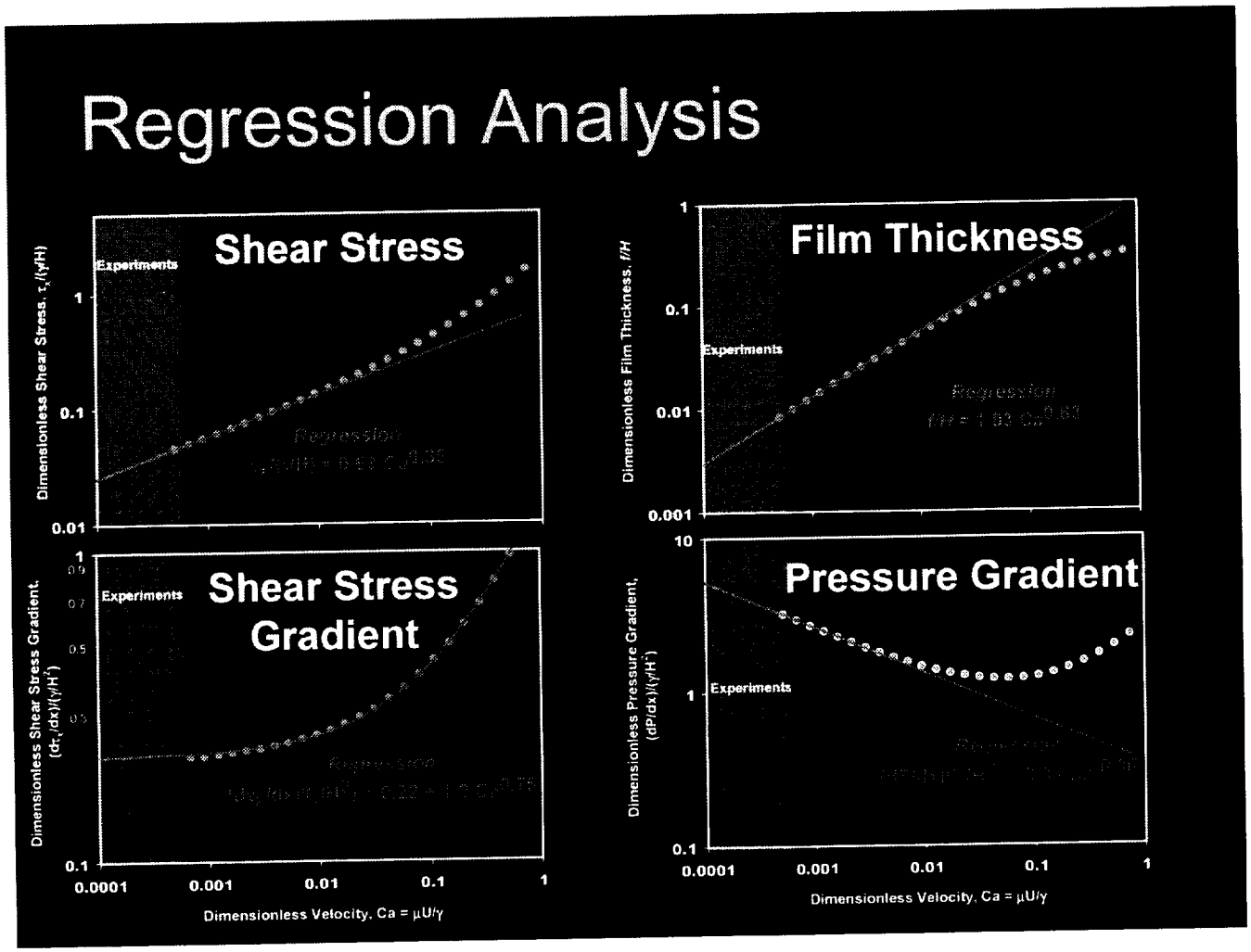
Regression Analysis
Shear Stress
Experiments
Dimensionless Shear Stress, $\tau_x/(\gamma/H)$
1
0.1
0.01
Film Thickness
Experiments
Dimensionless Film Thickness, f/H
1
0.1
0.01
0.001
Shear Stress Gradient
Experiments
Dimensionless Shear Stress Gradient, $(d\tau_x/dx)/(\gamma/H^2)$
1
0.9
0.7
0.5
0.3
0.1
Pressure Gradient
Experiments
Dimensionless Pressure Gradient, $(dP/dx)/(\gamma/H^2)$
10
1
0.1
0.0001
0.001
0.01
0.1
1
Dimensionless Velocity, Ca = μU/γ
Dimensionless Velocity, Ca = μU/γ

Predictions

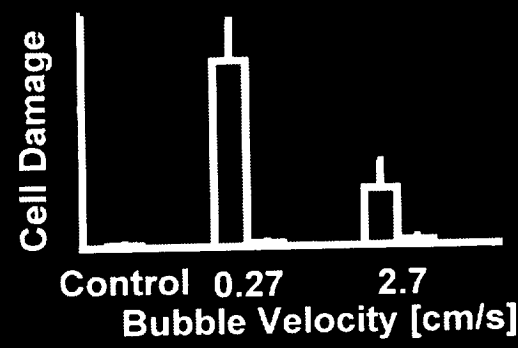

Fluid	Speed	Φ_s (dyn/cm²)	Φ_g (dyn/cm²)	P (dyn/cm²)	f (Ωm)
Saline	Slow	15.5			
Saline	Fast	34.3			
Infasurf	Slow	7.9			
Infasurf	Fast	17.5			

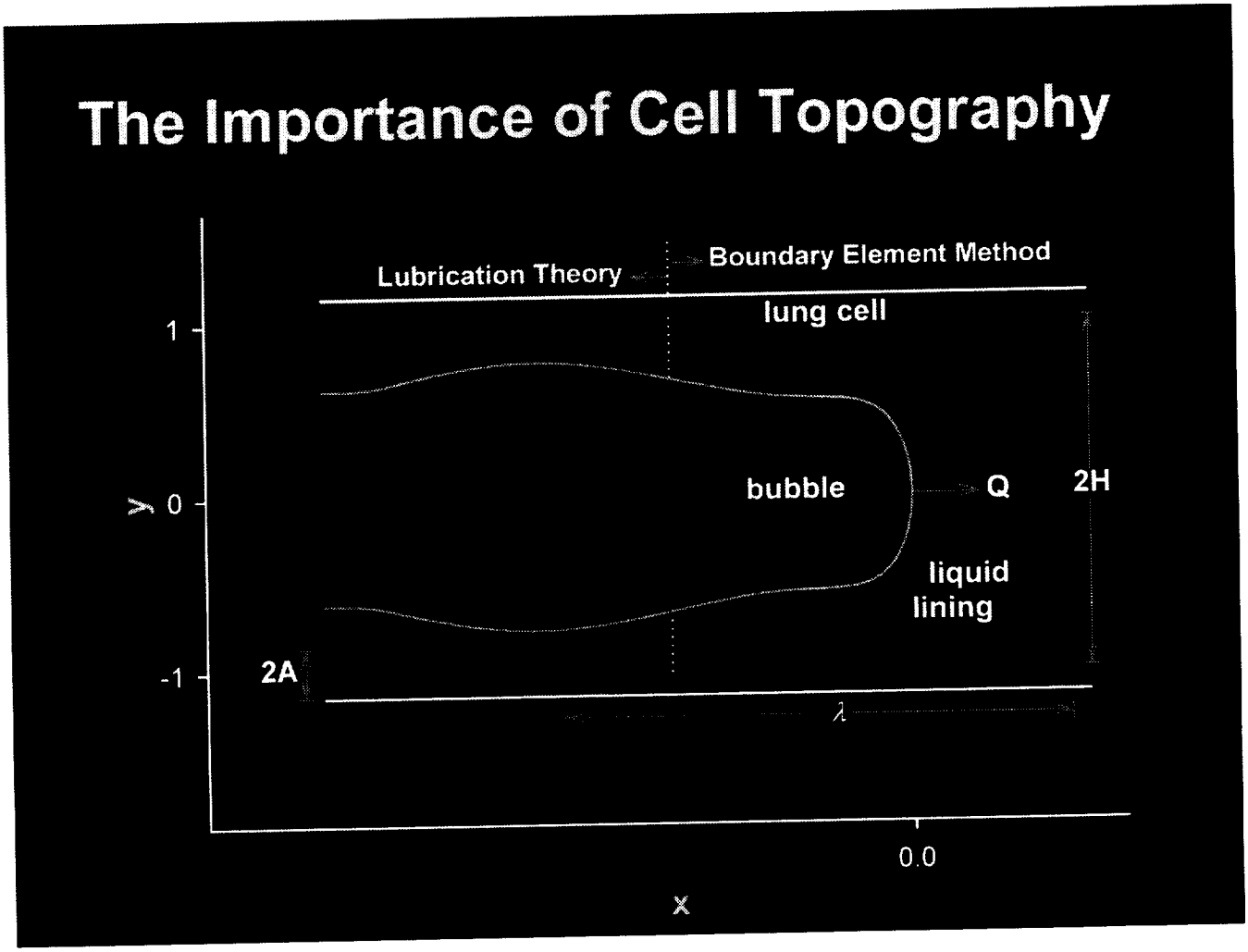
The Importance of Cell Topography
Lubrication Theory
Boundary Element Method
lung cell
1
0
-1
y
bubble
Q
2H
liquid
lining
2A
λ
0.0
x

Normal Stress Distribution

A/H = 0.1, λ/H = 2, Ca = 0.01

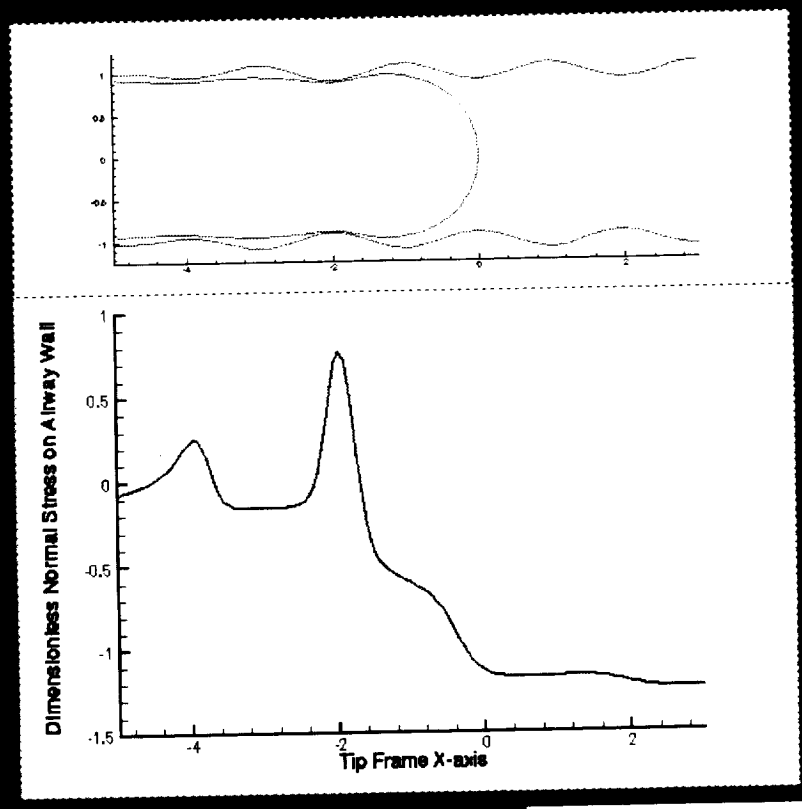

Click here to play movie

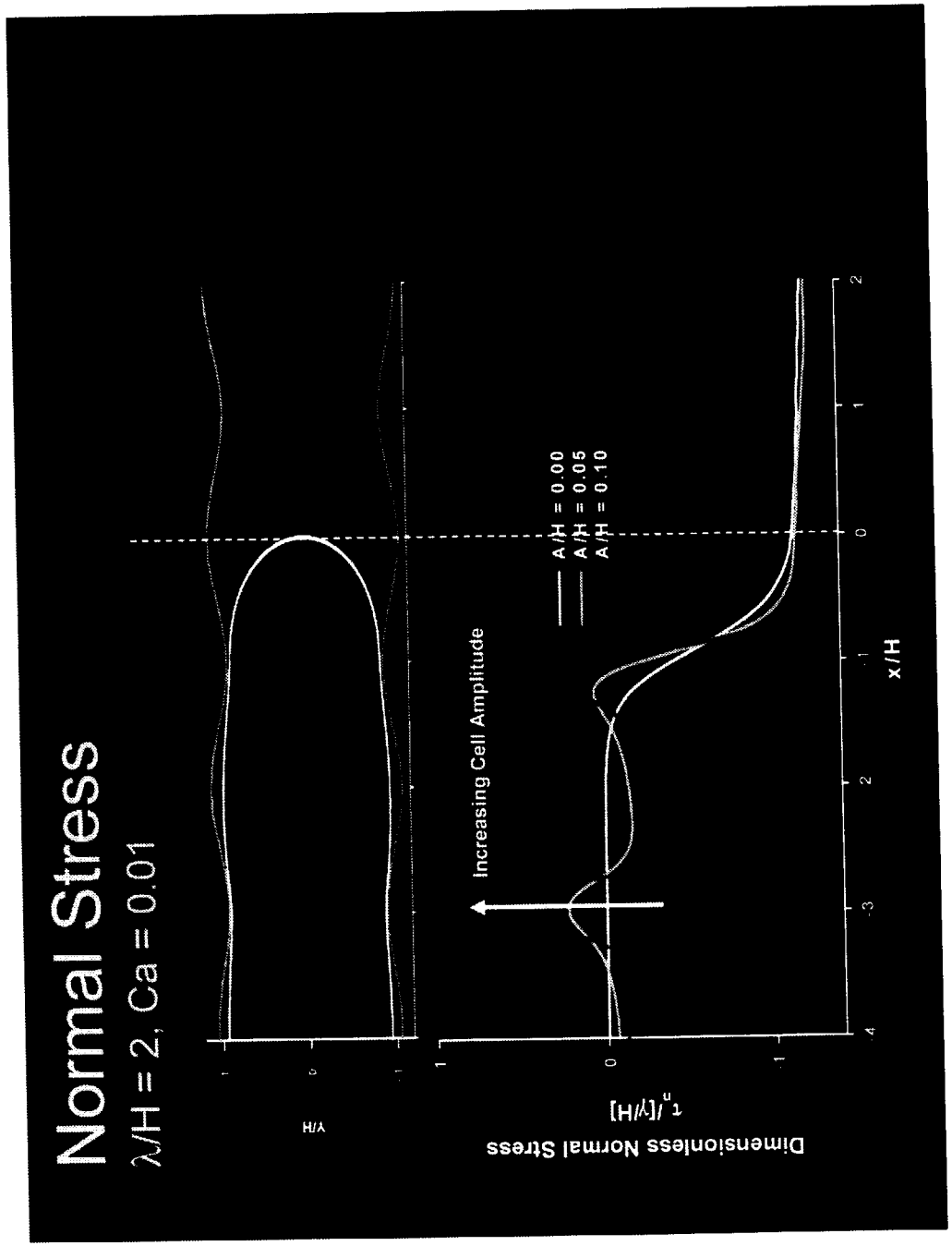
Normal Stress
λ/H = 2, Ca = 0.01
Y/H
Increasing Cell Amplitude
A/H = 0.00
A/H = 0.05
A/H = 0.10
Dimensionless Normal Stress
τn/[γ/H]
x/H

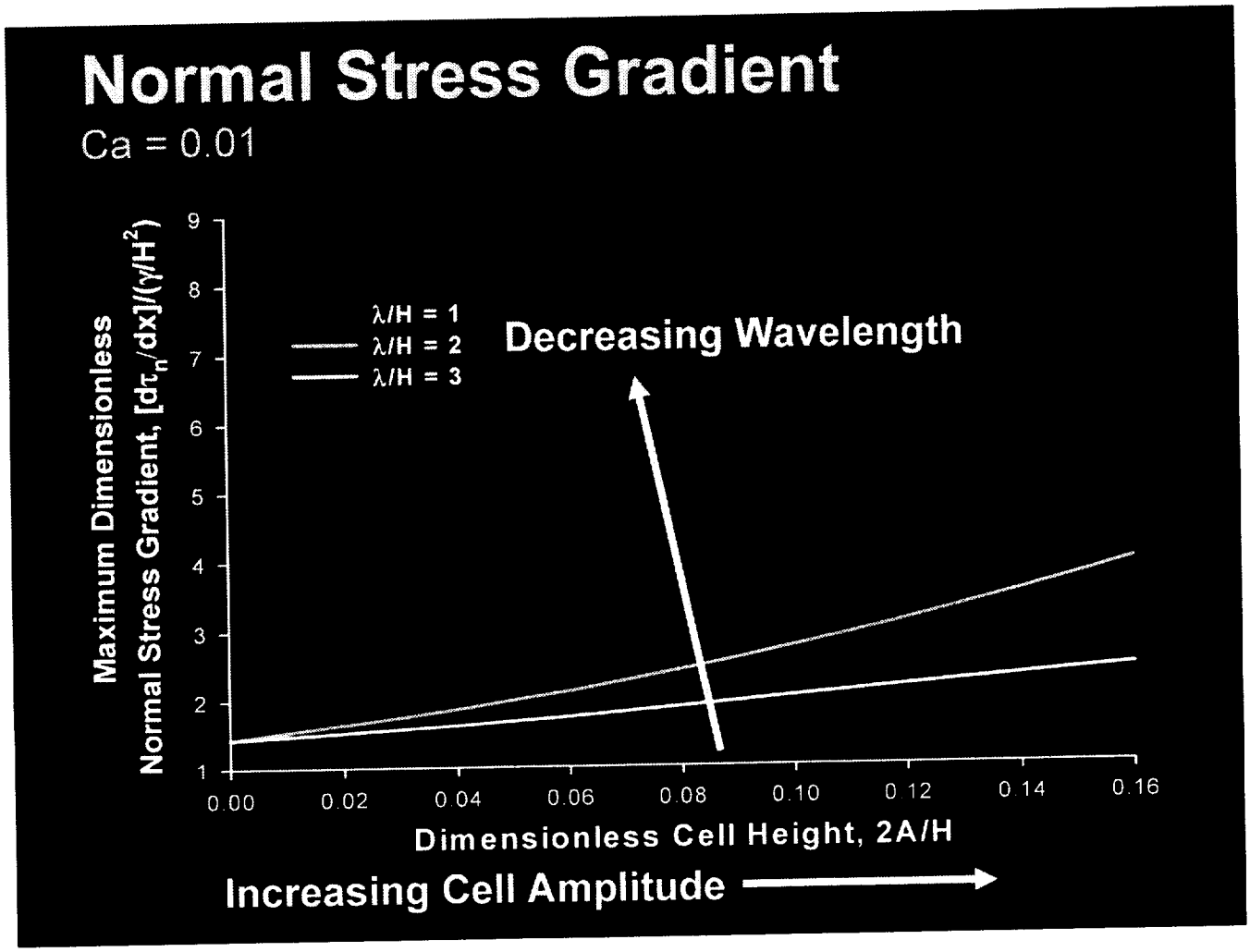
Normal Stress Gradient
Ca = 0.01
Maximum Dimensionless
Normal Stress Gradient, [dτn/dx]/(γ/H²)
λ/H = 1
λ/H = 2
λ/H = 3
Decreasing Wavelength
9
8
7
6
5
4
3
2
1
0.00
0.02
0.04
0.06
0.08
0.10
0.12
0.14
0.16
Dimensionless Cell Height, 2A/H
Increasing Cell Amplitude

Tangential Stress Distribution

A/H = 0.1, λ/H = 2, Ca = 0.01

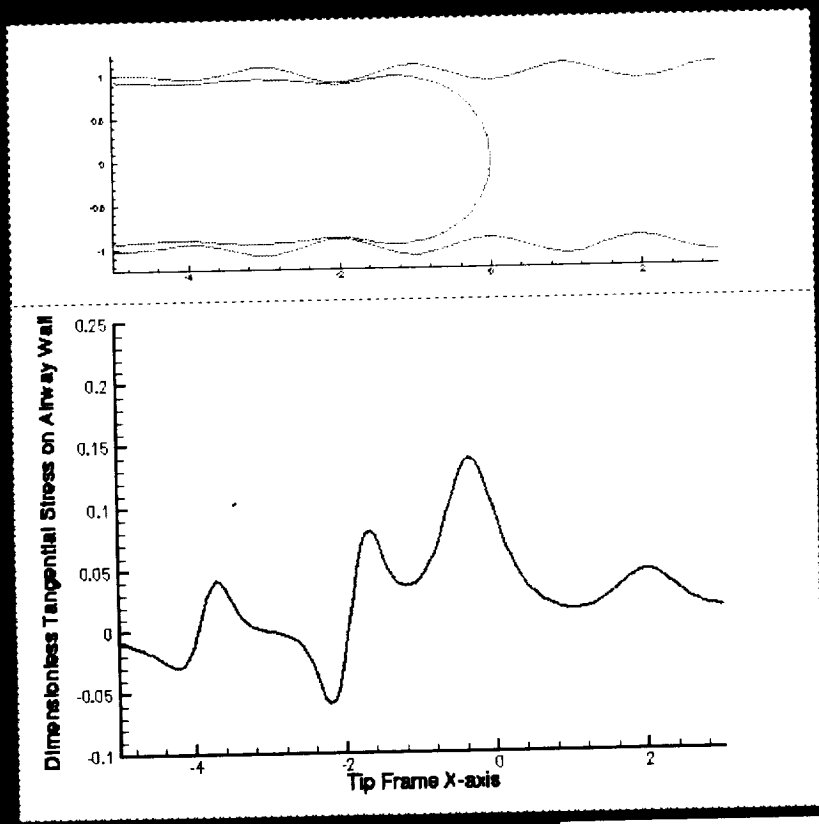

Click here to play movie

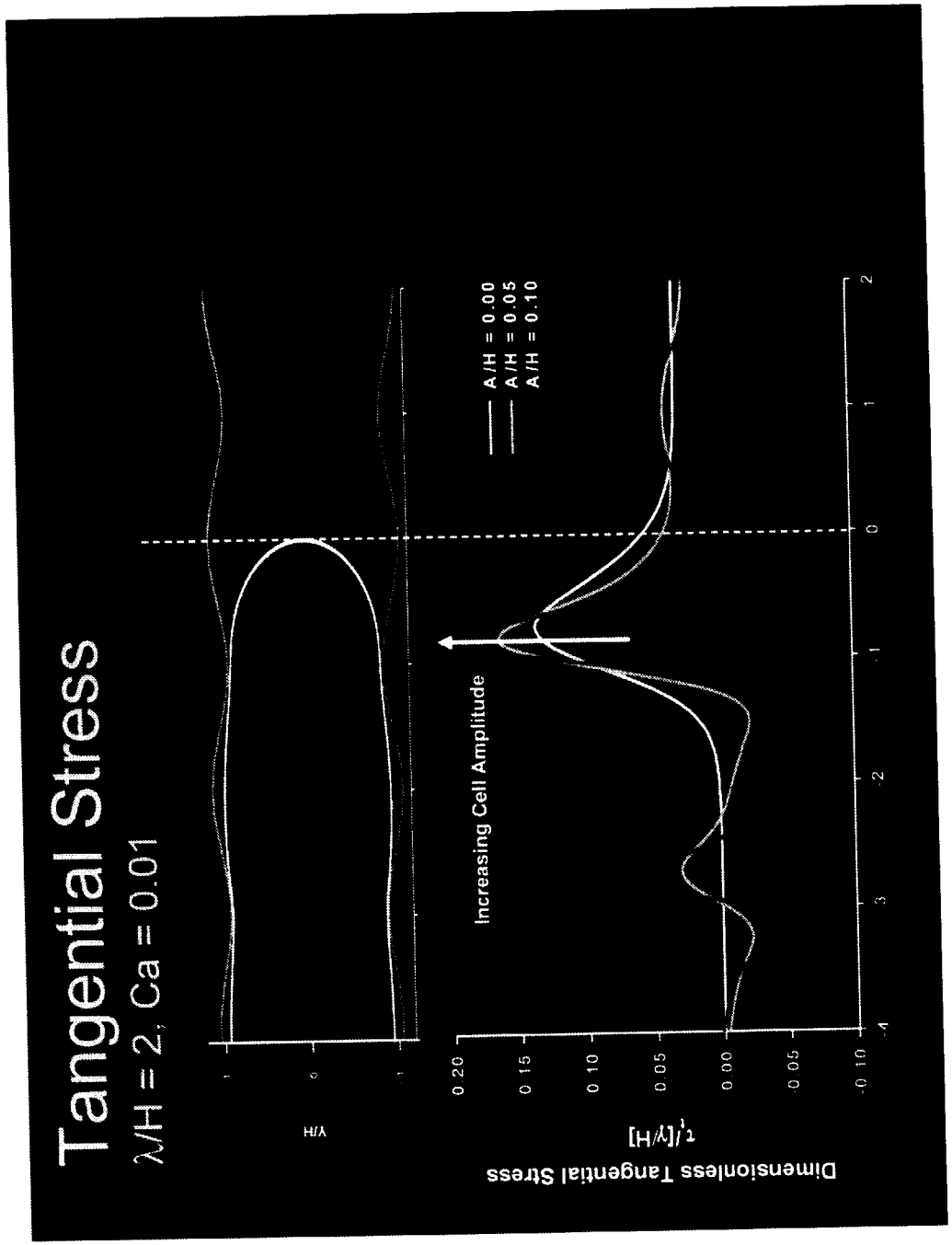
Tangential Stress
λ/H = 2, Ca = 0.01
Y/H
Increasing Cell Amplitude
A/H = 0.00
A/H = 0.05
A/H = 0.10
Dimensionless Tangential Stress
τ_t/[γ/H]
0.20
0.15
0.10
0.05
0.00
-0.05
-0.10
-4
-3
-2
-1
0
1
2

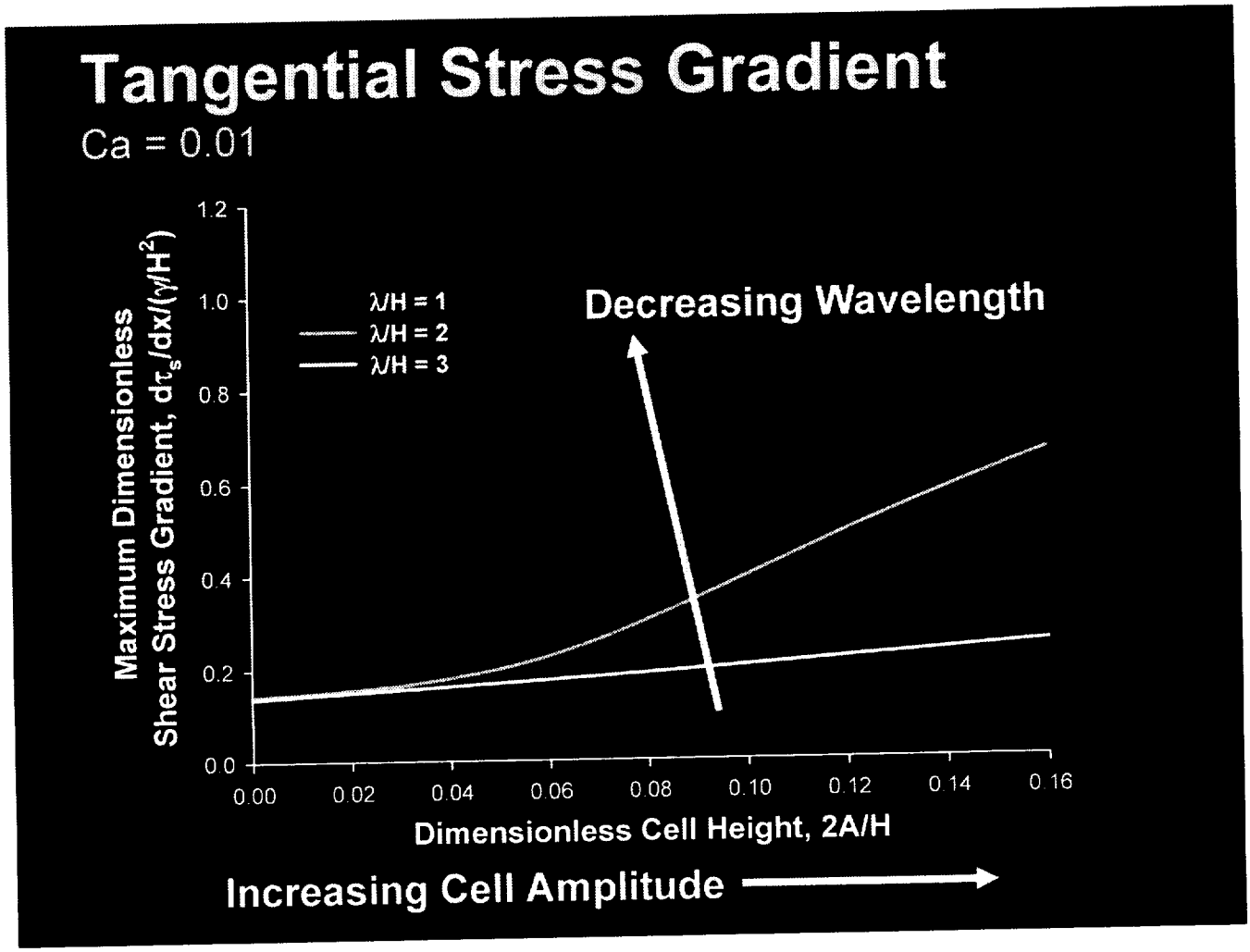
Tangential Stress Gradient
Ca = 0.01
Maximum Dimensionless
Shear Stress Gradient, $d\tau_s/dx/(\gamma/H^2)$
1.2
1.0
0.8
0.6
0.4
0.2
0.0
λ/H = 1
λ/H = 2
λ/H = 3
Decreasing Wavelength
0.00
0.02
0.04
0.06
0.08
0.10
0.12
0.14
0.16
Dimensionless Cell Height, 2A/H
Increasing Cell Amplitude

Substrate Denudation by Repetitive Bubble Progression (L2 cells, Infusion Rate 20 mL/min = ~ 2 cm/s)

Number of Bubble Passes

Control **1** **5** **20**

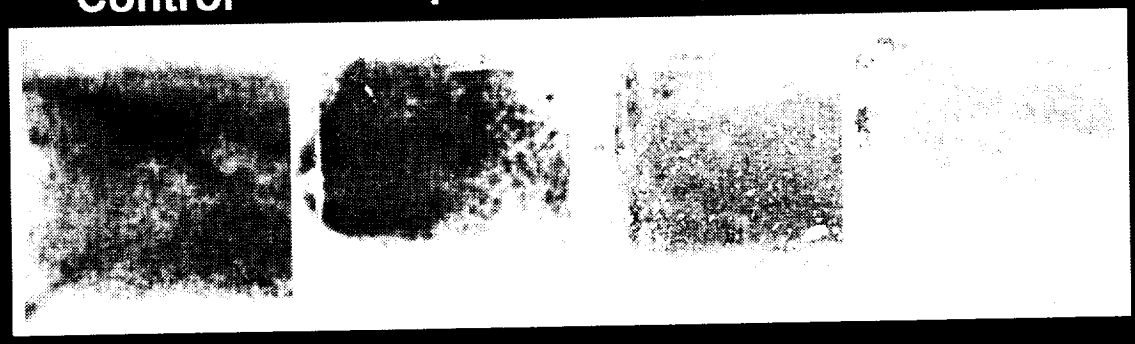

Repetitive "closure" and "reopening" of an occluded narrow channel lined with live lung epithelial cells significantly denudes the channel walls.

Conclusions

- Bubble progression inflicts significant injury on a monolayer of cells *in vitro*.
- The presence of pulmonary surfactant eliminates this injury.
- The injury is due to transient, steep pressure gradients, inducing an enormous pressure difference across the cell.
- Topological effects may be important.
- This model could potentially be used to further investigate airway reopening injury mechanisms, lung injury consequences, and surfactant replacement effectiveness.

PROTEIN VIRIAL COEFFICIENTS FROM SIZE EXCLUSION CHROMATOGRAPHY

Seth Fraden[A], Joshua Bloustine, Viatcheslav Berejnov
Martin Fisher School of Physics, Brandeis University

ABSTRACT

An improved method is presented for measuring protein virial coefficients from retention time measurements in size exclusion chromatography (SEC). Second virial coefficients for the self-interaction of lysozyme have been determined by analyzing the concentration dependence of the partition coefficient obtained from SEC studies on silica beads. Our SEC results show agreement with virial coefficients obtained by light scattering.

It is well known in the standard practice of size exclusion liquid chromatography (SEC) that the solute retention time depends sensitively on the solute's excluded volume. It has also been realized that the thermodynamic non-ideality resulting from any excluded volume leads to a *concentration* dependence of the retention time[1], and that such dependence can be utilized to quantify the second osmotic virial coefficient, B_2 by $\mathrm{Ln}\left(\frac{K_D}{K_0}\right) = 2B_2\frac{N_A}{M_w}C_i(1-K_D)$. Here K_D and K_0 are the SEC distribution coefficients for finite and zero concentration, respectively, M_w the solute molecular weight and N_A Avogadro's number. Second virial coefficients are often reported as $A_2 = B_2\frac{N_A}{M_w^2}$.

Winzor et al's[1] measurements of B_2 employed frontal elution liquid chromatography. Although frontal chromatography allows one to fix the solute concentration in the column directly, it requires a large amount of protein ($\approx 2.5g$) and (prohibitively) long experiment times (≈ 2 days). We extend their method to modern SEC, which necessitates a consideration of the solute concentration in the column. This adaptation drastically reduces the amount of protein ($\approx 25mg$) and time needed (≈ 2 hours) to measure B_2 by SEC. We show that our results for B_2 from SEC compare quantitatively well to light scattering measurements, and that SEC can track the evolution of B_2 from positive to negative values.

In the above discussion the crucial parameter C_i represents the solute concentration in the *mobile* phase of the migration zone, not the *injected* concentration, C_{nj}. Therefore one must relate C_i to measurable parameters. One measures the mass of solute molecules in the migration zone (m_{zone}) by integrating the concentration as a function of time curve (the peak) over the zone width (V_{zone}). Because the fraction of molecules in the mobile phase is V_{ret}/V_{Total} one has $C_i = \frac{m_{zone}}{V_{zone}}\frac{V_{Total}}{V_{ret}}$ where V_{Total} is the total volume and V_{ret} is the protein retention time.

[A] Address: 415 South St. MS 057, Waltham, MA 02454
fraden@brandeis.edu, fax: 781.736.2915, tel: 781.736.2888

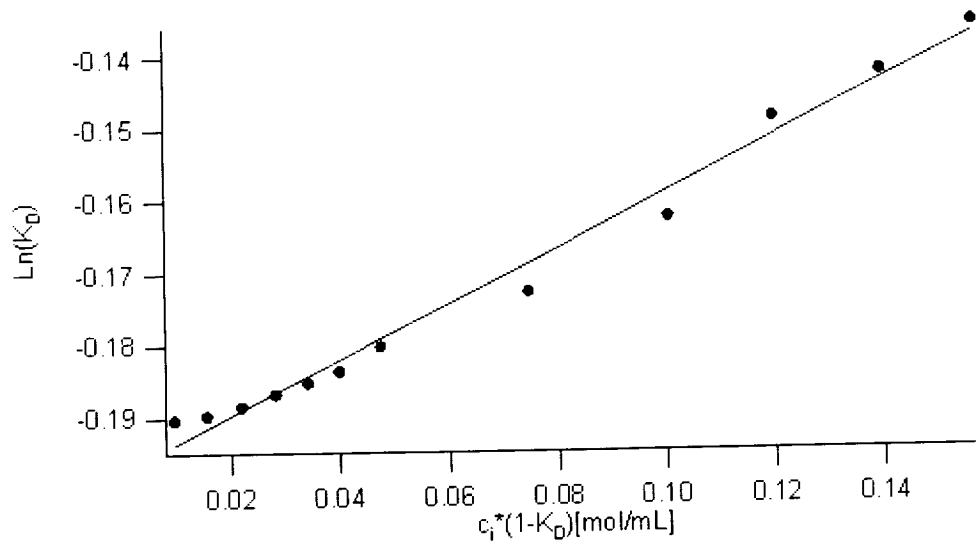

Lysozyme
Buffer: Sodium Acetate 0.05M pH 4.7
Concentration dependent distribution coefficient

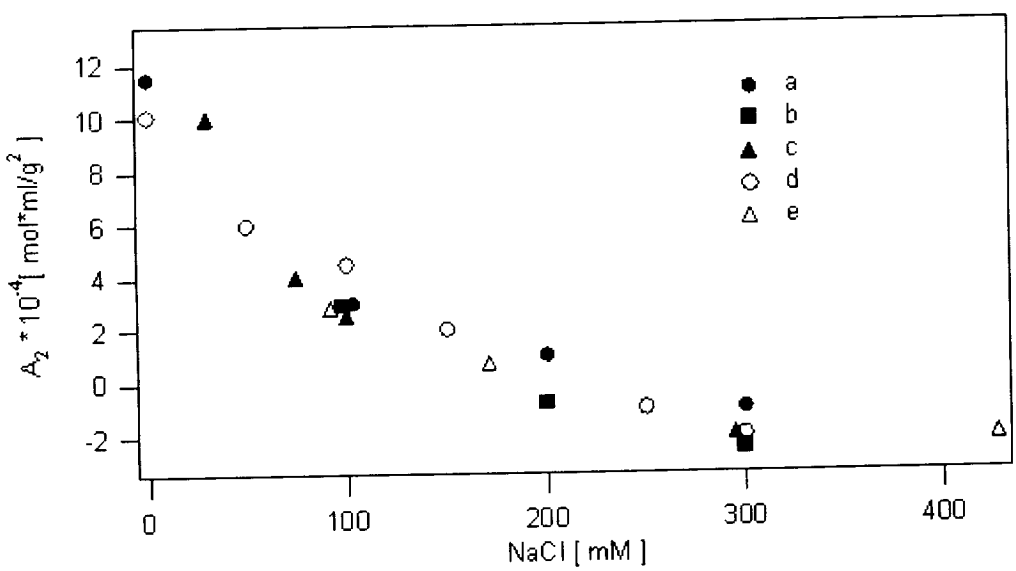

● a: Our SEC data
■ b: C. Gripon et al, *J. Cryst. Gr.*, **178**, 575(1997)
▲ c: O. Velev et al, *Biophys. J.*, **75**, 2682, (1998)
○ d: A. Kulkarni, *Masters Thesis*, U. Illinois(1999)
△ e: M. Muschol et al, *J. Chem. Phys.*, **103**, 10424, (1995)

[1] D.J. Winzor et al, *Biophys. Chem.*, **9**, 47 (1978)

B_2 or not B_2 ...?

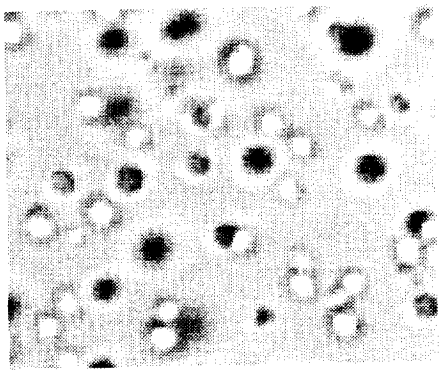

George Thurston
Tuhin Vermani
Joshua Bloustine
Emmanuel Belamie
Viatcheslav Berejnov

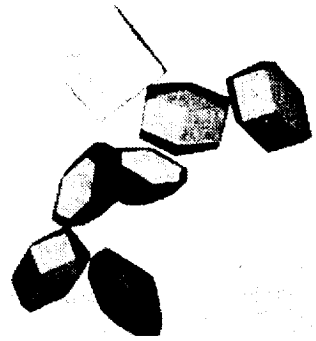

Complex Fluids Group
Brandeis University
www.elsie.brandeis.edu

Support: NASA

Protein Crystallization

Motivation

Structure implies function
X-ray diffraction provides structure
4,000 of 200,000 human proteins crystallized

Tasks

DNA sequence
Expression
Purification
Equilibrium phase diagram
Nucleation
Growth

B_2 or not B_2 … ?

Crystallization slot

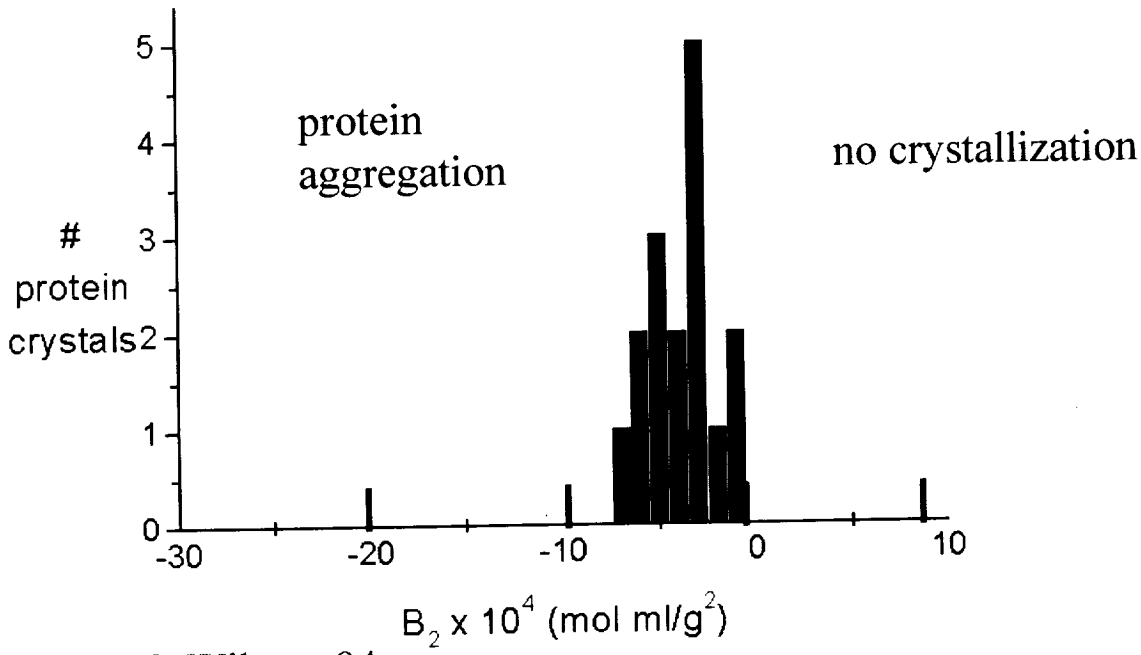

George & Wilson, 94

B_2 or not B_2 … ?

Single component equation of state

Osmotic pressure Π
density ρ

$$\frac{\Pi}{kT} = \rho + B_2(T)\rho^2 + B_3(T)\rho^3 + \ldots$$

Single component ρ

B_2 or not B_2 … ?

2nd virial coefficient B_2

$$B_2 = \frac{1}{2}\int\left(1 - e^{-U(r)/kT}\right)dV$$

$$B_2^{HS} = \frac{1}{2}\frac{4\pi\sigma^3}{3}$$

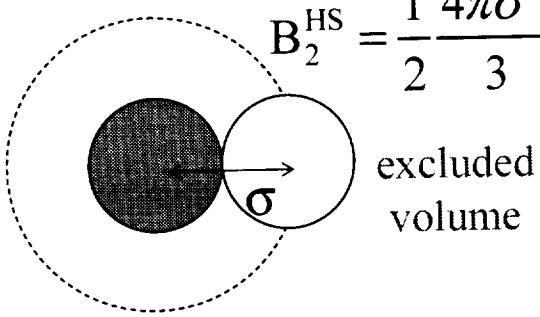

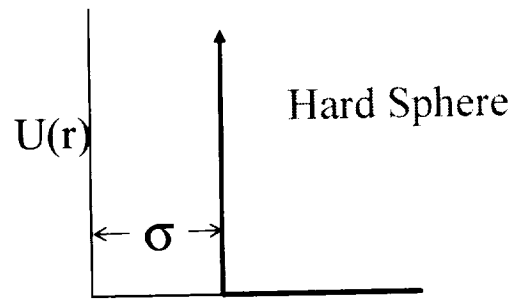

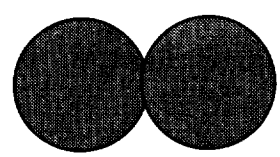

$U(r) = \infty$

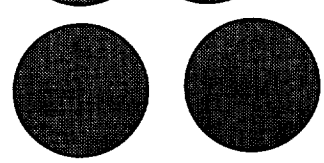

$U(r) = 0$

$B_2 > B_2^{HS}$ repulsion

$B_2 < B_2^{HS}$ attraction

B_2 or not B_2 … ?

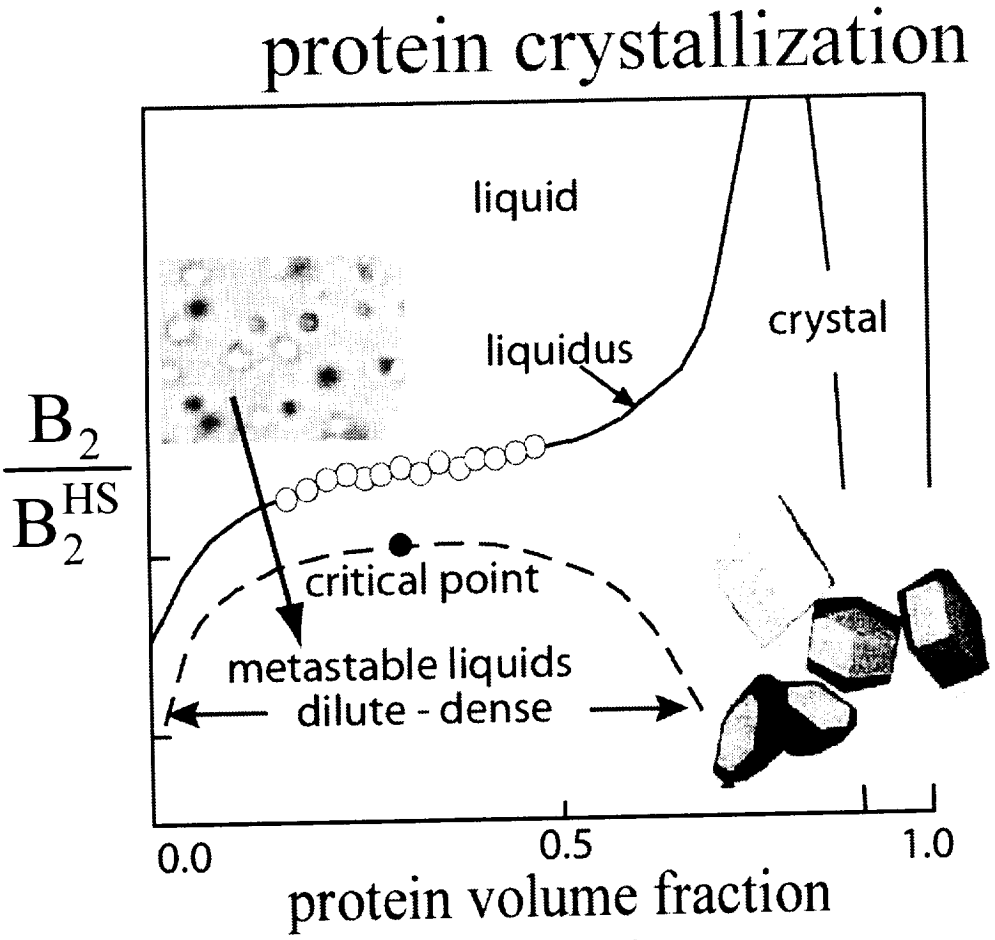

Rosenbaum, Zamora, Zukoski 96

B_2 or not B_2 … ?

mean field free energy density (per kT)

$$G(\phi, B) = \phi^2 (B-4) + \phi \,\mathrm{Log}(\phi) - \frac{\phi - 6\phi^2 + 4\phi^3}{(1-\phi)^2}$$

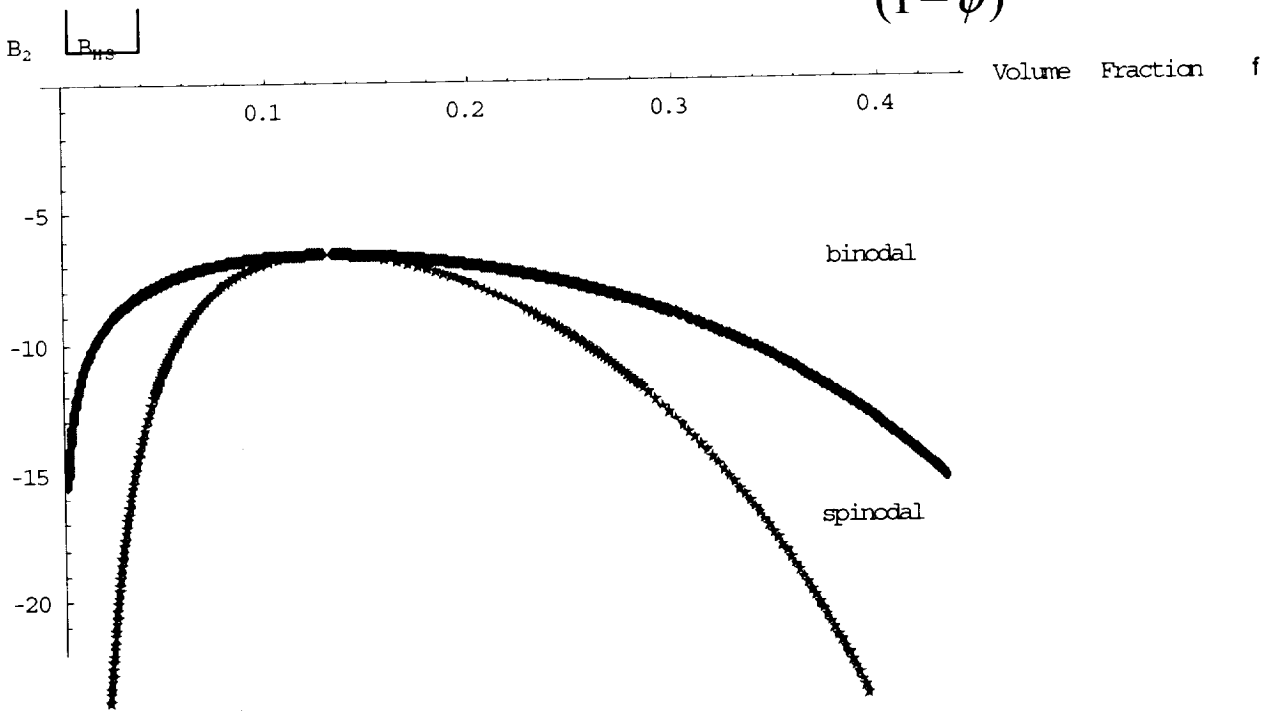

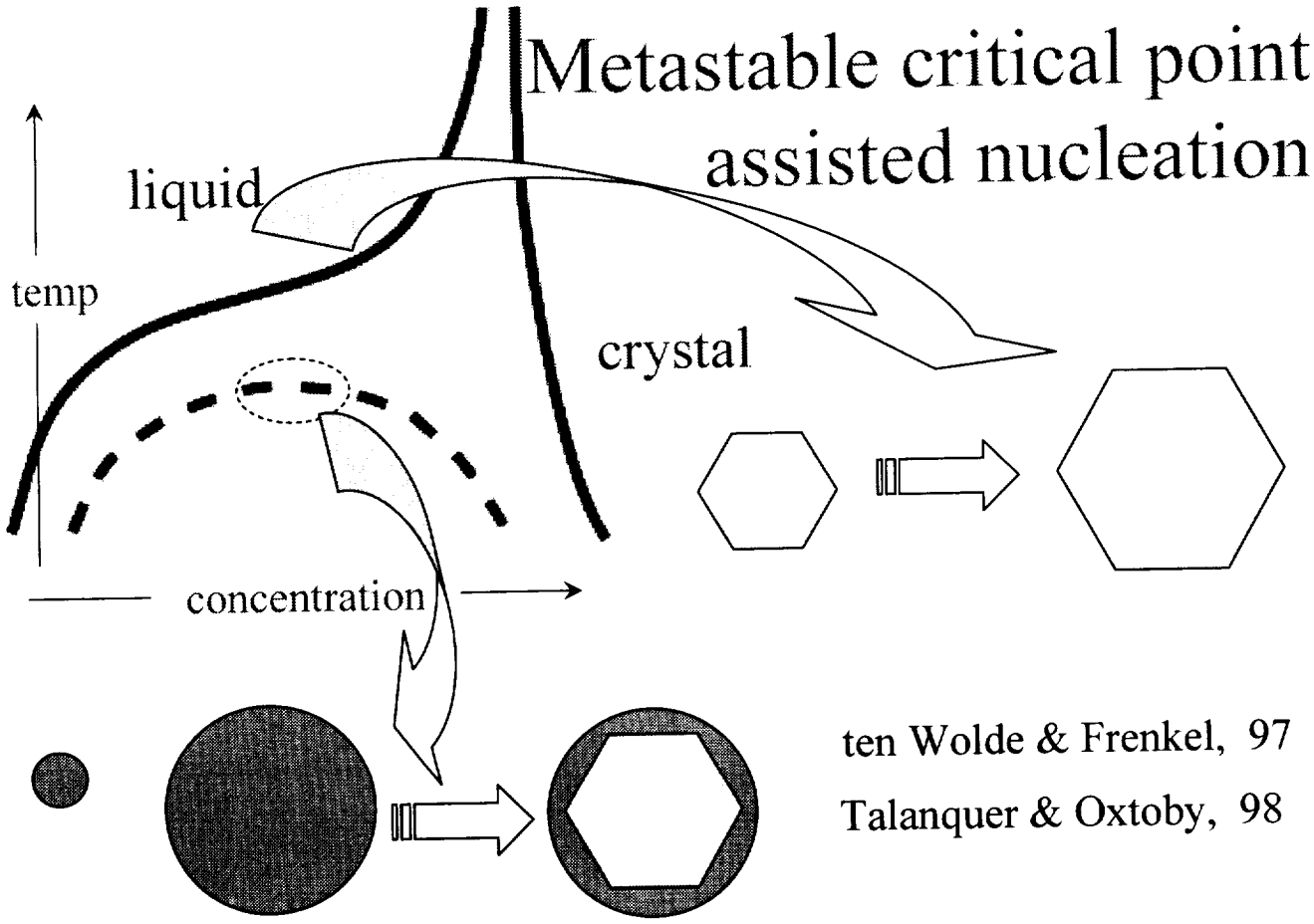
Metastable critical point
assisted nucleation
liquid
temp
crystal
concentration
ten Wolde & Frenkel, 97
Talanquer & Oxtoby, 98

B_2 or not B_2 … ?

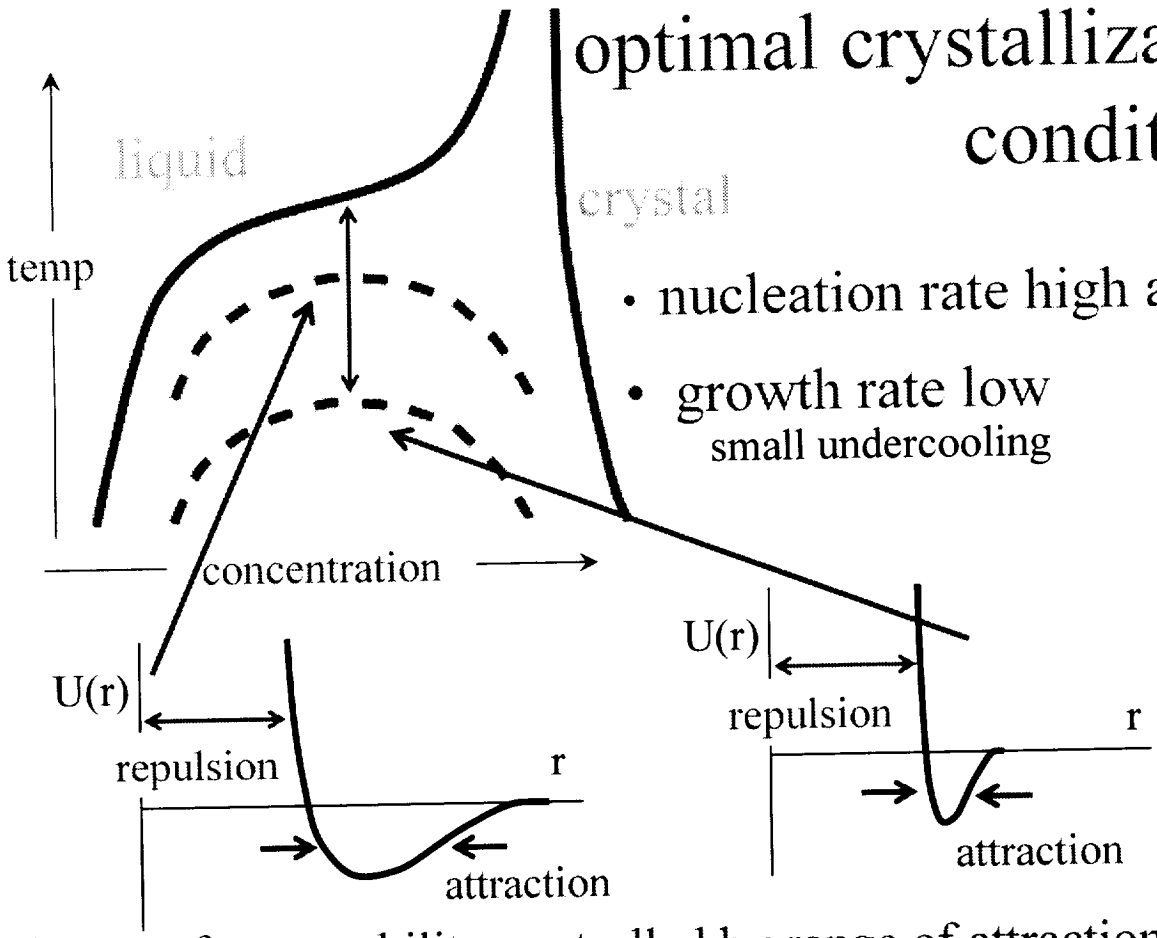

degree of metastability controlled by range of attraction

B_2 or not B_2 … ?

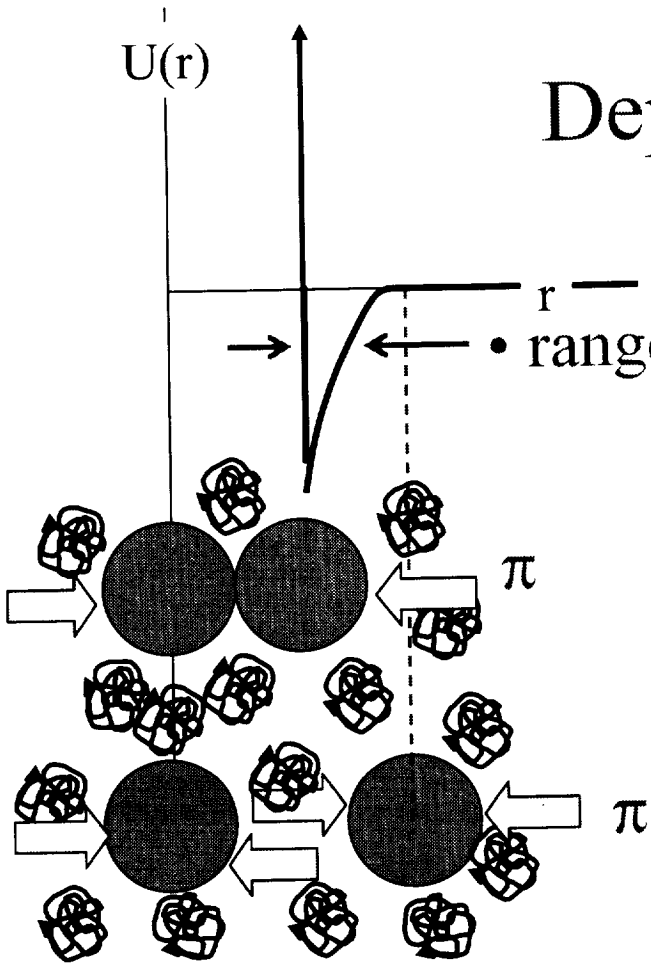

Depletion Attraction

- range of attraction equals polymer diameter
- depth of attraction proportional osmotic pressure

Asakura & Oosawa, 58

B_2 or not B_2 … ?

Depletion attraction & B_2

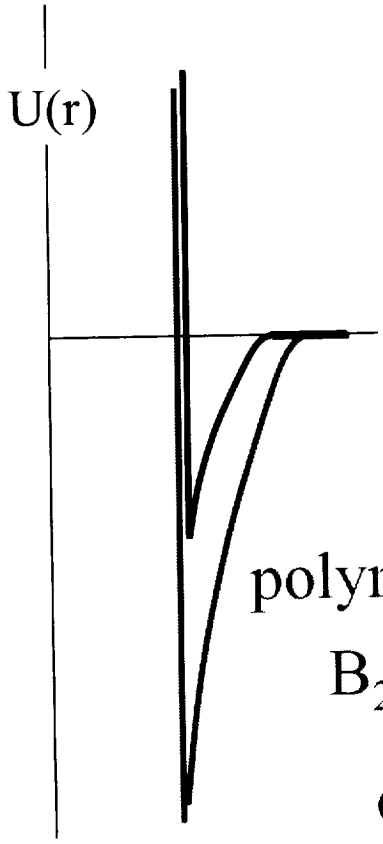

lysozyme / polymer mixtures

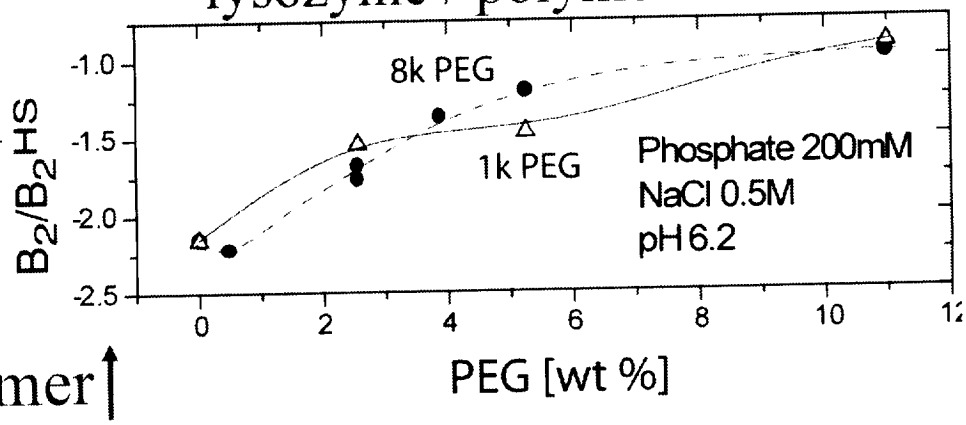

polymer↑

B_2↓

opposite to depletion prediction

B_2 or not B_2 … ?

Cloud Point & PEG/Lysozyme

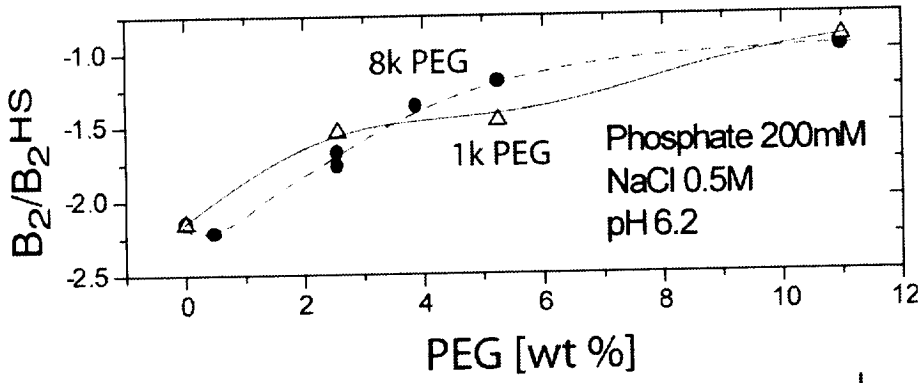

Depletion predicts

$B_2 \downarrow$ as [PEG] $\uparrow$

opposite observed!

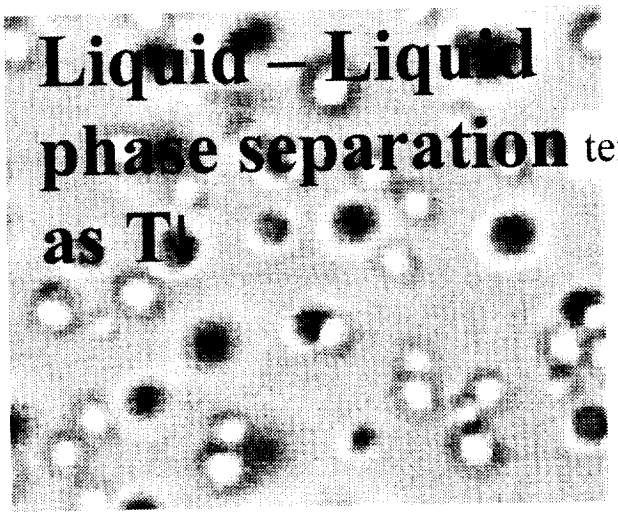

Liquid – Liquid phase separation as T↓

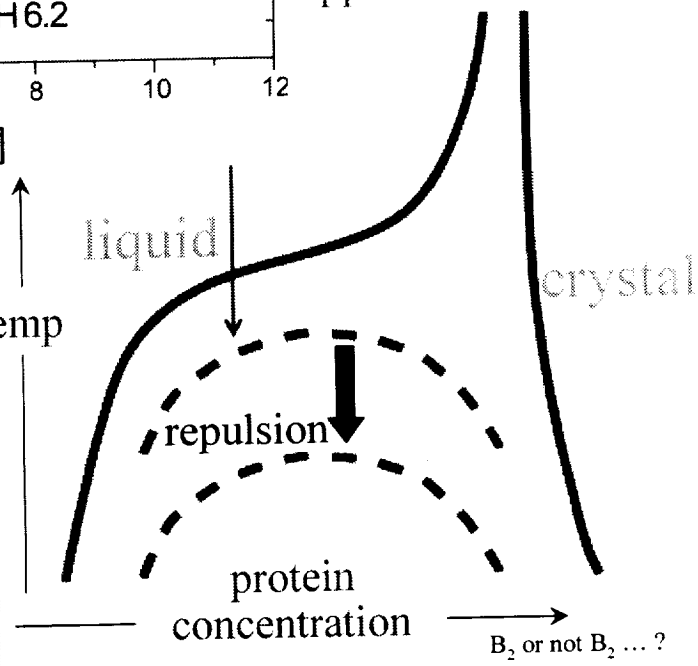

Does B_2 correlate with phase behavior?

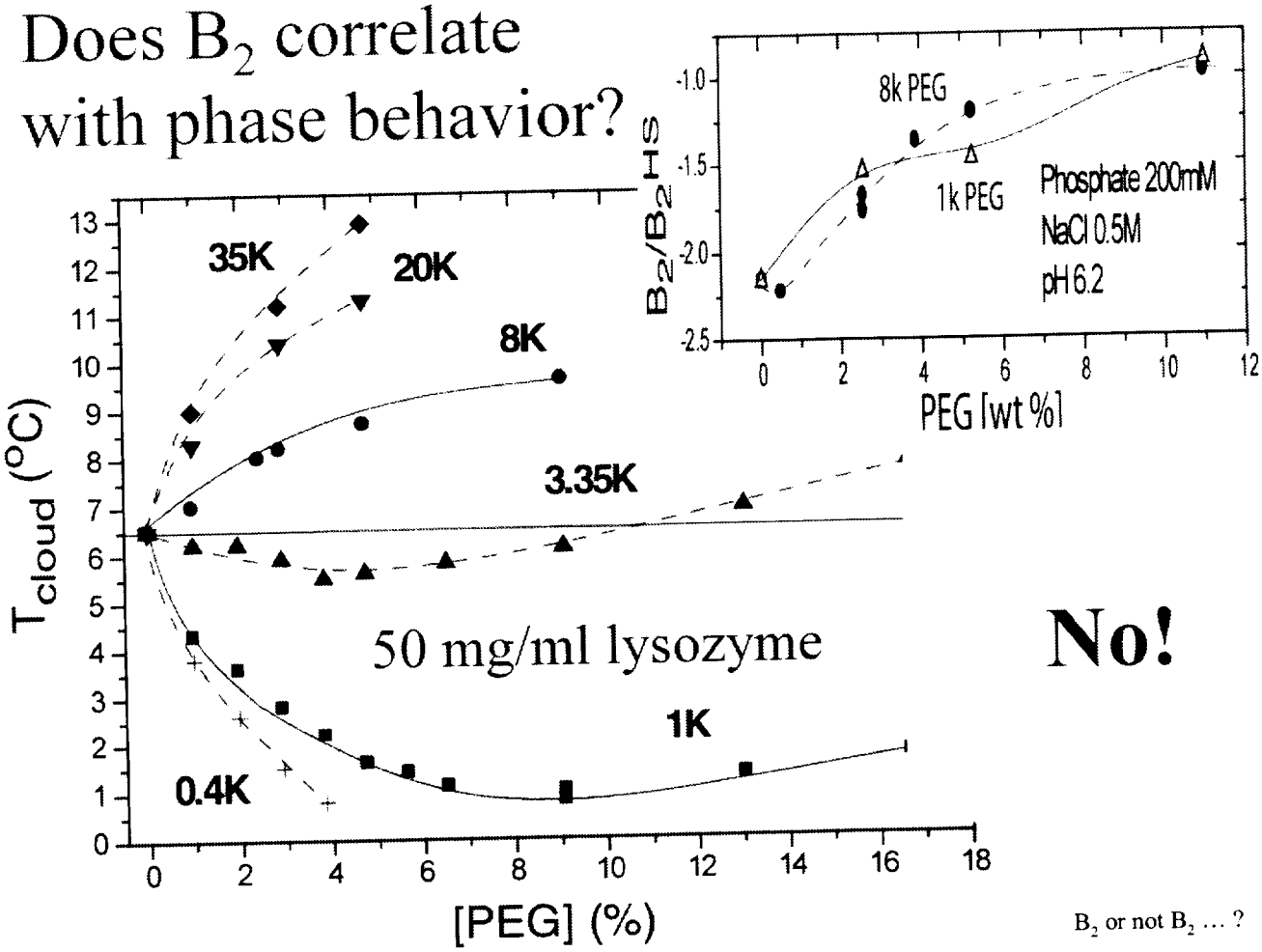

No!

B_2 or not B_2 … ?

Multi-component equation of state

Osmotic pressure Π
density ρ_1, ρ_2

$$\frac{\Pi}{kT} = \rho_1 + \rho_2 +$$

$$+ B_{11}(T)\rho_1^2 + B_{12}(T)\rho_1\rho_2 + B_{22}(T)\rho_2^2 +$$

$$+ C_{111}(T)\rho_1^3 + \boxed{3\,C_{112}(T)\rho_1^2\rho_2} + 3\,C_{122}(T)\rho_1\rho_2^2 + \ldots$$

depletion

B_2 or not B_2 … ?

High Pressure Liquid Chromatography HPLC

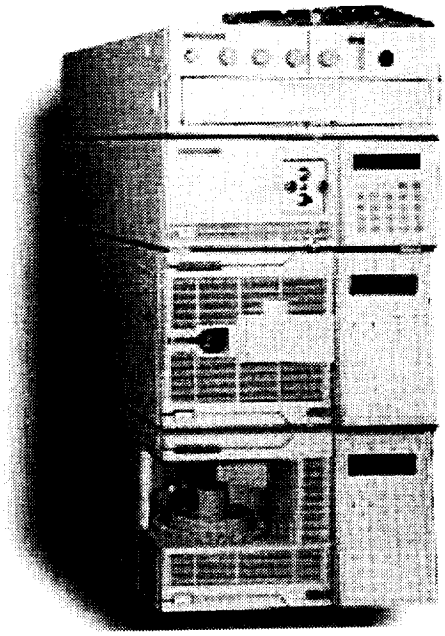

PEG

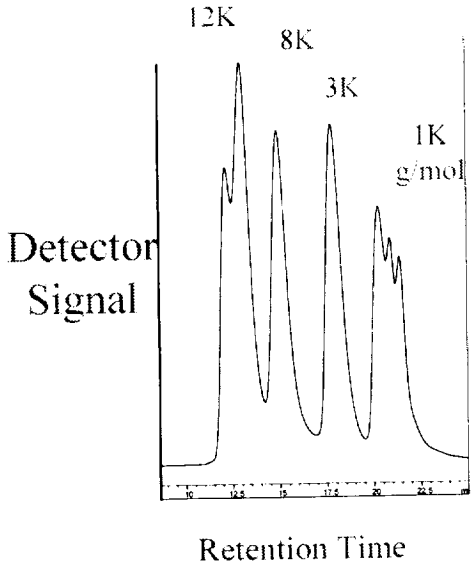

B_2 or not B_2 … ?

Size Exclusion Chromatography

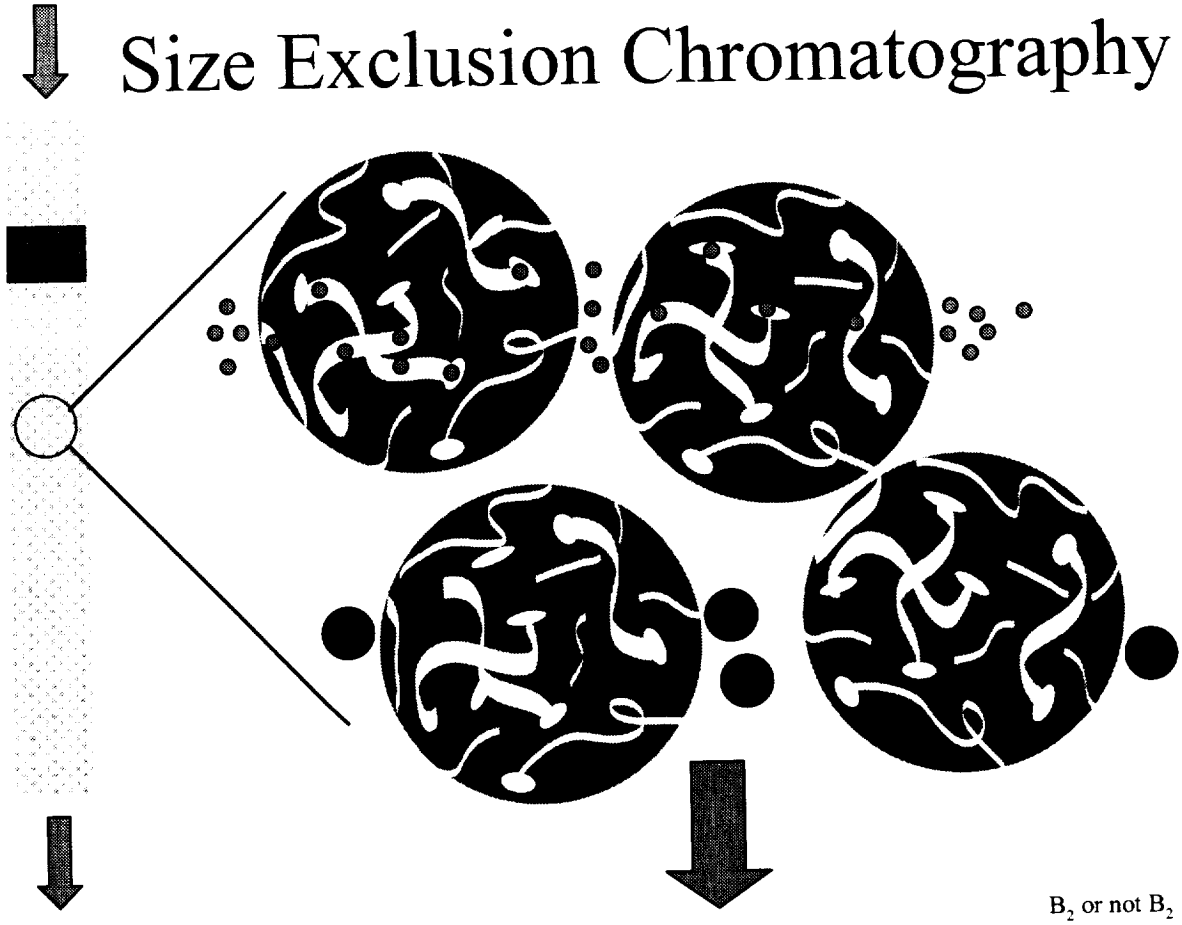

B_2 or not B_2 … ?

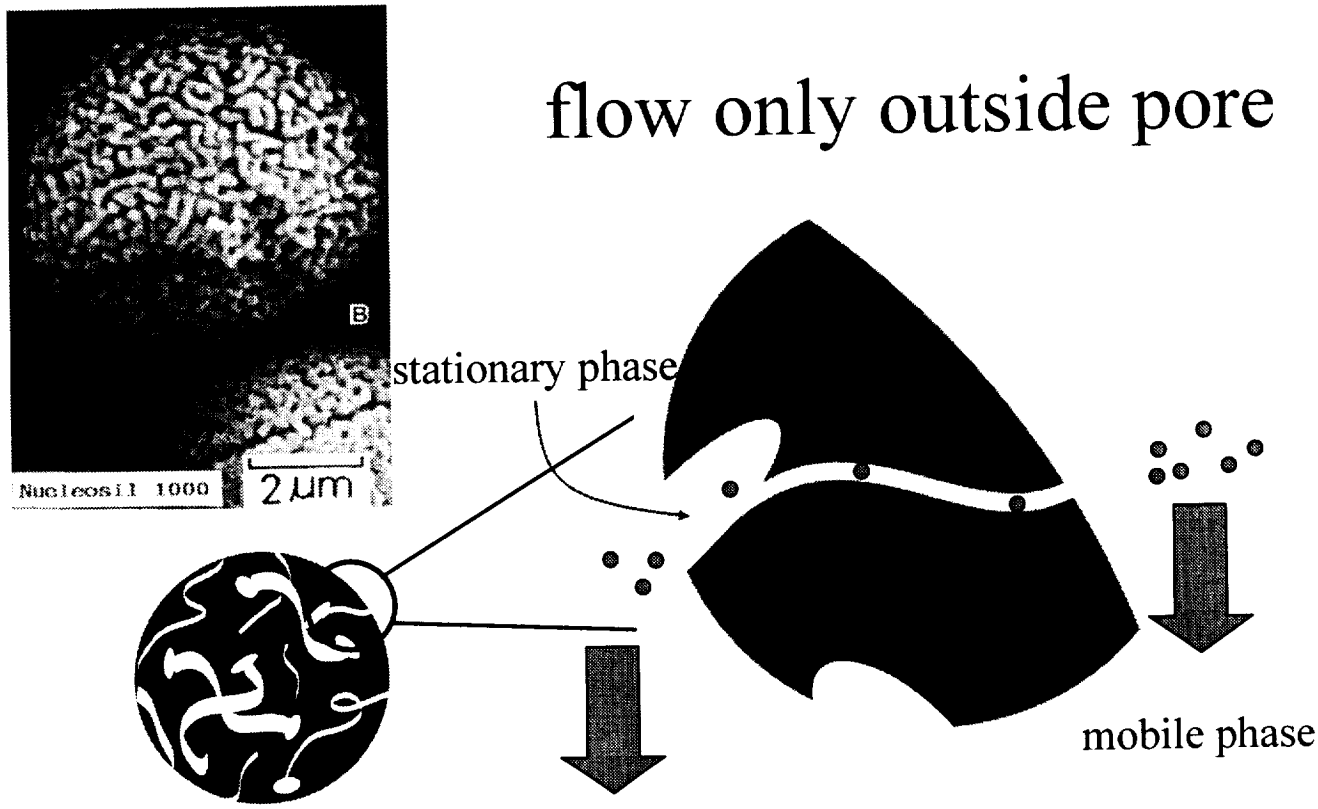
flow only outside pore
B
Nucleosil 1000
2 µm
stationary phase
mobile phase

B_2 or not B_2 … ?

plate model

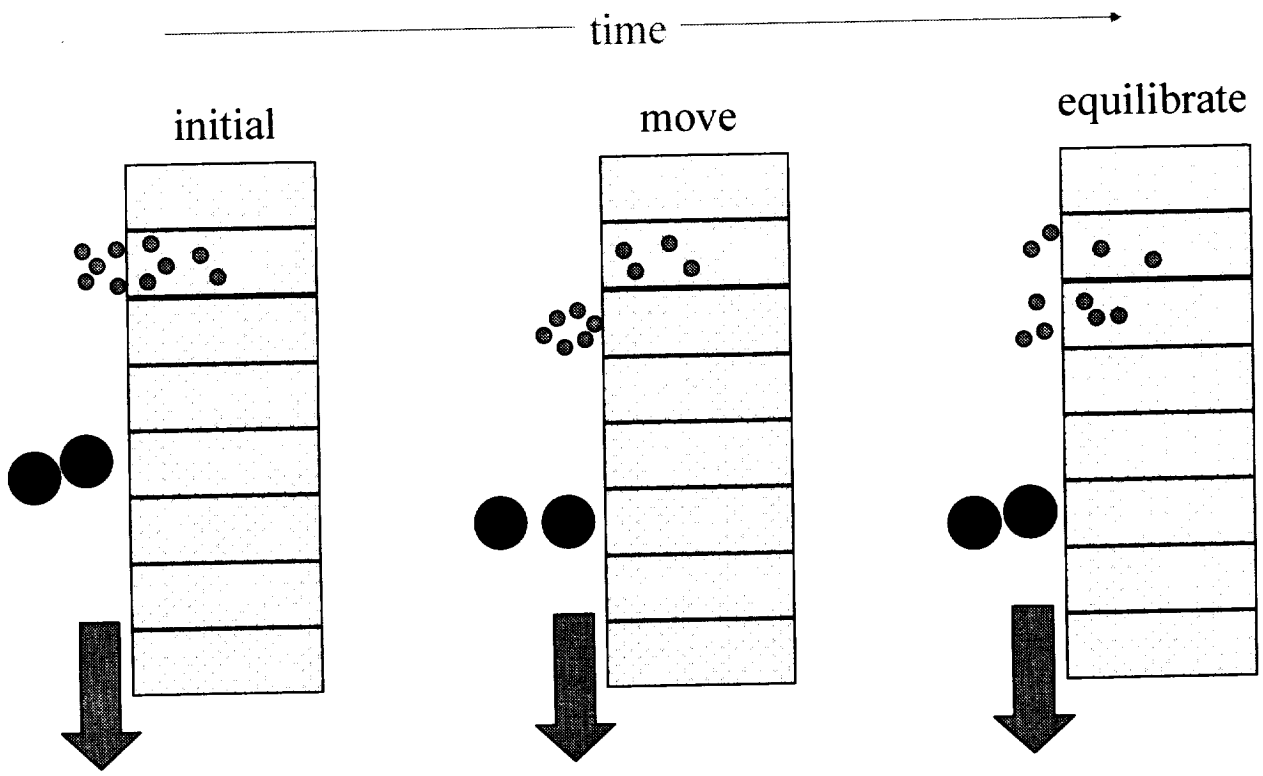

B_2 or not B_2 … ?

Size Exclusion Chromatography

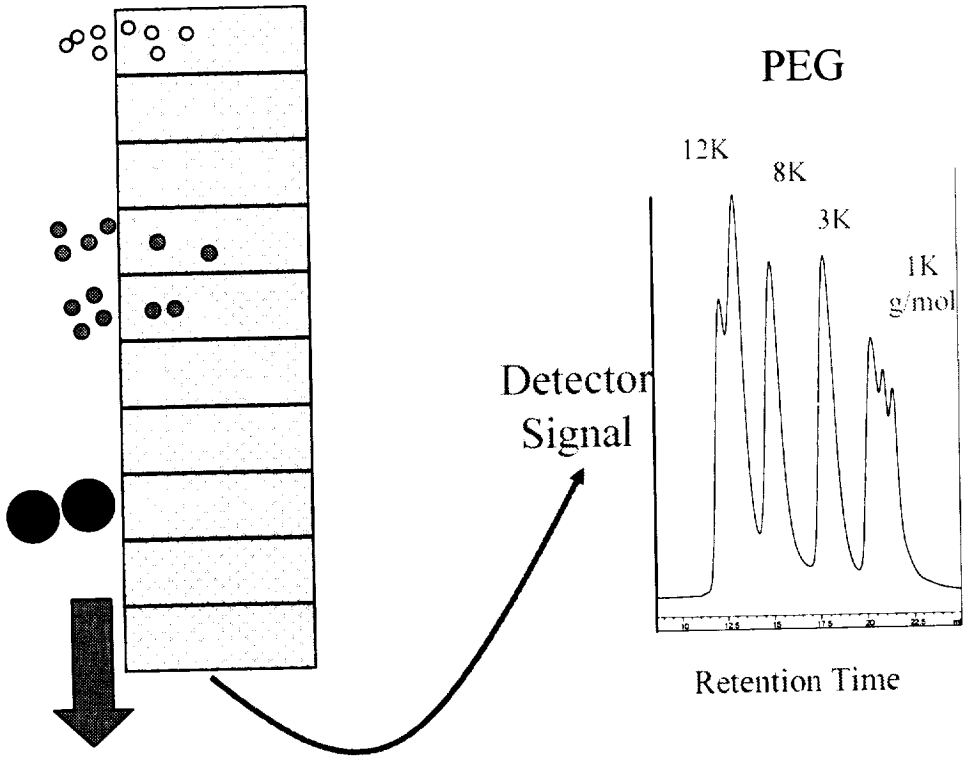

B_2 or not B_2 … ?

Theory

proportional
to retention time

$$\frac{\text{concentration in stationary phase}}{\text{concentration in mobile phase}} = K$$

equal to $e^{-\frac{\Delta G}{kT}}$

$$\mu_m^o + RT \ln c_m + RT \ln \gamma_m = \mu_s^o + RT \ln c_s + RT \ln \gamma_s$$

$$e^{\frac{\mu_m^o - \mu_s^o}{RT}} = K_o = \frac{c_s}{c_m} e^{\frac{2B_2 N_A}{M}(c_s - c_m)}$$

Winzor, Biophys. Chem. **9**, 47 (1978)

Chromatography and light scattering agree!

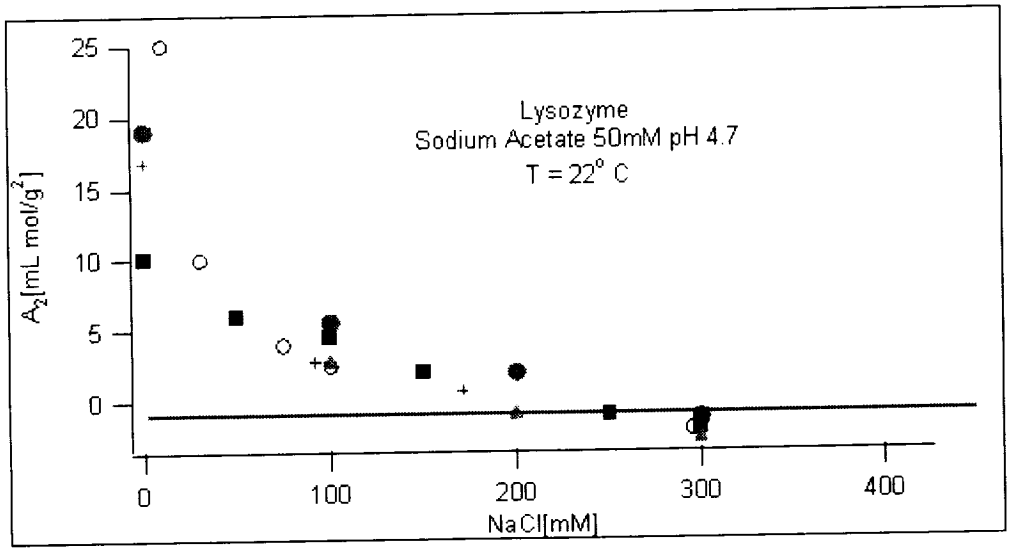

- ● Our SEC data
- + M. Muschol et al *J. Chem. Phys.*, 1995
- ■ A.Kulkarni *Thesis*, U. Illinois, 1999
- ○ O.D.Velev et al *Biophys. J.*, 1998
- ▲ C.Gripon et al *J. Cryst. Growth*, 1997

B_2 or not B_2 … ?

Conclusions

- depletion model fails for lysozyme / PEG
- B_2 does not correlate with liquid phase boundary

- why does depletion model fail?
  (potential of mean force inadequate – ternary phase diagram)
- extend chromatography to protein – polymer mixtures

www.elsie.brandeis.edu

B_2 or not B_2 … ?

MICRO-FLUID DYNAMICS IN AN EVAPORATING SESSILE DROPLET: APPLICATION TO DNA OPTICAL GENE MAPPING

Hua Hu, Lei Li, and Ronald Larson
Dept. of Chemical Engineering, Univ. of Michigan

ABSTRACT

The flow field proposed by a drying, sessile droplet has been used by Jing, et al. (1998) to stretch and adhere DNA molecules to derivatized glass substrate, as a preparation for optical gene analysis using restriction enzymes. We have carried out experimental, analytical, and numerical analysis of the flow field in an evaporating droplet, and combined this flow field with a Brownian dynamics analysis of polymer deformation to predict the conformations of DNA molecules adhered to the substrate in this flow. We have compared these predictions to experimental observations and measurements of the DNA configurations, obtaining excellent agreement. The results indicate that combined hydrodynamic/Brownian dynamic analyses can be used to design flows for micro-manipulation of DNA, for gene analysis.

The flow fields in the evaporating droplet, obtained from a finite element analysis and from an analytic lubrication analysis are similar qualitatively. However there are some quantitative differences that can be traced to the boundary condition at the air-fluid interface, which reduces to a zero axial gradient in radial velocity in the case of the lubrication approximation, but which does not quite hold in the numerical analysis, due to the radial gradient in evaporation rate. The analytic flow field is then combined with a Brownian dynamics method to predict the stretching and deposition of DNA molecules to a glass substrate treated with 3-aminopropyltriethoxysilane (APTES) to induce irreversible adsorption of DNA In the Brownian dynamics simulation, the DNA molecule is represented as a bead-spring chain, with parameters chosen from known elastic and hydrodynamic properties of lambda-phage DNA. Any bead coming into contact with the substrate due to a combination of flow and Brownian motion is "frozen" to the surface.

An image of DNA molecules adhered to the treated glass substrate is shown in Fig. 1. Fig. 2 analyzes the distribution of stretch length and orientation angle, relative to the radial flow direction, from many such images, and compares the results to the predictions of the Brownian dynamics simulations. The agreement is very good, indicating that analysis of DNA molecular dynamics and surface adhesion in complex flows is now possible. We are extending this work to flow in a channel, and to electrostatic manipulations of DNA molecules, with the aim of developing tools for manipulation of DNA single molecules in microfabricated devices. Such devices are of growing interest in the biomedical community and for space applications, including space flight.

Reference: Jing J., J. Reed, J. Huang, X. Hu, C. V. Clarke, J. Edington, D. Housman, T. S. Anantharaman, E.J. Huff, B. Mishra, B. Porter, A. Shenker, E. Wolfson, C. Hiort, R. Kantor, C.

Aston, D. C. Schwartz, "Automated high resolution optical mapping using arrayed, fluid-fixed DNA molecules," Proc. Natl. Acad. Sci. USA **95**, 8046-8051 (1998).

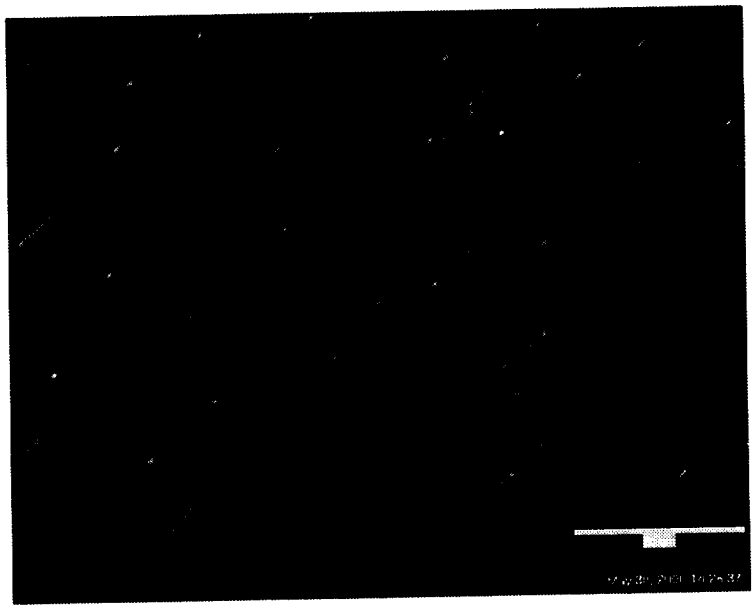

Fig. 1. Image of DNA adhered to substrate following drying droplet flow

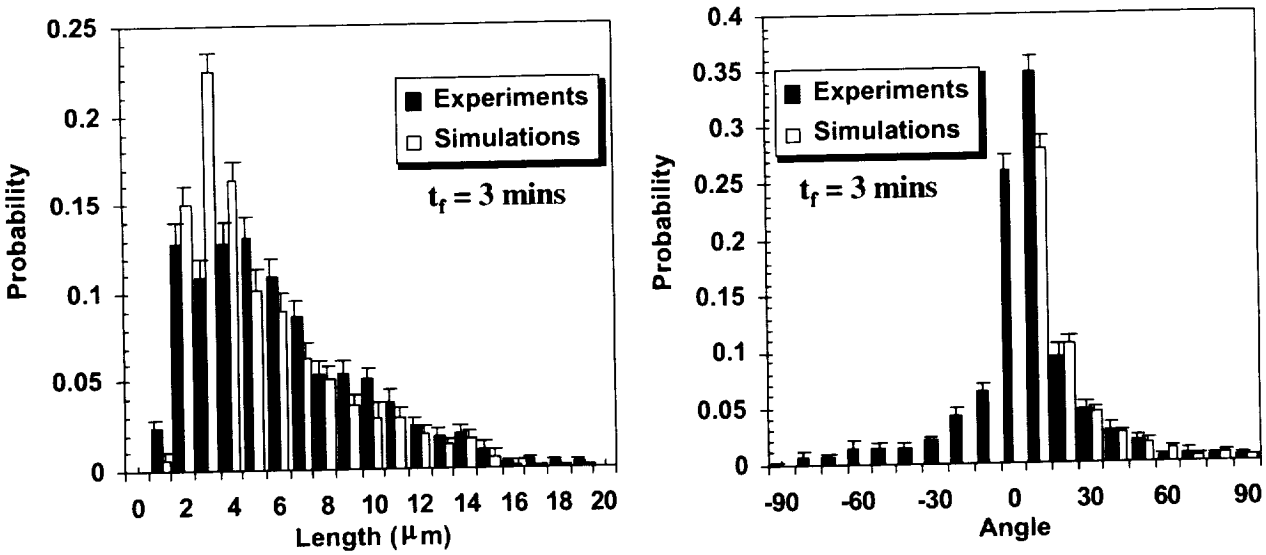

Fig. 2 Distribution of stretch and of orientation of lambda-phage DNA molecules resulting from drying droplet flow, under "fast" drying conditions

Micro-fluidic Dynamics in an Evaporating Droplet

Hua Hu and Ronald Larson
Department of Chemical Engineering
Univ. Of Michigan, Ann Arbor

Aug. 2002, NASA Micro-Gravity Research

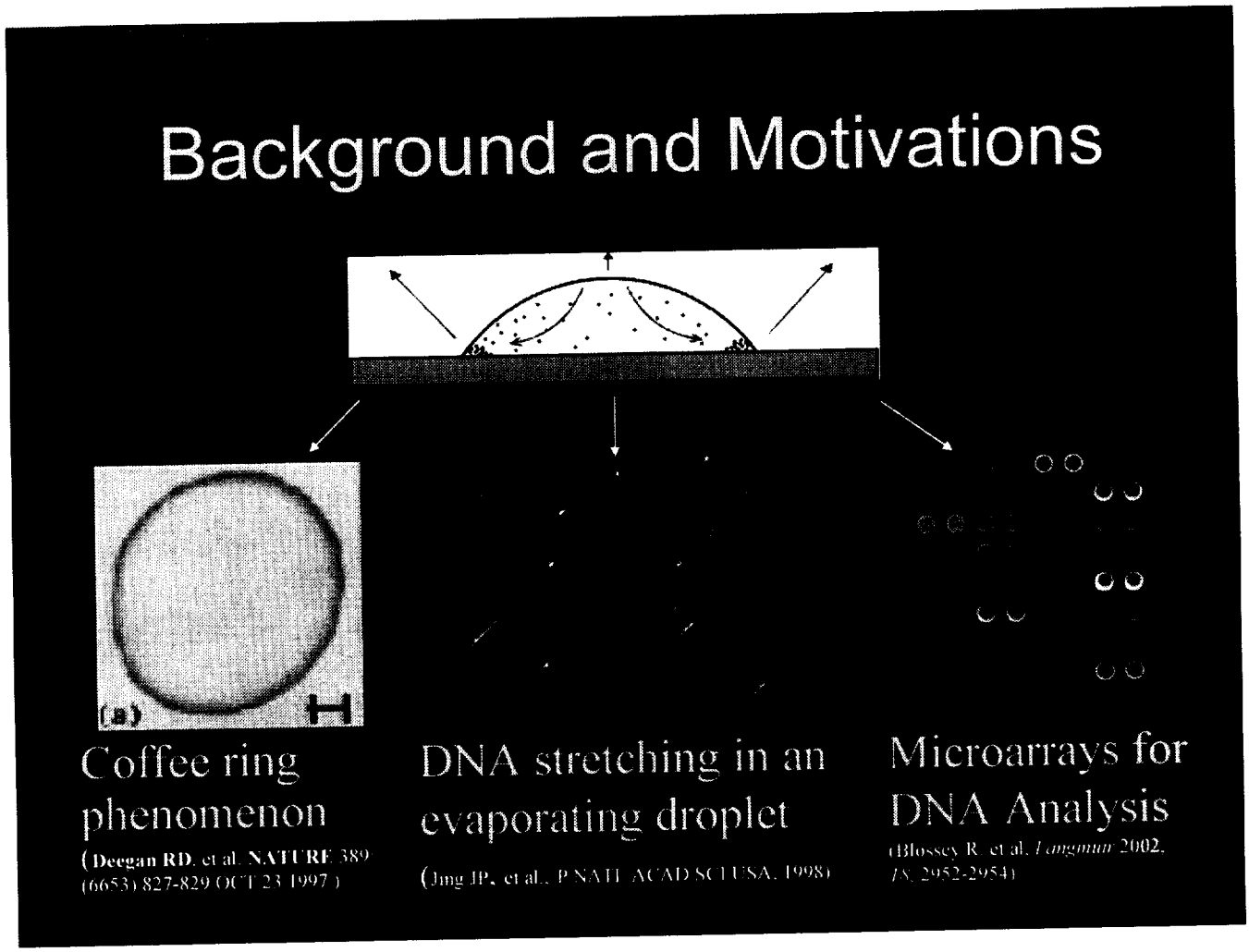
Background and Motivations
(a)
Coffee ring phenomenon
(Deegan RD, et al. NATURE 389 (6653) 827-829 OCT 23 1997)
DNA stretching in an evaporating droplet
(Jing JP, et al., P NATL ACAD SCI USA, 1998)
Microarrays for DNA Analysis
(Blossey R, et al. Langmuir 2002, 18, 2952-2954)

DNA Genomics in an Evaporating Droplet

(Schwartz et al.)

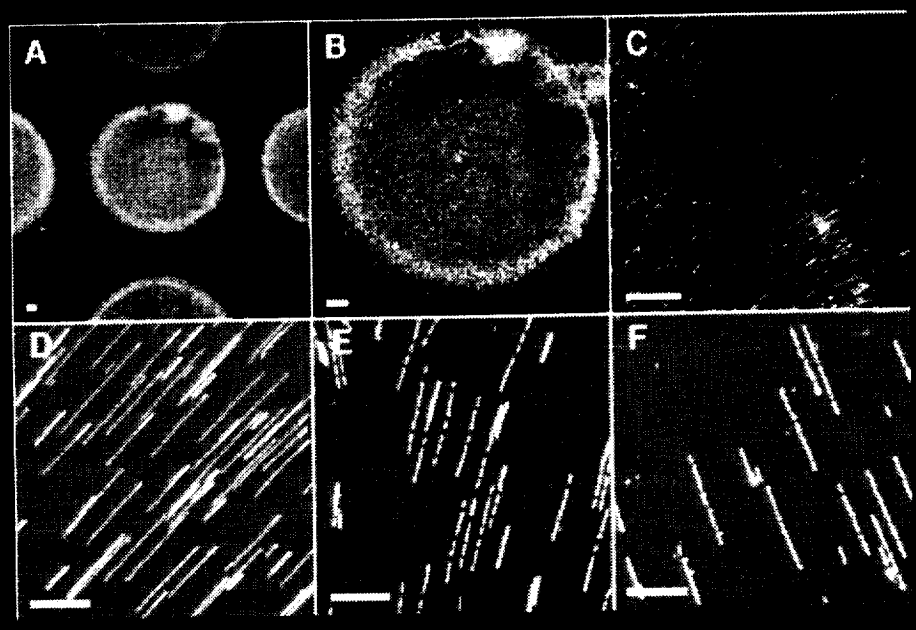

Theory: Dimensionless Group Numbers

$$Bo = \frac{\rho g h_o R}{\sigma} \approx 0.04 << 1$$

$$Ca = \frac{\mu \bar{u}_r}{\sigma} \approx 4 \times 10^{-8} << 1$$

$$\frac{c_v (1 - H)}{\rho} \approx 1.4 \times 10^{-5} << 1$$

$$\mathrm{Re} = \frac{\rho \bar{u}_r R}{\mu} \approx 0.003 << 1$$

$$St^{-1} = \frac{C_p \rho \bar{u}_r R}{h} \approx 0.02 << 1$$

Through these dimensionless numbers, we find that the mass, heat and momentum transfer in an evaporating droplet can all be regarded as pseudo-steady state processes.The energy and vapor transport equations can be largely decoupled from the liquid momentum equation. During the droplet evaporation, the droplet always remains a spherical shape. As a result, accurate semi-analytic solutions for the problem can be obtained.

Theory: Model

Mass, momentum and heat balances in three regions:

1. Vapor 2. Liquid 3.Vapor-liquid interface

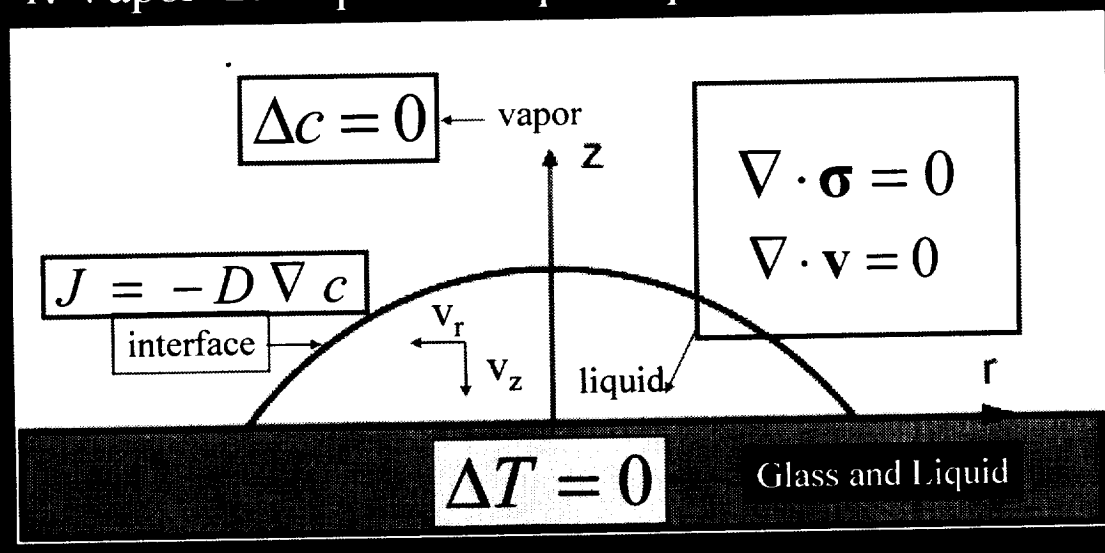

Flow is axisymmetric

Theory

Boundary conditions

Laplace equation in vapor	Flow equations	Laplace equation for temperature
$\begin{cases} r=\infty, z=\infty, c=c_v H \\ r>1, h=0, \dfrac{\partial c}{\partial z} \\ h=h(r), c=c_v \end{cases}$	* Without Marangoni effect 1. $z=0$, non-slip condition 2. Shear-stress-free interface $(u\cdot n)=u_\xi;\ (\tau\cdot t)=0$ * With Marangoni effect 1. $z=0$, non-slip condition 2. Shear stress on the surface $(u\cdot n)=u_\xi;\ (\tau\cdot t)=\dfrac{d\sigma}{d\eta}$	1. $z=0$, $r<=1$, T=const. 2. $z=0$, $r>1$, J=0. 3. $S=\{h(r,t)\mid r\le R\}$ heat flux: $J_h=H(\mathbf{J}\cdot\mathbf{n})$

* Lubrication assumption is applied to derive analytical solution

Results: Evaporation Flux

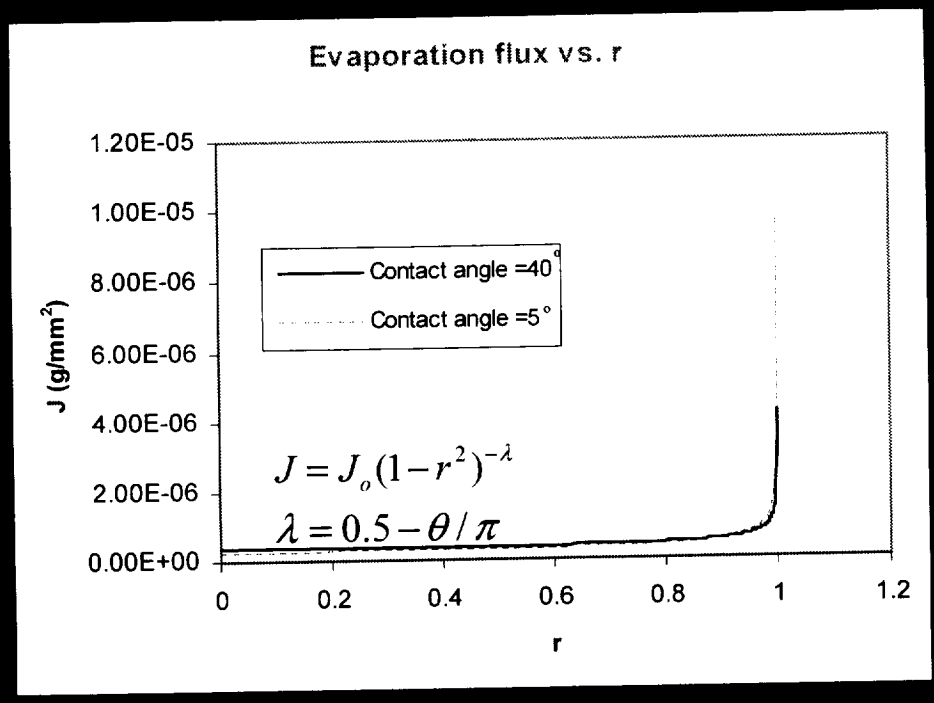

Results: Temperature Field

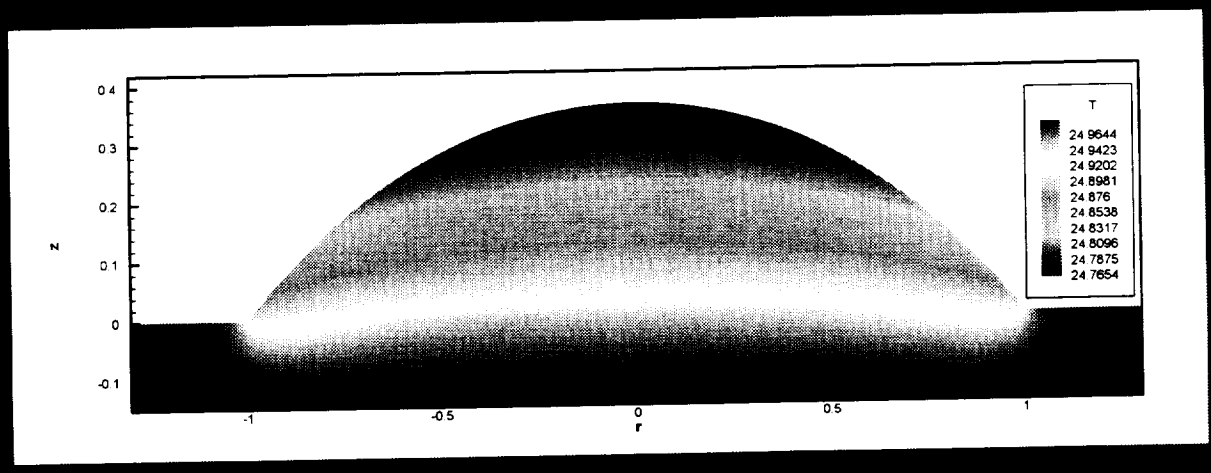

The temperature distribution on the droplet surface can be approximately fitted by equation: $T = k\tilde{r}^2 + c$

where, k and c are two fitting constants

Theory

Approximate analytical results with Marangoni force from lubrication assumption

$$\tilde{u}_r = \tilde{\bar{u}}_r\left(\frac{3\tilde{z}}{\tilde{h}} - \frac{3}{2}\frac{\tilde{z}^2}{\tilde{h}^2}\right) - Ma\tilde{r}\tilde{h}\frac{h_o}{R}\left(\frac{\tilde{z}}{\tilde{h}} - \frac{3}{2}\frac{\tilde{z}^2}{\tilde{h}^2}\right)$$

$$\tilde{u}_z = \frac{3}{4}\frac{1}{1-\tilde{t}}\left[1+\lambda(\theta)\left(1-\tilde{r}^2\right)^{-\lambda(\theta)-1}\right]\left(\frac{\tilde{z}^3}{3\tilde{h}^2} - \frac{\tilde{z}^2}{\tilde{h}}\right) +$$

$$\frac{3}{2}\frac{1}{1-\tilde{t}}\left[\left(1-\tilde{r}^2\right) - \left(1-\tilde{r}^2\right)^{-\lambda(\theta)}\right]\left(\frac{\tilde{z}^2}{2\tilde{h}^2} - \frac{\tilde{z}^3}{3\tilde{h}^3}\right)\tilde{h}(0,\tilde{t})$$

$$+ Ma\frac{h_o}{R}\left(\tilde{z}^2 - \frac{\tilde{z}^3}{\tilde{h}}\right) - Ma\tilde{r}^2\frac{h_o}{R}\left(\frac{\tilde{z}^3}{\tilde{h}^2}\right)\tilde{h}(0,\tilde{t})$$

$$Ma = \frac{\beta k t_f}{\mu R} \qquad \lambda(\theta) = \frac{1}{2} - \frac{\theta}{\pi}$$

Theory

Approximate analytical results without Marangoni force from lubrication assumption

$$\tilde{u}_r = \frac{3}{8}\frac{1}{1-\tilde{t}}\frac{1}{\tilde{r}}\left[(1-\tilde{r}^2)-(1-\tilde{r}^2)^{-\lambda(\theta)}\right]\left(\frac{\tilde{z}^2}{\tilde{h}^2}-2\frac{\tilde{z}}{\tilde{h}}\right)$$

$$\tilde{u}_z = \frac{3}{4}\frac{1}{1-\tilde{t}}\left[1+\lambda(\theta)(1-\tilde{r}^2)^{-\lambda(\theta)-1}\right]\left(\frac{\tilde{z}^3}{3\tilde{h}^2}-\frac{\tilde{z}^2}{\tilde{h}}\right)+$$

$$\frac{3}{2}\frac{1}{1-\tilde{t}}\left[(1-\tilde{r}^2)-(1-\tilde{r}^2)^{-\lambda(\theta)}\right]\left(\frac{\tilde{z}^2}{2\tilde{h}^2}-\frac{\tilde{z}^3}{3\tilde{h}^3}\right)\tilde{h}(0,\tilde{t})$$

$$\tilde{r}=\frac{r}{R} \quad \tilde{z}=\frac{z}{h_o} \quad \tilde{t}=\frac{t}{t_f} \quad \tilde{u}_r=\frac{u_r t_f}{R} \quad \tilde{u}_z=\frac{u_z t_f}{h_o} \quad \tilde{h}=\frac{h}{h_o} \quad \lambda(\theta)=\frac{1}{2}-\frac{\theta}{\pi}$$

Results: Velocity Field at Different Times

Velocity field w/o Marangoni stress, Ma = 0,
Initial contact angle θ=40°

Click here to play movie

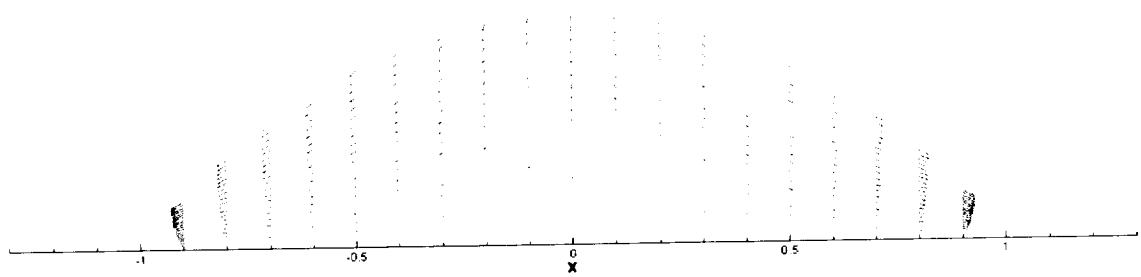

Results: Velocity Field at Different Times

Velocity field w Marangoni stress, Ma = 1193
Initial contact angle θ=40°

Click here to play movie

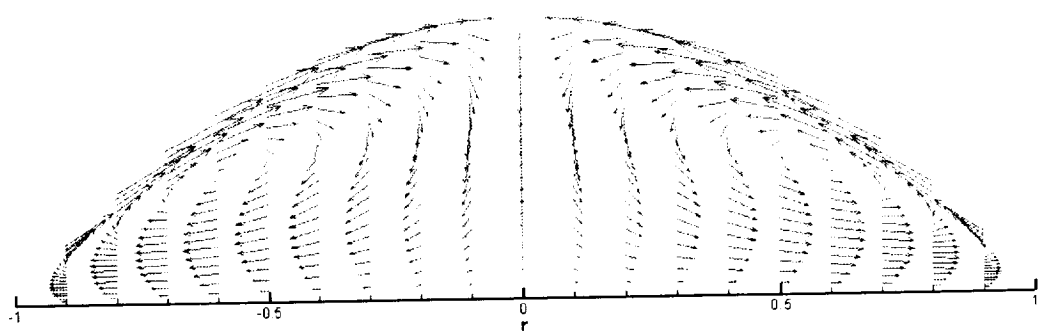

$Ma = \beta k t_f / \mu R = 1193$ β=0.1657erg/cm/C°, μ=0.01Poise, k=0.02 C°, t_f=360s, R=1mm

Theory: FEM Analysis

FEM models are developed for the following fields

- Vapor concentration distribution
  Extracting evaporation flux and boundary motion
- Temperature distribution
  Calculating the Marangoni force
- Velocity field

A mesh generated by Ansys6.0 software

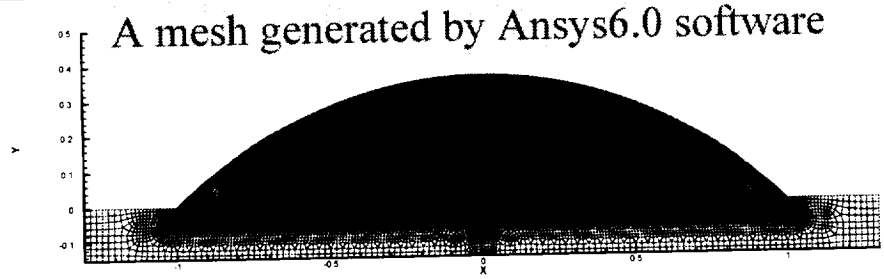

Results: Comparison Between FEM and Analytical Results, Ma=0

Comparison of velocity fields without Marangoni stress, Ma = 0
Contact angle, $\theta=40^{o}$

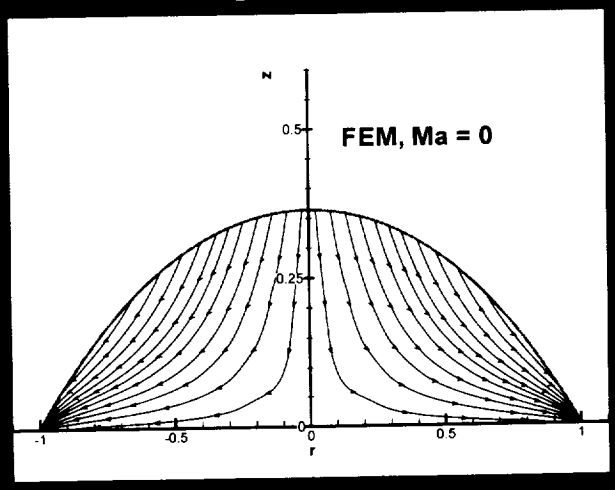

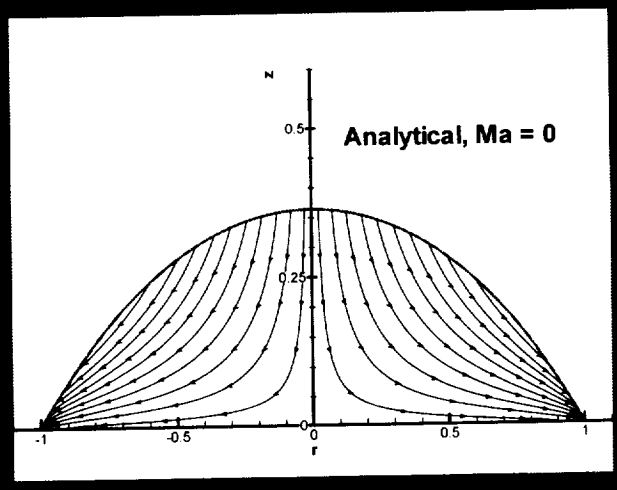

Results: Comparison Between FEM and Analytical Results, Ma=0

Comparison of velocity fields w/o Marangoni stress, Ma = 0,Contact angle, θ=40°

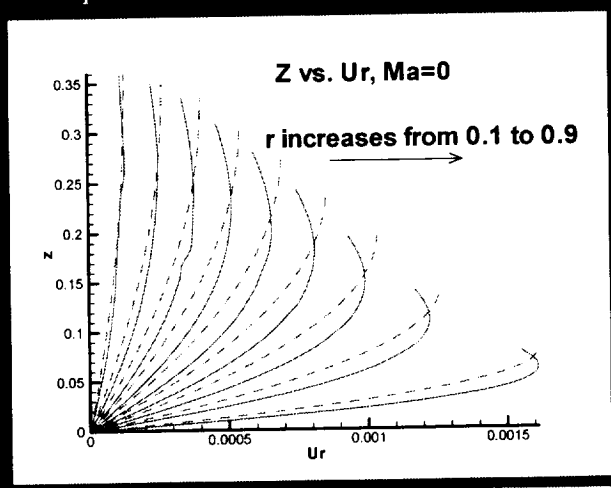

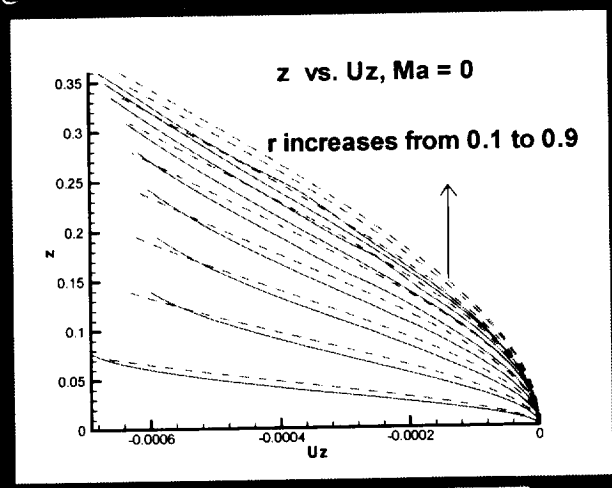

FEM results - - - - - - Analytical results

$$\tau_{rz}\Big|_{z=h(r,t)} = \mu\left(\frac{\partial u_r}{\partial z} + \frac{\partial u_z}{\partial r}\right)\Bigg|_{z=h(r,t)}$$

τ is the stress on the surface. Because u_z is a function of r and du_z/dr is not zero, when applying Lubrication theory du_r/dz must be a non-zero value to keep $\tau = 0$

Results: Comparison Between FEM and Analytical Results, Ma=0

Comparison of velocity fields without Marangoni stress, Ma = 0
Contact angle, $\theta=10^{o}$

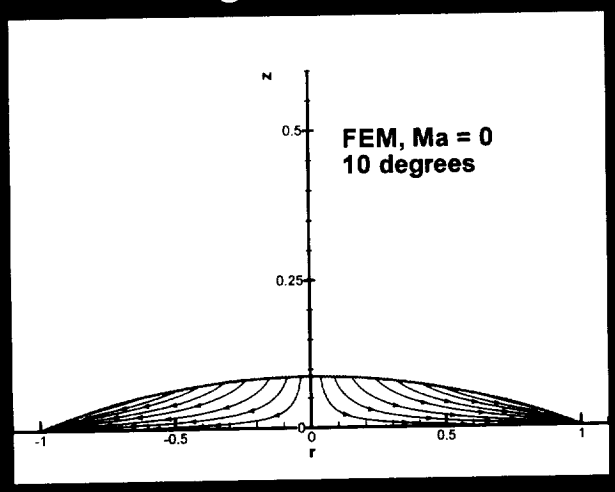

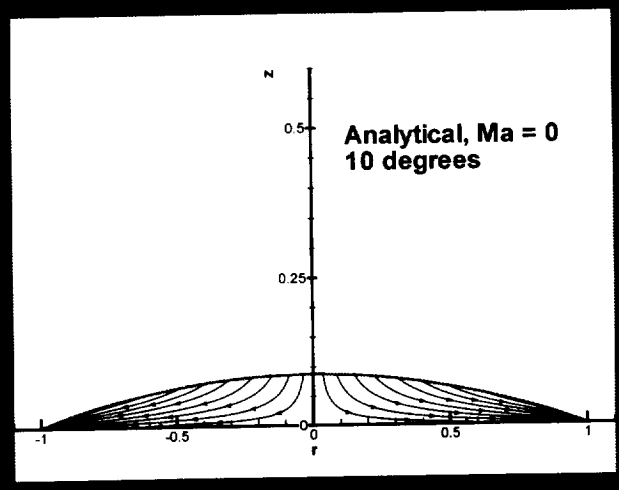

Results: Comparison Between FEM and Analytical Results, Ma=0

Comparison of velocity fields w/o Marangoni stress, Ma = 0, Contact angle, $\theta=10^{o}$

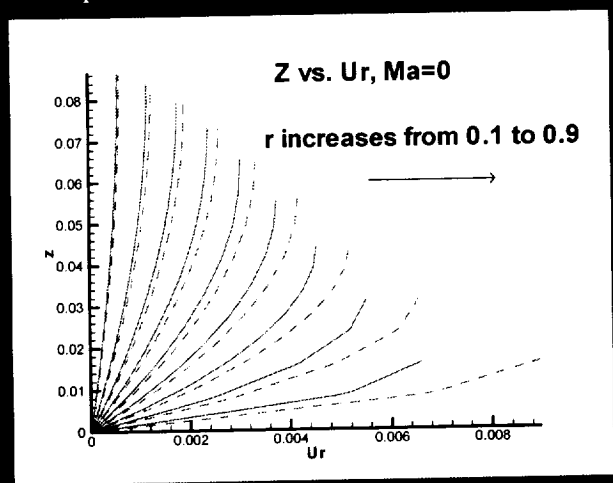

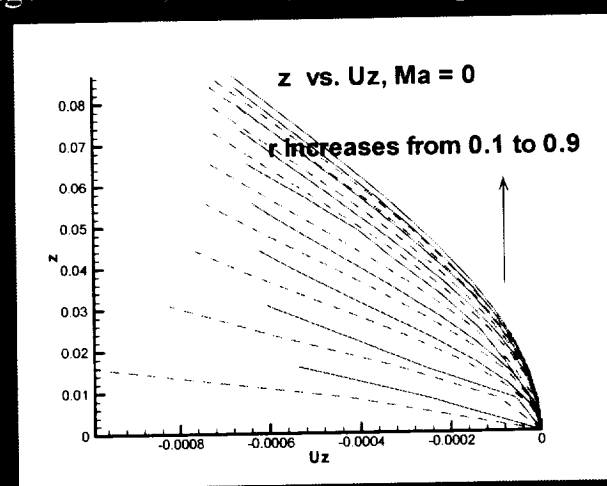

FEM results - - - - - - Analytical results

$$\tau_{rz}\Big|_{z=h(r,t)} = \mu\left(\frac{\partial u_r}{\partial z} + \frac{\partial u_z}{\partial r}\right)\Bigg|_{z=h(r,t)}$$

Even the droplet is flat, because du_r/dr is not zero, the difference between two predictions becomes large near the edge of the droplet

Results: Comparison Between FEM and Analytical Results, Ma=1193

Comparison of velocity fields with Marangoni stress, Ma = 1193
Contact angle, $\theta=10^{o}$

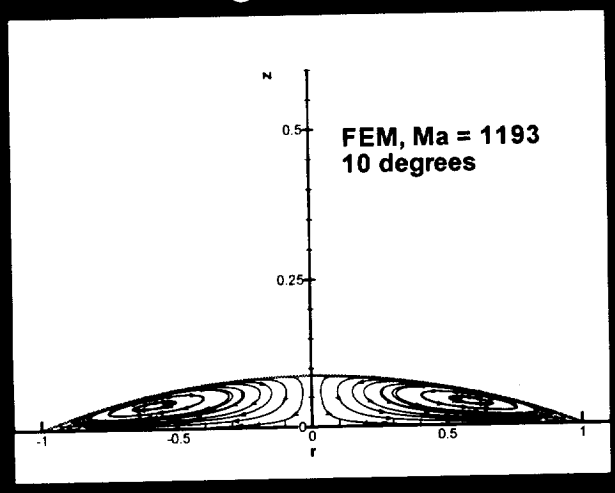

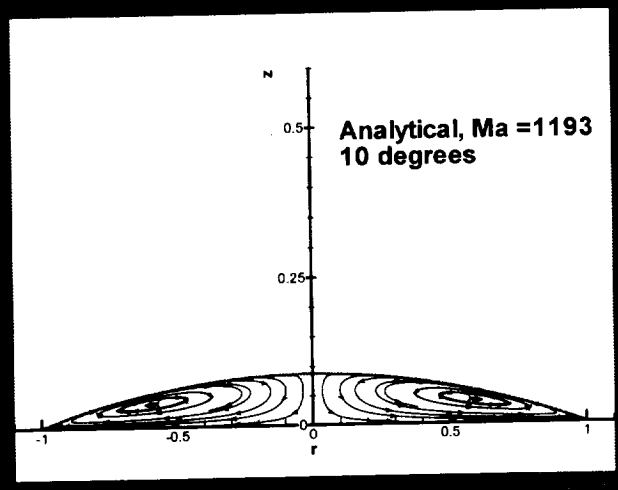

Results: Comparison Between FEM and Analytical Results, Ma=1193

Comparison of velocity fields with Marangoni stress, Ma = 1193
Contact angle, $\theta=10^{o}$

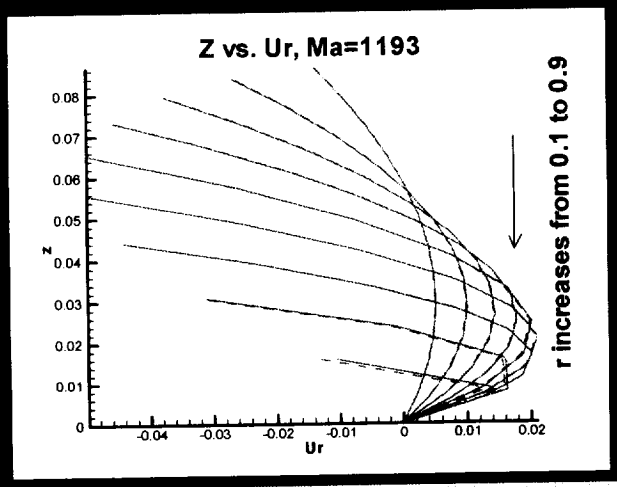

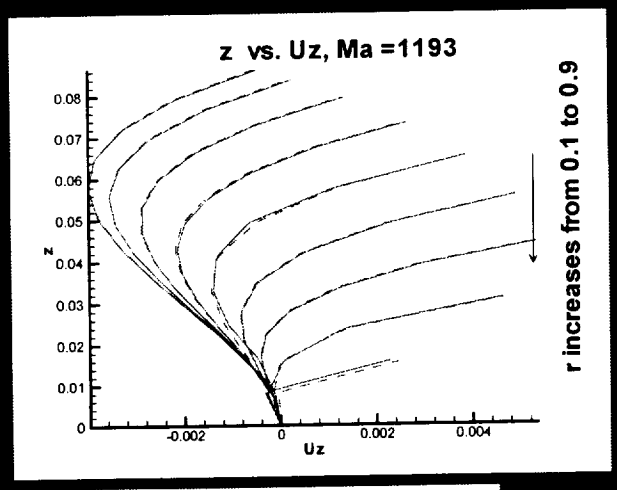

_____ FEM results - - - - - - Analytical results

Results: Comparison Between FEM and Analytical Results, Ma=1193

Comparison of velocity fields with Marangoni stress, Ma = 1193
Contact angle, θ=40°

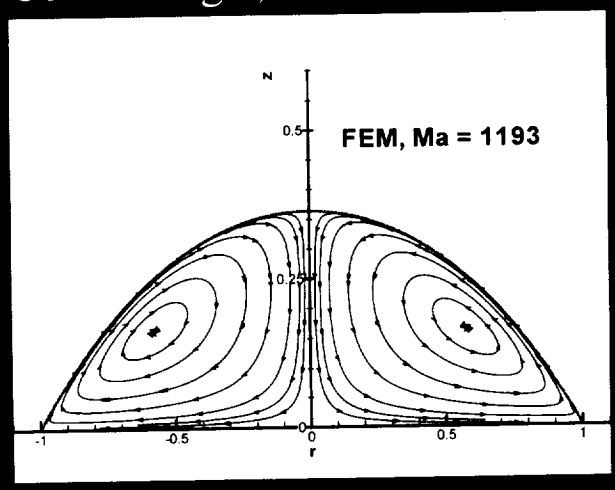

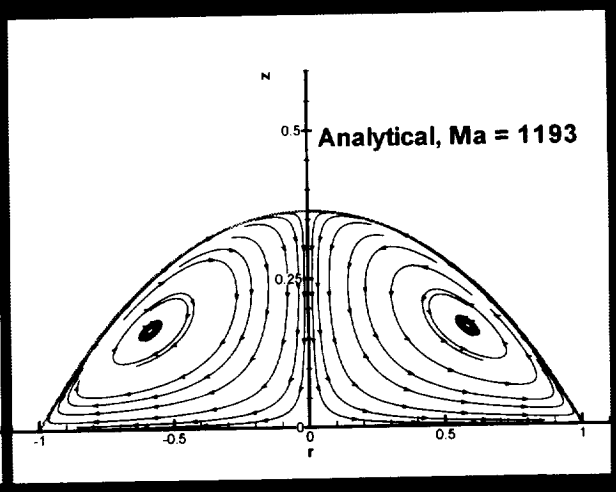

Results: Comparison Between FEM and Analytical Results, Ma=1193

Comparison of velocity fields with Marangoni stress, Ma = 1193
Contact angle, θ=40°

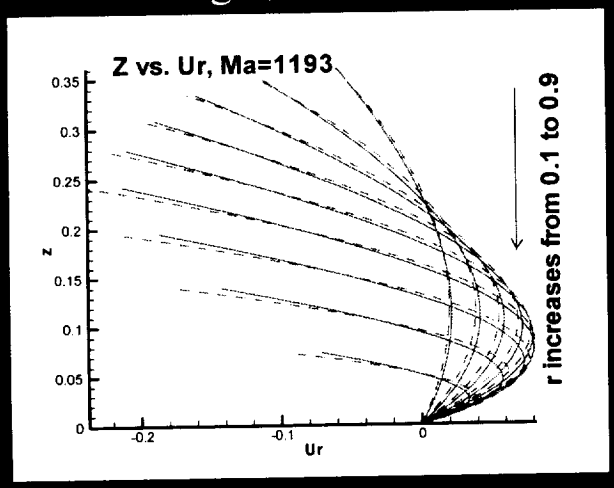

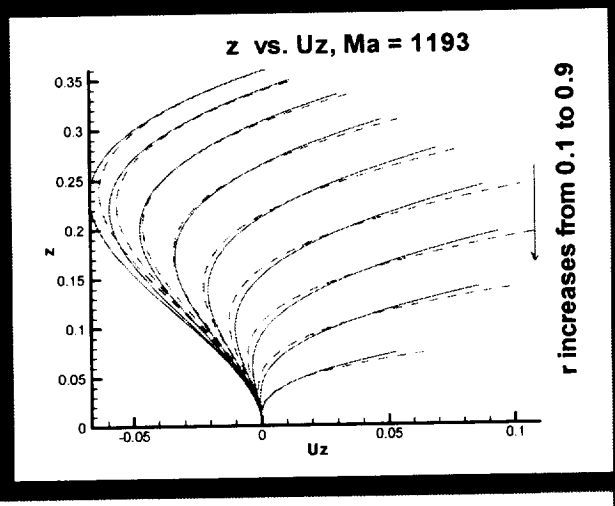

$$\tau_{rz}\Big|_{z=h} = \frac{d\sigma}{dr}$$

Marangoni stress has more effects on du_r/dz other than du_z/dr on the droplet surface

Experiments

Experimental apparatus

- 0.75micron fluorescent particle used as tracers (480/510nm)
- Compix SimplePCI image processing software

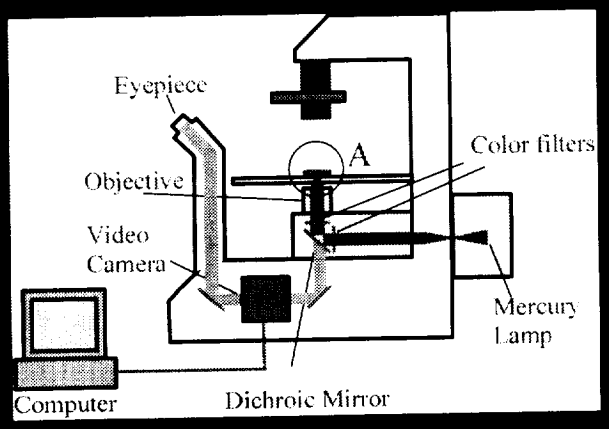

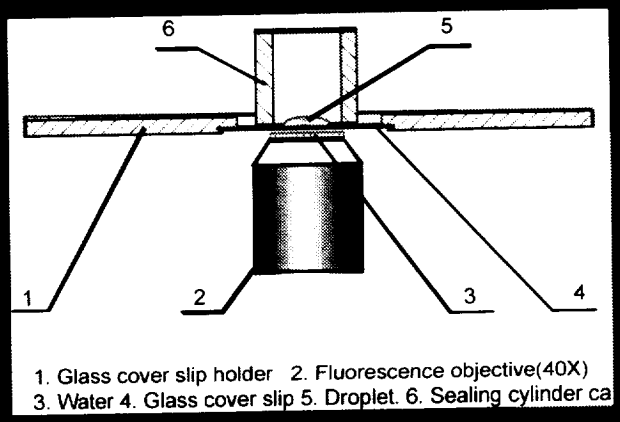

Experiments
Microscopic particle-tracking velocimetry
y = 0.1062x² + 1.7885x + 4.247
R² = 0.9996
particle image diameter (pixels)
Distance relative to the focal plane, z (μm)
Fig 4 The calibration curve
Z
r

Results: Comparison Between Experiments and Computations

Experimental results,
dimensionless t = 0.3

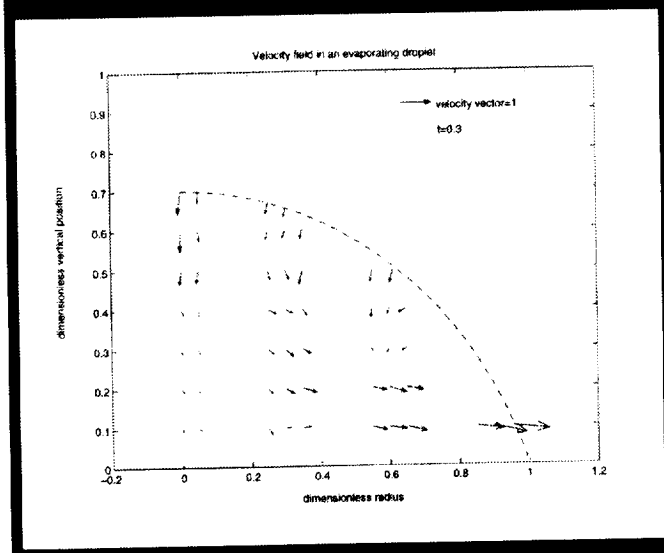

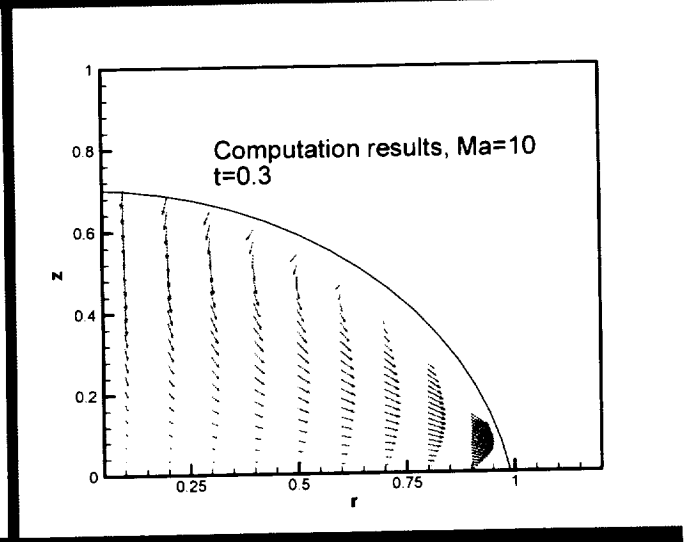

Velocity field (to reduce the effect of Brownian motion, 250-300 droplets are measured)

Results: Comparison Between Experiments and Computations

Experimental results,
dimensionless t = 0.5

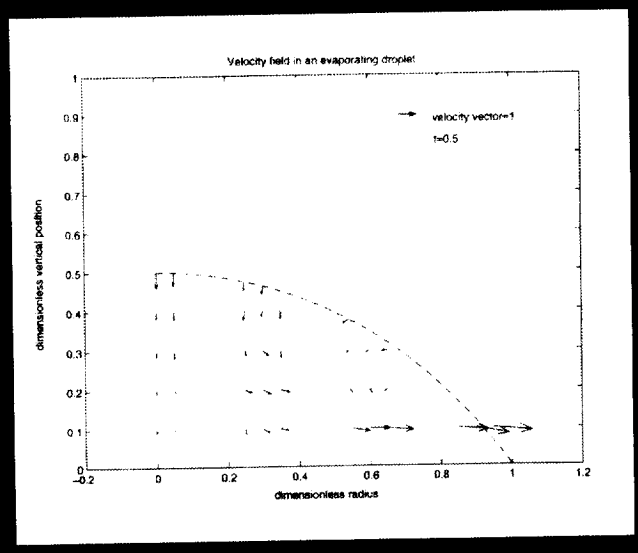

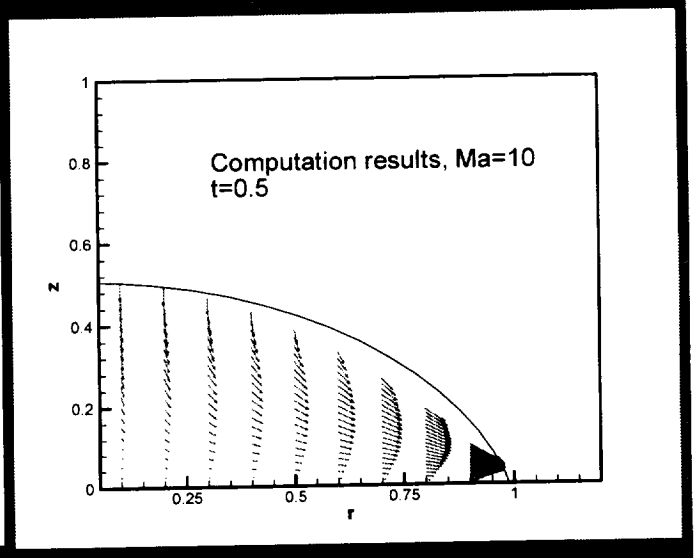

DNA Experiments: DNA image at high/low evaporation rate

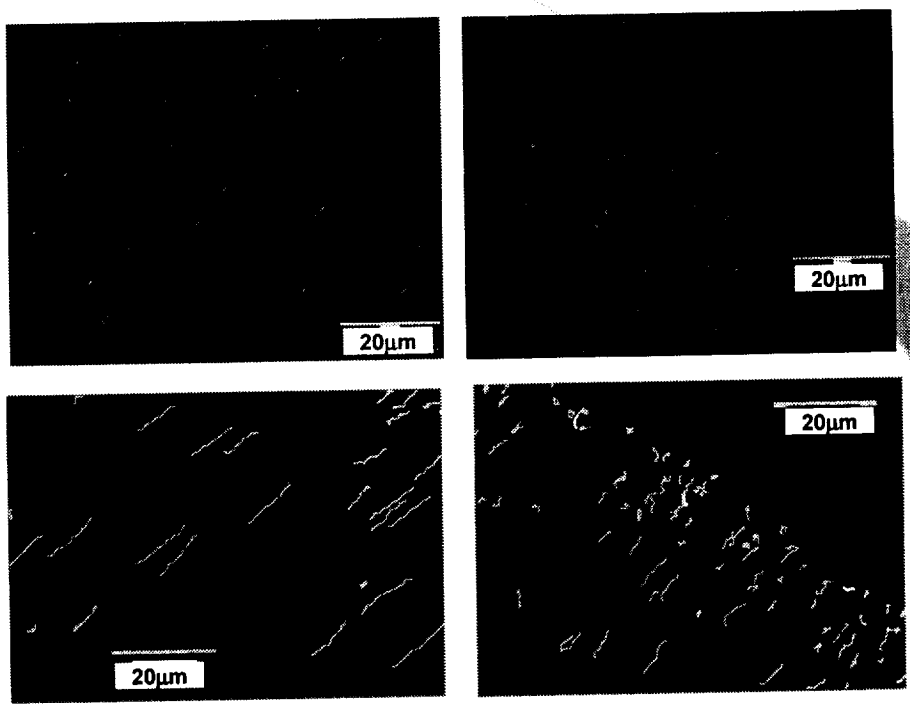

Comparison Between Simulations and Experiments in Drying Droplets

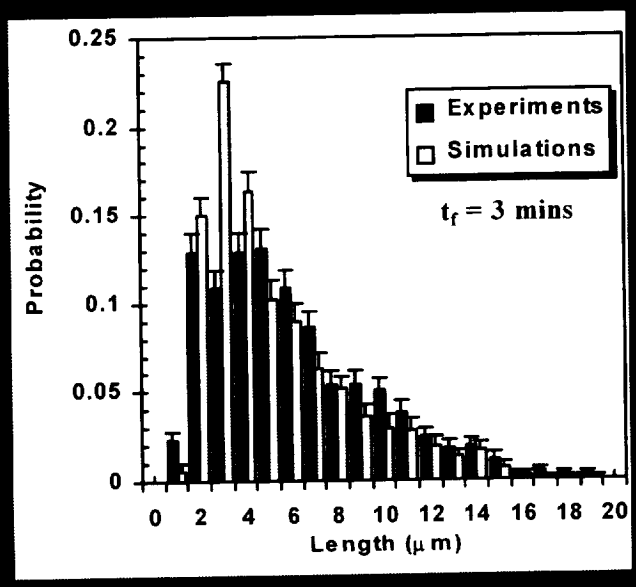

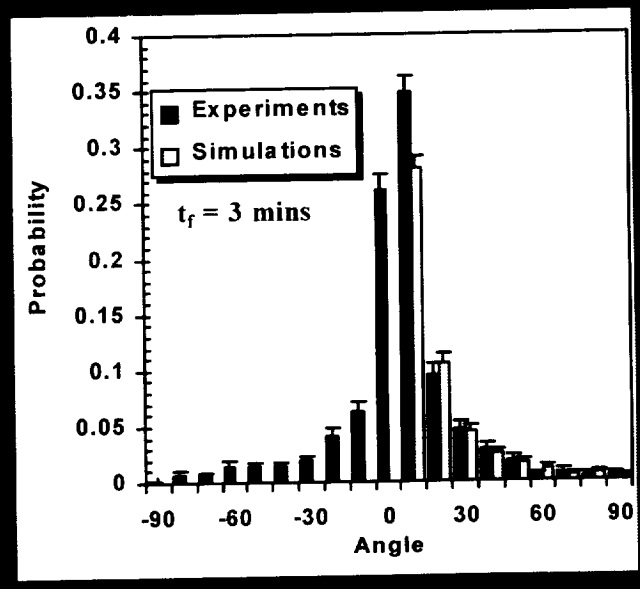

Droplet: simulation and experimental results at medium evaporation rate

Conclusions

FEM analysis show that the evaporation flux is singular near the edge of the droplet and the temperature profile on the vapor-liquid interface is non-uniform, which generates a Marangoni stress on the droplet surface.

The analytical solutions for the full velocity field in the evaporating droplet with/without Marangoni stress are first time derived basing on the lubrication theory. The approximated analytical results agree with the FEM analysis very well, especially when Marangoni flow is present.

Conclusions

Microscopic particle-tracking velocimetry is able to map the 3D velocity field from a 2D image. And the time-dependent flow fields in an evaporating droplet are obtained. A weak recirculation flow near the droplet surface is observed.

Using the theoretical velocity field, combined with Brownian dynamics simulations, quantitative predictions are made of the configurations of DNA molecules adsorbed onto the substrate.

NON-INVASIVE HEALTH DIAGNOSTICS USING EYE AS A "WINDOW TO THE BODY"

RAFAT R. ANSARI
NASA Glenn Research Center
Mail Stop 333-1, 21000 Brookpark Road
Cleveland, OH 44135
Tel: 216-433-5008, Fax: 216-977-7138, E-mail: rafat.r.ansari@grc.nasa.gov

ABSTRACT

As a "window to the body", the eye offers the opportunity to use light in various forms to detect ocular and systemic abnormalities long before clinical symptoms appear and help develop preventative/therapeutic countermeasures early. The effects of space travel on human body are similar to those of normal aging. For example, radiation exposure in space could lead to formation of cataracts and cancer by damaging the DNA and causing gene mutation. Additionally, the zero-gravity environment causes fluid shifts in the upper extremities of the body and changes the way blood flows and organ system performs. Here on Earth, cataract, age-related macular degeneration (AMD), diabetic retinopathy (DR), and glaucoma are major eye diseases and are expected to double in next two decades. To detect, prevent, and treat untoward effects of prolonged space travel in real-time requires the development of non-invasive diagnostic technologies that are compact and powerful. We are developing fiber-optic sensors to evaluate the ocular tissues in health, aging, and disease employing the techniques of dynamic light scattering (cataract, uveitis, Alzheimer's, glaucoma, DR, radiation damage, refractive surgery outcomes), auto-fluorescence (aging, DR), laser-Doppler flowmetry (choroidal blood flow), Raman spectroscopy (AMD), polarimetry (diabetes), and retinal oximetry (occult blood loss). The non-invasive feature of these technologies integrated in a head-mounted/goggles-like device permits frequent repetition of tests, enabling evaluation of the results to therapy that may ultimately be useful in various telemedicine applications on Earth and in space.
Acknowledgements: NASA-NIH and NASA-FDA Interagency Agreements, and John Glenn Biomedical Engineering Consortium. Collaborators: Manuel B. Datiles, MD and J. Samuel Zigler, Ph.D., (NEI/NIH), Michelle M. Chenault, Ph.D., (FDA), J. Sebag, MD (Doheny Eye Institute), Luigi Rovati, Ph.D., (University of Modena, Italy), Martial Geiser (Institute for Research in Ophthalmology, Switzerland), Marco F. Cabrera, Ph.D., (CWRU), Fabrice Moret (NCMR/HEVs), and James F. King (QSS/NASA).

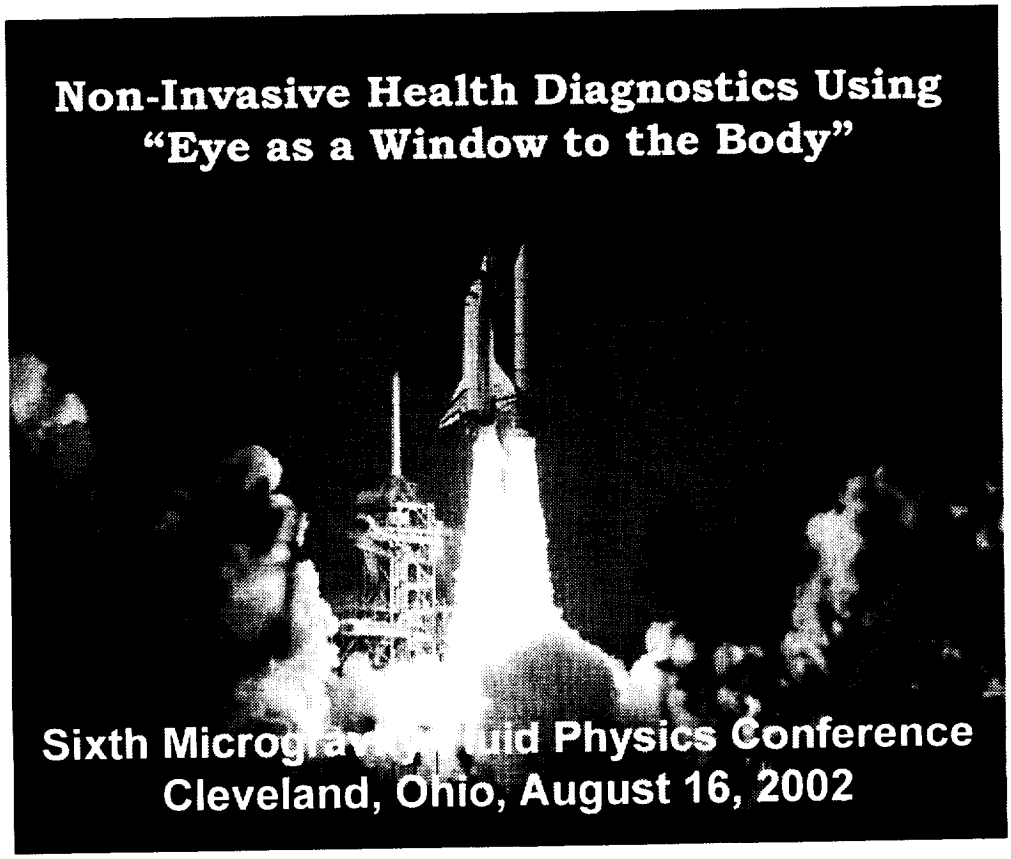

Contact:
Rafat R. Ansari, Ph.D.
Phone: 216–433–5008
email: rafat.r.ansari@grc.nasa.gov

81727
22

"EYE IS A WINDOW TO THE SOUL", JESUS, HOLY BIBLE

Can Eye be a "Window to the Body"?

Effects of Space Travel on the Human Body are Similar to that of Aging

Contact:
Rafat R. Ansari, Ph.D.
Phone: 216–433–5008
email: rafat.r.ansari@grc.nasa.gov

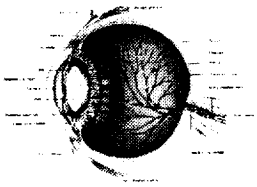

"MICROCOSM OF THE BODY"

- Eye is built like a camera.
- Light from cornea to the retina traverses through tissues that are representative of nearly every tissue type in the body.
- Cornea: typical extra-cellular matrix composed primarily of collagen.
- Aqueous: an ultrafiltrate of blood, containing most of the molecules found in serum at concentrations that are reflective of serum levels.
- Lens: highly organized array of crystallin proteins.
- Vitreous: similar in nature to the articular cartilage and synovial fluid found in joints.
- Retina and optic nerves are in fact part of the central nervous system.
- Since eye is easily accessed by light, the optical technologies can be used for the evaluation of structure and physiology in health, aging, and disease.

Contact:
Rafat R. Ansari, Ph.D.
Phone: 216–433–5008
email: rafat.r.ansari@grc.nasa.gov

AIM: DIAGNOSE DISEASES NON-INVASIVELY LONG BEFORE CLINICAL SYMPTOMS APPEAR	
OPTICAL TECHNIQUE	DISEASE
DYNAMIC LIGHT SCATTERING	CATARACT, RADIATION DAMAGE, VITREOPATHY, UVEITIS, CHOLESTEROL, ALZHEIMER'S, LASIK COMP
AUTOFLUORESCENCE	DIBETIC RETINOPATHY
LASER DOPLER VELOCIMETRY/FLOWMETRY	RETINAL DISEASE (AMD) DIABETIC RETINOPATHY
RAMAN	AGE-RELATED MACULAR DEGENERATION (AMD)
POLARIMETRY	DIABETES (BLOOD GLUCOSE MANAGEMENT)
OXIMETRY	DIABETES, STROKE, TRAUMA

Contact:
Rafat R. Ansari, Ph.D.
Phone: 216–433–5008
email: rafat.r.ansari@grc.nasa.gov

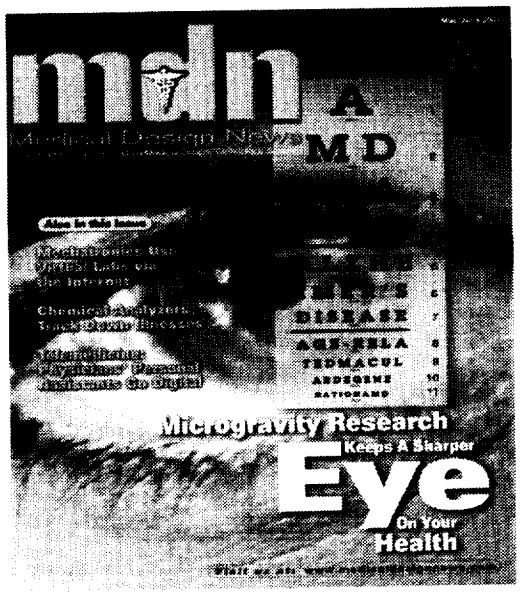

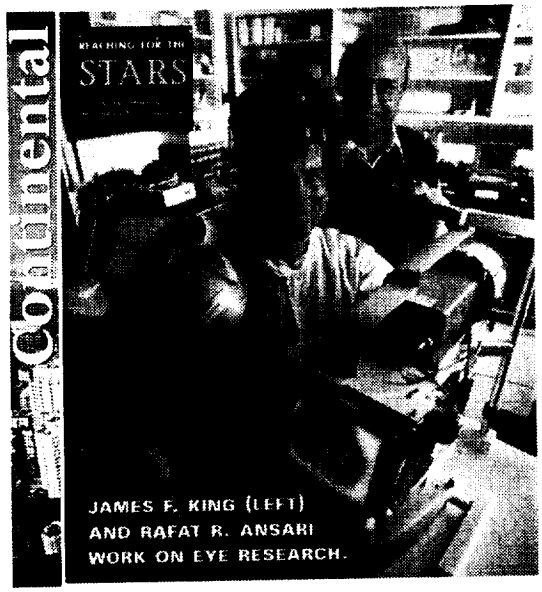

CNN / WebMD®

World

AMERICAN ACADEMY OF OPHTHALMOLOGY
The Eye M.D. Association

Contact:
Rafat R. Ansari, Ph.D.
Phone: 216–433–5008
email: rafat.r.ansari@grc.nasa.gov

IONIZING RADIATION CAN CAUSE GENES TO MUTATE

A CLINICAL STUDY FROM NASA JSC SHOWS THAT

Cataractogenesis due to *radiation* exposure is a risk factor.

(Cucinotta et al., "Space radiation and cataracts in astronauts", Radiation Research, Vol.156, No. 5, 460-466, Nov. 2001.)

Contact:
Rafat R. Ansari, Ph.D.
Phone: 216–433–5008
email: rafat.r.ansari@grc.nasa.gov

BLINDNESS DUE TO CATARACTS

- Worldwide, 50% of all blindness is due to cataracts
- No medical treatment
- 1.4 million cataract surgeries are performed each year in the U.S.
- $3.4 billion spent through Medicare
- 34 million Americans have cataracts over the age 65
- 70 million Americans will have cataracts in year 2030 compared to 34 million figure today

"A delay in cataract formation of about 10 years would reduce the prevalence of visually disabling cataract by about 45%"

(Carl Kupfer, MD, Director NEI/NIH, The Conquest of Cataract: A Global Challenge, trans. Ophthal., Soc., UK, 1985)

Contact:
Rafat R. Ansari, Ph.D.
Phone: 216–433–5008
email: rafat.r.ansari@grc.nasa.gov

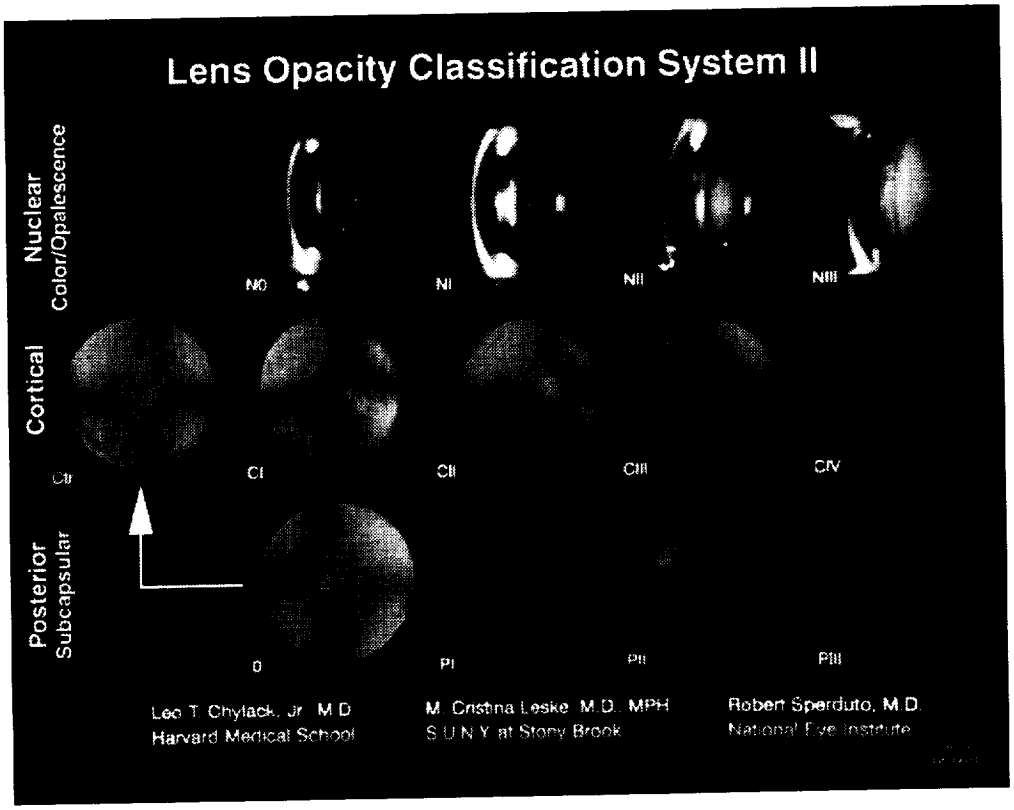

Contact:
Rafat R. Ansari, Ph.D.
Phone: 216–433–5008
email: rafat.r.ansari@grc.nasa.gov

Compact Dynamic Light Scattering (DLS) Fiber Optic Probe for Early Cataract Detection

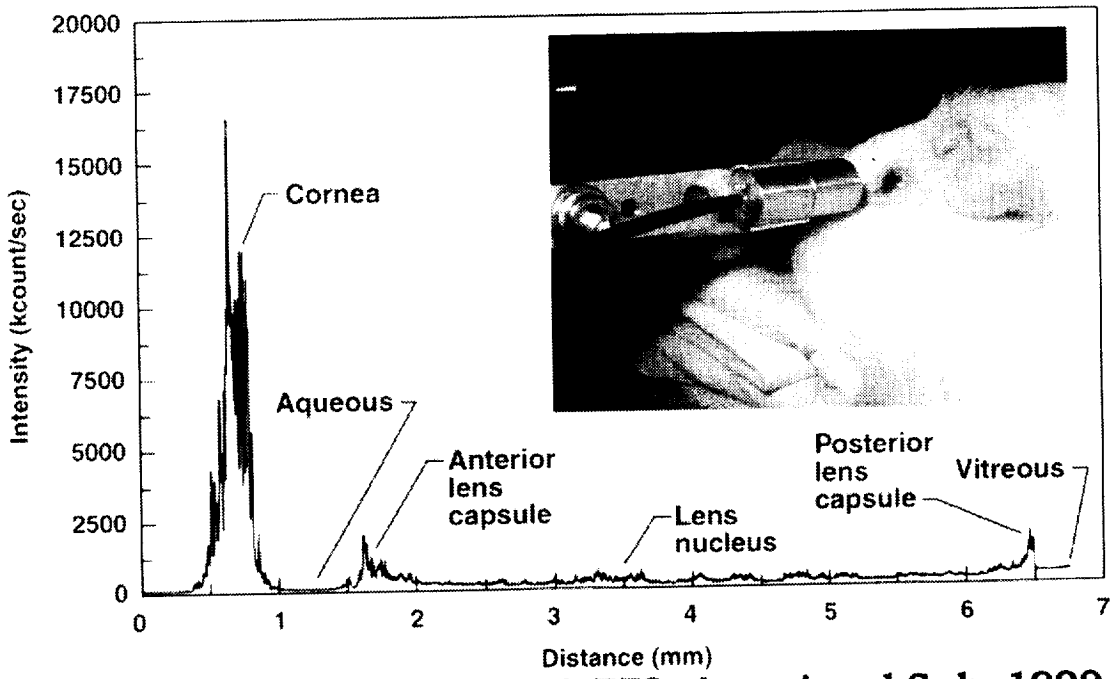

PATENT 5,973,779, Ansari and Suh, 1999

Contact:
Rafat R. Ansari, Ph.D.
Phone: 216–433–5008
email: rafat.r.ansari@grc.nasa.gov

Radiation Cataract

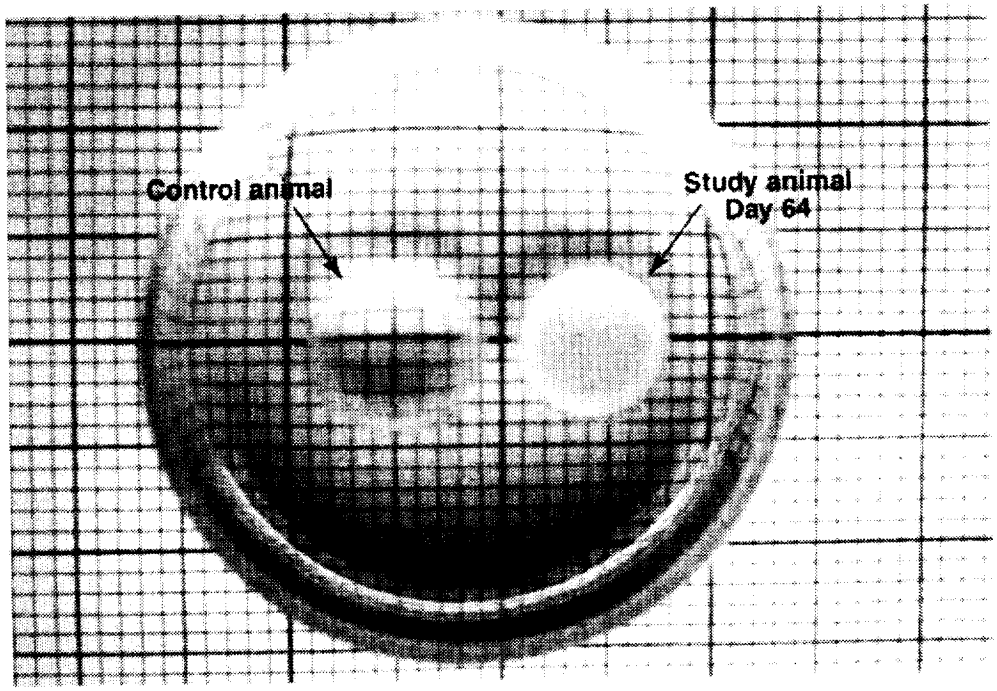

In Rabbits

Contact:
Rafat R. Ansari, Ph.D.
Phone: 216–433–5008
email: rafat.r.ansari@grc.nasa.gov

IN VITRO BIOCHEMICAL ANALYSIS

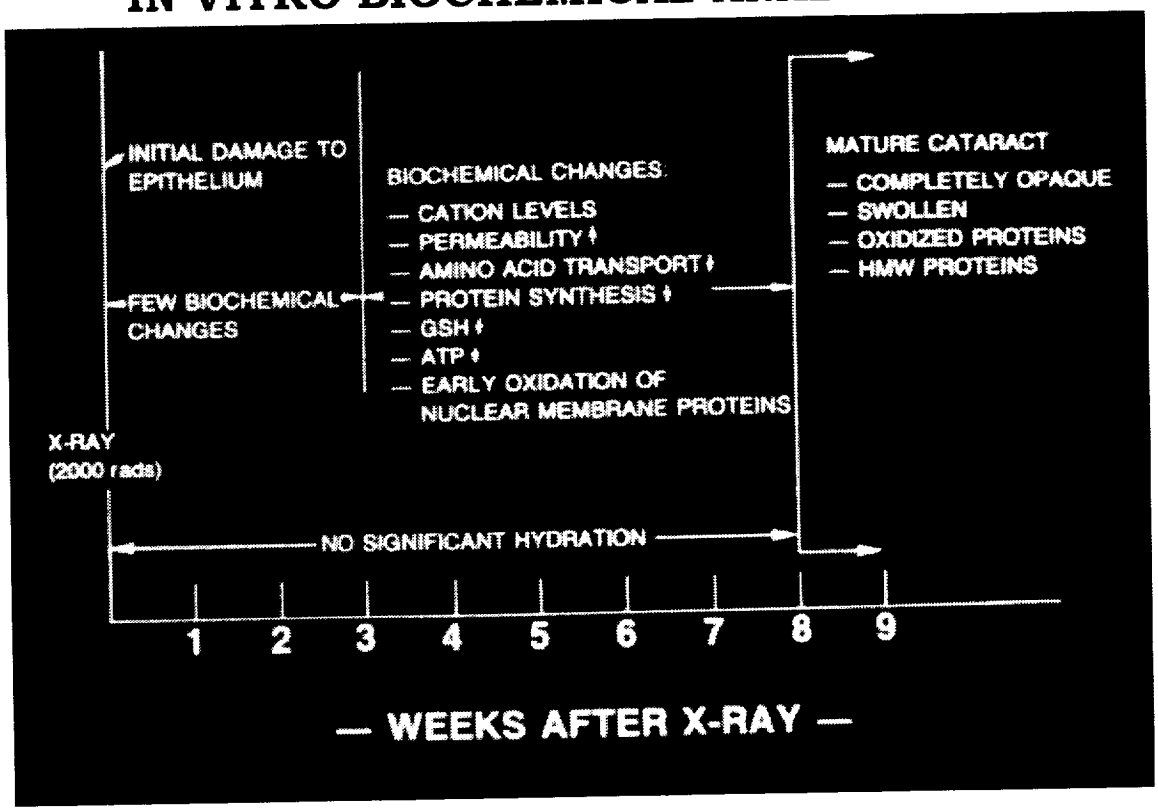

Contact:
Rafat R. Ansari, Ph.D.
Phone: 216–433–5008
email: rafat.r.ansari@grc.nasa.gov

Courtesy of Frank Giblin, Ph.D. Oakland University, MI

Environmental Ocular Toxicity: Effects of X-Ray Irradiation (DLS-Rabbit Study)

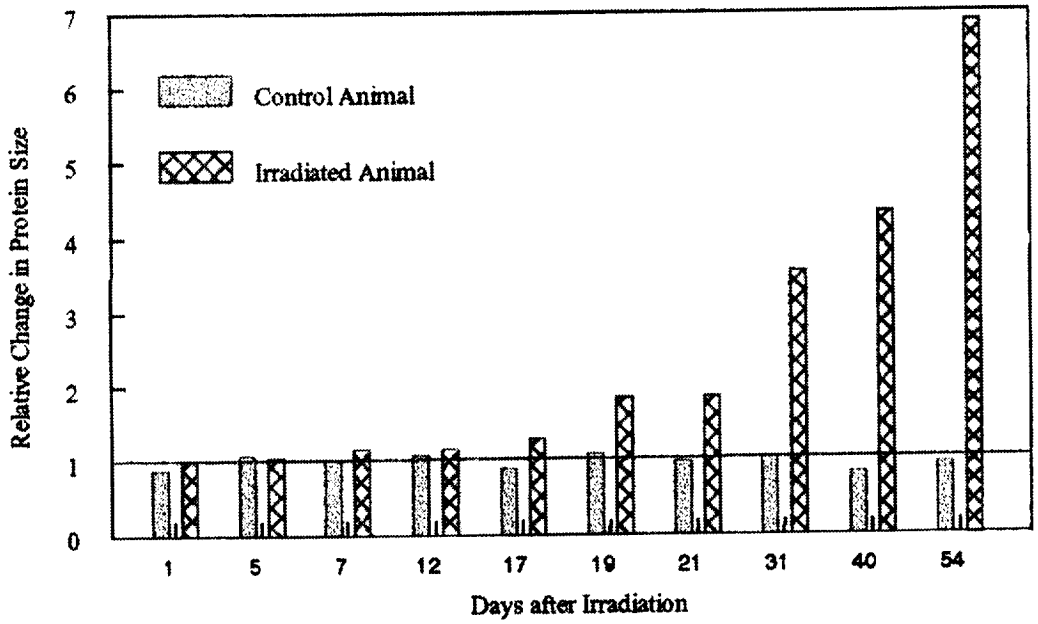

Outstanding Paper Award: Radiation Track, STAIF February, 2002

Contact:
Rafat R. Ansari, Ph.D.
Phone: 216–433–5008
email: rafat.r.ansari@grc.nasa.gov

Counter Measures: Cataract Treatment in Rats
2nd Day Post Injection Slit-Lamp Results

Control

Selenite only

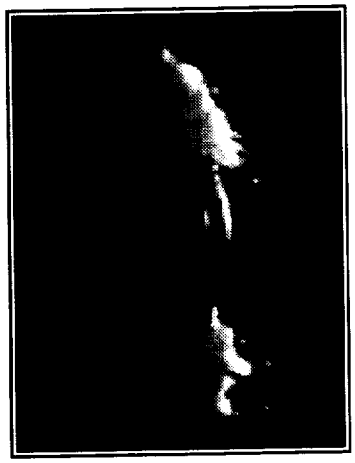

Pantethine prior to Selenite injection

Contact:
Rafat R. Ansari, Ph.D.
Phone: 216–433–5008
email: rafat.r.ansari@grc.nasa.gov

Cataract Treatment in Rats (One Day Post-Injection)
Non-Invasive DLS Screening (Static Mode)

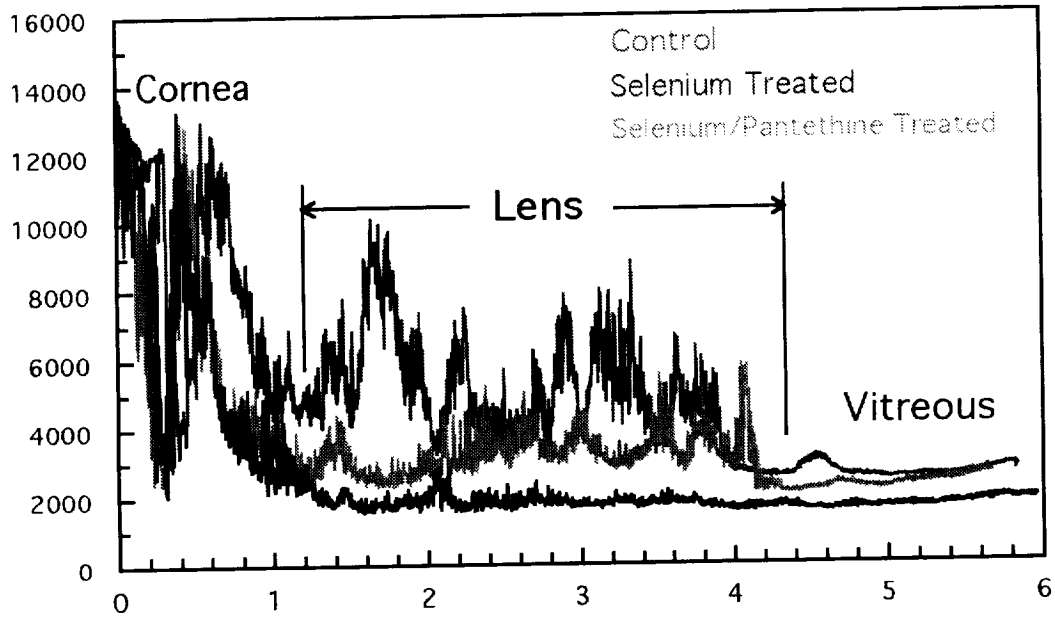

Contact:
Rafat R. Ansari, Ph.D.
Phone: 216–433–5008
email: rafat.r.ansari@grc.nasa.gov

Cataract Treatment in Rats
(One day post-injection)

Non-Invasive DLS Size Distribution In-Vivo Results

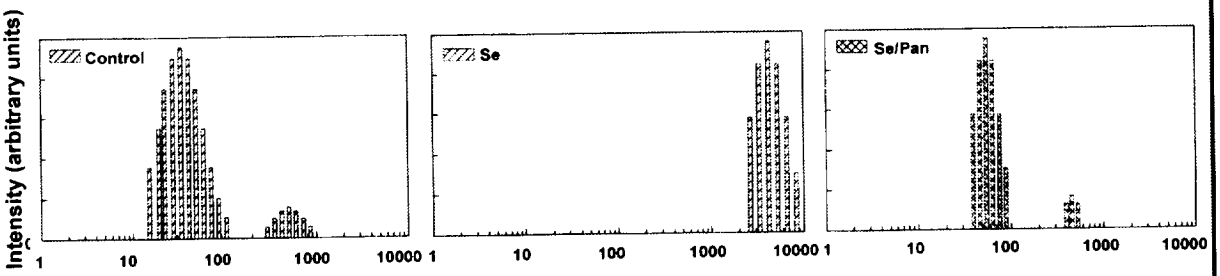

Nuclear Protein Crystallin diameter (nm)

Contact:
Rafat R. Ansari, Ph.D.
Phone: 216–433–5008
email: rafat.r.ansari@grc.nasa.gov

New NASA-Developed DLS Eye Diagnostics Device in Clinical Use at NEI/NIH

Cataract

Post LASIK Evaluation

Glaucoma

Alzheimer's

Uveitis

Vitreopathy

Diabetic Retinopathy

Drug screening

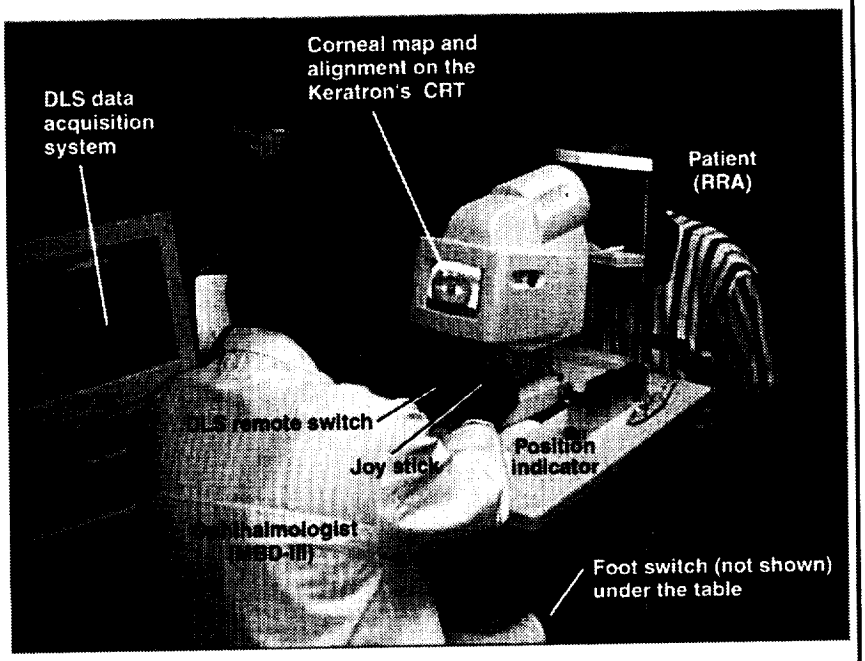

Exp. Eye Res., Vol. 74, 93-102, January, 2002

NIH-NASA Interagency Agreement

Contact:
Rafat R. Ansari, Ph.D.
Phone: 216–433–5008
email: rafat.r.ansari@grc.nasa.gov

Presently Fluorescene Angiography is the Most Widely Used Technique

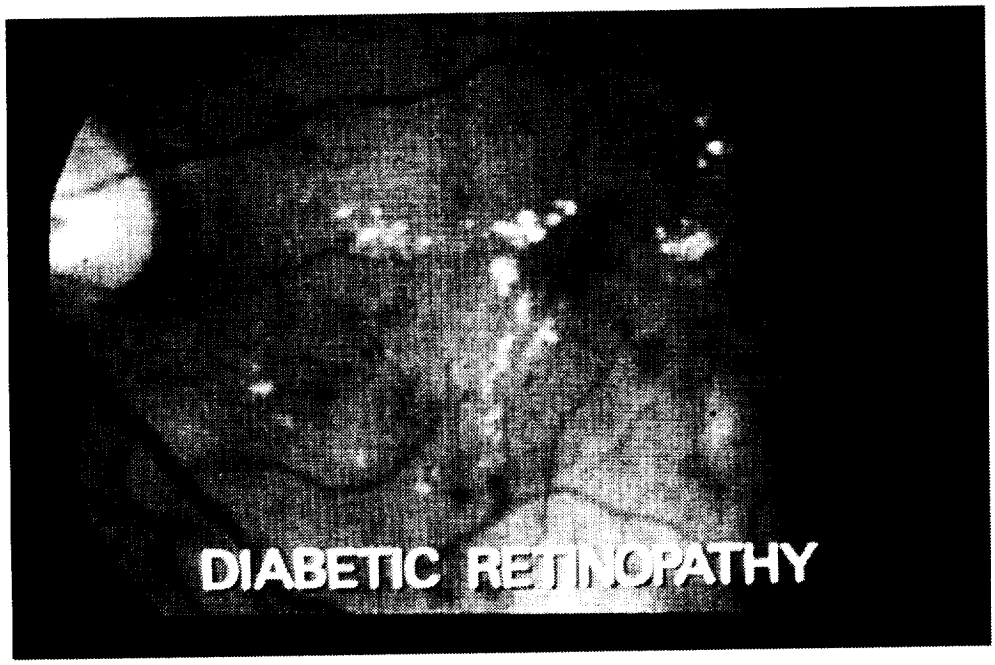

Contact:
Rafat R. Ansari, Ph.D.
Phone: 216–433–5008
email: rafat.r.ansari@grc.nasa.gov

Natural Fluorescence as a Function of Age (Oxidative Stress in Humans)

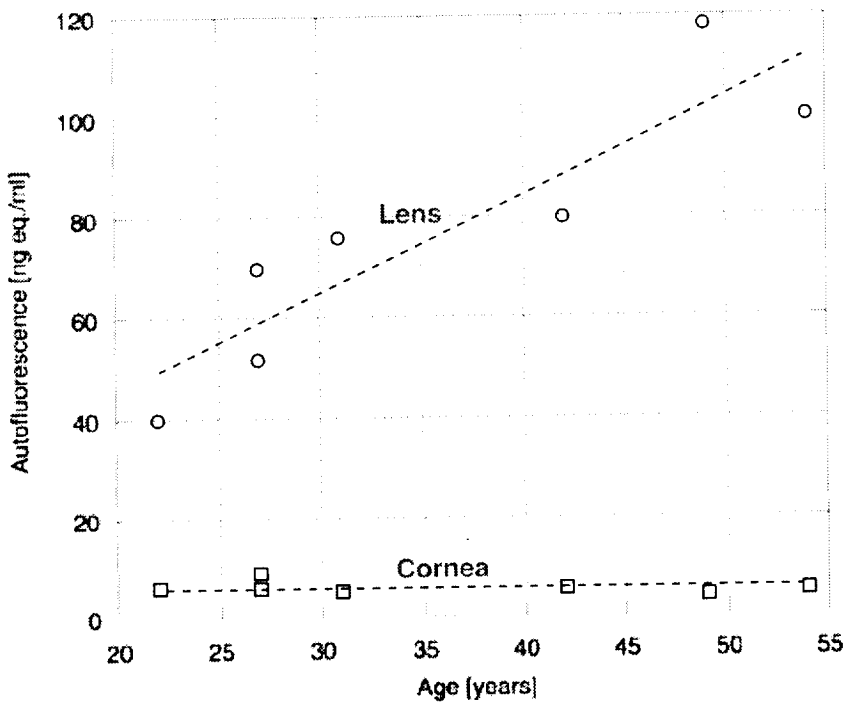

Contact:
Rafat R. Ansari, Ph.D.
Phone: 216–433–5008
email: rafat.r.ansari@grc.nasa.gov

SPIE, BiOS 2002

Corneal Auto-Fluorescence and Diabetic Retinopathy

Metabolically active Epithelial and Endothelial cells contain fluorophores: pyridine nucleotides (NADPH) and flavins (FMN and protein-linked flavins)

λ = 500-520 nm

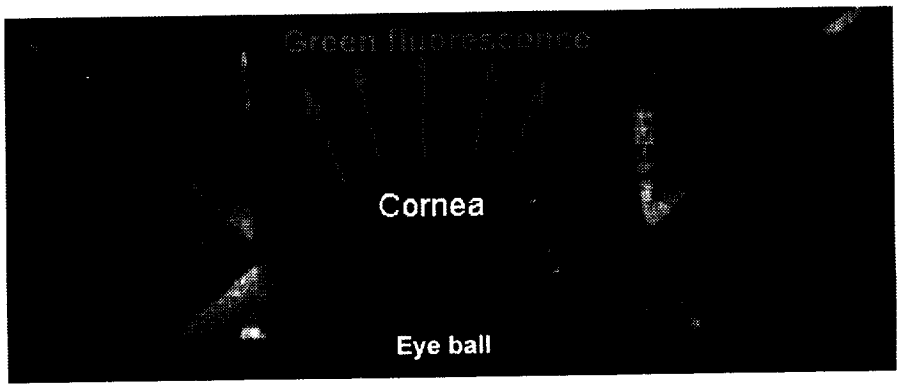

NADPH fluoresce in the reduced redox state and flavins in the oxidized redox state

Contact:
Rafat R. Ansari, Ph.D.
Phone: 216–433–5008
email: rafat.r.ansari@grc.nasa.gov

NON-INVASIVE
Autofluorescence Camera

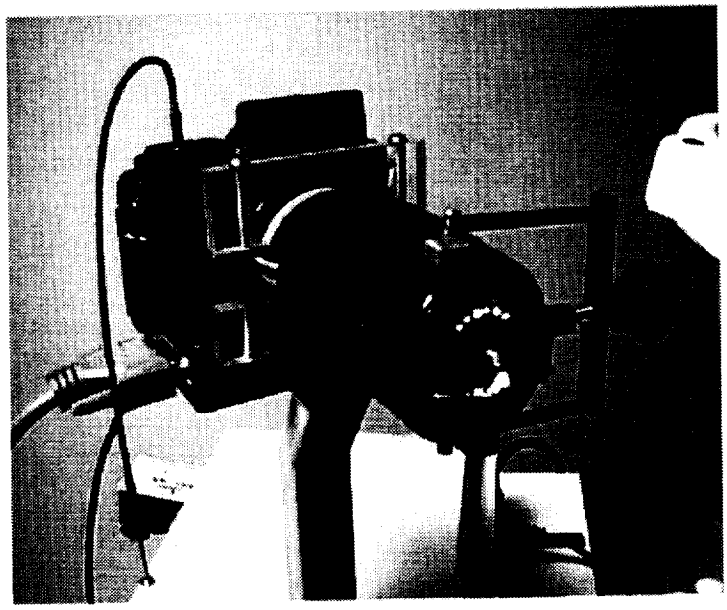

NO NEED for FLUORESCENE DYE INJECTIONS

NCMR-UNIVERSITY OF BRESCIA COOPERATIVE AGREEMENT

Contact:
Rafat R. Ansari, Ph.D.
Phone: 216–433–5008
email: rafat.r.ansari@grc.nasa.gov

Results of a Preliminary Clinical Test Performed on about 90 Diabetic Subjects

(the bars represent the standard error in the measurements)

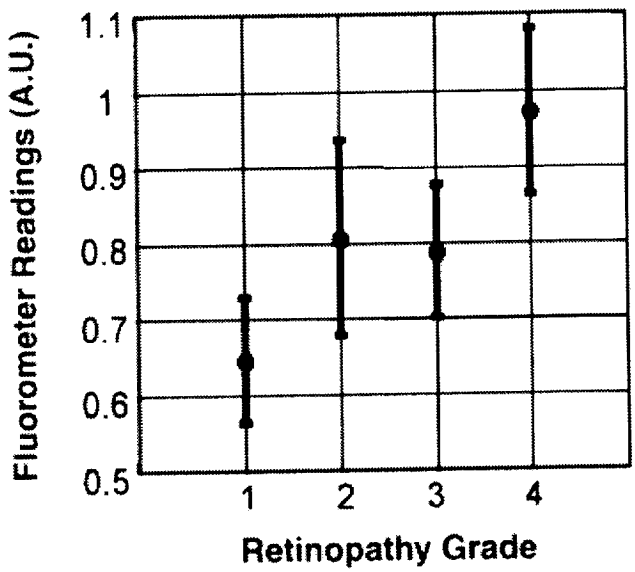

Contact:
Rafat R. Ansari, Ph.D.
Phone: 216–433–5008
email: rafat.r.ansari@grc.nasa.gov

JBO, Vol 3, 357-363, 1999

Astronauts Report Changes in Visual Acuity in Orbital Flight

On Earth

On-Orbit

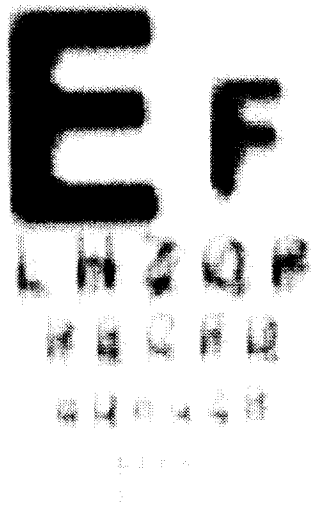

To this date this remain of unknown etiology

Contact:
Rafat R. Ansari, Ph.D.
Phone: 216–433–5008
email: rafat.r.ansari@grc.nasa.gov

Choroid may have an answer!

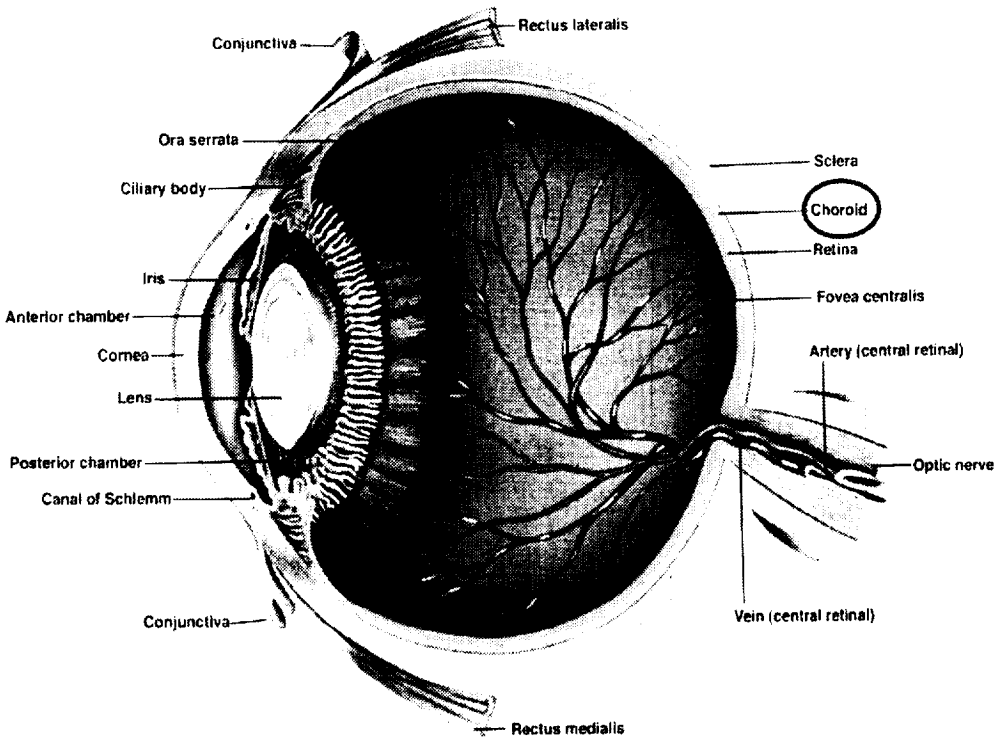

Contact:
Rafat R. Ansari, Ph.D.
Phone: 216–433–5008
email: rafat.r.ansari@grc.nasa.gov

HYPOTHESIS (in collaboration with Keith Manuel, OD, Flight Clinic, NASA JSC)

- Primarily, could choroidal engorgement mechanism and secondarily some curvature/shape-change mechanism of the cornea or lens be responsible for this change in VA?
- Since the choroid has no baroreceptors to autoregulate the choroid during fluid shifts as does the systemic vascular system, the choroid possibly remains engorged thereby pushing the macula forward, causing a hyperopic shift of the eye.
- KC-135 experiments could help answer this question.

Contact:
Rafat R. Ansari, Ph.D.
Phone: 216–433–5008
email: rafat.r.ansari@grc.nasa.gov

New Helmet-Mounted Laser Doppler Ocular Blood Flow Meter for Use on KC-135 Flights

Weight: ~2 Lbs

λ: 875 nm

Power: 100μW

Contact:
Rafat R. Ansari, Ph.D.
Phone: 216–433–5008
email: rafat.r.ansari@grc.nasa.gov

HERE ON EARTH LDF CAN ALSO BE USED FOR THE

EARLY DETECTION OF AMD

(Age Related Macular Degeneration)

AMD damages and destroys the central vision of up to 1 in 3 Americans in their lifetime and has no known cause or cure.

By the year 2025 the population of people over the age 65 in the U.S. will be 6 times higher than in 1990. AMD will soon take on aspects of an epidemic.

(Carl Kupfer, MD, Director NEI/NIH)

Contact:
Rafat R. Ansari, Ph.D.
Phone: 216–433–5008
email: rafat.r.ansari@grc.nasa.gov

DIABETES

"Between the time you wake up this morning and the time you wake up tomorrow morning, there are going to be 2,000 people diagnosed with diabetes. There will be 150 amputations, about 70 people who go blind from diabetes, and approximately 75 people who enter end-stage kidney disease programs because of diabetes."

(Frank Vinicor, MD, MPH, Director of the Division of Diabetes Translation, CDC)

Presently the only method available today to manage diabetes is the "Finger-Stick"

Contact:
Rafat R. Ansari, Ph.D.
Phone: 216–433–5008
email: rafat.r.ansari@grc.nasa.gov

Head-Mounted Glucose Meter

(Funded by John Glenn Biomedical Engineering Consortium)

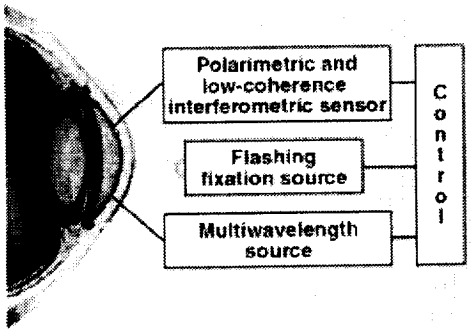

Ansari and Rovati (2002) patent pending
Ansari et al., J. App. Opt. 2002 in Review

Contact:
Rafat R. Ansari, Ph.D.
Phone: 216–433–5008
email: rafat.r.ansari@grc.nasa.gov

Present and Future

Remote Health Monitoring: for the Benefit of All Human Kind

Prototype head mounted eye disease monitoring system.

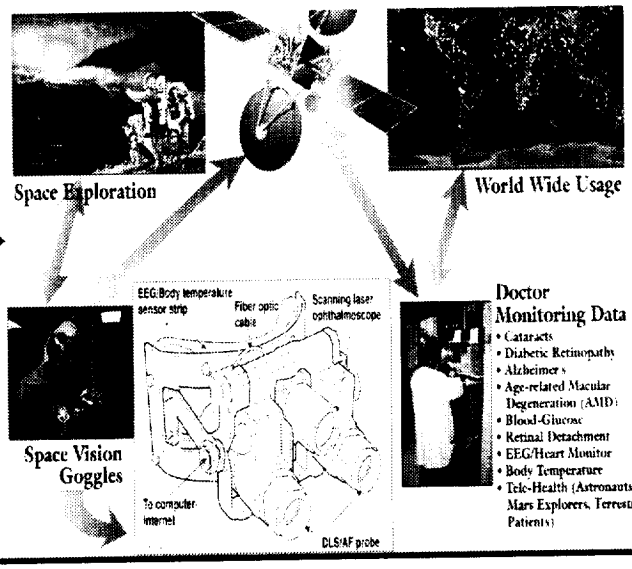

NASA JSC Critical Path Roadmap: Clinical Capabilities and Effective Countermeasures

Contact:
Rafat R. Ansari, Ph.D.
Phone: 216–433–5008
email: rafat.r.ansari@grc.nasa.gov

Collaborators

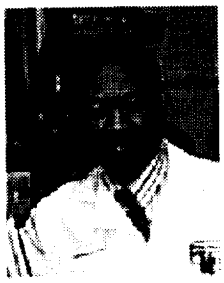

Manuel Datiles, MD
NIH/NEI

Jerry Sebag, MD
Doheny Eye Clinic.

Frank Giblin, Ph.D.
Oakland University

Luigi Rovati, PhD
U. of Modena

Martial Geiser
IRO Switzerland

John Clark, PhD
U. of Washington

Contact:
Rafat R. Ansari, Ph.D.
Phone: 216–433–5008
email: rafat.r.ansari@grc.nasa.gov

Session 6: Dynamics and Instabilities

CONTAINERLESS RIPPLE TURBULENCE

Seth Putterman and William Wright
Physics Department, University of California Los Angeles CA 90095

Walter Duval and Charles Panzarella
NASA Glenn Research Center, Cleveland OH

ABSTRACT

One of the longest standing unsolved problems in physics relates to the behavior of fluids that are driven far from equilibrium such as occurs when they become turbulent due to fast flow through a grid or tidal motions. In turbulent flows the distribution of vortex energy as a function of the inverse length scale [or wavenumber 'k']of motion is proportional to $1/k^{5/3}$ which is the celebrated law of Kolmogorov. Although this law gives a good description of the average motion, fluctuations around the average are huge. This stands in contrast with thermally activated motion where large fluctuations around thermal equilibrium are highly unfavorable. The problem of turbulence is the problem of understanding why large fluctuations are so prevalent which is also called the problem of "intermittency".

Turbulence is a remarkable problem in that its solution sits simultaneously at the forefront of physics, mathematics, engineering and computer science. A recent conference [March 2002] on "Statistical Hydrodynamics" organized by the Los Alamos Laboratory Center for Nonlinear Studies brought together researchers in all of these fields. Although turbulence is generally thought to be described by the Navier-Stokes Equations of fluid mechanics the solution as well as its existence has eluded researchers for over 100 years. In fact proof of the existence of such a solution qualifies for a 1M$ millennium prize.

As part of our NASA funded research we have proposed building a bridge between vortex turbulence and wave turbulence. The latter occurs when high amplitude waves of various wavelengths are allowed to mutually interact in a fluid. In particular we have proposed measuring the interaction of ripples [capillary waves] that run around on the surface of a fluid sphere suspended in a microgravity environment.

The problem of ripple turbulence poses similar mathematical challenges to the problem of vortex turbulence. The waves can have a high amplitude and a strong nonlinear interaction. Furthermore, the steady state distribution of energy again follows a Kolmogorov scaling law; in this case the ripple energy is distributed according to $1/k^{7/4}$. Again, in parallel with vortex turbulence ripple turbulence exhibits intermittency [Wright et al Science 278, 1609 (97)].

The problem of ripple turbulence presents an experimental opportunity to generate data in a controlled, benchmarked system. In particular the surface of a sphere is an ideal environment to study ripple turbulence. Waves run around the sphere and interact with each other, and the effect of walls is eliminated. In microgravity this state can be realized for over 2 decades of frequency.

Wave turbulence is a physically relevant problem in its own right. It has been studied on the surface of liquid hydrogen [Brazhnikov et al] and its application to Alfven waves in space is a source of debate.[P. Goldreich]. Of course, application of wave

turbulence perspectives to ocean waves has been a major success of V. E. Zakharov. [Kolmogorov Spectra of Turbulence, Springer, Berlin 1992].

The experiment which we plan to run in microgravity is conceptually straightforward. Ripples are excited on the surface of a spherical drop of fluid and then their amplitude is recorded with appropriate photography. A key challenge is posed by the need to stably position a 10cm diameter sphere of water in microgravity. Two methods are being developed. Orbitec is using controlled puffs of air from at least 6 independent directions to provided the positioning force. This approach has actually succeeded to position and stabilize a 4cm sphere during a KC 135 segment. Guigne International is using the radiation pressure of high frequency sound. These transducers have been organized into a device in the shape of a dodecahedron. This apparatus 'SPACE DRUMS' has already been approved for use for combustion synthesis experiments on the International Space Station.

A key opportunity presented by the ripple turbulence data is its use in driving the development of codes to simulate its properties. A head start on this aspect of the project is being developed at NASA Glenn Research Center.

SCIENCE REQUIREMENT

What are the differences in the way in which energy is distributed in turbulent flow and in thermal equilibrium ?

Thermal Equilibrium	**Turbulence**
Experimentally controlled parameter	
T = temperature	q = energy throughput = ergs/cm^{2}sec
Probability distribution for wave motion	
$P(\{\varepsilon\}, T) \sim e^{-\Sigma(\varepsilon_i/k_B T)}$	$P(\{\varepsilon\}, q) = ??$

$$\varepsilon_i = \text{energy in mode } i$$

$\langle \varepsilon_i \rangle = k_B T$	$\langle \varepsilon_k \rangle \sim \dfrac{q^{1/2} (\rho\sigma)^{1/4}}{k^{11/4}}$
"Equipartition"	"Kolmogorov cascade"
Gaussian	Intermittency
boring	interesting
	Competition between randomization and structure

Proposed Flight Experiment

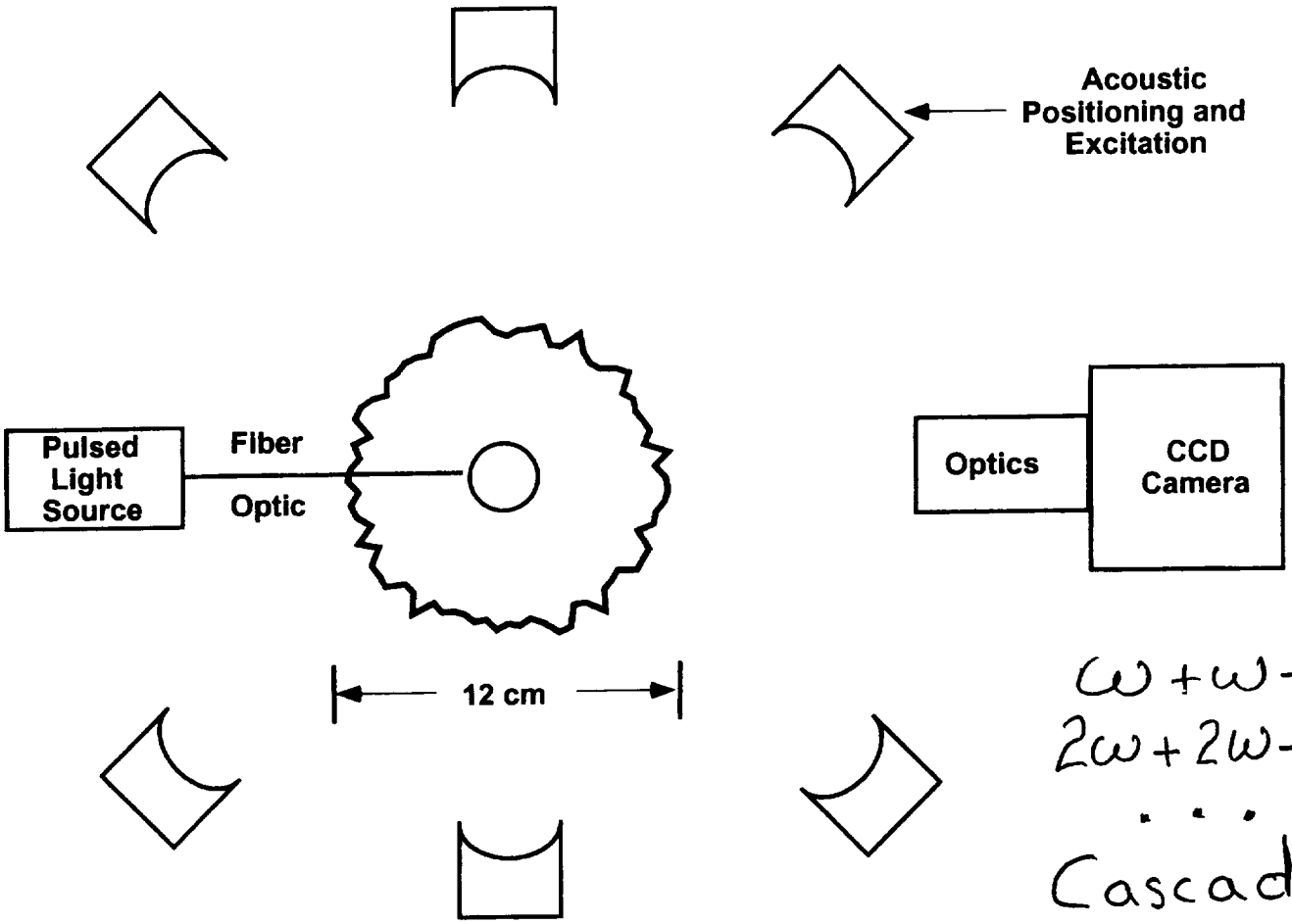

$\omega + \omega \rightarrow 2\omega$
$2\omega + 2\omega \rightarrow 4\omega$
...
Cascade

Big whorls have little whorls
Which feed on their velocity;
And little whorls have lesser whorls,
And so on to viscosity
(in the molecular sense) ... Richardson 1926

The wind comes in gusts ... attributed to Landau
1942 - Kazan

When I die and go to heaven there are two matters on which I hope for enlightenment. One is quantum electrodynamics and the other is turbulent motion of fluids. And about the former I am really optimistic.

Sir Horace Lamb 1932

Excitation and Measurement of Ripples [Ground-based]

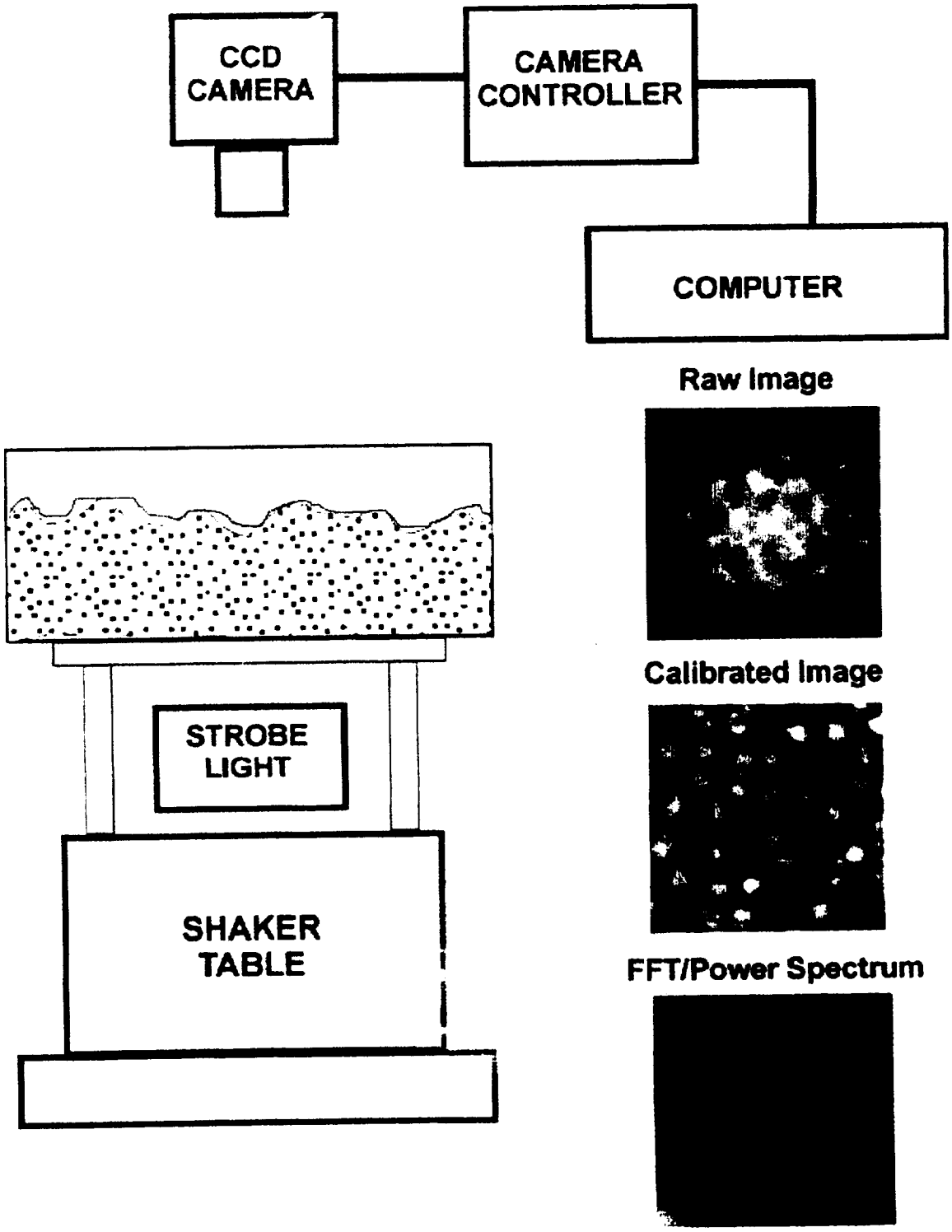

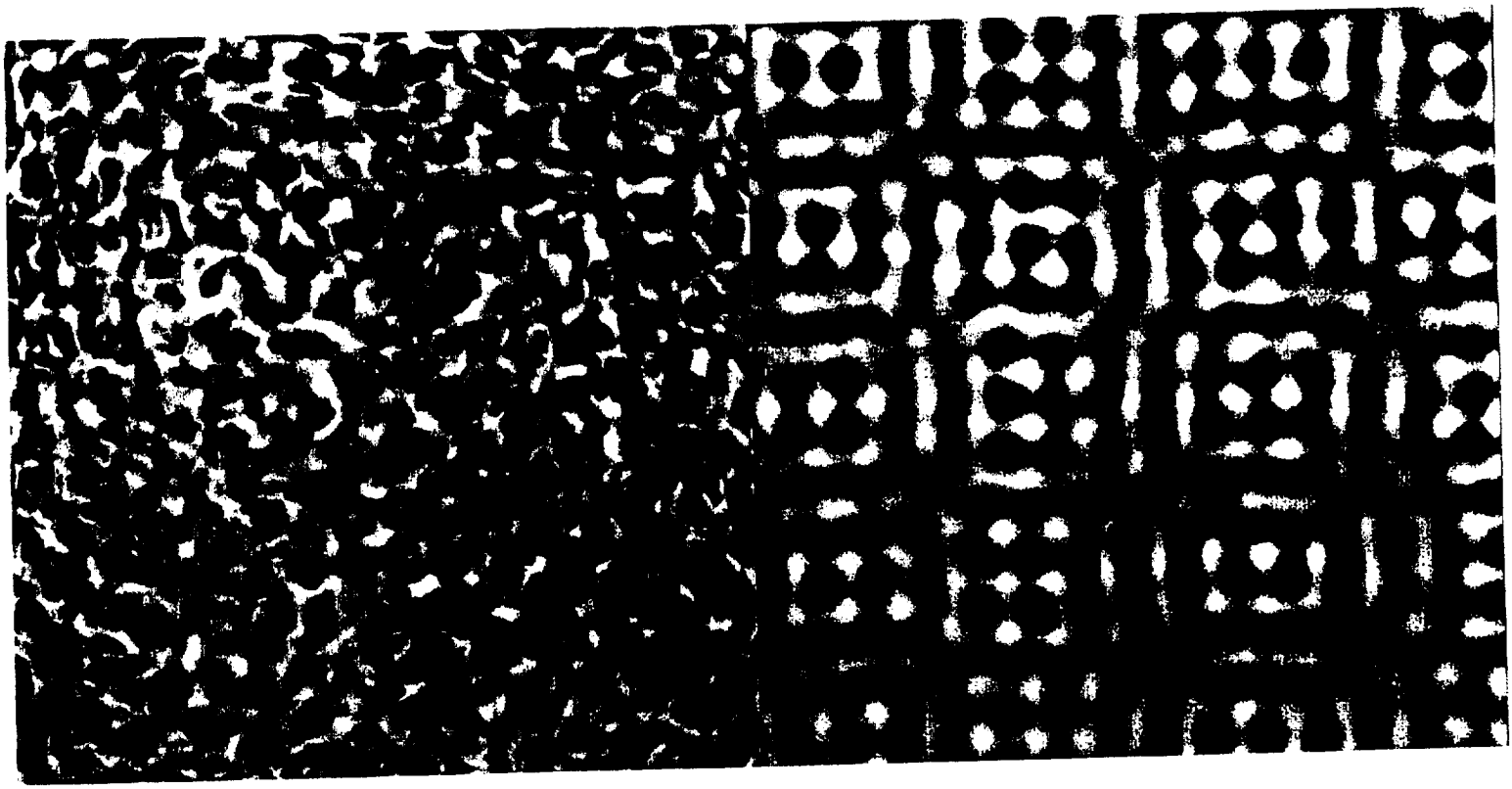

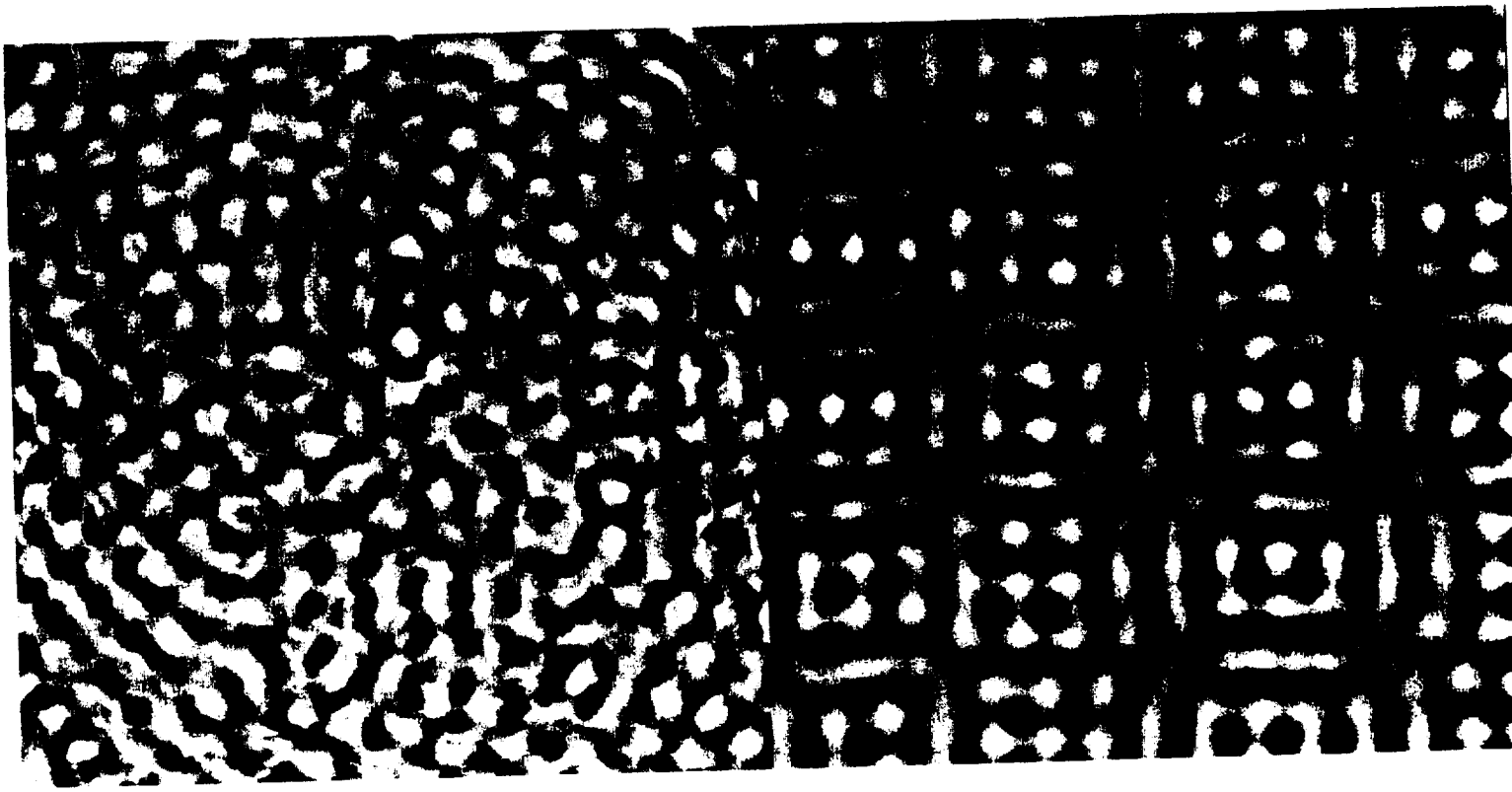

Power Spectrum of Ripple Turbulence

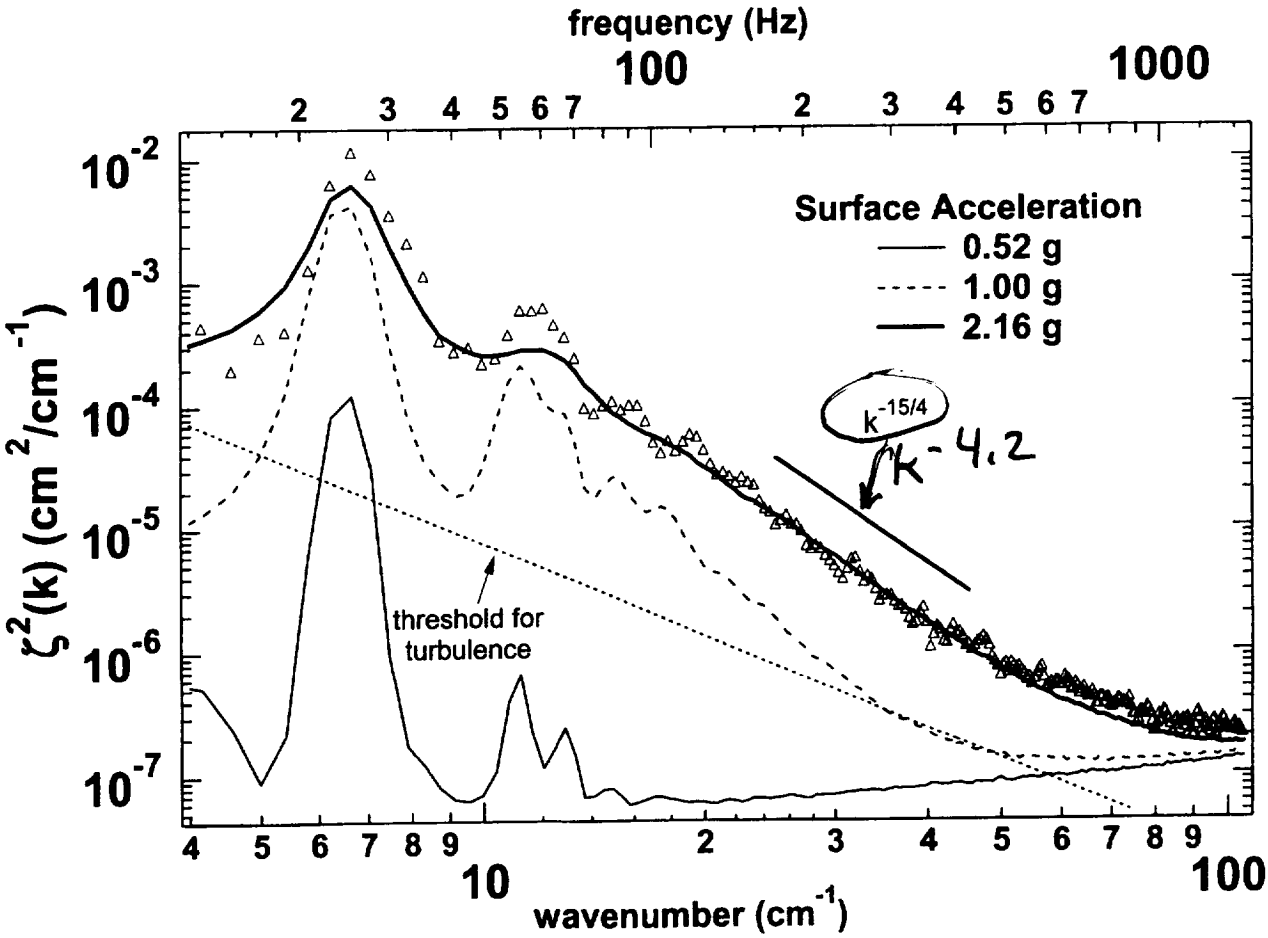

POWER SPECTRUM FOR RIPPLE TURBULENCE

$$\omega^2 = (\sigma/\rho)k^3$$

σ = surface tension

cascade from $k \to 2k$ =

$$\left.\frac{\partial E_k}{\partial t}\right]_+ = \omega_k G^2 E_k \frac{E_k}{\sigma} - 4\mu k^2 E_k$$

$E_k \cong \sigma k^2 \zeta_k^2$ = ripple energy between k and 2k

μ = kinematic viscosity ~ .01 cm²/s for water,
$G^2 = 8\pi^4/13$ = nonlinear coefficient

$$\left.\frac{\partial E_k}{\partial t}\right]_+ = q = \frac{\text{ergs}}{\text{cm}^2\text{s}} = \text{energy throughput}$$

in the steady state, $E_k \sim \left[q\sigma/g^2\omega_k\right]^{1/2}$.

therefore spectral density

$$e(\omega) \sim 1/\omega^{3/2}$$

$$\zeta^2(\omega) \simeq \frac{\sigma^{1/6} q^{1/2}/\rho^{2/3}}{\omega^{17/6}}; \zeta^2(k) \simeq \frac{q^{1/2}\rho^{1/4}/\sigma^{3/4}}{k^{15/4}}$$

$$\langle \zeta^2(r) \rangle = \langle \zeta^2(t) \rangle = \int \zeta^2(k)dk = \int \zeta^2(\omega)d\omega$$

OPERATIONAL DEFINITION OF TURBULENCE

$$\left(\frac{\partial E_k}{\partial t}\right)_+ = G^2 \omega_k E_k \frac{E_k}{\sigma} - 4\mu k^2 E_k$$

1) Interaction rate due to nonlinear scattering:

$$\frac{1}{\tau_{NL}} \equiv \frac{1}{\tau_+} \equiv G^2 \omega_k \frac{E_k}{\sigma} \gg 4\mu k^2$$

$$\text{or } M^2 > 1/G^2 Q,$$

where M is the Mach number and Q is the quality factor.

2) There must be many modes in the bandwidth determined by τ_+:

$$n(\omega)/\tau_+ \gg 1$$

where n is the density of modes

$$n(\omega) \approx \frac{S\omega^{1/3}}{3\pi(\sigma/\rho)^{2/3}}$$

and S is the surface area. $S = 10 \times 10\ cm^2$, $\frac{\omega}{2\pi} = 100\ Hz$

$n \sim 5$ seconds

<u>Turbulence, not Chaos !</u>

$M^2 \sim .1$, $G \sim 5.$

$n/\tau_+ \sim 10^4$

STOSSZAHL-ANSATZ

$$< I_i >= \int I_i P dI d\theta$$

Kinetic Equation for Waves:

$$d < I_i > / dt \sim \varepsilon^2 c^2 \sum \delta(\omega_{ijk}) < I_j I_k >$$

To close the equation requires a stosszahl ansatz -or equivalent:

$$< I_i I_j > = < I_i > < I_j >$$

RENORMALIZED WAVE VELOCITY:

$$\dot{\theta}_i = \omega_i + \int \dot{\phi}(I) dP d\theta = \omega_i + \int \dot{\phi}(I) P dI d\theta$$

where $\phi = \theta - \omega t$

$$P_1 \simeq i\pi\epsilon \sum_{ijk} \delta^-(\omega_{ijk}) c I^{3/2} e^{i\theta} \nabla \bar{P}$$

$$\frac{d}{dt}\left[< I_p I_q > - < I_p > < I_q >\right] \sim \epsilon^2 N C_{jk,q}$$

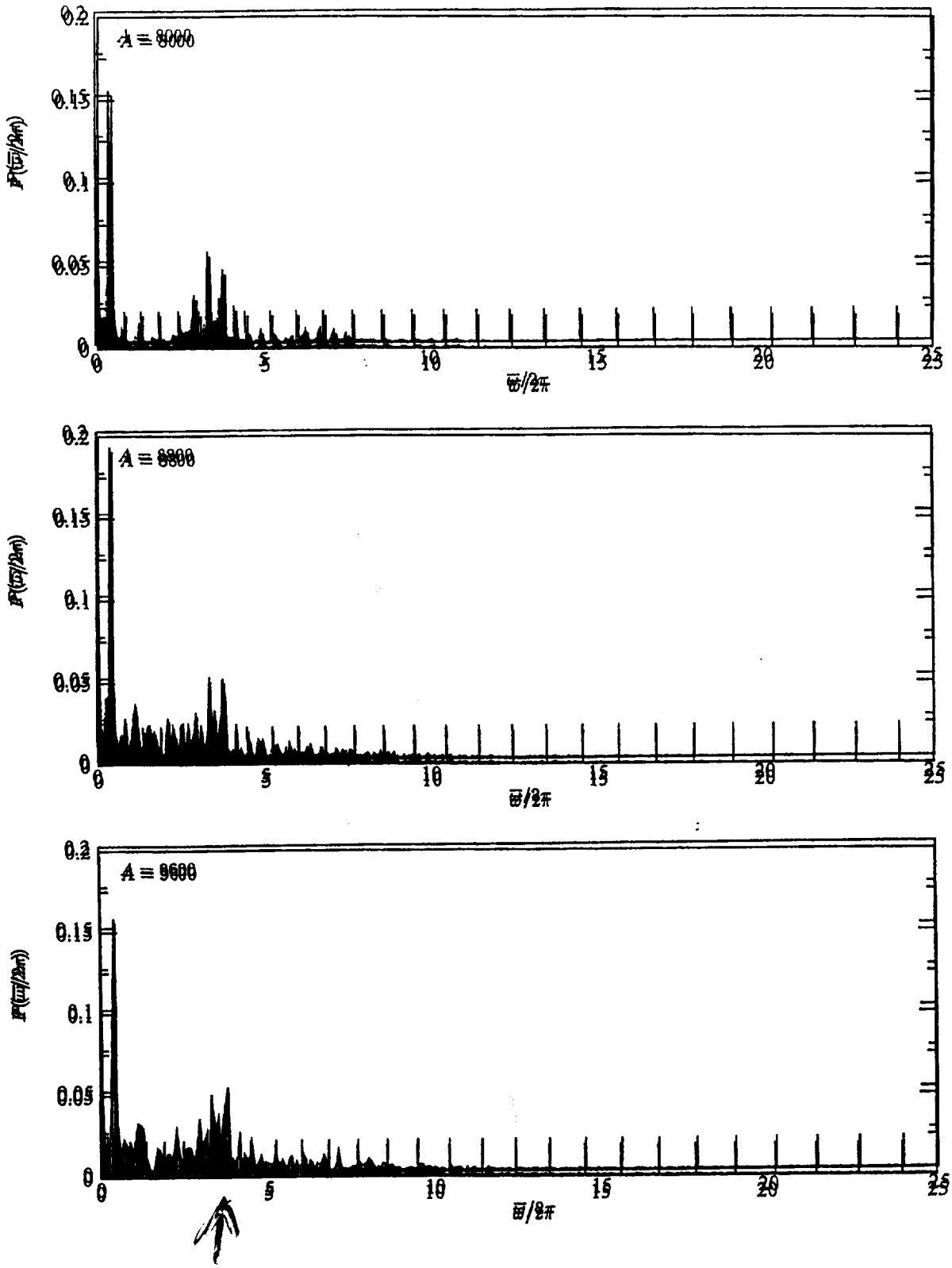

FIGURE 4. Power spectrum versus dimensionless frequency $\varpi/2\pi$ for the data shown in figure 2. The vertical lines along the frequency axis are the natural frequencies $\varpi_{l0}/(2\pi)$ for each of the symmetric spherical harmonics $l \equiv 2, \ldots, 80$.

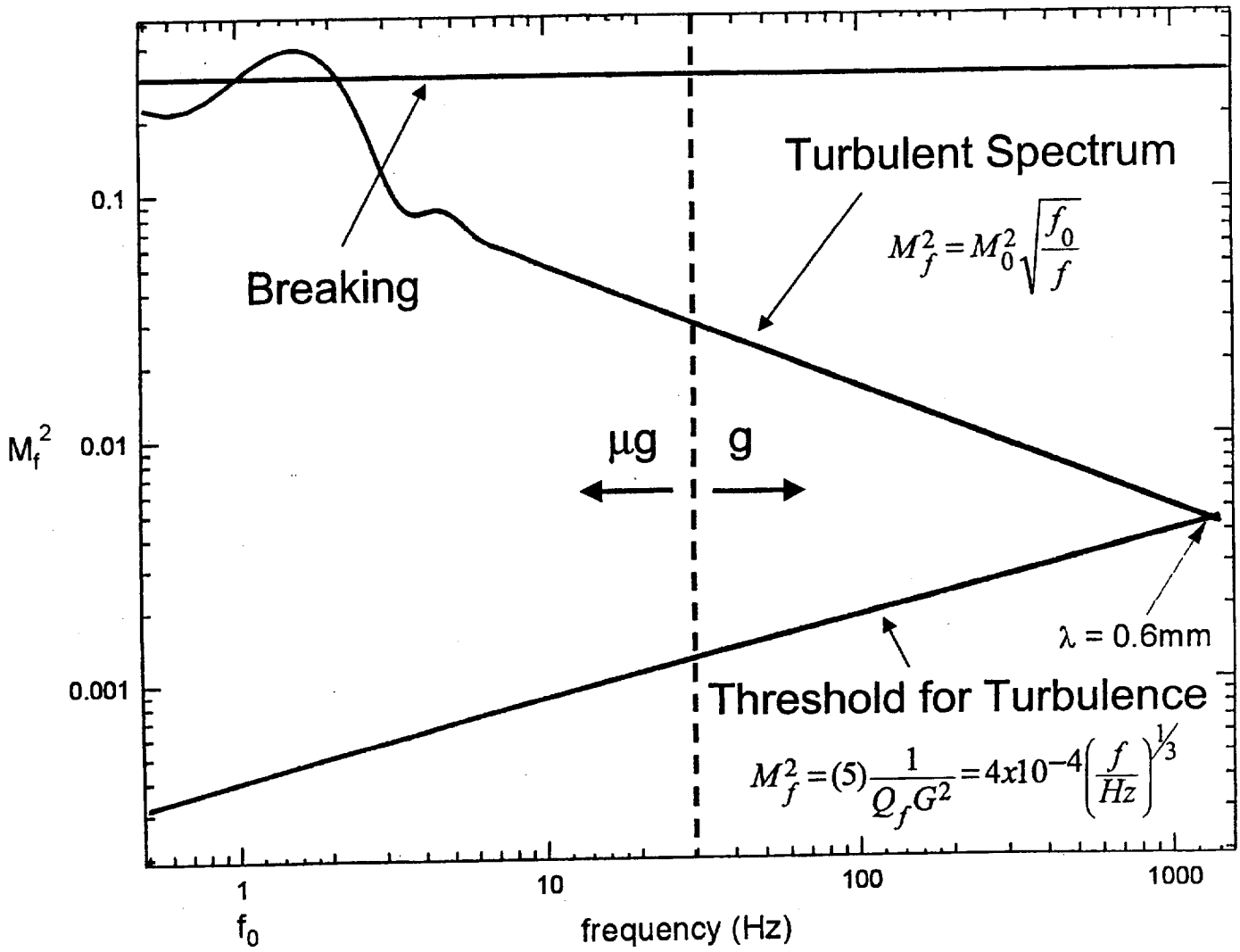
Turbulent Spectrum
$M_f^2 = M_0^2\sqrt{\frac{f_0}{f}}$
Breaking
μg
g
λ = 0.6mm
Threshold for Turbulence
$M_f^2 = (5)\frac{1}{Q_f G^2} = 4x10^{-4}\left(\frac{f}{Hz}\right)^{1/3}$
M_f^2
0.1
0.01
0.001
1
10
100
1000
f_0
frequency (Hz)

Fluctuations Around Kolmogorov Spectrum are Large

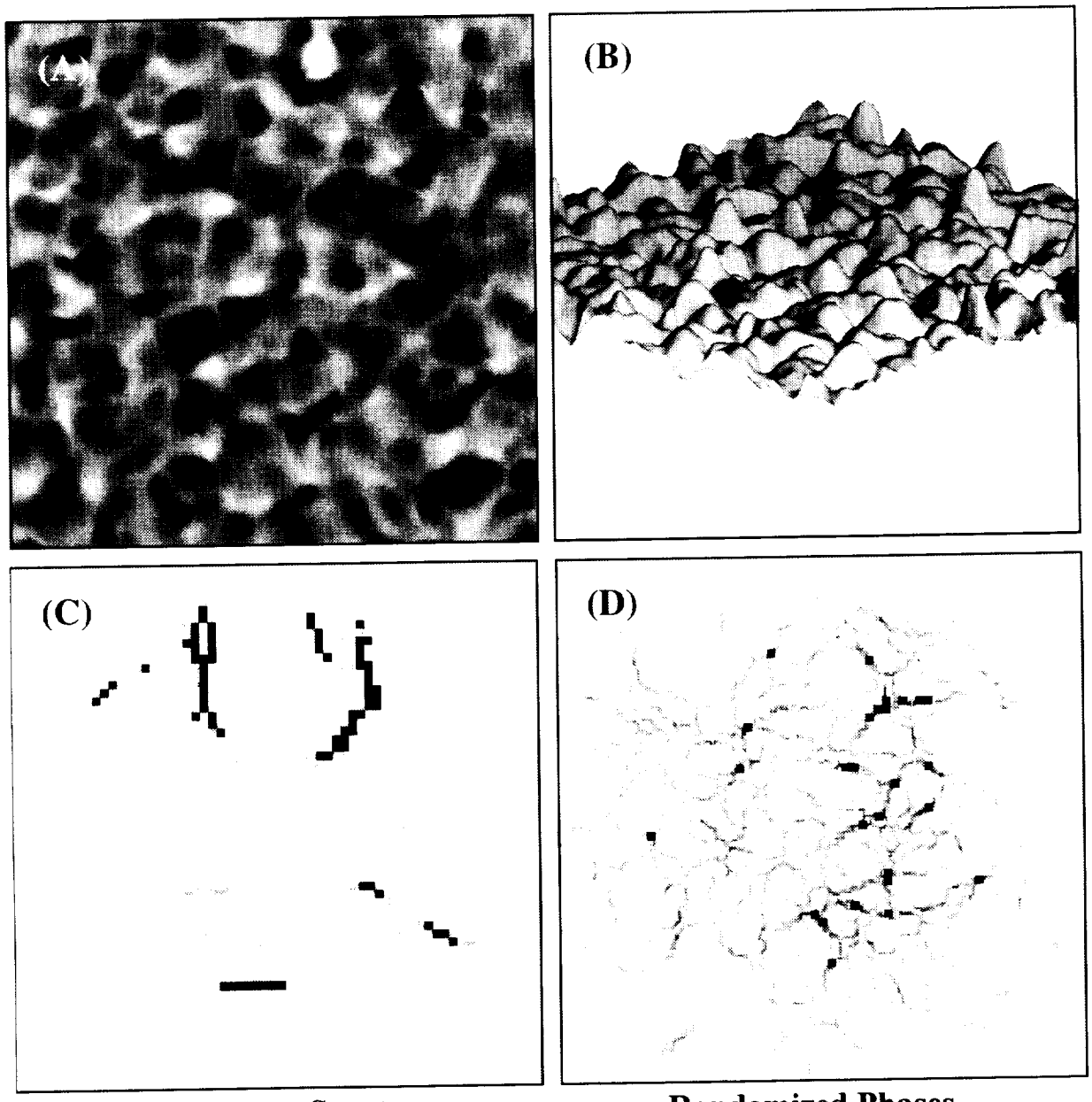

Kolmogorov Spectrum Measured Phases

Randomized Phases

$\left(\lambda_0 \nabla^2 \zeta\right)^2 > 5$ rms for 16 pixels are indicated by blackening those regions

Intermittency in Turbulence

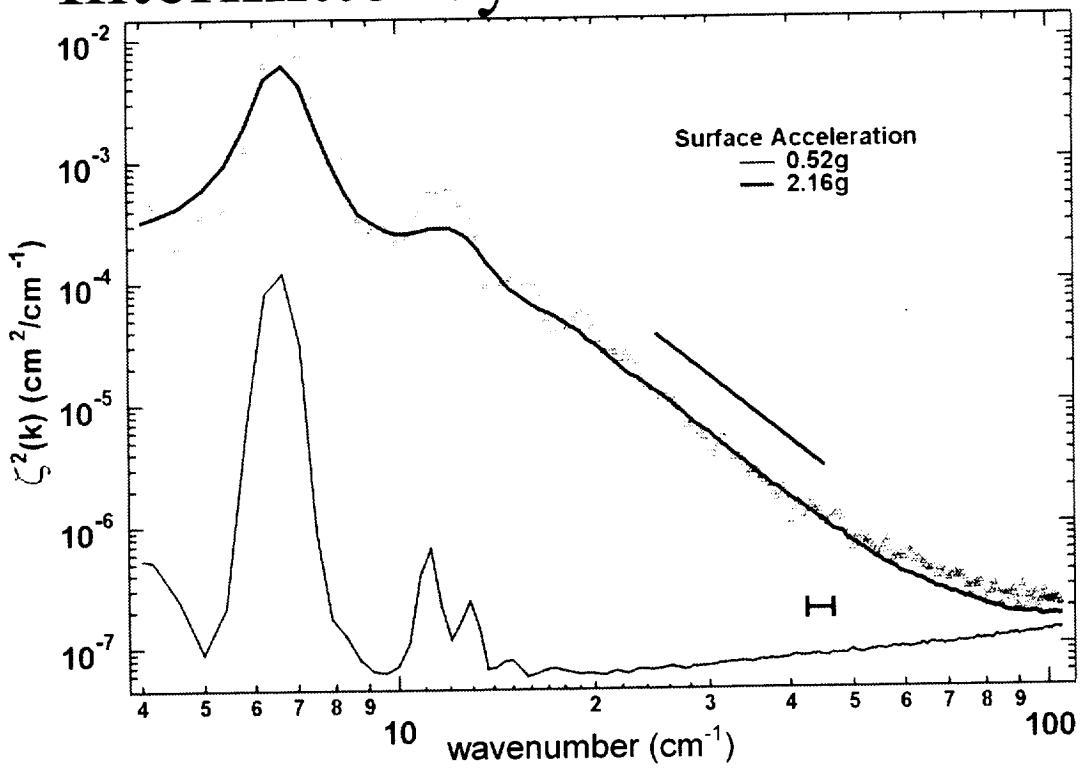

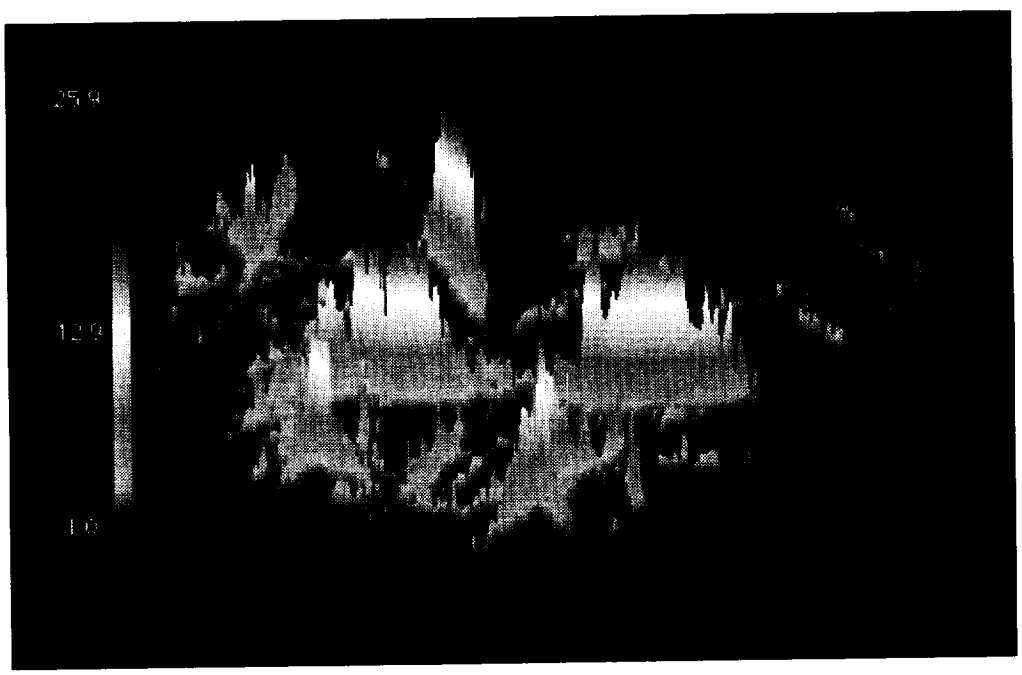

Plot of $\left(\lambda_0 \nabla^2 \zeta\right)^2 \propto$ local dissipation

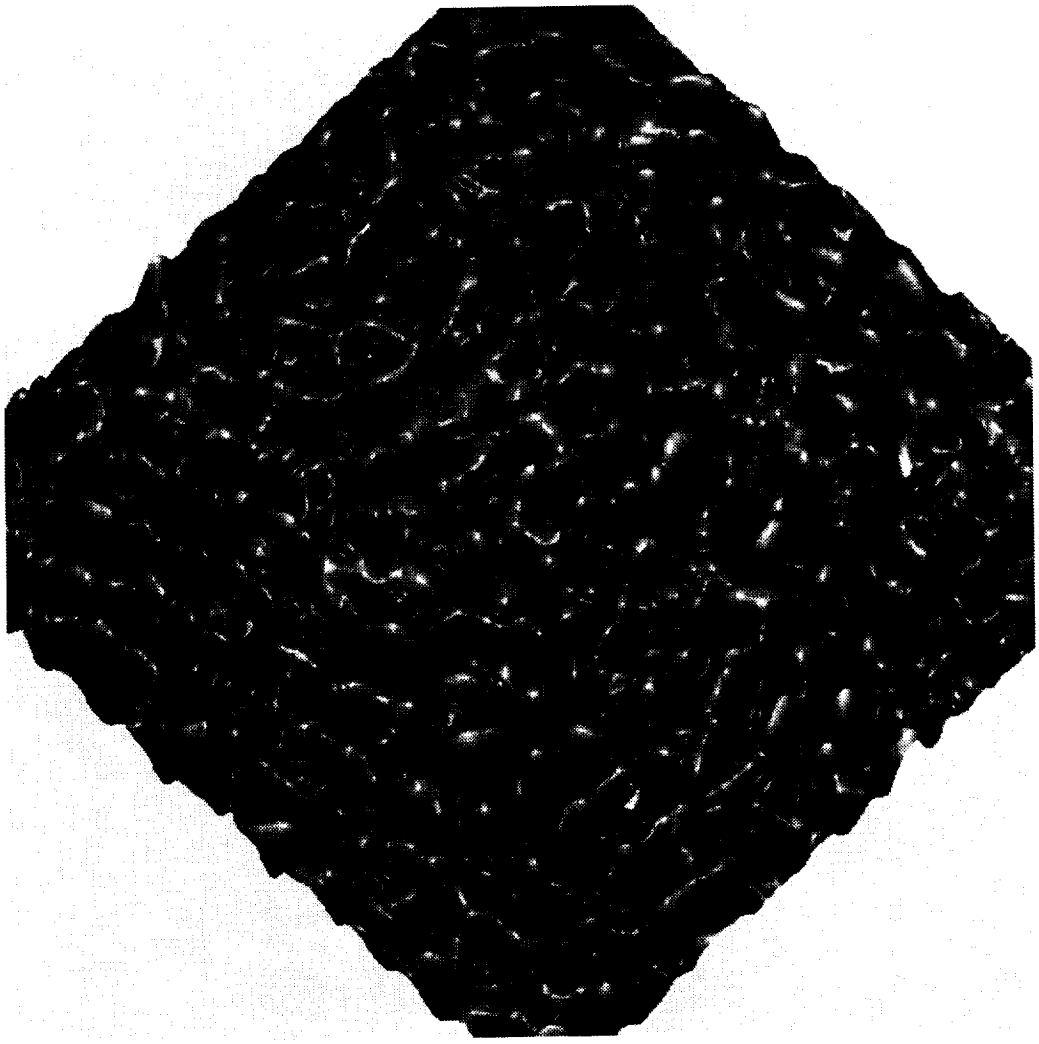

RippleHighAmpl

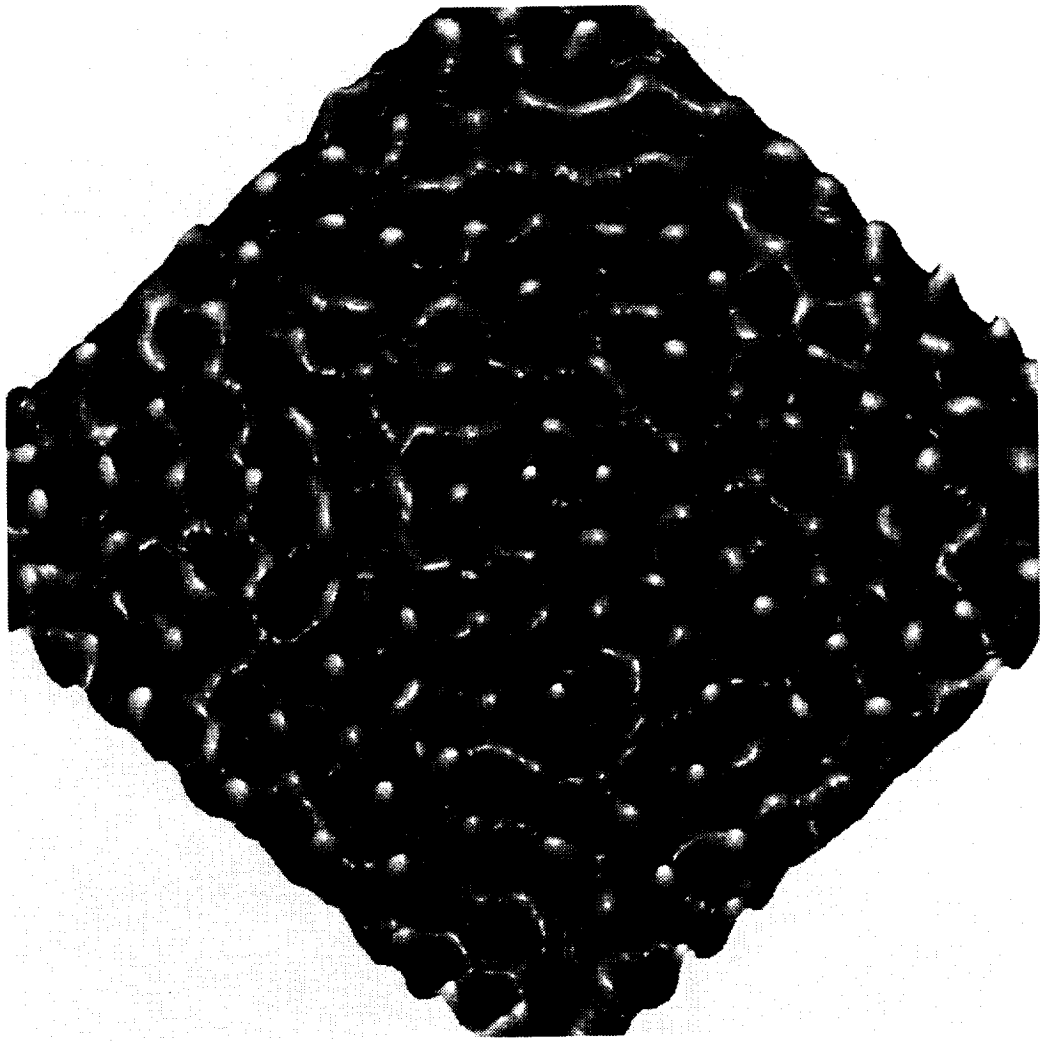

RippleMedAmpl

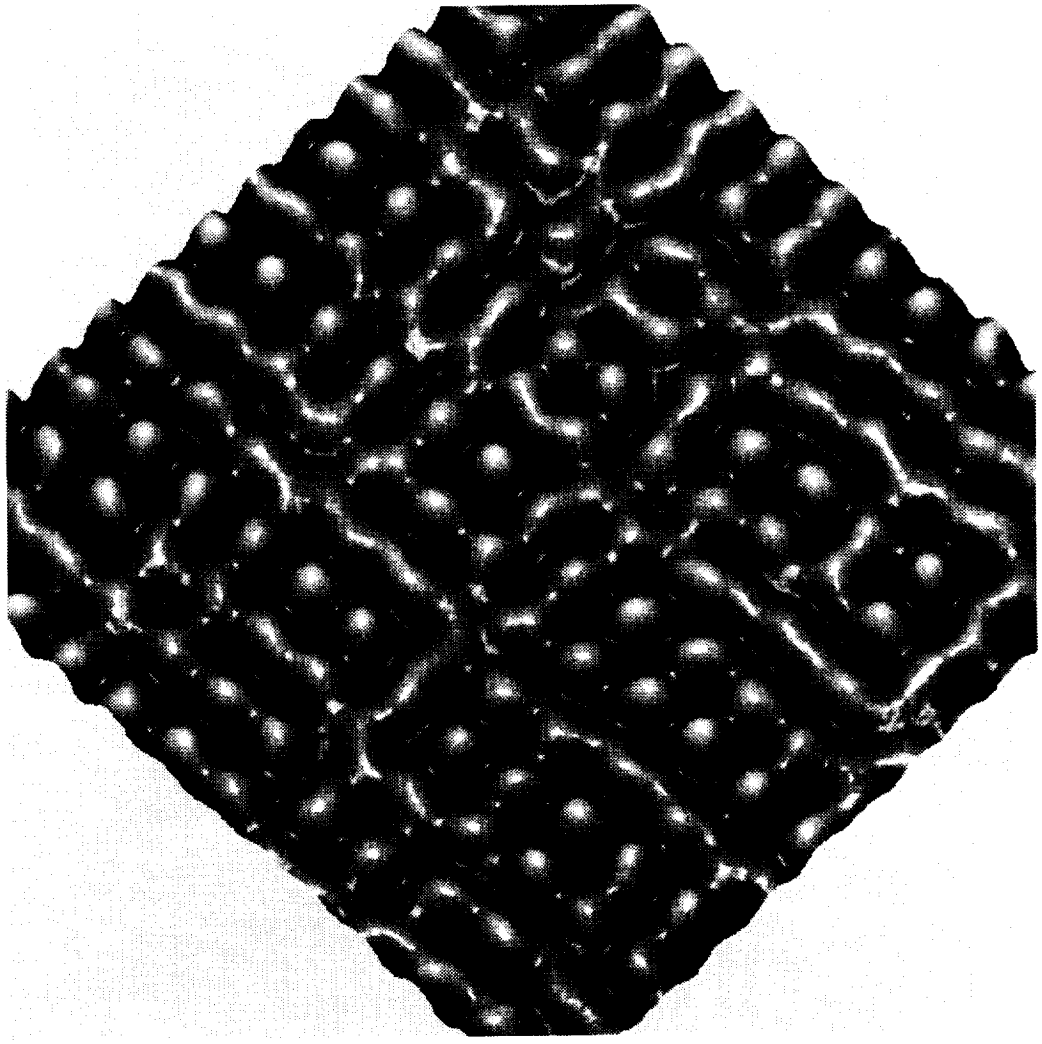

RippleLowAmpl

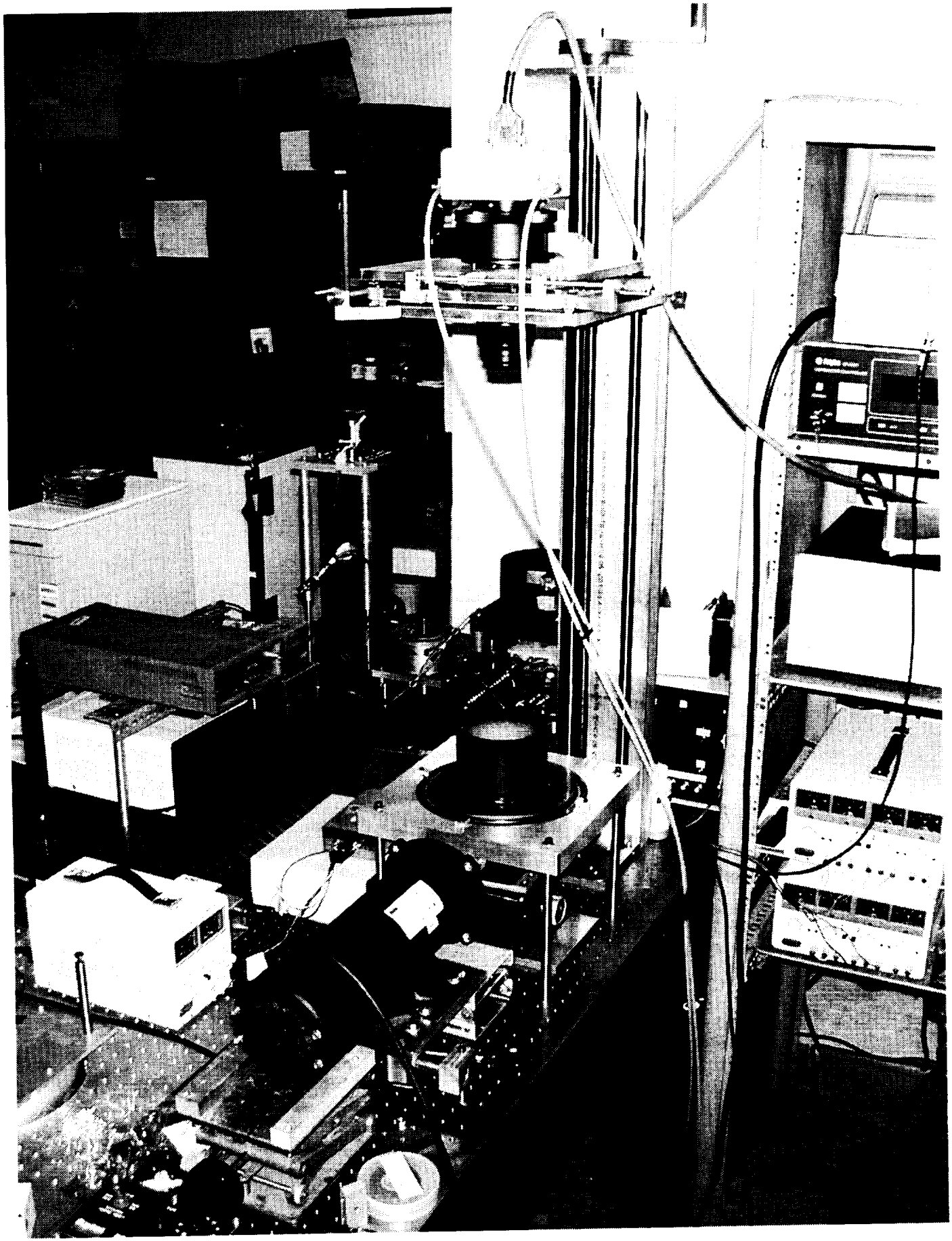

SB Apparatus

NASA/CP—2002-211212/VOL1

GUIGNÉ

Space-DRUMS®
Processing Chamber
and Material
Handling System

ISS Configuration
for inside Processing
Module

Launch ULF1

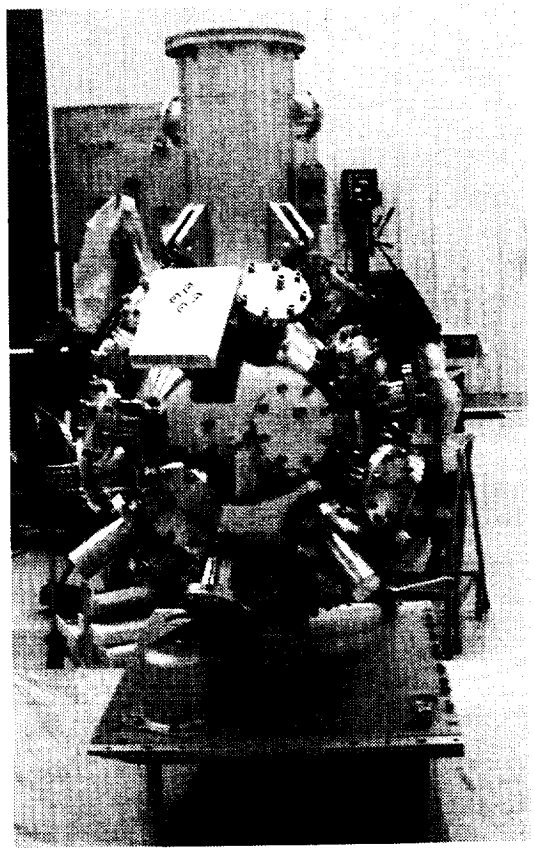

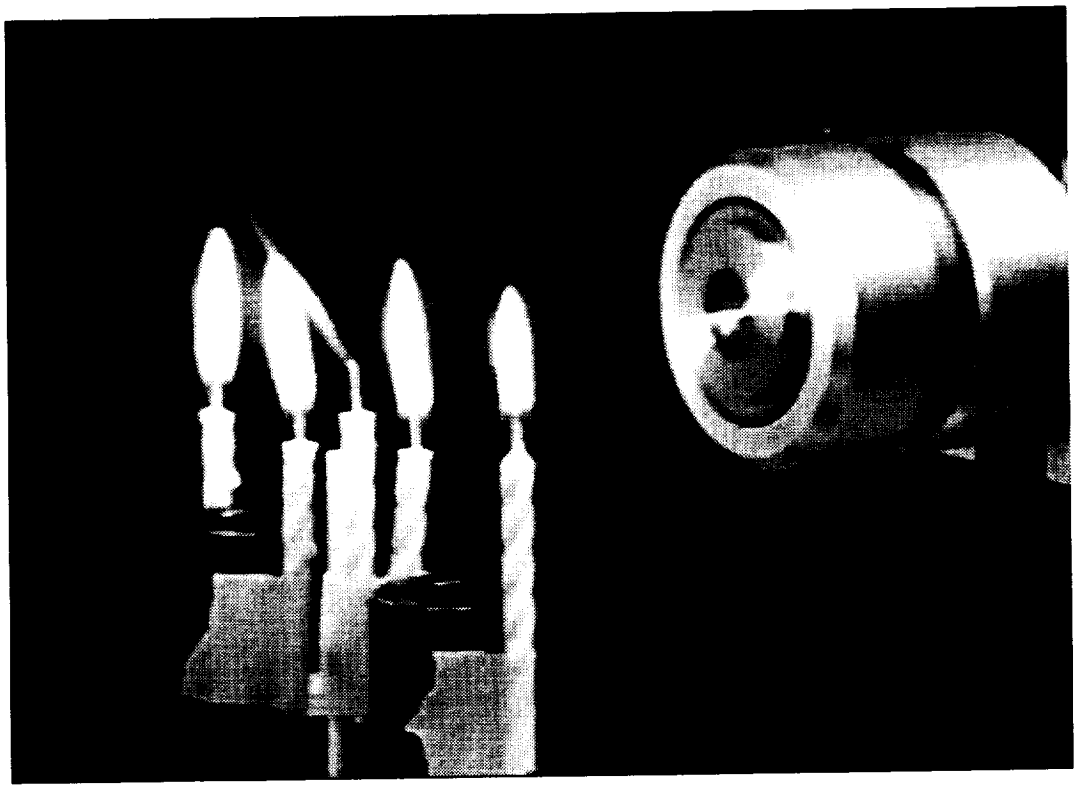

Candles.avi

OrbSphereNBigDrops.avi

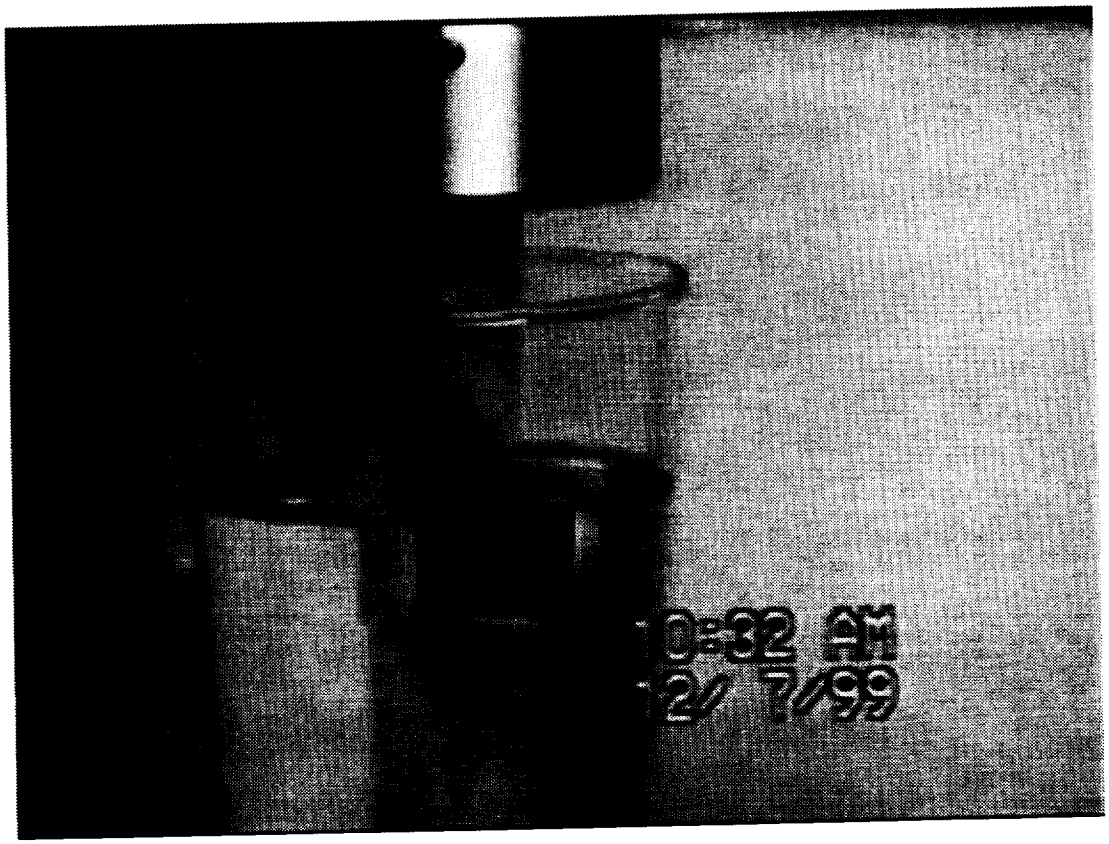

ProjDrivWater.avi

Phase separation, density fluctuations, and boiling near the liquid-gas critical point

John Hegseth, Ana Oprisan, and Arun Roy
Department of Physics, University of New Orleans, New Orleans, LA 70148
Telephone: 504-280-6706, FAX: 504-280-6048, E-mail: jhegseth@uno.edu

Vadim S. Nikolayev, Carole Lecoutre, D. Beysens, and Y. Garrabos
CEA and CNRS, ICMCB, Université de Bordeaux

ABSTRACT

A pure liquid-gas mixture is one of the simplest examples of a soft-matter system. In fact, when co-existing gas and liquid phases of pure fluid are heated to their critical point, large-scale density fluctuations make the fluid extremely compressible (to external forces), expandable (to heating), slows the diffusive transport, and decreases the surface tension. In principle these properties and others either diverge to infinity or converge to zero at the critical temperature. These properties lead to some very unusual behavior: large density gradients at the laboratory scale, a large mechanical response to heating, and perfect wetting of a solid wall by the liquid phase (zero contact-angle). We have further simplified this system by performing experiments in weightlessness (Mir spaces station). By controlling the fluid's temperature, these properties may be varied over large ranges in a single sample. When the fluid is driven out of equilibrium by a fast temperature quench from the single-phase (supercritical fluid) state into the two-phase state, we have observed universal growth laws of minority domains (gas bubbles) during phase separation. Prior to this quench we have also observed density fluctuations using optical microscopy near the critical point. When heat is applied to a liquid-gas mixture, we have observed a spectacular spreading of a gas bubble along a hot solid wall as well as gas bubble over-heating (where the interior of a gas bubble gains a higher temperature than the heating wall). Although this gas phase over-heating appears to violate the second law, it is really a transient our-of-equilibrium effect. Inside of these unusual bubbles we also have observed unusually large variations in liquid wetting film thickness that often appear to evolve into spreading contact lines on the sapphire wall when heat is applied.

We have observed coarsening and growth of minority domains (gas bubbles) in SF_6 near its liquid-gas critical point. Phase separation in our constant density samples was induced in our constant volume cells by temperature quenches in weightless conditions (Mir station), while visualizing density fluctuations and domain growth using optical microscopy. The optics of the formation of the density fluctuation images will be discussed. The well-known statistics of the density fluctuations provide natural space and time scales for domain growth. Previous experiments have documented two morphologies and two associated growth laws with a sharp transition between the two. This transition appears to be controlled by the minority volume fraction. While the slow, $t^{1/3}$ growth, for disconnected morphologies, is understood as a diffusion process, the fast growth, t^1 growth, for connected domains, is less well-understood. We will discuss several shallow quenching sequences at the critical density (±0.02%) and slightly off-critical where we have observed fast linear growth.

When a coexisting liquid-gas mixture of a single species fluid is heated into a single phase a complex transport and interfacial processes occurs in the two-phase fluid. This process, that is often called boiling, is important in many applications because of the large heat transfer that it facilitates. In the weightless environment of an orbiting space craft, the buoyancy force and all of the complications it causes is negligable. The perfect wetting by the liquid phase (zero contact-angle) near the critical temperature, T_C, will be replaced by liquid-gas-solid contact lines with a zero degree contact angle when a wetted wall dries from evaporation.

In this presentation, we also report on the behavior of a single bubble in a thin constant mass cell in several experiments where the cells are filled with fluid very close to the liquid-gas critical density and heated. These thin cells produce a considerable constraint on the bubble and allow the entire bubble to be observed as the heat is applied. Our experiments have recorded two types of behavior depending on the initial conditions and the constraints on the bubble. The first behavior is characterized by vigorous gas spreading over much of the heating copper side-wall near T_C, when the system's temperature, T, is increased at a constant rate past T_C. This behavior occurs when the bubble is free to move in the cell and is initially in contact with the highly conductive side-wall. We identify this behavior with the boiling crisis near the critical point, i.e., a reaction of the fluid to the heating surface where the heating surface becomes covered with gas. A likely mechanism for this spreading is revealed near the critical point by an analysis of the critical anomalies: the vapor recoil from evaporating fluid pushes the fluid near the liquid-gas-solid contact line at the edge of the bubble.

No gas bubble spreading is observed in the second type of behavior that occurs when a piston and temperature sensors, present inside of the cell, prevent the bubble from moving and touching the side-wall. This case did reveal that as the liquid-gas mixture is heated toward the critical point, gas phase over-heating is observed. Previously this gas phase over-heating was only observed when the temperature was quenched in a thick cell. Here, we have observed overheating in a thin cell when the temperature is ramped. More interestingly, this over-heating effect persists and increases when the temperature is ramped into the single-phase supercritical fluid state, where the liquid becomes high-density fluid and the gas become low-density fluid.

In both cases large distortions in the liquid wetting layer inside the bubble is also observed at lower T. The film distortions were sometimes continuous, appearing to be similar to a refracting (converging) lens. By ray tracing the shadow of a defocused grid through the cell and the film, we modeled this film shape as an ellipse. This showed that these films were much thicker than films typically found on Earth, by more than an order of magnitude. This large film thickness allows an explanation of the over-heating in this thin cell that is consistent with a previous explanation for thick cells. Other film structures appear as lines of almost discontinuous film thickness changes that propagate away from the bubble's edge into the bubble. We conclude that these are spreading contact lines. These spreading contact lines are usually observed near the region where the bubble touches the copper side-wall and they are also highly correlated with cell heating events. The zero contact-angle for these contact lines implies that an external stress is applied to create a large curvature change at these lines. Once again the vapor-recoil force is a good candidate for the cause of this additional stress.

Phase separation, density fluctuations, and boiling near the liquid-gas critical point

John Hegseth, Ana Oprisan, and Arun Roy
Department of Physics
University of New Orleans
New Orleans, LA 70148
E-mail:jhegseth@uno.edu

Vadim Nikolayev and Daniel Beysens
ESEME, Service des Basses Température, DSM/DFMRC, CEA/Grenoble
17, Avenue des Martyrs, F-38054 Grenoble Cedex 9, France
E-mail: beysens@drfmc.ceng.cea.fr

Yves Garrabos, and Carole Lecoutre-Chabot
ESEME, CNRS, Institut de Chimie de la Matière Condensée de Bordeaux
Université de Bordeaux I, 87, Avenue du Dr. Schweitzer
F-33608 Pessac Cedex, France
E-mail: garrabos@icmcb.u-bordeaux.fr

Background

- Near the liquid-gas critical point material and thermal properties vary considerably:

✓ **divergence of the isothermal compressibility**

✓ **divergence of the is thermal expansion coefficient**

✓ **vanishing of the thermal diffusivity**

✓ **vanishing of the surface tension**

- These experiments were performed in near-critical fluids on Mir using the Alice-II instrument, to suppress sedimentation, buoyancy driven flows, and gravitational constraints on the liquid-gas interface.

Instrument: Alice 2

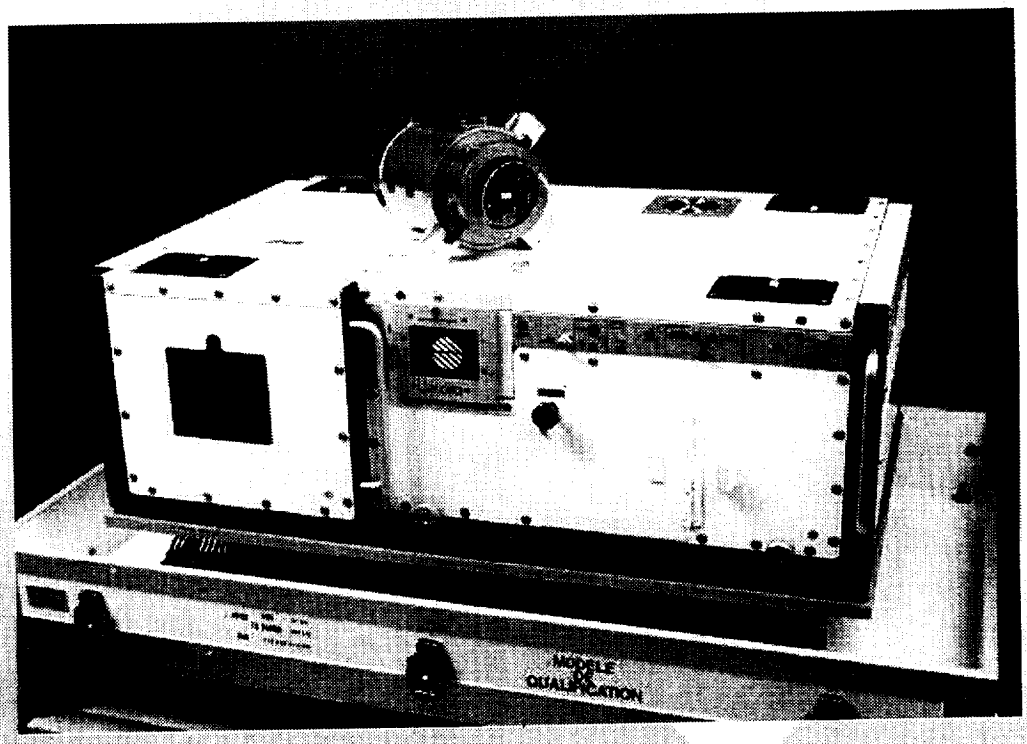

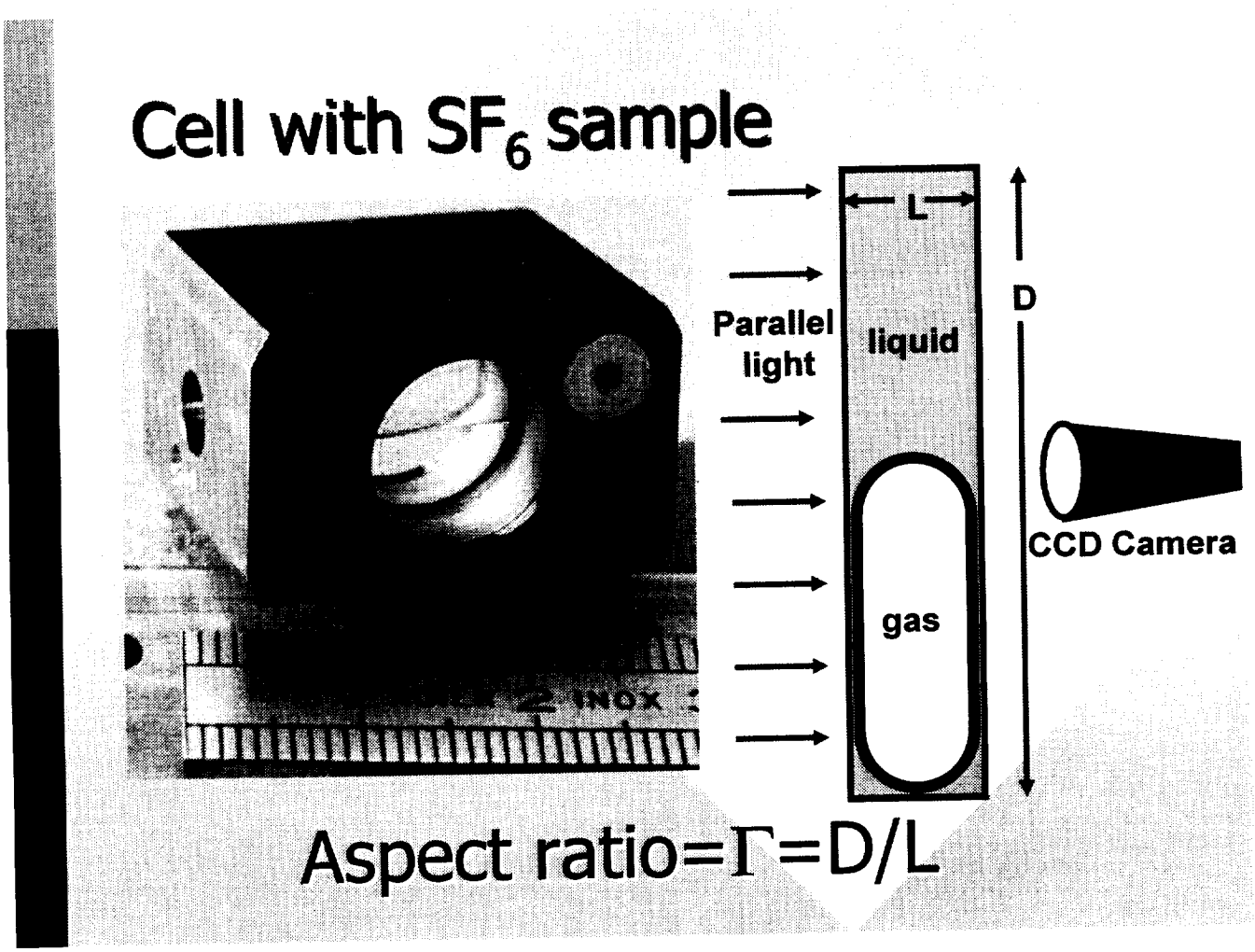
Cell with SF_6 sample
Parallel light
L
liquid
gas
D
CCD Camera
Aspect ratio=Γ=D/L

Variable volume cell with 3 thermistors and grid

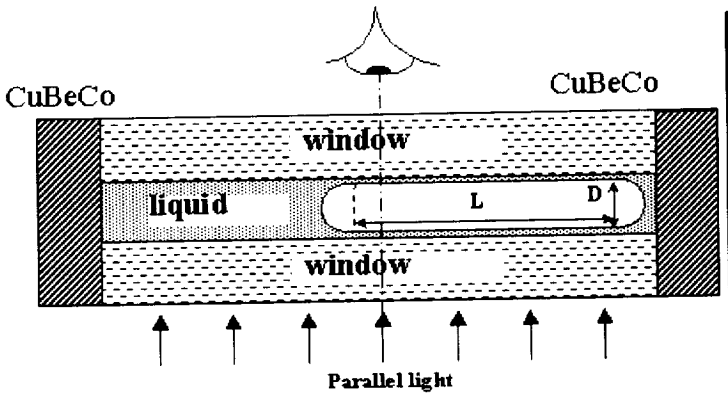

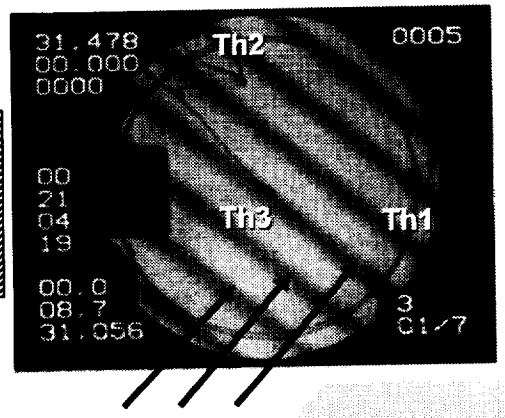

Shadows of a grid that shows density gradients

Ramp the temperature through T_c: see overheating

GMSF Experiment 1 Final Ramp $\delta\rho$=0

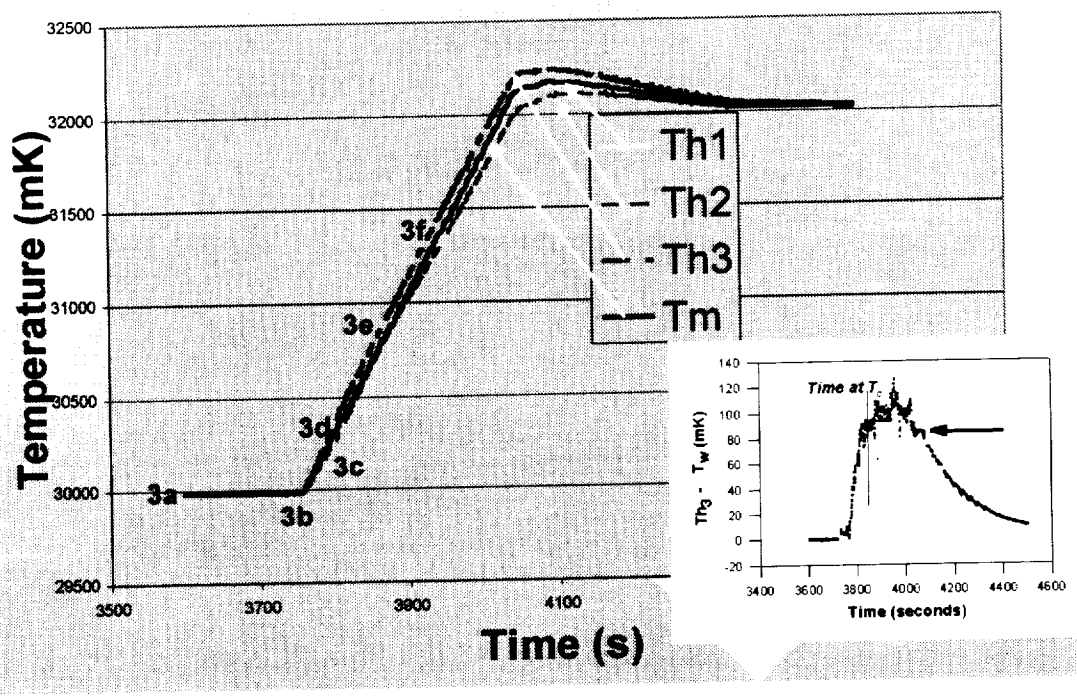

Overheating , no gas spreading

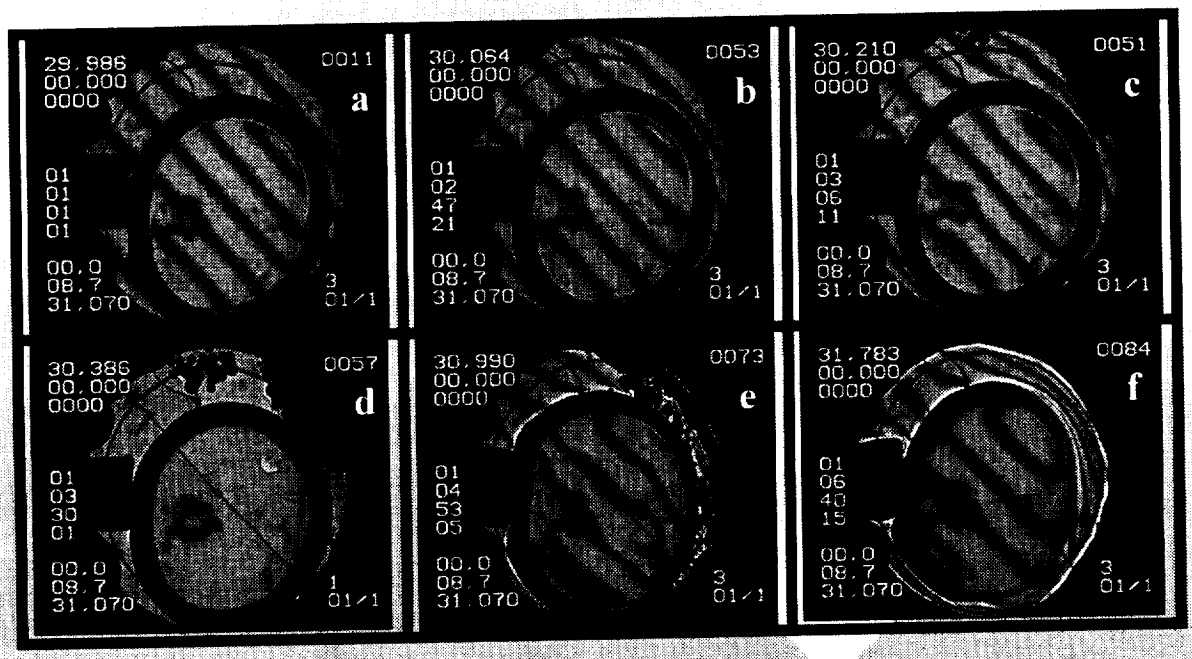

Gas spreads on side-wall near T_c, Γ=7.2

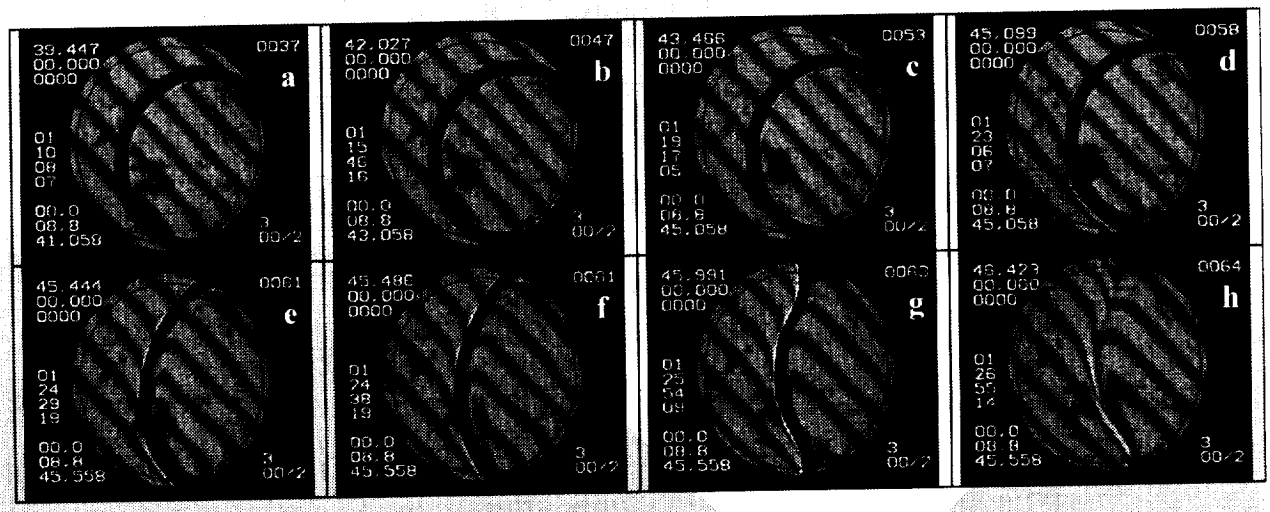

Spreading angle Γ=7.2

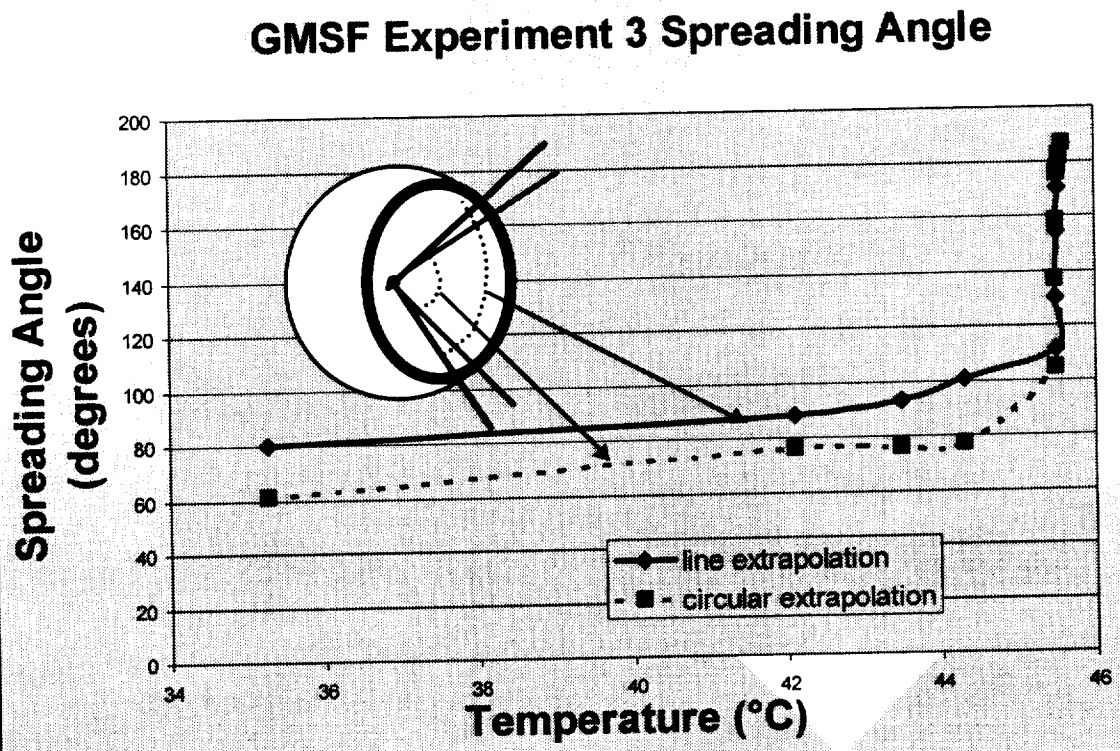

Same ramp, Γ=4.0

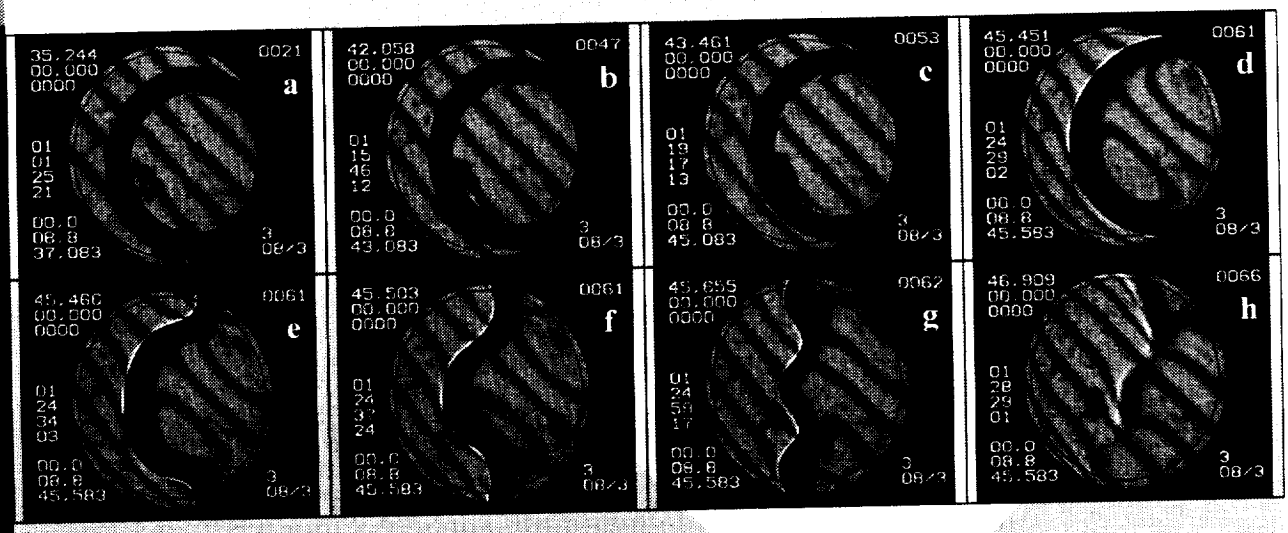

Spreading angle Γ=4.0

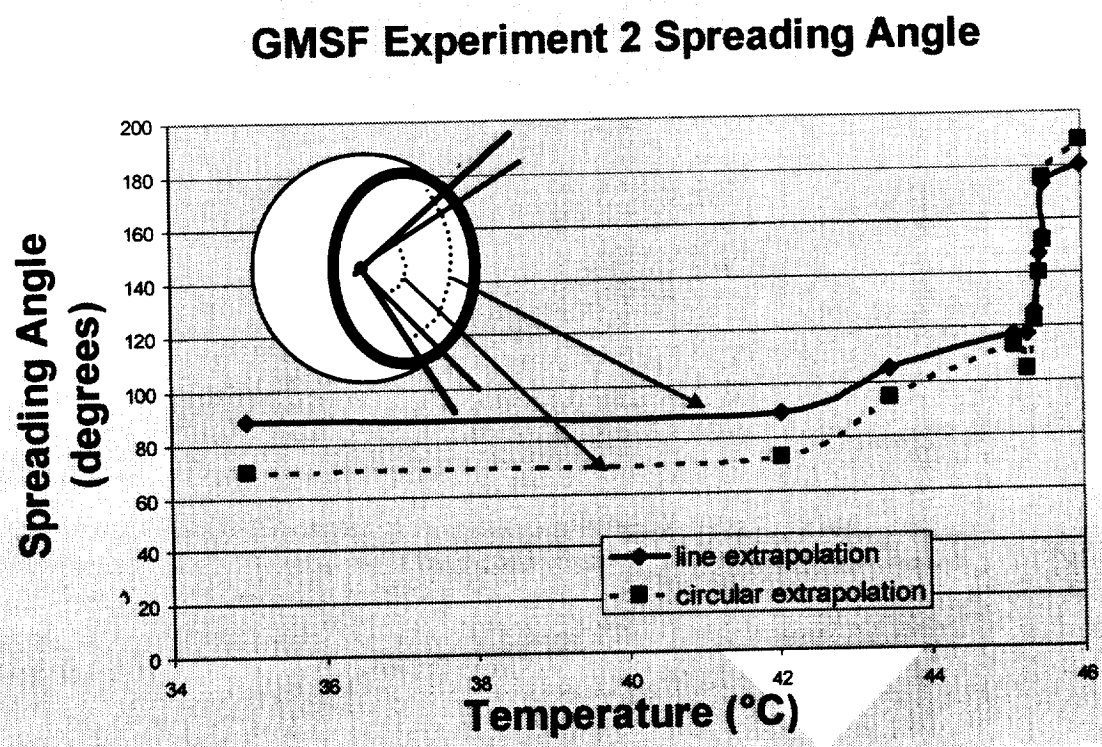

Simulation of recoil force from evaporation

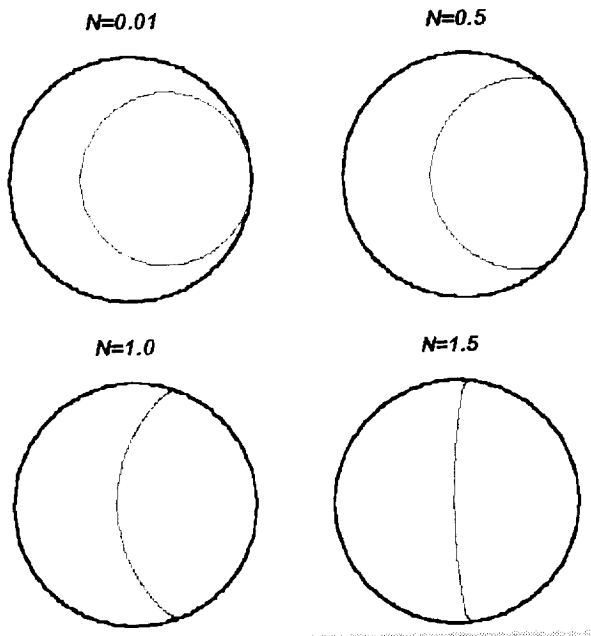

At the contact line near T_c the vapor recoil "thrust", P(x), strongly diverges: $N=\langle P\rangle/\sigma \sim (T_c-T)^{-2.3}$.

We have shown that this effect is also strong at high heat flux.

The gas overheating mechanism
(piston effect in two-phase fluids)

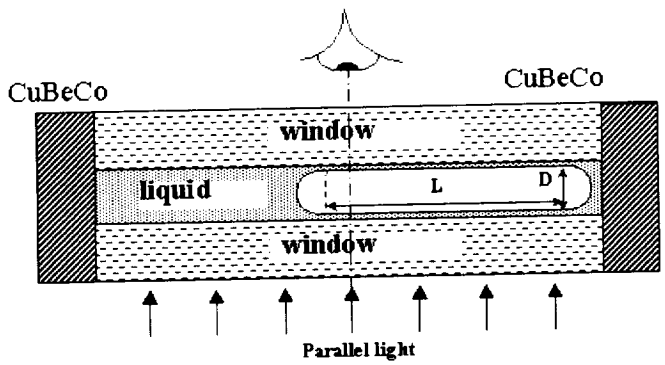

- The heat transfers from the walls to the liquid
- Low thermal diffusivity and large thermal expansion coefficient ⇒ the liquid region close to walls expands and compresses the gas bubble
- **Expanding boundary layer in liquid heats the gas bubble adiabatically (thermocompresibility of the gas allows it to become hotter than the heating walls).**

Observe large film distortions

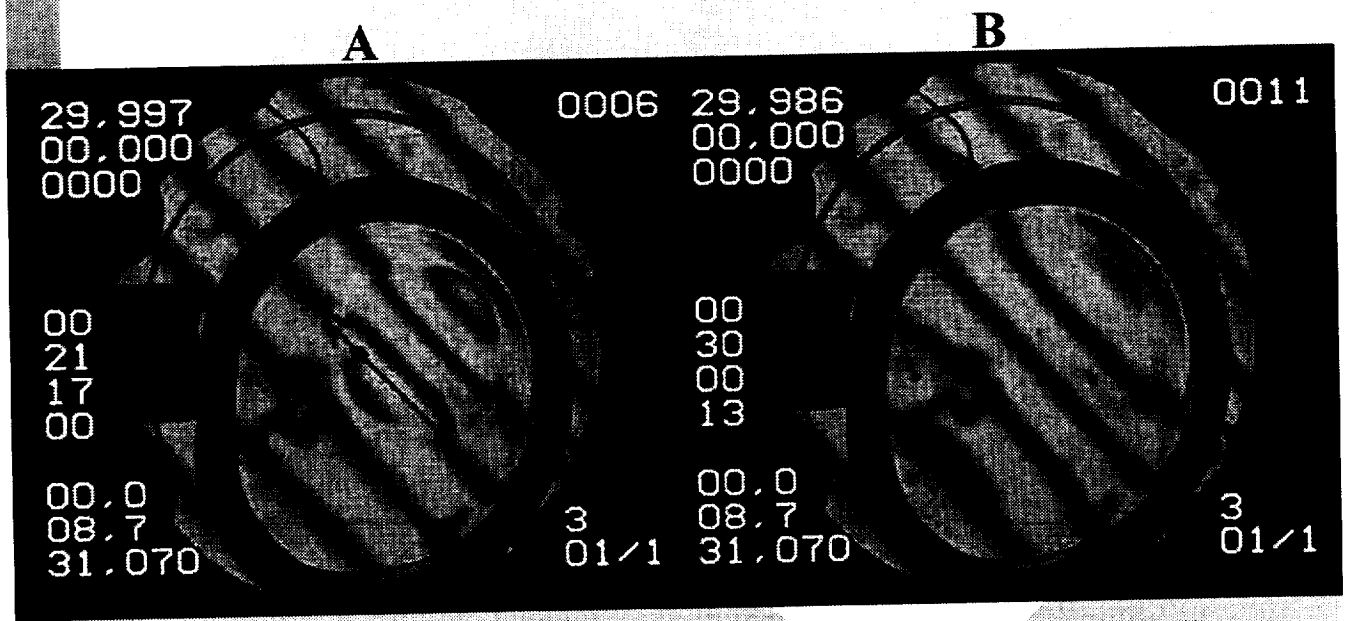

Experimentally observed displacements of the grid shadow.

Defocused grid shadow visualizes curved interfaces

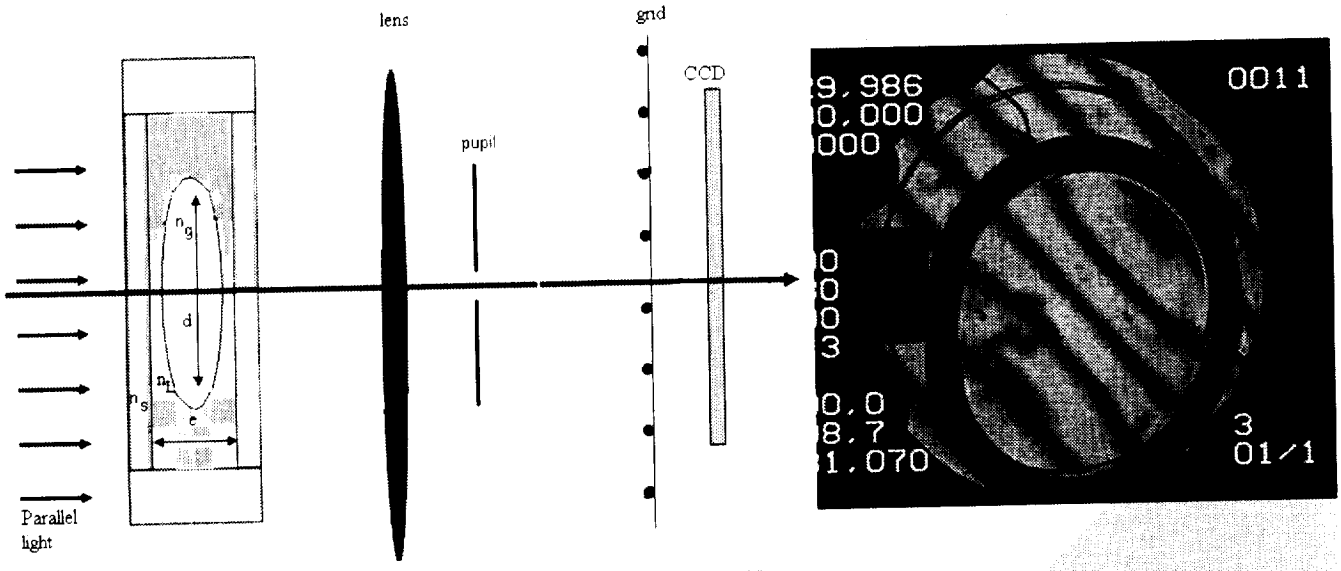

- flat liquid-gas interface (reference shadow)
- curved interface (displaced shadow)

Analytic and numerical results

Computation assumes an elliptic biconvex liquid film

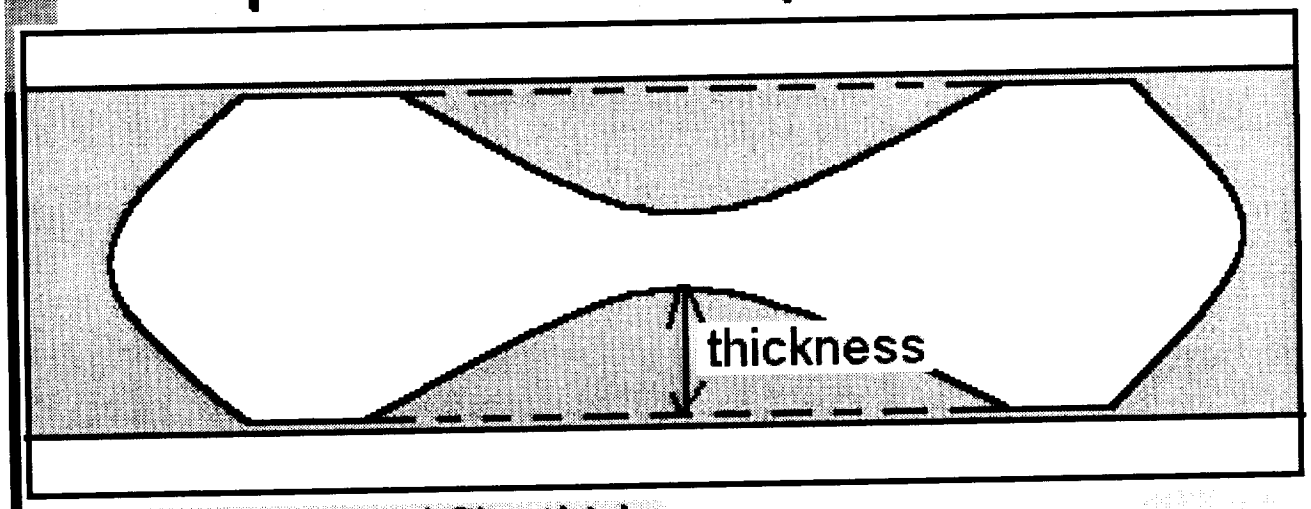

- Estimated liquid film thickness:

  t_A = 800-990 μm t_B = 280-320 μm

- Our results indicate that this is a **very thick** liquid film.

Film distortions move from heating

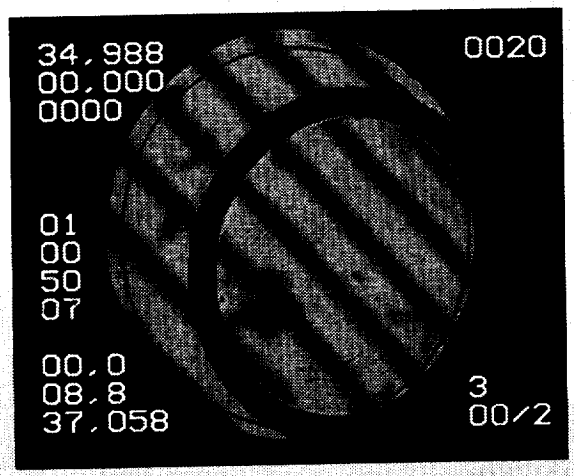

- T=constant

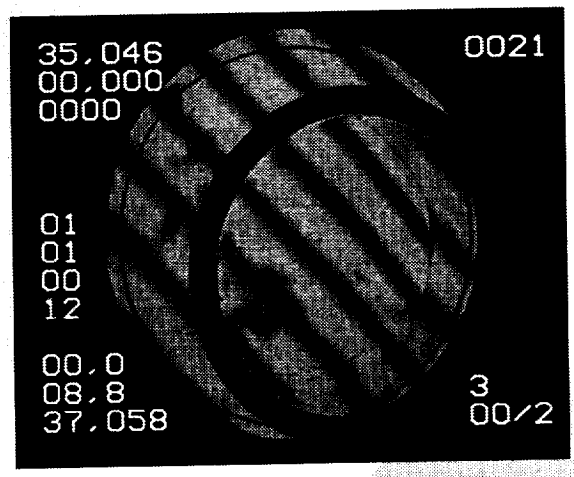

- T ramp begins

Boiling conclusions

- The liquid film has a **much larger thickness** than films found on Earth (1-2 magnitude orders).
- The liquid thick film isolate the gas phase from the wall allowing the gas overheating.
- See gas spreading on a solid wall close to the critical point when the gas bubble initially touches the wall.
- See thick film distortions that move in response to heat.

Critical fluctuations

- Observe fluctuations in space and time with microscope in ALICE 2.
- Studied fluctuation images in pure fluid SF_6 in weightlessness.
- Test optical technique with phase contrast and dark field microscopy using density matched binary mixture.

Density Fluctuations in SF_6

Time between images = 40 seconds

1 pixel=2 μ m

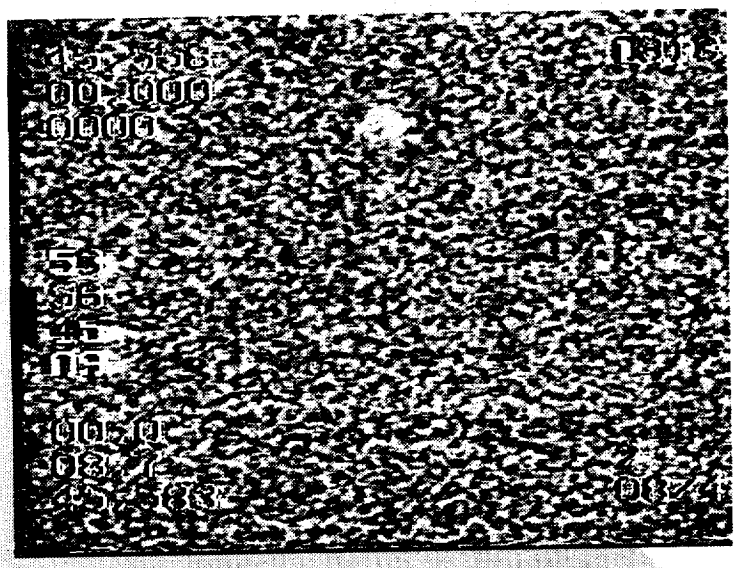

$\Delta\rho/\rho_c$=0.7%

$T-T_c \geq 10\mu K$

$\xi \leq 10\ \mu$ m

$\tau \geq 0.2$seconds

$a \leq 10\ \mu g$

Phase contrast and dark field microscopy

•BF bright field, nothing at F

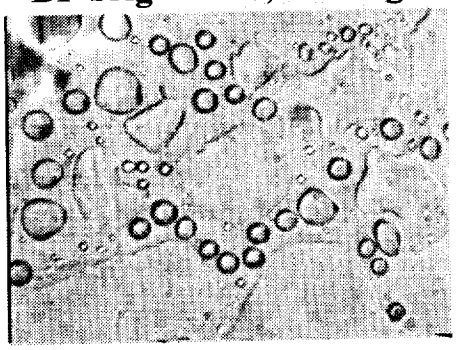

•PC, phase contrast, 1/4 waveplate at F

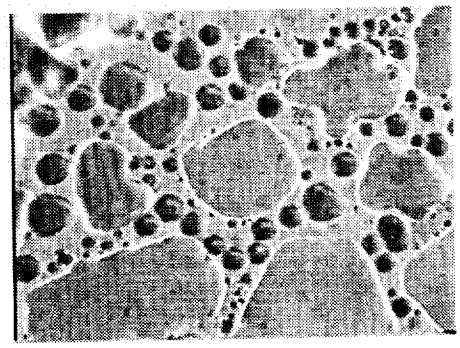

•DF, dark field, solid object at F

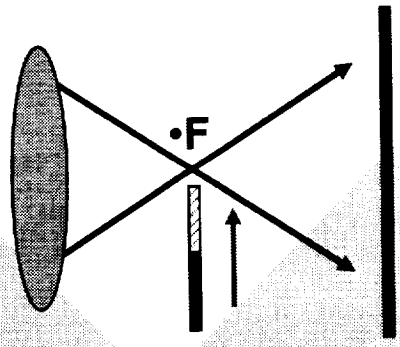

Visualizing fluctuations

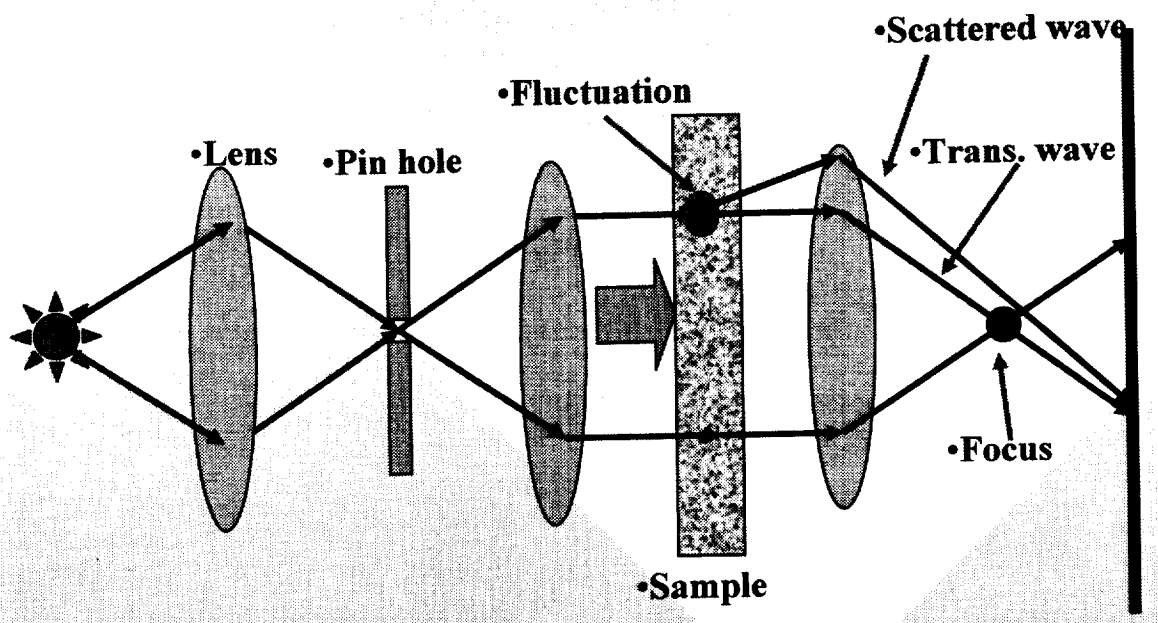

Interference mechanism $\delta I \propto (\delta\rho)^2$ for BF, $\delta I \propto \delta\rho$ for PC

- Decompose **E** into transmitted and scattered waves: $\mathbf{E} = \mathbf{E}_T + \mathbf{E}_S$, $I \propto \mathbf{E}^2 = \mathbf{E}_T^{\,2} + \mathbf{E}_S^2 + 2\,\mathbf{E}_T \bullet \mathbf{E}_S$.
- $\delta I(\mathbf{r},t) \propto \mathbf{E}_T \bullet \mathbf{E}_S = E_T E_S \cos\theta$, where $\theta \propto \delta n \propto \delta\rho$.
- BF image: $\cos\theta \approx 1 - \theta^2 \Rightarrow \delta I(\mathbf{r},t) \propto -\theta^2 \propto -\delta\rho^2$.
- PC image: $\mathbf{E}_T$ shifted by $\pi/2$. $\cos\theta \rightarrow \sin\theta \approx \theta$ $\Rightarrow \delta I(\mathbf{r},t) \propto \theta \propto \delta\rho$.

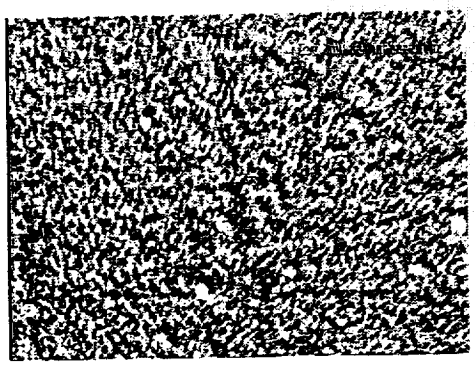

•BF, nothing at F

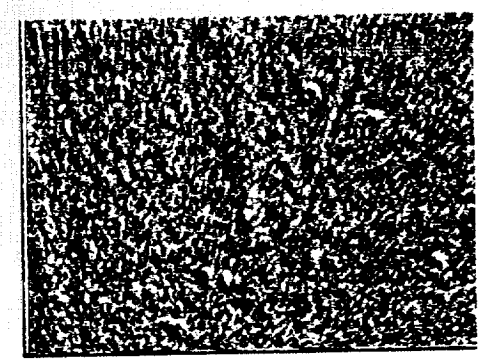

•PC, 1/4 waveplate at F

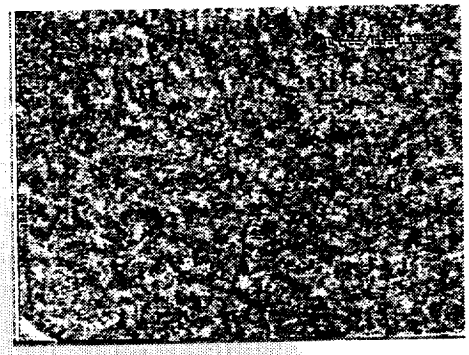

•DF, solid object at F

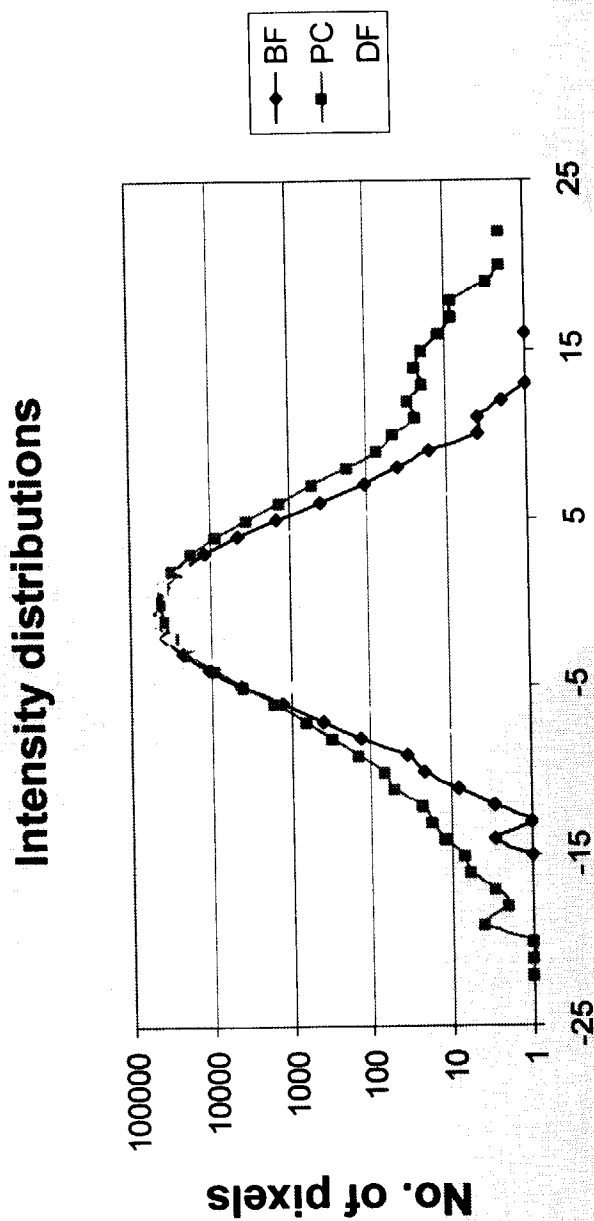
Intensity distributions
No. of pixels
100000
10000
1000
100
10
1
-25
-15
-5
5
15
25
<I> - I
BF
PC
DF

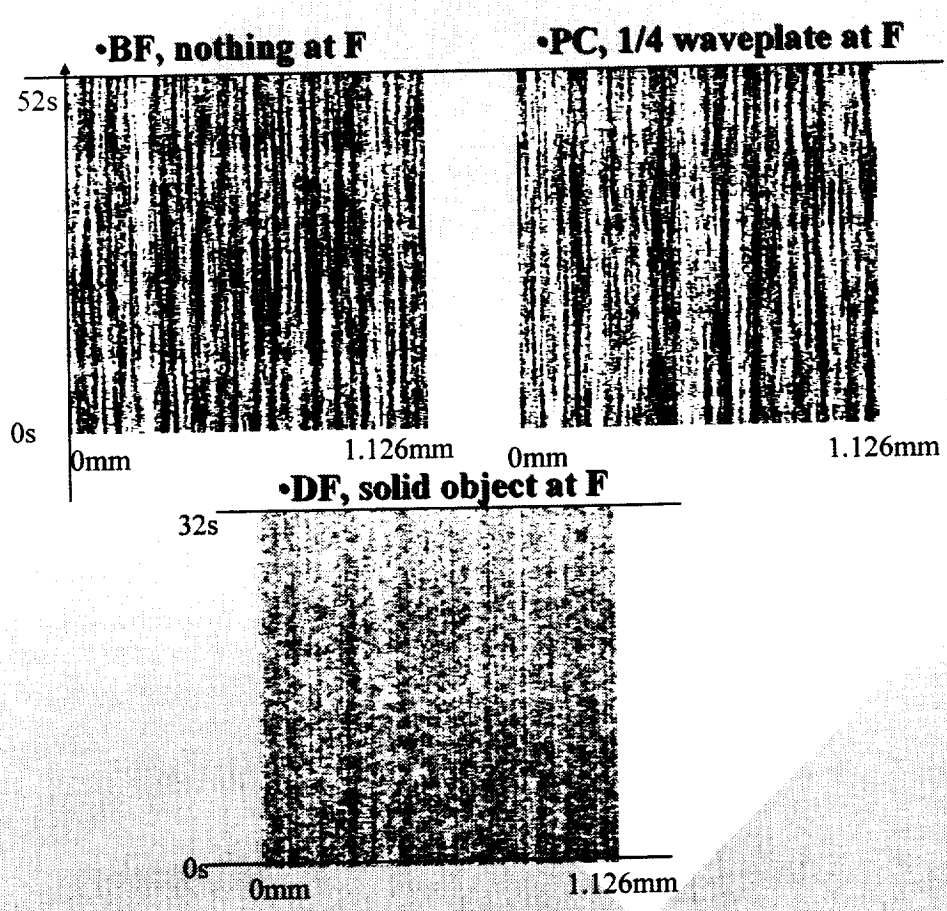
•BF, nothing at F
52s
0s
0mm
1.126mm
•PC, 1/4 waveplate at F
0mm
1.126mm
•DF, solid object at F
32s
0s
0mm
1.126mm

Extinction mechanism $\delta I \propto \delta \rho$

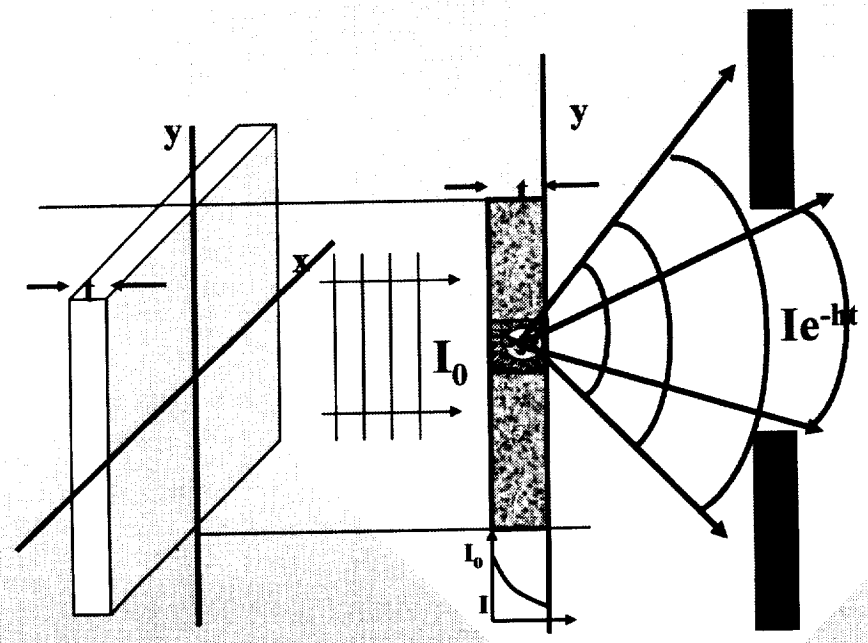

Extinction mechanism

- ***Scattering from critical opalescence***
- ***Pupil captures a fraction of the scattered light to make extinction coefficient, h.***
- ***Using Ornstein Zernicke scattering formula and Lorentz-Lorenz formula to get h and $\delta I \propto \delta \rho$***

Below T_c, fluctuations grow

0.3mK quench, $\delta\rho$=0.00

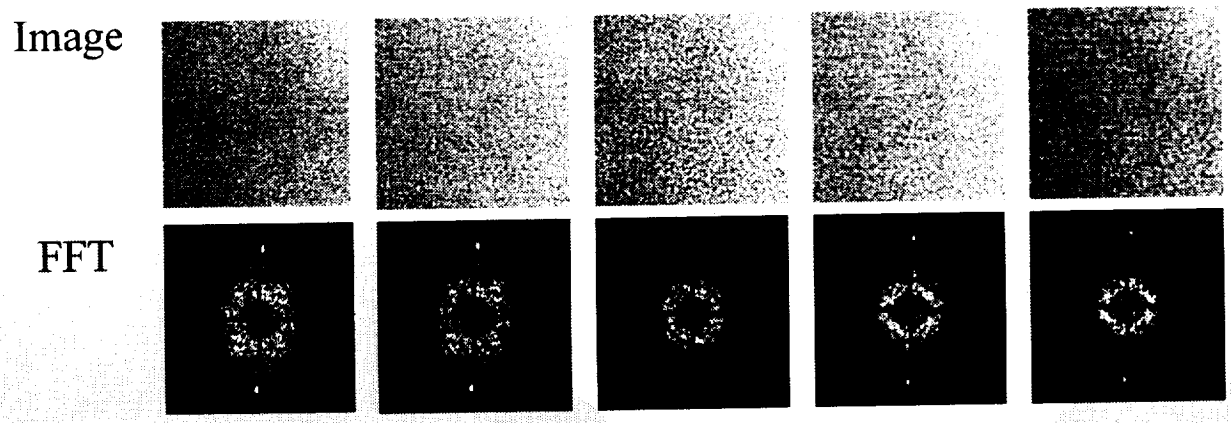

time

Phase separation

- Observe growing gas domains (bubbles) in space and time with microscopy in ALICE 2 in pure SF_6 & CO_2
- **Observed disconnected morphology that grows slowly (diffusion) and interconnected morphology that grows fast (hydrodynamics)**
- Observed morphology transition as the volume faction is increased

Liquid-gas phase separation

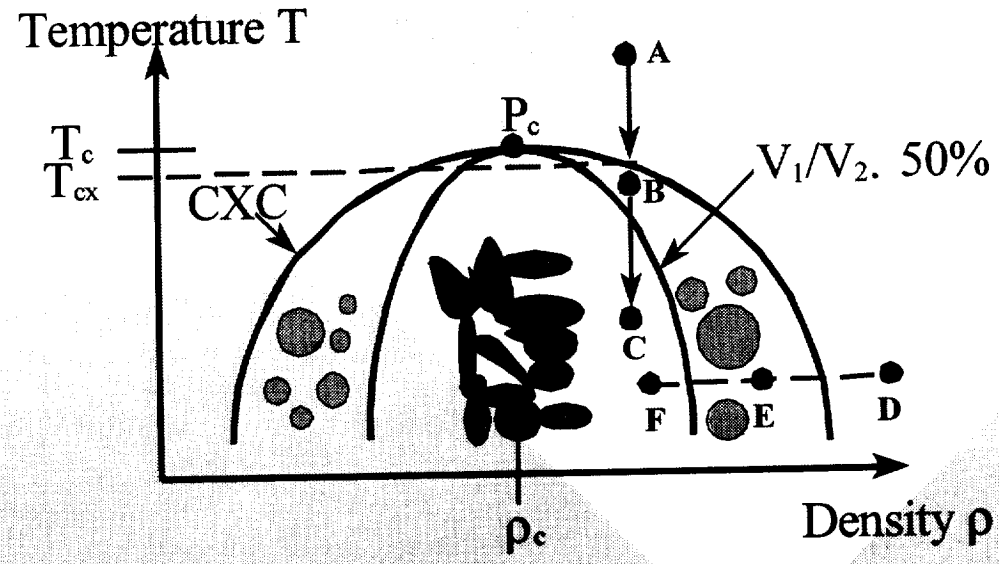

Natural space and time scales near T_C

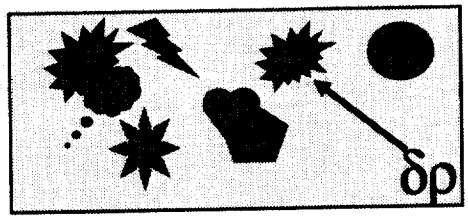

Density fluctuation correlation length:

$$\xi=\xi_0(T-T_C)^{-0.6}$$

Density fluctuation relaxation time:

$$\tau=\tau_0(T-T_C)^{-1.9}$$

Fast and slow growth laws

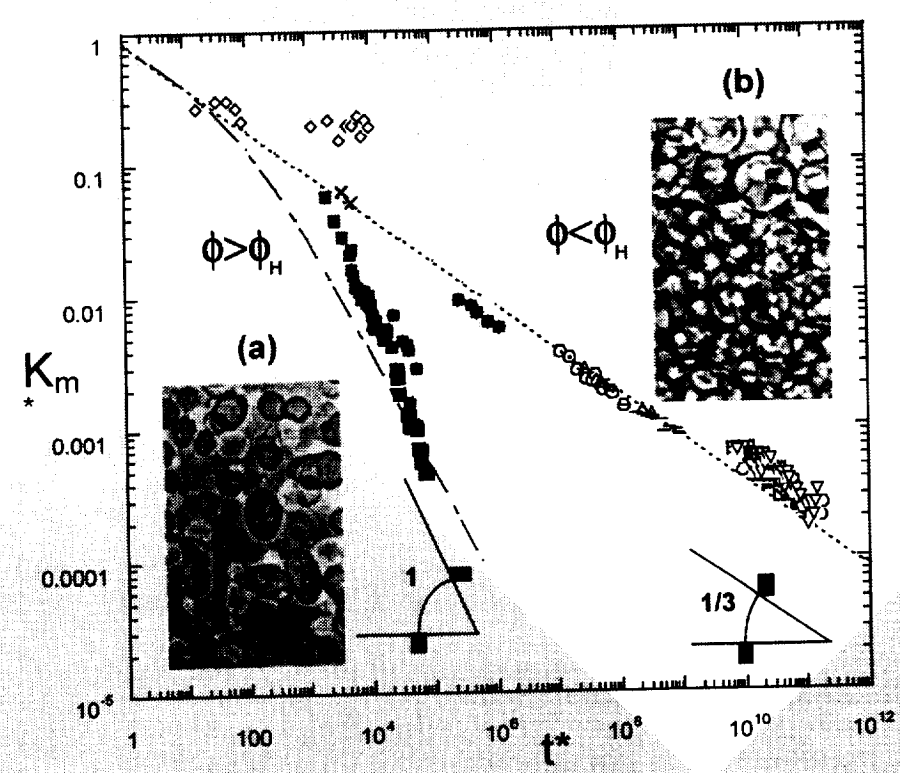

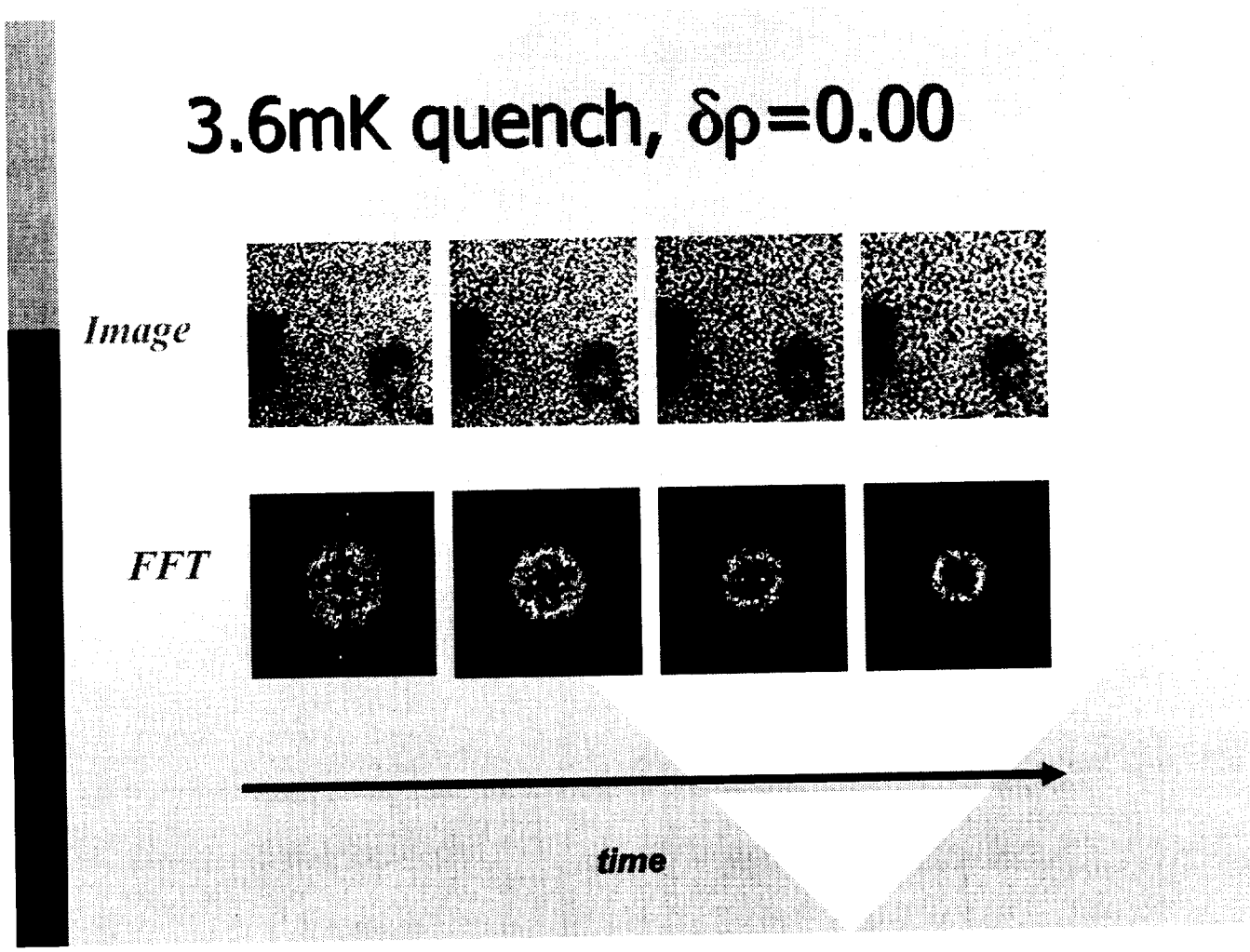
3.6mK quench, δρ=0.00
Image
FFT
time

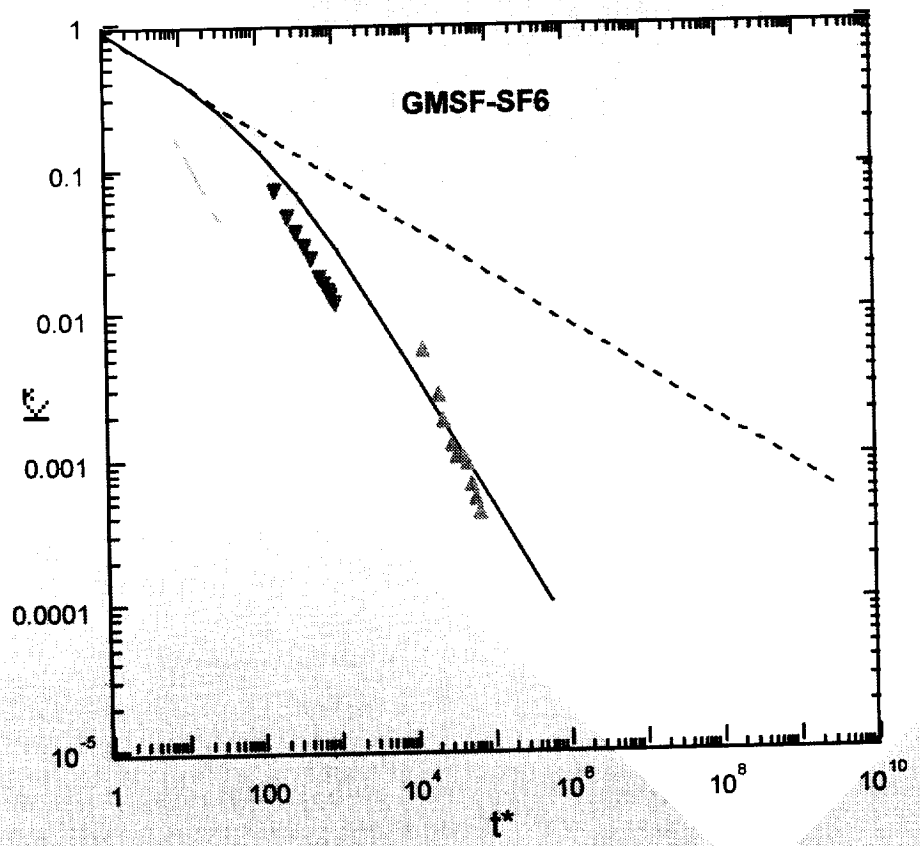
GMSF-SF6
1
0.1
0.01
0.001
0.0001
10^{-5}
K
1
100
10^4
10^6
10^8
10^{10}
t*

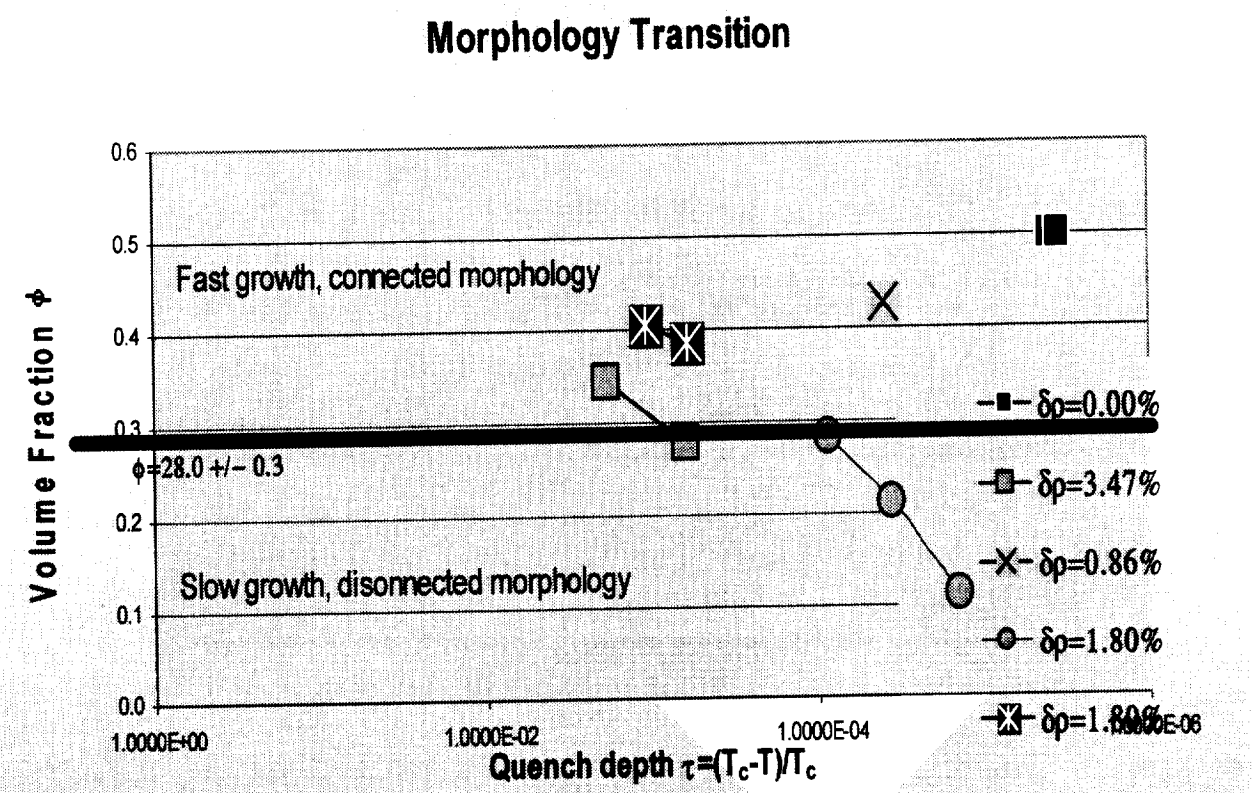
Morphology Transition
Volume Fraction ϕ
0.6
0.5
0.4
0.3
0.2
0.1
0.0
Fast growth, connected morphology
Slow growth, disonnected morphology
ϕ=28.0 +/- 0.3
δρ=0.00%
δρ=3.47%
δρ=0.86%
δρ=1.80%
1.0000E+00
1.0000E-02
1.0000E-04
Quench depth τ=(Tc-T)/Tc

Fast and slow growth from coalescence

Small volume fraction ϕ: Brownian motion

$L_M \sim R/\phi^{1/3} \sim (k_B T/6\pi\eta)t^{1/3}$

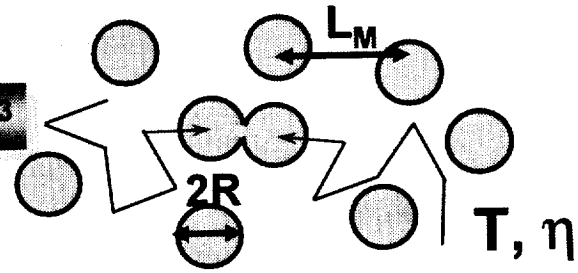

Large volume fraction: hydrodynamics interactions

$L_M \sim (\sigma/\eta)t$

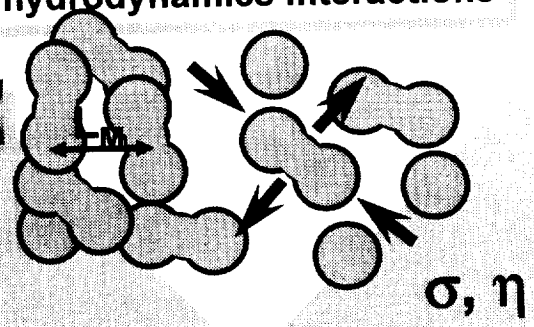

Conclusion

- Use microscopy to study statistics of density fluctuations close to T_c
- Study morphology transition and hydrodynamic interactions between bubbles close to T_c

Plan to do more on ISS with DECLIC

STRATIFIED TAYLOR-COUETTE FLOW WITH RADIAL GRAVITY

John Hart, Dan Ohlsen
Program in Atmospheric and Oceanic Sciences, Univerisity of Colorado, Boulder, CO 80309

Randall P. Tagg
Department of Physics, University of Colorado, Denver, CO 80217

Patrick D. Weidman
Department of Mechanical Engineering, University of Colorado, Boulder, CO 80309

ABSTRACT

An experiment to study stratified Taylor-Couette flow with radial, or cross-stream, gravity is being developed. The experiment uses ferromagnetic fluid (ferrofluid) and a unique stacked-magnet configuration to generate a strong (3 to 10 g) radial gravity field. In the microgravity environment this experiment will permit laboratory study of a wide range of stability, transitional, and turbulent flow problems in a simple re-entrant geometry. Important fundamental situations that can be implemented include thermal convection in a "vertical" shear flow, stably stratified shear flows, and stably or unstably stratified centrifugal (spiral) instabilities. Figure 1 (below) shows a sketch of the experiment, which also illustrates the basic-state flows expected in the terrestrial laboratory.

The linear stability problem for an axially and azimuthally invariant mean flow consisting of the exact analytically determined fields

$$\mathbf{V} = [\, 0, V_m(r), W_m(r) \,], \quad T = T_m(r)$$

has been solved numerically for the terrestrial case with both g_e and $g_m(r)$ present, and for the microgravity case where g_e is negligible. Modifications to the usual Taylor-Couette modes are found, along with new disturbance modes arising from the radial magnetic gravity.

In order to carry out meaningful experiments with this system, an effective visualization method for the opaque ferrofluid is required. Ultrasonic Doppler Velocimetry has been used to measure the velocity distributions in ferrofluid for a simple mechanically forced un-heated configuration. The experimental results are in good agreement with direct numerical simulations of the axisymmetric (2D) steady flow, suggesting that UDV is a very promising tool for studying circulations in this medium.

Other issues, such as determining the significance of non-Newtonian fluid effects, and predicting the nature of motions driven directly by magnet field imperfections (in height), have been studied theoretically, and will be summarized as time permits.

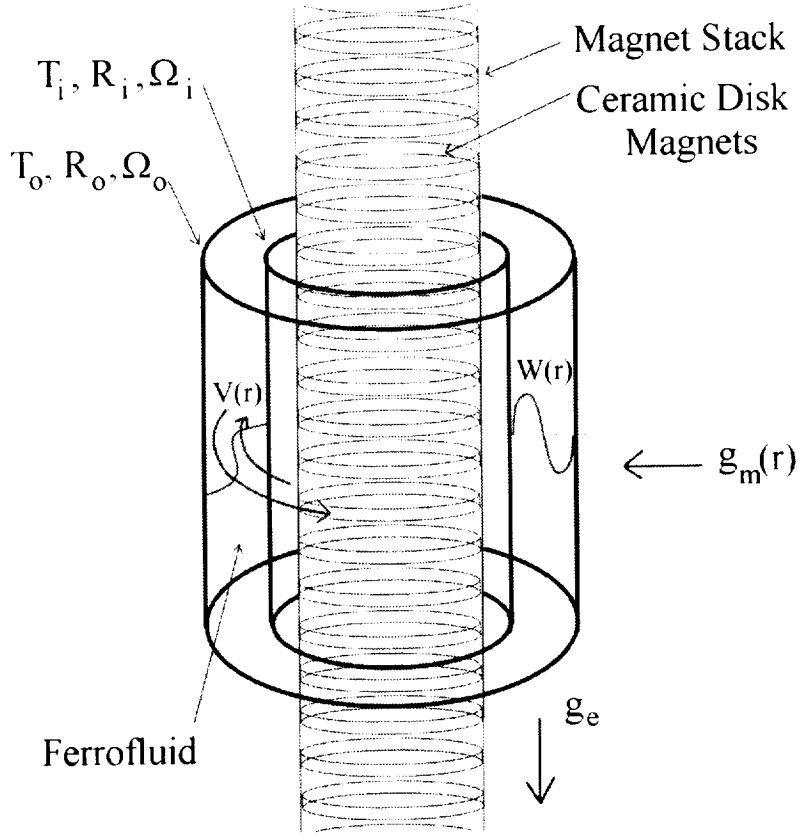

Figure 1. Stratified Taylor-Couette Flow. Radial gravity is achieved from the magnetization of the ferrofluid by the magnetic field created by a stack of high intensity disk magnets. The absolute magnitude of the **B**-field is almost exactly uniform in axial height z, and independent of azimuthal angle θ. This leads to a strong inwards-directed magnetic gravity $g_m(r)$. Flows are driven by differential rotation of the inner and outer walls that turn at rates Ω_i and Ω_o respectively, and by imposing either positive or negative radial thermal gradients across the annular gap via thermal baths at temperatures T_i and T_o.

PI: John E. Hart, Program in Atmospheric and Oceanic Sciences, Stadium 255UCB, University of Colorado, Boulder, CO 80309. hart@tack.colorado.edu 303-492-3524 (fax) 303-492-4248 (Lab).

STRATIFIED TAYLOR-COUETTE FLOW

with

RADIAL GRAVITY

John Hart, Dan Ohlsen, Patrick Weidman
University of Colorado, Boulder

Randy Tagg
University of Colorado, Denver

INTRODUCTION. Taylor-Couette flow between differentially rotating cylinders, and the related problem of rotating planar Couette flow, form paradigms in the study of instability, transition, and turbulence. A variation of substantial importance is the inclusion of buoyancy accelerations perpendicular to the axis of rotation. Buoyancy then acts in the same direction (radially) as centrifugal forces and competes or assists the latter in the generation of instabilities. If the density field is statically unstable (e.g. temperature decreases outwards and gravity is radially inwards), then it becomes possible to experimentally study the geophysically important case of vertically (i.e. radially) sheared convection. This paper reports on research aimed at attaining a robust experimental realization of Taylor-Couette flow with radial gravity.

The radial gravity is achieved by using a unique configuration of permanent magnets arranged along the axis of the apparatus. The working liquid is high-magnetization ferrofluid of low viscosity. Several questions have arisen in the implementation of the basic idea.

1) Ferrofluid is opaque. New visualization methods need to be developed.
2) What are the instabilities of Taylor-Couette flow in the presence of radial gravity and stratification? When does radial gravity swamp out terrestrial gravity?
3) Ferrofluid has non-Newtonian viscosity (because of the platelet suspension). How will this behavior the dynamics?
4) The magnet configuration has residual errors in the sense that small deviations from pure radial gravity will be present. These will cause anomalous motions. How big will these be and will they significantly affect the fundamental instabilities of stratified Taylor-Couette flow.

This paper summarizes recent research results on these problems.

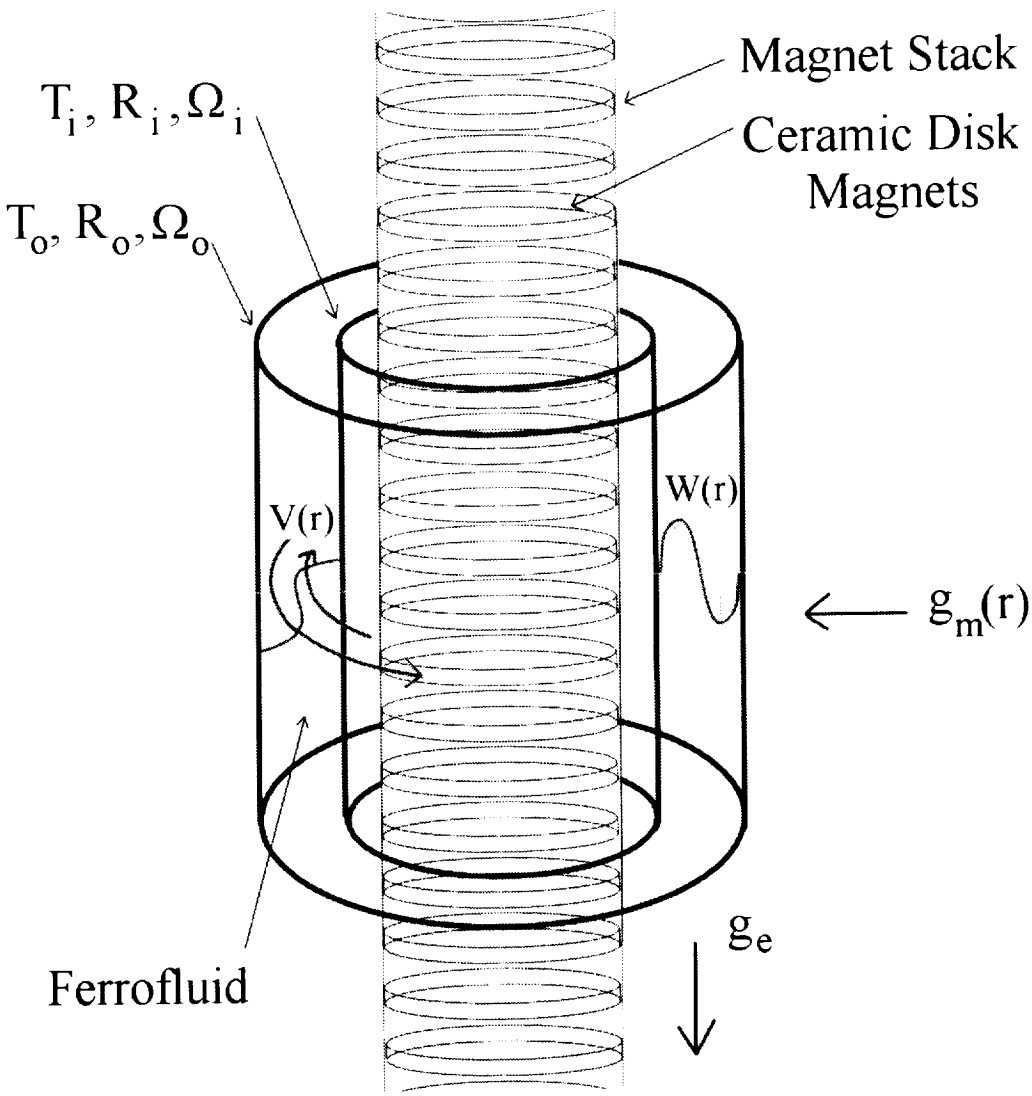

Fig. 1 Sketch of apparatus with vertical terrestrial gravity and radial magnetic gravity.

Figure 1 presents a conceptual design of the experiment. Ferrofluid is held in a Taylor-Couette cell whose walls can rotate and be heated differentially. The stack of Neodymium-Iron-Boron magnets leads to a magnetic gravity that is directed inwards and is a function of r (only) to lowest order. In the terrestrial lab, earth gravity can play a role. In the presence of heating an axial shear flow W(r) develops, in addition to the swirling flow V(r) generated by the differential rotation of the wall.

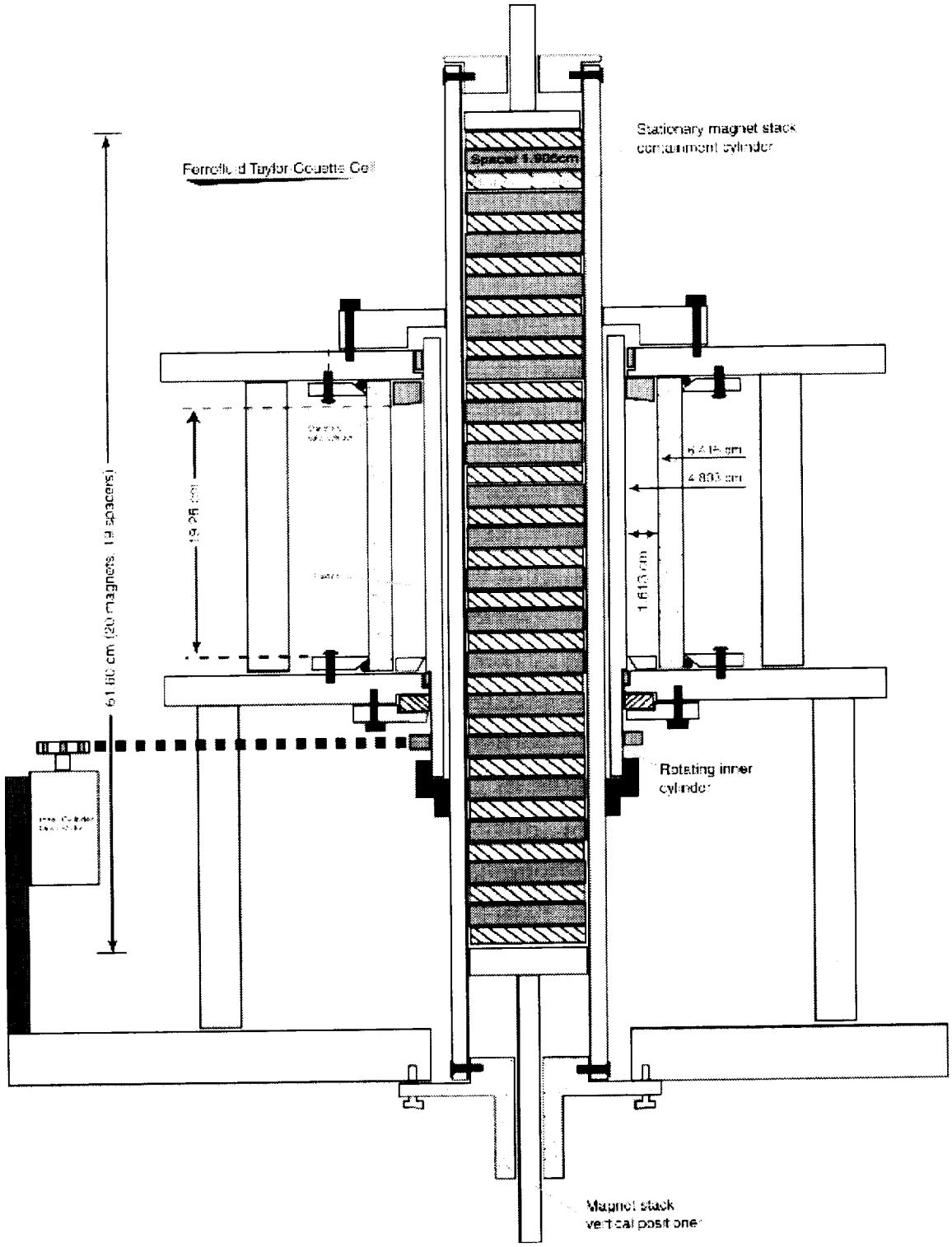

Fig. 2 Cross-section of actual apparatus showing typical dimensions.

Figure 2 illustrates the dimensions of our test cell. In this version only the inner wall is driven. To obtain differential rotation, the whole cell is placed on a rotating turntable. For the rest of this report, it is assumed that the outer rotation rate vanishes.

THE GENERATION OF RADIAL GRAVITY. The magnetic far-field of a tall stack of disk magnets, with vertical wavenumber k', is dominated by only the lowest vertical components. For a small gap width, and located far from the axis of rotation at r = 0, the magnetic potential is approximately given

$$\phi_m \propto e^{-k'r} \sin(k'z).$$

The magnitude of the resulting magnetic field is independent of z (though the vector B-field itself is strongly varying):

$$|B| \propto e^{-k'r}.$$

The magnetic body acceleration in a ferromagnetic fluid is

$$\vec{A} = \frac{\mu_o}{\rho_o}\left[\vec{M}\cdot\nabla\vec{H} + \nabla\times\vec{M}\times\vec{H}\right]$$
$$\propto -\alpha T M_s \nabla B \propto g_m(r)\ \alpha T\ \hat{r},$$

where M_s is the saturation magnetization of the ferrofluid, and, as is typical, $\vec{M} << and\ \vec{H}$ (to lowest order). Thus $B(r)$ is a "geopotential" that with this assumed symmetry leads to a radially directed gravity (Hart, 2002, provides more detail).

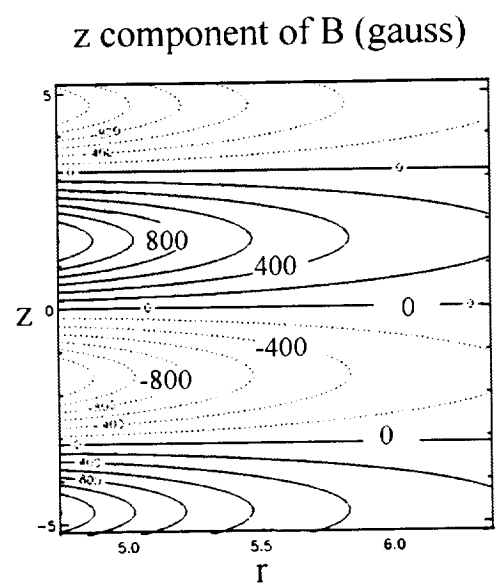

Figure 3. Computed B_z (r, z) for the situation of figure 2.

Figure 3 shows the results of a numerical solution of Maxwell's equations for the magnet stack actually used in our experiment. The z component of the magnetic field fluctuates strongly in r and with the periodicity of the magnet stack (twice the actual periodicity since the magnets are placed in the stack with poles NNSSNNSS....). Over the radius range r = 5cm to about 5.5cm the magnitude of the field has azimuthal symmetry and near axial symmetry (Figure 3, below). The magnetic geopotential is essential just a function of r, leading to a radial gravity. Our initial gap is wider, to support high Re experiments.

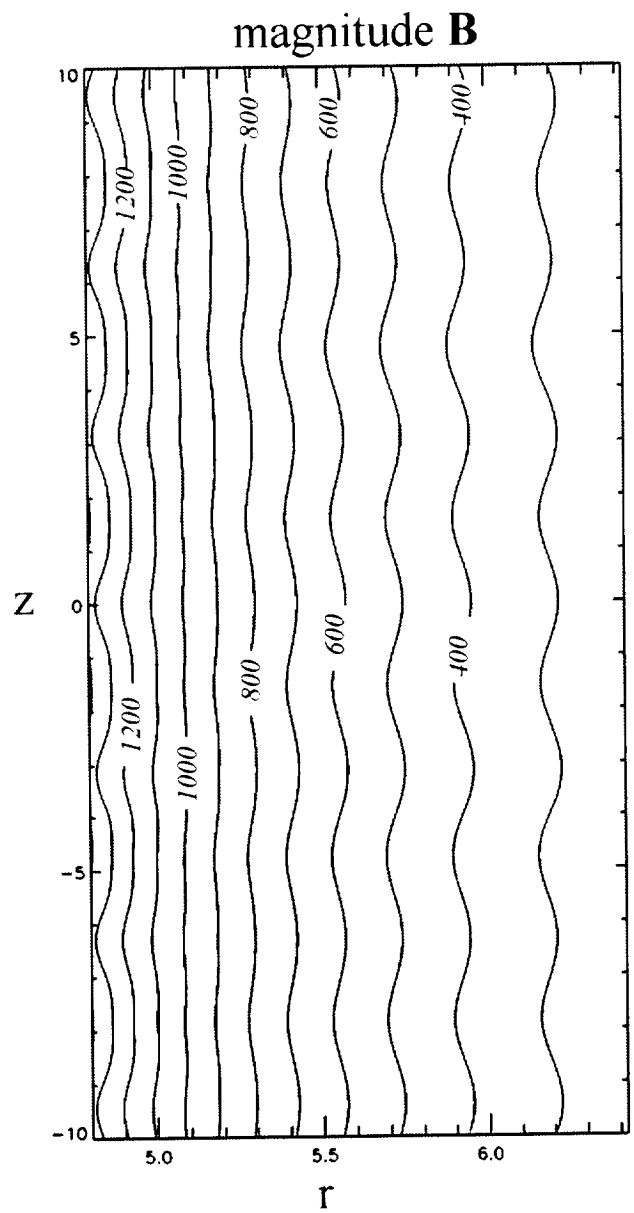

Figure 3. Magnitude of the magnetic field B

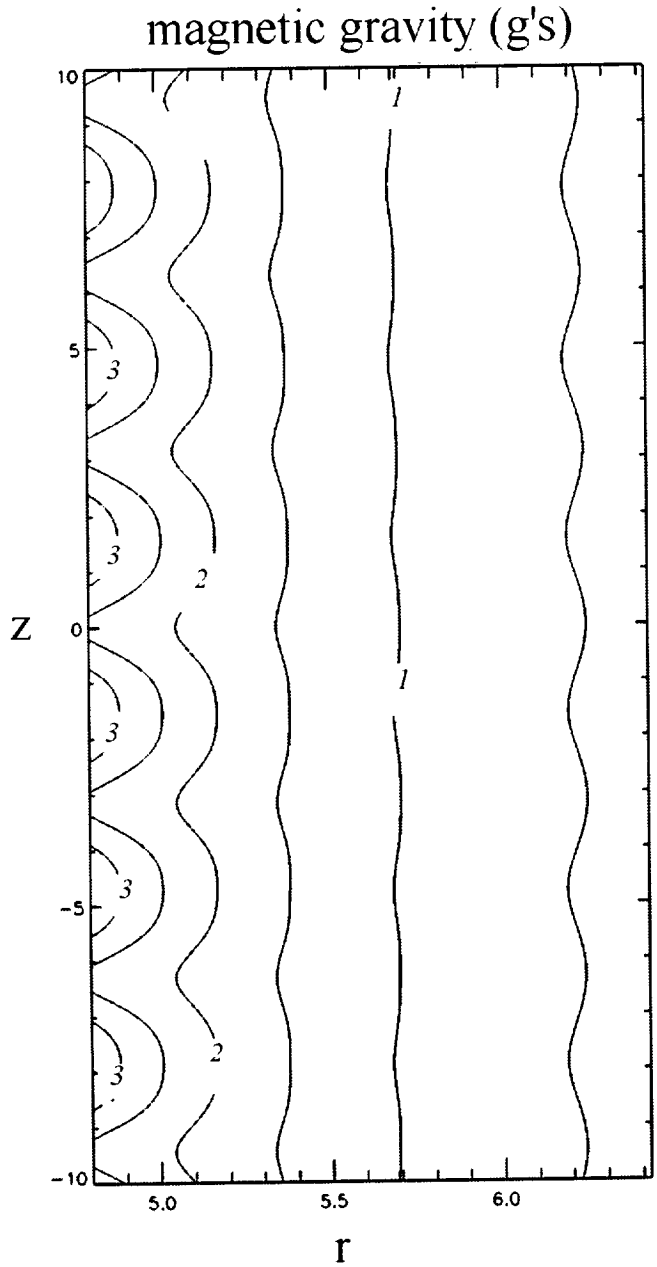

Figure 5. Magnetic gravity in terrestrial g's in the vicinity of r = 5cm using 3:1 water based ferrofluid and NIB magnets with about 2000G of vertical magnetization (from Edmund Scientific).

Even with 3:1 ferrofluid a ratio of magnetic to terrestrial gravity of about 2 can be obtained at the inner cylinder wall (Figure 5). At 1:1 the viscosity goes up to about 10 centistokes (thereby limiting the range of available Reynolds and Richardson numbers), but the magnetic to terrestrial gravity ratio become of order 10. Eventually we may rebuild our inner cylinder to set $R_i = 5.3cm$ in order to sit in a more uniform B region.

FLOW VISUALIZATION. The nearly 100% opacity of Ferrofluid presents a visualization problem. How will we observe flow regimes and make quantitative measurements of instabilities and turbulence.

1) In-situ miniature thermistor temperature sensors (or hot thermistor velocimeter).
2) Remote sensing via Ultrasonic Doppler Velocimetry Profiler

Item 1) represents old technology. It can be done, but the probes constitute a substantial obstacle to the flow, potentially altering regimes. At best, measurements at only a few points can be made simultaneously. Ultrasonic Doppler Velocimetry, on the other hand, returns a profile of line-of-sight velocity and is remote and non-perturbing.

We have tested a commercial UDP, the DOP2000, in a simple geometry, the differentially driven cylinder. Figures 6 - 8 illustrate this experiment, where a pure ferrofluid (of a given dilution) is driven to steady axisymmetric motion by the differential rotation of a disk or a cylinder. Measurements of radial velocity u vs. r are obtained at several heights z by mounting the ultrasonic probe to point in along a radius through the outer plexiglass wall at various locations up the side.

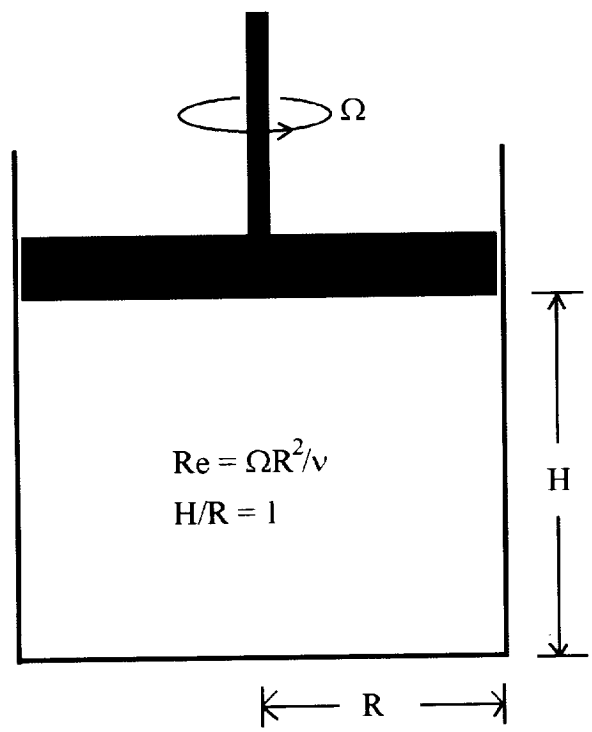

Figure 6. Cross-section of test cell for UDP with either an aluminum driving disk, or a driving disk consisting of a strong vertically-magnetized NeFeBo magnet. With the aspect ratio fixed at 1 this is a one- parameter system, involving only the Reynolds number Re.

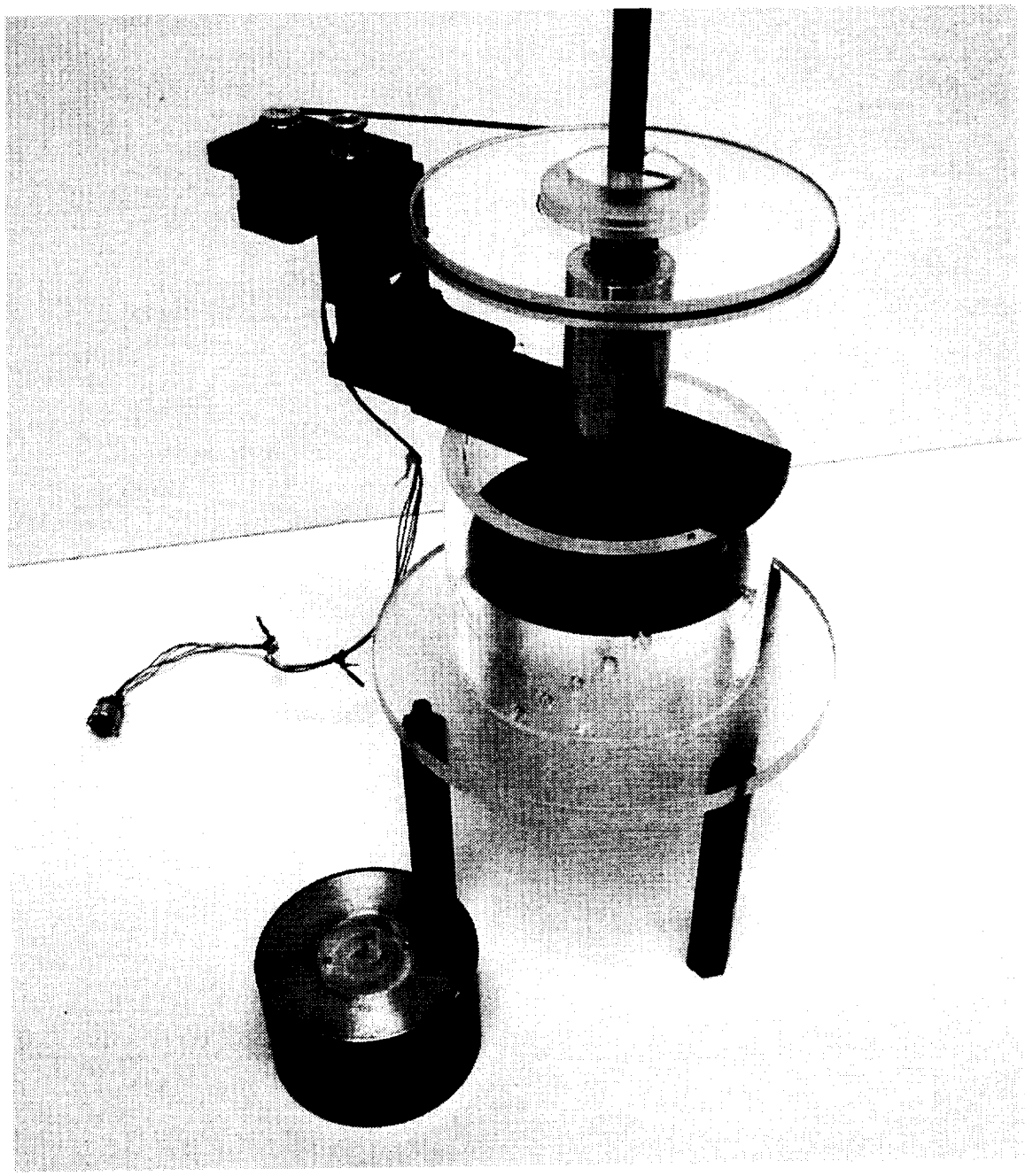

Figure 7. Test cell for Ultrasonic Doppler Velocimetry tests. Simple cylinder flow with a differentially rotating lid or a rotating inner cylinder.

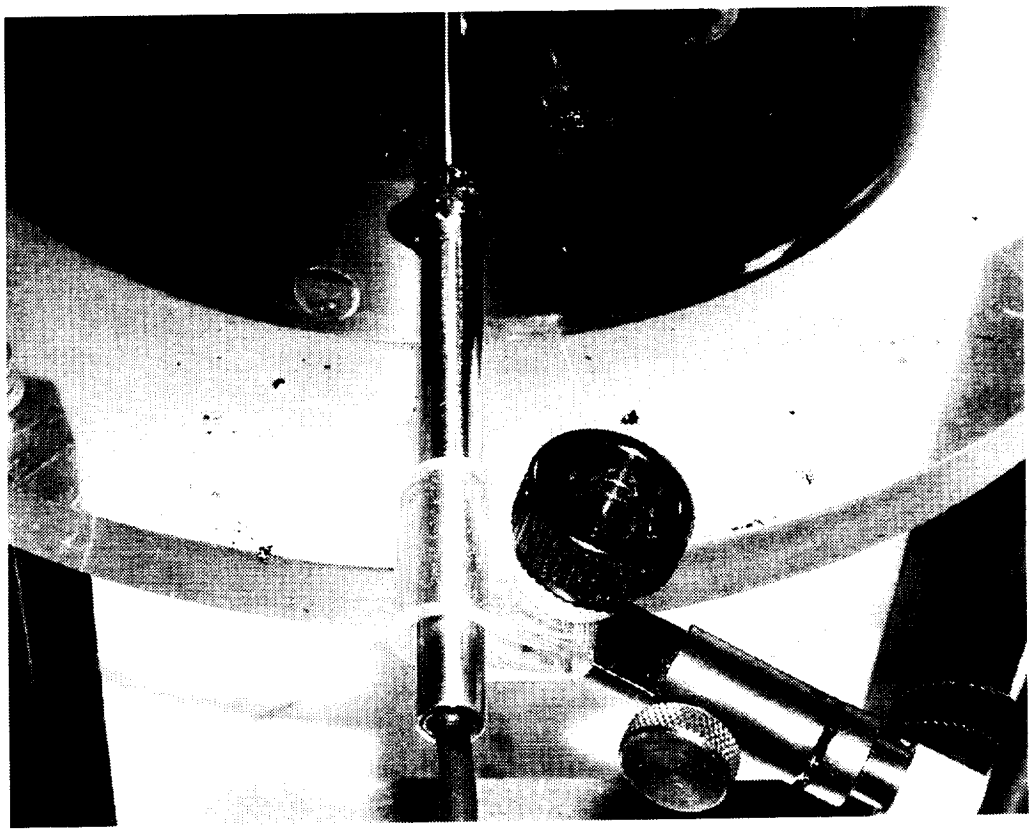

Figure 8. Probe mounted in the side of the cylinder. Holes are drilled into the plexiglass walls to within 2mm of the inner diameter. Note the dark opaque ferrofluid.

The instrument works quite well for quasi-steady flows (periods of motion less than about 1/3 second). 4MHz signals penetrate the full height of our test cell (Figure 2), while 8 or 10MHz pulses can be used to more accurately probe the radial structure (i.e. the higher frequencies are attenuated more rapidly, and thus are useful only over a distance of a couple of cm in full strength ferrofluid).

Figures 9 and 10 illustrate results obtained with the DOP2000. Agreement is good between the ultrasonic measurements and a finite-difference simulation of the expected 2D motion. Wavy structures in the experimental data near r = 1 need further investigation, but could be due to near field and wall reflection effects. Figure 10 shows that the presence of a strong vertical magnetic field at the driving surface is associated with a weaker circulation. This is believed caused by a non-Newtonian viscosity effect where the strong horizontal vorticity just below the3 disk rotates the particles out of alignment with the axial magnetic field, leading to new body forces. With Prof. Lopez we are in the process of attempting a non-Newtonian simulation of this phenomena.

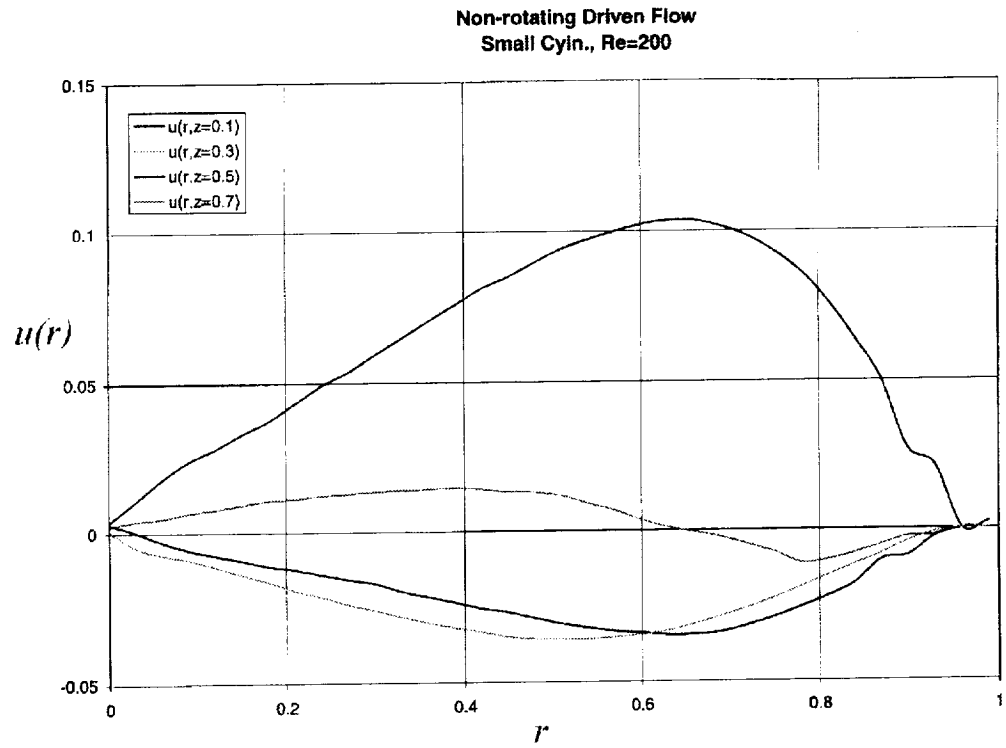

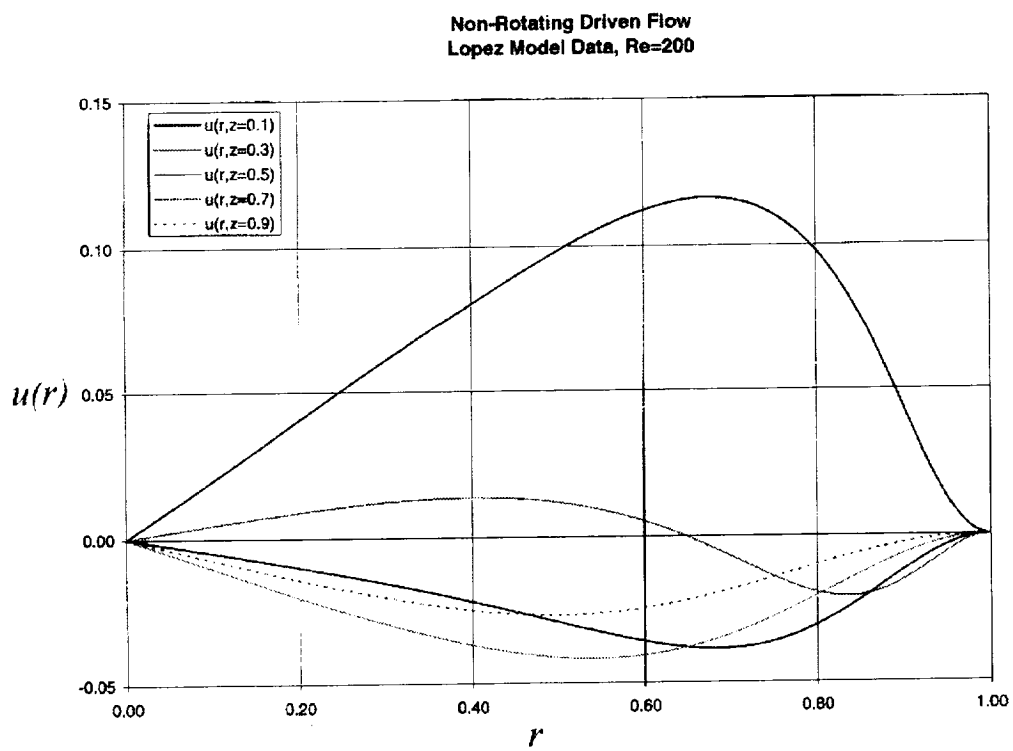

Figure 9. DOP2000 data vs. numeric DNS results (courtesy John Lopez)

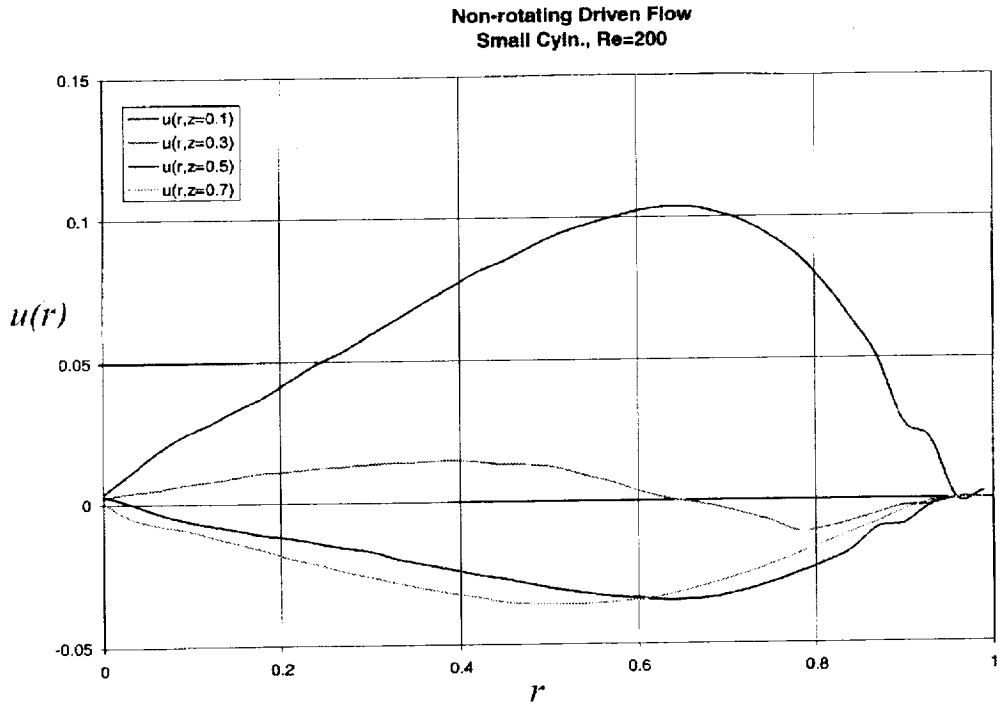

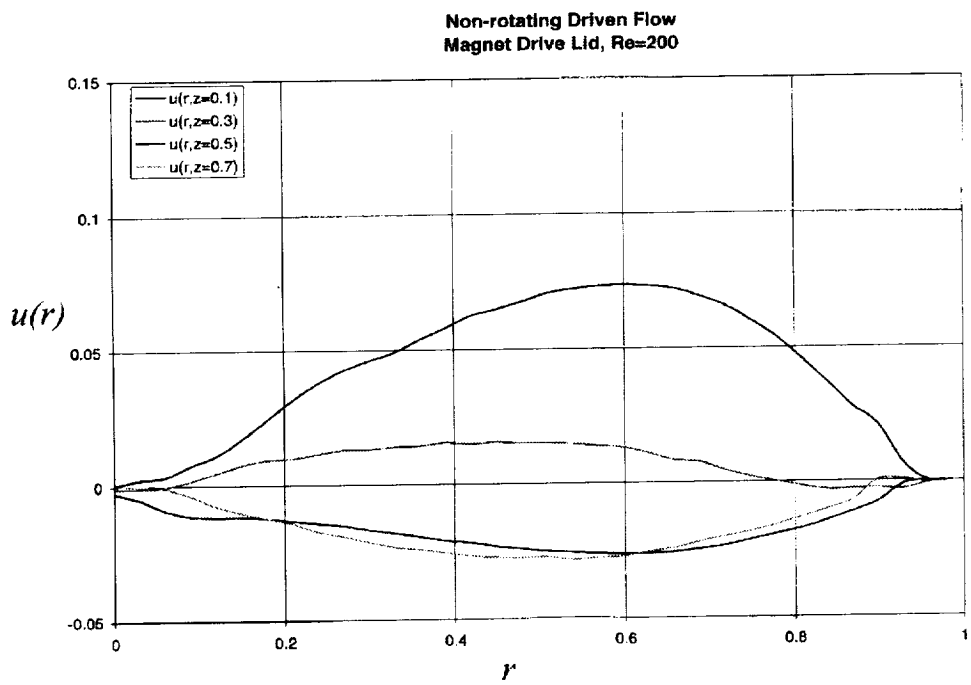

Figure 10. Measured radial velocity with the aluminum driving disk (top) and with a 2000G magnet as the drive disk (bottom).

THE LINEAR STABILITY PROBLEM. It is of considerable interest to investigate the instabilities expected in the combined gravity fields of figure 1. We have completed a numerical solution to obtain the growth rates for three-dimensional linear perturbations in a Newtonian fluid in which z variations of magnetic gravity are neglected. That is, the only magnetic effect is $g_m(r)\hat{r}$. Our analytical determined (exact) basic state is composed of:

$\bar{V}(r)\hat{\theta}$	The classic Taylor-Couette flow
$\bar{W}(r)\hat{z}$	The terrestrial-gravity buoyancy flow
$\bar{T}(r)$	The basic stratification w.r.t. radial $\vec{g}_m$. This stratification, under the action of terrestrial gravity, is what generates W(r)

The stability problem is solved numerically with rigid sidewalls. The linear modes are periodic in z with wavenumber k, and are periodic in azimuth with wavenumber m.

The parameters in the stability problem are:

$$\eta = R_i / R_o$$
$$\mathrm{Pr} = \nu / k$$
$$\mathrm{Gr} = g_e \alpha (T_i - T_o) D^3 / \nu^2$$
$$\mathrm{Re} = \Omega_i R_i D / \nu$$
$$g_m = g_m(R_i) / g_e$$

The stability equations are written out in Appendix 1.

Figures 11 and 12 illustrate results for a typical fluid with Prandtl number 18 and various levels of magnetic/terrestrial gravity. When $g_m = 0$ (no radial gravity), the vertical shear flow leads to a weak destabilization (i.e. a lower Re) as Gr increases. As g_m becomes large, the radial gravity, coupled with the statically unstable temperature gradient, leads to a dramatic destabilization. The modes at low Re and low Gr are essentially convective columns, aligned vertically into "longitudinal rolls" by W(r). When Gr is negative, the radial stratification is statically stable. For the modest magnitudes of Gr computed, there appears to be the counterintuitive result that large g_m actually destabilizes the motion relative to the zero radial gravity case. This could be related to the well-known destabilization of plane Couette flow by vertical shear (provided the Richardson number is small). Investigation of the physics underlying these results is under study.

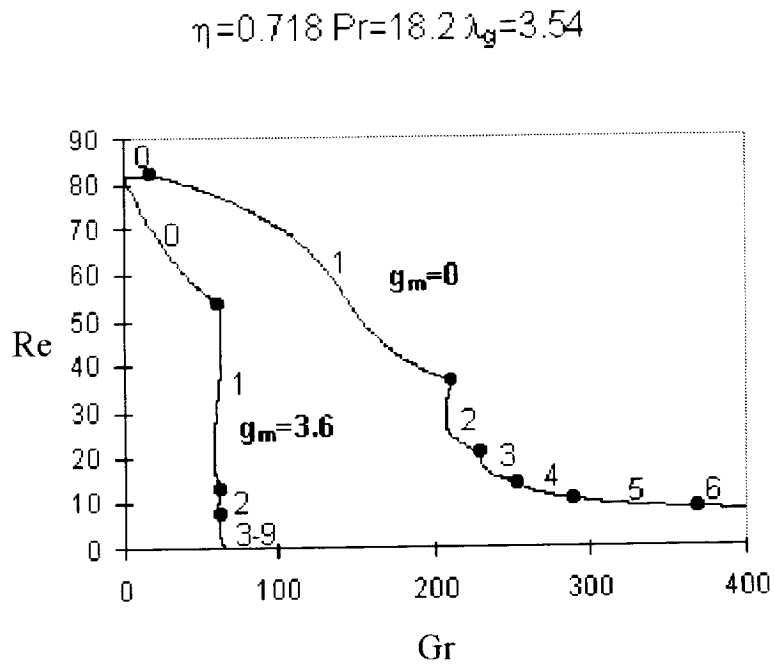

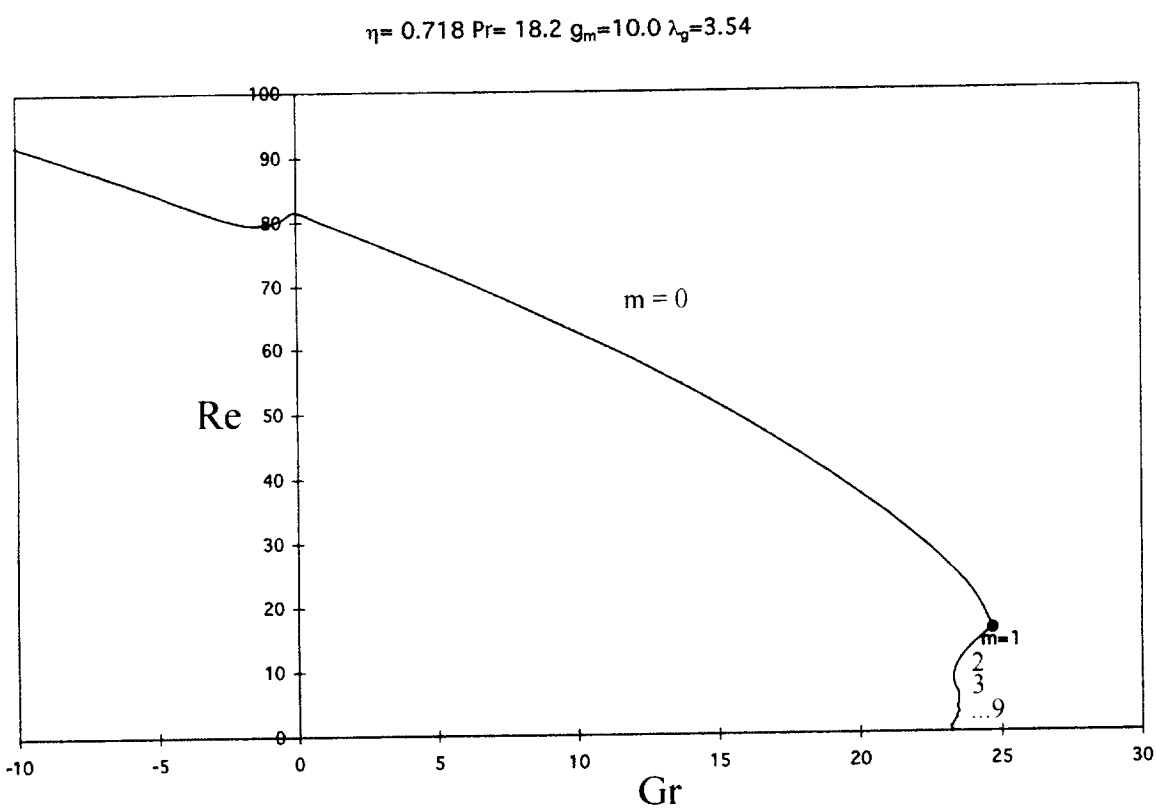

Figure 11. Neutral curves for three values of g_m .

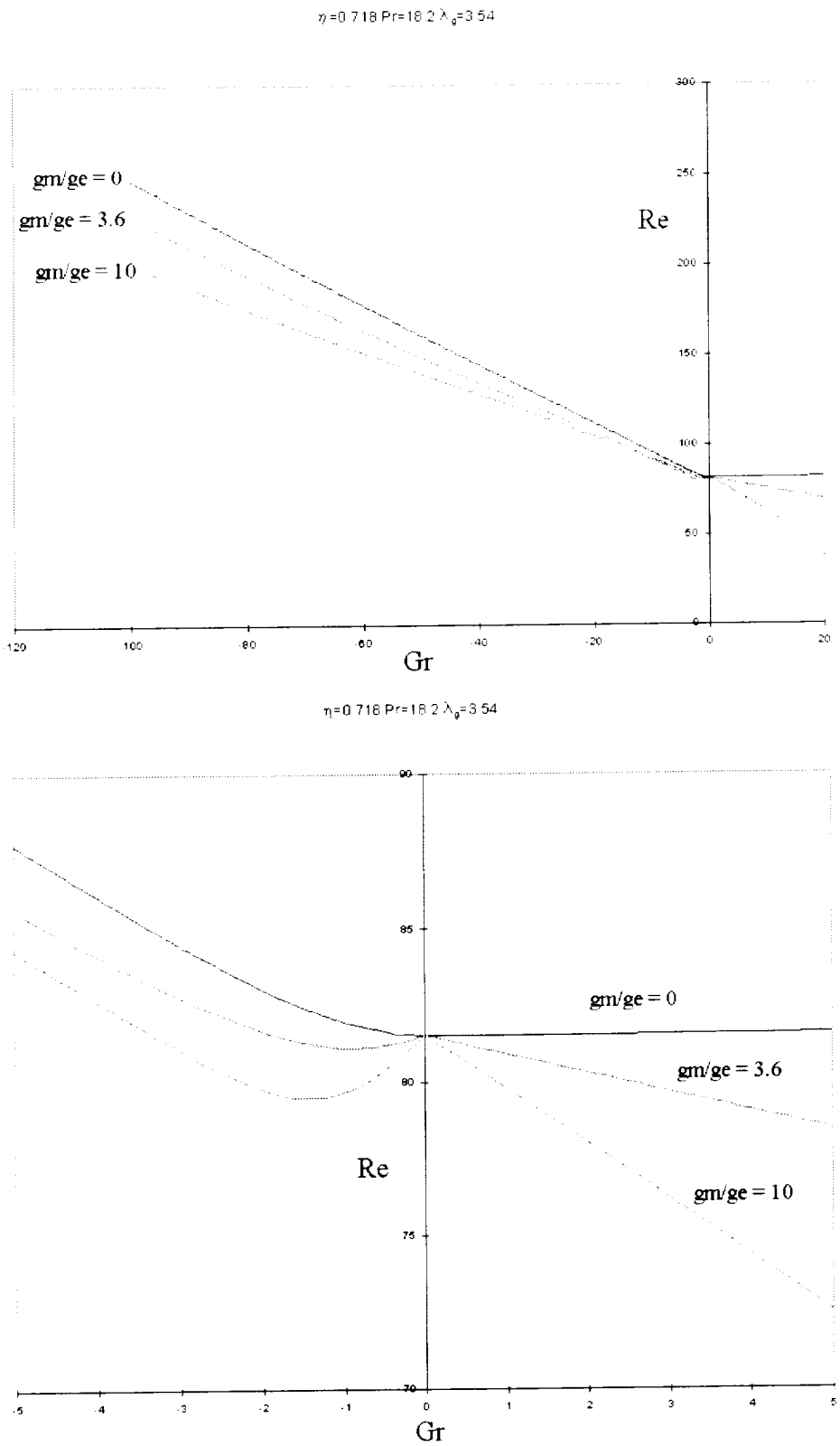

Figure 12. Stability results for weak heating.

Non-Newtonian Viscosity. Shearing of particles in the suspension by local fluid rotation leads to anisotropic viscosity. In the Shliomis Model (see Hart, 2002), the magnetization comes out of alignment with the imposed magnetic field. This "deviation magnetization" is small and given by the vorticity-field interaction

$$\vec{M}' = const * \left[(\nabla \times \vec{u}) \times \vec{B}_o \right]$$

New magnetic body forces associated, for example, with $\nabla \times \vec{M} \times \vec{B}_o$ drive secondary circulations that have the same vertical periodicity as magnetic field stack. These circulations can influence stability and can even resonate with linear modes of instability.

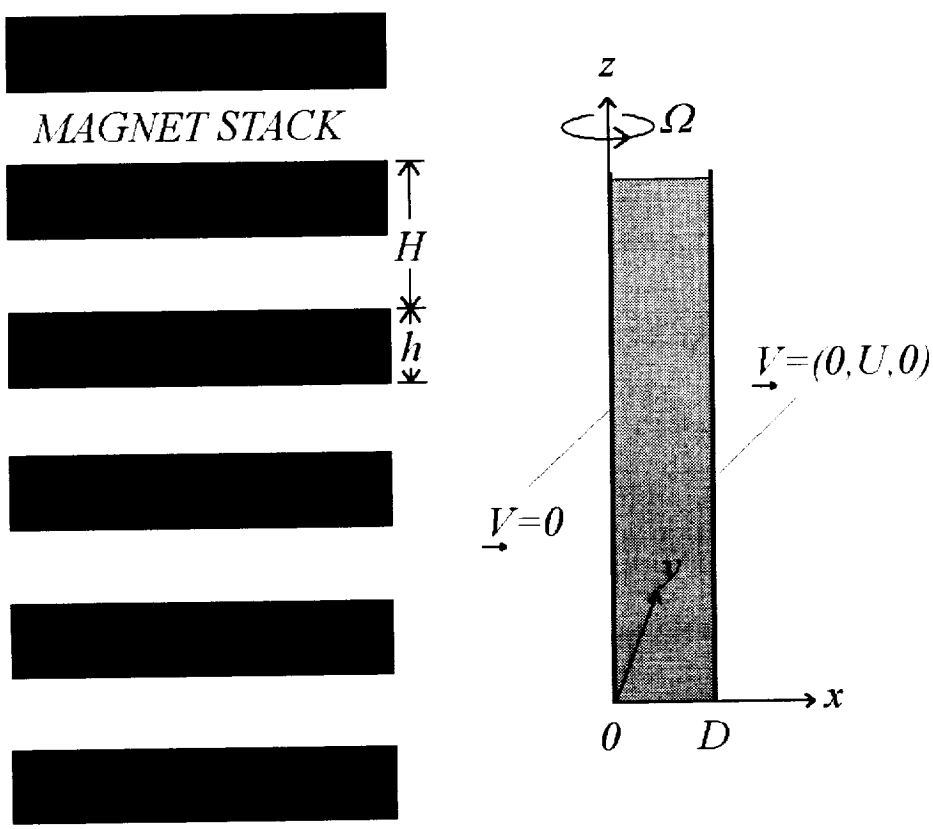

Fig. 13. Rotating channel model for analytic calculation of non-Newtonian effects on basic flows and stability.

In order to make analytical progress on assessing the magnitude of non-Newtonian effects in the system of figure 2, we unwrap the cylindrical geometry and study the dynamics in a simpler system of plane Couette flow in a narrow gap of rotating fluid. This is illustrated in figure 13. First, the interaction of the plane Couette flow (i.e. V(r) in the Taylor Cell) with the periodic fields (as in figure 3) drives a secondary circulation. For the system of figure 2, this is pretty weak, only a mm per second or less.

Nonetheless, this motion, along with anisotropic viscosity acting on the Taylor vortices themselves, can change the stability of the system. Figure 14 shows the results of a long and tedious analytical calculation of the fractional change of the critical parameter Q for the case of figure 13. Since $\delta = (Q - Q_c)/Q_c$ is small (where Q_c is the critical parameter with ordinary viscosity), the analysis shows that here non-Newtonian influences should be negligible (Hart, 2002).

Why is this different from the observation in figure 10 of significant non-Newtonian effects? There are two reasons. In the system of figures 6 – 7 the fluid contacts the magnet, while in figure 2 it is substantially removed from the magnet (so that fields and field gradients are weaker). More importantly, the basic flow of figure 13 (or figure 1) is smooth and spread over the entire gap. The vorticity is small or zero. The vorticity of linear perturbation is also relatively small since the linear modes have length scale D. However in the differentially driven cylinder the vorticity at the disk is huge, because the motion occurs in a boundary layer attached to the disk.

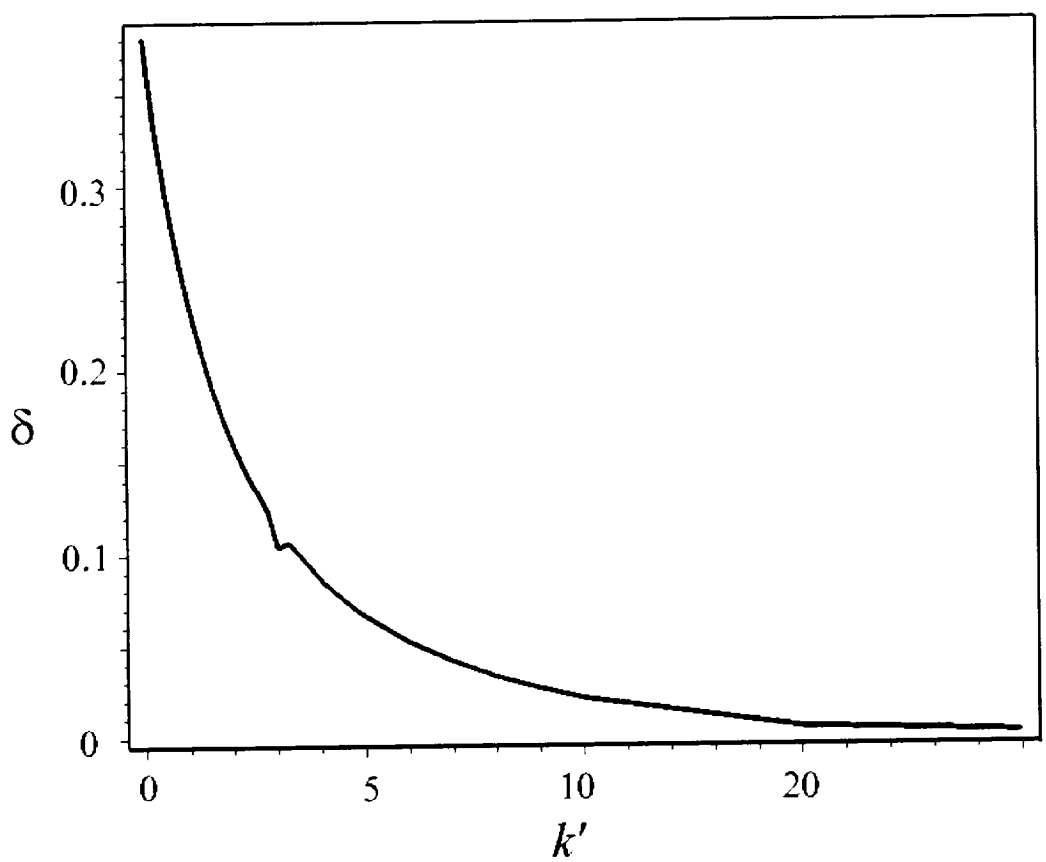

Fig. 14. Fractional change in critical Taylor number vs. magnetic stack wavenumber (for the most unstable axisymmetric mode with critical wavenumber 3.117)

Z-Dependent Magnetic Gravity. Small z–variations in magnetic gravity (in both direction and magnitude) cause unbalanced buoyancy forces when a radial temperature gradient is imposed:

$$\nabla \phi_m(r,z) \times \nabla \overline{T}(r) \neq 0$$

Weak cells with the same vertical periodicity of magnet stack form, and potentially can interact with linear instabilities and other flows of interest. Cells can be resonant with linear instabilities if k' = k.

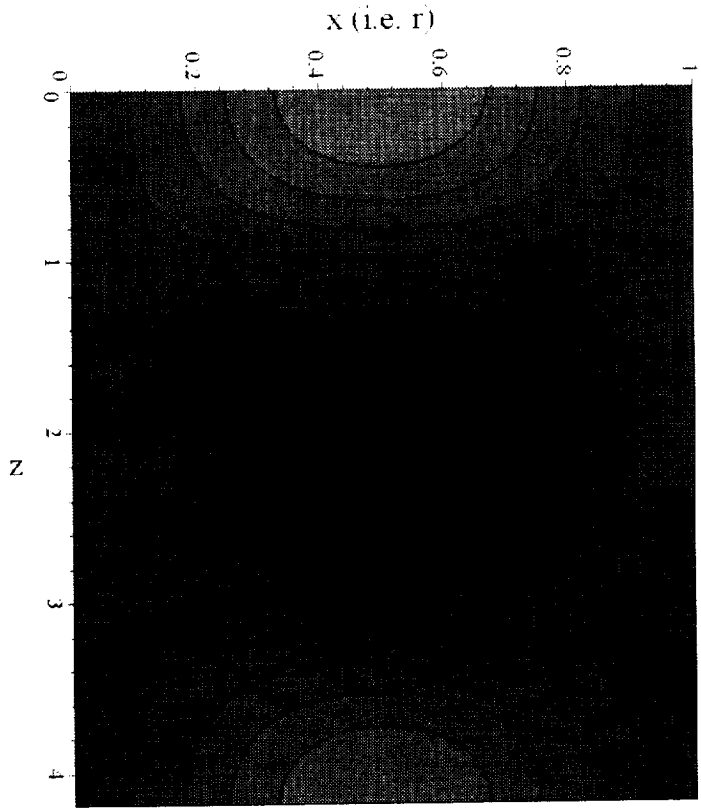

Fig. 15. Mean flow induced by z-varying magnetic gravity.

If gravity varies spatially, as in figure 5, motions will be generated even in the presence of an axially invariant thermal field T(r) or T (x). Figure 15 illustrates this. The motions are weak unless they happen to be resonant with one of the linear neutral modes in the system, whence they can be fairly significant (Hart, 2002a). However, this latter situation can be avoided by suitable choice of the magnet stack wavenumber k'. Nonetheless, the z-periodic mean flow and gravity can both affect the linear instability problem. Figure 16 illustrates the change in critical Taylor number (Re ^ 2) as the heating parameter Gr and the fluid properties (Pr) vary. Here

$$Q = Q_c + \varepsilon^2 \delta,$$

where $Q_c = 1707$ is the unperturbed critical point, and $\varepsilon \approx 0.2$, say, is the magnitude of the gravity fluctuations compared with the mean radial gravity.

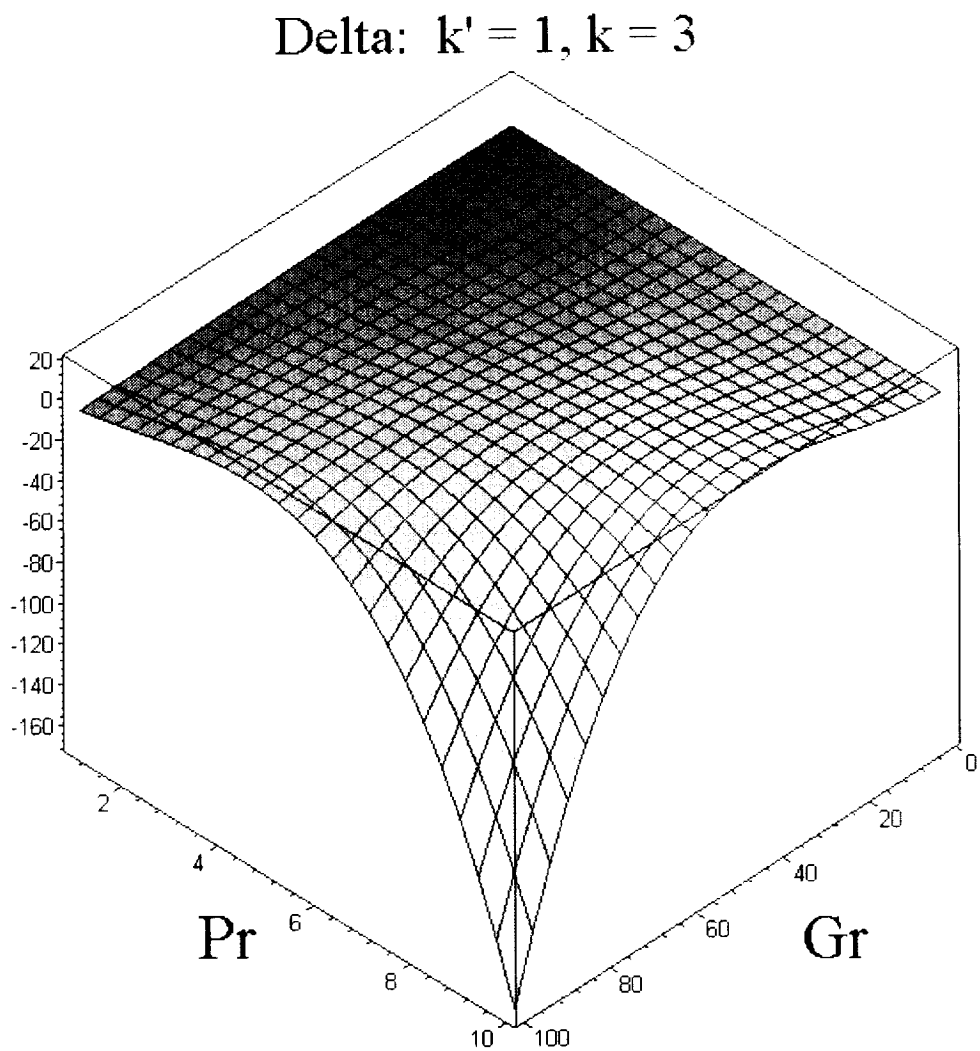

Fig. 16 Change of stability of the most dangerous mode for the cell of figure 13, vs. Gr and Pr. In this example unstable mode has a critical point of 1708 at k = 3.117. In this plot instability axial wavenumber k = 3 and k' (the magnet stack wavenumber) is 1.

It is interesting that at low Gr and Pr the z-varying gravity is stabilizing, while at larger Pr and Gr (or more specifically at larger Ra = Pr Gr) it is destabilizing. The former is easy to understand. The weak secondary circulation (figure 15) simply mixes up the basic stratification, stabilizing the interior and leading to steeper thermal gradients near the walls. Since the perturbations are not active near the walls (where their velocity vanishes), they are thus stabilized. Figure 17 shows the mean (z – independent) thermal gradient associated with the buoyancy circulation of figure 15. The destabilization at large Ra is more complicated, involving wave-wave interactions that reinforce the fundamental instability mode (Hart, 2002a).

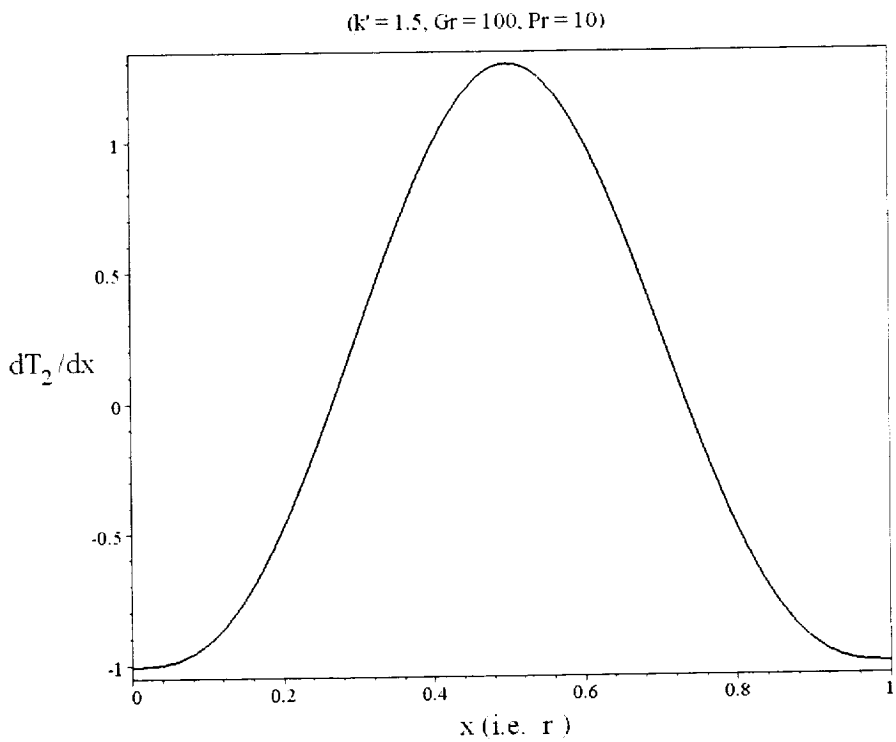

Fig. 16 Mean temperature gradient correction (to statically unstable basic state). The z-varying gravity circulation stabilizes the interior and destabilizes the edges. The net effect is to stabilize the system.

CONCLUSIONS AND FUTURE PLANS

A multi-g radial-gravity Taylor-Couette experiment has been built. Visualization via ultrasonic Doppler line-of-sight velocity profiling is feasible and demonstrably accurate.

Linear and weakly nonlinear theories have suggested that:

a) Non-Newtonian viscosity effects are small (10% or so).
b) z – variations of magnetic gravity may be more significant but are still relatively small (10 – 20%).
c) New modes of instability appear with radial gravity, and the classical modes are substantially altered.

Experiments using UDP on the full experiment will provide data with which to explore supercritical regimes of sheared convection, stably stratified centrifugal and shear flow instabilities, and other phenomena.

REFERENCES

Hart, J.E., "Ferromagnetic rotating Couette flow: the role of magnetic viscosity," *J. Fluid Mech.*, 453, 21 – 38, 2002.

Hart, J.E., "Instability and secondary motion in stratified rotating Couette flow with spatially periodic gravity," *J. Fluid Mech.*, to be submitted, October, 2002a.

Tagg, R., and Weidman, P., "Instability of Stratified Taylor-Couette Flow with Terrestrial and Radial Gravity," *J. Fluid Mech.*, in final preparation.

ACKNOWLEDGEMENTS

We thank NASA for supporting this research under grant NAG-3-2402 to the University of Colorado. Mr. Scott Kittelman provided invaluable assistance with the experiments.

APPENDIX: Linear Stability Problem with Basic States as Illustrated in Fig. 1

Small Disturbance Equations

Modal Disturbance Form

$$\begin{pmatrix} u(r,\phi,z) \\ v(r,\phi,z) \\ w(r,\phi,z) \\ \theta(r,\phi,z) \\ \pi(r,\phi,z) \end{pmatrix} = \begin{pmatrix} \overline{u}(r) \\ \overline{v}(r) \\ \overline{w}(r) \\ \overline{\theta}(r) \\ \overline{\pi}(r) \end{pmatrix} + \begin{pmatrix} U(r) \\ V(r) \\ i\,W(r) \\ \Theta(r) \\ \Pi(r) \end{pmatrix} \exp\{i\,(kz + m\phi - \omega) + \sigma t\}$$

Linearized Equations

$$X = \frac{dU}{dr} + \frac{1}{r}U - \Pi$$

$$\frac{dX}{dr} = \left[\left(\sigma + \frac{m^2}{r^2} + k^2\right) + i\left(-\omega + mR\frac{\overline{v}}{r} + kR\overline{w}\right)\right]U - 2\left(R\frac{\overline{v}}{r} - i\frac{m}{r^2}\right)V - \boxed{\frac{\gamma G}{R}f(r)\,\Theta}$$

$$Y = \frac{dV}{dr} + \frac{1}{r}V$$

$$\frac{dY}{dr} = \left[R\left(\frac{d\overline{v}}{dr} + \frac{\overline{v}}{r}\right) - i\frac{2m}{r^2}\right]U + \left[\left(\sigma + 2\frac{m^2}{r^2} + k^2\right) + i\left(-\omega + mR\frac{\overline{v}}{r} + kR\overline{w}\right)\right]V + i\frac{mk}{r}W - i\frac{m}{r}X$$

$$Z = \frac{dW}{dr}$$

$$\frac{dZ}{dr} = -iR\frac{\overline{w}}{dr}U - i\frac{mk}{r}V + \left[\left(\sigma + \frac{m^2}{r^2} + 2k^2\right) + i\left(-\omega + mR\frac{\overline{v}}{r} + kR\overline{w}\right)\right]W - kX - \frac{1}{r}Z + i\frac{G}{R}\,\Theta$$

$$Q = \frac{d\Theta}{dr}$$

$$\frac{dQ}{dr} = PR\frac{d\overline{\theta}}{dr}U + \left[\left(P\sigma + \frac{m^2}{r^2} + k^2\right) + iP\left(-\omega + mR\frac{\overline{v}}{r} + kR\overline{w}\right)\right]\,\Theta - \frac{1}{r}\,Q$$

Eigenvalue Problem

Neutral Stability: $(\sigma = 0)$

$$\boxed{F(R, G, P, \gamma, k, \omega, m, \eta, \mu) = 0}$$

AN EXPERIMENTAL INVESTIGATION OF INCOMPRESSIBLE RICHTMYER-MESHKOV INSTABILITY

J. W. Jacobs[†]
University of Arizona

C. E. Niederhaus
NASA Glenn Research Center

ABSTRACT

Richtmyer-Meshkov (RM) instability occurs when two different density fluids are impulsively accelerated in the direction normal to their nearly planar interface. The instability causes small perturbations on the interface to grow and eventually become a turbulent flow. It is closely related to Rayleigh-Taylor instability, which is the instability of a planar interface undergoing constant acceleration, such as caused by the suspension of a heavy fluid over a lighter one in the earth's gravitational field. Like the well-known Kelvin-Helmholtz instability, RM instability is a fundamental hydrodynamic instability which exhibits many of the nonlinear complexities that transform simple initial conditions into a complex turbulent flow. Furthermore, the simplicity of RM instability (in that it requires very few defining parameters), and the fact that it can be generated in a closed container, makes it an excellent test bed to study nonlinear stability theory as well as turbulent transport in a heterogeneous system. However, the fact that RM instability involves fluids of unequal densities which experience negligible gravitational force, except during the impulsive acceleration, requires RM instability experiments to be carried out under conditions of microgravity.

This experimental study investigates the instability of an interface between incompressible, miscible liquids with an initial sinusoidal perturbation. The impulsive acceleration is generated by bouncing a rectangular tank containing two different density liquids off a retractable vertical spring. The initial perturbation is produced prior to release by oscillating the tank in the horizontal direction to produce a standing wave. The instability evolves in microgravity as the tank travels up and then down the vertical rails of a drop tower until hitting a shock absorber at the bottom. Planar Laser Induced Fluorescence (PLIF) is employed to visualize the flow. PLIF images are captured by a video camera that travels with the tank. Figure 1 is as sequence of images showing the development of the instability from the initial sinusoidal disturbance far into the nonlinear regime which is characterized by the appearance of mushroom structures resulting from the coalescence of baroclinic vorticity produced by the impulsive acceleration. At later times in this sequence the vortex cores are observed to become unstable showing the beginnings of the transition to turbulence in this flow. The amplitude of the growing disturbance after the impulsive acceleration is measured and found to agree well with theoretical predictions. The effects of Reynolds number (based on circulation) on the development of the vortices and the transition to turbulence are also determined.

[†] Address: Department of Aerospace and Mechanical Engineering, University of Arizona, Tucson, AZ 85721; e-mail: jwjacobs@u.arizona.edu; phone: (520) 621-8459; fax: (520) 621-8191.

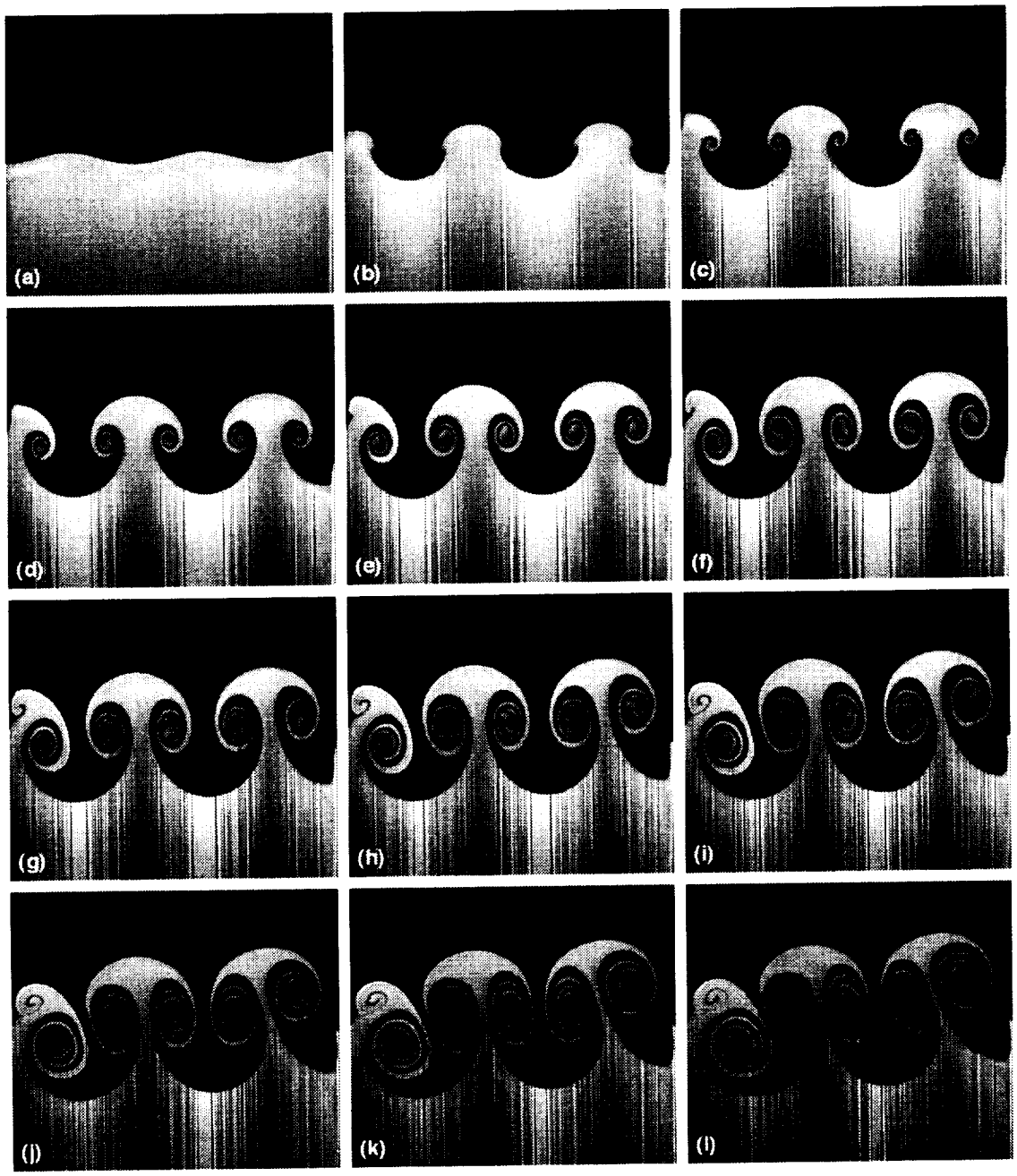

Figure 1. A sequence of images from an experiment showing the development of the RM instability. The initial sinusodial perturbation inverts (due to the acceleration direction) and then evolves into a mushroom pattern that is nearly symmetrical due to the moderate density difference (Atwood number of 0.15). At late times and high Reynolds number (2400 for this experiment based on circulation), an instability develops in the vortex cores, as can be seen beginning in (i). Times relative to the midpoint of spring impact are (a) −28 ms, (b) 88 ms, (c) 172 ms, (d) 255 ms, (e) 339 ms, (f) 422 ms, (g) 505 ms, (h) 589 ms, (i) 672 ms, (j) 756 ms, (k) 839 ms, and (l) 906 ms.

An Experimental Investigation of Incompressible Richtmyer-Meshkov Instability

J.W. Jacobs[†] and C.E. Niederhaus[‡]

[†]Department of Aerospace and Mechanical Engineering
University of Arizona

[‡]Microgravity Science Division
NASA Glenn Research Center

Richtmyer-Meshkov Instability

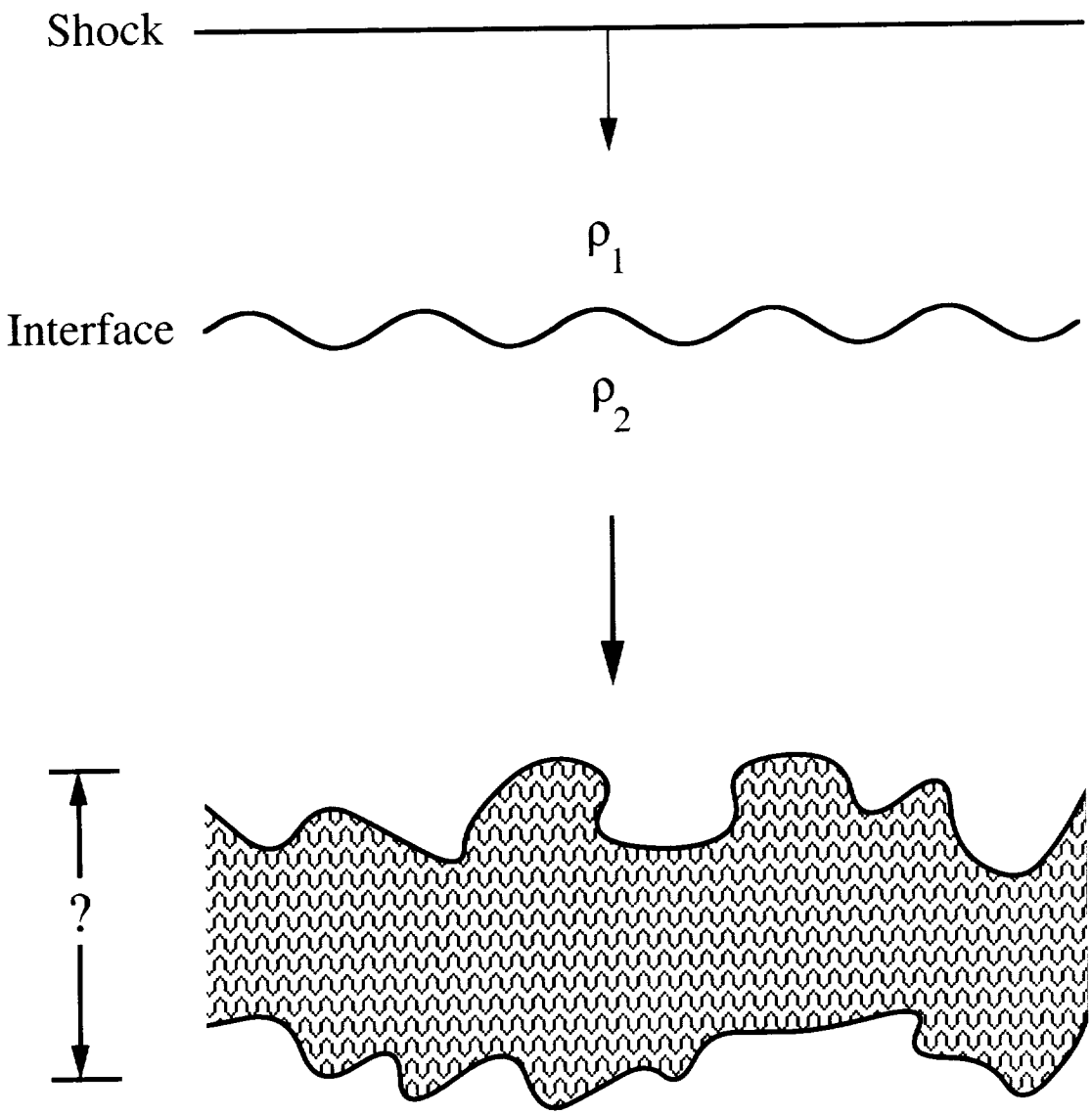

The National Ignition Facility

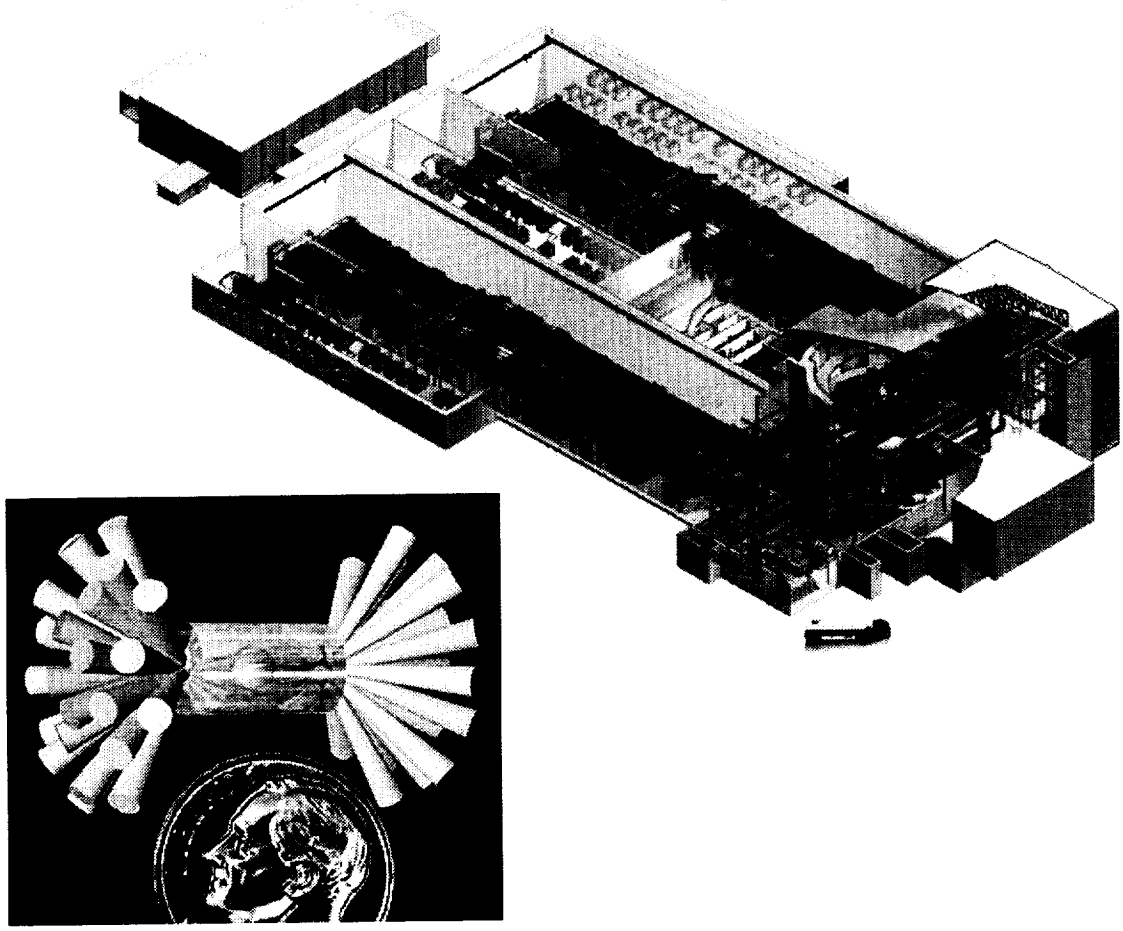

The Inertial Confinement Fusion Concept

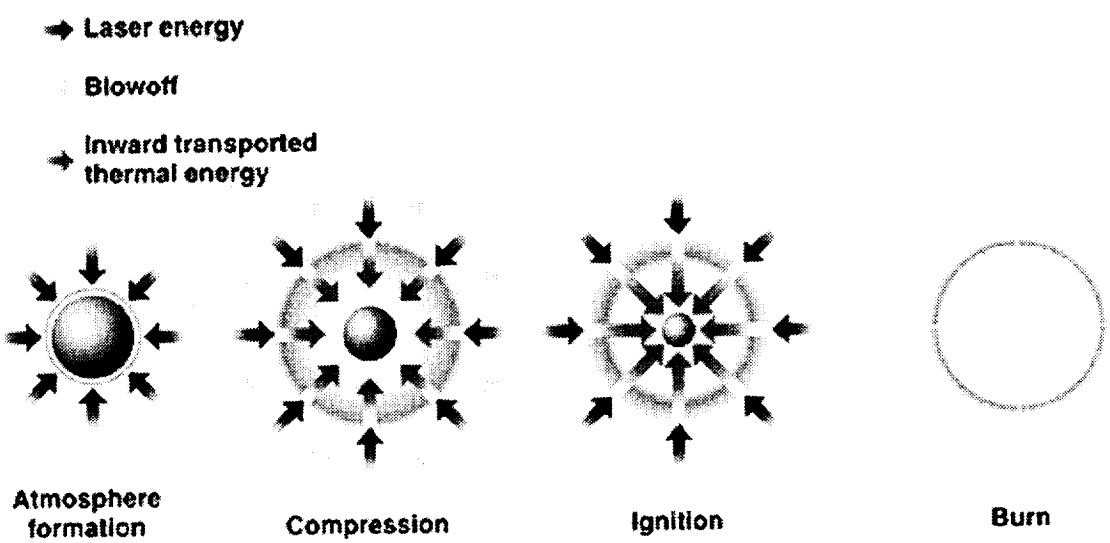

Shock Interaction with a Density Interface

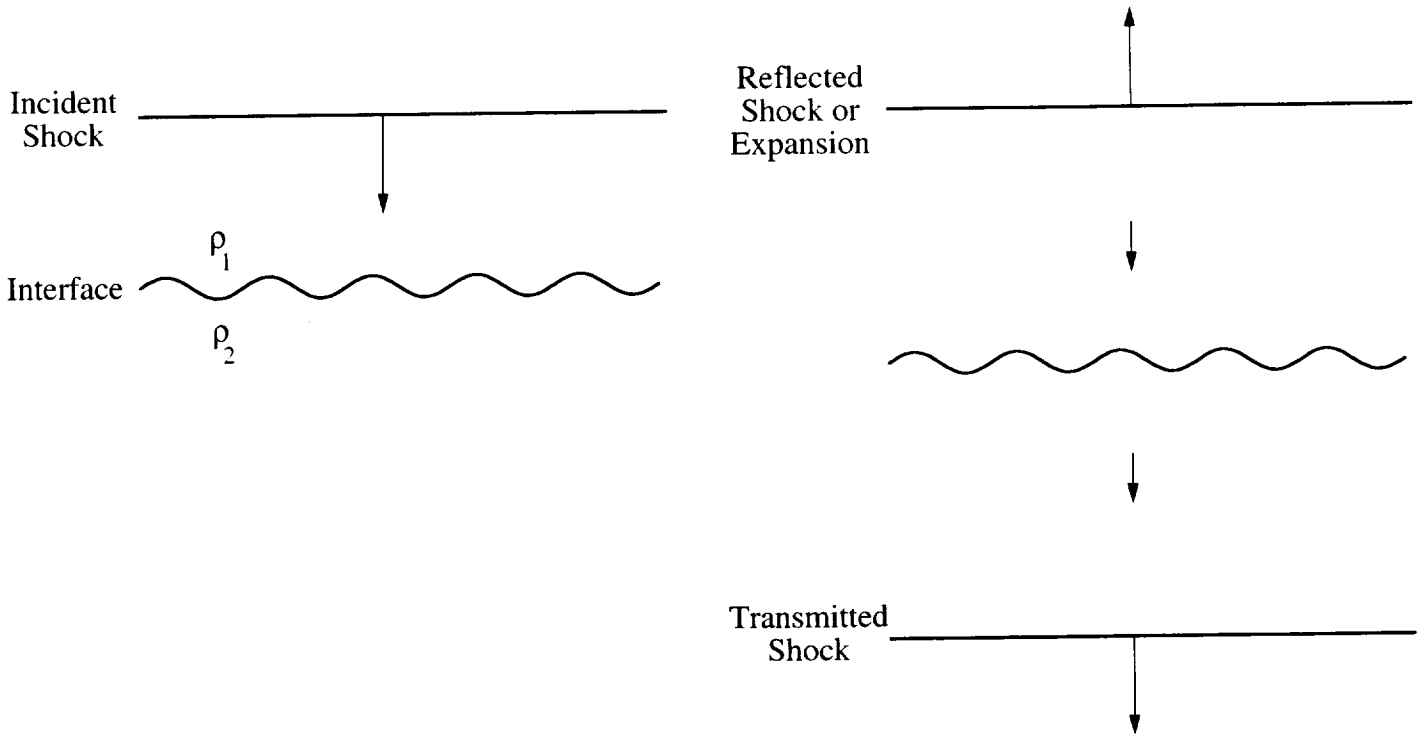

Incompressible RM Apparatus

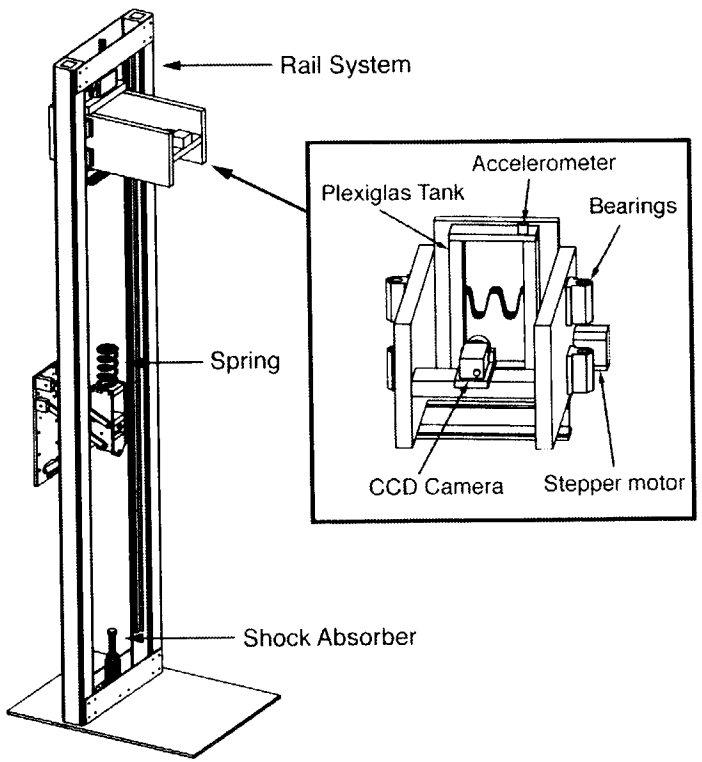

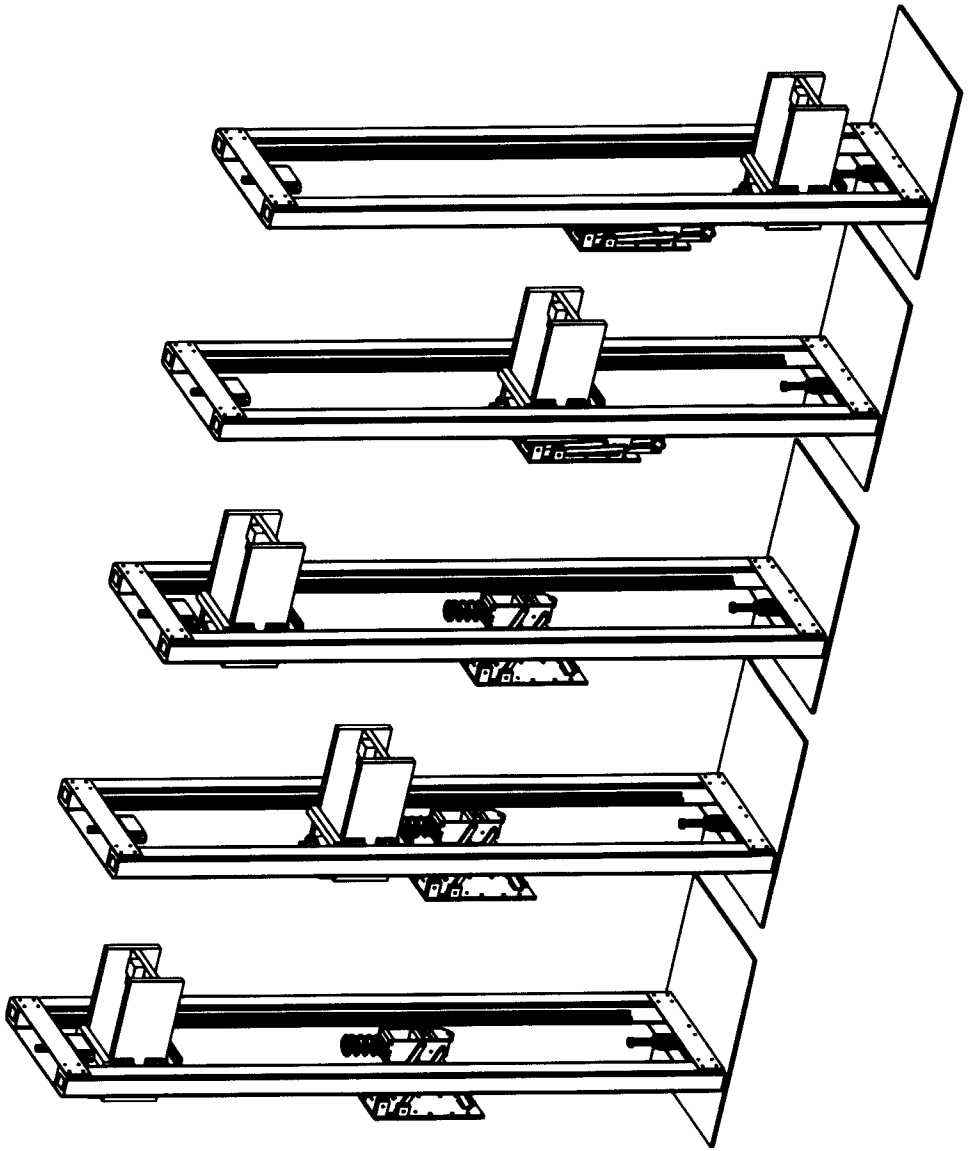

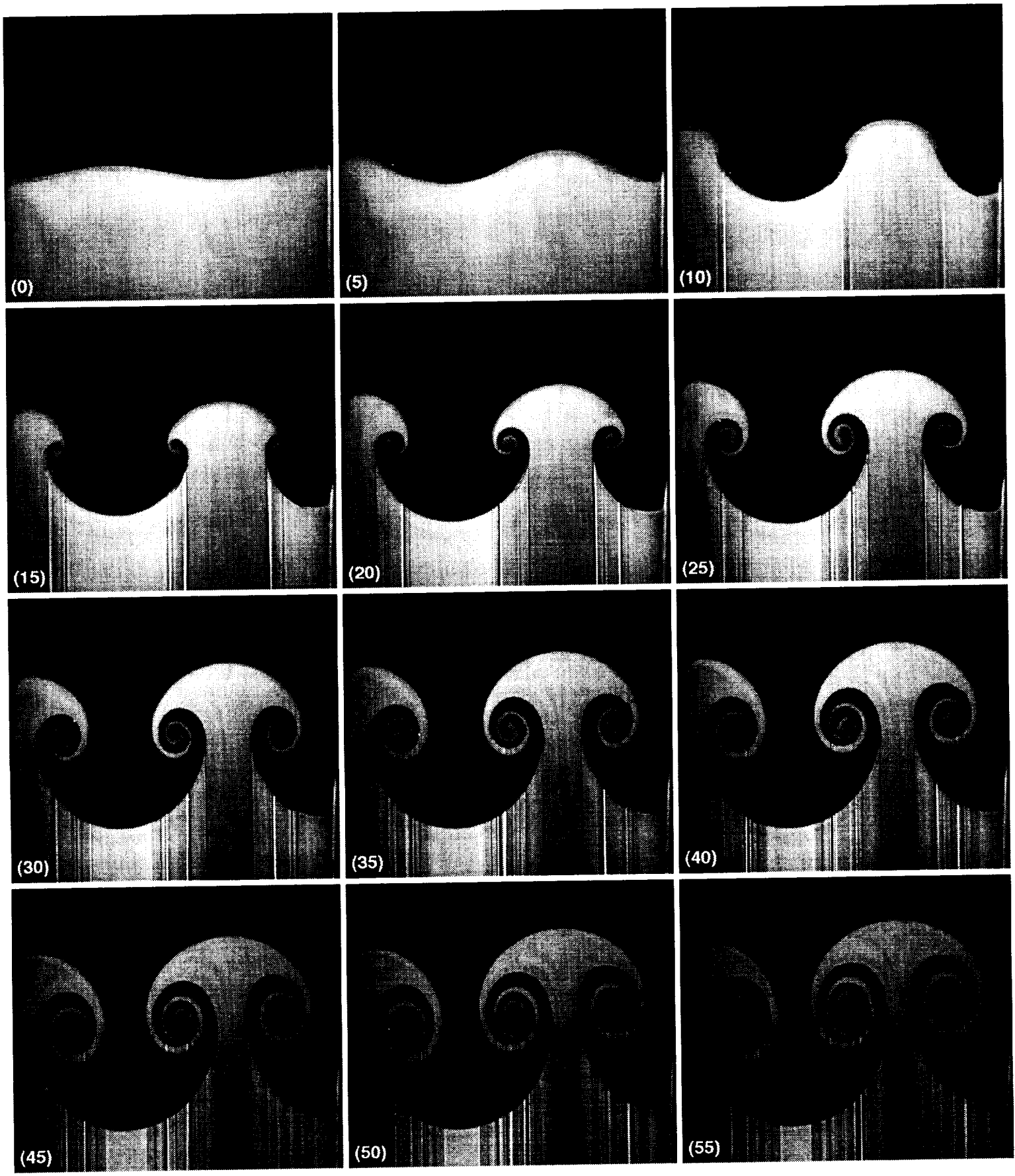
(0)
(5)
(10)
(15)
(20)
(25)
(30)
(35)
(40)
(45)
(50)
(55)

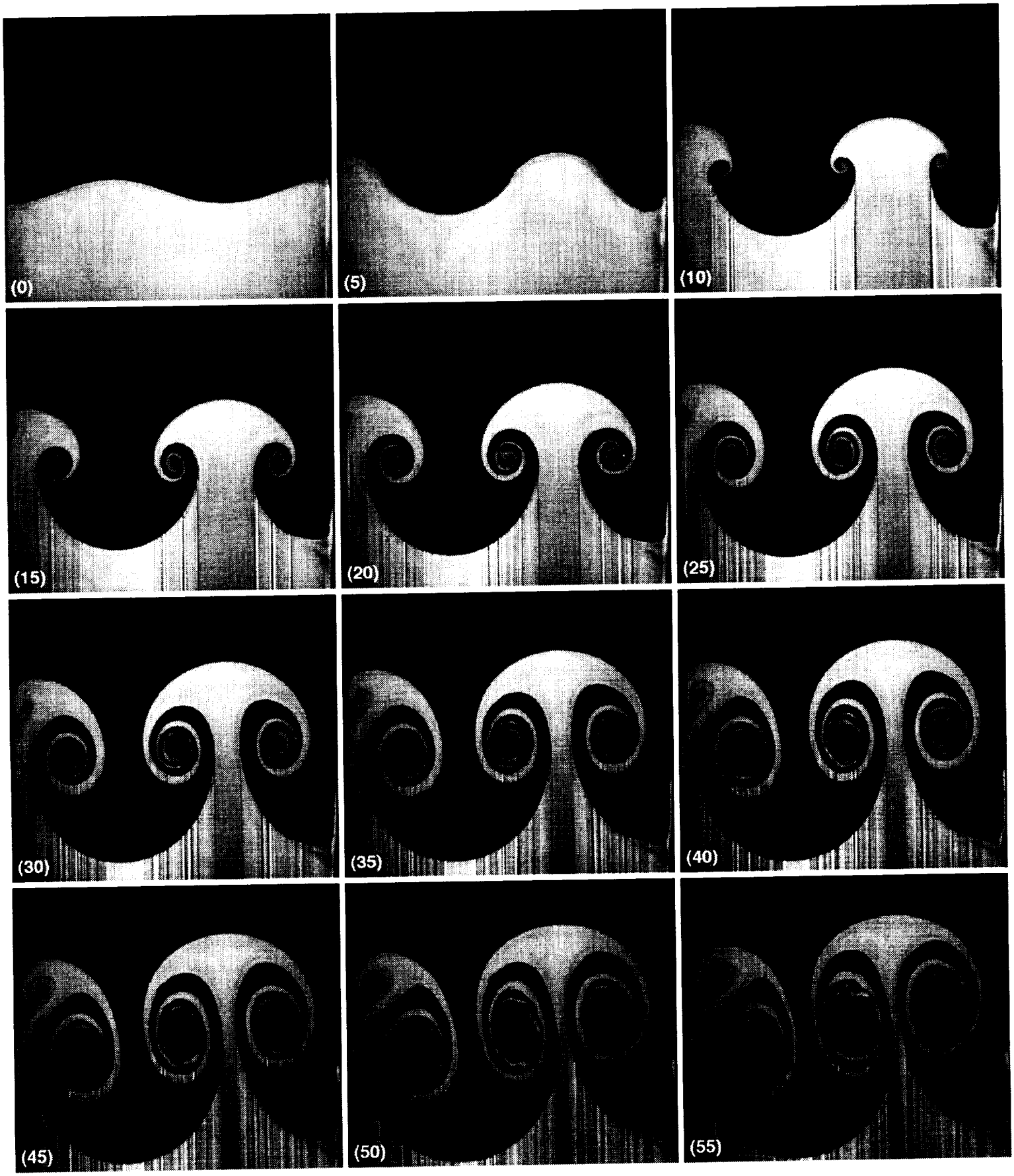
(0)
(5)
(10)
(15)
(20)
(25)
(30)
(35)
(40)
(45)
(50)
(55)

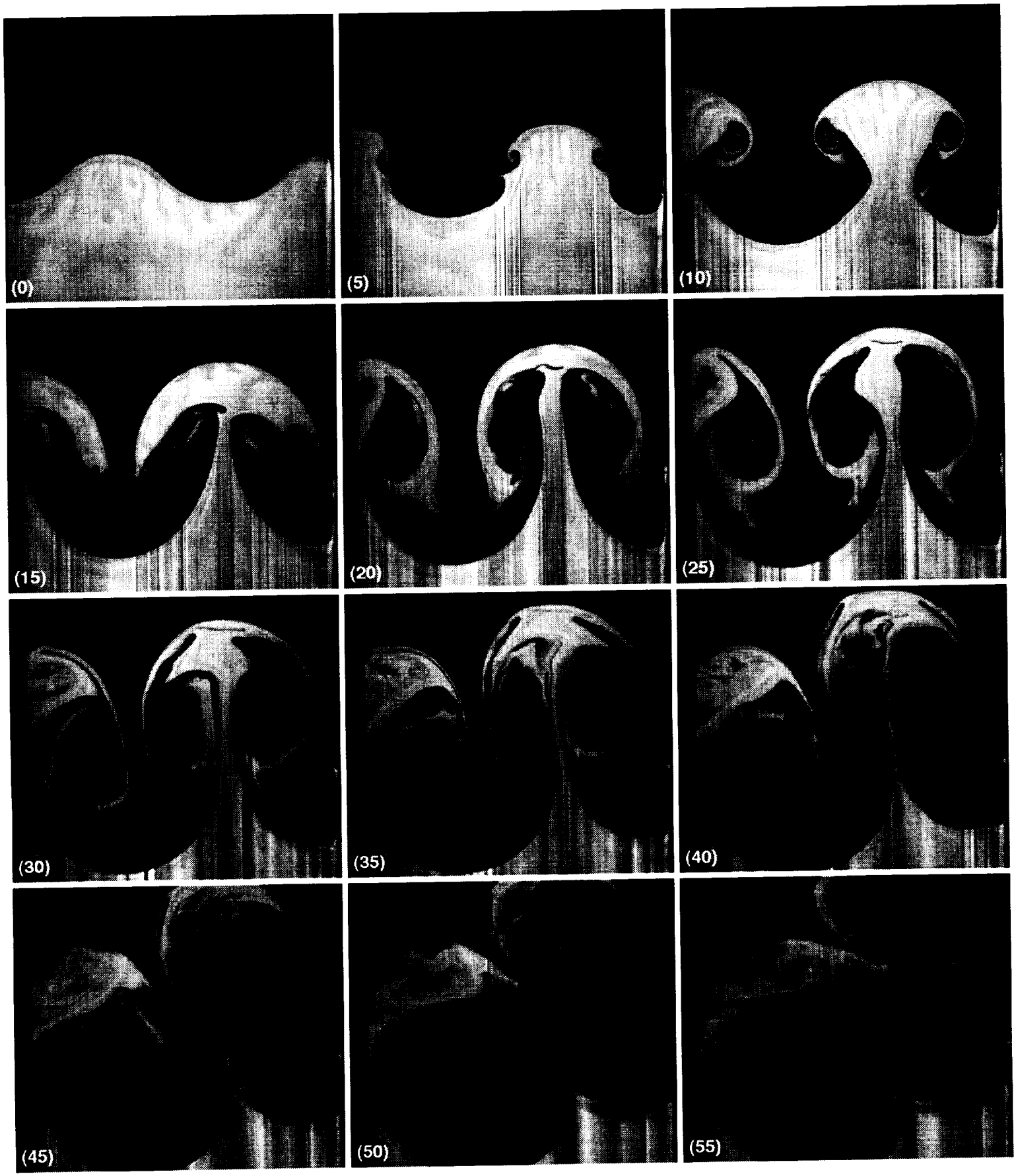
(0)
(5)
(10)
(15)
(20)
(25)
(30)
(35)
(40)
(45)
(50)
(55)

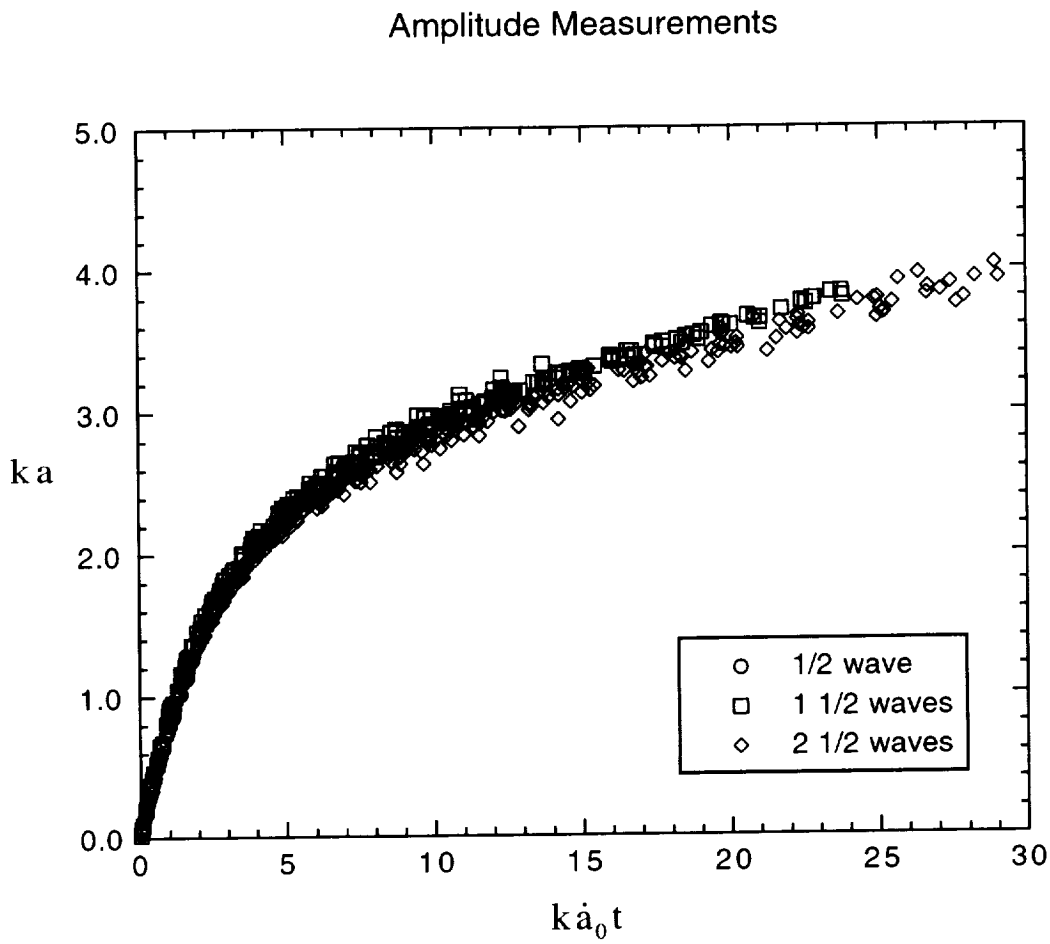
Amplitude Measurements
5.0
4.0
3.0
2.0
1.0
0.0
ka
0
5
10
15
20
25
30
$k\dot{a}_0 t$
1/2 wave
1 1/2 waves
2 1/2 waves

Stability Theory

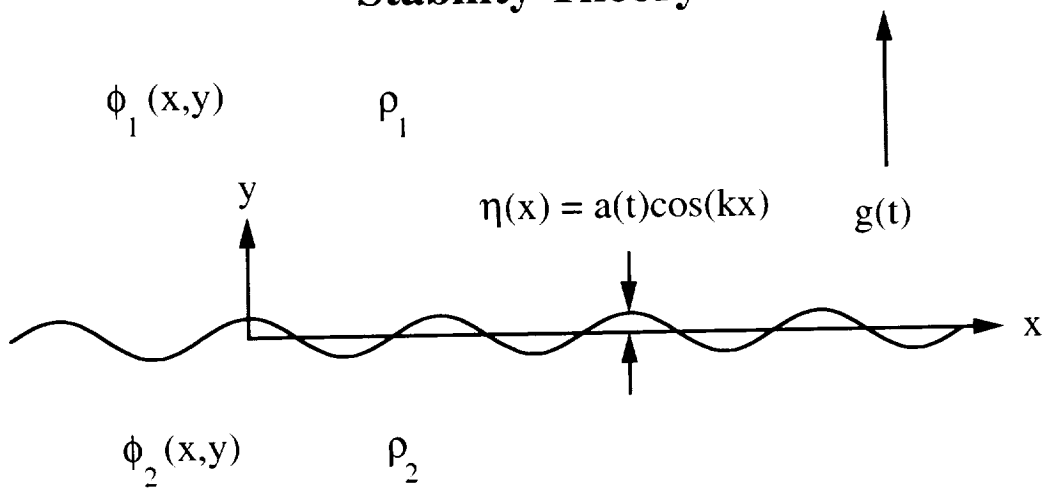

Linear Theory (Taylor 1950, Richtmyer 1960)

$$\boxed{\dot{a} = k\, a_0\, A\, \Delta V \equiv \dot{a}_0}$$

Atwood number: $A = \dfrac{\rho_2 - \rho_1}{\rho_2 + \rho_1}$

Weakly Nonlinear Theory (Zhang & Sohn, 1997)

$$\boxed{\dot{a} = \dot{a}_0\left[1 - (a_0 k)\dot{a}_0 k\, t + (A^2 - \tfrac{1}{2})\dot{a}_0{}^2 k^2 t^2 - \cdots\right]}$$

Padé approximant,

$$\boxed{\dot{a} = \dot{a}_0\left[\frac{1}{1 + (a_0 k)\dot{a}_0 k\, t + \max\left\{0,\, a_0{}^2 k^2 - A^2 + \tfrac{1}{2}\right\}\dot{a}_0{}^2 k^2 t^2}\right]}$$

when $A \le \dfrac{1}{2}$, $\dot{a} \to \dfrac{1}{t^2}$ as $t \to \infty$

Nonlinear Models

Vortex Model (Jacobs et al. 1995)

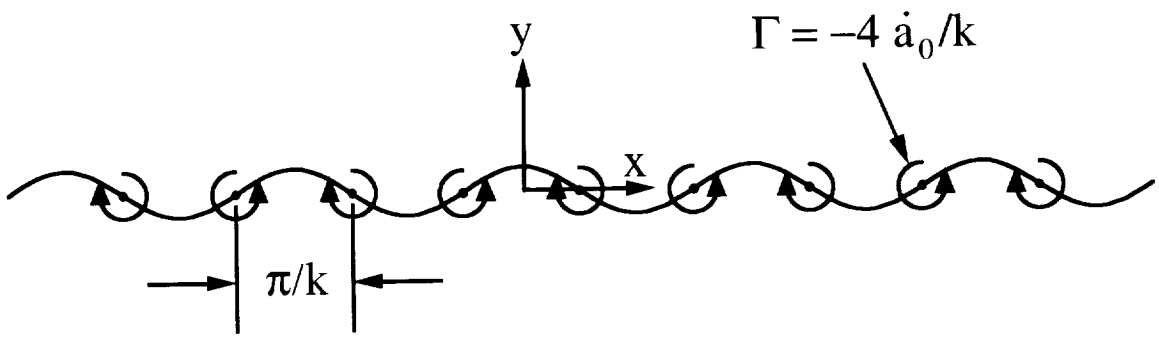

$$a(t) = \frac{1}{k}\sinh^{-1}\left[\frac{2}{\pi}k\,\dot{a}_0\,t + \sinh(k\,a_0)\right]$$

$$\boxed{\dot{a} \to \frac{1}{k\,t} \quad \text{as} \quad t \to \infty}$$

Empirical Model (Sadot el al. 1998)

$$\boxed{\dot{a}_{b/s} = \dot{a}_0 \frac{1 + \dot{a}_0 k\,t}{1 + (1 \pm A)\dot{a}_0 k\,t + \left[\frac{1 \pm A}{1 + A}\right]\frac{1}{2\pi C}\dot{a}_0^{\,2}k^2\,t^2}}$$

$$C = \begin{cases} 1/3\pi & A \geq 0.5 \\ 1/2\pi & A \to 0 \end{cases}$$

Small Atwood Number Correction (Niederhaus & Jacobs 2002)

$$\boxed{C = \frac{1}{2\pi(1 + A)} \quad \text{when} \quad A \to 0}$$

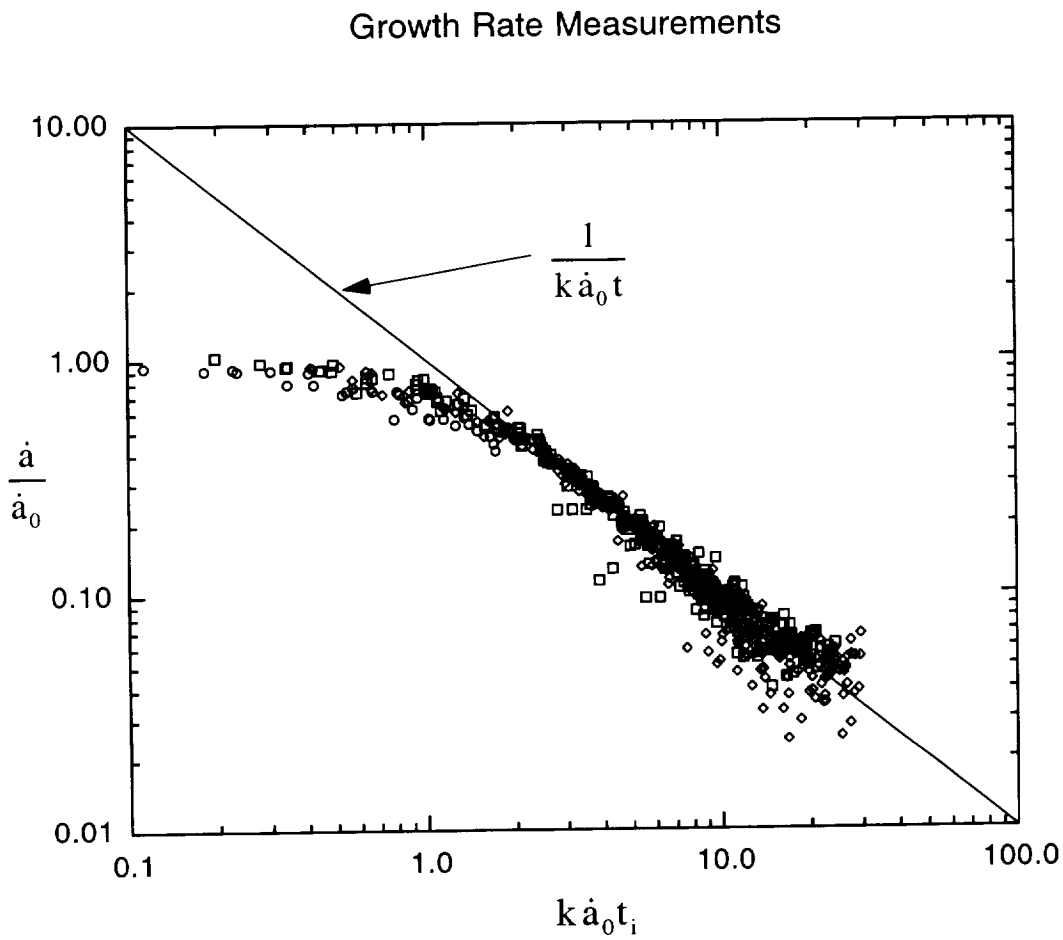
Growth Rate Measurements
10.00
1.00
0.10
0.01
0.1
1.0
10.0
100.0
$\frac{\dot{a}}{\dot{a}_0}$
$k\dot{a}_0 t_i$
$\frac{1}{k\dot{a}_0 t}$

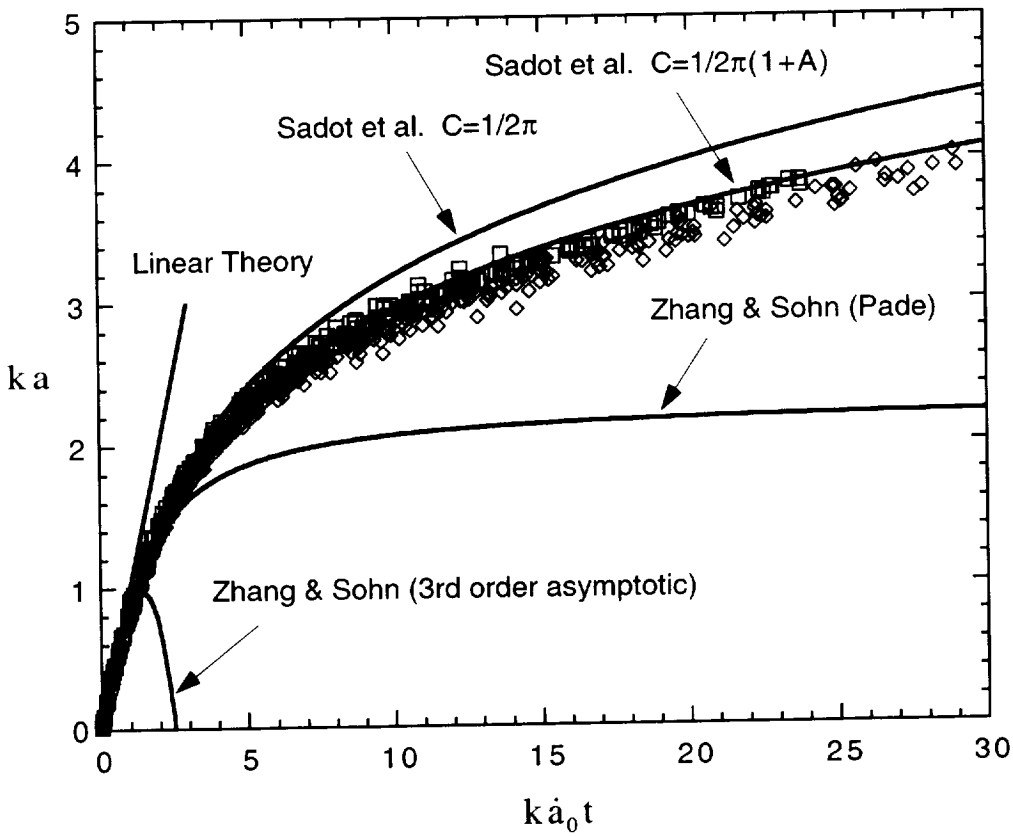
Sadot et al. C=1/2π(1+A)
Sadot et al. C=1/2π
Linear Theory
Zhang & Sohn (Pade)
Zhang & Sohn (3rd order asymptotic)
k a
k ȧ0 t
0
1
2
3
4
5
0
5
10
15
20
25
30

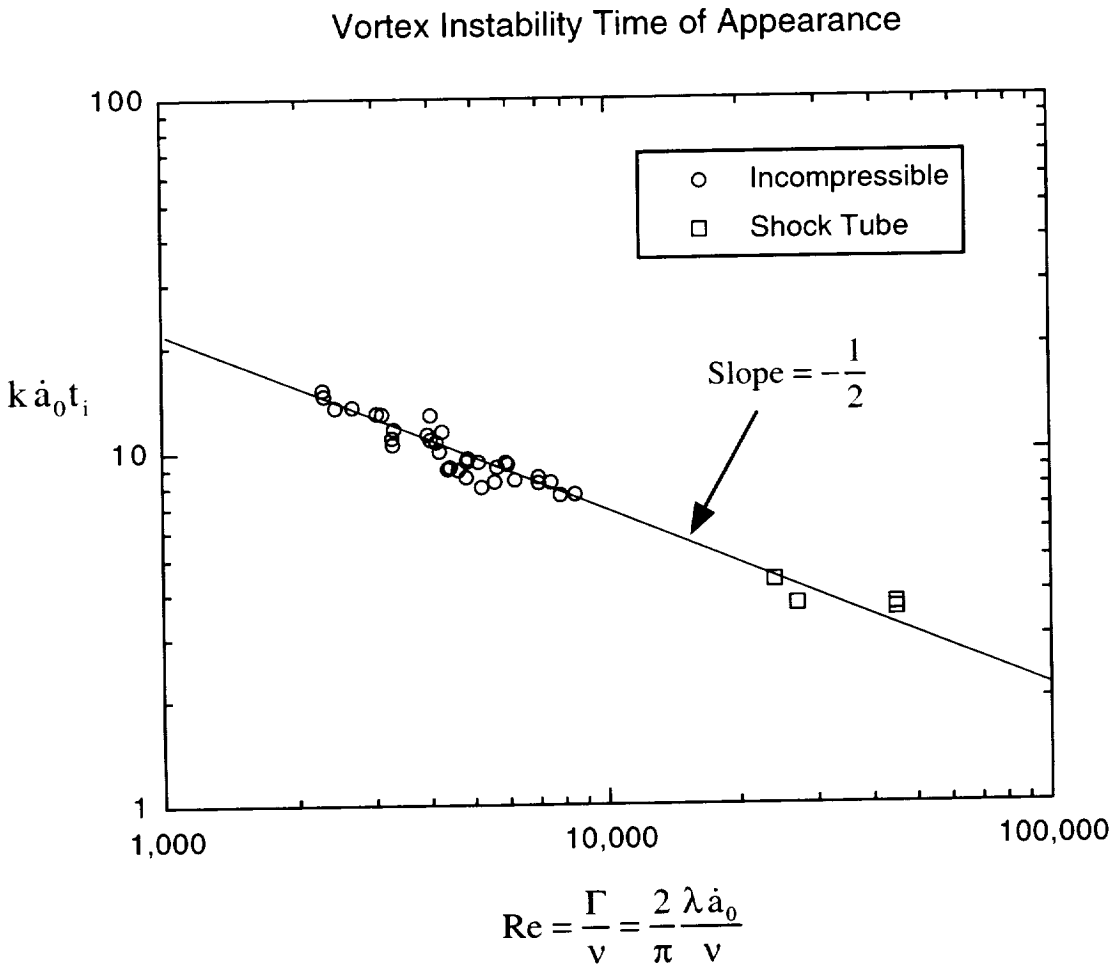
Vortex Instability Time of Appearance
100
10
1
1,000
10,000
100,000
Incompressible
Shock Tube
Slope = $-\frac{1}{2}$
$k\dot{a}_0 t_i$
$Re = \frac{\Gamma}{\nu} = \frac{2}{\pi}\frac{\lambda \dot{a}_0}{\nu}$

Kelvin-Helmholtz Instability

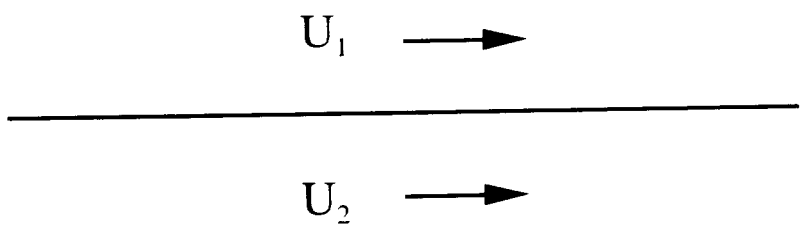

Kelvin-Helmholtz growth rate:

$$\sigma_{K-H} \sim \frac{U_1 - U_2}{\lambda_{K-H}} \sim \frac{\dot{a}_0}{\lambda_{K-H}} \sim \frac{1}{t_i}$$

Fastest growing wavelength:

$$\lambda_{K-H} \sim \text{Vorticity Thickness} \sim \sqrt{\nu/\varepsilon}$$

Strain rate:

$$\varepsilon \sim \frac{\dot{a}_0}{\lambda}$$

Dimensionless time of appearance:

$$\boxed{k\dot{a}_0 t_i \sim \sqrt{\frac{\nu}{\dot{a}_0 \lambda}} \sim Re^{-1/2}}$$

Conclusions

- Incompressible experiments have proven to be an excellent method for studying the late-time development of RM instability.
- Late-time amplitude measurements show Reynolds number independence and are in excellent agreement with nonlinear models.
- Late-time images show the instability of the vortex cores resulting in the transition to turbulence.
- Dimensionless vortex instability occurrence times for incompressible and compressible experiments show the same Reynolds number dependence.
- Future experiments in the GRC 2.2 Second Drop Tower will allow even later-time observations of the instability.

THE USE OF PULSATILE FLOW TO SEPARATE SPECIES

R. Narayanan, Professor
Department of Chemical Engineering
University of Florida

Aaron M. Thomas, Assistant Professor
Department of Chemical Engineering
University of Idaho

ABSTRACT

The removal of carbon dioxide from air is important in producing a habitable environment for the self-supporting space stations of the space program. Pulsatile flow is a novel way to help in the partial separation of different species from air by using a purely mechanical method. The advantage of this is that no chemicals are needed. Pulsatile flow also has the advantage that it can handle large volumes. While it is not expected that this process will replace existing methods of separation, it can surely be used as a means to assist in the overall separation process, possibly as a precursor to conventional methods. This work specifically focuses on the physics of pulsatile flow and its effect on the mass transfer of species and the separation that can be achieved. From the theoretical model that predicts the mass transfer and separation of species, we provide a physical explanation of the phenomena predicted by the models. If two dilute species are present in a carrier, the mass transfer of the faster diffusing species may be higher, lower, or the same as the slow diffusing species. This depends on the time constants associated with the system and the ability of a species to remain in the fast moving portion of the flow field. The difference in the mass transfer of each species can lead to a separation that can be used in a number of processes including the removal of carbon dioxide from the air. This phenomenon is modeled in an open tube geometry and in the annular space between two concentric cylinders. Further, in annular pulsatile flow, the effect of the inner cylinder being off center from the outer cylinder on the mass transfer and separation is also analyzed. Experiments were also conducted to verify the validity of the models and the viability of pulsatile flows as a separations procedure.

PHYSICS OF THE FLUID FLOW--MASS TRANSPORT INTERACTION

Picture a tube with a gas occupying a reservoir at each end. One of the reservoirs can be considered to hold a pure gas called the carrier while the other is a mixture of the carrier gas with a dilute amount of a single species as shown in Fig. 1 According to Fick's law for dilute species, the non-interacting particles will move from the mixture to the carrier gas from high to low concentration in a process involving pure molecular diffusion. Now, suppose that the fluid in the tube oscillates with no net flow from one reservoir to the other. This, for example, can be achieved with a piston. In the first half of a cycle of the piston stroke, a nearly parabolic flow profile is produced in the tube, provided that the frequency is not large. This in turn causes radial concentration gradients. The dilute species then diffuses from the core of the tube to the

boundary. In the second half of a cycle, the flow profile is reversed and the species moves from the boundary to the core where the concentration of the species is small compared to itw value at the boundary. In the first half of the next cycle of the piston stroke, the species that is in the fast moving core of the tube is convected down the tube and again radially diffuses

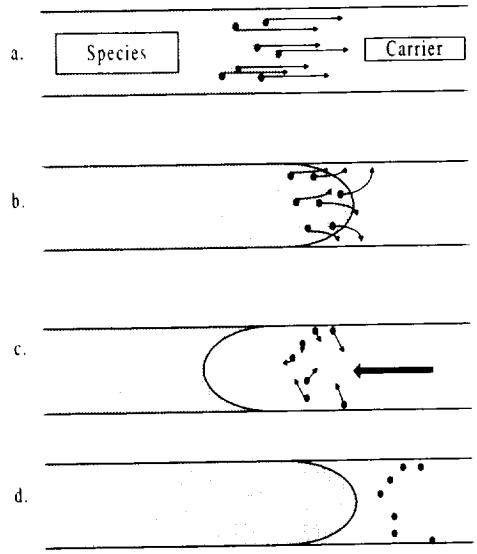

Figure 1. Dispersion mechanism for dilute species in pulsatile flow.

towards the wall of the tube. The species thus proceeds to move in this zigzag fashion down the tube giving a higher transport of it than by pure molecular diffusion, yet with no net flow between the two reservoirs. If another non-interacting dilute species were added to the mixture, the time constants of the system become very important due to the differing diffusion coefficients of the species, the frequency of oscillation, and the kinematic viscosity of the fluid. These different time constants can give rise to a separation of species due to the periodic flow. It is the relationship of the different time constants that govern the mass transfer for each species as well as an analysis of the mass transfer and separation of species for different geometries that are the focus of this research.

References:

a) Aaron M. Thomas, and R. Narayanan, Periodic flow and its effects on the mass transfer of a system and separation of species, Physics of Fluids, Vol 13, p 859, (2001.)

b) Thomas, A and Narayanan, R., " The Mechanism for Enhanced Mass Transfer in Oscillatory Flow- Comparison Between Wall Driven and Pressure Driven Flows", in press , Int. J. Heat and Mass Transfer, (2002)

c) Thomas, A. and Narayanan R., " The use of pulsatile flow to separate species", in press N.Y. Acad. Sciences (2002)

NASA/CP—2002-211212/VOL1

Mass Transfer and Separation of Species in Oscillating Flows

R. Narayanan
A. Thomas
University of Florida
Chemical Engineering

Motivation

- Separation of CO_2 or other species from air is important to the space program
- Periodic flow uses purely mechanical (non-chemical) means to *assist* in the separation
- Gain a better understanding of periodic flow to optimize a system to give a reasonable separation with a high throughput (mass transfer).

General Theory

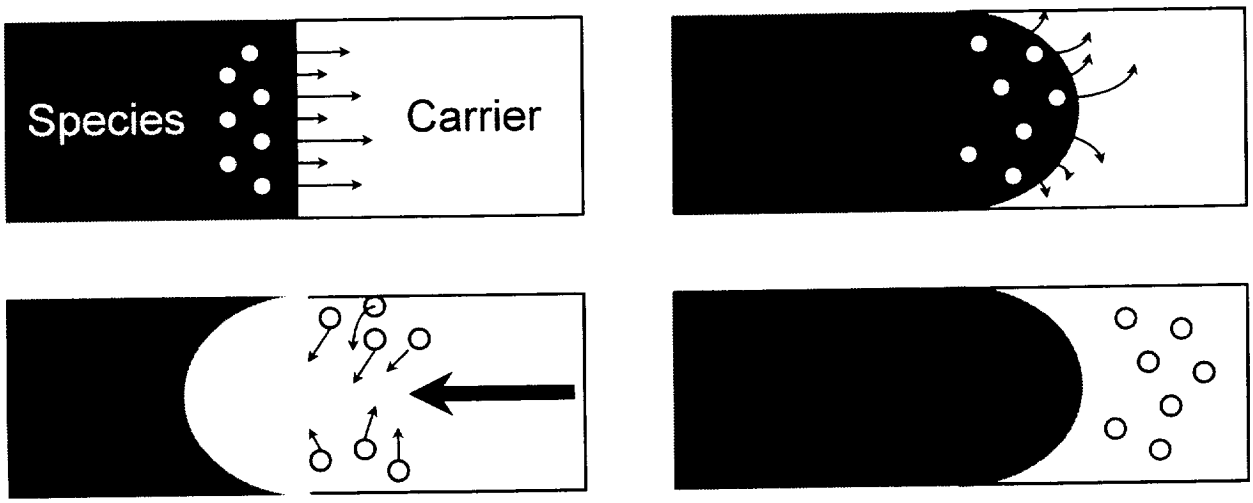

TRANPORT DURING OSCILLATING FLOW

Periodic Flow Setup

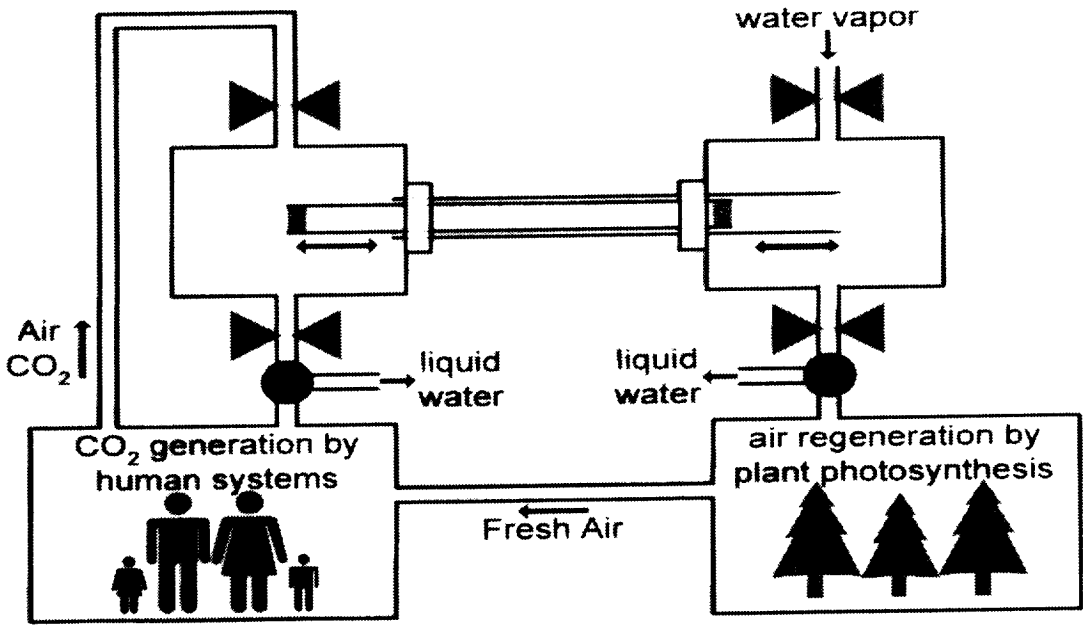

Pressure Driven System Between Two Flat Plates

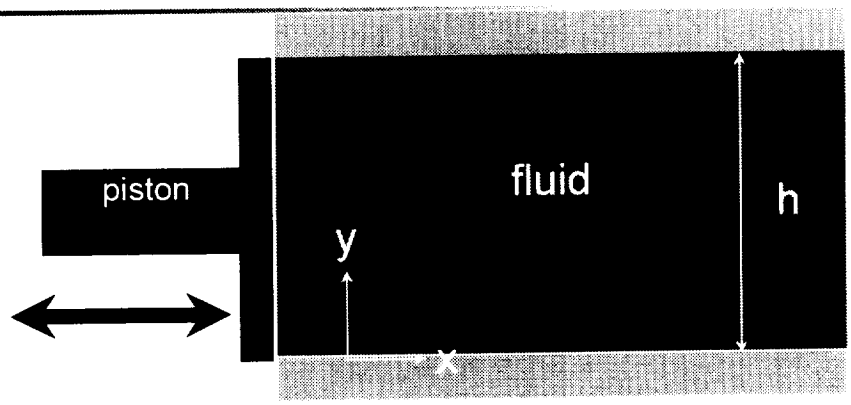

Piston Movement

$$x = \tfrac{1}{2} A \sin(\omega t)$$

$$FlowRate = h\frac{dx}{dt} = \tfrac{1}{4} A\omega h\left(e^{i\omega t} + e^{-i\omega t}\right)$$

Velocity Boundary Conditions

$V_x = 0$ at $y = 0$ and $y = h$

Concentration Boundary Conditions

$$\frac{\partial c}{\partial y} = 0 \quad \text{at } y = 0 \text{ and } y = h$$

Simple Model

$$\frac{\partial V_x}{\partial t} = -\frac{\Delta P}{L} + \nu \frac{\partial^2 V_x}{\partial y^2}$$

$$\frac{\partial c}{\partial t} + \frac{\partial c}{\partial x} V_x = D \frac{\partial^2 c}{\partial x^2} + D \frac{\partial^2 c}{\partial y^2}$$

$$V_x = 2\Re\left(\tilde{V}_x e^{-i\omega t}\right)$$

$$\bar{Q} = -\frac{D\left(c_2 - c_1\right)}{L} + \frac{2}{h}\Re\left[\int_0^h \tilde{V}_x \hat{c}\, dy\right]$$

Total Mass Transfer

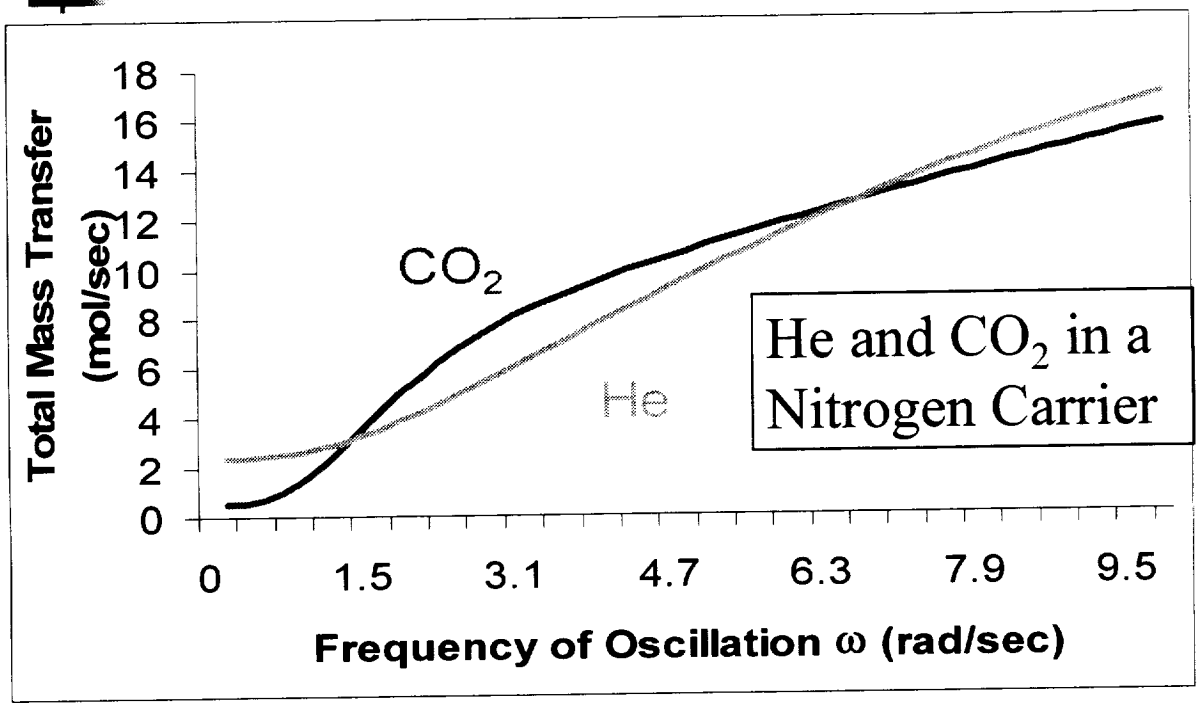

Separation of Species

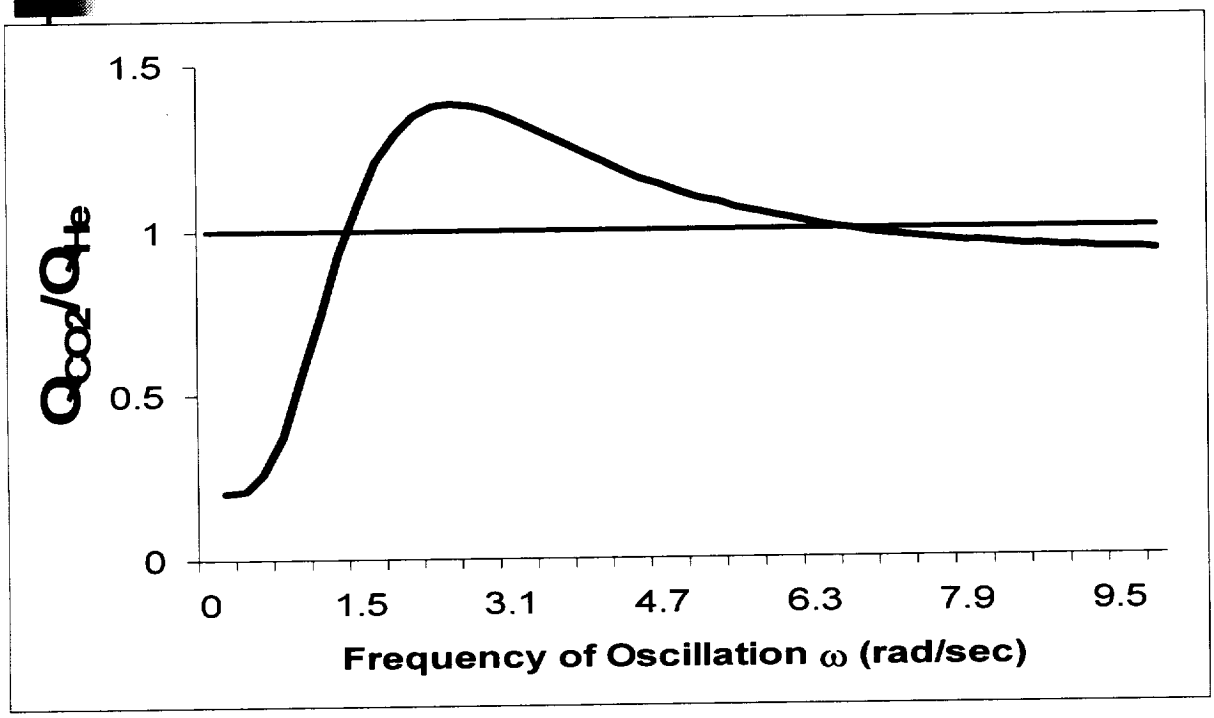

Convective Mass Transfer for Pressure versus Boundary

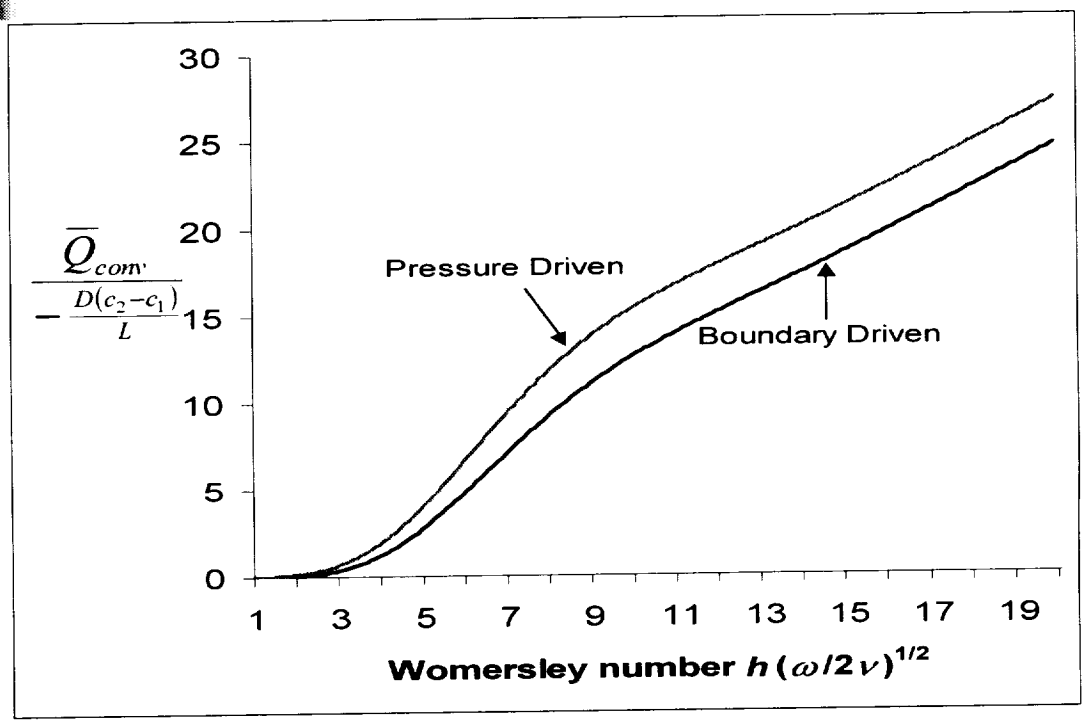

Pressure versus Boundary

- Power required to drive pressure driven flow higher that power for boundary driven flow

- *Convective* mass transfer per power for both configurations is the same

Open Tube Configuration

$$V_z = \frac{1}{2} A \omega \cos(\omega t)$$

Experimental Setup

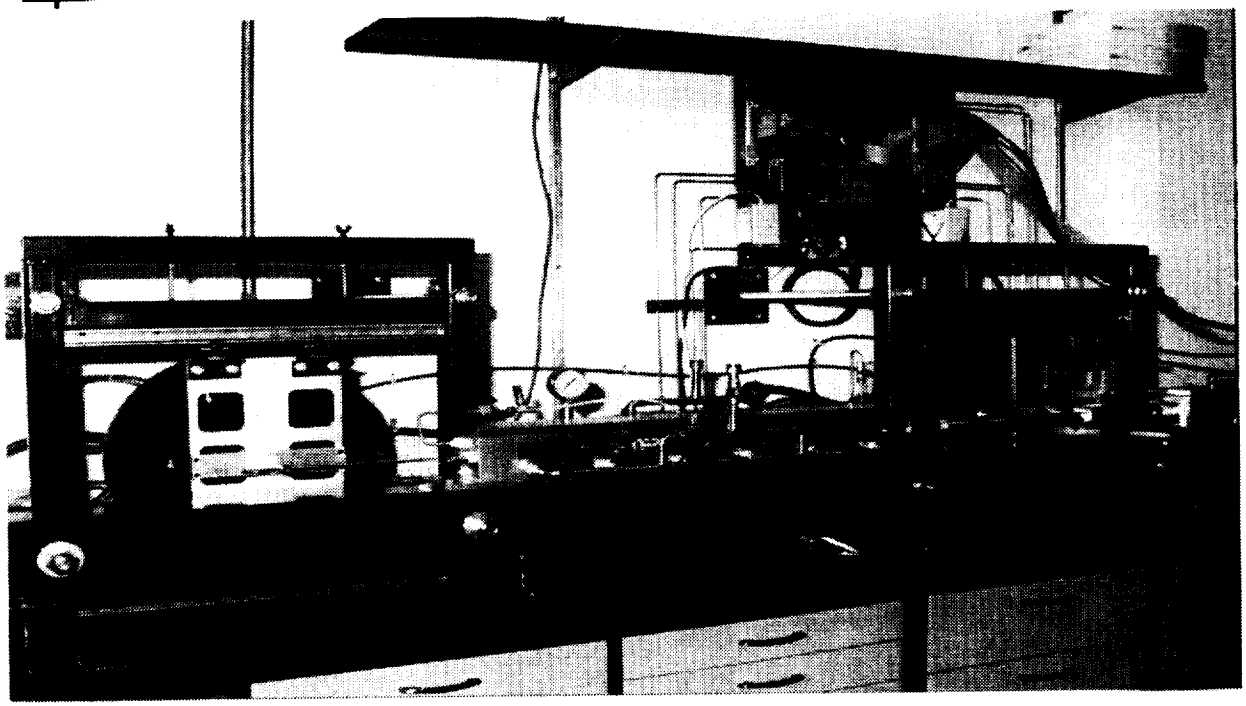

Separation Ratio for CO_2-CH_4 System

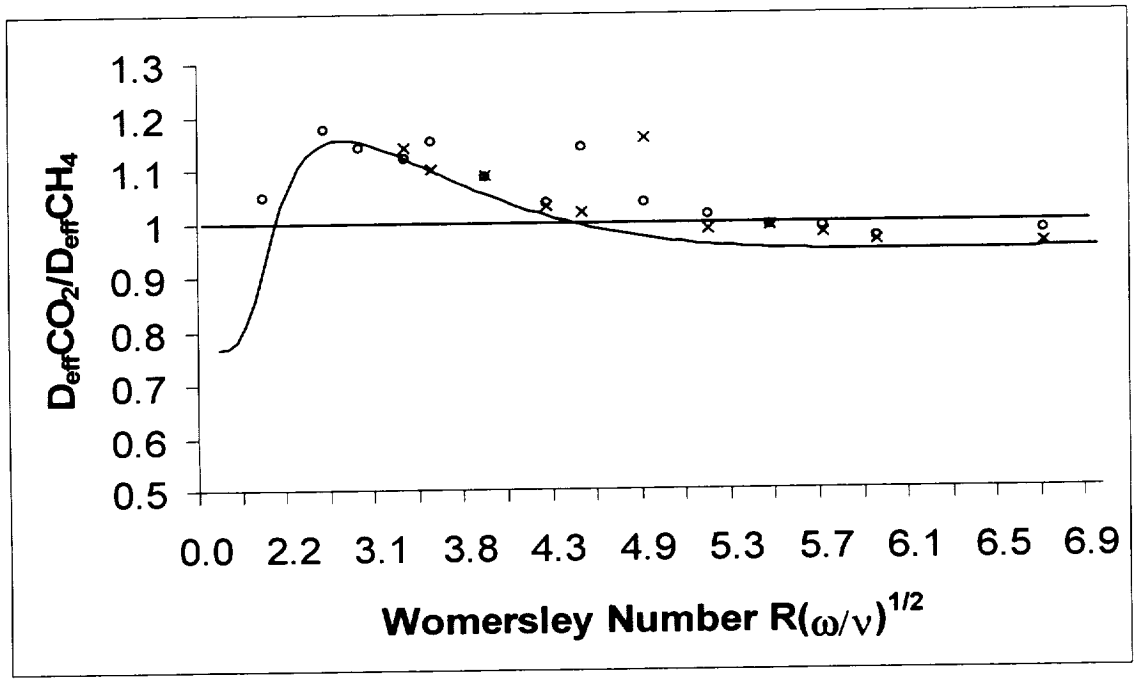

Separation Ratio for CH_4-He System

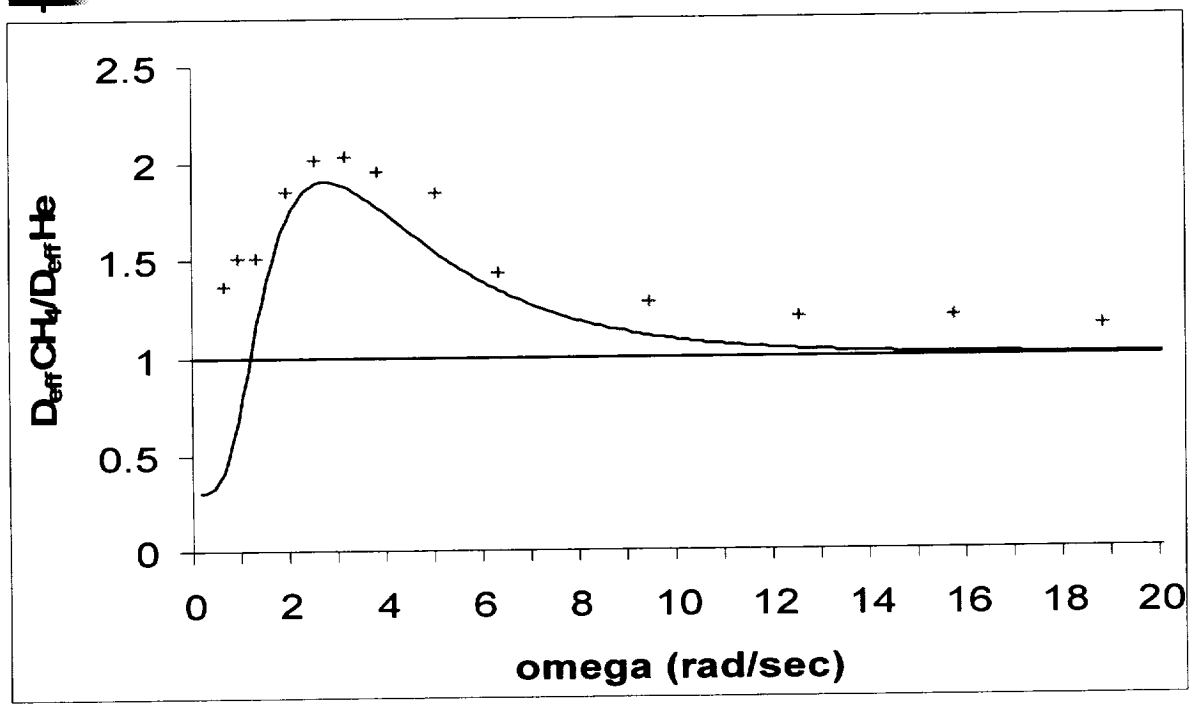

Annular Geometry

$$V_z = \frac{1}{2} A \omega \cos(\omega t)$$

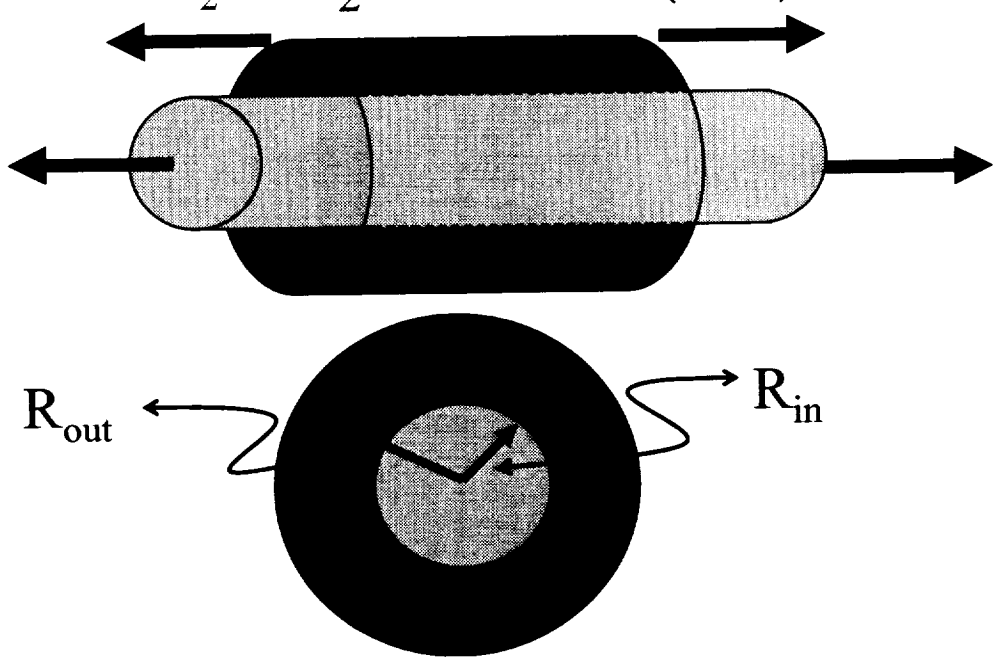

Comparison of Mass Transfer

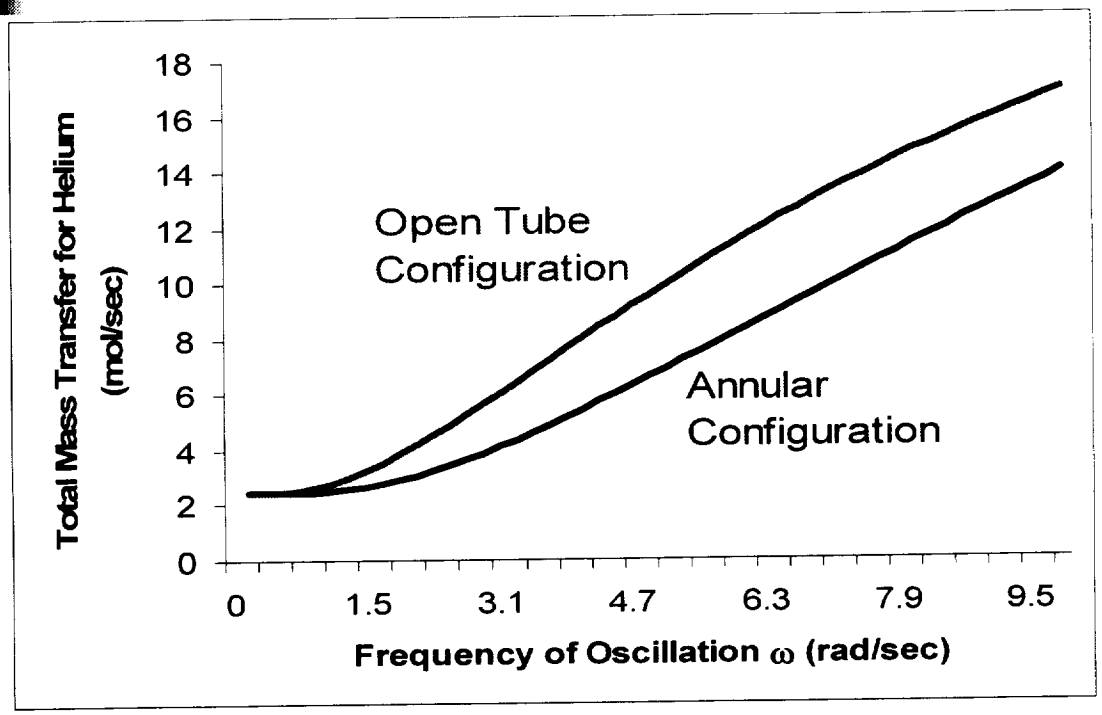

Comparison of Separation

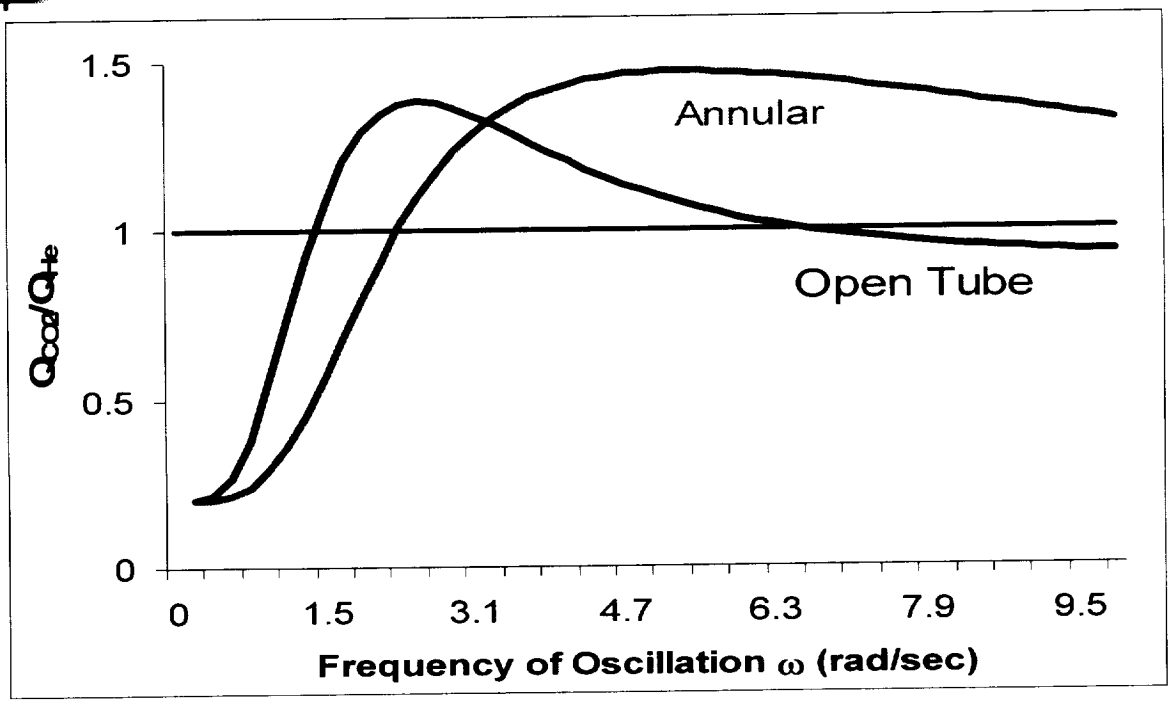

Motivation for Eccentric Geometry

- Experimental setup cannot ensure that the inner cylinder is exactly centered
- In steady Poiseuille flow, the eccentric annulus gives more flow than a regular annulus.

Eccentricity Geometry

$$R_{in,0}^2 = R_{in}^2 - 2\varepsilon R_{in}\cos\theta + \varepsilon^2$$

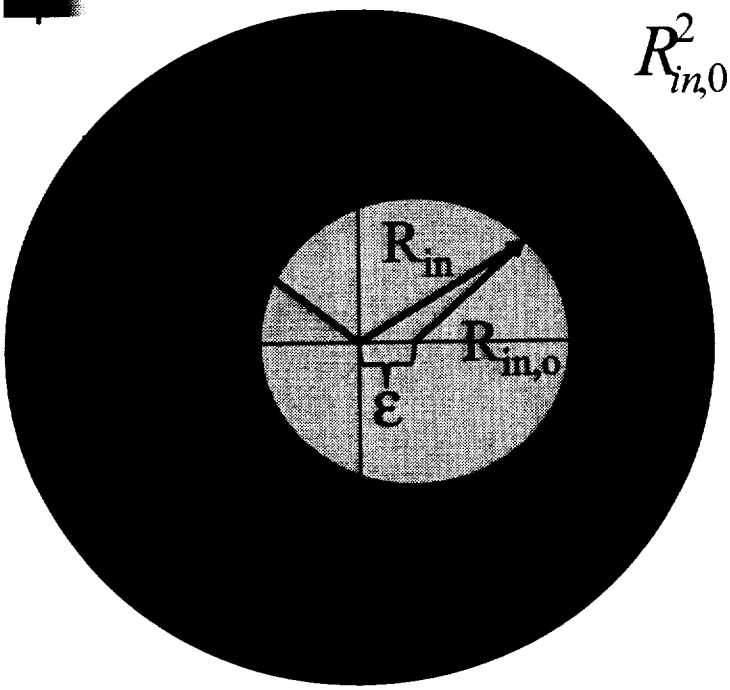

Effect on the Mass Transfer

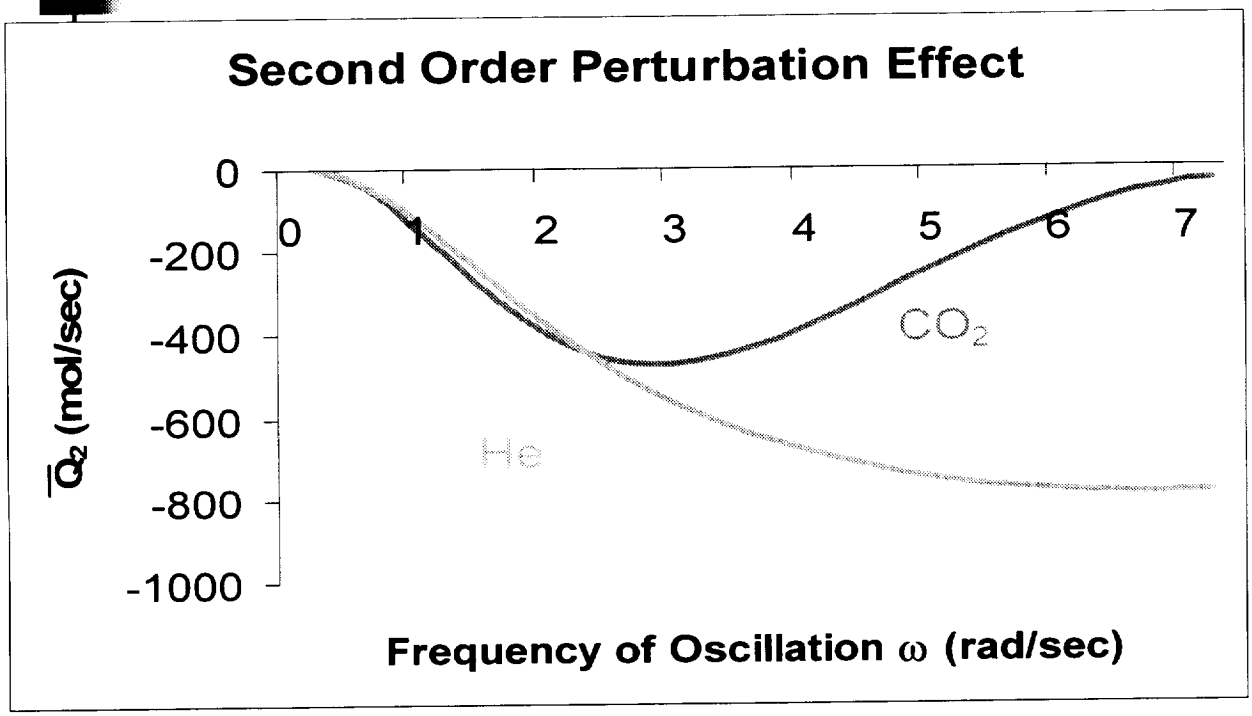

Effect on the Separation

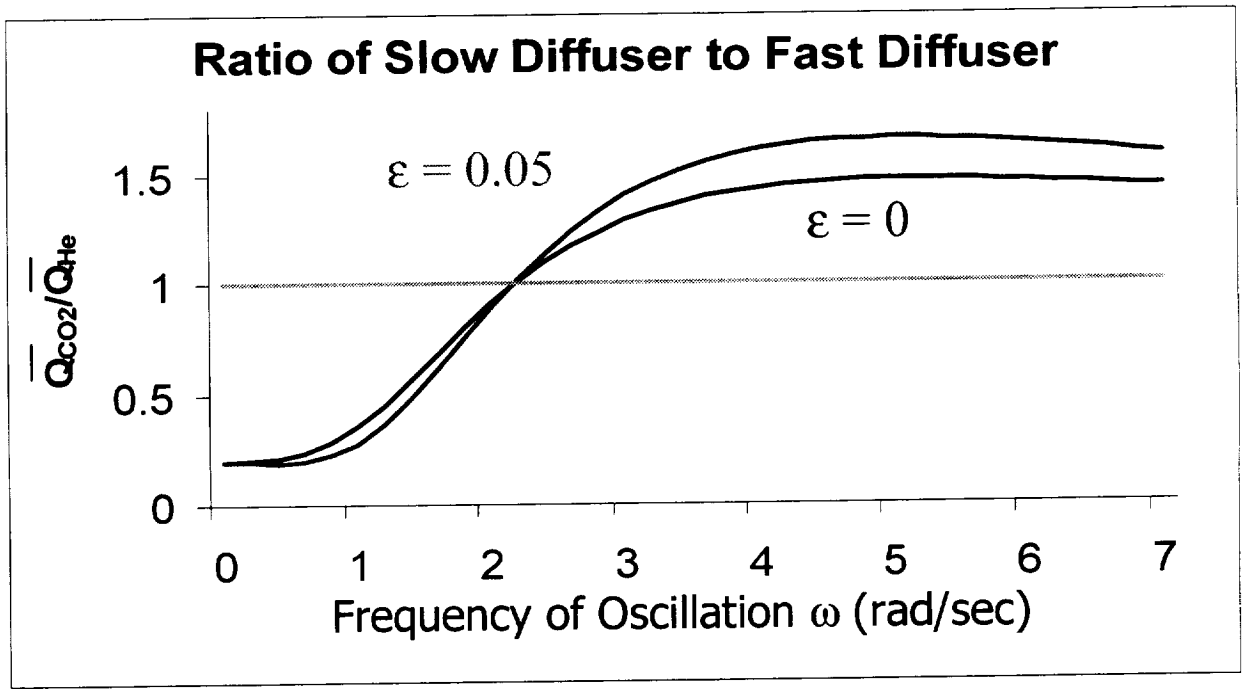

Results Summary

- Physics and Effect of geometry on the mass transfer and separation of species
  - Annular periodic flow is a viable configuration
  - Eccentric geometries may be beneficial
- Experiments agree quite well with the model

Future Work

- Examine non laminar effects and recessed geometries
- particle separation
- species separation in liquids
  in micro tubes using electrical potentials
- Study periodic flow with elastic walls (biological systems)

References

A. Thomas and and R. Narayanan, Physics of Fluids, **13**,p 859,2001

A. Thomas and R. Narayanan, Int.J Heat and Mass Transfer, to appear (2002)

PARTICLE PROXIMITY SENSORS: A NOVEL TECHNIQUE FOR VISUALIZING PARTICLE DEPOSITION IN SUSPENSION FLOWS

M. Yoda, B. C. Bailey and U. C. Andresen
G. Woodruff School of Mechanical Engineering, Georgia Institute of Technology

ABSTRACT

Efficient fluid reclamation is a critical technology for manned space exploration. Centrifugal filtration, where non-colloidal particles are deposited on filter fibers due to inertial impaction or direct interception, is a promising candidate for mechanical separation in variable gravity environments. Understanding how fluid inertia characterized by shear-based Reynolds number affects deposition is therefore critical in designing fluid reclamation systems for microgravity environments.

This work will develop "particle proximity sensors," or non-intrusive optical diagnostic techniques for directly visualizing where and when non-colloidal particles deposit upon, or contact, solid surfaces. Essentially, any particle near the surface will scatter light at a different wavelength from that scattered by particles in the bulk suspension. The particles next to the surface can then be easily isolated using a wavelength filter. The technique exploits the pH sensitivity of fluorophores and uses an applied electric potential to create a pH gradient next to the surface of interest.

The particle proximity sensors require aqueous chemistries. We have therefore developed and characterized a new *aqueous* model suspension system of polymethyl methacrylate (PMMA) particles suspended in a ternary mixture of the salt ammonium thiocyanate (NH_4SCN), water and glycerin. The model suspension has a refractive index $n = 1.4867$, a density $\rho = 1.19$ g/cm^3, a viscosity $\mu = 4.99$ cP at 22°C—giving a kinematic viscous four times that of water—and a pH of 4.5. Transmission measurements using both polydisperse and nearly monodisperse PMMA particles (diameters ranging from 106–212 μm and 75–90 μm, respectively) show that a 5% volume fraction suspension has an optical transmission through 1 cm of suspension that is 80% of that for the same solution without particles at 22.5°C when illuminated at 488 and 514.5 nm.[1] The optical transmission of this suspension is comparable to that of a suspension system used by other researchers for laser-Doppler velocimetry studies[2]. This aqueous system is less hazardous than previous model systems based on organic solvents and halogenated hydrocarbons. It is, with its relatively low viscosity, also useful for higher Reynolds number studies, including turbulent suspension flows.

---

[1] Bailey, B. C. and Yoda, M. (2001) An aqueous density- and refractive-index matched suspension system. Submitted to *Experiments in Fluids*

[2] Lyon, M. K. and Leal, L. G. (1998) An experimental study of he motion of concentrated suspensions in two-dimensional channel flow. Part I. Monodisperse systems. *J. Fluid Mech.* **363**, 25–56

Fluorescein in aqueous solution fluoresces at pH values above 6. The aqueous suspension is dyed with $O(1\ \mu M)$ disodium fluorescein. A weak electric current ($O(10\ \mu A)$) is applied across the suspension with the solid surface of interest as the cathode, creating a higher pH layer (due to depletion of protons by the cathode) next to the surface. The fluorescein then fluoresces only in this "boundary layer" region, whose thickness can be adjusted from $O(0.1–1$ mm) by adjusting the applied current. A particle illuminated by light from an argon-ion laser at 514.5 nm scatters light at 514.5 nm in the bulk fluid, and light at longer (about 520–600 nm) wavelengths in the fluorescent region next to the surface. The flow is imaged from the side or through the surface of interest using a nearly transparent layer of indium tin oxide on glass as the electrode. Preliminary experimental results characterizing the effect of a solid surface (*i.e.*, wall) at varying orientation on a single sedimenting particle will be presented using this technique.

We plan to also use particle proximity sensors to study inertial particle impaction upon a single filter fiber in centrifugal filtration, or a cylinder immersed in a simply sheared suspension. To this end, a plane Couette suspension flow facility to study simply sheared suspensions has been designed and built. Based upon a previously used apparatus for single-phase Newtonian fluid studies, the facility uses an endless belt stretched over and driven by two large rollers and a contraction at both ends of the test section to minimize end effects. The temperature-controlled suspension is confined inside the belt by a layer of heavy immiscible fluid at the bottom of the test section. Preliminary results on the rotation rate of a circular cylinder immersed in a simply sheared suspension in this new facility at various shear-based Reynolds number will be presented and compared with previous numerical and experimental results for a cylinder immersed in a single-phase fluid.

This ground-based project is a first step towards "heavy" and "light" suspension flow experiments in microgravity. Considering the current limitations of computational techniques in non-Stokesian, many-particle suspension simulations and our inability to decouple inertial and buoyancy effects upon Earth, microgravity environments present a unique opportunity to isolate and study the effects of differential particle-fluid inertia. In addition, particle proximity sensors could be a valuable diagnostic technique in studying several multiphase flow problems of importance in manned space exploration, such as dust deposition on solar arrays and seal degradation in dusty environments.

PI:	Minami Yoda
Mailing address:	School of Mechanical Engineering Georgia Institute of Technology 771 Ferst Dr., NE Atlanta, GA 30332–0405
E-mail address:	minami.yoda@me.gatech.edu
Fax number:	(404) 894-8496
Phone number:	(404) 894-6838

NASA/CP—2002-211212/VOL1

Particle Deposition in Suspensions: Cylinders in a Simply Sheared Suspension

M. Yoda, B.C. Bailey and U.C. Andresen
Mechanical Engineering

Georgia Institute of Technology

6th Microgravity Fluid Physics and Transport Phenomena Conference

Outline

- New model suspension system
- Experiments: cylinder in simple shear
- Particle proximity sensor technique

Motivation

- Study interaction of noncolloidal particles with solid surfaces in inertial solid-liquid suspension flows
  - Fluid and particle inertia (*Re* and *St*) effects
- Microgravity issues
  - Experimentally study density-mismatched suspension systems ⇒ Decouple inertial and buoyancy effects
  - Centrifugal filtration for fluid reclamation: separate particles via inertial impaction

Objectives

- Develop "particle proximity sensor": nonintrusive technique for visualizing noncolloidal particle interactions with solid surfaces
  - Use pH sensitive-fluorophores to create fluorescent "wall layer" with thickness ~ particle diameter
- Study particle deposition upon cylinders in simple shear flow of neutrally buoyant suspension
  - Models flow around filter fiber in centrifugal filtration
  - Noncircular cylinders and spheroids transition from time-periodic to stationary behavior [Ding & Aidun 00; Zettner & Yoda 01]

Model Suspension Systems

- Match refractive index n and density ρ of continuous/liquid and discrete/solid phases
  - Discrete phase: O(10-100 μm) PMMA particles ($n_D \approx 1.49$; $\rho = 1.19$ g/cm^3)
- High viscosity continuous phase
  - Triton X-100 1,6-dibromohexane, UCON 75-H ⇒ $\mu = 4.8$ P at 20°C [Lyon and Leal 98]
  - Water and Triton X-100 + $ZnCl_2$ ⇒ $\mu = 34$ P at 23°C [Krishnan *et al.* 96; Breedveld *et al.* 98]
- New low viscosity continuous phase
  - Water and glycerin + NH_4SCN ⇒ $\mu = 4.99$ cP at 22.5°C
  - Aqueous solution for fluorophore tracers

New Suspension System

- Match n of PMMA particles at λ = 488-514 nm
  - Maximize power $P(\phi)$ transmitted through 1 cm of constant-temperature fluid at various particle volume fractions ϕ by varying n of continuous phase
  - "Transmission" $T(\phi) = P(\phi) / P(0)$ [cm^{-1}]
  - $T_{max} \Rightarrow$ refractive index match
  - Two types of PMMA particles tested: polydisperse 106–212 μm sieved ICI Elvacite 2021 and nearly monodisperse 75–90 μm Bangs Laboratories
  - n_D: refractive index at λ = 589.3 nm

Transmission Data

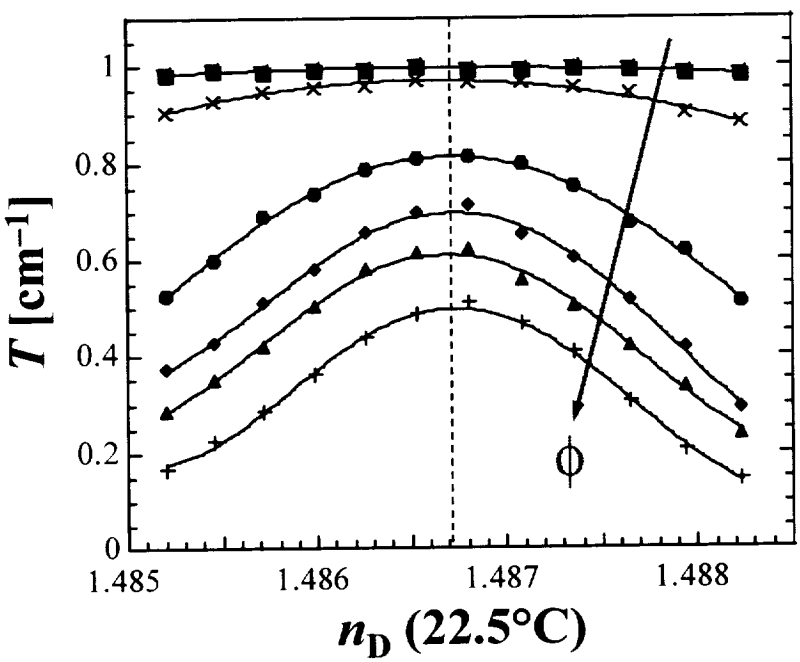

$$T_{max}(\phi) \equiv \frac{P_{max}(\phi)}{P(0)}$$

$$= 1 - 3.96\phi$$

- $T_{max} = 0.8$ for $\phi = 0.05$

■	$\phi = 0.0011$
×	$\phi = 0.0101$
●	$\phi = 0.0426$
◆	$\phi = 0.0788$
▲	$\phi = 0.0984$
+	$\phi = 0.1229$

T_{max} Comparison

- Compare w/suspension system of Lyon & Leal
  - New suspension: $T_{max} = 0.96$ for $\phi = 0.01$ at $\lambda = 488$–514 nm and 22.5°C
  - $T_{max} = 0.95$ for $\phi = 0.01$ at $\lambda = 488$ nm and 20°C [Lyon & Leal 1998]
  - Continuous phase: 50% w/w Triton X-100; 27% UCON-75-H-90000 (L&L used half UCON-75-H-450/half UCON-75-H-90000); 23% 1,6-dibromohexane
  - Discrete phase: < 106 μm sieved ICI Elvacite 2021
  - $T_{max} \approx 0.50$ for $\phi = 0.11$ at $\lambda = 488$ nm and 22°C
  - $T_{max} = 0.56$ for $\phi = 0.11$ and new suspension

Cylinder in Simple Shear

- Centrifugal filtration
  - Particles deposited upon rotating filter basket
  - Cylinder in simply sheared suspension models particle deposition upon single filter fiber in body-fixed frame

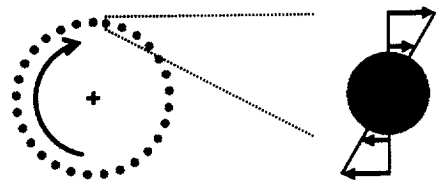

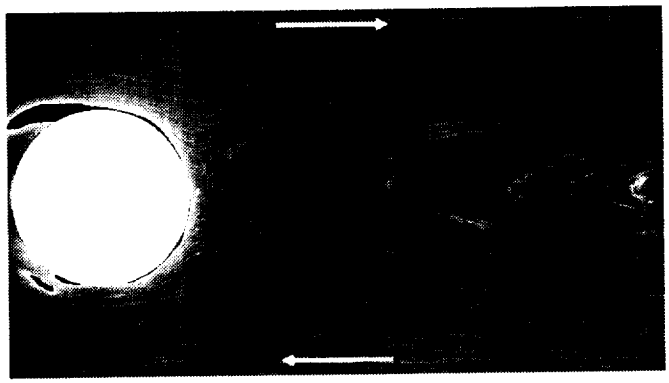

Pathlines for circular cylinder in single-phase simple shear at $Re = 8$

[Zettner & Yoda 2000]

Experimental Setup

- Plane Couette channel to study cylinders in simply sheared suspension
  - $Re_{ch} = L^2G/\nu \leq 600$
  - $Re = r^2G/\nu \leq 17$ ($\kappa = 2r/L \leq 0.33$)
  - $Re_a = a^2G/\nu \leq 0.17$ ($a/r \leq 0.1$)

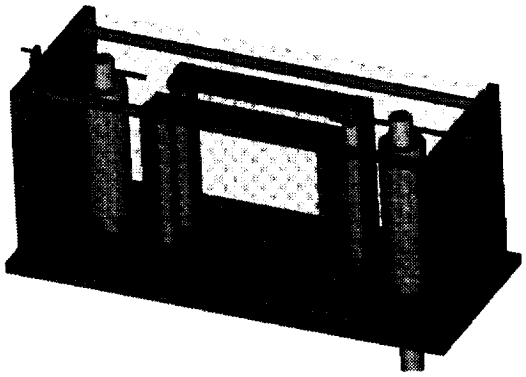

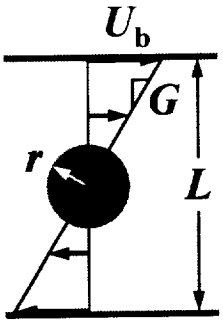

Plane Couette Channel

- Motor-driven endless Mylar belt supported by glass plates: adjustable width test section: L = 1.2–5 cm × 20.3 cm (h) × 16.5 cm (v)
- Contraction at ends of test section to minimize end effects (area ratio = 1–4)
- Initial tests with (corrosive) liquid suspension phase
- Total inventory 10 L; test section inventory 0.8–2.4 L

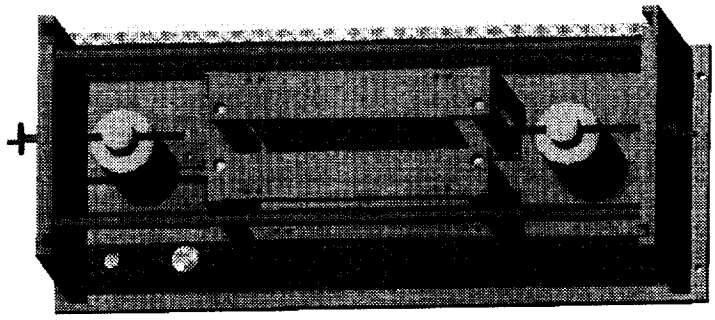

Cylinder in Simple Shear

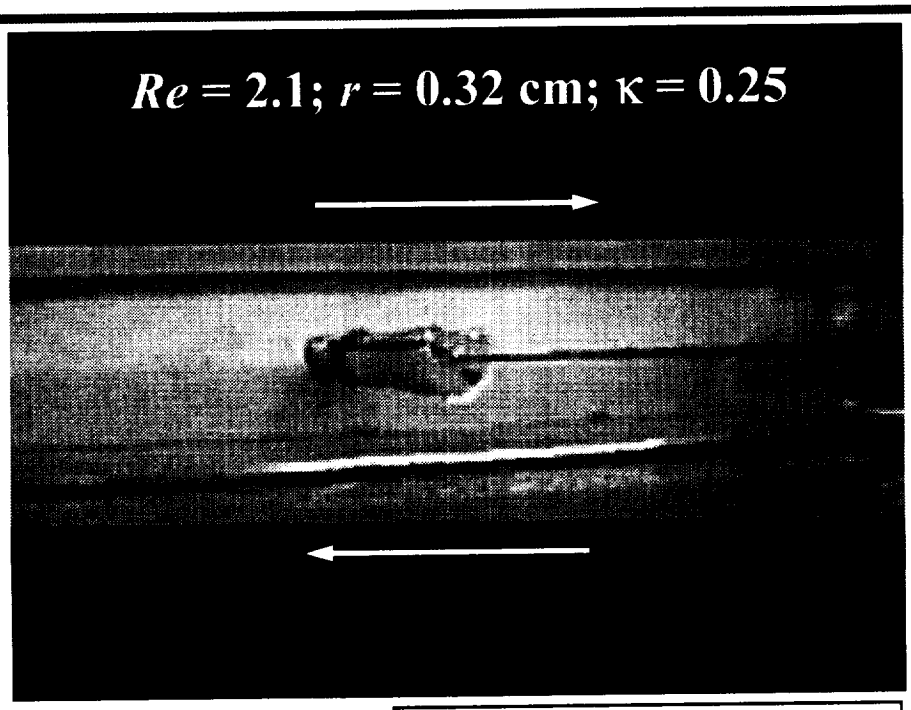

Click here to play movie

Particle Proximity Sensors

- Create fluorescent "wall layer" of $O(100\ \mu m)$
  - Apply $O(1\ V/cm,\ 10\ \mu A)$ voltage/current: wall = cathode
  - Cathode depletes protons, creating higher pH wall layer
  - Dye suspension with $O(1\ \mu M)$ fluorescein: bulk suspension pH = 4.5; fluorescein fluoresces at pH > 6
  - Illuminate at $\lambda = 514.5$ nm $\Rightarrow$ fluorescent wall layer
  - Layer thickness adjustable from $O(100–1000\ \mu m)$ by adjusting current
- Particles near wall scatter 520–600 nm fluorescence; those in bulk flow scatter 514.5 nm illumination
- Use wavelength filtration to distinguish between near-wall, bulk flow particles

Summary

- Developed and characterized new "low viscosity" aqueous suspension system
  - PMMA particles in water, glycerin and NH_4SCN
  - Optical properties comparable to previous model systems
- Built plane Couette channel for suspension studies
  - Testing cylinders with suspension liquid phase
- Particle proximity sensors
  - Created fluorescent wall layer $O(100\ \mu m)$ thick in new suspension system using applied potential difference
  - Use wavelength filtration to distinguish particles in wall layer from those in bulk flow

Future Work

- Plane Couette channel
  - Test with suspension
  - Noncircular cylinders, spheroids
- Particle proximity sensors
  - Light intensity across layer
  - Timescales of fluorescent layer formation, evolution
  - Calibrate technique in sedimentation flows
  - Cylinder in simply sheared suspension

Rotation Rates

- Initial single-phase data for circular cylinder
- Data low: friction in cylinder mounting

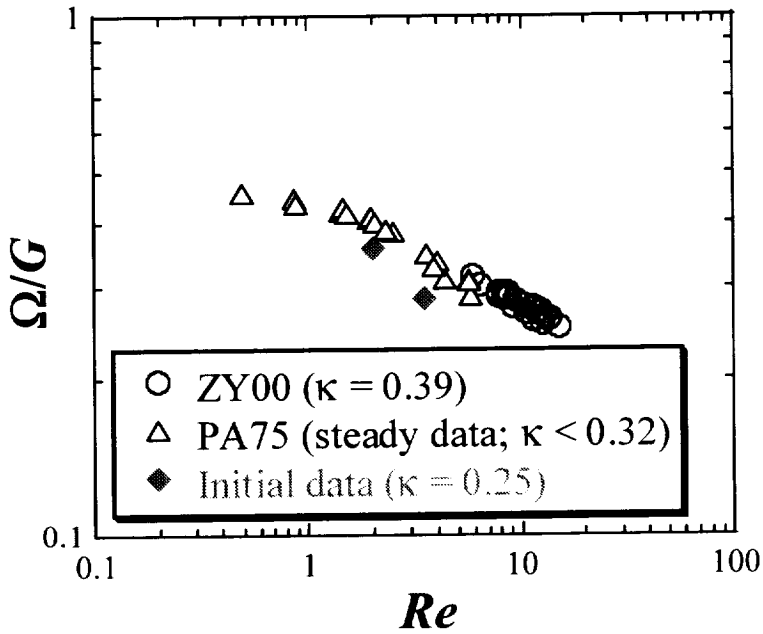

Effects of Gravity Modulation on the Convective Instabilities of a Horizontal Double-Diffusive Layer

Wen-Yau Chen, Cho Lik Chan, and C. F. Chen
University of Arizona
Aerospace and Mechanical Engineering Department
Tucson, AZ 85721

ABSTRACT

Linear stability analysis of a horizontal double-diffusive layer under gravity modulation is performed. The steady part of the gravity is in the vertical direction while the oscillating part of the gravity is arbitrary. In the absence of gravity modulation, two modes of instabilities are possible, they are steady finger and oscillatory diffusive modes. The gravity modulation excites synchronous and quasi-periodic modes in the case of steady finger convection. In the oscillatory diffusive case, synchronous, quasi-periodic and subharmonic modes are found.

We consider a horizontal fluid layer of thickness D stratified by a stable constant solute gradient characterized nondimensionally by the solute Rayleigh number $R_S = g_0\beta\Delta S D^3/\kappa\nu$ in which $\beta = \rho^{-1}\partial\rho/\partial S$, κ and ν are thermal diffusivity and kinematic viscosity of the fluid, ΔS is the difference in solute concentration across the layer maintained constant by the rigid diffusive upper and lower boundaries, and g_0 is the steady gravity field. The lower boundary is maintained at a temperature ΔT higher than that of the upper boundary. Instability occurs when the thermal Rayleigh number $R_T = g_0\alpha\Delta T D^3/\kappa\nu$ in which $\alpha = -\rho^{-1}\partial\rho/\partial T$ exceeds its critical value. Under steady gravity, the instability onsets in the oscillatory mode and the oscillation frequency, σ, depends on the wave number of the perturbation. Now, if the fluid layer is subjected to gravity modulation in the form $g = g_0\vec{k} + g_1\cos(\Omega t)\vec{e}$. Resonance may occur when Ω is some multiple of σ. Such resonance effects are the focus of our investigation. Also $\vec{k}$ is the unit vector in the vertical direction and $\vec{e}$ is the unit vector of the oscillating gravity direction.

We investigate the linear stability of such a system under gravity modulation based on the set of equations derived by Terrones and Chen (1993). The method of analysis according to Floquet theory is carried out with a double series expansion, Galerkin and Chebyshev, as used by Chen and Chen (1999) for convection in a vertical slot under gravity modulation. Numerical results are obtained for a liquid metal with Pr = 0.01, Le = 3333, $g_1/g_0 = 0.2$, and an initial $R_S = -3200$ [one of the examples given by Terrones and Chen (1993)]. Three modes, synchronous, quasi-periodic and subharmonic, were excited by gravity modulation. The subharmonic mode corresponds to the resonance and has the most destabilizing effect. The critical Rayleigh number versus modulation frequency for different directions of the oscillating part of the gravity is shown in Figure 1. The resonance effect is found to be increasing with angle (θ = 0 corresponds to horizontal and 90° means vertical). The maximum reduction in the critical thermal Rayleigh is 86%.

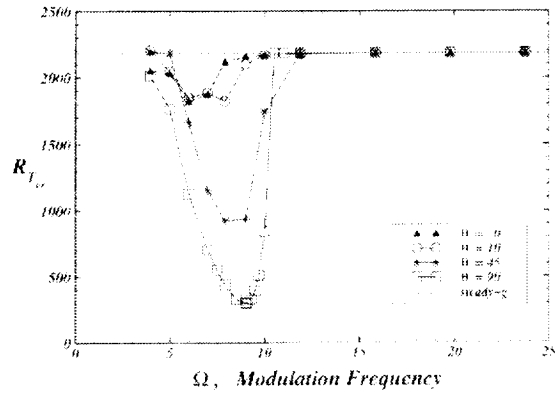

Figure 1. Resonance Curve vs Modulation Frequency

We also investigate the effect of gravity modulation on the steady finger instability case. Only synchronous and quasi-periodic modes exist. The results presented in Figure 2 corresponds to Pr = 7 Le = 100 $g_1/g_0 = 0.4$, and an initial $R_S = 100$. The gravity modulation has a small destabilizing effect on the onset of steady finger convection.

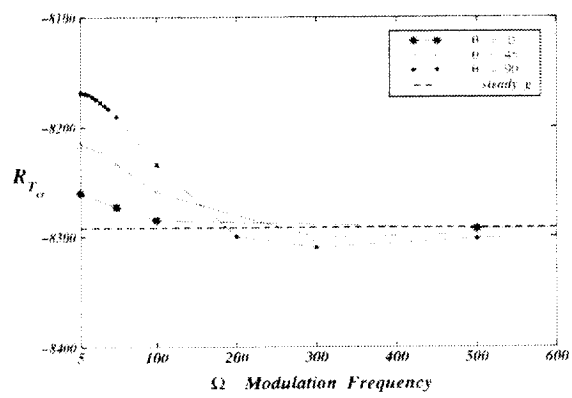

Figure 2. Critical Rayleigh Number versus Modulation Frequency

In this investigation, we found that resonance occurs only in the diffusive regime with modulation frequency being approximately twice the natural frequency. The destabilizing effect is most pronounced when the gravity modulation is in the same direction of the steady gravity vector. In the finger convection regime, gravity modulation causes slight destabilizing effect at low modulation frequencies.

References

Chen, W. Y. and Chen, F., 1999, "Effect of Gravity Modulation on the Stability of Convection in a Vertical Slot," *J. Fluid Mech.* **345**: 327-344.

Terrones, G. and Chen, C. F., 1993, "Convective Stability of Gravity-Modulated Doubly Cross-Diffusive Fluid Layers," *J. Fluid Mech.* **255**: 301-321.

NASA/CP—2002-211212/VOL1

Convective Instability of a Horizontal Double-Diffusive Layer Subjected to Steady Gravity and G-jitter in Arbitrary Directions

Wen-Yau Chen, Cho Lik Chan, and C. F. Chen

University of Arizona

Aerospace and Mechanical Engineering Department

Tucson, AZ 85721

Outline

- Linear theory
- Double diffusive layer
- Arbitrary angles
- Instability modes
- Preliminary results
- Conclusion

Linear theory

- Basic state
- Linearized perturbation equations
- Galerkin method to obtain the dynamical system
- Algebraic eigenvalue problem for steady g
- Floquet theory for time-periodic system
- Chebyshev expansion method to obtain the fundamental matrix for the determination of the Floquet exponents

Horizontal double diffusive layer steady vertical g_o

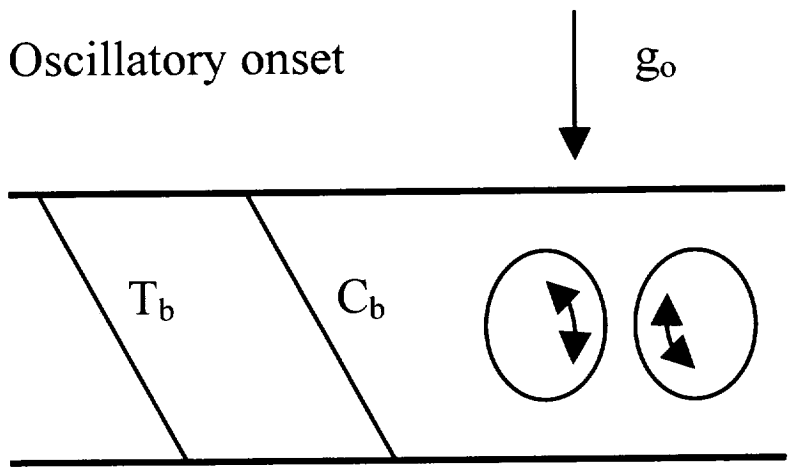

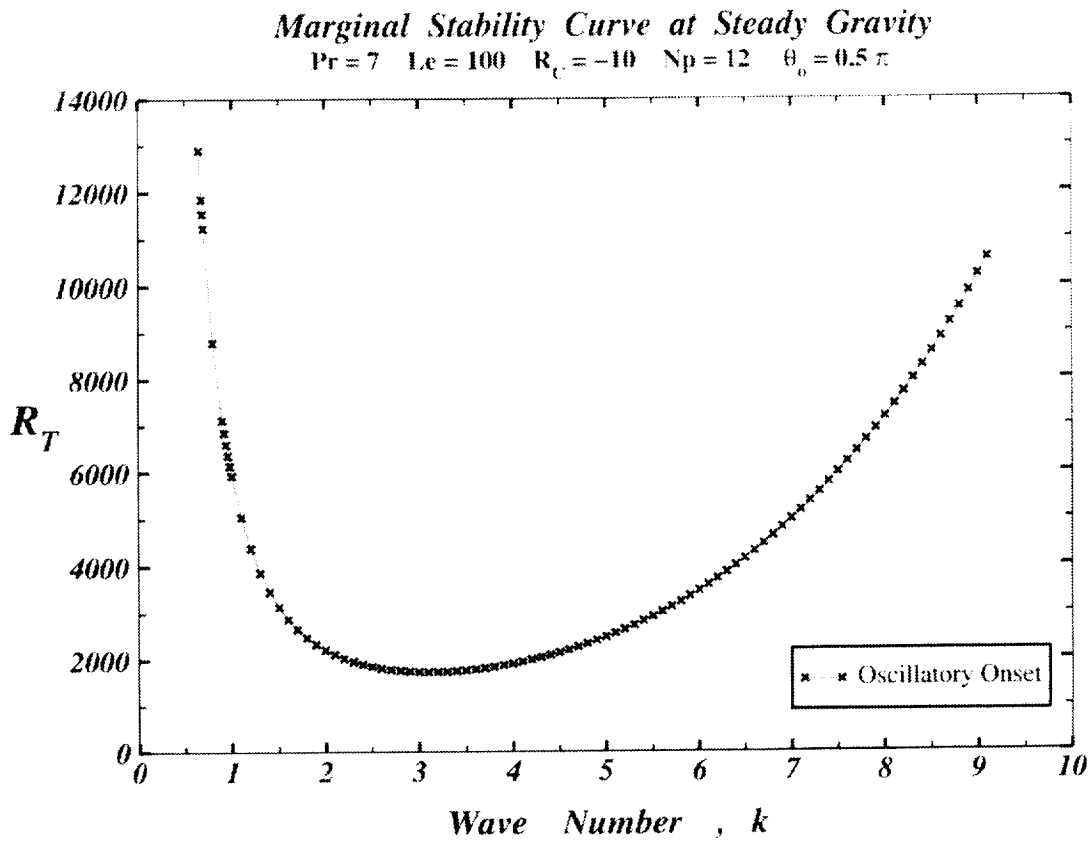
Marginal Stability Curve at Steady Gravity
Pr = 7 Le = 100 $R_C = -10$ Np = 12 $\theta_o = 0.5\pi$
R_T
14000
12000
10000
8000
6000
4000
2000
0
0
1
2
3
4
5
6
7
8
9
10
Wave Number , k
Oscillatory Onset

Horizontal double diffusive layer steady g_o inclined angle θ_o + modulation $g_1 \cos(\omega t)$ inclined angle θ_1

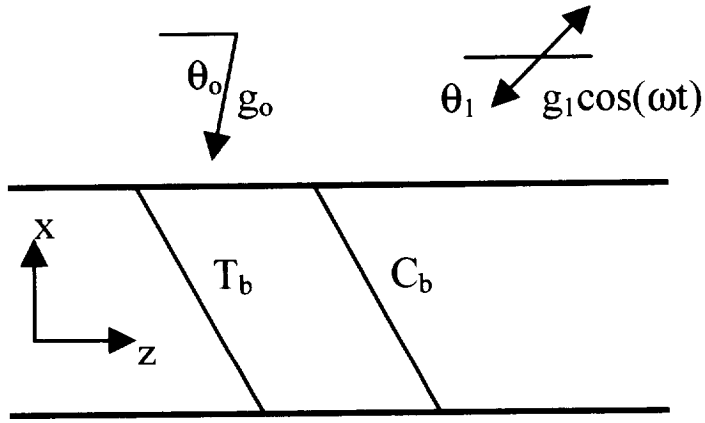

Combination of two problems

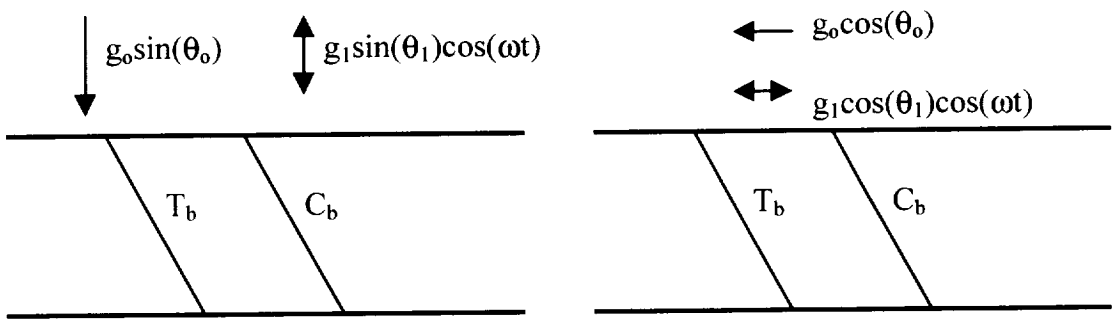

It is a vertical slot.

Rotate ccw 90°

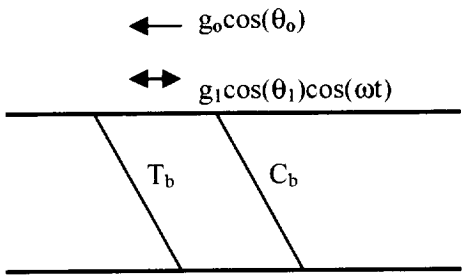

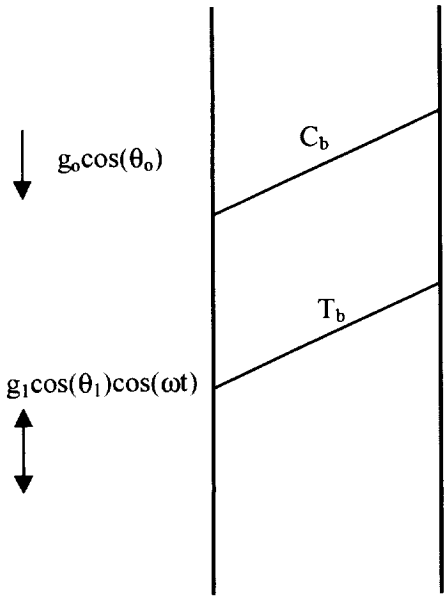

Basic state

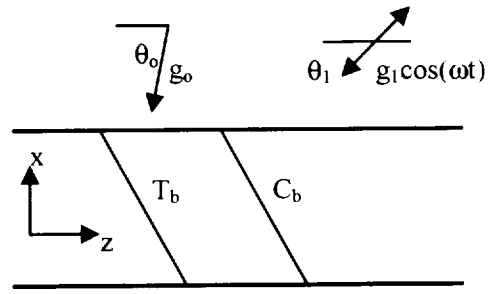

$$T_b = R_T\left(x+1/2\right),$$

$$C_b = R_C\left(x+1/2\right),$$

$$W_b = f\cos\left(\theta_o\right)\left[R_T + R_C\right]\left\{\frac{x^3}{6} - \frac{x}{24}\right\}$$

$$+ h\,\mathrm{Pr}^{3/2}\cos\left(\theta_1\right)\left[R_T + R_C\right]\cdot\left\{F_1\left(x\right)\cos\left(\Omega t\right) + F_2\left(x\right)\sin\left(\Omega t\right)\right\}$$

$$F_1\left(x\right) = a_1\sinh\left(\sqrt{\frac{\Omega}{2\,\mathrm{Pr}}}x\right)\cos\left(\sqrt{\frac{\Omega}{2\,\mathrm{Pr}}}x\right) + a_2\cosh\left(\sqrt{\frac{\Omega}{2\,\mathrm{Pr}}}x\right)\sin\left(\sqrt{\frac{\Omega}{2\,\mathrm{Pr}}}x\right)$$

$$F_2\left(x\right) = -bx + \left\{a_1\sinh\left(\sqrt{\frac{\Omega}{2\,\mathrm{Pr}}}x\right)\cos\left(\sqrt{\frac{\Omega}{2\,\mathrm{Pr}}}x\right) + a_2\cosh\left(\sqrt{\frac{\Omega}{2\,\mathrm{Pr}}}x\right)\sin\left(\sqrt{\frac{\Omega}{2\,\mathrm{Pr}}}x\right)\right\}$$

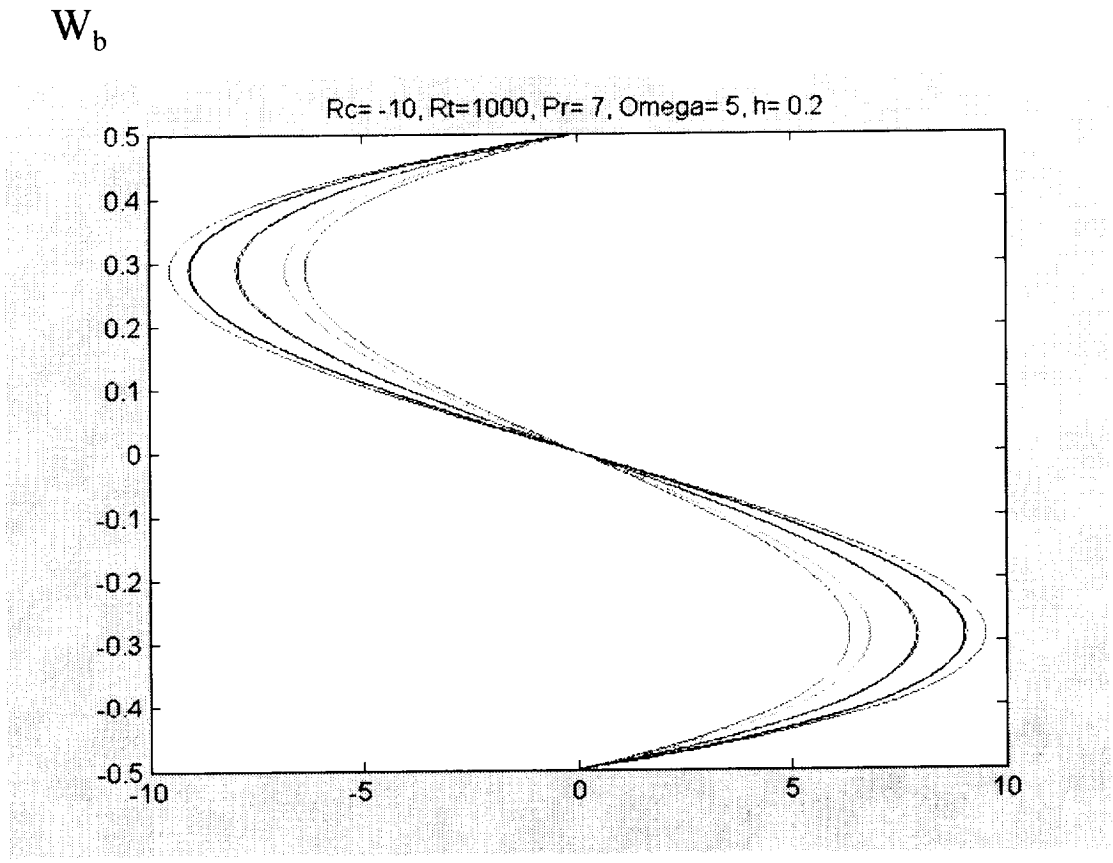
W_b
Rc= -10, Rt=1000, Pr= 7, Omega= 5, h= 0.2
0.5
0.4
0.3
0.2
0.1
0
-0.1
-0.2
-0.3
-0.4
-0.5
-10
-5
0
5
10

Vertical slot, single component

Thermal

- Ra_T, Pr
- Pr < 12.5 steady
- Pr > 12.5 oscillatory

Solutal

- Ra_C, Sc
- Sc < 12.5 steady
- Sc > 12.5 oscillatory

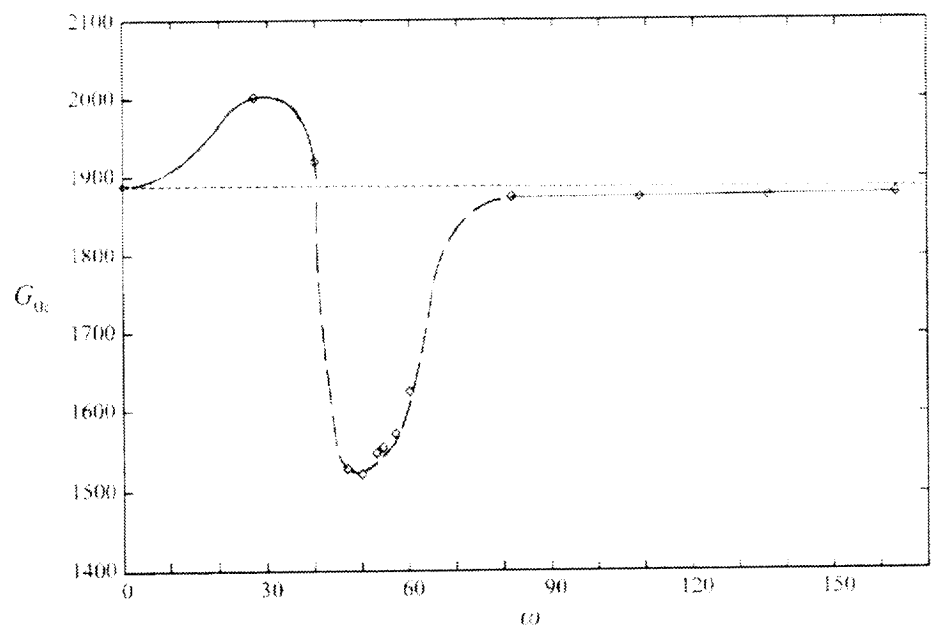

FIGURE 9. The critical Grashof number, G_{0c}, over a range of modulation frequencies, ω, for $Pr = 25$ at $g_1/g_0 = 0.5$. Note the resonant interaction in the frequency range $45 < \omega < 60$. ———, Quasi-periodic mode; - - - - -, subharmonic mode.

Chen and Chen, JFM 1999, v. 395, p. 327

Horizontal double diffusive layer steady vertical g_o+ vertical modulation $g_1 \cos(\omega t)$

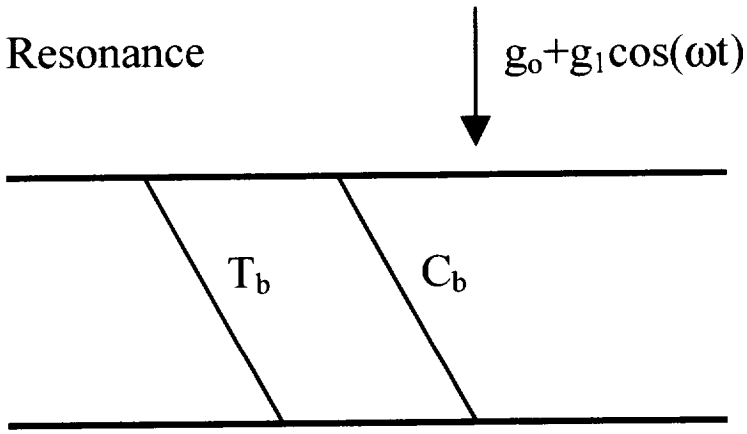

Wen-Yau Chen's thesis, December 2001, University of Arizona

R_{Tcr} vs Modulation Frequency

Pr = 0.01; Le= 3333; R_c= -3200

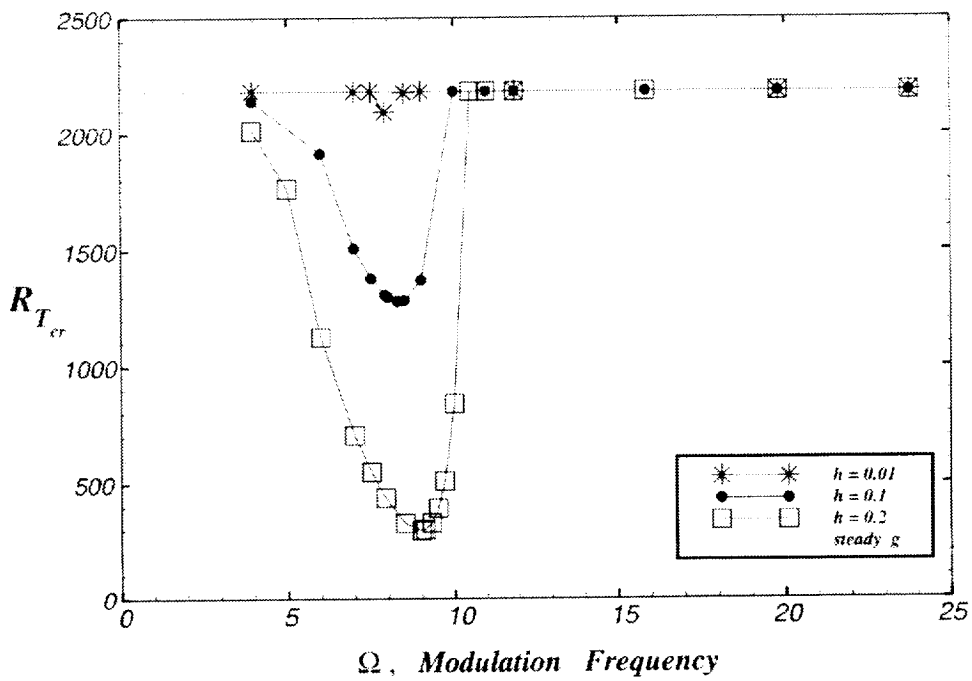

Wen-Yau Chen's thesis, December 2001, University of Arizona

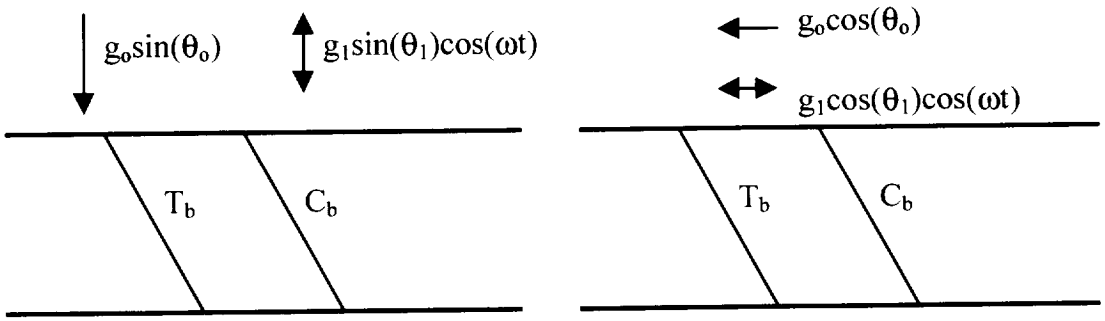

Bernard

Double diffusive

Resonance

Single component

Steady and unsteady

Resonance

Double diffusive

Horizontal double diffusive layer steady g_o inclined at an angle

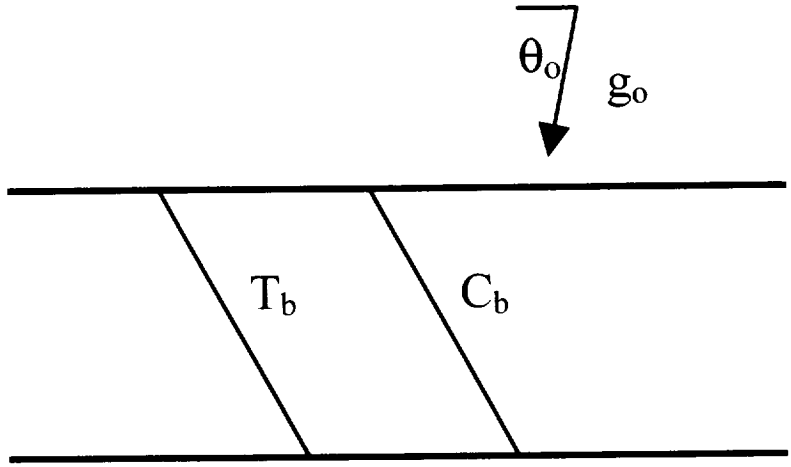

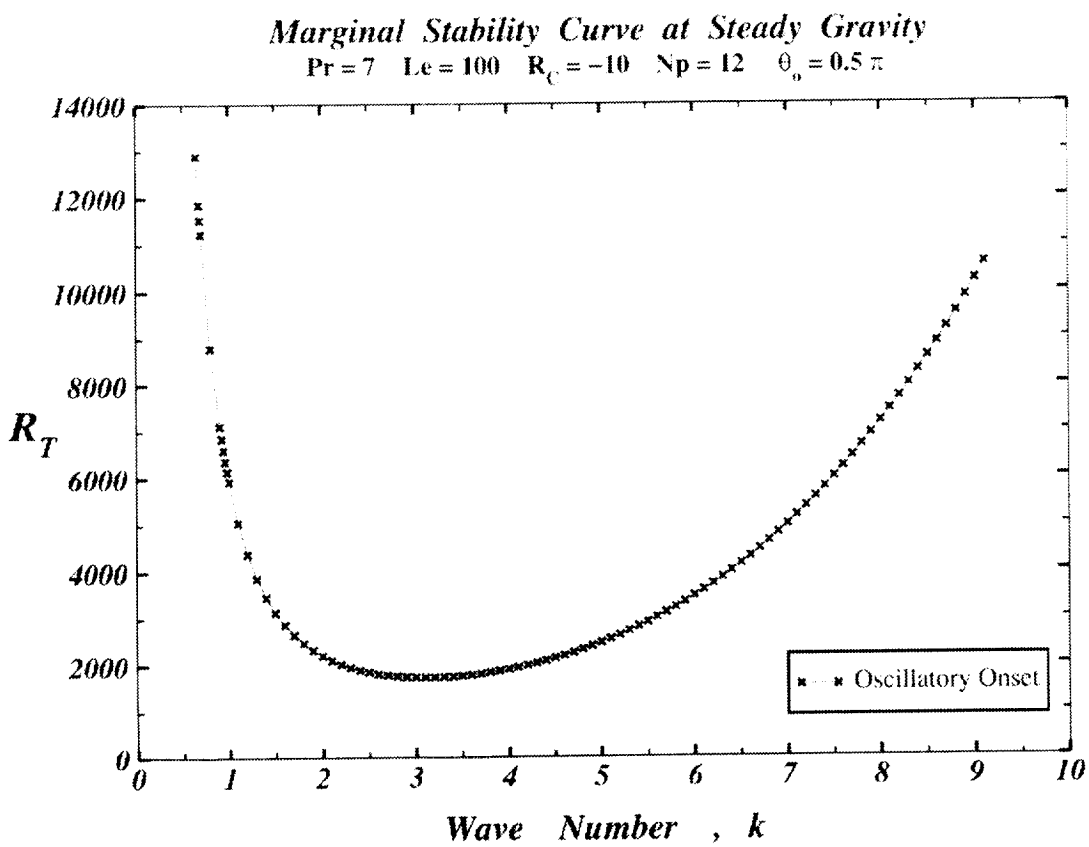
Marginal Stability Curve at Steady Gravity
Pr = 7 Le = 100 R_C = −10 Np = 12 θ_o = 0.5 π
14000
12000
10000
8000
6000
4000
2000
0
R_T
0
1
2
3
4
5
6
7
8
9
10
Wave Number , k
Oscillatory Onset

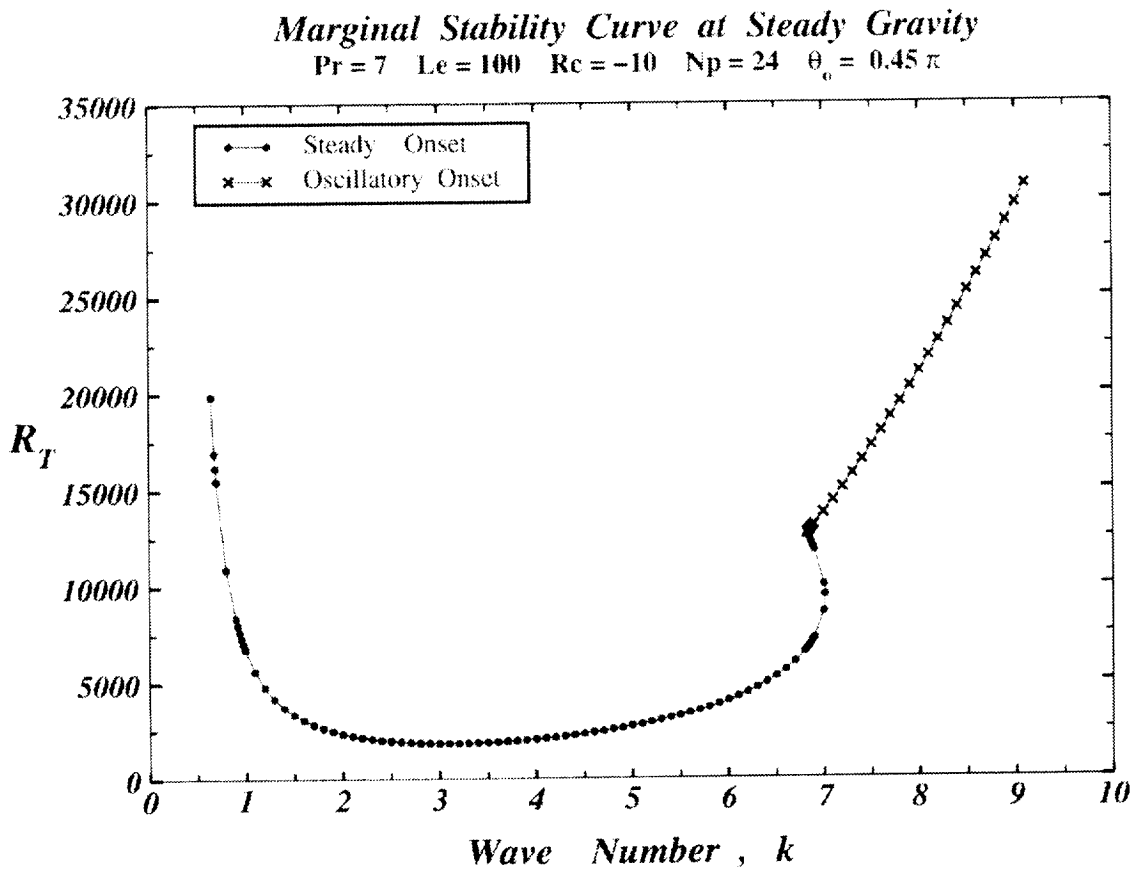
Marginal Stability Curve at Steady Gravity
Pr = 7 Le = 100 Rc = −10 Np = 24 θ_o = 0.45 π
Steady Onset
Oscillatory Onset
R_T
35000
30000
25000
20000
15000
10000
5000
0
0
1
2
3
4
5
6
7
8
9
10
Wave Number , k

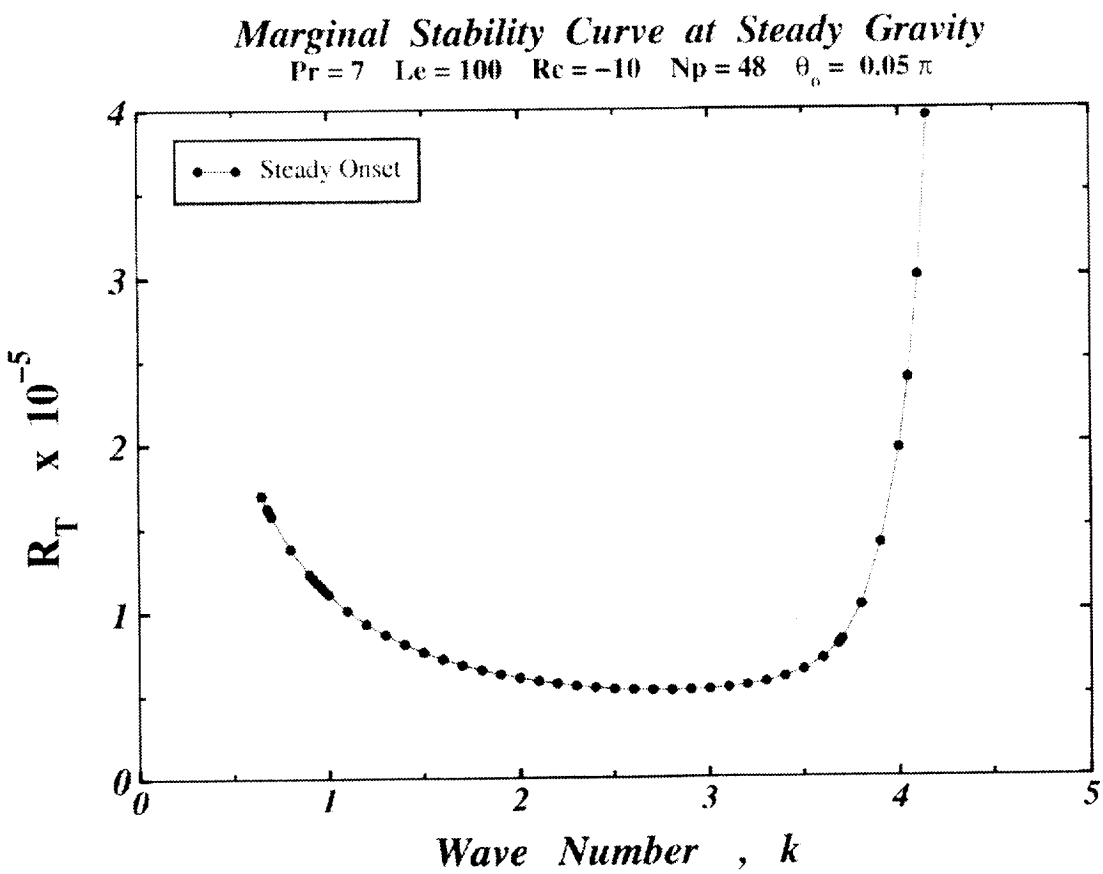
Marginal Stability Curve at Steady Gravity
Pr = 7 Le = 100 Rc = −10 Np = 48 θ0 = 0.05 π
Steady Onset
R_T x 10^-5
Wave Number , k
0
1
2
3
4
5

Conclusion

- Horizontal double diffusive layer
- Steady g_o arbitrary direction
- Modulation $g_1\cos(\omega t)$ in arbitrary direction
- Horizontal gravity component - vertical slot
- Many instability modes and their interaction

Future work

- Linear theory - different modes interaction
- Experimental investigation - vertical g steady and modulation
- Numerical simulation - 2-d double diffusive convection

Author Index

Acrivos, A. 346
Ainslie, K. 658
Aksay, I.A. 192
Andresen, U.C. 964
Ansari, R.R. 800

Bailey, A. 91
Bailey, B.C. 964
Banavar, J.R. 211
Bayer, I.S. 272
Behringer, R.P. 453
Berejnov, V. 745
Beysens, D. 855
Bilek, A.M. 714
Bloustine, J. 745
Bowen, J. 91
Brady, J.F. 386

Cannell, D.S. 325
Carpen, I.C. 386
Carpenter, B. 12
Chaikin, P.M. 133
Chan, C.L. 982
Chen, C.F. 982
Chen, W.-Y. 982
Chen, X. 242
Cheng, Z.-D. 133
Chiaramonte, F. 12
Christianson, R. 91
Cieplak, M. 211
Cipelletti, L. 91
Civelek, M. 658
Colwell, J.E. 395
Crocker, J.C. 637

Davis, S. 223
Dee, K.C. 714
Dhir, V.K. 529
Doherty, M. 91
Duval, W. 832

Eaton, J.K. 515
Eggers, J. 91

Finn, J.E. 620
Fraden, S. 745

Garanich, J. 658
Garoff, S. 242
Garrabos, Y. 855
Gasser, U. 91
Gast, A.P. 161
Gaver, D.P. 714
Goree, J. 163
Gropper, M. 161
Grotberg, J.B. 680

Halpern, D. 680
Hammer, D.A. 637
Harris, N.R. 658
Hart, J. 896
Hasan, M.M. 553
Hegseth, J. 855
Henry, C. 579
Hiddessen, A.L. 637
Homsy, G.M. 240
Horányi, M. 395
Hu, H. 769
Hwang, W. 515

Jacobs, J.W. 919
Jankovsky, A. 91
Jenkins, J.T. 370, 435

Khusid, B. 346
Kim, J. 579
Kim, M. 658
Koch, D.L. 477
Kondic, L. 453
Koplik, J. 211
Kurta, C. 91

Ladd, A.J.C. 417
Larson, R. 769
Lecoutre, C. 855
LeVan, M.D. 620
Li, L. 769
Lorik, T. 91
Louge, M.Y. 435

Manley, S. 91
Markarian, N. 346
Marston, P.L. 253
Megaridis, C.M. 272
Merkel, R. 161
Meyer, W.V. 133
Mudawar, I. 553

Narayanan, R. 938
Nayagam, V. 272
Neitzel, G.P. 293
Niederhaus, C.E. 919

Nikolaenko, G. 325
Nikolayev, V.S. 855

Ohlsen, D. 896
Oprisan, A. 855

Panzarella, C. 832
Phan, S.-E. 133
Plawsky, J.L. 606
Poulikakos, D. 272
Prasad, V. 91
Prisk, G.K. 24
Pusey, P. 91
Putterman, S. 832

Qiu, Z. 346

Ramé, E. 242
Ratanabanangkoon, P. 161
Reeves, A. 435
Ristenpart, W.D. 192
Robertson, S. 395
Roy, A. 855
Russel, W.B. 133

Sangani, A. 477
Saville, D.A. 192
Schoefield, A. 91
Segre, P. 91
Shiley, W. 91
Sickafoose, A.A. 395
Sridhar, K.R. 620

Tagg, R.P. 896
Tarbell, J.M. 658
Thiessen, D.B. 253
Thomas, A.M. 938
Tohver, V. 637
Trinh, E. 1
Tsang, Y.H. 477

Uter, B. 453

Volkov, I. 211

Walton, K.S. 620
Wang, Y.-X. 606
Ward, T. 240
Warrier, G.R. 529
Wayner, Jr., P.C. 606
Wei, W. 253
Weidman, P.D. 896
Weitz, D.A. 91, 417, 637
Wright, W. 832

Xu, H. 435

Yoda, M. 964
Yodh, A.G. 194

Zhang, H. 553
Zheng, L. 606
Zhu, J. 133

REPORT DOCUMENTATION PAGE

Form Approved
OMB No. 0704-0188

Public reporting burden for this collection of information is estimated to average 1 hour per response, including the time for reviewing instructions, searching existing data sources, gathering and maintaining the data needed, and completing and reviewing the collection of information. Send comments regarding this burden estimate or any other aspect of this collection of information, including suggestions for reducing this burden, to Washington Headquarters Services, Directorate for Information Operations and Reports, 1215 Jefferson Davis Highway, Suite 1204, Arlington, VA 22202-4302, and to the Office of Management and Budget, Paperwork Reduction Project (0704-0188), Washington, DC 20503.

1. AGENCY USE ONLY (*Leave blank*)

2. REPORT DATE
November 2002

3. REPORT TYPE AND DATES COVERED
Conference Publication

4. TITLE AND SUBTITLE
Sixth Microgravity Fluid Physics and Transport Phenomena Conference
Plenary and Sessions 1–6

5. FUNDING NUMBERS
WU–101–43–0B–00

6. AUTHOR(S)
Bhim Singh, compiler

7. PERFORMING ORGANIZATION NAME(S) AND ADDRESS(ES)
National Aeronautics and Space Administration
John H. Glenn Research Center at Lewis Field
Cleveland, Ohio 44135–3191

8. PERFORMING ORGANIZATION REPORT NUMBER
E–13064

9. SPONSORING/MONITORING AGENCY NAME(S) AND ADDRESS(ES)
National Aeronautics and Space Administration
Washington, DC 20546–0001

10. SPONSORING/MONITORING AGENCY REPORT NUMBER
NASA CP—2002-211212-VOL1

11. SUPPLEMENTARY NOTES
Plenary and Sessions 1–6 presentations of a conference cosponsored by the NASA Office of Life and Microgravity Sciences and Applications and the Fluid Physics and Transport Phenomena Discipline Working Group and hosted by NASA Glenn Research Center and the National Center for Microgravity Research on Fluids and Combustion, Cleveland, Ohio, August 14–16, 2002. Responsible person, Bhim Singh, organization code 6712, 216–433–5396.

12a. DISTRIBUTION/AVAILABILITY STATEMENT
Unclassified - Unlimited
Subject Category: 34 Distribution: Nonstandard
Available electronically at http://gltrs.grc.nasa.gov
This publication is available from the NASA Center for AeroSpace Information, 301–621–0390.

12b. DISTRIBUTION CODE

13. ABSTRACT ***(Maximum 200 words)***

The Sixth Microgravity Fluid Physics and Transport Phenomena Conference provides the scientific community the opportunity to view the current scope of the Microgravity Fluid Physics and Transport Phenomena Program, current research opportunities, and plans for the near future. The conference focuses not only on fundamental research but also on applications of this knowledge towards enabling future space exploration missions. A whole session dedicated to biological fluid physics shows increased emphasis that the program has placed on interdisciplinary research. The conference includes invited plenary talks, technical paper presentations, poster presentations, and exhibits. This CP is a compilation of the abstracts, presentations, and posters presented at the conference.

14. SUBJECT TERMS
Fluid dynamics; Fluid physics; Fluid mechanics; Microgravity; Reduced-gravity; Heat transfer; Multiphase flow; Complex fluids

15. NUMBER OF PAGES
1019

16. PRICE CODE

17. SECURITY CLASSIFICATION OF REPORT
Unclassified

18. SECURITY CLASSIFICATION OF THIS PAGE
Unclassified

19. SECURITY CLASSIFICATION OF ABSTRACT
Unclassified

20. LIMITATION OF ABSTRACT